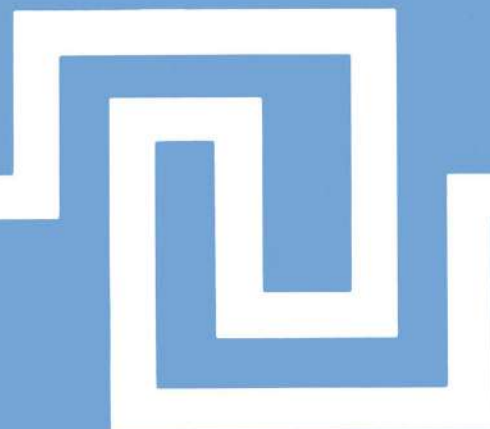


# Quantum Electrodynamics of Strong Fields Volume 1

Edited by  
W. Greiner



NATO ADVANCED STUDY INSTITUTES SERIES

**Series B: Physics**

# Quantum Electrodynamics of Strong Fields

## NATO ADVANCED STUDY INSTITUTES SERIES

A series of edited volumes comprising multifaceted studies of contemporary scientific issues by some of the best scientific minds in the world, assembled in cooperation with NATO Scientific Affairs Division.

### **Series B: Physics**

#### *Recent Volumes in this Series*

*Volume 78*—Excitations in Disordered Systems  
edited by M. F. Thorpe

*Volume 79*—Artificial Particle Beams in Space Plasma Studies  
edited by Bjørn Grandal

*Volume 80*—Quantum Electrodynamics of Strong Fields  
edited by W. Greiner

*Volume 81*—Electron Correlations in Solids, Molecules, and Atoms  
edited by Jozef T. Devreese and Fons Brosens

*Volume 82*—Structural Elements in Particle Physics and Statistical  
Mechanics  
edited by J. Honerkamp, K. Pohlmeyer, and H. Römer

*Volume 83*—Physics of Ion-Ion and Electron-Ion Collisions  
edited by F. Brouillard

*Volume 84*—Physical Processes in Laser-Materials Interactions  
edited by M. Bertolotti

*Volume 85*—Fundamental Interactions: *Cargèse 1981*  
edited by Maurice Lévy, Jean-Louis Basdevant, David Speiser,  
Jacques Weyers, Maurice Jacob, and Raymond Gastmans

*Volume 86*—Surface Mobilities on Solid Materials: Fundamental Concepts and  
Applications  
edited by Vu Thien Binh



This series is published by an international board of publishers in conjunction with NATO Scientific Affairs Division

**A** Life Sciences

Plenum Publishing Corporation

**B** Physics

London and New York

**C** Mathematical and  
Physical Sciences

D. Reidel Publishing Company  
Dordrecht, The Netherlands  
and Hingham, Massachusetts, USA

**D** Behavioral and  
Social Sciences

Martinus Nijhoff Publishers  
The Hague, The Netherlands

**E** Applied Sciences

# Quantum Electrodynamics of Strong Fields

Edited by

**W. Greiner**

*Johann Wolfgang Goethe University  
Frankfurt am Main, Federal Republic of Germany*

SPRINGER SCIENCE+BUSINESS MEDIA, LLC

---

Library of Congress Cataloging in Publication Data

NATO Advanced Study Institute on Quantum Electrodynamics of Strong Fields (1981:

Lahnstein, Germany)

Quantum electrodynamics of strong fields.

(NATO advanced study institutes series. Series B, Physics; v. 80)

"Proceedings of a NATO Advanced Study Institute of Quantum Electrodynamics of Strong Fields, held June 15-26, 1981, in Lahnstein, Federal Republic of Germany"—Verso t.p.

Bibliography: p.

Includes index.

1. Quantum electrodynamics—Congresses. 2. Heavy ion collisions—Congresses. 3. Quantum field theory—Congresses. I. Greiner, Walter, 1935-. II. North Atlantic Treaty Organization. III. Title IV Series.

QC679.N37 1981 537.6 82-5301

ISBN 978-1-4899-2141-3 ISBN 978-1-4899-2139-0 (eBook) AACR2

DOI 10.1007/978-1-4899-2139-0

---



Proceedings of a NATO Advanced Study Institute on Quantum Electrodynamics of Strong Fields, held June 15-26, 1981, in Lahnstein, Federal Republic of Germany

© Springer Science+Business Media New York 1983

Originally published by Plenum Press, New York in 1983

Softcover reprint of the hardcover 1st edition 1983

All rights reserved

No part of this book may be reproduced, stored in a retrieval system, or transmitted in any form or by any means, electronic, mechanical, photocopying, microfilming, recording, or otherwise, without written permission from the Publisher

## PREFACE

The NATO Advanced Study Institute on *Quantum Electrodynamics of Strong Fields* was held at Lahnstein on the Rhine from 15-26 June, 1981.

The school was devoted to the advances, theoretical and experimental, in the physics of strong fields made during the past decade. The topic of the first week was almost exclusively quantum electrodynamics, with discussions of symmetry breaking in the ground state, of the physics of heavy ion collisions and of precision tests of perturbative quantum electrodynamics. This was followed in the second week by the presentation of a broad range of other areas where strong fields occur, reaching from nuclear physics over quantum chromodynamics to gravitation theory and astrophysics.

We were fortunate to be able to call on a body of lecturers who not only have made considerable personal contributions to these advances but who are also noted for their lecturing skills. Their dedication for their subject was readily transmitted to the students resulting in a very successful school. This enthusiasm is also reflected in their contributions to these Proceedings which, as I believe, will in time become a standard source of reference for future work on the physics of strong fields and will help to spread the benefits of the school to a larger audience than those who were able to attend. I regret that the Soviet colleagues Ya. B. Zeldovich and V.S. Popov were unable to participate. They have made such important contributions to the field, that their presence would have certainly further contributed to the atmosphere of the meeting.

A special highlight was the historical lecture on "Early germs in quantum field theory in the history of quantum physics" by Friedrich Hund. He was personally involved in several aspects of the early development of molecular physics and also of quantum-electrodynamics (Klein's Paradox). In his lecture he exhibited the roots of the modern developments of QED of Strong Fields.

The School was sponsored by and had the support of the NATO Research Council, the Bundesministerium für Forschung und Technologie, and the Gesellschaft für Schwerionenforschung (GSI).

The meeting took place at the Dorint Hotel "Rhein-Lahn" just outside Lahnstein/Rhein which contributed with its facilities to the success of the school.

Finally, I wish to acknowledge the contributions made by all those who took part in organizing and running the school. Above all, my thanks go to my secretaries Mrs. Ruth Lasarzig and Ellen Pfister, who handled the correspondence before, during and after the school, managed the budget and helped to make these Proceedings possible. I am grateful to the Organizing Committee for their help in preparing the school, in particular I wish to thank my colleague Reiner Dreizler and many other members of the Institute of Theoretical Physics, Johann Wolfgang Goethe-University at Frankfurt/Main.

Walter Greiner

## CONTENTS

Opening Remarks . . . . .	1
W. Greiner	
The States of Quantum Electrodynamical Precision	
-- Theoretical Points of View . . . . .	25
G.W. Erickson	
Quantum Electrodynamics of Strong Fields . . . . .	41
B. Müller	
Atomic Collisions with Sticky Nuclei . . . . .	77
W.E. Meyerhof	
Positrons from Heavy Ion Collisions-Experiments at the UNILAC . . . . .	107
H. Backe et al.	
Heavy Ion Collision Induced Characteristic X-Ray Production - Cross Section Experiments . . . . .	135
P. Armbruster	
Experiments on the Excitation of the Innermost Electrons in Extremely Strong Fields . . . . .	155
F. Bosch	
Systematics and Discussion of Ionization Probability Measurements . . . . .	179
P. Armbruster	
Theory of Positron Creation in Supercritical Quasimolecules . . . . .	195
J. Reinhardt et al.	
Spectroscopy of Superheavy Quasimolecules . . . . .	233
G. Soff et al.	

Search for Spontaneous Positron Production in Heavy Ion Collisions . . . . .	273
H. Bokemeyer et al.	
Pair Creation in Heavy Ion-Atom Collisions . . . . .	293
P. Kienle	
δ-Ray Spectroscopy of Quasi-Atoms . . . . .	317
C. Kozhuharov	
2p <sub>0</sub> Molecular Orbital Radiation of Colliding Atoms: Dynamical Model Predictions Versus Experimental Data . . . . .	335
K.-H. Heinig, H.-U. Jäger, K.-H. Kaun, H. Richter, H. Woittennek	
Continuum X-Ray Emission in Adiabatic Heavy Ion-Atom Collisions . . . . .	359
P. Vincent	
Density Functional Approach to the Relativistic Many Body Problem . . . . .	383
R.M. Dreizler and E.K.U. Gross	
Experimental Tests of QED and Electroweak Theories in e <sup>+</sup> e <sup>-</sup> Annihilation at PETRA . . . . .	413
A. Böhm	
The Muon (g-2) Experiments at CERN . . . . .	441
E. Picasso	
Electron-Electron Correlation in Highly Charged Atoms . . . . .	463
W.R. Johnson and K. T. Cheng	
Variational Method for the Time-Dependent Dirac Equation . . . . .	489
J. Krause and M. Kleber	
Radiative Corrections in Strong Fields . . . . .	503
P.J. Mohr	
The Description of Excitation Processes in Ion-Atom Collisions . . . . .	521
J.S. Briggs	
Particle Condensates in Strongly Coupled Quantum Field Theory . . . . .	539
J. Rafelski	

Non-Perturbative Approach to the Long Distance Behavior of Yang-Mills Theory and the Problem of Quark Confinement in QCD . . . . .	583
M. Baker	
Pion Condensation . . . . .	635
J.M. Irvine	
Classical Solutions of Yang-Mills-Theory . . . . .	651
H. Mitter	
Particles in Strong Periodic Fields . . . . .	659
H. Mitter	
Precision Laser Spectroscopy of Hydrogen . . . . .	669
T.W. Hänsch	
Non-Linear Vacuum Polarization in Strong Fields . . . . .	685
M. Gyulassy	
Does Pion Condensation Prevent Pion Condensation? . . . . .	701
A. Faessler	
Short-Range Nucleon-Nucleon Interaction and QCD Potential Models . . . . .	737
C.S. Warke	
Quark Interchange in Bag-Model QCD . . . . .	745
H.J. Weber	
Nonperturbative Treatment of Magnetic Interactions at Short Distances and a Simple Magnetic Model of Matter . . . . .	755
A.O. Barut	
Strong Magnetic Fields . . . . .	783
N.D. Hari Dass	
Particle Production by the Gravitational Field . . . . .	789
P. Candelas	
Confining the Aether . . . . .	817
P. Candelas	
Early Germs of Quantum Field Theory in the History of Quantum Physics . . . . .	829
F. Hund	

Summary Talk: Theoretical . . . . .	837
L.C. Biedenharn	
Summary: Experimental Aspects . . . . .	853
J.S. Greenberg	
Contributors . . . . .	893
Index . . . . .	897

## OPENING REMARKS

Walter Greiner

Institut für Theoretische Physik  
der Johann Wolfgang Goethe-Universität  
Frankfurt am Main, Germany

I would like to welcome you at Lahnstein to our Nato Advanced Study Institute on *Quantum Electrodynamics of Strong Fields*. You came from many different parts of the world to attend this school, which deals with a novel field of physics with exciting new aspects and new insights. Thank you that you came!

Before I try to describe our motivation for the physics we shall be discussing during the next two weeks, let me thank a few institutions and persons, who have made this meeting possible. Above all my thanks go to the NATO Scientific Program, which sponsored this school. It was my friend Professor Arthur Scharmann from the University of Gießen, who, as a member of the Nato Scientific Council, directed my attention to this possibility and who helped very actively that it came about. I would like to express my gratitude to him. Second, I would like to thank Dr. D Hartwig and through him the Bundesministerium für Forschung und Technologie, who gave additional support to our school. And finally I thank Herrn H.O. Schuff, administrative general director of GSI and my colleague Professor P. Armbruster from GSI, who also made available some funds in support of this meeting.

As you may have noticed, I used four different phrases to describe our gathering here; namely Advanced Study Institute, School, Meeting, Conference. This is my intention. I want us to have something of everything: We should have a school, in which advanced new research is presented in the most pedagogical way so that our numerous young students and researchers can follow easily and get a smooth introduction into the new field. The lecturers should keep this in mind! I want also that the usual atmosphere of a scientific meeting or conference prevails here, since there are so many new, recent

developments in our field that they should be brought up, carefully discussed with opposing views being friendly confronted. I use the word friendly, because there is no need for disharmony. The various aspects of QED of strong fields seem to be so far-reaching and rich in content that there is enough for everybody in this area of research. Moreover, it is only harmony which can create new ideas for new adventures. This is certainly true for me, but I think that it is also true for most of you; if not for all of us.

I have been thinking for some time to find a proper title for our meeting. There were two favorites of mine: Should we call it "Physics of Strong Fields" or "QED of Strong Fields"? After conferring with my friends, Professor R. Dreizler, Professor B. Müller and Professor J. Rafelski, I decided to call it *QED of Strong Fields*. The reason was that it is the QED of strong fields-aspect, where the greatest and perhaps most exciting advances are made in the sense of true physics, with both theory and experiments closely interplaying, stimulating and checking each other. However, we did not leave out other aspects of strong fields. This is why our meeting addresses itself to the strong and overcritical field phenomena, nearly exclusively originating in heavy ion physics, during the first week, and then leading gently over to strong field aspects in other areas: Strong Laser Fields, Strong Nuclear Fields (pion condensation), Strong Colour Fields (Quarks and QCD) and Strong Gravitational Fields. Some of these strong field phenomena are related to each other. I hope that at the end of our two weeks we will see this more clearly. There will also be nuclear structure, atomic physics general, plasma physics, QED proper, (i.e. precision measurements,  $e^+e^-$  collisions), and cosmology entering our discussions. We should not hesitate to bring in these aspects where this is necessary for our understanding and for academic round-off. The breadth of our field indicates the richness and also the dangers: The richness, because it is so fascinating to see the connections and consequences of certain phenomena in nearly all physical areas; the danger, because we must be careful not to touch the problems only on the surface, but also go into depths, as it is expected from a scientist. In fact, I would say, this is the moral obligation of a scientist; to be not just colloquial and eloquent, but to strive for the roots and understanding of the problems.

The concept of the vacuum, its physical properties and their experimental verification will be of central interest in our meeting. It is therefore appropriate to recall the historical and philosophical roots of this concept.

#### HISTORICAL DEVELOPMENT OF VACUUM CONCEPTS

Since the days of the early Greek natural philosophers our view of the physical world has been dominated certain paradigms, i.e. specific pictures ("modellhafte Vorstellungen"), for selected

physical entities. Such entities are space, time and matter as the basis of natural philosophy or, more specifically, of physics. Therefore, it is no surprise that our conception of the "vacuum", intimately connected with the picture of space, time and matter, ranges among the most fundamental issues in the scientific interpretation of the world.

The picture of the vacuum has undergone perpetual modifications during the last twenty-five centuries as the available technologies have changed; often old, abandoned ideas have been resurrected when new information became accessible. Many aspects of today's conception of the vacuum date back to the ancient greek philosophy, but have only recently been established by modern experiments.

Two concepts have alternatively formed the ancient greek's point of view concerning the "vacuum": 1) "vacuum" is the void, separating material objects and allowing for their relative motion; and 2) "empty space" is not possible, i.e. the vacuum was conceived as a medium. In the Pythagorean point of view, "air" was identified with the void as a seat of pure numbers.

In the atomism of *Democritos*, (~400 BC) the vacuum manifests itself as "intervals that separate atom from atom and body from body, assuring their discreteness and possibility of motion". *Lucretius* (~60 BC) writes in 'De rerum natura', "all nature then, as it exists, by itself is founded on two things: there are bodies and there is void in which these bodies are placed and through which they move about". For *Plato* (~380 BC) a physical body was merely a part of space limited by geometrical surfaces containing nothing but empty space. For *Plato* physics was merely geometry, a point of view which finally led to *Einstein*'s geometric vision of the world and *J. Wheeler*'s geometrodynamics.

Opposed to that attitude we find the opinion of *Parmenides* (~480 BC), and *Melissos* (~350BC) "according to whom the universe was a compact plenum, one continuous unchanging whole". Also *Aristotle* (~350 BC) rejected the Platonic, Democritian and Pythagorean conception of space, and avoiding the notion of empty space he speaks of "space as the total sum of all places occupied by bodies, and of place (topos) as that part of space whose limits coincide with the limits of the occupying body. Rejecting the vacuum, Aristotle insisted that the containing body has to be everywhere in contact with the "contained". It was already around 450 B.C., when *Empedokles* actually performed an experiment with the "vacuum", using the so-called clepsydra or "water thief", a brazen sphere with an open neck and small holes in the bottom that was used as a kitchen ladle at that time. As a consequence the idea of a natural "horror vacui" was developed, i.e. the belief that nature tries to avoid the formation of vacuum. However, with the invention of the air pump (around 1640) and of the barometer (1643) it became clear

that the air can be removed from the interior of a vessel. The question remained, what kind of vacuum is formed if all air molecules are pumped out of the vessel.

Since then many different conceptions of the vacuum were developed by scientists, different vacua as carriers for different kinds of physical phenomena. *Newton's* laws of mechanics require an absolute space in order for the principle of inertia to make sense. He writes in his "Principia": "Absolute space, owing to its own nature, remains the same and fixed regardless of any relationship to any substance". In the eyes of *E. Mach*, *Newton's* absolute space was but an empty philosophical notion and should be replaced by an operational device to construct inertial frames. That idea developed into the requirement that the bundle of local inertial frames should be determined by the energy-momentum distribution in the universe (*Mach's principle*). In *Einstein's* theory of gravity it means that the bundle of local inertial frames is determined by *Einstein's* field equation combined with suitable initial values for energy-momentum and geometry on a spacelike hypersurface. As an experimental consequence, e.g., it is predicted that near the surface of the earth a free gyroscope, with its axis oriented perpendicular to the rotational axis of the earth, should precess at a rate of 0.05 seconds of arc per year (*Lense-Thirring-effect*). Attempts are underway to measure this precession in the near future by means of a gyroscope launched into orbit around the earth.

When the wave nature of light had been firmly established, the hypothesis of the vacuum as an elastic medium, the "ether", was developed in parallel to the theory of elasticity that was worked out in the early nineteenth century by *Navier*, *Cauchy*, *Poisson* and others. In this point of view the ether had to be a very firm, elastic body to account for the high velocity of light, but it had to impose practically no friction onto planetary motion. *Michelson's* experiment (1881) showed that the velocity of light is not influenced by the motion of the earth with respect to the ether by quantities of order  $(v/c)^2$ , and thus did away with the notion of the ether as an absolute system of reference. This development led to *Einstein's* principle of special relativity, saying that all inertial systems are physically equivalent. *Newton's* "absolute space" has lost most of its attributes, yet is not completely abandoned in *Einstein's* geometrodynamics. Accelerated frames are still "preferred" coordinate systems, although locally, within an infinitesimally small space-time volume, a freely falling system in a gravitational field may not be distinguished from a local inertial frame. When larger regions of space-time are considered, a true gravitational field is revealed by tidal forces and the radiation field of an "accelerated" charge can always be detected in the far zone.

Quantum mechanics and quantum field theory, finally, laid the grounds for our present conception of the nature of the vacuum. In

today's language, the vacuum consists of a polarizable gas of virtual particles, fluctuating randomly. It is found that, in the presence of strong external fields, the vacuum may even contain "real" particles. The paradigm of "virtual particles" not only expresses a philosophical notion, but directly implies observable effects:

- 1) The occurrence of spontaneous radiative emission from atoms and nuclei can be attributed to the action of the fluctuations of the virtual gas of photons;
- 2) the virtual particles cause effects of zero-point motion as in the *Casimir* effect. (Two conducting, uncharged plates attract each other in a vacuum environment with a force varying like the inverse fourth power of their separation). Hawking's effect of pair formation by a collapsing body may also be understood as a gravitational Casimir effect;
- 3) the electrostatic polarizability of the virtual fluctuations can be measured in the *Lamb* shift and *Delbrück* scattering. The electron in the hydrogen atom is subject not only to the Coulomb potential  $\phi$  of the nucleus but also to the fluctuation field of the virtual particles. If  $L$  is the typical dimension of the system, fluctuations in the electrostatic field strength are of the order

$$\Delta\epsilon \sim \frac{(hc)^{1/2}}{L^2}$$

This field causes a slight displacement  $\Delta x$  of the electron from the usual classical orbit, leading to a shift of atomic energy levels of the order  $\Delta E$ :

$$\Delta E \sim \frac{(\Delta x)^2}{2} \langle \nabla^2 \phi \rangle_{\text{average}}$$

Precise calculations give a difference of 1057,9 MHz between the energies of the  $2s_{1/2}$  and  $2p_{1/2}$  levels in hydrogen atom in beautiful agreement with experiment. The scattering of photons by an external electric field (*Delbrück* scattering) that is caused by interaction of the photons with virtual electrons and positrons has first been measured by R. Wilson.

- 4) According to E. Zavattini the magnetic polarizability of the vacuum might be measured by observing the rotation of the polarization of laser light travelling through strong magnetic fields. Experiments are actually in progress to determine this effect.

However, the most fascinating aspect of the vacuum of quantum field theory, which will be discussed extensively during this meeting, is the possibility that it allows for the creation of real

particles in strong, time-independent external fields. In such a case the normal vacuum state is unstable and decays into a new vacuum that contains real particles. This, in itself, is a deep philosophical and physical insight. But it is more than an academic problem, for two reasons: firstly, very strong electric fields are available for laboratory experiments that are presently in progress; secondly, it can be shown that the quantum theory of interacting fields may be constructed from the vacuum-to-vacuum amplitude  $W[J]$  of a quantized field in the presence of an arbitrary external source  $J$ . Effects that occur in strong external fields may, therefore, in some way be carried over to strongly coupled, interacting fields as they form the basis of the strong and superstrong interactions. In the following chapter we shall discuss some basic aspects of the vacuum break-down in strong external fields and the present situation of experimental tests.

#### THE VACUUM IN STRONG EXTERNAL ELECTRIC FIELDS (QED OF STRONG FIELDS):

QED dates back to the early days of Quantum Mechanics. It were giants of physics like *Heisenberg, Pauli, Dirac, Weisskopf, Schwinger, Feynman and Tomonaga* who created QED. What they initiated, however, is mainly QED of weak fields where perturbation techniques could be used. Therefore ordinarily physicists associate with QED high precision measurements, where small effects of order  $\alpha$  or  $\alpha^2$  and higher orders are established and compared with a renormalized perturbation theory. That there are effects of zeroth order, i.e. 'yes or no'-effects, which are most typical of the field theory we call QED, does not seem to be known by most scientists. The most typical of these effects is the change of the vacuum (more specifically: the electron-positron-vacuum) in overcritical fields. It was initiated in the work of our school in Frankfurt -I mention the names *Pieper, P.G. Reinhard, Müller, Rafelski, J. Reinhardt, Soff* (1968-today) - and by the Moscow school (*Zeldovich, Gershtein and Popov* (1969-1978)). This topic will be discussed in length later in this conference. I shall illustrate it shortly here to make clear what I mean. One of the basic features of relativistic quantum field theory is its character of a many-body theory. This aspect becomes important as soon as a quantum field is coupled to an external classical (i.e. unquantized) field: pairs of particles may be produced spontaneously out of the vacuum if the external field is sufficiently strong, either strongly space- or time-dependent. Normally one visualizes these two creation processes by two different pictures. In the static case one attributes the produced pairs to virtual fluctuations of the vacuum: due to the uncertainty relation even a free quantum field tends to produce pairs of mass  $m$ . The lifetime of the virtual pairs is of the order  $\Delta t - \frac{m}{mc^2}$ . If a virtual pair is separated during this time by more than a Compton wavelength and if it has gained more kinetic energy than twice its rest mass, the pair becomes real. It is important that the strong space dependence of the background field has to extend over a sufficiently large region: a potential difference of more

than 1 MeV in van de Graaff machine has a negligible probability for pair production.

This particle creation process will continue to take place until either the potential differences in the external field are reduced or the Pauli principle prevents further particle creation. If the Dirac field occupies a new ground state than we speak of a dynamically broken symmetry. The new ground state is called supercritical vacuum.

The first figure illustrates the binding energies for electrons in the central field of an extended nucleus with charge  $Z$ . The typical cut-off of the  $n s_{1/2}$  - and  $n p_{1/2}$  - levels at  $Z = \frac{1}{\alpha} = 137$  disappears because of the finite size of the nucleus. At  $Z = Z_{\text{crit}} = 173$  the  $1s_{1/2}$  - bound state dives into the negative energy continuum. It is there, where the system becomes overcritical. The fundamental phenomenon happening there is best illustrated in the hole-theory,

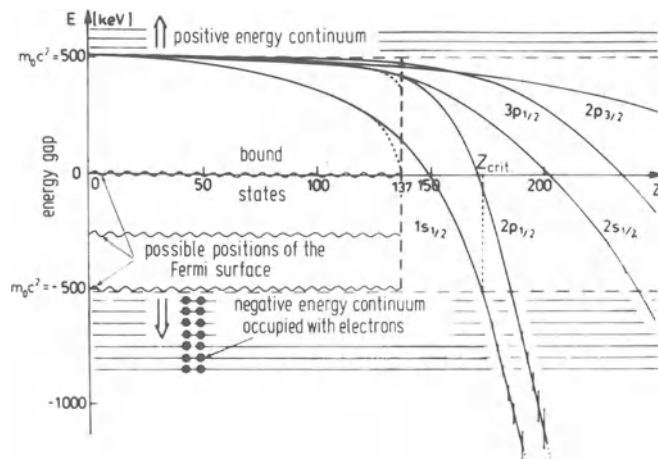


Fig. 1. The energy-spectrum of a Diracelectron in the central field of an extended nucleus with charge  $Z$ .

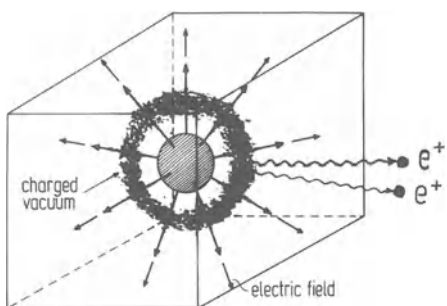


Fig. 2. "Veranschaulichung" of the vacuum in overcritical fields.

where the negative energy continuum states are all occupied with electrons in order to make atoms (i.e. the world) stable. This state, characterized by the Fermi energy at  $E_F = m_0 c$ , represents the neutral, particle-free-vacuum. It is here, that the above mentioned many-body character of QED becomes very obvious. For over-critical fields this is no more stable, but decays by spontaneous positron emission into a *charged vacuum*. If the external field is increased, beyond the critical value, vacua of higher and higher charge can be created.

The second figure gives a vivid view of the situation: The central nucleus in the middle of the cube creates the strong electrostatic field. With an "elementary-particle pump" (we theoreticians can invent such a thing) one may pump off all the elementary particles from the interior of the cube. The empty space in the box is then the neutral vacuum. If, however, the central charge  $Z$  will be increased (and through it the electric field), suddenly - at the critical charge  $Z_{cr}$  - a lightning in form of two positrons appears and at the same time two electrons form a cloud around the central nucleus, shielding it. The two positrons can easily be pumped away (they are free particles). The left-over electrons represent the charged vacuum. With crude force (i.e. substantial supply of energy) they could also be pumped out, but within about  $10^{-20}$  seconds again two positrons would be created and the electronic cloud would re-establish itself. We say: In the overcritical situation only the charged vacuum is stable.

This change of the vacuum is related to Klein's paradox. O. Klein found immediately after the invention of the Dirac equation in 1928 that the reflection and penetration of electron waves on a potential barrier,  $V_0$ , leads to strange results: For very high potential barriers there appears an unusually large penetration of electrons into the wall (about 83% for  $V_0 \rightarrow \infty$ ). Moreover, Klein observed that these electrons had negative energy. This was later on called *Klein's Paradox*. Sauter (1931) found essentially the same results in the more general case where the barrier is not sudden, but smoothed out. If the potential step of order  $m_0 c^2$  appears over a distance of the Compton wavelength  $d \lambda_e$ , the penetration of electrons into the classically forbidden region ceases. Hund introduced in 1940 the quantized field aspect by discussing the Klein-paradox in the frame-work of the hole-theory. The particles of negative energy in the high potential domain are then the positrons. In this picture there can be more reflected electrons than incoming ones, because the incoming ones can knock out an electron-positron pair at the surface of the well, whose electron moves with the reflected incoming electrons and whose positron travels inside the high potential. Particle creation by strong, infinitely extended *constant* electrostatic fields (which is related to the Klein paradox) was quantitatively predicted already by Heisenberg and Euler in 1936.

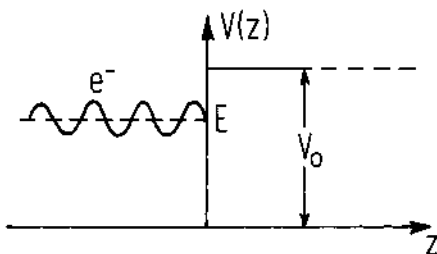


Fig. 3. Illustration of the Klein-paradox. If the barrier  $V_0$  becomes very high ( $V_0 \rightarrow \infty$ ), 83% of the electron wave will penetrate into the potential.

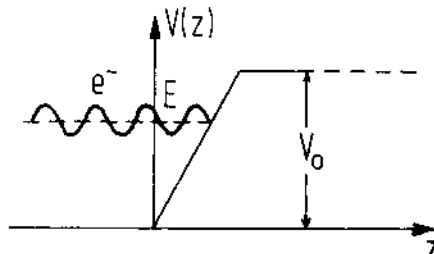


Fig. 4. Sauter studied the Klein-paradox for smoothed-out potential barriers.

Clearly, the pair creation in the case of Klein's paradox is stimulated by the incoming electron beam. This introduces some time-dependence, which is responsible for the knock-out of pairs from the barrier. It is similar to the induced pair creation, appearing in the time-dependent heavy ion collision.

The possibility of pair creation by the time dependence of an external gauge field results from the fact that a quantized field can be viewed as consisting of infinitely many harmonic oscillators ("modes"). If the quantized field is then excited from its ground state (i.e. from the vacuum state), real particles are produced. In some cases these two possibilities of pair creation by external gauge fields are connected by a gauge transformation: a globally static external gauge field may represent a dynamical field if only the gauge is suitably chosen. One simple example is the constant electrostatic field, which may be described by the static potential  $A = (E, r, \vec{0})$  but also by  $A_\mu = (0, E_t)$ .

At about the time of Hund's contribution, in 1939, Schiff, Snyder and J. Weinberg, in R. Oppenheimer's institute, discussed particles in a deep well. They found an energy spectrum of the type shown in the following figure for the Klein-Gordon equation. They mentioned that they expected similar results also for the Dirac-equation.

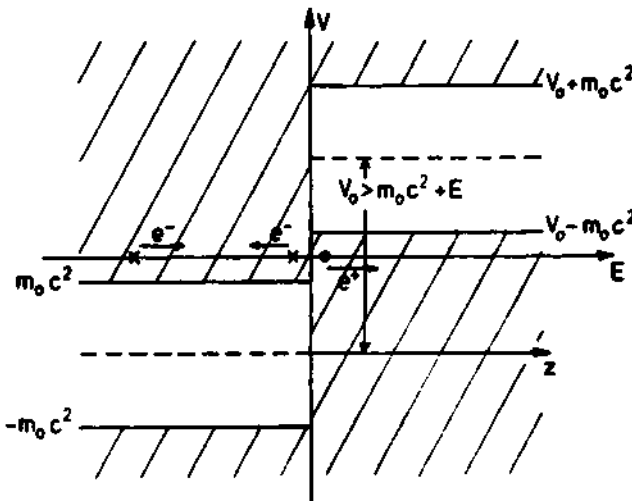


Fig. 5. By introducing the quantized-field aspect in the sense of the hole theory, Hund gave an explanation of the Klein-Gordon paradox: The incoming electrons could knock out additional electrons at the barrier and positrons would move inside the potential.

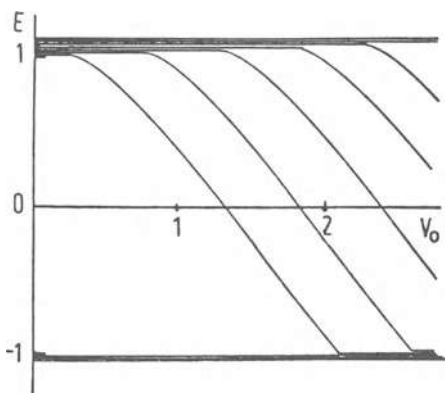


Fig. 6. The energy spectrum of a Klein-Gordon-particle in a steep square well potential according to Schiff, Snyder and Weinberg.

The same is true for the investigation of *Wheeler* and *Werner* from the year 1957, who studied superheavy nuclei, more or less hypothetically from the present point of view. They also solved the Dirac-equation for extended high-Z-nuclei up to Z=170 and found that the K-binding energy can reach  $2m_0c^2$ . The fact, that beyond Z=170 something fundamental happens has not been recognized by them.

The spontaneous positron emission in such an overcritical situation has first been recognized by *Voronkov* and *Kolesnikov* in 1960. It was a short, completely forgotten paper, recognized neither by us in Frankfurt nor by their colleagues in Moscow, the two schools which started the modern development and the complete clarification of the change of the vacuum in overcritical fields. It was communicated to us around 1977 by *Armbuster*, who had been approached by *Kolesnikov* at a Dubna-Conference, as he told us later on. Even though this very short "prehistoric" paper contained the correct idea it was of no relevance to the later physical developments. It should be mentioned that there appeared a paper called "Remark on the Klein-paradox" in context with atoms by *Beck*, *Steinwedel* and *Süßmann* in 1962, in which they say that if the binding energy for electrons in a potential becomes larger than  $2m_0c^2$ , those states "will be occupied". That they have not understood what is going on, is hidden in a footnote, in which they remark "that this occupation is - of course - not in the sense of a physical process, but according to some definition" they give. Clearly, they did not recognize the physics, even so they speak about pair creation, but, as indicated, in a confuse way.

The work which ultimately led to the physics of QED of super-critical fields was that of *Pieper* and *Greiner* in 1968/69 and - parallel to it - that of *Gershtein* and *Zeldovich* 1969/1970. I still recall the difficulties we had publishing our paper in *Zeitschrift für Physik*, where it was held up for nearly three quarters of a year. *J.H.D. Jensen* told me, that "his distinguished Heidelberg colleagues thought it is nonsense", but he finally printed the article. 1 1/2 years later he asked me to visit him. When he greeted me at the entrance of his institute (where he also lived) in the Philosophenweg in Heidelberg his first words were: "I have thought about the problem for quite a while; you are right, it were my distinguished colleagues who talked nonsense". He had meanwhile written a paper on the Klein-Paradox, together with *Dosch* and *V. Müller*, which he published in *Physica Norvegica* (1971). In the following time we had a number of very fruitful discussions until his sudden death.

The papers by *Müller*, *Rafelski* and *Greiner* 1971/72 clarified all the essential questions of the static supercritical atom. The creation of a charged vacuum around supercritical nuclei and its stability was described by *Rafelski*, *Müller* and *Greiner* 1973. The virtual vacuum polarization was already calculated by *Pieper* and *Greiner*, but studied again in context with non-linear electrodynamics of the

Born-Infeld-type by Rafelski, Fulcher, Soff, and Greiner (1971-74). Finally virtual vacuum polarization calculations in higher order  $Z\alpha$  were carried out by Gyulassy (1975) and by Rinker and Wilets. The static investigations were followed by the dynamical calculations for heavy ion collisions of Smith, J. Reinhardt, Soff, Müller and Greiner (1973- to date). These constitute a most important step for connecting theory and the observations; i.e. the bridge which makes out of a theoretical idea finally observable physics.

We will hear more about this work later on, so that there is no need for further discussing these aspects now.

Two more ideas were necessary before out of the theoretical concept of the charged vacuum in super critical fields became real physics: Even though quasi-stable islands of superheavy heavy nuclei were predicted around  $Z=114$  (Meldner (1967), Nilsson (1968), Mosel and Greiner (1968), Nix (1968)) and around  $Z=164$  (Mosel and Greiner (1969)) there was no hope that they could be produced fast and in sufficient quantity. Furthermore, the proton number (and hence the electric field) was not sufficiently large anyhow. The new idea was to betray nature and to use the short time two heavy, (e.g.) uranium nuclei are close to each other during a collision to simulate in this way a superheavy (quasi-) molecule or atom. We called these intermediate systems *superheavy quasimolecules*. The adiabaticity conditions were particularly fulfilled for the highly relativistic inner shell electrons in such systems. This idea was - again at the same time - suggested by the Frankfurt and Moscow schools.

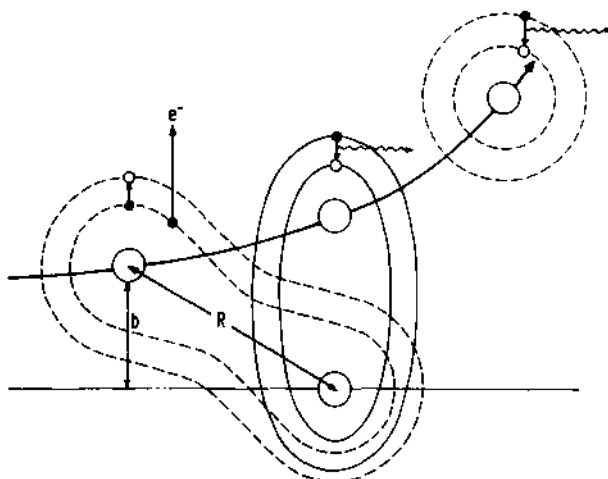


Fig. 7. Illustration of the basic idea of superheavy quasimolecules in heavy ion collisions: Since the relative motion of the two nuclei is relatively slow ( $v_{\text{ion}} \sim \frac{c}{20}$ ) compared to the motion of the inner electrons ( $v_e \sim c$ ), the latter are expected to circle around both centers.

As all ideas which finally turn out to be useful, it had its precursors: There existed for a long time the theoretical method for calculating ion-ion collisions not in Born-approximation, but according to the PSS-method (Perturbed Stationary State method). I refer to the fine paper by *Mott* (1934), in which he describes the timedeprendent molecular perturbation theory. It is also described in the book by *Mott* and *Massey* 1952, but dates back to the study of the electron promotion mechanism of molecular orbital theory by *F. Hund* (1927) and *R.S. Mulliken* (1928). The eigenfunctions of the quasimolecule appear in this method, which is also related to the Born-Oppenheimer approach.

*Hans Specht* in his thesis in 1965, in which he studied the ionisation of inner electron shells in nearly-adiabatic collisions of 5-80 MeV fission products with target atoms, spelled that out very clearly. He continued earlier work of *Armbruster* from the year 1961. Even much earlier, in 1934 *Coates* from Berkeley has observed what we now call quasi-molecular X-rays, where he already indicated that the X-ray bumps he observed might stem from an intermediate quasimolecular collision system. Again, as for many untimely discoveries, these works were of no relevance for the later developments.

The electron promotion mechanism and its enhancement due to quasi-molecular level-crossings was stressed by *Fano* and *Lichten* (1965) who interpreted  $\text{Ar}^+$ - $\text{Ar}$  inelastic collision experiments by *Afrosimov* et al. (1964) and by *Everhart* and *Kessel* (1965).

I do not know what led *Zeldovich* and *Gershtein* to the suggestion of the superheavy quasimolecules, I only can say how I came to this idea and promoted it in the inter-university GSI-seminars around 1969/70. It was the study of nuclear quasi-molecules, which *Scheid* and I had started in 1967 at Charlottesville/Virginia, where also the work with *Pieper* on electrons in superheavy nuclei was carried out. *Scheid* and I tried to explain the nuclear molecular resonances observed by *Bromley* (1960). It was then a small step from the nuclear to the electronic quasimolecule. In fact, the nuclear two center shell model, which we initiated in Frankfurt in 1968/69 to describe microscopically the nuclear quasi molecules was the direct predecessor of the *Two-Center-Dirac-Equation* studied by *B. Müller* in his thesis in 1972/73. This work is underlying all later developments of the dynamics of superheavy quasimolecular phenomena, which is culminating presently in the work of *Soff* and particularly that of *J. Reinhardt* on the dynamical studies of  $\delta$ -electron - K-vacancy - and positron production in heavy ion collisions, about which we will hear more later on.

Let me now turn to the third basic idea necessary for the development of supercritical QED as a field of physics, and that is the idea of using sticking (creating time delay and in the limit of very long sticking, even fusion) as a tool for observing the

relevant phenomena. The roots of this idea were grown already in 1973/74 when I spent a semester at Yale University. I took Berndt Müller along. The discovery of the quasimolecular X-rays by Saris, Mokler, Meyerhof, Greenberg, and somewhat later by Kaun and Wölfli was at full blossom. We had just suggested that the asymmetry of the quasimolecular x-ray spectrum could be dynamically induced and - as a consequence of this suggestion - I asked Allan Bromley and Jack Greenberg to check whether coincidence experiments of a sharp nuclear-molecular resonance with the quasimolecular x-rays could be set up. In a related development J. Reinhardt (1975), in his diploma thesis, looked for its effect in the bremsstrahlung spectrum of sticking heavy ions (nuclei). If the nuclei form for some time  $T$  a nuclear molecule (one might call it loosely nuclear sticking), the nuclear bremsstrahlung should develop a peak; the magnitude of the peak-structure is clearly a function of the sticking time  $T$ . This development lead in 1978 Rafelski, Müller and Greiner to suggest that indeed the nuclear time delay would be of great influence on the positron spectrum. If the two nuclei stick for one reason or another, the spontaneous positron decay line due to the decay of the neutral to the charged vacuum should appear. The longer the sticking time  $T$ , the more pronounced

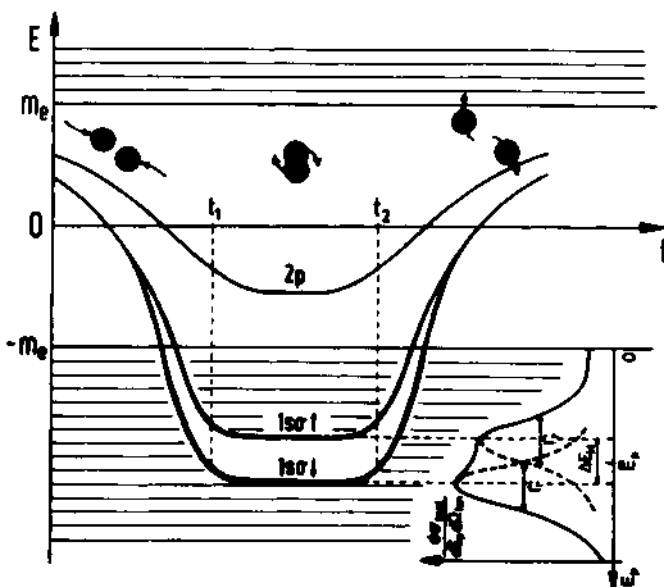


Fig. 8. Schematic diagram of the positron spectrum from overcritical heavy ion collisions with sticking (formation of superheavy nuclear systems).

should become the line-structure leading to an unanimous proof of Strong Field QED. *J. Reinhardt* (1979/80) has extended these investigations in his Ph.D.-thesis and incorporated it in a general formulation of positron production processes in under- and over-critical heavy ion collisions. In addition, it has been suggested that the superheavy nuclear system eventually formed in such sticking-processes might itself be excited and decay by supercritical internal conversion. The internal conversion rate in such superheavy systems increases by many orders of magnitude. Thus additional positron lines might appear at higher energies of the spectrum yielding information of the nuclear structure of the superheavy nuclear system formed in the collision. A schematic form of the expected spectrum is shown in the adjacent figure. The dynamically induced part of the spectrum is due to induced positron production and due to the direct positron production (shake-off of the vacuum polarisation cloud). These latter processes vary approximately like  $(Z_1+Z_2)^{19}$ , i.e. with an unusually high power in the sum of projectile and target charge. This prediction of *Soff, Müller and Greiner* has been experimentally verified through the early experiments of *Backe, Bokemeyer, Greenberg, Kankeleit et al.* (1978) and of *Kienle, Kozhuharov, Greenberg et al.* (1979).

As usual, the new idea of sticking was first laughed about and - also as usual - it had its predecessors: For proton-nucleus scattering time-delay effects of similar kind were suggested by *Eisberg* and *Yennie/Gugelot* (1960/1962) and by *Ciochetti and Molinari* (1965).

Other mile stones in the development of QED of strong fields are:

- 1) The observation of continuous x-ray spectra in various ion-ion collisions by *F. Saris* (1972), which were interpreted as quasi-molecular L-X-rays.
- 2) Nearly simultaneously with *Saris*, the GSI-Köln-group of *Armbuster, Mokler and Stein* (1972) observed a continuous X-ray-bump in the I-Au-collision, which was supposed to be the quasimolecular M-X-rays from the superheavy system.
- 3) The measurement of broad continuous x-ray spectra in Br-Br-collisions by *Meyerhof* (1973). These were interpreted as K-molecular x-rays.
- 4) Practically at the same time and with higher precision *Greenberg and Davies* (1974) confirmed the emission of quasi-molecular K-X-rays in Br-Br, Ni-Ni and other systems. They measured - for the first time - the asymmetry of the quasi-molecular spectrum, (which was - simultaneously - also investigated for the M-X- rays, mentioned under 2), by *Mokler et al.*). These measurements constituted the basis of

the final prove and identification of quasimolecular X-rays by *Meyerhof* (see 6).

- 5) The observation of K-quasimolecular X-rays from superheavy systems by *Kaun* and his associates (1975).
- 6) The rigorous confirmation of quasimolecules by *Meyerhof*, who measured the Doppler shift of quasimolecular X-rays (1975) using the asymmetry of the X-ray-spectrum predicted theoretically by *Müller* and *Greiner* and first identified experimentally by *Greenberg* and *Davies* (see 4)).
- 7) The first isolation of selected MO transitions to vacant  $1s\sigma$  states using the cascade coherence between MO and K x-rays by *Greenberg*, *O'Brien* and *Liarokapis* (1980).
- 8) The first observation of the tremendously enhanced K-vacancy creation in superheavy quasimolecules (*Greenberg*, *Schwalm* and *Bokemeyer*, 1977, the late *J. MacDonald*, *Armbruster* and collaborators 1978), *Meyerhof* and *Anholt* 1978). These experiments confirmed theoretical predictions by *Betz*, *Soff*, *Müller* and *Greiner* (1976). The phenomenon, due to relativistic electron motion, has been qualitatively anticipated already in the early work by *Rafelski*, *Müller* and *Greiner* (1972).
- 9) The use of the quasimolecular X-ray-asymmetry by *Wölfli* for a spectroscopy of quasatomic energies (1976). That the peaking of the asymmetry at the highest molecular (quasi-atomic) transition energies could eventually be used for a spectroscopy had been suggested by *Müller* and *Greiner* in their original paper. However, the special ansatz *Müller* and *Greiner* made for the interaction of the photon field with the rotations of the quasimolecular system was disputed, and later justified by *Gros*, *Müller* and *Greiner* (1976).
- 10) The use of the K-vacancy measurements for determination of binding energies (suggested by *Müller*, *Soff*, *Greiner* (1978) and experimentally realized by *Bosch*, *Armbruster* et al. (1979)).
- 11) The first positron experiments with heavy ions establishing the non-nuclear origin of these positrons and their energy-dependence (*Backe*, *Greenberg*, *Kankeleit*, *Bokemeyer* (1978)).
- 12) The first coincidence experiments of positrons and heavy ions (*Backe*, *Greenberg*, *Kankeleit* et al. (1978), *Kienle*, *Kozhuharov*, *Greenberg*, 1979).
- 13) The first observation of peaks in the coincidence positron spectrum by *Kienle*, *Kozhuharov*, *Bosch* et al. (1981) and by *Bokemeyer*, *Greenberg*, *Schwalm*, *Bethge*, *Vincent* et al. (1981). The second group has performed for the first time experiments with most kinematical parameters fully determined, which seems essential for reproducing the positron spectra.

These latter experiments seem to constitute an experimental break-through into an exciting future; possibly not only the discovery of the vacuum decay, but also that of superheavy nuclear systems with  $Z=180$  and higher, including their nuclear (and possibly also atomic) spectra. Whether this is all true as I describe it here, remains to be seen. Our conference will perhaps tell us more about it.

The intense study of the problem of electrons bound to strong potentials has stimulated interest in a number of similar, related problems. They can be divided into three groups, namely:

- a) bosons bound to strong electromagnetic and nuclear potentials;
- b) fermions and bosons in strong gravitational fields;
- c) the vacuum structure of strongly interacting fermions and bosons.

#### PION CONDENSATION

Let me now first discuss the efforts which dealt with the theory of bosons bound to strong potentials. Clearly, the concept here must be very different since it is the Pauli exclusion principle that stabilizes the charged vacuum in the case of fermions in over-critical fields.

Although the superbound boson system is theoretically a very interesting problem, there does not seem to be a prospect of experimental tests in atomic collisions in the future. This can be seen by noting that we need an external potential comparable in strength to the mass of the lightest meson, the pion ( $m_\pi = 139.6$  MeV), which requires nuclear charge of the order of  $Z=Rm_\pi \approx 2000$ . Here  $R$  describes the nuclear size. The above formula is valid only if  $Rm > 1$  and therefore does not apply to electrons bound in the nuclear Coulomb field.

As already mentioned, one of the earliest investigations of the solutions of the Klein-Gordon equation with a strong external potential was carried out by Schiff, Snyder and Weinberg (1940). They solved the problem of the square well potential and found that the spectrum behaves qualitatively differently from that of the Dirac equation with  $\frac{1}{r}$  potential as the potential strength is varied. They discovered that for a given state, there are two critical points; at a value  $V_0$  an antiparticle state with the same quantum numbers emerges from the negative energy continuum while at  $V_{cr}$  the particle and antiparticle states meet each other. No particle or antiparticle state with these particular quantum numbers is found

above  $V_{cr}$ . This situation is illustrated qualitatively in the figure below. Although this behaviour of the spectrum is suggestive for any potential, a different result was found later by *Bawin and Levine* (1975) for long-range potentials. In particular, they found that a cutt-off Coulomb potential has an eigenvalue spectrum similar to that of the Dirac equation.

*Snyder and Weinberg* successfully introduced a second quantization of the theory for potentials smaller than  $V_{cr}$  but made no attempt to treat the overcritical case. The theory remained at this point for a long time, with the exception of the technical development of first-order equations by *Feshbach and Villars* (1958).

The modern development of the subject which led to the understanding of the supercritical state was initiated by *Migdal* (1972), who was stimulated by the work on the overcritical Dirac equation. He recognized correctly that to stabilize the vacuum in the overcritical case, some higher-order effect must be included in the Hamiltonian. He, in particular, chose to consider a residual  $\lambda\phi^4$  term in the boson field Hamiltonian. His physical picture was based on the following considerations: as  $V$  approaches  $V_{cr}$ , the energy necessary to make a meson pair vanishes allowing an infinite number of pairs to be produced. To stabilize this situation, a positive definite part in the Hamiltonian is needed that would stop the production of the condensates when a certain meson density is reached.

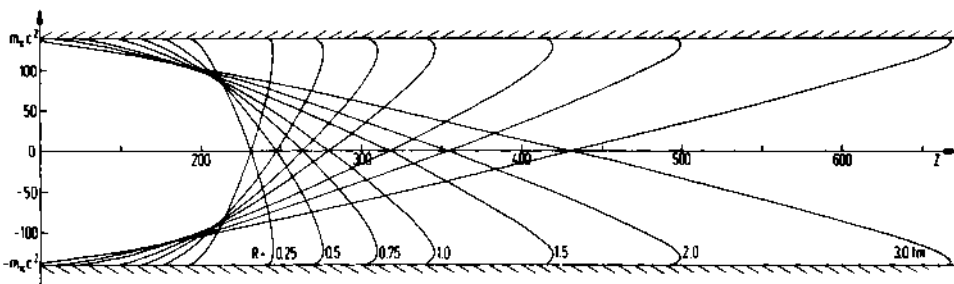


Fig. 9. Energy eigenvalues from the Klein-Gordon equation for a square well potential.

In a subsequent development, *Klein and Rafelski* (1975) showed that it is possible to consider the charge of the condensate itself as the stabilizing mechanism. They demonstrated that the repulsion, which is always present in any charge distribution of the meson condensate, suffices to stabilize the condensate. Their treatment was formally complete for both the under- and overcritical cases. A fully relativistic quasi-particle formalism was developed for  $V > V_{cr}$  and equations determining the Bose condensates were given. The self-consistent treatment was simplified by the use of the first-order Feshbach-Villars representation of the Klein-Gordon equation. In the original work of *Klein and Rafelski*, the lowest state of the supercritical system was considered to consist of a neutral Bose condensate. As subsequently pointed out by *Bawin and Lavine* (1975), the long-range character of the Coulomb potential allows the  $1s$  state to join the lower continuum. This led *Klein and Rafelski* (1975) to the conjecture that the neutral condensate must be replaced by a charged condensate in the long-range Coulomb field. The same authors confirmed this conjecture and described the properties of the charged condensate in 1977. In accordance with the charge conservation, a large number of free antimesons will be produced in this process. Furthermore, in view of the possibility of weak decay of charged vacuum other mechanisms leading to pion condensates in external fields have been considered.

There is another form of pion condensation, which comes about because nuclear matter itself may have excited states with the quantum numbers of a pion, i.e.  $0^-$ - $T=1$ -states. Now, as a function of nuclear density the effective nucleon-nucleon interaction will generally change. It turns out that such excited states (in normal nuclear matter) may become ground state in dense nuclear matter. A critical density of  $\rho_{cr} \approx 1.5 \rho_0$  has been predicted (*Migdal* (1971), *Brown and Weise* (1976)). *Gyulassy and Greiner* (1977, 1978) showed the stability of this new phase against temperature in hot, dense nuclear matter and suggested that the new phase might play a considerable role in shock waves (compression of nuclear matter) as they appear in relativistic heavy ion collisions (for a recent review of this subject see *J.A. Maruhn and Walter Greiner*: Relativistic Collisions: Theoretical Models, appearing in Heavy Ion Science, ed. *D.A. Bromley*, Plenum Publ. Corp. New York, 1982).

In particular precritical scattering analogous to critical opalescence should appear before the phase transition takes place and reduce the mean free path for nucleon-nucleon scattering, thus favoring the validity of nuclear hydrodynamics in relativistic heavy ion collisions (*Ruck, Gyulassy, Greiner* 1977). Later on it had been suggested by *M. Erickson and Delorme* (1979) that such precritical scattering might also be seen in electron scattering from a relatively dense light nucleus like  $C^{12}$ . It was called precursor -

effect. However, intensive searches for that effect were negative, (Weise (1981)), so that one must conclude, that the critical density for this second type of pion condensation is higher than  $\rho_{\text{crit}} > 1.5 \rho_0$ .

### STRONG GRAVITATIONAL FIELDS

The success of QED of strong fields raises the question, whether further instabilities of the Dirac vacuum, similar to the electrostatic instability, can occur in nature. Although many instabilities of the Dirac vacuum can be visualized by means of energy level diagrams based on the solutions of the classical field equation, they should ultimately be described in the framework of quantum field theory. For this purpose one needs a manifestly gauge-covariant formulation of the theory of the quantized Dirac field in the presence of external, classical gauge fields, which admits a description of particle creation. Such a formalism has, for example, been suggested by H. Rumpf (1976-78). In this formalism the description of pair creation by external fields becomes possible by introducing four (instead of two) classes of field modes, viz. ingoing and outgoing particle and antiparticle modes.

In various cases the ingoing/outgoing modes correspond to WKB-solutions of the quasiclassical theory in the corresponding asymptotic region ( $t \rightarrow \pm\infty$ ). A quantum field theory in the presence of external fields, which is based on solutions of the quasiclassical theory, has been known for some time, and theories of such type are frequently used for the calculation of particle creation rates in an expanding universe. (L. Parker 1969). However, we have to remark that Rumpf's particle definition in its present form is not applicable to situations where a new stable ground state of the supercritical Dirac system develops. In these cases one has to rely on the discussion of energy level diagrams. The stabilization of the supercritical vacuum can then be described by statistical methods that were first suggested by Müller and Rafelski (1975) for the highly charged supercritical vacuum in quantum electrodynamics. The way in which these models can be imbedded into a second quantized theory are described in the lectures of Müller and Rafelski.

Let me shortly sketch the general procedure for studying Dirac-particles in gauge-fields. One starts with the free Dirac action of spin-1/2 particles that have (internal) degrees of freedom with values on a semi-simple Lie group. Background fields are introduced into the action as gauge fields describing the parallel transport of the spinor from one space point to the next. Typical gauge groups are  $U(1)$  that forms the basis of QED, the Poincaré group  $\mathcal{P} \cong SL(2, \mathbb{C})$  that underlies the Einstein-Cartan theory of gravitation and the  $SU(n)$  groups that play such an important role in modern theories of elementary interactions (Yang-Mills theories). It turns out that the nature of the group has a profound influence on the stability or in-

stability of the Dirac vacuum in a strong, globally static gauge field.

The behaviour of fermions in the presence of external Yang-Mills fields is reviewed in a forthcoming Physics Report by Soffel, Müller and Greiner (1982). In general, non-abelian gauge theories such as the Einstein-Cartan theory or Yang-Mills theories introduce a complicated and rich vacuum structure into the Dirac system. The complications arise from the gauge freedom: gauge non-equivalent potentials may lead to identical field strengths (Wu-Yang ambiguity), but to a different behaviour of the Dirac field. On the other hand, locally gauge-equivalent potentials may lead to different vacuum structures which may be distinguished by global, topological properties.

For example, a uniformly accelerated observer should measure particles in the Minkowski vacuum. Here, the transformation from an observer at rest to a uniformly accelerated observer is a gauge transformation in the sense of Poincaré symmetry of the theory, but leads to a new vacuum structure, the vacuum of the accelerated observer. I guess that the problems herewith connected will show up in the lectures by Prof. Candelas.

The new vacuum structure of the accelerated observer means that the Fock-space of those states which are actually measured by a physical detector depends on the coordinate system of the observer and on the topology of the sub-manifold of the entire space-time, which is causally connected with the observer. Thus one has the apparent paradox that the gravitating part of matter can be described independent of a coordinate system in form of some covariant energy-momentum tensor  $T_{\mu\nu}$  (or the regularized expectation value of the energy-momentum operator  $\langle \hat{T}_{\mu\nu} \rangle_{\text{reg}}$ ), but that, on the other hand, the trajectory of the detector enters into the detection of field quanta, which is therefore a coordinate (or gauge) dependent phenomenon (Unruh 1976). This behaviour will particularly show up when the theory of fermions in Rindler space is discussed (Soffel, Müller and Greiner (1979)).

It turns out that the observer moving with a constant acceleration  $g$  in Minkowski space experiences a thermal flux of all kinds of fermions with effective temperature  $T = \frac{gh}{2ck}$  ( $k$  is Boltzmann's constant). This result, known for some time for particles with integer spin (Fulling 1973, Unruh 1976, Davies 1975, Sanchez 1979) depends crucially upon the fact that the uniformly accelerated observer in Minkowski space possesses an event horizon: there are parts of Minkowski space-time the observer cannot communicate with. Thus it is the geometric and topological structure of the sub-manifold naturally connected with the observer's state of motion which leads to the appearance of the thermal particle spectrum.

## VACUUM STRUCTURE OF STRONGLY INTERACTING FERMIONS AND BOSONS

Similar mechanisms are encountered when in a "Gedanken-experiment" the fine-structure constant is increased arbitrarily. At a certain point the bound positronium state could lead to an inherent instability of QED. But even before that point one finds a very instructive situation: muons, the heavy partners of electrons, can no more be produced as charged quanta. As  $\alpha \rightarrow \alpha_{cr} - 1$  the spontaneous production of a  $e^+e^-$  pair would become possible leading to a neutralized muon state with the muon charge being carried away by the electron field. At even greater values of  $\alpha \sim 1.5$  (?) one could argue that the electron field also develops an inherent instability.

The methods developed for the study of supercritical fields can successfully be applied to the study of gauge theories and in particular to the study of the structure of the QCD vacuum. One deals here simultaneously with a strongly coupled theory with the bose field having both attractive and repulsive self-interaction. Ignoring first a possible vacuum structure, i.e. working in the perturbative vacuum one considers the gauge field condensates around a Fermi source and describes the new ground state that must be constructed in order to have a satisfactory theory: a substantial screening of the color charge is found (Rafelski and Müller (1981).

However, from this study one learns that the essential aspect of the interaction is the *supercritical* attractive force between the spin 1 gluons and the color magnetic field when both are anti-parallel. This property can be further exploited to construct a new, nonperturbative global vacuum state.

This construction is based on an approximate evaluation of the zero point energy of the interacting gauge fields leading to the known concept of 'effective Lagrangian'. The supercritical binding of spin-1 gluons in colour-magnetic field lowers the energy density of the interacting ground state below that of the perturbative state globally (Savvidy 1977, N.K. Nielsen and Olesen 1978). Hence the usual vacuum state is quite different from the perturbative (naive) vacuum in which (perturbative) quarks are found. The ultimate description of the true QCD vacuum state in terms of the perturbative fields, similar in spirit to the BCS method, but certainly entirely different in its nature has not yet been accomplished, but bright young students are working on it. It is intrinsically related with the so-called confinement problem of QCD. The general problems associated with the quark-gluon ground state will be spread out during the course in the lectures by Rafelski and by M. Baker.

## CONCLUSION

Our aim in this meeting at Lahnstein is to present a synoptic view of the properties of the vacuum of particles in various strong fields. In particular, we want to convey the understanding that there are related phenomena connected with a change in the ground state for many different types of interaction. All these phenomena have in common that there exists some critical strength of the interaction at which it becomes energetically more favourable to produce particle-antiparticle pairs out of the vacuum. Depending on the geometry of the fields, either one species is emitted to infinity while the other species is retained in the interaction region or both, particles and antiparticles alike, remain localized, providing a real vacuum polarization. In any case, the effect of the pairs is to screen the external interaction. When the number of pairs produced is large, the screening effect becomes substantial and a self-consistent treatment is necessary.

The necessary condition under which such a change of the vacuum state (phase transition) can occur is that the field distinguishes the particles according to some quantum number, such as electric charge, spin, colour and so on. We may express this condition more formally by saying that the interaction must dynamically break some symmetry of the non-interacting theory. As a consequence, the changed ground state is characterized by the spontaneous global breaking of the symmetry, i.e. it is charged or carries spin, colour etc. Therefore, the theme of our discussions is really dynamical symmetry breaking in strong gauge fields. This phenomenon - that is our message - is typical for most strong external interactions and not the characteristic of a special one. Of course, the decay into a charged vacuum state in strong electromagnetic fields plays a distinguished role as the one example that is amenable to tests in the laboratory.

THE STATUS OF QUANTUM ELECTRODYNAMICAL PRECISION --  
THEORETICAL POINTS OF VIEW

G.W. Erickson

Physics Department  
University of California at Davis  
Davis, California 95616 USA

The most precise QED calculations<sup>1</sup> of atomic energy levels (one-electron Lamb shifts for small atomic numbers  $Z$ ) will be reviewed and compared with current precision measurements<sup>2</sup>. The nature of the  $Z\alpha$  dependence of these calculations will be considered in detail, including its validity and uncertainty for arbitrary energy levels and values of  $Z$ , comparison with results of complete numerical calculations<sup>3</sup> for a few levels at separate larger values of  $Z$ , and possible improvements using strong-field results near  $Z\alpha = 1$ .

**Summary:** Physical Significance of QED -  
Detailed Structure of EM Interactions:  
Electron Structure, Photon Structure, Vacuum Structure

Before we start studying quantum electrodynamics (QED) in Strong Fields with heavy colliding nuclei, it would be good to discuss QED in the more usual context of atomic physics. Here the ordinary electromagnetic fields of simple nuclei, like the proton, deuteron, and alpha particle, can be probed in detail. Without the complications of nuclear interactions, we can directly compare very high precision measurements with the predictions of QED.

I would especially like to point out the physical significance of the comparisons - just which details of the structure of the electromagnetic (EM) interaction - are being brought out in each comparison. We will see that it is primarily the EM structure of the electron that is involved in the Lamb shift (LS) and Hyperfine Splitting (HFS), while the EM structure of the photon and of the vacuum will be more important in strong fields.

If we wish to look at the smallest distances, then we must consider high energy experiments. Although these are not considered to be precision measurements, their results can be said to show that QED works well to at least very many GeV, and that electrons behave like QED-modified point charges down to  $2 \times 10^{-16}$  cm. However, at high energies, the non-EM interactions (the strong and weak interactions) start becoming intimately involved, so we cannot easily distinguish the effects of QED from the effects of quarks and weak currents. In any event, much more will be said of these small distance tests of QED by Böhm next week.

If we look to the highest precision to which QED is being tested, we must consider first the static magnetic moment of the electron, which is given to a precision of  $10^{-10}$  by

$$g = 2[1 + \frac{\alpha}{2\pi} - 0.328^+(\frac{\alpha}{\pi})^2 + 1.1765(\frac{\alpha}{\pi})^3 - 2.3(\frac{\alpha}{\pi})^4 + \dots]$$

$\pm 13$        $\pm 3.6$

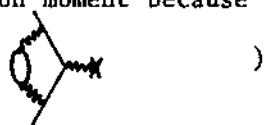
72 graphs (Levine & Roskies)  $\rightarrow$        $\uparrow$       } results as of  
891 graphs (Kinoshita & Lindquist)  $\longrightarrow$       } last Tuesday<sup>4,5</sup>

$$= 2[1 + (1.159.652.200 \pm 40) \times 10^{-12}]$$

(measurement<sup>6</sup> by Van Dyck et al., 1979)

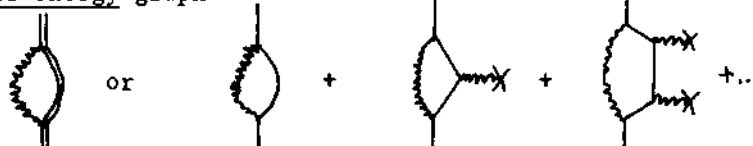
Whether or not you consider this as electron structure to  $10^{-10}$  or to  $10^{-7}$  precision ( $g = 2$  is Dirac,  $g-2$  is QED), it is the only QED calculation going to 8th order ( $\alpha^4$ ) in the QED perturbation expansion in order to compare with experiment. Difficulties are obvious when you consider that this order involves 891 Feynman graphs and that even the most precise independent value<sup>7</sup> of the fine structure constant ( $\alpha^{-1} = 137.035.963 \pm 0.000.015$ ) required to evaluate  $g-2$  yields an uncertainty ( $\pm 130 \times 10^{-12}$ ) larger than that in the measurement. In fact, if the 8th order terms were known better, the  $g-2$  measurement could be used to deduce a more precise fine structure constant. In any event, since the non-EM interactions ( $4 \times 10^{-12}$ ) are still smaller than the uncertainties, only QED is involved and it works well.

The muon moment differs from the electron moment because a number of graphs involving both leptons (starting with  $\longrightarrow$ ) do not have the same contribution for the heavier lepton (the muon) as for the lighter (the electron). However, the non-EM interactions ( $\sim 62 \pm 10 \times 10^{-9}$ ) are much more important (than for the electron  $g-2$ ) since the muon itself is much heavier. We will hear more about this measurement this afternoon from Picasso.



There will also be discussions later this week (Baker) and next week (Barut) on non-perturbative calculations.

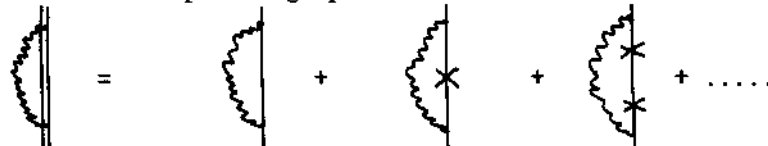
The lowest order contribution to  $g-2$  is from the vertex correction,  which is an electron structure term which is related to the electron self-energy graph



On the other hand, the photon-self-energy graph or vacuum polarization graph, is the leading correction to the structure of any photon, real or virtual. 

The effects can be seen in the LS or fine structure (FS) of simple (low  $Z$ ) atoms and are crucial in the description of high- $Z$  muonic atoms. If the field is strong enough, the virtual pair can become real, and Müller and Gyulassy will discuss the corresponding polarization and decay of the vacuum.

To explore the structure of the electron, we must start with the one-virtual-photon graph



and consider the nature of the interaction with a given potential, whether due to an electric or a magnetic field.

The magnetic part of the lowest order electron structure is  $\frac{\alpha}{2\pi}$  times the magnetic moment operator  $\frac{-e\hbar}{2mc}(\vec{\sigma} \cdot \vec{H} - i\vec{\alpha} \cdot \vec{E})$ .

For a pure Coulomb potential  $V = -Z\alpha/r$ , the magnetic field is zero, but the magnetic moment term contributes part of the Fine Structure Separation ( $P_{3/2} - P_{1/2}$ ) and part of the Lamb Shift ( $S_{1/2} - P_{1/2}$ ) due to the (mostly non-relativistic) expectation value

$$\langle n | \vec{\alpha} \cdot \vec{E} | n \rangle \simeq \frac{1}{4m^2} \int \phi_n^\dagger (\nabla^2 V + \frac{2}{r} \frac{dV}{dr} \vec{\sigma} \cdot \vec{L}) \phi_n$$

$$= \frac{(Z\alpha)^4 mc^2}{n^3} \frac{c_{\ell j}}{2\ell+1} \text{ where } c_{\ell j} = \begin{cases} 1/(\ell+1) & \text{for } j=\ell+\frac{1}{2} \\ -1/\ell & \text{for } j=\ell-\frac{1}{2} \end{cases} .$$

If there is a nuclear magnetic moment  $\vec{\mu}$  causing a vector potential  $\vec{A} = \vec{\mu} \times \vec{r} / r^3$ , then the magnetic part of the electron structure will modify the usual (non-QED) Hyperfine Structure

$$HFS = \frac{4|e|}{3m} \left(\frac{Zam}{n}\right)^3 \langle \vec{\sigma} \cdot \vec{\mu} \rangle$$

by a factor  $1 + \frac{\alpha}{2\pi} - \alpha(2\alpha)\left(\frac{5}{2} - \ln 2\right) + \dots$

It might be expected that the exceedingly precise (better than 1 part in  $10^{12}$ ) measurement of the HFS in Hydrogen might provide a high precision test of QED, but the calculated

$$HFS(H) = 1\ 420\ 406 \pm 4 \text{ kHz}$$

is limited in precision by nuclear structure corrections<sup>8</sup>. To avoid this, we can use a 0.06 ppm measurement of the HFS in muonium ( $4\ 463\ 302.90 \pm 0.27$  kHz) since the muon structure is given by QED, but here the calculated

$$HFS(\mu^+ e^-) = 4\ 463\ 307.7 \text{ kHz}$$

still has uncalculated parts as large as  $\pm 5$  kHz, as well as  $\pm 1.8$  kHz uncertainties due to a 0.4 ppm uncertainty in the muon moment (ratio to proton moment)

$$\mu_\mu / \mu_p = 3.183\ 344\ 8(12).$$

Other aspects of QED (virtual pair annihilation) are included in positronium HFS, where the measurements ( $203\ 384.9 \pm 1.2$  and  $203\ 387.0 \pm 1.6$  MHz) cannot be said to contradict the calculated

$$HFS(e^+ e^-) = 203\ 399.1 \pm 10.8 \text{ MHz}$$

because the next uncalculated term can be as large as -4.2 MHz.

In summary, these precise tests show that QED works (with no clear-out disagreements) but that more needs to be done to use the full precision of the measurements to test the theory.

Let us go back and consider what we mean by the EM structure of an electron, which we say is a point charge.

What is a point charge? Its interaction with an electromagnetic field is

$$j \cdot A = j_\mu(x) A^\mu(x),$$

while an extended charge might have

$$\int dx' j_\mu(x') f(x' - x) A^\mu(x).$$

The effect of an extended charge distribution  $\rho(r)$  on Rutherford scattering is

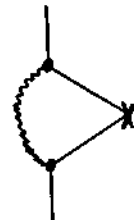
$$\frac{d\sigma}{d\Omega} = \left( \frac{d\sigma}{d\Omega} \right)_{\text{Ruth.}} \times |F(q^2)|^2$$



where  $F(q^2)$  is the charge form factor

$$F(q^2) = \int d^3r \rho(r) e^{iq \cdot r} \xrightarrow[q \rightarrow 0]{} 1 - \frac{q^2}{6} \langle r^2 \rangle + \frac{q^4}{120} \langle r^4 \rangle + \dots$$

In contrast, an electron is a point charge with  $j_\mu(x) = e\bar{\psi}(x)\gamma_\mu\psi(x)$  which interacts with external fields and/or virtual photons as a point charge. This is the way its QED interactions (such as 2nd order vertex corrections as in Bjorken and Drell<sup>9</sup> Sections 8.6, 8.7, and eq. 10.88) are calculated and understood. However, we can also consider those same QED interactions as equivalent to form factors  $F_1$  and  $F_2$  modifying the vertex as



$$e\gamma_\mu \rightarrow e\gamma_\mu F_1(q^2) + \frac{\alpha}{2\pi} \frac{e\hbar}{2mc} \sigma_{\mu\nu} iq^\nu F_2(q^2).$$

The corresponding magnetic form factor

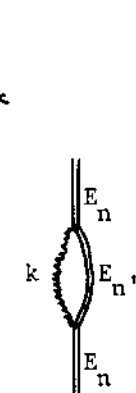
$$F_2(q^2) = \int_0^1 dx \frac{m^2}{m^2 + x(1-x)q^2}$$

has a static limit  $F_2(0) = 1$  whose coefficient is the anomalous magnetic moment  $g-2 = \alpha/2\pi$ . The charge form factor

$$F_1(q^2) = 1 - \frac{\alpha}{2\pi} \left\{ f\left(\frac{q^2}{m^2}\right) \ln \frac{m}{\lambda} - g\left(\frac{q^2}{m^2}\right) \right\}$$

cannot be used directly for a free electron because it diverges in the Infra-Red (virtual photon mass  $\lambda \rightarrow 0$ ). For example, electron scattering calculations must include bremsstrahlung of soft (Infra-Red) photons in order that the cross-section not depend on a fictitious photon mass  $\lambda$ . For the structure of a bound electron ( $E_n$ ) a photon mass is often used, although it is not needed because the intermediate states ( $E_{n'}$ ) → do not allow a virtual photon with arbitrarily small energy

$$\hbar\omega \equiv k = E_n - E_{n'} \neq 0.$$



However, there would still be an Infra-Red (IR) divergence in the zero binding limit ( $Z\alpha \rightarrow 0$ ,  $|E_n - E_{n'}| \propto (Z\alpha)^2 mc^2 \rightarrow 0$ ) and this appears as an IR logarithm

$$\ln \frac{m}{\lambda} \rightarrow \ln \frac{mc^2}{|E_n - E_{n'}|} \rightarrow \ln \frac{1}{(Z\alpha)^2}$$

in the non-relativistic limit  $|E_n - E_{n'}| \ll mc^2$ . Such IR behaviour dominates and complicates electron structure calculations and discussions.

In light atoms, the momenta are small ( $q^2 \sim (Z\alpha)^2 m^2 \ll m^2$ ) and the corresponding non-relativistic limit of the electron ( $F_1$ ) and vacuum polarization ( $\Pi$ ) form factors,

$$F_1(q^2) + \Pi(q^2) \xrightarrow{q^2 \rightarrow 0} 1 + \frac{\alpha}{3\pi} \left\{ \ln \frac{m}{\lambda} - \frac{3}{8} - \frac{1}{5} \right\} \frac{q^2}{m^2} + O\left(\frac{q^4}{m^4}\right),$$

contains the previously-discussed magnetic moment plus an additional interaction which is effectively the small number  $\frac{\alpha}{3\pi} \left[ \ln \frac{m}{\lambda} - \frac{3}{8} - \frac{1}{5} \right]$  times the interaction  $(q^2/m^2) e A^\mu$ . For the Coulomb potential  $A^\mu = -Ze \delta_\mu^\mu / r$  in coordinate space,  $q^2$  is  $-\nabla^2$  and our QED inter-

action  $q^2 A \rightarrow -\nabla^2(1/r) = 4\pi\delta(\vec{r})$  is a delta function, and thus causes an energy level shift which is  $[\ln(m/\lambda) - (3/8) - (1/5)]$  times an expectation value

$$\frac{\alpha}{3\pi} \frac{Z\alpha}{m^2} 4\pi \int d^3r \phi^*(\vec{r}) \delta(\vec{r}) \phi(\vec{r}) = \frac{4\alpha Z\alpha}{3m^2} |\phi(0)|^2$$

$$= \frac{4\alpha(Z\alpha)^4 mc^2}{3\pi n^3} \delta_{\ell_0}$$

which vanishes except for S-states and therefore is part (most) of the Lamb shift.

A different way to see this dominant feature of the Lamb shift is due to Ted Welton<sup>10</sup>. QED causes vacuum fluctuations in the electric field which causes fluctuations  $\delta\vec{r}$  in the position of an electron in the field. (This is a very direct way of viewing QED as causing an effective structure for a point charge.) The average  $\delta\vec{r}$  is zero (by symmetry) but the mean square fluctuation is given by a sum over frequencies

$$(\delta r)^2 = \frac{\alpha}{\pi} \left(\frac{h}{mc}\right)^2 \int \frac{dw}{w} = \frac{\alpha}{\pi m^2} \int \frac{dk}{k} .$$

The resulting energy shift is the difference between the Coulomb potential at the non-perturbed position  $\vec{r}_0$  and at the fluctuating position  $\vec{r} = \vec{r}_0 + \delta\vec{r}$ , expanded to leading non-vanishing order in  $\delta\vec{r}$ :

$$\begin{aligned} \Delta E_n &= \left\langle -\frac{Z\alpha}{r} - \frac{Z\alpha}{r_0} \right\rangle = -Z\alpha \left\langle \delta\vec{r} \cdot \vec{\nabla} \frac{1}{r} + \frac{(\delta r)^2}{6} \nabla^2 \frac{1}{r} + \dots \right\rangle \\ &= -Z\alpha \frac{(\delta r)^2}{6} \left\langle \nabla^2 \frac{1}{r} \right\rangle = \frac{-Z\alpha}{m^2} \frac{\alpha}{\pi} \int \frac{dk}{k} \left\langle -4\pi \delta(\vec{r}) \right\rangle \\ &= \frac{4\alpha(Z\alpha)^4 mc^2}{3\pi n^3} \delta_{\ell_0} \ln \frac{1}{(Z\alpha)^2}, \end{aligned}$$

where the UV cutoff is at relativistic energies  $k_{\max} \sim mc^2$ , and, as before, the IR cutoff is at atomic binding energies,  $k_{\min} \sim (Z\alpha)^2 mc^2$ .

In order to see how the IR logarithm is actually determined, and to see the source of terms higher order in  $Z\alpha$ , let us use a third view, that of the original non-relativistic (NR) calculation of Bethe<sup>11</sup>, where mass renormalization of the second-order perturbation due to  $j \cdot A$  (one  $A$  creates the photon, the other  $A$  destroys it) yields

$$\Delta E_n = \frac{2\alpha}{3\pi n^2} \int_0^\infty \frac{dk}{1+2k/mc^2} \sum_{n'} \frac{\langle n | \vec{p} | n' \rangle + \langle n' | \vec{p} | n \rangle (E_{n'} - E_n)}{k + E_{n'} - E_n} \quad (1)$$

where I have used a smooth cut-off factor  $(1+2k/mc^2)^{-1}$  in place of Bethe's  $k_{\max} \sim mc^2$ . Here, independently of our arbitrary choice of UV cut-off, we could see directly the logarithmic IR divergence  $\int_0^\infty dk/k$  if we would let  $E_{n'} - E_n \sim (Z\alpha)^2 mc^2$  completely vanish in the denominator. Instead, we obtain the leading logarithm and a remainder (higher order in  $(E_{n'} - E_n)/mc^2 \sim (Z\alpha)^2$ ) by using the identity

$$\int_0^\infty \frac{dk}{1+2k/mc^2} \frac{1}{k+E_{n'} - E_n} = \ell n \frac{mc^2/2}{|E_{n'} - E_n|} + \int_0^\infty \frac{dk}{1+2k/mc^2} \frac{1}{k+E_{n'} - E_n} \frac{E_{n'} - E_n}{mc^2/2}$$

Here the logarithm not only yields the by-now-familiar  $\delta_{\ell 0} \ell n(Z\alpha)^{-2}$  but also an additive constant

$$L_n \doteq \ell n \frac{(Z\alpha)^2 mc^2/2}{|E_{n'} - E_n|} \quad (3)$$

whose value may be calculated from Bethe's NR sum over states. This "Bethe logarithm"  $L_n$  can be shown to be independent of  $Z\alpha$  and turns out to be quite large (-3.0 to -2.7) and nearly independent of  $n$  for S-states and very small (<0.1) for non-S-states. Some values are tabulated at the end of the paper.

The exact result of all 2nd order QED effects may be written as

$$\Delta E_n^{(2)} = \frac{4\alpha(Z\alpha)^4 mc^2}{3\pi n^3} [\delta_{\ell 0} \ell n \frac{1}{(Z\alpha)^2} + B(n) + H(Z\alpha, n)] \quad (4)$$

(Exact)

where the complete  $(Z\alpha)^4$  coefficient is

$$B(n) = L_n + \frac{11}{24} \delta_{\ell 0} + \frac{3}{8} \frac{c_{\ell j}}{2\ell+1} \quad (5)$$

and the complete higher remainder has the behaviour

$$H(Z\alpha) = C_5 Z\alpha + (Z\alpha)^2 [C_{62} \ln^2(Z\alpha)^2 + C_{61} \ln(Z\alpha)^{-2} + G(Z\alpha)]. \quad (6)$$

An infinite sum (such as in Eq. 1) is needed for  $L_n$  and other terms analytic in  $(Z\alpha)^2$  ( $C_{60} = G(0)$ ,  $C_{80}$ , etc.). The non-analytic terms ( $\delta_{\ell_0} \ln \frac{1}{(Z\alpha)^2}$ ,  $C_5$ ,  $C_{62}$ ,  $C_{61}$ ) do not require such an infinite sum, and can use an expansion in powers of the potential, such as

$$\begin{array}{c} \parallel \quad \parallel \quad \parallel \quad \parallel \quad \parallel \\ = \quad + \quad \times \quad + \quad \times \quad + \dots , \\ \parallel \quad \parallel \quad \parallel \quad \parallel \quad \parallel \end{array}$$

and only require a few terms.

Before discussing calculational methods, let us consider the numerical history of the  $2S_1 - 2P_1$  Lamb shift in Hydrogen tabulated on the next page. Here we might point out the alternating periods of agreement and disagreement and the many unexpected changes in both theory and experiment due to error correction and/or accounting for unexpectedly large effects. For example, the 1949 status was seen at the time as a discrepancy because the  $\alpha(Z\alpha)^5$  coefficient was not expected to have the now-well-known large factor of  $2\pi$ . The opposite expectation, a known  $\alpha(Z\alpha)^6 \ln^2(Z\alpha)^2$  term in the direction needed to account for the  $\frac{1}{2}$  Megacycle difference in 1953, caused an assumption of no discrepancy until the 1957 discovery of an error in the 4th order  $g-2$  calculation, whose effect on the Lamb shift reduced the size of the difference but reversed its sign. This was then considered a discrepancy until the complete calculation and independent verification of the  $C_{62}$  and  $C_{61}$  coefficients in 1960-61. The resulting agreement was not left undisturbed, as the first independent measurement<sup>13</sup> cast doubt on the original measurements<sup>12</sup> and on the newly improved calculations<sup>14</sup>, which again (as in 1953) differed by  $\frac{1}{2}$  Megacycle but now included error limits for all calculated and uncalculated terms. Discovery<sup>15</sup> of an error in the "improved"  $\alpha^2(Z\alpha)^4$  calculations restored agreement and further improvements<sup>16</sup> in the calculations and experimental corrections<sup>17,18</sup> and new techniques<sup>19</sup> brought the agreement and its precision down to the next decimal place. As before, this agreement was not left undisturbed, and Mohr's entirely independent calculation<sup>3</sup> cast doubt on the presumed precision of my  $\alpha(Z\alpha)^6$  results<sup>16</sup> and independent measurements<sup>20</sup> cast doubt on their stated accuracies. Again, changes a few times larger than expected uncertainties are being made in the experiments<sup>22</sup> and are apparently necessary in the

calculations. At present, all values agree well within the 0.1 Megacycle accuracy that prevailed for a quarter of a century, and the current discussions<sup>2</sup> are in units of kilocycles.

Table I. Numerical History of the Lamb Shift in Hydrogen

<u>Theory</u>	<u>Experiment</u>
1040 MHz (1947) Bethe's NR calc.	(1947) $1000 \pm 100$ MHz
1051 (1949) $\alpha(Z\alpha)^4$	(1949) $1062 \pm 5$
1057.19 $\pm 0.16$ (1952) $\alpha(Z\alpha)^5\pi$	(1952) $1058.3 \pm 1$ (1953) $1057.77 \pm 0.10$ [Lamb <sup>12</sup> ]
1058.01 $\pm 0.13$ (1957) $\alpha^2$ Mag. Mom. correction	
1057.49 (1960) $\alpha(Z\alpha)^6 \ln^2(Z\alpha)^2$	
1057.77 (1961) $\alpha(Z\alpha)^6 \ln(Z\alpha)^2$	
1057.64 $\pm 0.21$ (1964) $\alpha(Z\alpha)^6$ [Erickson and Yennie <sup>14</sup> ]	(1965) $1058.07 \pm 0.10$ [Robiscoe <sup>13</sup> ]
1057.50 $\pm 0.11$ (1966) $\alpha^2(Z\alpha)^4$	
1057.56 $\pm 0.08$ (1967) $\alpha$ from $2e/h$	(1967) $1057.86 \pm 0.10$ [motional field corrections <sup>17</sup> ]
	(1969) $1057.90 \pm 0.10$ [non-Maxwellian vel. distr. in atomic beam <sup>18</sup> ]
1057.91 $\pm 0.16$ (1970) $\alpha^2(Z\alpha)^4$ correction <sup>15</sup>	
1057.910 $\pm 0.010$ (1971) $\alpha^2(Z\alpha)^4$ exact, $\alpha(Z\alpha)^6$ improved <sup>16,1</sup>	
1057.864 $\pm 0.014$ (1975) [Mohr <sup>3</sup> , extrap. from high Z]	(1975) $1057.893 \pm 0.02$ [Lundeen & Pipkin <sup>19</sup> ]
	(1976) $1057.862 \pm 0.02$ [Andrews & Newton <sup>20</sup> ]
1057.888 $\pm 0.013$ (1976) [larger proton size <sup>21</sup> ]	(1981) $1057.845 \pm 0.009$ [Lundeen & Pipkin <sup>22</sup> ]
	(1981) $1057.8583 \pm 0.0022$ [Sokolov <sup>23</sup> ]

Let us now consider the nature of my calculations<sup>1</sup> that allow the Lamb shift to be calculated for arbitrary states and extended from small  $Z\alpha$ . Peter Mohr's calculations<sup>3</sup> are more accurate at high  $Z$  but have only been done for a couple of states and can be extended from the calculated  $Z$  values only by interpolation or extrapolation; the mathematical form of the calculations do not allow much physical interpretation or modification without repeating the entire calculation. Since our intent here is understanding the physical significance, I will base the remaining discussion of higher order terms on the starting point of Bethe's NR calculation as modified in eq. (1) to match the style of the complete relativistic calculation<sup>14</sup>.

The equivalence of the sum-over-states form in eq. (1) and the operator form (resulting from a NR reduction<sup>14</sup> of the bound-state Green's function formulation) is most directly seen by replacing the energy difference  $E_{n'} - E_n$  in the numerator by a commutator

$$(E_{n'} - E_n) \langle n' | \vec{p} | n \rangle = \langle n' | [H, \vec{p}] | n \rangle = \langle n' | [V, \vec{p}] | n \rangle \quad (7)$$

and the energy in the denominator by an operator acting on the intermediate state as

$$\frac{1}{k + E_{n'} - E_n} |n'\rangle = \frac{1}{k + (p^2/2m + V) - E_n} |n'\rangle. \quad (8)$$

The sum over the complete set of states may then be removed and eq. (1) becomes

$$\begin{aligned} \Delta E_n &= \frac{2\alpha}{3\pi m^2} \int_0^\infty \frac{dk}{1 + 2k/mc^2} \langle n | \vec{p} \cdot \frac{1}{k + p^2/2m + V - E_n} [V, \vec{p}] | n \rangle \\ &= \frac{2\alpha}{3\pi} \int_0^\infty \frac{dx}{1+x} \langle n | \vec{p} \cdot \frac{1}{xm^2 + p^2 + 2mV + (2\alpha mc/n)^2} [V, \vec{p}] | n \rangle \quad (9) \end{aligned}$$

where  $x = 2k/mc^2$  is the photon energy in units of the electron rest energy, and  $E_n = -(Z\alpha)^2 mc^2 / 2n^2$  is the electron's energy in the bound state  $|n\rangle$ . The result can now be recognized as the entire leading part  $\Delta E(L)$  coming from the relativistic formulation<sup>14</sup> except that the  $x$  there is an integration variable used to combine the photon propagator with the bound electron propagator before integrating over photon four-momenta. In either case, infra-red

(IR) behaviour corresponds to the limit  $x \rightarrow 0$ . The other difference is in my arbitrary choice of convergence factor  $1/(1+2k/mc^2) = 1/(1+x)$  as simpler than the exact

$$\frac{1}{1+x} + x \int_0^1 du \frac{u}{4} \frac{6-3u-8u^2}{(1+ux)^2} = \frac{1}{1+x} + \frac{7x^2}{40} + O(x^3). \quad (10)$$

These have the same IR and near-IR behaviour, and the differences in results are small, such as the  $11/24$  in eq. (5). It should be understood that my calculations<sup>1</sup> include the exact form, but that, except for minor technical details, the simpler form  $1/(1+x)$  used in our examples contains all the relevant physical aspects of the calculation.

The separation of the lowest order operator is as in eq. (2), yielding

$$\begin{aligned} \frac{2\alpha}{3\pi} \langle n | \vec{p} \cdot \vec{\ell} n \frac{(mc)^2}{p^2 + 2mV + (Z\alpha mc/n)^2} \vec{z} [V, \vec{p}] | n \rangle \\ = \frac{4\alpha (Z\alpha)^4 mc^2}{3\pi n^3} \{ \ell n (Z\alpha)^{-2} + L_n \}. \end{aligned} \quad (11)$$

The operator formalism has not eliminated the need for an infinite sum but has only replaced a sum-over-states with an expression which can be evaluated as an infinite series in powers of the potential  $V$ . The advantage is that the leading terms can be evaluated directly in momentum space and contain the dominant  $Z\alpha$  behaviour. For example, the leading term of eq. (11) yields

$$\begin{aligned} \frac{8}{\pi} \int_0^\infty \frac{Z\alpha mc}{[p^2 + (Z\alpha mc)^2]^2} \ell n \frac{(mc)^2}{p^2 + (Z\alpha mc)^2} [1 - \frac{\tan^{-1}(p/Z\alpha mc)}{p/Z\alpha mc}] \\ = \ell n (Z\alpha)^{-2} - 2 - 2\ell n 2. \end{aligned} \quad (12)$$

for the ground state, and thus not only contains the exact  $\ell n (Z\alpha)^{-2}$  but also a constant,  $-2 - 2\ell n 2 = -3.4$ , which is the dominant part of the exact  $L_1 = -3.0$ . This technique for the lowest order operator is only an example (since the Bethe log has been calculated to high precision by a sum over states) but is the method used for all the higher order operators.

If we take the complete higher order remainder in eq. (2) and make the same operator replacements as in eq. (7) and (8), we obtain

$$\begin{aligned}\Delta E_n(\text{rem.}) &= \frac{4\alpha}{3\pi} \int_0^\infty \frac{dk}{1+2k/mc^2} \sum_n \frac{\langle nl \vec{p} | n' \rangle \cdot \langle n' | \vec{p} | n \rangle}{k+E_n - E_{n'}} \frac{(E_n - E_{n'})^2}{m^3} \\ &= \frac{4\alpha}{3\pi m} \int_0^\infty \frac{dx}{1+x} \langle nl | \vec{p}, v \rangle \cdot \frac{1}{xm^2 + p^2 + 2mV + (Z\alpha mc/n)^2} \langle v, \vec{p} | n \rangle. \quad (13)\end{aligned}$$

The leading term in the  $V$  expansion here is  $4\alpha(Z\alpha)^4 mc^2 / 3\pi n^3$  times

$$\begin{aligned}&\int_0^\infty \frac{dx}{1+x} \frac{4}{\pi} \int_0^\infty \frac{Z\alpha mc dp}{xm^2 + p^2 + (Z\alpha mc)^2} [1 - \frac{\tan^{-1}(p/Z\alpha mc)}{p/Z\alpha mc}]^2 \\ &= \frac{8Z\alpha \cos^{-1} Z\alpha}{\sqrt{1-(Z\alpha)^2}} - \frac{8(Z\alpha)^2}{1-(Z\alpha)^2} [(\ln Z\alpha)^2 + (\cos^{-1} Z\alpha)^2] + 2\Phi_3(Z\alpha) \quad (14)\end{aligned}$$

for the ground state;  $\Phi_3$  is a variety of tri-logarithmic function. The original calculation<sup>14</sup> only yielded the small  $Z\alpha$  behaviour

$$\begin{aligned}[4\pi Z\alpha - 8(Z\alpha)^2] - 2(Z\alpha)^2 [\ln^2(Z\alpha)^2 + \pi^2] \\ + (Z\alpha)^2 [8\ln 2 \ln(Z\alpha)^{-2} - 2\pi^2/3 - 8\ln^2 2] + 0(Z\alpha)^3 \quad (14a)\end{aligned}$$

and noted that the coefficients, like those in eq. (12), were either exact or the dominant part of known coefficients and therefore the large negative  $(Z\alpha)^2$  coefficient could also be expected to be dominant. The improved calculation<sup>16</sup> noted that each of the terms in eq. (14), although apparently singular at  $Z\alpha = 1$ , is quite well behaved (analytic in fact) and their sum should be expected to yield the dominant part of the exact result even for large  $Z$ .

The following technique was used to approximate the remainder of the  $V$  expansion for arbitrary  $Z\alpha$ . It is well-known that the  $Z\alpha$  dependence can be factored out of the NR wave function if we use a dimensionless momentum  $t = p/(Z\alpha mc/n)$ . For example, the momentum integral in eq. (14) can be rewritten as

$$I_0(y) = \frac{4}{\pi} \int_0^\infty \frac{dt}{1+y^2 t^2} [1 - \frac{\tan^{-1} t}{t}]^2 \quad (15a)$$

$$= \frac{2}{y} - 4\ln \frac{1+y}{y} + 4\ln 2 - 2y[\frac{\pi^2}{12} + \text{Li}_2(\frac{1-y}{1+y})] \quad (15b)$$

and yields a function (in terms of a dilogarithm  $\text{Li}_2$ ) of the single variable

$$y^2 = \frac{(Z\alpha)^2}{x^2 + (Z\alpha)^2}, \quad (16)$$

where  $0 \leq y \leq 1$ . If we use this  $y$  as an integration variable in place of  $x$ , eq. (14) becomes simply

$$\Phi_0(Z\alpha) = (Z\alpha)^2 \int_0^1 \frac{dy^2 I_0(y)}{y^2 + (1-y^2)(Z\alpha)^2}. \quad (17)$$

The same set of transformations will work for all remaining terms in the  $V$  expansion and will yield a  $Z\alpha$  dependence given by

$$\Phi_+(Z\alpha) = (Z\alpha)^2 \int_0^1 \frac{dy^2 I_+(y)}{y^2 + (1-y^2)(Z\alpha)^2} \quad (18)$$

where  $I_+(y)$  is a function which remains to be determined. The lower end point  $I_+(0) = 4\ln 2 - 2$  is entirely due to the next term in the  $V$  expansion, and yields a  $C_{61}$  contribution from

$$\Phi(Z\alpha) \xrightarrow[Z\alpha \rightarrow 0]{} (Z\alpha)^2 [I(0)\ln(Z\alpha)^2 + \int_0^1 dy^2 \frac{I(y) - I(0)}{y^2}], \quad (19)$$

a general identity for any function with finite  $I(0)$ . It is apparent that all terms in the expansion would be needed for the entire  $C_{60}$  contribution from  $\int_0^1 dy^2 [I_+ - I_+(0)]/y^2$ , and the contribution from any one term would require a difficult multiple momentum integration.

However, we can deduce the upper end point  $I_+(1) = \frac{\pi^2}{6} - \frac{3}{2}$  from the high  $Z\alpha$  limit

$$\Phi(Z\alpha) \xrightarrow[Z\alpha \rightarrow \infty]{} I(1)\ln(Z\alpha)^2 + \int_0^1 dy \frac{I(y) - I(1)}{1-y^2} \quad (20)$$

and can use it (and the deduced value of the integral  $\int [I_+ - I_+(1)]/[1-y^2]$ ) to determine a quadratic (in  $y^2$ ) approximation

$$I_+(y) \approx (1-y^2)I_+(0) + y^2I_+(1) + 2y^2(1-y^2)C. \quad (21)$$

The "trick" that makes these upper end deductions possible is simply to note that the entire (lower and higher order) operator expression (9) for infinite  $Z\alpha$  is of order  $\alpha(Z\alpha)^2 \ln(Z\alpha)^2$  and, therefore, the corresponding coefficient in eq. (9),

$$\ln(Z\alpha)^{-2} + B(n) + H(Z\alpha, n) \xrightarrow{Z\alpha \rightarrow \infty} 0$$

$$= [-1 + 2I_0(1) + 2I_+(1)]\ln(Z\alpha)^2 + [B + 2 \int_0^1 dy^2 \frac{I_0 + I_+ - I_0(1) - I_+(1)}{1-y^2}], \quad (22)$$

vanishes for infinite  $Z\alpha$ . Thus we deduce  $I_+(1) = \frac{1}{2} - I_0(1)$  and can choose  $C$  in eq. (21) to yield the deduced integral  $\int(I_+ - I_+(1))/[1-y^2]$ . Substitution of the simple approximation (21) into the simple integral (18) now yields a closed form approximation for  $\Phi_+(Z\alpha)$  that has the correct  $Z\alpha \rightarrow 0$  and  $Z\alpha \rightarrow \infty$  behavior.

Similar deductions and approximations can be made for the other parts of eq. (10) and for other large higher order terms not quite of the same NR form as eq. (1). For all other terms contributing to  $C_5$ ,  $C_{62}$ , or  $C_{61}$ , approximations are used that have the exact known  $Z\alpha \rightarrow 0$  behavior and are arbitrarily chosen to behave "reasonably" (that is, like other terms having the same small  $Z\alpha$  behavior) for larger  $Z\alpha$ . The results have been reasonably confirmed by Mohr's independent calculations<sup>3</sup> from  $Z=10$  to 100 (and by various measurements). In the table on the following page, our values of the  $G(Z\alpha)$  remainder for  $Z=10$  are given for a few states ( $1S$ ,  $2S_1$ ,  $2P_1$ ) and the  $n$ -dependent terms (the Bethe log, the coefficient  $C_{61}$  and my remainder  $G$ ) are tabulated for  $n < 6$ . Complete results are given in reference 1.

I should comment on omissions and future possibilities. (1) There are a number of terms of order  $(Z\alpha)^6$  that do not contribute to any lower order and therefore are not included. However, like the  $(Z\alpha)^4$  coefficient  $11/24$  in eq. (5), I would expect their net contribution to  $C_{60}$  to be smaller than  $\pm 1/2$ . (2) The relativistic corrections to the wave functions (and some of the operators) contribute to  $C_{62}$  and their  $C_{61}$  contributions, although not especially small individually, mostly cancel and leave a small net contribution. I have assumed they have a similarly small net contribution to  $G(Z\alpha)$  except for some calculated parts explicitly associated with the  $C_{62}$  contribution. (3) I would like to explore the possibility of using  $Z\alpha \approx 1$  behavior to tie down the relativistic corrections (as well as other terms), somewhat like the use of  $Z\alpha \rightarrow \infty$  behaviour in eq. (22). There are various simplifications at  $Z\alpha=1$  that encourage this possibility. This would turn out, among other things, to be a direct assault on the question of the size of QED effects as  $Z\alpha \rightarrow 1$  for pure Coulomb fields. There is hope that the answers might shed further light on QED in strong fields due to large nuclei with  $Z > 137$ .

Table II. State dependence of the Bethe log and other terms

n	$L_{nS}$	$L_{nP}$	$C_{61}$	$G_S^E(10\alpha)$	$G_S^M(10\alpha)$	$G_P^E(10\alpha)$	$G_P^M(10\alpha)$
1	-2.98		3.965	-17.5	-20.0		
2	-2.81	0.030	4.348	-16.4	-20.7	-0.40	-0.54
3	-2.77	0.038	4.31	-16.2		-0.46	
4	-2.75	0.041	4.26	-16.1		-0.48	
5	-2.74	0.044	4.22	-16.0		-0.50	

## REFERENCES

1. Glen W. Erickson, J. Phys. Chem. Ref. Data 6, 831-869 (1977).
2. Second International Conference on Precision Measurement and Fundamental Constants, 8-12 June 1981, National Bureau of Standards, Gaithersburg, Maryland USA.
3. Peter J. Mohr, Beam-Foil Spectroscopy, edited by I.A. Sellin and D.J. Pegg (Plenum, New York, 1976).
4. M.H. Levine and R. Roskies, paper B.14, ref. 2.
5. T. Kinoshita and W.B. Lindquist, paper B.15, ref. 2.
6. R.S. Van Dyck, Jr., P.B. Schwinberg, and H.G. Dehmelt, Bull. Am. Phys. Soc. 24, 758 (1979).
7. E.R. Williams and P.T. Olsen, Phys. Rev. Lett. 42, 1575 (1979).
8. S.D. Drell and J.D. Sullivan, Phys. Rev. 154, 1477 (1967).
9. J.D. Bjorken and S.D. Drell, Relativistic Quantum Mechanics, McGraw-Hill Book Co., New York (1964).
10. Theodore A. Welton, Phys. Rev. 74, 1157 (1948).
11. H.A. Bethe, Phys. Rev. 72, 339 (1947).
12. Sol Triebwasser, Edward S. Dayhoff, and Willis E. Lamb, Jr., Phys. Rev. 89, 98 (1953).
13. R.T. Robiscoe, Phys. Rev. 138, A22 (1965).
14. Glen W. Erickson and Donald R. Yennie, Ann. Phys. (N.Y.) 35, 271, 447 (1965).
15. Thomas Appelquist and Stanley J. Brodsky, Phys. Rev. Lett. 24, 562 (1970).
16. Glen W. Erickson, Phys. Rev. Lett. 27, 780 (1971).
17. R.T. Robiscoe, Phys. Rev. 168, 4 (1968).
18. R.T. Robiscoe and T.W. Shyn, Phys. Rev. Lett. 24, 559 (1970).
19. S.R. Lundein and F.M. Pipkin, Phys. Rev. Lett. 34, 1368 (1975).
20. D.A. Andrews and G. Newton, Phys. Rev. Lett. 37, 1254 (1976).
21. Peter J. Mohr, Fifth International Conference on Atomic Physics, Berkeley, 1976.
22. S.R. Lundein and F.M. Pipkin, Phys. Rev. Lett. 46, 232 (1981).
23. Yu. L. Sokolov, paper B.3 (as modified from the preliminary abstract), ref. 2.

## QUANTUM ELECTRODYNAMICS OF STRONG FIELDS

Berndt Müller

Institut für Theoretische Physik  
der Johann Wolfgang Goethe-Universität  
Frankfurt am Main, Germany

### INTRODUCTION

Our ability to calculate and predict the behaviour of charged particles in weak electromagnetic fields is primarily due to the relative smallness of the fine-structure constant  $\alpha$ . However, the atomic nucleus with  $Z$  protons can exercise a much stronger electromagnetic force on the surrounding electrons than could be described in perturbation theory, and we can foresee that the new expansion parameter  $(Z\alpha)$  can quite easily be of the order of unity. In these lectures we review the new phenomena that emerge for sufficiently large values of  $(Z\alpha)$  (for other reviews see refs. 1-4). A Discussion of the experimental tests of the theory that are presently underway is contained in the article by J. Reinhardt et al. in this volume, in the following referred to as [II].

A better measure of the strength of the electromagnetic interaction between electrons and nuclei in atoms is the energy that is required to remove an electron from its atomic orbit, as this does not depend on the details of the interaction. This ionization energy  $E_I$ , is, in the case of a hydrogen atom, about 13.6 eV, which is small compared with the electron mass,  $m_e = 511$  keV. However, as the number  $Z$  of protons in the nucleus increases, the ionization energy of the most tightly bound 1s electron increases initially as  $Z^2$ , and then even faster owing to relativistic effects. Thus in the case of a heavy atom such as uranium, the energy necessary to remove the most tightly bound 1s electron from the orbit around the atomic nucleus is a sizable fraction (about 20%) of the rest mass. If the 1s electron could be bound by the equivalent of, or even more than, its rest mass (this happens at  $Z \sim 150$ ), it would mean that such a (superheavy) ion would have the same or even less

weight with an electron in the orbit.

Since the heaviest atomic nucleus artificially created by man has 107 protons, it would seem that such considerations are largely academic. It may well be that this belief has so long delayed the development of the theory of strongly bound particles. However, two developments in the last decade have created interest in this subject. It has been suggested [5] that radioactive superheavy nuclei containing about 164 protons could be sufficiently long-lived to allow for a study of the atoms formed by them. In connection with investigations [6-8] of the electromagnetic properties of such superheavy elements, it has been realized [9,10] that in collisions of heavy ions tightly bound electrons can feel the combined attraction of the two nuclei. One may view this situation as if the electron would move in the combined Coulomb field corresponding to a superheavy nucleus of charge  $2Z$ . Considering, e.g. the case of a uranium-uranium collision, we find that the electrons experience attractive forces similar to those of a superheavy nucleus with 184 protons. Thus it seems that we have reason to try to understand the physics of strong binding.

The questions raised here are related to the Klein paradox: Shortly after the discovery of the Dirac equation, Klein [11] noted that a sufficiently high electromagnetic barrier shows abnormally large reflection coefficients that may even result in a larger number of reflected than incident particles. Only after solution of the problem of supercritical binding can this apparent paradox be fully resolved. Why do we call a Coulomb potential that is capable of binding an electron by more than  $2m_e$ , supercritical? To answer this question let us first consider the pair production process: normally, the minimum energy required in such a process is  $2m_e$ , but in the presence of a nucleus it is possible that we do not require the full energy in order to make an electron, since it can be bound to the nucleus. Thus the threshold for pair conversion of a  $\gamma$ -ray to an  $e^+e^-$  pair in the presence of a nucleus is

$$E_{\text{Min}}^Y = m_e + \epsilon \quad (1.1)$$

where  $\epsilon$  is the total energy of a bound K-shell electron (including its rest mass). Of course, this process is only possible if the K-shell is not already occupied by other electrons.

From the above energy balance we recognize that when  $\epsilon$  approaches  $-m_e$ , the minimum energy  $E_{\text{Min}}^Y$  required to create an  $e^+e^-$  pair approaches zero. At this critical point the energy of the bare nucleus is equal to the energy of the atom with a filled  $1s$  electron state and a free positron. And for supercritical potentials ( $\epsilon < -m_e$ ) we conclude that the energy of an ionized atom (without the  $1s$  electron, that is) is higher than the energy of an atom

and a free positron. Thus an ionized supercritical atom cannot be a stable ground state (vacuum state) even if left undisturbed from outside; the supercritical atom will spontaneously emit a positron, keeping in its vicinity the equivalent of negative charge often called real vacuum polarization. The bare nucleus, called neutral vacuum (vacuum state of the electron-positron field), is not a state of lowest energy -- the new state of lower energy, called the charged vacuum [12,13], is the nucleus surrounded by the real vacuum polarization charge. In this paragraph we have used the word 'vacuum' in the sense that the nucleus is a spectator, rather than a dynamical part of the system.

It has been suggested [7] that for a strong field with somewhat less than the critical field strength, it should be possible to regard a vacancy in the  $1s$  state as a bound positron state. Taking this view the appearance of a positron at infinity when the potential  $V$  becomes supercritical is viewed simply as the delocalization of a bound positron state. Thus we are again led to the conclusion that as  $V$  is increased adiabatically above  $V_{cr}$  spontaneous positron production will occur if the  $1s$  state is empty.

The following experimentally observable effect emerges as a consequence of the supercritical binding: in collisions of heavy ions an empty  $1s_0$  state can be bound by more than  $2m_e$ . Subsequently, a positron is emitted spontaneously; when the heavy ions separate again, the previously empty  $1s_0$  state is occupied by an electron. Of course, the actual physical situation is not that simple, since the heavy ion collision is a time-dependent process; thus there may not always be enough time to emit a positron. Furthermore, other QED processes may contribute. For example, we may expect direct pair production by the time-dependence of the electromagnetic potentials in the collision.

An elaborate effort of the Frankfurt group in recent years has led to detailed calculations [14-16] of the theoretically anticipated effects, in particular positrons emitted in heavy ion collisions with  $Z_1 + Z_2 > Z_{cr} \sim 173$ . This has led to a series of experiments described. Particular scepticism was directed towards these measurements, since a vacancy must be present near the colliding nuclei in order to obtain an observable effect. Thus a major effort has been necessary to understand the mechanisms of inner-shell ionization in heavy ion scattering; a whole new field of atomic physics has emerged. We will briefly enter into the discussion of these phenomena, as far as it is directly relevant to our present discussion.

While the current experimental information about pair production in heavy-ion collisions [17-19] is compatible with the predictions of strong field QED, the novel mechanism of spontaneous pair production has not yet been conclusively identified

due to the experimental difficulties. However, more recently new ideas [20] have emerged that are directed towards utilizing a prolonged time that heavy ions pass close to each other: it is hoped that under certain kinematic conditions due to nuclear interactions the colliding nuclei could stick to each other long enough to permit the observation of a clear peak in the positron spectrum that is characteristic of the neutral vacuum decay in supercritical fields. For theoretical details and a comparison with present experimental data cf. [II].

Let us now turn to a more academic question: What happens when the nuclear charge is further increased or if the nucleus is compressed to a point source? Apparently, more and more orbits will become bound beyond  $2m_e$  and the charge of the vacuum will increase rapidly. However, it is clear that the vacuum charge cannot grow faster than the nuclear charge because then the potential would soon become subcritical. In fact, it can be demonstrated that the vacuum charge density will increase at a pace roughly equal to the increase of the nuclear charge. This neutralization of external (nuclear) charge distributions by 'sparking' of the vacuum means that a large super-nucleus would not be surrounded by a large long-range Coulomb field. In much the same way, it is found that the apparent charge of a nucleus with  $Z > 137$  would be screened down to 137 if the nucleus could be compressed to a point. In fact, the vacuum charge density turns out to shrink in scale with the nuclear radius, so that the compression ultimately results in a point-like charge just at the threshold of criticality.

Two obvious fields of application are strong gravitational potentials and the strong interactions. While the physics of strong Yang-Mills fields will be discussed in the lectures of J. Rafelski [I], we only mention here the vacuum instabilities in strong gravitational and torsion fields. Two of the most interesting phenomena are the spontaneous discharge of charged black holes and the vacuum state with spin in the ECSK-theory of gravitation [21]. Other important applications pertain to intrinsically time-dependent field configurations, e.g. Hawking's black-hole evaporation, etc. [22,23]: For a discussion of these phenomena we refer to the lectures of P. Candelas at this conference.

#### SINGLE-PARTICLE THEORY OF SUPERCRITICAL FIELDS

In principle, the development of quantum electrodynamics of strong fields could have proceeded as soon as quantum field theory had been formulated about 40 years ago. The main obstacle was the fact that the solution of the Dirac equation (and also Klein Gordon equation) had not been understood for supercritical potentials. While already Heisenberg and Euler [24] and also Weisskopf [25] had proposed in the 1930's that strong external electric fields would lead to spontaneous pair creation and the subject had been

picked up by several other authors thereafter [7,8, 26-31] the crucial technical step has been the recognition [13, 32, 33] that the spectrum of the Dirac equation in supercritical fields contains a resonance in the negative energy continuum - continuously connected with the bound particle solutions as the strength of the potential decreases. This discovery was made in the years 1971-72 independently by the Frankfurt group [32, 33] and by Zel'dovich and Popov [13] in the Soviet Union. Without this resonance the spectrum is incomplete, and a consistent quantization of the electron field in the supercritical external potential is not possible. Only in a consistent theory that treats the  $(Z\alpha)$  effects correctly can further QED effects in order  $\alpha$ , which are naturally also present, be considered. However they have been found to be relatively unimportant, and we shall refer to the lectures of M. Gyulassy and P. Mohr at this conference for details. The characteristic properties of quantum electrodynamics of strong fields can be derived by considering only effects in order  $(Z\alpha)$ .

To describe electrons in an external electromagnetic field we use the Dirac equation for spin 1/2 particles:

$$[\gamma^\mu (p_\mu - eA_\mu) - m] \Psi(x) = 0, \quad (2.1)$$

where the four-component vector potential  $A_\mu$  is introduced by minimal coupling. For stationary states in a static electric field,  $A_0 = V(\vec{r})$ , the eigenvalue problem is:

$$H_D \Psi_n(\vec{r}) \equiv (\vec{\alpha} \cdot \vec{p} + \beta m + V(\vec{r})) \Psi_n(\vec{r}) = E_n \Psi_n(\vec{r}). \quad (2.2)$$

In the following we restrict to spherically symmetric potentials,  $V_0(r)$ , where the wavefunction has good angular momentum:

$$\Psi_{K\mu}(\vec{r}) = \begin{cases} g_K(r) \chi_K^\mu \\ i f_K(r) \chi_{-K}^\mu \end{cases} . \quad (2.3)$$

$g_K(r)$  and  $f_K(r)$  are the radial parts of the 'large' and 'small' components, respectively, and the  $\chi_K^\mu$  are the spinor spherical harmonics. The radial equations

$$\left( \frac{d}{dr} + \frac{K+1}{r} \right) g_K - (E + m - V_0(r)) f_K = 0 \quad (2.4)$$

$$\left( \frac{d}{dr} - \frac{K-1}{r} \right) f_K + (E - m - V_0(r)) g_K = 0$$

can be solved analytically for various simple potentials, e.g. for the point nucleus  $V_0(r) = -Z\alpha/r$ . The energy eigenvalues are known as Sommerfeld fine-structure formula:

$$E = m \left[ 1 + \left( \frac{Z\alpha}{n - |K| + \sqrt{K^2 + (Z\alpha)^2}} \right)^2 \right]^{-1/2}, \quad n=1,2,\dots \quad (2.5)$$

which exhibits a bifurcation singularity when  $(Z\alpha) \rightarrow |\kappa|$ :

$$f_j = \frac{1}{2}(r), \quad g_j = \frac{1}{2}(r) \sim r^{\sqrt{1-(Z\alpha)^2}} \quad \overline{(Z\alpha)} > 1 \quad r^{\pm i\sqrt{(Z\alpha)^2-1}}$$

Additional conditions are required to find the selfadjoint extension of the Hamilton operator  $H_D$ .

We therefore turn to the investigation of potentials that are due to the charge distribution of finite size nuclei:

$$V_0(r) = \begin{cases} -\frac{3}{2} \frac{Z\alpha}{R_n} \left(1 - \frac{r^2}{3R_n^2}\right) & : 0 \leq r \leq R_n \\ -\frac{Z\alpha}{r} & : R_n < r < \infty \end{cases} \quad (2.6)$$

Most of the recent calculations have relied on numerical integration techniques both inside and outside the nucleus of Eq. (9), although in the special case, Eq. (6), one can proceed further analytically [27]. In order to include also the effect of electron-electron interaction, Hartree-Fock-Slater calculations have been performed. Results for the energy eigenvalues are shown in Fig. 1. The eigenvalues decrease monotonically as the charge increases. None of the eigenvalues or the wave functions exhibit any unusual behaviour at  $Z\alpha = 1$ . The points at which the levels join the lower continuum are well isolated. The critical value of  $Z = Z^{cr}$  is  $\sim 170$ , where the  $1s$  level joins the lower continuum. The  $2p_{1/2}$  level joins the lower continuum at about  $Z = 183$ . The exact location of  $Z^{cr}$  is an important question for the experimental verification of the theory.

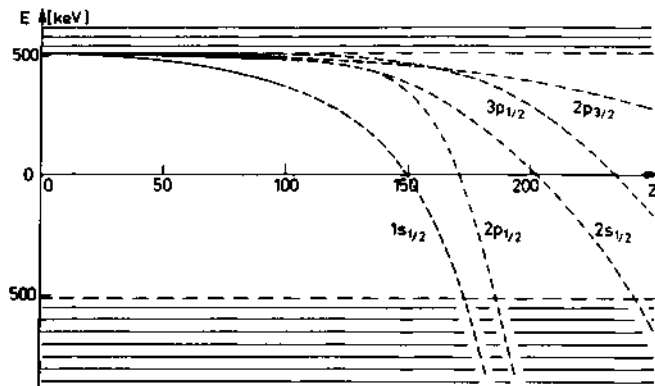


Fig. 1. The energies of the lowest atomic states versus the nuclear charge  $Z$ . Solid lines give the experimentally known region, dashed lines represent Hartree-Fock-Slater calculations.

To describe the supercritical atoms when the nuclear charge exceeds the critical value  $Z_{cr}$  and the  $1s_{1/2}$  state becomes degenerate with the negative-energy continuum we follow the approximate treatment developed in [32, 33] that makes use of Fano's method of treating auto-ionizing states [34]. We search for bound states of the Hamiltonian  $H_D$ , Eq. (2) with  $V(r;Z) \equiv Z \cdot U(r;Z)$ . The quantity  $U(r;Z)$  is depending on  $Z$  only slowly via the  $Z$ -N-dependent radius of the nuclear charge distribution. Within the range of atomic nuclei considered by us ( $170 < Z < 200$ ) this dependence is very weak and may initially be omitted for convenience:

$$V(r;Z) = Z \cdot U(r) . \quad (2.7)$$

We now make use of the fact that we know the solution to our problem for  $Z = Z_{cr} \approx 170$  and diagonalize  $H(Z=Z_{cr}+Z')$  in the basis of eigenstates given by  $H(Z_{cr})$ . Let  $|\phi\rangle$  be the  $1s$  bound state eigenfunction for  $Z = Z_{cr}$ , i.e.

$$H_D(Z_{cr}) |\phi\rangle = E_0 |\phi\rangle \approx -m |\phi\rangle \quad (2.8)$$

and  $|\psi_E\rangle$  be the  $s$ -continuum wave functions normalized to energy delta-functions:

$$H_D(Z_{cr}) |\psi_E\rangle = E |\psi_E\rangle , \quad E < -m . \quad (2.9)$$

$|\phi\rangle$  and the  $|\psi_E\rangle$  serve as a truncated ("reduced") basis for our diagonalization procedure. In doing so we neglect the small contribution from the higher bound  $ns$  states ( $n > 1$ ) which are widely separated from the  $1s$  bound state. We will need the matrix elements of  $H(Z_{cr}+Z')$  in our truncated basis

$$\langle \phi | H_D(Z_{cr}+Z') | \phi \rangle = E_0 + Z' \langle \phi | U | \phi \rangle \approx E_0 + \Delta E_0 \quad (2.10)$$

$$\langle \psi_E | H_D(Z_{cr}+Z') | \phi \rangle = Z' \langle \psi_E | U | \phi \rangle \approx V_E \quad (2.11)$$

$$\langle \psi_{E''} | H_D(Z_{cr}+Z') | \psi_{E'} \rangle = \approx E' \delta(E''-E') + Z' U_{E''E'} . \quad (2.12)$$

The matrix elements  $U_{E''E'}$  describe the rearrangement of the continuum states under the additional potential  $U(r)$ . For small  $Z'$  this effect may be neglected since its influence upon the  $1s$  bound state of second order. For large  $Z'$  the continuum states may be prediagonalized by constructing the solutions of the projected eigenvalue problem

$$P H_D(Z_{cr}+Z') P |\tilde{\psi}_E\rangle = E |\tilde{\psi}_E\rangle \quad (2.13)$$

where  $P=1-|\phi\rangle\langle\phi|$  is the operator that projects out the critical  $1s$ -state. For this continuum the matrix elements  $U_{E''E'}$  vanish identically. The projection method which is based on work in nuclear physics [35] has been extensively investigated by

J. Reinhardt [36] (see also II).

The aim is to find  $|\Psi_E\rangle$ , a continuum solution to the Dirac equation for  $Z > Z_{cr}$ . We may expand  $|\Psi_E\rangle$  within the space spanned by the truncated basis:

$$|\Psi_E\rangle = a(E)|\phi\rangle + \int_{|E'|>m} b_{E'}(E)|\psi_{E'}\rangle dE' \quad (2.14)$$

We are mainly interested in the effects on the bound state  $|\phi\rangle$  finding:

$$|a(E)|^2 = \frac{|v_E|^2}{[E - (E_o + \Delta E_o) - F(E)]^2 + \pi^2 |v_E|^4} \quad (2.15)$$

where  $F(E)$  is the principal value integral

$$F(E) = P \int_{|E'|>m} dE' \frac{|v_{E'}|^2}{E - E'} \quad (2.16)$$

The quantity  $|a(E)|^2$  is the probability that the 1s-electron bound in  $|\phi\rangle$  is embedded in  $|\Psi_E\rangle$  as the additional charge  $Z'$  is "switched on". The quantity  $|a(E)|^2$  has an obvious resonance behaviour. If  $v_E$  does not depend too strongly on the energy  $E$ , we may neglect  $F(E)$  with respect to  $\Delta E_o$  getting

$$\Gamma = 2\pi |v_{E_o + \Delta E_o}|^2 \quad (2.17)$$

Then, indeed, a Breit-Wigner shape is found with the resonance of width  $\Gamma$  peaked around  $E_o + \Delta E_o$ .

Since we have chosen  $E_o \approx -m$ ,  $\Delta E_o = -Z'\delta$  describes the energy shift of the bound 1s-state due to the additional charge  $Z'$ . The width  $\Gamma$  of the resonance is  $\Gamma = Z'^2 \gamma$ . Calculations [33] show that except very close to threshold

$$\delta \approx 30 \text{ KeV} , \quad \gamma \approx 0.05 \text{ KeV} \quad (2.18)$$

Thus we may explicitly show the  $Z'$ -dependence of Eq. (24):

$$|a(E)|^2 = \frac{1}{2\pi} \frac{Z'^2 \gamma}{[(E+m) + Z'\delta]^2 + \frac{1}{4} Z'^4 \gamma^2} , \quad Z' \geq 3 \quad (2.19)$$

From Eq. (19) we learn that the bound state  $|\phi\rangle$  "dives" into the negative energy continuum for  $Z > Z_{cr}$  proportional to  $Z' = (Z - Z_{cr})$ . At the same time it obtains a width  $\Gamma$  within the negative energy continuum that grows like  $Z'^2 = (Z - Z_{cr})^2$ .

Let us summarize. As the proton number of a nucleus with  $Z < Z_{cr}$  is steadily increased, the energy of K-shell electrons is decreased until at  $Z = Z_{cr}$  it reaches  $-m_e$ . During this process the

spatial extension of the K-shell electron charge distribution is also shrinking. When  $Z$  grows beyond  $Z_{cr}$  the bound 1s-state ceases to exist. But this does not mean that the K-shell electron cloud becomes delocalized. Indeed, according to Eq. (21) the bound state  $|\phi\rangle$  is shared by the negative energy continuum states in a typical resonance manner over a certain range of energy by Eq. (15). Due to the bound state admixture the negative energy continuum wavefunctions become strongly distorted around the nucleus. This additional distortion of the negative energy continuum due to the bound state can be called real charged vacuum polarization [12], because it is caused by a real electron state which joined the "ordinary vacuum states", i.e. the negative energy continuum. The charge densities induced by all the continuum states superpose to form an electron cloud of K-shell shape. This electron cloud created by the collective behaviour of all continuum states contains the charge of two electrons, since the total probability for finding the 1s-electron state  $|\phi\rangle$  in any of the continuum states is:

$$\int_{-\infty}^{-m_e c^2} dE |a(E)|^2 = 1. \quad (2.20)$$

Thus, the K-electron cloud remains localized in  $r$ -space.

We emphasize the surprising fact that it obtains an energy width  $\Gamma$ . This can be illustrated in the following way: Consider the Dirac equation with the cut-off Coulomb potential inside a finite sphere of radius  $a$ . Certain boundary conditions on the sphere have to be fulfilled. In this way the continuum is discretized, see Fig. 2. Fig. 2a shows the situation at  $Z=Z_{cr}$ , i.e. before diving. After diving (Fig. 2b) the 1s-bound state has joined the lower continuum and is spread over it. One sees that the K-shell electrons still exist, but are spread out energetically. Therefore a  $\gamma$ -absorption line from a 1s-2p-transition would acquire an additional width, the spreading

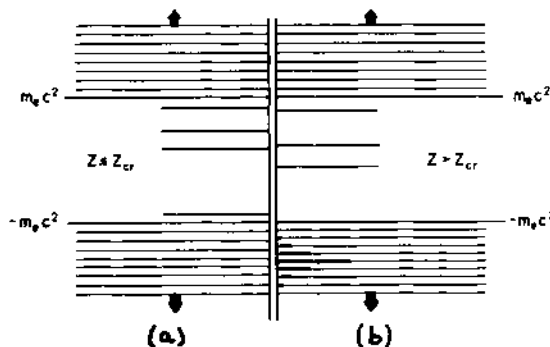


Fig. 2. Spreading of the bound state (solid line) over the negative energy continuum states (weak lines). Spectrum a) before and b) after diving.

width. The situation is different when the 1s-bound state is empty while  $Z$  is increased beyond  $Z_{cr}$ . Then - on grounds of charge conservation - one of the resulting continuum states  $|\Psi_E\rangle$  has to be empty - , i.e. a positron escapes. The kinetic energy of the escaping positron is not sharp, but has a Breit-Wigner type spectrum given by Eq. (24). Thus the width  $\Gamma$  is also the positron escape width. Of course, the positron-escape-process can be reserved. If positron scattering from nuclei with  $Z > Z_{cr}$  were observed, the scattering cross-section would have a resonance at  $E = |\Delta E|$  with a width  $\Gamma$ . The phase shift of the  $s_{1/2}$ -positron waves should go through  $\pi/2$  at this energy.

Returning now to the discussion of positron spectra we note that the probability per unit time for emission of positrons in the energy interval  $dE$  is given by Fermi's "Golden Rule":

$$p(E)dE = \frac{2\pi}{\hbar} |\langle \phi | H | \Psi_E \rangle|^2 \rho(E)dE = \frac{\frac{1}{2\pi} \Gamma_E dE}{[E - (E_0 + \Delta E_0)]^2 + \Gamma_E^2/4} \cdot \frac{\Gamma_E}{\hbar} . \quad (2.21)$$

This decay must be interpreted (see below) as the decay of the normal, neutral vacuum into a charged vacuum (charge  $2e$  for  $173 < Z < 184$ ) in overcritical fields. The normal vacuum state is absolutely stable up to  $Z = Z_{cr}$  and becomes unstable to spontaneous decay in supercritical fields. Only the charged vacuum (after two positrons were emitted) is stable in supercritical fields. The vacuum proceeds to become more highly charged as the supercritical fields are further increased. The above results can easily be generalized to several supercritical states embedded in the negative continuum.

The resonance behaviour of a supercritical state can be studied considering the exact continuum solutions [33, 37] of the Dirac equation for the electrostatic potential defined in Eq. (6). A phase shift  $\delta$  is determined from the ratio of the radial functions at the nuclear surface. The results for  $\sin^2(\delta - \delta_0)$  are represented in fig. 3. The background phase  $\delta_0$  is calculated using a nucleus with three protons less. The resonance in Fig. 3 is centered at  $E = -926$  keV and the full width at half maximum is  $\Gamma = 4.8$  keV. The results for the positions of the  $1s_{1/2}$  and  $1p_{1/2}$  resonances as functions of the nuclear charge are shown in Fig. 4. It was also shown that one could indeed parametrize the position and width of the resonance as in Eq. (18), for  $Z$  not very much greater than  $Z_{cr}$ . For values of  $Z$  very close to  $Z_{cr}$ , it is necessary to include in  $\gamma$  a damping factor which considers that the probability of finding low energy positrons near the nucleus is small when  $Z \approx Z_{cr}$ .

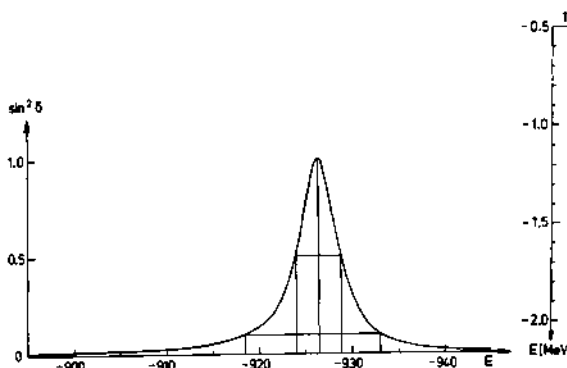


Fig. 3. The energy dependence of  $\sin^2(\delta - \delta_0)$  in an overcritical electrostatic potential  $Z=184$ .

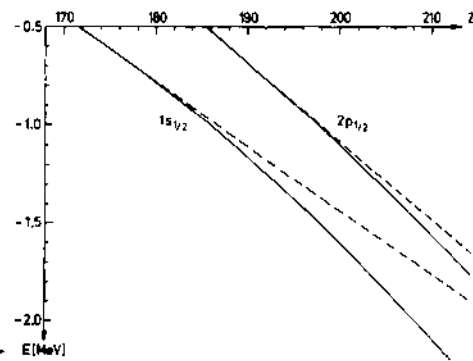


Fig. 4. The positions of the  $1s_{1/2}$  and  $2p_{1/2}$  resonances as functions of the nuclear charge.

#### SECOND QUANTIZATION OF THE DIRAC FIELD; THE VACUUM STATE

Strictly speaking, the treatment of single-particle orbits in Section 2 allows only the conclusion that the single-particle theory breaks down in the presence of a supercritical external field. By physical intuition we are able to guess the nature of the processes causing the break-down, viz. the spontaneous creation of particle-antiparticle pairs. A definite proof for this conjecture, along with the assertion that the supercritical system reaches a new stable configuration, can only be constructed within the framework of a many-particle theory, i.e. relativistic quantum field theory which simultaneously treats particles and antiparticles. In this section we briefly review the second quantization of the Dirac field in the presence of an external potential and discuss the nature of the ground-state [12, 64]. The abrupt change of the groundstate (phase transition) for sufficiently strong potentials, accompanied by pair-creation will be the subject of the following section.

In the process of second quantization the Dirac wavefunction  $\Psi(\vec{x}, t)$  is replaced by an operator-valued distribution  $\hat{\Psi}(\vec{x}, t)$  that acts in the Fock space of state vectors. The basic meaning of the operator  $\hat{\Psi}(\vec{x}, t)$  is that it annihilates a particle or creates an antiparticle at time  $t$  at the space-point  $\vec{x}$ . In many cases it is more practical to characterize particles not by position  $\vec{x}$  but by a normalizable wavefunction  $\Psi(\vec{x}, t)$ . If we have a complete set of such functions, we can divide it into a subset of functions describing particles and one describing antiparticles, which we shall denote symbolically by " $n>F$ " and " $n<F$ ", respectively. In the hole picture of Dirac the antiparticle states are considered as filled and therefore the boundary between particle and antiparticle states

has the quality of a generalized Fermi surface, from which the symbol "F" is derived. Accordingly we write:

$$\hat{\Psi}(\vec{x}, t) = \sum_{n>F} \hat{b}_n \Psi_n(\vec{x}, t) + \sum_{n<F} \hat{d}^+ \Psi_n(\vec{x}, t) . \quad (3.1)$$

$\hat{b}_n$  annihilates an electron in the single-particle state  $\Psi_n$ ,  $\hat{d}_n^+$  creates a positron in state  $\Psi_n$ . In this section we shall restrict ourselves to situations where the external potential is time-independent. Then it is allowed to assume that the functions  $\Psi_n$  are stationary states

$$\Psi_n(\vec{x}, t) = \varphi_n(\vec{x}) e^{-iE_n t} \quad (3.2)$$

where  $\varphi_n$  are eigenfunctions of the single particle Hamiltonian

$$H_D = \vec{p} \cdot (\vec{P} - e\vec{A}(\vec{x})) + \beta m + V(\vec{x}) . \quad (3.3)$$

The conjugate operator to  $\hat{\Psi}$  is denoted by  $\hat{\Psi}^+$ , creating an electron (destructing a positron) at  $(\vec{x}, t)$ . By well-known arguments involving Lorentz-invariance and causality the following equal-time anti-commutation relations on the field operators are imposed:

$$[\hat{\Psi}(\vec{x}, t), \hat{\Psi}(\vec{x}', t)]_+ = [\hat{\Psi}^+(\vec{x}, t), \hat{\Psi}^+(\vec{x}', t)]_+ = 0$$

$$[\hat{\Psi}(\vec{x}, t), \hat{\Psi}^+(\vec{x}', t)]_+ = \delta(\vec{x} - \vec{x}') . \quad (3.4)$$

The decompositions (1) and (4) lead to the relations

$$[\hat{b}_n, \hat{b}_m]_+ = [\hat{b}_n^+, \hat{b}_m^+]_+ = [\hat{d}_n, \hat{d}_m]_+ = [\hat{d}_n^+, \hat{d}_m^+]_+ = 0$$

$$[\hat{b}_n, \hat{b}_m^+]_+ = [\hat{d}_n, \hat{d}_m^+]_+ = \delta_{nm} . \quad (3.5)$$

These equations must be completed by an equation that determines the dynamical evolution of the field operators  $\hat{\Psi}, \hat{\Psi}^+$  or  $\hat{b}_n, \hat{b}_n^+$ . In the absence of two-body interactions it is convenient to work in the Heisenberg picture where the Fock-state-vector is time independent and the dynamics are determined by the operators according to Heisenberg's equations of motion

$$\frac{d\hat{A}}{dt} = i[\hat{H}, \hat{A}] \quad (3.6)$$

where  $\hat{H}$  is the Hamiltonian of the Dirac field.

Hermiticity of the Hamiltonian is achieved by complete symmetrization with respect to the field operator. After a partial integration one finds:

$$\hat{H} = \frac{1}{2} \int d^3x [\hat{\Psi}^+(\vec{x}, t), H_D \hat{\Psi}(\vec{x}, t)]_- + \frac{i}{2} \phi \int d\Sigma \cdot [\hat{\Psi}^+, \hat{\alpha} \hat{\Psi}]_- \quad (3.7)$$

For localized states the last surface term in Eq. (7) vanishes, but we shall see that it plays an important role in the transition to supercritical external fields.

In the same way one can construct an operator for the charge-current density:

$$\hat{j}^\mu(x) = \frac{e}{2} [\hat{\Psi}^+(x), \gamma^0 \gamma^\mu \hat{\Psi}(x)]_-, \quad (3.8)$$

and the total charge:

$$\hat{Q} = \frac{e}{2} \int d^3x [\hat{\Psi}^+, \hat{\Psi}]_- . \quad (3.9)$$

By explicit calculation it is easy to show that  $Q$  is a constant of motion (except for surface effects):

$$\frac{d}{dt} \hat{Q} = i [\hat{H}, \hat{Q}] = -\phi \int d\Sigma \cdot \hat{j} . \quad (3.10)$$

This equation allows us to rewrite Eq.(7) in the following way:

$$\hat{H}_{\text{loc}} = \frac{1}{2} \int d^3x [\hat{\Psi}, H_D \hat{\Psi}]_- = \hat{H} - \frac{i}{e} \frac{d}{dt} \hat{Q} \quad (3.11)$$

Let us for the moment neglect surface effects. In the representation of single-particle states the Hamiltonian and the charge operator take the following form:

$$\hat{H}_{\text{loc}} = \sum_{n>F} E_n \hat{b}_n^\dagger \hat{b}_n + \sum_{n<F} (-E_n) \hat{d}_n^\dagger \hat{d}_n + E_{\text{vac}} \quad (3.12)$$

and

$$\hat{Q} = e \left( \sum_{n>F} \hat{b}_n^\dagger \hat{b}_n - \sum_{n<F} \hat{d}_n^\dagger \hat{d}_n \right) + q_{\text{vac}} \quad (3.13)$$

where

$$E_{\text{vac}} = -\frac{i}{2\hbar} \sum_n |E_n| , \quad q_{\text{vac}} = -\frac{e}{2} \left( \sum_{n>F} 1 - \sum_{n<F} 1 \right) . \quad (3.14)$$

For given external potential,  $E_{\text{vac}}$  does not depend on the particular state vector of the system and can therefore be discarded re-normalizing the zero point of the energy scale. The operator combinations  $\hat{N} = \hat{b}_n^\dagger \hat{b}_n$  and  $\hat{N} = \hat{d}_n^\dagger \hat{d}_n$  have the properties of number operators counting electrons and positrons, respectively. It is easy to show that they can only take the eigenvalues 0 and 1, as allowed by the Pauli principle.

A little consideration tells one that the state of lowest energy, i.e. with the lowest expectation value of  $H_{loc}$ , is the one that is an eigenstate of eigenvalue zero with respect to all operators  $\hat{N}_n$  and  $\hat{N}_p$ , in combination with the following choice of the Fermi surface  $F_0$  which we shall also denote by  $E_F = 0$ :

$$E_n > 0 : "n>F_0" , \quad E_n < 0 : "n<F_0" . \quad (3.15)$$

In short, we obtain the state of lowest energy by dividing electron and positron states according to the sign of the energy eigenvalue and requiring that no particle or anti-particle be present. We shall call this state the absolute ground state or state of lowest energy  $|0, F_0\rangle$ .

For vanishing external potential the Dirac equation is charge conjugation invariant, and we have an equal number of states with  $n>F_0$  and  $n<F_0$ . As a consequence the ground state will have zero charge:  $q_{vac}(F_0) = \langle 0, F_0 | \hat{Q} | 0, F_0 \rangle = 0$ . Now consider an external attractive potential for electrons with a strength parameter  $\lambda$ :

$$V_\lambda(\vec{x}) = \lambda v(\vec{x}) \quad (3.16)$$

According to the discussion of section 2, for some strength  $\lambda$  the most strongly bound state acquires a binding energy equal to the rest mass  $m$  of the electron. For  $\lambda > \lambda_0$ :  $E(\lambda) < 0$  and this level is counted as a positron state. Therefore it is shifted from the sum over  $n>F_0$  to the sum  $n<F_0$ .

This changes the balance in the expression for  $q_{vac}$ :

$$\langle 0, F_0 | \hat{Q} | 0, F_0 \rangle = q_{vac}(F_0) = eN(\lambda)\theta(\lambda - \lambda_0) \quad (3.17)$$

where  $N(\lambda)$  denotes the number of states with a binding energy exceeding the rest mass  $m$ . We conclude that beyond a certain strength of the external potential the lowest energy state of the electron-positron field carries a non-zero charge (see Fig. 5). We note here that this state can only be reached if precisely the required number of electrons is supplied. Interesting as it may be, the lowest energy state is therefore a purely formal construction since the charge operator  $\hat{Q}$  is a constant of motion according to Eq. (10) as long as surface effects can be neglected. When the binding energy of a bound state is increased beyond  $m$ , its wavefunction remains localized - the surface effects vanish.

The situation is fundamentally different when the strength of the external potential is increased to the point  $\lambda$ , where one of the bound states is bound by twice the electron rest mass. As discussed in section 2, for  $\lambda > \lambda_0$ , the bound state becomes imbedded into the antiparticle scattering states as a resonance state. Due to the involvement of free scattering states boundary effects can no longer be excluded and we notice the difference between the local and global

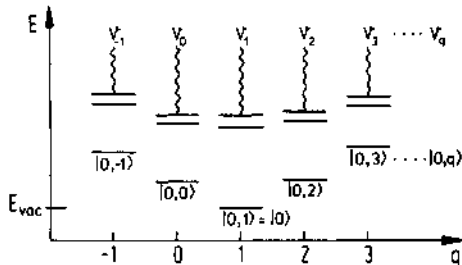


Fig. 5. The groundstates  $|0,q\rangle$  for the various charge subspaces  $V_i$  of the total Fock space. The absolute groundstate is  $|0,1\rangle$ .

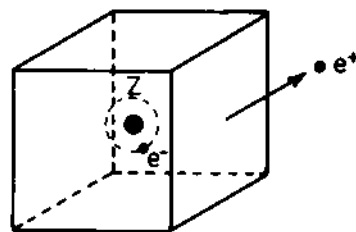


Fig. 6. When a state is supercritically bound, the atom must be treated as an open system.

state of the system, in particular the possibility to exchange particles with the surroundings develops. According to Eq. (10) the localized charge of the atomic system needs not to be conserved, if particles (or antiparticles) cross the boundary and at the same time the local Hamiltonian  $\hat{H}_{loc}$  acquires an imaginary part indicative of a decay process.

All this means that an atomic system can make a transition from one charge subspace  $V_i$  of the total Fock space to another subspace  $V_j$ , by the emission of an antiparticle (or particle). Each subspace is characterized by a different eigenvalue of the charge operator. In each sector (subspace) of the Fock space there is a state of lowest energy, the equilibrium state. It is most easily determined as the state that minimizes

$$\hat{K} = \hat{H}_{loc} + \hat{\mu} \hat{Q} \quad (3.18)$$

where it can be shown that the quantity  $\mu$ , the chemical potential, must be chosen as  $\mu = \frac{m}{e}$  in order to ensure that pair production is responsible for a transition from one charge sector to another - one member of the pair being emitted to infinity (see Fig. 6). We thus find the following condition for the equilibrium state:

$$\langle equil | \hat{H}_{loc} + \frac{m}{e} \hat{Q} | equil \rangle = \min. \quad (3.19)$$

By means of Eq. (12, 13) the operator  $\hat{H}_{loc} + \frac{m}{e} \hat{Q}$  can be rewritten as:

$$\hat{K} = \sum_{n>F} (E_n + m) \hat{b}_n^\dagger \hat{b}_n + \sum_{n<F} (-E_n - m) \hat{d}_n^\dagger \hat{d}_n + (E_{vac} + \frac{m}{e} q_{vac}), \quad (3.20)$$

Following the above line of arguments the equilibrium state with the lowest expectation value of  $\hat{K}$  is found by requiring

$$\hat{b}_n^{\dagger} | \text{equil} \rangle = 0 \quad \text{for } E_n > -m \quad (n > F_{-m}) \quad (3.21)$$

$$\hat{d}_n | \text{equil} \rangle = 0 \quad \text{for } E_n < -m \quad (n < F_{-m})$$

i.e. the Fermi energy must be  $E_F = -m$ .

This state is the state of an atomic system subject to a given external potential in the absence of interference from outside. In this state, all levels with  $E > -m$  are particle states and all levels with  $E < -m$  are antiparticle states. It is precisely the state we have called the charged vacuum state (for  $\lambda > \lambda_{cr}$ ) in section 2. We have now shown that a neutral atomic system in weak external field will develop into the state with  $E_F = -m$  after the potential has been increased to arbitrary strength and sufficient time has elapsed for the equilibrium to be established.

We may go one step further and ask for the charge density contained in the charged vacuum state. The formal expression

$$\langle \text{equil} | j^0(x) | \text{equil} \rangle = \frac{e}{2} \sum_{n < F} \frac{\psi^+(x)}{E} \psi_E^-(x) - \frac{e}{2} \sum_{n > F} \frac{\psi^+(x)}{E} \psi_E^-(x) \quad (3.22)$$

needs renormalization, but we can restrict the summation (integration) to a narrow energy interval around the resonance for our purpose of extracting the real vacuum charge. The results of such calculations are shown in Fig. 7 in comparison to the K-shell density of a subcritical atom. Note, in particular, that the charge density contains a node in the case of the supercritical 2s-state for  $Z=255$ .

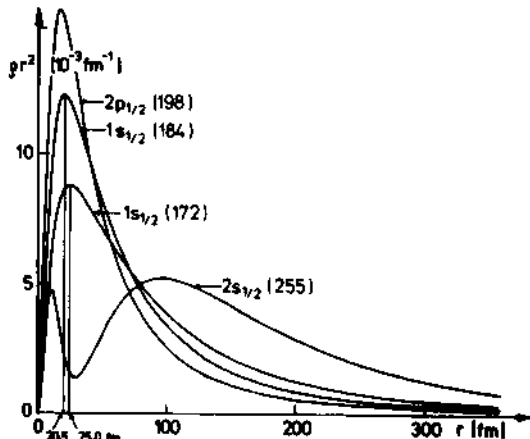


Fig. 7. Vacuum charge distributions for various supercritical states in comparison with the subcritical K-shell at  $Z=172$ .

## DECAY OF THE VACUUM STATE

Three types of experiments involving supercritical external field can be imagined, as illustrated in Fig. 8:

- (i) a subcritical but strong field is made supercritical for a certain finite period of time;
- (ii) a subcritical external field is rendered supercritical and made to remain so forever;
- (iii) everything is carried out in a supercritical field.

A prototype of the first kind - the only experiment presently feasible - is the sub-Coulomb barrier collision of very heavy ions, such as uranium on uranium, which is discussed in great detail ref. II. The second type of experiment would correspond, for instance, to the creation of a stable supercritical nucleus initially stripped of electrons by a nuclear fusion process. A typical experiment of the third kind would be resonant positron scattering on a (entirely hypothetical) supercritical atom and the observation of the resulting spontaneous pair creation.

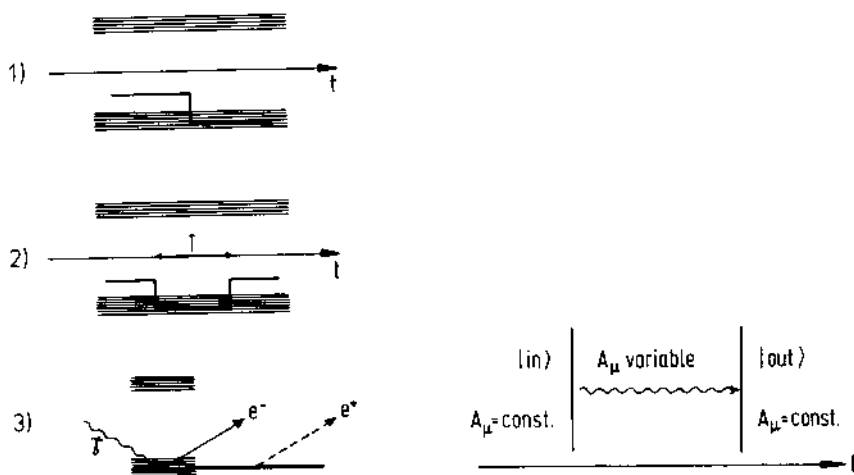


Fig. 8. The three different types of experiments with supercritical states.

Fig. 9. The in- and out-regions for time-dependent fields.

In this chapter we want to discuss the three types of experimental circumstances in turn from the standpoint of quantum field theory.

This will lead us to the conclusion that the instability of the neutral ground state in supercritical fields, previously asserted on the basis of several heuristic arguments, is a natural consequence [12] of field theory. To begin with, we have to explain how the information about observable quantities is extracted from quantum field theory.

We shall take the point of view that all observations on microscopic system undergoing a temporary change are made long before or long after that change has taken place, at time symbolically denoted as  $t = \pm\infty$  and called the in- and the out-region, respectively. We shall assume that the changes occur on a microscopic time scale and that the system is stationary at  $t \rightarrow \pm\infty$ . We shall continue to work in the Heisenberg picture, i.e. the Fock space vectors  $|\Omega\rangle$  of the system are fixed and all time dependence is carried by the operators.

We now make use of the two complete sets of solutions of the single-particle Dirac equation which are eigenstates in the past or in the future,  $\Psi_n^{(\pm)}(\vec{x}, t)$ , to obtain two different decompositions of the field operator (see Fig. 9)

$$\hat{\Psi}(\vec{x}, t) = \sum_{n>F} b_n^{(in)} \Psi_n^{(+)}(\vec{x}, t) + \sum_{n<F} d_n^{(in)} \Psi_n^{(+)}(\vec{x}, t) \quad (4.1a)$$

$$\hat{\Psi}(\vec{x}, t) = \sum_{n>F'} b_n^{(out)} \Psi_n^{(-)}(\vec{x}, t) + \sum_{n<F'} d_n^{(out)} \Psi_n^{(-)}(\vec{x}, t) \quad (4.1b)$$

The two sets  $F, F'$  denote the "filled" states (in Dirac's sense) in the in- and out-regions, respectively, and will be taken as the vacuum Fermi sets  $F_{-m}, F'_{-m}$  in the following. However, since the formalism remains equally valid for any initial state characterized by an arbitrary Fermi surface, we shall continue to write  $F$  and  $F'$  in this paragraph. The vacuum states before/after the experiment are then defined by the conditions

$$\hat{b}_n^{(in/out)} |0, \text{ in/out}\rangle = 0 \quad \text{for } n>F/F' \quad (4.2)$$

$$\hat{d}_n^{(in/out)} |0, \text{ in/out}\rangle = 0 \quad \text{for } n<F/F'$$

When the external field in the in-region differs from that in the out-region,  $F_{-m} = F'_{-m}$  and the two vacuum states will not be the same (although the Fermi energy is the same!). It is important to realize that the particle operators  $b_n^{(in)}, d_n^{(in)}$ , although being constant in time, differ from the particle operators  $b_n^{(out)}, d_n^{(out)}$  defined in the out-region. The reason for this is that the  $b_n^{(in)}, d_n^{(in)}$  do not correspond to physical particles outside of the stationary in-region. Physical particles are defined with respect to stationary wavefunctions, and the  $\Psi^{(-)}(\vec{x}, t)$  are not stationary in the out-region. Still, it is possible to relate the

operators for in-particles to those for the out-particles by projecting Eq. (1a) with  $\Psi_m^{(-)}$  and Eq. (1b) with  $\Psi_m^{(+)}$ . With the single-particle S-matrix elements

$$S_{mn} = \langle \Psi_m^{(-)} | \Psi_n^{(+)} \rangle \quad (4.3)$$

one finds that

$$\hat{b}_m^{(out)} = \left( \sum_{n>F} \hat{b}_n^{(in)} + \sum_{n<F} \hat{d}_n^{(in)\dagger} \right) S_{mn} \quad (4.4a)$$

$$\hat{d}_m^{(out)} = \left( \sum_{n>F} \hat{b}_n^{(in)\dagger} + \sum_{n<F} \hat{d}_n^{(in)} \right) S_{mn}^* \quad (4.4b)$$

In an experimental situation a state  $|\Omega\rangle$  is prepared in the in-region. For example, if we were to begin with the vacuum state then  $|\Omega\rangle = |0, in\rangle$ ; if starting with a single-particle state, we had  $|\Omega\rangle = \hat{b}_k^{(in)\dagger} |0, in\rangle$  etc. The measurements, on the other hand, are done in the out-region, so the corresponding operators act on the out-particles. Measuring the number of particles in a given state  $i>F'$  corresponds to taking the expectation value of the operator

$$\hat{N}_i^{(out)} = \hat{b}_i^{(out)\dagger} \hat{b}_i^{(out)} \quad (i>F') ,$$

which is easily evaluated with the help of relations (4a,b):

$$N_i = \langle o, in | \hat{N}_i^{(out)} | o, in \rangle = \sum_{n<F} |S_{in}|^2 \quad (4.5)$$

In the same way, one finds the number of out-antiparticles in a state  $k<F'$  to be given by

$$\bar{N}_k = \langle o, in | \hat{d}_k^{(out)\dagger} \hat{d}_k^{(out)} | o, in \rangle = \sum_{n>F} |S_{kn}|^2 \quad (4.6)$$

Since all observables in the out-region such as energy, charge etc. can be expressed in terms of expectation values of operators expressed in terms of the out-particle operators, every observable can be calculated from the single-particle amplitudes  $S_{mn}$ . This is a consequence of our neglect of true two-body interactions between Dirac particles as they would arise from the electromagnetic interactions of electrons with other electrons or positrons. Indeed, it can be shown that Eqs. (5a,b) hold in the Hartree-Fock approximation to quantum electrodynamics, but become invalid as correlations are taken into account.

We are now in position to calculate the effect upon the sub-critical vacuum state due to an external potential that becomes supercritical. We will consider both the cases (ii) and (i): The sub- and the supercritical potentials we take to be the same

as those discussed in section 2, denoted as  $V_{cr}$  and  $(V_{cr} + V')$ , respectively. We denote here the eigenstates in the subcritical potential by  $\psi_n$ , those in the supercritical potential by  $\Psi_n$ :

$$[-i\vec{\alpha} \cdot \vec{\nabla} + \beta m + V_{cr}] \psi_n = \varepsilon_n \psi_n , \quad (4.7)$$

$$[-i\vec{\alpha} \cdot \vec{\nabla} + \beta m + V_{cr} + V'] \Psi_n = E_n \Psi_n . \quad (4.8)$$

The subcritical and the supercritical bases are connected by a unitary transformation

$$\Psi_n = \sum_m C_{nm} \psi_m \quad (4.9)$$

which was explicitly calculated in section 2. If  $V'$  is switched on at  $t = t_0$ , we find that the forward-propagating wavefunctions prior to  $t_0$  are given by stationary subcritical functions:

$$\psi_n^{(+)}(x, t) = \psi_n(x) e^{-i\varepsilon_n t} \quad (t \leq t_0) \quad (4.10)$$

whereas the backward propagating functions after  $t_0$  are stationary in the supercritical basis:

$$\psi_m^{(-)}(x, t) = \Psi_m(x) e^{-iE_m t} \quad (t \geq t_0) . \quad (4.11)$$

Except for a phase factor, the S-matrix

$$S_{mn} = \langle \psi_m | \psi_n \rangle e^{i(E_m - \varepsilon_n)t_0} = C_{mn}^* e^{i(E_m - \varepsilon_n)t_0} \quad (4.12)$$

is given by the complex conjugate of the unitary transformation from the subcritical to the supercritical basis. When we start with the subcritical vacuum state,  $F_{-m}$ , containing all states with  $\varepsilon_n < -m$ , we find that the distribution of positrons at  $t = \infty$  is given by

$$\bar{N}_E = \sum_{n > F_m} |C_{E,n}|^2 , \quad E < -m . \quad (4.13)$$

If we reduce our Fock space to the positron continuum and the bound state that becomes supercritical, as we did in section 2, the sum reduces to a single term for the bound state,  $n = 0$ . In the terminology of section 2, we have  $C_{E,0} = a(E)$ , and hence:

$$\bar{N}_E = |a(E)|^2 = \frac{\Gamma/2\pi}{(E - E_r)^2 + \Gamma^2/4} . \quad (4.14)$$

Thus in the framework of quantum field theory the neutral vacuum state decays in a supercritical external potential, producing a positron distribution centered around the supercritical quasi-bound state resonance energy  $E_r$ .

In order to find out how the decay proceeds with time, we must switch off the additional potential  $V'$  after some time  $T$  and ask how far the neutral vacuum state has decayed during that period of time. In this situation it is convenient to evaluate  $S_{mn}$  at the time of the switch-off,  $t = t_0 + T$ . For  $t < t_0$  and  $t > t_0 + T$  the functions  $\psi_m^{(\pm)}$  propagate in the subcritical potential, whereas they propagate in the supercritical potential for  $t_0 < t < t_0 + T$ . This propagation can be described by the homogeneous Green's function for the supercritical potential:

$$S(x, t; x', t') = -i \sum_k \psi_k^{(-)}(x) \bar{\psi}_k^{(+)}(x') e^{-iE_k(t-t')} \quad (4.15)$$

After some calculation one finds for the single-particle S-matrix elements:

$$S_{mn} = \left\langle \psi_m^{(-)}(t_0 + T) | \psi_n^{(+)}(t_0 + T) \right\rangle = e^{i \sum_k C_{km} C_{kn}^* e^{-iE_k T}} \quad (4.16)$$

If again we restrict the Fock space to the subcritical positron states and the diverging bound state ( $n = 0$ ), the sum over intermediate supercritical states becomes an integral over the negative energy continuum:

$$|S_{mn}|^2 = \left| \int_{-\infty}^{-m} dE C_{E,m} C_{E,n}^* e^{-iET} \right|^2 \quad (4.17)$$

In the terminology of the autoionization model in section 2, we have  $C_{E,0} = a(E)$  and  $C_{E,\epsilon} = b_\epsilon(E)$ . Neglecting the continuum-continuum interaction, the following analytic expressions for these transformation coefficients (in the narrow resonance approximation) are found

$$a(E) = \frac{V_E^*}{E - E_r + \frac{i}{2}\Gamma} \quad , \quad \Gamma = 2\pi |V_E|_r^2 \quad (4.18)$$

$$b_\epsilon(E) = \delta(E - \epsilon) + \frac{a(E)V_\epsilon}{E - \epsilon + i\eta}$$

If we start with the subcritical vacuum state  $F_0$ , the positron distribution in the out-region is:

$$\bar{N}_\epsilon(T) = |S_{\epsilon,0}|^2 = |a^*(\epsilon)e^{-i\epsilon T} + \int_{-\infty}^{-m} dE \frac{|a(E)|^2}{E - \epsilon + i\eta} e^{-iET}|^2 \quad (4.19)$$

Closing the contour in the lower complex E-plane and neglecting contributions from the finite upper boundary, we find that only the

poles at  $E = E_r - \frac{i\Gamma}{2}$  and  $E = \varepsilon - i\Gamma$  contribute to the integral. The result of the calculation is [12]:

$$\bar{N}_\varepsilon(T) = |a(\varepsilon)|^2 \cdot |1 - e^{i(\varepsilon - E_r + \frac{i\Gamma}{2})T}|^2. \quad (4.20)$$

For times  $T$  long compared to the inverse resonance width  $\Gamma^{-1}$ , the positron distribution exponentially approaches that given by Eq. (14), but for small switch-on times  $T$ , the distribution is much broader than the resonance width:

$$\bar{N}_\varepsilon(T \ll \Gamma^{-1}) \sim |v_\varepsilon|^2 T^2 \left( \frac{\sin \frac{1}{2}T(\varepsilon - E_r)}{\frac{1}{2}T(\varepsilon - E_r)} \right)^2. \quad (4.21)$$

The width in this case is approximately  $h/T$ , caused by uncertainty of the energy of the dived bound state due to its short lifetime.

We conclude that the auto-ionization formula for the spectral shape of spontaneously emitted positrons is applicable when the supercritical state lives longer than its natural lifetime  $\tau = \Gamma^{-1}$ . We note that this condition may not be satisfied in the laboratory tests by means of heavy ion collisions. We can predict already at this point that the spectrum of positrons must be broadened, the width being determined by the time  $T_{\text{coll}}$ , during which the lowest bound state is supercritical. On the other hand, the probability that the hole in the supercritical bound state has not decayed after a time  $T$ , is found to be:

$$1 - N_0(T) = |S_{00}|^2 = \left| \int_{-\infty}^{-m} dE |a(E)|^2 e^{-iET} \right|^2 = e^{-\Gamma T}. \quad (4.22)$$

We conclude that the neutral vacuum state decays exponentially in a supercritical potential with a decay time  $\Gamma^{-1}$ . In case (iii) essentially the same result is obtained as in case (i). There may be some difference due to the fact that the preparation of the supercritical vacancy differs in these two cases (for (i) the potential strength is increased, whereas for (iii), e.g., the supercritical vacancy is created by a  $\gamma$ -ray.) That the spectrum of emitted particles (in our case: positrons) may depend on the way of preparation of the initial state, is a phenomenon well-known in quantum mechanics. We therefore refer to ref. 4 for a detailed treatment.

## VACUUM CHARGE AND VACUUM ENERGY

After the meaning and the nature of the vacuum state have been clarified, we are in a position to discuss the total charge and energy associated with it, as given by Eqs. (3,14). These expressions make little sense as they stand, because they involve divergent summations. In order to obtain well-defined expressions one proceeds in a number of steps [38]. First, one demands that in the absence of an external potential the vacuum carries no charge and no energy. After proper subtractions we proceed to the continuum limit and replace the summations by integrations. Finally, we expand in powers of the external potential and apply standard renormalization prescriptions to the lowest order terms. After resumming the series expansion we obtain definite expressions for  $q_{vac}$  and  $E_{vac}$  that are correct in all orders of the external field and clearly exhibit the phase transition at the critical field strength.

We make the simplifying assumption that there is no external vector potential,  $A = 0$ , and that the electrostatic potential is spherically symmetric,  $V(r)$  and of finite range with  $V(\infty) = 0$ . To be able to count states, we impose a suitable boundary condition on the Dirac wavefunctions at a finite, but large radius  $R$ . For good angular momentum waves (2.3) appropriate boundary conditions are  $f(R) = 0$ , or  $g(R) = 0$ . Let us first suppose that the external potential is weak and there is a well-defined gap separating positive energy and negative energy solutions of the Dirac equation as indicated in Fig. 10. For every value of the angular momentum quantum numbers  $\kappa, \mu$ , the positive energy eigenvalues  $E_n$  can then be counted according to growing energy ( $0 < E_1 < E_2 < \dots$ ), while the negative energy eigenvalues  $\bar{E}_n$  can be lined up with decreasing energy ( $0 > \bar{E}_1 > \bar{E}_2 > \dots$ ).

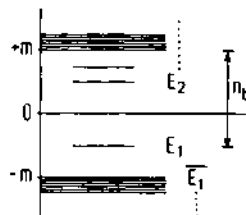


Fig. 10. Numbering of particle and antiparticle states according to energy.

In the case of vanishing external potential, the spectrum is symmetric around  $E = 0$ , i.e.,  $E_n = -\bar{E}_n$ . Then it is clear that  $q_{vac}[V=0] = 0$ , but

$$E_{vac}[V=0] = - \sum_{\kappa, \mu} \sum_{n=1}^{\infty} E_n^{\kappa, \mu} [V=0] \quad (5.1)$$

does not vanish. Since we have to define some reference point from which to measure energies, it seems reasonable to take the (infinite) energy of the Dirac vacuum in a vanishing potential as the standard. In this spirit we shall henceforth only be interested in the difference

$$E'_{\text{vac}}[V] = E_{\text{vac}}[V] - E_{\text{vac}}[V=0] . \quad (5.2)$$

We can then distinguish states for which the energy eigenvalue becomes independent of the boundary condition as  $R$  is increased further and further, i.e., the bound states, with  $-m \leq \lim_{R \rightarrow \infty} E_n(R) < +\infty$ , and those states that form the continuum in the limit  $R \rightarrow \infty$ . At distances larger than the range of the potential, these states have wavefunctions behaving like  $\sin(k_n r + \Delta_n[V])$  with  $k_n^2 = E_n^2 - m^2$ , and an analogous expression for the antiparticle states. For large  $R$ , the boundary condition  $f_n(R) = 0$  gives

$$n\pi = k_n R + \Delta_n[V] . \quad (5.3)$$

The phase shift  $\Delta_n$  is a functional of the potential. When the boundary at  $R$  is made to recede to infinity,  $E_n[V]$  and  $E_n[0]$  get infinitesimally close, such that

$$E_n[V] - E_n[0] \longrightarrow -\frac{1}{R} \frac{dE}{dk} \Big|_{k_n} (\Delta_n[V] - \Delta_n[0]) . \quad (5.4)$$

While the separation between the energy eigenvalues approaches zero, the number of states in a given momentum interval  $dk$  grows with  $k$  according to eq. (3):

$$dn = \frac{R}{\pi} dk + \frac{1}{\pi} \frac{d\Delta}{dk} dk . \quad (5.5)$$

In the limit  $R \rightarrow \infty$  the discrete sum over the "continuum" states becomes an integral:

$$\sum_{n=n_b+1}^{\infty} (E_n[V] - E_n[0]) \longrightarrow - \int_0^{\infty} dk \frac{dE}{dk} \frac{1}{\pi} \delta_k[V] . \quad (5.6)$$

Here we have introduced  $n_b$  to count the number of positive energy bound states and  $\delta_k[V] = \Delta[V] - \Delta[0]$  for the phase-shift caused by the potential. The full expression for the vacuum energy reads then:

$$E'_{\text{vac}}[V] \approx \sum_{\kappa, \mu} \left\{ \frac{1}{2} \sum_{n=1}^{n_b} (m - E_n^{\kappa\mu}[V]) + \frac{1}{2} \sum_{n=1}^{\bar{n}_b} (m + \bar{E}_n^{\kappa\mu}[V]) \right. \\ \left. + \frac{1}{2\pi} \int_m^{\infty} dE (\delta_E[V] + \delta_{-E}[V]) \right\} \quad (5.7)$$

since the bound states correspond to continuum states of infinitesimal kinetic energy in the case of vanishing potential.  $\bar{n}_b$  stands for the number of negative energy bound states. For the vacuum charge we obtain in a similar way

$$q_{vac} = -\frac{e}{2} \sum_{\kappa, \mu} \left\{ n_b - \bar{n}_b + \frac{1}{\pi} \int_m^{\infty} dE \frac{d}{dE} (\delta_E^{(V)} - \delta_{-E}^{(V)}) \right\}. \quad (5.8)$$

As they stand, eqs. (7,8) still involve divergent expressions. To see this, one has to investigate the high-energy behavior of the phase shifts  $\delta_E^{(\kappa\mu)}$ . If the potential  $V(r)$  has no singularities, the high-energy limit is exactly described by the WKB approximation which gives the following closed expression for the phase shift:

$$\delta_{WKB} = \int_{r_0[V]}^{\infty} dr \sqrt{(E-V)^2 - \frac{\kappa^2}{r^2} - m^2} - \int_{r_0}^{\infty} dr \sqrt{E^2 - \frac{\kappa^2}{r^2} - m^2}, \quad (5.9)$$

where  $r_0$ ,  $r_0[V]$  are the radii where the square roots vanish, respectively (the classical turning points). Taking the limit  $E \rightarrow \infty$  we find that

$$\lim_{E \rightarrow \infty} \delta_E^{(\kappa\mu)} = - \operatorname{sgn}(E) \int_0^{\infty} V(r) dr \quad (5.10)$$

independent of the angular momentum quantum numbers. As a consequence, the sum over  $\kappa$  and  $\mu$  in eq. (7) diverges:

$$\sum_{\kappa, \mu} \int_m^{\infty} dE \frac{d}{dE} (\delta_E^{(V)} - \delta_{-E}^{(V)}) = \sum_{\kappa, \mu} \left( -2 \int_0^{\infty} V(r) dr - \delta_m^{(\kappa\mu)} + \delta_{-m}^{(\kappa\mu)} \right). \quad (5.11)$$

Since the term linear in  $V$  cancels in the phase shift integral occurring in eq. (6), the integral is finite for every angular momentum channel. Still, the quadratic term in  $V$  in the sum over  $\kappa, \mu$  diverges, as can be seen by a more detailed argument. One easily checks that the  $V^3$  term cancels and that the quartic and all higher terms give finite contributions.

We conclude that, if the phase shift is expanded in powers of the external potential, the divergences arise from the lowest order term that contributes to the vacuum charge and energy, respectively. That the divergences are concentrated in the lowest order terms of a series expansion, is a typical property of a renormalizable field theory. The divergent terms must be absorbed in a renormalization of the electric coupling constant  $e$ . If we accept for a moment that this program can be carried through, we can give exact expressions for the vacuum charge and energy. We simply have to subtract the first order (Born) phase shift  $\delta_E^{(1(\kappa\mu))}$  from the exact phase shift  $\delta_E^{(\kappa\mu)}$  for the vacuum charge and the first and second order phase shift  $\delta_E^{(2(\kappa\mu))}$  for the vacuum energy:

$$\delta_E^{(k\mu)} = \delta_E^{(k\mu)} - \delta_E^{1(k\mu)} ; \quad \delta_E^{n(k\mu)} = \delta_E^{n(k\mu)} - \delta_E^{2(k\mu)} . \quad (5.12)$$

If we denote the part of the vacuum charge that is linear in the potential by  $q_{vac}^{(1)}$  and the part of the vacuum energy quadratic in  $V$  by  $E_{vac}^{(2)}$ , we find the following expressions:

$$q_{vac} = q_{vac}^{(1)} - \frac{e}{2} \sum_{k,\mu} \left\{ n_b - \bar{n}_b - \frac{1}{\pi} \delta_m^+ + \frac{1}{\pi} \delta_{-m}^- \right\} \quad (5.13)$$

$$E_{vac} = E_{vac}^{(2)} + \frac{1}{2} \sum_{k,\mu} \left\{ \sum_{n=1}^{n_b} (m - E_n) + \sum_{n=1}^{\bar{n}_b} (m + \bar{E}_n) + \right. \\ \left. + \frac{1}{\pi} \int_m^{\infty} dE (\delta_E^n + \delta_{-E}^n) \right\} . \quad (5.14)$$

We can draw a number of conclusions about the vacuum charge on purely physical grounds. Because of the quantization of electric charge,  $q_{vac}$  can take only values of multiples of  $e$ . Since  $q_{vac}$  was defined to be zero for vanishing potential, it cannot acquire a nonzero value in any order of perturbation theory for the external potential. To be discontinuous,  $q_{vac}^{(1)}$  cannot be of finite order in  $V$ . Thus  $q_{vac}^{(1)}$  must vanish. However,  $q_{vac}$  remains zero even beyond perturbation theory, as long as the potential is not strong enough to mix positive and negative energy states. In this region of "weak" external potentials, Levinson's phase-shift theorem is valid, which states that

$$n_b = \pi \delta_m = \pi \delta_m^+ , \quad \bar{n}_b = \pi \delta_{-m} = \pi \delta_{-m}^- \quad (5.15)$$

for nonsingular potentials of finite range. The equality of  $\delta_m$  and  $\delta_{-m}$  is an expression of the fact that the occurrence of bound states is a nonperturbative phenomenon. Equations (15) immediately yield the result that the vacuum does not carry a charge for weak potentials. In general we have

$$q_{vac} = - \frac{e}{2} \sum_{k,\mu} \left\{ n_b - \frac{1}{\pi} \delta_m - \bar{n}_b + \frac{1}{\pi} \delta_{-m} \right\} . \quad (5.16)$$

For strong fields  $q_{vac}$  acquires a nonzero value in the following way. Let us assume that  $V$  is attractive for particles ( $V \leq 0$ ) and that we consider the vacuum state with Fermi energy  $E_F = -m$ . At the critical strength of the potential,  $V_{cr}$ , the lowest bound state crosses the line  $E = -m$ , thereby diminishing  $n_b$  by one, and causing a jump of  $\pi$  in the phase shift  $\delta_{-m}$ . This is illustrated in Fig. 11, where curve 4 corresponds to a potential that has just become supercritical. Upon further increase of the potential, the bound state resonance moves through the antiparticle continuum, but does not cause any further change in  $\delta_{-m}$  until the next bound state dives in.

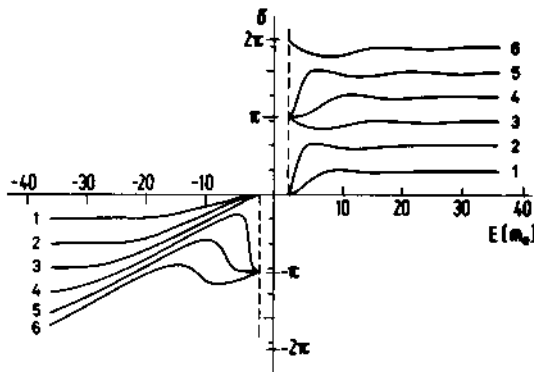


Fig. 11. Phase shifts for square-well potential of increasing depth. The supercritical resonance appears in curve 4. There are bound states between  $E = -1, +1$  for curves 3 and 6.

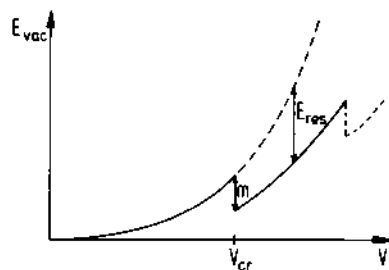


Fig. 12. Energy of the vacuum states as function of potential strength. The phase transition at  $V_{cr}$  leads to sudden lowering of the energy.

We may use Eq. (14) to find the contribution of the supercritical bound state resonance to the energy of the vacuum state. In the approximation of the autoionization model, the negative energy phase shift can be written as

$$\delta_E[V] \approx \delta_E[V_{cr}] - \text{arc tan} \frac{\Gamma}{2(E - E_{res})}, \quad (5.17)$$

where  $E_{res}$  is the energy of the center of the resonance. Carrying out the energy integration we find:

$$\int_m^{\infty} dE \delta''_{-E}[V] \approx \int_m^{\infty} dE \delta''_{-E}[V_{cr}] - (m + E_{res})\pi, \quad (5.18)$$

if the width is much smaller than the diving depth. Keeping in mind that the resonance comes from that bound state which is now missing from the first sum in eq. (14), we obtain the following approximate result for the vacuum energy in a slightly supercritical potential:

$$\begin{aligned} E_{vac}[V > V_{cr}] &= E_{vac}[V_{cr}] + \frac{1}{2} \left\{ -(m - E_{res}) + m + E_{res} \right\} \\ &= E_{vac}[V_{cr}] + E_{res}. \end{aligned} \quad (5.19)$$

This result corresponds to the picture that the supercritical bound state resonance is occupied by a particle whose energy must contribute to the energy of the charged vacuum an amount  $E_{res}$ .

We conclude that the energy of the vacuum state with  $E_F = -m$  exhibits a discontinuity of size  $(-m)$  at the critical strength of the external potential. This is illustrated in Fig. 12.

All that is left to do now, is to calculate the lowest-order terms  $q_{vac}^{(1)}$  and  $E_{vac}^{(2)}$  in Eqs. (12,13). In the diagrammatic perturbation expansion,  $q_{vac}$  and  $E_{vac}$  are represented by the Feynman diagrams:



By the standard methods of perturbative QED the lowest-order renormalized vacuum current density is found as [39]:

$$\left\langle \hat{o} | j^\mu(1)(x) | \hat{o} \right\rangle_{ren} = \int d^4x' \Pi_{ren}^{(1)}(x-x') j_{ext}^\mu(x') , \quad (5.20)$$

where  $\Pi_{ren}^{(1)}(p)$  is the first-order polarization function:

$$\begin{aligned} \Pi_{ren}^{(1)}(x-x') = & \frac{\int d^4p}{(2\pi)^4} e^{-ip(x-x')} \frac{\alpha}{3\pi} \left[ \frac{5}{3} + \frac{4m^2}{p^2} - \right. \\ & \left. - \left(1 + \frac{2m^2}{p^2}\right) \sqrt{1 - \frac{4m^2}{p^2}} \ln \frac{\sqrt{1 - \frac{4m^2}{p^2}} + 1}{\sqrt{1 - \frac{4m^2}{p^2}} - 1} \right] \end{aligned} \quad (5.21)$$

As an immediate consequence the total charge induced in the vacuum is zero in lowest-order perturbation theory:

$$q_{vac}^{(1)} = \int d^3x \left\langle \hat{o} | j^0(1)(\vec{x}, t) | \hat{o} \right\rangle_{ren} = 0 \quad (5.22)$$

if the external charge distribution is static.

The energy of the vacuum state in lowest order is obtained by calculating the electrostatic energy of the induced vacuum charge in the external potential:

$$E_{vac}^{(2)} = \int d^3x \left\langle \hat{o} | j^\mu(1)(x) | \hat{o} \right\rangle_{ren} A_\mu^{ext}(x) . \quad (5.23)$$

For a static external potential  $A_\mu^{ext}(\vec{x})$  generated by a static charge distribution this reduces to

$$E_{vac}^{(2)} = \int d^3x \int d^3x' A_\mu^{ext}(\vec{x}) j_\mu^0(\vec{x}') \cdot \Pi_{ren}^{(1)}(\vec{x}-\vec{x}') . \quad (5.24)$$

where  $\Pi(\vec{x}-\vec{x}')$  is the three-dimensional analogue of Eq. (21).

## SOLUTION OF THE POINT CHARGE PROBLEM [40,41]

In section 2 we have circumvented the breakdown of the Sommerfeld formula for  $Z\alpha > 1$  by introducing a finite size of the potential source. Still, the academic problem remains what would happen to a point charge when its strength exceeds the critical value  $Z\alpha = 1$ . Obviously, we must introduce a reasonable limiting process that leads to a point source with  $Z\alpha > 1$ . The most straightforward procedure is to introduce a finite radius  $R$  and to make  $R$  tend to zero. (Another possible procedure is to start from a nonlinear theory with a limiting electric field strength  $E_0$ , such as the Born-Infeld theory [42] and to consider the limit  $E_0 \rightarrow \infty$ . The same answer is found in this way.)

In Fig. 13 we show the energy eigenvalues of several inner electron states in the potential of a nucleus with  $Z=150$  protons as a function of the nuclear radius  $R$ . It is found that the binding energies of all  $j=\frac{1}{2}$ -states start to increase with  $1/R$  for sufficiently small values of  $R$ , whereas all higher angular momentum states readily approach a finite limit. We conclude that all states with  $j=\frac{1}{2}$  have a tendency to become supercritical in the point charge limit and, as a result, we have to take into account the screening due to the already supercritical levels when we want to carry out the limit process. This task is greatly facilitated by the fact that for all deeply bound ( $j=\frac{1}{2}$ ) states the radial density has maxima at the same distances from the source (see Fig. 14). The reason for this behaviour is that the Coulomb wavefunctions are Whittaker functions

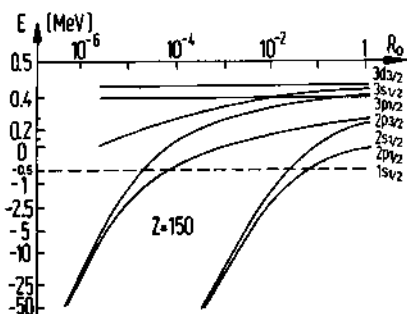


Fig. 13. Single particle energies of electronic states in the field of a shrinking nucleus with charge  $Z=150$  and radius  $R=R_0(2.5Z)^{1/3}$ .

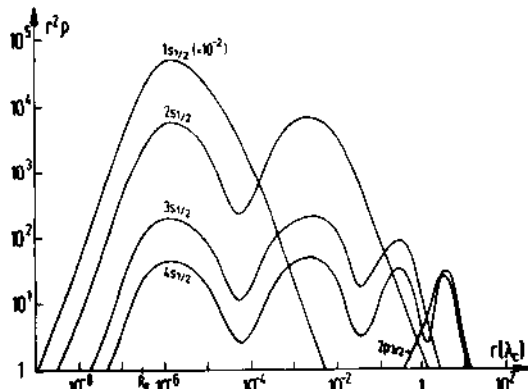


Fig. 14. Single particle densities (in arbitrary units) of some resonances and bound states for a nucleus with  $Z=150$  and  $R_0=10^{-5}$  fm.

$$M_{-Z\alpha E/p-1/2}, \pm i\sqrt{(Z\alpha)^2-1} (2ipr), p^2=E^2-m^2$$

which, for  $Z\alpha > 1$ ,  $pr \ll 1$  and  $|E|/m \gg 1$  give rise to a radial density distribution

$$pr^2 = N^2 e^{-\pi\gamma} [1 - \frac{2}{|\kappa| + (\gamma + Z\alpha)/|\kappa|} \sin (2\gamma \ln \frac{r}{R} + \phi)] \quad (6.1)$$

independent of  $E$  and the sign of  $\kappa$ . The real vacuum polarization density must, therefore, be also characterized by an undulatory structure with peaks and nodes separated by successive minima and maxima of the sine-function in Eq. (1).

The Thomas-Fermi method, which has been developed to treat the self-consistency of the screening of supercritical potentials [43, see also I], is not directly applicable to the point source problem, because  $|\nabla V|/V$  is of the same size as the potential  $V$  itself. A better approximation is obtained by writing the Dirac equation (2.4) in the second order form

$$u_{\pm}''(r) + p_{\text{eff}}(r)^2 u_{\pm}(r) = 0 \quad (6.2)$$

$$\text{with } p_{\text{eff}}(r)^2 = (E-V)^2 - m^2 - \frac{\kappa(\kappa \pm 1)}{r^2} \pm \frac{\kappa}{r} \frac{dV/dr}{E-V+m} \dots \quad (6.3)$$

where  $u_{\pm}$  stands for the radial functions  $g$  and  $f$ . One may now solve Eq. (2) in the WKB approximation. The radial variation of  $p_{\text{eff}}$  is shown in Fig. 15, where it is seen that there are two classically allowed regions. The inner region between  $r_-$  and  $r_+$  is the region where the supercritical vacuum charge density is located; the outer region beyond  $r_+$  contains the normal continuum tail of the wavefunction which does not contribute to the real vacuum polarization and will be neglected in our approach.

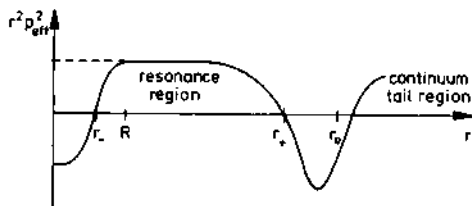


Fig. 15. The quasiclassical momentum for a supercritical nucleus. Dashed line; point charge.

In order to get a workable theory we have to neglect the higher derivatives in Eq. (3). However, this may not be done with the derivatives of the potential itself, but we may write  $V(r) = -Z(r)\alpha/r$ , with  $Z(r) \rightarrow Z$  at the source, and safely neglect derivatives of  $Z(r)$ . Obviously,  $Z(r)$  is the effectively screened charge. Adding the

so-called Langer correction we have

$$q_{\text{eff}}^2 = p_{\text{eff}}^2 - 1/4r^2 \quad (6.4)$$

and we may write down the WKB-solutions:

$$U_{\pm}(r) = N \left( \frac{E + Z\alpha/r \pm m}{q_{(\pm)}} \right)^{1/2} \sin \left( \frac{r}{r_i} q_{(\pm)} dr' + \frac{\pi}{4} \right). \quad (6.5)$$

The energies of the quasi-stationary states in the inner classically allowed region (the supercritical bound states) are determined from the Bohr-Sommerfeld condition

$$\int_{r_i}^{r_i} q_{(+)} dr' = (n + 1/2)\pi. \quad (6.6)$$

With the abbreviation  $\gamma(r)^2 = (Z\alpha)^2 - 1$  we then obtain the following expression for the vacuum charge density:

$$r^2 \rho_{\text{vac}} = 4N(r) Z(r)\alpha/\gamma(r) \sin^2 \left[ \int_{r_i}^r \gamma(r') dr' / r' + \eta \right] \quad (6.7)$$

$$\text{where } N(r_i)^{-1} = \frac{r_{i+1}}{r_i} \int_{r_i}^{r_{i+1}} dr' Z(r')\alpha/\gamma(r') \sin^2 \left[ \int_{r_i}^{r'} \gamma(r'') dr'' / r'' + \eta \right] \quad (6.8)$$

is chosen to normalize the total charge contained in any one of the peaks of the vacuum charge distribution between  $r_i$  and  $r_{i+1}$  (see Fig. 14). For self-consistency the vacuum charge must satisfy the Poisson equation:

$$d^2 Z(r)/dr^2 = 4\pi r \rho_{\text{vac}}. \quad (6.9)$$

The outer boundary of the vacuum charge distribution is fixed by the Fermi energy  $E_F = -m$  giving

$$q_F(r)^2 = -2Z(r)\alpha m/r + \gamma(r)^2/r^2. \quad (6.10)$$

The turning point is  $r_+^F$  with  $q_F(r_+^F) = 0$ . The total screening charge of the vacuum is determined by the condition

$$Z(r_+^F) = Z_N - \rho_{\text{vac}}, \quad (6.11)$$

where  $Z_N$  is the bare source charge. The solution  $Z(r)$  of Eq. (9) is shown in Fig. 16 for  $Z_N = 200$  and  $R = 10^{-5}$  fm. It is a smooth function with slight wiggles. Since the solution is numerically unstable for very small values of the source radius  $R$ , we have chosen to replace it by a step function that jumps by four units whenever the integrated vacuum charge has increased by four electron charges. It is clear that the average slope is the same, but the screening is underestimated by about 2 charge units.

With this recipe it is possible to solve the self-consistent screening equation down to extremely small source radii: as illustrated in Fig. 17, where  $Z(r^F)$  is shown as a function of  $R$  for  $Z_N=150$  and  $Z_N=200$ . More and more of the source charge is screened with

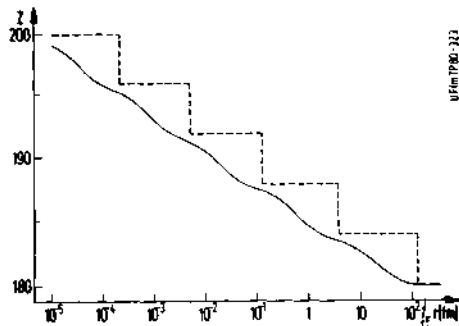


Fig. 16. Screening function  $Z(r) = -Vr/a$  for a nucleus with charge  $Z_N = 200$  and radius  $R = 10^{-5}$  fm. — Solution of the Poisson equation; --- approximate  $Z_{\text{eff}}$ .

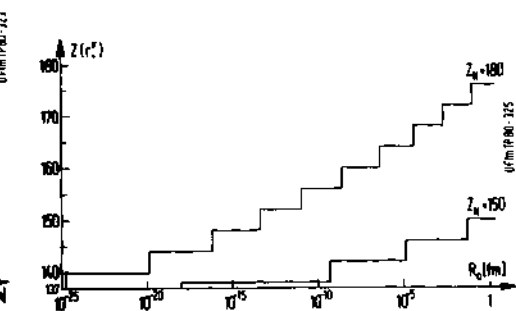


Fig. 17. Effective charge  $Z(r^F) = Z_N - Q_{\text{vac}}$  as function of the radius parameter  $R_0$  for two nuclei with charge  $Z_N = 150$  and  $200$ .

shrinking  $R$ , until the effectively unscreened charge becomes equal to 137. (Because we have not taken into account exchange interactions, the limit is uncertain by one unit of charge!) When the apparent source strength has been reduced to  $Z=137$ , no further bound state becomes supercritical, i.e. the screening no longer increases upon further reduction of the source radius.

We conclude:

- Sufficiently point-like charges are screened down to an apparent source strength of  $Z=137$ , i.e.  $Z\alpha=1$
- The vacuum charge is arranged in concentric shells ("onion"-layers) around the source. The layers are equidistant in the variable  $x=\gamma \ln(r/R)$ , as illustrated in the figure.

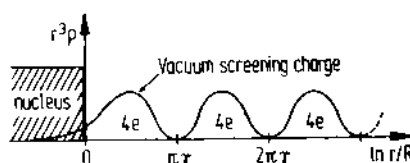


Fig. 18

- (c) The vacuum charge distribution shrinks in scale with the source charge. It also becomes point-like in the limit of a point source.
- (d) Virtual vacuum polarization (Uehling potential) only becomes important at  $r \sim m^{-1} \exp(3\pi/2\alpha) \sim 10^{-278} \text{ fm}$ . This is still quite another scale, so we may argue that the external field approximation is still valid for the type of source extension we consider here.

It is tempting to speculate on the relevance of these results for a strongly coupled field theory of elementary particles where, say,  $\alpha$  itself becomes large. If taken seriously, they would indicate that in such a theory the vacuum state is very much different from the perturbative free-field vacuum and the interaction between particles is strongly screened by the vacuum rearrangement. We wish, however, to add a word of caution: if  $\alpha$  itself is large, radiative corrections cannot be treated perturbatively but must be considered ab initio in the determination of the vacuum state. For a further discussion of this very interesting topic we refer to the lectures of J. Rafelski [I].

#### REFERENCES

- I. J. Rafelski, lectures at this conference.
- II. J. Reinhardt et al., lectures at this conference.
1. B. Müller, Ann. Rev. Nucl. Sci., 26:351 (1976).
2. J. Reinhardt and W. Greiner, Rep. Prog. Phys., 40:219 (1977).
3. J. Rafelski, L. P. Fulcher, and A. Klein, Phys. Lett. 38C:228 (1978).
4. J. Kirsch, B. Müller, and J. Rafelski, GSI-Report 81-5 (ISSN 0171-4546).
5. U. Mosel and W. Greiner, Z. Physik, 222:261 (1969); S. G. Nilsson, S. G. Thompson, and C. F. Tsang, Phys. Lett., 28B:458 (1969).
6. F. G. Werner and J. A. Wheeler, Phys. Rev., 109:126 (1958).
7. W. Pieper and W. Greiner, Z. f. Physik, 218:327 (1969).
8. D. Rein, Z. f. Physik, 221:423 (1969).
9. J. Rafelski, L. P. Fulcher, and W. Greiner, Phys. Rev. Letters, 27:958 (1971).
10. S. S. Gershtein and Y. B. Zeldovich, Lettre Nuovo Cimento, 1:835 (1969); [Soviet Phys. JETP 30:358 (1970)].
11. O. Klein, Z. f. Physik, 53:157 (1929).
12. J. Rafelski, B. Müller, and W. Greiner, Nucl. Phys., B38:585 (1974).
13. Y. B. Zeldovich and V. S. Popov, Soviet Phys. Uspekhi, 14:673 (1972).
14. B. Müller, V. Oberacker, J. Reinhardt, G. Soff, W. Greiner, and J. Rafelski, J. Phys. Soc. Japan 44 (Suppl):838 (1978).

15. J. Reinhardt, B. Müller, W. Greiner, in: "Coherence and Correlation in Atomic Collisions," ed. Kleinpoppken & Williams p. 331, Plenum Press (1980).
16. J. Reinhardt, W. Greiner, B. Müller, and G. Soff, in: Electronic and Atomic Collisions, ed. Oda & Takayanagi, p. 369, Amsterdam (1980).
17. H. Backe, L. Handschug, F. Hessberger, E. Kankeleit, L. Richter, F. Weik, R. Willwater, H. Bokemeyer, P. Vincent, Y. Nakayama, and J. S. Greenberg, Phys. Rev. Lett., 40:1443 (1978).
18. C. Kozhuharov, P. Kienle, E. Berdermann, H. Bokemeyer, J. S. Greenberg, Y. Nakayama, P. Vincent, H. Backe, L. Handschug, and E. Kankeleit, Phys. Rev. Lett., 42:376 (1979).
19. J. S. Greenberg, in: "Electronic and Atomic Collisions, ed. Oda & Takayanagi," p.351, Amsterdam (1980)
20. J. Rafelski, B. Müller, W. Greiner, Z. Physik, A285:49 (1978).
21. M. Soffel, B. Müller, and W. Greiner, Stability and Decay of the Dirac vacuum in strong external gauge fields, Physics Reports, to be published (1982).
22. S. W. Hawking, Nature, 248:30 (1974); Comm. Math. Phys. 43:199 (1975).
23. B. S. DeWitt, Phys. Reports, 19C:295 (1975).
24. W. Heisenberg and H. Euler, Z. Physik, 98:714 (1936).
25. V. Weisskopf, Phys. Z., 34:1 (1933).
26. L. I. Schiff, H. Snyder and J. Weinberg, Phys. Rev., 57:315 (1940).
27. I. Pomeranchuk and J. Smorodinsky, J. Phys. USSR, 9:97 (1945).
28. J. Schwinger, Phys. Rev., 82:664 (1951).
29. V. V. Vorokov and N. N. Kolesnikov, Sov. Phys. JETP 12:136 (1961).
30. F. Beck, H. Steinwedel, and G. Süssmann, Z. f. Physik, 171:189 (1963).
31. A. I. Akhiezer and V. B. Berestetskii, Quantum Electrodynamics, Interscience Publishers, New York (1965).
32. B. Müller, H. Peitz, J. Rafelski, and W. Greiner, Phys. Rev. Letters, 28:1235 (1972).
33. B. Müller, J. Rafelski, and W. Greiner, Z. f. Physik, 257:62 (1972).
34. U. Fano, Phys. Rev., 124:1866 (1961).
35. W. L. Wang and C. M. Shakin, Phys. Lett., 32B:421 (1970).
36. J. Reinhardt, B. Müller, and W. Greiner, Phys. Rev. A24: 103 (1981).
37. B. Müller, J. Rafelski, and W. Greiner, Nuovo Cimento, 18A:551 (1973).
38. J. Schwinger, Phys. Rev., 94:1362 (1954).
39. e.g. G. Källén, "Quantenelektrodynamik," in: "Handbuch der Physik V/1," Springer (1958).

40. P. Grtner, J. Reinhardt, B. Mller, and W. Greiner, Phys. Lett., 95B:181 (1980).
41. P. Grtner, U. Heinz, B. Mller, and W. Greiner, Z. Physik, A300:143 (1981).
42. M. Born and L. Infeld, Proc. Roy. Soc. A144:425 (1934).
43. B. Mller and J. Rafelski, Phys. Rev. Lett., 34:349 (1975).

# ATOMIC COLLISIONS WITH STICKY NUCLEI<sup>\*</sup>

W. E. Meyerhof <sup>\*\*</sup>

Department of Physics, Stanford University  
California 94305, USA, and Institute for  
Theoretical Physics, University of Frankfurt  
6 Frankfurt 1, Germany

## INTRODUCTION

These lectures describe a field of overlap between atomic and nuclear physics, which is receiving increasing attention since it might provide new information about nuclear and atomic collisions. I use the word "might", because, as you will see, the theoretical predictions are exciting and challenging, but the experiments are beset with severe backgrounds which make the detection of the desired effects very difficult.

Gugelot<sup>1</sup> first suggested that it should be possible to detect compound nucleus (CN) x-rays, i.e. atomic x-rays resulting from the formation of a relatively long-lived compound-nuclear system in a nuclear reaction. The interest in the detection of CN x-rays is twofold. From a nuclear physics point of view, the possibility exists to determine the life-time of the compound nucleus from the magnitude of the x-ray production cross section. From an atomic physics viewpoint, the possibility exists of determining the zero-impact-parameter ionization probability on the way into a collision,<sup>2</sup> a quantity of great theoretical interest, since normally only the way-in and -out probability is determined.<sup>3</sup> Also, if the energy of x-rays from (short-lived) super-heavy CN systems

---

\* Supported in part by the National Science Foundation under Grant No. PHY-80-15348.

\*\* Recipient of Alexander von Humboldt Foundation Award for Senior U.S. Scientists, 1980-81. Work done in collaboration with R. Anholt, J.F. Chemin, and Ch. Stoller.

could be determined, a new spectroscopic tool would be available to study atomic systems in which extreme relativistic effects are expected.<sup>4,5</sup>

The emission of CN x-rays from super-heavy systems, not yet detected, is related to positron emission, which has been detected (see the lectures by Backe, Bokemeyer, Greenberg, Kiende, Müller, and Reinhardt). The search for nuclear time-delay effects in positron emission<sup>6</sup> is presently under way.

Besides the possible formation of compound-nucleus x-rays in a nuclear reaction, there is another, more subtle, influence of nuclear time-delay effects on the production of target x-rays in an elastic or inelastic nuclear scattering reaction.<sup>8</sup> In principle, the target x-ray production probability can be used to estimate the nuclear time delay if the x-ray production process is understood, or, if the nuclear time delay is known, properties of the atomic vacancy-production amplitude can be investigated.<sup>9</sup> Theoretically, inner-shell target ionization in nuclear reactions induced by light projectiles has similarities to bremsstrahlung emission<sup>10-12</sup> by these projectiles: the former process involves (delta-) electron ejection, the latter photon production. A nuclear time-delay effect on projectile bremsstrahlung has been detected,<sup>13</sup> but is not discussed further in these lectures.

In the following sections, we begin with brief surveys of the pertinent aspects of nuclear and atomic collisions. The formation of CN x-rays produced by light and heavy projectiles is then discussed, as well as positron production by super-heavy compound systems. Finally, we consider target x-ray production in two types of nuclear reactions in which time delays are expected: resonance reactions with light projectiles and deep inelastic reactions with heavy projectiles.

#### SURVEY OF NUCLEAR REACTIONS

For the present purpose, a time-sequence view point of a nuclear reaction is useful.<sup>14-16</sup> If, for example, a complex nucleus is bombarded by a proton of several MeV energy, the first stage in the interaction is a partial reflection of the incoming proton wave function by the nuclear potential. This stage is called shape elastic scattering. The part of the proton wave function that enters the nucleus can undergo a series of processes, the first of which is the interaction with a single nucleon. Unless the incident or struck nucleons leave the nucleus ("direct interaction"), both nucleons can have further interactions with other nucleons, of increasing complexity. Finally, through many collisions, a complete sharing of the initial energy may take place, and a compound nucleus may be formed in which the initial mode of formation is no longer remembered. In principle, at any stage during the interaction, the system can find itself in a resonant condition, given a suitable projectile energy: there may a shape resonance (few-MeV width), a doorway or analog resonance (keV to

MeV width), or a CN resonance (eV to keV width). Hence, time delays from about  $10^{-21}$  to about  $10^{-15}$  sec can be expected in the nuclear-interaction process. (A rigorous time description of nuclear reactions can be found in Reference 16.)

For nuclear reactions induced by complex projectiles, microscopic (individual-nucleon) and macroscopic (statistical-average) treatments of the time sequence of the interaction have been used.<sup>17-18</sup> Experimentally, one finds with projectiles up to  $Z_p \approx 20$ , at bombarding energies that do not exceed the Coulomb barrier appreciably, the dominant nuclear process is fusion into a CN system.<sup>17,19</sup> If  $Z_p + Z_t \gtrsim 80$ , the compound nucleus decays mainly by neutron evaporation. Proton and alpha-particle evaporation occur for the lighter systems. If  $Z_p + Z_t \gtrsim 90$ , fission of the compound system becomes increasingly important. (Fission can also occur after neutron evaporation, in which case it is called sequential fission.) Independent of the mode of CN decay, the CN lifetime  $\tau_c$  is expected to be a very sensitive function of the excitation energy, and of the spin, of the compound nucleus. For example, for mass number  $A = 180$  and spin  $J = 60$ , the statistical model of neutron evaporation<sup>20</sup> predicts that  $\tau_c \approx 10^{-16}$  sec at 30 MeV and that  $\tau_c \approx 10^{-20}$  sec at 100 MeV excitation energy.<sup>19</sup> A weaker dependence of lifetime on excitation energy seems to be found in crystal-blocking experiments,<sup>21</sup> but the interpretation of such experiments is not simple.<sup>22</sup>

For projectiles with  $Z_p \gtrsim 30$ , at bombarding energies above the Coulomb barrier, deep-inelastic collisions are found to dominate the nuclear interaction.<sup>17,23</sup> A useful macroscopic model of this process assumes that in the collision the two nuclei stick together for a certain time in a quasi-molecular configuration and then fly apart. During cohesion, nucleons diffuse between the nuclei, resulting in an excitation of the system and in a spreading in  $Z$  and  $A$ , both of which increase with the sticking time. The temporal development of the diffusion process has been computed and indicates sticking times of the order of  $10^{-21}$  sec.<sup>24</sup> It has been suggested that the sticking time decreases exponentially with the impact parameter of the collision.<sup>25</sup>

#### SURVEY OF ATOMIC COLLISION PROCESSES

Our main interest is in K-vacancy production in atomic collisions, since only K x-rays have been used in the experiments discussed below. A useful viewpoint of such a collision is the semiclassical approximation, in which the nuclear motion is treated classically, but the electronic processes are calculated quantum mechanically.<sup>26</sup> Then, as the projectile passes through the target atom, a time-varying electric field acts on the K electron, which can cause an electronic transition from the K shell to empty bound states or to the continuum. In the de-excitation of the K-shell vacancy, x-rays or Auger electrons can be emitted; in super-heavy systems, positron emission can occur.<sup>5</sup> The de-excitation can take

place during the collision, i.e. while the projectile and target electron clouds overlap. The x-rays are then called "non-characteristic" or "molecular-orbital" x-rays. If the K-shell vacancy de-excites after the collision when the collision partners are well separated, "characteristic" or "separated-atom" x-rays are emitted.

Models of inner-shell vacancy production in collisions of heavy ions are based on an independent-electron picture, since the interelectronic coupling is weak compared to the electron-nuclear coupling. Two extreme models are in use.<sup>27</sup> In the "atomic model" one assumes that the inner-shell electronic wave function is only weakly perturbed by the projectile nucleus. Thus, one can use screened atomic wave functions for the initial and final states of the active inner-shell electron (i.e., the electron making the transition) in computing the transition amplitude.

In the "molecular" or "adiabatic model" the projectile and target inner-shell electron wave functions are assumed to adjust to both nuclei, so that diatomic molecular orbitals are formed around the projectile and target nuclei. During the collision, the internuclear separation vector  $\vec{R}$  of the instantaneous molecule changes length and rotates in the laboratory system. The forced time dependence of the molecular wave function of the active electron can cause a transition from the inner shell to vacant bound states or to the continuum. One finds that the transition matrix element can have a part which is proportional to time rate of change of  $R$ , called radial coupling, and a part which is proportional to the time rate of change of the orientation angle of  $\vec{R}$  with respect to the incident beam direction, called rotational coupling. Which coupling is effective depends on the quantum numbers of the initial and final molecular orbitals.

Figure 1 shows the lowest molecular-orbital (MO) energy levels of the  $^{53}\text{I} + ^{79}\text{Au}$  system as a function of  $R$ . The figure is taken from the work of Müller and Greiner<sup>28</sup> who were the first to make these type of calculations for relativistic electrons by solving the two-center Dirac equation. The only MO of interest to us is the lowest state, called  $1s\sigma$ . In sufficiently asymmetric collisions it receives vacancies mainly by radial coupling to the continuum (ionization). Reinhart et al. have calculated that in collisions of very heavy ions, multi-step electronic transitions via vacant bound states can cause more  $1s\sigma$  vacancies than direct ionization.<sup>29</sup>

Experiments have shown that the atomic model is applicable to collisions in which the projectile atomic number ( $Z_p$ ) is appreciably smaller than the target atomic number ( $Z_t$ ). The molecular model has been applied successfully when  $Z_p$  and  $Z_t$  are of comparable magnitude and when the projectile velocity is smaller than the Bohr velocity of the active (K) electron. The latter condition is fulfilled for  $\text{Ni} + \text{Ni}$  collisions if they are less energetic than  $\sim 1$  MeV/N and for  $\text{Pb} + \text{Pb}$  collisions if they are less energetic than  $\sim 100$  MeV/N.

We now turn to the effect of nuclear sticking on (K) x-ray production. As mentioned in the introduction, there are two types of effects, which correspond, respectively, to x-rays emitted

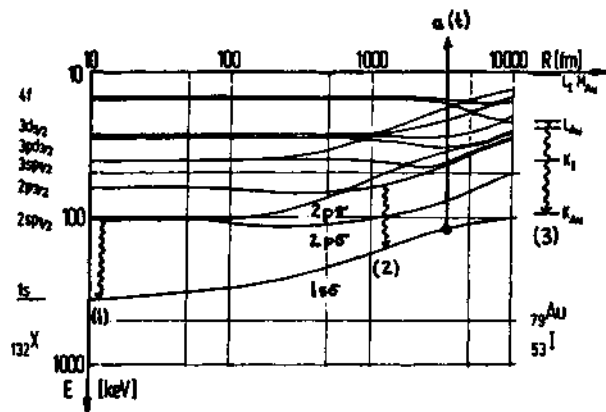


Fig. 1. Molecular - orbital (MO) energy level diagram for the  $^{53}\text{I} + ^{79}\text{Au}$  system (from Ref. 28). The lowest MO's of interest here are indicated:  $1s\sigma$ ,  $2p\sigma$ ,  $2p\pi$ , as well as the ionization amplitude  $a_{1s\sigma}(t)$  and three types of x-ray transitions: (1) CN or UA x-rays, (2) MO x-rays, (3) separated-atom x-rays.

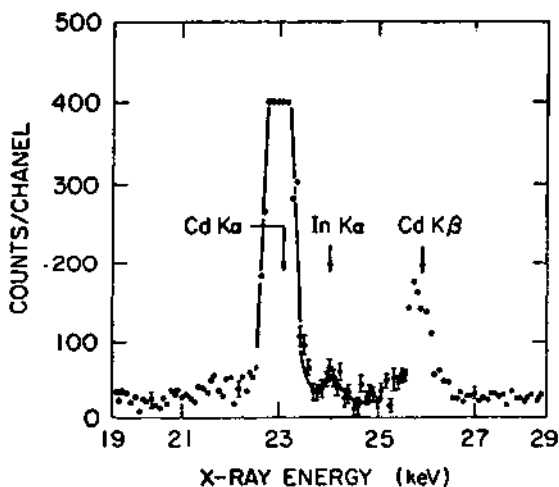


Fig. 2. X-ray spectrum from 12-MeV proton bombardment of  $^{106}\text{Cd}$  in coincidence with inelastic protons (energy window 5.5 to 10 MeV). Accidental coincidences have been subtracted. The In K $\alpha$  lines are due to CN formation. (From Ref. 34.)

during the atomic collision and x-rays emitted after the collision (see Fig. 1). Since x-ray production is coincident with a nuclear reaction, an effectively zero atomic impact parameter is selected in these collisions, even though there will be a range of impact parameters for the nuclear reaction. The electronic coupling then becomes purely radial.

In discussing the two classes of x-ray effects, we treat separately light projectiles, to which the atomic model of electron arrangement during the collision can be applied, and heavy projectiles, for which the molecular model of electronic arrangement is appropriate. In each case we provide a brief theoretical background and the experimental information and interpretation.

## EXPERIMENTS WITH COMPOUND NUCLEUS X-RAYS

### A. Light Projectiles

a. Theoretical background. Consider a proton or alpha particle bombarding a target nucleus and forming a compound nucleus with a cross section  $\sigma_R$ . Call  $P_{1/2}$  the probability of forming a K vacancy on the way into the collision (i.e. one-half of a complete atomic collision). Then  $\sigma_R P_{1/2}$  is the cross section for having a K vacancy in the united atom with atomic number  $Z_{UA} = Z_p + Z_t$ , where  $Z_p$  and  $Z_t$  are the projectile and target atomic numbers, respectively. Each such united atom (with a K vacancy) can decay by electronic filling of the K vacancy with a probability per unit time  $\lambda_K$  and by disintegration of the compound nucleus with a decay probability  $\lambda_c = 1/\tau_c$ . Hence the probability of K x-ray emission from the original united atom is equal to<sup>1,2</sup>

$$\omega_K \frac{\lambda_K}{\lambda_c + \lambda_K} , \quad (1)$$

where  $\omega_K$  is the K fluorescence yield. The cross section for K x-ray production in the entire nuclear reaction is

$$\sigma_{cx} = \sigma_R P_{1/2} \omega_K \frac{\lambda_K \tau_c}{1 + \lambda_K \tau_c} , \quad (2)$$

a formula first given by Gugelot<sup>1</sup> and reexamined by von Brentano and Kleber and by McVoy et al.<sup>3,6</sup>

Equation (1) assumes a simple exponential law for compound nucleus (CN) decay, which may not be correct in all situations<sup>1,6</sup>. Also it is assumed that K x-ray emission and CN decay are independent of each other, which is not true in all cases, as discussed below (Sec. 5.A.a). The exact calculation of  $P_{1/2}$  presents an interesting

theoretical problem.<sup>3,31</sup> It appears that, approximately,

$$P_{\frac{1}{2}} \approx \frac{1}{2} P_K(0) , \quad (3)$$

where  $P_K(b)$  is the K-vacancy production probability in a complete collision (way-in and way-out) at an atomic impact parameter  $b$ . For our purposes it is enough to note that one finds, approximately,<sup>32</sup>

$$P_K(0) \propto E_p^3 Z_p^2 / Z_t^8 , \quad (4)$$

where  $E_p$  is the projectile kinetic energy. For 12-MeV  $p + {}_{48}\text{Cd}$  collisions,  $P_K(0) \approx 7 \times 10^{-4}$ .<sup>33</sup>

b. Experimental results. The experimental difficulties in applying Gugelot's proposal to the determination of the CN lifetime  $\tau$  can be appreciated by the following example. Consider the 12-MeV  $p + {}^{106}_{48}\text{Cd}$  reaction.<sup>2,34</sup> Here, the CN formation cross section is  $\sigma_R \approx 0.7b$ , so that  $\sigma_R P_{\frac{1}{2}} \approx 2 \times 10^{-4} b$  represents the maximum cross section for the production of the united-atom  ${}^{107}\text{In}$  K x-rays. The latter cross section must be compared to an expected cross section of  $\sim 60b$  for the production of  ${}_{48}\text{Cd}$  K x-rays by the ordinary Coulomb ionization process. Furthermore, even the detection of  ${}^{107}\text{In}$  x-rays does not unambiguously signal the formation of the  ${}^{107}\text{In}$  compound nucleus, because the  ${}^{106}\text{Cd}$  ( $p, n$ ) reaction can form  ${}^{106}\text{In}$  in excited states as a reaction product. Internal conversion in the gamma decay of  ${}^{106}\text{In}^*$  will produce K x-rays which are indistinguishable from the K x-rays from  ${}^{107}\text{In}$  CN formation. This problem can be avoided by detecting only those In K x-rays which are in coincidence with inelastically scattered protons from the  ${}^{106}\text{Cd}$  ( $p, p'$ ) reaction. But, still, the energy interval of the inelastic protons must be judiciously chosen so that the decay of the  ${}^{107}\text{In}$  compound nucleus is signaled unambiguously.<sup>2,34</sup>

Figure 2 shows the x-ray spectrum in true coincidence with inelastic protons from the 12-MeV  $p + {}^{106}\text{Cd}$  reaction. Although the coincidence requirement reduces the Cd K x-rays enormously, it does not eliminate them, because they can be produced also by internal-conversion decay of  ${}^{106}\text{Cd}$  excited states which are populated in the  ${}^{106}\text{Cd}$  ( $p, p'$ ) reaction. Analysis of these and other<sup>35</sup> experiments gives the results shown in Table 1. Agreement with the statistical theory of CN decay appears to be good. For completeness, we mention an experiment of Hardy et al.<sup>36</sup> in which the compound atom  ${}^{69}\text{As}$  was formed, with a K vacancy, by electron capture from  ${}^{64}\text{Se}$ . In this decay,  ${}^{69}\text{As}$  can be produced in proton-unstable excited states. The K vacancy is then filled while the nucleus is  ${}^{69}\text{As}$  or while it is  ${}^{68}\text{Ge}$ . An expression similar to (1) leads to  $\tau_c$ .

TABLE 1

Reaction	Compound nucl. & excit. energy	$\tau_c$ (measured) (sec)	$\tau_c$ (calculated) (sec)	Ref.
10-MeV p + $^{106}\text{Cd}$	$^{107}\text{In}^*(14 \text{ MeV})$	$(6.5 \pm 4) \ 10^{-17}$	$11 \times 10^{-17}$	2
12-MeV p + $^{106}\text{Cd}$	$^{107}\text{In}^*(16 \text{ MeV})$	$(5.0 \pm 2.5) \ 10^{-17}$	$5 \times 10^{-17}$	2
10-MeV p + $^{112}\text{Sn}$	$^{113}\text{Sb}^*(13 \text{ MeV})$	$(4.0 \pm 3.8) \ 10^{-17}$		35
12-MeV p + $^{112}\text{Sn}$	$^{113}\text{Sb}^*(15 \text{ MeV})$	$(3.4 \pm 2.0) \ 10^{-17}$		35

### B. Heavy Projectiles

a. Theoretical background. The use of heavy projectiles for the measurement of  $\tau$  should be advantageous, for two reasons: according to Eq. (4) one expects a large increase in  $P_K(0)$  and, since  $Z_{UA}$  is well separated from  $Z_t$ , the CN K x-rays should be easily identified. Actually, relation (4) is no longer valid because the increased effective binding of the K electron by the passage of the projectile nucleus through the target must be taken into account<sup>37</sup> [this can be done very crudely by replacing  $Z_t$  by  $Z_{UA}$  in expression (4)]. Electronic relativistic effects also must be considered, which can enhance the ionization process by orders of magnitude.<sup>5,38</sup> Although, as described in Sec. (b) below, the advantages of using heavy projectiles are outweighed by severe disadvantages, it is of interest to consider a model calculation by Anholt<sup>38</sup> of CN x-ray production with heavy projectiles. Several concepts will appear which are useful for our later discussion.

Leaving aside for the moment the real nuclear processes which occur with heavy projectiles, let us consider the case of compound elastic scattering and trace out the time development of the lowest MO energy levels for the collision illustrated in Fig. 1. Figure 3 sketches the time dependence of the levels, assuming that the projectile and target nuclei stick together for a time  $T$  before they separate again. We now divide the time into three intervals  $-\infty$  to 0, 0 to  $T$  and  $T$  to  $\infty$ . If a vacancy existed in the  $1s0$  MO prior to the collision it could be filled by electronic transitions from the higher MO's with emission with MO x-rays in the first interval, with emission of CN x-rays in the second interval and with emission of MO x-rays and then separated-atom x-rays in the third interval. Hence MO and CN emission are intimately related (we postpone consideration of the separated-atom x-rays until Sec. 5.B.a). For a given initial state with wave function  $\psi_{in}$ , the probability of x-ray emission with angular frequency  $\omega_x$  is<sup>39</sup>

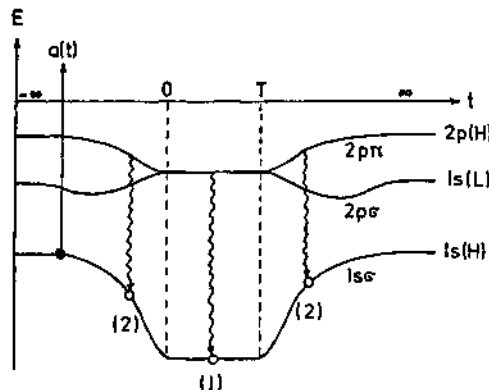


Fig. 3. Schematic time evolution of the  $1s\sigma$ ,  $2p\sigma$  and  $2p\pi$  MO energy levels (compare Fig. 1). It is assumed that during the time interval  $0$  to  $T$  the projectile and target nuclei form a CN system. Once a  $1s\sigma$  vacancy has been generated, MO x-rays (2) and CN x-rays (1) can be produced. (Separated atom x-rays are considered in Sec. 5.B.)

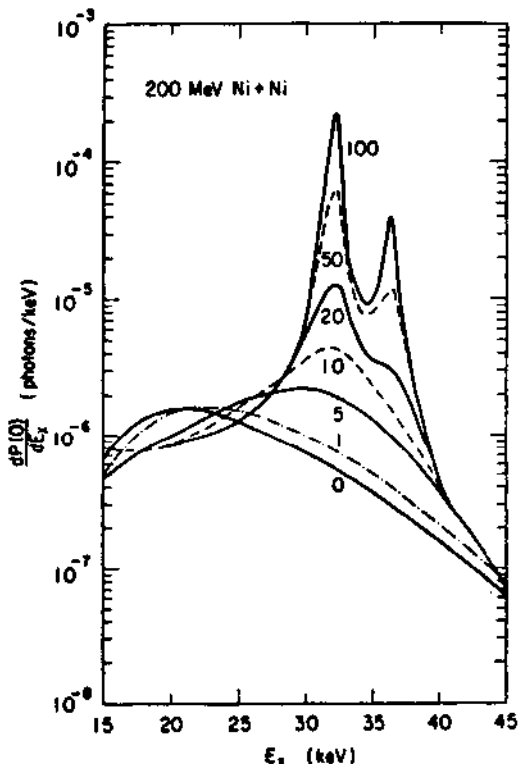


Fig. 4. Calculated x-ray spectra for 200-MeV Ni + Ni (central) collisions as a function of the CN lifetime  $\tau_c$ . The numbers adjacent to each curve give  $\omega_0 \tau_c$ , where  $\hbar \omega_0$  is the energy of the united-atom  $\text{K}\alpha$  line (32 keV). (From Ref. 39.)

$$\frac{dP}{d\omega_x} = \frac{2\omega_x}{3\pi\hbar c^3} |\vec{D}|^2 . \quad (5)$$

Here  $\vec{D}$  is a Fourier transform of the time-dependent dipole-velocity matrix element  $d[R(t)] = \langle \psi_{1s0} | \vec{e}r | \psi_{in} \rangle$ , with  $r$  denoting the electron coordinate:

$$\vec{D} = \int_{-\infty}^{\infty} dt \vec{d}(t) a_{1s0}(t) \exp [i \int_0^t [\omega_x - \Delta\omega(t')] dt'] , \quad (6)$$

where  $a_{1s0}(t)$  is the probability amplitude for having a  $1s0$  vacancy and  $\hbar\Delta\omega(t)$  is the energy separation of the initial and final ( $1s0$ ) MO's. By separating the time integral into the aforementioned three intervals, one finds that

$$\vec{D} = \vec{A} + \vec{B} e^{i\omega T - \lambda_K T/2} , \quad (7)$$

where  $\vec{A}$  and  $\vec{B}$  are complex quantities,  $\omega = \omega_x - \Delta\omega(0)$ , and  $\lambda_K$  is the decay probability per unit time of the united-atom K wacancy [see expression (1)]. Assuming exponential CN decay, the experimental probability of x-ray emission is computed from

$$\frac{dP}{d\omega_x} = \frac{2\omega_x}{3\pi\hbar c^3} \frac{1}{\tau_c} \int_0^{\infty} dT |\vec{D}|^2 \exp (-T/\tau_c) . \quad (8)$$

Figure 4 gives the x-ray emission spectra for various values of  $\omega_0\tau_c$ , where  $\hbar\omega_0$  ( $=\hbar\Delta\omega(0)$  for the  $2p\pi-1s0$  transition) is the united-atom K $\alpha$  x-ray energy. For  $\tau_c = 0$ , there is no CN formation and only MO x-rays are emitted. For increasing values of  $\omega_0\tau_c$ , the united-atom K x-ray spectrum appears and sharpens. This can be seen very simply by writing the uncertainty principle in the form

$$\tau_c \cdot \delta\omega_0 \approx 1 , \quad (9)$$

where  $\delta\omega_0$  is the width of a K line. Then,

$$\frac{\delta\omega_0}{\omega_0} \approx \frac{1}{\omega_0\tau_c} . \quad (10)$$

Anholt showed that integration of Eq. (8) over the x-ray frequencies near  $\Delta\omega(0)$  leads to expression (1).<sup>39</sup>

b. Experimental results. CN-forming nuclear reactions with heavy projectiles are not as simple as the preceding model calculation assumes (see Sec.2). The decay of the CN by neutron evaporation

produces excited "evaporation residues" (ER) whose deexcitation by internal conversion gives x-rays corresponding to  $Z_{UA}$ . Although these x-rays are indistinguishable from the  $Z_{UA}$  x-rays emitted during the CN lifetime, we made a survey of x-rays from a few 350-MeV  $^{36}\text{Kr}$ -induced reactions, with the hope that one might find contributions from the CN lifetime to the x-ray yield.<sup>46</sup> Figure 5 shows the x-ray spectra from  $^{28}\text{Ni}$ ,  $^{32}\text{Ge}$ ,  $^{19}\text{K}$ <sub>35</sub> $\text{Br}$  and  $^{39}\text{Y}$  targets. In each case, x-rays corresponding to  $Z_{UA}$  were found (shown in black), but our estimates indicate that internal conversion from ER decay can account completely for the intensity of the x-rays.

If  $Z_{\text{R}} + Z_{\text{C}} \gtrsim 90$ , ER formation is replaced by fission and the preceding difficulty should be avoided. Hence we investigated the reactions 250- to 288-MeV  $^{18}\text{Ar} + ^{82}\text{Pb}$  and  $^{18}\text{Ar} + ^{90}\text{Th}$  to search for  $Z_{UA} = 100$  and 108 x-rays. Since for 227-MeV  $^{136}\text{Xe} + ^{238}\text{U}$  the crystal blocking method<sup>21</sup> gives a lifetime of  $(3-8) \times 10^{-18}$  sec (probably from sequential fission after neutron evaporation), we expect a smaller value for  $\tau_c$  for the Ar induced reaction. From Eqs. (2) and (3) we then estimate a maximum CN K x-ray production probability per fission

$$\sigma_{\text{cx}} / \sigma_{\text{R}} \gtrsim 0.01 \quad . \quad (11)$$

This is based on the measured value<sup>41</sup>  $P_K(0) = 0.05$  and the calculated value<sup>42</sup>  $\lambda_K \approx 2.6 \times 10^{17} \text{ sec}^{-1}$ . It should be noted, though, that the estimate (3) may not be valid for these collisions and hence the estimate (11) may be incorrect.

Figure 6 shows the photon spectrum from 288-MeV Ar + Th in coincidence with particles within an energy interval corresponding to fission products.<sup>43</sup> A very high background is seen, presumably from the gamma decay of the excited fission products. In all the investigated reactions, we found a background of  $\sim 0.01$  photon/keV/fission, close to what is expected for slow-n fission of U or Th.<sup>44</sup> With a detector resolution of  $\sim 1$  keV, the expected CN x-ray production is submerged by the gamma-ray background. Only an upper limit  $\tau_c \gtrsim 10^{-18}$  sec can then be derived from our results, if the estimate (11) is correct.

#### 4.C. Emission of Positrons in Superheavy Collisions

The emission of positrons in superheavy collisions is discussed in other lectures and is mentioned here only for completeness. Theoretically, three processes are expected, called direct or shake-off, induced, and spontaneous. The direct process is the production of positrons due to the time-varying electromagnetic field caused by two heavy nuclei passing close to each other. The other two processes involve vacancies in the deeply bound MO levels. The induced process is conceptually similar to the formation of MO x-rays, except that the MO vacancies are filled by transitions of electrons from the negative-energy sea. The spontaneous process

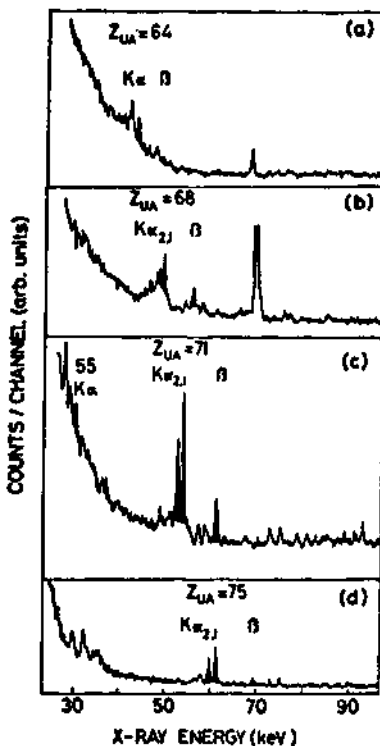


Fig. 5. Prompt x-ray spectra from 350-MeV  $^{36}\text{Kr}$  bombardment of various targets: (a)  $_{28}\text{Ni}$ , (b)  $_{32}\text{Ge}$ , (c)  $_{19}\text{K}_{35}\text{Br}$ , (d)  $_{39}\text{Y}$ . In each spectrum  $Z_{\text{UA}}$  and the expected united-atom K x-ray lines are indicated. The rising background at low x-ray energies is due to Mo x-rays. (From Ref. 40.)

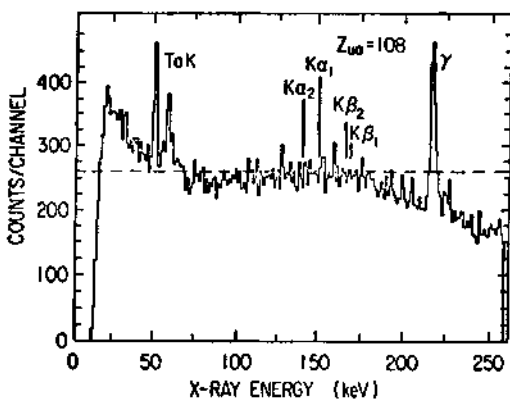


Fig. 6. Pulse-height spectrum in x-ray detector in coincidence with inelastic particle spectrum from 288-MeV  $^{36}\text{Ar} + ^{90}\text{Th}$  collisions. The UA K x-ray energies and relative intensities are indicated. Fluorescent x-rays from a Ta absorber appear. The gamma-ray is of unknown origin. The horizontal dashed line represents  $\sim 0.01$  photons/keV/reaction product. (From Ref. 41.)

is conceptually similar to the production of CN x-rays, except that the vacant united-atom MO must dive into the negative energy sea in order for it to be spontaneously filled by a negative-energy electron.

In detail, there are marked differences between the theory of MO + CN x-ray emission and that of induced + spontaneous positron emission:<sup>45</sup> (1) second-order processes involving electronic transitions to intermediate vacant MO states are much more important in positron emission than in x-ray emission, (2) the spontaneous positron emission amplitude differs in phase (by  $\pi/2$ ) from the induced emission amplitude, whereas the MO and CN x-ray emission amplitudes have an identical structure. Nevertheless, the effect of a nuclear sticking time<sup>6,7</sup> is again similar in the two cases: as the sticking time increases, a spontaneous positron line spectrum appears, analogous to the x-ray spectra shown in Fig. 4. Also, as the sticking time increases, the positron line spectrum becomes narrower until it reaches its natural width  $\Gamma$ , at which point the Gugelot equation (2) becomes approximately valid (with  $\lambda_K = \Gamma/\hbar$  and  $\omega_K = 1$ ).

The experimental situation is discussed in other lectures, particularly the question whether or not narrow lines recently found to be superimposed on the broader positron spectra are connected with nuclear sticking.

## 5. EXPERIMENTS WITH TARGET X-RAYS

### 5.A. Light projectiles

a. Theoretical background. We now turn to time-delay effects on target x-rays, i.e. on the vacancy-production probability in the target atom. For the reader not familiar with the application of time-dependent perturbation theory to electron excitation, a model problem is worked out in Appendix A (following the references).

In sufficiently asymmetric collisions, target K vacancies are produced predominately by ionization, with ejection of "delta electrons" whose energy is denoted by  $\epsilon$ . At zero impact parameter, the K-vacancy production probability is given by the semiclassical approximation as<sup>26</sup>

$$P_K(0) = 2 \int_0^\infty d\epsilon \sum_{\lambda\mu} |a_{\lambda\mu}(\epsilon)|^2 \quad (12)$$

where  $\lambda, \mu$  are the orbital and magnetic quantum numbers of the ejected electron. A factor 2 has been added to take into account the two K electrons. The amplitude  $a_{\lambda\mu}$  can be written in the form<sup>26</sup> [see App. A, Eq. (A14)]

$$a_{\lambda\mu} = \int_{-\infty}^{\infty} dt M_{\lambda\mu}(\epsilon, t) e^{i\omega t}, \quad (13)$$

where  $M_{\lambda\mu}$  is a Coulomb matrix element connecting the initial and

final electron states and  $\hbar\omega \equiv |E_K| + \epsilon$  is the energy which has to be imparted to the K electron with a binding energy  $E_K$  in order that it be ejected with the final kinetic energy  $\epsilon$ . For projectiles of velocity considerably less than the initial Bohr velocity of the K electron, the  $\lambda = 0$  term is dominant in Eq. (12).<sup>26</sup> Hence, for simplicity, we drop all higher terms in Eq. (12) and we drop the subscript  $\lambda\mu$  in Eq. (13). Breaking the integration in Eq. (13) into the time intervals  $-\infty$  to 0, 0 to  $T$ , and  $T$  to  $\infty$ , it is shown in App. A [Eq. (A29)] that for an elastic collision the ionization amplitude can be written

$$a = a'_{1/2} - e^{i\omega(0)T} a'^{*}_{1/2}, \quad (14)$$

where  $a'_{1/2}$  is the modified amplitude on the way into the collision [see Eq. (A30)].\*

Conceptually, Eq. (14) is clear: looking at  $a'_{1/2}$  as the ionization amplitude for a time-reversed nuclear decay, one must, after a time lapse  $T$  and a phase change  $\omega(0)T$ , add the ionization amplitude for the outgoing nuclear decay.<sup>8</sup> The probability  $P_K(0)$ , Eq. (12), must still be averaged over the distribution function  $p(T)$  of the sticking time:

$$\bar{P}_K(0) = \int_0^\infty dT p(T) P_K(0). \quad (15)$$

This semiclassical treatment of a nuclear collision is not suited for resonance reactions, nor does it include such effects as Coulomb-nuclear interference. A proper quantum mechanical treatment must be made,<sup>9,46-48</sup> which is sketched in App. B. This yields instead of Eq. (15), for  $\lambda = 0$  and elastic scattering,<sup>9\*\*</sup>

$$\bar{P}_K(0) = 2 \int_0^\infty dE |a'_{1/2} f[\theta, E - \hbar\omega(0)] - a'^{*}_{1/2} f(\theta, E)|^2 / |f(\theta, E)|^2. \quad (16)$$

Here  $f(\theta, E)$  is the elastic scattering amplitude for the projectile at a center-of-mass scattering angle  $\theta$  and kinetic energy  $E$ .

One can interpret Eq. (16) as follows. If the K electron is ionized on the way into the collision, the projectile has only an energy  $E - \hbar\omega$  left to initiate the nuclear reaction. If the K vacancy is produced only on the way out, the full energy  $E$  was available to the nuclear reaction. Hence, if  $f$  has a resonant behavior, the two terms in Eq. (16) will change magnitude as the resonance is

\* The probability  $P_K$  in Eq. (2) is related to  $a'_{1/2}$  by  $P_K = 2 \int_0^\infty dE |a'_{1/2}|^2$ .

\*\* The term proportional to  $a'^{*}_{1/2}$  differs in sign from Ref. 9, because the factor  $i$  is included in our definition of the amplitude  $a$  [Eq. (A14)].

traversed. The quantity  $\bar{P}_K(0)$  will reflect this variation. Of course, in a resonance reaction the time delay is known from the width of the resonance.<sup>13,16</sup> So, the interest of Eq. (16) lies in the fact that one has here the rare opportunity to determine the phase of  $a_K^1$  [see Eq. (19) below] and compare it to theories of ionization.<sup>2</sup>

In comparing the semiclassical expression (12) and (14) with the quantum mechanical expression (16), one sees that the phase factor  $e^{-i\omega(0)T}$  [suitably averaged by Eq. (15)] in the former theory is equivalent to the ratio  $f[\theta, E - \hbar\omega(0)]/f(E)$  in the latter theory. Expanding to first order in  $\omega(0)$ , the averaged semiclassical phase factor becomes

$$1 - i\omega(0)\tau , \quad (17)$$

assuming exponential decay with a mean life  $\tau$ . The ratio of the scattering amplitudes is, to first order in  $\omega(0)$ ,

$$1 - \hbar\omega(0)\partial\ln f/\partial E \Big|_E = 1 - i\omega(0)\tau' , \quad (18)$$

where  $\tau'$  is the reaction time.<sup>49</sup> As discussed by Blair,<sup>50</sup>  $\tau'$  can be imaginary and energy dependent; hence, the similarity between expressions (17) and (18) is partly superficial.

In the case of a simple resonant behavior of  $f(\theta, E)$ , if  $\hbar\omega(0)$  is much smaller than the width of the resonance,  $f(\theta, E)$  cancels out in Eq. (16). In that case no variation in  $\bar{P}_K(0)$  is expected, as the resonance is traversed.<sup>46-48</sup>

b. Experimental results. Two experiments have been done to date,<sup>9,51</sup> which are in agreement with the expected variation of  $\bar{P}_K$ , Eq. (16), across a resonance. Figure 7 taken from Ref. 51, shows the elastic scattering cross section in the neighborhood of the 5.16-MeV resonance in the  $^{88}\text{Sr}(p, p)$  reaction. This resonance has a width of  $\sim 19$  keV, which is of the same order of magnitude as the K-binding energy of Sr (16.1 keV). Hence a large effect in  $\bar{P}_K$  is expected – and found – as the resonance is traversed. In absolute value and in shape, the variation in  $\bar{P}_K$  agrees well with the ionization theory.<sup>55</sup> Similar agreement had been previously found<sup>9</sup> for a proton resonance in  $^{58}\text{Ni}$ . Since the  $^{88}\text{Sr}$  resonance requires a proton angular momentum  $\ell_p = 2$ , but the  $^{58}\text{Ni}$  resonance  $\ell_p = 0$ , the resonance effect on  $\bar{P}_K$  is not strongly dependent on the spin of the nuclear resonance.

A puzzling effect has been reported by Duinker et al.<sup>53</sup> for the 0.46-MeV elastic scattering resonance in the  $^{12}\text{C}(p, p)$  reaction. Here,  $\hbar\omega(0) \ll \Gamma[\hbar\omega(0) \approx 0.3 \text{ keV}, \Gamma \approx 35 \text{ keV}]^{54}$ , so that a very small resonance effect on  $\bar{P}_K$  is expected. Yet, a  $\sim 70\%$  variation was found across the resonance, which cannot be explained by present theory.<sup>46-48</sup>

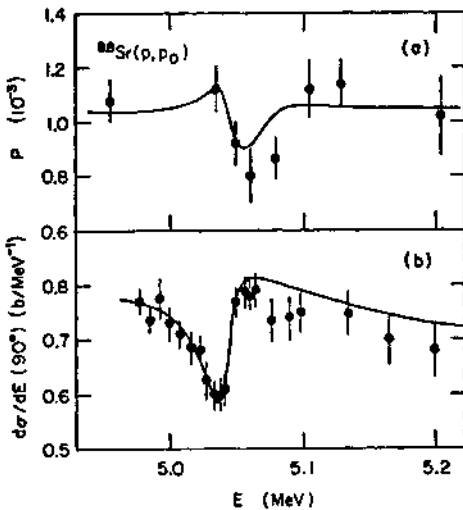


Fig. 7. (a) Ionization probability of  $^{88}\text{Sr}$  in coincidence with elastically scattered protons ( $90^\circ$  lab.). The curve has been computed using Eq. (16) and the ionization model of Ref. 55.

(b) Cross section of elastically scattered protons at  $90^\circ$  lab. angle from the reaction  $^{88}\text{Sr}(p,p)$ , as a function of bombarding energy. (From Ref. 51.)

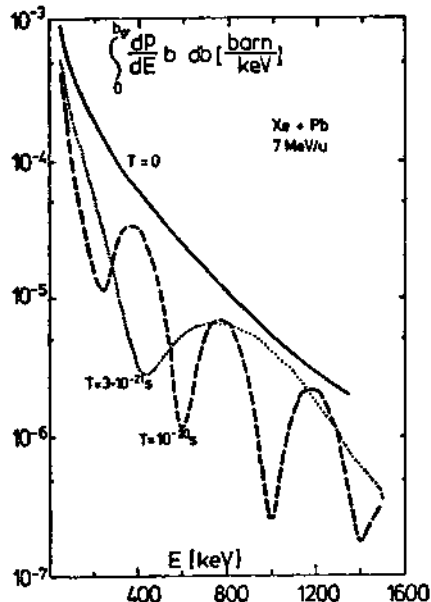


Fig. 8. Delta-electron spectrum from 7-MeV/N Xe + Pb reaction as a function of the nuclear sticking time  $T$  (from Ref. 56). Experimentally, one expects an added background of internal conversion electrons from the deexcitation gamma rays of the reaction products.

B. Heavy Projectiles

a. Theoretical background. As noted in Sec. 2, for projectiles with  $Z_p \gtrsim 30$ , at bombarding energies above the Coulomb barrier, deep-inelastic collisions dominate the nuclear interaction.<sup>17,23</sup> For these collisions the molecular model is appropriate [see App. A] and we can refer to Fig. 3 for a sketch of the time dependence of the  $1s\sigma$  MO energy. The effect of the nuclear sticking time on the amplitude  $a_{1s\sigma}(\infty)$ , i.e. the K-vacancy production amplitude in the higher-Z partner at the end of the collision, is given by Eq. (A26). Reinhardt et al.<sup>56</sup> propose that one should measure the delta-electron spectrum to obtain the sticking time. Anholt<sup>57</sup> suggests that one should measure the K x-ray production probability as a function of the total kinetic energy loss (TKEL) of the particles, which should reflect the sticking time.<sup>25</sup> We examine these two proposals briefly.

If one makes a model for a deep-inelastic nuclear reaction equivalent to an elastic process, one can use Eq. (A26), or the similar Eq. (14), to compute the ionization amplitude. Substitution into Eq. (12) then gives the delta-electron spectral yield per collision<sup>56</sup>

$$\frac{dP_K(0)}{d\epsilon} = 8|b_{1s\sigma}|^2 \sin^2 \left[ \frac{1}{2} \omega(0)T - \beta \right] , \quad (19)$$

where  $\hbar\omega(0) = |E_{1s\sigma}(0)| + \epsilon$  and  $\beta$  is the phase of the molecular-model ionization amplitude  $b_{1s\sigma}$ . This distribution must still be integrated over a sticking time distribution [Eq. (15)] in order to obtain the experimental spectrum  $\overline{dP_K(0)/d\epsilon}$ . Here one has to rely on various theoretical models.<sup>25,58</sup> Figure 8 shows the spectral shape computed by Soff et al.<sup>56</sup> using Eq. (19), but including higher order effects due to electronic transitions from the  $1s\sigma$  MO into vacant bound MO's. Soff et al. have also shown that inclusion of a realistic kinetic energy loss in the model has only little influence on the spectrum.

Anholt's proposal<sup>57</sup> is equivalent to the measurement of  $P_K(0)$  as a function of  $T$ . The expected dependence would be given by the integral of Eq. (19) over  $d\epsilon$ , if the incident and outgoing channels are identical. Anholt uses model calculations of Schröder et al.<sup>25</sup> and of Riedel et al.<sup>56</sup> to relate the sticking time to the TKEL ( $= -Q$ ) of the reaction products. The former model gives

$$T = T_0 e^{(TKEL)/Q_0} , \quad (20)$$

where  $T_0$  and  $Q_0$  are positive model-dependent, constants. The latter model takes into account the deformation of the reaction products and gives slightly longer sticking times for the same TKEL. Experimentally, the TKEL can be determined from the energy and lab.

angle of one reaction product,<sup>59</sup> assuming a binary process for the reaction.<sup>25</sup> Anholt's model calculations include the energy loss of the outgoing particles (see also Ref. 61). Figure 9 gives his predictions for the dependence of  $P_K(0)$  on TKEL for the 1130-MeV  $^{136}_{54}\text{Xe} + ^{209}_{83}\text{Bi}$  reactions.<sup>57,60</sup>

b. Experimental results. In order to apply Anholt's proposal,<sup>57</sup> we have made a measurement of the x-ray spectrum in coincidence with reaction products from the 1160-MeV  $^{136}_{54}\text{Xe} + \text{Pb}$  and  $^{136}_{54}\text{Xe} + \text{Th}$  reactions.<sup>62</sup> The x-rays were detected in a planar Ge detector at 90° to the beam. The particles were detected in a  $\Delta E$ -E system<sup>63</sup> consisting of a gas proportional detector and a surface barrier Si detector, placed at 35° (lab.) to the beam direction. The detector subtended a 8° half-angle cone at the target.

Figure 10 gives our preliminary results for the target-like (higher-Z) x-ray production probability  $P_x$  in coincidence with projectile-like or target-like particles. The curves AT show the model calculations of Anholt,<sup>60</sup> folded with a 50-MeV wide Q value resolution function. The experimental values of  $P_x$  exceed these predictions, increasingly more as the TKEL increases. The excess increase is reminiscent of the increase in the gamma-ray multiplicity of deep-inelastic nuclear reactions with increasing TKEL.<sup>17</sup> Hence, we believe that excess in  $P_x$  reflects the increase in the number of x-rays from internal conversion of the deexciting gamma cascades in the target-like nuclei. The dotted curves IC in Fig. 10 are measured gamma-ray intensity distributions as a function of TKEL, fitted along ordinate axis. One sees that the sum of the AT and IC curves can be made to agree with the measured dependence of  $P_x$  on TKEL.

Unfortunately, the presence of the internal conversion background makes it impossible to distinguish between the final resultant curves with a finite sticking time (heavy dash-dot curves in Fig. 10) and an assumed zero sticking time (heavy solid curves in Fig. 10). Nevertheless, we believe that with increasing united-atom Z values a situation can be produced (e.g. in U + U collisions), in which the atomic contribution to  $P_x$  exceeds the internal-conversion contribution, so that the sticking-time effect can be ascertained.

## OUTLOOK

The successful detection of sticking-time effects on x-rays produced in nuclear reactions<sup>2,9,35</sup> will inspire further work in this field. The incentive is high, because, in principle, the measurement of CN x-rays can determine nuclear lifetimes in the region of  $\sim 10^{-15}$  to  $\sim 10^{-18}$  sec and target x-ray methods are sensitive to nuclear delays from  $\sim 10^{-18}$  to  $\sim 10^{-21}$  sec.<sup>2</sup> Hence, the method has a potentially wide range of applicability. In particular, no other method is presently available to measure nuclear delay times in deep-inelastic heavy-ion reactions.<sup>64</sup> From an atomic physics point of view, one has here the opportunity to study details

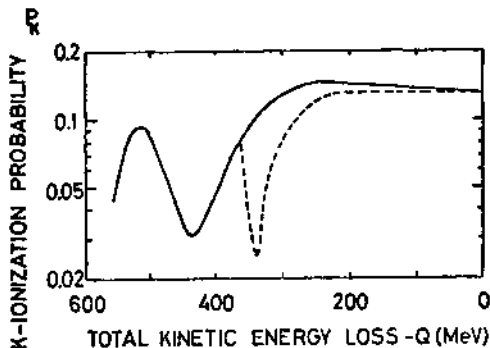


Fig. 9. Probability of creating target K vacancies in 1130-MeV  $Xe + Bi$  collisions at zero "atomic impact parameter", as a function of the total kinetic energy loss ( $= -Q$ ). Two different models for the sticking time dependence on  $Q$  have been assumed: solid curve Ref. 25, dashed curve Ref. 58. (From Refs. 57 and 60.)

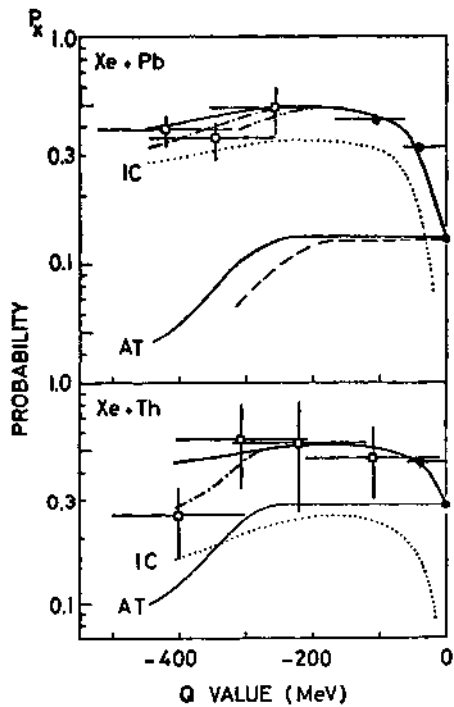


Fig. 10. Probability of target-like x-ray production in 1160-MeV  $Xe + Pb$  and  $Xe + Th$  reactions. The solid points represent  $P_x$  for coincidences with projectile-like particles, the open points  $P_x$  for coincidences with target-like particles. The curves AT and IC represent the calculated atomic and fitted internal-conversion contributions to  $P_x$ . The heavy curves are the summed values: the dash-dot curves assume the computed sticking-time effect, the solid curves assume zero sticking time. (From Ref. 62.)

of the ionization process, not accessible by other means. As experimental techniques develop further, one may expect to see much activity in this fascinating area of overlap between atomic and nuclear physics.

## REFERENCES

1. P. C. Gugelot, in Direct Interactions and Nuclear Reaction Mechanisms, Padua, E. Clementel and C. Villi, Eds. (Gordon and Breach, New York, 1962), p. 382.
2. J. F. Chemin, Doctor-of-Science Thesis, University of Bordeaux I (1978).
3. L. Kocbach, in Notes from the Nordic Spring Symposium on Atomic Inner Shell Phenomena, Geilo, Norway, J. M. Hansteen and R. Gundersen, Eds. (Department of Physics, University of Bergen, Norway, 1978), vol. II, p. 65.
4. J. Rafelski, private communication (1978).
5. J. Reinhardt and W. Greiner, *Repts. Prog. Phys.* 40, 219 (1977).
6. J. Rafelski, B. Müller, and W. Greiner, *Z. Physik A* 285, 49 (1978).
7. U. Müller, Diploma Thesis, Institute of Theoretical Physics, University of Frankfurt (1981).
8. G. Cochetti and A. Molinari, *Nuovo Cimento* 40B, 69 (1965).
9. J. S. Blair, P. Dyer, K. A. Snover, and T. A. Trainor, *Phys. Rev. Lett.* 41, 1712 (1978).
10. R. M. Eisberg, D. R. Yennie, and D. H. Wilkinson, *Nucl. Phys.* 18, 338 (1960).
11. H. Feshbach and D. R. Yennie, *Nucl. Phys.* 37, 150 (1962).
12. M. K. Liou, C. K. Liu, P. M. S. Lesser, and C. C. Trail, *Phys. Rev. C* 21, 518 (1980).
13. C. Maroni, I. Massa, and G. Vannini, *Nucl. Phys. A* 273, 429 (1976); C. C. Trail, P. M. S. Lesser, A. H. Bond, Jr., M. K. Liou, and C. K. Liu, *Phys. Rev. C* 21, 2131 (1980).
14. V. F. Weisskopf, *Rev. Mod. Phys.* 39, 174 (1957).
15. H. Feshbach, *Ann. Phys.* 5, 357 (1958) and 19, 287 (1960).
16. S. Yoshida, *Ann. Rev. Nucl. Sci.* 24, 1 (1974).
17. P. E. Hodgson, Nuclear Heavy-Ion Reactions (Clarendon Press, Oxford, England, 1978); R. Bass, Nuclear Reactions with Heavy Ions (Springer, Berlin, 1980).
18. M. Flocard, S. E. Koonin, and M. S. Weiss, *Phys. Rev. C* 17, 1682 (1978); P. Bonche, B. Grammaticos, and S. E. Koonin, *Phys. Rev. C* 17, 1700 (1978); S. E. Koonin, Calif. Inst. of Technology, W. K. Kellogg Rad. Lab., Preprint MAP-5 (1979).
19. M. Lefort, *J. Phys. (Paris) Colloq. C5* 37, 57 (1976) and *Rep. Progr. Phys.* 39, 129 (1976).
20. T. Erikson, *Adv. Phys.* 9, 425 (1960).
21. S. A. Karamayan, Yu. V. Melikov, and A. F. Tulinov, *Fiz. Elem. Chastits At. Yad.* 4, 456 (1973) [Sov. J. Part. Nucl. 4, 196 (1973)]; V. N. Bugrov, V. V. Kamanin, S. A. Karamayan, and S. P. Tret'Yakova, *Yad. Fiz.* 28, 303 (1978) [Sov. J. Nucl. Phys. 28, 153 (1978)].

22. J. U. Andersen, N. G. Chechnin, A. S. Jensen, K. Jørgensen, and E. Laegsgaard, *Nucl. Phys. A* 324, 39 (1979).
23. W. U. Schröder and J. R. Huizenga, *Ann. Rev. Nucl. Sci.* 27, 465 (1977).
24. L. G. Moretto and J. S. Sventek, *Phys. Lett.* 58B, 26 (1975); for other references see M. Lefort, *Z. Physik A* 299, 47 (1981).
25. W. U. Schröder, J. R. Birkelund, J. R. Huizenga, K. L. Wolf, and V. E. Viola, Jr., *Phys. Rep.* 45, 301 (1978).
26. J. Bang and J. M. Hansteen, *K. Dan. Videns. Selsk., Mat. Fys. Medd.* 31, No. 13 (1959).
27. W. Meyerhof and K. Taulbjerg, *Ann. Rev. Nucl. Sci.* 27, 279 (1977).
28. B. Müller and W. Greiner, *Z. Naturforsch.* 31a, 1 (1976).
29. J. Reinhardt, B. Müller, W. Greiner, and G. Soff, *Phys. Rev. Lett.* 43, 1307 (1979).
30. P. von Brentano and M. Kleber, *Phys. Lett.* 92B, 5 (1980); K. W. McVoy, X. T. Tang, and H. A. Weidenmüller, *Z. Physik A* 299, 195 (1981).
31. G. Ciochetti, A. Molinari, and R. Malvano, *Nuovo Cimento* 29, 1262 (1963).
32. W. Brandt, K. W. Jones, and H. W. Kraner, *Phys. Rev. Lett.* 30, 351 (1973).
33. J. F. Chemin, S. Andriamonje, J. Roturier, J. P. Thibaud, S. Joly, and J. Uzureau, in Electronic and Atomic Collisions, N. Oda and K. Takayanagi, Eds. (North Holland, Amsterdam, 1980), p. 313.
34. J. F. Chemin, S. Andriamonje, J. Roturier, B. Saboya, J. P. Thibaud, S. Joly, S. Platard, J. Uzureau, H. Lorent, J. M. Maison, and J. P. Shapira, *Nucl. Phys. A* 331, 407 (1979).
35. S. Röhrl, S. Hoppenau, and M. Dost, *Phys. Rev. Lett.* 43, 1300 (1979).
36. J. C. Hardy, J. A. Macdonald, H. Schmeing, H. R. Andrews, J. S. Geiger, R. L. Graham, T. Faestermann, E. T. H. Clifford, and K. P. Jackson, *Phys. Rev. Lett.* 37, 133 (1976).
37. W. Brandt, R. Laubert, and I. Sellin, *Phys. Lett.* 21, 518 (1966).
38. R. Anholt, *Phys. Rev. A* 17, 983 (1978).
39. R. Anholt, *Z. Physik A* 292, 123 (1979).
40. W. E. Meyerhof, R. Anholt, and W. Wölfl, *Phys. Lett.* 84B, 59 (1979).
41. R. Anholt, Ch. Stoller, J. F. Chemin and W. E. Meyerhof, unpublished results.
42. R. Anholt and J. O. Rasmussen, *Phys. Rev. A* 9, 585 (1974).
43. J. Peter, C. Ngô, and B. Tamain, *Nucl. Phys. A* 250, 351 (1975).
44. V. V. Verbinski, H. Weber, and R. E. Sund, *Phys. Rev. C* 7, 1173 (1973).
45. J. Reinhardt, G. Soff, B. Müller, and W. Greiner, *Progress in Particle and Nuclear Physics* 4, 547 (1980).
46. J. S. Blair and R. Anholt, to be published in *Phys. Rev. A*.
47. J. M. Feagin and L. Kocbach, to be published in *J. Phys. B*.
48. K. W. McVoy and H. A. Weidenmüller, to be published.
49. N. Austern, Direct Nuclear Reaction Theories (Wiley Interscience, New York, 1970).

50. J. S. Blair, Annual Report, Nuclear Physics Laboratory, University of Washington, Seattle (1980), p. 132.
51. J. F. Chemin, R. Anholt, Ch. Stoller, W. E. Meyerhof, and P. A. Amundsen, Phys. Rev. A 24, (in press).
52. W. Kretschmer and G. Graw, Phys. Rev. Lett. 27, 1294 (1971).
53. W. Duinker, J. van Eck, and A. Niehaus, Phys. Rev. Lett. 45, 2102 (1980).
54. E. A. Milne, Phys. Rev. 93, 762 (1954).
55. R. Anholt, Z. Physik A 295, 201 (1980).
56. J. Reinhardt, B. Müller, W. Greiner, and G. Soff, Z. Phys. A 292, 211 (1979); G. Soff, J. Reinhardt, B. Müller, and W. Greiner, Phys. Rev. Lett. 43, 1981 (1979).
57. R. Anholt, Phys. Lett. 88B, 262 (1979).
58. C. Riedel, G. Wolschin, and W. Nörenberg, Z. Physik A 290, 47 (1979).
59. R. D. Evans, The Atomic Nucleus, (McGraw Hill, New York, 1955), p. 411.
60. R. Anholt, unpublished results.
61. B. Müller and V. Oberacker, Phys. Rev. C. 22, 1909 (1980).
62. Ch. Stoller, J. F. Chemin, R. Anholt, W. E. Meyerhof, and W. Wölfl, to be published.
63. R. G. Markham, S. M. Austin, and H. Laumer, Nucl. Instr. Meth. 129, 141 (1975).
64. J. W. Harris, in Nuclear Physics with Heavy Ions and Mesons, R. Balian, M. Rho and G. Ripka, Eds. (North Holland, Amsterdam, 1978). p. 263.
65. D. H. Madison and E. Merzbacher, in Atomic Inner-Shell Processes, B. Crasemann, Ed. (Academic, New York, 1975) Vol. I, Sec. 1.5.
66. J. S. Briggs, Rep. Prog. Phys. 39, 217 (1976).
67. P. Amundsen, J. Phys. B 11, 3197 (1978); D. J. Jakubassa and P. A. Amundsen, J. Phys. B 12, L725 (1979).
68. L. I. Schiff, Quantum Mechanics (3rd ed.) (McGraw Hill, New York, 1968), Sec. 31.
69. Ref. 68, p. 289-290.
70. Ref. 68, p. 280-281.
71. J. S. Briggs, J. Phys. B 8, L 485 (1975).
72. W. E. Meyerhof, R. Anholt, J. F. Chemin, and Ch. Stoller, in Proceedings 18th Int. Winter Meeting on Nuclear Physics, Bormio, I. Iori, Ed. (University of Milan, Italy, 1980), p. 688.
73. L. Kocbach, Z. Physik A 279, 233 (1976).

## APPENDIX A. EXCITATION OF AN INNER-SHELL ELECTRON IN AN ATOMIC COLLISION WITH A LIGHT PROJECTILE IN THE SEMICLASSICAL APPROXIMATION. \*

Formulation of the problem

We consider a single electron initially bound to a (target) nucleus; the Hamiltonian for this system is  $H_0$ . A light projectile passes by and interacts with the electron through the Coulomb potential  $V[\mathbf{r}, \mathbf{R}(t)]$ , thereby exciting the electron to some bound state. (The problem is easily generalized to unbound states.) The vector  $\mathbf{R}(t)$  is the internuclear distance which, as a function of the time  $t$ , describes a classical trajectory. The electronic coordinate is denoted by  $\mathbf{r}$ . We want to show that to first order in  $V$  the atomic and molecular models give identical results for the  $t = \infty$  electron excitation probability, even if there is a time  $T$  during which the projectile and the target stick together.

The time-dependent Schrödinger equation can be written

$$i \frac{\partial \psi}{\partial t} = (H_0 + V)\psi , \quad (A1)$$

where atomic units ( $\hbar = e = m_e = 1$ ) have been used. To solve this equation, one uses as basis wave functions in the atomic model the eigenfunctions  $\psi_n(\mathbf{r})$  of  $H_0$ :

$$H_0 \psi_n = \epsilon_n \psi_n . \quad (A2)$$

In the molecular model, one uses as basis wave functions the eigenfunctions  $\phi_n(\vec{r}, \vec{R})$  of  $H_0 + V(\vec{r}, \vec{R})$ :

$$(H_0 + V)\phi_n = E_n \phi_n . \quad (A3)$$

One complication, which we ignore here by assuming the target nucleus to be very heavy compared to the projectile, is, that in  $\psi(\vec{r})$  the electron coordinate  $\vec{r}$  is measured with respect to the target nucleus instead of the center of mass (c.m.), as it should be. In the exact formulation of the problem, a recoil term must be added to  $V$  to correct for this defect.<sup>8,55,67</sup> In  $\phi_n$ , the electron coordinate  $\vec{r}$  is always measured with respect to the c.m.

If stationary perturbation theory is applied to Eq. (A3) by expanding  $\phi_n$  in terms of  $\psi_n$ , one finds, to first order in  $V$ ,<sup>68</sup>

$$E_n = \epsilon_n + V_{nn} , \quad (A4)$$

$$\phi_n = \psi_n - \sum_{m \neq n} (V_{nm} / \epsilon_{nm}) \psi_m , \quad (A5)$$

\*I am indebted to B. Müller for providing this material. More general treatments are given in Refs. 65 and 66.

where the following abbreviated notation has been used:

$$V_{nm} = \langle \psi_n | \vec{V}(\vec{r}, \vec{R}) | \psi_m \rangle , \quad (A6)$$

$$\varepsilon_{nm} = \varepsilon_n - \varepsilon_m . \quad (A7)$$

### Time-dependent perturbation theory

In the atomic model, one searches for a solution of Eq. (A1) by expanding  $\psi$  in terms of  $\psi_n$ :

$$\psi = \sum_n A_n(t) \psi_n(\vec{r}) \exp(-i\varepsilon_n t) , \quad (A8)$$

whereas in the molecular model one uses the expansion<sup>6,9</sup>

$$\psi = \sum_n b_n(t) \phi_n[\vec{R}(t)] \exp \left\{ -i \int_0^t E_n[\vec{R}(\tau)] d\tau \right\} . \quad (A9)$$

Substitution of expression (A8) into Eq. (A1) gives<sup>7,0</sup>

$$\dot{A}_n = -i \sum_m A_m V_{nm} \exp(i\varepsilon_{nm} t) . \quad (A10)$$

It is useful to eliminate the term  $m = n$  in the sum by the phase transformation

$$A_n(t) = a_n(t) \exp[-i \int_0^t V_{nn}(\tau) d\tau] . \quad (A11)$$

Substitution of Eq. (A11) into Eq. (A10) yields

$$\dot{a}_n = -i \sum_{m \neq n} a_m V_{nm} \exp[i \int_0^t E_{nm}(\tau) d\tau] , \quad (A12)$$

where Eq. (4) has been used, as well as the abbreviation

$$E_{nm} = \varepsilon_n - \varepsilon_m . \quad (A13)$$

To first order in  $V$ , only the initial amplitude  $a_0 \approx 1$  survives in the sum on the right hand side of Eq. (A12), so that

$$a_n(t) \approx -i \int_{-\infty}^t dt' V_{n0}(t') \exp[i \int_0^{t'} E_{n0}(\tau) d\tau] \quad (A14)$$

$$= - \int_{-\infty}^t dt' \frac{V_{n0}}{E_{n0}} \frac{\partial}{\partial t'} \left[ \exp[i \int_0^{t'} E_{n0} d\tau] \right] . \quad (A15)$$

Equation (A15) is convenient for the subsequent development. Integrating it by parts,

$$a_n(t) = - \left| \frac{V_{n0}}{E_{n0}} \exp[-i \int_0^t E_{n0} d\tau] \right|_{-\infty}^t + \int_{-\infty}^t dt' \left| \frac{\partial}{\partial t'} \left( \frac{V_{n0}}{E_{n0}} \right) \right| \exp[i \int_0^{t'} E_{n0} d\tau] . \quad (A16)$$

Because  $E_{n0}$  depends on  $t$  only through  $V(t)$  [Eq. (A4)], in the second term one can set, to first order in  $V$ ,

$$\frac{\partial}{\partial t} \left( \frac{V_{n0}}{E_{n0}} \right) \approx \frac{1}{E_{n0}} \langle \psi_n | \frac{\partial V}{\partial t} | \psi_0 \rangle . \quad (A17)$$

If the molecular wavefunction (A9) is substituted in Eq. (A1), one finds, using Eq. (A3) and choosing appropriate phases for the coefficients  $b_n$ ,<sup>6,9</sup> that to first order in  $\partial/\partial t$

$$b_n(t) \approx - \int_{-\infty}^t dt' \langle \phi_n | \frac{\partial \phi_0}{\partial t'} \rangle \exp[i \int_0^{t'} E_{n0} d\tau] . \quad (A18)$$

Using the (Feynman - Hellmann) theorem<sup>6,9</sup>

$$- \langle \phi_n | \frac{\partial \phi_m}{\partial t} \rangle = \frac{1}{E_{nm}} \langle \phi_n | \frac{\partial V}{\partial t} | \phi_m \rangle , \quad (A19)$$

one sees that to first order in  $V$  [Eq. (A5)], the right hand sides of expressions (A17) and (A19) are identical. Hence, within this approximation, the second term in expression (A16) represents  $b_n(t)$ :

$$a_n(t) = b_n(t) - \frac{V_{n0}(t)}{E_{n0}(t)} \exp[i \int_0^t E_{n0}(\tau) d\tau] , \quad (A20a)$$

where  $a_n$  and  $b_n$  are given by Eqs. (A14) and (A18), respectively, and where we have used the fact that  $V_{nm}(-\infty) = 0$ . Noting that also  $V_{nm}(\infty) = 0$ , Eq. (A20a) implies that, to first order in  $V$ ,

$$a_n(\infty) = b_n(\infty) . \quad (A20b)$$

Equation (A20a) is the desired connection between the atomic and molecular model amplitudes, whereas Eq. (A20b) shows that to first order in  $V$  the final amplitudes are identical in both models.

If one considers collisions systems which are near symmetric, recoil effects can no longer be ignored. A more complicated relation between the two amplitudes is then appropriate, which has been shown by Briggs<sup>71</sup> to simplify in collisions in which excitation at very close distances of approach is most important (see also Ref. 67 and lecture by Briggs).

### Time-delay effect

We now apply Eqs. (A14) and (A18) to the case of an atomic excitation accompanied by a nuclear reaction with a time delay  $T$ . For simplicity, we assume that the nuclear reaction involves elastic scattering. We first consider Eq. (A18).

If one refers the molecular wavefunction  $\phi$  to the internuclear axis  $\vec{R}$ , the time derivative  $\partial/\partial t$  in Eq. (A18) becomes, for the case of zero impact parameter,<sup>66</sup>

$$\partial/\partial t \rightarrow \dot{\vec{R}} \partial/\partial \vec{R} . \quad (A21)$$

Then, the final excitation amplitude in the molecular model can be written

$$b_n^{(\infty)} = [\int_{-\infty}^0 + \int_0^T + \int_T^\infty] dt \dot{\vec{R}} \langle \phi_n | \partial \phi_0 / \partial \vec{R} \rangle \cdot \exp[i \int_0^t E_{n0}(\tau) d\tau] . \quad (A22)$$

During the sticking time  $0 \rightarrow T$ ,  $\dot{\vec{R}} = 0$ ; hence the second integral is zero. Also, during the sticking time,  $E_{nm}(\tau) = E_{nm}(0) = \text{constant}$ , so that the third integral can be written

$$\exp[i E_{n0}(0) T] \int_T^\infty dt \dot{\vec{R}} \langle \phi_n | \partial \phi_0 / \partial \vec{R} \rangle \exp[i \int_T^t E_{n0}(\tau) d\tau] . \quad (A23)$$

Noting that for an elastic collision

$$R(-t) = R(t + T) , \quad (A24a)$$

$$E_{nm}(-t) = E_{nm}(t + T) , \quad (A24b)$$

$$\dot{R}(-t) = -\dot{R}(t + T) , \quad (A24c)$$

the integral in expression (A23) can be written as  $-b_n^*(0)$ , where

$$b_n^*(0) = \int_{-\infty}^0 dt \dot{\vec{R}} \langle \phi_n | \partial \phi_0 / \partial \vec{R} \rangle \exp[i \int_0^t E_{n0}(\tau) d\tau] . \quad (A25)$$

Hence, the excitation amplitude is

$$b_n^{(\infty)} = b_n^*(0) - b_n^*(0) \exp[i E_{n0}(0) T] . \quad (A26)$$

Equation (A14) for the atomic model amplitude can be treated in a similar way. Here, we use the facts that during the sticking time,  $v_{nm}(t) = v_{nm}(0) = \text{constant}$  and that, for an elastic collision,

$$v_{nm}(-t) = v_{nm}(t + T) . \quad (A27)$$

Then one finds

$$\begin{aligned} a_n(\infty) &= a_n(0) - a_n^*(0) \exp[i E_{n0}(0)T] \\ &\quad - i v_{n0}(0)T \int_0^T dt \exp[i E_{n0}(0)t] . \end{aligned} \quad (A28)$$

The integral is easily evaluated, and the last term becomes

$$- \frac{v_{n0}(0)}{E_{n0}(0)} \{ \exp[i E_{n0}(0)T] - 1 \} . \quad \text{Hence,}$$

$$a_n(\infty) = a_n'(0) - a_n'^*(0) \exp[i E_{n0}(0)T] , \quad (A29)$$

where

$$a_n'(0) = a_n(0) + v_{n0}(0)/E_{n0}(0) . \quad (A30)$$

We see that Eqs. (A26) and (A29) are consistent with Eq. (A20b), since according to Eq. (A20a)

$$b_n(0) = a_n'(0) . \quad (A31)$$

The second term in Eq. (A30) represents the excitation amplitude, calculated with the target wavefunction, due to the change in charge of the target nucleus as the projectile enters it. The term has been called adiabatic shake-off term.<sup>3</sup> Equation (A29) agrees with Ref. 8, since the factor  $i$  in Eq. (A14) has been factored out of Eq. (6) in Ref. 8. In the text, we have set  $a_{n0}(0) \equiv a_{1/2}$  and  $b_{n0}(0) \equiv b_{1/2}$ .

Equations (A14) and (A18) can both be written

$$\int_{-\infty}^t dt' M(t') \exp[i \int_0^{t'} E_{n0}(\tau) d\tau] \quad (A31)$$

where, in the atomic model,

$$M(t) = -i v_{n0}(t) , \quad M(-t) = M(t + T) , \quad (A32)$$

and, in the molecular model,

$$M(t) = - \hat{R} \langle \phi_n | \partial \phi_0 / \partial R \rangle , \quad M(-t) = -M(t + T) . \quad (A33)$$

Both relations can be combined in the form

$$M^*(-t) = -M(t + T) . \quad (A34)$$

Equations (A26), (A29) and (A32)-(A34) correct sign errors in Ref. 72.

If one applies the preceding treatment to ionization rather than excitation, one must use properly normalized continuum wavefunctions for the final state. One then finds for the delta - electron spectrum

$$dP/d\varepsilon = |b_n(\infty)|^2 \quad (A35)$$

and for the ionization probability

$$P = \int_0^\infty d\varepsilon |b_n(\infty)|^2 , \quad (A36)$$

where  $\varepsilon$  denotes the kinetic energy of the delta electron.

#### APPENDIX B. SKETCH OF THE DISTORTED - WAVE BORN APPROXIMATION DERIVATION.\*

We consider the same problem as in Appendix A, but use a quantum mechanical treatment for the projectile motion. The electronic motion will be described by the atomic model. This complete quantum mechanical treatment gives the combined cross section  $d\sigma_K/d\Omega_p$  for nuclear scattering and electronic (K shell) ionization (or excitation). To obtain the ionization probability one has to divide  $d\sigma_K/d\Omega_p$  by the nuclear scattering cross section  $d\sigma_p/d\Omega_p$ . (We again treat nuclear elastic scattering only.) The equation analogous to (A36) is

$$P = \frac{d\sigma_K/d\Omega_p}{d\sigma_p/d\Omega_p} = \frac{1}{|f(E)|^2} \sum_{\lambda, \mu} \int_0^\infty d\varepsilon |A_{\lambda\mu}(\varepsilon)|^2 \quad (B1)$$

Here the subscript p denotes projectile;  $f(E)$  is the elastic scattering amplitude. The scattering - ionization amplitude is given by ( $\hbar = e = m_e = 1$ )

$$A_{\lambda\mu}(\varepsilon) = \frac{\sqrt{KK'}}{2\pi v} \sum_{\ell, \ell'} \langle \chi_{\ell'}^-(\vec{K'}, \vec{R}) \psi_n(\vec{r}) | v | \chi_{\ell}^+(\vec{K}, \vec{R}) \psi_0(\vec{r}) \rangle , \quad (B2)$$

---

\* This material is based on the work of Refs. 46 and 47.

where  $V(\vec{r}, \vec{R})$  is the same projectile-electron interaction as in App. A. Recoil effects are again omitted. The initial and final momenta  $\vec{K}$  and  $\vec{K}'$  of the projectile are related to the energy  $\omega$  transferred to the electron:

$$\omega = (K^2 - K'^2)/(2M_p) \approx (K - K')v \quad , \quad (B3)$$

where  $M_p$  is the projectile mass. The projectile wave functions  $\chi_\ell$  and  $\chi_{\ell'}^*$  are characterized by the orbital angular momenta  $\ell$  and  $\ell'$  which are related to the orbital angular momentum  $\lambda$  transferred to the electron by

$$\vec{\ell} = \vec{\ell}' + \vec{\lambda} \quad . \quad (B4)$$

The index  $n$  on the  $\psi$  is meant to include  $\varepsilon, \lambda, \mu$ .

As suggested by Kochbach<sup>73</sup>, it is convenient to expand the potential  $V$  in spherical harmonics of  $\vec{r}$  and  $\vec{R}$ , yielding

$$\langle \psi_{n(\lambda\mu)} | v | \psi_0 \rangle = 4\pi(2\lambda + 1)^{-1} Y_{\lambda\mu}(\vec{R}) G_\lambda(R) \quad , \quad (B5)$$

where

$$G_\lambda(R) = -Z_p \langle U_n | r_{<}^\lambda r_{>}^{-\lambda-1} | U_0 \rangle \quad . \quad (B6)$$

Here,  $U$  is the radial part of  $\psi$  and  $r_{<}, r_{>}$  are the lesser or greater of  $r, R$ .

The projectile wave function is written in terms of the exact reduced radial wave function  $R_\ell(R)$  and the nuclear phase shift  $\delta_\ell$  as

$$\chi_\ell^+ = 4\pi(KR)^{-1} \sum_m i^\ell Y_{\ell m}^*(\vec{K}) \hat{Y}_{\ell m}(\vec{R}) e^{i\delta_\ell} R_\ell(KR) \quad (B7)$$

and  $\chi^-(\vec{K}') = [\chi^+(-\vec{K}')]^*$ . Substitution of Eqs. (B5-7) into Eq. (B2) then yields

$$A_{\lambda\mu} = \sum_{\ell, \ell'} C(\ell, \lambda, \ell') Y_{\ell', \mu}^*(\vec{K}') e^{i(\delta_\ell + \delta_{\ell'})} \cdot \int_0^\infty dR R_\ell(R) R_{\ell'}(R) G_\lambda(R) \quad , \quad (B8)$$

where  $C$  is a coefficient depending on the angular momenta  $\ell$ ,  $\lambda$ , and  $\ell'$ .

The method of Blair and Anholt<sup>46</sup> consists of evaluating the last integral by dividing the range of  $R$  into two regions, one of nuclear dimensions and one of atomic dimensions. The boundary between the two regions is denoted by  $R_0$ . For  $R > R_0$ , the projectile radial

wavefunction  $\mathcal{R}$  is replaced by its asymptotic value

$$\mathcal{R}_\lambda(R > R_0) \sim \dots e^{i(KR + \delta_\lambda)} + \text{c.c.} \quad (\text{B9})$$

The corresponding contribution to  $A_{\lambda\mu}$  consists of four terms

$$\begin{aligned} A_{\lambda\mu}(R > R_0) \sim & \int_{R_0}^{\infty} [\dots e^{2i\delta_\lambda} e^{i(K-K')R} + \dots e^{2i\delta_{\lambda'}} e^{i(K'-K)R} \\ & + \dots e^{2i(\delta_\lambda + \delta_{\lambda'})} e^{i(K+K')R} \\ & + \dots e^{-2i(\delta_\lambda + \delta_{\lambda'})} e^{-i(K+K')R}] G_\lambda(R) dR. \end{aligned} \quad (\text{B10})$$

The last two terms in Eq. (B10) are ignored because of the high frequency of oscillation of the factor  $\exp[i(K + K')R]$ . In the first two terms, the factor  $\exp[2i\delta_\lambda]$  eventually leads to the scattering amplitude  $f(E)$  and  $e^{2i\delta_{\lambda'}}$  to  $f(E - \hbar\omega)$ . The factor  $\exp[i(K - K')R] \approx \exp[i\omega R/v]$  [see Eq. (B3)], together with  $G_\lambda(R)$  [Eq. (B6)], leads to the ionization amplitude  $a_n(0)$  introduced in App. A.<sup>73</sup> Similarly, the factor  $\exp[-i(K - K')R]$  leads to  $-a_n^*(0)$ .

In the region  $R < R_0$ , it is sufficient to assume  $R \approx 0$  in  $G_\lambda(R)$ . One then finds that for  $\lambda > 0$  all contributions to  $A_{\lambda\mu}$  are negligible. For  $\lambda = 0$ ,  $G_0(0)$  is identical with the matrix element  $V_{n0}(0)$  introduced in App. A. Blair and Anholt<sup>46</sup> show that the corresponding contribution to  $A_{\lambda\mu}$  is just equal to the adiabatic shake off term

$$A_{\lambda\mu}(R < R_0) = [f(E) - f(E - \hbar\omega)] V_{n0}/\omega. \quad (\text{B11})$$

Adding the contributions (B10) and (B11), Eq. (16) of the text results.

POSITRONS FROM HEAVY ION COLLISIONS-EXPERIMENTS AT THE  
UNILAC\*

H. Backe<sup>1</sup>, W. Bonin, E. Kankeleit, M. Krämer,  
R. Krieg, V. Metag<sup>2</sup>, P. Senger, N. Trautmann<sup>3</sup>,  
F. Weik<sup>4</sup>, J.B. Wilhelm<sup>5</sup>

Institut für Kernphysik der TH Darmstadt

1 Institut für Physik der Universität Mainz

2 Max-Planck-Institut für Kernphysik, Heidelberg

3 Institut für Kernchemie der Universität Mainz

4 GSI, Darmstadt

present address: Lawrence Berkeley Laboratory,  
Berkeley, California 94720, USA

5 Los Alamos National Laboratory, Los Alamos  
New Mexico 87545, USA

ABSTRACT

Total positron production cross sections varying between a few  $\mu$ b and a few mb have been measured with a solenoidal spectrometer for various heavy ion scattering systems with united nuclear charges as high as 184 at beam energies between 3.6 and 5.9 MeV/u. The positron production probabilities for close ion atom collisions have been investigated for various scattering systems including the U + Cm system with a united nuclear charge of 188 at U - beam energies between 4.7 and 5.9 MeV/u and a scattering angle  $\theta_{lab} = 45^\circ \pm 10^\circ$ . In addition the energy distribution of the emitted positrons was investigated for the overcritical U + U and the undercritical U + Pb scattering system at a U - beam energy of 5.9 MeV/u and a scattering angle  $\theta_{lab} = 45^\circ \pm 10^\circ$ . No effects of a diving level have been observed in these measurements

---

\* presented by H. Backe

A positron spectrum taken for  $U + U$  at 8.4 MeV/u in coincidence to reaction products detected at  $\theta_{lab} = 45^\circ \pm 10^\circ$  probably indicates effects of a small time delay during nuclear contact.

## INTRODUCTION

Positron production in strong electrical fields has a long history ranging from the work of O. Klein<sup>1</sup> in 1929 which investigated the reflection behavior of electron waves impinging on a one dimensional step barrier potential with the aid of the, at the time, new Dirac theory to the very recent theoretical work of W. Greiner and coworkers in Frankfurt on positron production in superheavy atomic collision systems. In two recent articles this field has been extensively reviewed<sup>2,3</sup>. For the most recent theoretical status the reader is referred to the talk of B. Müller in this conference. It hopefully is, therefore, permissible not to repeat all the motivations to do experiments on positron creation in close collisions of very heavy ions (e.g.  $^{238}U$  on  $^{248}Cm$ ) but to go directly ahead and describe the experimental progress.

Experiments on this subject have been carried out at GSI in Darmstadt since 1976 when the UNILAC beam became available to experimentalists. At present three independent groups work on positron creation in heavy ion collisions with somewhat different experimental tools. We would like to review in this talk only the experiments performed with the solenoidal spectrometer installed at location X8 in the experimental area at GSI. In these experiments the positron production mechanism was investigated with special emphasis on overcritical situations i. e. for systems for which according to theoretical calculations the diving of the  $1s_\sigma$  level into the negative continuum (Dirac see) is expected to occur. In that case a  $1s_\sigma$  vacancy behaves like a bound positron which may give rise to pronounced deviations of the energy integrated positron production probability  $P_e^+$  from the exponential scaling behavior or possibly structures in the low energy part of the positron spectra  $dP_e^+/dE_e^+$ . For that reason  $P_e^+$  was measured for the overcritical  $U + Cm$  ( $Z_u = 188$ ), the  $U + U$  ( $Z_u = 184$ ), and the undercritical  $U + Pb$  ( $Z_u = 174$ )-systems under various dynamical conditions. In addition positron spectra have been measured for an overcritical  $U + U$  and an undercritical  $U + Pb$  system at a  $U$  beam energy of 5.9 MeV/u.

## DEFINITION OF THE PHYSICAL QUANTITIES

As P. Kienle pointed out in his talk on this conference the objective of positron spectroscopy in heavy ion collisions is to investigate a n-fold differential cross section with respect to various observables. However, the easiest thing from an experimental stand point is to avoid observation of parameters on which the cross section depends. Each experimentally parameter not observed is equivalent to an integration of the n-fold differential cross section. As an example, positron production may be studied as a function of always having electrons emitted in coincidence with a positron. If electrons are not observed the experiment simplifies considerably and the cross section being studied does no longer depend on the electron energy.

In this talk we will restrict ourselves primarily to the investigation of the double differential cross section

$$(d^2\sigma_{e^+}/(d\Omega_{\text{lab}} dE_{e^+})) (E_{e^+}, \theta_{\text{lab}}, E_1, Z_1, M_1, Z_2, M_2) \quad (1)$$

which is differential with respect to the positron energy  $E_{e^+}$  and the solid angle element  $d\Omega_{\text{lab}} = 2\pi \sin \theta_{\text{lab}} d\theta_{\text{lab}}$  in the laboratory system where  $\theta_{\text{lab}}$  is the scattering angle of projectiles or recoils relative to the beam direction. The cross section is in principle a function of the beam energy  $E_1$ , the charge numbers  $Z_1, Z_2$  and masses  $M_1, M_2$  of the projectile and target nuclei. It is more convenient, however, to measure the energy differential probability for positron production

$$\frac{dP_{e^+}^{\text{exp}}}{dE_{e^+}} = \frac{d^2\sigma_{e^+}/(d\Omega_{\text{lab}} dE_{e^+})}{d\sigma_{\text{Ruth}}/d\Omega_{\text{lab}}} = \frac{\Delta Z_{e^+}^{\text{exp}} / (\epsilon_{e^+} (E_{e^+}) h)}{\Delta E_{e^+} z_p} \quad (2)$$

which is obtained by normalizing the cross section (1) with respect to the Rutherford cross section for projectiles and target recoils:

$$d\sigma_{\text{Ruth}}/d\Omega_{\text{lab}} = (d\sigma_{\text{Ruth}}/d\Omega_{\text{lab}})^{\text{proj}} + (d\sigma_{\text{Ruth}}/d\Omega_{\text{lab}})^{\text{rec}} \quad (3)$$

Experimentally the number of positrons  $\Delta z_{e^+}^{\text{exp}}$  in an energy interval  $\Delta E_{e^+}$  (at energy  $E_{e^+}$ ) must be obtained in coin-

cidence with the number  $z_p$  of scattered particles. To get  $dP_{e^+}^{\text{exp}}/dE_{e^+}$  the right hand side of equation (2) must be evaluated taking into account the detection efficiency for positrons  $\epsilon_{e^+}(E_{e^+})$  and the fraction of time  $h$  the apparatus is ready for data taking. Equation (2) is only approximately valid because the particle counter has a finite acceptance angle  $\theta_{\text{lab}} \pm \Delta\theta_{\text{lab}}$ .

If  $dP_{e^+}^{\text{exp}}/dE_{e^+}$  is integrated over the positron energy the total positron production probability

$$P_{e^+}^{\text{exp}} = \frac{d\sigma_{e^+}/d\Omega_{\text{lab}}}{d\sigma_{\text{Ruth}}/d\Omega_{\text{lab}}} = \frac{z_{e^+}^{\text{exp}} / (\bar{\epsilon}_{e^+} + h)}{z_p} \quad (4)$$

is obtained. In this case a detector simply counting the number of positrons is sufficient. For positrons with a spectral distribution  $F(E_{e^+})$  the mean detection efficiency is

$$\bar{\epsilon}_{e^+} = (\int \epsilon_{e^+}(E_{e^+}) F(E_{e^+}) dE_{e^+}) / (\int F(E_{e^+}) dE_{e^+}) \quad (5)$$

Finally we can determine the total positron production cross section

$$\sigma_{e^+}^{\text{tot}} = P_{e^+}^{\text{exp}}(\theta_{\text{lab}}) (d\sigma_{\text{Ruth}}/d\Omega_{\text{lab}}) d\Omega_{\text{lab}} = \frac{z_{e^+}^{\text{tot}} / (\bar{\epsilon}_{e^+} + h)}{(Z_T/A) z_B} \quad (6)$$

The product  $(Z_T/A) z_B$  is the number of target nuclei  $Z_T$  per target area  $A$  times the number of projectiles  $z_B$ . This product is related to the number of particles  $z_M$  detected in a monitor counter of solid angle  $\Delta\Omega$  and the known Rutherford cross section by the expression

$$(Z_T/A) z_B = \frac{z_M/h}{\int (d\sigma_{\text{Ruth}}/d\Omega_{\text{lab}}) d\Omega_{\text{lab}}} \quad (7)$$

Positron yields and cross sections are often presented and discussed as a function of the distance of closest approach  $R_m$  in the Rutherford scattering process

$$R_m = a (1 + \epsilon) \quad (8)$$

Here  $2a$  is the minimum distance of closest approach in a head on collision

$$2a = ((M_1 + M_2)/(M_1 M_2)) \cdot (Z_1 Z_2 e^2 / (E_1 / M_1)) \quad (9)$$

and  $\epsilon$  the eccentricity for the scattering angle  $\theta_{cm}$  in the center of mass system

$$\epsilon = 1/\sin(\theta_{cm}/2) \quad (10)$$

For a symmetrical system like  $U + U$   $R_m$  is defined unambiguously only for  $\theta_{lab} = 45^\circ$  and this is therefore a preferred angle in the experiments described below.

It was shown by Kankeleit<sup>4,5</sup> that the scattering time defind as

$$2\hat{t} = (2a/v) (\epsilon + 1.6 + 0.45/\epsilon) \quad (11)$$

( $v = (2E_1/M_1)^{1/2}$  the projectile velocity at infinity) is an important quantity for understanding the positron production process. This is the time between the extrema of  $R(t)/R(t)$ , where  $R(t)$  is the relative distance and  $R(t)$  the relative radial velocity in the scattering process at the time  $t$ . For undercritical systems  $\hat{t}$  can be used to adequately describe the dynamically induced positron production. Positron yields have also been discussed as a function of the impact parameter<sup>6</sup>

$$b = a \operatorname{ctg}(\theta_{cm}/2) \quad (12)$$

For a typical  $U+U$  experiment at  $E = 5.9$  MeV/u and  $\theta_{lab} = 45^\circ$  these quantities are:  $2a = 17.36$  fm,  $\epsilon = 1.41$ ,  $R_m = 20.95$  fm,  $2\hat{t} = 1.71 \times 10^{-21}$  s,  $b = 8.68$  fm. The Rutherford cross section for the projectile in the laboratory system is  $d\sigma/d\Omega = 2.13b/\text{sr}$  and the integrated positron production probability is  $P_e^+ \approx 2 \times 10^{-4}$ .

In performing these experiments there is one important difficulty which should be mentioned. Through the Coulomb excitation process, nuclear levels of the collision partners may be excited which can decay by transitions having energies greater than  $2m_e c^2$ . Positrons created by internal pair conversion of these transitions cannot

be easily distinguished from atomic contributions since the time delay is only on the order of  $10^{-16}$ s to  $10^{-13}$ s. This precludes discrimination of these events using timing or recoil techniques. The procedure for correcting nuclear positron background is based on converting the observed  $\gamma$ -ray spectra into positron spectra and was first applied by Meyerhof et al<sup>7</sup>. This approach will be discussed in more detail in section 3.

#### THE EXPERIMENTAL SET-UP

A spectrometer for in-beam positron spectroscopy has to have a large collection efficiency and a broad energy acceptance band while at the same time effectively suppressing other background radiations like electrons,  $\gamma$ -rays and neutrons. These requirements are fairly well satisfied by a solenoidal positron transport system coupled with a Si(Li) detector for energy determination. The improved version of the solenoid used for the pioneering positron experiments<sup>8</sup> is shown schematically in Fig. 1. Positrons created in the target will spiral in the magnetic field to a Si(Li) detector assembly 88 cm away from the target. The magnetic mirror field configuration focuses all positrons with an emission angle  $\theta < 147^\circ$  with respect to the  $\zeta$ -axis to the detector.

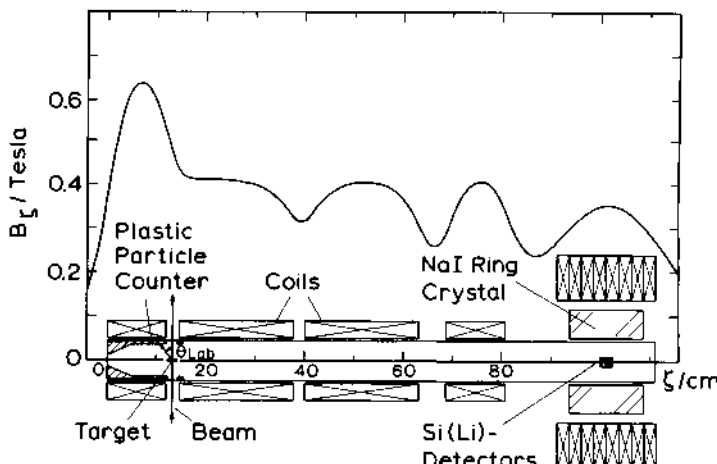


Fig. 1. Schematic drawing of the solenoid spectrometer. Also shown is the magnetic field on the  $\zeta$ -axis. The heavy ion beam enters the vacuum chamber perpendicular to the solenoid axis.

The accepted solid angle amounts to  $\Omega=9.3$  sr. Unfortunately, in the same manner all electrons resulting from Coulombic projectile-target electron interactions or internal conversion transitions of excited nuclear levels are also focused to the detector. To exclude detection of this very high electron background without appreciably decreasing the positron detection efficiency the detector system shown in Fig. 2 has been developed<sup>9</sup>. It consists of 2 Si(Li) diodes with a diameter of 20 mm and a thickness of 3 mm mounted with their surfaces parallel to the solenoid axis, one of them above, the other below it. The sensitive face of the upper detector is to the left, that of the lower one to the right. With this configuration positrons spiraling in a right hand manner have a high probability to enter the sensitive area of one of the Si (Li)-diodes. Electrons spiraling in the opposite direction are absorbed or scattered in the 3mm thick aluminium back cover of the detector. Only the very few electrons with an energy greater than about 1.4 MeV can penetrate the aluminium absorber.

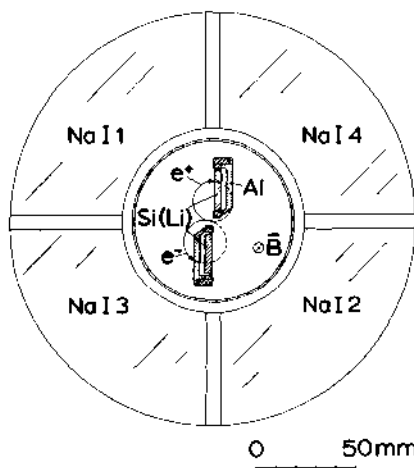


Fig. 2. The NaI-Si(Li) detector assembly for the detection of positrons in a view perpendicular to the solenoid axis at  $\zeta=102$  cm. The circular Si(Li) detectors have a diameter of 20 mm and a thickness of 3 mm. The fourfold segmented NaI ring crystal has the following dimensions: inner diameter 90 mm, outer diameter 204 mm, length 250 mm.

The suppression efficiency for electrons with this detector arrangement was tested using 365 keV electrons from a  $^{113}\text{Sn}$  source prepared on a target frame in a geometry similar to that used for the in-beam experiments. The results are presented in Fig. 3. If the polarity of the magnetic field is reversed the detection efficiency for electrons changes dramatically. From the corresponding intensities a geometrical suppression factor for 365 keV electrons of about 150 was determined. In spite of this strong suppression of electrons the Si(Li) counting rate observed for in-beam positron experiments is caused nearly entirely by electrons. In order to select the very few positrons, the Si(Li) diodes were surrounded by a 4-fold segmented NaI(Tl) ring crystal which permitted detection of the 511 keV annihilation radiation from the positron. To characterize a positron a coincidence was required between an event in the 511 keV region in one of the NaI(Tl) segments and the total energy region in the opposite one.

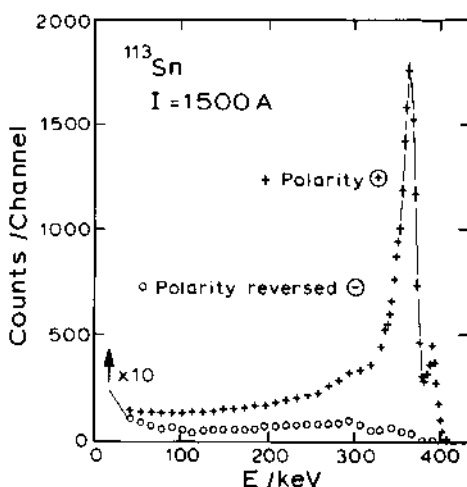


Fig. 3. Electron spectrum of a  $^{113}\text{Sn}$  source taken with the Si(Li) detector assembly as shown in Fig. 2. The magnet current was 1500 A with the two different polarities  $\oplus$  and  $\ominus$ . The lower spectrum is magnified by a factor of 10.

With this procedure a positron is detected unambiguously but true electron positron sum coincidences may deteriorate the spectral shape. Fortunately, the suppression factor of electrons is sufficiently high that electron positron sum coincidences contributed to less than 2 % of the events and therefore could be neglected.

Both Si(Li) diodes operate essentially independent of each other. This has several advantages. From a positron event with signals in both Si(Li) diodes for instance the fraction of electron positron sum coincidences can be determined. Also this assembly is useful in the search for peaks in the positron spectra. Such peaks are expected from a  $1s$  vacancy decay in a collision having a long time delay after nuclear contact<sup>10</sup>. Suppose a hypothetical superheavy nucleus is formed after a  $^{238}\text{U} + ^{238}\text{U}$  collision at 5.9 MeV/u and it emits positrons with a sharp energy of 300 keV. Such a superheavy nucleus moves with about 5.6% of the velocity of light. Positrons accepted by the magnetic field of the solenoid would be broadened in energy by the Doppler effect. The corresponding energy distribution is nearly rectangular with a width of 71 keV. A dip in the middle of this distribution is caused by positrons emitted with  $\theta > 147^\circ$  with respect of the  $\zeta$ -axis (cf. Fig. 1) of the solenoid since these positrons are not reflected by the magnetic mirror field configuration. The Si(Li) counters at the top and at the bottom are sensitive essentially to positrons emitted parallel or antiparallel relative to the beam direction, respectively. Therefore for these counters positron distributions are expected to result in two peaks separated by about 35 keV and having reduced width of also about 35 keV. Such an observation would be a very characteristic finger print for a positron peak.

The positron spectra have been unfolded numerically with a computer code using the detector response function (cf. Fig. 3). The detection efficiency was determined with intensity calibrated  $^{22}\text{Na}$  and  $^{68}\text{Ge}/\text{Ga}$  positron sources mounted on target frames. The calibration determination was performed in the same manner as in the in-beam experiment. The results are shown in Fig. 4 (lower curve).

The total positron production probability  $P_{e^+}$  can be obtained by integration of the energy spectrum. If this procedure is used only the fraction of positrons which strike the Si(Li)-detector are determined. Obviously, the detection efficiency can be increased by approximately a factor of 3 if the complete Si(Li) detector assembly is used as a passive positron catcher.

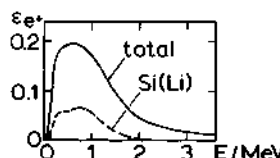


Fig. 4. Positron detection efficiency of the solenoid spectrometer. The lower dashed curve labeled "Si(Li)" corresponds to energy analyzed positrons. For the upper curve labeled "total" the Si(Li) detector assembly serves as a passive positron catcher only.

The detection efficiency shown in Fig. 4 (upper curve) decreases for low positron energies due to target self-absorption effects and for high energies because positrons get absorbed in the vacuum chamber or miss the catcher. Nevertheless, the shape of the detection efficiency is sufficiently flat in the relevant region between 0.2 and 1 MeV. As shown below only very few positrons have energies beyond this region.

Positrons were measured in coincidence with scattered particles, or target recoils, using a plastic scintillation counter with a thickness of  $50\mu\text{m}$  (Fig. 5). Recoils of light target contaminants like carbon or oxygen are electronically excluded from detection by pulse height discrimination. Fission products resulting from fusion reactions of projectiles with light target contaminants were kinematically excluded from entering the sensitive region of the plastic counter between  $35^\circ$  and  $55^\circ$ . For U beam energies below  $5.9 \text{ MeV/u}$  a small fraction of fission fragments from target projectile interactions could not be excluded from detection. However, positrons associated with these events were studied using two backward silicon surface barrier detectors (cf. Fig. 5). With this configuration elastic scattering events are excluded from detection provided the projectile mass  $M_1$  exceeds the target mass  $M_2$ .

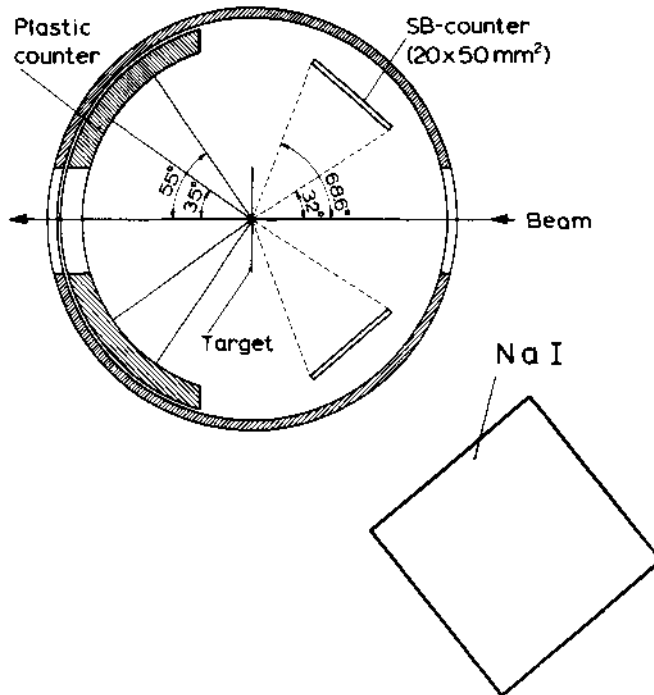


Fig. 5. The particle counters as viewed in a plane perpendicular to the solenoid axis at  $\zeta=13$  cm. Scattered particles, target recoils, and/or fission products are detected in a  $50\mu\text{m}$  thick plastic scintillator foil. Fission fragments from the projectile emitted in the backward hemisphere following nearly central collisions are detected with Silicon surface barrier detectors. Target  $\gamma$ -radiation is measured by a  $7.5 \times 7.5$  cm NaI detector.

#### EVALUATION OF ATOMIC POSITRONS

To calculate the atomic positron spectrum  $\Delta Z_e^{\text{atom}}/\Delta E_e^+$  with equation (2) the number of measured positrons  $\Delta Z_e^{\text{exp}}$  has to be corrected for several contributions

$$\Delta Z_e^{\text{atom}} = \Delta Z_e^{\text{exp}} - \Delta Z_e^{\text{int}}(z_1, M_1) - \Delta Z_e^{\text{int}}(z_2, M_2) - \Delta Z_e^{\text{ext}}(T) - \Delta Z_e^{\text{ext}}(S) \quad (13)$$

These corrections include positrons produced in the internal pair decay of excited levels in the projectile

and target nuclei ( $\Delta Z_e^{int} (Z_1, M_1)$  and  $\Delta Z_e^{int} (Z_2, M_2)$ )

as well as positrons from external pair conversion of target  $\gamma$ -rays in the target  $\Delta Z_e^{ext}(T)$  and in the solenoid  $\Delta Z_e^{ext}(S)$ . From test experiments and calculations it was concluded that

$$\Delta Z_e^{ext}(S) \approx 0 \quad (14)$$

On the other hand, the external pair creation in a  $1 \text{mg/cm}^2$  Pb or U target requires corrections on the order of 10% to the positron yield. Similar corrections have to be applied for the determination of the integral number  $Z_e^{atom}$  of positrons.

To correct for the internal pair conversion contribution, target  $\gamma$ -ray spectra have been measured using a  $7.5 \times 7.5 \text{ cm NaI(Tl)}$  detector in the configuration indicated in Fig. 5 under the same coincidence conditions with respect to scattered particles as in the positron determination. In case of neutron emission after nuclear reactions additional  $\gamma$ -rays are produced in the solenoidal material by  $(n, n'\gamma)$  reactions. This contribution must be subtracted to get the target  $\gamma$ -spectrum itself. Unfortunately, discrimination by means of a time of flight technique is not possible since the flight path from the target to e.g. the copper coils of the solenoid is too small.

For the  $^{208}\text{Pb} + ^{208}\text{Pb}$  scattering system the  $\gamma$ -ray spectrum is very simple because only the  $3^-$ -level at 2.614 MeV and the  $2^+$ -level at 4.09 MeV are populated by Coulomb excitation. In this case the correction procedure for nuclear positrons is straight forward.<sup>8</sup> To obtain the highest possible  $Z_u = Z_1 + Z_2$   $^{238}\text{U}$  beams have been used which results in the excitation of a large number of nuclear levels having unknown decay characteristics. This makes the subtraction procedure of nuclear positrons rather involved. A typical  $\gamma$ -spectrum is shown in Fig. 6.

After unfolding this spectrum with the response function of the NaI(Tl) detector the original  $\gamma$ -distribution  $dZ_\gamma / dE_\gamma (E_\gamma)$  can be transformed into a positron spectrum  $\gamma$

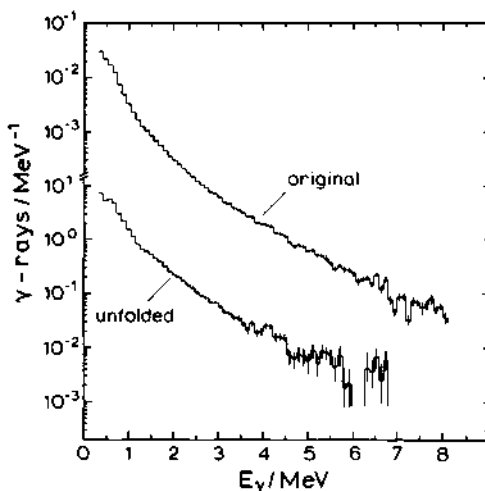


Fig. 6. Target  $\gamma$ -ray spectrum taken with the  $7.5 \times 7.5$  cm NaI detector shown in Fig. 5. A  $^{108}\text{Pd}$  target was bombarded with  $^{238}\text{U}$  projectiles with an energy of 5.9 MeV/u. The  $\gamma$ -ray spectra were recorded in coincidence with the  $^{108}\text{Pd}$  recoils, uniquely detected in the particle counter at  $\theta_{\text{lab}} = 45^\circ \pm 10^\circ$ .

using theoretical pair conversion coefficients<sup>11</sup>.  
 $d\beta_{M\lambda}/dE_{e^+}(E_\gamma, E_{e^+}, Z)$  of multipolarity  $M\lambda$

$$\frac{dZ_{e^+}}{dE_{e^+}}(E_{e^+}, M\lambda) = \frac{1}{2m_0c^2} \frac{dZ_\gamma}{dE_\gamma}(E_\gamma) \frac{d\beta_{M\lambda}}{dE_{e^+}}(E_\gamma, E_{e^+}, Z) \quad (15)$$

In Fig. 7 two positron spectra

$$\Delta P_{e^+}/\Delta E_{e^+} = (\Delta Z_{e^+}/\Delta E_{e^+}(E_{e^+}, M\lambda))/Z_p \quad (16)$$

are presented as calculated from the  $\gamma$ -distribution assuming E1 and E2 multipolarities, respectively.

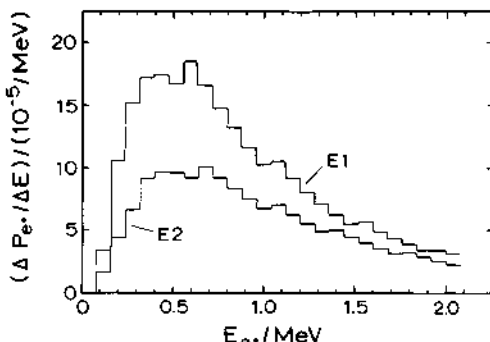


Fig. 7. Positron spectra as calculated from the unfolded  $\gamma$ -ray spectrum of Fig. 6 assuming E1 and E2 multipolarity.

There is a remarkable difference between these which emphasizes the difficulty in correcting for nuclear background positrons when the multipolarity of the  $\gamma$ -ray spectrum is unknown. However, the experimentally measured positron spectrum shown in Fig. 11 strongly suggests an E1 multipolarity if we make the plausible assumption that there are negligible amounts of atomic positrons created in the U + Pd scattering system.

Further informations about the  $\gamma$ -ray multipolarity can be gained from energy integrated positron yields which require much less beam time than positron spectra due to a higher total efficiency (cf. Fig. 4). We calculate

$$z_{e\gamma}^{\text{calc}}(M\lambda) = \int_0^{\infty} dE_e^+ \epsilon_e^{\text{tot}}(E_e^+) \frac{dz_e^+}{dE_e^+}(E_e^+, M\lambda) \quad (17)$$

and compare this number with the experimental value  $z_e^{\text{exp}}$  forming the ratio  $z_e^{\text{exp}} / z_{e\gamma}^{\text{calc}}(M\lambda)$ . For light scattering systems for which nuclear positron emission is expected to be dominant this ratio is nearly 1, with the assumption of E1-multipolarity for the nuclear  $\gamma$ -rays. However, it should be stressed that mixing of E1, M1 and

$E2$  multipolarities with the same mean feature as pure  $E1$  transitions cannot be excluded. In particular a possible contribution due to monopole conversion ( $EO$ ) is not taken care of by this procedure. In Fig. 8 the data have been normalized to unity in the region  $Z_u < 160$  by introduction of a factor  $f$  which is close to unity.

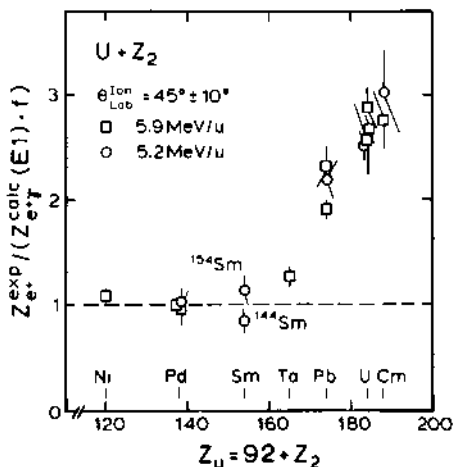


Fig. 8. Ratio of measured to calculated positron yields  $z_{e^+}^{\text{exp}} / (z_{e^+}^{\text{calc}}(\text{El}) \cdot f)$  as a function of the united nuclear charge  $Z_u$ , assuming  $E1$  multipolarity for the nuclear target  $\gamma$ -rays ( $\theta_{\text{lab}} = 45^\circ \pm 10^\circ$ , U-beam  $\square$  5.9 MeV/u,  $\circ$  5.2 MeV/u). For  $Z_u > 174$  there is a clear indication for a large number of excess positrons which are attributed to atomic processes.

The displayed ratio clearly exceeds unity for the  $U + Pb$ ,  $U + U$  and  $U + Cm$  scattering systems. This fraction of excess positrons is believed to originate from atomic processes for which we can write

$$z_e^{\text{atom}} = z_{e^+}^{\text{exp}} - z_{e^+}^{\text{ext}}(T) - z_{e^+}^{\text{calc}}(\text{El}) \cdot f \quad (18)$$

From comparison with equation (13) after consideration of

equation (14) we can identify the last term of (18) as the nuclear contribution of positrons:

$$z_{e^+}^{\text{calc}} (E1)f = z_{e^+}^{\text{int}}(Z_1, M_1) + z_{e^+}^{\text{int}}(Z_2, M_2) \quad (19)$$

However, it should be emphasised that this procedure is only correct if the multipolarity distribution of the  $\gamma$ -ray spectrum for the high  $Z_u = Z_1 + Z_2$  region ( $Z_u \geq 160$ ) for which atomic positrons are expected to contribute is not significantly different than in the low  $Z_u$  region ( $Z_u \leq 160$ ).

## RESULTS AND DISCUSSION

The experimental results obtained in this experiment can be grouped into three categories: (i) measurement of total positron production cross sections  $\sigma_{e^+}^{\text{tot}}$ , (ii) measurement of energy integrated positron production yields  $P_{e^+}$  and (iii) measurement of energy differential positron production yields  $\Delta P_{e^+}/\Delta E_{e^+}$ . Various scattering systems have been investigated in each group including systems with low  $Z_u = Z_1 + Z_2$  for which only emission of nuclear positrons is expected.

The total positron production cross section  $\sigma_{e^+}^{\text{tot}}$  is shown in Fig. 9 as a function of distance of closest approach in a head on collision, see equation (9). This parameter is particularly advantageous since the interaction radius

$$R_{\text{int}} = 1.16 (A_1^{1/3} + A_2^{1/3} + 2) \text{ fm} \quad (20)$$

defines two regions. Roughly speaking, for  $2a \geq R_{\text{int}}$  the collision partners follow essentially pure Rutherford trajectories and nuclear background positrons originate mainly from mutual Coulomb excitation of projectile and target nuclei. For  $2a \leq R_{\text{int}}$  nuclear reactions may contribute.

A strong target dependence of  $\sigma_{e^+}^{\text{tot}}$  for the nuclear systems  $^{238}\text{U} + ^{181}\text{Ta}$ ,  $^{238}\text{U} + ^{144,154}\text{Sm}$  and  $^{238}\text{U} + ^{108}\text{Pd}$  for  $2a = \text{const}$  can clearly be recognized. This reflects the  $Z$  and  $v$  dependence for Coulomb excitation of pair decaying nuclear levels in  $^{238}\text{U}$  and, possibly, a target

nuclear structure dependence. A nuclear structure effect may be responsible for the cross section difference observed in the  $^{238}\text{U} + ^{144,154}\text{Sm}$  scattering systems although it can not be completely excluded that this effect is caused by different contaminations with oxygen in the metallic  $^{144}\text{Sm}$  and  $^{154}\text{Sm}$  targets.

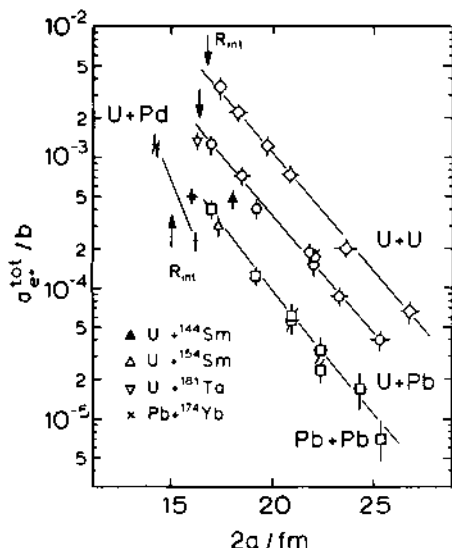


Fig. 9. Total positron production cross section (not corrected for nuclear positrons) for different scattering systems as a function of the closest approach in a head on collision  $2a$ , see equation (9). Indicated is also the interaction radius  $R_{int}$ , see equation (20).

The  $^{238}\text{U} + ^{238}\text{U}$ ,  $^{238}\text{U} + ^{208}\text{Pb}$  and  $^{208}\text{Pb} + ^{208}\text{Pb}$  systems have been investigated at different beam energies. The total cross sections follow, in the semilogarithmic representation of Fig. 9, straight lines. It is worth noting that cross sections have been measured in an interval from a few  $\mu\text{b}$  to a few  $\text{mb}$ .

The total atomic positron cross section (corrected for nuclear background positrons) could only be determined up to now for the Pb + Pb scattering system, see ref.8. No attempts have been made to correct the U + U and U + Pb systems since a  $\gamma$ -ray background continuum resulting from spurious  $\gamma$ -ray sources (slit scattering of the beam or reactions of the beam particles with light target contaminants) can hardly be distinguished from the target contribution itself. To be consistent in Fig.9 only the uncorrected positron cross sections are shown.

The total atomic positron production probability  $P_{e^+}$  is represented in Fig. 10 as a function of the scattering time  $2\hat{t}$  (eq. 11). As already mentioned in section 2 this time characterizes the dynamically induced positron creation for undercritical systems. We present this by following a model developed by Kankeleit<sup>4,5</sup>. He showed that the first order adiabatic transition amplitude

$$a(t=\infty) = -\int dt' \langle E_{e^-} | \partial/\partial t | E_{e^+} \rangle \exp(i(E_{e^-} - E_{e^+}) t'/\hbar) \quad (21)$$

can be written as

$$a(t=\infty) = (f(E_{e^+})g(E_{e^-}))^{1/2} \exp(-\hat{t}(E_{e^-} - E_{e^+})/\hbar) / (E_{e^-} - E_{e^+}) \quad (22)$$

The energy denominator  $(E_{e^-} - E_{e^+})$  originates from the application of the Hellmann-Feynman relation. The functions  $f(E_{e^+})$ ,  $g(E_{e^-})$  stem from the Coulomb repulsion of positrons or Coulomb attraction of electrons, respectively, in analogy to well known Fermi function in  $\beta$ -decay. Then, the double differential probability for pair creation can be expressed as:

$$d^2P_{e^+}/(dE_{e^+}dE_{e^-}) = f(E_{e^+})g(E_{e^-}) \exp(-2\hat{t}(E_{e^-} - E_{e^+})/\hbar) / (E_{e^-} - E_{e^+})^2 \quad (23)$$

We directly see that the transition amplitude factors into an exponential which contains the dynamical aspects of positron creation and functions  $f(E_{e^+})$  and  $g(E_{e^-})$  which are connected to the electron and positron wave functions in the initial and final state. When electrons are not detected in the experiment we have to integrate over  $E_{e^-}$  and obtain the positron spectrum:

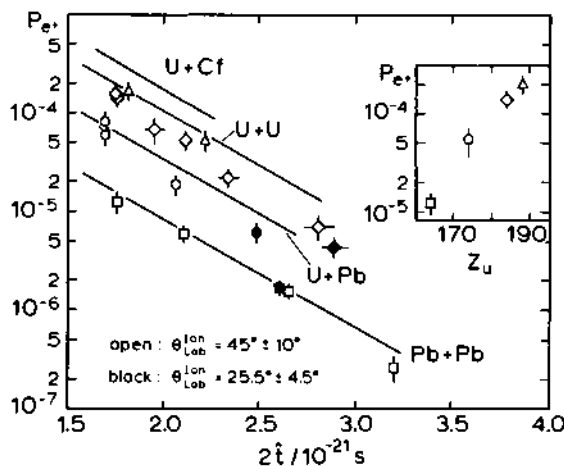


Fig. 10. The total atomic positron probability  $P_{e+}$  for different systems as a function of scattering time  $2t$ . The following designations are used:  $\Delta$  U+Cf,  $\diamond$  U+U,  $\square$  U+Pb,  $\circ$  Pb+Pb. Open points represent  $\theta_{\text{Lab}}^{\text{ion}} = 45^\circ \pm 10^\circ$ , black points  $25.5^\circ \pm 4.5^\circ$ . The full lines represent theoretical calculations<sup>12</sup>. The insert shows the  $Z_u$  dependence of  $P_{e+}$  for the fixed scattering time  $2t = 1.75 \times 10^{-21} \text{ s}$ .

$$dP_{e+}/dE_{e+} = h(E_{e+}, \hat{t}) \exp(-2\hat{t}(E_{e+} + 2m_0c^2)/\hbar) \quad (24)$$

The function  $h(E_{e+}, \hat{t})$  is responsible for the decrease of the positron intensity at low energy which has been observed experimentally (cf. fig. 11). If we are interested in the total positron probability only, a further integration over  $E_{e+}$  has to be performed yielding:

$$P_{e+} = i(t) \exp(-2\hat{t}(2m_0c^2)/\hbar) \quad (25)$$

These simple considerations can, therefore, explain that the nearly exponential slopes observed in both  $dP_{e+}/dE_{e+}$

(at sufficiently high positron energies  $E_{e+}$ ) and in  $P_{e+}(t)$  are the results of the simple dynamical aspects of collisional positron creation. On the other hand, the absolute positron production yield and/or deviations from the exponential slope can provide detailed physical

information regarding the wave function in the matrix element  $\langle E_e^- | \partial/\partial t | E_e^+ \rangle$  of equation (21). For this to be true, however, it must be assured that such deviations are not caused by interferences with higher order terms in the perturbation expansion which theoretical calculations<sup>12</sup> imply may not be negligible. Keeping this reservation in mind conclusions drawn from this model must be accepted with caution.

From fig. 10 we see that  $P_e^+$  can be for every scattering system approximated by an exponential function. No distinct effects of level diving are observed in  $P_e^+$  for the U+Cm and U+U points at lowest scattering time even though these systems are expected to be overcritical. This is also true for the  $Z_u$  dependence of  $P_e^+$  as shown in the insert of fig. 10 for the fixed scattering time  $2\hat{t} = 1.75 \times 10^{-21} \text{ s}$ . In fact the positron probability can be approximated by the simple relation:

$$P_e^+ \approx Z_u^{-20.3} \quad (26)$$

The absence of effects of a diving level, within the experimental errors of about 30%, may be a consequence of insufficient experimental sensitivity in the measurement of the total positron yield  $P_e^+$ .

A more sensitive determination for diving characteristics would be expected to be obtained by directly measuring the low energy portion of the positron spectra. Fig. 11 presents the measured spectra corrected for the detection response function and efficiency. The spectrum of the low  $Z_u = 138$  system, U+Pd, for which only nuclear positrons are expected can be reproduced by converting the target  $\gamma$ -ray distribution into a positron spectrum assuming E1 multipolarity. The nuclear background contributions for the U + Pb and U+U systems have similarly been determined. Comparing the overcritical U+U spectrum with the undercritical U+Pb spectrum we can suspect small deviations in the U+U system in the low energy part of the spectrum. However, preliminary results of a repeated experiment were not able to reproduce these deviations. Finally we compare the positron production yields with theoretical calculations<sup>12</sup>. The slopes of these calculations as shown in fig. 11, agree quite well with the experiment.

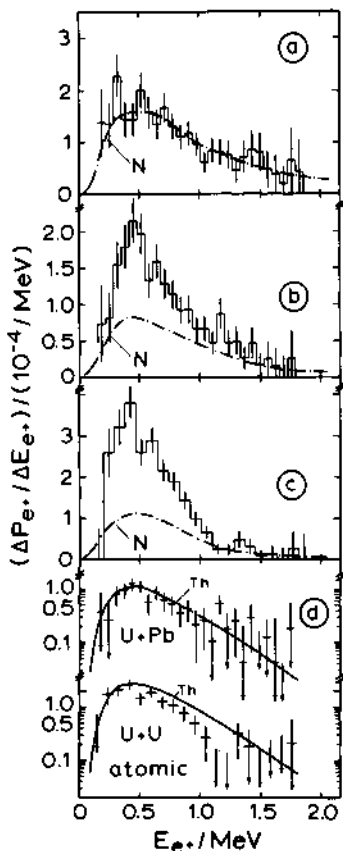


Fig. 11. Positron spectra  $\Delta P_{e+}/\Delta E_{e+}$  for (a) the nuclear U+Pd, (b) the undercritical U+Pd, (c) the overcritical U+U systems at a U beam energy of 5.9 MeV/u and  $\theta_{\text{lab}} = 45^\circ \pm 10^\circ$ . The dashed dotted curves "N" indicate nuclear positrons as derived from  $\gamma$ -ray spectra, assuming E1 multipolarity. (d) is a semilogarithmic presentation of the spectra of atomic positrons compared to theoretical calculations<sup>12</sup> indicated by "Th".

Nevertheless, there is some indication for increasing deviations of these calculations from the experimental findings as  $Z_u$  increases from 164 to 188. However, at this point it must be stressed that the absolute experimental errors are at present about 30%. If the indicated deviations continue to persist with improved experimental results their consequences must be investigated.

These experiments demonstrate that the diving process, if it occurs at all, does not show up in strong deviations of the total positron production cross section, the total positron production probability or positron spectra as gained for undercritical systems. These findings are in agreement with recent theoretical calculations<sup>12</sup>.

#### OUTLOOK

All experiments described in the preceeding sections have been performed for scattering systems in which the collision partners follow nearly pure Rutherford trajectories. For the  $^{238}\text{U} + ^{238}\text{U}$  systems at 5.9 MeV/u e.g. the distance of closest approach  $R_m$  (cf. eq. (8)) approaches only for very central collisions the interaction radius given by equation (20)  $R_{int}=16.7$  fm. One can speculate that only these very central collisions bring about nuclear sticking times of about  $10^{-20}\text{s}$  resulting in a decay of  $1s_0$  vacancies by emission of monochromatic positrons. Principally, such a mechanism of monochromatic positron emission was first proposed by Rafelski et al<sup>10</sup>. However, in the course of these experiments we have tried to investigate positron spectra obtained in the presence of a perturbation of the Rutherford trajectory due to nuclear contact at a beam energy as high as 8.4 MeV/u. At such an energy the grazing angle defined by  $R_{int}=R_m$  is  $70^\circ$  in the CM system. Collisions at impact parameters smaller than 8.7 fm (cf. equation (12)) result in nuclear contact with energy dissipation and consequently, most probably, fission of the very fragile  $^{238}\text{U}$  nuclei. Indeed, with the plastic particle counter shown in Fig. 5 with a sensitive region  $35^\circ < \theta_{lab} < 55^\circ$  for all angles  $0 < \psi < 360^\circ$  no kinematic sum coincidences of two  $^{238}\text{U}$  nuclei were observed at 8.4 MeV/u indicating that at least one of the U nuclei must have undergone fission.

Positron spectra were taken as described in section 3 in coincidence to a signal in the plastic particle counter caused by reaction products. The nuclear

background contribution of positrons was measured by replacing the  $^{238}\text{U}$  target by a  $^{108}\text{Pd}$  target. A preliminary background corrected positron spectrum exhibits a remarkable feature. Above an energy of 700 keV the spectrum drops off more rapidly than the reference spectrum taken of 5.9 MeV/u in coincidence to Rutherford scattered particles while from equation (22) and calculations based on pure Rutherford trajectories<sup>13</sup> just the opposite is expected. This effect may indicate a small time delay ( $\approx 10^{-21}\text{s}$ ) during the nuclear contact in connection with changed kinematical conditions in the outgoing channel. This is in agreement with recent calculations 5,13.

One very interesting aspect of positron spectroscopy after nuclear contact is the fact that nuclear positrons contribute unexpectedly little to the total yield (less than  $\approx 40\%$  for  $E_{e^+} = 500\text{keV}$  for  $\text{U}+\text{U}$  at 8.4 MeV/u). The reason for this may be that most of the dissipated energy is evaporated from the fission fragments by neutrons. While the neutron multiplicity increases as a function of the dissipated energy the multiplicity for  $\gamma$ -rays with energies above  $2m_{\text{O}}c^2$  increases at most only weakly. This fact makes future experiments feasible in which positron spectra are investigated as a function of the dissipated energy employing improved experimental techniques.

For future experiments the solenoid at location X8 in the experimental area at GSI will be replaced by a so called Torispectrometer<sup>14</sup> shown in Fig. 12. The main feature of this new instrument is the ability to separate electrons and positrons and to measure them simultaneously in different detectors. This is achieved by a S-shaped field configuration produced by pancake coils surrounding two quarters of a toroidal tube. Electrons and positrons leaving the target experience, in the bent magnetic field of the first quarter torus, a drift in their guiding center perpendicular to the spectrometer plane. According to the charges,  $q$ , this drift is opposite for electrons and positrons. It is designed to give complete separation of positrons from electrons (which are absorbed in a detector), while the positrons are left free to pass into the second quarter torus in which the drift is reversed. A broad band acceptance of positrons with an efficiency of more than 20% is expected. Around the target sufficient space is available to install position sensitive particle counters with the ability to determine precisely the impact parameter in the scattering process.

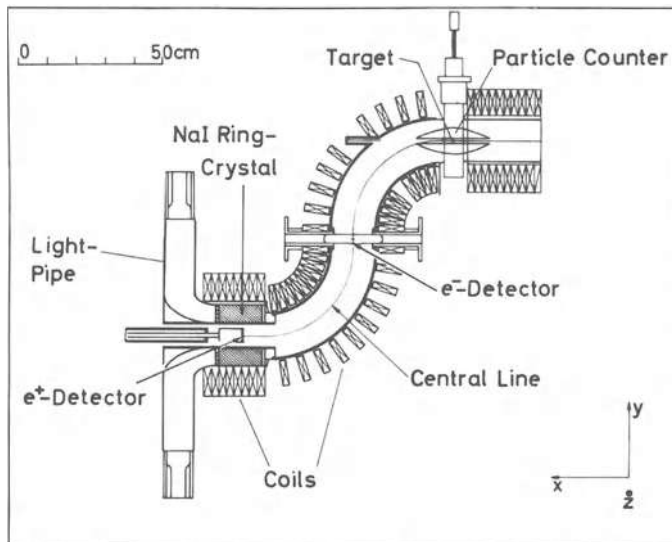


Fig. 12. Torispectrometer, beam direction and z-drift is perpendicular to the plane of drawing<sup>14</sup>.

This could be of great importance since small physical effects at specific distances of closest approach in the collision process may be obscured with a particle counter accepting a wide  $\theta_{\text{lab}}$  band. This clearly was demonstrated by the results presented by H. Bokemeyer and P. Kienle on this conference. With the increase of the detection efficiency for positrons the final accuracy in the atomic positron spectra may be limited by uncertainties in the correction of nuclear background positrons. For example, if an accuracy of 5% is required in the atomic positron spectra after subtraction of a 40% nuclear background contribution, this background has to be known with an accuracy of 7.5%. Future experiments will have to establish whether the  $\gamma$ -ray positron conversion procedure described above can be sufficiently improved to achieve this accuracy or whether new methods will be required. The first of these to be mentioned should be a proposed channeling experiment<sup>15</sup>. In this experiment, which uses a single U crystal, a blocking effect is expected for the atomic processes and not for the delayed nuclear positrons.

Another technique for obtaining information

about the multipolarity of the nuclear  $\gamma$ -ray continuum is from measuring the electron spectrum in coincidence with positrons. First attempts to do this have been performed with the old solenoid spectrometer. Two Si(Li) detectors for electrons have been installed within the short coil at  $\zeta = 6$  cm (cf. Fig.1) in a similar geometry as the positron counters at the other side. Electrons below an energy of about 400 keV were geometrically eliminated. In a test experiment electron spectra have been measured in coincidence to positrons for U+U at 5.9 MeV/u and  $\theta_{\text{lab}} = 45^\circ \pm 10^\circ$ . A preliminary analysis of this experiment indicates that the electron spectrum taken in coincidence with positrons exhibits a flatter descent as a function of energy than the corresponding electron spectrum not in coincidence with positrons. The reason for this effect lies in the distinct difference in the slope of  $\beta$ -electrons and electrons from nuclear pair decay. This offers a possibility of obtaining additional information about positrons from nuclear pair decay.

#### ACKNOWLEDGEMENTS

We gratefully acknowledge the collaboration with H. Bokemeyer, J.S. Greenberg, F. Heßberger, W. Engelhardt, M. Mutterer, Y. Nakayama, L. Richter, P. Vincent, and R. Willwater in the early stage of the experiment. We thank the GSI target laboratory lead by H. Folger as well as H. Krieger and H.-J. Maier for preparing the targets. Especially we would like to thank J. Foh from the TH Darmstadt for developing essential parts of the electronics needed to measure positron spectra. We are in debt to R. Köhler, M. Kollatz and U. Meyer for their help during the runs.

This work was supported by the Bundesministerium für Forschung und Technologie.

#### REFERENCES

1. O. Klein, Z. Physik 53, 157 (1929)
2. J. Reinhardt, W. Greiner, Rep. Progr. Phys. 40, 219 (1977)
3. J. Rafelski, L. Fulcher, A. Klein, Phys. Rep. 38C, 227 (1978)
4. E. Kankeleit, in: Nuclear Interactions, ed. by B.A. Robson, Lecture Notes in Physics Vol. 92. Springer-Verlag, New-York 1979, p.306

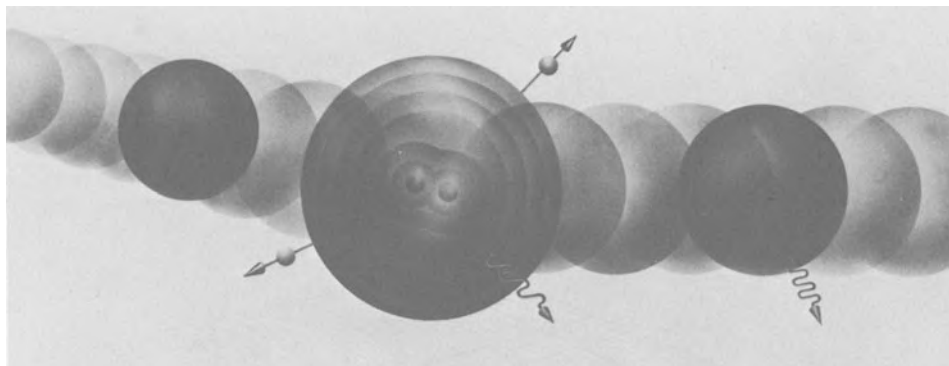
5. E. Kankeleit, Nucleonika 25, 253 (1980)
6. P. Armbruster, P. Kienle, Z.Physik A 291, 399 (1979)
7. W.E. Meyerhof, R. Anholt, Y.El. Masri, D. Cline, F.S. Stephens, R. Diamond, Phys.Lett. B 69, 41 (1977)
8. H. Backe, L. Handschug, F. Heßberger, E. Kankeleit, L. Richter, F. Weik, R. Willwater, H. Bokemeyer, P. Vincent, Y. Nakayama, J.S. Greenberg, Phys.Rev.Letters 40, 1443 (1978)
9. H. Backe, W. Bonin, E. Kankeleit, W. Patzner, P. Senger, F. Weik, GSI Scient.Rep.1979, GSI 80-3, p.168 ISSN 0174-0814
10. J. Rafelski, B. Müller, W. Greiner, Z.Physik A 285, 49 (1978)
11. P. Schlüter, G. Soff, W. Greiner, Z.Physik A 286, 149 (1978)
12. J. Reinhardt, B. Müller, W. Greiner, UFTP Reprint 34/1980
13. J. Reinhardt, U.Müller, B. Müller, W. Greiner, UFTP Reprint 63/1981
14. E. Kankeleit, R. Köhler, M. Kollatz, M. Krämer, R. Krieg, P. Senger, H. Backe, GSI Scient. Rep.1980, GSI 81-2 p. 195 ISSN 0174-0814
15. K.G. Kaun, S.A. Karamyan, JINR P 7-11420, Dubna 1978 and GSI-tr-9/78 (Übersetzung P. Strehl)

## EXPERIMENTAL STUDIES ON PHANTOMS -

### ELECTRONIC CONFIGURATIONS OF ATOMS BEYOND THE STABLE ONES

This topic will be covered by 3 lectures

- (1) Heavy Ion Collision Induced Characteristic X-Ray Production -  
Cross section Experiments  
(P. Armbruster)
- (2) Experiments on the Excitation of the Innermost Electrons in  
Extremely Strong Fields - Ionization Probability Experiments  
(F. Bosch)
- (3) Systematics and Discussions of Ionization Probability Measure-  
ments  
(P. Armbruster)



The object of our study, the intermediate collision system -  
superheavy Quasiatom-PHANTOM - PHANTOM (E. Malwitz)

HEAVY ION COLLISION INDUCED CHARACTERISTIC X-RAY PRODUCTION -  
CROSS SECTION EXPERIMENTS

P. Armbruster

Ges. f. Schwerionenforschung mbH  
P.O. Box 11 05 41  
D-6100 Darmstadt, FRG

INTRODUCTION

The number of electrons found in an atomic collision of two heavy nuclei may exceed the number of electrons of stable atoms considerably. Combined systems of  $(Z_1+Z_2)$  as large as 190 are experimentally feasible. For inner-shell electrons with orbital velocities  $u$  approaching the velocity of light, a collision velocity  $v$  smaller than 0.15 c still guarantees a combined Coulomb field acting on the electrons sufficiently long in order to make them feel as in an atom of combined atomic number. The combined nuclear charge  $(Z_1+Z_2)$  governs the electronic collision phenomena, which demand to be understood knowledge about the properties of atoms beyond the natural ones, or as the latter are in lack of stable nuclear systems not accessible, the collision phenomena convey messages from the world of not existing atoms - the superheavy quasiatoms - PHANTOMS - PHANTOMS.

15 % of the velocity of light corresponds to ion energies of 10 MeV/u, which became available for the heaviest ions with the operation of the UNILAC 1975 and the first U-beams, April 1st, 1976. Experiments on quasiatoms have developed to one of the fruitful branches of the GSI research program. This series of lectures tries to start from a series of earlier experiments reminding us that atomic physics is a well established field since long, and will conduct us to a description of our recent experiments and their interpretation as a key to a coming PHANTOM-spectroscopy.

Fig. 1 gives the world of atomic collision phenomena presented by their most important parameters : The velocity ratio  $v/u$  and the effective atomic number  $(Z_1+Z_2)/n$ . The condition of adiabaticity

$v < u/2\pi$  defines the world of quasiatoms, in the regime  $u/2\pi < v < u$  nonadiabatic collision dynamics is prevailing, for  $v > u$  few electron systems are found, the binding of most electrons is negligible. For  $v \gg u$  no electrons are bound, atomic physics with fully stripped ions is left. Limiting ourselves to studies on K-, L-, and M-shells of PHANTOMS ( $Z \geq 108$ ) the upper left corner of the figure with  $Z_1+Z_2/n > 36$  and  $v/u < 0.15$  has to be reached in our experiments. As all observable consequences of a collision tend to disappear for very low collision velocities, we set as a lower limit

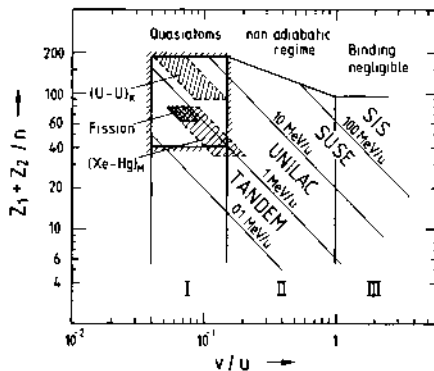


Fig. 1. The different fields of research in atomic collision studies together with the specific energies obtained with different accelerators presented in the plane  $Z_1+Z_2/n$  versus  $v/u$ .

of our experiment  $v/u > 0.04$ . The M-shell of the PHANTOM with atomic number  $Z = 108$  may still be studied with beam energies of  $0.02 \text{ MeV/u}$ , the energy for K-shell studies of atomic number  $Z = 190$  should not exceed  $10 \text{ MeV/u}$ . Heavy ions in the upper part of the periodic table and in the energy range of  $(0.02 - 10) \text{ MeV/u}$  are the necessary tool for our game. They are delivered in the lower energy range  $(0.02 - 0.5) \text{ MeV/u}$  by electrostatic accelerators as Van-de-Graafs or Tandem Van-de-Graafs, or by a natural source - fission of heavy nuclei -,  $E/A = (0.4 - 1) \text{ MeV/u}$ . It is here where the earlier studies began.

## EARLY EXPERIMENTS

In 1934 W.M. Coates /1/ published his atomic collision experiments using 2.8 MeV mercury beams delivered from a Sloan-Lawrence structure. This energy actually is just at the lower limit we defined for studies of PHANTOMS. In the abstract of his paper Coates introduced "the temporarily formed quasi-molecule" in order to explain his results. In spite of the poor measuring devices for x-ray energies at his time many features of later experiments are found in his work. It must be considered, especially in the discussion of the results as one of the most intuitive contributions to the field, which I regret not to have read in the time when I started my own experiments 25 years after Coates published his work.

Then a recoil fission product separator installed at the Munique Swimming Pool Reactor allowed to produce a beam of 100 fission products per second in the energy range (0.4 - 1) MeV/u /2/. With this beam a number of inner-shell ionization experiments became possible. Fig. 2 shows the uranium M-spectrum produced in a 42 MeV heavy fission product-uranium collision. The spectrum was measured with a proportional counter. My note book gives May 17th, 1961, thus certifying that I am talking about the same things since then. The cross section of about 1 Megabarn, we know now, cannot be understood unless it is related to the properties of a PHANTOM of  $Z = 146$ . Then we formulated /3/ : "Electron exchange phenomena in the quasi-molecular configuration of the electron shells during the nearly

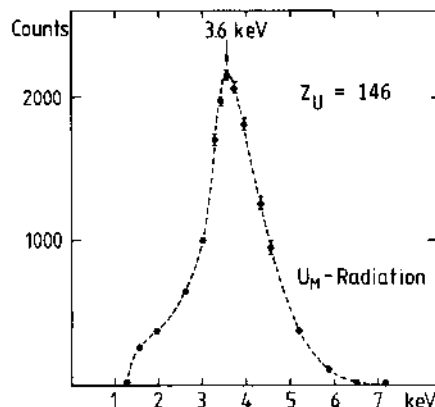


Fig. 2. Megabarn U-M spectrum induced in 42 MeV heavy fission product collision demonstrating action of  $Z = 146$  PHANTOM.

adiabatic collision seem to be responsible for the increase in the cross section". A comprehensive presentation of the Munique experiments has been given in the thesis of H.J. Specht /4/, out of which I have taken Fig. 3. The cross section of fission product L-shell excitation as a function of the atomic number of the collision partner is shown. Maxima in the ionization cross section have been found,

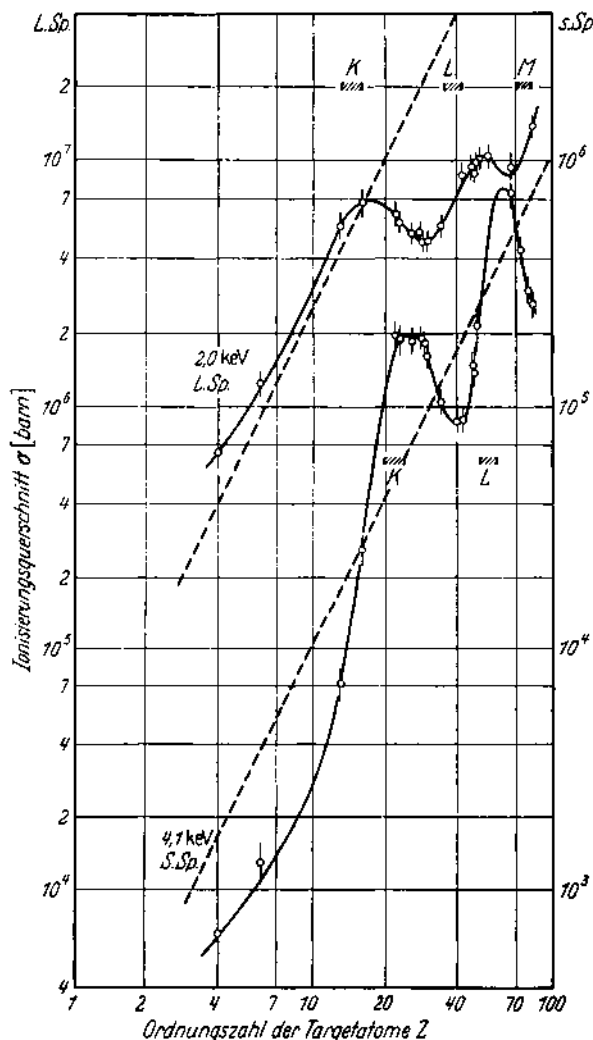


Fig. 3. Ionization cross section of fission product L-shell at 74 MeV and 42 MeV, respectively, as a functions of  $Z_2$ . Level-matching areas are indicated, /4/.

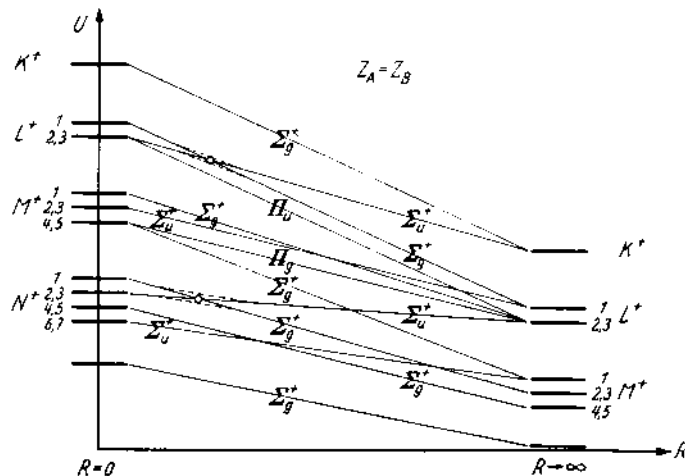


Fig. 4. Correlation diagram for a symmetric collision system, /4/.

which coincide with the energy matching of shells of the collision partners. The structure of the  $Z_2$ -dependence reflects the properties of the combined systems. The L-L level matching has been discussed using a correlation diagram, Fig. 4, which is drawn up-side-down mirror reflected compared to the schemes we know since the paper of Fano and Lichten /5/ published in the same year. The famous 4fo-orbital connecting the L-shell of the collision partners to the N-shell of the combined system is shown correctly in the correlation diagram.

The idea of electron promotion in the molecular system introduced by Fano and Lichten to explain the ionization of the Ar L-shell has been adapted to our fission product ionization experiments. Fig. 5a shows the extrapolation of the then existing cross section measurements using the concept of molecular orbitals of the combined system to predict the K-K level matching and its cross section /6/. Fig. 5b is a compilation of the now existing measurements done with Tandem beams /7/ showing that the prediction was off only by a factor of 4.

W. Meyerhof gave the quantitative description of the structures by the vacancy sharing mechanism between molecular orbitals /8/. But the early cross section measurements already established the concept of the intermediate molecular system and its underlying molecular orbitals. The combined system was needed to understand the ionization of the collision partners. The increased confidence in this concept allowed to study the molecular system itself. The first orbitals discussed were the promoting ones, which lead to the large cross sections, the demoting ones leading to increased binding in the quasimolecule in the early experiments still were hidden.

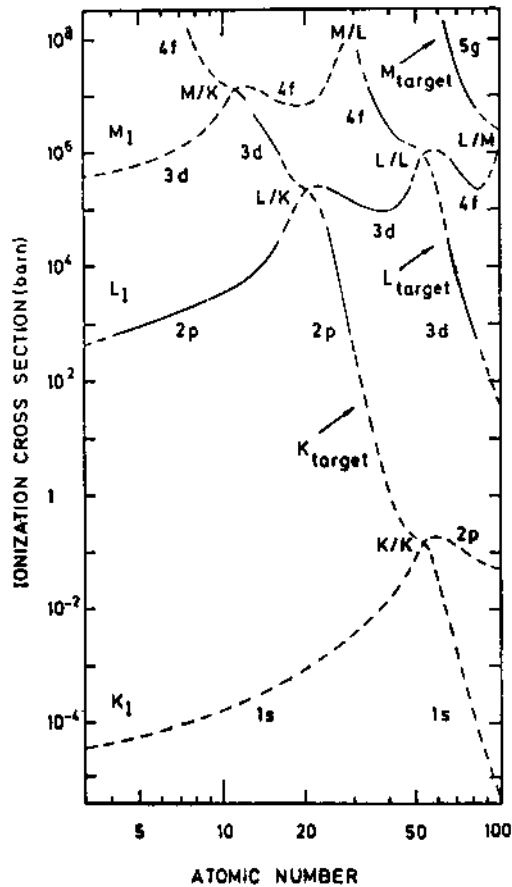


Fig. 5a. 42 MeV heavy fission product cross sections of Fig. 4 (full lines) extrapolated using the promotion mechanism. The state of the promoted electron in the united system is indicated, /6/.

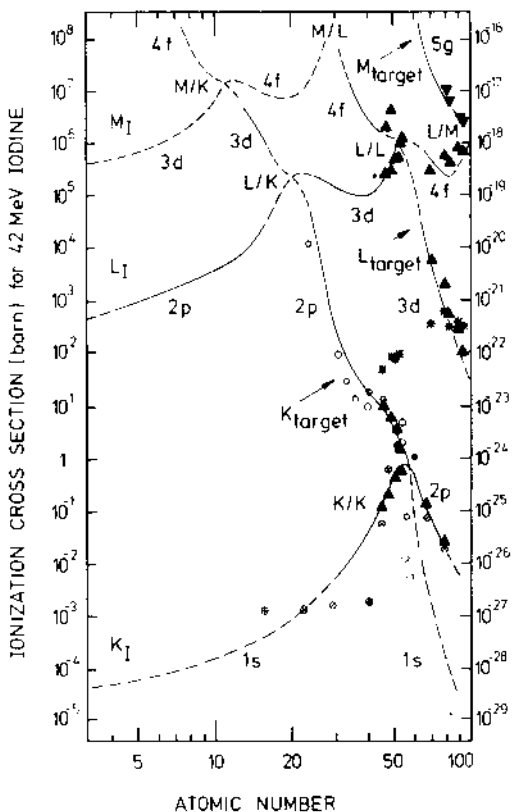


Fig. 5b. Cross sections from Ref. /7/ added to Fig. 5a.

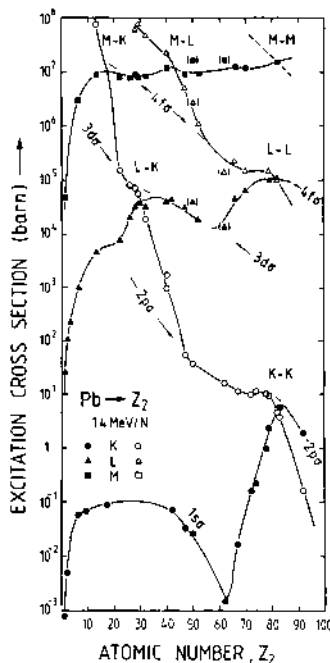


Fig. 6. Cross section of 1.4 MeV/u  
 $Pb \rightarrow Z_2$  collisions, /9/.

Fig. 6 shows the cross sections obtained recently in 1.4 MeV/u Pb-bombardments /9/. The molecular structure of the now really superheavy quasiatoms - the PHANTOMS - is reflected again in the cross sections. The minimum in the K-ionization cross section of lead at  $Z_2 = 62$  collisions is a message from a demoting or diving orbital. The ionization out of the  $1s\sigma$ -orbital is strongly decreased due to the increased binding energy of the innermost electrons. The main goal of the experiments described in the next section is to learn about the innermost demoting levels in PHANTOMS. The experiments are in some aspects easier to interpret than the earlier ones, as the complicated interplay of promoting orbitals with higher orbitals is of no importance. But the full complexity of atomic collision processes comprises all orbitals. The different interaction between orbitals and their coupling schemes for the heaviest collision systems is a wide and open field for future experiments, which just has been touched in first attempts /9/.

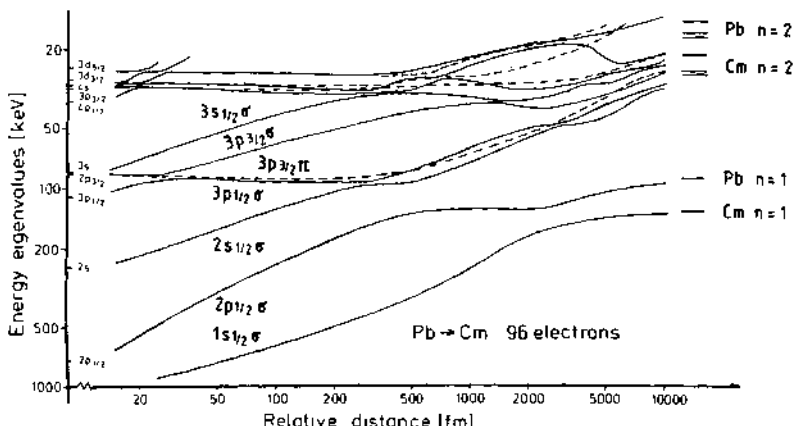
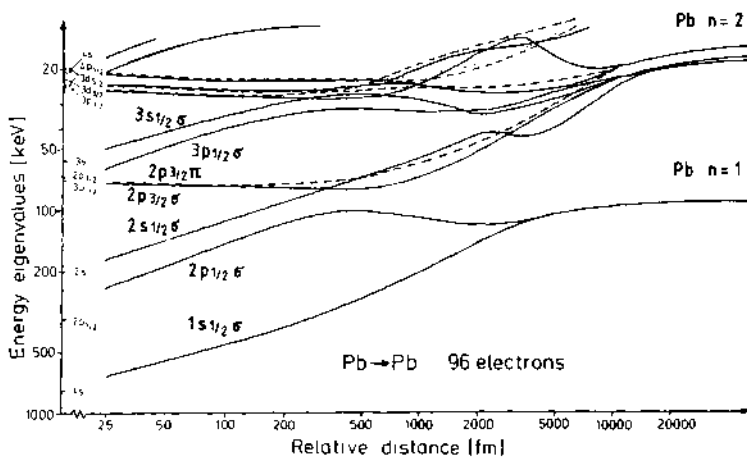
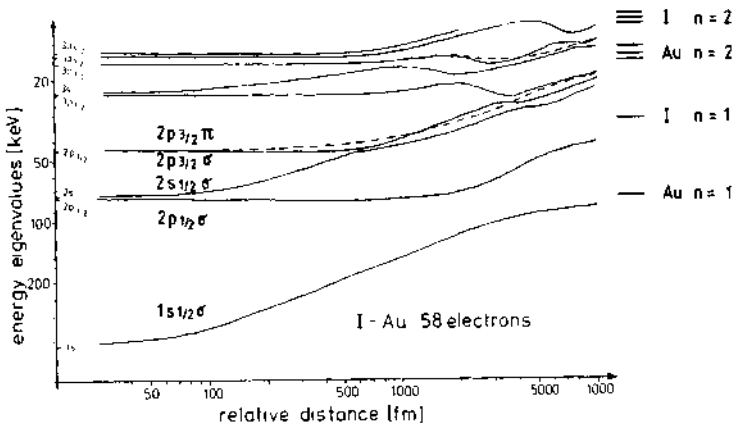


Fig. 7. Many electron, selfconsistent relativistic Hartree-Fock-Slater correlation diagram due to Fricke et al., /10/.

## TOTAL IONIZATION CROSS SECTIONS OF PHANTOMS

In this section we will discuss experiments concerning the ionization of inner-shells of PHANTOMS. We have learnt in the last section, whenever orbitals of a given shell in the separated atoms are connected to higher lying orbitals in the combined system, these promoting orbitals will mainly carry the ionization found after the collision in one of the collision partners. If the Coulomb field in the combined system is increased, it will mainly manifest itself as strongly increased binding for the unshielded inner-shell electrons. The ionization of these deeply bound shells may be small and hidden in large ionization cross sections out of the promoting orbitals. Inner-shell ionization of PHANTOMS may be observed, if orbitals are well separated of each other. The separation between orbitals increases with increasing atomic number and decreasing principal quantum number. K-shell ionization of slightly asymmetric collision systems with the highest atomic numbers are the most promising subjects of our studies.

The heaviest system studied until now is the (Pb+Cm)-system,  $Z = 178$ . The forthcoming lecture of F. Bosch is mainly devoted to this collision system, a recent correlation diagram of which is shown in Fig. 7, /10/. The diagram demonstrates the principal features of the theoretical predictions :

- (1) A binding energy of the  $1s\sigma$ -orbital approaching and diving into the lower continuum, which is reached at  $Z = 173$  as shown first by Voronkov et al. /11/.
- (2) There is no coupling from the  $1s\sigma$ -orbital by level crossings to higher orbitals.
- (3) As a function of distance between the charge centers the combined atom binding energies are observed only for very small separation distances. Even near the diving point at 18 fm, /12/, the slope  $dE_{1s\sigma}/dR$  is still 20 keV/fm.

It is clear from the correlation diagram that the experimental verification of the strongly increased binding of inner-shell electrons demands ionization at very small impact parameters. The possible observation of PHANTOM-ionization is governed by the size of this ionization probability, which is reflected in the total ionization cross section.

Measurements of total cross sections were the first to be performed at GSI when beams became available. The experimental set-up used is shown in Fig. 8. The following group took part in the measurements during the years 1976 - 1978.

B. Anholt	(Stanford)
P. Armbruster	(GSI)
H.H. Behncke	
F. Folkmann	(Aarhus Univ.)
S. Hagmann	(GSI)
D. Liesen	
J. MacDonald†	(KSU, Manhattan)
P.H. Mokler	(GSI)

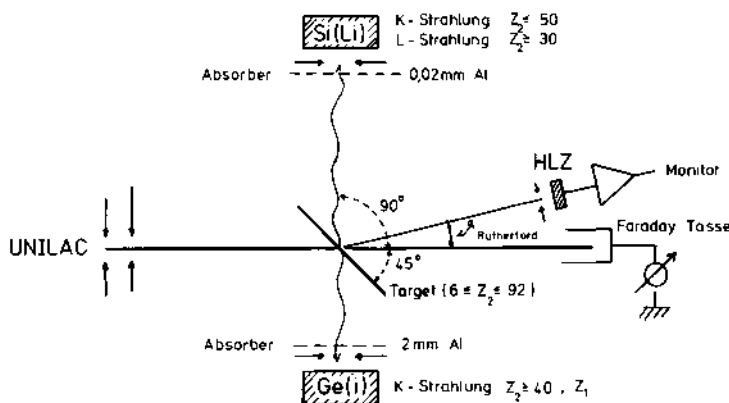


Fig. 8. Set-up to measure total cross sections used at the UNILAC experiments.

These measurements, /13,14/, will be discussed in the following, measurements of the differential ionization probability  $P(b)$  in the lecture of F. Bosch. From integral x-ray spectra we may derive the higher moments of  $P(b)$

$$\sigma = 2\pi \int_0^\infty bP(b)db \quad \text{first moment of } P(b) \quad (1)$$

$$\langle b \rangle = 2\pi \int_0^\infty b^2 P(b)db/\sigma \quad \text{second moment of } P(b)$$

The first moment is obtained via the integral count rate in an x-ray line, the second moment from the line width at  $90^\circ$  observation angle /15,16/

$$\langle b \rangle_{2,1} = 2a \frac{v}{c} \cdot \frac{A_{1,2}}{A_1 + A_2} \cdot \frac{1.03}{(\delta E/E)_{2,1}^{90^\circ}}$$

with  $2a$  the distance of closest approach, and  $A_1$  and  $A_2$  the masses of projectile and target atom, respectively. The indices 1 and 2 refer to the projectile and target atom. The line broadening increases with decreasing collision velocity and increasing atomic number.

Fig. 9 shows spectra of the (Pb-Au) system,  $Z = 161$  at three different energies /15/. The line broadening may be seen directly from the raw x-ray spectra. The analysis of the spectra gives line intensities - cross sections, line energies - information on higher shell occupation, and line widths - average impact parameters. Cross sections have been measured in the energy range (1.4 - 5.9) MeV/u for Xe-, Pb-, and U-beams bombarding different targets. K-shell ionization cross sections have been obtained. As example the cross sections for Pb-bombardments at 4.7 MeV/u are given in Fig. 10. The vacancy sharing at the K-K level matching point reflects the higher ionization out of the  $2p_{1/2}\sigma$ -orbital. 1s $\sigma$ -ionization prevails for  $Z_2 < 70$  and  $Z_2 > 94$ . Fig. 11 shows corresponding cross sections for U-ions at 3.6 MeV/u. The matching of the K-K-shells, L-L-shells, and K-L-shells is demonstrated by the vacancy sharing between corresponding orbitals in the PHANTOMS.

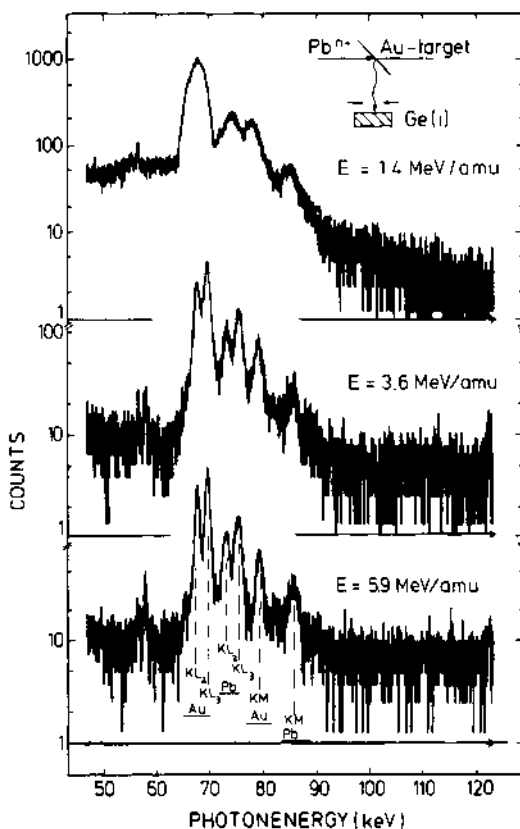


Fig. 9. X-ray spectra from  $\text{Pb} \rightarrow \text{Au}$  collisions at the different collision energies demonstrating the kinematical broadening of the K-lines, /15/.

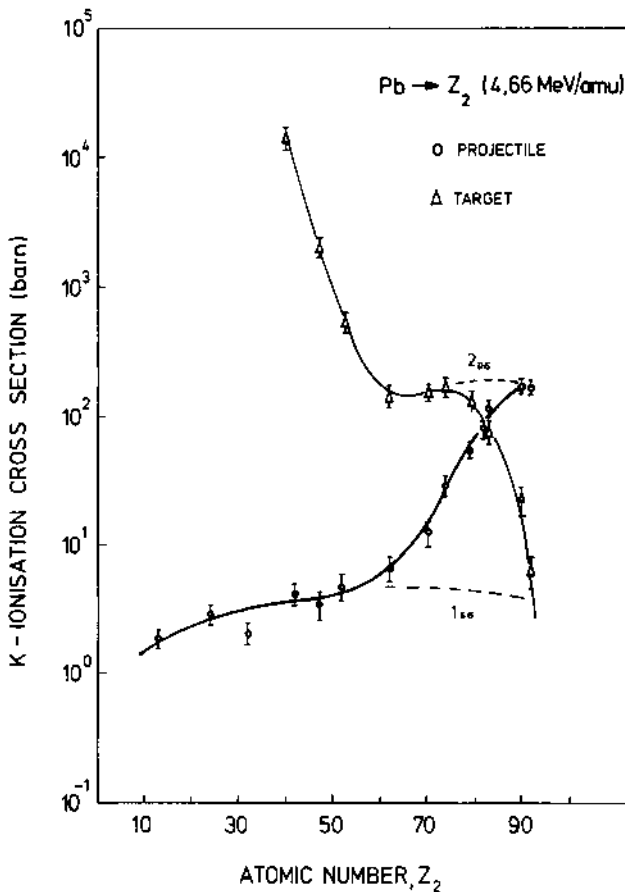


Fig. 10. Cross sections for 4.7 MeV/u  $Pb \rightarrow Z_2$  bombardments, /13/.

The high values of the ionization cross sections for 1s<sub>0</sub>-ionization of more than 1b even for  $Z$ -values of up to 170 was the sensational finding. The dip indicated even for  $Z=144$  at 1.4 MeV/u, Fig. 6, and earlier measurements at still lower energies /17/ extrapolated to the highest  $Z$ -values with their strongly increased binding gave values of the cross section below the mb-range. Contrarily, our Frankfurt colleagues /18/ had predicted large cross sections and their prediction was fully approved. The experimental values were even a factor of three larger than the calculated ones. Out of a demoting strongly bound orbital ionization with cross sections of several barns has become possible. 0°-line shape analysis /19/, which give directly  $P(b)$  (discussed in the lecture of F. Bosch), or line width analysis, such as Fig. 9, showed average impact parameters in the range smaller than 100 fm. Four months after the first U-beams at

the UNILAC, in August, 1976, from first exploratory cross section measurements of P.H. Mokler et al. it was evident that the cross sections were large, and the impact parameters probably small, that is ionization probabilities for close collisions could be expected in the percent range. The experiments of K-shell ionization of the heaviest systems will be faster than those done previously. Nature was kind to us, and the Frankfurt theoreticians even knew she will be, before we started.

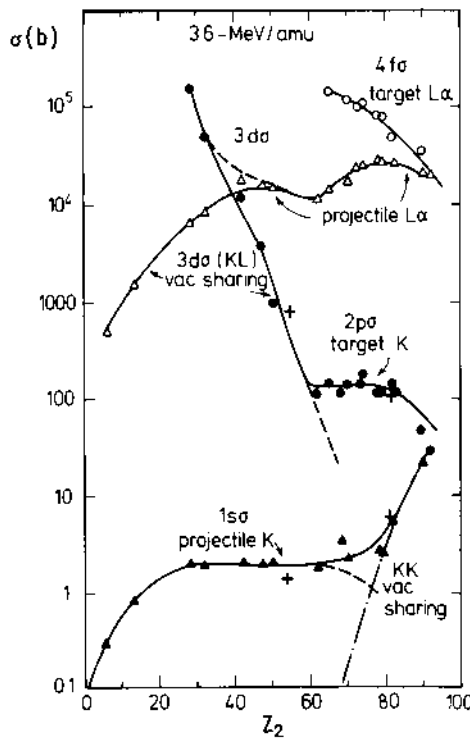


Fig. 11. Cross sections for 3.6 MeV/u  $U \rightarrow Z_2$  bombardments, /14/.

Anholt /20/, analyzing the data introduced a three factor formula, which takes into account the main physical effects. Comparing the K-shell ionization of lead in proton and lead bombardments, we should expect a ratio between Pb and p induced ionization of about 200. This ratio is the product of a factor  $7 \times 10^3$  due to the  $Z_1^2$ -scaling of the ionization cross sections, a factor  $6 \times 10^{-7}$

due to the increased binding of the molecular orbitals, and finally, a factor  $4 \times 10^4$  which is due to the relativistic wave functions of the PHANTOMS. This latter factor is the key to all further experiments and will be discussed by many speakers at this school. We will come back to the problem in the discussion of the ionization probability data.

The energy dependence of the cross section is very steep in the range below 3 MeV/u. For energies between (3 - 6) MeV/u the cross section for  $1s\sigma$ -ionization increases with a power of  $(3.0 \pm 0.3)$  for the (Pb-Mo) system,  $Z = 124$ . For heavier systems the increase is even weaker. The  $2p_{1/2}\sigma$ -cross sections in the same energy range increase slower with a power  $(1.4 \pm 0.4)$ , /13/.

Figs. 12 and 13 give the cross sections for  $1s\sigma$  and  $2p_{1/2}\sigma$  ionization as a function of the combined atomic number for 3 bombarding energies. The cross section governed by the properties of

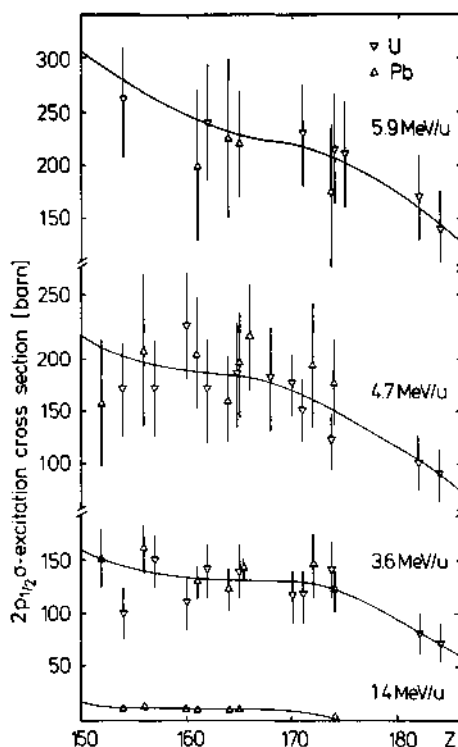


Fig. 12.  $2p_{1/2}\sigma$ -excitation cross section for  $Pb + Z_2$  and  $U + Z_2$  collisions in the energy range (1.4-5.9) MeV/u. Full lines are to guide the eye. The increase towards smaller Z-values is determined by measured values beyond  $Z \sim 150$ , /15/.

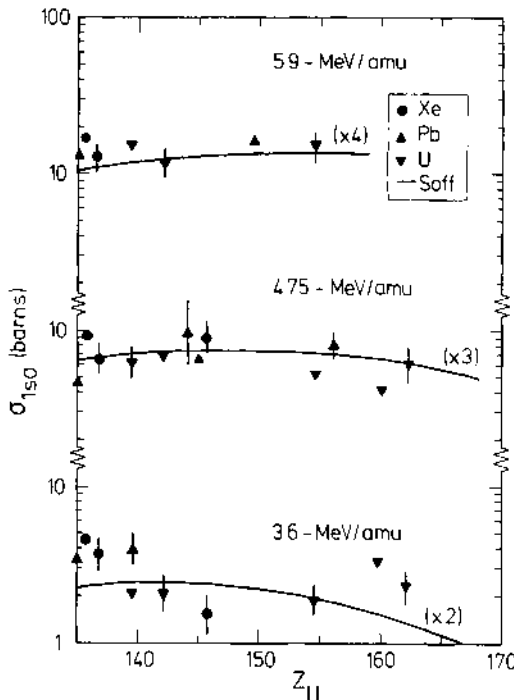


Fig. 13.  $1s\sigma$  cross sections for  $Xe, Pb, U \rightarrow Z$  collisions in the energy range (3.6-5.9) MeV/u compared to calculations, /18/, neglecting multiple ionization processes. The numbers in brackets are factors the calculated values have been multiplied with, /14/.

the combined system is not allowed to depend on the mass asymmetry of the collision partners. Different combinations giving the same PHANTOM have to have the same cross section. This is actually fulfilled as seen from the figures. The comparison to theory /18,21/ refers to the calculation neglecting multistep excitation, which underestimated the cross sections by factors given in brackets. In spite of increased binding for larger  $Z$ -values the relativistic enhancement compensates at least up to  $Z$ -values of 170. The cross sections are nearly constant. A slight decrease for  $2p_{1/2}\sigma$ -excitation beyond  $Z = 170$  is indicated by the data. Fig. 14 compares the cross sections at 5.9 MeV/u for the ionization of the  $2p_{1/2}\sigma$ -orbital, the  $1s\sigma$ -orbital, and the lower continuum /22/ as a function of  $(Z_1+Z_2)$ .

The relativistic enhancement factor makes the cross sections out of the discrete demoting states large and constant, and out of the lower continuum states strongly increasing. The latter remain small, of the order the  $1s\sigma$ -cross section would have been without relativistic enhancement. Looking at the experiments searching for positrons in the sub-mb range gives an appropriate impression, what a gift the large ionization cross sections have been to the experimentalists doing x-ray experiments.

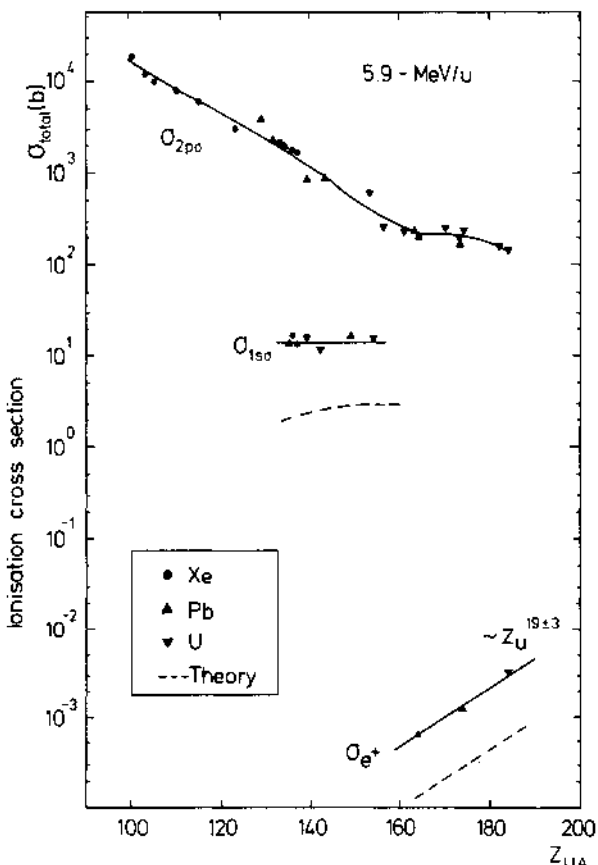


Fig. 14. Cross sections at 5.9 MeV/u for ionization out of the  $2p_{1/2}\sigma$  and  $1s\sigma$  molecular levels, and the lower continuum.

#### OUTLOOK TO NUCLEAR PHYSICS APPLICATIONS

Nuclear physicists are attracted by atomic physics, as the atomic phenomena might be used to learn about their proper problems. These are the reaction times in nuclear processes, the atomic number of unknown reaction products, or the application of atomic processes to build better detectors.

The attempts to measure lifetimes in heavy ion reactions using atomic ionization processes until now all failed (see contribution of W. Meyerhof to this school), or are questionable in their interpretation (see the discussions on the lines in the  $e^+$ -energy spectra during this school).

The finding of x-rays from the electronic rearrangement processes after a heavy ion reaction never succeeded until now. It was shown in 1962 by H. Hohmann /23/ that the x-rays observed in fission were all due to internal conversion processes of the excited fission products. The x-ray production thus depends on the individual nuclear structure of the reaction products, and is no well defined mean to determine production cross sections of the produced elements, unless their level schemes are already known. Similar experiences have been made recently at GSI in heavy ion reaction studies searching for x-rays from fusion-fission or deep inelastic reactions. The nuclear  $\gamma$ -radiation in the reaction drowned the x-rays, which were searched for.

A method making use of the very large cross sections of projectile x-ray excitation in atomic collisions is to my knowledge the only successful application of the experimental findings presented in the preceding sections. It was invented after the failure of H. Hohmann's experiments to determine the atomic numbers of primary fission fragments and applied to solve this problem /24/. The mass separated fission product beam /2/ was passed through a thin target foil and the collision induced x-rays were energy analyzed. As the cross sections are reaching Megabarns high yields of x-rays per fragment become possible. The collision induced x-rays served as element detector for fast recoils from a nuclear reaction.

Element analysis within  $\mu$ sec after the reaction - the separation time for the recoils - is of general value. A first application to the analysis of evaporation residues has been performed recently at GSI /25/. The elemental composition of a velocity separated heavy evaporation residue beam was analyzed making use of an analysis of  $L_\alpha$  x-rays, which were produced with cross sections of several tens of kilobarns. The resolution obtained using Si(Li)-detectors was superior to the best  $\Delta E-E$  ionization chambers ( $Z/\Delta Z = 75$ ). However, even with the high x-ray cross sections the total detection efficiency per fragment is of the order of some percent compared to 1 for  $\Delta E-E$ -ionization chambers.

As a demonstrative example of the technique, by which once we intended to analyze beams of superheavy elements /26/, we made use of it to detect the x-rays from fusion of copper and tin. Since 6000 years copper and tin gives bronze, but as modern alchemists we demonstrated that a second transmutation into gold is possible, a transmutation old alchemists searched for centuries. Fig. 15 gives the recoil separator SHIP and the detection system, Einstein's

magic box of transmutations. Moreover, it shows the  $L_{\alpha}$  x-rays induced in the evaporation residues after separation and passage through a tin converter. Clearly we produced isotopes of gold. The god's father Zeus  $\gamma$  (Sn) united with Aphrodite  $\varphi$  (Cu), the foamborne, vanished, transmuted and resurrected as Apollo  $\Theta$  (Au), the god of light. Apollo (Au) passing by his father Zeus (Sn) after his astonishing divine birth cannot resist to lift his identity by sending a glitter, modern alchemists registered as x-ray spectrum.

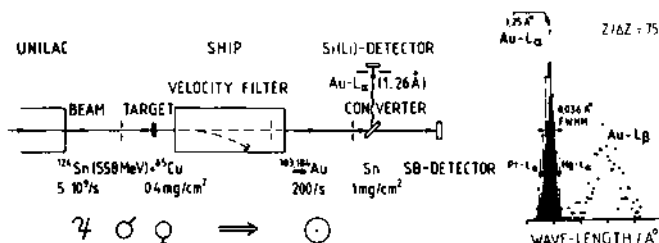


Fig. 15. Einstein's shrine of transmutation and spectrum of Apollo's glitter.

#### MEASUREMENTS OF IONIZATION PROBABILITY

The success of the theory of Bang and Hansteen /27/ in demonstrating the equivalence of an impact parameter presentation of collision induced x-ray production with a fully quantummechanical wave presentation /28/ made clear, that projectile scattering angle and impact parameter can be related uniquely, and scattering angle dependent differential measurements directly give the impact parameter dependent ionization probability  $P(b)$ . Early attempts to measure  $P(b)$  with fission products failed. The high intensity I-beams available at Tandem accelerators allowed the first  $P(b)$ -measurement for inner-shell x-ray excitation /29/. The  $P(b)$  for L x-ray excitation in the nearly symmetric (I-Te) system,  $Z = 105$ , was measured by H.J. Stein et al. in 1969. In the discussion of his thesis /30/ a correlation diagram for  $Z = 104$  was presented, where for the first time for the levels of the united system we had to introduce x-ray energies not available experimentally. At that time it became clear that atomic physics may profit from and contribute to the then eagerly discussed superheavy elements. As everybody then believed they will be produced in large amounts, nobody took such an esoteric contribution too seriously. Molecular x-rays and the idea to use  $P(b)$ -measurement to determine binding energies still were not borne at that time.

A first exploratory experiment to measure  $P(b)$  in the (Xe-Au) system,  $Z = 133$ , was initiated by the late J. MacDonald still in 1976 /31/. It proved for the first time directly the high values of  $P(b)$  for selected values of  $b$ .

The variety of further experiments done at GSI is presented in the lecture II given by F. Bosch.

## REFERENCES

1. W.M. Coates, P.R. 46, 542 (1934)
2. P. Armbruster, Z. Phys. 166, 341 (1962)
3. P. Armbruster, H.J. Specht, A. Vollmer, ANL-Report 6797, 464 (1963);  
P. Armbruster, E. Roeckl, H.J. Specht, A. Vollmer, Z. Naturforschung 9a, 1301 (1964)
4. H.J. Specht, Z. Phys. 185, 301 (1965)
5. U. Fano, W. Lichten, Phys. Rev. Letters 14, 627 (1965)
6. P. Armbruster, P.H. Mokler, H.-J. Stein, Proc. Int. Conf. Inner Shell Ionization Phenomena, Atlanta (1972),  
R. Fink, S. Ranson, J. Palms, P. Rao (eds.), CONF-720404 (Vol. 1), 396 (1973)
7. S. Hagmann, P. Armbruster, G. Kraft, P.H. Mokler, H.-J. Stein, Z. Physik A288, 353 (1978)
8. W. Meyerhof, Phys. Rev. Lett. 31, 1341 (1973)
9. W.A. Schönfeldt, Dissertation Üni. Köln (1981), GSI-Report 81-7
10. B. Fricke, T. Morović, W.-D. Sepp, A. Rosen, D.E. Ellis, Phys. Lett. 59A, 375 (1976);  
W.D. Sepp, B. Fricke, T. Morović, Phys. Lett. 81A, 258 (1981);  
B. Fricke, private communication
11. V.V. Voronkov, N.N. Kolesnikov, JETP (U.S.S.R.) 39, 189 (1960)
12. G. Soff, J. Reinhardt, W. Betz, J. Rafelski, Phys. Scr. 17, 417 (1978)
13. H.-H. Behncke, P. Armbruster, F. Folkmann, S. Hagmann, J.R. MacDonald, P.H. Mokler, Z. Physik A289, 333 (1979)
14. R. Anholt, H.-H. Behncke, S. Hagmann, P. Armbruster, F. Folkmann, P.H. Mokler, Z. Physik A289, 349 (1979)
15. S. Hagmann, P. Armbruster, H.-H. Behncke, D. Liesen, P.H. Mokler, Z. Physik A289, 1 (1980)
16. S. Hagmann, P. Armbruster, F. Folkmann, G. Kraft, P.H. Mokler, Phys. Lett. A61, 451 (1977)
17. W. Meyerhof, Phys. Rev. A10, 1005 (1974)
18. W. Betz, G. Soff, B. Müller, W. Greiner, Phys. Rev. Lett. 37, 1046 (1976)
19. J.S. Greenberg, H. Bokemeyer, H. Emling, E. Grosse, D. Schwalm, F. Bosch, Phys. Rev. Lett. 39, 1404 (1977)
20. R. Anholt, W. Meyerhof, Phys. Rev. A16, 190 (1977)
21. B. Müller, G. Soff, W. Greiner, V. Ceausescu, Z. Physik A285, 27 (1978)

22. H. Backe, L. Handschug, F. Hessberger, E. Kankeleit, L. Richter, F. Weik, R. Willwater, H. Bokemeyer, P. Vincent, Y. Nakayama, J.S. Greenberg, Phys. Rev. Lett. 40, 1443 (1978)
23. H. Hohmann, Z. Physik 172, 143 (1963)
24. P. Armbruster, D. Hovestadt, H. Meister, H.J. Specht, Nucl. Phys. 54, 586 (1964)
25. W. Faust, P. Armbruster, S. Hofmann, G. Münzenberg, H. Ewald, K. Güttner, Journal of Radioanalytical Chemistry 55, 175 (1980)
26. P. Armbruster, P.H. Mokler, H.J. Stein, Phys. Rev. Letters 27, 1623 (1971)
27. J. Bang, J.M. Hansteen, Kgl. Danske Videnskab. Selskab, Mat.-Fys. Medd. 31, no. 13 (1959)
28. W. Henneberg, Z. Physik 86, 592 (1933)
29. H.-J. Stein, H.O. Lutz, P.H. Mokler, P. Armbruster, Phys. Rev. A5, 2126 (1972)
30. H.-J. Stein, Dissertation T.H. Aachen D82, 1971
31. J.R. MacDonald, P. Armbruster, H.-H. Behncke, F. Folkmann, S. Hagmann, D. Liesen, P.H. Mokler, A. Warczak, Z. Physik A284, 57 (1978)

EXPERIMENTS ON THE EXCITATION OF THE INNERMOST ELECTRONS  
IN EXTREMELY STRONG FIELDS

Fritz Bosch\*

Ges. f. Schwerionenforschung mbH  
P.O. Box 11 05 41  
D-6100 Darmstadt, FRG

I would like to give you an *experimental* talk. After so many exciting theoretical lectures, in which the whole physics was lovingly embraced, it is a very troublesome job to find the little spot still left for the experimentalist. Now, theoretical people have both the task and the liberty to go far away within their power of imagination.

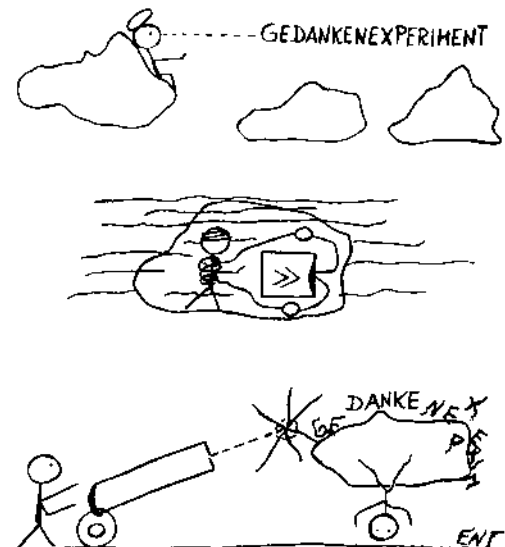


Fig. 1. Theoretical and experimental physicists, shown in their natural order.

"Above the clouds", however, "the freedom should be boundless, all troubles and all perturbations there are small".\*\*

Experimentalists, on the other hand, have to stay on earth, nearby their detectors and in the middle of the clouds, not seeing anything most of the time. But, since the most dirty experiment is able to kill the most beautiful theory at one blow, just theorists should consider for some minutes the experimental dirt in order to comprehend at least the difference between gedankenexperiments and the real ones. Moreover, also in order to conceive why they have to wait so many weeks or even months for a few shabby experimental data.

Actually, we have caused the deep indignation of our dear friend, the *experimentalist* Prof. Kienle, by whom we were nastily insulted as "Schwerionenbeamte" ("heavy ion clerks"). Now, Prof. Kienle, coming from the Top-University Munich (TUM), has no time anymore for the ordinary pursuits of a physicist; after having arrived in the House of Lords, he rather studies the last week Phys. Rev. Letters contemplating thereby the navel of the world, placed somewhere in the English Garden.

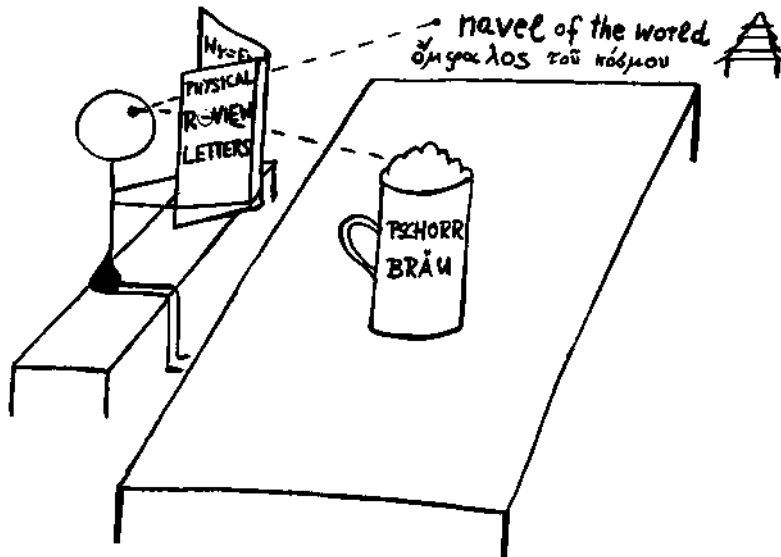


Fig. 2. Prof. Kienle during his daily strenuous job in the English Garden of Munich.

We, as clerks in the marsh of physics, on the contrary, have the time to be always poring over old books in order to learn trivialities, for example, how an experiment has to be performed. During these studies, however, we succeeded to find the GOLDEN RULES for experimentalists in developing the thoughts of the early pre-socratic philosophers :

NATURE IS SIMPLE

(Anaximandros)

Therefore, complicated experiments are wrong. Experiments have to be simple (GOLDEN RULE I).

NATURE LIKES TO HIDE ITSELF

(Heraclite)

Therefore, one has to ask the right questions. Experiments have to be simple but clever (GOLDEN RULE II).

NATURE HAS TWO FACES, A BRIGHT ONE AND  
A DARK ONE, WHICH ALWAYS APPEAR TOGETHER

(Heraclite)

Therefore, experiments have to transform dirty effects into gold (GOLDEN RULE III).

NATURE IS IN ALL THINGS AND THE  
VERY SAME IN ALL THINGS

(Parmenides)

Therefore, flat and structureless spectra are just so important or unimportant as wiggles and peaks (GOLDEN RULE IV).

These rules we tried to take to heart in performing our experiments on inner shell excitation in superheavy collision systems. Working on it in the dark catacombes of the UNILAC accelerator, however, we resembled the residents of Kafka's castle rather than the world navel spectators in the bright green of the English Garden ...

Up to now, it has remained a dream only to detect or to produce stable superheavy atoms ( $\alpha Z \gtrsim 1$ ), because NATURE refuses obstinately to open this box of Pandora. But, lately, we got the permission at least for a transient glance onto their shadows, since we became able to bring two heavy atoms closely together during a heavy ion-atom collision.

In a head-on collision of Pb on Pb with 5 MeV/u for example, which is a little below the Coulomb barrier, the nuclei approach to a distance of  $\approx 20$  fm and, thus, for a time of roughly  $10^{-20}$  s the innermost electrons perceive a combined charge  $Z = 164$ , supposed they are able to adjust their motion at once onto the instantaneous electromagnetic field. For that the velocity of the projectile has to be small as compared to the velocity of the bound electron :

$v_p \ll v_e$ . The question arises, of course, which specific information about the most strongly bound electrons one may obtain within this extremely short time ( $10^{-20}$ s) when a combined atomic system  $\alpha Z > 1$  exists. We shall see, however, that the experiment itself clarifies this still open question.

What happens during a collision of two heavy atoms with an energy below the Coulomb barrier? The bound electrons may be excited or ionized, picking up the appropriate Fourier frequencies from the time changing Coulomb field; the vacancies are filled either after the separation by characteristic x-radiation or, still during the collision, by quasimolecular x-rays. Moreover, electrons of the negative energy continuum are allowed to jump either into states of the positive continuum or into vacant bound orbitals.

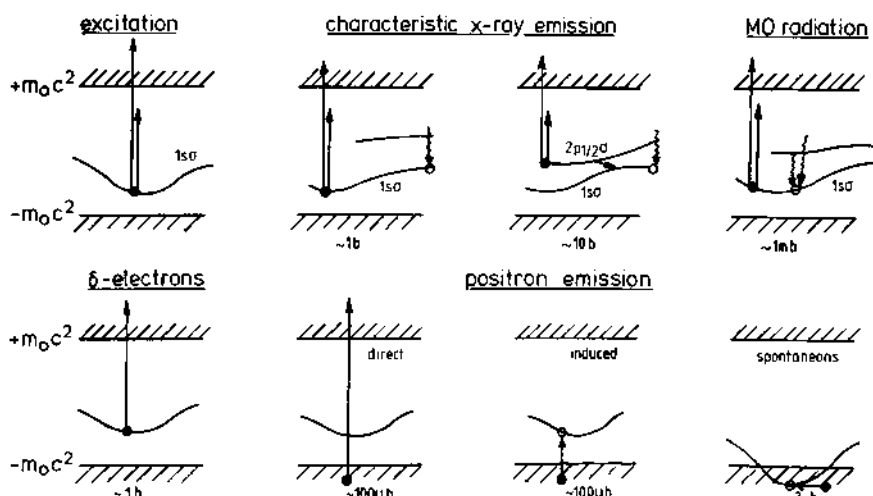


Fig. 3. Some excitation mechanism in heavy ion-atom collisions.

These processes just described could be investigated in detail by the following types of experiments :

- (1) Measurement of the inner shell excitation probability as a function of the impact parameter;
- (2) Analysis of the spectral distribution of the ionized electrons stemming from inner shells;
- (3) Investigation of the quasimolecular x-radiation;
- (4) Search for non-nuclear positrons.

I shall report, however, onto experiments concerning the first topic only. For the other ones I refer to the lectures given by Dr. Kozuharov, Dr. Vincent, Dr. Backe, Dr. Bokemeyer, and Prof. Kienle.

In detail I shall present both the methods and results of inner shell excitation experiments, performed at superheavy collision systems ( $\alpha Z \gtrsim 1$ ) together with a preliminary interpretation of the data, which is based on both simple and fundamental physical principles. All forthcoming questions, however, which are closely connected with those data, as inner shell binding energies and wave functions of superheavy quasiatoms, are discussed fully in the lectures given by Prof. Armbruster.

IMPACT PARAMETER DEPENDENCE OF THE  $1s\sigma$  EXCITATION IN COLLISION SYSTEMS  $\alpha(Z_1+Z_2) \gtrsim \alpha Z \gtrsim 1$

The Line-Shape Method

During an adiabatic collision ( $v_p \ll v_e$ ) the  $1s$ -state of the heavier atom changes to the  $1s\sigma$  orbital with respect to a quasimolecular basis set. Therefore, an excitation of a  $1s\sigma$  electron leads to an exit channel with a  $1s$  vacancy in the heavier atom which is filled by characteristic K- $\chi$  radiation.

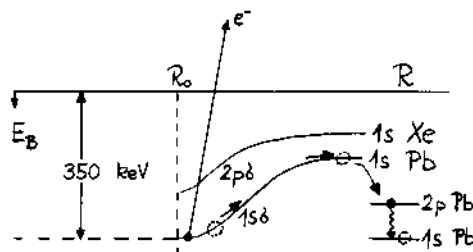


Fig. 4. Formation of the innermost quasimolecular orbitals as a function of the internuclear distance  $R$ , shown at the example of the  $Xe+Pb$  ( $Z=136$ ) system. The excitation of a  $1s\sigma$  electron during the collision leads to a K-vacancy of the heavier atom, which is filled by characteristic K- $\chi$  radiation.

Obviously, the natural way to investigate the impact parameter dependence of the  $1s\sigma$  excitation would be a coincidence measurement between the scattered projectile (by that defining the impact parameter) and the K- $\chi$  radiation of the heavier atom. In the first experiment<sup>1</sup>, performed at a superheavy collision system, however, a completely different technique was used, which tried to comply with the Golden Rules I, II, and III, as mentioned previously.

This method benefits from a simple physical fact : Provided that the detector, recording the characteristic x-radiation, is located at  $0^\circ$  with respect to the beam direction, it exists a one-to-one relationship between the scattering angle and the - Doppler shifted - photon energy, *independent* of the azimuthal scattering angle.

In this respect the  $0^\circ$  observation angle is unique :

$$E = E_0 \left\{ 1 + \frac{v_{CM}}{c} (1 - \cos \theta_{CM}) \right\} \quad (1a)$$

$$b = a \operatorname{ctg} \left( \frac{\theta_{CM}}{2} \right) \quad (1b)$$

Eq. (1a) provides the photon energy  $E$ , emitted by the recoiling target;  $E_0$  is the unshifted energy,  $v_{CM}$  and  $\theta_{CM}$  is the velocity and the projectile scattering angle, respectively, in the CM-system. Eq. (1b) contains the connection between the impact parameter  $b$ , the scattering angle  $\theta_{CM}$  and the minimum distance  $2a$  in a head-on collision.

From Eqs. (1a) and (1b) one gets for the Doppler shift  $\Delta E$  of the energy  $E = E - E_0$  :

$$\Delta E = 2E_0 \frac{v_{CM}}{c} \frac{a^2}{a^2 + b^2} \quad (2)$$

and as the cross section  $dN(\Delta E)$  for photons with an energy shift  $\Delta E$  :

$$dn(\Delta E) \propto 2b P(b) \frac{db}{d(\Delta E)} d(\Delta E) \quad (3)$$

where  $P(b)$  is the excitation probability of the corresponding electron orbital. Finally, one obtains for the differential cross section :

$$\frac{dN(\Delta E)}{d(\Delta E)} \propto \frac{2c}{E_0 v_{CM}} \frac{a^2}{4} \left( 1 + \left( \frac{b}{a} \right)^2 \right) \left( \frac{E}{E_0} \right)^2 P(b) \quad (4)$$

It follows from Eqs (3) and (4) that the number of x-rays with a fixed Doppler shift  $\Delta E$  is proportional to the excitation probability  $P(b)$  at that impact parameter  $b$ , which corresponds to  $\Delta E$  according to Eq. (2). The measurement of the spectral distribution of the x-ray energy, therefore provides immediately the *relative* excitation probability  $P(b)$ , without the need of any additional coincidence condition. In order to obtain the *absolute* number of  $P(b)$ , however, further information is required, e.g. the total excitation cross section  $\sigma = 2\pi \int_0^\infty b \cdot P(b) db$ .

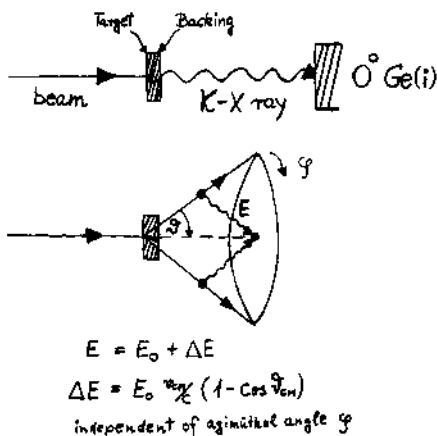


Fig. 5. Scheme of the line shape method. For a scattering angle  $\theta$  the Doppler shift  $\Delta E$  of the characteristic K-radiation becomes independent of  $\phi$ , if and only if, the x-ray detector is placed at  $0^\circ$  (or  $180^\circ$ ) with respect to the beam direction. Then, via Eqs. (1b) and (2) a one-to-one correspondence between impact parameter  $b$  and x-ray energy  $E$  is established.

The first experiment was performed on the collision systems Xe+Pb and U+Pb at a projectile energy of 4.7 MeV/u, whereby in both cases the K-x radiation of the target (Pb) was investigated. Thus, for the Xe+Pb system the  $1s\sigma$  - and for the U+Pb system the  $2p\sigma$  - excitation probability was obtained. The  $1 \text{ mg/cm}^2$   $^{208}\text{Pb}$ -targets were evaporated onto  $25 \text{ mg/cm}^2$  Ni-backings, in order to stop the beam. Since the lifetime of a Pb K-shell vacancy ( $\approx 10^{-17} \text{ s}$ ) is much shorter than the slowing down time in the backing ( $\approx 10^{-12} \text{ s}$ ) the backing thickness does not distort the line shape of the x-rays. Furthermore, the total Doppler width of the Pb  $K_{\alpha 1}$ -line, as extracted from Eq. (2) ( $\approx 8 \text{ keV}$ ) is an order of magnitude larger than the x-ray detector resolution of  $\approx 500 \text{ eV}$  (at 75 keV). Finally, the collision systems and the kinematic were chosen in such a way that the line shape of the  $K_{\alpha 1}$ -line does not overlap to the  $K_{\beta}$ -line (remember that in the case of target radiation the line shape arises on the high energy side of the unshifted line).

In Fig. 6 the Pb K-line for both collision systems Xe+Pb and U+Pb is shown, as recorded by the  $0^\circ$  Ge(i)-counter. In the lowest part of Fig. 6a the Pb K-radiation of a Bi-source is drawn for comparison. Apart from the pronounced line shape one notes both a shift and a broadening of the "reaction" Pb-line due to multiple vacancies in outer shells. At the top the spectrum is drawn, which was recorded by a counter placed at  $90^\circ$ .

The solid line in this spectrum represents the  $90^\circ$  line shape calculated with that  $P(b)$ , which was extracted from the measured  $0^\circ$  line-shape (cf. the inset; in Figs. 6a and 6b the impact parameter is called " $\rho$ " instead of " $b$ "). Obviously, this calculated line serves as a proof, whether  $P(b)$  was determined correctly from the  $0^\circ$ -data. For the absolute normalization of  $P(b)$  the value  $\sigma_K = 5 \cdot 10^{-24} \text{ cm}^2$  was used, measured by Behncke et al.<sup>2</sup>. It should be stressed (cf. the impact parameter scales, drawn at the bottom of Figs. 6a and 6b) that the line shape method is extremely sensitive just at the small impact parameters ( $0 \leq b \leq 30 \text{ fm}$ ).

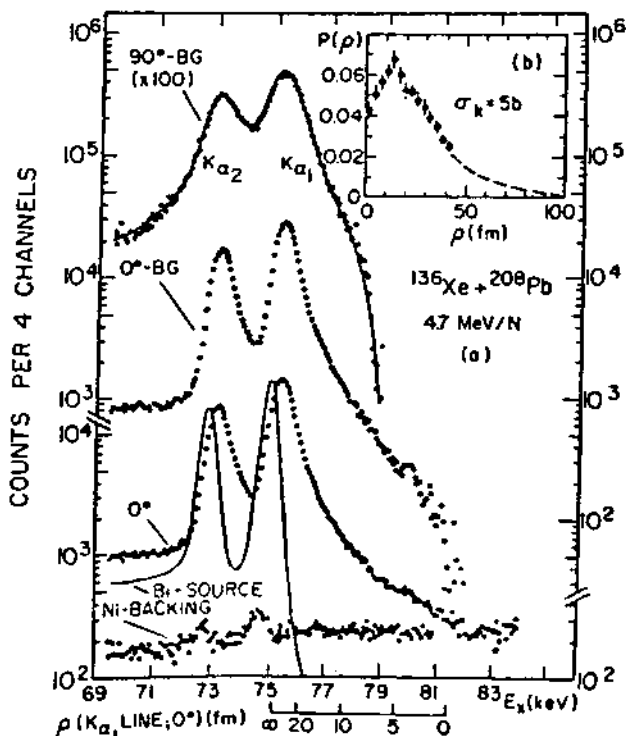


Fig. 6a.  $K_\alpha$ -line profiles of Pb from  $^{136}\text{Xe} + ^{208}\text{Pb}$  collisions observed at  $0^\circ$  before and after background (BG) subtraction and at  $90^\circ$  after BG subtraction. The inset shows the iso excitation probability  $P(\rho)$  for this system, extracted from the  $0^\circ$  line shape, as described in the text.

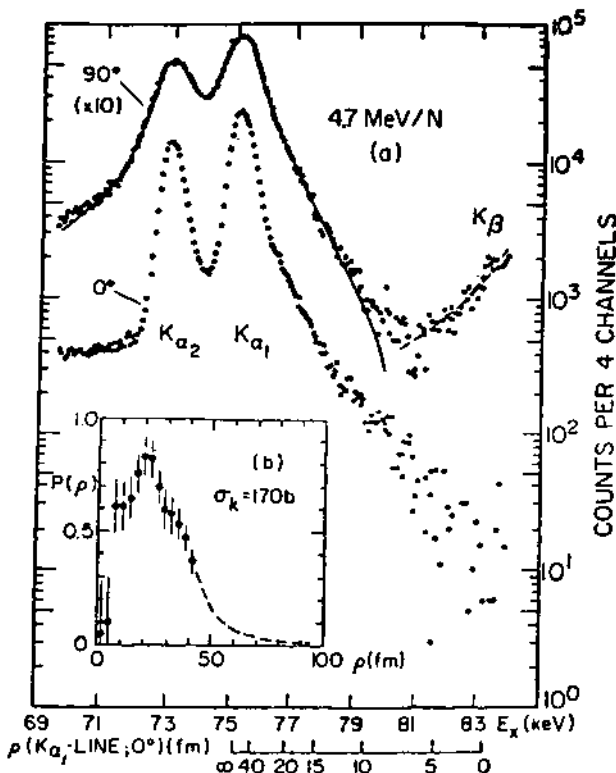


Fig. 6b.  $K_{\alpha}$ -line profile of Pb from  $^{238}\text{U}+^{208}\text{Pb}$  collisions observed at  $0^\circ$  and  $90^\circ$  after background subtraction. The inset shows the  $2\sigma$  excitation probability  $P(b)$  for this system, extracted from the  $0^\circ$  line shape. Further explanations are given in the text.

The prominent general features of this first measured  $1s\sigma$  excitation probability on a superheavy collision system ( $Z=136$ ) are :

- (i) A concentration of large excitation probabilities (in the order of  $10^{-1}$ ) at small impact parameters, and
- (ii) A pronounced dependence of  $P(b)$  on  $b$ . More than 50 % of the total cross section of a  $1s\sigma$  vacancy is contributed by collisions with  $b \leq 45$  fm. From that it must be concluded that the  $1s\sigma$  excitation occurs mainly at impact parameters much smaller than the K-shell radius of the united system (for  $\text{Xe}+\text{Pb}$   $\langle r \rangle_K \approx 220$  fm).

Similar conclusions can be taken from the  $2p\sigma$  measurement ( $U+Pb$ ), presented in Fig. 6b. In this system, however,  $P(b)$  reaches an order of 1 exhibiting a pronounced peak-structure at  $\approx 20$  fm, which could be explained by an important contribution of rotational coupling to the excitation mechanism.

By these first measurements using the line shape method, it is demonstrated clearly that the inner shell excitation in super-heavy collision systems is restricted onto a surprisingly small range of impact parameters. The reasons for that as well as the conclusions resulting from that I shall discuss in detail at the end of the next section.

The Doppler shift method, indeed, perfectly follows the Golden Rules I, II, and III. Especially Rule III seems to be realized in an ideal manner : The Doppler shift, usually a dirty effect in spectroscopy, was transformed into a Doppler gift granting at one blow the whole information on the inner shell excitation probability by the single data of one Germanium diode, provided only, that it was placed at the "right" position.

#### The Coincidence Method

Our Golden Rules resemble the Pole-star, the Great Bear, Cassiopeia, Orion, and the other stars, which serve as invariable fixed points for the sailor - but only, if the sky is clear. Often, however, these stars are darkened by clouds and the sailor has to content with other orienting lines. Actually, the clouds obscuring the line shape method are competing processes as vacancy sharing and Coulomb excitation, which can appear together with the pure inner shell excitation. Thus, becoming unfaithful to the promises of simplicity and cleverness, the inner shell experimentalist has to retreat mostly to the "pedestrian" method of coincidence technique in doing his job. By this means, however, the most precise data about inner shell excitation in superheavy quasiatoms have been obtained since the first experiment of MacDonald et al.<sup>3</sup>.

An excitation of a  $1s\sigma$  electron leads to an exit channel with a  $1s$  vacancy in the heavier atom which is filled by characteristic K-x radiation, as I have mentioned previously. Similarly an excitation of the neighbouring  $2p\sigma$  shell leads to a  $1s$  hole in the lighter atom.

In an experiment, where coincidences between the scattered projectiles (defining thereby the impact parameter) and characteristic K-x rays are recorded, the measured quantities therefore are

$$P^H(\theta) = \frac{N_c^H(\theta)}{N(\theta) \epsilon(K^H)} \quad \text{and} \quad P^L(\theta) = \frac{N_c^L(\theta)}{N(\theta) \epsilon(K^L)} \quad (5)$$

where  $N_c^H(\theta)$  and  $N_c^L(\theta)$  are the particles, which are coincident with characteristic  $K_x$  radiation of the heavier and lighter atom, respectively.  $\epsilon(K^H)$  and  $\epsilon(K^L)$  are the x-ray counter efficiencies at the corresponding energies, and  $N(\theta)$  is the number of particles scattered into an angle  $\theta$  with respect to beam direction.  $\theta$  can be transformed into the impact parameter  $b$ , with the aid of

$$b = a \operatorname{ctg} \theta^{\text{CM}} / 2 \quad (1b)$$

where  $a$  is half the minimum distance in a head-on collision.

$P^H(\theta)$ , however, is not yet the desired excitation probability of the  $1s\sigma$  orbital,  $P_{1s\sigma}$ . The reason is, that the same final state as in  $1s\sigma$  excitation is observed, whenever a vacancy produced at first in the  $2p\sigma$  shell is shared into the  $1s\sigma$  orbital. Therefore, in order to obtain  $P_{1s\sigma}$ , one has to correct  $P^H$  for vacancy sharing according to<sup>4</sup> :

$$P_{1s\sigma} = \frac{(1-w)P^H - wP^L}{1 - 2w} \quad (6)$$

where  $w$  is the sharing probability  $2p\sigma \rightarrow 1s\sigma$ .

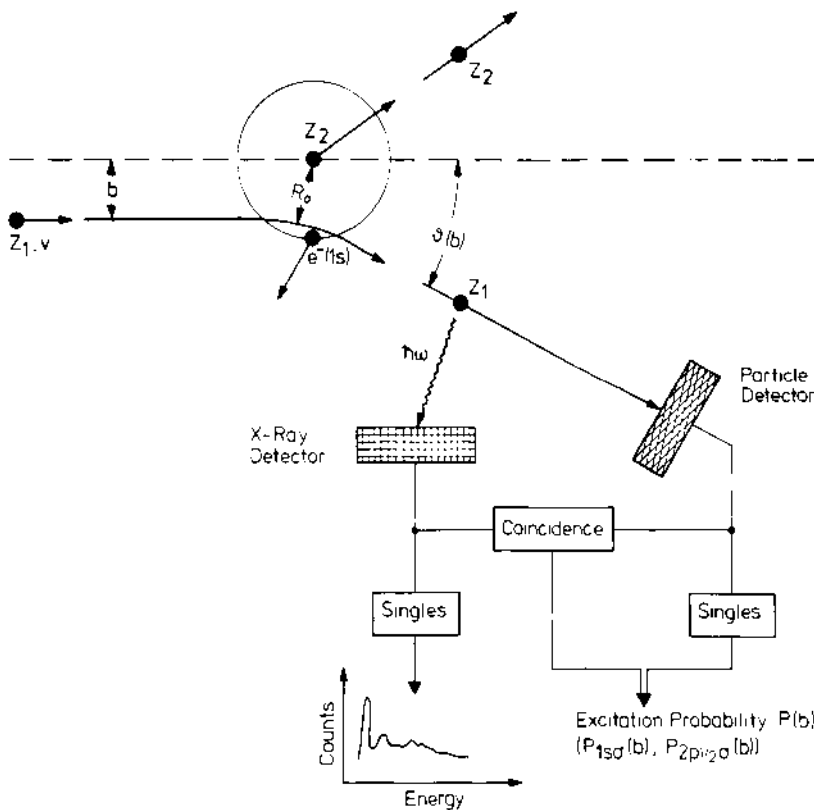


Figure 7

In Fig. 7 we show the experimental set up, used usually for that purpose. The scattered particles are recorded in a position of the inner shell excitation probability using the coincidence technique.

sensitive parallel plate avalanche counter and the characteristic  $K_x$ -rays of both atoms in an intrinsic Ge-diode. A typical spectrum, obtained in this way for the system Sm on Pb ( $Z=144$ ) is presented as the left side of Fig. 8<sup>5</sup>. At the right side we see the same data but corrected for vacancy sharing. Although the sharing probability is a few percent only for that rather asymmetric system ( $\Delta Z=20$ ), the sharing contribution is still important at large  $b$ , whereas at small  $b$  ( $b \lesssim 100$  fm) the correction may be neglected practically.

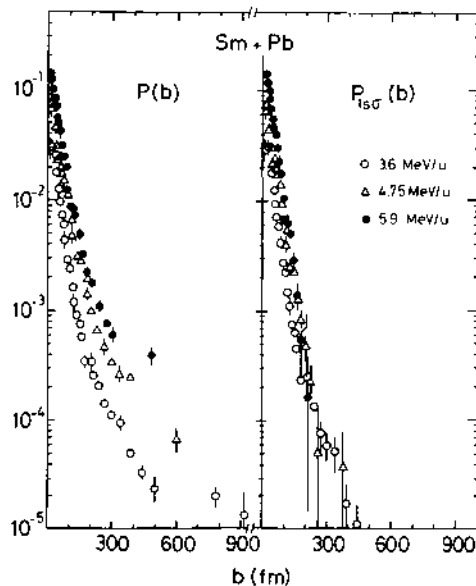


Fig. 8. The system Sm+Pb ( $Z_1+Z_2=144$ ).

Left side: Scattered Sm-particles in coincidence with Pb-K radiation, yielding  $P^H(b)$ , Eq. (5).

Right side: The same spectrum corrected for vacancy sharing yields  $P_{1s0}(b)$ , Eq. (6).

In order to understand now the completely new features, which arise in superheavy collision systems  $\alpha Z \gtrsim 1$  we show for comparison in Fig. 9 a typical "normal" collision system, Ne on Ni ( $Z=38$ )<sup>6</sup>. One notes immediately the following main differences :

- ( i) The excitation probability  $P_{1s0}$  reaches an order of  $\approx 10^{-3}$  as compared to  $\approx 10^{-1}$ .

- (ii)  $P_{1s0}$  is rather constant over a region in the order of the K-shell radius of Ne+Ni ( $r \approx 1400$  fm), whereas in Sm+Pb the probability is decreasing exponentially with a decay width of  $\approx 30$  fm !

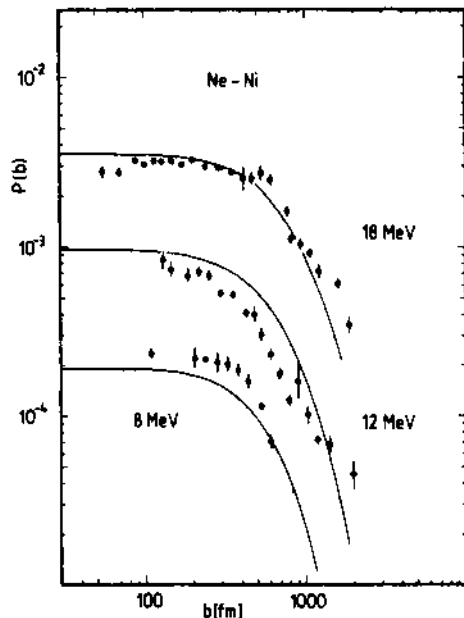


Fig. 9.  $1s0$  excitation probability for the "normal" collision system Ne+Ni ( $Z_1+Z_2=38$ ).

Let us try first to explain these differences rather roughly but based on both simple and general physical concepts. In order to excite or ionize a bound electron, the colliding nuclei have to transfer energy and momentum. One should note, however, that in contrast to a typical electron scattering experiment, for example, that momentum transfer can never be observed directly by measuring the deflection angle  $\theta$  of the projectile, since the scattering process is always dominated by the Rutherford scattering of both nuclei. Thus, measuring  $\theta$  we define the impact parameter  $b$  and nothing else !

Now, the relation between the momentum transfer  $\vec{q}_0$  onto the K-shell electron, its initial momentum  $\vec{k}_i$  and its mean momentum  $\langle \vec{k}_i \rangle$  is changing drastically when going from  $\alpha Z \ll 1$  to  $\alpha Z \approx 1$  or even to  $\alpha Z \gtrsim 1$  (cf. the following Table 1) :

$$|\vec{q}_0| = \frac{\Delta E}{\hbar v} = \frac{E_B + E_f}{\hbar v}; \quad \vec{q}_0 + \vec{k}_i = \vec{k}_f \quad (7)$$

where  $\vec{k}_i$ ,  $\vec{k}_f$  are the initial and final momenta of the electron,  $E_B$  and  $E_f$  its binding and final kinetic energy, respectively. Now,  $|\vec{k}_f|$  being always small against  $|\vec{q}_0|$ ,  $|\vec{k}_i|$  has to be in the order of  $|\vec{q}_0|$ :  $|\vec{k}_i| \approx |\vec{q}_0|$ .

TABLE I\*

$Z_1 + Z_2$	$(\hbar k_i)^2 \approx \left(\frac{E_B}{v}\right)^2$ [MeV $^2/c^2$ ]	$\langle (\hbar k_i)^2 \rangle = \left(\frac{Z\hbar}{a_0}\right)^2$	$k_i^2 / \langle k_i^2 \rangle$
20	$1.6 \cdot 10^{-3}$	$5.5 \cdot 10^{-3}$	0.3
40	$3.2 \cdot 10^{-2}$	$2.2 \cdot 10^{-2}$	1.4
60	$19 \cdot 10^{-2}$	$5 \cdot 10^{-2}$	3.8
80	$6.9 \cdot 10^{-1}$	$0.9 \cdot 10^{-1}$	7.7
100	2	0.14	14.3
120**	4.1	0.20	20.5
140**	7.6	0.27	28.1
160**	13.1	0.35	37.5
180**	20.9	0.45	46.4

\*) calculated for  $v/c = 0.1$  and  $E_f = 0$ .

\*\*) extrapolated nonrelativistically

For large  $Z$  the initial momentum of a K-electron has to be much larger than its mean momentum in order to be ionized - in sharp contrast to small  $Z$ . These high momenta, however, are available in a very restricted space only around the origin. Thus, for large  $Z$  K-shell ionization can not happen but in a region small as compared to the K-shell radius. In addition, relativistic effects (increase of the binding energy and shrinking of the wave function, cf. Fig. 10) are enhancing this effect drastically.

Therefore,

- (i) for  $aZ \gtrsim 1$  1s $\sigma$  excitation does not occur but at very small impact parameters  $b$  of the colliding nuclei;

and

- (ii) from the dependence of excitation on the impact parameter one gets information about the electrons of the practically combined system, that is of the superheavy quasiatom existing for only  $\approx 10^{-20}$  s.

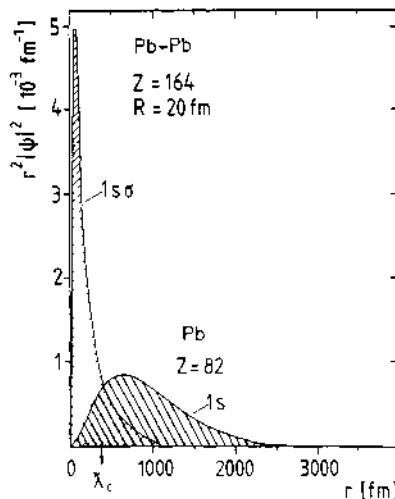


Fig. 10.  $1s$  wave function of  $\text{Pb}$  and  $1s\sigma$  wave function for the  $\text{Pb}+\text{Pb}$  quasiatom (from <sup>7</sup>). The dramatic shrinking of the  $1s\sigma$  wave function (caused by relativistic effects) leads to a  $1s\sigma$ -radius of some 120 fm at an internuclear distance of 20 fm!

In Fig. 11 we show most of the  $1s\sigma$  excitation probabilities measured up to now in the region  $aZ \gtrsim 1$   $\text{\AA}$ . In every experiment the same main properties are reproduced: A very restricted region of excitation together with a strong exponential increase and finally the high excitation probabilities themselves. Most surprising is probably that the physics of inner shell excitation becomes simple again at superheavy collision systems nearly as in a collision  $p$  on  $H$ : All other electrons are well separated by a large energy gap, therefore, correlations are rather unimportant. The moving charges offer as a Fourier transform of their time changing Coulomb field some frequencies and all we need is to find a bound electron with the appropriate initial momentum in order to fulfill energy and momentum conservation. Such electrons, however, can not be found but in a very restricted space and during a very short time, when the combined quasatomic system exists.

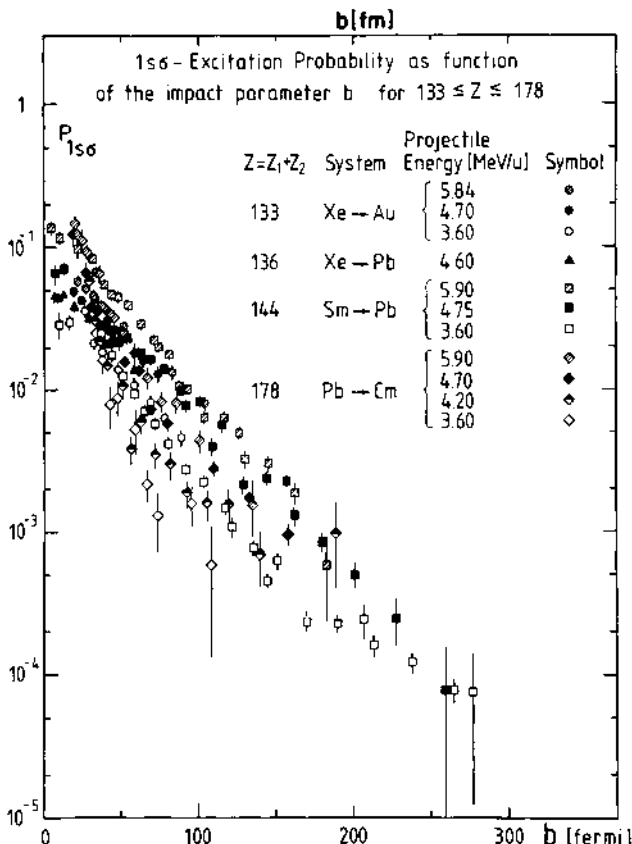


Fig. 11.  $P_{1s6}$ -data for several collision systems in the region  $\alpha Z \approx 1$ .

Now, after these coarse and qualitative remarks, which explained nevertheless the key point, we are prepared to discuss the physics on a more mathematical base. This task, however, is done in the contribution of Prof. Armbruster, where especially the possibility is examined to extract  $1s\sigma$  binding energies for super-heavy quasiatoms from the measured  $1s\sigma$  excitation probabilities.

#### Another Doppler Method

K-holes which are produced by internal conversion following nuclear Coulomb excitation "simulate" the same final state as the holes directly produced in the collision by the time changing

Coulomb field. And the smaller the impact parameters are, the more important becomes this process of internal conversion (C). Usually, one disentangles the two types of K-hole excitation by the following method : One measures the intensity of "all"  $\gamma$ -lines and takes into account the angular distribution of the  $\gamma$ -rays and the appropriate K-conversion coefficients. At *very small* impact parameters ( $b \lesssim 20$  fm), however, this procedure is too incorrect because there are generated even more holes by an C-process than by direct atomic excitation (A) and, therefore, one has to find a more suitable method.

Is there any *physical* difference between C- and A-produced K-holes ? Yes, there is ! By a C-process namely the K-hole originates just after the mean lifetime of the corresponding excited nuclear state, whereas an A-process generates the K-hole immediately, that is in the collision itself.

Let us discuss in more detail, for instance at the collision system Pb+Cm. The lifetimes of all members of the ground state band of Cm are in the order of a picosecond or longer ( $\tau^{30+} \approx 0.5$  ps). Therefore, no characteristic Cm K-radiation which fills a K-hole due to a C-process can occur earlier than  $\approx 10^{-12}$  s after the collision. The Cm K-rays following an A-process, on the other hand, already appear  $\approx 10^{-17}$  s (that is the mean lifetime of a Cm K-hole) after the collision.

How one could transform now these different time scales of  $10^{-12}$  s and  $10^{-17}$  s, respectively, into physically distinct observables ? The answer is : Via the Doppler effect. We use the  $10^{-12}$  s for decelerating in a backing the recoiling Cm ions; then all Cm K-x rays following C have as their non-interchangeable signature a *smaller* Doppler shift as compared with those K-x rays, which are due to an A-process.

The details of the experimental set up are shown in Fig. 12. A lead beam of 5.4 MeV/u ( $v/c = 0.107$ ) hits the Cm target ( $\approx 400 \mu\text{g/cm}^2$  thick), which is backed with  $4 \text{ mg/cm}^2$  Ti. Target and backing are tilted on  $30^\circ$  with respect to the beam direction. The scattered particles are recorded in two position sensitive parallel plate avalanche counters (with delay-line output); the  $\gamma$ - and x-radiation is detected by an intrinsic Ge-diode, placed behind the particle counter at right. The small impact parameters  $2 \text{ fm} \leq b \leq 10 \text{ fm}$  correspond to the branch B of the kinematical curves of Fig. 13 (Cm-recoils scattered into "Peter" between  $17^\circ$  and  $47^\circ$ ). Now the Cm K-x rays following an A-process are emitted from a Cm nucleus with the *full* initial velocity  $\langle v/c \rangle = 0.07$ , the K-x rays due to a C-process, on the other hand, always proceed from a Cm-nucleus which has traversed already the backing (passage time  $\leq 0.4 \cdot 10^{-12}$  s), and therefore, is *slowed down* ( $\langle v/c \rangle = 0.047$ ). Hence, for the two kinds of Cm-K x radiation ( $E_{K\alpha_1} = 109 \text{ keV}$ ) a

difference in energy arises in the order of  $\approx 2.5$  keV. Furthermore, the tilt angle of the target was chosen in such a way that this difference is approximately the same for all Cm-recoils reaching the particle counter at right ( $17^\circ \leq \theta \leq 47^\circ$ ).

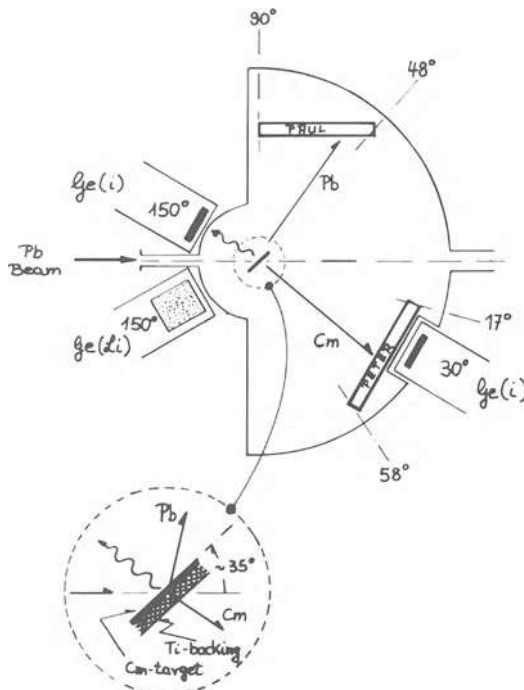


Fig. 12. Experimental set up for the measurement of the 1s0 excitation probability in the Pb-Cm system at very small impact parameters. The inset shows the tilted Cm-target, backed with  $4\text{mg}/\text{cm}^2$  Ti.

We see that at least five conditions have to be fulfilled to make the method described working successfully :

- ( i) The lifetime  $\tau_\gamma$  of all nuclear states involved should be in the order of picoseconds or longer (because otherwise no sufficient slowing of the recoils can be obtained)
 
$$\tau_\gamma \gtrsim 10^{-12} \text{ s}$$
- ( ii) The passage time  $\Delta t$  through the decelerating backing has to be smaller than the nuclear lifetimes (because otherwise the "C"-lines are smeared out)
 
$$\Delta t < \tau_\gamma$$

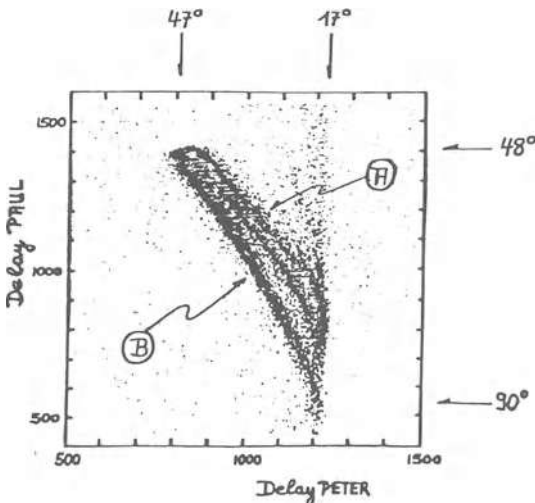


Fig. 13. The two Kinematical branches in the Pb+Cm System. Branch "B" represents all events, where Cm is scattered into the counter at right (with respect to the beam) corresponding to small impact parameters.

- (iii) The difference in Doppler shift  $\Delta E_x$  between C- and A-lines, respectively, has to be much larger than the intrinsic resolution  $E_{\text{Res}}$  of the x-ray counter

$$\Delta E_x \gg E_{\text{Res}}$$

- (iv) The Doppler shifted  $K_x$ -lines should not overlap with other lines of the spectrum, and
- (v) The backing should not influence too much the essential spectrum (in our case the grazing angle  $Cm + Ti$  was  $13^\circ$ ).

Finally, we point out that it would be not at all convenient to stop completely the recoil in the backing, because one needs in any case clean kinematic coincidences between both particle counters.

At this point we are reminded necessarily to the line shape method discussed previously. Why that complicated and tricky coincidence experiment could not be replaced by a simple line shape measurement, in the spirit of our GOLDEN RULES, which were proclaimed so showy by us ??

The reason is a very trivial one. In order that the line shape method can work, the slowing down time in the backing (where the beam is stopped completely) has to be smaller than the lifetimes of all possibly Coulomb excited nuclear levels. Now, alas, the slowing down time is 2 or 3 picoseconds, a little too large referring to

the Cm-levels ! Indeed, NATURE hides itself sometimes in a very deep hole !

Fig. 14 shows a preliminary result of the experiment<sup>9</sup>. In the upper part the complete spectrum is drawn, as recorded by the intrinsic Ge-counter, in the lower part the region of the Cm-K<sub>α</sub> lines is shown enlarged. Clearly, the K<sub>α<sub>1</sub></sub><sup>A</sup>- and the K<sub>α<sub>2</sub></sub><sup>C</sup>-lines, respectively, are well separated from all other lines, whereas the K<sub>α<sub>2</sub></sub><sup>A</sup>- and K<sub>α<sub>1</sub></sub><sup>C</sup>-lines are overlapping strongly. Using the literature-values, however, for the branching ratio of K<sub>α<sub>2</sub></sub><sup>C</sup> and K<sub>α<sub>1</sub></sub><sup>C</sup>, respectively, this line can be easily unfolded, too. (The branching ratio should not deviate from the literature, because the inner shells are most probably rearranged after 10<sup>-12</sup> s).

Fig. 14 represents the complete coincidence spectrum, which includes all impact parameters from 2 fm up to 10 fm. In order to obtain the differential excitation probability, one has to put the appropriate cuts on the "B"-branch of the particle spectrum.

The preliminary result is shown in the left part of Fig. 15. For the impact parameters  $b \geq 13$  fm the amount of C-induced 1s $\sigma$ -holes was obtained in the usual way, summing up "all" Cm- $\gamma$ -lines recorded by the 30° Ge(i) (up to the 14<sup>+</sup> + 12<sup>+</sup> transition) and taking into account the  $\gamma$ -angular distributions and the respective K-conversion factors. Independently, however, the  $\gamma$ -lines were recorded by a second counter (GeLi), placed at 150° (cf. Fig. 12); both data sets agree perfectly within their statistical errors. Thus, the separation of C- and A-induced 1s $\sigma$  excitation, respectively, seems to be very reliable for the larger impact parameters, ( $b \geq 13$  fm), too.

In any case, the feasibility is demonstrated for the first time to separate "hardwarelike" atomic processes, which take place at time scales of 10<sup>-17</sup> s and 10<sup>-12</sup> s, respectively.

## SUMMARY

In very heavy ion-atom collisions excitation of the innermost electrons takes place at very small internuclear distances only. The simple reason for that lies in the discrepancy of the mean momentum and the momentum needed for excitation, respectively, of the bound electron. Therefore, when investigating either the excitation probability as a function of the internuclear distance or the spectral distribution of the emitted electrons, nature allows a glance onto both binding energy and momentum distribution of the most deeply bound orbitals of superheavy quasiatoms.

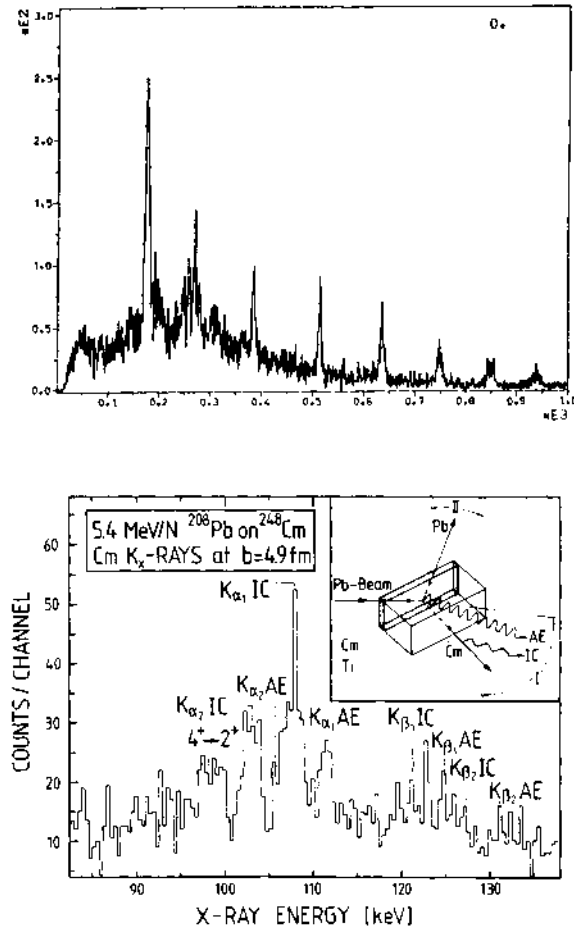


Fig. 14. x- and  $\gamma$ -spectrum recorded by the intrinsic Ge-diode. In the lower part the region of Cm K-radiation is drawn enlarged. The Cm  $K_{\alpha_1}$ -line due to direct atomic excitation ( $K_{\alpha_1}^A$ ) appears well separated from the other ones.

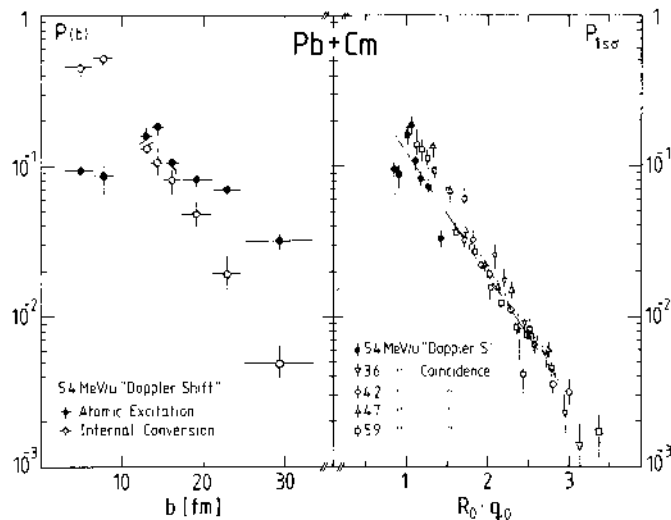


Fig. 15. Left side: Cm K-hole production in the collision of 5.4 MeV/u Pb on Cm at very small impact parameters  $b$ . Black symbols: "direct" (atomic)  $1s_0$ -excitation; open symbols: Cm K-holes produced by internal conversion following nuclear Coulomb excitation. Both processes were separated using the "Doppler Shift Technique", described in the text. These data are still *preliminary*.  
Right side: "Doppler Shift"-data (black symbols) together with previous measurements (open symbols) versus  $R_0 \cdot q_0 \equiv R_0 \cdot E_{1s0}(R_0)/\hbar v$ . ( $E_{1s0}(R_0)$  from Ref.<sup>10</sup>). The full line gives the theoretical prediction  $P_{1s0} = \frac{1}{2} D(Z) \exp \{-2R_0 q_0\}$ , with  $\frac{1}{2} D(Z) = 1.05$ , as obtained in the previous measurement<sup>8</sup>.

Quasiatoms formed in heavy ion encounters are still the only objects allowing a glance into the hidden territory  $aZ > 1$ . They may be used in future, too, in order to investigate the largest electric and magnetic fields ever produced over regions of atomic dimensions. Thus, this field of research will remain a stimulating one for a long while - at least as long as these "shadows" are not substituted by their counterparts, the real superheavy atoms.

Coming from the border  
 Of times and galaxies  
 For whiles, alas, much shorter  
 Than hasty memories

Awaking just in heavy ion beams  
 Are you "as stuff as dreams  
 And your little life  
 Is rounded with a sleep".\*\*\*

May be you dive  
 Into the Sea so deep  
 O shadows in the flight -

But there remains no flavour  
 Nor memory, whenever  
 You're going back to night.

#### ADDENDUM

I have to supply my contribution by the fifth GOLDEN RULE (cf. Fig. 15). It is, however, not a clue for planned experiments, but a more or less bitter experience *after* many cumbersome measurements :

NATURE ALWAYS IS ONE STEP FURTHER  
 THAN EXPERIMENTALISTS

Therefore, we have to learn from NATURE even more than from theory. (GOLDEN RULE V and at the same time experience of 300 years of physics history).

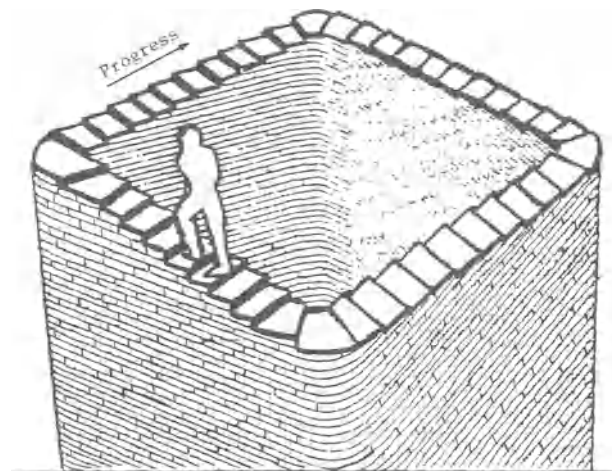


Fig. 16. NATURE always is one step further. (Picture by M.C. Escher)

## REFERENCES

1. J. S. Greenberg, H. Bokemeyer, H. Emling, E. Grosse, D. Schwalm, and F. Bosch, Phys. Rev. Lett. 39, 1404 (1977)
2. H. H. Behncke, P. Armbruster, F. Folkmann, S. Hagmann, J. R. MacDonald, and P. H. Mokler, Z. Phys. A289, 333 (1978)
3. J. R. MacDonald, P. Armbruster, H. H. Behncke, F. Folkmann, S. Hagmann, D. Liesen, P. H. Mokler, and A. Warczak, Z. Phys. A284, 57 (1978)
4. W. E. Meyerhof, Phys. Rev. Lett. 31, 1341 (1973)
5. D. Liesen, P. Armbruster, F. Bosch, D. Maor, P. H. Mokler, H. Schmidt-Böcking, R. Schuch, and A. Warczak, to be published
6. W. Schadt, K. E. Stiebing, R. Frieling, K. Bethge, I. Tserruya, R. Schuch, and H. Schmidt-Böcking, MPI-HD, Jahresbericht 1979, p. 112
7. G. Soff, W. Greiner, W. Betz, and B. Müller, Phys. Rev. A20, 169 (1979)
8. D. Liesen, P. Armbruster, F. Bosch, P. H. Mokler, H. Schmidt-Böcking, R. Schuch, J. Wilhelmy, and H. J. Wollersheim, Phys. Rev. Lett. 44, 983 (1980); F. Bosch, P. Armbruster, D. Liesen, D. Maor, P. H. Mokler, H. Schmidt-Böcking, and R. Schuch, Z. Phys. A296, 11 (1980)
9. P. Armbruster, H. Bokemeyer, F. Bosch, H. Emling, H. Folger, J. S. Greenberg, E. Grosse, S. Ito, R. Kulessa, D. Liesen, D. Maor, R. Schulé, D. Schwalm, and N. Trautmann, to be published
10. G. Soff, J. Reinhardt, W. Betz, and J. Rafelski, Phys. Scripta 17, 417 (1978)

\*) This lecture was prepared in collaboration with D. Liesen, P. Armbruster, P. H. Mokler, D. Maor, H. Schmidt-Böcking, R. Schuch, H. Emling, and D. Schwalm.

\*\*) This sentence is the refrain of Reinhard Mey's song : "Über den Wolken ...".

\*\*\*) Yes, you have recognized it. These unforgettable lines we owe to William Shakespeare.

## SYSTEMATICS AND DISCUSSION OF IONIZATION

### PROBABILITY MEASUREMENTS

P. Armbruster

Ges. f. Schwerionenforschung mbH  
P.O. Box 11 05 41  
D-6100 Darmstadt, FRG

Two principal ingredients enter the description of the collision of the two collision partners, the wave functions of the electrons involved in the ionization process and the kinematics of the collision.

The kinematics will be illucidated by a semiclassical consideration. It will give us an appropriate length scaling parameter. The time changing Coulomb field during a collision is created by charges moving on Rutherford trajectories. The average Fourier-frequency in the turning point of the trajectory is characterized by the velocity  $v$  of the collision partners and the impact parameter  $b$

$$\bar{\omega}_{\text{coll}} = \frac{v}{b}$$

Interpreting a direct ionization process - ionization in one step from an initial state to a final state - according to the correspondence principle as a resonance process we get

$$\langle \bar{\omega}_{\text{coll}} \rangle = \omega_{\text{if}}$$

with  $\langle \bar{\omega}_{\text{coll}} \rangle$  the average Fourier-frequency averaged over all impact parameters and  $\omega_{\text{if}}$  the energy difference between the initial and final state.

$$\frac{v}{\langle b \rangle} = \frac{E_{\text{if}}}{\hbar}$$

$$\langle b \rangle = \frac{\hbar v}{E_{\text{if}}} \equiv q_0^{-1}$$

Ionization occurs at those impact parameters which equal  $q_0^{-1}$ , the inverse of the momentum transfer needed to overcome the energy gap  $E_{if}$ . Highly bound electrons in low velocity ( $v/u < 1$ ) collisions need small distances between the collision partners to get ionized. This finding in first approximation is independent of the wave functions. For  $E_{if} = 1$  MeV and  $v/c = 0.1$  we get  $\langle b \rangle = 18$  fm. The natural unit of length is  $q_0^{-1}$ . The product  $\langle b \rangle q_0$  is a number not far from one, as was shown in Ref. 27. This relation was called in Ref. /32/ the Bang-Hansteen scaling rule.

What do we know about relativistic wave functions ? They are constricted in space compared to nonrelativistic ones, that is they are blown up in momentum space.

For the small distances, which are of only importance, as we know from our kinematics consideration, the monopole part of the two-center wave function governs the game. Church and Weneser /33/ investigating  $E0$ -conversion in heavy nuclei first treated monopole excitation using relativistic wave functions. The wave functions for small distances between the collision partners  $R$  are not constant, as in the nonrelativistic case but increasing with decreasing distance. For the center between the two partners  $r = 0$  holds in good approximation that the electron density for bound and continuum states is proportional to  $R^{-2}$  /34/.

$$\Psi(0, R)\Psi^*(0, R) \sim \frac{1}{R^2} -$$

The overlap of the wave functions for  $r = 0$  is :

$$\Psi_i(0, R)\Psi_f^*(0, R) \sim \frac{1}{R^2} -$$

For the radial matrix elements then follows :

$$\langle \Psi_f \frac{\partial}{\partial R} \Psi_i \rangle \sim \frac{1}{R}$$

a relation, which was found directly solving exactly the two-center Dirac problem /21,35/.

This relation is the fundamental assumption entering all calculations of ionization in the monopole approximation for relativistic wave functions. It reflects the fact that in momentum space there is an increased probability to find at small values of  $R$  the high momenta of electrons, which are a necessary condition to get large ionization probabilities at small values of  $R_0$ , which themselves from the kinematics point of view are the second necessary condition to be fulfilled. This gives the large enhancement factor of ( $10^4$ - $10^5$ ) for ionization in highly relativistic systems.

In Fig. 1 we plotted our data for the most intensively investigated systems as a function of  $R_0 q_0$  with  $R_0$  the distance of

closest approach in a collision with impact parameter  $b$ . To calculate  $q_0$  we inserted for  $E_{\text{if}}$  the value  $E_{1s\sigma}$  at  $R_0$  with  $E_{1s\sigma}$  taken from the static two-center calculations of Soff et al. /12/. Over orders of magnitude the logarithm of the ionization probability is linear in  $R_0 q_0$ . Besides statistical fluctuations only the points for  $R_0 < 50$  fm in the (Pb-Cm)-system do not follow this trend /36/. We will discuss this deviation later in the last section. From the data we derive a scaling law :

$$P(b)_{1s\sigma} = \frac{1}{2} D(Z) \exp(-mR_0 q_0)$$

with  $1/2 D(Z)$  and  $m$  as open parameters.

Fig. 2 shows the same data normalized to 1 at  $R_0 q_0 = 0$  giving once more the scaling and showing the common slope  $m = 2$  for all systems investigated in the range  $130 < Z < 178$ .

The measurements of  $\delta$ -electrons in coincidence with x-rays /37/ or of positrons allow to fix the energy transfer ( $E_{\text{if}} + E_{\delta}$ ), or  $E_{\text{if}} + E_{e^+}$ , respectively. The  $\delta$ -electron measurements of W. Koenig /37/ have given the slope  $m = 2$  for the (I+Pb) system,  $Z = 135$ , over a large range of energy transfers. A plot of recent data on  $e^+$ -production is given in the contribution of P. Kienle. Here again for the ionization of the lower continuum the slope  $m = 2$  is found /38/.

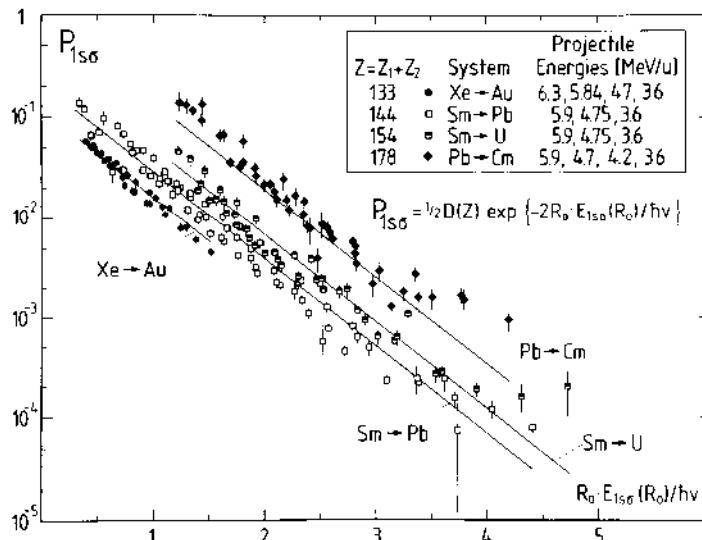


Fig. 1.  $1s\sigma$  excitation probabilities  $P_{1s\sigma}$  versus  $R_0 q_0$  for all systems measured up to now with  $Z \geq 1$ . The binding energies  $E_{1s\sigma}(R_0)$  to calculate  $q_0$  are taken from /12/.

Assuming the scaling law with  $m = 2$  its integration gives the total cross section

$$\sigma_{1s\sigma} = \frac{1}{2} D(Z) \cdot \pi \cdot \langle q_0 \rangle^{-2} \cdot \frac{1+\zeta}{2} \exp(-2\zeta)$$

with  $\zeta = 2a/\langle b \rangle$  and  $\langle b \rangle$  from the equality :

$$\langle b \rangle = \frac{\hbar v}{E_{1s\sigma} \langle R_0 \rangle} \approx \langle R_0 \rangle \sqrt{\langle R_0 \rangle - 2a}$$

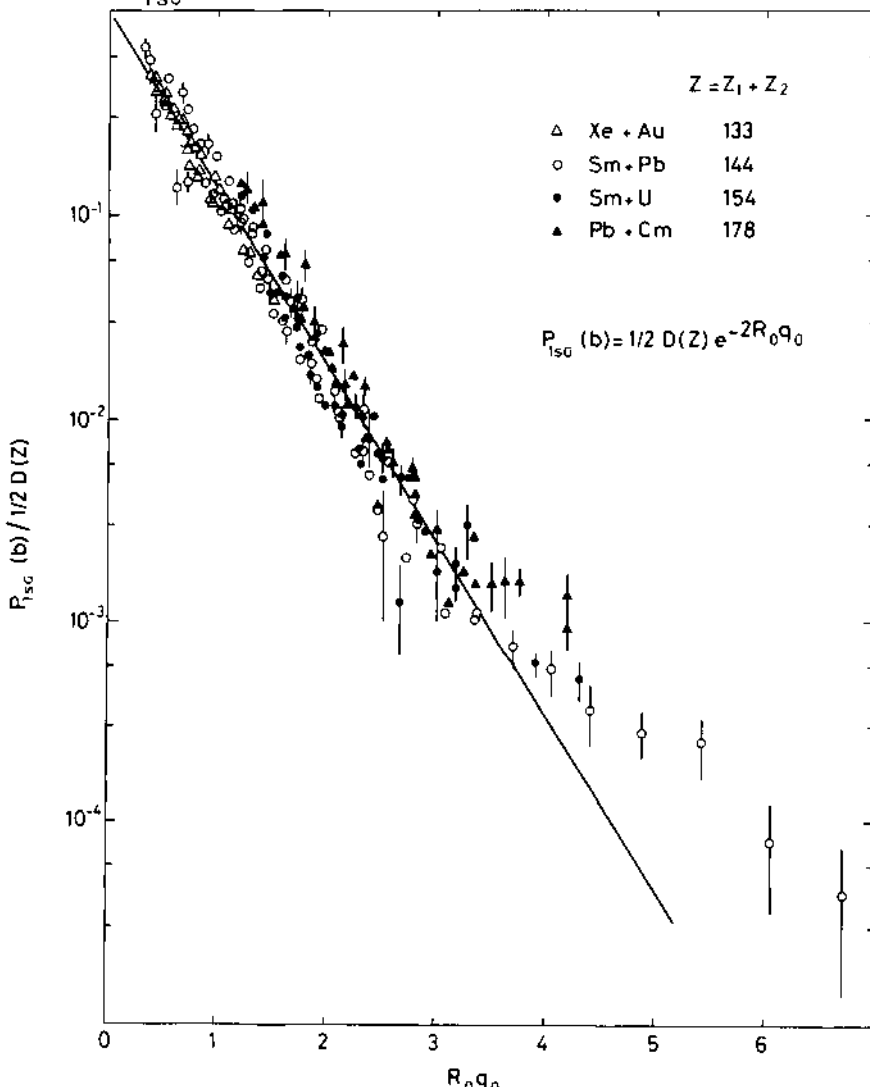


Fig. 2. Normalized  $1s\sigma$  excitation probabilities  $P_{1s\sigma} / (1/2 D(Z))$  versus  $R_0 q_0$ . The factors  $D(Z)$  have been obtained for each individual system by least square fit to the data of Fig. 1. The full line demonstrates the slope  $m = 2$ .

From the total cross sections further values of  $\frac{1}{2}D(Z)$  have been determined. They are given together with the values from Fig. 1 in Fig. 3 as a function of  $Z$ . For comparison the calculated values from Ref. /35/ are shown. The cross sections from Fig. 12 of the previous chapter are compared to the calculated ones using the values  $\frac{1}{2}D(Z)$  from Ref. /35/ shown in Fig. 4.

We conclude from our analysis :

- (1)  $q_0^{-1}$  is an appropriate length scaling parameter leading to a linear presentation of  $\ln P(R_0 q_0)$ . The calculated static values  $E_{1s0} = \epsilon(Z)/R_0 \alpha(Z)$  are needed for this scaling procedure.
- (2) A simple scaling law exists for  $Z > 130$

$$P(b)_{1s0} \approx \frac{1}{2} D(Z) \exp(-m R_0 q_0)$$

The values of  $\frac{1}{2}D(Z)$  are found in the range (0.01 - 1) in good agreement with those given in Ref. /35/. The slope for all systems including those with fixed energy transfer is  $m = 2 \pm 0.1$ .

In the following we want to sketch the derivation of the scaling law found in our experiments /39/. It is a first order perturbation calculation starting from

$$a(E_f, E_i) = - \int_{-\infty}^{+\infty} dt \langle f | \frac{\partial}{\partial t} | i \rangle \exp(-\frac{i}{\hbar} \int_{-\infty}^{t'} [E_f - E_i(t')] dt')$$

with the assumption made :

- (1) Monopole approximation for the potential-breathing sphere potential

$$V(r, R) = \begin{cases} -2Z\alpha/R & r \leq R/2 \\ -Z\alpha/r & r \geq R/2 \end{cases}$$

- (2) Radial coupling between  $E_i$  and  $E_f$

$$\partial/\partial t \rightarrow \dot{R} \partial/\partial R$$

- (3) For the matrix element

$$\langle f | \frac{\partial}{\partial R} | i \rangle = \left( \frac{D(Z)}{4\pi m_0 c^2} \right)^{1/2} \cdot \frac{1}{R}$$

Until here we follow an earlier paper of Müller et al. /21/.

- (4) The final state is assumed to be the upper continuum limit.

$$w(E_f) = m_0 c^2 \delta(m_0 c^2 - E_f)$$

Fig. 3.  
 $D(Z)$  values extracted from measured total  $1s\sigma$  cross sections /13,14/ and from  $P_{1s\sigma}(b)$  data. The full line gives the theoretical  $D(Z)$  values calculated in /35/.

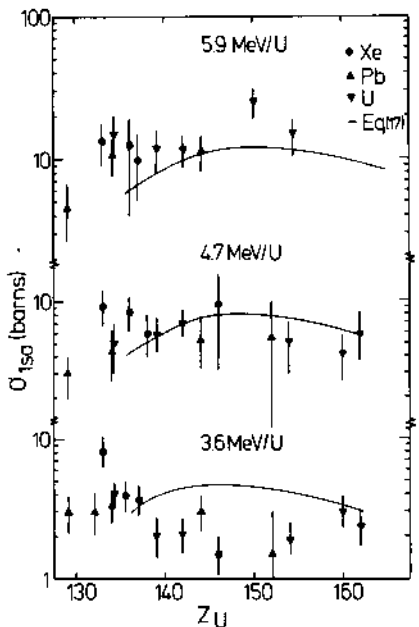
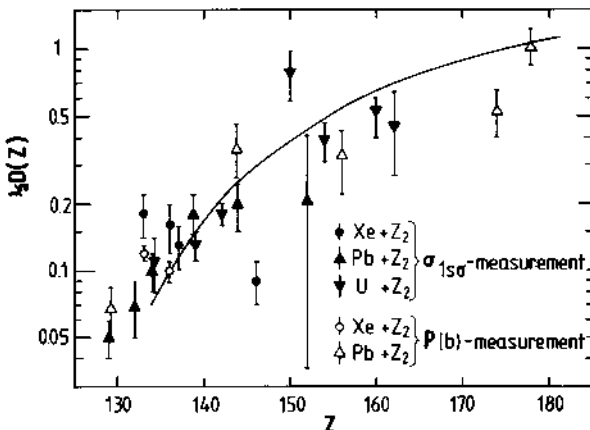


Fig. 4.  
Measured  $1s\sigma$  cross section /13,14/ compared to the integration of  $P_{1s\sigma}$  using the  $D(Z)$  values of /35/.

Here we neglect the discrete final states leading to larger ionization versus the higher lying continuum leading to smaller ionization, as shown in Fig. 5. The multistep processes are neglected as well via discrete as continuum states.

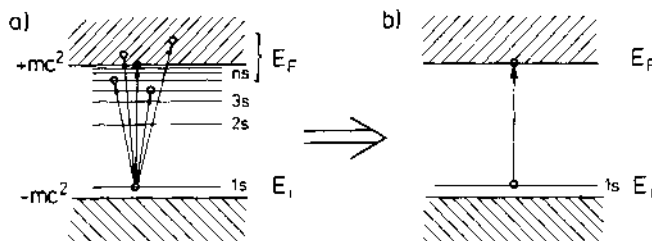


Fig. 5. (a) Excitation and ionization of the 1s-electron into discrete and continuum states;  
 (b) Substitute to (a), ionization into one single at the continuum limit.

- (5)  $E_i(R')$  is replaced by  $E_i(R_0)$ , a neglection which is shown in Ref. /39/ to be compensated by approximations made in the numerics of the phase factor.

A scaling law

$$P(b) = \frac{1}{2} D(Z) \exp[-2R_0 q_0(R_0)]$$

with

$$q_0 = E_{1s\sigma}(R_0)/\hbar v$$

is found to hold for  $\alpha Z \geq 1$  and  $R_0 \gg a$ . The scaling law is exactly the expression, which we have found prior from the data analysis.

From the agreement between the experiments and this first order perturbation theory with the assumptions discussed, we follow :

- (1) The basic theoretical finding for relativistic wave functions  $-\psi(0, R) \sim 1/R$  - is experimentally approved. It gives the slope  $m = 2$ .
- (2) The multistep processes which have been taken into account by the recent coupled channel calculations by Reinhardt et al. /40/ will not change the slope  $m = 2$ . This was first shown by Kankeleit /34/ for a two-step process.
- (3) The absolute values of  $\frac{1}{2}D(Z)$  are reasonably well reproduced by a replacement of the average energy transfer by  $E_{1s\sigma}(R_0)$ .  $D(Z)$  is treated as a free parameter in our calculation. The derivation of its size is given in Ref. /35/ and has found further foundation in the coupled channel calculations /40/.

The finding of  $\frac{1}{2}D(Z)$  between (0.05 - 1) explains the large ionization cross sections, that is the relativistic enhancement of ionization in highly relativistic collisions. The finding of the small impact parameters carrying the ionization is of less fundamental importance, as it reflects simply kinematics, which could have been learnt directly from the early paper of Bang-Hansteen /27/. Looking back to our measurements we may say, the first exploratory cross section determination by Mokler et al. in 1976 already has given the proper message, which was predicted by Greiner and his colleagues :

"In highly relativistic collisions at proper velocities ionization probabilities tend to values not far from 100 %"

#### PHANTOM-SPECTROSCOPY

The finding of a generally valid scaling law with a well-defined slope factor for a large range of Z-values and its simple structure as a three-parameter formula -  $D(Z)$  the Z-dependent absolute normalization constant, and  $E_{1s0}(R_0) = \epsilon(Z)/R_0^\alpha(Z)$  with  $\epsilon(Z)$  and  $\alpha(Z)$  as two Z-dependent parameters describing the  $R_0$ -dependence of the bin-binding energy  $E(R)$  - encourages to extract out of the  $P(b)$ -data not only  $D(Z)$ , as done in the preceeding section, but the spectroscopic important information concerning  $E_{1s0}(R_0)$  directly. This idea was put forward by B. Müller et al. /21/. But the scaling law derived in their paper is wrong, and so is a paper on  $1s0$ -binding energies of our group using their scaling /41/. Spectroscopy had to wait for the experiments setting up the scaling law and its theoretical derivation *a posteriori*. The recent coupled channel calculations per se will never give an analytical expression, which allows to extract one quantity, as  $E_{1s0}(R_0)$ . The best simply structured scaling law approximating the much more complicated physical process is the one we presented. In the sense of inverting this scaling we propagate its application to the  $P(b)$ -data to extract spectroscopic information. PHANTOM-spectroscopy is a big word for a poor kind of information on the average energy transfer in the ionization process. But as there is nothing else known about the existence of atoms beyond atomic number 107 even some first experimental information on binding energies of PHANTOMS is of general interest. The lifetimes of PHANTOMS are the collision times  $\hbar/mcv \sim 10^{-20}$  s giving an uncertainty in all energies of at least 50 keV. The accuracy of the PHANTOM-spectroscopy is restricted principally to about 5 %. In the sense of a 5 % accurate determination of mean binding energies of the ionized electrons the spectroscopy discussed in the following should be understood.

We used three methods to extract spectroscopic information :

- (1) If the slope of  $dE_i/dR_0$  is small, that is the energy  $E_i(R_0)$  is not changing much over the impact parameter range investigated,

we may obtain from the slope of  $P(b)$  a lower limit of  $E_i(R_0)$ , as  $dE_i/dR_0 < 0$

$$E_{1s\sigma}(R_0) \geq \frac{1}{2} \hbar v \cdot d \ln P(b) / dR_0$$

This evaluation avoids the fixing of  $\frac{1}{2}D(Z)$ . Its accuracy is about (10 - 15) % for systems in the Z-range 130 - 150. Fig. 21 gives the evaluation for the (Xe-Au)-system, Z = 133 at 4 energies. The agreement with the calculated energies of Soff et al. /12/ is satisfying.

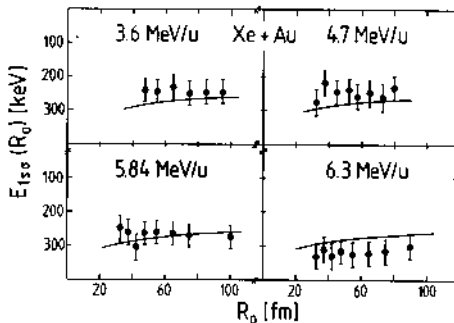


Fig. 6. Lower bound for the  $1s\sigma$  binding energy as function of  $R$ . The full line gives the theoretical energies, /12/.

- (2) Independent of the details of the wave functions exists, as was shown in the last section, a general kinematical relation between  $\langle b \rangle$  and  $\langle q_0 \rangle$ .

$$\langle b \rangle \langle q_0 \rangle = C$$

with  $C = 2/m$ . This scaling law goes back to Bang and Hansteen /27/ and has recently been rediscussed by the same authors /42/. In Ref. /39/ we derived

$$E_i \langle R_0 \rangle = \frac{\hbar v}{\langle b \rangle} \left( 1 + \frac{2a^2}{\langle b \rangle^2} \right)$$

In the energy range investigated, (3 - 6) MeV/u holds

$$\begin{aligned} C &= 1.00 - 1.12 & \text{for } 1s\sigma\text{-ionization and } Z > 130 \\ C &= 0.8 & \text{for } 2p\frac{1}{2}\sigma\text{-ionization and } Z < 150 \end{aligned}$$

Fig. 7 shows  $P_{2p\frac{1}{2}\sigma}$  as a function of  $R_0 q_0$  for the (Pb-Cm) system to prove  $m = 2.5$ .  $C = 0.8$  is assumed for  $2p\frac{1}{2}\sigma$ -ionization instead of  $C = 1.0 - 1.12$  as used for  $1s\sigma$  and ionization of the lower continuum /38/.

From the  $90^\circ$ -line widths of different collision systems the value of  $\langle b \rangle$  has been derived /32/, Fig. 9. Figure 8 gives

the binding energies of the  $2p_{1/2}\sigma$ -orbitals at  $R_0 = 100$  fm for systems in the range of  $Z = 148 - 174$  compared to the calculated values /12/ and the nonrelativistic extrapolation. The doubling of the binding energy for the heaviest systems is convincingly demonstrated.

(3) The inversion of the scaling law gives

$$E_{1s\sigma}(R_0) = \epsilon(Z)/R_0^{\alpha(Z)} = \frac{\hbar v}{2R_0} \ln[D(Z)/2P(b)]$$

For the systems shown in Fig. 9 a least square 3-parameter fit has been fitted to the data.  $E_{1s\sigma}(R_0)$  as a function of  $R_0$  is given together with the data points and the calculated (dotted lines) values /12/. For the (Pb+Cm)-system we omitted the data points for  $R_0 < 50$  fm. The increasing slope for higher  $Z$ -systems is reproduced excellently. Binding energies as high as 700 keV in the  $Z = 178$  system are obtained.

Finally, in Fig. 10 we present a plot of binding energies of atoms between  $Z = (1 - 200)$ . The values are known experimentally up to Nobelium,  $Z = 102$ , the rest is calculated according to Fricke et al. /43/. We present in this plot our binding energies at  $R_0 = 50$  fm again together with the calculated values /12/. The theoretically predicted trend is reproduced down to about 700 keV.

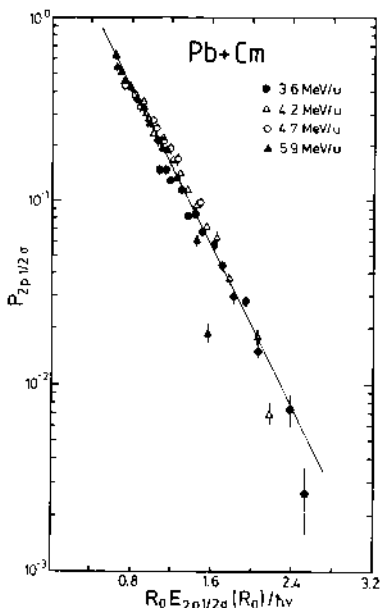


Fig. 7.  $2p\sigma$  excitation probabilities  $P_{2p_{1/2}\sigma}$  versus  $R_0 a_0$  for the (Pb+Cm) system. The fitted straight line has a slope  $m=2.5$ .

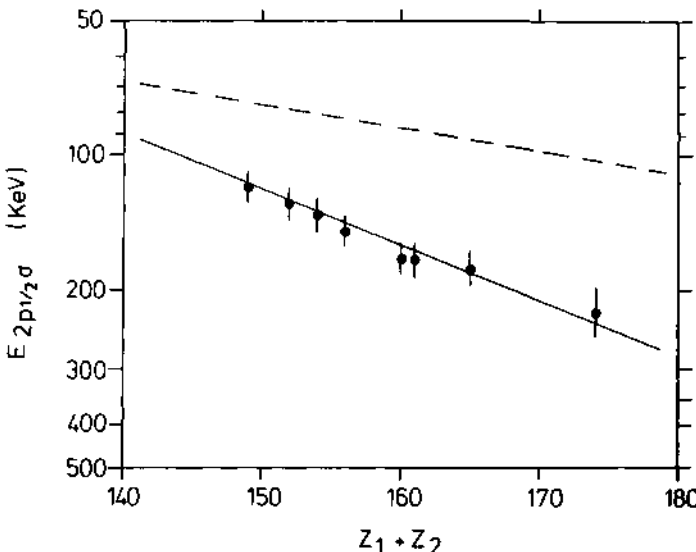


Fig. 8.  $2p_{1/2}\sigma$  binding energies at  $R_0 = 100$  fm for different collision systems. The solid line gives the calculated energies /12/, the dotted line the nonrelativistic extrapolation, /32/.

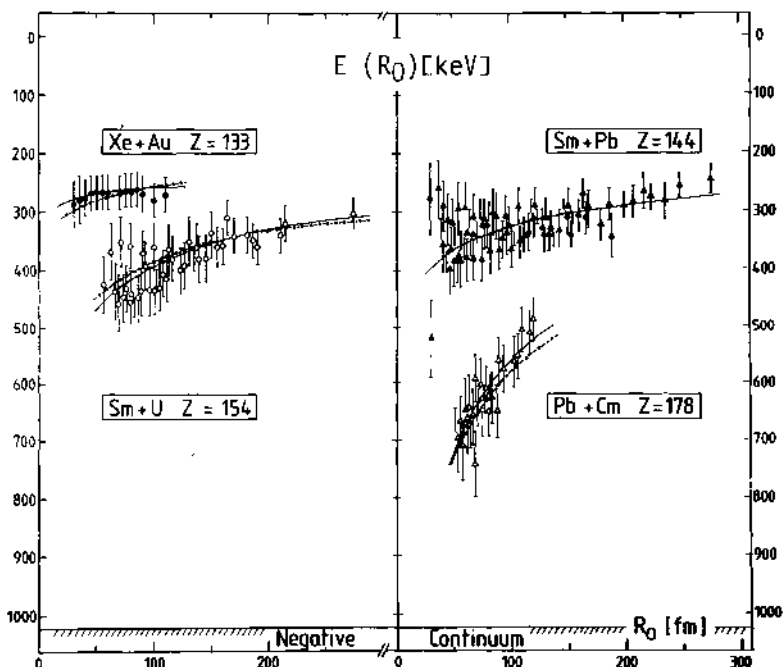


Fig. 9.  $1s\sigma$  binding energies as a function of  $R_0$  for different collision systems. The full line is a least square fit to the data, the dotted lines are theoretical predictions, /12/.

Our hope is that similar plots with more data points for at least the two innermost orbitals  $1s\sigma$  and  $2p_{1/2}\sigma$  may become one of the lasting contributions of GSI-research to atomic physics.

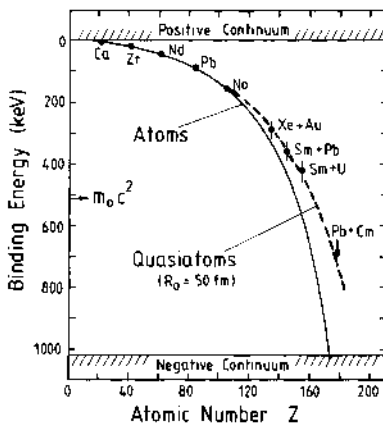


Fig. 10. K-binding energies of atoms in the range 1-200 and calculated binding energies for  $R_0 = 50$  fm /12,43/ in comparison with our measured values.

#### UNSOLVED QUESTIONS

##### $2p_{1/2}\sigma$ -Excitation

The  $2p_{1/2}\sigma$ -ionization for the heaviest systems is not well understood. The slope factor  $m = 2.5$ , Fig. 8, points to a stronger increase of  $\psi(0,R)$  than the  $1/R$ -dependence found for  $1s\sigma$ -ionization and ionization of the lower continuum. Why are wavefunctions of  $2p_{1/2}$ -electrons still more concentrated than wavefunctions for  $1s$ -electrons? Fig. 11 shows average  $2p_{1/2}\sigma$ -excitation probabilities obtained from cross section measurements and  $90^\circ$ -line width analysis /15/ in the range (3.6 - 5.9) MeV/u. The excitation probability has energy-independent, Z-independent values between (50 - 80) %. In the Z-range below 170 the highest ionization is not observed for the highest energy, but for a smaller one. It was shown /44/ in the (Pb-Au) system,  $Z = 161$ , that a maximum of the excitation probability exists at about 4.7 MeV/u. First calculations of Soff /45/ give an energy increasing and Z-decreasing dependence, which is completely off compared to the measurements. The relativistic enhancement for  $2p_{1/2}$ -electrons compensates the strongly increasing binding energies in such a way, that for all systems inspite of binding energies differing by nearly a factor of two, and collision energies changing

from (3.6 - 5.9) MeV/u the excitation probabilities are found constant at a very high absolute value.

Further measurements are needed to corroborate this result and to establish a scaling law for  $2p^{1/2}\sigma$ -excitation allowing to extract absolute values of a quantity corresponding to  $1/2D(Z)$  as found for  $1s\sigma$ -ionization. For the study of  $2p^{1/2}\sigma$ -ionization slightly asymmetric collision systems are recommended, as in symmetric systems ionization from higher levels and strong vacancy sharing cannot be excluded.

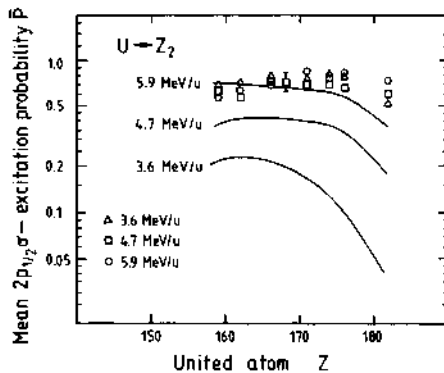


Fig. 11. Mean  $2p^{1/2}\sigma$  excitation probabilities /15/ for different  $U \rightarrow Z_0$  collision systems. The full curves give  $P$  values for central collisions calculated in /45/.

#### 1s $\sigma$ -Excitation in the (Pb-Cm)-System Below 50 fm

Fig. 12 demonstrates that the ionization in the (Pb-Cm) system,  $Z = 178$ , for all three energies investigated at distances smaller than 50 fm is found to be too large compared to the established scaling law. This increase is not as many thought due to nuclear Coulomb excitation, as was shown convincingly in the experiment described in Lecture II by F. Bosch. As the mean  $R_0$ -values for  $1s\sigma$ -excitation are in the range of (30 - 40) fm, that is below 50 fm, the main contribution to the  $1s\sigma$ -excitation seems to be largely increased. The increase is about 60 % above the extrapolated scaling.

What might be an explanation for the increased ionization ?

- (1) As we discussed in the previous topic there are very large excitation probabilities for the higher orbitals in the heaviest system, which are not reproduced by the theory. Even the coupled channel calculations will thus underestimate two-step processes involving the  $2p$ - and  $2s$ -orbitals. A large contribution from multi-step processes might explain the experimental finding

of higher excitation probabilities. But why the restriction to  $R_0$ -values smaller than 50 fm, and why at a Z-value of 178?

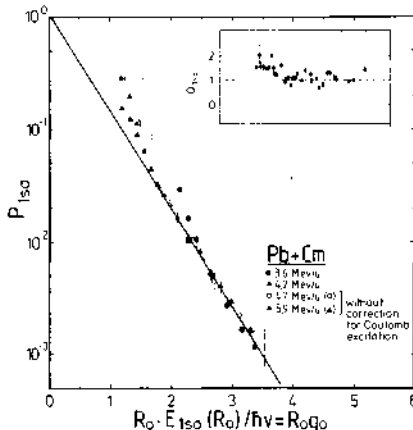


Fig. 12.  $1s0$  excitation probability for the (Pb+Cm) systems as a function of  $R_0 q_0$ . The deviation from the  $m = 2$  scaling law for  $R_0 < 50$  fm is seen for all energies. The insert shows the ratio between the measured and extrapolated values.

- (2) The adiabaticity for strongly diving orbitals - in our case  $dE/dR = 20$  keV/fm - may not be fulfilled. In the range of distances where the ionization occurs the energy still changes by hundreds of keV. Does the electron still follow the binding energies calculated for static systems? A breakdown of the scaling due to a breakdown of the assumptions made for the wave functions  $\psi(0, R) \propto R = \text{const.}$  is not very probable, as the scaling still holds for  $e^+$ -production and at large values of  $R$ . Increased ionization would follow if the effective energy transfers would be smaller than the static binding energies in the turning point. Will the diving of a vacancy into the lower continuum be prevented? How much will the contributions to  $e^+$ -production from multistep processes via  $1s0$ -vacancies be reduced?

These questions intimately connect the x-ray experiments to one of the main topics discussed in this school, the  $e^+$ -production.

A  $\delta$ -electron experiment in the (Pb-Cm) system will decouple the wave function and energy transfer contribution to the slope factor in the scaling law. Such an experiment may decide whether a scaling with  $m = 2$  still holds, and what the energy transfers at distances smaller than 50 fm really are.

The x-ray experiments until now leave open the fundamental question, whether electrons with binding energies larger than 700 keV can be detected and ionized in atomic collisions, or whether the dynamics of the collision forbids their ionization. As long as simple x-ray experiments below the Coulomb barrier leave open such fundamental questions, we should be very careful in overinterpreting the much more complex  $e^+$ -experiments above the Coulomb barrier. Spontaneous  $e^+$ -production needs a vacancy to be produced first. The problems in atomic collision physics are intimately correlated. X-ray,  $\delta$ -electron, and  $e^+$ -experiments must be done in parallel. Our more experimentally oriented approach to solve open problems has been advertised by F. Bosch. A one-sided approach to a peculiar aspect of the highly relativistic collision process will delay our final understanding of this most interesting complex phenomenon, even if this aspect is advertised as the most important one.

#### ACKNOWLEDGEMENT

I am indebted to many scientists I have had the pleasure to collaborate with. In my lectures I tried to present their work knowing I will not be able to give proper credit to each of them. My special thanks go to the members of the GSI atomic physics group, who have carried the experiments I discussed, F. Bosch, D. Liesen, D. Maor, P.H. Mokler, and W.A. Schönfeldt.

#### REFERENCES

References 1 to 31 are to be found in the preceding chapter, pages 135-154.

32. P. Armbruster, H.-H. Behncke, S. Hagmann, D. Liesen, F. Folkmann, P.H. Mokler, Z. Phys. A288, 277 (1978)
33. E.L. Church, J. Weneser, Phys. Rev. 103, 1035 (1956)
34. E. Kankeleit, Nukleonika 25, 252 (1980), Proceedings of the 12th Summer School, Mikolajki, Poland (1979)
35. G. Soff, W. Greiner, W. Betz, B. Müller, Phys. Rev. A20, 169 (1979)
36. D. Liesen, P. Armbruster, F. Bosch, S. Hagmann, H. Schmidt-Böcking, P.H. Mokler, H.J. Wollersheim, R. Schuch, J.B. Wilhelmy, Phys. Rev. Lett. 44, 983 (1980)
37. W. Koenig, private communication
38. P. Armbruster, P. Kienle, Z. Physik A291, 399 (1979)
39. F. Bosch, D. Liesen, P. Armbruster, D. Maor, P.H. Mokler, H. Schmidt-Böcking, R. Schuch, Z. Physik A296, 11 (1980)
40. J. Reinhardt, B. Müller, W. Greiner, G. Soff, Phys. Rev. Lett. 43, 1307 (1979)
41. H.-H. Behncke, D. Liesen, S. Hagmann, P.H. Mokler, P. Armbruster, Z. Physik A288, 35 (1978)
42. J. Bang, J.M. Hansteen, Physica Scripta 22, 609 (1981)
43. B. Fricke, G. Soff, At. and Nucl. Data Tabl. 19, 83 (1977)

44. D. Liesen, P. Armbruster, H.-H. Behncke, F. Bosch,  
S. Hagmann, P.H. Mokler, H. Schmidt-Böcking, R. Schuch,  
Proceedings of the XIth International Conference on the  
Physics of Electronic and Atomic Collisions, Kyoto,  
29 August - 4 September 1979, N. Oda, K. Takayanagi (eds.)  
p. 337, Amsterdam, North-Holland Publ. Comp. 1979
45. G. Soff, B. Müller, W. Greiner, Phys. Rev. Lett. 40,  
540 (1978)

## THEORY OF POSITRON CREATION IN SUPERCRITICAL QUASIMOLECULES

U. Müller, J. Reinhardt\*, T. de Reus, P. Schlüter  
G. Soff\*\*, K.H. Wietschorke, B Müller, and W. Greiner

Institut für Theoretische Physik  
der Johann Wolfgang Goethe-Universität  
Robert-Mayer-Straße 8-10  
Postfach 111 932  
D-6000 Frankfurt am Main, West Germany

\*\*Gesellschaft für Schwerionenforschung mbH  
Planckstraße 1  
Postfach 11 05 41  
D-6100 Darmstadt 11, West Germany

### ABSTRACT

Collisions of very heavy ions at energies close to the Coulomb barrier are discussed as a unique tool to study the behaviour of the electron-positron field in the presence of strong external electromagnetic fields. Theoretical predictions for positron production rates are compared with experimental results. Emphasis is laid on effects due to nuclear time delay and on the influence of electron screening for both sub- and supercritical collision systems. Internal electron-positron pair production from electric monopole transitions is investigated for atoms with charge number up to  $Z \approx 170$ .

### 1. INTRODUCTION

The behaviour of electronic states in a strong external electrostatic Coulomb-potential  $V(r) = -Z\alpha/r$  is a matter of investigation since the beginnings of relativistic quantum mechanics (for more details cf. the review articles 1 and Ref. 2). It is well-known that the spectrum of the Dirac equation with a weak external

\*Talk presented by J. Reinhardt.

potential consists of a set of bound levels, within  $-mc^2 < E_n < +mc^2$ , and two continua with positive and negative frequencies. However, at  $Z = 1/\alpha \approx 137$  the Dirac equation for point nuclei ceases to have stable  $s$ - and  $p_{1/2}$ -wave solutions, in general the Sommerfeld finestructure-formula yields complex energy eigenvalues for  $Z\alpha > |\kappa|$ . This singular behaviour is cured by the finite extension of the nucleus, the bound states then can be traced<sup>3</sup> beyond the value  $Z\alpha = |\kappa|$ . Note that, as a consequence, the wavefunctions of  $s$ - and  $p_{1/2}$ -wave electrons become extremely sensitive to the nuclear charge distribution.

At  $Z \approx 150$  (assuming normal nuclear density) the K-shell electrons have lost all their rest energy due to strong binding in the Coulomb potential,  $E_{1s} \approx 0$ . We enter the truly relativistic region where relativistic effects are no longer a small perturbation, but dominate the behaviour of the inner-shell electrons. Increasing the nuclear charge up to  $Z \approx 173$  the  $1s$ -state enters the negative energy continuum,  $E_{1s} < -mc^2$ ; the binding energy has reached the threshold where spontaneous pair production becomes possible. At this point the spectrum of eigenstates of the Dirac equation is subject to a characteristic change: The  $1s$ -state becomes a resonance in the lower energy continuum.

In a Gedankenexperiment it is possible to increase the charge of a bare nucleus from  $Z < Z_{cr} \approx 173$  to  $Z > Z_{cr}$ , the unoccupied  $1s$ -state will then be filled under emission of two (due to spin-degeneracy) positrons. The new stable ground state of the system consists of the nucleus plus two electrons in the K-shell; it is called the charged vacuum<sup>4, 5</sup>. The experimental exploration of this new phenomenon would constitute an important test of the theory of Quantum Electrodynamics (QED) in the region of strong fields.

At present, however, the unique way of extending the periodic table of elements, where these atomic effects can be pursued, lies in heavy ion collisions. By now it is well-known and generally accepted that during slow (in terms of the K-shell electron velocity) collisions of heavy atoms a quasimolecule is formed and finally, at closest approach, a quasiatom. We have learnt that this becomes the closer to the truth the heavier the ions are. Experimentally the upper boundary is given by the heaviest available combination of projectile and target, presently U-Cm, i.e.  $Z = 188$ .

In such scattering experiments, however, the dynamics of the collision becomes extremely important. The time-scale must be sufficiently long to allow the electron (positron) to adjust to the variation of the combined Coulomb field of the two nuclei. Since the typical velocities required to bring the nuclei close together are about  $v/c \approx .1$ , the adiabatic picture is meaningful only for electrons in relativistic motion. The theoretical description of the dynamics of the electronic states is outlined in Section 2.

In this contribution we will concentrate on positron creation, while various other excitation processes in collisions of very highly charged systems will be discussed by G. Soff et al.<sup>6</sup>. In particular, it is our aim to give an adequate description for positron production in supercritical collision systems, where  $Z_T + Z_P$  exceeds 173. The theoretical basis is laid in Section 2, where also a method, based on a projection operator technique, is introduced to treat the time dependent  $\text{ls}\sigma$ -resonance. The theoretical description is extended to the case of nuclear reactions with time delay in Section 3.

Numerical results for positron production in several collision systems are discussed in Section 4 and compared with presently available experimental data. The effects of a nuclear time delay (Section 5) and the influence of electron screening (Section 6) on positron production rates are investigated separately.

Section 7 was motivated by the recently observed structure <sup>7,8</sup> in the energy distribution of positrons emitted in collisions of very heavy ions like U-Th, U-U, and U-Cm. Having discussed the observations in terms of the mechanism of spontaneous positron emission, we investigate in addition if internal electron-positron pair conversion from electric monopole transitions can explain the observed spectra.

## 2. DYNAMICS OF ELECTRONIC STATES IN THE COMBINED FIELD OF TWO COLLIDING HEAVY IONS

To describe the production of positrons - as well as K-hole formation or  $\delta$ -electron excitation<sup>9</sup> - in a heavy ion collision it is essential to account for the strong Coulomb force experienced by the electron-positron field in the vicinity of the colliding nuclei. Since the adiabaticity criterion is satisfied for the motion of innershell electrons, it is most natural to adopt the quasi-molecular picture<sup>10</sup>. In the semiclassical approximation we have to solve the time-dependent two-centre Dirac equation

$$i\hbar \partial/\partial t \phi_i(\vec{R}(t)) = H_{TCD}(\vec{R}(t)) \phi_i(\vec{R}(t)), \quad (1)$$

where  $H_{TCD}(\vec{R}(t))$  is the two-centre Hamiltonian depending on the time-dependent internuclear distance  $\vec{R}(t)$ . Eq. 1 determines the motion of a single electron (initially in state  $i$ ) in the external time-varying electromagnetic field generated by the two colliding ions.

The time-dependent wavefunction  $\phi_i(\vec{R}(t))$  is expanded in terms of the complete basis of stationary molecular states  $\psi_j(\vec{R})$

$$\phi_i(\vec{R}(t)) = \sum_j a_{ij}(t) \psi_j(\vec{R}(t)) \exp \{-i\chi_j(t)\}, \quad (2)$$

where the states  $\psi_j(\vec{R})$  are solutions of the stationary two-centre

Dirac equation calculated for fixed internuclear distances  $\vec{R}$  with energy eigenvalues  $E_j(R)$ . The sum includes the set of bound states as well as the upper and lower continua. The phase factor  $\chi_j(t)$  is conveniently chosen so as to eliminate the diagonal matrixelement of the Hamiltonian, i.e.

$$\chi_j(t) = 1/\hbar \int dt' \langle \varphi_j(t') | H(\vec{R}(t')) | \varphi_j(t') \rangle . \quad (3)$$

The resulting system of coupled differential equations for the expansion amplitudes  $a_{ij}$ , equivalent to eq. 1, is

$$\begin{aligned} \dot{a}_{ij}(t) = & - \sum_{k \neq j} a_{ik}(t) \langle \varphi_j | \partial/\partial t + i/\hbar H | \varphi_k \rangle . \\ & \cdot \exp \{ -i(\chi_k - \chi_j) \} \end{aligned} \quad (4)$$

with the initial condition  $a_{ij}(-\infty) = \delta_{ij}$ .

Solving the coupled channel eqs. 4 numerically we make the following approximations: magnetic<sup>11</sup> and retardation effects are neglected, the multipole expansion of the two-centre potential<sup>12</sup> is restricted to the monopole- ( $l=0$ ) term. Therefore the time derivative operator  $\partial/\partial t$  in eq. 4 can be reduced to  $\vec{R}\partial/\partial R$  (radial coupling). Concerning the problem of spurious long-range couplings which can be corrected by using "translation factors", we refer to the work of Heinz et al.<sup>13</sup>. Details on the computation and properties of wavefunctions and matrixelements are given in Refs. 12, 14, 15.

To calculate the various possible excitations one has to solve a problem with infinitely many particles, since according to Dirac's hole picture the negative continuum is occupied with electrons. In addition various bound states may be occupied. If one neglects the electron-electron two-body-interaction it turns out, however, that it is sufficient to solve the one-electron problem and to include the effect of the Pauli-principle only afterwards<sup>14, 16</sup>.

The probability for excitation of particles in a level above the Fermi surface  $p > F$  or holes in a state  $q < F$  can be deduced completely from the single particle transition amplitudes

$$N_p = \sum_{r < F} |a_{rp}|^2 \quad \text{for} \quad p > F , \quad (5)$$

$$N_q = \sum_{r > F} |a_{rq}|^2 \quad \text{for} \quad q < F , \quad (6)$$

where  $F$  denotes the Fermi level up to which the states are occupied prior to the collision.

The number of correlated particle-hole pairs is given by

$$N_{p,q} = N_p \cdot N_q + \left| \sum_{r < F} a_{rp}^* a_{rq} \right|^2. \quad (7)$$

The same formula holds also in the case of particle-particle or hole-hole-correlations if the sign of the second term is inverted. The first term of eq. 7 describes statistical coincidences while the sum contains coherent correlation effects. This formula should, e.g., be applied to analyze experiments like those presently performed for coincidences between positrons and  $\delta$ -electrons.

We emphasize the fact that eq. 4 exhibits two kinds of coupling operators. If the set  $\varphi_i(\vec{R})$  consists of exact eigensolutions of the adiabatic Hamiltonian, as assumed so far, only dynamical couplings due to the time derivative operator  $\partial/\partial t$ , acting on the parametric time-dependence of the wave functions, are present. Otherwise, the second term will cause a potential-coupling for each non-eigenstate. This will be of importance in the following.

In supercritical collisions the resonance property of the  $1s\sigma$ -state must be handled with care. In Refs. 14, 17 a formalism is developed, which avoids those difficulties and moreover has heuristic value for the interpretation of the positron creation process. The method is based on the observation that the continuum wavefunction of the supercritical system ( $Z_1 + Z_2 > 173$ ) at resonance energy  $E = E_{res}$  is quite similar to the discrete  $1s\sigma$ -state in the subcritical  $p$ -case except for an oscillating tail - small in amplitude - reaching out to infinity. This structure reflects the occurrence of a tunneling process through the gap separating the particle- and antiparticle solutions of the Dirac equation (cf. the problem of Klein's paradox<sup>18, 19</sup>).

Apart from the asymptotic behaviour the  $1s\sigma$ -wavefunction retains much of its identity, e.g. the strongly localized charge distribution having the extension of the atomic K-shell. Many properties, e.g. the radial matrixelements for ionization, may be continued smoothly to the supercritical region just by neglecting the tail of the wavefunction.

This idea can be used to develop a general method to treat resonance scattering. In this context Wang and Shakin<sup>20</sup> introduced a projection formalism for resonances in the nuclear continuum shell model: After having defined a normalizable quasibound wavefunction  $\phi_R$ , a new continuum  $\varphi_{Ep}$  is constructed which spans a subspace orthogonal to  $\phi_R$  and replaces the old continuum  $\varphi_{Ep}$ . Here  $\varphi_{Ep}$  satisfies the Dirac equation

$$(H_{TCD} - E_p) |\varphi_{Ep}\rangle = 0 \quad (8)$$

and contains the resonance;  $E_p$  denotes the energy of the positron. The modified continuum wavefunctions  $\tilde{\psi}_{E_p}$  are eigenstates of a projected Hamiltonian

$$(P \ H \ P - E_p) \ |\tilde{\psi}_{E_p}\rangle = 0 , \quad (9)$$

with

$$\begin{aligned} P = 1 - Q : &= \int dE_p |\tilde{\psi}_{E_p}\rangle \langle \tilde{\psi}_{E_p}| , \\ Q = |\phi_R\rangle \langle \phi_R| + \sum_{\alpha} |\phi_{\alpha}\rangle \langle \phi_{\alpha}| , \end{aligned} \quad (10)$$

where  $Q$  is an operator projecting on the resonance state  $\phi_R$  and on all higher bound and electron continuum states  $\phi_{\alpha}$ . If  $\phi_R$  was chosen judiciously (this problem is discussed in Ref. 14) the newly defined modified continuum  $\tilde{\psi}_{E_p}$  will no longer show resonance behaviour. Using eqs. 10 and the orthogonality relations, eq. 9 may be transformed to a more explicit form

$$(H - E_p) \ |\tilde{\psi}_{E_p}\rangle = \langle \phi_R | H | \tilde{\psi}_{E_p}\rangle | \phi_R \rangle . \quad (11)$$

The modified continuum states satisfy the original Dirac equation supplemented by an inhomogeneous term containing an integral over the solution  $\tilde{\psi}_{E_p}$ .

If the states  $\phi_R$  and  $\tilde{\psi}_{E_p}$  are used as part of the basis in eq. 2 the  $1s\sigma$ -state couples to the positron continuum by two separate coupling operators

$$R \langle \tilde{\psi}_{E_p} | \partial / \partial R | \phi_R \rangle + i / \hbar \langle \tilde{\psi}_{E_p} | H | \phi_R \rangle . \quad (12)$$

The second matrixelement arises since  $\phi_R$  and  $\tilde{\psi}_{E_p}$  are not exact eigenstates of the two-centre Hamiltonian  $H$ . It does not depend on the nuclear motion and leads, in the static limit  $R(t) = \text{const} < R_{\text{cr}}^{21}$ , to an exponential decay of a hole prepared in  $\phi_R$  with the width

$$\Gamma = 2\pi \left| \langle \tilde{\psi}_{E_p} | H | \phi_R \rangle \right|^2 . \quad (13)$$

The values of  $\Gamma$  deduced by this method agree well with the exact widths obtained by a phase shift analysis of the old continuum  $\psi_{E_p}$ .

The developed formalism thus has led to the emergence of "induced" and "spontaneous" positron coupling, the latter resulting from the presence of an unstable state  $\phi_R$  in the expansion basis. In practice, however, this does not result in a threshold behaviour

at the border of the supercritical region. Firstly both coupling matrixelements enter via their Fourier transforms depending on the time development of the heavy ion collision. Their contributions have to be added coherently so that in a given collision there is no physical way to distinguish between them. Secondly in Coulomb collisions the rapid variation of the quasimolecular potential causes significant contributions from the dynamical coupling, whereas the period of time for which the internuclear distance  $R(t)$  is less than  $R_{cr}$  is usually very short ( $\sim 10^{-21}$  sec) compared to the decay time of the  $1s\sigma$ -resonance ( $\sim 10^{-19}$  sec).

Therefore, the predicted production rates and energy spectra of positrons continue smoothly from the subcritical to the supercritical region (cf. Sec. 4). It turns out that the emergence of a new coupling in eq. 12 is accompanied by a reduction of the radial matrixelements  $\langle \tilde{\psi}_{Ep} | \partial/\partial R | \phi_R \rangle$  and both effects nearly cancel in collisions on Coulomb trajectories. This can be understood from Fig. 1, where the strength of both couplings is shown as a function of time.

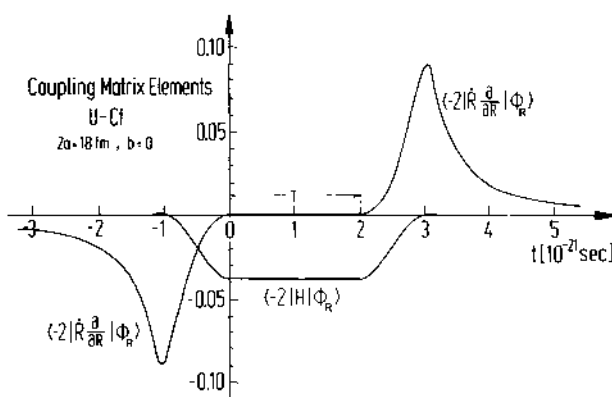


Fig. 1. The matrixelements of "radial coupling" and "spontaneous decay",  $\langle \tilde{\psi}_{Ep} | R \partial/\partial R | \phi_R \rangle$  and  $\langle \tilde{\psi}_{Ep} | H | \phi_R \rangle$ , joining the  $1s$ -resonance and the positron state of energy  $E = -2 mc^2$  is shown as a function of collision time  $t$ . The nuclei are assumed to stick together for a time  $T = 2 \cdot 10^{-21}$  sec. To demonstrate the effect most clearly, a head-on U-Cf collision at  $2a = 18$  fm has been chosen. In pure Rutherford scattering the delay time  $T$  is obsolete.

As discussed in the following sections qualitative deviations of the positron production rate in supercritical collision systems are expected only under favourable conditions, i.e. in encounters with a prolonged interaction time.

### 3. THE INFLUENCE OF A TIME DELAY ON EXCITATION PROBABILITIES

Since the "spontaneous" and "dynamical" couplings exhibit a different functional dependence on the nuclear motion (the "induced" coupling is proportional to the velocity  $\dot{R}$  while the "spontaneous" part depends only on the distance  $R$ ), an increase in collision time can be expected to provide a clear signature for supercritical collisions. Therefore Rafelski et al.<sup>22</sup> suggested the study of positron emission in heavy ion reactions at bombarding energies above the Coulomb barrier, where the formation of a di-nuclear system or of a compound nucleus would eventually lead to a time delay within the bounds of the critical distance  $R_{cr}$ . During this delay time  $T$  the spontaneous decay of the  $1s0$ -resonance, by filling dynamically created K-shell holes under emission of positrons, might be strongly enhanced.

In addition to the general interest this effect could also prove to be important for the study of nuclear reactions. Although several other methods<sup>23-27</sup> have been proposed to investigate the reaction time in deep inelastic nuclear collisions or the life time of compound nuclei by its influence on atomic processes, positron spectroscopy may be the most sensitive method (in very heavy systems) because the delay could result in an increase of the yield at resonance by one or two orders of magnitude.

In order to obtain a rough estimate for the effect of a time delay during the collision we discuss the solution of eq. 4 in time-dependent perturbation theory (although this approximation is not sufficient to obtain quantitatively reliable results).

In a schematic model the nuclear motion starts on a Rutherford hyperbola with initial kinematic parameters  $\{E_i, b_i\}$  (energy and impact parameter), stops at  $t=0$  and sets in again at  $t=T$ , i.e.  $R=R_{min}$  for  $0 \leq t \leq T$ . The outgoing path is assumed to be a second Coulomb trajectory with final kinematic parameters  $\{E_f, b_f\}$ .

Then eq. 4 is solved by a time integral between  $-\infty$  and  $+\infty$ , which can be split in three parts:  $-\infty < t < 0$ ,  $0 \leq t \leq T$ , and  $T < t < +\infty$ . Due to the vanishing radial velocity  $\dot{R}$  in the central region, only the potential or "spontaneous" coupling between the  $1s0$ -state and the positron continuum is effective here. This is illustrated in Fig. 1 for the example of a time delay  $T = 2 \cdot 10^{-21}$  sec.

With the abbreviation

$$M_{ij} = \langle \varphi_i | R \partial / \partial R + i / \hbar H | \varphi_j \rangle = D_{ij} + i H_{ij} \quad (14)$$

and the relation

$$M_{ij}(R(t)) = - M_{ij}^*(R(-t)) , \quad (15)$$

we obtain for the first order transition amplitude  $a_{ij}$  for  $t \rightarrow \infty$

$$\begin{aligned} a_{ij}^{(1)}(\infty) &= \int_{-\infty}^{\infty} dt M_{ji}(t) \exp\{-i(\chi_i(t) - \chi_j(t))\} \\ &= a_{ij}^{(1)}(0) - e^{-i(E_i - E_j)T/\hbar} \tilde{a}_{ij}^{(1)*}(0) \\ &\quad - \frac{e^{-i(E_i - E_j)T/\hbar}}{E_i - E_j} H_{ji}(R_{\min}) , \end{aligned} \quad (16)$$

where the third term is present only in supercritical collisions and it only couples the  $1s$  and positron continuum states. The tilde,  $\tilde{a}_{ij}^{(1)}$ , indicates that the amplitude has to be taken for a half-trajectory with the kinematic parameters of the outgoing branch  $\{E_f, b_f\}$  (for an elastic collision we have  $\tilde{a}_{ij}^{(1)}(0) = a_{ij}^{(1)}(0)$ ). The energies are those at the distance of nuclear delay:  $E_i = E_i(R_{\min})$ . Eq. 16 applies only if state  $i$  is brought empty in the collision, whereas in a realistic experiment inner shell vacancies have to be created dynamically during the collision. Therefore multistep excitation, i.e. higher - order processes, must be investigated.

Since the excitation probabilities are given by the square of the amplitudes, the time delay will lead to oscillations as a function of delay time  $T$  or of particle energy  $E$ . They are due to interference of the excitations taking place on the incoming and outgoing branch of the trajectory, with relative phases depending on  $T$  and  $E$ . Equivalent interference effects have been discussed for  $\delta$ -electron spectra<sup>27</sup> and K-hole formation<sup>26</sup>. In addition eq. 16 contains a term increasing monotonically with  $T$ , which is - for the case  $i \equiv 1s$ ,  $j \equiv \tilde{\varphi}_{EP}$  - proportional to  $H_{EP, 1s}(R_{\min})$ . It has to be added coherently to the combination of amplitudes in eq. 16. An estimate of the influence of this term that is appropriate for values of  $T$  large compared with the Coulomb collision time, but shorter than the spontaneous decay time of the  $1s\sigma$ -resonance, is obtained by simply disregarding the excitations in the region outside  $0 \leq t \leq T$ . The number of positrons with energy  $E$  then reads

$$\frac{dP^{e^+}}{dE} = \sum_{i>F} |a_{i,E}^{(\infty)}|^2 \approx$$

$$\approx P_{1s}(0) \frac{\Gamma}{2\pi} T^2 \cdot \left( \frac{\sin(E-E_{1s})T/2\hbar}{(E-E_{1s})T/2\hbar} \right)^2 \quad (17)$$

The spectrum of positrons thus develops a line at the position of the resonance,  $E_{1s\sigma}$ , which becomes increasingly narrow with growing delay time  $T$ . The width of the line is  $\Delta E_{1/2} \sim 5.56 \hbar/T$  (FWHM). The total intensity

$$p^{e+} = \int_{-\infty}^{-mc^2} dE (dp^{e+}/dE) \approx P_{1s}(0) \Gamma T/\hbar \quad (18)$$

grows linearly with  $T$ . We note that eqs. 17 and 18 are valid only for  $\Gamma T \ll \hbar$  since the filling of the K-vacancy has been neglected. In the case of very long times  $T$  the spectrum approximately takes on a Breit-Wigner shape with the natural line width  $\Gamma$ .

As mentioned above it is not sufficient to solve eq. 4 in time-dependent perturbation theory, because quantitatively reliable results cannot be obtained. Multi-step processes are of great importance, therefore coupled channel calculations have to be carried out. On the other hand the need for numerical calculations can be substantially reduced by use of the identity<sup>28</sup>

$$a_{ij}^{(\infty)} = \sum_{kl} a_{ik}(0) A_{kl}(T) \tilde{a}_{jl}(0) , \quad (19)$$

with

$$A_{kl}(T) = \delta_{kl} \exp \{-i/\hbar E_k (R_{\min}) \cdot T\} , \quad (20)$$

which connects the final transition amplitude  $a_{ij}^{(\infty)}$  with those at time  $t=0$ , denoted by  $a_{ik}^{(0)}$ . Within the schematic model eq. 19 allows easily for variation of the free parameter  $T$ , once the set of expansion coefficients for half-trajectories with incoming and outgoing kinematics has been calculated.

As it stands, eq. 19 is valid only for subcritical collisions, where no transitions take place at  $0 \leq t \leq T$ . If, e.g., the  $1s\sigma$ -state is supercritical during nuclear contact, the exponential factor in eq. 19 must be replaced by an off-diagonal matrix for those states that participate in the spontaneous decay<sup>29</sup>. The transition amplitudes can also be integrated numerically to time  $t=T/2$ , the matrix  $A_{kl}$  in eq. 19 then simply becomes the unit matrix  $\delta_{kl}$ . Trivially the same is true in the case of undelayed collisions with  $T=0$ .

Up to now the discussion was based on the very simple schematic model of the reaction described above. Most of our results were calculated within this model, where heavy-ion collisions at energy above the barrier are considered. On the other hand, at nuclear contact attractive and dissipative nuclear forces begin to act, the trajectory  $R(t)$  deviates from the usual Rutherford orbit but the

radial velocity  $R$  does not necessarily vanish for  $0 \leq t \leq T$ . Therefore more realistic calculations have to be performed for trajectories taking into account nuclear forces. These results will be presented in Section 5.

#### 4. POSITRON CREATION - THEORETICAL PREDICTIONS AND EXPERIMENTAL RESULTS

Since beams of very heavy ions at energies close to the Coulomb barrier or even above have become available at the Gesellschaft für Schwerionenforschung (GSI) in Darmstadt, a number of experiments has been performed to study positron emission in highly charged collision systems. At the same time, experiments measuring K-hole and  $\delta$ -electron production have yielded independent information on the excitation mechanism and have served to strengthen confidence in the underlying theoretical framework, see Ref. 9.

Before we will reflect on experimental results for positron creation and their comparison with theory, we first want to discuss the main theoretical predictions. The first calculations had been performed in the framework of perturbation theory<sup>14, 30</sup> which describes much of the physics involved in the excitation processes. However, the growing importance of multi-step processes indicates that perturbative calculations are of limited validity. In the following, therefore, we will present the results of coupled channel calculations<sup>14</sup>.

We have solved the system of differential equations using the monopole approximation including up to 8 bound states and ~15 states in the upper continuum, separately for the angular momentum channels  $\kappa = +1$  and  $\kappa = -1$ . The integration was performed with a standard Hamming predictor-corrector routine taking about 1500 steps in time. Since the probability for positron excitation is small compared to unity, it is sufficient to include only one positronic state at a time when varying  $E_p$ , i.e. the lower continuum can be coupled in perturbation theory<sup>14</sup>.

We will present coupled-channel calculations in four different heavy ion collision systems, Pb-Pb, Pb-U, U-U, U-Cf with the total charges  $Z_T + Z_p = 164, 174, 184, 190$  (Fig. 2). The impact energy per nucleon was kept constant at  $E_{\text{lab}} = 5.9$  MeV/u.

Positron emission rates increase very fast with total nuclear charge, flattening somewhat for the highest  $Z$ -values. If parametrized by a power law  $(Z_T + Z_p)^n$  the power takes values of 20 down to 13. Here a Fermi-level at  $F = 3s\sigma, 4p_{1/2}\sigma$  is assumed, i.e. the states above the  $3s\sigma$ - and  $4p_{1/2}\sigma$ -levels are empty, which should give an upper bound for positron production rates. If the distance of closest approach  $R_{\min}$  is kept fixed instead of the impact velocity,  $n$  becomes still larger. In collisions of bare nuclei

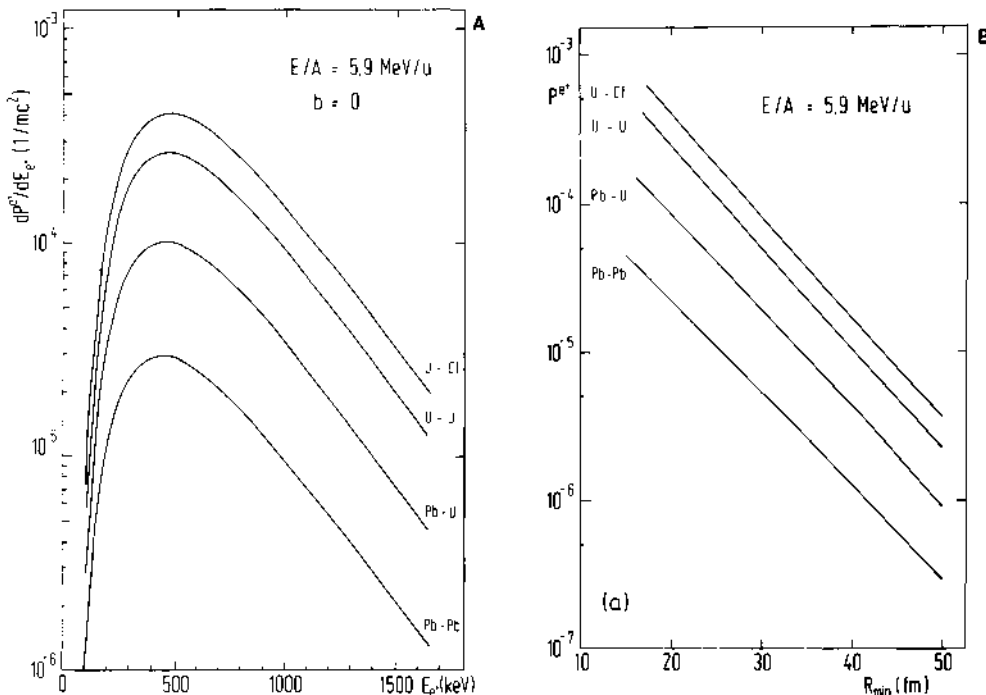


Fig. 2. a) Energy spectra of positrons created in 5.9 MeV/u head-on collisions of Pb-Pb, Pb-U, U-U, and U-Cf. The results are calculated in the coupled-channel approach assuming initial occupation up to the states  $3s0$  and  $4p_{1/2}0$  ( $F=3$ ). - b) Emission probability of positrons in 5.9 MeV/u collisions as a function of distance of closest approach  $R_{\min}$  ( $F=3$ ).

( $F=0$ ) positron production is increased by up to two orders of magnitude. Here also the Z-dependence is extremely steep ( $n=29$ ). Mainly responsible for this effect is the contribution of the  $1s$ -state which in normal collisions ( $F>0$ ) is suppressed due to the small K-vacancy probability. If the K-shell is empty it becomes the dominant final state for pair production. This clearly reflects the strong coupling between the  $1s$ -state and the antiparticle continuum which it approaches and even enters in the supercritical region. In all cases investigated the channels  $\kappa = -1$  and  $\kappa = +1$  contribute about equally to the total result.

Fig. 2a shows the energy spectra of positrons  $dP/dE_p$  produced in 5.9 MeV/u head-on collisions ( $F=3$ ). As is well known, the emission of low-energy positrons is suppressed by Coulomb repulsion while at high energies the spectra fall off exponentially in analogy to the spectra of  $\delta$ -electrons. The shapes do not differ qualitatively from the perturbative results. Obviously they are practically independent of the charge of the collision system.

As a further theoretical prediction Fig. 2b displays the impact parameter dependence of positron production. The abscissa is the distance of closest approach  $R_{\min}$ , which is related to impact parameter  $b$  by  $R_{\min} = a(1 + \sqrt{1 + (b/a)^2})$ . A nearly perfect exponential decrease of the curves is noted. The high value of the slope is understandable in terms of the energy transfer required to produce a pair. Therefore the impact parameter dependence is much weaker in the case  $F=0$  where the gap between the lowest empty state (iso) and the positron continuum becomes small or vanishes.

The displayed results demonstrate remarkable features of the pair production mechanism in "slow" collisions of highly charged nuclei. In particular, the large excitation rates and their high sensitivity on total nuclear charge in the region  $Z_T + Z_p \approx Z_{cr}$  are characteristic for the action of the time-dependent strong Coulomb field.

Now we turn to the discussion of experimental results and their comparison with the described predictions. But first we want to point out a major problem in analyzing the experimental data.

Already for bombarding energies well below the Coulomb barrier ( $E \sim 0.8E_C$ ) the nuclei can be excited by Coulomb excitation (which even may cause "Coulomb-fission"<sup>31, 32</sup>), the emitted photons with energy above 1022 keV can undergo pair conversion. Although this process takes place long after the collisions ( $\sim 10^{-13}$  sec, while "atomic" positrons are emitted within  $\sim 10^{-20}$  sec), it cannot be distinguished experimentally from the quasimolecular mechanism by ordinary methods (The use of the nuclear blocking effect has been suggested by Kaun and Karamyan<sup>33</sup>), resulting in a background which is difficult to handle. For nuclei with a simple level-structure (e.g.,  $^{208}\text{Pb}$ ; 2<sup>+</sup>, 3<sup>-</sup>) Coulomb excitation can be calculated. The resulting pair creation is then deduced from the theoretically<sup>34</sup> known conversion coefficients<sup>35</sup>. Otherwise one has to measure simultaneously the  $\gamma$ -spectrum and fold it with the conversion coefficients<sup>36</sup>. Here one has to know - or to assume - the  $\gamma$ -ray multipolarity. Monopole conversion (see Section 7) cannot be handled by this method.

In collisions with lighter targets, where the combined charge of projectile and target nucleus,  $Z_u = Z_p + Z_T$ , is well below the critical charge so that no significant contribution of atomic positrons is expected, the  $\gamma$ -ray spectra have been measured. The data can be fitted nicely by pair conversion if  $E$  multipolarity is assumed. Beginning in the region  $Z_p + Z_T \gtrsim 160$ , however, all experiments have found an increase which could not be explained by nuclear conversion alone (Fig. 3). This was the first hint for "atomic" positron production in heavy-ion collisions and, up to now, all conclusions had to rely on the described procedure for background

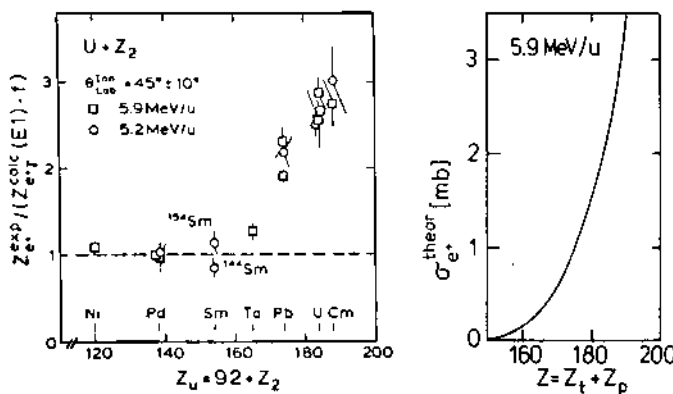


Fig. 3. In the left part the ratio between measured positron production rates and the expected pair conversion rates deduced from the nuclear  $\gamma$ -spectra,  $Z_{e^+}^{\text{exp}} / [Z_{e^+}^{\text{calc}}(\gamma, E1) \cdot f]$ , is displayed as a function of the united charge  $Z_u = 92 + Z_2$ . If E1 multipolarity is assumed,  $f=1$ . For  $Z_u > 170$  an increase in positron emission is observed, which cannot be explained by nuclear excitation processes<sup>37</sup>. The right part shows theoretical predictions for the positron cross section,  $\sigma_{e^+}(Z)$ , in heavy ion collisions at  $E=5.9$  MeV/u. A strong increase is expected.

subtraction.

The first generation of experiments further established the dependence of positron excitation rates on the kinematic conditions as well as on the combined charge  $Z_u$ . Fig. 4 shows results of Kozhuharov et al.<sup>38</sup> for three collision systems, Pb-Pb, U-Pb, and U-U, at 5.8 MeV/u bombarding energy, measured with an orange-type  $\beta$ -spectrometer. The positron production probability in an energy window  $E(e^+) = 490-50$  keV is shown as a function of projectile cm-scattering angle  $\theta_{\text{cm}}$ . The nuclear background is subtracted. Because target and projectile cannot be distinguished in the experiment, the theoretical values have been symmetrized with respect to forward and recoil scattering.

The shape of the theoretical curves is in quite good agreement with the experimental data. Also the  $Z$ -dependent increase is well described, which spans an order of a magnitude while  $\Delta Z/Z$  is only 12%. On the other hand the absolute magnitude of the theoretical

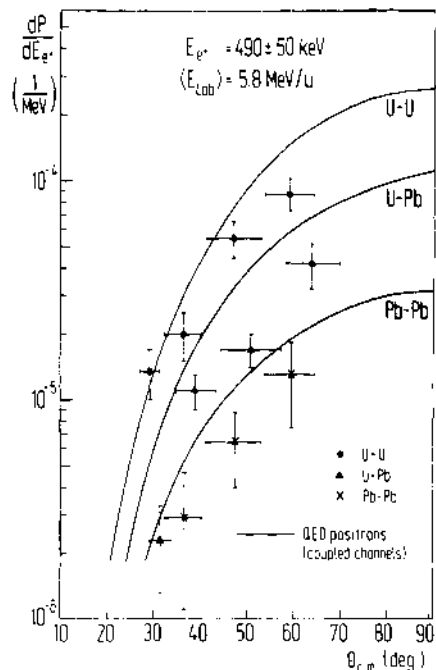


Fig. 4. For MeV/u Pb-Pb, Pb-U, and U-U collisions positron production probability in an energy window  $E_{e^+} = 490 \pm 50$  keV is displayed as a function of projectile scattering angle  $\theta_{cm}$ . The experimental data are taken from Kozhuharov et al.<sup>38</sup>. Here, the nuclear background is subtracted.

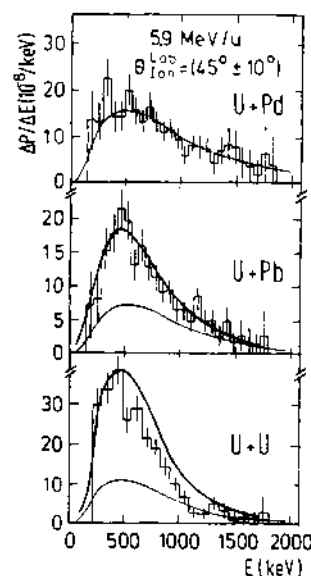


Fig. 5. Spectra of emitted positrons in 5.9 MeV/u collisions measured by Backe et al.<sup>41,42</sup> in coincidence with ions scattered in the angular window  $\theta_{lab} = 45^\circ \pm 10^\circ$ . The spectrum in the lightest system, U-Pd, is explained by nuclear pair conversion alone (light line). In the U-Pb and U-U systems the sum of nuclear and calculated atomic positron production rates (full lines) is displayed.

values is generally too high.

Using another type of experimental set-up, a solenoidal spectrometer, Backe et al.<sup>39</sup> obtained integrated and differential positron probabilities for various impact parameters for the heavy-ion collision systems Pb-Pb, Pb-U, U-U, and U-Cm. As in the experiment described above general agreement with theory is found. In the Pb-Pb case and, for smaller distances of closest approach, even in Pb-U and U-U collisions the data seem to agree also in absolute values, in contrast to the experiment discussed above. But in the heaviest accessible system U-Cm ( $Z = 188$ ) and for larger distances  $R_{min}$  theory again has a tendency to overestimate the measured data. The experi-

mental slopes are somewhat steeper than predicted, while the Z-dependence is overestimated - a trend, which seems to be continued also in new experimental data<sup>40</sup>.

For given kinematic parameters {E, b} the Z-dependence of the total positron probabilities is given by  $Z^{-17}$ , for lighter systems as well as for heavier ones<sup>41</sup>. From these data no qualitative signature for the "diving" of the  $1s\sigma$ -state in U-U, U-Cm collisions can be extracted, in agreement with theoretical predictions.

More sensitive information can be obtained by the measurement of energy spectra of positrons detected in coincidence with the scattered ions. Their knowledge is most useful if one wants to find deviations hinting to the positron creation mechanism.

Fig. 5 shows the first published positron spectra of Backe et al.<sup>41, 42</sup> for three collision systems, U-Pd, U-Pb, and U-U, at 5.9 MeV/u bombarding energy; the ions are detected in an angular window  $\theta_{\text{lab}} = 45^\circ \pm 10^\circ$ . For U-Pd (Z=138) no atomic positrons are expected, the data can be fully accounted for by nuclear conversion (light curve). Extrapolating this procedure to the U-Pb system (light curve) the sum of background and calculated QED positron rates (full curve) is in excellent agreement with the observed emission rates. In the spectrum of the supercritical U-U system ( $E_{1s} \approx 1200$  keV for  $R_{\text{min}} \approx 21$  fm) some deviations are seen.

Two possible sources which could cause deviations in the shape of the positron spectra from the results presented so far will be discussed in the next two sections.

##### 5. TIME DELAY EFFECTS

To obtain theoretical predictions for positron production it is essential to include the "spontaneous" coupling for collisions where the  $1s\sigma$ -state joins the lower continuum. If it is left out of the calculation the resulting positron spectra would be strongly altered: The "induced" radial coupling is changed at the same time as the spontaneous coupling becomes important. Both contributions add up coherently and cannot be observed separately<sup>14</sup>. A promising strategy to get a clear qualitative signature for the diving process will be to modify the time structure and to select heavy-ion collisions with prolonged nuclear contact time<sup>22</sup>. Such nuclear reactions are expected to occur at energies close to or above the Coulomb barrier. The nuclear delay time  $T$  should provide a handle to distinguish supercritical systems.

Within the schematic trajectory model which was described in Section 3 we have performed coupled channel calculations for the

four heavy-ion collision systems Pb-Pb, Pb-U, U-U, and U-Cm, corresponding to  $Z_{\text{united}} = 164, 174, 184$ , and 188, respectively. As in the preceding section the contributions of s- and  $p_{1/2}$ -partial waves ( $\kappa=1$ ), which are nearly equal for Coulomb trajectories<sup>14, 30</sup>, are taken into account

Independently of assumptions on the incoming and outgoing path, of dissipation of nuclear kinetic energy or angular momentum, and of the position of the Fermi level, all positron spectra exhibit the following features:

In subcritical collision systems ( $Z_T + Z_P \leq 173$ ) a delay time causes modulations in the positron spectrum with a width  $\Delta E = 2\pi\hbar/T$ . In Fig. 6a positron spectra are displayed for a Pb-Pb collision ( $E_{\text{lab}} = 8.73$  MeV/u,  $b=7.11$  fm,  $F=3s0, 4p_{1/2}, 0$ ) with delay times  $T=0$  (pure Rutherford scattering),  $3\cdot$ ,  $6\cdot$ , and  $10 \cdot 10^{-21}$  sec. The modulations are due to interference effects in much the same way as predicted for the  $\delta$ -electron spectra in deep inelastic heavy-ion collisions<sup>15</sup>. Fig. 6b shows the corresponding spectra for a Pb-U collision ( $E_{\text{lab}} = 8.97$  MeV/u,  $b=7.27$  fm,  $F=3$ ), a system, which is just at the border to supercriticality. The spectra of Figs. 6a, b are qualitatively similar, although the heavier system is characterized by the presence of constructive interference.

In addition to the oscillatory interference patterns an enhancement of positron production in time-delayed supercritical collisions is observed, where the binding energy of the lowest bound states exceeds the value  $2mc^2$ . For long delay times a distinct peak in the positron spectrum is found at the location of the supercritical bound state resonance (binding energy minus  $2mc^2$ ) due to the spontaneous pair-creation mechanism, as discussed in Section 3. A detailed analysis of the spectra reveals that this peak emerges gradually as  $Z_u + Z_T + Z_P$  exceeds  $Z_{\text{cr}}$ .

Positron spectra for the supercritical system U-U ( $E_{\text{lab}} = 7.35$  MeV/u,  $b=3.72$  fm,  $F=3$ ) are shown in Fig. 6c. With increasing delay time the position of the maximum drifts slowly from the kinematic maximum to the "resonance energy", which depends on the combined charge, the separation of the two nuclei and on the nuclear charge distribution (cf. Ref. 29).

The integrated positron emission probability  $P_e^+$  as a function of  $T$  for these three collision systems and for U-Cm ( $E_{\text{lab}} = 7.5$  MeV/u,  $b=3.74$  fm,  $F=3$ ) is displayed in Fig. 6d, where the solid lines denote s-state-, the dashed lines  $p_{1/2}$ -state contributions. The absolute values,  $P_e^+(T=0)$ , should not be compared since the impact energies are chosen differently. However, the variation of  $P_e^+$  with delay time  $T$  is of particular interest. In the investigated

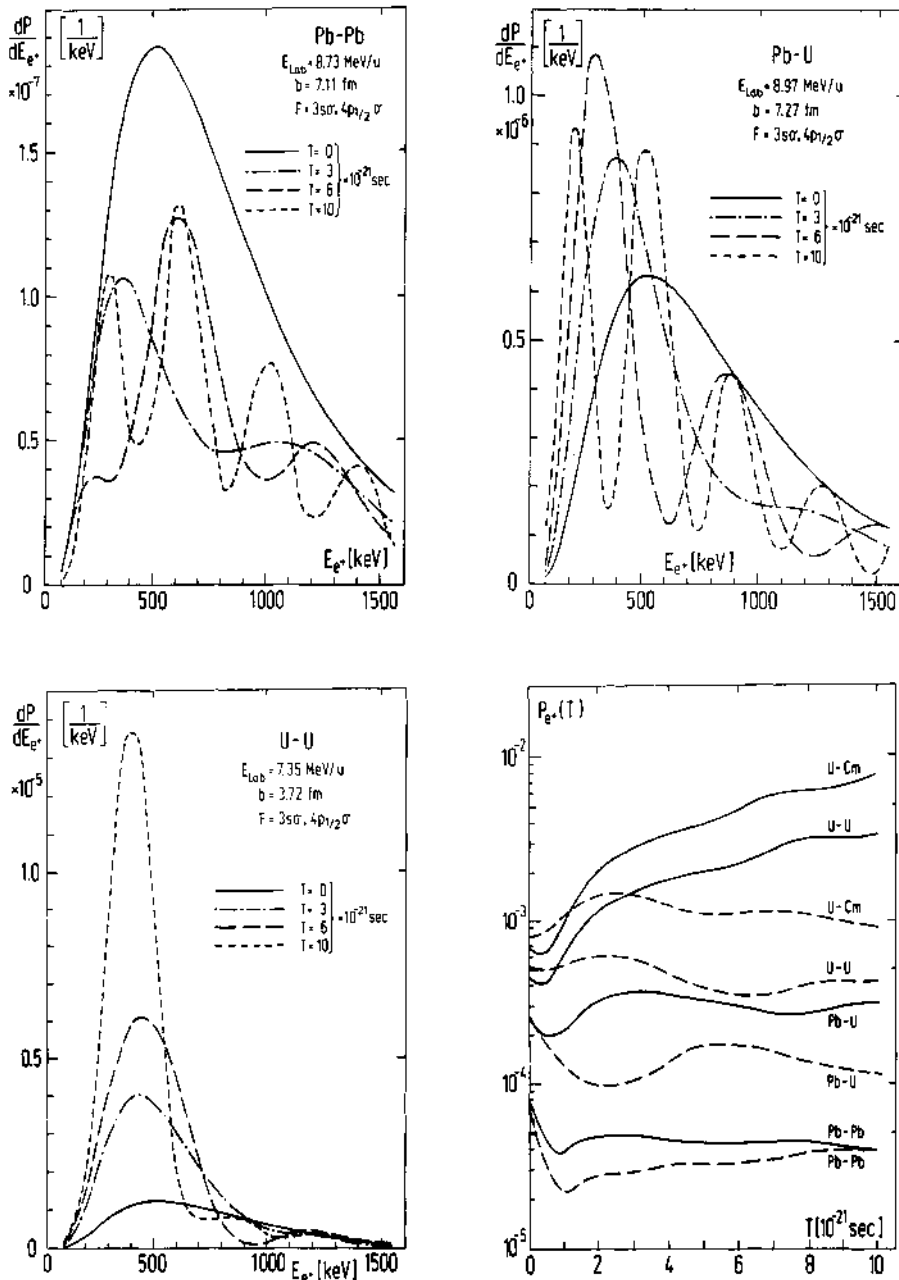


Fig. 6. Spectra of positrons created in subcritical (parts a,b) and supercritical (part c) heavy ion collisions assuming grazing Coulomb trajectory (full lines) and nuclear reactions leading to delay times  $T=3 \times 10^{-21} \text{ sec}$ ,  $6 \times 10^{-21} \text{ sec}$ , and  $10 \times 10^{-21} \text{ sec}$ , resp., using the schematic model for the trajectory. The (continued)

kinematic parameters  $\{E, b\}$  chosen are displayed within the figures, dissipation of energy or angular momentum is not taken into account. A Fermi level  $F=3s\sigma$ ,  $4p_{1/2}\sigma$  is assumed. Whereas for the lighter collision systems modulations in the positron spectra are present, a distinct peak at the "resonance" energy  $E_{1s0}(R_{\min})$  builds up for systems with  $Z_u > 173$ .- Part d: Probability for the emission of positrons, integrated over kinetic positron energy, as a function of reaction time  $T$ . Full lines: contribution of s-partial waves, dashed lines:  $p_{1/2}$ -partial waves' contribution. For the supercritical systems U-U and U-Cm  $P_e^+$ ,  $s$  increases strongly with  $T$ .

subcritical systems,  $P_e^+(T)$  remains roughly unchanged or is even reduced by up to a factor two due to destructive interference between incoming and outgoing path. In the supercritical systems the probability rises approximately in linear relation with  $T$ , which reflects the increasing contribution of the spontaneous decay (cf. eq. 18). In the schematic model its slope depends on the separation of the two nuclei,  $R_{\min}$ ; in general it depends also on the time-dependent charge distribution during nuclear contact. At small values of  $T$  interference effects seem to prevail even in supercritical collisions.

The results described so far were obtained within the schematic model for the nuclear motion. It facilitates a systematic study of the time delay effect and allows for an investigation of the conceptually interesting limit of large sticking times.

To analyze a given experiment, however, the employed nuclear trajectories should be consistent with the elastic and inelastic heavy-ion scattering data. Many reaction models with different degrees of refinement have been discussed in the literature. We have calculated<sup>29</sup> trajectories with the macroscopic models of Błocki et al., using the proximity potential and friction force<sup>43</sup>, of Gross and Kalinowski<sup>44</sup> and of Schmidt et al.<sup>45</sup>, which accounts for neck formation. The model parameters are determined in Refs. 43-45 by fitting the measured deflection function and energy loss. Fig. 7a displays the trajectories, compared with a Rutherford orbit, for a head-on U-U collision with bombarding energy  $E_{\text{lab}} = 7.5$  MeV/u. Strong deviations from Coulomb trajectory are found, energy loss up to ~30% (for model III) can be obtained.

We have performed coupled channel calculations with the trajectories of models I and III which are "extreme" with respect to minimal approach, time delay and energy loss. The resulting modified spectra are shown in Fig. 7b (s- plus  $p_{1/2}$ -states). As expected a longer delay time  $\Delta T$  causes an increase of positron production in the s-channel. On the other hand the change in kinematics causes a drift to lower kinetic energies in the  $p_{1/2}$ -partial

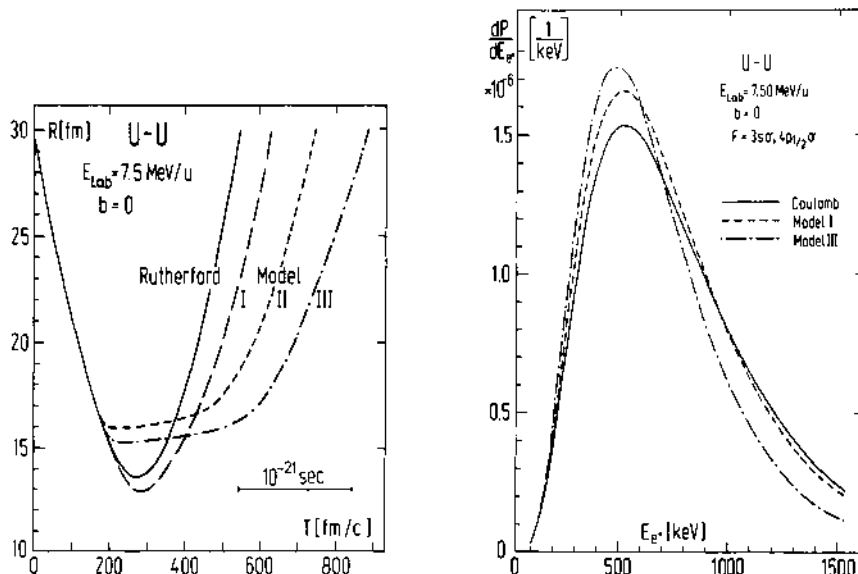


Fig. 7. Left part: Nuclear trajectories for a head-on U-U collision at 7.5 MeV/u lab. energy assuming a pure Coulomb orbit (full line) and various models for the dissipative nucleus-nucleus interaction. Trajectory I: Proximity potential of Blocki et al.<sup>43</sup>, II: friction model of Gross and Kalinowski<sup>44</sup>, and III: model of Schmidt et al.<sup>45</sup> including neck formation. - Right part: Spectra of positrons ( $s$ - plus  $p_{1/2}$ -partial waves) for Rutherford and nuclear trajectories depicted in part a.

wave spectra due to destructive interference. Both effects taken together lead to an enhancement of the maximum and a drift towards lower energies also in the total spectrum.

New measurements of Backe et al.<sup>46</sup> seem to indicate such tendencies: In U-U and U-Cm collisions at  $E_{\text{lab}} = 7.5$  MeV/u, i.e. above the Coulomb barrier, positron spectra have been measured in coincidence with fission fragments in order to get a signature for close nuclear contact. A first preliminary analysis shows an enhancement of  $dP/dE_e$  at lower kinetic energies in qualitative agreement with Fig. 7b.

For a quantitative comparison one has to integrate the impact parameter-dependent positron spectra over all values of  $b$  which lead to a nuclear reaction, weighted by the corresponding probability  $w(b)$  to induce nuclear fission

$$\frac{dp_e^+}{dE_e^+} = \int b db \frac{dp_e^+}{dE_e^+}(b) w(b) / \int b db w(b) . \quad (21)$$

Calculating the positron spectra for different impact parameters within model III and performing the integration eq. 21 with a primitive weight factor  $w(b)=1$  for  $b < b_{\text{grazing}}$  and  $w(b)=0$  elsewhere, there remains, however, an unexplained energy shift of  $\sim 50$  keV in the experimental data in comparison with the theoretical curves. Furthermore, as mentioned in Section 4, the theoretical values have to be reduced by an overall factor  $\sim 2/3$ . For the influence of electron screening see Section 6.

As another interesting theoretical problem one might speculate about the presence of nuclear collisions with very long reaction times. How would positron spectra look like if, at a given scattering angle, a superposition of Rutherford scattering and long-lasting nuclear reactions is assumed? Obviously, the positron creation probability  $P_e^+(\theta)$  is defined as the ratio

$$P_e^+(\theta) = \left( \frac{d\sigma_e^+}{d\theta}(\theta) + \frac{d\sigma_e^+}{d\theta}(\pi-\theta) \right) / \left( \frac{d\sigma}{d\theta}(\theta) + \frac{d\sigma}{d\theta}(\pi-\theta) \right) , \quad (22)$$

where the second terms are always present when discrimination between projectile and target nuclei is not experimentally feasible. If, for the sake of simplicity,  $d\sigma_e^+/d\theta$  and  $d\sigma/d\theta$  are assumed to be a superposition of just two contributions, one for Rutherford and one for nuclear scattering with definite delay time  $T$ , the positron probability assigned to the "line" then reads

$$\begin{aligned} P_e^+(\theta) &= \frac{\frac{d\sigma^N}{d\theta}(\theta) P_e^+(T) + \frac{d\sigma^N}{d\theta}(\pi-\theta) P_e^+(T)}{\frac{d\sigma^R}{d\theta}(\theta) + \frac{d\sigma^N}{d\theta}(\theta) + \frac{d\sigma^R}{d\theta}(\pi-\theta) + \frac{d\sigma^N}{d\theta}(\pi-\theta)} \\ &\approx \frac{\frac{d\sigma^N}{d\theta}(\theta) + \frac{d\sigma^N}{d\theta}(\pi-\theta)}{\frac{d\sigma^R}{d\theta}(\theta) + \frac{d\sigma^R}{d\theta}(\pi-\theta)} P_e^+(T) \equiv q \cdot P_e^+(T) . \end{aligned} \quad (23)$$

Thus the value of  $q$  can be used as a measure of the relative cross section of reactions leading to long contact times.

Motivated by recent experimental results<sup>7, 8</sup>, which will be discussed below, we performed calculations for the heavy-ion collision

system U-U at 5.79 MeV/u bombarding energy. Assuming an isotropic break-up of the long-living compound system ( $T=4 \cdot 10^{-20}$  sec), a ratio  $q \approx 2.4 \cdot 10^{-3}$ , and a shrinking of the internuclear distance  $R(t)$  to values smaller 2a (corresponding to a "resonance" energy at 370 keV), one gets Fig. 8. Due to the isotropic angular distribution  $d\sigma^N/d\theta$  of the nuclear reaction component, a line is observable in the posi-

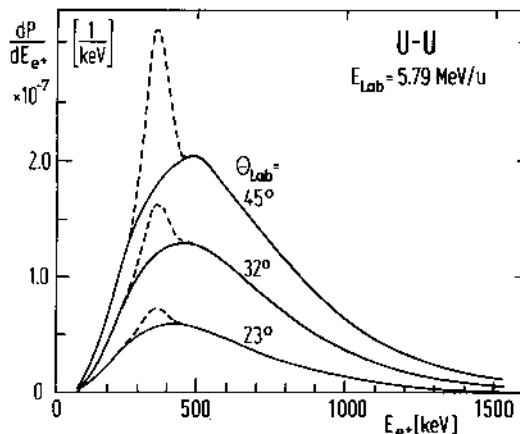


Fig. 8. Spectra of positrons emitted in 5.79 MeV/u U-U collisions in coincidence with a scattered nucleus for three selected lab-ion angles. The fully drawn curves are calculated assuming Rutherford scattering only. The dashed lines show the effect of an additional nuclear reaction with a lifetime  $T=4 \cdot 10^{-20}$  sec. A relative fraction of  $q=2.4 \cdot 10^{-3}$  reactions per elastically scattered ion (at  $45^\circ$ ) has been assumed. The curves at smaller angles have been drawn under the assumption of isotropic distribution of the reaction fragments in the reaction plane.

tron spectrum at all ion scattering angles. However, it is most pronounced under  $\theta_{\text{CM}} = 90^\circ$ , being suppressed at other angles relative to the elastic scattering cross section. If the long-living compound system fragmentates into a rather narrow angular window, the peak structure would disappear at forward (backward) scattering angles.

As mentioned above two experimental groups<sup>7, 8</sup> recently have performed experiments with U-Th, U-U, and U-Cm at energies close to the Coulomb barrier. Contrary to the results of Backe et al.<sup>4,6</sup> their positron spectra seem to show remarkable structures.

C. Kozhuharov, P. Kienle et al.<sup>7</sup> measured at 5.8 MeV/u beam-energy positron spectra in coincidence with ions scattered into various narrow angular windows, using an orange-type  $\beta$ -spectrometer. A preliminary analysis shows sharp maxima in the spectra that are most pronounced under laboratory scattering angles around  $\theta_{\text{lab}} \sim 45^\circ$ . In the U-U measurement the position of the peak was found to be located at  $\sim 370$  keV with a width of about  $\sim 90$  keV (FWHM), for U-Th the effect is less well established. After subtraction of a smooth background the number of positrons per detected ion emitted in the peak is roughly  $10^{-5}$  at  $\theta \sim 45^\circ$ .

If the observed structure is of quasimolecular origin, it must be produced in very long-lasting nuclear reactions. If one compares the experimental width with spectra from coupled channel calculations based on the schematic sticking model a minimum value  $T \sim 4 \cdot 10^{-20}$  sec is required. Should the observed line width have instrumental origins or be due to additional broadening effects the reaction time  $T$  would have to be even longer. Taking the coupled channel results the probability for positron production in a delayed ( $T = 4 \cdot 10^{-20}$  sec) collision should be  $\sim 4.7 \cdot 10^{-3}$ , which have to be compared with the observed probability  $\sim 10^{-5}$ . Thus a fraction of  $q = P_e^+ / (P_e^+ + \text{theor}) \approx 2 \cdot 10^{-3}$  delayed collisions per elastically scattered ion is sufficient to produce the observed effect (at  $45^\circ$ ). This number should serve only for a general orientation, since it depends on the details of the model assumed.

Similar features were detected in the experiment of H. Bokemeyer, J.S. Greenberg et al.<sup>8</sup> in U-U and U-Cm collisions. When displaying their data for U-U for different narrow scattering angle windows  $\theta_{\text{lab}}$  the differential positron spectra exhibit prominent peak structures at different kinetic energies  $E_e^+$ .

Thus the three experimental groups performing positron-spectroscopy at GSI, Darmstadt, so far have obtained different spectra. Backe's data<sup>4,6</sup> show no significant structures, while Berdermann et al.<sup>7</sup> and Bokemeyer et al.<sup>8</sup> reported similar, but not identical observations on peak structure. One might suppose that those peaks are caused by nuclear background processes. However, nuclear transitions of, e.g., multipolarity  $E1$  or  $E2$  should also be observable in the emitted photon spectra, provided that proper Doppler shift corrections are performed<sup>4,7</sup>. Whether the peaks can be caused by  $E0$ -processes will be discussed in Section 7.

On the other hand, if a sharply focussed nuclear reaction takes

place it is not surprising that an experiment not triggering for the optimal kinematic conditions might smear out any evidence for structure. Further investigations are needed to settle this question. Should the observed phenomena indeed be caused by reactions with a very long time scale, this would have far reaching consequences for the physics of nuclear systems in the superheavy region.

## 6. THE EFFECTS OF ELECTRON SCREENING ON POSITRON PRODUCTION RATES

In our discussion electron screening has been neglected so far. In order to clarify its gross features we choose the simple non-relativistic Thomas-Fermi model<sup>48</sup> and apply it to the calculations of basis wavefunctions in the framework of the monopole approximation. According to this model the semiclassical electron density reads

$$\rho(r) = 1/(3\pi^2\hbar^3) \cdot (2m)^{3/2} (E_F - V_{\text{eff}}(r))^{3/2}. \quad (24)$$

The potential is expressed by

$$V_{\text{eff}}(r) = V_{\text{nucl}} + V_{\text{ee}} = -Ze^2/r \cdot \phi(r), \quad (25)$$

where  $\phi(r)$  is a screening function. Using Poisson's equation we arrive at the nonrelativistic Thomas-Fermi equation

$$\frac{d^2\phi(x)}{dx^2} = \frac{\phi^{3/2}(x)}{x^{1/2}}. \quad (26)$$

For practical calculations we used an approximation to the solution of eq. 26 proposed by Latter<sup>49</sup>

$$\phi(x) = \left( \sum_{j=0}^6 a_j x^{j/2} \right)^{-1}, \quad (27).$$

where the  $a_j$  are given constants<sup>50</sup>. Strictly speaking this approximation is valid only in the nonrelativistic case for pointlike nuclei. But it was shown<sup>51</sup> that relativistic corrections are partially cancelled by the electron exchange terms for large nuclear charge  $Z$ . Eq. 26 yields vanishing electron screening at the origin, which is wrong for extended nuclei. We circumvented this problem by choosing the following local modified nonrelativistic Thomas-Fermi potential

$$U(r, R) = \phi(x) \left[ 1 - \frac{a(R)R_+}{(r+R_+)} \right] V_0(r, R), \quad (28)$$

where  $V_0(r, R)$  is the monopole part of the two-centre potential,  $R_+$  denotes  $R/2 + r_n$  with  $R$  the two-centre distance and  $r_n$  the main nuclear radius. In eq. 26  $x=r/b$  is a dimensionless quantity, with

$$b = 1/4 + (9\pi^2/2Z)^{1/3} a_0, \quad (29)$$

$a$  the Bohr radius.  $a(R)$  is a fit parameter which matches the  $1s\sigma$ -binding energy of the heavy-ion system to Hartree-Fock-Slater values. It turns out that then even the binding energies of the weaker bound states, e.g. up to  $5s\sigma$ , correspond within 7% in the TF and HFS models.

The resulting production rates for a head-on U-U collision at 5.9 MeV/u bombarding energy are displayed in Fig. 9a. A shift of the maximum towards lower positron energies by an amount of about 50 keV can be deduced. Recent, not completely analyzed measurements of Backe et al.<sup>46</sup> tend to confirm this shift. Fig. 9b shows the positron spectrum resulting from a U-Cm collision at 5.8 MeV/u. This system with higher combined charge shows a smaller shift of the maximum by about 30 keV.

Let us investigate now how screening affects the spectra in heavy-ion collisions where nuclear contact and time delay occurs. Fig. 9c shows positron production rates for a U-U collision,  $E_{\text{lab}}=8.5$  MeV/u,  $b=6.5$  fm (corresponding to nuclear contact for spherical nuclei), with time delay  $T=10^{-20}$  sec within the schematic model. We have to distinguish between the positron line emerging at  $\sim 400$  keV (unscreened case) and 300 keV (screened case), respectively, and the oscillations at higher kinetic energies which are inversely proportional to the sticking time. The peak shift is essentially due to the reduction of binding energy of the supercritical  $1s\sigma$ -level, which amounts to  $\sim 100$  keV. The latter structures are also shifted by  $\sim 100$  keV towards lower energies.

Caused by the reduction of the decay width due to screening we observe a decrease in intensity of the line by about 30% relative to previous results neglecting the screening effect. We also evaluated positron spectra of time delayed collisions for the system U-Cm at  $E_{\text{lab}}=7.5$  MeV/u and found similar results (Fig. 9d).

In Section 5 we have discussed positron creation in U-U collisions at 7.5 MeV/u considering nuclear trajectories originating from classical friction models. Fig. 10 shows the change of the positron spectrum for collisions with varying degree of nuclear contact. Part a displays the trajectories  $R(t)$  calculated in the model of Schmidt et al.<sup>45</sup> for several orbital angular momenta from  $l=0$  head-on (same as in Fig. 7a) to  $l=400$   $\text{\AA}$  near grazing collisions. In Fig. 10b we present a reevaluation of the positron spectrum including the influence of electron screening. As expected, an energy-shift (of  $\sim 55$  keV) towards lower kinetic energies is observed. However, the cross section (cf. eq. 21) is reduced only by about 10% which is not quite enough to obtain quantitative agreement with the experimental data of Ref. 46.

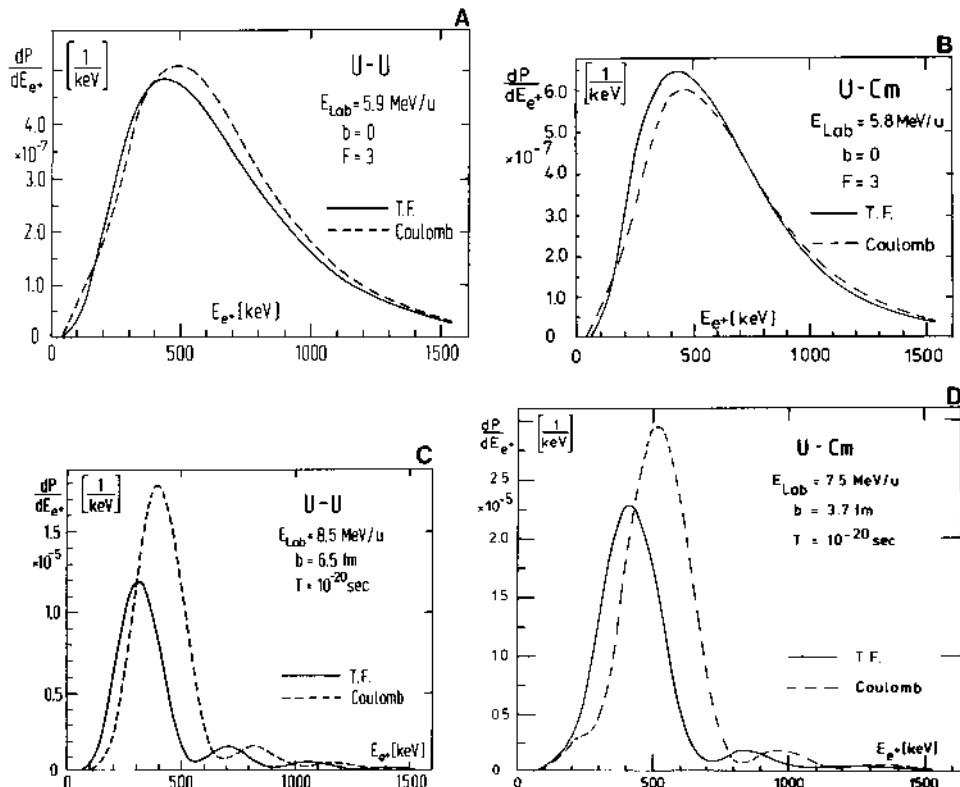


Fig. 9. Spectra of emitted positrons in heavy ion collisions. Coulomb potential (dashed lines) and a Thomas-Fermi screened potential (full lines) are investigated. Part (a) shows a head-on  $U \rightarrow U$  collision at  $5.9 \text{ MeV/u}$ , part (b) displays a  $U \rightarrow \text{Cm}$  collision,  $E_{\text{lab}} = 5.8 \text{ MeV/u}$ ,  $b = 0$ . Rutherford trajectories and  $F = 3s\sigma$ ,  $4p_3\sigma$  are assumed. Parts (c), (d): In the case of time delayed supercritical collisions the positron spectra for screened (full lines) and unscreened (dashed ones) potential differ not only in their magnitude but also in the position of the "spontaneous" line. Spectra of a  $U \rightarrow U$  collision,  $E_{\text{lab}} = 8.5 \text{ MeV/u}$ ,  $b = 6.5 \text{ fm}$  (part c) and a  $U \rightarrow \text{Cm}$  collision,  $E_{\text{lab}} = 7.5 \text{ MeV/u}$ ,  $b = 3.7 \text{ fm}$ , are shown assuming a delay time  $T = 10^{-20} \text{ sec}$ .

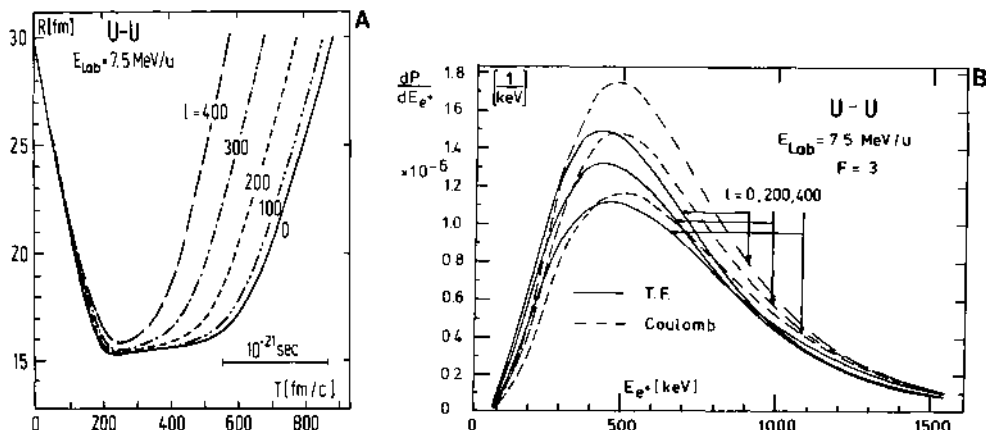


Fig. 10. Part a: Nuclear trajectories calculated in the friction model of Ref. 45 for 7.5 MeV/u U-U collisions at various values of the orbital angular momentum  $l$  between 0 and 400  $\hbar$ . - Part b: Energy spectra of positrons emitted in U-U 7.5 MeV/u collisions assuming nuclear trajectories depicted in part a) for  $l=0, 200$ , and  $400 \hbar$ . Screened Thomas-Fermi and unscreened Coulomb-potential are investigated. The results for  $s$ - and  $p_{1/2}$ -partial waves have been added.

## 7. INTERNAL ELECTRON-POSITRON PAIR PRODUCTION FROM ELECTRIC MONOPOLE TRANSITIONS

Our theoretical investigations are partly motivated by the recently observed structures<sup>7,8</sup> in the energy distribution of emitted positrons which have been produced in collisions of very heavy ions like U-Th, U-U, and U-Cm. These systems are supercritical and in principle may lead to spontaneous positron production. In Section 5 we have discussed this effect in detail.

A second, more conventional explanation for this peculiar structure was proposed: Intrinsic nuclear excitations may take place either by Coulomb excitation or by transfer reactions. The nuclear transition can be accompanied by internal electron-positron pair creation<sup>34,52,53</sup>. Contrary to E0-processes nuclear transitions of multipolarity E1 or E2 should also be observable in the emitted photon spectra provided that proper Doppler shift corrections are performed<sup>47</sup>. Here we will prove the following assertion: If the observed structure in the positron distribution originates from E0-pair production one should definitely see also a peak in the high energy part ( $E_e^+ > 1 \text{ MeV}$ ) of the  $\delta$ -electron distribution originating from K-shell conversion.

Nuclear EO-transitions are characterized by the absence of single photon emissions, because a photon must carry at least one unit of angular momentum. Therefore EO-transitions predominantly occur by bound state electron conversion or by internal electron-positron pair creation. The latter process requires nuclear transition energies  $\hbar\omega$  larger than twice the electron rest mass  $mc^2$ . The basic processes under investigation are depicted schematically in Fig. 11. The nucleus which undergoes EO-transition is labelled by its initial and final state angular momenta  $J_i$ ,  $J_f = J_i$  and eigen-energies  $E_i, E_f = E_i - \hbar\omega$ . Process a) describes the electron-positron pair creation. An electron of the negative energy continuum ( $\epsilon = -E < mc^2$ ) with Dirac quantum number  $\kappa$  is lifted to the positive energy continuum. The final state energy obviously amounts to  $E' = \epsilon + \hbar\omega$  whereas the angular momentum quantum number remains unchanged. Since neither the initial electron state energy nor the final state energy is fixed one expects a continuous energy distribution for the emitted positrons.

Process b) indicates the conversion of a K-shell electron ( $n=1$ ,  $l=0$ ,  $j=\frac{1}{2}$ ,  $\kappa=-1$ ) with energy eigenvalue  $E_{1s}$ . Thus bound states with definite energies are involved. Energy conservation then simply causes monoenergetic lepton emission for a fixed nuclear transition energy  $\hbar\omega$ .

Process c) symbolizes monoenergetic positron production. Here an electron of the negative energy continuum is excited to a bound state, e.g., to the  $1s_{1/2}$ -state. This represents a rather rare process since it requires a vacant bound state with a large overlap with the nuclear interior. If we investigate a realistic heavy-ion collision of  $^{92}\text{U}$  on  $^{92}\text{U}$  with a bombarding energy close to the Coulomb barrier, the number of created K-vacancies per collision with impact parameter  $b \leq 20$  fm is typically of the order of 10%<sup>12,15,54</sup>. The transition time (X-ray decay) of an electron from a higher shell to the K-shell is<sup>55</sup> about  $10^{-17}$  sec. This has to be compared with nuclear transition times of about  $10^{-13}$  sec, after which conversion takes place. Hence the K-vacancy will be decayed before it could eventually be filled again due to pair conversion of a nuclear state.

Therefore the monoenergetic positron formation is suppressed in contrast to ordinary K-shell conversion by at least 7 orders of magnitude, because one can conclude<sup>56</sup> that the EO-conversion of a K-shell electron has a probability<sub>+</sub> larger by about 3 orders of magnitude than the monoenergetic  $e^-$ -production where the electron occupies the vacant K-shell. This ratio even increases by one order of magnitude if one considers higher bound states in relation to the positron production process. Thus process c) can be neglected completely.

Therefore, the ratio  $\eta$  of the two conversion probabilities  $P_{e^+, e^-}$  for electron-positron pair creation and  $P_{e^-}$  for the ionization of bound state electrons

$$\eta = \frac{P_{e^+, e^-}}{P_{e^-}} \quad (30)$$

must be investigated more closely. The differential ratio with respect to the positron energy  $E$  obviously is

$$\frac{d\eta}{dE} = \frac{dP_{e^+, e^-}}{dE} / P_{e^-} \quad (31)$$

and consequently

$$\eta = \frac{\frac{d\eta}{dE}}{\frac{dP_{e^+, e^-}}{dE}} = \frac{d\eta}{dE} \frac{dE}{dP_{e^+, e^-}} \quad (32)$$

The investigation of such a ratio is motivated by the following considerations: The calculation of the nuclear E0-transition probability implies the precise knowledge of the initial and final state nuclear wavefunction, which clearly is model-dependent. Therefore it seems to be more advantageous to perform model-independent evaluations by considering the ratio of two different conversion probabilities. In this ratio the nuclear transition matrix element drops out, thereby avoiding difficulties with the specific nuclear structure.

The final expressions for the conversion probabilities entering eq. 31 are to lowest order in  $r$

$$\frac{dP_{e^+, e^-}}{dE} \propto |M|^2 \sum_{\kappa=-1}^+ |C_{e^+, e^-}|^2, \quad (33)$$

$$P_{e^-} \propto |M|^2 \sum_m |C_{e^-}|^2, \quad (34)$$

where  $M$  denotes the nuclear E0 matrix element

$$M = \int_0^\infty dV \sum_n \left| \vec{r}_n \right|^2 r_n^2, \quad (35)$$

and  $C$  is a normalization factor

$$C = \lim_{r \rightarrow 0} \frac{ff' + gg'}{r^{2j-1}} . \quad (36)$$

Here  $f, f'$  and  $g, g'$  are the radial Dirac wavefunctions belonging to the initial and final state of the electron, respectively.  $\Sigma'$  in eq. 34 denotes the sum over all occupied states  $(E_m, j_m)$  excluding the summation over magnetic substates; in eq. 33 only  $j=1/2$  ( $\kappa=\pm 1$ ) states are taken into account.

Thus the ratio eq. 31 now reads

$$\frac{d\eta}{dE} = \sum_{\kappa=\pm 1} |C_{e^+} e^-|^2 / \sum_m |C_{e^-}|^2 , \quad (37)$$

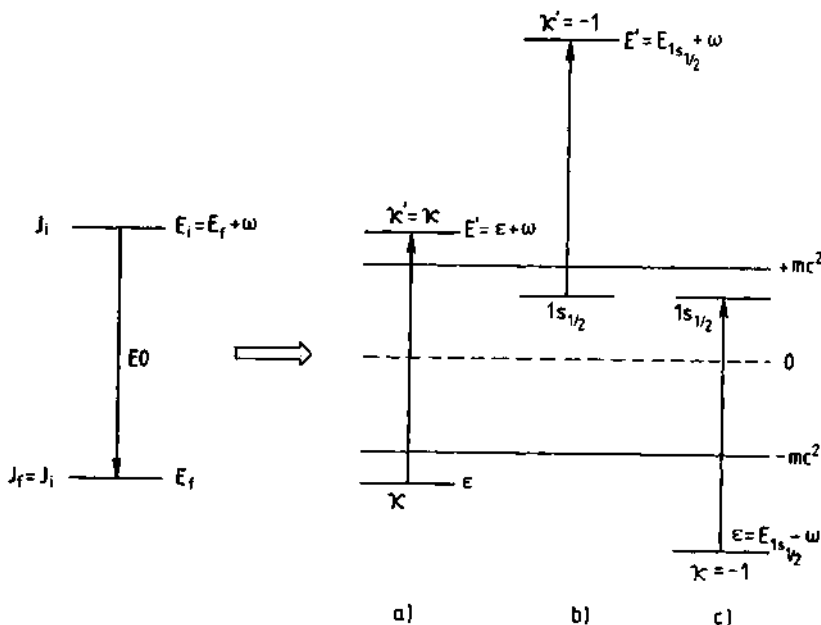


Fig. 11. Schematic representation of electron conversion processes accompanying nuclear E0-transition from a state  $\{E_i, J_i\}$  to a state  $\{E_f = E_i - \hbar\omega, J_f = J_i\}$ . a) Electron-positron pair production leading to a continuous energy distribution of positrons and electrons. b) Conversion of K-shell electrons - a monoenergetic electron-positron mechanism. c) Monoenergetic positron-production - a negligible process.

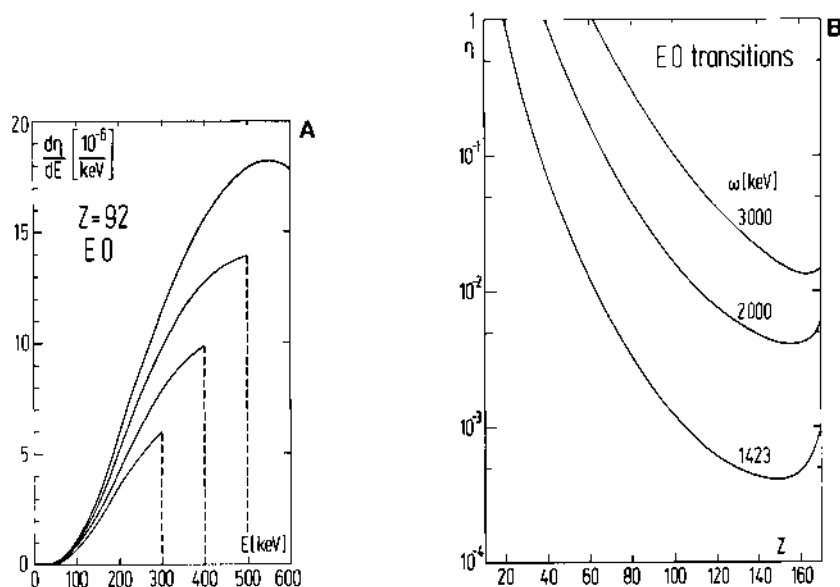


Fig. 12. a) Differential conversion probability ratio  $d\eta/dE$  with respect to the kinetic positron energy  $E$  for nuclear  $E0$ -transitions in  $^{92}\text{U}$ . Nuclear transition energies  $\hbar\omega = 1323$  keV, 1423 keV, 1523 keV, and 1623 keV are considered, corresponding to maximum kinetic positron energies of  $E_{\text{max}} = 300$  keV, 400 keV, 500 keV, and 600 keV. - b)  $Z$ -dependence of  $\eta$  for nuclear  $E0$ -transition energies  $\hbar\omega = 1423$  keV, 2000 keV, and 3000 keV, resp..

where the nuclear matrixelement drops out. Due to eq. 36 the ratio  $\eta$  of pair conversion to bound state electron conversion is completely determined by the density of the electron wavefunctions at the nuclear origin.

According to eqs. 37 and 36 we computed the differential conversion ratio  $d\eta/dE$  with respect to the positron energy  $E$  for  $E0$ -transitions. As bound state only the atomic K-shell has been taken into account. The conversion probability of higher bound states is at least one order of magnitude smaller. For the nucleus  $^{92}\text{U}$  the energy distribution of emitted positrons is depicted in Fig. 12a. Nuclear transition energies of 1323 keV, 1423 keV, 1523 keV, and 1623 keV are considered, which correspond to maximum positron energies of  $E_{\text{max}} = 300$  keV, 400 keV, 500 keV, and 600 keV, respectively.

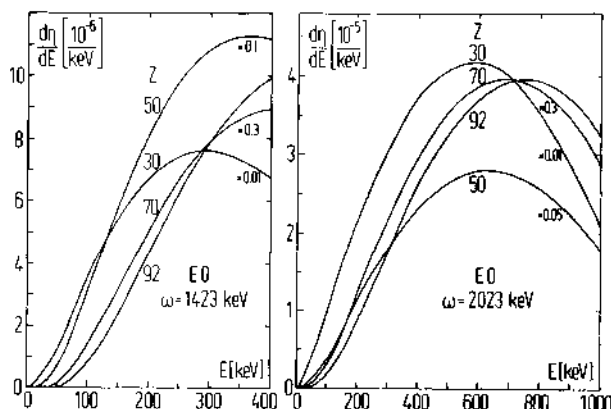


Fig. 13. Z-dependence of the differential conversion probability ratio  $dn/dE$  versus the kinetic positron energy  $E$  for EO-transitions with  $\hbar\omega=1423$  keV (left part) and  $\hbar\omega=2023$  keV (right part). The lines have been multiplied by different factors for each charge  $Z$ .

The spectra are centered around  $E_{\max}^{\text{kin}}$ , reflecting the strong Coulomb repulsion of low energetic positrons.

Figs. 13 display the change of  $dn/dE$  with the nuclear charge  $Z$  for the transition energies  $\hbar\omega=1423$  keV and  $\hbar\omega=2023$  keV, respectively. With decreasing  $Z$  and increasing  $\hbar\omega$  the energy distribution of positrons becomes more symmetric and therefore resembles the electron spectrum. The numerical integration of eq. 37 yields the dimensionless ratio  $\eta$ . It is presented in Fig. 12b versus the nuclear charge  $Z$  for transition energies  $\hbar\omega=1423$  keV, 2000 keV, and 3000 keV. These calculations are also extended to the region of superheavy nuclei ( $Z>100$ ).  $\eta$  decreases monotonically until almost critical systems ( $Z\sim 170$ ) are reached, where the binding energy of the  $1s_{1/2}^-$  state exceeds twice the electron rest mass and the bound state gets imbedded as a resonance into the negative energy continuum. The onset of this behaviour is reflected in a slight increase of  $\eta$  around  $Z\sim 160$ . However, the numerator of eq. 37 and therefore the pair production probability increases by almost 4 orders of magnitude if the nuclear charge is extended from  $Z=92$  to  $Z=169$ . In consequence the nuclear transition time due to internal

pair creation decreases by 4 orders of magnitude in the considered Z-range.

Comparing  $\eta$  in the region from oxygen ( $Z=8$ ) to Polonium ( $Z=84$ ) with experimental and other theoretical data<sup>57</sup> fair agreement is achieved.

Thus we can discuss the probability that the recently observed structures in positron spectra originates from nuclear EO-transitions. One convincing argument against this interpretation is related to the shape of the  $e^+$ -energy distribution. According to Fig. 12a the halfwidth of the spectra should be at least  $\Delta E \gtrsim 150$  keV. However, the observed structure is much narrower. The second argument is connected with the energy distribution of the emitted  $\delta$ -electrons. The measured differential positron production probability  $dP_{e^+}/dE$  with respect to the kinetic positron energy at  $E \sim 400$  keV for  $U-8$  collisions with a bombarding energy of  $E_{\text{lab}}^{\text{ion}} = 5.9$  MeV/u and ion scattering angles of  $\theta_{\text{lab}} = 45^\circ \pm 10^\circ$  amounts to  $dP_{e^+}/dE \approx 10^{-7}$  / keV<sup>7,26</sup>.

Assuming that these positrons are of pure nuclear origin one can easily deduce the probability  $P_N$  for nuclear excitation

$$P_N \approx \frac{dP_{e^+}}{dE} / \frac{dn}{dE} \approx 10^{-2} . \quad (38)$$

In principle the competing K-shell conversion should lead to a sharp line in the electron spectra at  $E_{e^-} \approx 1300$  keV.

However, the experimental energy resolution for these high energy electrons is presently not better than  $\Delta E_{e^-} = 25$  keV, which therefore yields a differential  $e^-$ -production probability of

$$dP_{e^-}/dE_{e^-} \approx P_N/\Delta E_{e^-} = 4 \cdot 10^{-4} / \text{keV} . \quad (39)$$

This is still by a factor  $F=40$  larger than the expected  $\delta$ -electron production rate<sup>15, 54</sup> of  $dP_{e^-}/dE_{e^-} \approx 10^{-5} / \text{keV}$  at a kinetic electron energy of  $E_{e^-} \approx 1300$  keV, which results from dynamical electron excitations during the collision. The factor  $F$  can be increased by an order of magnitude if one measures the emitted electrons in coincidence with the decaying K-vacancy (e.g.,  $K_{\alpha}$ -radiation). Hence we can conclude: If the observed structure in the positron spectra is caused by nuclear EO-transitions one should also observe a distinct peak in the  $\delta$ -electron distribution at  $E_{e^-} \approx 1300$  keV. Furthermore we emphasize that sharp peaks in the  $e^-$  energy distribution of emitted positrons with a halfwidth of less than 100 keV may not originate from nuclear EO-conversion processes.

## CONCLUSIONS

We have studied the mechanisms of ionization and pair production in collisions of very heavy ions within the framework of a dynamical theory of excitation based on the quasimolecular picture. Massive relativistic effects in the wavefunctions of electrons and positrons in  $s^{1/2}$  and  $p_{1/2}$ -states, caused by the coherent action of the Coulomb field generated by the two nuclei, are reflected in the excitation rates.

We have developed a theory which properly takes into account the resonance character of the "dived" 1s-state. The results of our coupled channel calculations indicate that no sharp threshold effects are to be expected at the border of the supercritical region, in accordance with the notion of dynamical collision broadening. Collisions above the Coulomb barrier characterized by a sufficiently long reaction time may help to identify the process of spontaneous positron production.

The experiments performed so far have convincingly established the predicted strong increase of positron production in collisions with very high total nuclear charge and its concentration on close collisions. There remain some discrepancies with theory in absolute magnitude, in the slope of  $Pe^+(b)$ , and, possibly, in the shape of the positron spectra. On the other hand, if the experimental data of Refs. 7,8 are confirmed and if no other explanation of the positron line in the region 300-400 keV can be found, then one is led to the conclusion that this already constitutes the quantitative proof for the existence of a spontaneous change of the ground state (the "vacuum decay"). The possibility that the structures in the positron spectra might be caused by E0-conversion due to nuclear deexcitation has been discussed. The results of Section 7 offer a way to decide whether the observed structures can be explained by background.

The experimental findings open up a multitude of interesting questions and speculations as to the nuclear physics of the unexpected reaction mechanism, the central question being: are there meta-stable superheavy nuclei in the range  $Z \sim 160-190$ ? More experimental and theoretical information and investigation is required before definite conclusions can be drawn.

## ACKNOWLEDGEMENTS

We acknowledge very fruitful discussions with H. Backe, K. Bethge, H. Bokemeyer, F. Bosch, J.S. Greenberg, A. Gruppe, P. Kienle, Ch. Kozuharov, M. Krämer, D. Schwalm, J. Schweppe, and P. Senger concerning their experiments.

This work was supported by the Bundesministerium für Forschung

und Technologie (BMFT) and the Deutsche Forschungsgemeinschaft (DFG). One of us (G.S.) acknowledges the support of the DFG - Heisenberg Programm.

## REFERENCES

1. J. Reinhardt, W. Greiner, *Rep. Prog. Phys.* 40:219 (1977).  
J. Rafelski, L.P. Fulcher, and A. Klein, *Phys. Rep.* 38C:227 (1978).
2. B. Müller, *Lectures at this conference.*
3. W. Pieper and W. Greiner, *Z. Physik* 218:327 (1969).
4. J. Rafelski, B. Müller, and W. Greiner, *Nucl. Phys.* B68:585 (1974).
5. L. Fulcher and A. Klein, *Phys. Rev.* D8:2455 (1973).
6. T. de Reus, U. Müller, J. Reinhardt, P. Schlüter, K. H. Wetschork, B. Müller, W. Greiner, and G. Soff, *Contribution at this conference.*
7. E. Berdermann, F. Bosch, M. Clemente, F. Güttner, P. Kienle, W. König, C. Kozhuharov, B. Martin, B. Povh, H. Tsertos, W. Wagner, and Th. Walcher, *GSI Scientific Report 1980, GSI 81-2*:128 (1981).
8. H. Bokemeyer, H. Folger, H. Grein, S. Ito, D. Schwalm, P. Vincent, K. Bethge, A. Gruppe, R. Schulé, M. Waldschmidt, J. S. Greenberg, J. Schweppe, and N. Trautmann, *GSI Scientific Report 1980, GSI 81-2*:127 (1981).
9. See Ref. 6 and further references herein.
10. J. Theis, J. Reinhardt, and B. Müller, *J. Phys.* B12:L479 (1979).
11. J. Rafelski and B. Müller, *Phys. Rev. Lett.* 36:517 (1976).
12. G. Soff, W. Greiner, W. Betz, and B. Müller, *Phys. Rev.* A20:169 (1979).
13. U. Heinz, W. Greiner, and B. Müller, *Phys. Rev.* A23:562 (1981).
14. J. Reinhardt, B. Müller, and W. Greiner, *Phys. Rev.* A24:103 (1981).
15. G. Soff, J. Reinhardt, B. Müller, and W. Greiner, *Z. Physik* A294:137 (1980).
16. J. F. Reading, *Phys. Rev.* A8:3262 (1973).
17. J. Reinhardt, B. Müller, and W. Greiner, in: "Coherence and Correlation in Atomic Collisions", H. Kleinpoppen and J.F. Williams, eds., Plenum New York, p. 331 (1980).
18. O. Klein, *Z. Physik* 53:157 (1929).
19. F. Hund, *Z. Physik* 117:1 (1941).
20. W. L. Wang and C. M. Shakin, *Phys. Lett.* 32B:421 (1970).
21. K.-H. Wietschorke, B. Müller, W. Greiner, and G. Soff, *J. Phys.* B12:L31 (1979).
22. J. Rafelski, B. Müller, and W. Greiner, *Z. Physik* A285:49 (1978).
23. See, e.g.: W. E. Meyerhof, R. Anholt, J. F. Chemin, and Ch. Stoller, in: Proc. of the XVIII. Internat. Winter Meeting on Nucl. Phys., Bormio (Italy), p. 688 (1980) and references herein.
24. R. Anholt, *Phys. Lett.* 88B:262 (1979).

25. R. Anholt, Z. Physik A292:123 (1979).
26. U. Müller, J. Reinhardt, G. Soff, B. Müller, and W. Greiner, Z. Physik A297:357 (1980).
27. G. Soff, J. Reinhardt, B. Müller, and W. Greiner, Phys. Rev. Lett. 43:1981 (1979).
28. B. Müller and V. Oberacker, Phys. Rev. C22:1909 (1980).
29. J. Reinhardt, U. Müller, B. Müller, and W. Greiner, Z. Physik A, in print; UFTP-preprint 63/1981, Frankfurt (1981).
30. J. Reinhardt, V. Oberacker, B. Müller, W. Greiner, and G. Soff, Phys. Lett. 78B:183 (1978).
31. V. Oberacker, W. Greiner, H. Kruse, and W. T. Pinkston, Phys. Rev. C20:1453 (1979).
32. H. Backe, F. Weik, P. A. Butler, V. Metag, J. B. Wilhelmy, D. Habs, G. Himmels, H. J. Specht, Phys. Rev. Lett. 43:1077 (1979).
33. K. G. Kaun and S. A. Karamyan, JINR preprint P7-11420, Dubna (1978).
34. P. Schlüter, G. Soff, and W. Greiner, Z. Physik A286:149 (1978).
35. V. Oberacker, G. Soff, and W. Greiner, Phys. Rev. Lett. 36:1024 (1976); V. Oberacker, G. Soff, and W. Greiner, Nucl. Phys. A259:324 (1976).
36. W. Meyerhof, R. Anholt, Y. El Masri, I. Y. Lee, D. Cline, F. S. Stephens, and R. M. Diamond, Phys. Lett. 69B:41 (1977).
37. H. Backe, in: "Present Status and Aims in Quantum Electrodynamics", Lecture Notes in Physics, vol. 143, G. Gräff, E. Klempf, and G. Werth, eds., Springer, Berlin, Heidelberg, New York, p. 277 (1981).
38. C. Kozuharov, P. Kienle, E. Berdermann, H. Bokemeyer, J. S. Greenberg, Y. Nakayama, P. Vincent, H. Backe, L. Handschug, and E. Kankeleit, Phys. Rev. Lett. 42:376 (1979).
39. H. Backe, L. Handschug, F. Hessberger, E. Kankeleit, L. Richter, F. Weik, R. Willwater, H. Bokemeyer, P. Vincent, Y. Nakayama, and J. S. Greenberg, Phys. Rev. Lett. 40:1443 (1978).
40. A. Bałanda, K. Bethge, H. Bokemeyer, H. Folger, J. S. Greenberg, H. Grein, A. Gruppe, S. Ito, S. Matsuki, R. Schulé, D. Schwalm, J. Schweppe, P. Vincent, and M. Waldschmidt, GSI preprint 80-16, Darmstadt (1980).
41. H. Backe, W. Bonin, W. Engelhardt, E. Kankeleit, M. Mutterer, P. Senger, F. Weik, R. Willwater, V. Metag, and J. B. Wilhelmy, GSI Scientific Report 1979, GSI 80-3:101 (1980).
42. H. Backe, W. Bonin, W. Engelhardt, E. Kankeleit, M. Mutterer, P. Senger, F. Weik, R. Willwater, V. Metag, and J. B. Wilhelmy, "Positron Production in Heavy Ion Collisions", preprint (1979).
43. J. Błocki, J. Randrup, W. J. Świątecki, and C. F. Tsang, Ann. of Phys. 105:427 (1977).
44. D. H. E. Gross and H. Kalinowski, Phys. Rep. 45:175 (1978).
45. R. Schmidt, V. D. Toneev, and G. Wolschin, Nucl. Phys. A311:247 (1978).

46. H. Backe, W. Bonin, E. Kankeleit, R. Köhler, M. Kollatz, M. Krämer, R. Krieg, V. Metag, and P. Senger, *Verhandl. DPG(VI)* 16:794 (1981).
47. R. B. Piercey, J. H. Hamilton, A. V. Ramayya, H. Emling, P. Fuchs, E. Grosse, D. Schwalm, H. J. Wollersheim, N. Trautmann, A. Faessler, M. Ploszajczak, *Phys. Rev. Lett.* 46:415 (1981).
48. L. H. Thomas, *Proc. Camb. Phil. Soc.* 23:542 (1926).
49. R. Latter, *Phys. Rev.* 99:150 and 1854 (1955).
50. N. H. March, "Self-consistent Fields in Atoms", Pergamon Press, Oxford, p. 72 (1975).
51. E. K. U. Gross and J. Rafelski, *Phys. Rev.* A20:44 (1979).
52. P. Schlüter, G. Soff, and W. Greiner, *Phys. Rep.* 75:327 (1981).
53. P. Schlüter and G. Soff, *Atomic Data and Nuclear Data Tables* 24:509 (1979).
54. G. Soff, B. Müller, and W. Greiner, *Z. Physik A* 299:189 (1981).
55. R. Anholt and J. O. Rasmussen, *Phys. Rev.* A9:585 (1974).
56. G. Soff, P. Schlüter, and W. Greiner, *Z. Physik A*, in print; GSI 81-23 preprint, Darmstadt (1981).
57. R. J. Lombard, Ch. F. Perdrisat, and J. H. Brunner, *Nucl. Phys.* A110:41 (1968).

## SPECTROSCOPY OF SUPERHEAVY QUASIMOLECULES

G. Soff<sup>1</sup>, T. de Reus<sup>2</sup>, U. Müller<sup>2</sup>, J. Reinhardt<sup>2</sup>,  
P. Schlüter<sup>2</sup>, K.H. Wietschorke<sup>2</sup>, B. Müller<sup>2</sup>, and  
W. Greiner<sup>2</sup>

<sup>1</sup>Gesellschaft für Schwerionenforschung mbH  
Planckstraße 1, Postfach 11 05 41  
D-6100 Darmstadt 11, West Germany

<sup>2</sup>Institute für Theoretische Physik der  
Johann Wolfgang Goethe-Universität  
Robert-Mayer-Straße 8-10, Postfach 111 932  
D-6000 Frankfurt am Main, West Germany

### ABSTRACT

A systematical investigation of  $1s\sigma$ -ionization probabilities and  $\delta$ -electron production rates in heavy ion collisions is performed. We present their charge dependence from  $Z_1+Z_2=134$  up to  $Z_1+Z_2=184$  and compare our results with recent experimental data. The influence of electron screening on vacancy formation and the possibility to use  $\delta$ -electron spectra in collisions with nuclear sticking as an 'atomic clock' are also discussed. Strong magnetic fields ( $|B_{\text{max}}| \sim 10^{16}$  G) in heavy ion collisions are expected to cause spin polarizations of the  $1s\sigma$ -vacancies and emitted  $\delta$ -electrons in the order of 5-10%.

### INTRODUCTION

Collisions of very heavy ions with bombarding energies close to the Coulomb barrier offer us the possibility to perform a spectroscopy of electronic states in transient superheavy systems within a charge range of  $100 \leq Z \leq 190$  ( $^{92}\text{U} + ^{98}\text{Cf}$ ).

The pivotal question to answer is whether the binding energy of the strongest bound electronic state can reach or exceed the electron rest mass.

An important task in this connection is the investigation of electron excitation processes in superheavy systems. Two possible excitation mechanisms are visualized in Fig. 1. As an example we consider the schematic level structure for a head-on collision of Pb + Cm with a total charge  $Z = 178$  at 5.9 MeV/u bombarding energy. Binding energies of the adiabatic  $1s\sigma$  - and  $2s\sigma$ - states<sup>1</sup> are displayed versus the internuclear separation  $R$ . The turning point between incoming and outgoing trajectory is given by  $R_{\min} = 17$  fm.

A typical one-step excitation process is the direct ionization from the  $1s\sigma$ - state to the positive continuum. In addition the multi-step processes play an important role. Actually they form the dominant part of inner shell vacancy production probabilities. An example for a two-step process is depicted in Fig. 1, where a  $2s\sigma$ - electron is ionized to the continuum. The remaining hole is filled by the  $1s\sigma$ - electron which leaves a vacancy in the K-shell. Since initial and final state of both processes are indistinguishable, they have to be treated coherently. This is achieved by solving coupled channel equations for the electron occupation amplitudes of the quasimolecular adiabatic states.

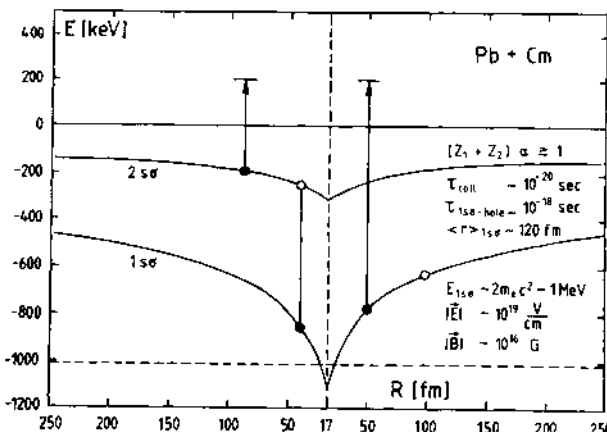


Fig. 1. Binding energies of the  $1s\sigma$  and  $2s\sigma$  state versus internuclear separation for the Pb+Cm system. One-step and two-step electron excitation processes are indicated qualitatively. On the right hand side characteristic numbers describing the collision are given.

A typical feature in collisions of very heavy ions is the shrinkage of the  $1s\sigma$ - wavefunction at shortest internuclear distances. Sticking to our example  $\text{Pb} + \text{Cm}$  at  $E_{\text{lab}} = 5.9 \text{ MeV/u}$  we find a radial expectation value for the  $1s\sigma$  orbital of about 120 fm at the distance of closest approach.

Due to this extreme localization (within the Compton wavelength of an electron,  $\lambda_e = 386 \text{ fm}$ ) transfer of high momenta components to the strongly bound electrons resulting from the nuclear motion becomes possible. Therefore  $\delta$ -electrons up to kinetic energies of 2 MeV can be observed experimentally<sup>2</sup>, whereas the classically allowed maximum energy transfer to an electron at rest is about 10 keV.

After a short theoretical survey in Chapter 2 we present the systematics of the  $1s\sigma$ -binding energies, K-vacancy formation and  $\delta$ -electron production (Chapter 3) with respect to the total nuclear charge  $Z$ . In Chapter 4 the experimental vacancy production rates are compared with our coupled channel results. The influence of an initially unsharp Fermi surface and electron screening on K-hole production is discussed in Chapter 5.

We compare measured  $\delta$ -electron cross sections of superheavy systems with our calculations in Chapter 6.

In collisions where the combined nuclear charge  $Z_1 + Z_2$  exceeds 174 the  $1s\sigma$ -state is expected to 'dive into' the negative energy continuum. The very strong time-varying Coulomb field which causes this effect amounts to about  $10^{19} \text{ V/cm}$ . Furthermore the nuclear motion is a source of an extremely strong magnetic field in the order of  $10^{16} \text{ G}$ . The consequences of this fact which causes a partial polarization of K-holes and emitted  $\delta$ -electrons<sup>3</sup> are discussed in Chapter 7.

## THEORETICAL FUNDAMENTALS

In this chapter we summarize the essential equations upon which our calculations are based. We emphasize that in superheavy quasi-molecules a fully relativistic treatment of the electron motion is absolutely necessary since the combined charge  $Z = Z_1 + Z_2 \gtrsim 1/\alpha$  and the electron binding energies become comparable with the electron rest mass or even exceed it.

In a completely adiabatic picture electronic binding energies and wave functions therefore have been evaluated by the stationary solutions of the two centre Dirac equation ( $\hbar = c = 1$ )

$$[\vec{\alpha} \cdot \vec{p} + \beta m_e + V_{\text{TC}} - E_n(R(t))] \phi_n(r, R) = 0 \quad (1)$$

with

$$V_{TC} = -z_1 e^2 / |\vec{r} - \vec{R}/2| - z_2 e^2 / |\vec{r} + \vec{R}/2| \quad \cdot \quad (2)$$

After expanding the two-centre potential of eq. (2) into multipoles and restricting ourselves to the dominant monopole part  $V_0$  we obtain two first-order coupled differential equations

$$\begin{aligned} d/dr u_1 &= -\kappa/r u_1 + (E + m - V_0) u_2 & , \\ d/dr u_2 &= - (E - m - V_0) u_1 + \kappa/r u_2 & , \end{aligned} \quad (3)$$

where  $u_1 = r \cdot g(r)$  and  $u_2 = r \cdot f(r)$ .

The radial dependence of the upper and lower components of a  $1s_0$ -wave function for a combined nuclear charge  $Z=169$  ( $Z\alpha > 1$ ) is shown in Fig. 2. A striking feature is the almost equal absolute amplitude of both components between 10 and 100 fm emphasizing the necessity to perform relativistic calculations.

If we want to describe the dynamical evolution of an electron involving two colliding nuclei we thus have to solve the time-dependent two-centre Dirac equation

$$i\partial/\partial t \Phi_i(\vec{R}(t)) = H_{TCD}(\vec{R}(t)) \Phi_i(\vec{R}(t)) \quad . \quad (4)$$

$H_{TCD}$  is the relativistic two-centre Hamiltonian which depends sensitively on the internuclear separation  $R(t)$ . For this reason it is

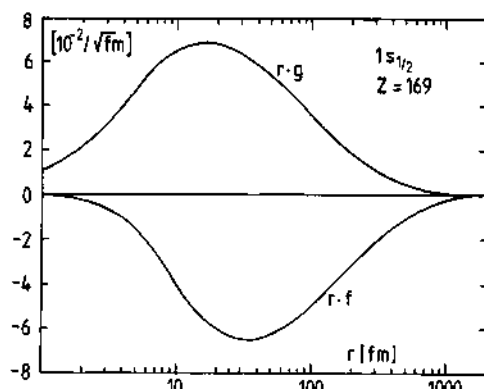


Fig. 2. Radial components of the  $1s_0$ -wave function for a total nuclear charge  $Z = 169$ .

useful to expand the total wave function  $\Phi_i$  into Born-Oppenheimer states  $\phi_n$  which are represented by the stationary molecular states of eq. (1). The expansion reads

$$\Phi_i(t) = \sum_j a_{ij}(t) \phi_j(\vec{R}(t)) \exp(-i\chi_j(t)) , \quad (5)$$

where the sum includes an integration over continuum states with positive and negative energies. The phase factors  $\chi_j$  are chosen as

$$\chi_j(t) = \int_0^t dt' \langle \phi_j(\vec{R}(t')) | H_{TCD}(\vec{R}(t')) | \phi_j(\vec{R}(t')) \rangle . \quad (6)$$

Inserting the expansion of eq. (5) into eq. (4) and projecting with stationary eigenfunctions of eq. (1) we obtain the following set of first-order coupled differential equations for the occupation amplitudes  $a_{ij}(t)$

$$\dot{a}_{ij}(t) = - \sum_k a_{ik}(t) \langle \phi_j | \partial/\partial t | \phi_k \rangle \exp\{+i(\chi_j - \chi_k)\} . \quad (7)$$

The time derivative operator can be expressed in terms of a radial and a rotational coupling

$$\partial/\partial t \rightarrow \vec{R} \cdot \partial/\partial \vec{R} - i\vec{w} \cdot \vec{j} . \quad (8)$$

Our calculations are restricted to radial couplings only.

Concerning the many electron problem we first state that the full time-dependent wave functions  $\Phi_i(t)$  form a complete and orthogonal basis set at each time  $t$ . This can be concluded from the unitarity of the time-development operator

$$\langle \Phi_j(t) | \Phi_i(t) \rangle = \delta_{ij} \quad (9)$$

or equivalently

$$\sum_i a_{ki}^* a_{li} = \sum_i a_{ik}^* a_{il} = \delta_{kl} . \quad (10)$$

Therefore the set  $\Phi_i(t)$ , already containing the dynamical excitations, can be used as a basis for solving the many-particle problem. To do this, one can expand the total wave function in a basis of many-electron configurations which may be represented by Slater determinants of the single particle basis functions  $\Phi_i$ . The amplitude for exciting a final configuration starting from a given initial configuration turns out to be just the determinant of the corresponding single-particle amplitudes  $a_{ij}(t)$ .

Therefore the number of physical particles  $p$  or holes  $q$  in a particular level can be deduced completely from the single-particle amplitudes

$$N_p = \sum_{r < F} |a_{rp}|^2 \quad \text{for } p > F , \quad (11)$$

$$N_q = \sum_{r>F} |a_{rq}|^2 \quad \text{for } q < F \quad . \quad (12)$$

$F$  denotes the Fermi surface of occupied states. For the number of correlated particle - hole pairs  $N_{p,q}$  one finds

$$N_{p,q} = N_p \cdot N_q + \left| \sum_{r < F} a_{rp}^* a_{rq} \right|^2 . \quad (13)$$

This formula should be applied to analyze experiments like those presently performed for coincidences between electrons and  $1s\sigma$ - vacancy formation. Eq. (13) holds also for particle-particle or hole-hole correlations if the sign of the second term is inverted.

The differential probability for the emission of an  $Es\sigma$ -  $\delta$ - electron with energy  $E$  and definite spin projection measured in coincidence with a  $1s\sigma$ - vacancy having the same spin projection is given by

$$(dP/dE)_{\text{coinc}} = \sum_{r < F} |a_{r,Es\sigma}|^2 (1 - \sum_{r' < F} |a_{r',1s\sigma}|^2) + \left| \sum_{r < F} a_{r,Es\sigma}^* a_{r,1s\sigma} \right|^2 . \quad (14)$$

In coincidence experiments with a particle  $p$  and an additional hole  $q$  a problem arises from accidental coincidences since in measurements there is usually no distinction between a  $\delta$ - electron with spin up and a  $1s\sigma$ - vacancy with spin down.

In order to obtain the total number of particle-hole pairs we have to perform a summation before comparing with experimental data

$$N_{p,q}^{\text{tot}} = 2 (N_{p,q} + N_p \cdot N_q) , \quad (15)$$

where the last term describes accidental coincidences.

#### SYSTEMATICAL INVESTIGATION OF K-HOLE FORMATION AND $\delta$ - ELECTRON PRODUCTION

In this chapter we present our theoretical results for the inner-shell ionizations and  $\delta$ - electron production probabilities. An essential ingredient here is the precise knowledge about the  $1s\sigma$ - binding energy and wave function. Fig. 3a shows the dependence of  $1s\sigma$ - total energy on the internuclear separation  $R$  of two

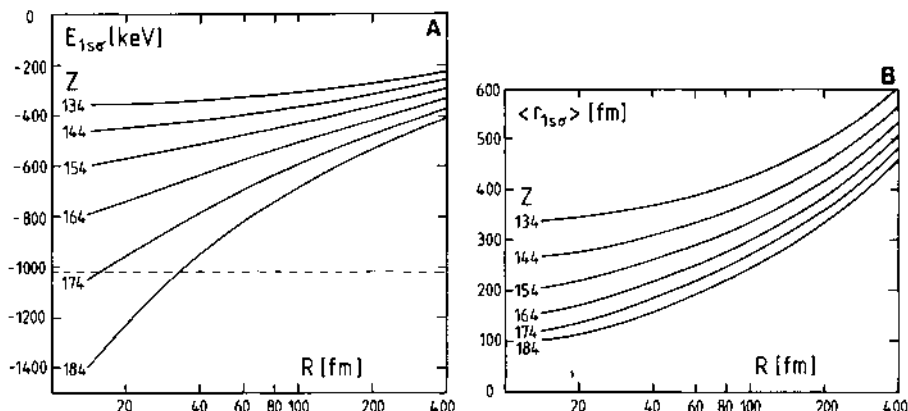


Fig. 3. (a) Binding energies of the  $1s\sigma$ - state in dependence on the internuclear separation  $R$  for various total charges  $Z$ . - (b) Corresponding radial expectation values  $\langle r_{1s\sigma} \rangle$ .

colliding nuclei in a semilogarithmical representation. The different curves belong to different united charges  $Z_1+Z_2$  denoted by  $Z=134$  to  $Z=184$ . We observe that the binding energy increases with decreasing nuclear distance, but it increases the more the heavier the system is. For the system U+U with united charge  $Z=184$  the binding energy rises by more than 1 MeV in the considered range of internuclear separation. Here we enter the truly relativistic region where relativistic effects are no longer a small perturbation, but dominate the behaviour of inner-shell electrons, cf. Fig. 2.

In Fig. 3b we have drawn the radial expectation value  $\langle r_{1s\sigma} \rangle$  of the  $1s\sigma$ - level in dependence on the internuclear separation  $R$  for combined charges  $Z=134$  up to  $Z=184$ . For fixed distance  $R$  the  $1s\sigma$ -wave function shrinks the heavier the systems are.

Binding energies as well as the radial expectation value  $\langle r_{1s\sigma} \rangle$  play an important, but contrary role when calculating K-hole formation and  $\delta$ - electron production. Whereas a strong increase in the binding energy hinders, e.g., the ionization of an electron from the K-shell - thus producing a K-hole and, eventually, a  $\delta$ - electron - the strong decrease of  $\langle r_{1s\sigma} \rangle$  leads to high Fourier frequencies in the pulse spectrum - thus stimulating K- shell ionization. Therefore one can predict a maximum for K-hole production rates,  $P_{1s\sigma}$ , around  $Z \sim 170$  (Fig. 4).

Subsequently we investigate this effect more systematically for K-hole formation as well as for  $\delta$ - electron production rates. For this purpose we evaluated K-vacancy production rates for various combined nuclear charges  $Z=134$  up to  $Z=184$ . We present coupled

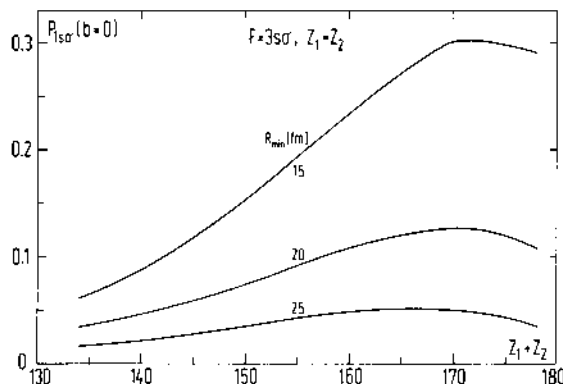


Fig. 4. The dependence of  $P_{1s0}(b=0)$  on total nuclear charge  $Z_1+Z_2$  in superheavy systems. Collisions with a distance of closest approach  $R_{\min} = 15, 20$ , and  $25$  fm are considered.

channel calculations stressing the  $Z$ - dependence of  $P_{1s0}(b)$  in Fig. 5. Part a shows K-hole production rates for charges  $Z \leq 164$ . We observe an increasing slope with rising binding energy. Vacancy formation increases especially for small impact parameters as a consequence of the sharp localized  $1s0^-$  state. The latter effect allows the transfer of high Fourier frequencies to the K-shell originating from the nuclear motion, thus leading to increased K-hole production.

In Fig. 5b combined nuclear charges beyond  $Z=164$  are considered. In this region the ionization probabilities decrease due to the extremely strong binding energy which amounts nearly twice the electron rest mass, reflecting the preceding remarks concerning Fig. 4.

Another observable quantity where the influence of  $1s0^-$  binding energies and the radial expectation value  $\langle r_{1s0} \rangle$  can be demonstrated is the differential emission probability of  $\delta^-$  electrons as a function of the kinetic electron energy. In Fig. 6  $\delta^-$  electron cross sections are displayed for systems with united charge  $Z=134$  up to  $Z=184$ . The  $\delta^-$  electrons have to be measured in coincidence with  $1s0^-$  vacancies according to eq. (14). In all calculations we chose a Fermi level of  $F=3s0$  and a bombarding energy  $E_{\text{lab}}=4.7$  MeV/u. Asymmetric systems are considered.

In the region of united charge  $Z < 164$  the  $\delta^-$  electron cross section rises with increasing  $Z$ . The high-kinetic part with  $E_{e^-} > 500$  keV grows faster than the low-kinetic one. This is due to the stronger localization of the  $1s0^-$  orbit which allows for high momenta transfer as described above. But if the united charge exceeds  $Z \sim 170$

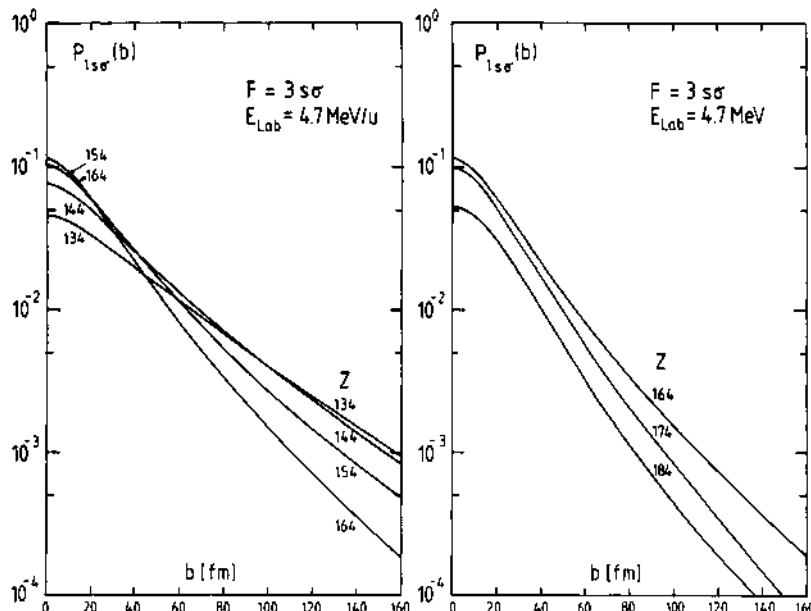


Fig. 5. Number of created  $1s\sigma$ - vacancies versus impact parameter  $b$ . The different curves belong to different total charges  $Z$ . Asymmetric systems are assumed. Part (a) for  $Z \leq 164$ , part (b) for  $Z \geq 164$ .

the influence of the rapidly increasing  $1s\sigma$ - binding energy becomes dominant. Thus the emission cross section even diminishes which is shown for  $Z=184$ .

Therefore it would be highly desirable to measure K-hole formation and  $\delta$ - electron cross sections more systematically in dependence on the united charge  $Z$  in order to verify the interplay of strong binding and sharp localization in ionization processes.

#### 4. VACANCY FORMATION IN COMPARISON WITH EXPERIMENTAL DATA

Now we turn to the discussion of K- and L- hole production in heavy and superheavy systems. According to eq. (12) we calculated the number of created  $1s\sigma$ - vacancies per collision for the systems Xe-Au at  $E_{\text{lab}}=4.7$  MeV/u and Xe+Pb at different bombarding energies. In our calculations we chose  $F=3$  corresponding to the last bound state occupied initially. The first measurements of K-hole probabilities were performed by Greenberg et al.<sup>4</sup> for Xe-Pb and Pb+U.

The results for Xe+Au are plotted in comparison with experimental data of D. Liesen et al.<sup>5</sup>, in Fig. 7a. We find fair agreement up to impact parameters  $b \leq 90$  fm. Beyond this value the measured data are underestimated.

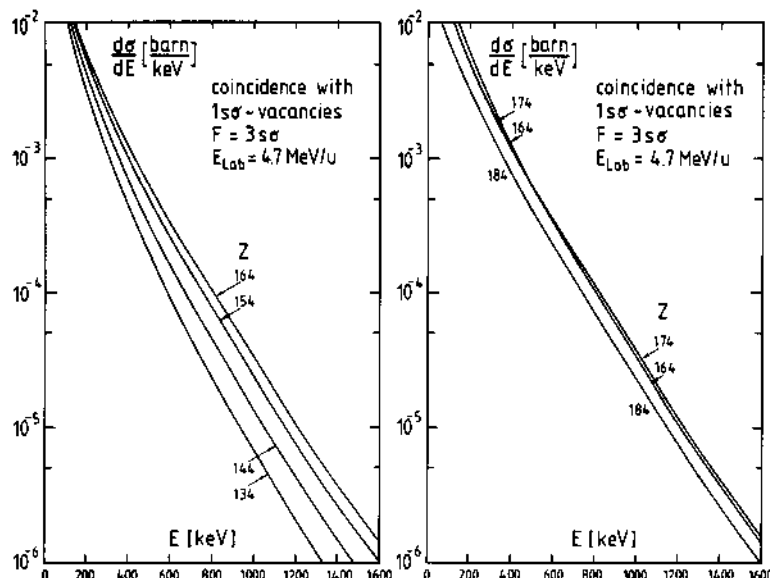


Fig. 6.  $\delta$ - electron distributions in coincidence with  $1s\sigma$ - vacancies versus the kinetic electron energy for different combined charges  $Z$ .

Similar agreement is achieved for the dependence on the bombarding energy  $E$  at fixed impact parameters  $b$  which is shown in Fig. 7b.

A system of comparable combined charge is Xe+Pb. Experimental data of Anholt et al.<sup>6</sup> are in remarkable agreement with our coupled channel results for  $P_{1s\sigma}(b)$  at  $E_{lab}=4.6$  MeV/u (solid line in Fig. 8a). At  $E_{lab}=7.2$  MeV/u we only find fair agreement for small impact parameters. Furthermore K-vacancy production within first order time-dependent perturbation theory is presented (dashed line). In comparison to our coupled channel results these values are off by a factor 3 - 5, stressing that it is indispensable to take into account multi-step excitations. Scaling laws<sup>7</sup> which are based on simplifying approximations within the framework of first-order time-dependent perturbation theory are useful to determine the dependence of  $1s\sigma$ -vacancy production on kinematical parameters  $\{b, E_{ion}\}$ . They fail, however, in predicting the measured data quantitatively.

A systematical investigation of vacancy formation should also comprise  $2p_{3/2}\sigma$ - hole measurements which are rarely available up to now. In Fig. 8b we also display  $2p_{3/2}\sigma$ - vacancy production rates for the system Xe+Pb versus the impact parameter at  $E_{lab}=3.6$  MeV/u choosing  $F=3p_{1/2}\sigma$ . The prevailing difference from K- vacancy rates is a drastic decrease of the slopes which stem - beside other things - from the increased spatial-extended  $2p_{3/2}\sigma$ - orbital. Since L-shell electrons have a smaller binding energy the concerning va-

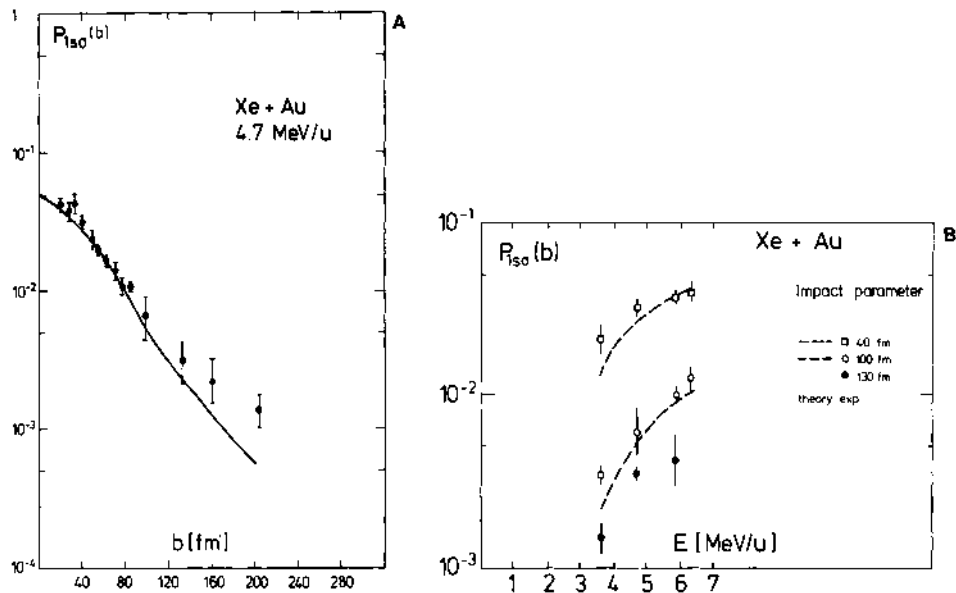


Fig. 7. (a) Number of created  $1s\sigma$ -vacancies per  $Xe+Au$  collision at 4.7. MeV/u laboratory energy as a function of impact parameter  $b$ . Also shown are experimental data of D. Liesen et al.,<sup>5</sup> (b) Bombarding energy dependence of the number of created  $1s\sigma$ -vacancies in the  $Xe+Au$  system<sup>5</sup> for some specific impact parameters.

cancy yields increase at fixed bombarding energy. The dashed lines indicate the effect of electron screening and are calculated by means of the model discussed in Chapter 5.

One of the heaviest systems accessible to experimental investigation concerning  $1s\sigma$ -ionization is  $Pb+Cm$  with a combined nuclear charge of  $Z_1+Z_2=178$ . In Fig. 9a we compare our results with experimental data of D. Liesen et al.<sup>6</sup>. Calculations including multi-step excitation processes are indicated by the full line.  $F=4s\sigma$  is assumed. In order to estimate the effect of electron screening we use reduced binding energies adjusted to the Hartree-Fock values<sup>9,10</sup> known in the limits  $R \rightarrow 0, \infty$  while retaining the coupling matrix elements. A considerable increase of  $P(b)$  is found, shown by the dashed lines in Fig. 9. At  $E_{lab}=5.9$  MeV/u the results with reduced binding energies are in fair agreement with experiment except for small impact parameters and values  $b \geq 90$  fm. Calculations for  $Pb+Cm$  including matrix elements which are determined by Hartree-Fock wave functions are in progress. However, it is not expected that the new results will deviate drastically from the corrected values presented here.

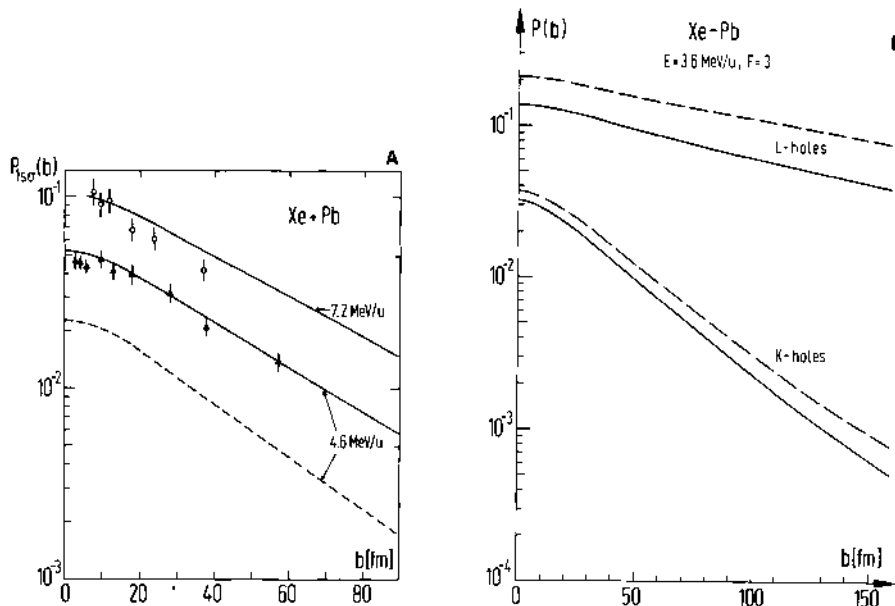


Fig. 8. (a)  $1s0^-$  vacancy production rates in a  $Xe+Pb$  collision at 4.6 MeV/u and 7.2 MeV/u versus impact parameter  $b$ . (solid lines). Also indicated is a result obtained within first-order time-dependent perturbation theory (dashed line). The experimental data are taken from Anholt et al.<sup>6</sup> (b) The same system investigated at  $E_{lab}=3.6 \text{ MeV/u}$ ,  $2p_{1/2}^{0-}$  and  $1s0^-$  vacancy production rates are compared. Results including electron screening are indicated by dashed lines.

Fig. 9b shows  $P_{1s0}(b)$  for the smaller bombarding energy  $E_{lab}=3.6 \text{ MeV/u}$ . Beside a consistent underestimation of the ionization probability for small impact parameters and values of  $b > 90 \text{ fm}$  (compare Fig. 7a with Fig. 9a) we now find a clear discrepancy between calculated and measured data. In order to clarify this deviation it would be desirable to obtain also  $\delta$ -electron spectra in coincidence with characteristic  $Cm - K - X$ -rays in dependence on  $b$ . Although screening effects cannot account for this discrepancies it is necessary to incorporate them into future calculations. For a further discussion of screening effects we refer to Chapter 5.

Another essential point to be considered is the influence of two-centre effects like translation factors and level crossings. If we want to incorporate them it is indispensable to evaluate the exact two-centre continuum states.

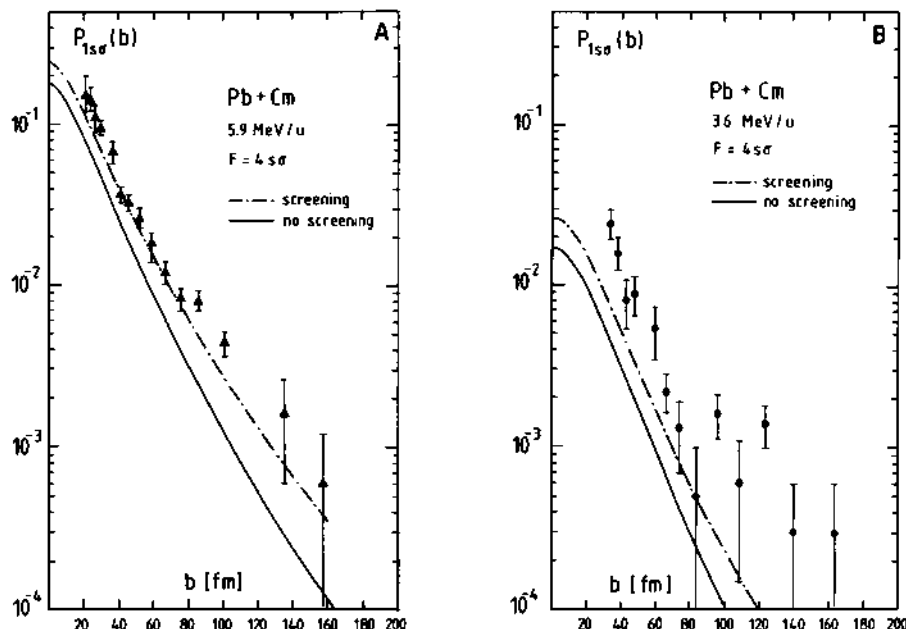


Fig. 9. (a) The system Pb+Cm is investigated concerning K-holes at 5.9 MeV/u lab energy. The dashed-dotted line represents results where the binding energies have been modified to include electron screening corrections. (b) The same as in part a for 3.6 MeV/u. Experimental data are taken from Ref. 8.

#### THE EFFECTS OF AN INITIALLY STATISTICAL OCCUPATION AND OF ELECTRON SCREENING ON VACANCY PRODUCTION

Comparing the measured K-hole production rates of the system Pb+Cm at 5.9 MeV/u with our theoretical predictions, represented by the solid line in Fig. 10a, one observes an overall slight underestimation of the experimental data. At lower bombarding energies (e.g.,  $E_{\text{lab}} = 4.7 \text{ MeV/u}$ ) the discrepancies between experiment and theory increased especially for small impact parameters.

We investigated the question, how a change in the initial electron distribution might modify the shape of the K-shell vacancy production.

For this purpose we assume the initial state  $|F_n\rangle$  to be a mixture of many-body states which are occupied<sup>11</sup> with a possibility  $w_n$  instead of being clearly distinguishable states filled up to a certain Fermi level. We express the number of particles in a level

p by means of the creation and annihilation operators for particles

$$N_p = \sum_n w_n \langle F_n | \hat{b}_p \hat{b}_p^\dagger | F_n \rangle = \sum_n w_n \sum_{r \in F} |a_{rp}|^2 \quad (16)$$

where  $a_{rp}$  are the expansion coefficients used in eq. (7). The occupation probabilities  $w_n$  can be taken from statistical mechanics if we demand our system to be in a thermal equilibrium at  $T=\text{const}^{12}$

$$w_i = \frac{\exp \{-\beta (E_i - \mu N_i)\}}{\sum_n \exp \{-\beta (E_n - \mu N_n)\}} = \rho_i / Z \quad (17)$$

Here  $\beta = 1/kT$  is the inverse temperature,  $\mu$  the chemical potential and  $N_i$  the number of particles in the many-body level  $i$ . The grand distribution function  $\rho_i$  is expressed by

$$\rho_i = \langle F_i | \hat{\rho} | F_i \rangle, \quad \hat{\rho} = \exp \{-\beta (\hat{H} - \mu \hat{N})\}. \quad (18)$$

Thus

$$w_i = \langle F_i | \hat{\rho} | F_i \rangle / (\text{tr} \hat{\rho}), \quad (19)$$

since  $Z = \text{tr} \hat{\rho}$ .

Requiring a system of noninteracting fermions, i.e.  $\{\hat{b}_k^\dagger, \hat{b}_j\} = \delta_{kj}$ , for which we denote the grand distribution function as  $\rho_i^0$ , one obtains

$$\rho_i^0 = \langle F_i | \exp \{-\beta \sum_k (\epsilon_k - \mu) n_k^1\} | F_i \rangle. \quad (20)$$

$n_k^1$  has the meaning of an occupation factor for the  $k^{\text{th}}$  level in the many-body state  $i$  (0 or 1) and  $\mu$  now indicates the Fermi energy. Using eqs. (19) and (17) we arrive at

$$w_i = \frac{\prod_k \exp \{-\beta (\epsilon_k - \mu) n_k^1\}}{\prod_k (1 + \exp \{-\beta (\epsilon_k - \mu)\})}. \quad (21)$$

For the number of particles and holes in the levels p and q one obtains<sup>11</sup>

$$N_p = \sum_r |a_{rp}|^2 (1 + \exp \{\beta (\epsilon_r - \mu)\})^{-1}, \quad (22)$$

$$N_q = \sum_r |a_{rq}|^2 (1 + \exp \{-\beta (\epsilon_r - \mu)\})^{-1}. \quad (23)$$

Eqs. (22) and (23) reproduce the familiar results<sup>13</sup> for vanishing temperature  $T=1/k\beta \rightarrow 0$ . These expressions are restricted to noninteracting fermions but remain valid in cases where the interaction can be described by a mean potential.

Using eq. (23) we investigated the behaviour of K-vacancy production rates for the system Pb+Cm at bombarding energies of  $E_{\text{lab}} = 5.9 \text{ MeV/u}$  and  $4.7 \text{ MeV/u}$  at different temperatures  $T$ .

The full line in Fig. 10a indicates calculations of Refs. 13,14; although including multi-step excitation processes the experimental data are still underestimated. 'Switching on' temperature a general increase of the K-vacancy production can be observed. In Fig. 10a the curve for  $kT=12 \text{ keV}$  fits quite well the experimental data of Ref. 8 but the discrepancies at small impact parameters  $b$  still remain. They aggravate with decreasing bombarding energy as displayed in Fig. 10b. In both pictures we observe a flattening of the curves with rising temperature at high impact parameters causing an overestimation of the experimental data. In our model this is caused by those K-holes which are already present before the collision of the two heavy ions takes place, since they are generated by the Fermi distribution of eq. (23). These curves at very high temperatures are

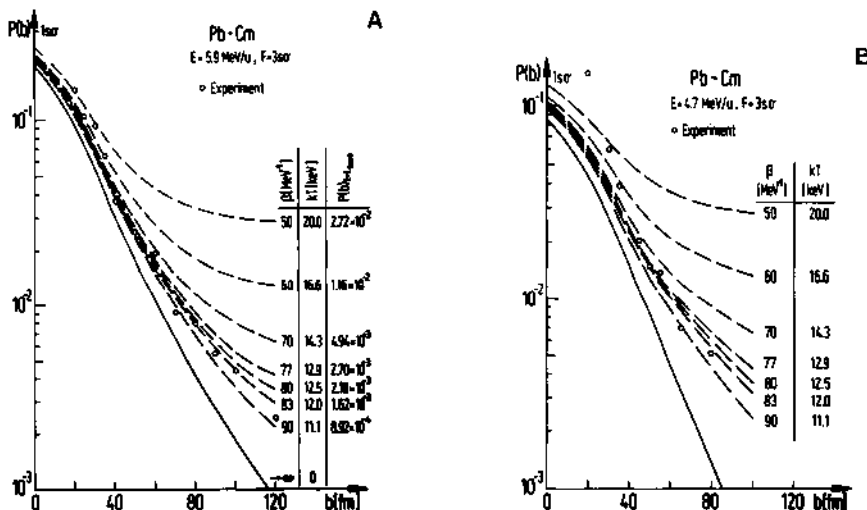


Fig. 10. (a) The increase of  $1s0^-$  vacancy production with rising temperature  $T$  for the system Pb+Cm at  $E_{\text{lab}} = 5.9 \text{ MeV/u}$  is indicated by the dashed lines. Numbers of K-holes initially present due to eq. (23) are listed in the third column. Also shown are experimental data of Ref. 8. The full line is obtained without temperature modification. (b) The same as before but at smaller bombarding energy  $E_{\text{lab}} = 4.7 \text{ MeV/u}$ .

of course not realistic because they result from K-vacancy probabilities up to  $2.7 \cdot 10^{-2}$  initially present. But even in such cases the strong increase at small impact parameters cannot be reproduced.

Therefore this simple ansatz of an initially statistical Fermi surface due to a temperature-dependent occupation distribution surely is inapt to account for the deviations between theoretical predictions and experimental data concerning K-vacancy production rates at small impact parameters.

However we can see that the slopes of  $P_{150}(b)$  in Fig. 10 are reproduced quite well for distant collisions ( $b > 40$  fm) assuming a temperature of  $kT \sim 12$  keV. Probably this is an indication for K-holes initially present due to thermal excitation.

Referring to the preceding remarks it appears desirable to find out the influence of electron screening effects on vacancy production rates. From common sense an increase of K-hole formation is expected.

The most simple ansatz for describing screening is the non-relativistic Thomas-Fermi model which can serve to discuss the main trend of the electron-electron interaction. According to Ref. 15 the semiclassical electron density becomes

$$\rho(r) = 1/3\pi^2 \hbar^3 (2m)^{3/2} (E_F - v_{\text{eff}}(r))^{3/2}. \quad (24)$$

$v_{\text{eff}}$  contains the Coulomb potential and the electron-electron interaction part. From a variational principle one minimizes the total energy and finds  $E_F = -\lambda$ , where  $\lambda$  is a Lagrange multiplier taking into account the conservation of the total particle number.  $E_F$  can be recognized as the chemical potential at vanishing temperature  $T=0$ . Thomas and Fermi chose the ansatz

$$v_{\text{eff}}(r) = v_n + v_{ee} = -Ze^2/r \Phi(r), \quad (25)$$

which is the limit for extended nuclei if  $r > R_+$ , cf. eq. (29).  $\Phi(r)$  denotes the screening function. Inserting this into the Poisson equation one is led to the non-relativistic Thomas-Fermi equation

$$d^2/dr^2 \Phi(r) = \Phi(r)^{3/2}/\sqrt{r}. \quad (26)$$

The dimensionless variable  $x$  is defined by eq. (30). In our calculations we used an approximation proposed by Latter<sup>16</sup>

$$\Phi(x) = \left( \sum_{j=0}^6 a_j x^{j/2} \right)^{-1}, \quad (27)$$

where  $a_j$  are familiar constants<sup>17</sup>.

The asymptotic behaviour of  $\phi(x)$  reads

$$\phi(0) = 1 \quad , \quad \phi(x \gg 1) \sim x^{-3} \quad , \quad \phi''(x \ll 1) \sim x^{-1/2} \quad .$$

Thus

$$\rho(x \ll 1) \sim x^{-3/2} \quad , \quad \rho(x \gg 1) \sim x^{-6} \quad (28)$$

$\phi(x)$  is valid for pointlike nuclei and yields vanishing screening for  $x \rightarrow 0$  which is wrong for extended nuclei. For supercritical systems we achieve finite screening at the origin with eq. (29).

Another problem arises from the non-relativistic treatment, but fortunately it was shown<sup>18</sup> that the electron exchange terms nearly cancel the relativistic corrections for large  $Z$ . Therefore in the case of large nuclear charges the non-relativistic TF-model should be a reasonable approximation with the exception of small inter-nuclear distances.

We investigated the systems Xe+Pb and Pb+U using eq. (27). Taking into account electron-electron interaction it was necessary to evaluate modified wave functions using eq. (1) with the potential for extended nuclei multiplied by the screening function of eq. (25). The dominant changes in binding energies and matrix elements  $\langle \phi_i | \partial/\partial R | \phi_k \rangle$  can be briefly summarized as follows:

a) For bound states we find a strong decrease of the binding energies with increasing main quantum number (Fig. 11a) due to the reduced Coulomb attraction. This causes a reduction of the transition probabilities, e.g., between the  $1s0$ -state and weaker bound levels as shown in Fig. 11b.

b) The probability-density for positron wave functions of low kinetic energy increases drastically in the vicinity of the centre of charge origin. Transitions involving such states therefore yield larger matrix elements.

c) Since screening causes smaller binding energies the  $1s0$ -level does not 'dive' into the negative energy continuum as deep as it would do in the case of a pure Coulomb potential.

Inserting these binding energies and matrix elements into the coupled channel equations we evaluated K- and L- vacancy production rates for the systems Xe+Pb and Pb+U at different bombarding energies choosing a Fermi level  $F=3$ . Referring to an impact parameter range  $0 \leq b \leq 20$  fm we find an increase of about 13% for K- and L- hole production at  $E_{lab}=5.9$  MeV/u considering the system Pb+U (Fig. 12a).

The same system was also investigated at  $E_{lab}=3.6$  MeV/u and

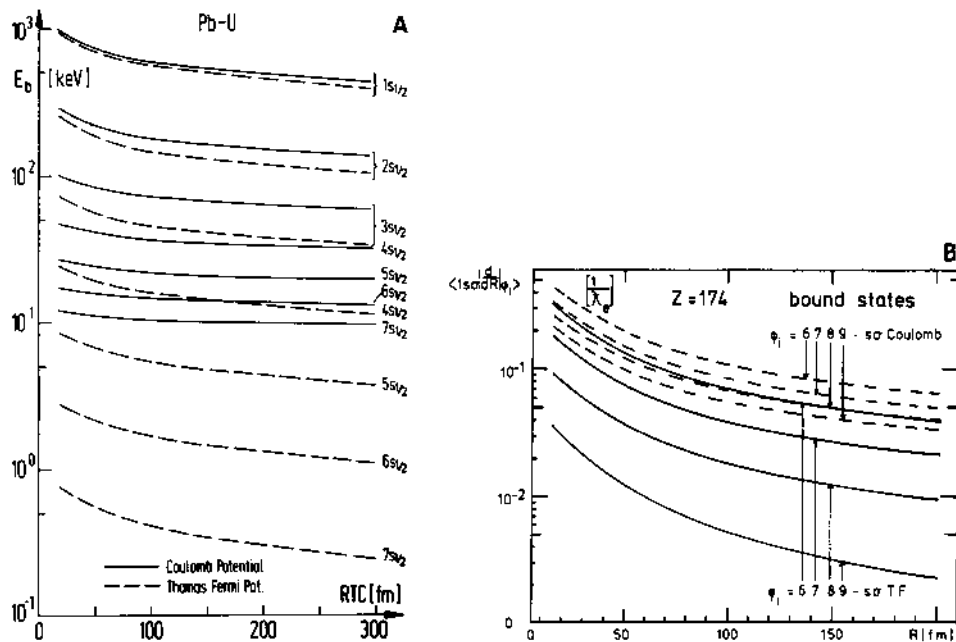


Fig. 11. (a) Binding energies for bound states versus internuclear separation  $R$  for total nuclear charge  $Z=174$ . The dashed lines indicate results including electron screening.  
 (b) Radial coupling matrix elements between bound states for the same system. Now the full lines indicate calculations obtained by the potential of eq. (25).

$E_{\text{lab}}=8.9$  MeV/u. We find that the higher the lab energy is chosen the weaker the screening effects turn out. Since at high bombarding energies the inner-shells play a dominant role this is plausible, because the TF-potential hardly changes the transitions between. e.g.,  $1s0^-$  and  $2s0^-$  states.

We also observe a decreasing slope with increasing impact parameter as a result of the reduced binding energies for weaker bound states.

Another important feature of screening is its different influence on  $s$ - and  $p$ - states which emerges especially at lower combined charge  $Z$ . Calculations for the system Xe+Pb which were performed at  $E_{\text{lab}}=3.6$  MeV/u, 4.7 MeV/u, and 5.9 MeV/u will elucidate this point. Plotting the data for  $E_{\text{lab}}=4.7$  MeV/u (Fig. 12b) we find a tremendous increase of the  $2p_{1/2}0^-$ - vacancy production rates which exceed calculations using a pure Coulomb potential by about 40%. In contrast to this the  $1s0^-$  vacancy formation only rises by approx-

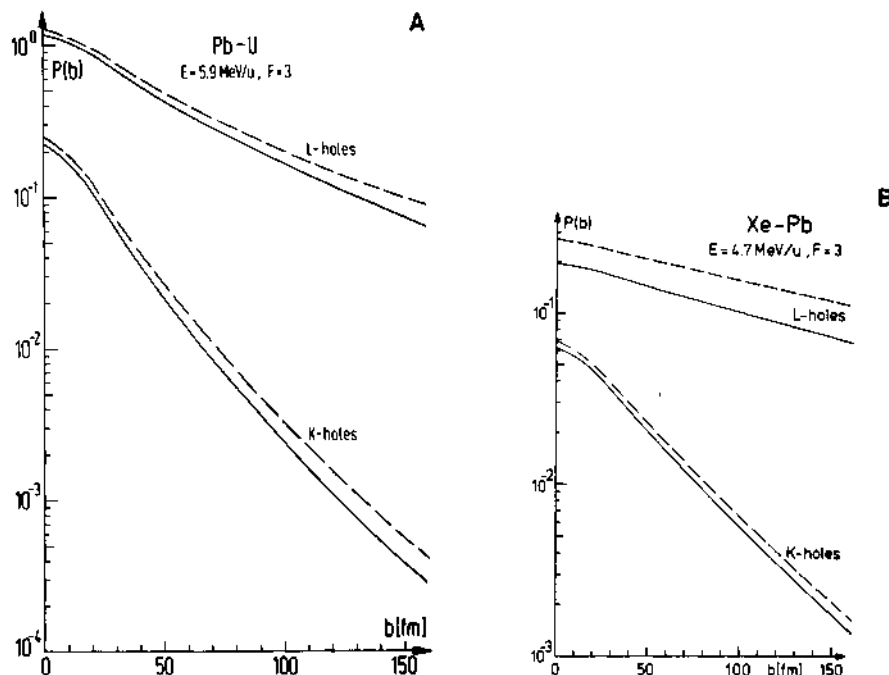


Fig. 12. (a) Comparison between  $\text{iso-}$  and  $2p_{1/2}\sigma$ -vacancy production rates for the system  $\text{Pb+U}$  at  $E_{\text{lab}}=5.9$  MeV/u. The results including electron screening are indicated by dashed lines. (b) The same as in part a, but for the lighter system  $\text{Xe+Pb}$  for  $E_{\text{lab}}=4.7$  MeV/u.

imately 10%. Thus it would be of great interest to have the opportunity of a comparison with experimental data, as one has for K-holes, in order to affirm or to reject this prediction.

It was already mentioned above that the simple non-relativistic Thomas-Fermi model for pointlike nuclei yields a vanishing screening function  $\Phi(x)$  at the origin. This can be circumvented by using the following modified potential

$$U(r, R) = \Phi(x) [1 - a(R)R_+/(r+R_+)] V_0(r, R) , \quad (29)$$

where  $V_0(r, R)$  is the monopole part of the two-centre potential and  $R_+ = R/2 + R_n$ .  $R$  denotes the two-centre separation and  $R_n$  the nuclear radius. The spatial distance is dimensionless according to

$$r = bx, \quad (30)$$

where

$$b = 1/4 (9\pi^2/2Z)^{1/3} a_0$$

and  $a_0$  denotes the Bohr radius.

For two-centre distances smaller than a critical value<sup>9,10</sup>  $R_{cr}$  the  $1s\sigma$ -state 'dives' into the negative continuum ( $E < -m_e c^2$ ). This occurs for the systems U+U and U+Cm. Therefore we have to apply the projection formalism developed in Ref. 11 in order to take into account also spontaneous couplings  $\langle \phi_{Ep} | H | \phi_R \rangle$ . We calculated K-hole production rates for the systems U+U at  $E_{lab} = 5.9$  MeV/u and U+Cm at  $E_{lab} = 5.8$  MeV/u using the potential of eq. (29), cf. Fig. 13. We again find an increase in K-hole formation for different Fermi surfaces  $F=2$  till  $F=4$ , respectively, by about 15-20%.

The increase of L-hole production due to screening is comparable to that of K-holes in contrast to the system K-Pb. By means of this feature one should be able to decide whether screening effects show up as have been discussed here. According to our results we expect notable deviations in  $2p_{3/2}\sigma$ -vacancy production rates for lighter systems like Xe-Pb.

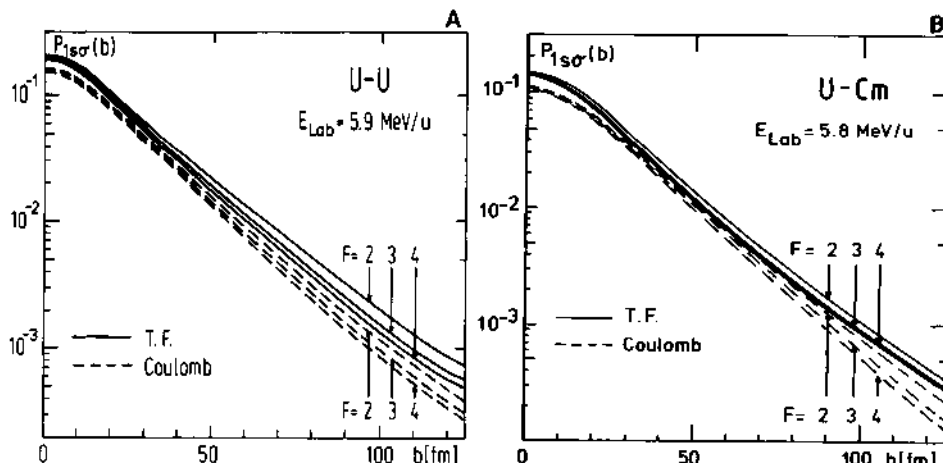


Fig. 13. (a) K-hole production in a U+U collision at  $E_{lab} = 5.9$  MeV/u is investigated choosing different Fermi levels  $F=2s\sigma$ ,  $3s\sigma$ , and  $4s\sigma$ , respectively, and is compared to results obtained with the potential of eq. (29), denoted by full lines. (b) As in part a, but for U+Cm at  $E_{lab} = 5.8$  MeV/u.

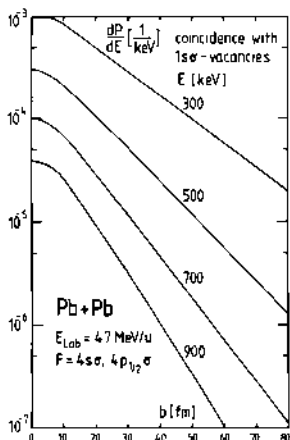


Fig. 14. Production probabilities with  $1s\sigma$ -vacancies versus impact parameter  $b$ , considering a  $\text{Pb}+\text{Pb}$  collision at  $E_{\text{lab}}=4.7$  MeV/u. The different curves belong to different kinetic electron energies.

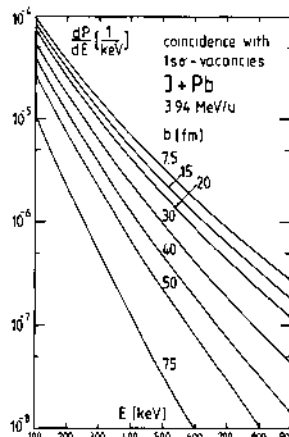


Fig. 15. As in Figure 14 but for the lighter system  $\text{J}+\text{Pb}$  at  $E_{\text{lab}}=3.94$  MeV/u.

#### δ- ELECTRONS - COMPARISON OF THEORETICAL PREDICTIONS WITH RECENT EXPERIMENTAL DATA

In this chapter we turn to the discussion of  $\delta$ - electron emission in superheavy collision systems. The differential production probability of  $\delta$ - electrons measured in coincidence with a  $1s\sigma$ - vacancy is displayed in Fig. 14 as a function of the classical impact parameter  $b$ . The superheavy system  $\text{Pb}+\text{Pb}$  at  $E_{\text{lab}}=4.7$  MeV/u is under investigation. The various curves correspond to different electron energies  $E_e=300, \dots, 900$  keV. For  $b \geq 15$  fm the curves show an exponential fall-off, which is steepest for the highest energy  $E$ . At smaller impact parameters the curves pitch down. As initial bound states we take into account the  $1s\sigma$ - up to the  $4s\sigma$ - state and the  $2p_{1/2}\sigma$  - up to the  $4p_{1/2}\sigma$  - level, which is denoted by the Fermi level  $F$ . However, one should state that also higher bound states may lead to a considerable contribution in the  $\delta$ - ray spectrum.

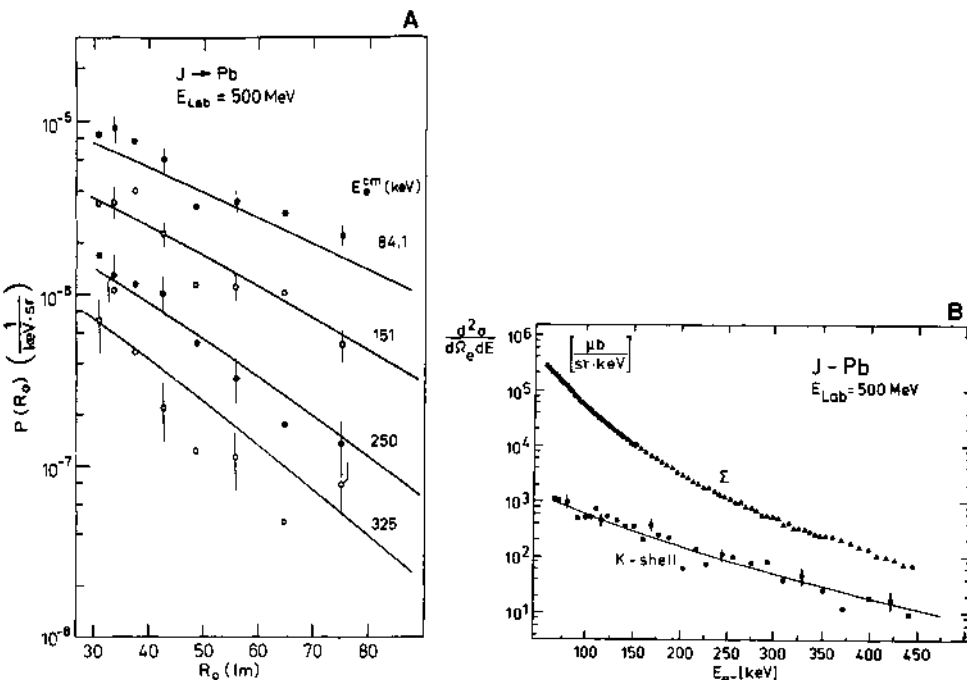


Fig. 16. (a) Triple coincidence measurements<sup>19</sup> (scattering angle,  $\delta$ - electron energy, and K- hole formation) of  $\delta$ - electrons versus  $R_0 = R_{\min}$  in the system J+Pb at  $E_{\text{lab}} = 500$  MeV. Different curves belong to different kinetic electron energies. (b) Total  $\delta$ - electron distribution (triangles) and  $\delta$ - electrons in coincidence with K- vacancies for the same system versus kinetic electron energies are results of Ref. 19. The latter data are compared with absolute values of coupled channel calculations.

For the J+Pb system with  $Z_1 + Z_2 = 135$  the  $\delta$ - electron spectra are shown as a function of the kinetic electron energy at various impact parameters  $b = 7.5$  fm up to  $b = 75$  fm (Fig. 15). The dependence is again of exponential form and less steep for more central collisions.

A comparison with experimental data is presented in Fig. 16 for the system J+Pb,  $E_{\text{lab}} = 500$  MeV. Part a shows a triple coincidence measurement (scattering angle,  $\delta$ - electron energy, and K- hole formation) by W. König, C. Kozuharov et al.<sup>19</sup>. Good agreement is achieved for all cm- kinetic electron energies and for all impact parameters. In part b the double differential electron cross section  $d^2\sigma/d\Omega dE$  is

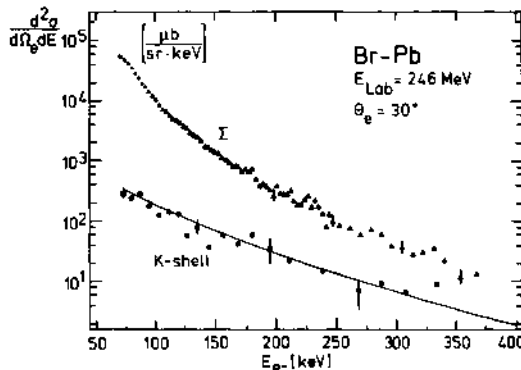


Fig. 17. The system Br+Pb at  $E_{\text{lab}} = 264$  MeV is under investigation with respect to the total  $\delta$ - electron distribution (triangles) and  $\delta$ - ray emission in coincidence with 1 $\sigma$ - vacancies. The double differential cross section is displayed versus the kinetic electron energy and compared with coupled channel results for the coincidence measurement.

displayed<sup>19</sup>. The triangles denote the total spectrum of emitted  $\delta$ - electrons. The experimental data representing coincidence measurements with K- vacancies are in overall agreement with our theoretical calculations. Also for the lower Z- system Br+Pb fair agreement with the measured data of Ref. 19 is achieved (Fig. 17).

The  $\delta$ - electron distribution of the system Pb+Sn in coincidence with 1 $\sigma$ - vacancies is displayed in Fig. 18. For comparison with experimental data of Kozhuharov et al.<sup>20</sup> we divided our results by  $4\pi$  assuming a spherical symmetric angular distribution of the  $\delta$ - ray emission. The latter assumption was verified experimentally<sup>20</sup>. We obtain a theoretical cross section which slightly underestimates the measured data.

In a last comparison with experimental results we show total  $\delta$ - electron production rates for a Pb+Pb collision<sup>14,21,22</sup> (Fig. 19). Again the experiment exceeds the theoretical values by about a factor of three. It could be that higher bound states yield considerable contributions to the electron spectrum. Also the modification of the binding energies due to electron screening is expected to shift the theoretical predictions towards higher kinetic energy.

On the other hand it should be noted that all calculations agree with the exponential slope of the energy distribution of emitted electrons found experimentally, cf. Figs. 16-19. In general better agreement is achieved if the  $\delta$ - electrons are measured in coincidence with K- vacancies of the heavier collision partner in asymmetric

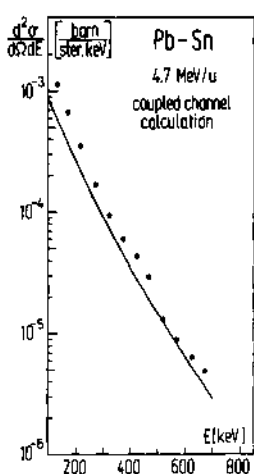


Fig. 18.  $\delta$ -ray spectrum for the Pb+Sn system which should be measured in coincidence with  $1s\sigma$ -vacancy formation. The data are divided by  $4\pi$  and compared with measurements of Kozhuharov et al.<sup>20</sup>. The experimental error bars are not drawn.

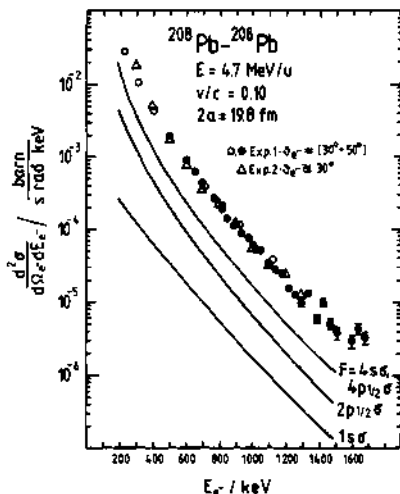


Fig. 19. Total  $\delta$ -electron distribution versus kinetic electron energy for the Pb+Pb quasimolecule as well as the various portions of the  $1s\sigma$ - and  $2p_{1/2}\sigma$ - initial bound states. Comparison with experimental data of C. Kozhuharov et al.<sup>20</sup>.

systems.

Finally we discuss the influence of a nuclear time delay in deep - inelastic heavy - ion reactions on  $\delta$ - electron spectra<sup>23,24</sup>. To determine the excitation amplitudes in delayed collisions, we make the simplest possible ansatz for the nuclear motion. The branches of two Rutherford hyperbolas having the same distance of closest approach  $R_{\min}$  are joined by a section without any radial motion. The delay time  $T$  is taken as a free parameter. The effect of the reaction then enters via an additional phase in the set of coupled differential equations (7) for the occupation amplitudes  $a_{ij}(t)$ .

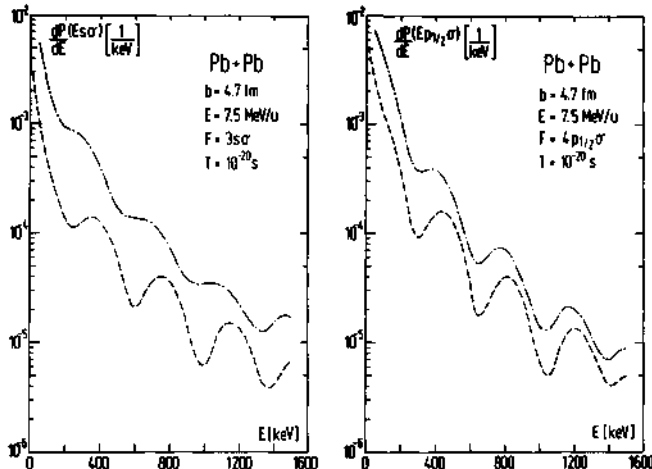


Fig. 20. Differential emission probability of  $\delta$ - electrons in dependence on the kinetic electron energy for the system Pb+Pb at  $E_{\text{lab}} = 7.5$  MeV/u and  $b = 4.7$  fm. A nuclear sticking time of  $T = 10^{-20}$  sec is assumed. In part a the dashed-dotted line denotes the total  $\delta$ - electron spectrum, whereas the dashed line indicates  $\delta$ - ray emission in coincidence with  $1s_0$ - vacancies choosing  $F = 3s_0$ . Part b shows the corresponding results for  $P_{1/2}^0$ -partial waves.

We calculate  $\delta$ - electron spectra in the heavy-ion collisions Pb+Pb, Pb+U, U+U, and U+Cm, where the nuclei stick together for about  $10^{-21}$  to  $10^{-20}$  sec. In a perturbation theoretical treatment the spectra will show interference patterns<sup>23,24</sup> with an energy width  $\Delta E = \hbar/T$ , which was confirmed by coupled channel calculations for the collision system Xe+Pb. Investigating heavier collision systems the predicted structure is increasingly suppressed. Fig. 20 shows the spectra of emitted  $\delta$ - electrons (left part s - contribution only, right part  $P_{1/2}^0$ -partial waves only) in a Pb+Pb collision at  $E_{\text{lab}} = 7.5$  MeV/u,  $b = 4.7$  fm, choosing a delay time  $T = 10^{-20}$  sec. The bound states are assumed to be initially occupied up to  $3s_0$ ,  $4p_{1/2}^0$ , respectively. The dashed-dotted lines denote the total spectra, the dashed ones display  $\delta$ - electron distributions in coincidence with K- vacancy formation according to eq. (14).

Although the individual emission spectra remain oscillatory patterns, the superposition of the contributions from several electron shells destroy much of the structure contrary to the case of Xe+Pb. Therefore it is advantageous to measure  $\delta$ -electrons in coincidence with K-shell ionization. Under this condition the interference patterns should retain an amplitude sufficient to be observable even in very heavy collision systems if the reaction time is defined sharply enough and the severe nuclear background can be separated<sup>25</sup>.

#### SPIN POLARIZATION OF ELECTRONS BY STRONG COLLISIONAL MAGNETIC FIELDS

The strongest magnetic fields on a microscopic scale accessible to experimental observation are created<sup>26</sup> in heavy ion collisions with  $(Z_1+Z_2)\alpha > 1$ . The maximum magnetic field strength may reach values in the order of  $|B_{\max}| = 10^{16}$  G.

In superheavy quasimolecules the  $1s\sigma$ -electron moves almost adiabatically close to the nuclei and is highly localized. Hence it may serve as a test particle for the high- $\vec{B}$  limit of Quantumelectrodynamics. The strong collisional magnetic fields cause a spin polarization of electrons which will be discussed in this chapter.

In the following discussion we neglect electron screening and retardation effects which should have only small influence on polarization<sup>27</sup>. We now have to solve the coupled channel equations (7) taking into account the scalar and vector potentials in the transverse Coulomb gauge. For this purpose we split the relativistic Hamiltonian into two parts,

$$H = H_0 + H' \quad (31)$$

where  $H_0$  is given in eq. (1).  $H'$  contains any interaction responsible for electron excitations which is not included in  $H_0$ . In the case of magnetic interactions it is given by

$$H' = -\vec{a} \cdot \vec{A} \quad (32)$$

with the vector potential  $\vec{A}$  created by the current of both colliding ions. Inserting the ansatz (5) into eq. (4) followed by projection leads to a set of first-order coupled differential equations for the occupation amplitudes  $a_{ij}(t)$ .

$$\dot{a}_{ij}(t) = -\sum_k a_{ik}(t) \{ \langle \phi_j | \partial/\partial t | \phi_k \rangle + i \langle \phi_j | H'(t) | \phi_k \rangle \} \exp(i\chi_{jk}) \quad (33)$$

with the phases

$$\chi_{jk} = \chi_j - \chi_k \quad . \quad (34)$$

In contrast to eq. (7) there occurs an additional magnetic interaction term resulting from the vector potential  $\vec{A}$  which reads in the Coulomb gauge

$$\begin{aligned}\vec{A}_C(\vec{r}, t) &= - \sum_{i=1,2} \frac{z_i e^2 \vec{v}_i(t)}{2 |\vec{r} - \vec{R}_i(t)|} - \\ &- \sum_{i=1,2} \frac{z_i e^2 \vec{v}_i(t) \cdot [\vec{r} - \vec{R}_i(t)] [\vec{r} - \vec{R}_i(t)]}{2 |\vec{r} - \vec{R}_i(t)|^3} \\ &= \vec{A}_C^{(1)} + \vec{A}_C^{(2)}.\end{aligned}\quad (35)$$

The corresponding result in the Lorentz-gauge  $\vec{A}_L(\vec{r}, t)$  becomes

$$\vec{A}_L(\vec{r}, t) = 2 \vec{A}_C^{(1)}(\vec{r}, t). \quad (36)$$

For simplicity we restrict our derivations to symmetric systems with

$$z_1 = z_2 = z \quad (37)$$

and use nuclear trajectories prescribed as Rutherford hyperbolas in the x-z plane, where the z-axis connects both nuclei. The matrixelements resulting from the interaction term in eq. (32) are evaluated in the monopole approximation since exact continuum solutions of the two-centre Dirac equation are unknown up to now. Due to selection rules or triangle rules we find that all contributions to couplings between s-states with the same magnetic quantum number just cancel in the Coulomb gauge

$$\langle s' \pm \frac{1}{2} | H'_{\text{Coulomb}} | s \pm \frac{1}{2} \rangle = 0. \quad (38)$$

This is different from the Lorentz gauge, where we obtain

$$\langle s' \pm \frac{1}{2} | H'_{\text{Lorentz}} | s \pm \frac{1}{2} \rangle = - \frac{2e^2}{3} i v_R \int_0^\infty r^2 dr \frac{r <}{r >} (fg' - f'g) . \quad (39)$$

However, also in this case there is no contribution to the Zeeman splitting: Due to the minus sign in the integrand of eq. (39) the diagonal matrix elements ( $s' = s$ ) vanish. For the spin flip transitions we find in summary the simple result

$$\langle s' \mp \frac{1}{2} | H' | s \pm \frac{1}{2} \rangle = \pm \frac{2e^2}{3} i v_\phi \int_0^\infty r^2 dr \frac{r <}{r >} (fg' + f'g) = \quad (40)$$

$$= \mp i A_{s', -, s, +} \quad (41)$$

which is the same in the Coulomb as well as in the Lorentz gauge. The only contributing rotational matrixelement in the monopole approximation leads to

$$\langle s\pm \frac{1}{2} | -i\vec{\omega} \cdot \vec{j} | s\pm \frac{1}{2} \rangle = \pm bv_\infty/2R^2 . \quad (42)$$

Up to now we only discussed the fate of a single electron influenced by the collision dynamics. In order to describe the many-electron problem the field operator  $\psi$  is expanded<sup>28</sup> in terms of the complete adiabatic basis states  $\phi_q$ . This leads us to expressions for the number operators of particles  $N_{q+}^Y$  and holes  $N_{q-}^Y$  with a given spin projection along a marked axis  $y$ . The spin polarization of holes  $q$  along the  $y$  axis is defined by

$$n_q = (N_{q+}^Y - N_{q-}^Y) / (N_{q+}^Y + N_{q-}^Y) \quad (43)$$

and correspondingly for particles

$$n_p = (N_{p+}^Y - N_{p-}^Y) / (N_{p+}^Y + N_{p-}^Y) . \quad (44)$$

Using symmetry, time-reversal-symmetry and completeness relations of the expansion coefficients  $a_{i+j\pm}$  to a given spin projection we can rewrite the two preceding equations into

$$n_q = \frac{2\text{Im} \left( \sum_{r < F} a_{q-,r+}^* a_{q-,r-} \right)}{\sum_{\substack{i=1 \\ r < F}} |a_{q-,r-}|^2 - \sum_{r < F} |a_{q-,r+}|^2} , \quad (45)$$

$$n_p = \frac{2\text{Im} \left( \sum_{r < F} a_{r-,p+}^* a_{r-,p-} \right)}{\sum_{\substack{r < F \\ r < F}} |a_{r-,p-}|^2 + \sum_{r < F} |a_{r-,p+}|^2} . \quad (46)$$

The solutions for a modified set of coupled channel equations<sup>3</sup> containing expressions for  $\dot{a}_{i+j+}$ ,  $\dot{a}_{i+j-}$ ,  $\dot{a}_{i-j-}$ ,  $\dot{a}_{i-j+}$  also take into account the rotational coupling eq. (42), the diagonal and off-diagonal magnetic interaction and as usual the radial coupling.

We only consider results for the collision Pb+Cm ( $Z_1+Z_2=178$ ) hence being the heaviest system investigated with respect to iso-ionization probabilities.

As a main result we found that the additional magnetic interaction does not change the total ionization probabilities but leads to spin polarization of electron states. The created polarization is preserved during the collision despite the importance of multi-step excitation processes. As dominant effect the Zeeman splitting of the iso- state gives rise to a stronger ionization of one of the usually degenerated spin states whereas the other becomes less

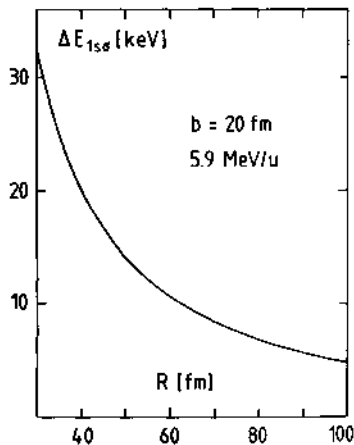


Fig. 21. Zeeman Splitting of the  $1s\sigma$ -state induced by the strong magnetic field in the collision system  $Z_1+Z_2=178$ .

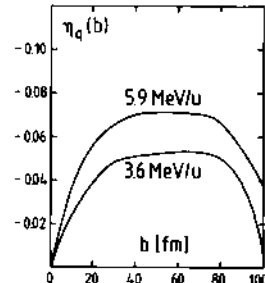


Fig. 22. Spin polarizations of  $1s\sigma$ -vacancies versus impact parameter  $b$ .  $E_{lab}=3.6$  MeV/u and 5.9 MeV/u, respectively.

ionized. However, the total sum remains almost exactly the same as obtained with the radial coupling only.

The Zeeman splitting of the  $1s\sigma$ - level as function of inter-nuclear separation  $R$  is given in Fig. 21 for a collision with  $E_{lab}=5.9$  MeV/u and  $b=20$  fm. Using eq. (41) it has been evaluated according to

$$\Delta E_{1s\sigma} = 2 |A_{1s+\sigma, 1s-\sigma}| . \quad (47)$$

At the distance of closest approach it reaches a maximum value of  $\Delta E(R=30 \text{ fm})=32 \text{ keV}$ .

The spin polarization  $\eta_q$  of created  $1s\sigma$ -vacancies has been calculated according to eq. (45). Its dependence on the impact parameter  $b$  is presented in Fig. 22. As can be seen,  $\eta_q=0$  for head-on collisions since the rotational velocity  $v_\phi$  is zero in this case. Its maximum is obtained for medium impact parameters between  $b=30$  and  $80$  fm. For larger impact parameters (distances) the magnetic field is too small in order to influence ionization processes. This theoretical prediction still needs experimental verification. The

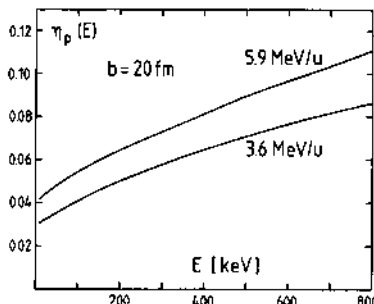


Fig. 23. The spin polarizations of emitted  $\delta$ - electrons stemming directly from the  $1s\sigma$ - state is displayed versus the kinetic electron energy, using eq. (46).

spin polarization  $\eta_p$  of  $\delta$ - electrons versus kinetic electron energy  $E$  stemming directly from ionization of the  $1s\sigma$ - state, cf. eq. (46), is presented in Fig. 23 for  $b=20$  fm. Correlation effects are not considered in this case. Larger polarizations are found for increasing  $\delta$ - electron energy.

Ionization measurements of  $1s\sigma$ - electrons and  $\delta$ - electron spectroscopy therefore may yield direct information about the behaviour of electrons in strong magnetic fields.

#### CONCLUSIONS

We have discussed systematically the charge dependence of vacancy formation and  $\delta$ - electron production rates open to experimental verification. The steep increase at small impact parameters was explained by the strong localization of the  $1s\sigma$ - state caused by relativistic effects. Furthermore we predict a maximum for vacancy and  $\delta$ - electron production rates around  $Z_1+Z_2=170$  due to the interplay of the extremely strong  $1s\sigma$ - binding energy and the radial

expectation value  $\langle r_{1s0} \rangle$ .

Comparing our coupled channel results with experimental data we pointed out that the inclusion of multi-step processes is indispensable to obtain reasonable absolute values. This is emphasized by results obtained within first order time-dependent perturbation theory which underestimate the measured data by factors 3-5.

Beside the expansion of  $\phi(R(t))$  into stationary eigenstates a variational principle for the calculation of K- hole production rates in lighter systems is proposed in Ref. 29 which is also applicable to heavy collision systems.

Considering vacancy formation we find fair agreement with experimental data except for small impact parameters and distant collisions, where we slightly deviate from the experimental results. However, the present discrepancies in collisions far below the Coulomb barrier (e.g.,  $Pb+Cm$   $E_{lab} = 3.6$  MeV/u) still need clarification.

The  $\delta$ - electron spectra are partially in excellent agreement with measured values of Kozhuharov and König et al.<sup>19</sup>. We find that the slope is reproduced very well for all  $\delta$ - electron energies. Considering  $\delta$ - electron production rates in a  $Pb+Pb$  collision in coincidence with final K- vacancies of the heavier collision partner, our calculations slightly underestimate the experimental results. We expect that electron screening will shift the present results towards higher energies.

The influence of electron screening was investigated with respect to vacancy formation. We found an increase of vacancy production up to 40% for  $2p_{1/2}^0$ - holes considering  $Xe+Pb$ .

In nuclear reactions with a time delay  $T$  we predict interference patterns in  $\delta$ -electron spectra having an energy width of  $\Delta E = \hbar/T$  thus offering the opportunity to measure nuclear reaction times.

As a measurable quantity for the strong magnetic fields in heavy ion collisions we predict a Zeeman splitting of the  $1s0^-$  state yielding measurable spin polarizations of  $1s0^-$  vacancies and emitted  $\delta$ - electrons.

#### REFERENCES

1. Conceptual ideas on atomic excitation processes in scattering of very heavy ions were presented by K. Smith, B. Müller, and W. Greiner, J. Phys. B8: 75 (1975); first calculations were performed by W. Betz, G. Soff, B. Müller, and W. Greiner, Phys. Rev. Lett. 37: 1046 (1976). For more details see G.

- Soff, W. Greiner, W. Betz, and B. Müller, Phys. Rev. A20: 169 (1979).
2. C. Kozuharov, in: 'Electronic and Atomic Collisions', S. Datz, ed., North Holland, Amsterdam (1981).
3. G. Soff, J. Reinhardt, and W. Greiner, Phys. Rev. A23: 701 (1981).
4. J. S. Greenberg, H. Bokemeyer, H. Emling, E. Grosse, D. Schwalm, and F. Bosch, Phys. Rev. Lett. 39: 1404 (1977).
5. D. Liesen, P. Armbruster, H.-H. Behncke, and S. Hagmann, Z. Physik A288: 417 (1978).
- D. Liesen, P. Armbruster, H. H. Behncke, F. Bosch, S. Hagmann, P. H. Mokler, H. Schmidt-Böcking, and R. Schuch, in: 'Electronic and Atomic Collisions', N. Oda and K. Takayanagi, eds., North Holland, Amsterdam (1980), p. 337.
6. R. Anholt, W. E. Meyerhof, and C. Stoller, Z. Physik A291: 287 (1979).
- R. Anholt, W. E. Meyerhof, C. Stoller, and J. F. Chemin, in: 'Proc. of the 7th Internat. Conf. on Atomic Physics', Cambridge, Mass. (1980).
7. B. Müller, G. Soff, W. Greiner, and V. Ceausescu, Z. Phys. A285: 27 (1978);  
G. Soff, B. Müller, and W. Greiner, Phys. Rev. Lett. 40: 540 (1978).
8. D. Liesen, P. Armbruster, F. Bosch, S. Hagmann, P. H. Mokler, H. J. Wollersheim, H. Schmidt-Böcking, R. Schuch, and J. B. Wilhelmy, Phys. Rev. Lett. 44: 983 (1980).
9. B. Fricke and G. Soff, Atomic Data and Nuclear Tables 19: 83 (1977).
10. K. H. Wietschorke, B. Müller, W. Greiner, and G. Soff, J. Phys. B12: L31 (1979).
11. J. Reinhardt, thesis, Frankfurt (1979);  
J. Reinhardt, B. Müller, and W. Greiner, Phys. Rev. A24: 103 (1981).
12. R. D. Mattuck, 'A Guide to Feynman Diagrams in the Many-body Problem', McGraw-Hill, New York (1976).
13. J. Reinhardt, B. Müller, and W. Greiner, Phys. Rev. Lett. 43: 1307 (1979).
14. G. Soff, B. Müller, and W. Greiner, Z. Physik A299: 189 (1981).
15. L. H. Thomas, Proc. Camb. Phil. Soc. 23: 542, and 35: 197 (1926).
16. R. Latter, Phys. Rev. 99: 150 and 1854 (1955).
17. N. H. March, 'Self-consistent Fields in Atoms', Pergamon, Oxford (1975), p. 72.
18. E. K. U. Gross and J. Rafelski, Phys. Rev. A20: 44 (1979).
19. F. Gütter, W. König, B. Martin, B. Povh, H. Skapa, J. Soltani, Th. Walcher, F. Bosch, and C. Kozuharov, 'Study of High Energetic Electrons Emitted During Heavy Ion Collisions', preprint (1981), and contribution at this Conference.
20. E. Berdermann, F. Bosch, H. Bokemeyer, M. Clemente, F. Gütter, P. Kienle, W. König, C. Kozuharov, B. Martin, B. Povh, H. Tsertos, and Th. Walcher, GSI - Scientific Report 1979, GSI 80-3: 100 (1980).

21. E. Berdermann, H. Bokemeyer, F. Bosch, M. Clemente, F. Güttner, P. Kienle, W. König, C. Kozhuharov, H. Krimm, B. Martin, B. Povh, K. Traxel, and Th. Walcher, GSI Jahresbericht 1978, GSI 79-11: 95 (1979).
22. H. Bokemeyer, in: 'Proc. of the Predeal Internat. School, Heavy Ion Physics', A. Berinde, V. Ceausescu, I. A. Dorobantu, eds., Romania (1978), p. 489.
23. J. Reinhardt, B. Müller, W. Greiner, and G. Soff, Z. Physik A292: 211 (1979).
24. G. Soff, J. Reinhardt, B. Müller, and W. Greiner, Phys. Rev. Lett. 43: 1981 (1979).
25. R. Anholt, private communications.
26. J. Rafelski and B. Müller, Phys. Rev. Lett. 36: 517 (1976).
27. D. Kolb, W.-D. Sepp, B. Fricke, and T. Morović, Z. Physik A286: 169 (1978).
28. G. Soff, J. Reinhardt, B. Müller, and W. Greiner, Z. Physik A294: 137 (1980).
29. M. Kleber and K. Unterseer, Z. Physik A292: 311 (1979); M. Kleber, contribution at this Conference.

#### ACKNOWLEDGEMENTS

We acknowledge very fruitful discussions with P. Armbruster, H. Backe, H. Bokemeyer, F. Bosch, W. Koenig, Ch. Kozhuharov, D. Liesen, and D. Schwalm, concerning their experiments.

This work was supported by the Bundesministerium für Forschung und Technologie (BMFT) and the Deutsche Forschungsgemeinschaft (DFG). One of us (G.S.) acknowledges the support of the DFG - Heisenberg Programm.

APPENDIX: SCALING LAWS FOR  $1s\sigma$ -IONIZATION OF SUPERHEAVY QUASIMOLECULES

As discussed in detail in our contribution, ionization of the lowest quasimolecular boundstates is an essential prerequisite for the occurrence of many atomic phenomena in heavy ion collisions, such as spontaneous and induced positron creation, characteristic K-X-rays, delta electrons and quasimolecular K-X-rays. The numerical calculations have shown the probability for the creation of a vacancy in such a collision is an extremely sensitive function of impact parameter  $b$ , relative impact velocity  $v$ , as well as of the magnitude of the binding energy and localization of the wavefunction during the collision.

It is, therefore, an obvious aim to derive a simple, analytical relationship among these quantities that replaces the scaling law of Bang and Hansteen [1] which is valid only for very asymmetric, light collision systems. Such a scaling law was first obtained by several of us [2] within the framework of first-order perturbation theory (which, as we now know, does not give the correct size of the ionization probability). Its derivation was based on the following characteristic features valid for all superheavy quasimolecules:

- (a) Ionization takes place predominantly at very small internuclear distances, where the monopole approximation provides an excellent approximation to the binding energies of, and transition matrix elements between, quasimolecular states.
- (b) Ionization of the  $1s\sigma$ -level is dominated by radial coupling. The rotational coupling does not seem to play an important rôle because the relevant matrix elements vanish at small distances.
- (c) The radial coupling matrix elements  $\langle f | \partial/\partial R | i \rangle$  exhibit a very strong peak at the point of closest approach of the two nuclei. The detailed shape of these matrix elements at large internuclear separations, especially the choice of translation factors is therefore only of minor importance. For small and intermediate distances  $R$  a good parametrization of the radial matrix element is achieved by:

$$\langle E_{1s\sigma} | \partial/\partial R | 1s\sigma \rangle = \frac{d(E, Z)}{R} \quad (1)$$

where  $E$  is the energy of the emitted electron and  $Z = Z_p + Z_t$  is the total (central) charge of the system.

- (d) The matrix element is a smooth function of  $E$ . The electrons are mainly ionized into states with less than 1 MeV

kinetic energy. The transition strength in this range can be approximated by

$$d(E, Z) = d_0(Z) \left( \frac{m c^2}{E} \right)^{\gamma/2} \quad (2)$$

where  $\gamma$  is a slowly varying function of  $Z$ .

With these parametrizations the amplitude for ejecting an electron from the  $1s_0$  state into the continuum takes the form:

$$\begin{aligned} a(E) = & - \int_{-\infty}^{\infty} dt \dot{R}(t) \langle \partial / \partial R | 1s \rangle \cdot e^{i \frac{1}{\hbar} \int_0^t dt' (E - E_{1s}(t'))} = \\ & = -d \int_{-\infty}^{\infty} dt \frac{\dot{R}(t)}{R(t)} \exp \left[ i \frac{1}{\hbar} \int_0^t dt' \Delta E(R(t')) \right] \end{aligned} \quad (3)$$

where  $\Delta E = E - E_{1s}$  is the instantaneous transition energy. For a Coulomb trajectory the radial velocity is given by

$$\dot{R}(R) = \frac{v}{R} \sqrt{(R - R_0)(R + R_0 - 2a)} \operatorname{sgn}(t) \quad (4)$$

with the distances of closest approach

$$R_0 = a + \sqrt{a^2 + b^2}, \quad a = \frac{Z_1 Z_2 e^2}{2 E_{CM}} \quad (5)$$

for impact parameter  $b$ , centre-of-mass bombarding energy  $E_{CM}$  and velocity  $v$  at infinity.

A crude estimate of the integral (3) can be obtained from an investigation of the singularities of the integrand  $(\dot{R}/R)$  in the complex time plane. First, let us, for convenience, replace the variable transition energy  $\Delta E(t)$  by its value at the distance of closest approach:  $\Delta E_0 = E - E_{1s}(R_0)$ . From the equation of motion

$$\ddot{R} = v^2 \left\{ \frac{a}{R^2} + \frac{R_0(R_0 - 2a)}{R^3} \right\} \quad (6)$$

it is easy to show that  $|R(t)|$  can at most grow as a quadratic polynomial in the limit  $|t| \rightarrow \infty$ . Therefore the integration contour in Eq. (3) can be closed in the upper half complex  $t$ -plane, reducing the integral to one around all singularities of the function  $(\dot{R}/R)$  in this region (see Fig. 1).

From Eqs. (4) and (6) one can prove that the only singular points of this function can be the points where  $R(t)$  vanishes. By integrating (4) into the inverse function  $t(R)$ , or by inspecting the parametric representation

$$R = a(\varepsilon \cosh(\xi) + 1), \quad t = \frac{a}{v}(\varepsilon \sinh(\xi) + \xi) \quad (7)$$

(with the eccentricity  $\varepsilon = (R_0 - a)/a$ ), it is found that all zeroes of  $R(t)$  must lie on the imaginary time-axis, the closest to the origin

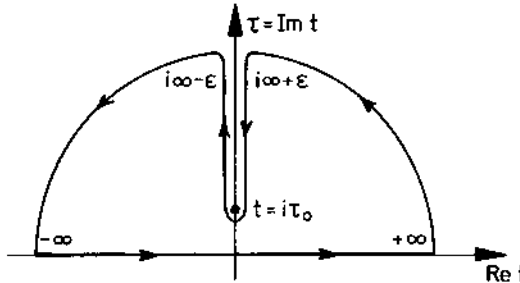


Fig. 1. Integration contour for Eq. (3) in the complex time plane. All singularities are located on the imaginary axis.

being given by [7]

$$\begin{aligned} \tau_0 = \text{Im}(t_0) &= \frac{1}{v} \left[ \sqrt{R_0(R_0 - 2a)} - a \cos^{-1} \left( \frac{a}{R_0 - a} \right) + \pi \right] = \\ &= \frac{a}{v} \left[ \sqrt{\varepsilon^2 - 1} + \pi - \cos^{-1} \frac{1}{\varepsilon} \right] = \\ &= \frac{1}{v} \left[ b + a \left( \pi - \tan^{-1} \frac{b}{a} \right) \right]. \end{aligned} \quad (8)$$

The transition amplitude (3) can, therefore, be written as an integral over the discontinuity of the function  $(\dot{R}/R)$  across the imaginary time-axis from  $i\tau_0$  to infinity. Writing  $t = i(\tau_0 + x)$  one has

$$a(E) = -d \exp \left[ -\frac{\tau_0 \Delta E_0}{\hbar} \right] \int_0^\infty dx \text{disc} \left( \frac{\dot{R}(x+i\varepsilon)}{R(x+i\varepsilon)} \right) \exp \left[ -\frac{x \Delta E_0}{\hbar} \right]. \quad (9)$$

The remaining integral is basically a small number, the dominant contribution coming from a pole term at  $x=0$  that yields a factor  $\pi$

(The factor is slightly  $\epsilon$ -dependent.). One can therefore write approximatively

$$|a(E)|^2 \approx -\pi^2 d_0^{-2} (mc^2/E)^\gamma \exp\left[-\frac{2\tau_0 \Delta E_0}{\hbar}\right]. \quad (10)$$

Equation (10) reproduces the numerically known fact that the energy spectrum of ionized electrons falls off exponentially, apart from the weak energy dependence of the matrix element.

In order to obtain the total ionization probability  $P(b)$ , an integration over  $E$  must be performed:

$$\begin{aligned} P(b) &= \int_{mc^2}^{\infty} dE |a(E)|^2 = \\ &= \frac{1}{4} D(Z) \exp\left(-\frac{2\tau_0}{\hbar} E_{1s}(R_0)\right) \left(\frac{2\tau_0}{\hbar} mc^2\right)^{\gamma-1} \Gamma\left(1-\gamma, \frac{2\tau_0}{\hbar} mc^2\right). \end{aligned} \quad (11)$$

Here  $\Gamma$  denotes the incomplete gamma function<sup>[3]</sup>, while the dimensionless factor

$$D(Z) = 4\pi^2 d_0^{-2} mc^2 \quad (12)$$

can be easily calculated from the quasimolecular wavefunctions. It is shown in Fig. 2.

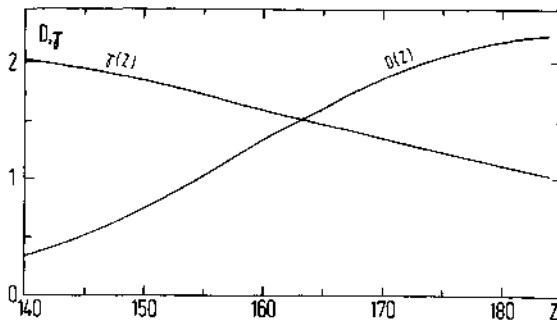


Fig. 2. The strength function  $D(Z)$  for  $1s0$ -ionization.

The rapid increase in the region  $140 \leq Z \leq 170$  is due to the relativistic shrinking of the  $1s0$ -wave function setting in for  $Z > 137$  (diving effect). For even larger  $Z$ , the transition strength  $D(Z)$

begins to level off so that the strong increase in binding energy  $E_B(R_0, Z) = mc^2 - E_{1s}(R_0)$  dominates in formula (11).

The assumption that the transition energy  $\Delta E$  does not change with time is, of course, incorrect. Since  $\Delta E$  approaches a constant value in the separated atomic limit  $R \rightarrow \infty$ , the integration contour can still be closed at infinity. However, further singularities may be introduced in the complex  $t$ -plane by the phase factor in Eq. (3). For superheavy quasimolecules the variation of the binding energy in the united atom limit is known to be simple [4]:

$$\Delta E(R) \sim \Delta E_0 \cdot (R_0/R)^v \text{ with } v \sim 0.3. \quad (13)$$

In this case no further singularity is introduced on the imaginary time-axis below  $\tau_0$ , the first zero of  $R(t)$ . The derivation of Eq. (10) then goes through unchanged, only the exponential factor is modified to

$$\begin{aligned} \exp \left[ -\frac{2}{\hbar v} \int_0^{\tau_0} dt \Delta E(R(it)) \right] = \\ = \exp \left[ -\frac{2\Delta E_0 R_0}{\hbar v} \sqrt{\frac{\varepsilon+1}{\varepsilon-1}} B\left(\frac{1}{2}, 2-v\right) {}_2F_1\left(\frac{1}{2}, 2-v, \frac{5}{2} - v, -\frac{\varepsilon+1}{\varepsilon-1}\right) \right] \quad (14) \end{aligned}$$

While the general impact parameter dependence is seen to become fairly complicated, it is of interest to compare the two formulas in the limits  $b \rightarrow 0$  and  $b \rightarrow \infty$ . Writing the exponential factor as

$$\exp \left[ -\frac{2\Delta E_0 R_0}{\hbar v} \alpha(b) \right], \quad \text{Eq. (10) yields}$$

$$\alpha(b \rightarrow 0) = \frac{\pi}{2} \approx 1.57; \quad \alpha(b \rightarrow \infty) = 1 \quad (15a)$$

whereas Eq. (14) gives the corrected values

$$\alpha(b \rightarrow 0) = \sqrt{\pi} = 1.77; \quad \alpha(b \rightarrow \infty) \sim 1.2. \quad (15b)$$

A scaling law of the type (11) was first derived in ref. 2, but with slightly different and more severe approximations that yielded a correction factor  $\alpha = \sqrt{2R_0}/(R_0 - a)$  with the limits  $\alpha(0) = 2$  and  $\alpha(\infty) = \sqrt{2} = 1.41$ , respectively. A similar scaling law has, subsequently, been put forward by F. Bosch et al. [5]. Bosch neglected the second term in Eq. (8), obtaining an exponential factor  $\exp \left[ -\frac{2(R_0 - a)\Delta E_0}{\hbar v} \right]$  corresponding to  $\alpha(0) = \frac{1}{2}$  and  $\alpha(\infty) = 1$ . Still, the authors claimed good agreement of their scaling law with the experimental data that exceed the exact results of first-order perturbation theory by a factor 3 to 5. This agreement was, however, accidentally caused by an incorrect integration over final state energies. The correct integration yields a formula analogous to Eq. (11) but with a modified value of  $\tau_0$ . Since  $v\tau_0 - b = a(\pi - \tan^{-1} \frac{1b}{a})$

approaches the constant value  $a_2^{\frac{\pi}{2}}$  for  $b \rightarrow \infty$ , Bosch's scaling law gives the correct slope of  $P(b)$  for large impact parameters but continues to stay above the true first-order result by a substantial factor.

The various versions of the scaling law are compared with the exact numerical result for  $P(b)$ , in first-order perturbation theory, in Fig. 3. Best agreement is found for the scaling laws (11) and (14)

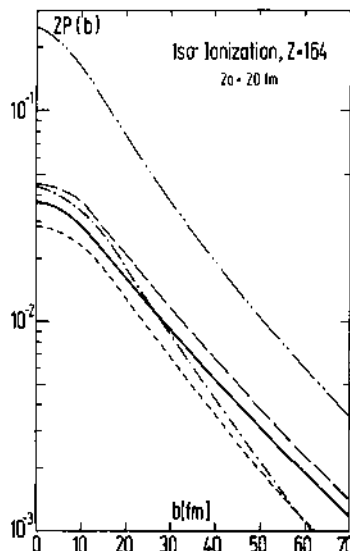


Fig. 3. Impact parameter dependence of iso-ionization for various models: exact first-order result (—), Eq. (11) (—), Eq. (14) with variable binding (---), the model of ref. 2 (---) and Bosch's law (—).

with a slight edge in favour of the model without variable binding energy. The scaling law of ref. 2 yields a slightly different slope, but is in good absolute agreement for  $b$  between 0 and 50 fm, whereas Bosch et al.'s law strongly overestimates the correct result. For a further and more detailed comparison of the various scaling models we refer to a forthcoming article of G. Soff et al. [6].

The gravest concern, whether any of these scaling laws are applicable towards a spectroscopic analysis of binding energies in superheavy quasimolecules, come from the numerically established fact that ionization in these systems cannot be understood but

through coupled-channel calculations. A careful comparison of the impact parameter- and velocity-dependence of  $P(b)$  with and without the inclusion of such multi-step ionization mechanisms shows that besides the overall increase there is also a change in the kinematical dependences [6]. It is tempting to speculate that this may be caused by an effective reduction of the ionization threshold by multi-step processes, but there is, at present, no clear proof or disproof of such ideas. More work in this direction is clearly needed. If scaling laws for multi-step (not just two-step) processes cannot be derived, it is probably necessary to allow for parametrized perturbations of the quasimolecular states and determine their size from a comparison of computer calculations with the experimental data.

## REFERENCES

1. J. Bang, J. M. Hansteen, Mat. Fys. Medd. Dan. Vid. Selskab 31, No. 3 (1959).
2. B. Müller, G. Soff, W. Greiner, V. Ceausescu, Z. Physik A285, 27 (1978).
3. A factor  $xY^{-1}$  was accidentally omitted in the definition of the exponential integral  $E_x(x)$  in ref. 2. However, this does not affect the validity of Eqs.(8) and (9) in that article.
4. G. Soff, J. Reinhardt, W. Betz, Physica Scripta 17, 417 (1978).
5. F. Bosch, D. Liesen, P. Armbruster, D. Moor, P. H. Mokler, H. Schmidt-Böcking, R. Schuch, Z. Physik A296, 11 (1980).
6. G. Soff et al., to be published.
7. The quantity  $\tau_0$  can be regarded as the characteristic collision time of a Coulomb trajectory. Similar expressions have been suggested by H. Backe, in: Trends in Physics 1978 (Proc. 4th EPS conference) p. 445, Ed. M. M. Woolfson, Bristol 1979. E. Kankeleit, Nukleonika 25, 253(1980). Their characteristic time  $\hat{t}$  differs from our  $\tau_0$  by less than 5 percent over the whole range of impact parameters.

## SEARCH FOR SPONTANEOUS POSITRON PRODUCTION IN HEAVY-ION COLLISIONS

H. Bokemeyer<sup>\*</sup>, K. Bethge<sup>1</sup>, H. Folger, J.S. Greenberg<sup>1</sup>,  
H. Grein, A. Gruppe<sup>2</sup>, S. Ito, R. Schule<sup>2</sup>, D. Schwalm,  
J. Schwepp<sup>1</sup>, N. Trautmann<sup>3</sup>, P. Vincent<sup>4</sup>, M. Waldschmidt<sup>2</sup>

GSI, 61 Darmstadt, West Germany

<sup>1</sup>Yale University, New Haven, Conn., USA

<sup>2</sup>University of Frankfurt, 6 Frankfurt, West Germany

<sup>3</sup>University of Mainz, 65 Mainz, West Germany

<sup>4</sup>GSI and Rutgers University, New Brunswick, N.J., USA

### INTRODUCTION

In collisions between heavy ions with heavy target atoms distances of closest approach deep within the atomic K-shell radii are achieved. When using projectile velocities which are slow compared to the orbital velocities of the inner-shell electrons, these electrons will adjust their orbitals during the course of such collisions, evolving for small internuclear separations into a quasiamionic system with a charge number  $Z_{ua}$  of the united atom (for an U+U-collision at 1.4 GeV projectile energy, for example, the distance of closest approach in a head-on collision is 17 fm while the K-shell radius<sup>1</sup> of an atom with  $Z_{ua}=92+92=184$  amounts to  $\sim 120$  fm). In this manner transient, collision constructed quasimolecules are formed, and their formation provides a vehicle through which the behaviour of electrons in extremely large Coulomb fields may be studied.<sup>2</sup>

---

<sup>\*</sup>Presented by H. Bokemeyer

In view of the adiabatic nature of heavy ion collisions a successful theoretical description of the behaviour of innermost electron wave-functions has been obtained using molecular basis-states which are solutions to the two-center Dirac equation as a function of inter-nuclear separation  $R$ .<sup>3</sup> However, despite their adiabatic character, these atomic collisions are usually inelastic, and information on the most strongly bound  $1s\sigma$  quasimolecular state may be gained by observation of its excitation and/or subsequent decay, namely  $\delta$ -electrons<sup>4</sup>, molecular orbital (MO)<sup>5</sup> and characteristic X-rays<sup>6,7,8</sup>. Abundant experimental evidence now exists that quasimolecules are indeed formed in heavy ion atom collisions.

One of the most exciting consequences of the formation of quasimolecules is expected for *close* encounters between two very heavy ions, where  $Z_{ua}$  exceeds the critical value  $Z_{crit} = 173$ .<sup>3</sup> For such collision systems, the binding energies of the  $1s\sigma$ -electrons are expected to be larger than twice the rest-mass energy of the electron, namely  $2m_e c^2$ . Under these conditions, vacancies in the  $1s\sigma$  orbital may be spontaneously filled with the creation of a bound electron - free positron pair. The search for this process of spontaneous positron production is the central goal of the experiment described in this lecture and of similar measurements discussed in other contributions to this workshop by P. Kienle and H. Backe. Indeed, the study of strong field QED in the quasimolecular collision system<sup>9</sup> is one of the principal subjects of this conference.

But this search is not uninterrupted by problems of a basic nature. Due to the time-variation of the Coulomb field during the course of such collisions, electrons can be excited from the negative energy continuum, both into empty quasimolecular orbits as well as directly to the positive energy continuum thereby leaving a hole in the negative energy continuum, which means creating a free positron. This so-called induced pair production process competes principally with the spontaneous process being sought. For quasiatoms where the two collision partners are moving on trajectories characteristic for pure Rutherford scattering, the spontaneous and the induced processes are predicted to result in a broad bell-shape like positron

energy spectrum centered at  $\sim 500$  keV and it may thus not be possible to distinguish the two contributions experimentally. If, however, the time the quasiatom remains at the distance of closest approach is prolonged (e.g. by forming a composite nuclear system of finite ( $>10^{-21}$  sec) lifetime), then the two  $e^+$ -production processes are expected to behave differently and to give rise to characteristic structures in the  $e^+$ -energy spectra. Experimental complications arise furthermore from the excitation of nuclear states above 1 MeV during the course of the collision as positrons may be produced in the decay of these states via internal pair production. Thus any experiment seeking to distinguish spontaneous positron production from other sources of positron emission in heavy ion collisions should not only allow the measurement of the energy of the emitted positrons with good resolution but should also provide information about the impact parameter (respectively the distance of closest approach  $R_{\min}$ ) and the inelasticity of the corresponding collision and should also pursue a systematic investigation of the various processes as a function of  $Z_{ua}$  and the projectile energy.

We report at this time on our most recent results from such experiments. Anomalous behaviour of the particle angular distribution coincident to specific positron spectral energy regions as well as peaked structures in high resolution energy spectra measurements have been found. Section II discusses the experimental apparatus with which the measurements were performed. In section III results are presented and the possible relationship of the anomalous positron angular distributions and peaked structures to spontaneous positron emission is discussed.

#### EXPERIMENTAL SET-UP

Since the  $e^+$ -production cross-section is rather small ( $\sim 100$   $\mu$ barn<sup>10</sup>) the apparatus had to be optimized for highest detection efficiency and background suppression. A solenoid-Si(Li) spectrometer system (figure 1) called EPOS<sup>11</sup> was constructed for this purpose and set up at the UNILAC in Darmstadt. The spectrometer combines high  $e^+$ -detection efficiency for all relevant  $e^+$ -energies

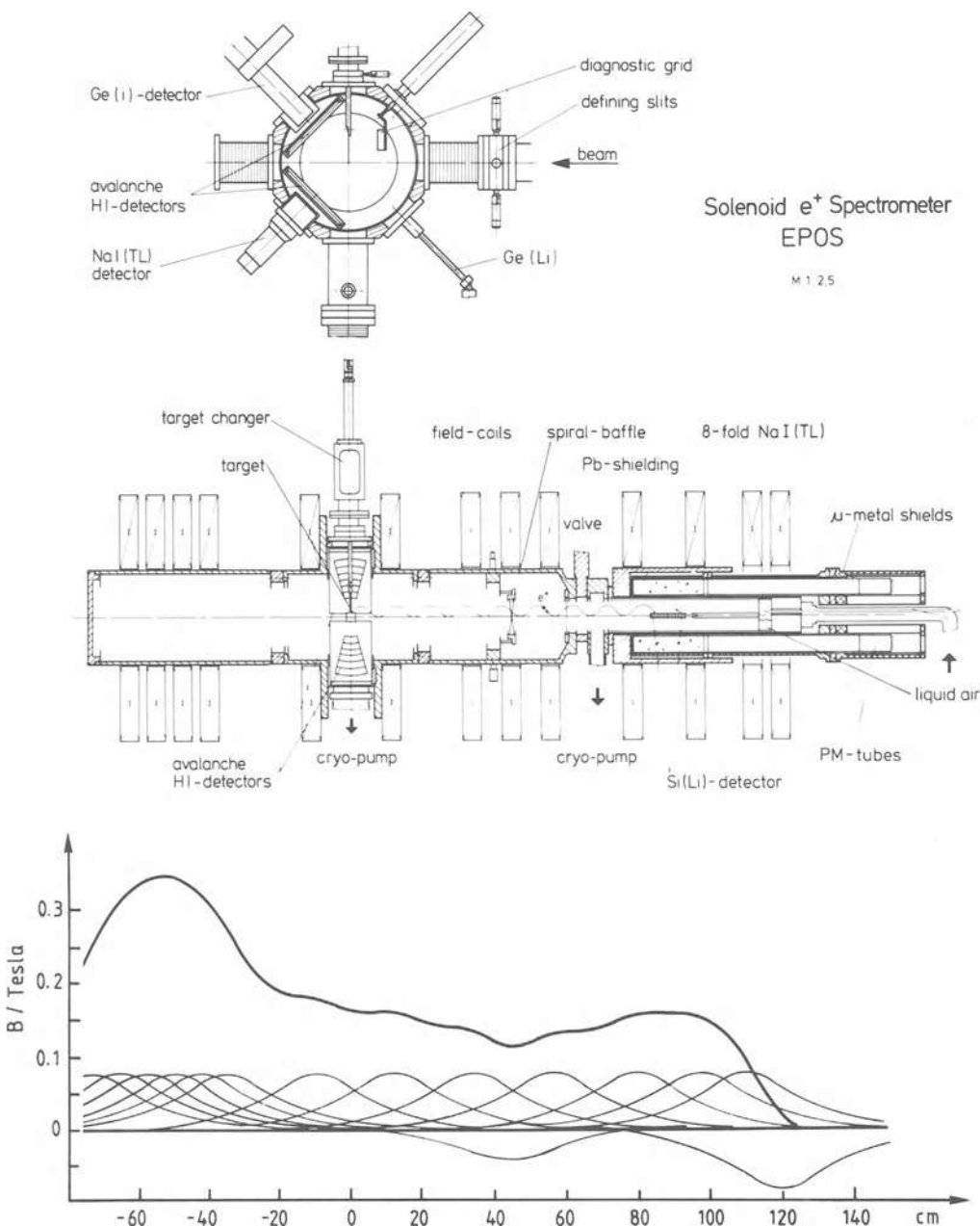


Fig. 1. Plane-view of the solenoid system EPOS used in the present experiment. Also shown is the magnetic field distribution along the solenoid axis.

with a simultaneous measurement of both scattered particles over a large angular range. The system exploits two basic features of solenoidal transport fields in order to achieve maximum background suppression: the opposite spiral directions of oppositely charged particles and the fact that the particles return to the field-lines passing through their point of creation.

A magnetic solenoid, perpendicular to the beam direction, is used to transport positrons on spiraling trajectories from the target to the positron counter. The magnetic field is produced by 12 'Donut'-coils<sup>12</sup> which can be moved separately. A suppression of  $\delta$ -electrons being emitted in every heavy ion collision is achieved by a carefully constructed spiral baffle; these  $\delta$ -electrons are several orders of magnitude more intense than the positrons, and therefore have to be suppressed in order to reduce the singles counting rates in the  $e^+$ -detector and to avoid sum coincidences between positrons and electrons. The transport-efficiency for positrons is maximized by making use of a magnetic mirror on the side of the target opposite to the  $e^+$ -detector and a field-decrease at the position of the spiral baffle. The resulting broad-band efficiency (figure 2) scales with  $B_t/\eta$  ( $B_t$  = magnetic field at the target,  $\eta$  = momentum of the positron). Thus the flat top of the efficiency curve can be moved to the  $e^+$ -energy region of interest by simply adjusting the electric current in the coils.

Background counts in the  $e^+$ -detector due to the leakage of scattered electrons through the baffle and due to other possible background sources outside the target are reduced by using a pencil-like  $e^+$ -detector located along the solenoid axis. The coaxial geometry of the  $e^+$ -detector combines maximum efficiency for target-produced positrons with minimum sensitivity for positrons and electrons which have been scattered or do not originate from the target.<sup>13</sup> Positrons are identified by demanding coincidences between the  $e^+$ -detector and at least one of the two 511 keV annihilation  $\gamma$ -quanta of the positron by using an eight-fold cylindrical NaI-detector array surrounding the  $e^+$ -counter. By summing up the signals of the 8 separate NaI-crystals electronically and requiring a total  $\gamma$ -sum  $E_{\Sigma} \geq 440$  keV

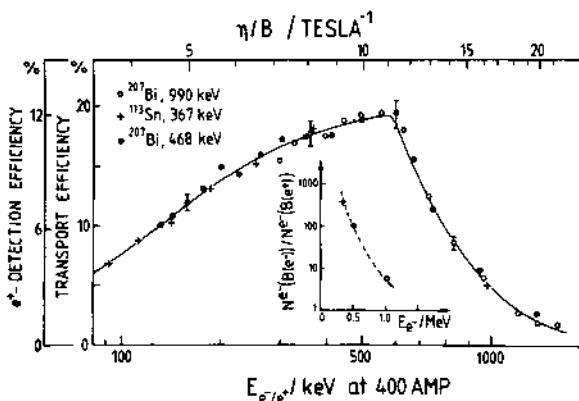


Fig. 2. Transport and  $e^+$ -detection efficiency as a function of  $B_t/n$  ( $B_t$  = magnetic field at the target position and  $n = e^+$ -momentum in units of  $m_e c$ ).

Insert:  $e^-$ -suppression factor (ratio of total  $e^-$ -transmission for opposite field-settings) as a function of the kinetic electron energy.

(to exclude low-energy  $\gamma$ -rays), the NaI-efficiency reaches  $\approx 58\%$  per positron detected in the  $e^+$ -counter.

The pencil-like positron detector (figure 3) consists of two coaxially drifted Si(Li)-detectors of 1 cm outer diameter, 2.5 mm sensitive thickness and 5 cm length each. The detectors are mounted closely one behind the other on a cooling-rod. To protect the (cooled) detector surface the detector vacuum is separated from the vacuum of the solenoid system by a 2  $\mu$  thick aluminized mylar-foil. Special precaution has been taken to avoid an electrical break-through along the front-surface of the detector in the presence of the strong magnetic field. The energy resolution of the  $e^+$ -detector is better than 10 keV for the 662 keV conversion electron line of  $^{137}Cs$ ; this resolution is much better than the expected width

of an  $e^+$ -line measured in-beam, which will be mainly determined by the maximum Doppler-broadening  $2\Delta E_D$  of the positrons emitted in flight, where  $\Delta E_D$  is given in first order in  $\beta = v/c$  by

$$\Delta E_D = E_e \beta \sqrt{2(m_e c^2/E_e) + 1}$$

This broadening results in a width of  $2\Delta E_D \approx 126$  keV (63 keV) for a 300 keV line and  $\beta=0.1$  ( $\beta=0.05$ ). The value of  $\beta=0.1$  is typical if the emitting system is one of the heavy collision products. The  $\beta=0.05$  value would be associated with a quasiatom moving with the velocity of the center of mass in the laboratory.

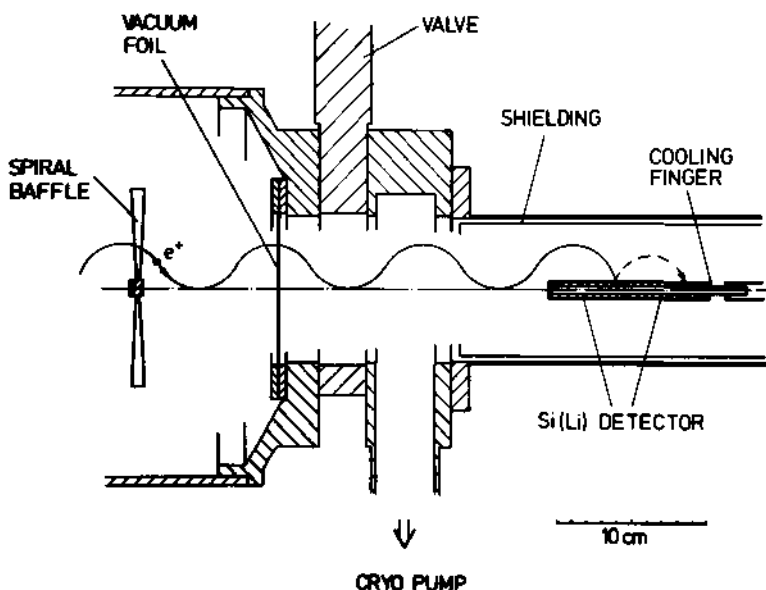


Fig. 3. Enlarged view of the Si(Li) detector arrangement used to measure the kinetic energy of the positrons. The Si(Li)-detector is cooled close to liquid-air temperature by a temperature-controlled feed-through cryostat (not shown in the figure) of very slim shape in order to fit into the surrounding NaI-detector arrangement (see fig. 1).

Backscattering from the Si(Li)-detector leads to low energetic tails in the line-shape of the  $e^+$ -detector. This effect is reduced in this set-up due to the repetitive return of scattered positrons (or electrons) to the counter in the presence of the solenoidal magnetic field. A typical line shape observed for an  $e^-$ -conversion line is shown in figure 4. The shape for a single  $e^+$ -line will have in addition a high energy tail due to the Compton-scattering of one or both of the 511 keV annihilation  $\gamma$ -rays in the Si(Li)-crystal. Because of the lack of a radioactive single-line  $e^+$ -emitter this effect has been studied with a  $^{22}\text{Na}$ -source (figure 5) and found to be of the order of 10 % for our  $e^+$ -identifying condition  $E_{\Sigma} \geq 440$  keV.

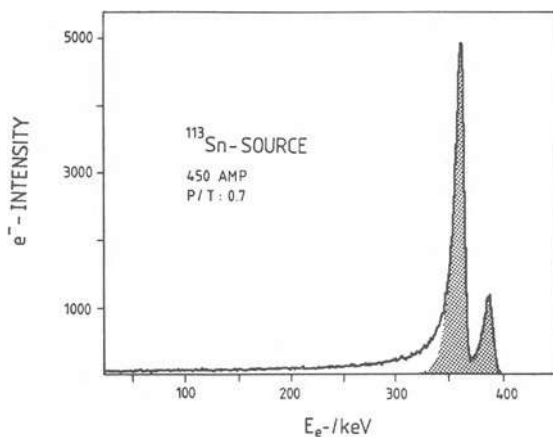


Fig. 4. Typical line-shape observed for conversion electrons emitted from a  $^{113}\text{Sn}$ -source mounted at the target-position. The solenoid current was set to 450 Amp, providing optimal transmission for this energy region. The peak to total ratio is 70 %.

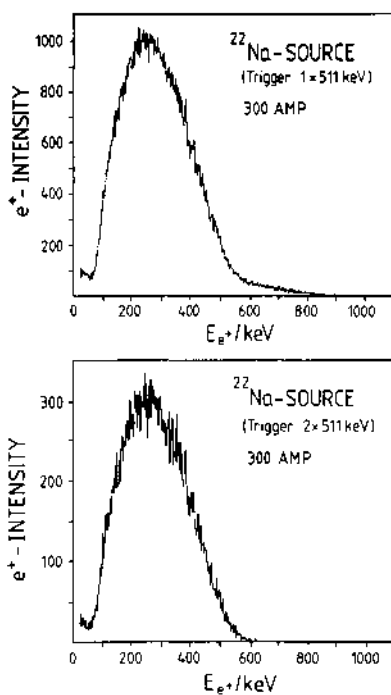


Fig. 5. Investigation of the summing of the  $e^+$ -energy signal with a signal caused by additional scattering of one or both of the two 511 keV annihilation  $\gamma$ -rays in the Si(Li)-detector. The upper graph shows the  $e^+$ -spectrum of a  $^{22}\text{Na}$ -source obtained by requiring  $E_\gamma \geq 440$  keV in the surrounding NaI-detector; this corresponds to our  $e^+$ -identifying condition used in the analysis of the present experiment. The summing effect is clearly visible and can be quantitatively deduced by comparing this spectrum to the one obtained by requiring that both 511 keV  $\gamma$ -rays deposit all their energy in the NaI-crystal ( $E_\gamma > 910$  keV) (lower graph).

Both the scattered projectile and the recoiling target nucleus are detected in two symmetrically arranged parallel-plate avalanche-detectors with continuous delay-line read-out.<sup>14</sup> The cathodes of these detectors are structured as to form a 'meander' delay-line whose delay is directly proportional to the polar angle  $\vartheta$  of the detected particle relative to the beam axis. The angular acceptance of each of the two particle detectors is  $20^\circ < \vartheta < 70^\circ$  at constant  $\Delta\phi=60^\circ$ . In addition to the particle scattering-angle information the time of flight difference between both particles as well as a rough Z-information via the energy-loss of the particles in the detector-gas is obtained.

The coincident detection of both particles has several advantages. For asymmetric systems such as U+Pb, the impact parameter, respectively the distance of closest approach  $R_{\min}$ , can be determined uniquely under the assumption of Rutherford scattering conditions from the kinematic  $(\vartheta_1, \vartheta_2)$ -correlation (figure 6). For symmetric systems like U+U, the distinction of close from distant collisions is principally impossible. However, information on the energy-loss during the collision (Q-value) can be obtained from the sum of the two scattering angles  $(\vartheta_1 + \vartheta_2)$ , which should be  $90^\circ$  for elastic and  $<90^\circ$  for inelastic events. This allows a study of the positron emission not only as a function of the scattering angle  $\vartheta$  but also as a function of the inelasticity of the collision process. The Q-resolution obtained around  $45^\circ$  is about 35 MeV and is equally determined by the finite angular resolution of the detectors ( $\Delta\vartheta=0.4^\circ$ ) and small angle scattering in the target. Furthermore, the kinematic coincidence can be used together with the rough Z-identification of the detected ions to select desired reaction channels and discriminate against background from the target-backing and/or covering foils. Although the set-up allows for the selection of binary, so-called quasielastic events, it should be noted, that separation of reaction-channels involving the transfer of a few nucleons is not possible as long as both resulting nuclei are stable against fission.

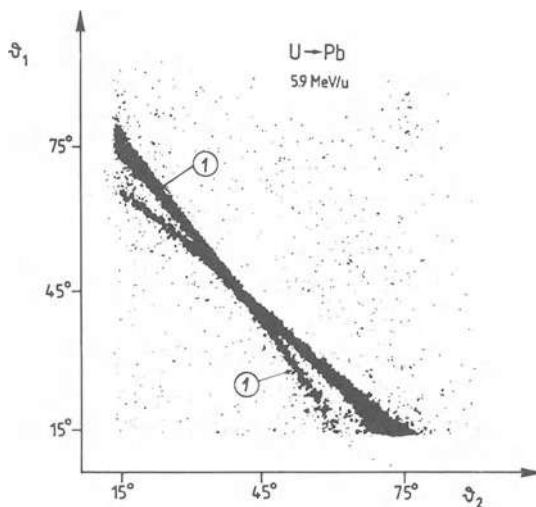


Fig. 6. Intensity of scattered particles as a function of the two laboratory scattering angles  $\vartheta_1$  and  $\vartheta_2$  observed in the upper (Otto) and lower (Uwe) heavy ion detector, respectively, for the system  $^{238}\text{U}+^{208}\text{Pb}$  at 5.9 MeV/u. Close and distant collisions can be separated completely with the exception of the  $45^\circ$ -region (an event in branch 1 corresponds to U being observed in 'Uwe' and Pb in 'Otto').

The contribution of positrons from nuclear internal pair creation amounts e.g. in U+U-collisions up to 30 % of the observed positron yield. To determine this contribution the corresponding  $\gamma$ -ray spectrum is measured by means of a 3" x 3" NaI-detector operated in coincidence with the heavy ion detectors.<sup>15</sup> As proposed in ref. 10 the nuclear  $e^+$ -spectrum can be deduced from the unfolded  $\gamma$ -spectrum using the differential internal pair-conversion coefficient for high Z elements<sup>16</sup>. Since for this procedure the multipolarities of the  $\gamma$ -rays have to be known, they were established semi-empirically through systematic studies of the  $e^+$ -production in low Z systems

(e.g.  $^{238}\text{U} + ^{154}\text{Sm}$ ,  $^{238}\text{U} + ^{165}\text{Ho}$ ) where quasiatomic  $e^+$ -production has been proved to be negligible<sup>10</sup>.

The experimental data are fed via an event-type oriented electronic set-up to the GSI on-line data accumulation system. All information is stored event by event in order to allow for variable selective analysis of the data.

## EXPERIMENTS AND RESULTS

In the first experiments with the new solenoid system EPOS, a pencil-like plastic-scintillator was used to measure  $e^+$ -energies instead of the Si(Li)-detector presently installed. In these studies, measurements of the impact parameter dependence of positron production for the system  $^{238}\text{U} + ^{248}\text{Cm}$  at U-energies of 4.3 and 5.8 MeV/u have been carried out. For both bombarding energies the U+Cm-system, whose combined charge is  $Z_{ua} = 188$ , is expected to become critical for scattering angles within the range subtended by the two particle detectors. The observed dependence for high and low positron energies on the distance of closest approach  $R_{\min}$  is shown in figure 7.<sup>17</sup> In the nearly symmetric U+Cm-system close from distant collisions could not be resolved experimentally; therefore it was assumed that the more intense branch of the Rutherford cross-section determines the  $R_{\min}$ -value. Note that the nuclear contribution to the observed positron yield has been subtracted according to the procedures described at the end of section II. For the two  $^{238}\text{U} + ^{248}\text{Cm}$ -systems studied the nuclear background amounts with increasing  $R_{\min}$  and for low (high) positron energies to 17%(8%)-23%(18%) and 17%(7%)-15%(14%) for  $E(^{238}\text{U}) = 5.8$  MeV and 4.3 MeV/u, respectively. At both beam-energies the observed  $R_{\min}$ -dependence for the atomic  $e^+$ -production appears to be steeper for the lower than for the higher  $e^+$ -energy group. As the opposite behaviour is expected for induced  $e^+$ -emission, our findings could indicate for the first time the presence of an additional positron production process in the U+Cm-collision system at low positron kinetic energies.

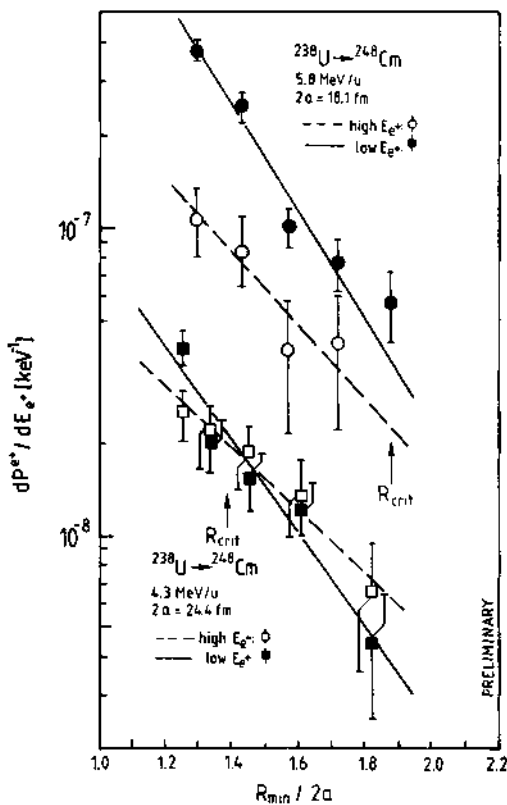


Fig. 7. The atomic  $e^+$ -production probability for low and high energy positrons as a function of the distance of closest approach  $R_{\min}$  for the U+Cm-collision system at two projectile energies of 5.8 MeV/u (low  $E_{e^+}$ : 250 keV  $\leq E_{e^+} \leq 500$  keV; high  $E_{e^+}$ : 600 keV  $\leq E_{e^+} \leq 900$  keV) and 4.3 MeV/u (low  $E_{e^+}$ : 200 keV  $\leq E_{e^+} \leq 500$  keV; high  $E_{e^+}$ : 500 keV  $\leq E_{e^+} \leq 800$  keV).

In subsequent experiments the Si(Li)-detector discussed in sect. II was employed to measure the  $e^+$ -energies. In these studies we investigated in particular the two critical collision systems  $^{238}U + ^{248}Cm$  ( $Z_{ua} = 188$ ) at  $E(^{238}U) = 4.7, 5.9$  MeV/u and  $^{238}U + ^{238}U$  ( $Z_{ua} = 184$ ) at  $E(^{238}U) = 5.8, 5.9, 6.0$  MeV/u as well as the (for the range of scattering angles accessible to us) subcritical system  $^{238}U + ^{208}Pb$  ( $Z_{ua} = 174$ ) at  $E(^{238}U) = 5.9$  MeV/u. In addition, some low Z systems like  $^{238}U + ^{154}Sm$  have been studied to investigate the nuclear background component. With the exception of the 4.7 MeV/u run the U-beam energies are close to the Coulomb barrier and it is known that at these energies nuclear reactions are starting to occur. The analysis of these data is still in progress. We will therefore concentrate in the following discussion on one aspect of the data which we find particularly exciting.

Figure 8 shows the total  $e^+$ -spectra observed for the two systems  $^{238}U + ^{238}U$  and  $^{238}U + ^{248}Cm$  at  $E(^{238}U) = 5.9$  MeV/u. The spectra are integrated over all observed scattering angles ( $20^\circ \leq \vartheta_1 \leq 70^\circ$ ) and over all elastic and quasielastic two-body events. We note that these spectra are not corrected for nuclear  $e^+$ -contributions and for the solenoid transport-efficiency, which partly determines the shape of the spectra at lowest and highest  $e^+$ -energies. While the overall bell-shape form of the  $e^+$ -spectra with a maximum around 500 keV is in agreement with earlier findings and theoretical predictions based on Rutherford trajectories for the two collision partners, there seems to exist the exciting possibility of additional peak-like structures. This possibility lead us to a detailed examination of the positron spectra under special kinematic conditions in order to try to enunciate the structure and gain information about its possible origins.

In figure 9b the most striking result for the  $^{238}U + ^{238}U$ -measurement at  $E(^{238}U) = 5.9$  MeV/u is shown. The spectrum was obtained by selecting the time of flight difference and the anode pulse-height corresponding to binary events, by subtracting random events, and by requiring  $11^\circ \leq |\Delta\vartheta| \leq 19^\circ$  and  $89.2^\circ \leq \Sigma\vartheta \leq 89.8^\circ$ , where  $\Delta\vartheta$

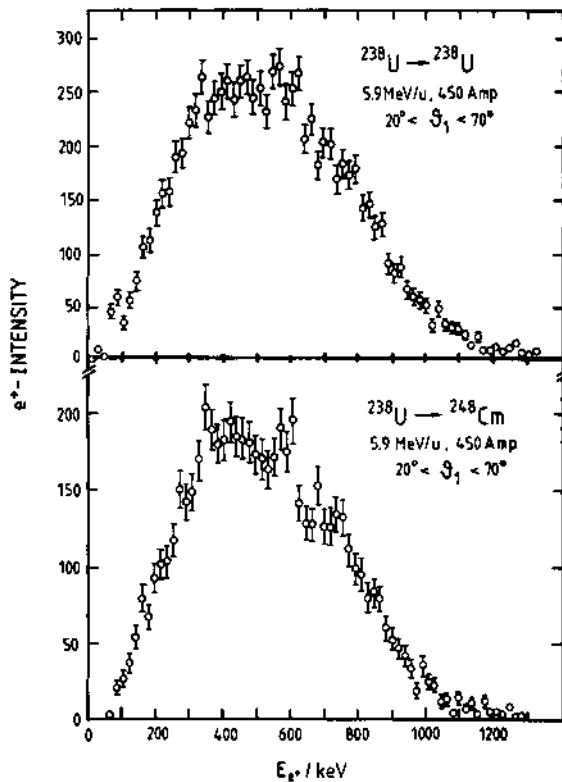


Fig. 8.  $e^+$ -energy spectra for the system  $^{238}\text{U} + ^{238}\text{U}$  and  $^{238}\text{U} + ^{248}\text{Cm}$  at 5.9 MeV/u projectile energy integrated over particle scattering angles between  $20^\circ$  and  $70^\circ$ . The spectra are not corrected for the solenoid transport efficiency and for the line-shape of the Si(Li)-detector. The contribution of nuclear  $e^+$ -production is not subtracted.

and  $\Sigma\vartheta$  are defined by  $\Delta\vartheta = \vartheta_1 - \vartheta_2$  and  $\Sigma\vartheta = \vartheta_1 + \vartheta_2$ , respectively. The kinematic window on  $\Delta\vartheta$  corresponds to selecting events with  $35.5^\circ \leq \vartheta_1 \leq 39.5^\circ$  or  $50.5^\circ \leq \vartheta_1 \leq 54.5^\circ$  if elastic scattering is assumed. These two  $\vartheta$ -regions can be considered together because of the symmetry of the experimental set-up around  $\Delta\vartheta=0^\circ$ . The window on  $\Sigma\vartheta$  corresponds to slightly inelastic events (note that  $\Sigma\vartheta=90^\circ$  for elastic scattering), and the selected width is equivalent to a Q-value window of about  $\Delta Q = 15$  MeV (assuming inelastic scattering with no mass-transfer). With these conditions two peak-like structures centered around positron energies of  $\sim 320$  keV and  $\sim 590$  keV are observed. In connection with the rather narrow Q-window, which amounts to only approximately one third of the experimental Q-resolution it should be noted that these structures are still present - although less pronounced - if a very broad  $\Sigma\vartheta$ -window of approximately 100 MeV centered around the maximum of the observed  $\Sigma\vartheta$ -distribution is selected. The structures are obviously not produced by the Q-cut but rather found to be related to events of slight inelasticity.

In figure 9a the positron spectrum obtained for  $25^\circ \leq |\Delta\vartheta| \leq 35^\circ$  (corresponding to  $27.5^\circ \leq \vartheta_1 \leq 32.5^\circ$  and  $57.5^\circ \leq \vartheta_1 \leq 62.5^\circ$ ) under otherwise identical conditions to the data in fig. 9b are shown. The shape of this spectrum is in agreement within statistics with the bell-shaped curve one expects theoretically by assuming Rutherford trajectories<sup>18</sup> (solid curve). By adjusting the height of this spectrum to the experimental one and using the theoretical impact parameter dependence, one obtains the corresponding theoretical spectrum for scattering angles satisfying  $11^\circ \leq |\Delta\vartheta| \leq 19^\circ$ , which is represented in fig. 9b by the solid line. The comparison clearly exhibits the additional structure observed in the experimental spectrum for  $11^\circ \leq |\Delta\vartheta| \leq 19^\circ$ . This  $\Delta\vartheta$ -dependence itself excludes the possibility that the structure is caused by instrumental effects connected with the  $e^+$ -detection. Moreover, the corresponding  $\gamma$ -ray spectra observed for the relevant scattering angles are smooth and do not show any pronounced structure, implying that the structure does not originate from internal pair production. There remains, however, the possibility that there are strong E0-transitions occurring in the decay of the reaction products, which would not be

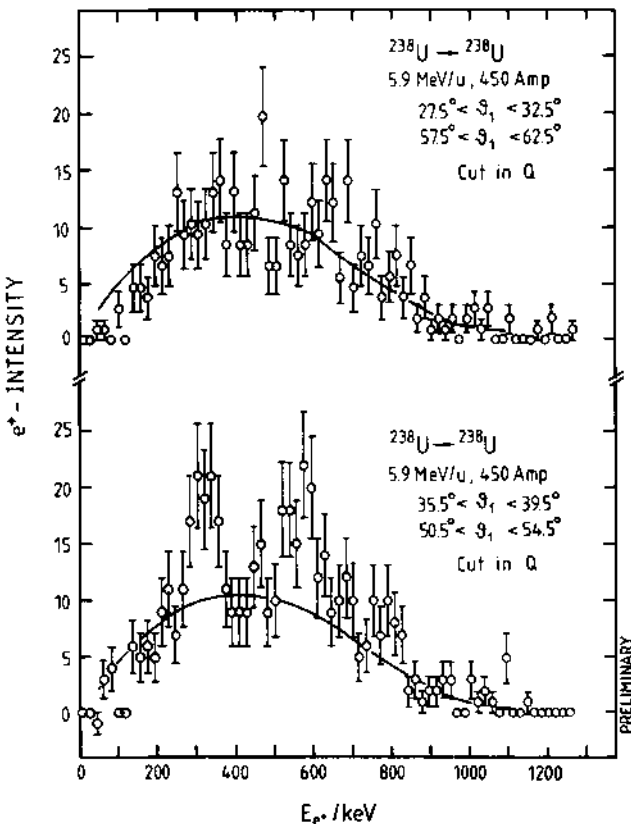


Fig. 9: Two selected  $e^+$ -energy spectra observed in  $^{238}\text{U} + ^{238}\text{U}$ -collisions at 5.9 MeV/u and kinematic conditions as explained in the text. The spectra are not corrected for the solenoid transport-efficiency, the Doppler-broadening the Si(Li)-detector line-shape and nuclear background. The solid lines represent the theoretical spectra<sup>18</sup> normalized to the upper spectrum.

visible in the  $\gamma$ -ray spectrum but might contribute via internal pair production to the measured positron spectrum. However, possible EO-contributions from the decay of Coulomb-excited  $^{238}\text{U}$  nuclei can be ruled out as a rather smooth  $\Delta\vartheta$ -dependence is expected in this case in contrast to the observed behaviour. On the other hand, the  $\Delta\vartheta$ - as well as  $\Sigma\vartheta$ -dependence of the structure is consistent with expectations for products produced in reactions involving the transfer of a few nucleons. Although it is difficult to conceive how the roughly triangular shapes of  $e^+$ -spectra resulting from the internal pair production of EO-transitions could possibly explain the form of the peaks observed, such an explanation can presently not be excluded.

Besides a possible nuclear origin of the observed structures there exists the possibility that they may signify the production of spontaneous positrons. If the times the collision systems remain critical are prolonged due to nuclear interactions, an enhancement of the spontaneous  $e^+$ -production probability is expected at focussed positron kinetic energies<sup>19</sup> although rather long unexpected time delays of up to  $10^{-20}$  sec would be required in this case<sup>20</sup> in order to explain the observed line-width of the structure. There may be also an alternative mechanism that could lead to peaked structures. Time delay processes could produce a phase-shift in the excitation amplitudes for dynamic positrons between incoming and outgoing parts of the nuclear trajectory, which would result in an interference pattern in the positron energy spectra<sup>20</sup> although again rather long time delays are required.

However, before drawing any far reaching conclusions from the experimental data presented, we feel that the following questions should be solved. First of all one must show by further analysis that the structures are not produced by some yet unknown background effects associated with one of the event selecting criteria. Secondly, the reproducibility of the effect has to be shown and its systematic dependence on  $Z_{\text{ua}}$  and the incident projectile energy must be studied. Finally it has to be demonstrated that the structures are not related to internal EO-pair conversion. An elegant way to

distinguish between a quasiamionic and nuclear origin of the structures would be to measure the velocity of the emitting system via the Doppler-shift of the peaks. While the velocity  $\beta$  of the quasiamion is the velocity of the center of mass ( $\beta=0.5$  for 5.9 MeV/u  $^{238}\text{U}$  impinging on  $^{238}\text{U}$ ) the velocities of the reaction products depend on  $\vartheta_1$  and reach values up to  $\beta=0.1$ . This different velocity behaviour results in different Doppler-shifts of the peaks when observed as a function of the relative angle between the recoiling reaction products and the  $e^+$ -emission direction.

Obviously the studies of positron production in collision constructed quasimolecules are far from completion, but the present results suggest that their further pursue could lead to exciting insights in both the atomic *and* nuclear physics of heavy ion collision systems.

## REFERENCES

1. G. Soff, B. Müller, Z. Physik A280(1977)243
2. W. Pieper and W. Greiner, Z. Physik 218(1968)327
3. J. Reinhardt, W. Betz, J. Kirsch, B. Müller, W. Greiner, G. Soff, Nukleonika 25(1980)225
4. E. Berdermann, F. Bosch, H. Bokemeyer, M. Clemente, F. Gütter, P. Kienle, W. König, C. Kozuharov, B. Martin, B. Povh, H. Tsertos, Th. Walcher, GSI Darmstadt, Scientific Report 1978, GSI 80-3(1980)100 C. Kozuharov in S. Datz, ed., Electronic and Atomic Collisions 1981, XXIII ICPEAC 1981, to be published in North Holland Publ. Company, Amsterdam and London, (1982)
5. K.E. Stiebing, K. Bethge, W. Schadt, H. Schmidt-Böcking, F. Bosch, D. Liesen, D. Maor, P.H. Mokler, P. Vincent, S. Hagmann, R. Schuch, GSI Darmstadt, Scientific Report 1980, GSI 81-2(1981)126
6. J.S. Greenberg, H. Bokemeyer, H. Emling, E. Grosse, D. Schwalm and F. Bosch, Phys. Rev. Lett. 39(1977)1404
7. R. Anholt, W.E. Meyerhof, Ch. Stoller, Z. Physik A291(1979)287

8. D. Liesen, P. Armbruster, H.-H. Behncke, and S. Hagmann, Z. Physik A288(1978)417
9. U. Müller, T. de Reus, W. Greiner, J. Kirsch, B. Müller, J. Reinhardt, G. Soff, K.H. Wietschorke, Inst. für Theor. Phys. d. Univ. Frankfurt, UFTP Preprint 58(1981)
10. H. Backe, L. Handschug, F. Hessberger, E. Kankeleit, L. Richter, F. Weik, R. Willwater, H. Bokemeyer, P. Vincent, Y. Nakayama, J.S. Greenberg, Phys. Rev. Lett. 40(1978)1443
11. A. Balanda, K. Bethge, H. Bokemeyer, H. Folger, J.S. Greenberg, H. Grein, A. Gruppe, S. Ito, S. Matsuki, R. Schule, D. Schwalm, J. Schweppe, P. Vincent, M. Waldschmidt, GSI Darmstadt, GSI-Preprint 80-16(1980)
12. G. zu Putlitz, priv. comm.: water-cooled field-coils of 260 mm inner diameter, usually called pancake coils.
13. G.A. Burginyon and J.S. Greenberg, Nucl. Inst. Meth. 41(1966)109
14. P. Fuchs, H. Emling, E. Grosse, D. Schwalm, H.J. Wollersheim, R. Schulze, GSI Darmstadt, Jahresbericht 1977, GSI-J-1-78(1978)
15. W.E. Meyerhof, R. Anholt, Y. El Masri, I.Y. Lee, D. Cline, F.S. Stephens, R. M. Diamond, Phys. Lett. 69B(1977)41
16. P. Schlüter, G. Soff, W. Greiner, Z. Physik A286(1978)149
17. H. Bokemeyer, H. Folger, H. Grein, S. Ito, D. Schwalm, P. Vincent, K. Bethge, A. Gruppe, R. Schule, M. Waldschmidt, J.S. Greenberg, J. Schweppe, N. Trautmann, GSI Darmstadt, Scientific Report 1980, GSI 81-2(1981)127
18. J. Reinhardt, priv. communication
19. J. Rafelski, B. Müller, W. Greiner, Z. Phys. A285(1978)49
20. J. Reinhardt, U. Müller, B. Müller, W. Greiner, Universität Frankfurt, UFTP Preprint 63(1981), to be published in Phys. Rev. Lett.

## PAIR CREATION IN HEAVY ION-ATOM COLLISIONS

P. Kienle

Physik-Department, Technische Universität  
München  
D-8046 Garching

### INTRODUCTION

The experimental problem: F. T. O (for theoreticians only).

Fig. 1 sketches the experimental problem simplified for a nuclear collision leading to a binary reaction accompanied by pair-creation. For the binary reaction (two nuclei in the exit channel) it is assumed that the charge  $\Delta Z = (Z'_p - Z_p)$  the mass  $\Delta A = (A'_p - A_p)$  and the energy  $T_p - (T'_p + T'_t) = Q$  may be transferred. A theoretician dreams of somebody, who would measure the n-fold differential cross section:

$$d^n\sigma(z_p, z_t, T_p, \theta'_p, Q, \Delta Z, \Delta A, T_{e+}, \theta_{e+}, \varphi_{e+}, T_{e-}, \dots) \quad (1)$$

This seems to be nearly impossible, but all quantities may be of some relevance. So we control or measure them nearly all by now.

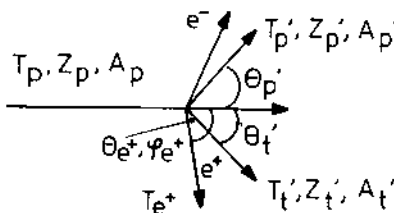


Fig. 1. Schematics of a binary reaction leading to pair creation.

The lecture will treat the following topics. In section 1 we deal with early experiments, which revealed pair-creation induced by the time changing strong di-nuclear Coulombfield of the quasi molecular system. In these experiments the positron creation probability for a defined positron energy and direction was measured as function of the scattering angle and the combined

$$\text{charge } Z_u = Z_p + Z_t : d\sigma(\theta', p', Z_p, Z_t) T_p, T_{e^+}, \theta_{e^+}.$$

Section 2 describes improvements of the experimental methods, which increased the positron detection efficiency by an order of magnitude and allowed the determination of kinematic coincidences between the particles in the exit channel, which are used to measure  $\Delta A$  and  $Q$ .

With this equipment positron spectra were observed for various scattering angles, which indicated the presence of linelike structures superimposed on a continuous spectrum, as described in section 3 for U+U-collisions.

Section 4 mentions some preliminary results on excitation functions for pair-creation, which indicate, that the linestructure in the positron spectrum appears at bombarding energies around the Coulomb barrier.

Section 5 deals with positron spectra from U-Th-collisions.

In the concluding section 6, some very recent results on high resolution positron spectra from U-U-collisions are presented.

#### FIRST EXPERIMENTS ON PAIR PRODUCTION USING U-BEAMS. THE REAL EXPERIMENTAL PROBLEMS: F. E. O. (for experimentalists only).

Due to their small creation probabilities, positrons have to be identified and their energies have to be measured in coincidence with scattered ions with the highest possible detection efficiency, in the presence of a huge radiation field ( $\delta$ -rays, X-rays,  $\gamma$ -rays and neutrons). This was achieved<sup>1)</sup> by using a large solid angle  $\beta$ -spectrometer of the "orange" type, which focused only positrons in selected momentum bins (charge- and momentum filter) on a positron detection system, which measures the kinetic energy and for further background reduction one annihilation quantum.

The total positron detection efficiency was 2.6 %, the accepted momentum bin amounted to  $\Delta p/p \approx 15 \%$ . An improved version of this apparatus will be described in section 2.

The other very difficult experimental problem to solve was a reliable determination of the positron background from nuclear transitions, excited during the collision. Following a suggestion by Meyerhof et al.<sup>2)</sup>, we measured also the  $\gamma$ -ray spectrum in coincidence with the scattered ions. It was assumed<sup>1)</sup> that the number of observed positrons in coincidence with scattered particles,  $N_{e+p}$ , originate from two sources, one for which the number of positrons is proportional to the number of scattered particles  $N_p$ , with  $P_{e+}$  being the "atomic" positron creation probability, and the other for which the positron number is proportional to the number of  $\gamma$ -rays, with an energy above the value  $E = 2m_0c^2 + T_{e+}$ . Then one expresses  $N_{e+p}$  as follows:

$$N_{e+p} = \varepsilon_{e+}(P_{e+} \cdot N_p + \alpha \cdot N_\gamma (E_\gamma \geq 2m_0c^2 + T_{e+})) \quad (2)$$

The proportionality constant  $\alpha$  of the  $\gamma$ -correlated nuclear positron background was determined experimentally from the following observation. Fig. 2 shows<sup>1)</sup> the ratio of observed positrons and  $\gamma$ -rays for collisions of 5.9 MeV/u  $^{238}\text{U}$ -ions with various target atoms as function of the united charge of the collision system  $Z_u = Z_p + Z_t$ . Note that for low  $Z_u$  this ratio is independent of the united charge - also from the scattering angle - and increases very steeply with  $Z_u$  for values of  $Z_u$  larger than 160. The constant value of the positron- $\gamma$ -ratio, as exhibited by the low  $Z_u$ -collision systems is ascribed to pair-creation following nuclear excitation, whereas the steep rise of positron production at high  $Z_u$  is due to atomic processes. Note, that it is only due to the very strong increase of the transition probability with larger Coulombfield, that the atomic pair-creation process becomes observable above the inherent nuclear background. In very high  $Z_u$ -collision-systems, which are most interesting, the ratio of atomic positrons to nuclear background becomes about 3 : 1.

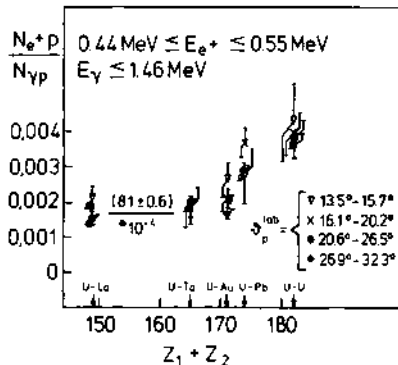


Fig. 2. Number of observed positrons  $N_{e+p}$  per number of observed  $\gamma$ -rays  $N_{\gamma p}$  (in arbitrary units) in coincidence with particles scattered into angular ranges indicated as function of the charge of the collision system.

In order to investigate the origin of the observed atomic positrons in more detail, the impact parameter and the  $Z_u$ -dependence of the pair-creation probability was investigated. For this the pair-creation probability per particle, observed at a scattering angle  $\theta$ , defined as:

$$P_{e+}(\theta) = \frac{N_{e+p}^{\text{atomic}}}{N_p} / \epsilon_{e+} \quad (3)$$

was measured for three heavy collision systems: U+U, U+Pb and Pb+Pb in the range of scattering angles between  $13.5^\circ < \theta_{\text{lab}} < 32.3^\circ$ . The positron detection efficiency of the apparatus,  $\epsilon_{e+}$ , was determined using calibrated positron sources. From the whole positron spectrum an energy window centred around 478 keV with a width of 108 keV was selected for these first measurements.

Fig. 3 shows the impact parameter dependence<sup>3)</sup> of the positron production for the three collision systems as function of the impact parameter  $b$ . The impact parameter was determined from the scattering angle  $\theta$  by assuming Rutherford trajectories. Here a problem arises. In the symmetric collision systems U+U and Pb+Pb, events from scattering angles  $\theta$  and  $(\pi - \theta)$  are principally indistinguishable. For the Pb-U-system our experimental set up could not distinguish Pb from U. The problem was approximately solved by assuming that in the low angle range investigated, the number of positrons in

coincidence with the events belonging to a scattering angle  $\theta$  is much higher compared with those belonging to the rarer collisions with scattering angle  $(\pi - \theta)$ . Physically this amounts to the assumption that the Rutherford cross section drops faster with increasing angle than the pair-creation probability rises. This was checked recently by Baland et al.<sup>4)</sup> for the U-Pb-system using a kinematic coincidence spectrometer which allowed to separate U- and Pb-ions. What was even more important, the kinematic coincidence method allowed to measure  $P(b)$  in the U-Pb-system down to very small impact parameters.

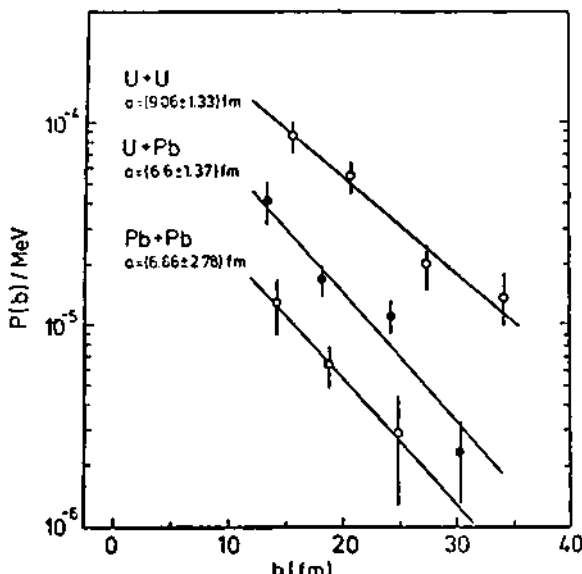


Fig. 3. Impact parameter dependence of the production probability of positrons  $P(b)$  per MeV at  $(478 \pm 54)$  keV positron energy for  $(U+U)$ ,  $(U+Pb)$ , and  $(Pb+Pb)$  - collisions at 5.9 MeV/u bombarding energy. The solid lines represent fits of the data to the relation  $P(b) = P(0) \exp(-b/a)$ . The values for the fall off constant  $a$  are given for various systems.

In discussing the impact parameter dependence of positron creation as shown in Fig. 3, one notes an exponential fall off of  $P(b)$  with a characteristic fall off constant  $a$ , as also shown in Fig. 3. Armbruster and the present author<sup>3)</sup> showed, that the magnitude of  $a$

is related to the minimum momentum transfer  $q_o$  and thus to the energy transfer  $\Delta E$  induced by the time changing Coulombfield, which leads to pair-creation. Using a scaling law first proposed by Bang and Hansteen for Coulomb ionisation by light ions<sup>5)</sup> and recently extended<sup>6)</sup> to heavy ion-atom collisions by incorporating the idea of the united atom approximation to the description of inner shell vacancy production or pair-creation one expects for  $P(b)$  the following expression:

$$P(b) \approx \exp(-2q_o b) \quad (4)$$

which should be valid for  $b > 1/q_o = \bar{b}$ , the impact parameter at which the cross section reaches a maximum. The minimum momentum transfer  $q_o$  necessary for the transition is related to the energy transfer by the expression:

$$q_o = \frac{\Delta E}{\hbar v} \quad (5)$$

If one inserts (5) in (4), one arrives at a different form of the same scaling law

$$P(b) \approx \exp\left(-\frac{\Delta E}{\hbar} \hat{t}\right) \quad (6)$$

with  $\hat{t} = \frac{2R}{v} \approx \frac{2b}{v}$  for  $b \gg R_o = (z_p z_t e^2)/E_{CM}$

which was recently derived by Kankeleit<sup>7)</sup>.

Note that according to the scaling law for Coulomb ionisation the observed fall off constant  $a$  of  $P(b)$  is related, using (4) and (5), to the energy transfer  $\Delta E$  by the expression:

$$a = 1/2q_o = \frac{\hbar v}{2\Delta E} \quad (7)$$

For the measurements shown in Fig. 3,  $\Delta E$  is known to some accuracy, because

$$\Delta E = 2m_o c^2 + T_{e+} + T_{e-} \quad (8)$$

where the positron kinetic energy  $T_{e+}$  has been observed. If one assumes that the average energy  $\langle T_{e-} \rangle$  transferred to the  $\delta$ -rays, which are associated with the positrons in pair-creation process, is small compared with  $2m_o c^2 + T_{e+}$ , one indeed knows  $\Delta E$ . For a collision at a

bombarding energy of 5.9 MeV/u, corresponding to a relative velocity  $v/c = 0.11$  one expects for the creation of 480 keV positrons a fall off constant  $a = 7.2$  fm, which is in good agreement with the results gained from a fit to the experimental values for all three collision systems as shown in Fig. 3. From this we conclude that the production probability for 480 keV positrons shows for all three collision systems including the overcritical (U+U)-system, within an accuracy of about 20 % the impact parameter dependence expected from a simple scaling law, which holds for all Coulomb collision induced processes, in which the time changing Coulombfield transfers momentum and energy to electrons or pairs. This result is substantiated by a recent theoretical proposition of Bang and Hansteen<sup>6)</sup>, who could show the validity of their scaling law for ionization and pair-creation even in the presence of a strong contribution of two step processes, as expected to occur theoretically.

Another interesting early observation concerning the positron production probability is its strong increase with increasing united charge  $Z_u = Z_1 + Z_2$  of the collision system. The data shown in Fig. 3 indicate an exponential increase with  $Z_u$  or a power law with  $Z_u^{+17}$ <sup>7)</sup>! This can be explained quantitatively<sup>8)</sup> by semi-classical collision theories in which the pair-creation is induced by the time changing monopole field in the quasi molecular basis. The strong increase of the pair-creation probability with  $Z_u$  reflects the strong relativistic contraction of the wave functions at the origin in the domain of the strong Coulombfield acting around the turning point of the collision. In fact it is the extreme increase of the radial coupling matrix elements with  $Z_u$  in the high field regime, which makes the observation of atomic pair-creation in Coulomb collisions possible, because only for systems with  $Z_u > 162$  it becomes larger than the nuclear positron background.

In summary one can say that the early experiments on positron production, in which the impact parameter and  $Z_u$ -dependance was studied, revealed that pair-creation is induced by the time dependant, strong Coulombfield produced by the dinuclear system at small internuclear distances. In order to explain quantita-

tively<sup>9)</sup> the observed transition probabilities multistep processes had to be introduced in the quasimolecular description of the process. No evidence of spontaneous positron decay in overcritical systems had been seen.

In order to study more elaborately the characteristics of the pair-creation process, especially the spectral shape of the positrons and its dependence from the kinematic variables of the collision, the experimental techniques had to be improved using a more efficient positron detection method.

## 2. IMPROVED EXPERIMENTAL METHODS

Fig. 4 shows schematically our improved set up for measurements of positron spectra in coincidence with scattered ions using an "orange type"  $\beta$ -spectrometer for positron detection and an anular scattering angle sensitive parallel plate avalanche counter for detecting the scattered ions in kinematic coincidence.

Positrons emitted from a target between  $30^\circ$  and  $70^\circ$  relative to the beam direction can be focused by the toroidal magnetic field, produced by 60 coils on a special detection system, which accepts a momentum bite of 14 %. The positron detection system, shown in Fig. 5, consists of a 12 cm long, tapered ( $\phi = 12-16$  mm) plastic scintillator coupled with optimized light collection efficiency on a photomultiplier tube, placed along the axis of the spectrometer in the region of the momentum focus. The positrons are stopped in the scintillator and produce an energy proportional signal with an energy resolution of 17 % at 500 keV. Figure 6a shows a pulse hight spectrum of the plastic scintillator in coincidence with scattered ions, with the spectrometer current set such that positrons with energies between 415 keV and 505 keV hit the scintillator. One sees a clear peak above a small background in the pulse hight spectrum of the plastic scintillator corresponding to the focused positron energy. The background rises strongly in the pulse hight regime belonging to positron energies lower than 150 keV. The background can be further reduced by requiring a coincidence with a signal from an anular proportional counter surrounding the plastic scintillator as shown in Fig. 6b,c. This proportional counter is made position sensitive by subdivision of the outer cathode foil. Thus the accepted momentum bite of 14 % can be subdivided into several bins for better momentum resolution. The total positron detection efficiency is up to 15 % of  $4\pi$  (depending on the accepted angular range) in a momentum bite of 14 %. The response func-

tion is independant of energy. A positron spectrum is measured by scanning the magnetic field up and down in a selected number of steps within a certain momentum range. The scanning is controlled by a preselected number of counts of ions scattered into the avalanche detector.

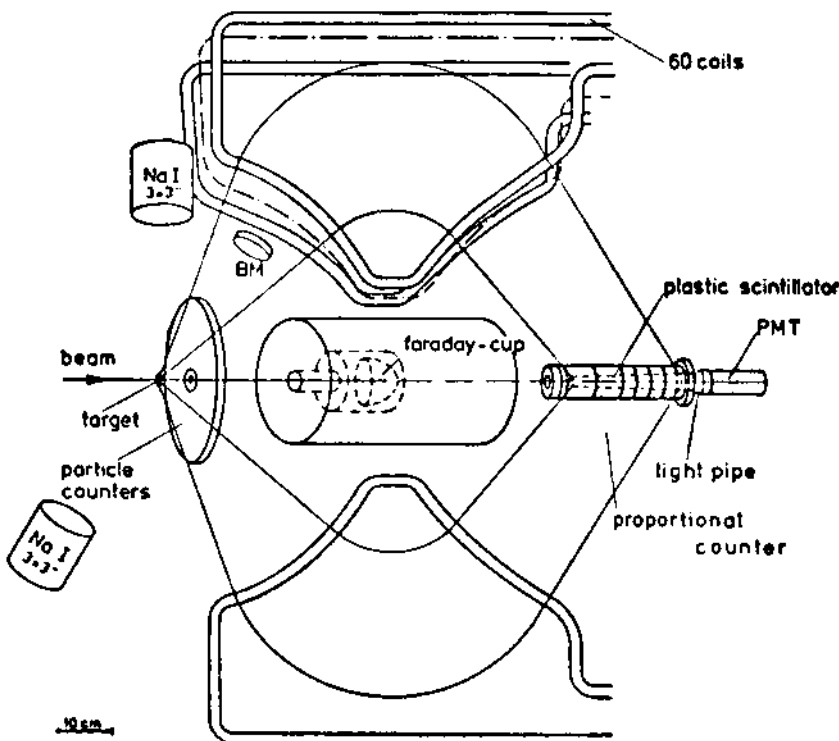


Fig. 4. Schematic drawing of an experimental set up to measure positron production in heavy ion-atom collisions in coincidence with scattered particles. Positrons are focused by the toroidal field of an "Orange" type  $\beta$ -spectrometer on a conically shaped plastic-scintillator, surrounded by a positron sensitive proportional counter. Scattered ions are detected by an annular parallel plate avalanche counter, with 16 concentric anode rings. BM indicates a Si-beam monitor.  $\gamma$ -rays are detected by NaJ-scintillation counters.

As mentioned before, scattered ions and recoils from the target are detected by an annular parallel plate avalanche counter, the anode of which is subdivided into 8 to 16 concentric rings which make it angle sensitive. In order to handle high countrates - up to  $10^7$ /s instantaneous - each ring is read out independant-

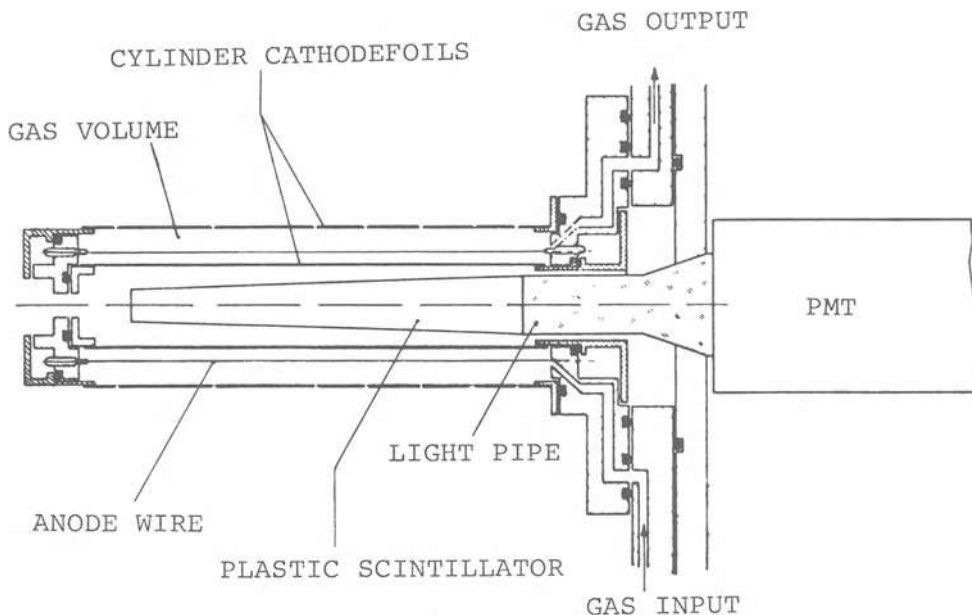


Fig. 5. The positron detection system, consisting of a conically shaped plastic scintillator, coupled to a photomultiplier. The scintillator is surrounded by a cylindrical, transmission proportional counter, whose outer cathode foil is divided in four (or six) rings, to get position information.

ly. We used three types of counters either transmission type for the  $\beta^+$ -particles, non-transmission type, or hybrids with the inner section non-transmissive and the outer one transmissive. The transmission counters had the advantage that ions and recoils scattered into a large angular range ( $15^\circ - 70^\circ$ ) could be accepted. The disadvantage was reduction of the positron detection efficiency up to a factor of two due to scattering in the entrance and exit foils of the detector. So the last run was made with a non-transmission type detector which accepted scattered ions in the range from  $12^\circ$  to  $51^\circ$ . Therefore the positron acceptance angle had to be cut down to values between  $52.4^\circ$  and  $70^\circ$ , reducing the detection efficiency to 8 %. Also kinematic coincidences could be registered only in a limited angular range ( $\pm 5 \%$ ) around  $\theta_{\text{lab}} = 45^\circ$ .

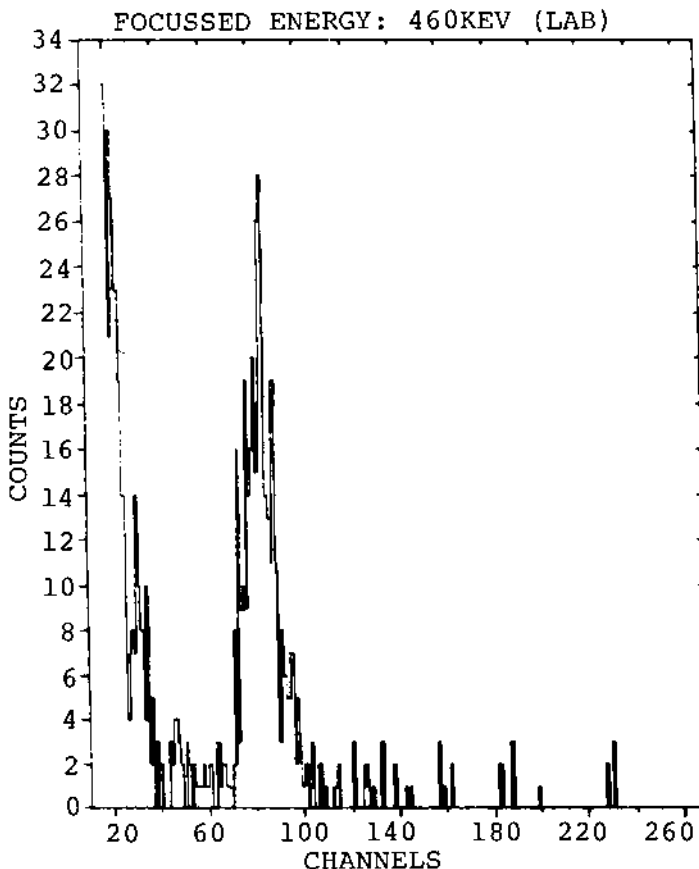


Fig. 6a. A typical plastic scintillator spectrum, with focussed positron between 415 and 505 keV (lab.) in coincidence with scattered ions. One recognizes the low background in the focussed energy interval but the strong increase of background below an energy of 150 keV.

In this context a word to the problem of Doppler-shift and Dopplerbroadening seems to be appropriate. If one assumes that the positrons detected are emitted from the quasimolecular system, one notes that due to the axial symmetry of the reaction- and the detection system together with the limited angular range of positron acceptance, the Dopplershift of the observed positrons can be corrected for (c.m. energy, and c.m. cross section) with good accuracy. But what is even more important in case of line structures in the positron spectrum: the Doppler broadening is very small. For future experiments it may be crucial to test the

assumption that positron "lines" are emitted from the quasimolecular system. This could be done by introducing also a " $\varphi$ "-sensitivity in our ion- and positron detectors, which can be easily incorporated in our apparatus with simple modifications. In case of quasimolecular positron "lines" there would be no " $\varphi$ "-dependance in the spectrum, whereas one should find one in case of "nuclear" positrons, which are emitted from the scattered ions or the recoils.

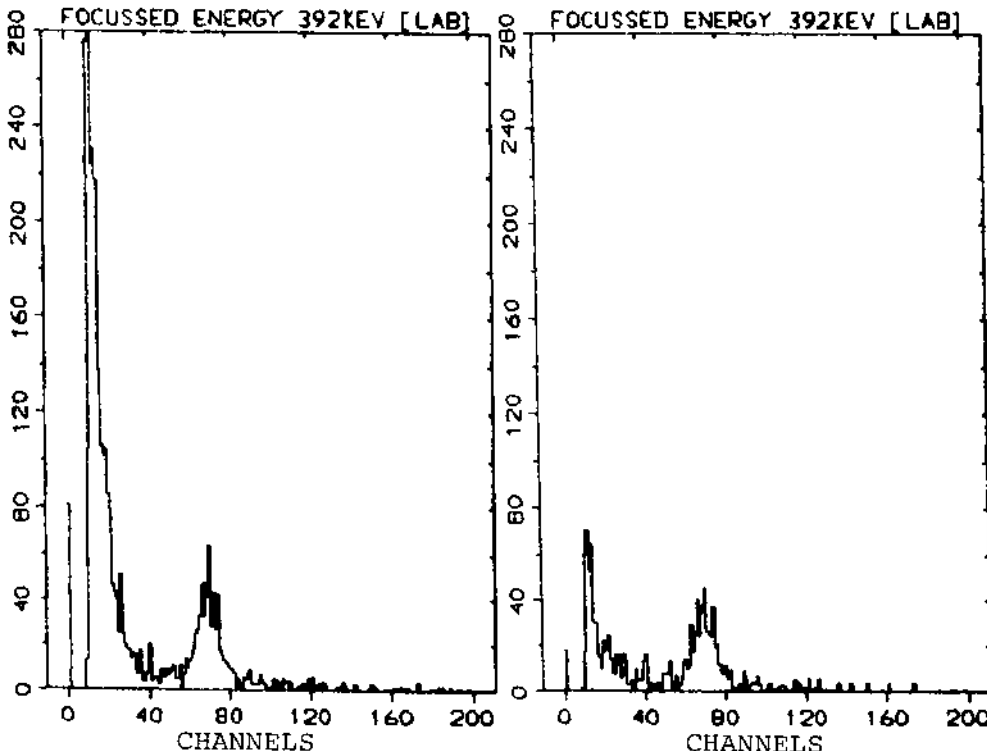


Fig. 6b,c. The background, especially at low energies ( $\leq 150$  keV) can further be reduced by requiring a coincidence between the plastic scintillator and the annular proportional counter. Fig. 6b shows a scintillator spectrum without coincidence (mean focussed positron energy: 392 keV) and Fig. 6c shows the same spectrum in coincidence with the proportional counter.

Very important for our experiments were Si-detectors, mounted around  $45^\circ$  relative to the beam, which monitored the energy spectra of the scattered ions. In this way we could control continuously the degree of

target deterioration, which resulted in a downward shift of the effective bombarding energy including low energy tails. We tried various methods of target preparation, rolled metallic foils, evaporation of metals on a carbon-foil and covering it by a further C-foil, and evaporation of metal oxides on C-foils. None of the methods led to completely stable targets, when bombarding these foils with thicknesses between  $300 \mu\text{g/cm}^2$  and  $1 \text{ mg/cm}^2$  with  $1 - 2 \text{ pA}$   $^{238}\text{U}$ -beams. Therefore we usually changed the target when the beam monitor signaled a certain deterioration. Future experiments require still better targets and better controls.

The  $\gamma$ -ray spectra were recorded by two 3" x 3" NaJ-scintillation counters placed at  $90^\circ$  and  $150^\circ$  relative to the beam in coincidence with scattered particles.

Before and after each positron experiment we took  $\delta$ -ray spectra in coincidence with scattered ions using the identical set up but switching only the direction of the toroidal field to focus electrons. In this way we could easily set up the whole experiment making use of the copious  $\delta$ -ray production and could also search for internal conversion lines.

### 3. POSITRON SPECTRA FROM U-U-COLLISIONS

Fig. 7 shows positron-production probabilities per keV energy interval as function of the positron kinetic-energy after conversion into the c.m. frame for  $^{238}\text{U}$ - $^{238}\text{U}$ -collisions at 5.9 MeV/u bombarding energy for four ranges of scattering angles. The targets were rolled metallic foils of  $1 \text{ mg/cm}^2$  thick  $^{238}\text{U}$ , which could reasonable well stand a beam current of about 1 pA. After deterioration, signaled by low energy tails in the scattered particle spectrum, the target was changed. Nuclear background, as determined from the simultaneously measured  $\gamma$ -spectra has not been subtracted. The positron spectra in coincidence with ions scattered to angles smaller than  $37^\circ$  are broad and mostly structureless with maxima between 450 and 500 keV positron energy and exponentially decaying high energy tails. They are reasonably well reproduced<sup>9)</sup> by a semiclassical collision model based on Rutherford trajectories, in which pair-creation induced by the time changing Coulombfield is determined by a coupled channel calculation in the adiabatic basis of a two center Coulombfield.

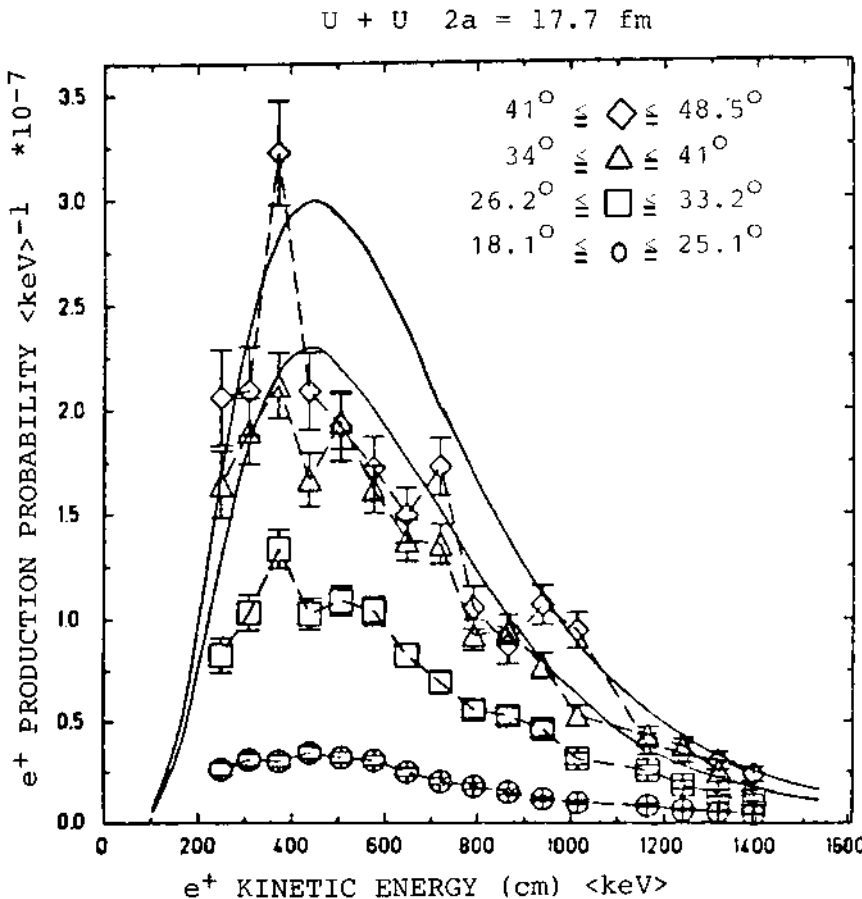


Fig. 7. Positron production probability  $dP/dE$  per keV as a function of the positron kinetic energy in the c.m. system for  $(U+U)$ -collisions at 5.9 MeV/u bombarding energy in coincidence with ions scattered into 4 angular ranges indicated. The solid lines are calculated spectra for Coulomb collisions by Reinhardt et al.<sup>9)</sup>.

#### The positron spectrum in coincidence with ions

scattered between  $41.9^\circ$  and  $48.5^\circ$  in the lab system shows a "line" like structure peaked at about 370 keV and possibly weaker ones around 720 and 950 keV. A subdivision of the positron spectrum in the momentum band around 370 keV into six parts using the positron information from the proportional counter confirms the existence of a relatively sharp "line" with a width of

90 keV and an energy integrated probability of about  $10^{-5}$ . Figure 8 shows additional positron spectra from subsequent experiments with  $^{238}\text{U}$ - $^{238}\text{U}$ -collisions at 5.9 MeV/u bombarding energies. The targets  $500 \mu\text{g}/\text{cm}^2$  metalic  $^{238}\text{U}$ , sandwiched between  $20 \mu\text{g}/\text{cm}^2$  thick C-foils showed again deterioration which was kept as small as possible by a frequent change.

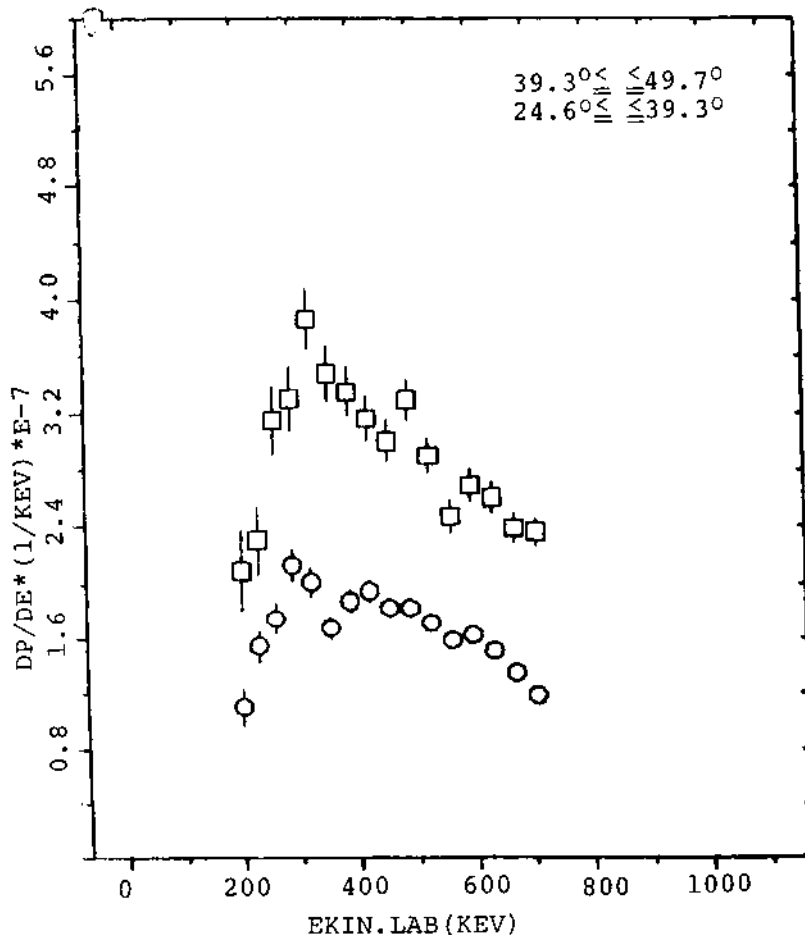


Fig. 8. Positron production probability  $dP/dE$  per keV as a function of the positron kinetic energy in the lab. system for  $(\text{U}+\text{U})$ -collisions at 5.9 MeV/u bombarding energy (very recent data).

The positron spectrum in coincidence with ions scattered between angles of  $39.3^\circ$  to  $49.7^\circ$  shows again a strong indication of a "line" at about 335 keV (lab. system) corresponding to 315 keV in the c.m. frame superimposed on a broad distribution. The main difference with respect to the "line" indicated in the spectrum of Fig. 7 is a shift of the maximum by about 55 keV. The energy integrated intensity and the width of the "line" is similar as in the previous experiment. We could not find until now an experimental deficiency which could easily explain this apparent "line" shift. Thus more experiments have been performed. (see section 6).

#### 4. EXCITATION FUNCTIONS OF PAIR-CREATION IN U+U COLLISIONS

More experiments were recently performed for a better understanding of the experimental conditions under which the "line" structures becomes observable in the positron spectrum. Especially the dependence of the positron spectrum on the bombarding energy seem to be interesting in view of the difficulties with the reproducibility of the "line" energy and the target deterioration. Therefore using  $^{238}\text{U}$ -targets of  $300 \mu\text{g/cm}^2$  sandwiched between two carbon-foils, excitation functions for the positron spectra were measured in steps of about 100 keV/u (the target thickness corresponded to an energy loss of about 85 keV/u) between 5.73 MeV/u and 6.20 MeV/u which was supposed to cover the energy range around the Coulomb barrier of U-U-collisions. Unfortunately the statistics of some of the runs turned out to be insufficient to give clear evidence for "line" structures.

Figures 9a and 9b show positron spectra in coincidence with particles scattered between  $41.5^\circ$  and  $50.3^\circ$  as well  $25.3^\circ$  and  $35.9^\circ$  respectively, for  $^{238}\text{U}$ - $^{238}\text{U}$  at the bombarding energies indicated. A very weak indication of a possible "line" structure at energies around 330 keV (lab.) and a still weaker one at about 500 keV seems to be indicated in most individual spectra coincident with particles scattered around  $45^\circ$ . There is also a threshold like increase of the positron yield between 300 and 700 keV positron energy indicated in these spectra. The "line" structure as well as the threshold like increase is not well recognizable in the positron spectra in coincidence with ions scattered around  $30^\circ$ .

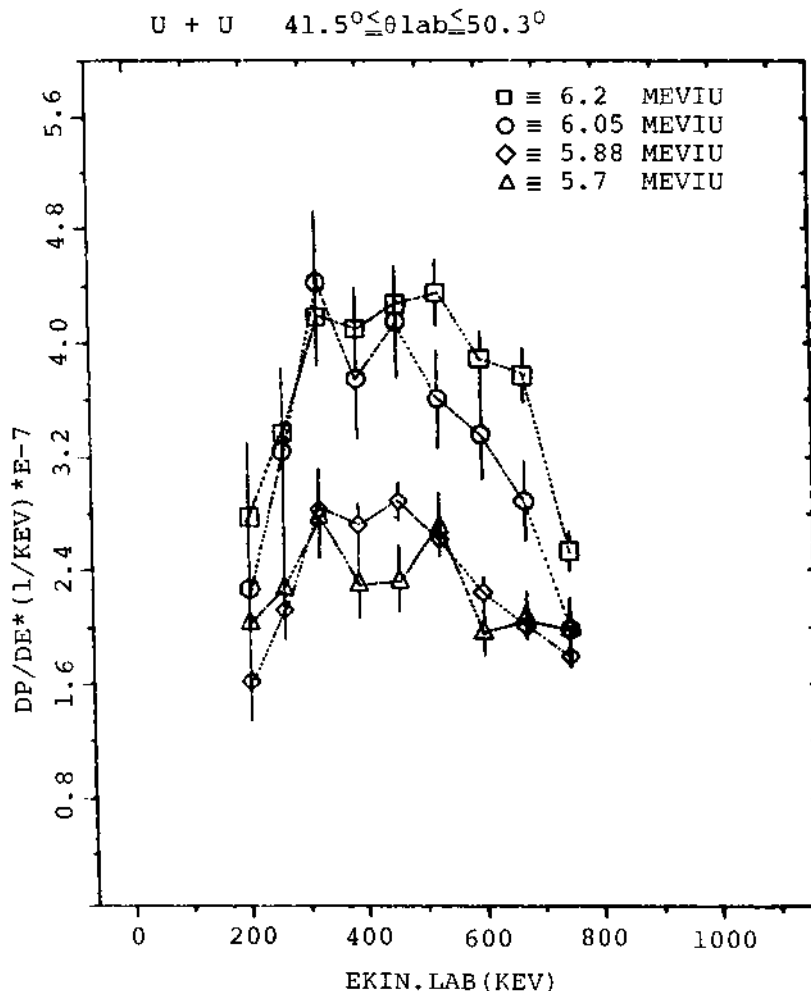


Fig. 9a. Positron production probability per keV as a function of the positron kinetic energy in the lab. frame for  $(U+U)$ -collisions at bombarding energies of 6.2 MeV/u ( $\square$ ), 6.05 MeV/u ( $\circ$ ), 5.88 MeV/u ( $\diamond$ ), and 5.7 MeV/u ( $\Delta$ ). The ion scattering angle range was  $41.5^\circ \leq \theta_{\text{lab}} \leq 50.3^\circ$ .

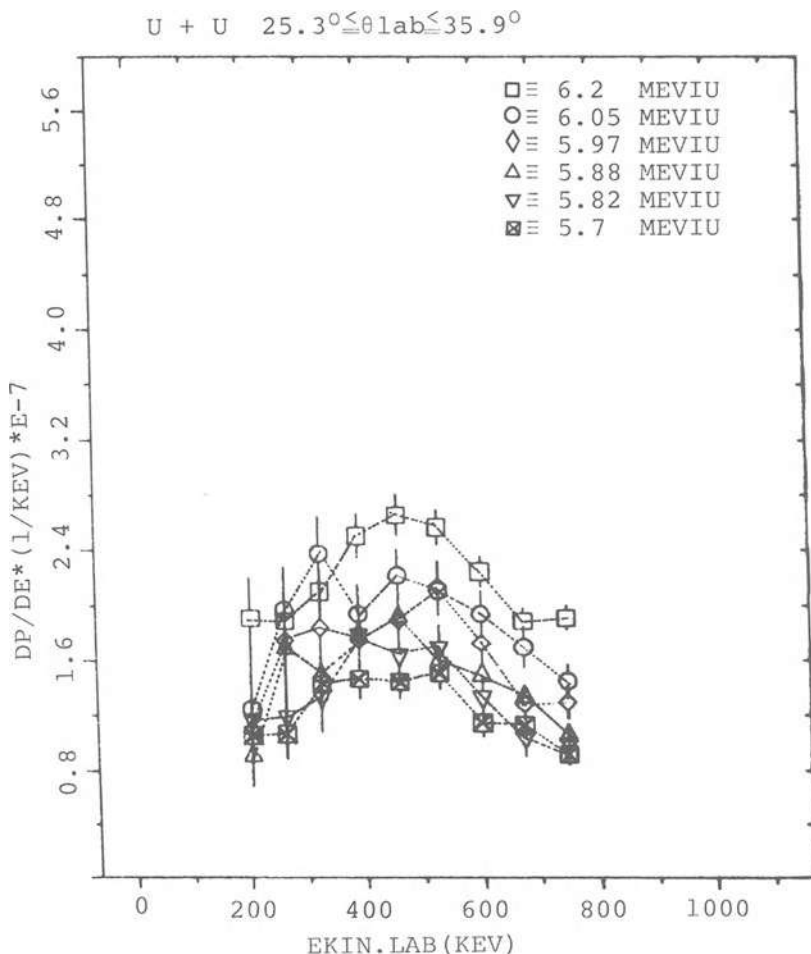


Fig. 9b. Positron production probability per keV as a function of the positron energy in the lab. frame for (U+U) collisions at bombarding energies of 6.2 MeV/u (□), 6.05 MeV/u (○), 5.97 MeV/u (◇), 5.88 MeV/u (△), 5.82 MeV/u (▽) and 5.7 MeV/u (■). The ion scattering angular range was  $25.3^\circ < \theta_{\text{lab}} < 35.9^\circ$ .

Figure 10 shows "45°"-data for the positron spectra gained at 6.2 and 6.05 MeV/u (above threshold) and 5.88, 5.82 and 5.70 MeV/u (below threshold) respectively. Both sum spectra show weak indications of "line" structures. This seems to indicate that the observed "line" structures do not depend very sensitively on the bom-

bardening energy. High resolution experiments, described in section 6 reveal high sensitivity of the energy of the positron fine structures on bombarding energy.

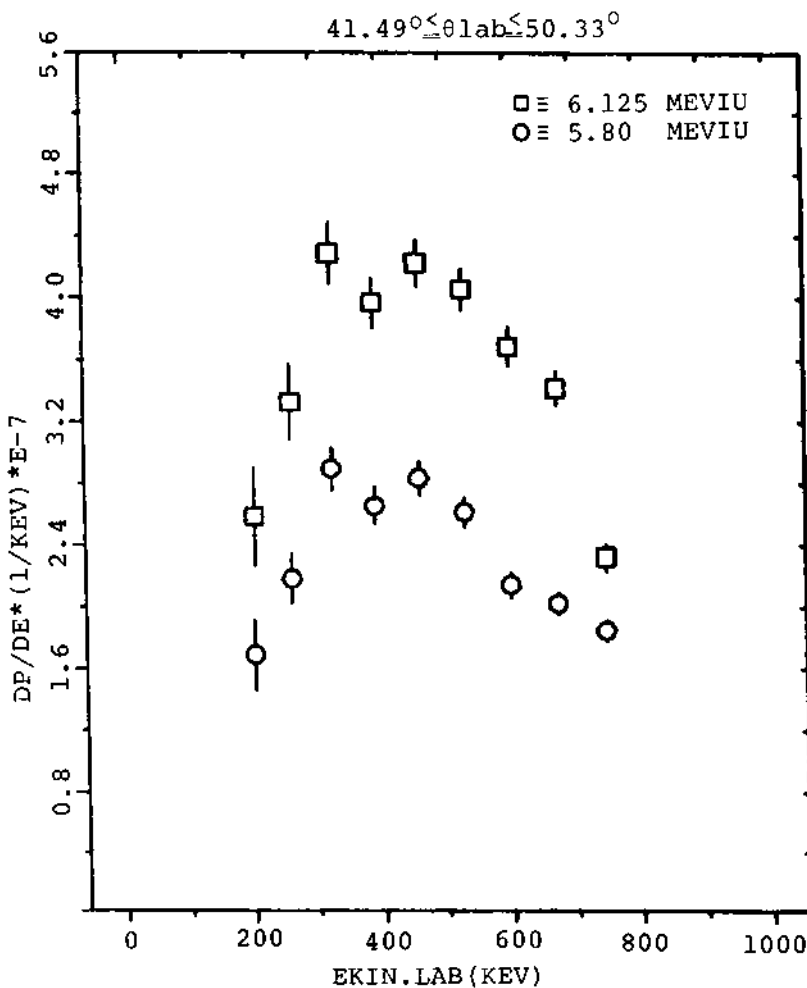


Fig. 10. Positron production probability per keV as a function of the positron energy in the lab. frame for bombarding energies of 6.2 and 6.05 MeV/u (□) and 5.88, 5.82, 5.7 MeV/u (○). The ion scattering angular range was  $41.5^\circ < \theta_{\text{lab}} < 50.3^\circ$ .

From this I should like to summarize, that we seem to have observed in a series of experiments in the positron spectra from U-U-collisions at bombarding energies around the Coulomb barrier positron "line"structures at various positron energies, superimposed on continuous

distribution especially pronounced at scattering angles around  $45^\circ$ . The exact form of these structures remains to be studied.

## 5. POSITRON SPECTRA FROM $^{238}\text{U}$ - $^{232}\text{Th}$ -COLLISIONS

A series of measurements using  $^{238}\text{U}$ -beams and  $^{232}\text{Th}$ -targets have also been performed. First positron spectra from  $^{238}\text{U}$ - $^{232}\text{Th}$ -collisions indicated also a "line" structure with about 50 keV lower energy than that from  $^{238}\text{U}$ - $^{238}\text{U}$ -collisions. Figure 11 shows recently evaluated positron data from  $^{238}\text{U}$ - $^{232}\text{Th}$ -collisions at 5.9 MeV bombarding energy. Positrons in coincidence with ions scattered between  $\theta_{\text{lab}} = 40^\circ - 50^\circ$  indicate a very weak "line" structure at 290 keV lab. energy, which may persist in the positron spectra in coincidence with ions scattered to smaller angles.

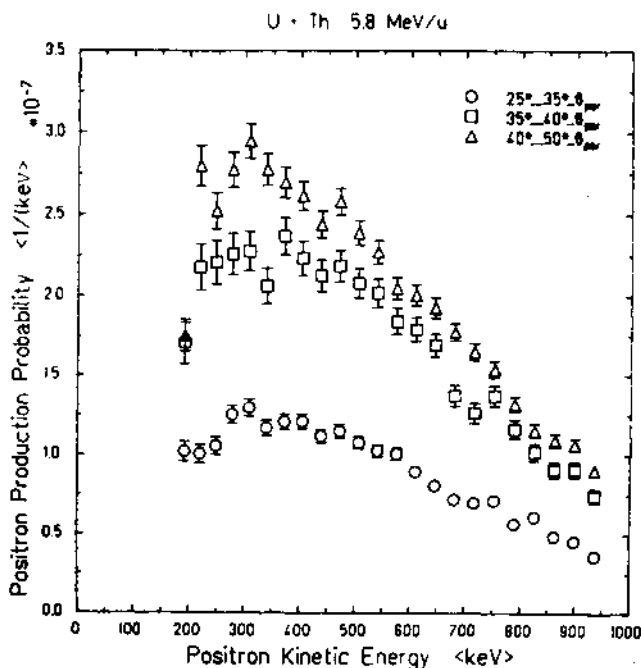


Fig. 11. Positron production probability per keV as function of the positron kinetic energy (c.m. frame) for (U+Th)-collisions at 5.8 MeV/u bombarding energies. The ion scattering angular ranges are

$25^\circ < \theta_p < 35^\circ$  (○),  $35^\circ \leq \theta_p \leq 40^\circ$  (□) and  
 $40^\circ \leq \theta_p \leq 50^\circ$  (△).

## 6. HIGH RESOLUTION POSITRON SPECTRA

Very recently we could analyze some of the U-U-data with improved momentum resolution by making use of the position sensitive proportional detector which subdivided the momentum bin of 13 % - as shown in all previous spectra - into 4 about equal parts. Figure 12a shows the positron spectrum in coincidence with particles

scattered between  $41.5^\circ$  and  $50.3^\circ$  as measured with the scintillation detector alone at a bombarding energy of 5.7 MeV/u. This spectrum which was taken with a momentum resolution of about 13 % has been already shown in Fig. 9a. Figure 12b shows a positron spectrum composed of the spectra gained using the information from the 4 cathode rings of the proportional counter in a completely independant data analysis. One notes a remarkable structure on the positron spectra, with maxima at about 320 keV, 520 keV and possibly 700 keV. There may be a further "maximum" at lower energies. If one sums up the corresponding 4 points from the cathodes which belong to the same magnetic field setting one arrives at the spectrum shown in Fig. 12c, which is comparable with the one using the scintillator counter only (Fig. 12a), as it should be, if the two independant evaluations are consistent.

Preliminary evaluation of the data at various bombarding energies indicates, that at fixed scattering angle the energy of the positron "line" pattern shifts measurably with small changes of the bombarding energy in a characteristic way. This shift of the "line" pattern imposes a very severe requirement on keeping the effective bombarding energy constant. Next we have to investigate the scattering angle dependence of the positron "line" pattern using the data with resolved "lines". Although it is premature to say anything definite on the origin of "line" structures in the positron spectrum shown in Fig. 12b, we think that it points strongly at an interference phenomenon in positron creation. We think, that an interference of the transition amplitudes for spontaneous positron creation from the incoming and the outgoing collision should occur, because in this case the positron energy is directly related with the internuclear distance. The interference effect of spontaneous positron decay from the entrance and exit channel may be enhanced by additional interference with the amplitudes of induced pair-creation, which by itself could not cause a "line" structure.

We have to evaluate first all our data and think about them. We also would like to ask our impatient

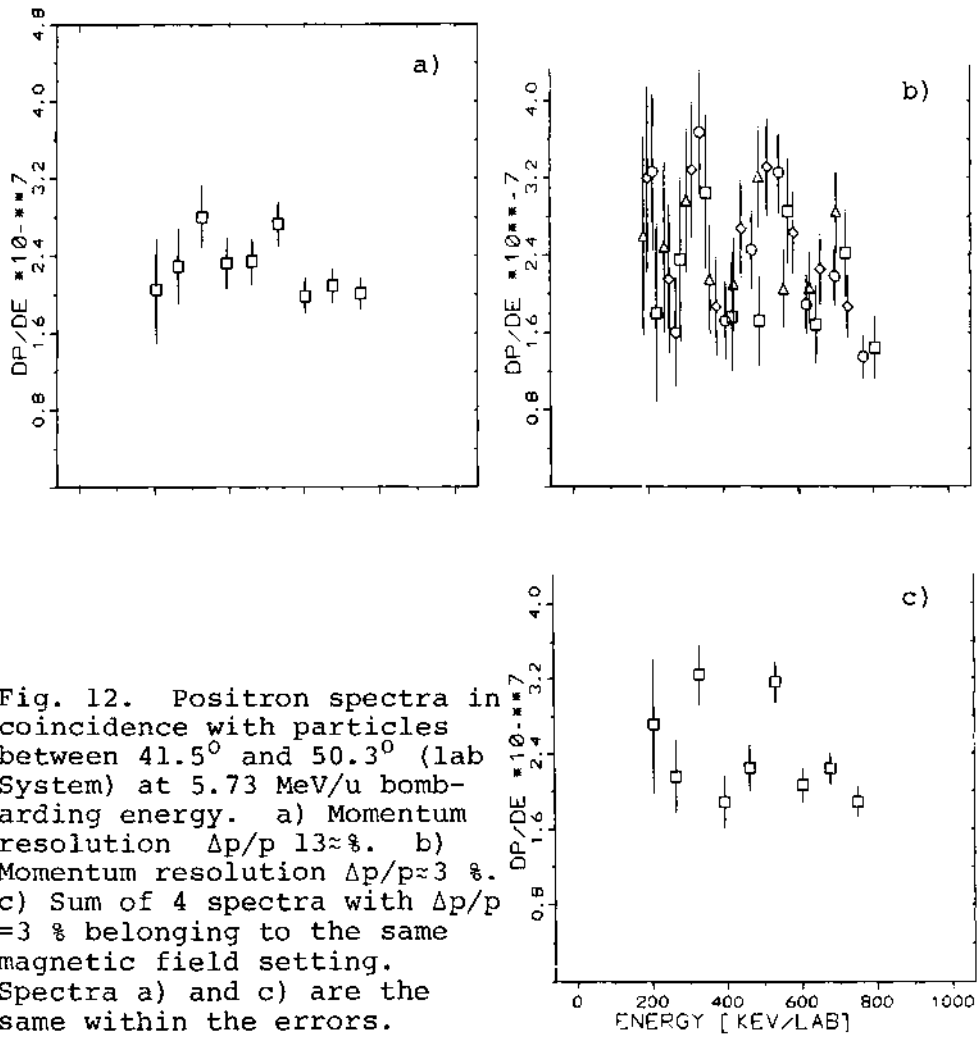


Fig. 12. Positron spectra in coincidence with particles between  $41.5^\circ$  and  $50.3^\circ$  (lab system) at 5.73 MeV/u bombarding energy. a) Momentum resolution  $\Delta p/p \approx 13\%$ . b) Momentum resolution  $\Delta p/p \approx 3\%$ . c) Sum of 4 spectra with  $\Delta p/p = 3\%$  belonging to the same magnetic field setting. Spectra a) and c) are the same within the errors.

theoretician friends to give us a chance to do things right.

Vorrede - Gegenrede - Nachrede:

Vorrede: When I have used the word "we", in the sense that "we have done something", I meant all others except me. Especially I meant my dear friends Dr. Bosch and Dr. Kozuharov, who have fulfilled their hard duties loyally and steadily like one would expect according to their prominent positions as "heavy ion civil servants = Schwerionenbeamte" of the Bundesrepublik Deutschland. Then I meant my two Greeks - "one for love and one for peaks"<sup>11)</sup> - Eleni Berdermann and H. Tsertos. I meant especially our "Mädchen für Alles". W. Wagner, who is so attracted by the GSI, that it takes him only 2 hr 25 minutes to rush from Munich to the GSI with his Porsche. I hope he enjoys such rides also in the future. Then there is my Dr.-student M. Clemente who can breathe deeply again and dream of stars and friendlier galaxis. Last not least I meant Dr. W. Koenig from the Max-Planck-Institute Heidelberg, who could not be stopped by anybody to bring the flavour of the excellency from the Max-Planck-Society in our "Chaoten-haufen". Anyway it was also big fun and I thank them all sincerely. It would have been impossible without anyone of you.

Gegenrede: Dear Dr. Bosch, please be not insulted by my titulation, I meant it quite sincere. You know that I am the only real civil servant of the whole team, a bavarian of course, and this gives me indeed the privilege to sit from time to time at the Chinese-Tower of the English Garden. I drink also a beer and read a newspaper but you are wrong it was always the "Abendzeitung" and never the "Physical Review Letters". You know very well that too much of education may become hinderly for creativity.

Nachrede: I must apologize that the written version of my lectures differs especially in the last sections considerable from the original presentation, during which I said: "Caution, the data are only few days old its interpretation may be all wrong". I had very recently with my good friend D. Liesen whom I gave the title "Schwerionenbeamter" first, an exciting discussion on "oscillations in coincident Mo-Anger spectra emitted in 450 keV Kr<sup>+4</sup> + Kr-collision" by D. Liesen,

A. N. Zinoviev and F. W. Saris, which inspired us to think of an interference pattern in the positron spectra in a similar way. But again we should be given a chance to look more at our data.

#### REFERENCES

1. C. Kozhuharov, P. Kienle, E. Berdermann, H. Bokemeyer, J. S. Greenberg, Y. Nakayama, P. Vincent, H. Backe, L. Handschug, and E. Kankeleit, Phys. Rev. Lett. 42, 376 (1979)
2. W. E. Meyerhof, R. Anholt, Y. El Masri, I. Y. Lee, D. Cline, F. S. Stephens, and R. M. Diamond, Phys. Lett. 69B, 41 (1977)
3. P. Armbruster and P. Kienle, Z. Physik A291, 399 (1979)
4. A. Balandia, K. Bethge, H. Bokemeyer, H. Folger, J. S. Greenberg, H. Grein, A. Gruppe, S. Ito, S. Matsukim, R. Schule, D. Schwalm, J. Schweppe, P. Vincent, M. Waldschmidt, GSI-Bericht 80-16
5. J. Bang and J. M. Hansteen, Kgl. Dan. Vid. Selsk., Mat.-Fys. Medd. 31, no 13 (1959)
6. J. Bang and J. M. Hansteen, Phys. Lett. 72A, 218 (1979); Physica Scripta 22, 609 (1981)
7. E. Kankeleit, 12. Summer School Mikolajki Poland (1979)
8. J. Reinhardt, V. Oberacker, B. Müller, W. Greiner, and G. Soff, Phys. Lett. 78B, 183 (1978)
9. J. Reinhardt et al. UFTP Preprint 34, (1980)
10. P. Kienle, Proceedings of the th General Conference of the EPS, Istanbul, Sept. 7 - 11 (1981)
11. W. Czech in a bavarian-english Gstanzerl for the first time presented to public at midnight of August 27, 1981, while celebrating "5 Jahre Experimente bei GSI".

## δ-RAY SPECTROSCOPY OF QUASI-ATOMS

C. Kozhuharov

Ges. f. Schwerionenforschung mbH  
P.O. Box 11 05 41  
D-6100 Darmstadt, W. Germany

### INTRODUCTION

The subject of our studies is the spectroscopy of high energy δ-rays, emitted in collisions of very heavy ions. In this experimental talk I would like to discuss collision systems with combined charge ( $Z_u = Z_p + Z_t$ ) of the projectile ( $Z_p$ ) and the target ( $Z_t$ ) atoms about equal or larger than the reciprocal of the fine structure constant :  $Z_u \cdot \alpha \gtrsim 1$ . Furthermore, we concentrate on δ-electrons with very high energies - above 100 keV up to 2000 keV. It is easy to be understood qualitatively that a large energy and momentum transfer to a bound electron is possible only if the initial momentum of the electron is also very high - i.e. high energy δ-rays originate mostly from the sharper localized, strongly bound innermost shells. For very heavy quasi-atoms one expects a rapid increase of the high-momentum components as a consequence of the enormous relativistic "shrinking" of the electronic wave functions <sup>1,2,3</sup>. Hence, the high energy tail of the δ-ray spectrum can be attributed to the high energy component of the momentum distribution of strongly bound quasatomic electrons and, thus, provide information about their wave function and energy.

### EXPERIMENTAL ARRANGEMENTS

Two experimental set-ups possessing somewhat complementary features were utilized: An iron-free "orange"-type β-spectrometer <sup>4</sup> and an achromatic electron channel <sup>5</sup>.

Figure 1 shows a schematic view of the "orange"-type β-spectrometer, in which a toroidal magnetic field produced by 60 current coils is used to momentum analyze and focus electrons emitted from

the target onto a small, cone-shaped plastic scintillator counter.

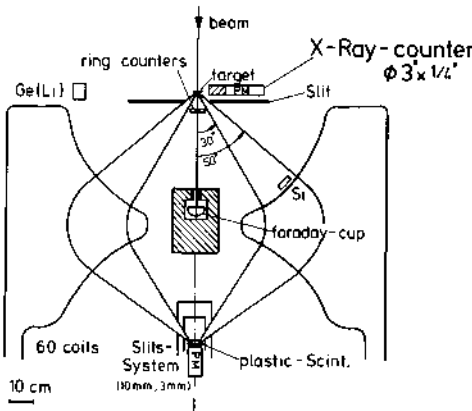


Fig. 1. Experimental set-up in the iron-free "orange"-type  $\beta$ -spectrometer. Momentum resolution  $(\Delta p/p) = 0.08$ , transmission  $T = 1$  srad. Coincidence measurements with scattered particles and/or X-rays are performed.

The momentum direction of the emitted  $\delta$ -rays is defined by the entrance slits. Two configurations have been used - one shown in Fig. 2a, where all electrons emitted between  $30^\circ$  and  $50^\circ$  ( $\theta_\delta$ ) relative to the beam direction and within a momentum band of  $(\Delta p/p) = 0.018$  were focussed and the second configuration - with  $50^\circ \leq \theta_\delta \leq 70^\circ$  and  $(\Delta p/p) = 0.014$ . The transmission efficiency in both cases run to 0.08 of  $4\pi$  (1 srad). The large transmission renders possible the detection of small  $\delta$ -ray intensities and the performance of coincident measurements with X-rays and/or with scattered particles. Characteristic K-X-rays were detected by two  $\phi 3'' \times 1$  cm NaI scintillator counters, mounted 4.5 cm away from the target. All particles, scattered between  $9.5^\circ$  and  $27^\circ$  (arrangement shown in Fig. 2a) or between  $16^\circ$  and  $48^\circ$  (second configuration, not shown here) relative to the beam axis were detected by an annular parallel-plate avalanche counter. Its active area was subdivided into 8 concentric rings with individual read-out, each capable of operating up to countings rates of  $10^6$  sec $^{-1}$ . Kinematical particle coincidences between particular rings were also possible, allowing an unambiguous definition of scattered particle trajectories for asymmetric collision systems. The magne-

tic field of the spectrometer was swept repeatedly up and down focussing  $\delta$ -rays with energies typically between 150 keV and 2.4 MeV. The measuring time after each field adjustment was normalized to the number of elastically scattered particles, detected by a Si-surface barrier monitor counter (BM). The multi-parameter data were recorded event-by-event, together with the normalization spectra and the corresponding instantaneous value of the spectrometer magnetic field. Self-supported  $\sim 1 \text{ mg/cm}^2$  metallic foils of  $^{238}\text{U}$ ,  $^{232}\text{Th}$ ,  $^{208}\text{Pb}$ ,  $^{197}\text{Au}$ , and  $^{120}\text{Sn}$  were bombarded with  $^{208}\text{Pb}$ -ions, accelerated up to 4.7 MeV/u ( $v_\infty/c = 0.10$ ) at GSI Darmstadt.

The experiments with the achromatic magnetic electron channel, shown in Fig. 2 were performed both at the Heidelberg MP Tandem van de Graaff accelerator: C-, S-, and Ni-beam (and in combination with the postaccelerator - Ni-, Br-, and I-ions, respectively) as well as at UNILAC accelerator: (Pb-ions). Zr, Pr, Pb, and U foils of thicknesses  $0.5 \div 1 \text{ mg/cm}^2$  were used as targets.

$$\Delta p/p = 12\%$$

$$\Delta\Omega = 4.1 \text{ msr}$$

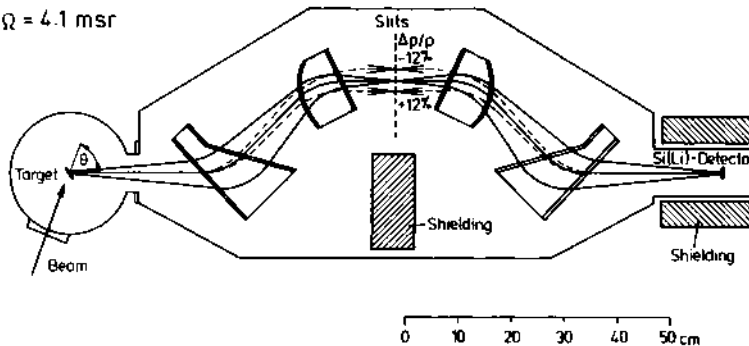


Fig. 2. Achromatic magnetic electron channel (the parallel-plate avalanche particle counter and the NaI-counters for X-rays are not shown in the Figure). The variable electron detection angle  $\theta$  allows measurements of  $\delta$ -angular distribution.

The channel separates a momentum byte of  $(\Delta p/p) = 0.24$  and focusses it with a transmission of 4 msrad onto a cooled Si(Li) counter, which energy resolution ran to 2.5 keV at 1 MeV. Similar as in the "orange" spectrometer, X-ray counters (two  $\phi 2" \times 1 \text{ cm}$  NaI scintillator counters) and particle-counters (annular parallel-plate avalanche counter with a  $\theta$ -sensitive anode and a  $\phi$ -sensitive cathode) were mounted in the scattering chamber (not shown in the figure). Unlike the "orange" spectrometer the relative small solid angle allows better definition of the  $\delta$ -ray emission angle relative

to the beam axis or (combined with the  $\theta$ - and  $\phi$ -information from the particle counter) relative to the trajectory of the scattered particles. The channel can be rotated in the plane around the target, thus allowing angular distribution measurements.

Since the bombarding energies are about 20 % below the Coulomb barrier elastic scattering with Rutherford trajectories of the projectile and target nuclei is considered. This (and the native modesty of the crew) allows to reduce the "F.T.O."-n-fold differential cross section <sup>6</sup> for binary reaction to a measurable 3-fold one :  $d^3\sigma/d\Omega_\delta dE_\delta d\Omega_{ion}$  as a function of the  $\delta$ -ray kinetic energy  $E_\delta$ , relative ion velocity  $v_\infty$ , united atom charge  $Z_u$ , and the particle scattering angle (lab.)  $\Omega_{ion}$ . The emission probability for a  $\delta$ -ray with energy  $E_\delta$  per collision is given by :

$$p = \left( \frac{d^3\sigma}{d\Omega_\delta dE_\delta d\Omega_{ion}} \right) / \left( \frac{d\sigma_{Ruth}}{d\Omega_{ion}} \right) \quad (1)$$

and can be extracted from the measured  $\delta$ -ray yields in coincidence with particles scattered through an angle  $\Omega_{ion}$  and from the simultaneously recorded particle counting rates. For asymmetric collision systems the data are also presented as a function of the distance of closest approach  $R_{min}$  or the impact parameter  $b$ , defined as follows :

$$R_{min} = a \left( 1 + \csc \frac{\theta_{CM}}{2} \right) \quad (2)$$

$$b = a \operatorname{ctg} \frac{\theta_{CM}}{2} \quad (3)$$

with :  $2a = Z_p Z_{te}^2 / E_{CM}$  - collision diameter (distance of closest approach for head-on collision).

From the investigation of  $\delta$ -ray production probabilities as a function of the distance of closest approach  $R_{min}$  or the impact parameter  $b$ , one expects not only more detailed information about the mechanism of Coulomb ionization. The ion trajectory must be taken into consideration for very heavy collision systems, since the binding energies of the innermost shells are expected to vary strongly with the internuclear separation, especially at very small distances <sup>3</sup>. On the other hand the impact parameter dependence represents a very sensitive test for scaling laws, as already discussed for ionization probabilities determined via X-ray measurements <sup>1,2</sup> or for positron emission probabilities per collision <sup>6</sup>. Unlike X-ray measurements the energy transfer is determined for fixed  $\delta$ -ray energy, provided that the binding energy is known; and vice versa - if the validity of the scaling law is established - unknown binding energies of electrons in superheavy colliding systems can be experimentally determined to some extent.

Double differential cross sections ( $d^2\sigma/d\Omega_\delta dE_\delta$ ) - i.e. Eq. (1) integrated over all impact parameters - have been also extracted from measured single δ-ray energy distributions, normalized to the number of elastically scattered particles detected by the beam monitor counter.

As already mentioned above, K-X-ray associated with δ-ray emission (the latter both single as well as in coincidence with scattered particles) were recorded simultaneously.

#### EXPERIMENTAL RESULTS AND DISCUSSION

Extending our very first experiments with lighter ions <sup>7,8</sup> to much heavier systems, we ask first of all whether the observed δ-electrons still originate from the quasi-atom. Let us, therefore, look first at the dependence of the δ-ray emission on the united charge number  $Z_u$ . The principal features reflected in the spectra displayed in Fig. 3 are :

- ( i) The very high kinetic energies of the δ-rays observed: Up to 750 keV for the  $Pb \rightarrow Sn$  collision system with  $Z_u = 132$  and 1.7 MeV for the  $Pb \rightarrow Pb$  system with  $Z_u = 164$ . Recently, we succeeded to measure δ-rays with reasonable statistics at kinetic energies of 2.4 MeV emitted in  $U + Pb$  collisions. This kinetic energy is more than 20 times higher than the binding energy of K-electrons in U-atoms and lets one for-taste the magnitude of the momentum transfer to the bound electrons;
- ( ii) The large difference in the intensities of the  $Pb-Sn$  and  $Pb-Pb$  spectra of more than one order of magnitude;
- (iii) The much steeper fall-off of the  $Pb-Sn$  spectrum, reflecting the relative lack of high momentum component of the bound state wave functions compared to the  $Pb-Pb$  distribution.

All of these imply that the electrons have been emitted from bound quasi-atomic states, where, due to the  $Z_u$ -dependent relativistic contraction of the wave function, large momentum transfers to strongly localized bound electrons become possible. This is also corroborated by the data in Fig. 4, in which the double-differential cross section ( $d^2\sigma/d\Omega dE$ ) at given kinetic energy  $E_\delta = 470$  MeV is displayed versus the united charge  $Z_u$  for the systems  $C+Pb$ ;  $Ni+Pb$ ;  $Pb+Pr$ ;  $Pb+Au$ ;  $Pb+Pb$ ; and  $Pb+Th$  measured also at the same relative ion velocity.

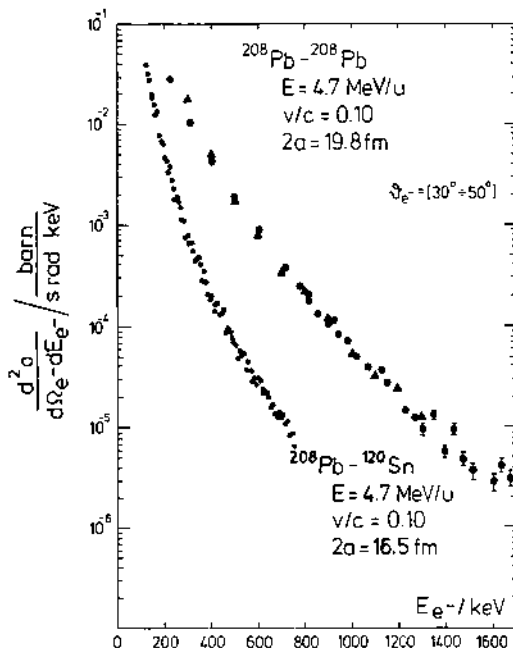


Fig. 3.  $\delta$ -ray spectra from Pb+Pb ( $Z_u = 164$ ) and Pb+Sn ( $Z_u = 132$ ) collision systems measured at the same relative velocity ( $v_\infty/c$ ) = 0.10. Also indicated are the distances of closest approach for a head-on collision  $2a$ . The data are from <sup>9</sup>.

The increase of the cross section over four orders of magnitude, whereas  $Z_u$  only doubles, demonstrates again the characteristic behaviour of bound state wave functions in superheavy quasi-atoms. For lower  $Z_u$  the ionized electrons originate predominantly from the L-shell <sup>5,10</sup> with binding energies much smaller than the kinetic energy observed - i.e. at given  $\delta$ -ray energy the energy transfer required  $\Delta E = |BE| + E_\delta$  is determined by  $E_\delta$ . The latter does not apply to the heavier systems, where the saturation of the  $Z_u$ -dependence observed is partially due to the stronger binding. This is easy to be understood qualitatively: The K-shell is expected to be more sharply localized than the L-shell also at very high  $Z_u$  - i.e. the value of the high energy component should be higher for K-electrons in the region of initial momenta considered.

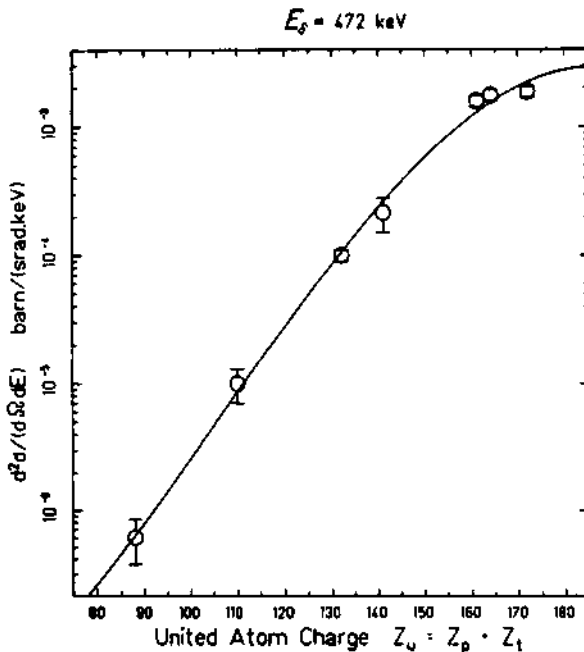


Fig. 4. Double-differential cross section for  $\delta$ -ray emission at fixed c.m. electron kinetic energy of 427 keV for the collision systems: C+Pb; Ni+Pb; Pb+Sn; Pb+Pr; Pb+Au; Pb+Pb; and Pb+Th. The relative ion velocity is  $v_\infty/c = 0.10$  (the data point for Ni+Pb has been extrapolated from  $v_\infty/c = 0.091$ ). The data are from <sup>9,5,10</sup>.

However, the ionization probability depends also on the energy transfer needed ( $\Delta E = E_\delta + |BE|$ ) to induce transition from a state with binding energy BE to continuum state with  $E_\delta$ . Thus, the stronger binding can cancel to some extent the effects of sharper localization.

#### ASYMMETRIC COLLISION SYSTEMS WITH $Z + \alpha \approx 1$

The spectra shown in the previous chapter represent a superposition of contributions from several inner shells - mostly from  $1s\sigma$ ,  $2p_{1/2}\sigma$ , and  $2s\sigma$ -quasi-atomic states. A preferential observation of the contributions from a particular quasi-atomic shell to the total  $\delta$ -ray spectrum is possible, if only  $\delta$ -rays, asso-

ciated with an emission of characteristic X-rays of one of the collision partners are being detected. The vacancy left in a shell after  $\delta$ -electron emission decays in a time of  $\tau_{\text{hole}} \approx 10^{-17} \div 10^{-18}$  sec, which is much longer than the collision time  $\tau_{\text{coll}} \approx 10^{-20}$  sec - i.e. the decay occurs after the nuclei are well separated and the quasi-molecular picture does not hold. It has been pointed out already <sup>1,2,3</sup> that for asymmetric collisions ( $Z_p \neq Z_t$ ) a vacancy produced in the  $1s\sigma$ -state of the quasi-atom becomes a K-hole in

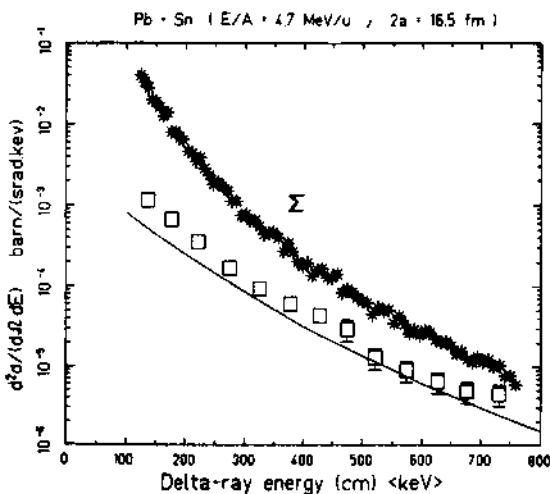


Fig. 5a.  $\delta$ -ray spectrum from  $\text{Pb} + \text{Sn}$  collisions at  $(v_{\infty}/c) = 0.10$  associated with K-X-rays from lead ( $\square$ ) is compared with results of coupled channel calculations performed by Soff et al. <sup>11</sup>, which include multistep processes. Also shown is the single  $\delta$ -ray spectrum ( $\Sigma$ ). (The data are from Ref. 9).

the heavier collision partner.

For two systems with similar united charge  $Z_u$   $\delta$ -rays associated with K-X-rays of the heavier collision partner have been measured. In Fig. 5a the results for  $^{208}\text{Pb} + ^{120}\text{Sn}$  collisions ( $Z_u = 132$ ) are shown together with the single spectrum ( $\Sigma$ ).

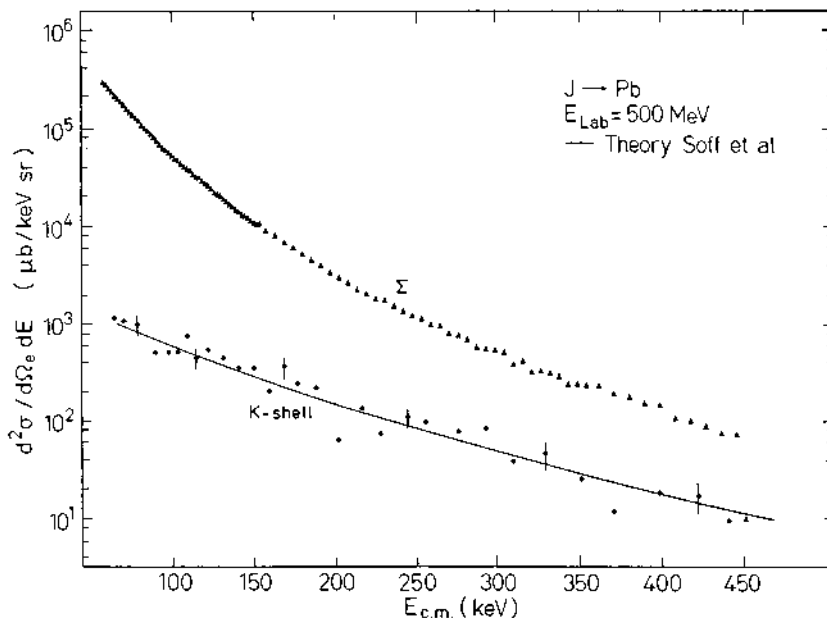


Fig. 5b: The same as in Fig. 5a for  $I \rightarrow Pb$  collisions at  $(v_\infty/c) = 0.09$ . (The data are from Ref. 12).

The measurements were performed with the "orange"-type  $\beta$ -spectrometer at GSI Darmstadt. The relative ion velocity ran to  $(v_\infty/c) = 0.10$ . The corresponding spectra for the system  $^{127}I \rightarrow ^{208}Pb$  are presented in Fig. 5b. The data were taken at MPI Heidelberg at slightly different ion velocity  $(v_\infty/c) = 0.09$  with the achromatic electron channel. The solid lines in Figs. 5a and 5b represent results of coupled channel calculations performed by Soff et al.<sup>11,3</sup> for  $\delta$ -ray emission in coincidence with an  $1s\sigma$ -vacancy creation. Also included are multistep processes - i.e. the ejected electron can be re-scattered during the collision to higher energy. These calculations reproduce very well both the absolute  $\delta$ -ray yields as well as their energy distribution. It should be emphasized again, that the good agreement between the theoretical calculations (which adopt the quasi-atom-picture) with measurements performed with two different experimental arrangements and with inverse projectile-target combinations strongly corroborate the expectations to exploit in this way the characteristic behaviour of the innermost  $1s\sigma$  bound state in the Pb-Cm quasi-atom ( $Z_u = 178$ ).

In collisions of very heavy ions the multiplicity of  $\delta$ -ray emission per collision is higher than unity for low  $\delta$ -ray kinetic energies. It is possible, therefore, to detect a  $\delta$ -electron ionized from a higher shell in a collision, in which a K-hole has been also

produced and X-ray detected. Such "background" processes are also included in the theory of Soff et al.<sup>11,3</sup>, however, it slightly underestimates the experimental values for  $Pb \rightarrow Sn$ , particularly at low  $\delta$ -ray energies.

The contributions of the K-shell to the total cross section ( $\Sigma$ ) are very small at low kinetic energies (less than 1 % at 40 keV) and do not become significant until the energy reaches very high values. They exhibit a slope not as steep as for the single spectrum but similar to that of the Pb-Pb distribution in Fig. 3. As already mentioned, the lower intensity can be explained by the larger momentum transfer required to emit a K-electron with respect to the much weaker bound L-electrons. On the other hand we also know that higher momenta can be transferred at rather small impact parameters  $b$ , due to the higher Fourier frequencies available in the Coulomb collision. Fig. 6 shows  $\delta$ -ray emission probabilities per collision as a function of the distance of closest approach  $R_{min}$  for two fixed  $\delta$ -ray kinetic energies 540 and 720 keV, at which the K-shell contributions are more significant.

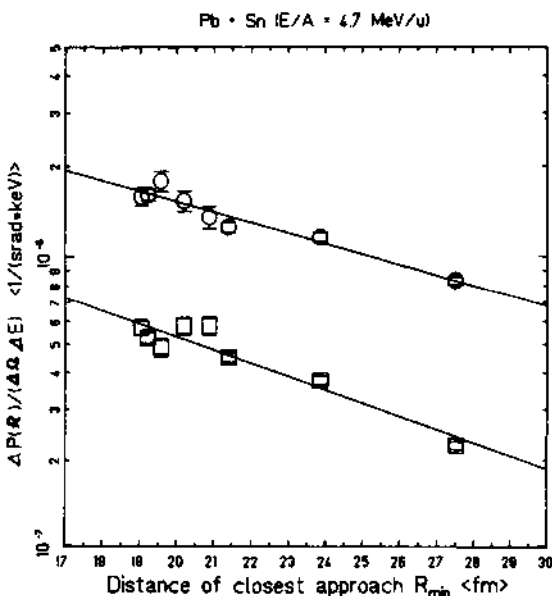


Fig. 6.  $\delta$ -ray emission probability for  $Pb + Sn$  collisions as a function of the distance of closest approach  $R_{min}$  for fixed  $\delta$ -ray energies: (○) 540 keV and (□) 720 keV. The solid line represents a fit to the data with  $P \propto \exp(-2R_{min}(E_{\delta} + |BE|)/E_{\infty})$ ;  $(v_{\infty}/c) = 0.10$ . Data are from Ref. 9.

The slope of the emission probability distributions exhibits an exponential fall-off, steeper for higher kinetic energies according also to expectation based on an analytical model <sup>13</sup> or on a scaling law, already discussed at this Conference <sup>2,6</sup>. The solid lines in Fig. 6 represent a least square fit to the data using  $P \propto \exp[-2R_{\min}q_{\min}]$ . From the fitted value of  $q_{\min} = (\Delta E/\hbar v_{\infty})$  the energy transfer  $\Delta E$  needed for the ionization can be extracted and runs to reasonable values of  $\Delta E = 790$  keV for  $E_{\delta} = 540$  keV and  $\Delta E = 1.03$  MeV for  $E_{\delta} = 720$  keV. No reasonable agreement with the data is achieved, however, if not only the slope but also the absolute values of the data are fitted. Similar behaviour is observed for the  $I \rightarrow Pb$  system for lower δ-ray kinetic energies and larger distances of closest approach  $R_{\min}$  <sup>14</sup>. Nevertheless, it is interesting to note that the slope of the emission probabilities is well described by a simple exponential fall-off ( $\exp[-2R_{\min}q_{\min}]$ ), also valid for L-electrons and apparently for multistep excitations too.

As we have heard before <sup>3</sup>, the dependence on the distance of closest approach of the emission probabilities for electrons from the K-shell of the  $(I \rightarrow Pb)$ -united atom are described perfectly well by the theory, which includes multistep processes <sup>3</sup>, thus emphasizing the role of the latter and the advantages of giving an experimental talk after the data were "lovingly embraced in a theoretical lecture" <sup>2</sup>.

#### VERY HEAVY COLLISION SYSTEMS

$^{208}Pb + ^{208}Pb$  collisions at bombarding energy far below the Coulomb barrier were studied first. Because of its nuclear structure this system gives an unique opportunity to study δ-ray spectra without any distortion due to nuclear de-excitation via internal conversion or internal pair creation, respectively. The disadvantages are also evident :

- (i) The contributions from the innermost  $1s\sigma$  bound state cannot be separated by a K-X-ray coincidence requirement.
- (ii) The ion trajectory can be defined unambiguously only for scattering through an angle of  $\theta_{CM} = \pi/2$ .

In Fig. 7 the measured double-differential cross sections <sup>9</sup> are compared with results of coupled channel calculations performed by Soff et al. <sup>3,11</sup>, which include multistep excitation processes. Shown are the calculated total δ-ray distribution, representing a sum over all initial bound states up to  $4s\sigma-$  and  $4p_{1/2}\sigma$ -state, as well as contributions from the  $1s\sigma-$  and  $2p_{1/2}\sigma$ -state.

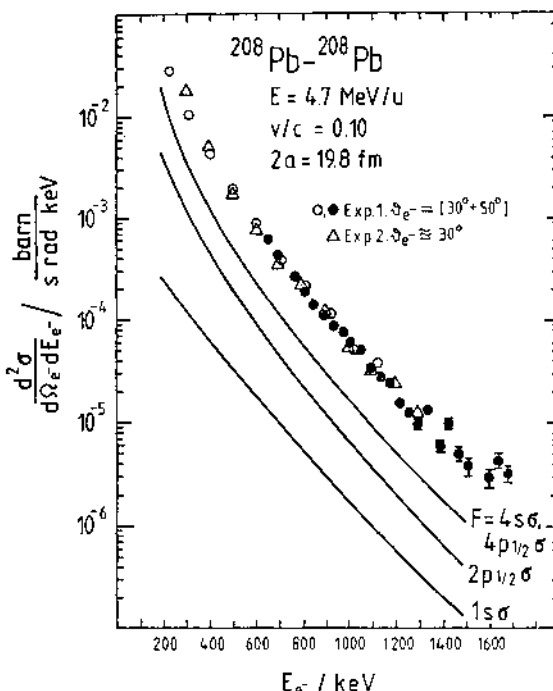


Fig. 7.  $\delta$ -ray spectra from  $^{208}\text{Pb} + ^{208}\text{Pb}$  at 4.7 MeV/u bombarding energy (Exp. 1 - "orange"- $\beta$ -spectrometer; Ex. 2 - achromatic electron channel). The solid lines represent results of coupled channel calculations performed by Soff et al. <sup>3,11</sup> for the total spectrum ( $F = 4s\sigma$ ,  $4p_{1/2}\sigma$  denotes the Fermi surface) and for contributions from the  $1s\sigma$  and  $2p_{1/2}\sigma$ -states, respectively.

The experimental data exceed the calculated values by a factor of about three. The slope of the measured spectrum, however, is reproduced well. It should be noted in this context that perturbation theory values <sup>15,16</sup> also agree in the shape with the measured spectrum, underestimating the data by more than a factor of 6. The pronounced difference between the contributions from  $1s\sigma$ - and  $2p_{1/2}\sigma$ -states, shown in Fig. 7, demonstrate again that the emission process depends strongly on the energy (or momentum-) transfer  $\Delta E = |BE| + E_{\min}$  required and that the  $1s\sigma$ -binding energy cannot be neglected even at  $\delta$ -ray kinetic energies as high as 1.7 MeV.

The dependence of the emission probabilities on the ion scattering angle at several fixed δ-ray kinetic energies between 470 keV and 1.8 MeV is given in Fig. 8.

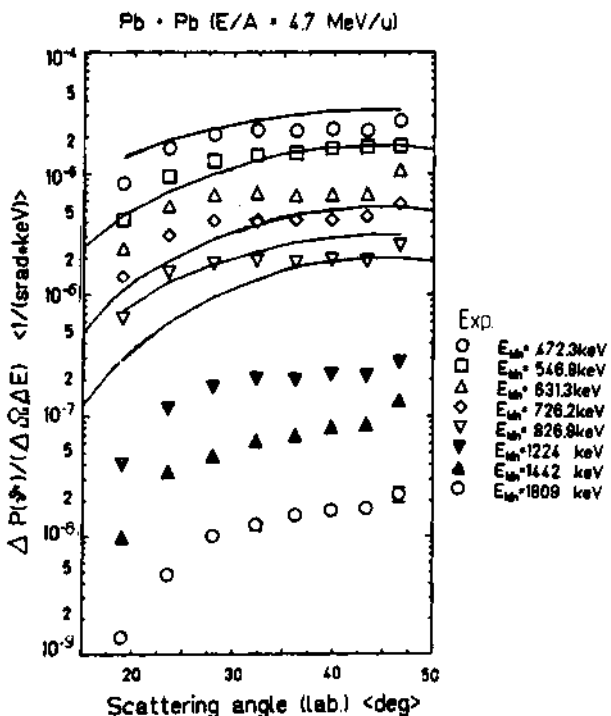


Fig. 8. δ-ray emission probabilities as a function of the scattering angle of the detected ion for kinetic energies of the δ-electrons between 470 keV and 1.8 MeV as indicated. The solid lines represent theoretical calculations of Soff et al. for following energies (from the top) 400, 500, 700, 800, and 900 keV. The curves for 400 and 800 keV are calculated for δ-ray-particle coincidences only, whereas those for 500, 700, and 900 keV for triple coincidences - δ-ray-particles - K-X-ray <sup>3,11</sup>.

The experimental data represent the total emission probability - i.e. contributions from several inner shells are superimposed. The results of the triple coincidence measurement - i.e. δ-ray-scattered particles and K-X-rays - do not show, within the limits

of error, any significant deviations from the distributions presented in Fig. 8. From this one has to conclude that a large fraction of the K-X-rays observed is not associated with holes in the  $1s\sigma$ - or  $2p_{1/2}\sigma$ -states but results from vacancies produced in higher shells (with ionization probabilities in the order of unity), which may couple to the  $1s\sigma$ -orbital in the outgoing phase of the collision. This finding allows to compare the data in Fig. 8 with calculated impact parameter dependences both of the total as well as of the K-X-ray coincident  $\delta$ -ray emission probabilities <sup>3,11</sup>. Since the scattering particles are identical, the emission probabilities for impact parameter  $b(\theta)$  and those for  $b(\pi-\theta)$  have been weighted with the corresponding Rutherford cross section and folded. The agreement with the experimental data is surprisingly good, keeping in mind the factor of three difference between the total energy distributions presented in Fig. 7. Apparently, the  $\delta$ -ray emission associated with particles scattered through small angles is underestimated by the theory, especially for higher  $\delta$ -ray kinetic energies, at which the effects of rotational coupling (not included in the theory) can be neglected. Further experiments are planned to study this unexpected behaviour, with additional emphasis of the dependence on the relative ion velocity.

Finally, I would like to comment very briefly the results of our measurements at bombarding energies at the Coulomb barrier. It has been pointed out <sup>3,17</sup> that if the observed structures in the positron spectra <sup>6,18,19</sup> are caused by nuclear EO transitions, one should also observe a distinct peak in the  $\delta$ -ray distribution at approximately  $E_{e^-} \approx 1300$  keV. This prediction is based on the calculated ratio of the probabilities for internal pair creation and for internal conversion <sup>20</sup>.

The fact, no such distinct peak is observed in the spectrum presented in Fig. 9 should be interpreted very cautious - the data are still *preliminary*, which can be seen for instance from the arbitrary calibration of the emission probabilities. It should be emphasized too that no Doppler-shift and Doppler-broadening corrections have been made. Sum spectra for U+U and U+Pb have been evaluated in order to obtain better statistics. Displayed in Fig. 9 (from the top) are :

- ( i) The total  $\delta$ -ray production probability associated with particles scattered through an angle  $15^\circ < \theta < 50^\circ$ , analyzed with a broad momentum window ( $\Delta p/p = 0.127$ );
- ( ii) The same - analyzed with a narrow window ( $\Delta p/p \approx 0.02$ ). The energy resolution is defined by the Doppler broadening;
- (iii) The same as the total ( $\Delta p/p = 0.127$ ) with additional U-K-X-ray coincidence requirement.

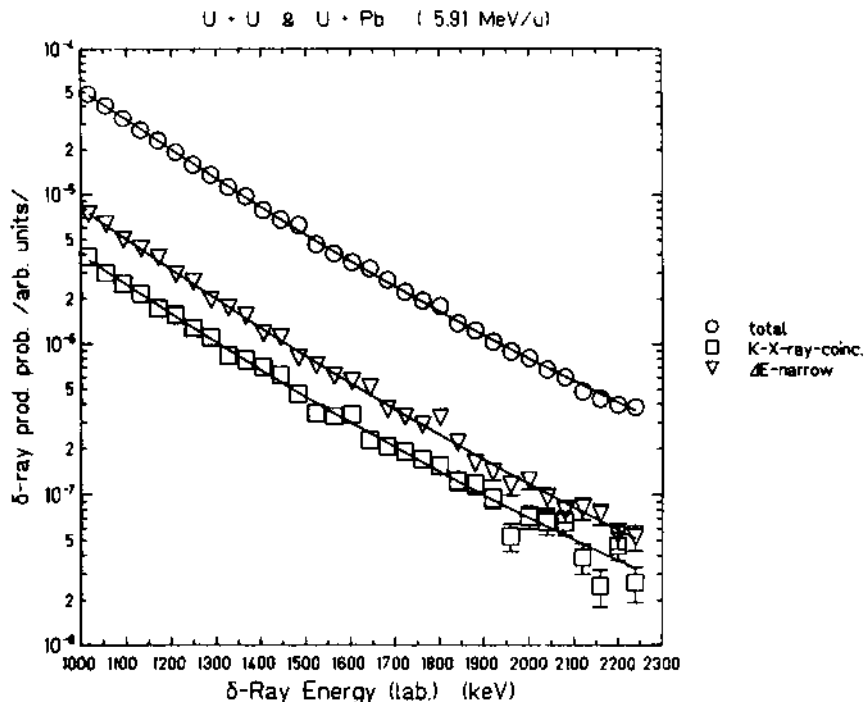


Fig. 9:  $\delta$ -ray production probabilities associated with particles scattered through an angle  $15^\circ < \theta < 50^\circ$  for  $U+U$  and  $U+Pb$  collision systems at 5.91 MeV/u bombarding energy. From the top (○) - spectrum measured with broad momentum window -  $\Delta p/p = 0.127$ ; (▽) the same measured with a narrow momentum window  $\Delta p/p \approx 0.02$ ; (□)  $\delta$ -rays associated with K-X-rays of U (broad window).

The experiments presented here have been carried out by GSI-Heidelberg-Munich collaboration with following members :  
F. Bosch and C. Kozuharov (GSI); F. Güttner, W. Koenig, B. Martin, B. Povh, H. Skapa, J. Soltani, Th. Walcher (MPI für Kernphysik, Heidelberg); E. Berdermann, M. Clemente, P. Kienle, H. Tsertos, W. Wagner (Technische Universität München).

This work has been supported by BMFT.

#### REFERENCES

1. P. Armbruster, contribution to this Conference
2. F. Bosch, contribution to this Conference
3. G. Soff, contribution to this Conference

4. E. Moll, E. Kankeleit, Nukleonik 7 (1965) 180
5. H. Krimm, Diplomarbeit, Universität Heidelberg, 1978  
(unpublished)
6. P. Kienle, contribution to this Conference
7. C. Kozhuharov, P. Kienle, D.H. Jakubaša, M. Kleber,  
Phys. Rev. Lett. 33 (1977) 540
8. F. Bosch, H. Krimm, B. Martin, B. Povh, Th. Walcher,  
K. Traxel, Phys. Lett. 78B (1978) 568
9. E. Berdermann, H. Bokemeyer, F. Bosch, M. Clemente,  
F. Güttner, P. Kienle, W. Koenig, C. Kozhuharov,  
H. Krimm, B. Martin, B. Povh, K. Traxel, Th. Walcher,  
GSI-Jahresbericht (1978) p. 95  
E. Berdermann, H. Bokemeyer, F. Bosch, M. Clemente,  
F. Güttner, P. Kienle, C. Kozhuharov, H. Krimm, B. Martin,  
B. Povh, K. Traxel, Th. Walcher, Verh. DPG (VI) 14 (1979)  
492  
E. Berdermann, F. Bosch, H. Bokemeyer, M. Clemente,  
F. Güttner, P. Kienle, W. Koenig, C. Kozhuharov, B. Martin,  
B. Povh, H. Tsertos, Th. Walcher, GSI-Scientific Report  
(1979) p. 100  
E. Berdermann, H. Bokemeyer, F. Bosch, M. Clemente,  
F. Güttner, P. Kienle, W. Koenig, C. Kozhuharov, B. Martin,  
B. Povh, H. Tsertos, Th. Walcher, Verh. DPG (VI) 15 (1980)  
1168
10. F. Güttner, Diplomarbeit, Universität Heidelberg, 1979  
(unpublished)
11. G. Soff, J. Reinhardt, B. Müller, and W. Greiner, Z. Physik  
A294 (1980) 137
12. J. Soltani, Diplomarbeit, Universität Heidelberg, 1980  
(unpublished)
13. B. Müller, G. Soff, W. Greiner, V. Ceausescu, Z. Phys.  
A285 (1978) 27
14. H. Skapa, Diplomarbeit, Universität Heidelberg, 1980  
(unpublished)
15. G. Soff, W. Betz, B. Müller, W. Greiner, E. Merzbacher,  
Phys. Lett. 65A (1978) 19
16. D. H. Jakubaša, Z. Phys. A293 (1979) 281

17. J. Reinhardt, contribution to this Conference
18. H. Bokemeyer, contribution to this Conference
19. H. Backe, contribution to this Conference
20. G. Soff, P. Schlüter, W. Greiner, preprint GSI-81-23,  
1981

## 2p $\sigma$ MOLECULAR ORBITAL RADIATION OF COLLIDING ATOMS:

### DYNAMICAL-MODEL PREDICTIONS VERSUS EXPERIMENTAL DATA

K.-H. Heinig, H.-U. Jäger, K.-H. Kaun, H. Richter  
and H. Woittennek

Akademie der Wissenschaften der DDR  
Zentralinstitut für Kernforschung Rossendorf bei Dresden

#### INTRODUCTION

In the recent years the problem of the observation of quasi-molecules and of quasimolecular Roentgen emission in heavy ion-atom collisions was very important in view of the electronic structure of heavy quasiatoms with effective atomic numbers much higher than 100 and for the observation of new Processes of quantum electrodynamics in very strong electromagnetic fields. The formation and the radiative decay of quasimolecules with inner-shell vacancies in energetic ion-atom collisions manifest themselves in the x-ray spectra. The drastic change of electronic binding energies at small internuclear distances causes a collision broadening of the characteristic lines of the colliding atoms. Compared with the collision broadening at thermal energies, in energetic heavy ion collisions this effect becomes so strong that a new notation has been introduced, namely quasimolecular x-ray continua or molecular orbital (MO) radiation. These quasimolecular x-ray continua have been extensively studied during the last few years. Some of their characteristic properties such as energy limits and yields can be estimated qualitatively in a simple way from correlation diagrams of quasimolecular orbitals and collision times.

Symmetric or nearly symmetric collisions ( $Z_1 \approx Z_2$ ) in the medium-mass region with ion energies of about 1MeV/amu have been systematically studied using the Dubna heavy-ion cyclotron U300. In the high-energy part of the x-ray continuum situated above all characteristic lines emitted, two distinct x-ray continua have been identified which proved to be both of quasimolecular origin. It is the aim of the present contribution to review this experimental work and the corresponding dynamical-model calculations. To understand the compli-

cated radiation processes in such a complex system as a rotating, transiently formed quasimolecule, the influence of approximations in the dynamical model on the spectral distribution of the continuous x-ray spectra is discussed. Additionally, preliminary results on the impact parameter dependence of the quasimolecular x-rays will be presented.

#### THE PROPERTIES OF THE QUASIMOLECULAR X-RAY CONTINUA

Now it is well known and generally accepted that during slow (with respect to inner-shell electron velocity) collisions of heavy atoms a quasimolecule or even a quasiatom is formed. This concept was proposed by Fano and Lichten (1965) when they explained data on electron ejection from the pioneering Ar + Ar collision experiments (Afrosimov et al. 1964, Everhart and Kessel 1965). They used correlation diagrams to understand the promotion process of inner-shell

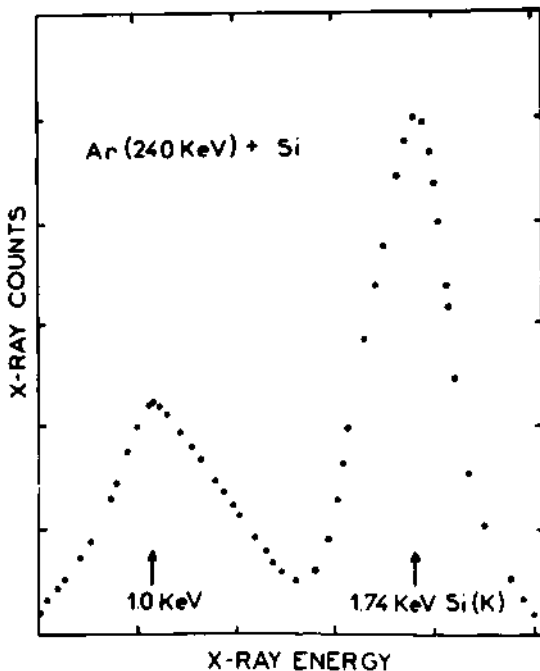


Fig. 1. Direct signature of the quasimolecule formed in the Ar + Si collision experiment of Saris et al. (1972). The continuous distribution of x rays at  $E_x \approx 1\text{keV}$  was found to be L x-radiation of the quasimolecular system Ar + Ar.

electrons to states of lower binding energy. The observation of non-characteristic continuous x-ray spectra has given a direct signature of the quasimolecule formed. Quasimolecular continuous x-ray emission was first seen by Saris et al. (1972). In their Ar + Si collision experiment they observed at  $E_x \approx 1\text{keV}$  an x-ray continuum which was found to be quasimolecular L x-radiation emitted after a collision cascade  $\text{Si} + \text{Ar} \rightarrow \text{Si} + \text{Ar}(2p^{-1})$ ,  $\text{Ar} + \text{Ar}(2p^{-1}) \rightarrow [\text{Ar}+\text{Ar}] (2p\pi^{-1})$ . The experimental spectrum of this radiation is shown in Fig. 1. Quasimolecular M x-radiation of superheavy systems was first found by Mokler et al. (1972). They investigated the quasimolecular  $4f \rightarrow 3d$  radiative transitions in the collision system I + Au. In 1973, high-energy quasimolecular K x-rays were obtained in the Br + Br experiment made in Stanford (Meyerhof et al. 1973) and in the Ge + Ge experiment performed in Dubna (Gippner et al. 1973, 1974). The group at Dubna studied preferentially characteristic and quasimolecular K x-rays of symmetric collision systems such as Ni + Ni, Ge + Ge, Kr + Kr, Nb + Nb, La + La and Bi + Bi at incident ion energies of about 1MeV/amu (see Kaun et al. 1976, 1977). Fig. 2 shows a typical x-ray spectrum observed in these experiments. It was measured in collisions of 67MeV Nb ions with the atoms of a target of  $1\text{mg/cm}^2$  thickness made of pure metallic niobium.

Besides the intense K x-ray lines of the Nb atoms and the absor-

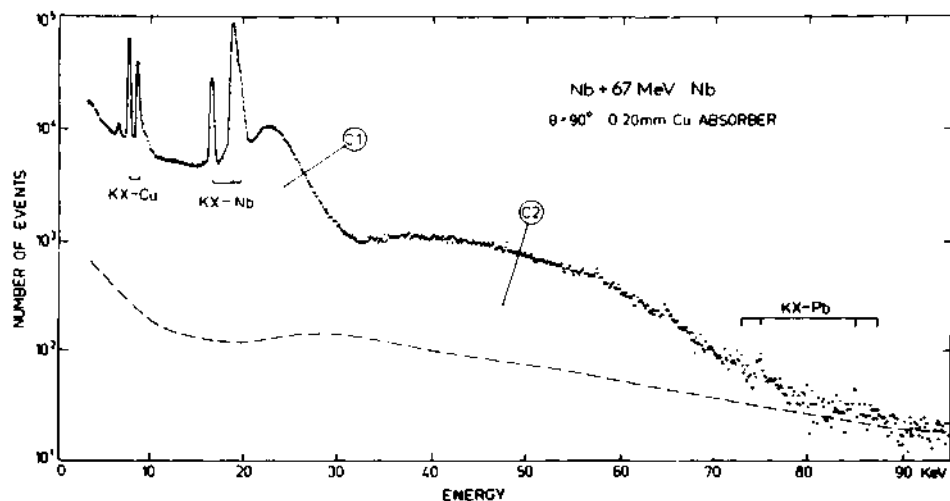


Fig. 2. The experimental spectrum measured by bombarding a Nb target with 67 MeV Nb ions. Besides the intense K x-ray lines of the Nb atoms and the absorber material, the spectrum contains a radiation continuum which ranges up to about the united-atom K x-ray lines and has a two-component structure. The dashed line represents the sum of electronic bremsstrahlung and of the delayed background measured.

ber material (0.2mm Cu), the spectrum shown in Fig. 2 contains a continuous intensity distribution which ranges up to about the united-atom K x-ray energies. We found in the Nb + Nb, Ge + Ge and La + La experiments that this continuum consists of a low-energy and a high-energy component denoted by us as C1 and C2, respectively. The high-energy continuum identified in the first experiment of Meyerhof et al. (1973) appeared to be identical with the continuum called here C2. It is the  $1s\sigma$  MO radiation searched for in ion-atom collision experiments from the very beginning. Thus, our main problem consisted in an explanation of the C1 continuum.

At first we discussed the possibility that the observed x-ray spectra contain significant contributions from other radiation processes like

- (a) bremsstrahlung of secondary electrons (SEB),
- (b) nucleus-nucleus bremsstrahlung (NNB),
- (c) radiative electron capture (REC) and
- (d) Compton scattering of Coulomb excited nuclear  $\lambda$  rays.

As collision systems having only high-lying nuclear states were used, the latter type of background radiation is negligible. The radiative electron capture into the K shell causes a peaked spectrum centered

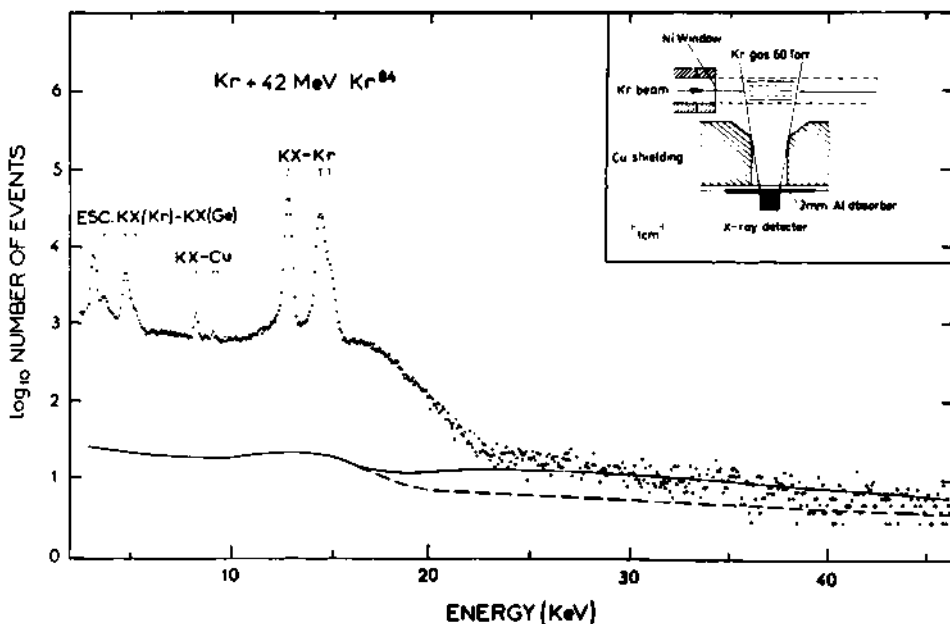


Fig. 3. The x-ray spectrum measured by bombarding a Kr gas target with 42 MeV Kr ions. The dotted line shows the background measured without gas in the target chamber. The solid line presents the sum of this background and the calculated nuclear (El) and electronic bremsstrahlung.

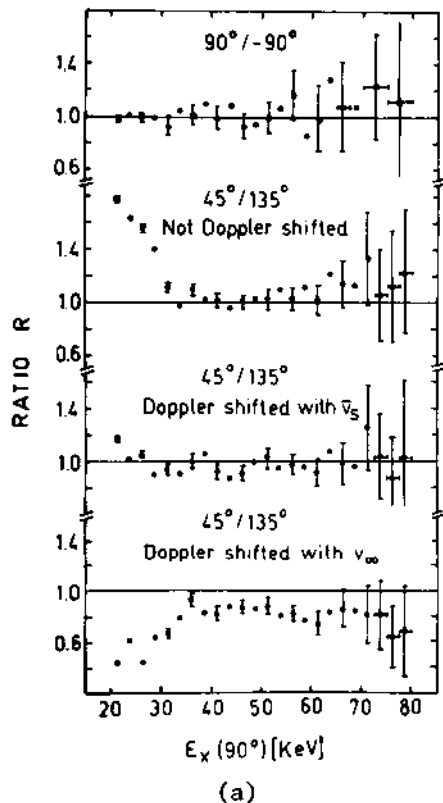
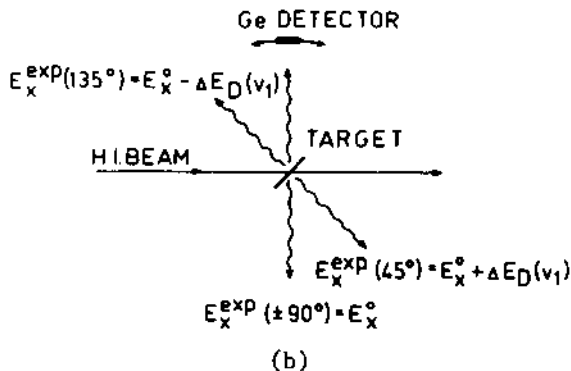


Fig. 4. Doppler shift measurements show that the emitter velocity obtained for the whole continuous x-ray distribution between 20keV  $E_x$  80keV coincides with the center-of-mass velocity of the corresponding quasimolecule. It indicates that both the components C1 and C2 originate from quasimolecular transitions.

(a) The principal arrangement for Doppler shift measurements.

(b) Ratios of normalized x-ray spectra from Nb + 67MeV Nb collisions.

around

$$E_x = E_K + \frac{1}{2} m_e v^2 ,$$

where  $E_K$  is the projectile K-ionization energy. For the collision systems considered here the second term is lower than 1keV. Therefore REC can give no essential contribution, neither to the C1 continuum nor to the C2 continuum. This statement is confirmed by a gas-target experiment. Fig. 3 shows the experimental set-up and the x-ray spectrum measured for the collision system Kr + 42MeV Kr. In this experiment, K-vacancies produced in the projectile in a close collision are filled during the time before the next collision partner is reached. Therefore REC is not expected to be observed. But the low-energy C1 continuum is clearly present in Fig. 3, it must have another origin. A further important result of the Kr + Kr experiment consists in the fact that the C2 continuum is absent.

For SEB and NNB, the x-ray yields calculated by Gippner (1975, 1978) are included in Figs. 2, 3, 14. All the competing radiation processes mentioned prove to give negligible contributions in the spectral region where the C1 and C2 x-ray continua are observed.

Further information on the continua C1 and C2 has been obtained by measuring the velocity of the radiation source using the Doppler-shift method (Meyerhof et al. 1975, Frank et al. 1976). The Doppler-shift analysis of the x-ray spectra measured at polar angles  $45^\circ$  and  $135^\circ$  with respect to the beam direction (Fig. 4a) reveals that the

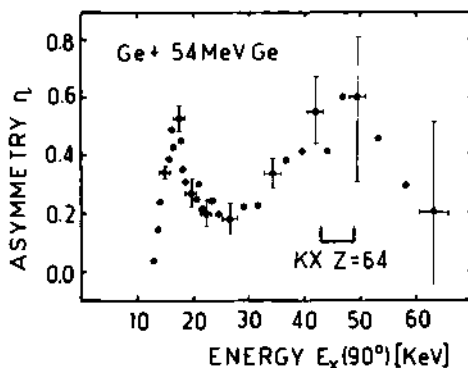


Fig. 5. The anisotropy  $\eta = I(90^\circ)/I(0^\circ) - 1$  of the quasimolecular x-ray spectra obtained in Ge + 54MeV Ge measurements. One finds that  $\eta$  has maxima just at energies which correspond to the maximum energies of the two continuum components C1 and C2 of the quasimolecular spectrum observed.

C1 continuum as well as the C2 continuum are emitted by a system moving with the center-of-mass velocity of the transiently formed quasimolecule (Fig. 4b). Knowing this emitter velocity a x-ray spectrum observed at any angle can be corrected for the Doppler shift, too. If after this correction the angular anisotropy  $\eta(E)$  of the radiation is drawn versus the x-ray energy  $E_x$  (Fig. 5), one finds again a similar behaviour of the C1 and C2 radiation. The angular anisotropy reaches typically values of 50% and has maxima at the high-energy limits of C1 and C2 radiation, respectively.

Up to now we summarized in the present talk all the experimental results which indicate that the two distinct x-ray continua C1 and C2 are both of quasimolecular origin. In the following we present a discussion based more on theoretical concepts and show first how the maximum energies (Fig. 6) and intensities of these x-ray continua can be explained (Heinig et al. 1976). In the solid-target experiments with medium-mass collision partners and impact energies of the order 1 MeV/amu, quasimolecular 1s $\sigma$  vacancies are created preferentially via a two-collision process (Meyerhof et al. 1974). During a "first" collision a 2p $\pi$  vacancy being present or having produced at the beginning of this collision can be transferred to the 2p $\sigma$  orbit because of the strong 2p $\sigma$ -2p $\pi$  rotational coupling at small internuclear distances (Lichten 1967). Considering in the following only symmetric systems ( $Z_1 = Z_2$ ), a 2p $\sigma$  vacancy appears after the collision with probability 1/2 as K-vacancy in the projectile and survives to some extent the time passing until the next close collision

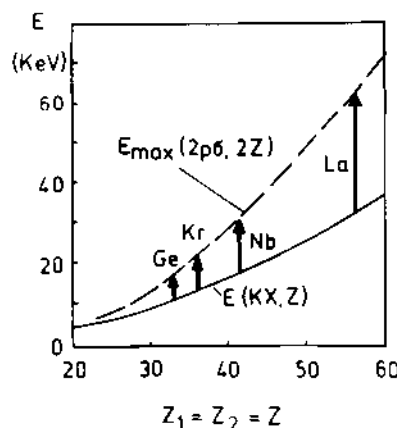


Fig. 6. The maximum binding energies  $E_{\max}$  of quasimolecular 2p $\sigma$  levels agree with the "endpoint energies" of the C1 components measured in our experiments with Ge, Kr, Nb and La ions.

of the projectile with any target atom. Then quasimolecular orbits are generated again and the incoming K-vacancy is shared (Meyerhof 1973) between the  $1s\sigma$  and  $2p\sigma$  orbits. In each moment of such a collision cascade the existing vacancy can be filled up by radiative electronic transitions. There are emitted (Fig. 7) either characteristic K x-ray quanta or  $2p\sigma$  or  $1s\sigma$  MO-radiation quanta. The maximum transition energies calculated for electronic transitions into the  $2p\sigma$  and  $1s\sigma$  MO's (Figs. 6, 8) agree approximately with the maximum photon energies being observed for the continua C1 and C2, respectively. For the collision systems considered, the  $1s\sigma$  (C2) radiation is much less intense than the  $2p\sigma$  (C1) radiation since the number of  $1s\sigma$  vacancies existing during the collision cascade is much smaller than the number of  $2p\sigma$  vacancies. The difference is roughly described by a factor  $v \cdot n \cdot (\pi r_K^2)/4 \cdot \Gamma_K$ , where  $v$ ,  $\Gamma_K$ ,  $n$  and  $r_K$  are the projectile velocity, the total decay rate, the atomic density in the target and the mean K-shell radius, respectively.

#### DYNAMICAL-MODEL CALCULATIONS OF $2p\sigma$ AND $1s\sigma$ MO RADIATION

For a better understanding of MO radiation it is necessary to carry out extensive calculations. In our earlier calculations (Heinig et al. 1977) we obtained for the  $\text{Ni} + 39\text{MeV Ni}$  collision system a

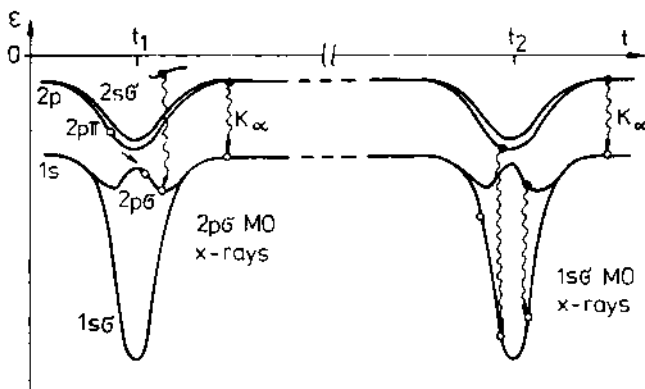


Fig. 7. Scheme of the quasimolecular one-collision  $2p\sigma$  and two-collision  $1s\sigma$  MO radiation. One-collision  $2p\sigma$  MO radiation (C1 continuum) can be emitted in each K-vacancy producing collision and is therefore much more intense than  $1s\sigma$  MO radiation (C2 continuum) from a rather improbable subsequent collision of a projectile having a K-vacancy.

spectral distribution of MO radiation which is very similar to the measured one. But an essential approximation consisted in the assumption of sudden 2p $\sigma$ -vacancy production at the distance of closest approach. It has been shown (Anholt 1976, Heinig et al. 1977, 1978) that such a description provides an unrealistically intense radiation tail of Lorentzian shape which was predicted to exceed even the two-collision 1s $\sigma$  MO radiation in collision systems with  $Z_1=Z_2 \geq 32$ . In the present contribution we apply a more straightforward method to the calculation of spectral yields. This approach allows to include the electron slip in the initial and final states of the radiating quasimolecule as well as the time dependence of the

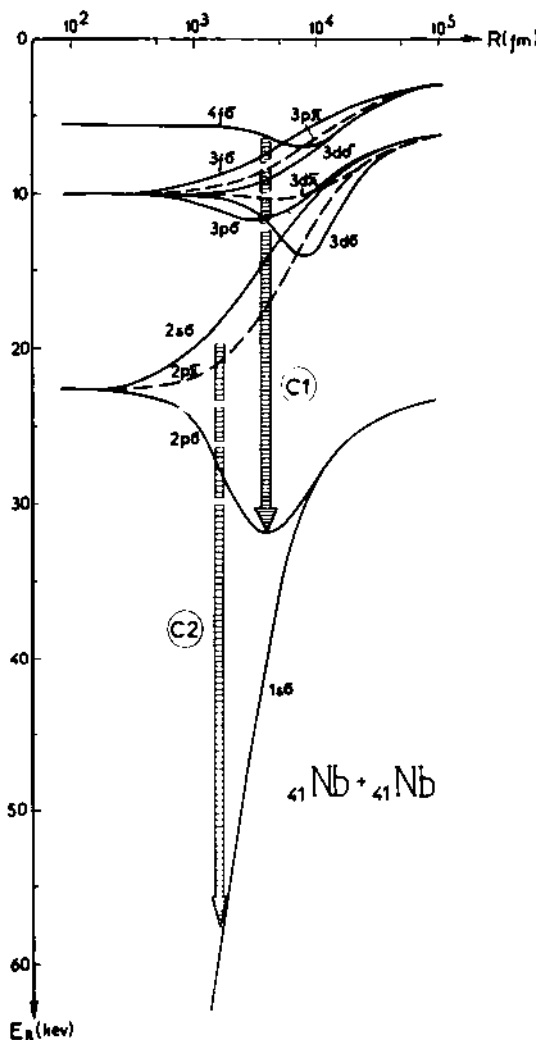


Fig. 8. Correlation diagram for the quasimolecular electronic binding energies of the system Nb + Nb (Truskova 1976).

dipole matrix elements and of the orientation of the molecular axis. By the aid of this calculation we can give relevant predictions for the impact parameter dependence of the spectra and the intensity of the  $2p\sigma$  MO radiation tail. We focus our attention to the investigation of one-collision  $2p\sigma$  MO radiation, but the two-collision  $1s\sigma$  MO radiation is also evaluated in order to compare the predictions with experimental data. The dynamical model applied (Jäger et al. 1981) is of comparable accuracy with models which have recently been used to study preferentially  $1s\sigma$  MO radiation (Anholt 1978, 1979, Briggs et al. 1979, Kirsch et al. 1979). For the description of the quasimolecular electronic system, of the radiation field and of their interactions we make the following approximations.

- (i) We restrict ourselves to one-vacancy states.
- (ii) Concerning the mixing of the adiabatic MO states by the operator  $\partial/\partial t$ , only rotational couplings are taken into account. Rotational coupling is considered between the quasimolecular  $2p$ ,  $3p$  and  $3d$  states, respectively.
- (iii) The emission of x-ray quanta is treated in perturbation theory.

Using these restrictions our calculation of the  $2p\sigma$  MO radiation can be explained by a simple physical scheme: It is assumed that there is a vacancy in the  $2p\pi$  level at the beginning of the collision (initial condition). During the collision this vacancy is distributed among the  $2p\sigma$  and  $2p\pi$  states due to rotational coupling ("electron slip"). A MO x-ray quantum is emitted by a radiative transition of an outer-electron distributed among the  $2d\sigma$ ,  $3d\pi$  and  $3d$  states into the  $(2p\sigma, 2p\pi)$ -vacancy. The vacancy appearing now in the  $3d$  MO states has to be distributed among these states in such a way that after the collision it will have been transferred

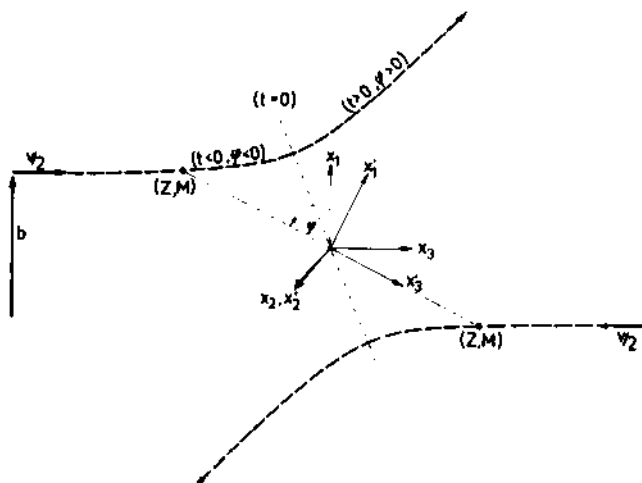


Fig. 9. The center-of-mass reference frame  $(x_1, x_2, x_3)$  and the molecular reference frame  $(x'_1, x'_2, x'_3)$  rotating.

by rotational coupling into a defined atomic state (future condition). From the mathematical point of view this means that different radiative transitions between adiabatic quasimolecular states have to be summed up coherently.

Let the energies  $\epsilon_n(R(t))$  and functions  $\chi_n(\vec{r}', R(t))$  be the nonrelativistic solutions of the stationary one-electron-two-center problem in the molecular reference frame (Fig. 9). Then the electronic states of the radiating quasimolecule

$$\varphi_j^{(i)}(t), \varphi_j^{(f)}(t)$$

having before (after) the collision a vacancy in the  $j$ 'th MO are assumed to be one-hole states

$$\varphi_j^{(i)}(t) = \sum_1 a_{j,1}^{(i)}(t) e^{-\frac{1}{\hbar} \int_{-\infty}^t (E_C - \omega_1) dt'} c_1 |0_C\rangle . \quad (1)$$

In the ansatz (1) a many-electron core state  $|0_C\rangle$  filled up to the Fermi level and its energy  $E_C(R(t))$  are introduced. The symbol  $c$  denotes an electron annihilation operator. In first-order perturbation theory concerning the interaction with the radiation field, one can introduce the wave function

$$\psi_{nm}(t) = \varphi_n^{(i)} |0_{ph}\rangle + c_k^+ \varphi_m^{(f)} e^{-i\omega_k^+ t} a_{k\lambda}^+ |0_{ph}\rangle \quad (2)$$

where  $|0_{ph}\rangle$ ,  $a_k^+$ ,  $\omega_k^+$  and  $c_k^+ \lambda$  denote the photon vacuum, the creation operator of a proton with wave vector  $\vec{k}$  and polarization  $\lambda$ , the photon energy and the radiation amplitude, respectively. The coefficients of the trial function  $\psi_{nm}(t)$  are obtained from the Schrödinger equation

$$- \frac{\hbar}{i} \frac{\partial}{\partial t} \psi_{nm}(t) = H \psi_{nm}(t) \quad (3)$$

with the Hamiltonian

$$H = H_e + H_r + H_{er} \quad (4)$$

which consists of three terms, the electronic Hamiltonian of the quasimolecule

$$H_e = E_C + \sum_1 \epsilon_1 :c_1^+ c_1: , \quad (5)$$

the Hamiltonian of the radiation field

$$H_r = \sum_{\vec{k}\lambda} \hbar \omega_{\vec{k}}^+ \vec{a}_{\vec{k}\lambda}^+ \vec{a}_{\vec{k}\lambda}^- \quad (6)$$

and an interaction term describing photon emission which is taken in dipole approximation

$$H_{er} = -i \sqrt{\frac{2\pi \hbar e^2}{L^3 c}} \sum_{\vec{k}, \lambda} \frac{\omega_{1m}}{\sqrt{|\vec{k}|}} \langle 1 | \vec{r}' \cdot \vec{e}_{\lambda} | m \rangle c_1^+ c_m \vec{a}_{\vec{k}\lambda}^+ , \quad (7)$$

$$\omega_{1m} = (\epsilon_1 - \epsilon_m)/\hbar , \quad \vec{r}' = U \vec{r} .$$

Here the (time-dependent) transformation matrix  $U$  appears as the electronic system and the radiation field are treated in the rotating, non-inertial molecular reference frame and in the center-of-mass reference frame, respectively (Fig. 9).

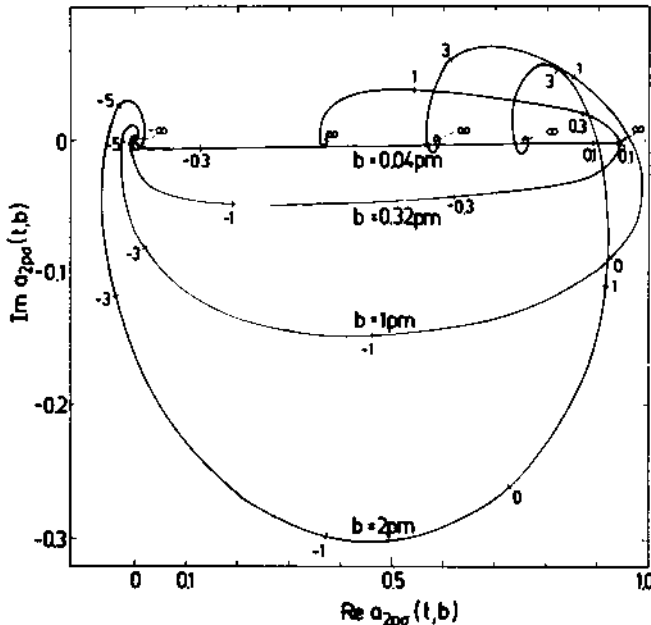


Fig. 10. Real and imaginary parts of the vacancy-amplitude  
(i)  $a_{2p\pi_x, 2p\sigma}(t, b)$

for the collision system  $^{60}\text{Ni} + 39\text{MeV}^{60}\text{Ni}$ . The numbers along the curves label selected times  $t$  (in  $10^{-19}\text{s}$ ).

Inserting the trial wave function  $\psi_{nm}(t)$  into the Schrödinger equation and projecting on basis states, we get differential equations for the orbital occupation amplitudes

$$\dot{a}_{j,n}(t) = \sum_1 a_{j,1}(t) \frac{bv}{R^2} f(R) e^{-i \int_{-\infty}^t \omega_{1n} dt}, \quad (8)$$

and the radiation amplitudes

$$\dot{c}_{k\lambda}(t) = \frac{2\pi e^2}{L^3 \hbar \omega} \sum_{j,1} \left( a_{m,j}^{(f)}(t) \right) * a_{n,1}^{(i)}(t) \omega_{1j} \langle 1 | \vec{r} \cdot \vec{e}_\lambda | j \rangle \cdot$$

$$i\omega t - i \int_{-\infty}^t \omega_{1j} dt,$$

$$(9)$$

where the symbols  $b$ ,  $\vec{e}_\lambda$  and  $f(R)$  stand for the impact parameter, the polarization vector of the photon and the rotational-coupling matrix elements corrected for plane-wave translational factors, respectively.

The coefficients  $a(t)$  are obtained by solving the system of coupled equations (8) with special assumptions on the initial (or final) configurations of the quasimolecule. In Fig. 10 the vacancy amplitude

$$a_{2p\pi_x, 2p\sigma}^{(i)}(t, b)$$

of the molecular 2p state having initially a vacancy in the  $2p\pi$  MO

$$a_{2p\pi_x, 2p\pi_x}^{(i)}(-\infty) = 1, \quad a_{2p\pi_x, 2p\sigma}^{(i)}(-\infty) = 0$$

is shown. For the occupation amplitudes of the quasimolecular 3d states, the "perfect slipping solution" is used which is obtained from equation (8) by the approximations  $\omega_{1n}(R)=0$  and  $f(R)=f(0)$ .

Integrating equation (9) over time and summing up over all final states  $m$ , we get the probability for the emission of a photon of frequency  $\omega$  into a solid angle  $\Omega$  by radiative transitions from the initial state  $n$  to all final states  $m$

$$\frac{dP^n}{d\omega d\omega} = \frac{e^2 \omega}{4\pi^2 \hbar c^3} \sum_{m,\lambda} \left| \sum_{j,1} \int_{-\infty}^{\infty} dt \left( a_{m,j}^{(f)} \right)^* a_{n,1}^{(i)} \omega_{1j} \right. \\ \left. \cdot \langle \vec{r}' \vec{u}_\lambda^+ | j \rangle e^{i\omega t} - i \int_{-\infty}^t \omega_{1j} dt' \right|^2 \quad (10)$$

Since we are here not interested in the angular distribution of the x-rays we integrate over the solid angle. Furthermore we divide by the vacancy transfer probability

$$P(b) = \left| a_{2p\pi, 2p\sigma}^{(i)}(t \rightarrow) \right|^2 \quad (11)$$

in order to normalize the radiation yield to the number of K-vacancies produced in the collision. Finally, the formula for the spectral yield per K-vacancy to be numerically evaluated has the form

$$I_{2p\sigma}^{oc}(\omega, b) = \frac{1}{P(b)} \int d\Omega \frac{dP}{d\omega d\Omega} \\ = \frac{2e^2}{3\pi\hbar c^3 P(b)} \sum_m \sum_{s=1}^3 \left| \sum_{j,1} \sum_{r=1}^3 \frac{1}{(\omega - \omega_{1j}^0)} \int_{-\infty}^{\infty} dt e^{i(\omega - \omega_{1j}^0)t} \right. \\ \left. \frac{d}{dt} \left[ \left( a_{m,j}^{(f)} \right)^* a_{2p\pi, 1} \omega_{1j} \vec{u}_{rs} \langle 1 | x_r' | j \rangle e^{-i \int_{-\infty}^t (\omega_{1j} - \omega_{1j}^0) dt} \right] \right|^2 \quad (12)$$

The matrix elements of electron coordinates  $x'$  have been simply scaled (with 1/2) from values evaluated for the hydrogen molecule ion (Ramaker and Peek 1973, Truskova 1978). In Fig. 11 we present all matrix elements which enter in our calculations. In experiments without impact parameter selection a mean spectral yield per K-vacancy is observed. Such mean spectral yields have been evaluated from

$$\overline{I(\omega)} = \left( \int_0^{b_{\max}} 2\pi b P(b) I(\omega, b) db \right) / \left( \int_0^{b_{\max}} 2\pi b P(b) db \right) \quad (13)$$

results  $(\omega, b)$ ,  $P(b)$  given at about 30 impact parameters.

The two-collision 2p $\sigma$  MO radiation is negligible in comparison to the one-collision one. The formula derived for the two-collision 1s $\sigma$  MO radiation yield per K-vacancy  $I_{1s\sigma}^{tc}(\omega)$  is rather similar to equation (12). It can be concluded from eq. (12) in a formal way by introducing

(i) the substitutions

$$P(b) \rightarrow 1, \quad a_{2p\pi, j}^{(i)} \rightarrow a_{1s\sigma, j}^{(i)} = \delta_{1s\sigma, j},$$

- (ii) a factor  $v/d_K$  resulting from the sum over all secondary collisions (Macek and Briggs 1974).  
 (iii) a factor 1/2 taking into account sharing of the incoming K-vacancy into both the 1s $\sigma$  and 2p $\sigma$  MO.

We think that it is useful to demonstrate the effect of some improvements incorporated in our dynamical model. For this purpose

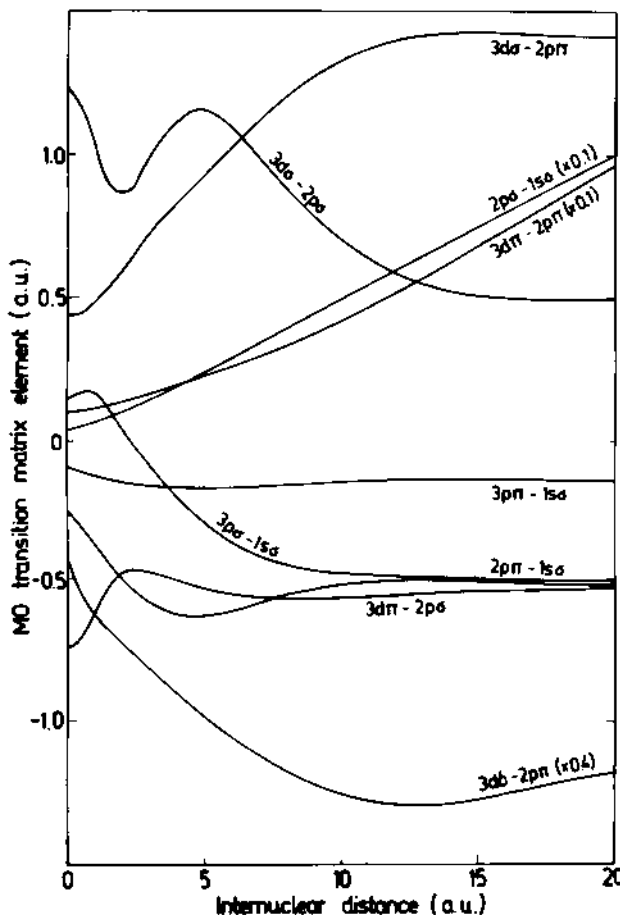


Fig. 11. Dipole matrix elements  $\langle 1|x_3^i|j\rangle$  or  $\langle 1|x_1^i|j\rangle$  of the H<sub>2</sub><sup>+</sup> molecule (Truskova 1978) used in our calculations.

we consider the mean spectral yield  $I(\omega)$  (equation 13) for selected strong radiative transitions in the system  $^{60}\text{Ni} + 39\text{ MeV}^{60}\text{Ni}$  (Fig. 12). This system was investigated already in a paper (Heinig et al. 1977) where  $\omega_{1j} < 1 | x'_m | j \rangle = \text{constant}$  and a sudden  $2p\sigma$ -vacancy production at  $t=0$  were assumed, and the electron slip in initial and final states and the rotation of the molecular axis were neglected. The effect of

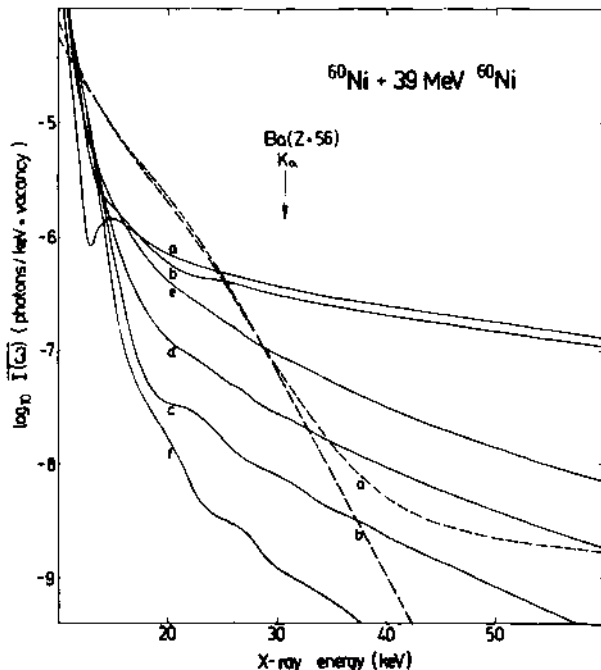


Fig. 12. The dependence of one-collision  $2p\sigma$  MO radiation (full curves; final states  $\gamma_j$  with  $j=3d\pi_x, 3d\pi_y$ ) and of two-collision  $1s\sigma$  MO radiation (broken curves; final states:  $j=2p\pi_z, 2p\pi_x$ ) on approximations in the dynamical calculations. The full and broken lines labeled 'a' are results of Heinig et al. (1977) whereas the full line 'f' and the broken line 'b' are results of our present dynamical calculation. The two results 'a' and 'f' differ in equation (12) by the approximations

$$\omega_{1j} < 1 | x'_m | j \rangle = \text{constant} \quad (\text{I}), \quad a_{2p\pi_x, 2p\sigma}^{(i)} \sim \theta(t) \quad (\text{II}),$$

$$U_{mn} = \delta_{mn} \quad (\text{III}), \quad a_{2p\pi_x, 2p\pi_x}^{(i)} = 0 \quad (\text{IV}),$$

$$a(f) = \delta_{k,1} \quad k, 1 \quad (\text{V}).$$

The effect of each of these approximations is shown step by step ('a' corresponds to approximations (I)-(V), 'b' to (II)-(V), 'c' to (III)-(V), 'd' to (IV)-(V) and 'e' to (V) respectively.

all these approximations on the one-collision 2p $\sigma$  MO radiation is shown in Fig. 12. Below the quasistatic MO radiation limit ( $E \lesssim 10$  keV for the 3d $\pi \rightarrow$ 2p $\sigma$  transition), shape and intensity of the quasimolecular (C1) spectrum depend sensitively on the transition matrix elements (Fig. 11). All other approximations influence only the high-energy MO radiation tail. Whereas initially (Heinig et al. 1977) the 2p $\sigma$  MO radiation tail was predicted to exceed even the two-collision 1s $\sigma$  MO radiation at high x-ray energies, now a tail (curve 'f' in Fig. 12) is calculated which is not expected to be observed in solid-target experiments.

The strong dependence of the calculated MO radiation tail on the model can be explained. The Mo radiation tail reflects the short-time behaviour of collisions with small impact parameters (Heinig et al. 1978). In such collisions the electron clouds cannot follow the rapid motion ("rotation") of the nuclei, they stay fixed in space (perfect electron slip). As a consequence the expression

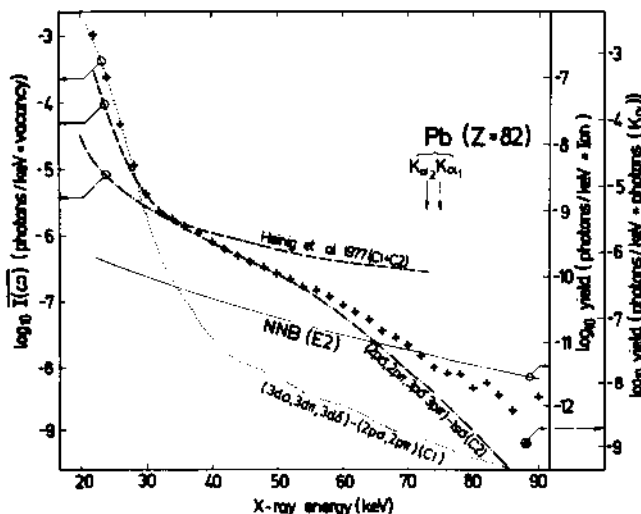


Fig. 13. Comparison of experimental and theoretical photon yields in Nb + 67 MeV Nb collisions. The spectrum (see also Fig. 2) is corrected for detector efficiency, the delayed background has been subtracted. The E2 NNB (full line) calculated for this experiment is shown, but has not been subtracted from the spectrum. The theoretical results presented are mean spectral yields (13) for the one-collision 2p $\sigma$  MO radiation (C1; dotted line) and for the two-collision 1s $\sigma$  MO radiation (C2; chain line). Besides a result (C1+C2; broken line) of our previous calculations (Heinig et al. 1977) is given.

$$\sum_{j,1,m} a_{2p\pi_x,j}^{(i)} \left( a_{k,1}^{(f)} \right)^* U_{mn} \langle 1 | x_m^i | j \rangle$$

of equation (10) is even constant in the perfect-slipping approximation although the quantities in it are oscillating time-dependent functions. Neglecting the time dependence of any quantity only, the whole expression becomes strongly time-dependent, and an unrealistic intensity of high-frequency Fourier components is evaluated in equation (12). Thus, the low intensity of the high-energy MO radiation tail is well predicted only in a dynamical approach which correctly takes into account both the direct (rotation matrix; transition matrix elements for states with different projection quantum numbers) and the indirect (rotational coupling) dependences on quasimolecule orientation.

Now we discuss mean spectral yields (13) calculated by taking

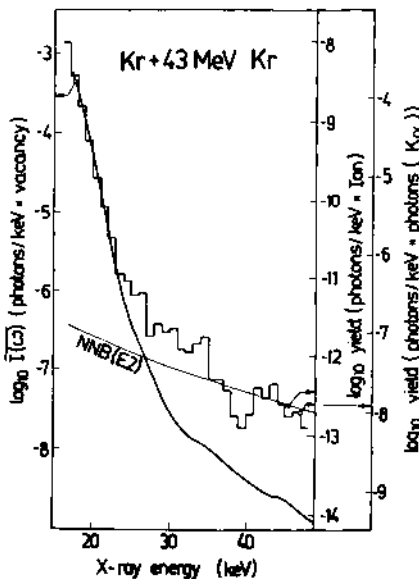


Fig. 14. The one-collision  $2p_0$  MO radiation in the gas-target experiment  $\text{Kr} + 43\text{MeV Kr}$ . The spectrum (see also Fig. 3) is corrected for detector efficiency and for background effects (prompt background, SEB, E1 NNB). The E2 NNB and the mean one-collision  $2p_0$  MO radiation yield (13) (thick full line) have been calculated (Jäger et al. 1981).

into account all partial transitions of the types (3d $\sigma$ , 3d $\pi$ , 3d $\delta$ , 3s $\sigma$ )  $\rightarrow$  (2p $\sigma$ , 2p $\pi$ ) and (2p $\sigma$ , 2p $\pi$ , 3p $\sigma$ , 3p $\pi$ )  $\rightarrow$  (1s $\sigma$ ). For the Nb + 67MeV Nb collision system we compare our calculated yields per K-vacancy with the yield per characteristic photon measured (Fig. 13). These two quantities differ by the K-shell fluorescence yield which should be about 0.8 for a Nb atom having a few additional L-vacancies (Bambynek et al. 1972, Greenberg et al. 1977). Apart from this factor 0.8 expected, we find that our calculated intensity is 1.4 times smaller than the measured one. Deviations of this order of magnitude may arise from uncertainties in the correlation diagrams and transition matrix elements and partly from neglected transitions (e.g. 4d $\pi$   $\rightarrow$  2p $\sigma$ ). In Fig. 13 the experimental and theoretical results refer to different scales and are arranged in such a way that the shape of the spectra can be easily compared. The shape of the whole measured x-ray spectrum is well explained, the unreasonable high MO radiation tails (Heinig et al. 1977) are no longer present.

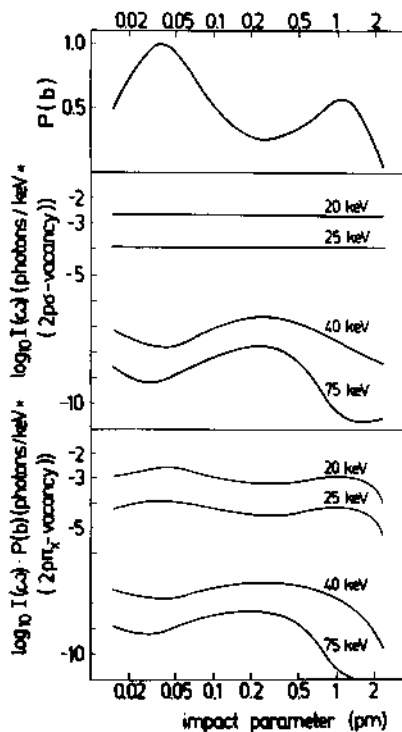


Fig. 15. The one-collision 2p $\sigma$  MO radiation yield in Nb + 67MeV Nb collisions versus impact parameter and for different photon energies. The two yields presented differ by the probability  $P(b)$  of 2p $\sigma$  - 2p $\sigma$  vacancy transfer given on the top of the figure.

The explanation of the two-component structure of the x-ray spectrum by one-collision  $2p\sigma$  and two-collision  $1s\sigma$  MO radiation (Heinig et al. 1976, Kaun et al. 1977) is now supported by the results of a dynamical calculation, too.

Using a gas target instead of the solid one, the two-collision radiation ( $C_2$  continuum) can be suppressed by more than 3 orders of magnitude. Therefore the one-collision  $2p\sigma$  MO radiation tail could be observable in such experiments. In Fig. 14 we compare the mean yield calculated for the one-collision  $2p\sigma$  MO radiation in  $Kr + 43\text{MeV}$   $Kr$  collisions with the spectrum measured. It can be seen that the low-energy part of the experimental spectrum can be explained by one-collision  $2p\sigma$  MO radiation whereas the high-energy part consists of the  $E2$  component of NNB. The intensity of the  $2p\sigma$  MO radiation tail is too low to be visible. Therefore, more definite conclusions on this tail cannot be drawn from the available gas-target experiment.

In experiments where the non-characteristic x-ray quanta are measured in coincidence with the scattered ions, more information about the radiating system can be obtained. Theoretical predictions on the impact parameter dependence of MO radiation have been presented in nearly all recent dynamical calculations (Anhold and Meyerhof 1977, Briggs et al. 1979, Kirsch et al. 1979). The impact parameter dependence of the one-collision yield (12) is given in Fig. 15. For the intense one-collision  $2p\sigma$  MO radiation below  $E_x \lesssim 30\text{KeV}$ ,

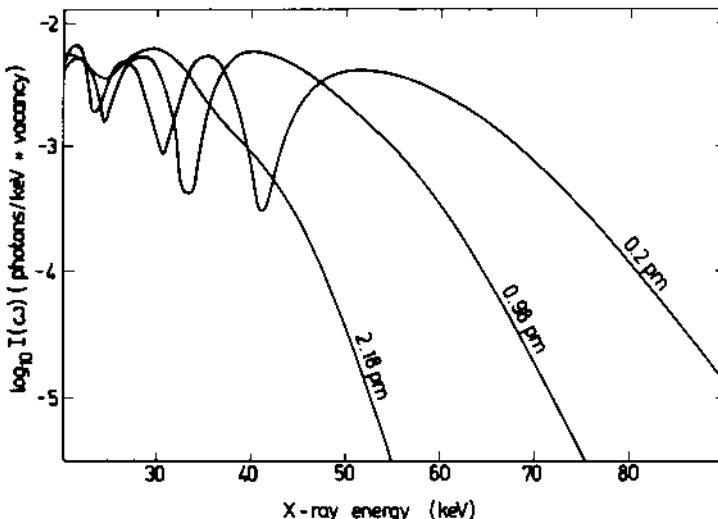


Fig. 16. Two-collision  $1s\sigma$  MO radiation in the  $Nb + 67\text{MeV}$   $Nb$  system predicted for different impact parameters.

Fig. 15 shows that the spectral yield per 2p $\sigma$  - vacancy is expected to be nearly independent on the impact parameter. A slight impact parameter dependence can only be found in this region if the yield per initial 2p $\pi_x$  - vacancy is considered. This quantity reflects the properties of the vacancy transfer probability P(b).

Concerning the impact parameter dependence of two-collision 1s $\sigma$  MO radiation (Fig. 16) it is complicated to substantiate the predictions by experiment because in reality impinging ions have a K-va-

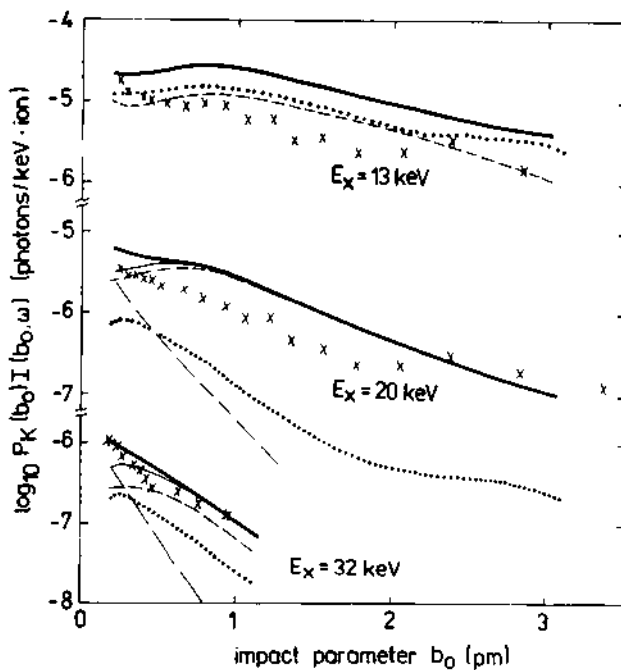


Fig. 17. The impact parameter dependence of MO radiation in a Ni-90MeV Ni coincidence experiment (Schmidt-Böcking et al. 1981). The contributions of one-collision 2p $\sigma$  (dotted lines) and two-collision 1s $\sigma$  (dashed lines) MO radiation to the predicted impact parameter dependent MO radiation yield (thin solid lines) are given for different x-ray energies. The theoretical yields have been calculated using the measured K-vacancy production probability. Additionally, the one collision 1s $\sigma$  MO radiation obtained from a crude estimation is shown (chain lines) for  $E_x = 20\text{ keV}$  and  $32\text{ keV}$  and has been added (thick solid lines) show the total sum).

cancy are already deflected out of the beam direction in a foregoing, vacancy-producing collision. In order to obtain the yield which will be observed in experiment at a total deflection angle  $\theta_0$  of the two-collision process the  $1s\sigma$  MO radiation yields calculated for impact parameters  $b$  of the second collision have to be folded with K-vacancy production probabilities  $P(b_1)$  depending on the impact parameters  $b_1$  of the foregoing collisions (Schmidt-Böcking et al. 1981). Since the vacancy transfer probability  $P(b)$  of the two-state rotational coupling model (11) is known to deviate in its shape from the K-vacancy production probabilities  $P_K(b)$  obtained in recent coincidence experiments (Annett et al. 1979, Schuch et al. 1980), the theoretical yields (12) have been folded with measured probabilities  $P_K(b)$ . In Fig. 17, MO x-ray spectra of Ni + Ni coincidence experiments (Bethge et al. 1978, Stiebing et al. 1979, Schuch et al. 1981) are compared with such folded impact parameter dependent MO radiation yields (Schmidt-Böcking et al. 1981). The measured and calculated data have a similar shape for effective impact parameters  $b_0 > 0.4\text{pm}$ . The data measured at smaller impact parameters seem to deviate significantly from theory. If one adds a one-collision  $1s\sigma$  MO radiation yield estimated in a crude manner to the sum of one-collision  $2p\sigma$  and two-collision  $1s\sigma$  MO radiation yield, the agreement between theory and experiment at small impact parameters can be improved.

## REFERENCES

- Afrosimov, V. V., Gordeev, Yu. S., Panov, M. N., and Fedorenko, N. V., 1964, Zh. Tekhn. Fiz., 34:1613, 1624, 1637.
- Anholt, R., 1976, J. Phys. B: Atom. Molec. Phys., 9:L249
- Anholt, R., 1978, Z. Phys., A288:257.
- Anholt, R., 1979, Z. Phys., A291:289.
- Anholt, R., and Meyerhof, W. E., 1977, Phys. Rev., A16:913.
- Annett, C. H., Curnutte, B., and Cocke, C. L., 1979, Phys. Rev., A19:1038.
- Bambynek, W., Crasemann, B., Fink, R. W., Freund, H.-U., Mark, H. Swift, C. D., Price, R. E., and Venugopala, Rao P., 1972, Rev. Mod. Phys., 44:716.
- Bethge, K., Gaukler, G., Himmelle, G., Lichtenberg, W., Nolte, G., Schmidt-Böcking, H., Schuch, R., Specht, H. J., Stiebing, K., Tserruya, I., Vincent, P., and Anholt, R., 1978, in: "annual report", Max-Planck-Institut für Kernphysik, Heidelberg.
- Briggs, J. S., Macek, J. H., and Taulbjerg, K., 1979, J. Phys. B: Atom. Molec. Phys., 12:1457.
- Everhart, E., and Kessel, Q.C., 1965, Phys. Rev. Lett., 14:247.
- Fano, U., and Lichten, W., 1965, Phys. Rev. Lett., 14:627.
- Frank, W., Gippner, P., Kaun, K.-H., Manfrass, P., and Tretyakov, Yu. P., 1976, Z. Phys., 4277:333.
- Gippner, P., 1975, Dubna Report, JINR E7-8843.
- Gippner, P., 1978, Dubna Report, JINR E7-11431.
- Gippner, P., Kaun, K.-H., Neubert, W., Stary, F. and Schulze, W., 1973, Dubna Report, JINR E7-7636.

- Gippner, P., Kaun, K.-H., Neubert, W., Stary, F. and Schulze, W., 1974, Nucl. Phys., A230:509.
- Greenberg, J. S., Vincent, P., and Lichten, W., 1977, Phys. Rev., A16:964.
- Heinig, K.-H., Jäger, H.-U., Munchow, L., Richter, H., and Woittennek, H., 1978, J. Phys. B: Atom. Colec. Phys., 11:115.
- Heinig, K.-H., Jäger, H.-U., Richter, H., and Woittennek, H., 1976, Phys. Lett., 60B:249.
- Heinig, K.-H., Jäger, H.-U., Richter, H., Woittennek, H., Frank, W., Gippner, P., Kaun, K.-H., and Manfrass, P., 1977, J. Phys. B: Atom. Molec. Phys., 10:1321.
- Jäger, H.-U., Gippner, P., Heinig, K.-H., Richter, H., Truskova, N. F., and Woittennek, H., 1981, J. Phys. B: Atom. Molec.
- Kaun, K.-H., Frank, W., and Manfrass, P., 1976, The Structure of Quasi-Molecular K x-ray Spectra from Heavy Ion Collisions, in: Proc. II. Intern. Conf. "Inner Shell Ionisation Phenomena", Vol. 2, Mehlhorn, W., and Brenn, R., eds., Universität Freiburg, Germany.
- Kaun, K.-H., Manfrass, P., and Frank, W., 1977, Particles and Nuclei (Moscow), 8:1246.
- Kirsch, J., Betz, W., Reinhardt, J., Müller, B., Greiner, W., and Soff, G., 1979, Z. Phys., A292:227.
- Lichten, W., 1967, Phys. Rev., 164:131.
- Macek, J. H., and Briggs, J. S., 1974, J. Phys. B: Atom. Molec. Phys., 7:1312, Corrigendum 8:156.
- Meyerhof, W. E., 1973, Phys. Rev. Lett., 31:1341.
- Meyerhof, W. E., Saylor, T. K., and Anholt, R., 1975, Phys. Rev., A12:2641.
- Meyerhof, W. E., Saylor, T. K., Lazarus, S. M., Little, W. A., Trippe, B. B., and Chase, L. F., 1973, Phys. Rev. Lett., 30:1279, Corrigendum 32:502.
- Meyerhof, W. E., Saylor, T. K., Lazarus, S. M., Little, W. A., Trippe, B. B., Chase, L. F., and Anholt, R., 1974, Phys. Rev. Lett., 32:1279.
- Mokler, P. H., Stein, H. J., and Armbruster, P., 1972, Phys. Rev. Lett., 29:827.
- Ramaker, D. E., and Peek, J. M., 1973, Atomic Data, 5:167.
- Saris, F. W., van der Weg, W. F., Tawara, H., and Laubert, R., 1972, Phys. Rev. Lett., 28:717.
- Schuch, R., Nolte, G., and Schmidt-Böcking, H., 1980, Phys. Rev., A22:1447.
- Schuch, R., Schmidt-Böcking, H., and Tserruya, I., 1981, Phys. Lett., 82A:453.
- Schmidt-Böcking, H., Anholt, R., Schuch, R., Vincent, P., Stiebing, K., and Jäger, H.-U., to be published.
- Stiebing, K. E., Specht, H. J., Schuch, R., Schmidt-Böcking, H., Nolte, G., Lichtenberg, W., Bethge, K., Anholt, R., and Vincent, P., 1979, in: "annual report", Max-Planck-Institut für Kernphysik, Heidelberg.

Truskova, N. F., 1976, Dubna Report, JINR P11-10207.  
Truskova, N. F., 1978, Dubna Report, JINR P11-11218.

## CONTINUUM X-RAY EMISSION IN ADIABATIC HEAVY ION-ATOM COLLISIONS

P. Vincent\*

Department of Physics and Astronomy  
Rutgers University  
New Brunswick, New Jersey 08903

### ABSTRACT

A brief review of the current status of experiments on quasimolecular x-ray production in heavy ion collisions is given. Facts about continuum x-ray emissions learned from measurements on lighter systems provide the groundwork for the extension of studies to the heaviest possible collision systems. Increasingly detailed experiments explore the differential properties of the molecular orbital x-rays and provide for simpler and more direct comparisons between experiment and calculation.

### INTRODUCTION

In heavy ion collisions, distances of closest approach deep within the K shell radii of the two collision partners are attainable using projectiles whose velocity is slow compared to those of the inner shell electrons. Under such conditions, these electrons will have time to readjust their orbits to the combined

---

\*Invited speaker NATO International School on Quantum Electrodynamics of Strong Fields, Lahnstein/Rein, West Germany.

Supported in part by the National Science Foundation.

charge of the target plus slowly moving projectile nuclei and, in so doing, experience increasing binding energies for decreasing internuclear separations. In this way, a collision-constructed quasimolecular electron system is formed, whose innermost orbitals evolve towards those of the united projectile - target atom for the smallest internuclear separations. A qualitative measure of the velocity and distance scales involved in such collisions is given by a comparison of the distance of closest internuclear approach  $R_o$  to the radius  $R_K$  of the atomic K shell, and the projectile velocity  $v_p$ , to that of the bound K shell electron  $v_K$ . For 70 MeV Ni + Ni collisions  $R_o = 30$  fm,  $R_K = 3000$  fm,  $v_p/c = 0.05$ , and  $v_K/c = 0.2$ . For 1 GeV Pb + Pb collisions,  $R_o = 20$  fm,  $R_K = 800$  fm,  $v_p/c = 0.1$  and  $v_K/c = 0.6$ .

Since heavy ion collisions near the Coulomb barrier are (from the point of view of K shell electrons) slow, one may be able to utilize such collisions to explore the properties of electrons experiencing extremely strong binding. Despite their slowness, these atomic collisions are usually inelastic and spectroscopic information on strongly bound electron states may be gained either through observations of the ionization of these orbitals or by measurements of their subsequent decay. Although the characteristic K x-rays produced in heavy ion collisions actually decay long after the collisions are over, their cross sections and impact parameter excitation probabilities reflect the excitation characteristics of the electrons during the collision.<sup>1</sup> Alternatively, direct measurements of the ionized electrons themselves ( $\delta$  electrons)<sup>2</sup> probe the properties of the most strongly bound molecular wavefunctions. In addition, observations of molecular positron production<sup>3</sup> and molecular orbital x-ray transitions, both contain information on excitation and decay processes during the collision. Molecular orbital x-rays (Mo x-rays) are transitions which take place in the quasimolecule during the course of the collision. We will concentrate here on a review of their properties, starting first with somewhat lighter collision systems, and progressing to a discussion of the most interesting heavy collisions.

#### LIGHTER SYSTEMS

Figure 1 gives the energy level solutions to the two centered Dirac equation for the Ni + Ni quasi-molecule.<sup>4</sup> Shown as wiggly lines, are Mo x-ray transitions into collision produced vacancies in the K-like

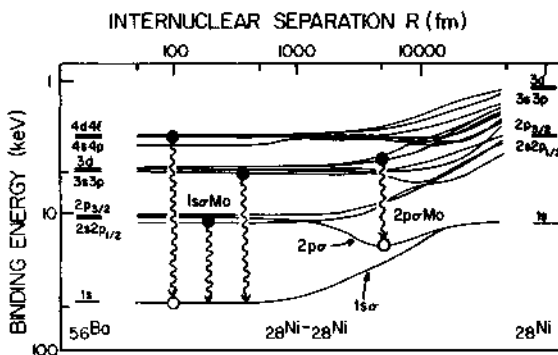


Fig. 1. Molecular orbital correlation diagram for the Ni + Ni quasimolecule showing decay of  $1s\sigma$  and  $2p\sigma$  Mo x-rays.

orbital of the quasimolecule ( $1s\sigma$ Mo) and into the minimum in the L-like  $2p\sigma$  state ( $2p\sigma$ Mo). The  $2p\sigma$ Mo radiation has also been called "Cl" x-rays for historical reasons.<sup>5</sup> One particularly striking feature of the correlation diagram for this somewhat lighter system is the nearly constant value of the  $1s\sigma$  binding energy for all internuclear separations below approximately 1000 fm, a feature which is not present in very heavy quasimolecules.

In Figure 2, examples of x-ray spectra given off in Ni + Ni collisions are shown.<sup>6</sup> The peaks labeled  $K_\alpha$  and  $K_\beta$  are the characteristic K x-ray emissions from Ni, and the continuum band extending from these x-rays to beyond the  $K_\alpha$  transition energy of the united Ba atom at 32 keV is composed of quasimolecular x-rays. A strong absorber is used to attenuate the dominant low energy characteristic x-rays and reduce counting rates to manageable levels. The small bump visible in the spectra at approximately 15 keV is due to two-electron, one-photon transitions into doubly vacant Ni K shells.<sup>7</sup> Two particularly striking features of these data are their featureless continuum character and their extension to transition energies beyond the united atom

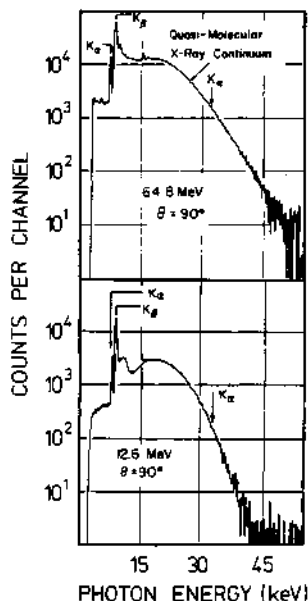


Fig. 2. Exemplary x-ray spectra from  $^{58}\text{Ni} + ^{58}\text{Ni}$  collision systems at two projectile bombarding energies taken at 90 degrees to the beam direction.

static limit, the latter feature becoming more pronounced at higher bombarding energies. Both these features reflect the intrinsically dynamic nature of the collisions and the resulting collision broadening of the static molecular orbitals shown in Figure 1.

In Figure 3 examples of extracted Mo x-ray production cross sections from three collision systems are shown.<sup>6</sup> The two component character of the absorption, efficiency corrected spectra is apparent. The lower component has been identified as L-like radiation into the minimum in the  $2p\sigma$  orbital ( $2p\sigma\text{Mo}$  or "Cl" in Figure 1),<sup>5</sup> and the upper component as  $1s\sigma\text{Mo}$  x-rays.<sup>8</sup> We note that these two components scale systematically to higher x-ray energies as the combined charge of the

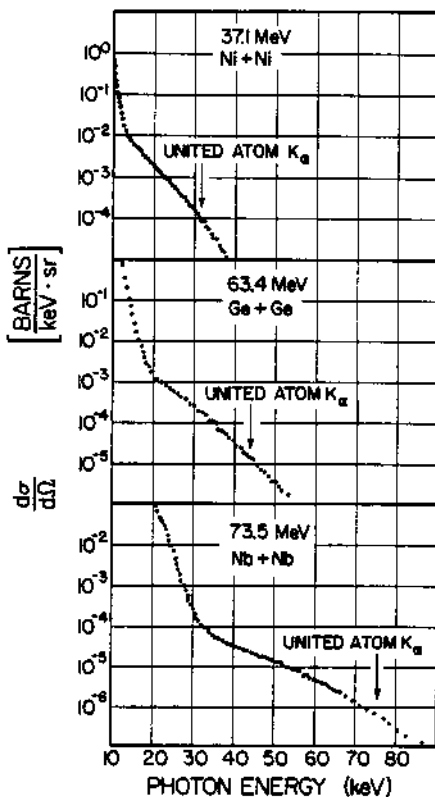


Fig. 3. Extracted cross sections for continuum x-ray production in three selected collision systems illustrating the two component features of the Mo x-ray radiation.

projectile and target nuclei is increased. This two-component structure and its scaling reflect the basic validity of the static molecular orbital view of these collisions. However, the continuum nature of the radiation and its extension to x-ray energies beyond the united atom limit serve as constant reminders that the dynamic character of these collisions plays a dominant role in all quasimolecular phenomena.

Figure 4 shows results of measurements of the directional anisotropy of the continuum radiation.<sup>6</sup> This anisotropy is defined as the ratio of the x-ray intensity at 90° to the beam direction to that at 0° minus 1.  $(I(90^\circ)/(I(0^\circ) - 1))$ . Peaks in the anisotropy

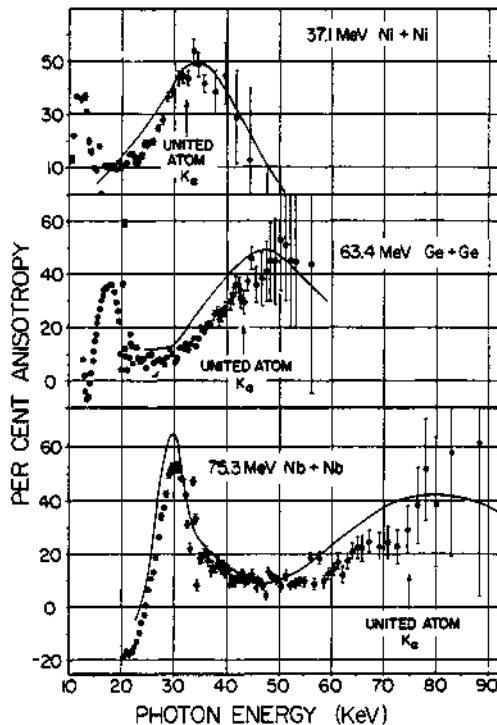


Fig. 4. Results for the directional anisotropy of the Mo x-rays for three selected quasimolecules in comparison to calculations by Anholt (solid lines).<sup>10</sup>

ratios are observed for all collision systems.<sup>9</sup> The low x-ray energy peak occurs near the point where the two component structures illustrated in Figure 3 cross, and the high energy peak occurs in the vicinity of the united atom K x-ray energy. The solid lines drawn through the data in Figure 4 are calculations of the anisotropy due to Anholt.<sup>10</sup> These calculations have shown that the peaks are caused by the alignment of molecular orbitals with large transition rates, an alignment which reflects very general properties of correlation diagrams for lighter collision systems. Systematic measurements of these peaks by Stoller, Wölfli, and collaborators<sup>11</sup> have established a semi-empirical relationship between the upper energy peak and the K x-ray transition energy of the united atom. These observations generated enthusiasm that extension of such angular distribution measurements to very heavy

collision systems would allow for a relatively straight-forward spectroscopy of superheavy quasiatoms using Mo x-rays.

In addition to these general features of Mo x-ray spectra from lighter collision systems, subsequent, more extensive studies of the radiation have resulted in a number of more detailed discoveries of their properties. Examination of dynamic effects through measurements of the slopes with which the extensions or tails of the spectra above the static united atom limits fall off with photon energy, and comparisons of these results with calculations, have led to a better understanding of Mo x-ray production mechanisms.<sup>12</sup> Vacancies in the most deeply bound ls<sub>0</sub> molecular orbital must be produced before their subsequent decay into Mo K x-rays. In solid targets, with which most measurements are performed, vacancy production may occur in the same collision where the Mo x-ray decays (one collision process) or in a prior collision (two collision process).<sup>13</sup> Studies of the projectile velocity dependence of the dynamic tails and, in particular, experiments with gas targets<sup>14</sup> have provided important insight into which mechanism is dominant in solid targets. In addition, investigations of the scaling properties of radiation below the united atom limit from various collision systems have been performed.<sup>15</sup> The picture emerging from all these studies is that the two collision process generally dominates Mo x-ray production in lighter solid targets, but admixtures of one collision events are significant especially at higher projectile velocities.

All measurements mentioned up to this point have been singles measurements. Coincidence measurements determining correlations between scattered particles and/or x-rays produced in the same collision have also been performed. The first of such measurements by Schmidt-Böcking and collaborators determined the impact parameter dependent probability for continuum x-ray production.<sup>16</sup> Figure 5 illustrates a recent example of such experiments for 90 MeV <sup>58</sup>Ni + <sup>58</sup>Ni collisions.<sup>17</sup> The impact parameter dependences for Mo x-rays at 20 and 32 keV are compared with two collision calculations by Anholt.<sup>18</sup> The dashed line gives calculated results assuming that a vacancy was brought into the second collision along the initial beam direction. The solid curve gives the final result including the actual angular distribution of vacancies produced in the first collision ( $P_K(b)$  in Figure 5). The excess experimental

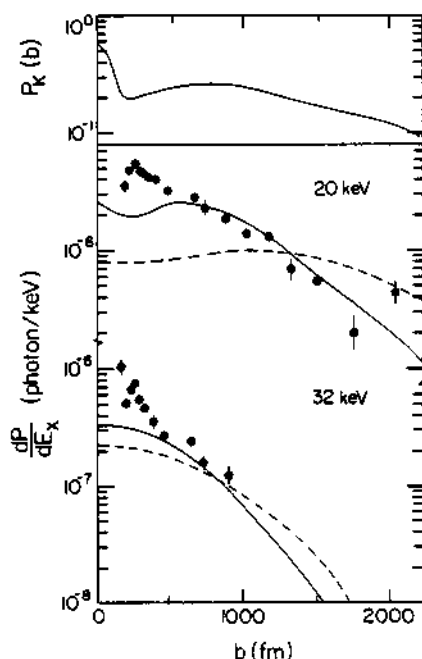


Fig. 5. Top: Impact parameter dependence for characteristic K x-rays. Bottom: comparison of measurement to two collision calculations of the impact parameter dependence for Mo x-ray production.  $^{58}\text{Ni} + ^{58}\text{Ni}$  collisions at 90 MeV.

intensity at small impact parameters is interpreted as contributions from one collision Mo x-rays to the two collision yield.

Other recent coincidence experiments have determined the impact parameter dependent azimuthal angular distribution of the Mo x-rays.<sup>19</sup> In such measurements, the scattering plane of the projectile is defined with a particle x-ray coincidence and the azimuthal angular distribution of the Mo x-rays is measured with respect to this plane. Results indicate that full dynamical calculations of the collision process<sup>10</sup> including the rotation of the internuclear axis during the collision and the effects of this rotation on the quasimolecular electronic wavefunctions<sup>20,10</sup> are more successful in reproducing experimental azimuthal anisotropies than other model calculations.<sup>21</sup>

A third type of coincidence experiment first proposed by Greenberg and collaborators is designed to determine the amount of  $1s\sigma$ Mo intensity due to electron transitions from the  $2p\sigma$  to the  $1s\sigma$  orbital.<sup>22</sup> By measuring coincidences between these emissions and cascading K x-rays which fill the vacancies left in the  $2p\sigma$  orbital by the initial Mo x-ray decay (see Figure 1), the fraction of  $2p\sigma$  to  $1s\sigma$  transitions can be isolated from other continuum x-rays. Initial investigations with the Nb + Nb collision system demonstrated the general feasibility of such cascade measurements, while showing that coincidences due to independent excitation of double vacancies in one and two collision processes can also make large contributions to the measured intensities.<sup>22</sup> Further discussion of such cascade measurements follows below when experimental results for the Pb + Pb collision system are presented and reviewed.

#### HEAVY SYSTEMS

Figure 6 shows the electron binding energy solutions to the two center Dirac equation for the Pb + Pb quasi-

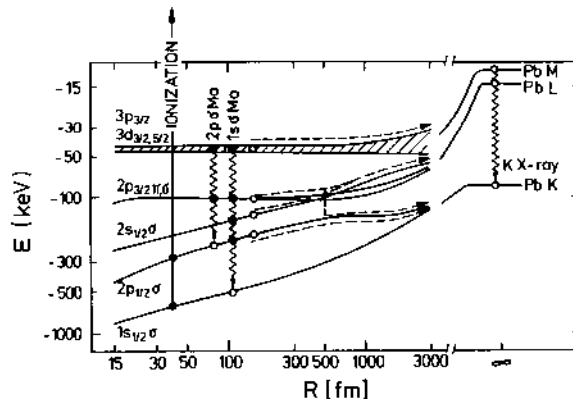


Fig. 6. The correlation diagram for the Pb + Pb quasi-molecule showing the excitation and decay of inner quasimolecular orbitals during and after the collision.

molecule.<sup>2,3</sup> The very high binding energies achieved for small internuclear separations and the accompanying large spin-orbit splitting of the molecular states are striking features of these highly relativistic quasi-molecules. The runway effect present in lighter collision systems has disappeared and, in fact, binding energies increase at increasingly rapid rates as the projectile and target nuclei approach each other.

Examination of the correlation diagram for relativistic quasimolecules shows that simple comparisons between velocities and distances of the kind given in the introduction can be misleading. The ratio  $v_K/v_p$  actually increases for the relativistic systems, and therefore, from the point of view of K electrons, the superheavy collisions are slower. However, due to the rapid change in the inner molecular wave functions with decreasing internuclear separation, these relativistic systems are actually less adiabatic than their lighter counter parts.

Sharp increases in production probabilities to large values at small impact parameters have been observed in the K x-ray,<sup>1</sup>  $\delta$ -electron,<sup>2</sup> and positron channels.<sup>3</sup> These observations indicate rapid changes in the deeply bound molecular wavefunctions at small internuclear separations. Although large vacancy production probabilities concentrated at small internuclear separations have allowed experimentalists to observe very strong binding phenomena in heavy ion collisions, the very fact that excitation accompanies strong binding implies that efforts to extract spectroscopic information from such experiments<sup>2,4</sup> are being made at precisely those times during the collision when the orbitals are the least adiabatic. For this reason, only average properties of the wavefunctions can be probed.

Figure 7 gives results for Mo x-ray thick target yields per projectile from the  $^{208}\text{Pb} + ^{208}\text{Pb}$  collision system at 4.2 MeV/amu.<sup>2,5</sup> The yields reveal a three component structure with measurable x-ray energies beyond 1 MeV. The solid line in the top part of the picture gives Kirsch et al. calculations of the  $^{1s0}\text{Mo}$  intensity and the dashed line the background from nucleus-nucleus bremsstrahlung.<sup>2,6</sup> The agreement between experiment and calculation above 500 keV is fairly good. The cause of discrepancies below 400 keV is uncertain.

In the bottom part of Figure 7, results for the

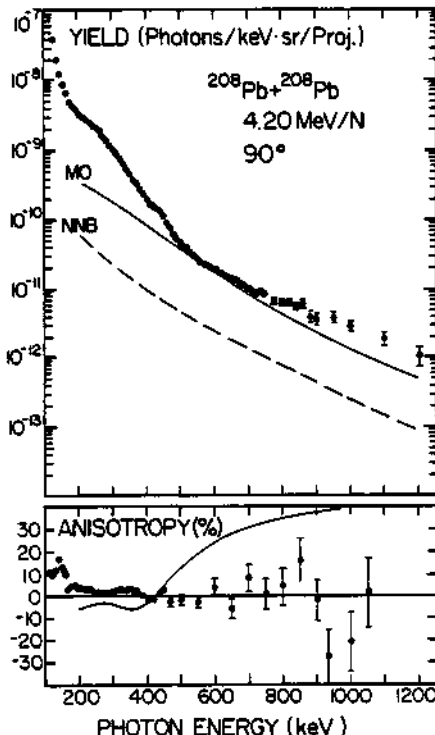


Fig. 7. Thick target yields and associated directional anisotropies for Mo x-rays emitted in 4.2 MeV/amu  $^{208}\text{Pb} + ^{208}\text{Pb}$  collisions and their comparison to theory (solid lines) by Kirsch et al.<sup>26</sup>

directional anisotropy of the continuum x-rays are shown in comparison to calculations by Kirsch et al.<sup>26</sup> The characteristic rise in the anisotropy near the united atom K x-ray energy observed in lighter systems and expected here by Kirsch, is conspicuously absent. Only small anisotropies are observable at very low photon energies. Therefore, the rather straightforward spectroscopy suggested by the scaling features of Mo x-ray anisotropies in lighter collision systems, does not appear to be feasible in the interesting relativistic cases. This disappointing result was actually predicted by Anholt,<sup>10</sup> who argued against the kind of alignment in relativistic molecular orbits which is responsible for peaking effects in the non-relativistic systems.

Figure 8 shows results of the measured impact parameter dependences for Mo x-ray production in 4.2 MeV/amu  $^{208}\text{Pb} + ^{208}\text{Pb}$  collisions due to Schmidt-Böcking<sup>27</sup> and collaborators. The top part of the figure gives results for the characteristic K x-rays and the bottom portion those for the Mo x-rays. Careful examination of the  $P(b)$  data for the K shell ( $P_K(b)$ ) indicates a slight rise in the probability below approximately 50 fm. At Mo x-ray photon energies, this rise becomes increasingly apparent and the two component structure of the Mo x-ray  $P(b)$  is quite clear.

The ratio of the  $1s_{1/2}\sigma$  orbital ionization probability to that of the  $2p_{1/2}\sigma$  increases strongly with united atom  $Z$ , and the lifetime of K vacancies decreases rapidly. For these reasons, the dominant production mechanism for Mo K x-rays in the heaviest quasimolecules is the one collision process. This facilitates interpretation of the heavy system  $P(b)$  data, since in contrast to lighter systems no folding of the K x-ray

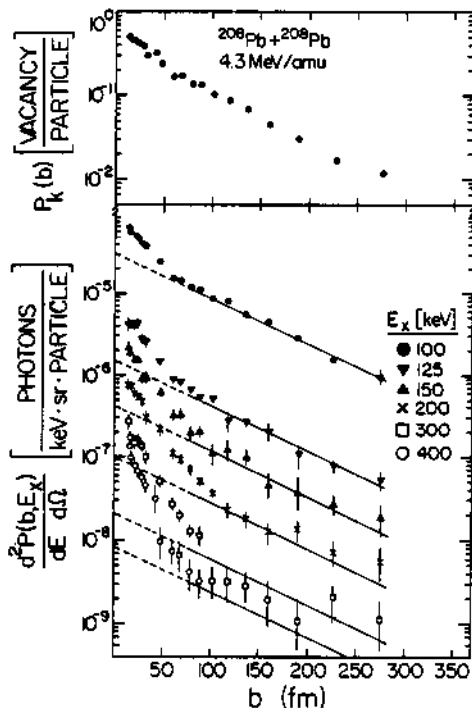


Fig. 8. Impact parameter dependence of Mo x-rays from 4.3 MeV/amu  $^{208}\text{Pb} + ^{208}\text{Pb}$  collisions showing two component structure of continuum x-ray  $P(b)$ .

P(b) from the first collision is necessary.<sup>18</sup>

Analysis of the slopes of the two Mo x-ray P(b) components within the context of first order perturbation theory<sup>24</sup> leads to the conclusion that the steeply falling component reflects ionization and decay of the  $1s_{1/2}\sigma$  orbital and the other component corresponds to radiation from  $2p_{1/2}\sigma$  orbital excitation.<sup>27</sup> These results illustrate nicely the continuity between Mo x-ray radiation and characteristic K x-ray emissions, and suggest that a separation between  $1s_{1/2}\sigma$  and  $2p_{1/2}\sigma$  excitations based on P(b) measurements of Mo x-ray emission is quite feasible.

In the preceding section on lighter systems mention was made of coincidence measurements between Mo and characteristic x-rays from Nb + Nb collisions.<sup>22</sup> The basic idea behind such types of experiments is illustrated in Figure 6. When a vacancy in the  $1s_{1/2}\sigma$  orbital decays through a  $2p_{1/2}\sigma$  to  $1s_{1/2}\sigma$  transition, the resulting  $2p_{1/2}\sigma$  vacancy will usually survive the collision and decay into a K x-ray. Therefore, a cascade relationship exists between  $2p_{1/2}\sigma \rightarrow 1s_{1/2}\sigma$  Mo x-rays and K x-rays, and a coincidence between the two may be used to isolate these transitions from other Mo x-ray contributions. As suggested in Figure 6, the actual situation is considerably more complicated than this, since double vacancy production in a single collision and/or other Mo transitions whose resulting vacancy couples down to the K shell will also result in the production of one continuum and one characteristic x-ray.

Figure 9 shows the results of such a coincidence measurement for 4.8 MeV/amu  $^{208}\text{Pb} + ^{208}\text{Pb}$  collisions.<sup>28</sup> The double vacancy (non-cascade) contribution to the coincidence cross section may be calculated assuming independent excitation of the two vacancies. This double vacancy contribution will depend upon the size and shape of the P(b) for the K x-rays, and the relative size and shape of the  $1s_{1/2}\sigma$  and  $2p_{1/2}\sigma$  Mo x-ray P(b) curves. In the bottom part of Figure 9, the ratio of measured coincidence to singles cross sections is plotted versus photon energy. The two horizontal lines represent the calculated double vacancy cross section to singles cross section ratios assuming that Mo x-rays are completely due to decays of the  $2p_{1/2}\sigma$  (bottom) or  $1s_{1/2}\sigma$  (top) orbitals. One sees that the observed coincidence to singles ratios can be explained as due solely to independently excited double vacancies.

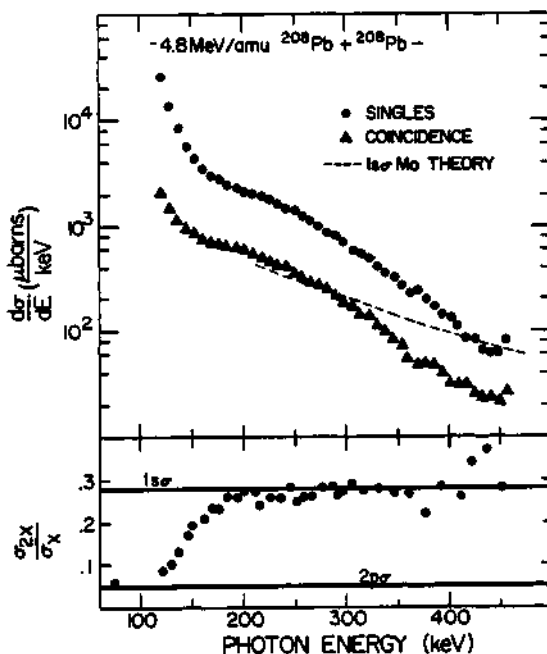


Fig. 9. Singles and K x-ray-Mo x-ray coincidence cross sections from 4.8 MeV/amu  $^{208}\text{Pb} + ^{208}\text{Pb}$  collisions. The dashed line represents singles Mo x-rays from the  $1s_0$  orbital as calculated by Kirsch et al.<sup>26</sup> See text for explanation.

simply by choosing a suitable mixture of  $1s_{1/2}\sigma$  to  $2p_{1/2}\sigma$  Mo x-ray intensities as a function of photon energy. Such a mixture would indicate a significantly higher cross section for  $1s_{1/2}\sigma$  Mo x-rays than that calculated by Kirsch et al. (dashed line in upper part of Figure).<sup>26</sup> The discrepancy between these results and those due to Kirsch can be explained by three possibilities: 1) Significant contributions from cascade coincidences are present in the coincidence cross section. 2) Kirsch's calculated  $1s_{1/2}\sigma$  Mo cross sections are too low at low photon energies. 3) The model of independent excitation is invalid. Which of these possibilities are in fact the case remain interesting unresolved questions.

## BACKGROUND RADIATION

Due to the continuum nature of Mo x-ray transitions, the identification of this radiation as quasimolecular in origin as well as its separation and distinction from competing background sources of x-rays, has been of major concern to these studies. In this section, a brief sketch of the major sources of background radiation will be given.

Secondary electron bremsstrahlung from high energy  $\delta$  electrons produced in these collisions is one source of continuum x-rays. Extensive studies of the bremsstrahlung cross sections from electron-atom scattering have been made. The central problem in calculating this contribution to the Mo x-ray spectra, is the lack of information concerning the cross section for  $\delta$  electron production, particularly in lighter collision systems. Since bremsstrahlung interactions occur not only in the target but also in other materials near the target (walls of target chamber, target frame, etc.), further complications arise in calculating this background for any particular experimental geometry.<sup>29</sup>

Nucleus-nucleus bremsstrahlung cross sections are well known. Use of symmetric collision systems (same atomic number and same isotope) eliminates the prominent dipole term leaving first order contributions from quadrupole radiation only. The quadrupole contribution is generally small compared to Mo x-ray intensities in both lighter and heavy collision systems.<sup>30</sup>

Radiative electron capture of a target electron into a projectile K vacancy has been studied to some extent. This background reflects non-adiabatic aspects of the collision and therefore increases with projectile velocity. Results show that this background presents problems only in very fast collisions and then is usually dominant only in the x-ray region directly above the characteristic K x-ray lines.<sup>31</sup>

Radiative ionization is a process by which a  $\delta$  electron produces bremsstrahlung on its way out of the collision due to its de-acceleration by the nuclear charges. Several attempts have been made to calculate this source of x-ray radiation in lighter collision systems. Due to the extreme difficulty in calculating direct  $1s\sigma$  ionization cross sections in lighter quasi-molecular systems,<sup>32</sup> very little is known about this

possible source of background.<sup>33</sup>

Coulomb excitation of low lying nuclear states and/or nuclear reactions both produce  $\gamma$ -ray backgrounds which interfere with measurements of Mo x-rays. In general, these cross sections increase more rapidly with increasing bombarding energy than those for Mo x-ray production. For most adiabatic lighter collision systems, choice of projectile and target nuclei with high lying first excited nuclear states is usually sufficient to reduce this background to negligible proportions. For the heaviest collision systems, such a choice becomes increasingly difficult and for the relativistic quasimolecules, nuclear background is easily the largest source of competing intensity to the Mo x-ray radiations.

In singles measurements significant background contributions may also come from residual radioactivity in the materials surrounding the experimental apparatus. Since these room backgrounds are randomly correlated in time to the Mo x-rays, any coincidence requirement (scattered particle, K x-ray, etc.) will eliminate this source of background radiation. Thick Pb shields must be constructed in singles experiments to reduce this background to manageable proportions.

Figure 10 shows a singles spectrum for the  $^{208}\text{Pb} + ^{208}\text{Pb}$  collision system at 4.8 MeV/amu, taken with a 3" x 3" NaI crystal.<sup>28</sup> Also shown in the figure for comparison purposes are calculated background intensities from nucleus-nucleus bremsstrahlung (NNB) and an upper bound to contributions from secondary electron bremsstrahlung (SEB). The highly Doppler broadened lines from  $^{207}\text{Pb}$  and  $^{206}\text{Pb}$  represent less than one percent isotopic contamination of the  $^{208}\text{Pb} + ^{208}\text{Pb}$  system. Despite the use of isotopically enriched  $^{208}\text{Pb}$  targets and beams, this small amount of contamination by nuclei with low lying levels produces significant backgrounds. Coulomb excitation of the 2.6 MeV  $^{208}\text{Pb}$  line and the resulting Compton tail generated by this line in the NaI detector is the next largest source of background. This situation can be improved by using highly enriched targets and beams, as well as by reducing the incident bombarding energy. However, the presence of these large backgrounds from nuclear excitations has limited current studies in very heavy systems to  $^{208}\text{Pb} + ^{208}\text{Pb}$  collisions only. Extension of these measurements to still heavier non-spherical

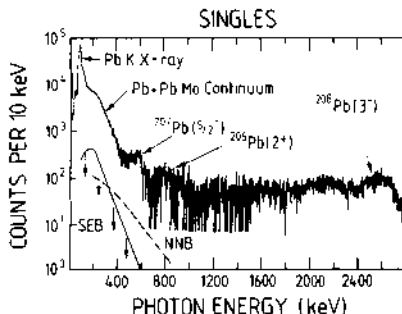


Fig. 10. Singles spectrum from 4.8 MeV/amu  $^{208}\text{Pb} + ^{208}\text{Pb}$  collisions showing secondary electron bremsstrahlung (SEB-solid line) and nucleus-nucleus bremsstrahlung (NNB-dashed line) backgrounds.

nuclear systems such as  $^{238}\text{U} + ^{238}\text{U}$  without significant experimental suppression of these backgrounds is not possible. Furthermore, the means by which such a suppression might be performed are unclear at the present time and certainly represent a challenge to future experimentalists.

Despite the problems and uncertainties surrounding background contributions, the experimentalist has been able to convince himself in both studies of lighter and heavy collisions, that Mo x-rays are in fact being observed. This has been done through observations of the scaling properties of the radiation and its directional anisotropy with the united atom nuclear charge as well as by detailed comparisons with calculations. In addition to these means, continuum x-rays may be identified as quasimolecular in origin by using the Doppler shift of the Mo x-rays to determine the velocity of their emitter.

If one assumes that the angular distribution of the Mo x-rays with respect to the beam direction is the same in the forward and backward directions, the difference in forward-backward laboratory intensities (for example 45 and 135 degrees) due to the Doppler shift, and relativistic solid angle effects may be used to actually measure the velocity with which the emitter of the

radiation was travelling at the time of x-ray emission. Application of this idea was first proposed by Meyerhof<sup>34</sup> who showed that Mo x-ray radiation indeed originates from the center of mass of the projectile-target system. Figure 11 shows more detailed studies of the emitter velocity of radiation from  $^{58}\text{Ni} + ^{58}\text{Ni}$  collisions at 64.8 and 12.6 MeV.<sup>35</sup> The directional anisotropy of the radiation may be used in conjunction with the extracted emitter velocities to identify the sources of continuum radiation in various photon-energy regions. The increase in emitter velocity in the 64.8 MeV data at low photon energies in conjunction with the rise in the directional anisotropy, serve to identify contributions from radioactive electron capture. At higher photon energies, the radiation is emitted with the center of mass velocity

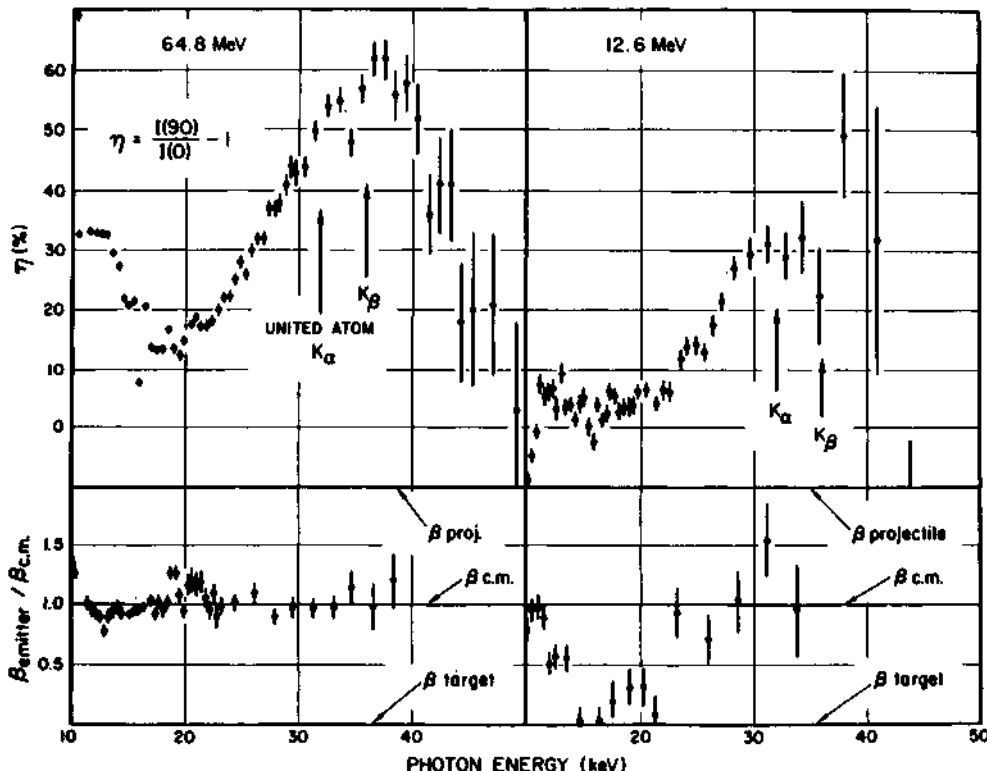


Fig. 11. Anisotropies (upper part of figure - called  $\eta$ ) and extracted emitter velocities (in units of the center of mass velocity - bottom part of figure) for continuum x-rays from  $\text{Ni} + \text{Ni}$  collisions.

of the projectile-target system indicating a dominance of Mo x-rays. The 12.6 MeV results indicate a decrease in the emitter velocity between 15-20 keV which remains unexplained. At higher energies the rise to center of mass velocities is characteristic of Mo x-ray emission.

Figure 12 shows Doppler shift measurement results for 4.8 MeV/amu  $^{209}\text{Bi} + ^{209}\text{Bi}$  collisions.<sup>36</sup> In the figure the anisotropy ratios  $I(137.5^\circ)/I(42.5^\circ) - 1$  are plotted versus photon energy for various emitter velocity assumptions. The upper results labelled  $V_p$  are the ratios corrected for Doppler shifts and relativistic solid angle effects corresponding to the projectile velocity, the middle points to the velocity of the center of mass system, and the lower points assume no Doppler shift. Only when the measured intensities are corrected for Doppler effects and relativistic solid angle corrections corresponding to 90% of the center of mass velocity, is forward-backward symmetry achieved. The use of 90%  $v_{cm}$  rather than 100% is due to the use of thick targets in these experiments and reflects energy loss of the projectile ions in the thick target. These results provide further evidence that the observed emissions are indeed quasimolecular in origin.

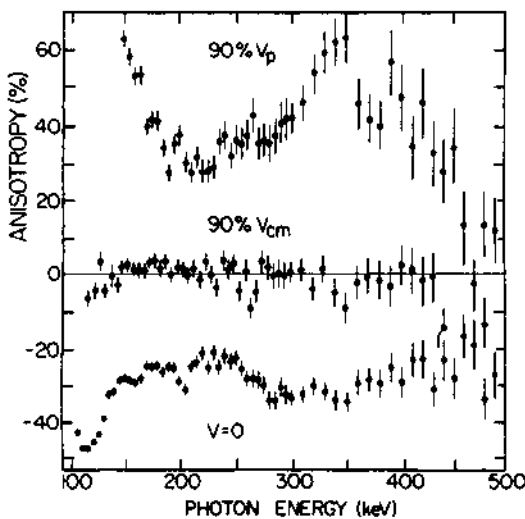


Fig. 12. Forward-backward continuum x-ray anisotropies calculated for 3 different emitter velocities of the continuum x-rays. Symmetry is obtained only for the case where the radiation is assumed to be emitted from the center of mass of the projectile-target system.

## CONCLUSIONS

Quasimolecular x-ray emissions provide direct evidence for the formation of molecular orbitals during the course of heavy ion collisions. In particular, the two component structures and directional anisotropies from lighter systems and their associated scaling with the united atom charge, provide relatively simple and direct indications that high electron binding occurs during the course of such collisions. The straightforward spectroscopy based on anisotropy measurements in lighter systems cannot be extended to superheavy quasimolecules. As a result, more detailed experiments exploring the differential properties of these x-rays using coincidence measurement techniques have assumed increasingly important roles. The impact parameter dependence measurements both in lighter and heavier systems provide a means by which  $1s_{1/2}^{50}\text{Mo}$  and  $2p_{1/2}^{50}\text{Mo}$  radiative yields can be separated and distinguished from each other. Cascade measurements have demonstrated the degree to which independent and correlated double vacancy producing mechanisms can provide more detailed information on excitation and radiative decay probabilities in these collisions.

The lack of structure in these spectra and the significant role of dynamic effects particularly in the vicinity of the united atom configuration caution us against hopes for a highly accurate quantitative spectroscopy of superheavy atoms. Nevertheless, studies of  $\delta$  electron, positron, K x-ray, and Mo x-ray production certainly all provide complementary information on the interactions responsible for excitation and decay processes in these collisions. Detailed studies of the differential and scaling properties of these various emissions will provide, through comparison to theory, checks on the matrix elements which actually govern the behavior of electrons in the very strong electric fields associated with these collisions.

## REFERENCES

1. J. S. Greenberg, H. Bokemeyer, H. Emling, E. Grosse, D. Schwalm, and F. Bosch, Phys. Rev. Lett. 39 (1977) 1404.  
R. Anholt, W. E. Meyerhof, and Ch. Stoller, Z. Phys. A291 (1979) 287.  
D. Liesen, P. Armbruster, F. Bosch, S. Hagmann,

- P. H. Mokler, H. J. Wollersheim, H. Schmidt-Böcking, R. Schuch, and J. B. Wilhemy, Phys. Rev. Lett. 44 (1980) 983.
- F. Bosch, D. Liesen, P. Armbruster, D. Maor, P. H. Mokler, H. Schmidt-Böcking, and R. Schuch, Z. Physik A296 (1980) 11.
2. C. Kozuharov, P. Kienle, D. H. Jakubassa, and M. Kleber, Phys. Rev. Lett. 39 (1977) 540.
- E. Berdemann, F. Bosch, H. Bokemeyer, M. Clemente, F. Güttner, P. Kienle, W. König, C. Kozuharov, B. Martin, B. Povh, H. Tsertos, and Th. Walcher, GSI Annual Report (1979) 137.
3. H. Backe, L. Handshug, F. Hessberger, E. Kankeleit, L. Richter, F. Weik, R. Willwater, H. Bokemeyer, P. Vincent, Y. Nakayama, and J. S. Greenberg, Phys. Rev. Lett. 40 (1978) 1443.
- C. Kohzuharov, P. Kienle, E. Berdemann, H. Bokemeyer, J. S. Greenberg, Y. Nakayama, P. Vincent, H. Backe, L. Handschug, and E. Kankeleit, Phys. Rev. Lett. 42 (1979) 376.
- J. Reinhardt, B. Müller, W. Greiner, Phys. Rev. A24 (1981) 97.
4. B. Müller, J. Rafelski, and W. Greiner, Phys. Lett. 49B (1973) 5.
5. K. H. Heinig, H. U. Jaeger, H. Richter, and H. Woittennik, Phys. Lett. 60B (1976) 249.
- K. H. Kaun, P. Manfrass, and W. Frank, Particles and Nuclei (Moskow) 8 (1977) 1246.
6. P. Vincent, "The X-Ray Spectroscopy of Electronic Quasimolecules," Ph.D. Thesis Yale University (1977) unpublished.
- J. S. Greenberg, C. K. Davis, and P. Vincent, Phys. Rev. Lett. 33 (1974) 473.
- P. Vincent, C. K. Davis, and J. S. Greenberg, Phys. Rev. A18 (1978) 1878.
- P. Vincent and J. S. Greenberg, to be published.
7. W. Wölfli, Ch. Stoller, B. Bonani, M. Suter, and M. Stöckli, Phys. Rev. Lett. 35 (1975) 656.
- J. S. Greenberg, P. Vincent, and W. Lichten, Phys. Rev. A16 (1977) 964.
- W. L. Luken, J. S. Greenberg, and P. Vincent, Phys. Rev. A15 (1977) 2305.
- Ch. Stoller, W. Wölfli, G. Bonani, M. Stöckli, and M. Suter, Phys. Rev. A15 (1977) 990.
8. W. E. Meyerhof, T. K. Saylor, S. M. Lazarus, W. A. Little, B. B. Triplett, and L. F. Chase, Jr., Phys. Rev. Lett. 30 (1973) 1279
- C. K. Davis and J. S. Greenberg, Phys. Rev. Lett. 32 (1974) 1215.

9. K. H. Kaun, P. Manfrass, and W. Frank, Ref. 5.  
P. H. Mokler, H. J. Stein, and P. Armbruster,  
Phys. Rev. Lett. 29 (1972) 827.  
Ch. Stoller, W. Wölfli, G. Bonani, M. Stöckli,  
and M. Suter, J. Phys. B10 (1977) L347.
10. R. Anholt, Z. Physik A288 (1978) 257.
11. C. H. Stoller, W. Wölfli, G. Bonani, M. Stöckli,  
and M. Suter, Ref. 9.
12. J. H. Macek and J. S. Briggs, J. Phys. B7 (1974)  
1312.  
H. D. Betz, F. Bell, H. Panke, W. Stehling, E.  
Spindler, and M. Kleber, Phys. Rev. Lett. 34  
(1975) 1256.  
P. Vincent and J. S. Greenberg, J. Phys. B12  
(1979) L641.
13. W. E. Meyerhof, T. K. Saylor, S. M. Lazarus,  
A. D. Little, B. B. Triplett, L. F. Chase, Jr.,  
and R. Anholt, Phys. Rev. Lett. 32 (1974) 1279.  
J. H. Macek and J. S. Briggs, Ref. 12.  
R. Anholt, "Scattering Angle Dependence of Double-  
Collision Processes," (1981) to be published.
14. F. Bell, H. D. Betz, H. Panke, E. Spindler,  
W. Stehling, and M. Kleber, Phys. Rev. Lett. 35  
(1975) 841.  
R. Laubert, R. S. Peterson, J. P. Forester,  
K. H. Liao, P. M. Griffin, H. Hayden, S. B. Elston,  
D. J. Pett, R. S. Thoe, and I. A. Sellin, Phys.  
Rev. Lett. 36 (1976) 1574.  
H. Schmidt-Böcking, R. Schuch, I. Tserruya,  
R. Schulé, H. J. Specht, and K. Bethge, Z. Physik  
A284 (1978) 39.  
H. Schmidt-Böcking, W. Lichtenberg, R. Schuch,  
J. Volpp, and I. Tserruya, Phys. Rev. Lett. 41  
(1978) 859.  
Ch. Stoller, R. Anholt, and W. E. Meyerhof,  
"Molecular Orbital X-Rays and Their Anisotropies  
in Heavy-Ion Collisions in Solids and Gases,"  
(1981) to be published.
15. R. Anholt, Z. Physik A289 (1978) 41.
16. H. Schmidt-Böcking, I. Tserruya, H. Zekl, and  
K. Bethge, Nucl. Instrum. Meth. 120 (1974) 329
17. H. Schmidt-Böcking, R. Anholt, R. Schuch, P.  
Vincent, K. Stiebing, H. U. Jäger, "Impact Para-  
meter Dependence of Quasimolecular K-radiation  
in 90 MeV Ni + Ni Collisions," (1981) to be  
published.
18. R. Anholt, Ref. 13.
19. P. Bürgy, G. Bonani, E. Morenzoni, M. Stöckli,  
Ch. Stoller, M. Suter, and W. Wölfli, Z. Physik  
A300 (1981) 105.

- H. Schmidt-Böcking, R. Schuch, I. Tserruya, Inst. für Kernphysik, Univ. Frankfurt Annual Report (1980) 53, and to be published.
- R. Anholt, "Theory of the Azimuthal Angular Distribution of Molecular Orbital X-Ray Emission," (1981) to be published.
20. M. Gros, B. Müller, and W. Greiner, J. Phys. B9 (1976) 1849.  
J. S. Briggs and K. Dettman, J. Phys. B10 (1977) 1113.
21. W. Wölfli, Ch. Stoller, G. Bonani, M. Stöckli, M. Suter, and W. Däppen, Z. Phys. A286 (1978) 249.  
H. Hartung and B. Fricke, Z. Phys. A288 (1978) 345.
22. J. J. O'Brien, E. Liarokapis, and J. S. Greenberg, Phys. Rev. Lett. 44 (1980) 386.
23. G. Soff, W. Greiner, W. Betz, and B. Müller, Phys. Rev. A20 (1979) 169.
24. F. Bosch, D. Liesen, P. Armbruster, D. Maor, P. H. Mokler, H. Schmidt-Böcking, and R. Schuch, Ref. 1.  
D. Liesen, P. Armbruster, F. Bosch, S. Hagmann, P. H. Mokler, H. J. Wollersheim, H. Schmidt-Böcking, R. Schuch, and J. B. Wilhemy, Ref. 1.
25. W. E. Meyerhof, D. L. Clark, Ch. Stoller, E. Morenzoni, W. Wölfli, F. Folkmann, P. Vincent, P. H. Mokler, and P. Armbruster, Phys. Lett. 70A (1979) 303  
Ch. Stoller, E. Morenzoni, W. Wölfli, W. E. Meyerhof, F. Folkmann, P. Vincent, P. H. Mokler, and P. Armbruster, Z. Physik A297 (1980) 93.
26. J. Kirsch, W. Betz, J. Reinhardt, G. Soff, B. Müller, and W. Greiner, Phys. Lett. 72B (1978) 298; Z. Physik A292 (1979) 227.  
J. Kirsch, Ph.D. Thesis, University of Frankfurt (1980) unpublished.
27. K. E. Stiebing, K. Bethge, W. Schadt, H. Schmidt-Böcking, F. Bosch, D. Liesen, D. Maor, P. H. Mokler, P. Vincent, S. Hagmann, R. Schuch, GSI Annual Report (1980) 126; Inst. Kernphysik, Univ. Frankfurt Annual Report (1980) 49, and to be published.
28. P. Vincent, D. Schwalm, H. Bokemeyer, H. Emling, E. Grosse, J. S. Greenberg, Proc. XVIII International Wint. Meeting on Nucl. Phys., Bormio (1980) 718, and to be published.
29. C. M. Lee, L. Kissel, R. H. Pratt, H. K. Tseng, Phys. Rev. A13 (1976) 1714.  
E. Berdemann, F. Bosch, H. Bokemeyer, M. Clemente, F. Gütter, P. Kienle, W. König, C. Kozhuharov, B. Martin, B. Povh, H. Tsertos, and Th. Walcher,

- Ref. 2.
30. J. Reinhardt, G. Soff, W. Greiner, Z. Phys. A276 (1976) 28.  
H. P. Trautvetter, J. S. Greenberg, and P. Vincent, Phys. Rev. Lett. 37 (1976) 202.
31. H. W. Schnopper, H. D. Betz, J. P. Delvaille, K. Kalata, A. R. Sohval, K. W. Jones, and H. E. Wegner, Phys. Rev. Lett. 29 (1972) 898.  
E. Spindler, H. D. Betz, F. Bell, Phys. Rev. Lett. 42 (1979) 832.
32. W. Thorson and J. H. Choi, Phys. Rev. A15 (1977) 550.
33. D. H. Jakubassa and M. Kleber, Z. Phys. A273 (1975) 29.
34. W. E. Meyerhof, T. K. Saylor, and R. Anholt, Phys. Rev. A12 (1975) 2641.
35. P. Vincent, C. K. Davis, and J. S. Greenberg, Ref. 6.
36. Ch. Stoller, E. Morenzoni, W. Wölfli, W. E. Meyerhof, F. Folkmann, P. Vincent, P. H. Mokler, and P. Armbruster, Ref. 25.

DENSITY FUNCTIONAL APPROACH TO THE RELATIVISTIC  
MANY BODY PROBLEM

R.M. Dreizler and E.K.U. Gross

Institut für Theoretische Physik  
Universität Frankfurt, W. Germany

INTRODUCTION

The effects of strong Coulomb fields on electrons can be investigated in heavy ion collisions. Unfortunately the ideal set up for such an experiment: the collision of a heavy nucleus from a target atom stripped of all the electrons but one, can not be realised very easily. The strong field effects do occur against the background of many electron physics.

In order to deal with the many body problem involved, one has to develop some reasonably simple as well as reasonably accurate methods. We hope to achieve this goal with the aid of density functional methods.

We first take a look at the two (Coulomb) centre situation in the adiabatic approximation. The internuclear separation changes sufficiently slowly, so that the electron cloud is able to adapt itself to the nuclear geometry at every instance. This situation is described by the Born-Oppenheimer approximation in which the electronic Hamiltonian has the form

$$H_{el} = \sum_i t_i + \sum_{i,\alpha} v_n (r_i, R_\alpha) + \frac{1}{2} \sum \frac{e^2}{|r_i - r_j|} .$$

The solution of the many body problem with two charge centres is very tedious, even in the HF-limit. In molecular physics the internuclear separation is large enough, so that the situation can be described in terms of frozen atomic cores and a few valence electrons. If on the other hand, the two systems are pushed

together fairly closely, it is obvious that this notion will not be adequate.

If one searches the literature for two centre HF calculations, one finds (with a few valiant exceptions), that they are restricted to systems with less than 20 electrons. This is the reason why we attempted to activate density functional methods, which are relatively independent of the number of particles involved.

If the process is not adiabatic, one has to search for an alternative approach. As a starting point one then relies on the impact parameter approximation. One assumes that in view of the dominant nuclear masses on the atomic scale, the relative motion of the nuclei can be described in terms of a classical trajectory  $\underline{R}(t)$ . The electronic Hamiltonian becomes time dependent

$$H_{el} = \sum t_i + \sum_{i,\alpha} v_n (\underline{r}_i, \underline{R}_\alpha(t)) + \frac{1}{2} \sum \frac{e^2}{|\underline{r}_i - \underline{r}_j|} .$$

If one assumes furthermore that the electronic wave function depends parametrically on the internuclear separation as well as explicitly on the time

$$\psi = \psi(\underline{r}_1 \dots \underline{r}_A, \underline{R}(t), t) ,$$

the time dependent Schrödinger eq. for the electrons takes the form

$$i\partial_t \psi|_{\text{exp}} = (H_{el}(t) - i\dot{\underline{R}} \cdot \nabla_{\underline{R}}) \psi .$$

The time differentiation is separated into an explicit as well as an implicit term. The implicit term contains the socalled translational (the contribution in direction of the internuclear axis) as well as the rotational coupling terms. These two coupling terms describe the dominant dynamic response of the electrons to the nuclear motion.

If one aimed for a density functional approach of this situation, one would have to set up a theory (or model) that describes the time development of the density. We have started to tackle this question<sup>1</sup>, but for the present we will stay with the adiabatic situation indicated before and report on the following topics

- Definition of density functional methods,
- assembly of the basic equations in the nonrelativistic case,
- an indication of the quality<sup>2</sup> of results obtained in the nonrelativistic case.

- Discussion of first attempts to extend these ideas to relativistic situations.
- Outline of a consistent density functional approach to relativistic systems.

### NONRELATIVISTIC DENSITY FUNCTIONAL THEORY

The foundation of density functional methods is the theorem of Hohenberg and Kohn<sup>3</sup>. It states in its simplest version:

The groundstate energy of a many particle system (with two body interactions) is a unique, continuous functional of the density alone

$$E_0 = E_0 [\rho].$$

This statement is far from trivial. It is obviously possible to generate a given number by means of a suitable chosen functional. The statement of the theorem is however: The functional is universal. The same functional is supposed to describe atoms (neutral or ionised), molecules, nuclei etc. The only difference is the form of the potentials used for a given system and the form of the boundary conditions to be specified.

The functional in question can not be specified exactly. At present there are two regimes, for which approximate forms of the functional have been discussed.

Regime 1: We have small, but otherwise arbitrary deviations from a constant density

$$\rho(\underline{r}) = \bar{\rho} + \delta\rho(\underline{r}) \quad , \quad |\delta\rho(\underline{r})|/\bar{\rho} \ll 1.$$

The situation is most appropriate for the discussion of solid state problems. An approximate form of the functional in question can then be derived by the many body methods used for the discussion of the inhomogeneous electron gas.

Regime 2: We have a slowly varying but otherwise arbitrary density. This condition is usually specified by

$$|\nabla\rho|/\rho \ll K_F .$$

This situation is supposed to apply to atomic, molecular and nuclear systems. An approximate form of the functional can be derived by the gradient expansion technique, first introduced by Kirzhnits<sup>4</sup>. This expansion technique has a strong parallel to the semiclassical expansion technique of Wigner<sup>5</sup> and Kirkwood<sup>6</sup>.

In the following we present a derivation of the functional for the regime 2. We split the exact ground state energy of an interacting Coulomb system into the kinetic energy  $E_{\text{kin}}$ , the external potential energy  $E_{\text{en}}$ , the particle-particle interaction  $E_{\text{ee}}$ , the exchange contribution  $E_{\text{ex}}$  and the correlation part  $E_{\text{cor}}$

$$E_0 = E_{\text{kin}} + E_{\text{en}} + E_{\text{ee}} + E_{\text{ex}} + E_{\text{cor}}.$$

In detail we have (natural units  $\hbar=c=1$  are used throughout this paper)

$$E_{\text{kin}} = \int d^3r \int d^3r' \delta(\underline{r}-\underline{r}') \left[ -\frac{\Delta}{2m} \rho(\underline{r}, \underline{r}') \right] \equiv \int d^3r \tau(\underline{r}) \quad (1)$$

$$E_{\text{en}} = \int d^3r \rho(\underline{r}) v_n(\underline{r}), \quad (2)$$

$v_n(\underline{r})$  is the nuclear potential corresponding to either atomic, molecular or solid state situations.

$$E_{\text{ee}} = \frac{e^2}{2} \int d^3r \int d^3r' \frac{\rho(\underline{r}) \rho(\underline{r}')}{|\underline{r}-\underline{r}'|} \quad (3)$$

$$E_{\text{ex}} = -\frac{e^2}{2} \int d^3r \int d^3r' \frac{\rho(\underline{r}, \underline{r}') \rho(\underline{r}', \underline{r})}{|\underline{r}-\underline{r}'|} \equiv \int d^3r e_x(\underline{r}) \quad (4)$$

$$E_{\text{cor}} = \frac{e^2}{2} \int d^3r \int d^3r' \frac{\rho^{(2)}(\underline{r}\underline{r}', \underline{r}\underline{r}')}{|\underline{r}-\underline{r}'|} - E_{\text{ee}} - E_{\text{ex}}. \quad (5)$$

For the sake of brevity spin degrees of freedom are suppressed here. For later use we have expressed the kinetic energy as well as the exchange energy by the corresponding energy densities  $\tau(\underline{r})$  and  $e_x(\underline{r})$ .

Within this paper we shall restrict ourselves to the HF-limit, i.e. we neglect the correlation energy

$$E_{\text{cor}} \equiv 0.$$

It should be mentioned however, that various attempts<sup>7,8</sup> to calculate correlation effects within the density functional theory can be found in the literature.

In the HF limit one can obtain a suitable representation of the one particle density operator by the following argument. We

start with the HF variational equation

$$(\hat{t} + \hat{v}_{\text{eff}}) |\alpha\rangle = \epsilon_{\alpha} |\alpha\rangle . \quad (6)$$

The one particle density matrix then has the form

$$\begin{aligned} \langle \underline{r} | \hat{\rho} | \underline{r}' \rangle &= \rho(\underline{r}, \underline{r}') \\ &= \int_{\alpha} n_{\alpha} \langle \underline{r} | \alpha \rangle \langle \alpha | \underline{r}' \rangle . \end{aligned}$$

The occupation number  $n_{\alpha}$  (1 for occupied levels, 0 for unoccupied levels) can be represented with a step function involving the Fermi-level  $\epsilon_F$

$$= \int_{\alpha} \theta(\epsilon_F - \epsilon_{\alpha}) \langle \underline{r} | \alpha \rangle \langle \alpha | \underline{r}' \rangle$$

or in operator form

$$= \int_{\alpha} \langle \underline{r} | \theta(\epsilon_F - \hat{t} - \hat{v}_{\text{eff}}) | \alpha \rangle \langle \alpha | \underline{r}' \rangle .$$

By use of the completeness of the HF single particle basis we obtain

$$= \langle \underline{r} | \theta(\epsilon_F - \hat{t} - \hat{v}_{\text{eff}}) | \underline{r}' \rangle .$$

For convenience we introduce a "Fermi energy operator" by

$$\hat{E}_F = \epsilon_F - \hat{v}_{\text{eff}}$$

and extract from the simple argument above, the well known representation

$$\hat{\rho} = \theta(\hat{E}_F - \hat{t}) . \quad (7)$$

The kinetic energy density can, with a similar argument, be contracted into the formal expression

$$\tau(\underline{r}) = \frac{1}{2} \langle \underline{r} | \hat{t} \hat{\rho} + \hat{\rho} \hat{t} | \underline{r} \rangle . \quad (8)$$

In order to evaluate these formal expressions the complete system of plane waves  $|\underline{k}\rangle$  is inserted

$$\rho(\underline{r}, \underline{r}') = 2 \int d^3k \langle \underline{r} | \theta(\hat{E}_F - \hat{t}) | \underline{k} \rangle \langle \underline{k} | \underline{r}' \rangle . \quad (9)$$

The plane wave states are eigenfunctions of the kinetic energy operator

$$\hat{t}|\underline{k}\rangle = \frac{\mathbf{k}^2}{2m} |\underline{k}\rangle .$$

The problem that we then face, is the evaluation of the matrix elements of an operator valued function, whose arguments do not commute

$$[\hat{E}_F, \hat{t}] \neq 0 .$$

We assume that the HF-problem (6) can be approximated to any required accuracy by an appropriate local problem (knowledge of the corresponding local potential is not required as it will be eliminated in the end). If we assume in addition as a lowest order approximation that the operators  $E_F$  and  $t$  do commute (the effects due to the actual noncommutativity are discussed below in a systematic fashion), we obtain for the density matrix

$$\rho_o(\underline{r}, \underline{r}') = \frac{2}{(2\pi)^3} \int d^3k \theta(E_F(\underline{r}) - \frac{\mathbf{k}^2}{2m}) e^{i\mathbf{k} \cdot (\underline{r}-\underline{r}')} . \quad (10)$$

Introducing a "position dependent Fermi momentum"

$$K_F(\underline{r}) = \sqrt{2mE_F(\underline{r})}$$

the integral above is readily evaluated yielding

$$\rho_o(\underline{r}, \underline{r}') = \frac{K_F^2}{\pi^2} j_1(K_F y) \frac{1}{y} \quad \text{with} \quad y = |\underline{r}-\underline{r}'| . \quad (11)$$

In the limit  $y \rightarrow 0$  one obtains

$$\rho_o(\underline{r}) = \frac{1}{3\pi^2} K_F^3(\underline{r}) . \quad (12)$$

A similar calculation gives for the kinetic energy density

$$\begin{aligned} \tau_o(\underline{r}) &= \frac{2}{(2\pi)^3} \int d^3k \frac{\mathbf{k}^2}{2m} \theta(E_F(\underline{r}) - \frac{\mathbf{k}^2}{2m}) \\ &= \frac{1}{10m\pi^2} K_F^5(\underline{r}) . \end{aligned} \quad (13)$$

These are the wellknown relations of the Thomas Fermi (TF)-model. Eliminating the unknown local Fermi momentum  $K_F$  in favor of the density one obtains for the kinetic energy

$$\tau_0(\underline{x}) = \frac{3}{10m} (3\pi^2)^{2/3} \rho_0(\underline{x})^{5/3} . \quad (14)$$

We note one particular point: At the intermediate level (equations (12) and (13)) we have a turning point problem, i.e. the quantity

$$K_F(\underline{x}) = [2m(\epsilon_F - v_{\text{eff}}(\underline{x}))]^{1/2}$$

vanishes on some surface in the asymptotic region (since  $v_{\text{eff}}$  is purely attractive and  $\epsilon_F < 0$ ) and is not defined outside. With the elimination of  $K_F$  in favor of  $\rho$  we have implicitly set up a continuation into the (semi-classically forbidden) outer region.

In order to go beyond the lowest order approximation we are left with the problem of calculating the operator function

$$\hat{f}(\hat{a}+\hat{b}) |a\rangle$$

for the case that  $|a\rangle$  is an eigenstate of the operator  $\hat{a}$ , and that  $\hat{a}$  and  $\hat{b}$  do not commute. The question is resolved by the following argument. First, we use the Laplace representation

$$\hat{f}(\hat{a}+\hat{b}) |a\rangle = \int d\lambda c(\lambda) \exp[\lambda(\hat{a}+\hat{b})] |a\rangle$$

and the factorisation of the exponential operator

$$\exp[\lambda(\hat{a}+\hat{b})] = \exp[\lambda\hat{b}] \hat{K}(\lambda) \exp[\lambda\hat{a}] . \quad (15)$$

For the operator  $\hat{K}$  a differential equation of the form

$$\frac{d\hat{K}}{d\lambda} = [\hat{a}, \hat{K}] + \exp(-\lambda\hat{b}) [\hat{a}, \exp(\lambda\hat{b})] \hat{K}(\lambda) \quad (16)$$

with the initial condition

$$\hat{K}(0) = 1$$

can be derived. In order to solve this equation one expands  $\hat{K}$  into a power series in  $\lambda$

$$\hat{K}(\lambda) = \sum_{n=0}^{\infty} \lambda^n \hat{K}_n . \quad (17)$$

For the operators  $O_n$  one obtains from the differential equation (16) the recursion formula

$$\hat{o}_n = \frac{1}{n} ([\hat{a}, \hat{o}_{n-1}] + \sum_{i=1}^n \hat{c}_i \hat{o}_{n-1-i})$$

$$\text{with } \hat{c}_i = \frac{(-1)^i}{i!} \underbrace{[b, [b, [\dots [b, a] \dots]]]}_{i \text{ times}}. \quad (18)$$

The initial values for the recursion are

$$\hat{0}_0 = 1 \quad \hat{0}_1 = 0 \quad .$$

Then we proceed as follows: By use of equation (15) the exponential operator acting on the eigenfunctions of  $\hat{a}$  gives

$$\exp[\lambda(\hat{a}+\hat{b})] |a\rangle = \exp[\lambda\hat{b}] \hat{K}(\lambda) \exp[\lambda\hat{a}] |a\rangle$$

$$= \exp[\lambda(\hat{a}+\hat{b})] \hat{K}(\lambda) |a\rangle .$$

Here we have recollected the exponential operator with the eigenvalues of  $\lambda$  at the cost of introducing the operator  $\hat{K}(\lambda)$ . Inserting the expansion (17) for  $\hat{K}$  and using the formal derivative of the operator valued function

$$f^{(n)}(\hat{Q}) = \frac{d^n f(\hat{Q})}{dQ^n} = \int d\lambda c(\lambda) \lambda^n \exp[\lambda \hat{Q}]$$

one obtains the final result

$$f(\hat{a} + \hat{b}) |a\rangle = \sum_{n=0}^{\infty} f^{(n)}(a+b) \hat{a}_n |a\rangle . \quad (19)$$

For the final exploitation one sets

$$f \rightarrow \theta, \quad \hat{a} \rightarrow -\hat{t} \quad \text{and} \quad \hat{b} \rightarrow \hat{E}_F.$$

If one again uses the local representation of  $E_F$ , the commutators involved in (18), correspond to gradients of  $E_F(r)$ . The commutators can be evaluated in a straightforward manner. If one restricts oneself to the second order in gradient terms  $\Delta E_F$ ,  $(\nabla E_F)^2$  one has to go to  $\hat{O}_4$ , for an expansion to fourth order gradient terms  $\Delta^2 E_F$ ,  $(\nabla E_F)^4$ , etc., one has to go to  $\hat{O}_8$ . These expansions are then

introduced into the representation of density, kinetic energy density and exchange energy density. The integration over momentum space (as well as spatial coordinates in the case of the exchange energy density) can be executed directly, yielding to second order the following expressions:

$$\rho(\underline{r}) = \frac{K_F(\underline{r})^3}{3\pi^2} + \frac{1}{24\pi^2} \frac{\Delta K_F^2}{K_F} - \frac{1}{96\pi^2} \frac{(\nabla K_F^2)^2}{K_F^3} + \dots \quad (20)$$

$$\tau(\underline{r}) = \frac{K_F(\underline{r})^5}{10m\pi^2} - \frac{1}{48m\pi^2} \frac{K_F \Delta K_F^2}{K_F} - \frac{1}{64m\pi^2} \frac{(\nabla K_F^2)^2}{K_F} + \dots \quad (21)$$

$$e_X(\underline{r}) = - \frac{e^2}{4\pi^3} \frac{K_F(\underline{r})^4}{K_F^2} - \frac{e^2}{576\pi^3} \frac{(\nabla K_F^2)^2}{K_F^2} + \dots \quad . \quad (22)$$

The lowest order is again the TF-result. The formal expansion parameter is  $\frac{m}{\hbar}$ . Thus we have at this stage again a semiclassical statement, including the WKB like turning point problem discussed before. This problem can be overcome if one eliminates the Fermi momentum in favor of the density (consistently to second order). The result of this process is

$$\tau(\underline{r}) = c_1 \rho(\underline{r})^{5/3} + c_2 \frac{(\nabla \rho)^2}{\rho(\underline{r})} \quad (23)$$

$$e_X(\underline{r}) = - c_3 \rho(\underline{r})^{4/3} - c_4 \frac{(\nabla \rho)^2}{\rho(\underline{r})^{4/3}} \quad (24)$$

$$\text{with } c_1 = \frac{3}{10m} (3\pi^2)^{2/3} \quad c_2 = \frac{1}{72m}$$

$$c_3 = e^2 \frac{3}{4} \left(\frac{3}{\pi}\right)^{1/3} \quad c_4 = \frac{7e^2}{432\pi (3\pi^2)^{1/3}} \quad .$$

These are the approximate functionals that will be used in the following. The next question to be answered is how these functionals can be applied to atomic and nuclear physics problems. There are essentially two options:

Option I: Derive a set of variational equations

$$\delta_{\rho} (E_o[\rho] + v_o \int \rho(\underline{r}) d^3r) = 0 \quad (25)$$

from which the density (and hence the groundstate energy and other quantities derived from the density) can be determined.

Option II: Rely only on the representation of the exchange term and use it to set up a HF-Slater like problem

$$t + v_n + \left[ \frac{\delta E_{ee}}{\delta \rho} + \frac{\delta E_{ex}}{\delta \rho} \right] \varphi_i = e_i \varphi_i \quad (26)$$

from which orbitals and orbital energies are determined in a self-consistent fashion.

For the problem, we are going to consider, i.e. the calculation of the electronic structure of diatomic systems, we have actually used a combination of the two options.

Step 1: Calculate the density with option I.

Step 2: Insert this density into the expressions for

$\frac{\delta E_{ee}}{\delta \rho}$  and  $\frac{\delta E_{ex}}{\delta \rho}$  and solve the orbital problem (26). The hope

is to obtain reasonably consistent results without tackling the selfconsistency problem.

We first look at atomic systems, where a full comparison with HF results is possible. Fig. 1 shows the density for the Kr atom ( $r\rho$  is plotted as a function of  $\sqrt{r}$ ) calculated in step 1 from the so-called Thomas-Fermi-Dirac-Weizsäcker (TFDW) functional which contains the first two terms of the kinetic energy density (23) and the lowest order (Dirac) term of the exchange energy density (24). The TFDW density averages beautifully over the shell structure. For exactly this reason it will only be able to reproduce quantities that do not depend sensitively on shell effects.

The total energy is a quantity that does not depend strongly on the shell fluctuations. This is illustrated in Table 1 which contains the result of a careful numerical solution of the TFDW problem. One notes that the TFDW energies agree with the HF values to better than 4% over the whole periodic table.

A number of authors have discussed the use of an adjustable coefficient  $c_2$  of the gradient term in (23) in order to allow for an effective correction of the terms neglected in the expansion.

Table 1. Atomic groundstate energies in atomic units (a.u.): Comparison of TFDW-results with HF- and TF-results. ((1): Calculation with  $c_2=1/72m$ , (2): with  $c_2=1/40m$ ).

System	$-E_{HF}$	$-E_{TFDW}^{(1)}$	$-E_{TFDW}^{(2)}$	$-E_{TF}$
Ne(10)	128.55	139.89	128.80	165.62
Ar(18)	526.82	561.82	524.75	652.76
Kr(36)	2752.1	2897.2	2744.3	3289.7
Xe(54)	7232.1	7558.7	7309.2	8472.9
Au(79)	17865	18575	17817	20586
Rn(86)	21867	22699	21799	25096
U(92)	25664	26618	25586	29373
Fm(100)	31283	32409	31187	35682
(120)	48203	49838	48069	54578

This can actually be determined from the noninteracting (hydrogen-like) problem. One finds that a factor of 1.8 gives agreement with HF-values to better than 0.4% over the full range of charge numbers.

For the discussion of diatomic systems we use the result for atoms in the sense, that we adopt the same factor. We thus rely on the theorem of Hohenberg and Kohn that the same functional should be as adequate for more complex systems.

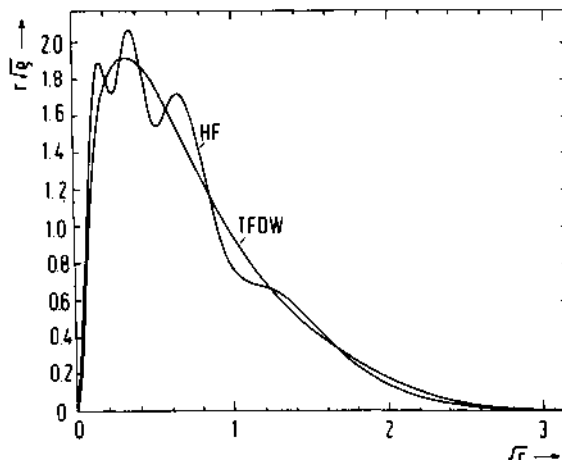


Fig. 1. The density of the Kr atom.

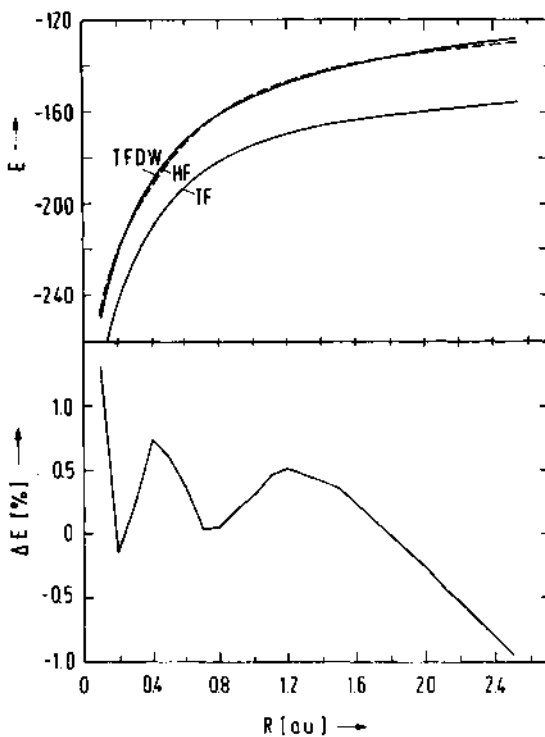


Fig. 2. The total electronic energy as a function of the internuclear separation for the N-N system.

In Fig. 2 we show the corresponding TFDW energy as a function of the internuclear separation for the system N-N. The agreement with HF-groundstate energies is better than 2%. The corresponding electronic density is then used to carry through step 2 of our programme consisting of the solution of the single particle eigenvalue problem (26) for two centre systems. Fig. 3 shows a comparison of the correlation diagram with HF results for the 14 electron system N-N. The agreement lies within a few per cent.

It should be emphasized that within this approach we can with a very reasonable increase in computing time generate as accurate correlation diagrams for heavier systems. As an example Fig. 4 shows the correlation diagram for the occupied orbitals of the 70 electron system I-Cl. This system represents a borderline case for the nonrelativistic treatment. For heavier systems relativistic effects have to be taken into account.

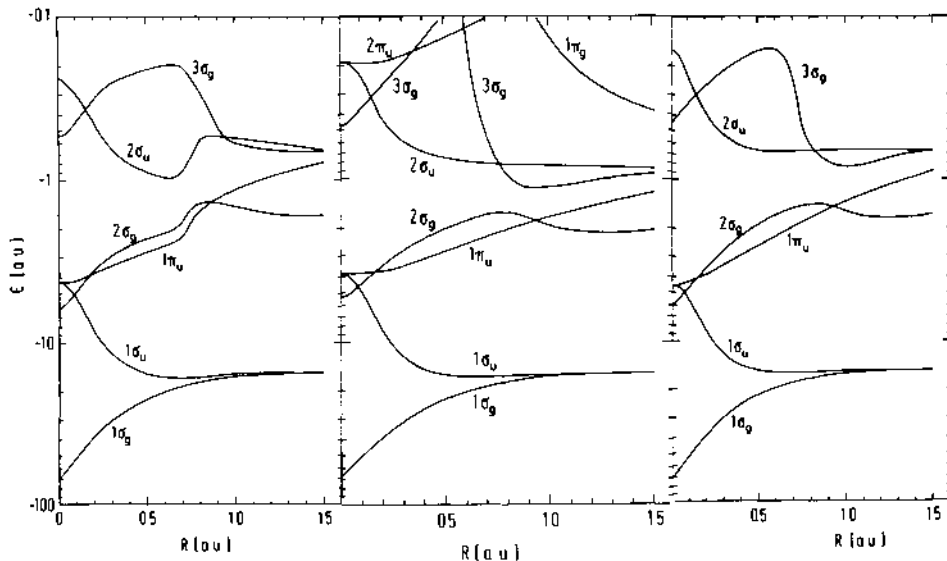


Fig. 3. Correlation diagrams for the N-N system (from left to right: HF-result, results of the variable screening model (Phys. Rev. A11, 1973, 1975)), result on the basis of the TFDW approach.

#### RELATIVISTIC DENSITY FUNCTIONAL THEORY

In this section we first discuss the relativistic TF (RTF) model which dates back to 1932<sup>10</sup>. In addition to this lowest order we then derive a second order gradient correction of the kinetic energy density within the Foldy Wouthuysen (FW) approximation. The FWTFDW model turns out to give satisfactory results for weakly relativistic systems up to  $Z \approx 90$ . Finally a fully relativistic gradient expansion on the basis of the Dirac equation is discussed.

The RTF density is calculated in analogy to the nonrelativistic TF density (10) from

$$\rho_O(\underline{r}) = \frac{2}{(2\pi)^3} \int d^3k \theta(E_F(\underline{r}) - E_K) \quad (27)$$

$$\text{with } E_K = [k^2 + m^2]^{1/2} \quad (28)$$

$$\text{and } E_F = [k_F^2 + m^2]^{1/2}. \quad (29)$$

$$\text{This yields } \rho_O(\underline{r}) = \frac{1}{3\pi^2} k_F^3 \quad (30)$$

The kinetic energy density has to be calculated with the relativistic formula

$$\begin{aligned}\tau_o(\underline{r}) &= \frac{2}{(2\pi)^3} \int d^3k \theta(E_F(\underline{r}) - E_K) E_K - m\rho_o(\underline{r}) \\ &= \frac{m^4}{\pi^2} \left( \frac{1}{8} [x(2x^2+1) \sqrt{x^2+1} - \text{Arsh } x] - \frac{1}{3} x^3 \right) \quad (31)\end{aligned}$$

with  $x = K_F/m$ .

The elimination of  $K_F$  corresponds to the replacement

$$x = \frac{(3\pi^2)^{1/3}}{m} \rho_o(\underline{r}).$$

The variational equation (25) corresponds to a functional relation between the total electrostatic potential and the density. If one inserts this relation into Poissons equation one obtains for neutral systems

$$\Delta V_{\text{rel}} = \sigma \cdot (-V_{\text{rel}})^{3/2} \left[ 1 - \frac{V_{\text{rel}}}{2m} \right]^{3/2}, \quad \sigma = -\frac{8\sqrt{2}}{3\pi} e^2 m^{3/2}. \quad (32)$$

This nonlinear differential equation for the determination of  $V$  (and hence  $\rho$ ) is to be compared with the corresponding well known nonrelativistic TF equation

$$\Delta V = \sigma \cdot (-V)^{3/2}. \quad (33)$$

The relativistic correction  $\left[ 1 - \frac{V_{\text{rel}}}{2m} \right]^{3/2}$  shows some reasonable features: It increases with increasing  $Z$  and it contributes particularly for small values of  $r$ , i.e. for the innermost electrons. On the other hand, however, it overestimates the relativistic effects: Since the right hand sides of equation (32) and (33) are proportional to the density we obtain in the vicinity of the atomic nucleus

$$\begin{aligned}\rho_{\text{TF}} &\sim r^{-3/2} \\ \rho_{\text{RTF}} &\sim r^{-3}\end{aligned}$$

i.e. the RTF density is not integrable. It can in fact be shown that the RTF equation (32) does not even possess solutions for pointlike nuclear boundary conditions.<sup>11</sup>

There is a very hesitating history of attempts to correct this deficiency: The simplest remedy already suggested by Jensen in 1933<sup>12</sup> is the introduction of an extended nucleus instead of the point source. The problem is however: The nuclear dimensions are so small on the atomic scale that the incorrect  $1/r^3$  behavior sets in before the cut-off procedure takes over.

Therefore, Ashby and Holzman<sup>13</sup> introduced a hybrid model by using simple relativistic K-shell orbitals to describe the inner part of the density distribution and matched the TF density at a distance  $r_0$  from the point charge. As a condition to determine the point  $r_0$  they required the kinetic energy functional to be continuous at this point. It turns out that  $r_0$  moves inward with increasing  $Z$  so that no solution could be found for  $Z > 87$ .

A look at the nonrelativistic case suggests that the deficiency can be remedied by considering the gradient terms. The first suggestion along these lines is due to Rudkjøbing<sup>14</sup> who proposed an old version of the once iterated Dirac equation as a starting point. In this equation the spin orbit term is made explicit and contributes to the density of states. The resulting correction for the variational equation is then

$$\Delta v_{\text{rel}} = -\frac{4e^2}{3\pi} \left[ (m - v_{\text{rel}})^2 - m^2 - \left( r \frac{dv_{\text{rel}}}{dr} \right)^2 \right]^{3/2} . \quad (34)$$

If the spin orbit term is neglected, this equation reduces to the RTF equation (32). In the limit  $r \rightarrow 0$  the right hand side (i.e. the density) is proportional to  $r^{-3/2}$ . Unfortunately the solution does not only behave like the nonrelativistic solution at the origin, it agrees with the classical solution practically completely. The correction goes in the wrong direction.

We have undertaken a systematic approach to provide a gradient expansion on the basis of the FW-method<sup>15</sup>. The basic idea is: (a) to represent the relativistic density operator by

$$\hat{\rho} = \theta(\epsilon_F - [\hat{\alpha} \cdot \hat{p} + \hat{\beta}m + \hat{v}_{\text{eff}}])$$

which is the equivalent of our starting point in the nonrelativistic case (eq.(7)) and (b) to approximate the Dirac operator by its FW-representation to second order in  $(p/m)$

$$\hat{h}_{\text{eff}} = \beta [p^2 + m^2]^{1/2} + \hat{v}_{\text{eff}} + \frac{1}{4m^2} \hat{\alpha} \cdot (\hat{\nabla} v_{\text{eff}}) \hat{x} \hat{p} + \frac{1}{8m^2} \Delta v_{\text{eff}} .$$

The gradient expansion can then be set up in complete analogy to the nonrelativistic case. The final result for the kinetic energy density looks as follows

$$\tau_{FW}(\underline{r}) = \tau_o(\underline{r}) + \frac{1}{72m} \frac{(\nabla \rho)^2}{\rho(\underline{r})} B_{FW}(x)$$

$$\text{with } B_{FW}(x) = \frac{1}{\sqrt{1+x^2}} \left[ 1 + \frac{x^4}{2} - \frac{x^2}{1+x^2} + \frac{2}{3} \frac{x^4}{(1+x^2)^2} \right]$$

$$\text{and } x = \frac{(3\pi^2)^{1/3}}{m} \rho(\underline{r})^{1/3} .$$

$\tau_o(\underline{r})$  is given by the lowest order expression (31). For small densities  $x \ll 1$  one finds  $B(x) \rightarrow 1$  which is the proper nonrelativistic limit. Some results obtained on the basis of this density functional are given in Table 2. The calculations are for neutral atomic systems. One notices (for the corrected coefficient  $c_2 = 1.8/72m$ ) that the agreement with Dirac Fock results is not as good as in the nonrelativistic case for light to medium atoms, but still acceptable as a first attempt. For heavier systems ( $Z \gtrsim 90$ ) the deviation increases fairly rapidly, i.e. the weakly relativistic approximation inherent in the second order FW representation is not sufficient. Thus, we finally have to face a fully relativistic treatment.

As in the nonrelativistic case, the starting point is the total groundstate energy of the system within the single particle approximation (i.e. we neglect the correlation energy):

$$\begin{aligned} E_o^{(\text{rel})} = & \text{tr} \left[ \int d^3r \int d^3r' \delta(\underline{r}-\underline{r}') (-i\alpha \cdot \nabla_{\underline{r}} + \beta m) \rho(\underline{r}, \underline{r}') \right. \\ & + \int d^3r \rho(\underline{r}, \underline{r}) v_n(\underline{r}) \\ & + \frac{1}{2} \int d^3r \int d^3r' \rho(\underline{r}, \underline{r}) v(\underline{r}, \underline{r}') \rho(\underline{r}', \underline{r}') \\ & \left. - \frac{1}{2} \int d^3r \int d^3r' \rho(\underline{r}, \underline{r}') v(\underline{r}, \underline{r}') \rho(\underline{r}', \underline{r}) \right] . \end{aligned} \quad (35)$$

Again,  $v_n(\underline{r})$  is the nuclear Coulomb potential. The particle-particle interaction is given by the series

$$v(\underline{r}, \underline{r}') = \frac{e^2}{|\underline{r}-\underline{r}'|} - \frac{e^2}{2} \left[ \frac{\underline{\alpha} \cdot \underline{\alpha}'}{|\underline{r}-\underline{r}'|} + \frac{\underline{\alpha} \cdot (\underline{r}-\underline{r}') \underline{\alpha}' \cdot (\underline{r}-\underline{r}')}{|\underline{r}-\underline{r}'|^3} \right] + \dots$$

In the following we restrict ourselves to the lowest order, i.e. the nonrelativistic Coulomb interaction. The inclusion of higher orders, as e.g. the Breit interaction, does not pose principle difficulties.

Table 2. Atomic groundstate energies in a.u.: Comparison of DF-results with results obtained by the density functional methods explained in the text, ((1): FW-version, (2): Simplified fully relativistic version).

$Z$	$-E_{HF}$	$-E_{DF}$	$-E_{RTFDW}^{(1)}$	$-E_{RTFDW}^{(2)}$
10	128.55	128.67	129.60	128.53
36	2752.1	2787.3	2862.0	2736.0
70	18392	14052	14202	13608
92	25664	28011	27363	26739
110	39225	44950	42012	42071
120	48203	57387	51773	52742

The density matrix

$$\rho(\underline{r}, \underline{r}') = \sum_{\substack{\text{occ. bound} \\ \text{states}}} \Phi_V(\underline{r}) \Phi_V(\underline{r}')^+ \quad (36)$$

consists of the above sum over the occupied bound states of the corresponding Dirac Fock variational equation

$$\hat{h}_{\text{eff}} \Phi_V(\underline{r}) = \epsilon_V \Phi_V(\underline{r}) \quad , \quad \hat{h}_{\text{eff}} = \hat{\alpha} \cdot \hat{\underline{p}} + \hat{\beta} m + \hat{v}_{\text{eff}} \quad (37)$$

It should be noted that each element  $\rho(\underline{r}, \underline{r}')$  of the density matrix (36), by definition, is a  $4 \times 4$  matrix. Therefore, the ground-state energy (35) as well as the single particle density are obtained by taking the trace

$$\rho(\underline{r}) = \text{tr } \rho(\underline{r}, \underline{r}) \quad . \quad (38)$$

In order to approximate the kinetic energy and the exchange energy by functionals of the one particle density (38) alone, we have to represent the density matrix in terms of an appropriately chosen density operator. The question is how this operator looks like in the relativistic case. We shall first consider the nonrelativistic form

$$\hat{\rho} = \theta(\epsilon_F - \hat{h}_{\text{eff}}) = \theta(\hat{E}_F - \hat{t}) \quad (39)$$

$$\text{with } \hat{E}_F = \epsilon_F - \hat{v}_{\text{eff}} \quad (40)$$

$$\hat{t} = \hat{\alpha} \cdot \hat{\underline{p}} + \hat{\beta} m \quad . \quad (41)$$

The following investigation will reveal that this ansatz is not yet the complete answer.

We make use of the completeness of the Dirac spinors

$$1 = \sum_{ST} \int d^3k \left| \underline{k}_{ST} \right\rangle \left\langle \underline{k}_{ST} \right| \quad (42)$$

whose standard representation in configuration space is given by

$$\left\langle \underline{r} \right| \left| \underline{k}_{ST} \right\rangle = \frac{1}{(2\pi)^{3/2}} u_s^T(\underline{k}) e^{i \underline{k} \cdot \underline{r}}$$

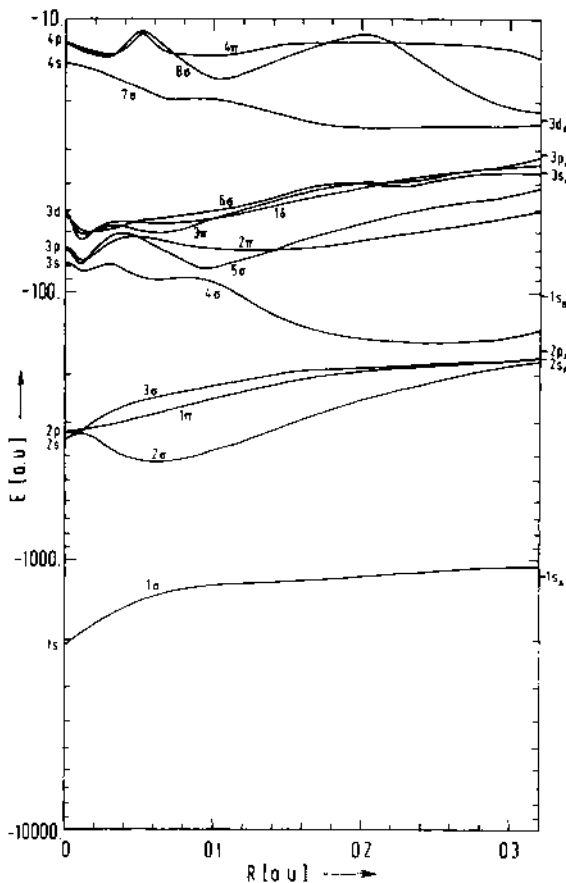


Fig. 4. Correlation diagram for the 70 electron system I-Cl.

$$\text{with } u_s^{(+)}(\underline{k}) = \left[ \frac{E_k + m}{2E_k} \right]^{1/2} \begin{pmatrix} \chi_s \\ \frac{\sigma \cdot \underline{k}}{E_k + m} \chi_s \end{pmatrix}$$

$$\text{and } u_s^{(-)}(\underline{k}) = \left[ \frac{E_k + m}{2E_k} \right]^{1/2} \begin{pmatrix} \frac{-\sigma \cdot \underline{k}}{E_k + m} \chi_s \\ \chi_s \end{pmatrix}$$

The index  $s=\pm 1/2$  denotes the spin, while  $T=(+), (-)$  classifies positive and negative energy solutions.

The gradient expansion of the density matrix is then obtained from

$$\begin{aligned} \rho(\underline{r}, \underline{r}') &= \langle \underline{r} | \theta(E_F - \hat{t}) | \underline{r}' \rangle \\ &= \sum_{ST} \int d^3k \langle \underline{r} | \theta(E_F - \hat{t}) | \underline{k} s T \rangle \langle \underline{k} s T | \underline{r}' \rangle \end{aligned}$$

by use of the mathematical theorem (19). If only the lowest order

$$\theta(E_F(\underline{r}) - \hat{t}) | \underline{k} s T \rangle = \theta(E_F(\underline{r}) \pm E_k) | \underline{k} s T \rangle$$

(" - " for  $T = (+)$ , "+ " for  $T = (-)$ )

is taken into account one obtains for the density matrix

$$\begin{aligned} \rho_O(\underline{r}, \underline{r}') &= \int d^3k \theta(E_F(\underline{r}) - E_k) \sum_s \langle \underline{r} | \underline{k} s (+) \rangle \langle \underline{k} s (+) | \underline{r}' \rangle \\ &\quad + \int d^3k \theta(E_F(\underline{r}) + E_k) \sum_s \langle \underline{r} | \underline{k} s (-) \rangle \langle \underline{k} s (-) | \underline{r}' \rangle \\ &= \int_{K_F} \frac{d^3k}{(2\pi)^3} e^{i \underline{k} \cdot (\underline{r} - \underline{r}')} M_O^{(+)}(\underline{k}) \\ &\quad + \int_{\infty} \frac{d^3k}{(2\pi)^3} e^{i \underline{k} \cdot (\underline{r} - \underline{r}')} M_O^{(-)}(\underline{k}) \end{aligned} \quad (43)$$

$$\text{with } M_0^{(\pm)}(\underline{k}) = \frac{1}{2E_{\underline{k}}} \begin{pmatrix} (E_{\underline{k}}^{\pm m}) & \pm \underline{\sigma} \cdot \underline{k} \\ \pm \underline{\sigma} \cdot \underline{k} & (E_{\underline{k}}^{\mp m}) \end{pmatrix} \quad (44)$$

In the case of the positive energy solutions the step function yields an upper boundary for the integral (namely the Fermi momentum  $K_F$ , defined in eq. (29) while for the negative energy solutions the step function retains the value 1 everywhere (since both  $E_F$  and  $E_K$  are positive quantities). Therefore, the second term in (43) which arises from the negative energy solutions is divergent. The divergence somehow originates from the integration over the whole filled Dirac sea. So, at first glance, one might think that the correct lowest order density matrix is obtained just by dropping the divergent term. The remaining (convergent) term in (43) leads to the classical RTF model discussed above (eqs. (30) to (32)). Unfortunately, it is impossible to proceed in the same fashion for the higher orders of the expansion (19). The series consists of well defined terms but on the whole it is divergent. So one does not know which terms have to be dropped and which have to be kept.

In order to overcome this difficulty we take another look at the origin of the divergence. The precise reason, sketched on Fig. 5, is the following: In the nonrelativistic case the spectrum of the Hamiltonian  $\hat{h}_{\text{eff}}$  consists of positive continuum states and bound states from which the occupied ones are extracted by means of the step function. In the relativistic case, i.e. for the Dirac Hamiltonian, the discrete levels cannot be arbitrarily strongly bound. Instead, we have negative continuum states, and the completeness relation of the Dirac Fock single particle basis contains both the positive and the negative continuum states as well as the bound states. Therefore, the nonrelativistic form of the density operator yields a wrong density matrix. In comparison to the correct density matrix (36) it consists not only of the occupied bound states but contains the negative continuum states in addition:

$$\begin{aligned} \rho(\underline{r}, \underline{r}') &= \langle \underline{r} | \theta(\epsilon_F - \hat{h}_{\text{eff}}) | \underline{r}' \rangle \\ &= \int_V \langle \underline{r} | \theta(\epsilon_F - \epsilon_V) | v \rangle \langle v | \underline{r}' \rangle \\ &= \sum_{\text{occ. bound states}} \phi_V(\underline{r}) \phi_V(\underline{r}')^+ + \int_V \phi_V(\underline{r}) \phi_V(\underline{r}')^+ . \end{aligned}$$

This additional term is the origin of the divergence.

From the above consideration it is evident that the correct relativistic density operator must be constructed in such a way

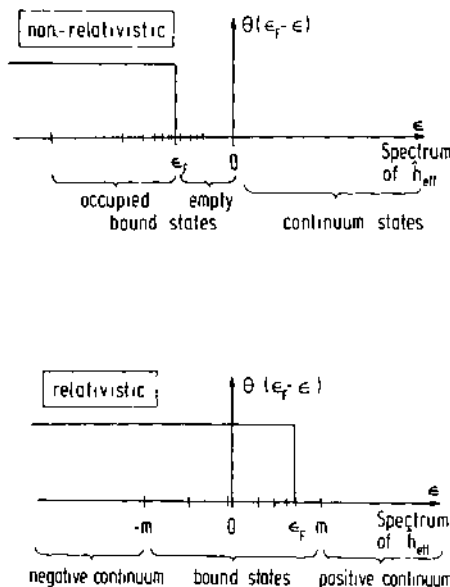


Fig. 5. Schematic representation of the occupation numbers for an effective single particle problem based on the Schrödinger equation and the (divergent) relativistic extension.

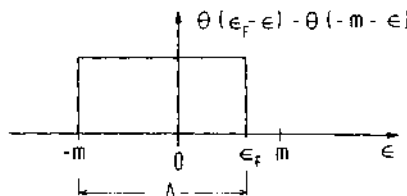


Fig. 6. Schematic representation of the occupation numbers for the relativistic problem.

that only a window of the occupied bound states is extracted from the whole spectrum of  $\hat{h}_{\text{eff}}$ . This aim is most easily achieved by the difference of two step functions

$$\hat{\rho}_{\text{rel}} = \theta(\epsilon_F - \hat{h}_{\text{eff}}) - \theta(-m - \hat{h}_{\text{eff}}) . \quad (45)$$

This function is shown in Fig. 6. As in the nonrelativistic case we summarize the Fermi energy  $\epsilon_F$  and the effective potential in a "Fermi energy operator"  $\hat{E}_F$ . A similar quantity  $\hat{G}_F$  arises from the second step function

$$\hat{\rho}_{\text{rel}} = \theta(\hat{E}_F - \hat{t}) - \theta(\hat{G}_F - \hat{t})$$

$$\text{with } \hat{E}_F = \epsilon_F - \hat{v}_{\text{eff}}$$

$$\hat{G}_F = -m - \hat{v}_{\text{eff}} .$$

$\hat{t}$  is still the Dirac operator (41). It should be pointed out that the difference between the operators  $\hat{E}_F$  and  $\hat{G}_F$  is a constant  $\Delta$  (namely the width of the window) which amounts to approximately  $2m$ .

$$\hat{E}_F - \hat{G}_F = \epsilon_F + m =: \Delta (\approx 2m) \quad (46)$$

The relativistic gradient expansion of the density matrix is then obtained by insertion of the complete system of free Dirac spinors (42)

$$\begin{aligned} \rho(\underline{r}, \underline{r}') &= \langle \underline{r} | \hat{\rho}_{\text{rel}} | \underline{r}' \rangle \\ &= \sum_{sT} \int d^3k \langle \underline{r} | \theta(\hat{E}_F(\underline{r}) - \hat{t}) | \underline{k} sT \rangle \langle \underline{k} sT | \underline{r}' \rangle \\ &\quad - \sum_{sT} \int d^3k \langle \underline{r} | \theta(\hat{G}_F(\underline{r}) - \hat{t}) | \underline{k} sT \rangle \langle \underline{k} sT | \underline{r}' \rangle . \end{aligned} \quad (47)$$

If the mathematical theorem (19) is applied twice in the last expression we obtain two formally identical series, one depending on  $\hat{E}_F$ , the other depending on  $\hat{G}_F$ . It turns out that all divergent contributions cancel each other. This is most easily demonstrated for the lowest order where we obtain:

$$\rho_o(\underline{r}, \underline{r}') = \int \frac{d^3k}{(2\pi)^3} \theta(E_F(\underline{r}) - E_K) e^{i\underline{k} \cdot (\underline{r} - \underline{r}')} M_o^{(+)}(\underline{k})$$

$$\begin{aligned}
 & + \int \frac{d^3 k}{(2\pi)^3} \theta(E_F(\underline{r}) + E_K) e^{i \underline{k} \cdot (\underline{r} - \underline{r}')} M_O^{(-)}(\underline{k}) \\
 & - \int \frac{d^3 k}{(2\pi)^3} \theta(G_F(\underline{r}) - E_K) e^{i \underline{k} \cdot (\underline{r} - \underline{r}')} M_O^{(+)}(\underline{k}) \\
 & - \int \frac{d^3 k}{(2\pi)^3} \theta(G_F(\underline{r}) + E_K) e^{i \underline{k} \cdot (\underline{r} - \underline{r}')} M_O^{(-)}(\underline{k}) . \quad (48)
 \end{aligned}$$

The matrices  $M_O^{(\pm)}(\underline{k})$  are given by (44). The second and the fourth term of (48), both divergent, cancel each other. The first term corresponds to the classical RTF model while the third one gives an additional contribution if  $G_F > m$ . In terms of the effective potential this inequality means

$$v_{\text{eff}}(\underline{r}) < -2m . \quad (49)$$

Thus, we obtain a correction to the classical RTF model in the region where the potential is more attractive than  $-2m$ .

For the density we obtain

$$\rho_O(\underline{r}) = \rho_1(\underline{r}) - \rho_2(\underline{r}) \quad (50)$$

$$\text{with } \rho_1(\underline{r}) = \frac{1}{3\pi^2} K_F^3 , \quad K_F(v_{\text{eff}}) = \left[ \frac{E_F^2 - m^2}{v_{\text{eff}}} \right]^{1/2} = \left[ (\epsilon_F - v_{\text{eff}})^2 - m^2 \right]^{1/2} \quad (51)$$

$$\text{and } \rho_2(\underline{r}) = \frac{1}{3\pi^2} q_F^3 , \quad q_F(v_{\text{eff}}) = \begin{cases} \left[ \frac{G_F^2 - m^2}{v_{\text{eff}}} \right]^{1/2} = \left[ (-m - v_{\text{eff}})^2 - m^2 \right]^{1/2} \\ 0 \quad \text{if } v_{\text{eff}} > -2m \end{cases} \quad (52)$$

This means, we have a weakly relativistic domain where the density equals the classical contribution  $\rho_1$  and, in addition, we have a highly relativistic domain, where the "correction"  $\rho_2$  comes into the game. This is illustrated in Figs. 7a, b where the density is shown as a function of the effective potential and as a function of the distance  $r$  from the nuclear point charge.

For pointlike nuclei the density is still divergent. But, in contrast to the classical RTF-model, the density is integrable: In the vicinity of the nucleus we obtain

$$\rho_O(r) \underset{v_{\text{eff}} \ll -2m}{\propto} (v_{\text{eff}})^2 \propto \left( \frac{Z}{r} \right)^2 .$$

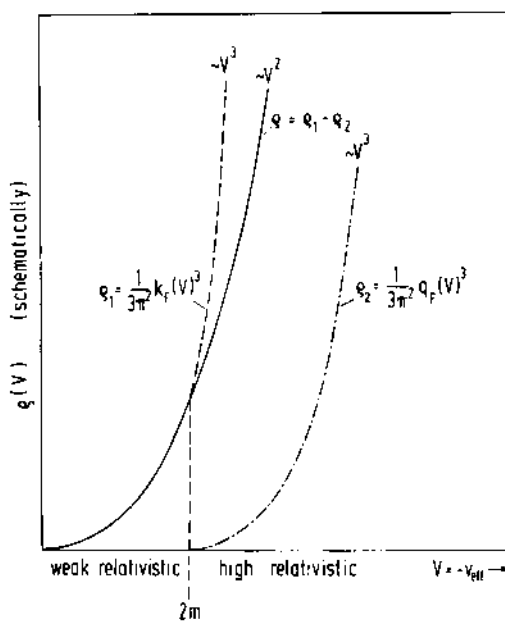


Fig. 7a. The relativistic TF density for an atomic system as a function of the effective potential.

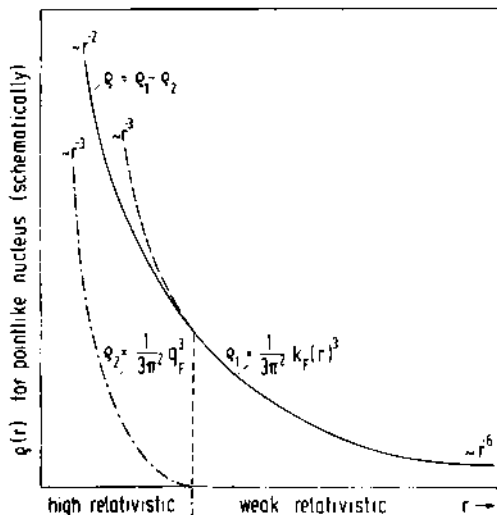


Fig. 7b. As in Fig. 7a as a function of the distance from a point charge.

It should be noted that the density  $\rho_2$  can be expressed as a simple function of  $\rho_1$  by means of the fundamental equation  $G_F = E_F - \Delta$  :

$$\begin{aligned}\rho_2 &= \frac{1}{3\pi^2} q_F^3 = \frac{1}{3\pi^2} \left[ G_F^2 - m^2 \right]^{3/2} = \frac{1}{3\pi^2} \left[ (E_F - \Delta)^2 - m^2 \right]^{3/2} \\ &= \frac{1}{3\pi^2} \left[ \left( \left[ (3\pi^2 \rho_1)^{2/3} + m^2 \right]^{1/2} - \Delta \right)^2 - m^2 \right]^{3/2}.\end{aligned}$$

For the kinetic energy density we obtain twice the classical RTF-expression (31):

$$\tau_0(\underline{r}) = \tau_0(x) + \tau_0(y) \quad (53)$$

where the first term depends on  $\rho_1$  via

$$x := K_F/m = (3\pi^2 \rho_1)^{1/3} / m \quad (54)$$

while the second term depends on  $\rho_2$  via

$$y := q_F/m = (3\pi^2 \rho_2)^{1/3} / m. \quad (55)$$

The calculation of the exchange energy density is more complicated because a product of two density matrices and an additional integration have to be carried through (see eq. (4)). The traditional relativistic exchange energy density (to lowest order of the gradient expansion) which corresponds to the RTF kinetic energy density (31) has first been calculated by Jancovici in 1962<sup>16</sup>. He derived the following expression

$$\begin{aligned}e_x^{(0)}(\underline{r}) &= -\frac{e^2 m^4}{(2\pi)^3} \cdot \left[ x^4 + \frac{2}{3} x^2 E_x^2 - \frac{2}{3} E_x^4 \ln(E_x^2) \right. \\ &\quad \left. + \frac{4}{3} x^3 E_x \text{Arsh } x - (xE_x - \text{Arsh } x)^2 \right] \quad (56)\end{aligned}$$

$$\text{with } E_x = \sqrt{x^2 + 1}.$$

Due to the high relativistic correction  $\rho_2$  we now obtain the following extension

$$e_x^{(0)}(\underline{r}) = -\frac{e^2 m^4}{(2\pi)^3} \cdot \left[ (x-y)(x^3 - y^3) + \frac{2}{3} (xE_x - yE_y)^2 \right]$$

$$\begin{aligned}
 & -\frac{2}{3} E_x^4 \ln(E_x^2) + \frac{2}{3} (E_x^4 + E_y^4) \ln \left( \frac{E_x E_y + 1 + xy}{E_x E_y + 1 - xy} \right) - \frac{2}{3} E_y^4 \ln(E_y^2) \\
 & - \left[ (x^2 - y^2)^2 + \frac{1}{6} (E_x - E_y)^4 \right] \ln \left( \frac{x-y}{x+y} \right) \\
 & + \frac{4}{3} (x^3 E_x - y^3 E_y) (\text{Arsh } x - \text{Arsh } y) - \left[ [x E_x - y E_y] - [\text{Arsh } x - \text{Arsh } y] \right]^2 \quad (57)
 \end{aligned}$$

For  $y=0$  this expression reduces to Jancovici's result. An important application of this expression should be the use of the derivative

$$v_x = \frac{\partial e_x^{(0)}}{\partial p_0}$$

as an effective exchange potential in relativistic HF-Slater-like calculations.

Let us finally discuss the higher order terms of the gradient expansion. These are obtained by application of the mathematical theorem (19) to equation (47). This yields for the density

$$\begin{aligned}
 \rho(\underline{r}) = & \sum_{sT} \int d^3 k \sum_{n=0}^{\infty} \theta^{(n)} (E_F \pm E_K) \langle \underline{k} sT | \underline{r} \rangle \langle \underline{r} | \hat{\mathcal{O}}_n | \underline{k} sT \rangle \\
 & - \sum_{sT} \int d^3 k \sum_{n=0}^{\infty} \theta^{(n)} (G_F \pm E_K) \langle \underline{k} sT | \underline{r} \rangle \langle \underline{r} | \hat{\mathcal{O}}_n | \underline{k} sT \rangle .
 \end{aligned}$$

The operators  $\hat{\mathcal{O}}_n$  are calculated from (18) by insertion of the Dirac operator

$$\hat{a} = -\hat{t} = -\underline{a} \cdot \hat{\underline{p}} - \beta \mathbf{m} .$$

As before, we evaluate the operators up to second order gradients of  $E_F(\underline{r})$  and  $G_F(\underline{r})$ . A detailed analysis shows that, in contrast to the nonrelativistic case, each operator  $\hat{\mathcal{O}}_n$  contains first and second order gradient terms. Therefore, the series over  $n$  have to be resummed. This problem is solved by use of the Taylor expansion of the step function

$$\theta(x+a) = \sum_{n=0}^{\infty} \frac{1}{n!} \theta^{(n)} (x-a) (2a)^n$$

which is a well defined object in the theory of distributions<sup>17</sup>. The result at the semiclassical stage looks as follows:

$$\rho(\underline{r}) = \rho_1 [E_F] - \rho_2 [G_F] \quad (58)$$

$$\text{with } \rho_1 [E_F] = \frac{1}{3\pi^2} (K_F^3 + f(E_F)) (\nabla E_F)^2 + g(E_F) \Delta E_F \quad (59)$$

$$\rho_2 [G_F] = \frac{1}{3\pi^2} (G_F^3 + f(G_F)) (\nabla G_F)^2 + g(G_F) \Delta G_F \quad (60)$$

$$\text{and } f(E_F) = -\frac{1}{8} \frac{E_F^2}{K_F^3} + \frac{3}{8} \frac{1}{K_F}$$

$$g(E_F) = \frac{1}{4} \frac{E_F}{K_F} + \frac{1}{2} \operatorname{Arsh} \left( \frac{K_F}{m} \right) \quad .$$

For the kinetic energy density one obtains

$$\tau(\underline{r}) = \tau_O(E_F) + \frac{1}{3\pi^2} (h(E_F) (\nabla E_F)^2 + k(E_F) \Delta E_F)$$

$$- \tau_O(G_F) - \frac{1}{3\pi^2} (h(G_F) (\nabla G_F)^2 + k(G_F) \Delta G_F)$$

$$\text{with } h(E_F) = \frac{1}{4} \frac{E_F}{K_F} - \frac{1}{8} \frac{E_F^3}{K_F^3} - \frac{1}{4} \operatorname{Arsh} \left( \frac{K_F}{m} \right)$$

$$k(E_F) = \frac{1}{4} \frac{E_F^2}{K_F} + \frac{1}{4} \frac{E_F}{K_F} \quad .$$

In the final step we invert the functionals  $\rho_1 [E_F]$  and  $\rho_2 [G_F]$  and eliminate in  $\tau(\underline{r})$   $E_F$  in favour of  $\rho_1$  and  $G_F$  in favour of  $\rho_2$ . The final result is

$$\tau(\underline{r}) = \tau_O(x) + \frac{1}{72m} B(x) \frac{(\nabla \rho_1)^2}{\rho_1} - \tau_O(y) - \frac{1}{72m} B(y) \frac{(\nabla \rho_2)^2}{\rho_2} \quad (61)$$

$$\text{with } B(z) = \frac{1}{\sqrt{1+z^2}} + \frac{2z}{1+z^2} \operatorname{Arsh} z \quad . \quad (62)$$

The quantities  $x$  and  $y$  are given by (54) and (55).

In contrast to the lowest order,  $\rho_2$  cannot be expressed as a simple function of  $\rho_1$ . Instead we have the following differential relation

$$g[\rho_1, \rho_2] := E_F[\rho_1] - G_F[\rho_2] - \Delta = 0 \quad (63)$$

where the functionals  $E_F[\rho_1]$  and  $G_F[\rho_2]$  are the inversions (to second order) of (59) and (60).

For the total groundstate energy we thus obtain

$$E_o^{\text{rel}} = \int d^3r \tau[\rho_1, \rho_2] + \int d^3r e_x^{(o)}(\rho_1, \rho_2)$$

$$+ \int d^3r v_n(\underline{r}) [\rho_1(\underline{r}) - \rho_2(\underline{r})]$$

$$+ \frac{1}{2} \int d^3r \int d^3r' [\rho_1(\underline{r}) - \rho_2(\underline{r})] \frac{e^2}{|\underline{r} - \underline{r}'|} [\rho_1(\underline{r}) - \rho_2(\underline{r})]$$

where the functionals (61) and (57) have to be inserted for the kinetic and the exchange energy density. The corresponding variational principle looks as follows

$$\delta \left( E_o^{\text{rel}} + v_o \int d^3r (\rho_1(\underline{r}) - \rho_2(\underline{r})) + \int d^3r l(\underline{r}) g[\rho_1, \rho_2] \right) = 0 .$$

The Lagrangian multiplier  $v_o$  guarantees a fixed particle number while the subsidiary condition (63), which relates  $\rho_1$  and  $\rho_2$ , is included by means of the "Lagrangian multiplier function"  $l(\underline{r})$ .

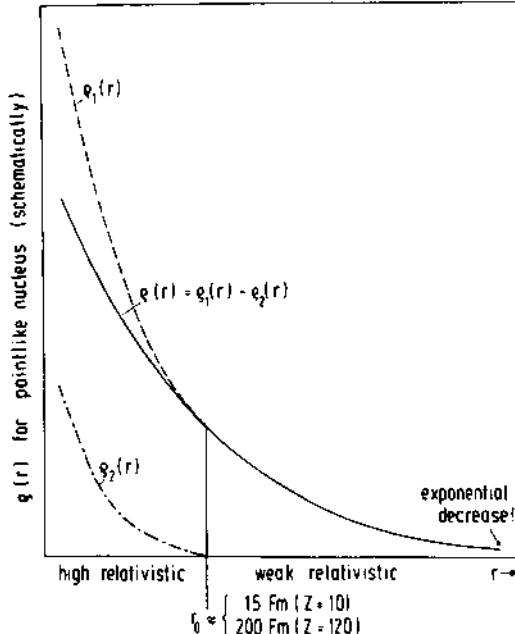


Fig. 8. Schematic representation of the solution of the RTFDW variational equations.

The corresponding variational equations have not been solved so far. A qualitative discussion of the solution is shown in Fig. 8. As before, we have a dominant contribution  $\rho_1$  to the density and a correction  $\rho_2$  in the highly relativistic region near the nucleus. In contrast to the lowest order, the density is expected to be less singular at the position of the nucleus and decreases exponentially in the asymptotic region.

Numerical results have been obtained so far only for a simplified version of the full set of equations in which we set  $\rho_2=150$ . The results for the total atomic energies are given in the last column of Table 2. It turns out that for the heaviest systems the results are already slightly better than those obtained within the second order FW-approximation. Of course, this is not yet the final answer. The numerical solution of the complete set of variational equations is envisaged as a near future problem.

Finally it should be pointed out that the fully relativistic expression (62) for the kinetic energy density is completely general. It holds for any bound relativistic many Fermion system, independent of the particular external potential and independent of the particle-particle interaction. Therefore, a variety of applications can be expected in many fields of physics.

#### REFERENCES

1. M. Horbatsch and R.M. Dreizler, *Z.Phys.* A300, 119 (1981)  
H.J. Lüddecke and R.M. Dreizler, *J.Phys.* B14, 2191 (1981)
2. E.K.U. Gross and R.M. Dreizler, *Phys.Rev.* A20, 1798 (1979)  
A. Toepfer, E.K.U. Gross and R.M. Dreizler, *Phys.Rev.* A20, 1808 (1979)  
R.M. Dreizler, E.K.U. Gross and A. Toepfer, *Phys.Lett.* A71, 49 (1979)  
A. Toepfer, E.K.U. Gross and R.M. Dreizler, *Z.Phys.* 298, 167 (1980)
3. P. Hohenberg and W. Kohn, *Phys.Rev.* 136, B864 (1964)
4. D.A. Kirzhnits, *Field Theoretical Methods in Many Body Systems*, Pergamon Press (Oxford 1967)
5. E. Wigner, *Phys.Rev.* 40, 749 (1932)
6. J.G. Kirkwood, *Phys.Rev.* 44, 31 (1933)
7. S. Ma and K. Brueckner, *Phys.Rev.* 165, 18 (1968)
8. D.J.W. Geldart and M. Rasolt, *Phys.Rev.* B13, 1477 (1976)
9. J. Desclaux, *At. Data And Nucl. Data Tab.* 12, 311 (1973)
10. M.S. Vallarta and N. Rosen, *Phys.Rev.* 41, 708 (1932)
11. E.K.U. Gross, A. Toepfer, B. Jacob and R.M. Dreizler, *Proc. XVIIth International Winter Meeting on Nuclear Physics in Bormio*, p.84, *Instituto Nazionale di Fisica Nucleare, Milano* (1979)

12. H. Jensen, Z.Phys. 82, 794 (1933)
13. N. Ashby and M.A. Holzman, Phys.Rev. A 1, 764 (1970)
14. M. Rudkjøbing, Kgl. Danske Videnskab Selskab, Mat.-Fys. Medd. 27, No 5 (1952)
15. E.K.U. Gross and R.M. Dreizler, Phys.Lett. A81, 447 (1981)
16. B. Jancovici, Nuovo Cim. 25, 428 (1962)
17. F. Constantinescu, Distributionen und ihre Anwendungen in der Physik, p. 59 ff., Teubner, Stuttgart (1974)

Experimental Tests of QED and Electroweak Theories in  
 $e^+e^-$  Annihilations at PETRA

A. Böhm

III. Phys. Institut, RWTH Aachen  
D 5100 Aachen, Germany

ABSTRACT

Experimental results from  $e^+e^-$  reactions at PETRA on tests of QED and electro-weak theories are reviewed. The leptonic reactions  $e^+e^- \rightarrow e^+e^-$ ,  $\gamma\gamma$ ,  $\mu^+\mu^-$  and  $\tau^+\tau^-$  and hadron production via  $e^+e^- \rightarrow q\bar{q}$  have been measured. The cross-sections calculated from QED agree well with the experimental values. A quantitative measure of the agreement with QED is obtained by inserting form-factors into the cross-section and deriving limits on the cut-off parameters. Assuming the validity of QED a search for weak interaction effects is performed, which results in stringent limits for the coupling constants of weak neutral current interactions.

INTRODUCTION

Tests of QED at high energies and high momentum transfers have the advantage of being sensitive to a deviation from QED in the lowest order term of the fine structure constant  $\alpha$ . Thus they are especially suited for detecting and measuring possible new interactions or for finding deviations at short distances. For example, at high energies we expect to see the effects of weak neutral current interactions, as they rise with the c. m. energy squared. An example of a deviation from QED at short distances is the modification of the cross-section which would appear if the leptons or quarks have an internal structure. High energy tests of QED complement tests at low energies<sup>1</sup> like the g-2 experiments or the measurements of the fine and hyperfine structure in atoms, which are very precise and mainly test the

higher-order calculations of QED including the renormalization procedure.

I will review<sup>2</sup> here tests of QED performed at the electron-positron storage ring PETRA at the Deutsches Elektronensynchrotron DESY in Hamburg. This storage ring<sup>3</sup> actually reaches energies and momentum transfers up to 36 GeV and it is at the moment the best instrument for high energy tests of QED. The reactions measured at PETRA are

- (1)  $e^+e^- \rightarrow e^+e^-$  Bhabha scattering,  
 (2)  $e^+e^- \rightarrow \gamma\gamma$  annihilation into two photons,

pair production of  $\mu$  and  $\tau$ -leptons

- (3)  $e^+e^- \rightarrow \mu^+\mu^-$   
 (4)  $e^+e^- \rightarrow \tau^+\tau^-$

and production of quark-antiquark pairs in the hadronic cross-section

- (5)  $e^+e^- \rightarrow q\bar{q} \rightarrow \text{hadrons}$

The measurements have been performed by five experiments named CELLO, JADE, MARK J, PLUTO and TASSO. These experiments use large and complex detectors which are constructed to measure the reactions (1) to (5) within a solid angle of nearly  $4\pi$ . For a more detailed description of the detectors and the measurements the reader is referred to the original publications of the different experiments<sup>4-8</sup>. Here only a short comment should be made about the detection of  $\tau$ -leptons.

The  $\tau$ -lepton<sup>9</sup> has a very short lifetime, which is theoretically expected to be about  $3 \cdot 10^{-13}$ s. Therefore it decays within less than a millimeter from the production point and it can only be detected by its decay products. With a branching ratio of about 17% the  $\tau$ -lepton decays leptonically as  $\tau^- \rightarrow e^-\bar{\nu}_e \nu_\tau$  or  $\tau^- \rightarrow \mu^-\bar{\nu}_\mu \nu_\tau$ , and in the remaining 66% it decays into hadrons and a  $\tau$ -neutrino. In none of the decays do we observe the full c.m. energy, owing to the undetected neutrinos. In addition the hadronic decays are characterized by a low multiplicity of charged particles, which is mainly one or three. Therefore the  $\tau$ -decays can easily be separated from hadronic events resulting from quark-antiquark production, which have a high multiplicity of charged particles of about 12 at  $\sqrt{s} = 30$  GeV and where the energy of all particles adds up to the c. m. energy. For illustration fig. 1 displays an event with  $\tau$ -pair production and fig. 2 shows the usual hadronic event with two jets.

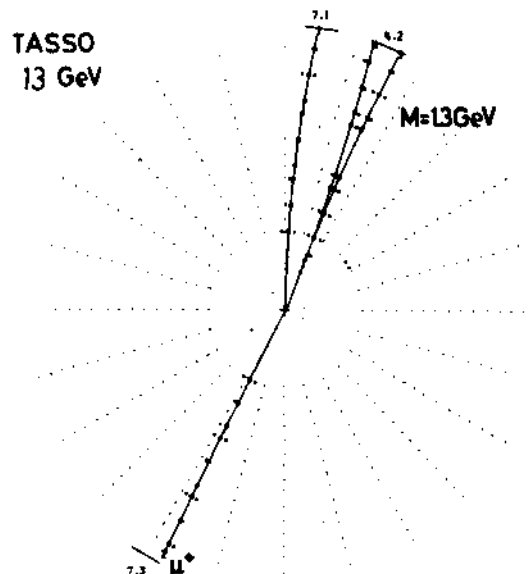


Fig. 1. A  $\tau$ -pair production event observed at  $\sqrt{s} = 13$  GeV by TASSO. Only tracks of charged particles are shown. The positive  $\tau$ -lepton decays into a muon and neutrinos, the negative  $\tau$ -lepton decays into three charged hadrons and a neutrino.

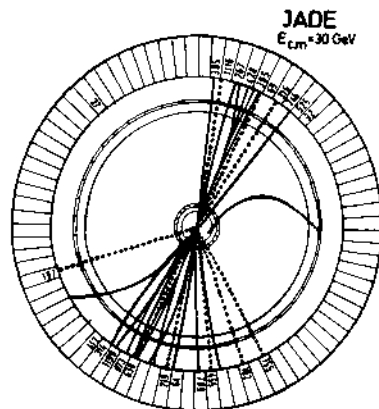


Fig. 2. A hadronic event with two jets measured at  $\sqrt{s} = 30$  GeV by JADE. The charged particle tracks are indicated by solid lines, the neutral particle tracks by dotted lines. The energy deposited in the lead-glass shower-counter is given in units of MeV.

For all reactions (1) to (5) the measured event rate  $dN/dt$  is converted into a cross-section  $\sigma$  with the relation  $dN/dt = \sigma \cdot L$ . The luminosity  $L$  is measured by the small angle Bhabha-scattering, where no deviation from QED is expected. With the insertion of stronger focussing quadrupoles, the so-called low beta scheme<sup>10</sup>, PETRA reached a luminosity of  $1.5 \cdot 10^{31} \text{ cm}^{-2}\text{s}^{-1}$  at 34 GeV and a luminosity integrated over a day up to  $700 \text{ nb}^{-1}$ . The lowest order QED cross-section for production of pointlike, singly charged particles is given by

$$\sigma_{\text{pt}} = \frac{4\pi\alpha^2}{3s} = \frac{87 \text{ nb GeV}^2}{s} .$$

For a c. m. energy squared of  $s = 1225 \text{ GeV}^2$  we therefore have a cross-section of  $\sigma_{\text{pt}} = 0.071 \text{ nb}$ , which with the above stated maximal luminosity, gives 50  $\mu$ -pair events per day. Even if this rate is reduced in longer runs and by experimental cuts and acceptance, a high statistics sample of several thousand  $\mu$ -pairs can be collected within a year. This would enable a substantial improvement in the results discussed in this article, which often suffer from a lack of statistics.

#### COMPARISON WITH THEORY

The theoretical cross-sections of QED reactions have a simple and compact form only in lowest order of  $\alpha$ . The next order calculation is included as radiative corrections. As shown in fig. 3 for the reaction  $ee \rightarrow \mu\mu$  these diagrams contain virtual radiative corrections, like vacuum polarisation or vertex corrections, and real photon bremsstrahlung. The radiative corrections<sup>11</sup> applied here take into account contributions up to order  $\alpha^3$ , which arise from an interference between the lowest order  $\alpha^2$  and the  $\alpha^4$  graphs in fig. 3.

The radiative corrections are typically 10 % to 20 %. Of this, the hadronic vacuum polarisation amounts to about 4 %. Unfortunately radiative corrections depend on the detector and the selection criteria for events. We therefore adopt the following procedure for testing QED: a measured cross-section, say  $d\sigma/d\Omega$  is corrected for radiative effects  $\delta_r$  and hadronic vacuum polarisation  $\delta_h$  and then compared to the lowest order QED cross-section  $d\sigma_0/d\Omega$

$$\frac{d\sigma}{d\Omega} (1 - \delta_r - \delta_h) = \frac{d\sigma_0}{d\Omega} (1 + \delta)$$

A departure from QED measured by the deviation  $\delta$  could have two main origins:

Firstly, leptons interact with a new force at high energies. This is predicted for the weak interaction and already observed in the SLAC polarized electron-deuterium scattering<sup>12</sup>. Thus QED is a part of a larger theory, which will finally include all

interactions. If weak interaction effects are important, we have to study  $e^+e^-$  annihilation in the framework of electroweak theories, mainly the very successful theory of Glashow, Salam and Weinberg (GSW)<sup>13</sup>.

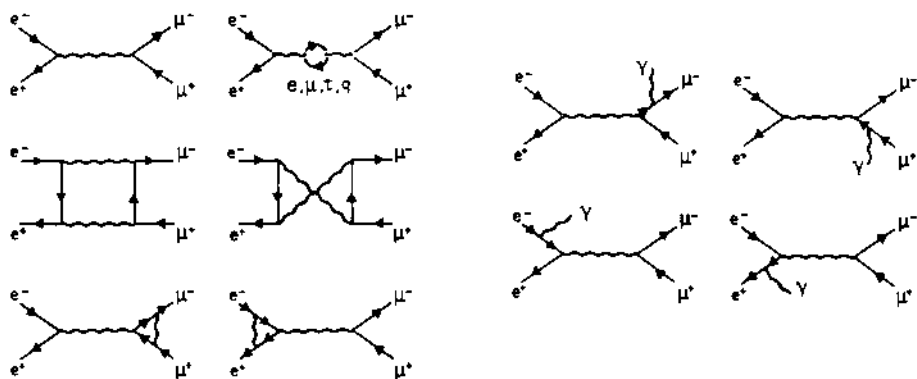


Fig. 3. Feynman graphs contributing up to order  $\alpha^4$  to the reaction  $ee \rightarrow \mu^+ \mu^-$ . The first diagram shows the lowest order  $\alpha^2$  contribution. The second diagram shows the leptonic and hadronic vacuum polarization. The remaining graphs indicate the virtual photon correction and the real photon bremsstrahlung.

Secondly, a departure from QED can be related to the fact that we are studying QED at high energies and momentum transfer, i. e. at short distances. The sources for a modification of QED could be:

- A deviation from the pointlike nature of leptons.
- The exchange of a heavy photon-like object.
- The existence of a heavy lepton  $e^*$  with quantum numbers like the electron.

These sources will modify vertices and/or propagators. Deviations from QED are generally parametrized<sup>14</sup> in terms of a form factor  $F(q^2)$

$$F(q^2) = 1 \mp \frac{q^2}{q^2 - \Lambda_{\pm}^2} \approx 1 \pm \frac{q^2}{\Lambda_{\pm}^2}$$

The first expression is used by CELLO, JADE, MARK J and TASSO, while PLUTO uses the second expression.

For a moment we will neglect the weak interaction and consider the modification of cross-sections due to formfactors. By comparing the measured data with theoretical predictions which

contain formfactors, we are able to obtain lower limits on cut-off parameters. To illustrate the significance of a cut-off parameter we neglect the relativistic definition of a formfactor and transform it with a Fourier transformation into a spatial distribution. Then we can give two interpretations of a cut-off parameter  $\Lambda$ :

- The exchange of a heavy photon modifies the photon propagator  $\frac{1}{q^2}$  to  $\frac{1}{q^2} F(q^2)$ . Within the above mentioned restriction this means a modification of the Coulomb potential  $\frac{1}{r}$  to  $\frac{1}{r} (1 - e^{-\Lambda r})$ , which can be translated into a distance  $R = \frac{1}{\Lambda}$
- If leptons are not pointlike particles, but have a finite charge radius, then the formfactor corresponds to a charge distribution  $\rho(r) \sim e^{-\Lambda r}$ , where  $R = \frac{1}{\Lambda}$  is a measure of the charge radius.

PETRA experiments limit the cut-off parameters to typically  $\Lambda \gtrsim 100$  GeV, which therefore corresponds to a distance of  $R \lesssim 2 \cdot 10^{-16}$  cm.

We now turn to the question of how formfactors modify the cross-section. Firstly fig. 4 shows the unmodified, lowest order QED cross-sections for reaction (1) to (4).

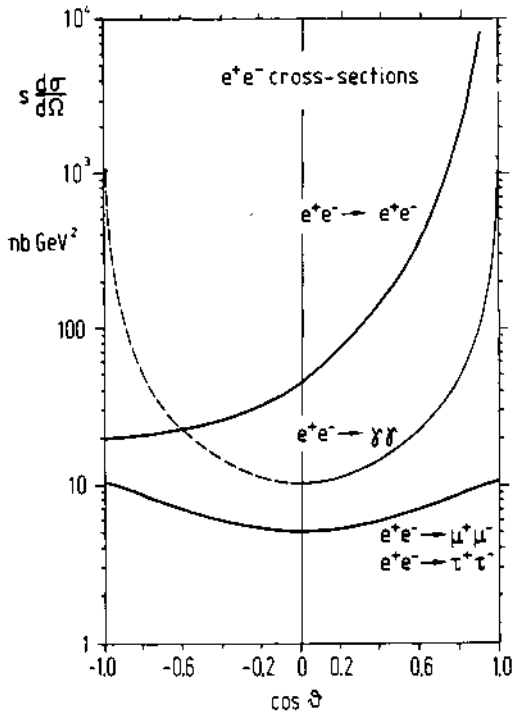


Fig. 4. Angular distribution in lowest order QED calculation for the reactions  $e^+e^- \rightarrow e^+e^-$ ,  $e^+e^- \rightarrow \gamma\gamma$  and  $e^+e^- \rightarrow \mu^+\mu^-$  or  $\tau^+\tau^-$ .

Due to spacelike contributions the reactions  $ee \rightarrow ee$  and  $ee \rightarrow \gamma\gamma$  have a very strong forward peak in the angular distributions, while the  $\mu$ -pair and  $\tau$ -pair cross-sections are rather flat. At very large scattering angles all cross-sections are of similar magnitude.

In order to demonstrate how cross-sections are modified by formfactors we will discuss  $\mu$ -pair production and Bhabha scattering in more detail. In the reaction  $e^+e^- \rightarrow \mu^+\mu^-$  only the formfactor  $F_t$  for the timelike exchange of a photon appears

$$\frac{2s}{\alpha^2} \frac{d\sigma}{d\Omega} = \frac{q^4 + q'^4}{s^2} |F_t(s)|^2 \quad (1)$$

where  $q^2 = -\frac{s}{2}(1 - \cos \theta)$  and  $q'^2 = -\frac{s}{2}(1 + \cos \theta)$  and  $\theta$  is the angle between the incoming lepton and outgoing lepton of the same charge. If we compare this cross-section with the unmodified cross-section  $\frac{d\sigma_0}{d\Omega}$ , we have a deviation  $\delta$  defined by

$$\frac{d\sigma}{d\Omega} = \frac{d\sigma_0}{d\Omega} (1 + \delta)$$

For  $\sqrt{s} = 35$  GeV and  $\Lambda_t = 100$  GeV the cross-section would change by  $\delta = \pm 25\%$ , if we use the parametrization with  $\Lambda_+$  or  $\Lambda_-$  respectively. Such large changes of the cross-section should be easily measurable.

Now we turn to the differential cross-section of Bhabha scattering. It is slightly more complicated, as we have contributions from both timelike and a spacelike exchange of a photon. The modified cross-section results in

$$\begin{aligned} \frac{2s}{\alpha^2} \frac{d\sigma}{d\Omega} = & \frac{q^4 + s^2}{q^4} |F_s(q^2)|^2 + \frac{2q'^4}{q^2 s} \operatorname{Re} (F_s(q^2) \cdot F^*(q^2)) \\ & + \frac{q'^4 + q^4}{s^2} |F_t(s)|^2 \end{aligned} \quad (2)$$

For  $\sqrt{s} = 35$  GeV and  $\Lambda_s = \Lambda_t = 100$  GeV the deviation, maximal at  $\theta = 90^\circ$ , amounts to  $\delta = \pm 12\%$ . Again such a deviation should be detectable, because the cross-section of Bhabha scattering at  $\theta = 90^\circ$  is nine times larger than the  $\mu$ -pair cross-section (fig. 4) and thus has correspondingly smaller statistical errors. To simplify the discussion and to shorten the list of results in this article I will not distinguish between timelike and spacelike formfactors and from now on set  $\Lambda_s = \Lambda_t = \Lambda$ . Fig. 5a indicates how the deviation from QED varies with  $\cos \theta$  for different cut-off parameters. The curves are calculated for an experiment like MARK J which does not measure the charge of the scattered

electron. Otherwise the curves extend to scattering angles of  $180^\circ$ , where the deviation  $\delta$  is again zero, if one uses the above listed parametrization for the formfactor and sets  $\Lambda_t$  equal to  $\Lambda_s$ .

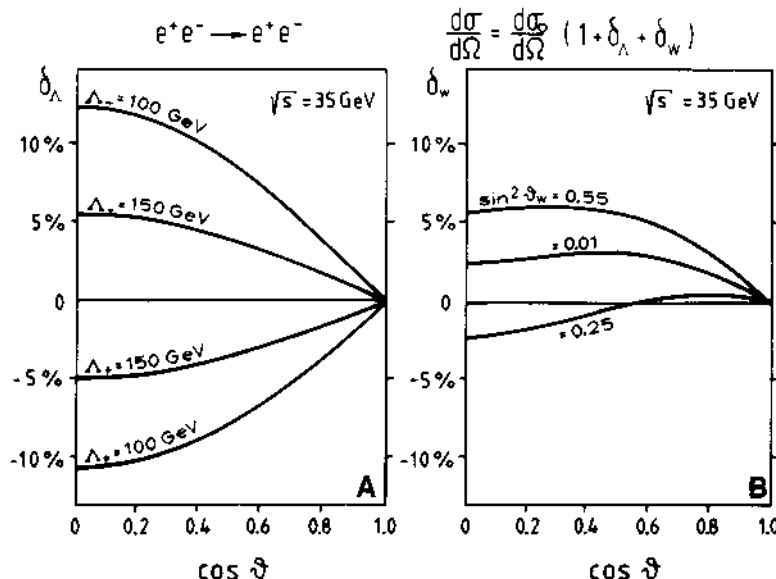


Fig. 5. (a) Relative deviation  $\delta$  of the angular distribution of Bhabha scattering for different values of the cut-off parameters  $\Lambda_+$  and  $\Lambda_-$ . It is compared in (b) with the deviations expected from the weak interaction theory (GSW) for different values of the weak mixing angle.

It is very interesting to compare the modification of Bhabha scattering due to formfactors with the deviation expected from the electroweak theory. This is done in fig. 5b for different values of the weak mixing angles  $\sin^2 \theta_w$  in the GSW-theory. Clearly deviations less than 5 % or cutoff parameters larger than 150 GeV should be evaluated including weak interaction effects. This has not yet been done consistently by all groups. But if one limits the weak mixing angle to  $\sin^2 \theta_w = 0.220 \pm 0.014$  as measured in the neutrino scattering<sup>15</sup>, then the inclusion of weak interactions does not alter significantly the limits on the cut-off parameters, which are obtained by neglecting weak interactions. This statement will soon be invalid, if more data and higher energies improve the precision and sensitivity of the experiments. We will return to weak interactions in chapter 5.

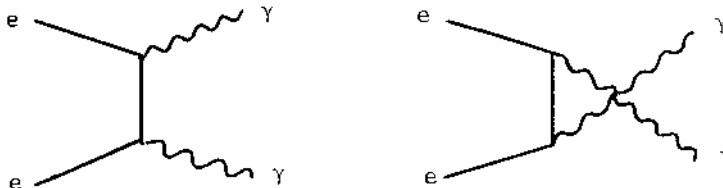
## RESULTS ON QED TESTS

A large number of results<sup>4-8</sup> on tests of QED has been obtained by the PETRA experiments CELLO, JADE, MARK J, PLUTO and TASSO. It is sometimes necessary to show only a selection or typical examples, but in the final table of cut-off parameters all results available up to June 1980 are included.

We first consider the reaction  $e^+e^- \rightarrow \gamma\gamma$ . Its angular distribution (fig. 4) has the form

$$\frac{2s}{\alpha^2} \frac{d\sigma}{d\Omega} = \frac{q'^2}{q^2} + \frac{q^2}{q'^2} \quad (3)$$

which arises from the two lowest order graphs



The reaction  $ee \rightarrow \gamma\gamma$  is a pure QED process, where effects of weak interactions can be neglected, as they appear only in higher orders. Also the effect due to vacuum polarisation is absent in this reaction. Therefore the reaction  $ee \rightarrow \gamma\gamma$  seems to be a very good candidate for testing QED. Unfortunately it is less sensitive to modifications of the electron propagator, which cancel due to current conservation. It can be shown<sup>16</sup> that a formfactor for this reaction should have the form

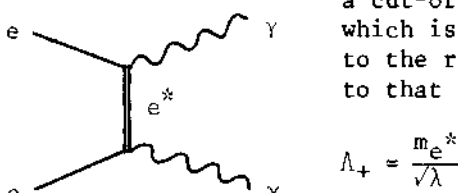
$$F(q^2) = 1 \pm \frac{q^4}{\Lambda^4}$$

Inserting this formfactor into the theoretical cross-section causes a deviation from QED, which for the same cut-off parameter as in Bhabha scattering is smaller due to the dependence on the fourth power of  $\Lambda$ . As an example for  $\Lambda = 50$  GeV we should observe a deviation from QED of 12 % at an angle of 90° and at  $\sqrt{s} = 35$  GeV.

Because the angular distribution has a sharp forward peak (fig. 4), we prefer to plot the ratio of the measured cross-section  $d\sigma/d\Omega$  to the one predicted by QED (fig. 6). The measurements agree within the errors, which are still very large due to a lack of statistics. A quantitative comparison with the QED prediction results in lower limits on cut-off parameters, which are typically about 50 GeV with 95 % confidence. The exact values of the different experiments are listed in table I at the end of this chapter. An alternative interpretation can be made

by exchanging a hypothetical heavy electron<sup>17</sup> of mass  $m_e^*$ , which should have the same quantum numbers as the electron. In this case

a cut-off parameter can be defined, which is connected to the mass  $m_e^*$  and to the relative coupling  $\lambda$  with respect to that of the electron by



Therefore, if the heavy electron has the same electromagnetic coupling constant as the electron, then the cut-off parameter gives directly a limit on the mass of a heavy electron. Again PETRA experiments limit the cut-off parameter  $\Lambda$  to typically 50 GeV with 95 % confidence.

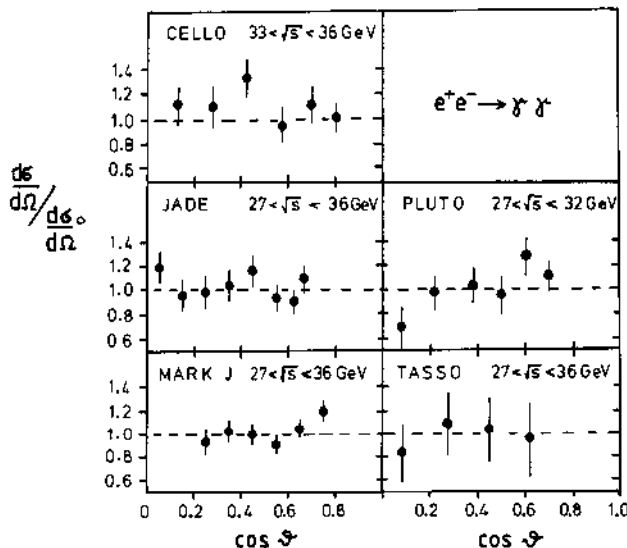


Fig. 6. Ratio of the measured cross-section for  $e^+e^- \rightarrow \gamma\gamma$  to the theoretical lowest order QED cross-section.

Now we turn to the results on Bhabha scattering. Again we prefer to display the measured angular distribution divided by the QED expectation (fig. 7).

Because the data are corrected for radiative effects, they can be directly compared to the lowest order QED cross-section, which is given by equation (2) if the formfactors are set to unity. For experiments which measure the charge of the scattered electron, the angular distribution extends to scattering angles larger than 90° and negative values of  $\cos\theta$ . Dividing the measured radiatively corrected cross-section by the theoretical QED cross-section is a very sensitive method for finding deviations. As we see no deviation within errors, we can conclude that the QED predictions are valid for the reaction  $e^+e^- \rightarrow e^+e^-$ . It even seems that the agreement slightly improves if one includes weak interaction effects as also shown in fig. 7.

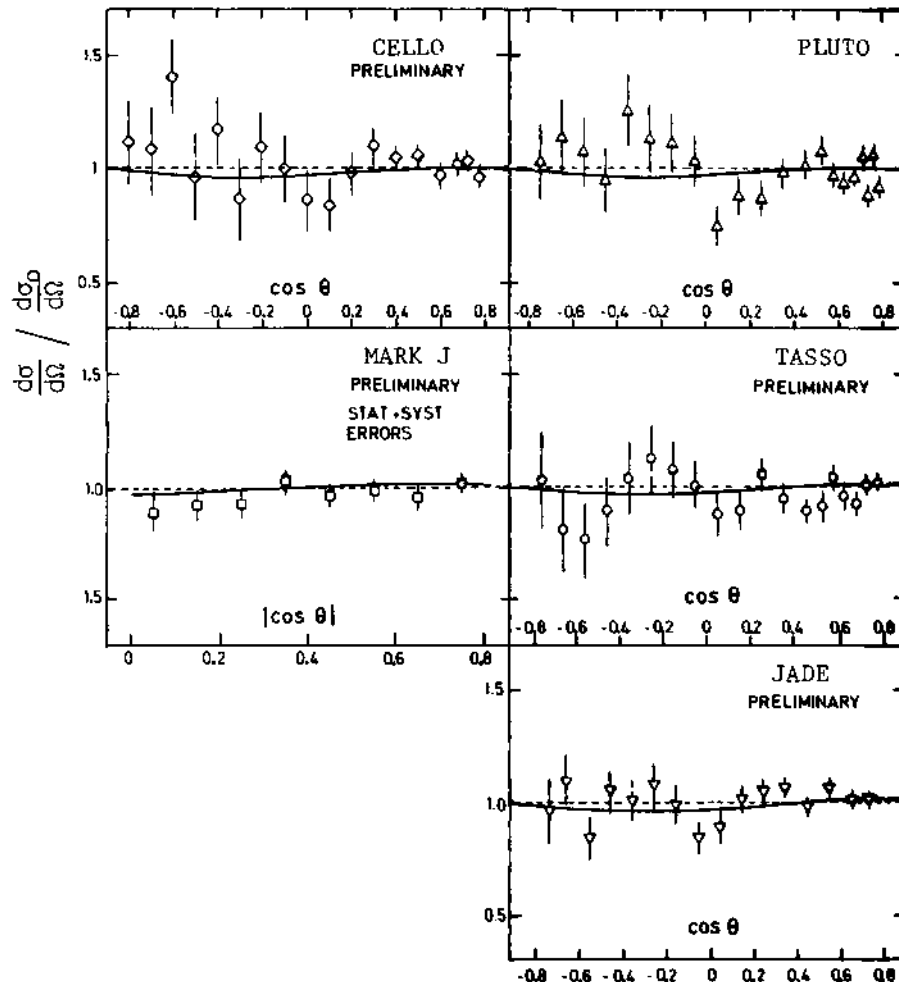


Fig. 7. Results on the reaction  $e^+e^- \rightarrow e^+e^-$ . The measured cross-section divided by the theoretical QED cross-section (dotted line) is plotted. The prediction, which includes weak interaction with the GSW-theory for  $\sin^2 \theta_W = 0.22$  (solid line) is also indicated.

A good agreement with the QED prediction is also found for the cross-section of the reactions  $e^+e^- \rightarrow \mu^+\mu^-$  and  $e^+e^- \rightarrow \tau^+\tau^-$ . Fig. 8 and fig. 9 show the total cross-section as a function of the c. m. energy between  $\sqrt{s} = 12$  GeV and 36 GeV.

Although individual points on fig. 8 and fig. 9 have rather different errors depending on the measuring time spent at each energy, they follow well within errors the pointlike cross-section  $\sigma = 4\pi\alpha^2/3s$ . Fig. 8 also indicates how the energy dependence of the cross-section varies, if the cut-off parameter is 100 GeV.

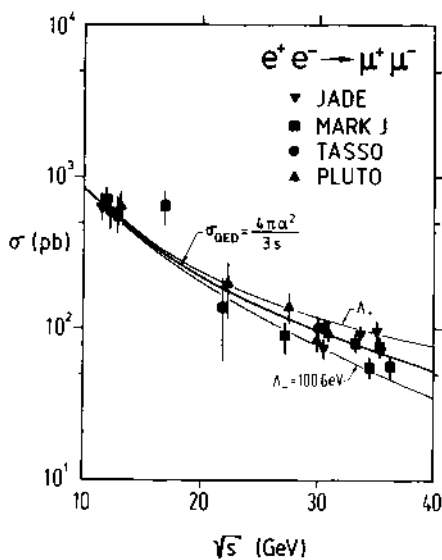


Fig. 8. Cross-section for  $e^+e^- \rightarrow \mu^+\mu^-$  as a function of energy. The lowest order QED cross-section and the limits corresponding to a cut-off parameter of 100 GeV are also indicated.

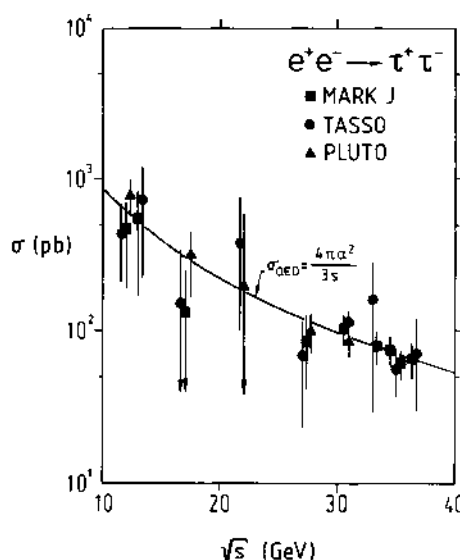


Fig. 9. Energy dependence of the  $\tau$ -pair cross-section compared with the QED prediction.

Finally we can express the agreement with QED by lower limits on the cut-off parameters, which are summarized in table 1.

Summarizing the tests of QED with reactions (1) to (4), we can say that QED is valid up to  $s = 1225 \text{ GeV}^2$  and  $q^2 \approx 1000 \text{ GeV}^2$ . Leptons are pointlike particles with a charge radius smaller than  $2 \cdot 10^{-16} \text{ cm}$ . This result is especially remarkable for the  $\tau$ -lepton, because it is very heavy and has a mass about twice that of the proton.

Table I. Summary of lower limits on cut-off parameters for reactions (1) to (4). The values are given in GeV. The confidence level is 95%.

ee  $\rightarrow$  ee

	CELLO	JADE	MARKJ	PLUTO	TASSO
$\Lambda_+$	83	119	128	80	140
$\Lambda_-$	155	138	161	234	296

ee  $\rightarrow$   $\gamma\gamma$   $F(q^2) = 1 \pm q^4/\Lambda_+^4$

$\Lambda_+$	-	-	51	46	-
$\Lambda_-$	-	-	41	36	-

heavy electron:  $\Lambda_+^2(e^*) = \frac{M^2_e}{\lambda}$

$\Lambda_+(e^*)$	43	52	51	46	34
$\Lambda_-(e^*)$	48	50	49	-	42

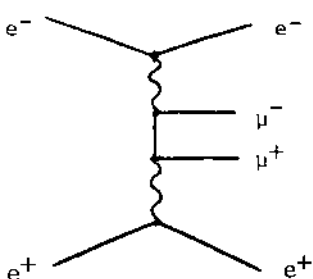
ee  $\rightarrow \mu\mu$

$\Lambda_+$	-	146	194	107	80
$\Lambda_-$	-	126	153	101	118

ee  $\rightarrow \tau\tau$

$\Lambda_+$	-	-	126	79	68
$\Lambda_-$	-	-	116	63	103
	CELLO	JADE	MARKJ	PLUTO	TASSO

Before we turn to weak interactions two additional results should be mentioned. QED has been tested at PETRA in the two photon exchange reaction  $e^+e^- \rightarrow e^+e^-\mu^+\mu^-$ . The process is of the



order  $\alpha^4$  and therefore allows a test of the higher orders of QED. The measured cross-section<sup>18</sup> agrees well with the QED prediction, but formfactors have not been studied.

Another important result concerning QED, has been obtained from a search for a new heavy lepton, which should be added as a fourth generation to the leptons e,  $\mu$  and  $\tau$ . No new charged heavy lepton has been observed and the experiments give the following limits of the mass  $M_L$  with 95 % confidence<sup>19</sup>.

$M_L > 17$	GeV	JADE
$M_L > 15$	GeV	MARK J
$M_L > 14.5$	GeV	PLUTO
and $M_L > 15.5$	GeV	TASSO

### FORM FACTORS OF QUARKS

The pair production of quarks,  $e^+e^- \rightarrow q\bar{q} \rightarrow \text{hadrons}$ , can be studied in the same way as lepton production. If quarks are pointlike fermions, the cross-section is proportional to

$$\sigma_{\text{pt}} = \frac{4\pi\alpha^2}{3s}$$

If a quark of flavor  $i$  has a charge  $Q_i$ , the ratio  $R$  of the hadronic cross-section to the pointlike cross-section is given by the sum of the square of the charges multiplied by three to take into account the three colors.

$$R_o = \frac{\sigma(ee \rightarrow \text{hadrons})}{\sigma_{\text{pt}}} = 3 \sum Q_i^2$$

For five known quarks  $u, d, s, c, b$  with the charge assignment of  $Q = -1/3$  for  $d, s, b$  and  $Q = +2/3$  for  $u$  and  $c$  we expect  $R = 11/3 = 3.67$ .

The ratio  $R$  is slightly modified by strong interactions and by weak interactions. In the framework of quantum chromodynamics (QCD) the strong interaction causes a gluonic radiative correction  $\delta_{\text{QCD}}$

$$R_{\text{QCD}} = 3 \sum Q_i^2 (1 + \delta_{\text{QCD}})$$

The correction can be calculated<sup>20</sup> in second order QCD from the strong coupling constant  $\alpha_s$  and the number of quark flavors, which is taken to be  $N = 5$ .

$$\delta_{\text{QCD}} = \frac{\alpha_s}{\pi} (1 + 1.40 \frac{\alpha_s}{\pi})$$

If we take  $\alpha_s = 0.17 \pm 0.04$  as measured by PETRA experiments<sup>21</sup> at  $\sqrt{s} \approx 30$  GeV, the correction is  $(5.8 \pm 1.4)\%$ . It increases to  $(7.3 \pm 2.0)\%$  at  $\sqrt{s} = 12$  GeV, because the strong coupling constant  $\alpha_s$  varies proportionally to  $(\ln s/\Lambda^2)^{-1}$  in QCD. A scale parameter  $\Lambda = 240$  MeV was used to compute the correction.

The effects of weak interactions on the ratio  $R$  are very small, as long as we assume the validity of the GSW theory and set  $\sin^2 \theta_w = 0.220 \pm 0.014$  as measured in neutrino experiments<sup>15</sup> and electron-deuterium scattering<sup>12</sup>. If we write again

$$R_w = R_0 (1 + \delta_w),$$

we find a correction of  $\delta_w = (+ 0.7 \pm 0.7) \%$  at  $\sqrt{s} = 35 \text{ GeV}$ . It is proportional to the c.m. energy squared  $s$  and is therefore negligible at lower energies.

In principle we can use the measurement of  $R$  to extract a value for either  $\alpha_s$  or  $\sin^2\theta_w$  or for both. Unfortunately the effects are very small in comparison to the systematic error, which is approximately 10 %. But as the systematic error should be practically energy independent, a measurement of  $\sin^2\theta_w$  has been attempted, which will be discussed in the next chapter.

At present we assume a modification of the QED cross-section due to a deviation from the pointlike nature of the quarks. In analogy to the case of  $ee \rightarrow \mu\mu$ , we would expect a modification of the hadronic cross-section and the ratio  $R$  by a formfactor

$$R_\Lambda = R \cdot F^2(q^2) = R_0 (1 + \delta_w) (1 + \delta_{QCD}) F^2(q^2)$$

For the quark formfactor  $F(q^2)$  we take the same parametrization as previously used for leptons. We allow the measurements of the ratio  $R$  to vary within the statistical and systematical errors and compare them with the modified ratio  $R_\Lambda$ . In this way we find lower limits on the cut-off parameter  $\Lambda$  for quarks. The MARK J experiment obtains  $\Lambda_+ = 190 \text{ GeV}$  and  $\Lambda_- = 285 \text{ GeV}$  with 95 % confidence (fig. 10). As the data<sup>22</sup>

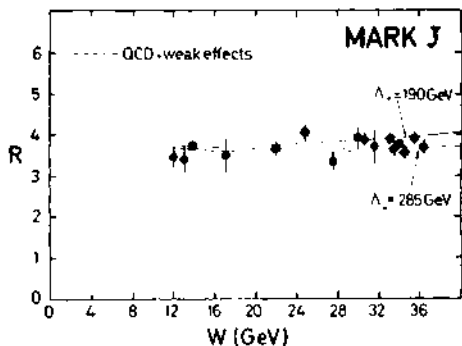


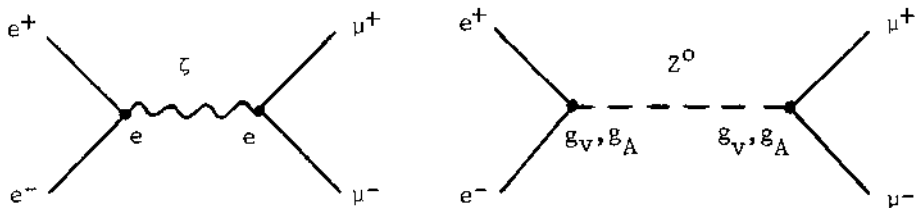
Fig. 10. Measurements of the ratio  $R$  as a function of the c.m. energy  $w$ . Indicated are also the theoretical curves with QCD and weak effects and its variations for  $\Lambda_+ = 190 \text{ GeV}$  and  $\Lambda_- = 285 \text{ GeV}$ .

have an overall systematic error of 10 %, the cut-off parameters are not determined by the absolute value of the hadronic cross-section but by its energy dependence, which is measured over a wide range as shown in fig. 10. From the limits of the cut-off

parameters we can conclude, with the precautions mentioned in chapter 2, that quarks are pointlike particles with a charge radius of less than  $10^{-16}$  cm.

### WEAK NEUTRAL CURRENT INTERACTION

From electroweak theories and the discovery of weak neutral currents in neutrino experiments<sup>23</sup> and in electron deuterium scattering<sup>12</sup> we also expect to observe weak effect in  $e^+e^-$  reactions. They arise from the fact that leptons couple not only to photons with a strength of  $e = \sqrt{4\pi\alpha}$ , but also to the neutral  $Z^0$  boson.



In the interaction lagrangian we therefore have an electromagnetic and a weak part

$$L_{\text{int}} = -\sqrt{4\pi\alpha} \bar{\ell} \gamma^\mu \ell A_\mu - m_Z \sqrt{2G_F} \bar{\ell} \gamma^\mu (g_V + g_A \gamma_5) \ell Z_\mu$$

$$\text{where } G_F = \frac{1,02 \cdot 10^{-5} \text{ GeV}}{m_p^2} \text{ and } m_p \text{ is the mass of the proton}$$

and  $m_Z$  is the mass of the  $Z^0$ . As long as we do not have longitudinally polarized beams the observed cross-section only depends on the square of the coupling constants  $g_V$  and  $g_A$ .

In this article, we will restrict our discussion to models with a single  $Z^0$ . Then weak interaction effects in  $e^+e^-$  reactions are determined by the three parameters  $g_V$ ,  $g_A$  and  $m_Z$ . In the GSW - theory they depend only on a single parameter, the weak mixing angle  $\sin^2 \theta_W$ .

$$g_V^2 = \frac{1}{4} (1 - 4 \sin^2 \theta_W)^2$$

$$g_A^2 = \frac{1}{4}$$

$$m_Z = \frac{37.4 \text{ GeV}}{\sin \theta_W \cos \theta_W}$$

If we insert the value  $\sin^2 \theta_W = 0.22$ , we find  $m_Z = 90$  GeV and  $g_V^2 = 0.004$ . This shows, that weak effects due to the vector coupling constant will be very small and difficult to measure. But we can reverse the argument. If we find no weak effects with respect to the vector coupling and are able to set a limit for  $g_V^2$  say smaller than 0.05 then the weak mixing angle would be  $\sin^2 \theta_W = 0.25 \pm 0.11$ . As we will see later, this is the 68 % confidence limit PETRA experiments reach studying leptonic interactions.

We now assume the validity of QED and search for weak interaction effects in  $e^+e^-$  reactions<sup>2,24</sup>. Firstly we discuss the reactions  $e^+e^- \rightarrow \mu^+\mu^-$  and  $e^+e^- \rightarrow \tau^+\tau^-$ , where we can measure the cross-sections  $\sigma_{\mu\mu}$ ,  $\sigma_{\tau\tau}$  and the angular distributions. We again divide the cross-sections  $\sigma_{\mu\mu}$  and  $\sigma_{\tau\tau}$  by the pointlike cross-section  $\sigma_{pt} = 4\pi\alpha^2/3s$  and call this ratio  $R_{\mu\mu}$  and  $R_{\tau\tau}$  respectively. If weak interactions are included, they have the form<sup>25</sup>

$$R_{\tau\tau} = R_{\mu\mu} = 1 + 8\chi g_V^2 + 16\chi^2 (g_V^2 + g_A^2)^2$$

where

$$\chi = \frac{G_F}{8\sqrt{2} \pi \alpha} \frac{s \cdot m_Z^2}{s - m_Z^2} = \frac{4.5 \cdot 10^{-5}}{GeV^2} \frac{s \cdot m_Z^2}{s - m_Z^2}$$

The angular distribution is expected to show a forward-backward asymmetry, where the angle  $\theta$  is measured between the incoming electron and the outgoing lepton of the same charge. The asymmetry  $A$  depends mainly on the axial-vector coupling  $g_A$

$$A \approx 6\chi g_A^2 = \frac{2.7 \cdot 10^{-4}}{GeV^2} g_A^2 s \frac{m_Z^2}{s - m_Z^2}$$

We see that the asymmetry rises with the square of the c. m. energy and contains a propagator term with the mass of the  $Z^0$  boson. To measure the asymmetry, the c. m. energy should be as high as possible. At  $\sqrt{s} = 35$  GeV and for  $g_A^2 = 0.25$  we expect an asymmetry of - 9 %. At PETRA measurements were performed in the range of 27 to 35 GeV with a typical average of 33 GeV. Fig. 11 shows the individual measurements of JADE, MARK J, PLUTO and TASSO and fig. 12 the combined angular distribution, which has the form  $1 + \cos^2 \theta$  as predicted by QED.

Four experiments have measured the forward-backward asymmetry. The results are listed in Table II and compared to the theoretical expectations. Unfortunately, the data have large errors due to a lack of statistics. We therefore combine all PETRA measurements and obtain an asymmetry  $A_{\mu\mu} = (-2.8 \pm 3.4)\%$ , which should be -6.7 % in the standard  $SU(2) \times U(1)$  theory.

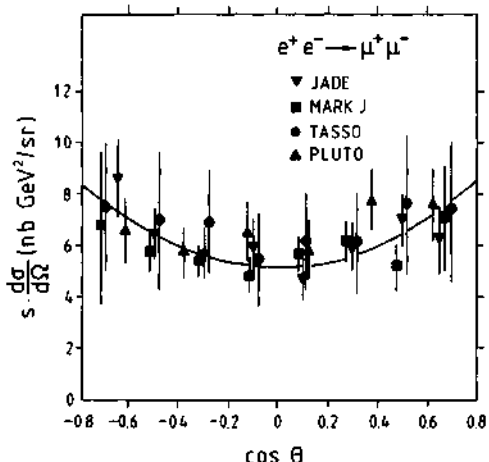


Fig. 11. Angular distribution of  $\mu$ -pair production measured by PETRA experiments at energies between 27 and 35 GeV

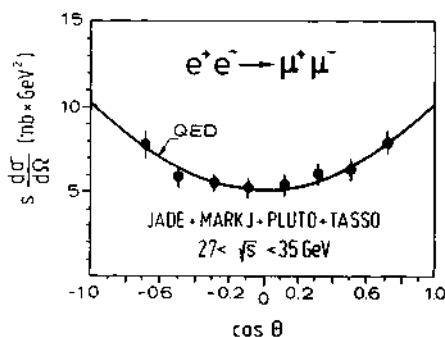


Fig. 12. Combined angular distribution of  $\mu$ -pair production from PETRA experiments

Table II. PETRA results on the forward-backward asymmetry for  $\mu$ -pair production. The theoretical values are obtained with  $g_A^2=0.25$  and include a cut on the angular acceptance.

	JADE	MARK J	PLUTO	TASSO
$A_{\mu\mu}$ in %	-5±6	-1±6	+7±10	-7±7
EXPECTED	-6.6	-7.7	-5.8	-6.6

With 95 % confidence the combined asymmetry is larger than -8.4 %. From this value the following limits can be determined, again with 95 % confidence:

- 1) If we set  $g_A^2 = 1/4$ , as predicted by the standard  $SU(2) \times U(1)$  theory, we find  $m_Z > 59$  GeV.
- 2) Reversing the argument, we find  $|g_A| < 0.56$ , where  $g_A = -0.5$  is expected in the standard  $SU(2) \times U(1)$  theory.
- 3) Instead of  $g_A^2$  we really measure the product of axial coupling of the electron and the muon,  $g_A^e \cdot g_A^\mu$ . If we again set  $g_A^2 = -0.5$  we can give a limit of the axial coupling of the neutral current interaction for the muon without the use of  $\mu$ -e universality

$$|g_A^\mu| < 0.63.$$

The limits for 2) and 3) are obtained with the assumption of  $m_Z = \infty$ , which gives the weakest constraints of the coupling constants.

First results have been obtained on the asymmetry of the reaction  $e^+e^- \rightarrow \tau^+\tau^-$ . The results are listed in Table III.

Table III. Results of the MARK J and TASSO experiment on the asymmetry  $A_{\tau\tau}$  of the  $\tau$ -pair production at  $27 < \sqrt{s} < 36$  GeV.

	$A_{\tau\tau}$	expected from GWS-theory
MARK J	$(-6 \pm 12) \%$	-7 %
TASSO	$(0 \pm 11) \%$	-7.5 %
combined	$(-3 \pm 8) \%$	-7 %

From the combined measurement, we can set a limit on the axial - vector coupling of the  $\tau$ -lepton, which is  $|g_A^\tau| < 1.3$ , if we set  $|g_A^e| = 0.5$ . The results on these asymmetries still suffer from a lack of statistics, but as the measurements are in progress more precise results are expected in the near future<sup>26</sup>.

Electroweak effects can also be studied in the angular distribution of Bhabha scattering, which depends on  $\sin^2\theta_W$  or more generally on  $g_V^2$ ,  $g_A^2$  and  $m_Z$ . Its functional form<sup>27</sup> is rather complicated and will not be presented here. Instead fig. 5 b shows the change of the angular distribution for different values of the weak mixing angle. As weak interaction effects are negligible at small scattering angles, we are able to measure the luminosity at these angles. Measurements at large scattering angles can therefore be used to study neutral currents. Firstly we restrict our discussion to the standard  $SU(2) \times U(1)$  theory of Glashow, Salam and Weinberg, where we have only one free parameter  $\sin^2\theta_W$ . We do not attempt to fit all leptonic reaction individually, but perform a common fit to the leptonic reactions (1) to (4), in

order to increase the statistical significance. Table IV displays the results of the PETRA experiments<sup>4-8</sup>.

Table IV: Results on  $\sin^2 \theta_w$  for  $27 < \sqrt{s} < 36$  GeV.

group	limit on $\sin^2 \theta_w$ with 95 % confidence		final states used	$\sin^2 \theta_w$ with one standard deviation error
	lower	upper		
CELLO			ee	$0.25 \pm 0.15$
JADE	0.04	0.46	ee, $\mu\mu$ , $A_{\mu\mu}$	$0.25 \pm 0.15$
MARK J	0.06	0.42	ee, $\mu\mu$ , $\tau\tau$ , $A_{\mu\mu}$	$0.24 \pm 0.12$
PLUTO	-	0.52	ee, $\mu\mu$ , $\tau\tau$ , $A_{\mu\mu}$	$0.22 \pm 0.22$
TASSO	0.06	0.43	ee, $A_{\mu\mu}$	$0.24 \pm 0.11$

Next we discuss a more general case, still with a single  $Z^0$ , but without restricting the vector and axial coupling constants. This gives 3 parameters  $m_Z$ ,  $g_V$  and  $g_A$ , but setting  $m_Z$  to infinity leads to the most pessimistic limits. Very similar results for  $g_V$  and  $g_A$  are obtained with  $m_Z = 90$  GeV, because the effects of weak interactions only change by 18 % at  $\sqrt{s} = 35$  GeV, if the mass of the  $Z^0$  is varied between 90 GeV and infinity. Four experiments have determined the range of the values for  $g_V^2$  and  $g_A^2$  varying one coupling constant independently of the other. Table V list the results, obtained with 68 % confidence, and compares them to the values expected in the GSW-theory with  $\sin^2 \theta_w = 0.22$ .

Table V: Results (68% conf.) for  $g_V^2$  and  $g_A^2$  at  $27 < \sqrt{s} < 36$  GeV. The theoretical expectation of the GSW-theory is calculated with  $\sin^2 \theta_w = 0.22$

experiment	$g_V^2$	$g_A^2$
JADE	$0.01 \pm 0.08$	$0.18 \pm 0.16$
MARK J	$-0.04 \pm 0.09$	$0.20 \pm 0.17$
PLUTO	$-0.02 \pm 0.15 \pm 0.07$	$-0.19 \pm 0.24 \pm 0.02$
TASSO	$-0.14 \pm 0.12$	$0.25 \pm 0.14$
expected with $\sin^2 \theta_w = 0.22$	0.004	0.25

It is clear that the values for the neutral weak coupling constants  $g_V^2$  and  $g_A^2$  are correlated. Therefore a contour of allowed values in the  $g_V^2$ ,  $g_A^2$ -plane should be determined. Fig. 13 shows the 95 % confidence contour determined by the MARK J experiment and compares it with the results from table V. Neutrino experiments allow two solutions where the vectorlike solution is clearly ruled out by

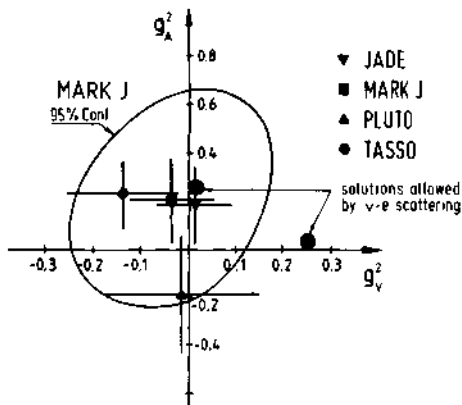


Fig. 13. Results of  $g_V^2$  and  $g_A^2$  obtained by PETRA experiments with 68 % confidence. Indicated are also the 95 % confidence contour from MARK J and the two solutions, allowed by the neutrino experiments<sup>29</sup>.

the 95 % confidence contour of the MARK J experiment<sup>28</sup>. The comparison with the results of the neutrino experiments<sup>29</sup> is more detailed if one displays the results in the  $g_V$ ,  $g_A$  plane. This has been done by the MARK J experiment (fig. 14).

In this plane the allowed region has a fourfold symmetry due to the fact that  $e^+e^-$ -experiments measure only the square of the coupling constant. Combining the MARK J and the neutrino scattering

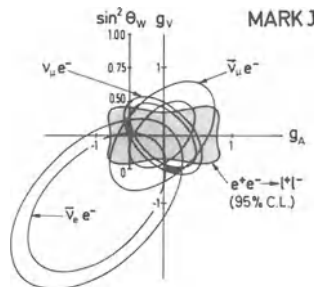


Fig. 14. The shaded area contains the values of  $g_V$  and  $g_A$ , which are allowed with 95 % confidence. It is obtained by MARK J from a measurement of leptonic reactions in  $e^+e^-$  annihilations. The regions between the concentric ellipses are the 68 % confidence limits from neutrino experiments. The black area indicates their overlap<sup>29,30</sup>.

results the vectorlike solution for  $g_V$  and  $g_A$  is ruled out<sup>28</sup>. This confirms the conclusion drawn on the basis of deep inelastic neutrino nucleon scattering and electron deuterium scattering<sup>31,32</sup> but with the MARK J result the selection of the axialvector dominant solution is made by purely leptonic reactions. It should be added<sup>33</sup> that this conclusion is reached only in models with a single  $Z^0$ . Otherwise there is an additional scale parameter between the coupling constants  $g_V$  and  $g_A$  measured in  $e^+e^-$  annihilations, and those measured in neutrino electron scattering. This scale parameter is close to one as tested in neutrino nucleon scattering<sup>15</sup>.

### WEAK INTERACTION EFFECTS IN $e^+e^- \rightarrow q\bar{q}$

Effects of weak interactions can also be studied in the hadronic cross-section  $e^+e^- \rightarrow q\bar{q} \rightarrow \text{hadrons}$ . Similarly to chapter 4 we discuss the ratio  $R$  of the hadronic cross-section divided by the pointlike cross-section. Similarly to the reaction  $ee \rightarrow \mu\mu$ , a quark of flavor  $f$  and charge  $Q_f$  contributes to  $R$  by<sup>24</sup>

$$R_f = 3 \left[ Q_f^2 + 8\chi Q_f g_V v_f + 16\chi^2 (g_V^2 + g_A^2) (v_f^2 + a_f^2) \right]$$

where  $g_V$  and  $g_A$  are the coupling constants of the electron and  $v_f$  and  $a_f$  those of the quark of flavour  $f$ . In the GSW-theory the quark couplings are given by

$$v_f = \begin{cases} 1/2 - 4/3 \sin^2 \theta_W & \text{for } f = u \text{ and } c \\ -1/2 + 2/3 \sin^2 \theta_W & \text{for } f = d, s \text{ and } b \end{cases}$$

$$a_f = \begin{cases} +1/2 & \text{for } f = u \text{ and } c \\ -1/2 & \text{for } d, s, \text{ and } b \end{cases}$$

The variable  $\chi$  is defined as in chapter 5

$$\chi = \frac{4.5 \cdot 10^{-5}}{\text{GeV}^2} \cdot \frac{s \cdot m_Z^2}{s - m_Z^2}$$

To simplify the expression for  $R_f$  we have neglected a part of the  $Z^0$  propagator term which contains the width of the  $Z^0$ . The contribution of all five known quarks  $u, d, s, c$  and  $b$  to the hadronic cross-section is given by a sum over all  $R_f$

$$R = \sum_{f=1}^5 R_f (1 + \delta_{\text{QCD}})$$

where we also included corrections due to strong interactions (QCD).

At first one might think that effects of weak interaction in the hadronic cross-section are too small to be measured, but the value of  $R$  changes by 10 % if the weak mixing angle varies between 0.10 and 0.30 at  $\sqrt{s} = 35$  GeV. Again this variation seems to be too small in view of the relatively large systematic error of 10 %, but this error is an overall normalization error independent of the c. m. energy, where as the effects of weak interaction depend on the c. m. energy squared. Therefore comparing measurements at different energies allows the determination of the weak mixing angle from hadronic reactions. The measurements of the MARK J experiment are shown in fig. 15.

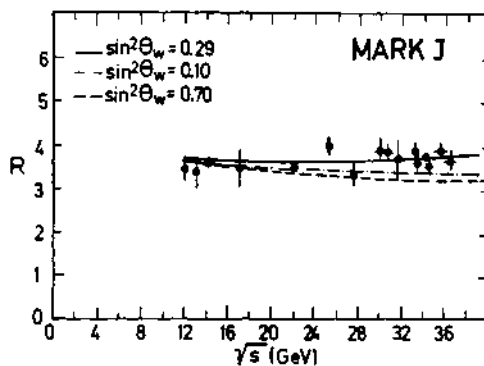


Fig. 15. Measurements of the relative hadronic cross-section by MARK J at different c.m. energies, compared to the theoretical predictions for three values of  $\sin^2 \theta_w$ .

A similar analysis has been performed by the JADE experiment<sup>35</sup>. The results of both experiments are

$$\sin^2 \theta_w = 0.27 \pm 0.34 \quad \text{MARK J}$$

$$\sin^2 \theta_w = 0.22 \pm 0.08 \quad \text{JADE}$$

where the JADE result takes the leptonic interactions into account, in order to limit the error for large values of  $\sin^2 \theta_w$ . If a combined fit to the measurements on the leptonic and hadronic reactions is performed, the MARK J group obtains  $\sin^2 \theta_w = 0.27 \pm 0.08$ . We do not attempt to average the results of both groups as systematic errors might be dominating. The precision of  $\sin^2 \theta_w$  determined by hadronic reactions in  $e^+e^-$ -annihilations is not yet comparable to those of the neutrino experiments and electron deuterium scattering, but the PETRA measurements test the GSW-theory in the region of high  $q^2$  and with heavy quarks, like  $c$  and  $b$ , which are practically unmeasurable in current neutrino experiments.

## CONCLUSIONS

The tests of QED and electro-weak theories performed at PETRA lead to the following conclusion:

1. QED is valid in  $e^+e^-$  annihilations up to  $s = 1225 \text{ GeV}^2$  and  $q^2 \approx 1000 \text{ GeV}^2$ .
2. No effects of formfactors have been detected in the reactions  $e^+e^- \rightarrow e^+e^-$ ,  $\gamma\gamma$ ,  $\mu^+\mu^-$ ,  $\tau^+\tau^-$  and  $q\bar{q}$ . The limits of cut-off parameters are higher than 100 GeV except for  $\gamma\gamma$ .
3. The lepton, including the  $\tau$ -lepton, and the quarks are pointlike particles with a charge radius less than  $2 \cdot 10^{-16} \text{ cm}$ .
4. A new charged heavy lepton with a mass smaller than 17 GeV does not exist.
5. The search for weak interaction effects leads to strong limits on the parameters of neutral currents and tests the theories at very large  $s$  and  $q^2$ .
6. Leptonic and hadronic reactions in  $e^+e^-$  annihilations are well described by the standard  $SU(2) \times U(1)$  theory with  $\sin^2\theta_W = 0.25 \pm 0.08$ . This test includes measurements of pair production of heavy quarks.
7. The vector and axial-vector couplings of the weak neutral currents can be uniquely determined in theories with a single  $Z^0$  by purely leptonic interactions.

## ACKNOWLEDGEMENT

I wish to thank the members of the CELLO, JADE, PLUTO, TASSO collaborations and my colleagues from the MARK J group for discussion and for providing me with unpublished data. The support of the DESY directorate, Profs. Lohrmann and V. Soergel, and the hospitality of the organizers of this conference, especially Prof. W. Greiner, are gratefully acknowledged. I wish to thank Drs. D. P. Barber, W. Krenz, L. M. Sehgal and R. Schulte for comments and discussions and Miss B. Breuer for careful typing of the manuscript.

## REFERENCES

1. S. J. Brodsky and S. D. Drell, *Annu. Rev. Nucl. Sci.* 20, 147 (1970);  
B. E. Lautrup, A. Peterman and E. de Rafael, *Phys. Reports* 3C, 193 (1972);  
G. P. Lepage, Cornell University preprint CLNS 80/474 (1980);  
G. P. Lepage and D. R. Yennie, Cornell University preprint CLNS 81/499 (1981) and references therein.

2. R. Marshall, XV Rencontre de Moriond, Les Arcs, 1980 and Rutherford Lab. report RL-80-29;  
 A. Böhm, Proc. of the XXth Int. Conf. on High Energy Physics, Madison (1980) and Aachen report PITHA 80/9 (1980);  
 M. Pohl, XVI Rencontre de Moriond, Les Arcs, 1981 and Aachen report PITHA 81/10  
 P. Dittmann and V. Hepp, DESY report 81/030 (1981).
3. PETRA Proposal (updated version), DESY, Hamburg (February 1976);  
 G. - A. Voss, The 19 GeV  $e^+e^-$  Storage Ring, Internal Report, DESY M79/16 and Phys. Blätter 36, 267 (1980).
4. CELLO: M. J. Schachter, DESY report 80/128 (1980);  
 H. - J. Behrengs et al., Phys. Lett. 103B, 148 (1981)
5. JADE collaboration: W. Bartel et al., Phys. Lett. 88B, 171 (1979);  
 Phys. Lett. 92B, 206 (1980); Phys. Lett. 99B, 281 (1981).
6. MARK J Collaboration: D. P. Barber et al., Physics Reports 63, 337 (1980); Phys. Rev. Lett. 42, 1110 (1979); Phys. Rev. Lett. 43, 1915 (1979);  
 Phys. Lett. 95B, 149 (1980); Phys. Lett. 99B, 495 (1981).  
 J. P. Revol, M. I. T. thesis, 1981 (unpublished)
7. PLUTO Collaboration: Ch. Berger et al., Z. Phys. C4, 269 (1980);  
 Z. Phys. C1, 343 (1979); Z. Phys. C7, 289 (1981); Phys. Lett. 94B, 87 (1980); Phys. Lett. 99B, 489 (1981).
8. TASSO Collaboration: R. Brandelik et al., Phys. Lett. 83B, 261 (1979); Phys. Lett. 92B, 199 (1980); Phys. Lett. 94B, 259 (1980).
9. M. L. Perl et al., Phys. Rev. Lett. 35, 1489 (1975);  
 G. Feldman et al., Phys. Rev. Lett. 38, 117 (1977);  
 J. Burmester et al., Phys. Lett. 68B, 297 (1977) and 68B, 301 (1977)  
 For a recent review on the  $\tau$ -lepton, see M. Perl, Ann. Rev. Nucl. Part. Sci. 30, 299 (1980) and references therein.
10. K. W. Robinson and G.-A. Voss, Int. Symposium on Storage Rings, Vol. 8, Paris, 1966;  
 J. Rossbach, DESY Internal Report M-81/10 (1981);  
 K. Steffen, Internal Note, March 6, 1980.
11. F. A. Berends, K. J. F. Gaemers and R. Gastmans, Nucl. Phys. B57, 381 (1973); Nucl. Phys. B63, 381 (1973); Nucl. Phys. B68, 541 (1974);  
 F. A. Berends and G. J. Komen, Phys. Lett. 63B, 432 (1976);  
 F. A. Berends and R. Kleiss, Nucl. Phys. B177, 237 (1981) and private communication.
12. C. Y. Prescott et al., Phys. Lett. 77B, 347 (1978); Phys. Lett. 84B, 524 (1979).

13. S. L. Glashow, *Nucl. Phys.* 22, 579 (1961);  
 S. Weinberg, *Phys. Rev. Lett.* 19, 1264 (1967) and *Phys. Rev. D5*, 1412 (1972);  
 A. Salam, Proc. 8th Nobel Symp. (Aspensgaden, 1968), Almquist and Wiksell, Stockholm 1968, p. 367.
14. H. Salecker, *Zeits. Naturforsch.* 8a, 16 (1953) and 10a, 349 (1955);  
 S. D. Drell, *Ann. Phys. (N. Y.)* 4, 75 (1958);  
 T. D. Lee and G. C. Wick, *Phys. Rev. D2*, 1033 (1970).
15. M. Jonker et al., *Phys. Lett.* 99B, 265 (1981);  
 Similar results are obtained from an analysis of earlier data by  
 J. E. Kim et al., *Rev. of Mod. Phys.* 53, 211 (1981);  
 I. Liede and M. Roos, *Phys. Lett.* 82B, 89 (1979);  
 see also ref. 12 and ref. 32.
16. J. A. Mc Clure and S. D. Drell, *Nuovo Cim.* 37, 1638 (1965);  
 N. M. Kroll, *Nuovo Cim.* 45A, 65 (1966).
17. A. Litke, Harvard University thesis 1970 (unpublished).
18. MARK-J Collab.: D.P. Barber et al., *Phys. Rep.* 63, 337 (1980);  
 PLUTO Collab.: Ch. Berger et al., *Phys. Lett.* 94B, 254 (1980).
19. JADE Collab., D. Cords, DESY Report 80/92 and Proc. of the  
 XXth Int. Conf. on High Energy Physics, Madison, (1981);  
 MARK J Collab., D. P. Barber et al., *Phys. Rev. Lett.* 45, 1904 (1980);  
 PLUTO Collab., Ch. Berger et al., *Phys. Lett.* 99B, 489 (1981);  
 O. Meyer, University of Wuppertal thesis (unpublished);  
 TASSO Collab., R. Brandelik et al., DESY Report 80/108 (1980).
20. K. G. Chetyrkin et al., *Phys. Lett.* 85B, 277 (1979);  
 M. Dine and J. Sapierstein, *Phys. Rev. Lett.* 43, 668 (1979);  
 W. Celmaster and R. Cousalves, *Phys. Rev. Lett.* 44, 560 (1980).
21. D. P. Barber et al., *Phys. Lett.* 89B, 139 (1979);  
 W. Bartel et al., *Phys. Lett.* 91B, 142 (1980);  
 R. Brandelik et. al., *Phys. Lett.* 94B, 437 (1980);  
 H. Newman, Proc. XX Int. Conf. on High Energy Physics, Madison (1980), p. 627;  
 S. Yamada, *ibid.*, p. 616;  
 For recent reviews see  
 P. Söding and G. Wolf, DESY Report 81-013 (1981)  
 W. Braunschweig, Invited talk at the 1981 Int. Symp. on Lepton and Photon Interactions at High Energies, Bonn, 1981.
22. D. P. Barber et al., *Phys. Rev. Lett.* 42, 1113 (1979); *Phys. Lett.* 85B, 463 (1979) and H. Rykaczewski, Thesis, RWTH Aachen, Aachen internal report AC INTERN 81-05, 1981.
23. F. J. Hasert et al., *Phys. Lett.* 46B, 121 (1973); *Phys. Lett.* 46B, 138 (1973).

24. N. Wright and J.H. Sakurai, Phys. Rev. D22 (1980) 220;  
E.H. de Groot and D. Schildknecht, Bielefeld preprint, BI-TP  
80/08, May 1980
25. J. Ellis and M.K. Gaillard, CERN yellow report CERN 76-18, p.21.
26. More data on the reaction  $e^+e^- \rightarrow \mu^+\mu^-$  have been analysed by  
JADE, MARK J and TASSO. The new combined asymmetry is  
 $A_{\mu\mu} = (-7.7 \pm 2.4) \%$  where  $-7.8 \%$  is expected. It represents  
for the first time a statistically significant effect of weak  
neutral currents in  $e^+e^-$  annihilations. This result has been  
presented by J. Branson, invited talk at the 1981 Int. Sym.  
on Lepton and Photon Interactions at High Energies, Bonn,  
Aug. 1981.
27. R. Budny, Phys. Lett. 55B, 227 (1975).
28. D.P. Barber et al., Phys. Lett. 95B, 149 (1980).
29. H. Faissner, New Phenomena in Lepton-Hadron Physics (1979), ed.  
D.E. Fries and J. Wess (Plenum Publishing Corp., New York),  
p. 371;  
H. Reithler, Phys. Blätter 35, 630 (1979);  
F.W. Bullock, Proc. of Neutrino 79, Bergen 1979, p. 398;  
R.H. Heisterberg et al., Phys. Rev. Lett. 44 (1980) 635;  
L.W. Mo, Contribution to Neutrino 80, Erice (1980), and  
private communication H. Faissner and H. Reithler.
30. A new result on elastic  $\bar{\nu}_\mu e$ -scattering by the CHARM collabora-  
tion is not yet included in fig. 14. M. Jonker et al.,  
Phys. Lett. 105B, 242 (1981).
31. J.J. Sakurai, Proc. Neutrino-79, Bergen (1979), Vol. 1, p. 267.
32. For recent reviews on the status of neutral currents see:  
L.M. Sehgal, Aachen Report PITHA 80/17  
F.W. Büsser, Proc. of the Int. Conf. on Neutrino  
Physics and Astrophysics, Wailea, Hawaii, 1981 and ref. 15.
33. P.Q. Hung and J.J. Sakurai, Phys. Lett. 69B, 323 (1977).
34. D.P. Barber et al., Phys. Rev. Lett. 46, 1663 (1981).
35. W. Bartel et al., Phys. Lett. 101B, 361 (1981).

## THE MUON ( $g - 2$ ) EXPERIMENTS AT CERN

Emilio Picasso

CERN, Geneva, Switzerland  
and Scuola Normale Superiore, Pisa, Italy

### INTRODUCTION

In this lecture I shall discuss measurements of the dipole moments of free electrons and muons, and the lifetime of free muons. I shall discuss these experiments in terms of physical principle rather than technical details; full accounts of the experimental methods may be found in the original papers to which reference is made in some of the review articles given below<sup>1</sup>).

I note that a totally free particle is an idealized concept, and I use the term to mean particles so weakly bound that any shift in the value of the measured quantity due to this containment is negligibly small.

The  $g$ -factor of the muon (and electron) is a dimensionless number which relates its magnetic dipole moment to its intrinsic angular momentum. Classically the dipole moments can arise from either charges or currents. For example, the circulation current, due to an orbiting particle with an electric charge  $e$  and mass  $m$ , has associated with it a magnetic dipole moment  $\vec{\mu}_L$  given by

$$\vec{\mu}_L = \frac{e}{2mc} \vec{L} \quad (1)$$

where  $\vec{L}$  is the orbital angular momentum.

Alternatively, the electric dipole moment possessed by certain polar molecules is due to the relative displacement of the centre of positive and negative electric charge distribu-

tions. Thus we have examples of a magnetic dipole moment and electric dipole moment both having their origines in electric charge. It is of interest to note that all electromagnetic phenomena are explained in terms of electric charges and their currents; there is not place, as yet, for magnetic charges. In particular the intrinsic magnetic dipole moments of all particles can be considered, in the classical picture, to be made up of circulation electric currents and not of distributed magnetic charges<sup>2)</sup>. This is just one aspect of the basic asymmetry between the electric and magnetic parts of electromagnetism which is apparent from Maxwell's equations. The argument, first proposed by Dirac<sup>3)</sup>, that the existence of magnetic charge leads naturally to the quantization of both magnetic and electric charges, still stands as a challenge to physicists, both theoretical and experimental, to find a proper place for the magnetic monopole in the electromagnetic theory and establish its physical reality.

For a particle with both magnetic and electric dipole moments the electromagnetic interaction Hamiltonian contains a part

$$H = -\vec{\mu}_m \cdot \vec{B} - \vec{\mu}_e \cdot \vec{E} , \quad (2)$$

where  $\vec{B}$  and  $\vec{E}$  are the magnetic and electric field strengths and  $\vec{\mu}_m$  and  $\vec{\mu}_e$  are the magnetic and electric dipole moment operators. Following the general form of (1) and treating the electric dipole moment analogously to the magnetic dipole moment one can write

$$\vec{\mu}_m = g \frac{e}{2mc} \frac{(\vec{\sigma})}{2} ; \quad \vec{\mu}_e = f \frac{e}{2mc} \frac{(\vec{\sigma})}{2} \quad (3)$$

where the components of  $\vec{\sigma}$  are the three Pauli spin matrices and for the negative lepton we have to insert the charge  $e = -|e|$ . Introducing the Bohr magneton  $\mu_0 = eh/2mc$ , these equations can be simplified to

$$\vec{\mu}_m = g\mu_0 \frac{\vec{\sigma}}{2} ; \quad \vec{D} \equiv \vec{\mu}_e = f\mu_0 \frac{\vec{\sigma}}{2} \quad (4)$$

where I have taken the opportunity to introduce the conventional symbol for the electric dipole moment,  $\vec{D}$ .

The g-factor represents a fundamental propriety related to electromagnetism, if the particle participates in any other interactions which endow it with an internal structure then the value of its g-factor will reflect this departure from the point-like nature implied by the Dirac equation. The proton with

a g-factor of 5.586 is an example of such a case. However, even in the absence of an intrinsic structure the quantum nature of the electromagnetic interaction itself also modified the g-factor. This modification is quite small and it has become conventional to define a magnetic moment anomaly "a" such that

$$g = 2(1 + a) \quad (5)$$

which has given rise to the title (g - 2) experiments.

The motivation for these experiments is twofold. The first aim is to check that the quantum theory of electromagnetism correctly predicts the value of the magnetic moment anomaly without need of modification. The second aim is to look for the effects of interactions outside electromagnetism; in particular, this second aim is associated with the mystery of the muon mass. The question arises as to what type of process generates that large mass. I should like to mention here that some advantage occurs from this large mass in the use of the muon as a probe of effects at small distances.

Quantum electrodynamics (QED) can be considered as a clearly defined mathematical procedure whereby any process involving the interaction of the photon and charged lepton fields may be calculated to any order of approximation. It is not without its controversial points. The existence of infinities within its structure remain difficult to accept, in fact, their presence precludes any real understanding of the fundamental constants such as charge and mass. The increasing order of the approximation involves the calculation of more and more successive interactions between the photon and the lepton fields. All these terms depend upon the renormalization procedure in which the sum of the bare lepton mass and its (infinite) radiative correction is put equal to the observed rest mass of the particle, while the sum of the bare lepton charge and its (infinite) radiative correction is put equal to the observed electronic charge.

The target of experimentalists in QED is to check the theory at smaller and smaller distances, searching for any evidence of the structure of lepton or of some new interaction which may explain the difference in mass between the electron and the muon. Experimentalists in doing so are measuring the effects of the higher order corrections, including renormalization. These measurements need to be performed with extreme precision and there has developed a friendly rivalry between theorists and experimentalists which has pushed the comparison between theory and experiment to finer and finer limits. The atomic-physics experiments, together with the measurements of the lepton magnetic moments, have provided the arena for this fruitful confrontation.

2.

The lepton g-factor may be expressed as a perturbation expansion of the form

$$g_\ell = 2 \left\{ 1 + \sum_n A_n^{(\ell)} \left( \frac{\alpha}{\pi} \right)^n + \sum_n B_n^{(\ell)} \left( \frac{\alpha}{\pi} \right)^n \right\} = e, \mu, \dots, \quad (6)$$

where  $\ell$  stands for either electron or muon or tau leptons, and  $g = 2$  just represents the result of the Dirac relativistic theory. The higher order terms involve an increasing number of interactions between photon and lepton fields and consequently take the form of a power series in the square of the coupling constant, that is, a series in the fine structure constant  $\alpha$ . The anomaly  $a$  is defined by

$$a_\ell \equiv \frac{(g - 2)}{2} = \sum_n A_n^{(\ell)} \left( \frac{\alpha}{\pi} \right)^n + \sum_n B_n^{(\ell)} \left( \frac{\alpha}{\pi} \right)^n. \quad (7)$$

The coefficients  $A$  and  $B$  are distinguished in that the former are independent of the lepton mass, while the latter are functions of the ratio of the mass of the external lepton to that of the lepton in the vacuum polarization loops. Thus the first sequence of terms is identical for both electron and muon, while the second sequence, which commence at  $n = 2$  is only significant in the case of the muon anomaly owing to the fact that  $m_\mu$  is about 200 times larger than  $m_e$ .

The coefficient of the leading term was first shown to be  $A_1 = 0.5$  by Schwinger<sup>4)</sup> and so it can be seen that the order of magnitude of the anomaly  $a$  is  $10^{-3}$ . From this it is apparent that a direct measurement of the anomaly offers the prospect of a much higher precision than a measurement of  $g$  itself. It should be pointed out, however, that theory predicts the value of  $g$  in total since there is no a priori reason why it should be close to the value 2. In table 1. I list the values of the perturbation expansion coefficients together with the complete contribution to the anomaly.

Table 1.  
Coefficients of the perturbation  
series in  $(\alpha/\pi)$  for  $a_\ell$  up to  $(\alpha/\pi)^4$

$n$	$A_n^{(\ell)}$	$B_n^{(\mu)}$	$10^9 \times A_n^{(\ell)} \left( \frac{\alpha}{\pi} \right)$	$10^9 \times B_n^{(\mu)} \left( \frac{\alpha}{\pi} \right)$
1	0.5	0	$1161409.8 \pm 0.3$	
2	-0.32848	1.09426	-1772.3	5904.1
3	$1.188 \pm 0.017$	$23.26 \pm 0.05$	$14.9 \pm 0.2$	$291.5 \pm 0.6$
4	?	$128 \pm 70$	?	$3.7 \pm 2.1$

The numerical values in the last two columns have been obtained using

$$\alpha^{-1} = 137.035987(29) \quad (8)$$

as given by Olsen and Williams<sup>5)</sup> after combining their new measurement of the proton gyromagnetic ratio at low field with the value e/h obtained from the a.c. Josephson effect<sup>6)</sup>.

The Feynman graphs contributing to the coefficients  $A_1$ ,  $A_2$  and  $B_2$  are shown in fig. 1. Putting the numerical results together and recalling that the  $B$  coefficients for the electron are negligible, one obtains the predicted values for the anomaly according to QED:

$$\begin{aligned} a_e^{\text{QED}} &= (1159652.4 \pm 0.4) \times 10^{-9} \\ a_p^{\text{QED}} &= (1165851.7 \pm 2.3) \times 10^{-9} \end{aligned} \quad (9)$$

where the errors are the quadratic sum of those due to the uncertainty in  $\alpha^{-1}$  and those arising from the numerical calculations.

The calculation of the anomaly within QED can in principle be carried through with limitless precision, as more and more terms are reduced to an analytical form. However, it should be noted that at each order the number of graphs increases considerably. There is only one contributing to  $B_2^{(0)}$ , 24 diagrams are associated with  $B_3^{(0)}$ , and 469 diagrams remain for  $B_4^{(0)}$ . Thus the rapidly increasing complexity of the calculations forms a barrier to indefinite improvements in precision.

The strong-interaction contribution to the anomaly appears through the vacuum polarization into virtual hadronic state.

Accurate theoretical calculations are not yet possible, but fortunately use can be made of the relationship between this virtual process and the total hadronic cross-section for the annihilation of electrons and positrons. Dispersion theory provide the link between the two. If one assume single-photon dominance, one obtains:

$$a_\mu(h) = \frac{1}{4\pi^3} \int_{4m^2/\pi}^{\infty} ds \sigma_{e^+ e^- \rightarrow \text{hadrons}}(s) \cdot K(s) \quad (10)$$

where  $s$  is the total  $e^+ e^-$  centre of mass energy squared.

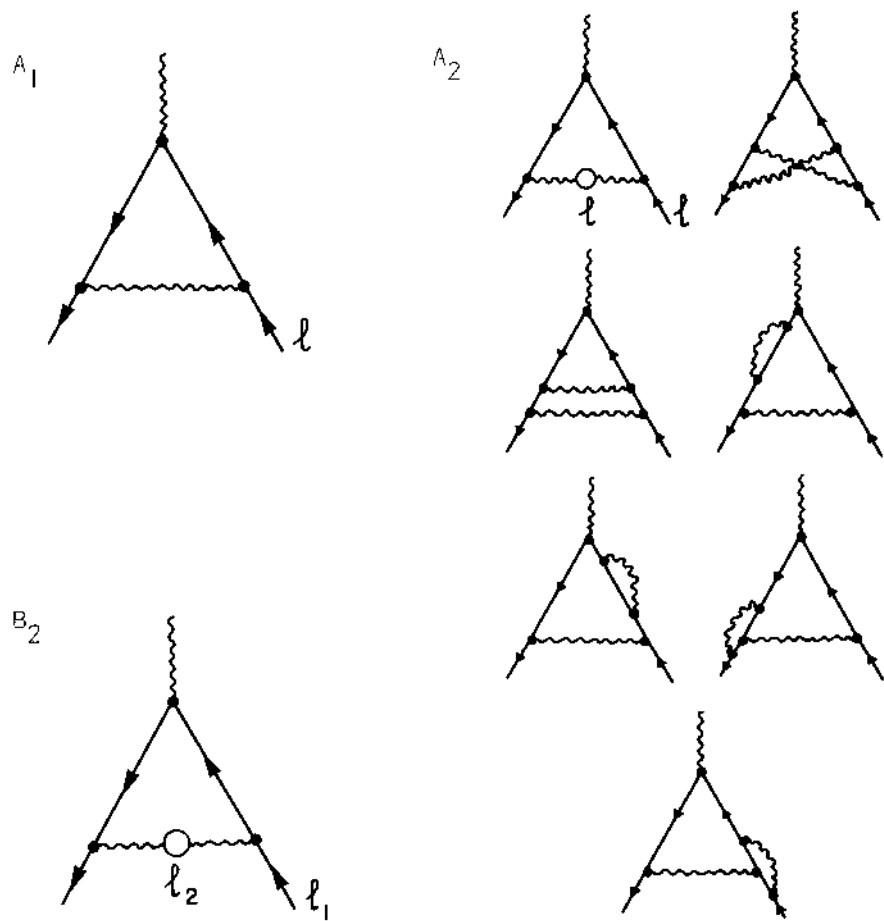


Fig. 1. Feynman graphs contributing to  $A_1$ ,  $A_2$  and  $B_2$ .

The function  $K(s)$  is a purely QED quantity, which results from the combination of the two lepton propagators and the propagator of a virtual photon with mass  $\sqrt{s}$  at the lepton vertex. The  $K(s)$  is positive definite in the region of integration and for  $s \gg m^2$  has a limiting value

$$K(s \rightarrow \infty) = \frac{1}{3} \frac{m^2}{s} \quad (11)$$

The equation (11) indicates that the contribution to the electron anomaly will be some  $10^{-5}$  times that of the muon anomaly.

The most recent evaluation<sup>7)</sup> gives

$$a_\mu(h) = (66.7 \pm 8.1) \times 10^{-9} \quad (12)$$

I should note that the relative smallness of the hadronic contribution to the electron anomaly ( $< 10^{-11}$ ) renders it an essentially QED quantity; the corollary of this statement being, of course, that it is less sensitive to a breakdown of QED through vacuum polarization effects.

To end I must take into account the contribution of the weak interaction to the anomalous magnetic moment of the muon. The four-fermion weak interaction is negligibly small ( $\sim 10^{-12}$ ), but in the renormalizable gauge theories there are specific effects on the anomaly arising from the emission and reabsorption of virtual intermediate bosons. However, in general the size of the contribution is critically dependent upon the parameters of the theory and only in the simplest standard version<sup>8)</sup> are the parameters sufficiently well established to give predictions for the muon anomaly of  $(2.1 \pm 0.2) \times 10^{-9}$ .

The addition of the contributions of strong and weak interactions to the value of the muon anomaly calculated in QED yields for the most recent theoretical prediction:

$$a_\mu(\text{theory}) = (1165921 \pm 8.3) \times 10^{-9} \quad (13)$$

3.

The experimental technique employed in the measurements of the lepton g-factors naturally fall into two groups, the resonance and precession methods. In both technique the lepton is in a static magnetic field, but while the precession method involves the direct observation of the spin precession, the resonance method involves the application of oscillatory electromagnetic

field and the observation of the induced transitions between the lepton energy levels.

I start by considering a simple configuration in which the muon moves with a low velocity on a circular orbit in a plane perpendicular to an uniform static magnetic field  $\vec{B} = (0, 0, B_z)$ . The momentum vector rotates at the cyclotron angular frequency  $\omega_c$  given by

$$\vec{\omega} = \frac{e\vec{B}}{mc} \quad (14)$$

while the Larmor spin precession frequency is the same as for the particle at rest

$$\vec{\omega}_L = \frac{2\mu \vec{B}}{h} = g \left( \frac{e\vec{B}}{2mc} \right) = \left( 1 + a_\mu \right) \left( \frac{e\vec{B}}{mc} \right) \quad (15)$$

For  $g = 2$  these two frequencies are equal and the muon would maintain its initial polarization direction with respect to its momentum vector. For  $g > 2$  the spin turns faster than the momentum vector; the relative frequency  $\omega_a$  being given by

$$\vec{\omega}_a = \vec{\omega}_L - \vec{\omega}_c = a_\mu \left( \frac{e}{mc} \right) \vec{B} \quad (16)$$

This is the basic equation for  $(g - 2)$  precession experiments. The equation (16) underlines the basis of the experiments which is to contain the particle orbits in a known magnetic field and measure the angle between the spin and direction of motion as a function of time. The value  $(e/mc)$  is deduced from the spin precession frequency of muons at rest. This latter result is obtained in a different experiment, but the two values of  $B$  are both measured in terms of the proton magnetic resonance frequency and consequently the measurement of  $\omega_a$  and  $\omega_L$  can be used to deduce  $a$ .

A muon makes about a thousand turns in the field for the relative spin direction to rotate through one cycle. Thus an accurate measurement of the anomaly will require the muons to be stored for many thousand of turns. This give rise to a particular problem with muons since their lifetime at rest is only 2.2  $\mu$ sec. To some extent this difficulty can be avoided by making use of relativistic time dilation and in the three CERN experiments there is a clear trend towards the use of muons of higher and higher energies. I must reexamine the basic equations with which I started this discussion since they were derived specially for low velocities.

The cyclotron frequency must now be written as

$$\vec{\omega}_c = \frac{e\vec{B}}{\gamma mc} \quad (17)$$

where  $\gamma = (1 - \beta^2)^{\frac{1}{2}}$  and  $\beta = v/c$ .

The circular motion of the particle leads to a relativistic effect first pointed out by Thomas<sup>9</sup>) in which the particle rest frame, when viewed from the laboratory appears to rotate with a precession frequency  $\vec{\omega}_T$  given by

$$\vec{\omega}_T = \left(1 - \frac{1}{\gamma}\right) \frac{e\vec{B}}{mc} \quad (18)$$

This angular velocity is in the opposite sense to the spin precession in the muon rest frame and so the net angular rotation frequency of the spin in the laboratory is

$$\vec{\omega}_s \equiv \vec{\omega}_L - \vec{\omega}_T = \left(a_\mu + \frac{1}{\gamma}\right) \left(\frac{e}{mc}\right) \vec{B} \quad (19)$$

From (19) and (17) I obtain

$$\vec{\omega}_a \equiv \vec{\omega}_s - \vec{\omega}_c = a_\mu \left(\frac{e}{mc}\right) \vec{B} \quad (20)$$

The (g - 2) precession frequency is unaffected by time dilation since the relativistic treatment leads to the same conclusion as our previous discussion.

I briefly recall that the principal features of the lepton (g - 2) experiment are a polarized source, a uniform magnetic field and a polarimeter. An effective polarimeter would be one which measures  $s, \beta$  as function of the storage time spent in the magnetic field<sup>1</sup>). This quantity oscillated with the frequency  $\omega_a$ . The muons are produced by the decay of pions in flight, and are born longitudinally polarized in the pion rest frame. Furthermore the muon waves a flag to show which way its spin is pointing at the moment of decay; in fact, in the process  $\mu^+ \rightarrow e^+ + \nu + \bar{\nu}_\mu$ , the electron angular distribution has its maximum in the direction of the muon spin. By observing a large number of decays from an ensemble of muons, one can measure the mean spin direction to any desired accuracy. Thus, the pion-muon decay and the muon-electron decay provide a very simple polarized source and an efficient

polarimeter. The ideal ( $g - 2$ ) experiment consists, then, of trapping longitudinally polarized muons in a uniform magnetic field and measuring the precession frequency  $\omega_a$  of the spin relative to the velocity vector via the decay electron asymmetry.

I have to draw your attention to the fact that the phenomenon under consideration is oscillatory in nature, like the motion of a pendulum, and therefore the more oscillations we measure then the more precise will be the determination of the angular frequency  $\omega_a$ . Therefore it is advantageous to store charged particles in the uniform magnetic field for as long as possible. In the case of the measurement of the ( $g - 2$ ) of electrons, this is easily achieved, the electron being stable particles. In the case of the muon it is necessary to dilate the lifetime by going to high energies. In doing this a real gain is made since, as we have seen, the angular frequency  $\omega_a$  does not depend upon the muon energy. Thus through the lengthening of the muon lifetime, as measured in the laboratory, the storage time is increased, and the ( $g - 2$ ) modulation of the decay electrons can be followed out over a longer period of time ( $\tau = \gamma \tau_0$ . It has been done good use of special relativity!).

I should like to describe briefly only the third experiment carried out at CERN. This is the more precise one. One of the major difficulty in the ( $g - 2$ ) precession experiment as I have described using formula (20) is the use of a radial magnetic field gradient necessary to provide the vertical focusing; this implies a magnetic field variation typically of  $\pm 0.1\%$  over the aperture in which the muons are stored, and a corresponding radial dependence of  $\omega_a$ . Even if the mean radius is determined precisely after injection, uncertainty in radius would arise from uncontrolled muon losses. A better experiment can be done if one removes the dependence of  $\omega_a$  on  $r$  without destroying the vertical focusing. The forces that hold the muon in its orbit and give focusing for small deviations from equilibrium arise from what appears in the muons rest frame as an electric field, while the spin precession arises from what appears there as a magnetic field. These two fields may be varied independently by applying suitable magnetic and electric fields in the laboratory frame. The equations of the motion in classical configuration of transverse fields ( $\vec{B} \cdot \vec{B} = \vec{E} \cdot \vec{E} = 0$ ) are

$$\frac{d\vec{\beta}}{dt} = \vec{\omega}_c \times \vec{\beta} \quad ; \quad \frac{d\vec{\sigma}}{dt} = \vec{\omega}_s \times \vec{\sigma} \quad (21)$$

where  $\omega_c$  and  $\omega_s$  are shifted from the values given in equations (17) and (19) owing to the presence of the electric field. They are now given by (10)

$$\vec{\omega}_c = \frac{e}{mc} \left[ \frac{\vec{B}}{\gamma} - \left( \frac{\gamma}{\gamma^2-1} \right) \vec{\beta} \times \vec{E} \right] \quad (22)$$

$$\vec{\omega}_s = \frac{e}{mc} \left[ \left( a + \frac{1}{\gamma} \right) \vec{B} - \left( \frac{1}{\gamma^2-1} - a - \frac{\gamma}{\gamma^2-1} \right) \vec{\beta} \times \vec{E} \right] \quad (23)$$

in which the additional electric field terms are evident. The precession of the spin relative to the velocity vector is

$$\vec{\omega}_a \equiv \vec{\omega}_s - \vec{\omega}_c = \frac{e}{mc} \left[ a \vec{B} - \left( \frac{1}{\gamma^2-1} - a \right) \vec{\beta} \times \vec{E} \right] \quad (24)$$

$$\vec{\omega}'_a = \vec{\omega}_a + \frac{e}{mc} \left( \frac{1}{\gamma^2-1} - a \right) \vec{\beta} \times \vec{E} \quad (25)$$

This equation emphasizes the point that the trapping potential shifts the observed frequency from desired value  $\omega_a$ . This shift is zero for the special choice of particle energy equivalent to

$$\gamma = \left( 1 + \frac{1}{a} \right)^{\frac{1}{2}} = 29.3 \quad (26)$$

For muons this is equivalent to a momentum of 3.098 GeV and it is at this value that the muon storage ring is designed to operate.

This equation tells us that, if we seek to reduce the problems of magnetic-field averaging by making  $B$  uniform and employ an electric field for vertical focusing, then there is a shift in the relative spin precession frequency away from the desired value  $\omega_a$ . However, it is also clear that this shift is zero if  $\gamma$  satisfies the value given in equation (26). Of course, in practice  $\vec{B}$  is not completely uniform and there is some spread of muon momentum ( $\pm 0.7\%$ ) about the central "magic" value, but the overall result of this particular choice of design means that the uncertainties in obtaining "a" from the measured precession frequency are at the level of a few p.p.m. To apply the corrections due to the slight inhomogeneity of the magnetic and the effect of the electric fields, the momentum or equilibrium orbit distribution of the muon sample is measured by observing the fast rotation of a narrow muon bunch at early times.

## 4.

A plan view of the storage ring is shown in Fig. 2. At each cycle of the CERN Proton Synchrotron a pion beam with momentum spread of  $\pm 0.75\%$  is injected into the volume where the muons are to be stored by means of a pulsed inflector. The pions have slightly higher momentum than the 3.098 GeV/c for which the magnetic field of the storage ring is set. Consequently they tend to leave the ring on the outside, but before they do so about a tenth of them decay. The over-all trapping efficiency of stored muons produced per injected pion is about  $10^{-4}$ . The advantage of this method of producing the stored muon population is that the sample has high initial polarization in excess of 90% owing to the fact that the muons are selected from the top 1.5 % of the available momentum range and hence maximum use is made of the complete polarization of the muons in the pion rest frame. We have already discussed the crucial role that parity non-conservation plays in both the provision and detection of the muon polarization<sup>1</sup>).

As can be seen from Fig. 2 the storage ring consisted of 40 bending magnets placed around the circumference of a ring of 14 m diameter. The magnets were C-shaped in section with their open sides towards the centre of the ring, and had pole pieces so shaped that their ends fitted together to form a 40-sided polygon.

The electrodes (also shown in cross-section in Fig. 2), which provided the trapping potential for vertical motion of the particles, were mounted inside vacuum tank sections which each covered a sector of the ring equivalent to four magnets blocks in length. To accommodate the pion inflector a complete sector was left free of electrodes, and in order to keep the closed orbit distortion to a minimum the sector diametrically opposite the inflector was also left without electric field.

The decay electrons were detected by 22 energy-sensitive shower counters spread evenly around the inside of the ring. The time spectrum of the recorded counts is displayed in Fig. 3. The characteristic exponential decay can clearly be seen, as can the modulation at the  $(g - 2)$  frequency which is due to the selection of the larger pulse heights; that is, just the application of an energy cut on the decay electrons as discussed in reference<sup>1</sup>.

In order to apply the small corrections due to the slight inhomogeneity of the magnetic field and the effect of the electric field, it is necessary to know how the muon momenta or equilibrium orbits are distributed. This is measured by observing the rotation of the narrow (10 nsec) bunch of muons around the ring just after injection. At this early time the decay electron time spectrum clearly shows the rotating bunch, and the way in which this bunch

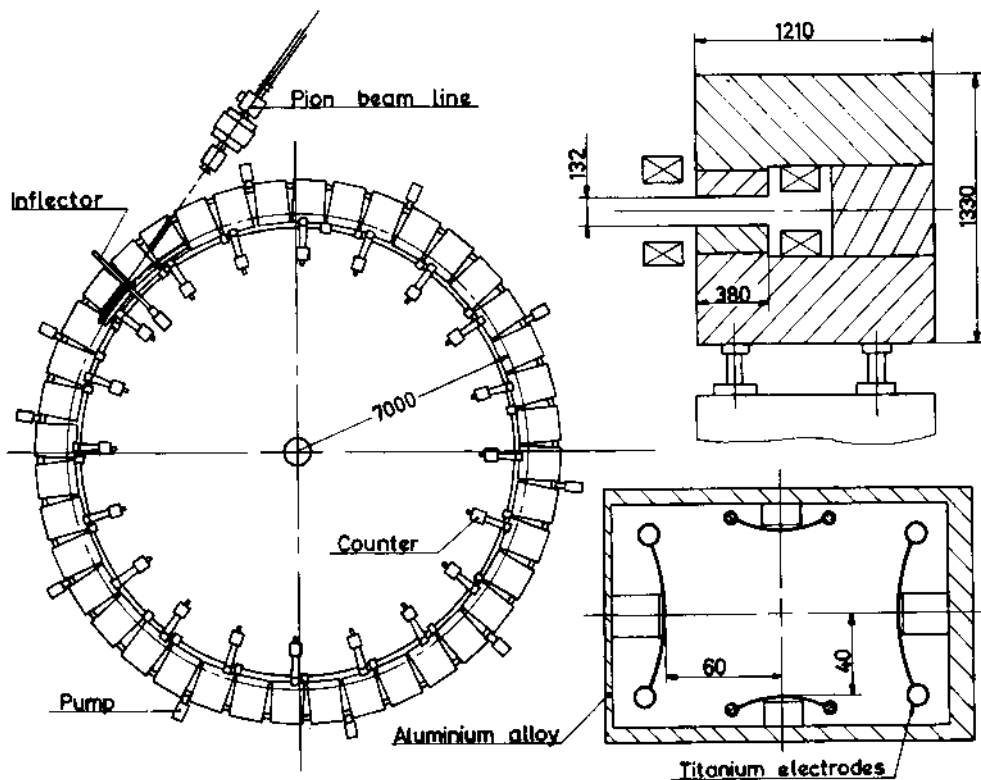


Fig. 2. Scheme of the muon storage ring, which consists of 40 contiguous magnet blocks. The open side of the C-shaped yoke (upper right) faces the centre of the ring. The cross-section of the vacuum chamber and electric quadrupole is shown at the bottom right. The decay electrons are detected by 20 counters. Dimensions are in mm.

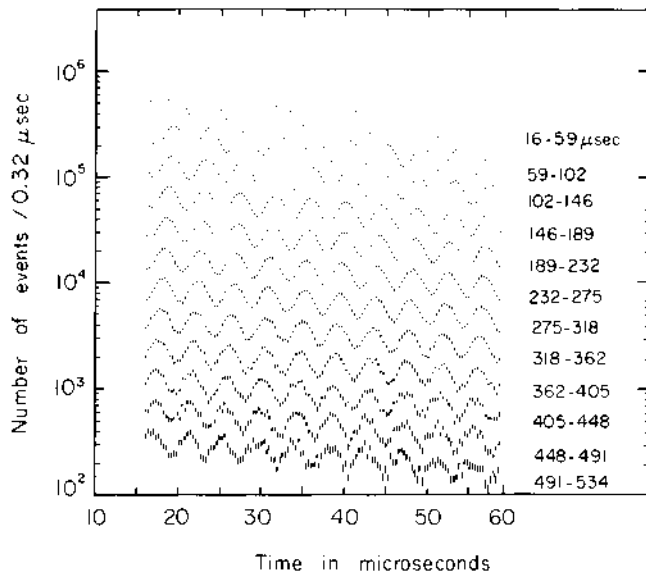


Fig. 3. Time distribution of decay electrons. The time range shown is  $(g - 2)$  cycles.

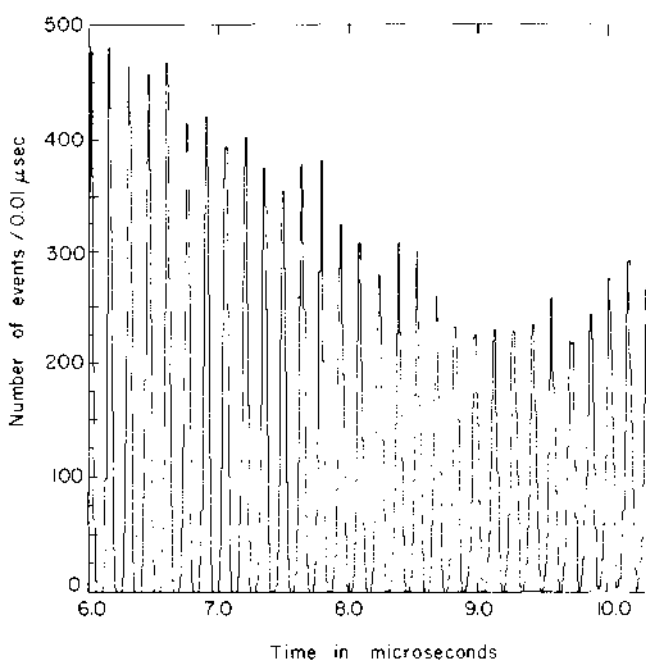


Fig. 4. The fast rotation pattern. This is the count rate at early time which clearly shows the muon bunch rotating around the ring with a period of 147 ns.

disperses in time is used to obtain the momentum distribution, see fig. 4.

The value of  $\omega_a$  obtained from the data, as shown in Fig. 3, was converted into a value of the anomaly by means of the magnetic field measurements. These were made at about a quarter of a million points throughout the storage volume both before and after a sequence of runs. The field values were obtained in terms of the proton magnetic resonance frequency and, after averaging over the muon equilibrium orbit distribution and applying corrections for shielding and calibration of the probes, the resulting mean magnetic field seen by the muon sample was expressed in terms of the effective mean Larmor frequency of protons in vacuum. The over-all average value of  $R$ , the ratio of the  $(g - 2)$  frequency to this effective mean Larmor frequency, was <sup>1)</sup>

$$R = 3.707213(27) \times 10^{-3} . \quad (27)$$

The final step in obtaining the anomaly  $a$  requires the ratio  $\lambda$  of the Larmor frequency of the muon to that of the proton (or equivalently the ratio of their magnetic moments). Recent measurements of this ratio have been made by Crowe et al.<sup>11)</sup> and Casperson et al.<sup>12)</sup>. The two values are in good agreement, and the weighted average is

$$\lambda = 3.1833417(39) , \quad (28)$$

which, when inserted into the equation

$$a_\mu = R/(\lambda - R) , \quad (29)$$

gives the results <sup>1)</sup>

$$a_\mu^+ = (1165912 \pm 11) \times 10^{-9} \quad (39)$$

$$a_\mu^- = (1165938 \pm 12) \times 10^{-9}$$

which together provide the average experimental value of the muon anomaly,

$$a_\mu = (1165924 \pm 8) \times 10^{-9} , \quad (31)$$

in excellent agreement with the theoretical prediction

$$a_{\mu} = (1165920 \pm 10) \times 10^{-9}. \quad (32)$$

5.

I will discuss here briefly the principle used by Dehmelt and his co-workers<sup>13)</sup> to measure the  $(g - 2)$  of the electron. This is a spectacular experiment where ingenuity, elegance and ability makes of an experiment a piece of art.

In general the measurements of the lepton g-factors are made on leptons trapped in a region of homogeneous magnetic field, and in order that the measurement may be made to high precision it is necessary that the additional field which provides the trapping should not greatly perturb the system.

In the Dehmelt's experiment the electrons are confined within a Penning trap which takes the form of a uniform magnetic field of 18.3 KG within a cylindrically symmetric electric quadrupole field superimposed. The electric potential  $V(r, z)$  has the form

$$V(r, z) = \frac{V_0}{b^2}(r^2 - 2z^2) \quad (33)$$

This potential is provided by two caps ( $V = -V_0$ ) shaped to the surfaces,  $z_s^2 = 1/2 (r^2 + b^2)$ , and a ring electrode ( $V = +V_0$ ) which has the shape  $r^2 = b^2 + 2z^2$ ; the dimension  $b$  equals 0.473 cm.

The non-relativistic Hamiltonian for the electron, including the spin-dependent part, is given by

$$H = \frac{\vec{p}^2}{2m} - eV + \mu_0 \frac{g}{2} (\vec{\sigma} \cdot \vec{B}) \quad (34)$$

where the kinetic momentum operator has the minimal coupling form

$$\vec{p} = -i\hbar\vec{v} + e \frac{\vec{A}}{c} \quad (35)$$

For a uniform magnetic field  $B = (0, 0, B_z)$ , the vector potential is

$$\vec{A} = \left( -y \frac{B_z}{2}, x \frac{B_z}{2}, 0 \right) \quad (36)$$

The Schrödinger equation with this Hamiltonian has been solved by Sokolow and Pavlenko, and the eigenvalues are given in terms of the integer quantum numbers  $n$ ,  $n_z$  and  $n_m$ , and the spin quantum number  $m_s$  by

$$E = \hbar (n + 1/2)\omega_c' + (n_z + 1/2)\omega_z - (n + 1/2)\omega_m + \omega_L m_s \quad (37)$$

$$n, n_z, n_m = 0, 1, 2, \dots, \quad m_s = \pm 1/2$$

The first term involves the cyclotron orbital motion at the modified frequency given by

$$\omega_c' = \frac{eB}{mc} - \omega_m = \omega_0 - \omega_m; \quad \frac{\omega_c'}{2\pi} = 51 \text{ GHz} \quad (38)$$

The second term is due to the quantized axial oscillations whose fundamental frequency depends only upon the electrostatic field,

$$\omega_z = 2 \left( \frac{V_0 e}{mb^2} \right)^{1/2}; \quad \frac{\omega_z}{2\pi} = 59 \text{ MHz} \quad (39)$$

The third term represents the contribution to the energy from the magnetron oscillations which is slow in comparison with the cyclotron motion. In this ideal axial symmetric trap the centre of the cyclotron orbit circulates around the x-axis with the frequency

$$\omega_m = \frac{\omega_0}{2} \left[ 1 - \left( 1 - \frac{2\omega_z^2}{\omega_0^2} \right)^{1/2} \right]; \quad \frac{\omega_m}{2\pi} = 34 \text{ KHz} \quad (40)$$

Among all these frequencies the following relation exists

$$2\omega_c' \cdot \omega_m = \omega_z^2 \quad (41)$$

The final term in eq. (37) is just the energy due to the two possible orientations of the electron spin with respect to  $B_z$  (i.e.  $m_s = \pm 1/2$ )

The inequality

$$0 < \frac{eV_0}{b^2} < \frac{e^2 B^2}{8mc} \quad (42)$$

defines the domain of the applied voltage  $V_0$  for which the electron will remain confined within the trap. - The lower limit has to be satisfied in order that the vertical motion is stable while the upper limit ensures stability of the radial motion.

In the limit of extremely weak trapping potential ( $V_0 \rightarrow 0$ ) the energy eigenvalues reduce to the Rabi-Landau levels

$$E = \hbar\omega_0 \left[ n + \frac{1}{2} + \frac{g}{2} m_s \right] \quad (43)$$

The determination of the anomaly  $a_e$  involves the measurement of the ratio of the frequencies  $\omega_a$  and  $\omega_0$ . This ratio can be written

$$a_e = \frac{\omega_a}{\omega_0} = \frac{\omega'_a - \omega_m}{\omega'_c + \omega_m} \quad (44)$$

where  $\omega_a = \omega_L - \omega_c$ . Thus in order to obtain  $a_e$  three frequencies have to be measured, and in practice these frequencies are  $\omega_c$ ,  $\omega_a$  and  $\omega_m$ , from which  $\omega_m$  may be deduced by means of equation (41).

The remarkable feature of the electron ( $g - 2$ ) experiment is that measurements are made on a single electron confined in the trap. The description of the very elegant ( $g - 2$ ) electron and positron experiments will require a new lecture that has not been planned. I do invite the students here present to study the literature of the electron ( $g - 2$ ) experiment published by Dehmelt and co-workers because it constitutes a short but elegant course in atomic physics and in advanced technology.

The results obtained by Dehmelt and co-workers are the following:

$$a_e^{\text{exp}} = 1159652200(40) \times 10^{-12} \quad (45)$$

to be compared with the best theoretical value of  $a_e$  to order  $\alpha^3$ :

$$a_e^{\text{the}} = 1159652569(150) \times 10^{-12} \quad (46)$$

For positrons:

$$a_{e^+}^{\text{exp}} = 1159652222(50) \times 10^{-12} \quad (47)$$

By combining the measured electron and positron anomalies one obtain a preliminary matter/antimatter comparison of

$$g(e^+)/g(e^-) = 1 + (22 \pm 64) \times 10^{-12} \quad (48)$$

The same ratio for the muons is

$$g(+)/g(-) = 1 - (26 \pm 16) \times 10^{-9} \quad (49)$$

The two experiments consist of trapping either muons or electrons in an electromagnetic trap. In the case of the electron the trap is typically  $1 \text{ cm}^3$  and in the case of the muon it is about  $4 \times 10^5 \text{ cm}^3$ . In the electron experiment an electron has been trapped for at least one day, in the muon experiment  $1.4 \times 10^8$  decay muons has been recorded. If one take into account that each of them has a dilated lifetime of  $64 \mu\text{sec}$  it has been explored in total about  $10^4 \text{ sec}$  i.e.  $1/8$  of a day.

This is what one have to pay if one wishes to make an experiment with an unstable particle!

In doing an experiment with muons one profits from the mass square dependence of the many effects which have been mentioned above in the text. It is clear that the two experiments test QED and in the case of the muons other effects are explored.

## 6.

In the muon experiment an accurate measurement of the muon lifetime in a circular orbit has been done. This experiment provides a stringent test of Einstein's theory of special relativity. As a bonus it sheds light on the so-called twin paradox, gives an upper limit to the granularity of space time, and tests the CPT invariance of weak intraction.

The muon is an unstable particle, and can therefore be regarded as a clock and used to measure the time dilation predicted by special relativity. The existence of cosmic-ray muons at ground level supports the idea of time dilation, for, if the muon lifetime was not lengthened in flight, they would all decay in the upper atmosphere<sup>14)</sup>. Experiments verifying the time dilation in a straight path have also been made with high energy accelerators<sup>15)</sup>. Recently Hafele and Keating<sup>16)</sup> loaded cesium atomic clock on to a commercial aircraft on an around-the-world trip and verified the time dilation at low velocity with an accuracy of about 10 %.

In the CERN Muon Storage Ring, the muon performs a round trip and so when compared with the muon at rest the experiment mimics closely the twin paradox already discussed in Einstein's first paper<sup>17)</sup>. The circulating muons, although they return again and

again to the same place, should remain younger than their stay-at-home brothers. It is indeed observed that the moving muons live longer, in agreement to one part in a thousand with the prediction of special relativity. The stationary twin's time scale is given by the muon decay rate at rest determined in a separate experiment.

An accurate measurement of the muon lifetime in a circular orbit at  $\gamma \simeq 29.3$  requires high orbit stability in a short time interval (a few hundred microseconds), for any loss of muons will set a limit to the accuracy of the measurement. The stability in the Muon Storage Ring was achieved by using a scraping system that shifted the muon orbits at early times in order to "scrape off" those muons most likely to be lost.

The experiment consisted of measuring the decay electron counting rate

$$N(t) = N_0 \exp(-t/\tau) [1 - A \cos(\omega_0 t + \sigma)] \quad (50)$$

and the fitting procedure gave the value of  $\tau = \gamma \tau_0$ . The value of  $\gamma$  was given by

$$\gamma = \lambda f_p / (1 + a) f_r = 29.327(4) \quad (51)$$

where  $f_r$  is the rotation frequency of the muons and is a measured quantity in the Ring. The best value for the lifetime at rest is  $2.19711(8) \text{ sec}^{18}$ , which gives a predicted value of  $\tau = 64.435(9) \mu\text{sec}$ .

The experimental value obtained by fitting the decay electron counting rate is  $\tau = 64.378(29) \mu\text{sec}$  in good agreement with the expected value; thus the transformation of time is validated to an accuracy of  $-(0.9 \pm 0.4) \times 10^{-3}$ . Corrections were made in order to measure the muon lifetime with an accuracy of 0.1 % for residual small loss of stored muons, for variations of the photomultiplier gain accompanying the recovery from the initial flash, and the background counts due to stored protons, in the case of  $\mu^+$ .

Another check on relativity theory can be obtained by comparing  $(g - 2)$  measurements carried out at different value of  $\gamma$ . It is worthwhile pointing out that in the case of the electron, for example, the value of the rest-frame electron magnetic moment, extracted on the basis of the quantum electrodynamic model from the Michigan data for 100 keV electrons exhibiting a 20% relativistic mass increase, agrees with the value measured at University of Washington for a  $\sim 1 \text{ meV}$  electron to 3 parts to  $10^9$ . This constitutes another rather stringent test of the model for a kinetic energy variation of  $1:10^8$ .

In the case of the muon, where the relativistic effects are dominant similar test and with comparable accuracy can be established. As pointed out by Combley and co-workers<sup>19)</sup> when comparing the (g - 2) experiments at different values of the conclusions are model dependent, but one can make a plausible case that these results confirm the relativistic transformation laws for magnetic field and mass, as well as for time.

## REFERENCES

1. F. H. Combley, F.J.M. Farley and E. Picasso, Phys. Rep. A68:95 (1981).  
F. J. M. Farley and E. Picasso, Ann. Rev. Nucl. Part. Sci. 29:243 (1979).  
J. H. Field, E. Picasso and F.H. Combley, Sov. Phys. Usp. 22:199 (1979).  
F. H. Combley, Report on Progress in Physics, 42:1889 (1979).
2. J. D. Jackson, CERN 77:17 (1977).
3. P. A. M. Dirac, Proc. Roy. Soc. 133A:60 (1931); Phys. Rev. 74:817 (1948).
4. J. S. Schwinger, Phys. Rev. 73:416 (1948); Phys. Rev. 75:898 (1949).
5. P. T. Olsen and E.R. Williams, Atomic Masses and Fundamental Constants 5:538 (1975) (New York, Plenum Press).
6. B. D. Josephson, Phys. Letters 1:251 (1962).
7. J. Calmet, S. Narison, M. Perrottet and E. de Rafael, Rev. Mod. Phys. 49:21 (1977).
8. A. Salam in Elementary Particles, ed. N. Svartholm, pp. 367. Stockholm, ed. Almqvist & Wikjells, 1968.  
S. Weinberg, Phys. Rev. Lett. 19:1264 (1967).
9. L. H. Thomas, Nature 117:514 (1926).
10. J. Bailey and E. Picasso, Progr. Nucl. Phys. 12:43 (1970).
11. K. M. Crowe, J.F. Hague, J.E. Rothberg, A. Schenck, D. L. Williams, R.W. Williams, K.K. Youngs, Phys. Rev. D5:2145 (1972).
12. D. E. Casperson, T.W. Crane, A.B. Denison, P.O. Egan, V.W. Hughes, F.G. Mariam, H. Orth, H.W. Reist, P.A. Souder, R.D. Stambaugh, P.A. Thompson, G. zu Putlitz, Phys. Rev. Lett. 38:956 (1977).

13. R. S. Van Dyck, P.B. Schwinberg, H.G. Dehmelt, Phys. Rev.Lett. 38:310 (1977).  
H. G. Dehmelt in *Atomic Physics*, ed. D. Kleppner and Pipkin, Plenum 1981.  
P. B. Schwinberg, R.S. Van Dyck and H.G. Dehmelt (to be published) Preliminary comparison of the positron and electron spin anomalies, Dept. of Phys. University of Washington, Seattle, Washington 98195.
14. B. Rossi, D.B. Hall, Phys. Rev. 59:223 (1941).
15. J. Bailey, K. Borer, F. Combley, H. Drummm, F.J.M. Farley, J.H. Field, W. Flegel, P.M. Hattersley, F. Krienen, F. Lange, E. Picasso, W. von Rüden, *Nature* 268:301 (1977).
16. J. C. Hafek and Keating, *Science* 177:166 (1972).
17. A. Einstein, *Ann. Phys.* 17:891 (1905).
18. M. P. Bolandin, V.N. Crebenyuk, V.G. Zinov, A.D. Konin, A.N. Ponomarev, *Sov. Phys. Jetp.* 40:811 (1974).
19. F. Combley, F.J.M. Farley, J.H. Field, E. Picasso, *Phys. Rev. Lett.* 42:1383 (1979).

## ELECTRON-ELECTRON CORRELATION IN HIGHLY CHARGED ATOMS

W.R. Johnson and K.T. Cheng

Department of Physics  
University of Notre Dame  
Notre Dame, Indiana 46556

and

Argonne National Laboratory  
Argonne, Illinois 60439

### ABSTRACT

The relativistic random-phase approximation (RRPA) is introduced to account for electron-electron correlation in atoms and ions of high nuclear charge where non-relativistic many-body methods are inadequate. To provide a basis for this study of the RRPA, the Dirac-Fock (DF) theory is reviewed. Applications of the DF equations to determine inner-electron binding energies in heavy atoms are given illustrating the influence of relativistic effects in situations where correlations are unimportant. The RRPA equations are derived as natural generalizations of the DF equations. Examples of RRPA calculations of discrete excitations and of photoionization are given illustrating situations where both relativistic and correlation effects play important roles.

### REVIEW OF THE DIRAC-FOCK THEORY

To set a framework for our study of correlation effects in highly charged atoms we briefly review the central field DF approach to atomic structure calculations. The Dirac-Fock theory is based on an approximate relativistic Hamiltonian<sup>1</sup>

$$H_0 = \sum_{i=1}^N h_i + \sum_{i>j} \frac{e^2}{r_{ij}} \quad (1.1)$$

where  $h = \vec{a} \cdot \vec{p} + \beta m - e^2 Z/r$  is the usual one-electron Dirac Hamiltonian. Although the application of  $H_0$  to atomic structure problems has been criticized,<sup>3-5</sup> its use in connection with DF calculations has been recently justified from the point of view of quantum electrodynamics.<sup>6</sup> A DF wave function is constructed as a Slater determinant of single-electron Dirac orbitals  $u_i(\vec{r})$  in parallel with the usual non-relativistic Hartree-Fock (HF) procedure. These orbitals  $u_i(\vec{r})$  are assumed to be orthonormal positive energy solutions to a central field Dirac equation. The expectation value of the Hamiltonian  $H_0$  in Eq. (1.1) is then expressed as a functional of the orbitals  $u_i(\vec{r})$  and the variational principle is applied to this functional to obtain the DF equations for the orbitals  $u_i$ :

$$(h+V)u_i = \epsilon_i u_i \quad i=1, \dots, N \quad (1.2)$$

The quantity  $V$  is a self-consistent DF potential

$$V u = \sum_{i=1}^N e^2 \int \frac{d^3 r'}{|\vec{r} - \vec{r}'|} [(u_i^\dagger u_i)' u - (u_i^\dagger u)' u_i] \quad (1.3)$$

The equations (1.2) and (1.3) are similar to the non-relativistic HF equations but there are two important differences; the single-electron Hamiltonian  $h$  is a Dirac Hamiltonian and the orbitals  $u_i(\vec{r})$  are Dirac orbitals. The Dirac orbitals  $u_i(\vec{r})$  may be separated into radial and spin-angle functions and Eqs. (1.2) and (1.3) reduced to coupled radial equations.<sup>7</sup> Positive energy solutions to the resulting radial self-consistent field equations may then be obtained numerically.<sup>8</sup>

The DF eigenvalue  $\epsilon_i$  has the physical significance of being the "frozen-orbital" approximation to the binding energy of an electron in state  $i$ .<sup>9</sup> To get some notion of the importance of relativistic effects in situations where correlation is expected to be insignificant we compare the non-relativistic HF eigenvalues and the relativistic DF eigenvalues with experimentally measured K-shell binding energies.

In Figure 1 we plot experimental K-shell binding

energies determined by Bearden and Burr<sup>10</sup> against  $Z$ . It is interesting to note that the non-relativistic Coulomb binding energy of a 1s electron ( $Z^2$ Ry) gives a good approximation to the data in Figure 1, but this agreement arises only because of an accidental cancellation between relativistic and screening effects.

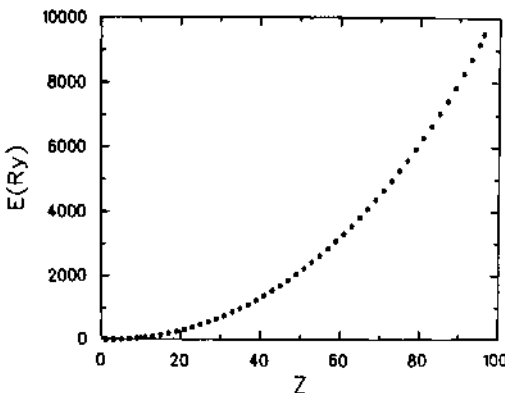


Fig. 1. Experimental K-shell binding energies as determined by Bearden and Burr, Ref. 10, are plotted against nuclear charge.

In Fig. 2 HF eigenvalues<sup>11</sup> and DF eigenvalues<sup>12</sup> are compared with the data from Figure 1. The error in the HF approximation varies from -3% at  $Z=10$  to 12% at  $Z=90$ . The error at low  $Z$  is primarily due to the relaxation and correlation effects not included in the "frozen-orbital" HF approximation while the error at high  $Z$  is mainly due to relativity. To see that this is indeed the case we note that the DF approximation in Fig. 2 agrees with the HF approximation at low  $Z$  where electronic velocities are small and reduces the discrepancy between the HF approximation and measurement

from 12% to -1% at high  $Z$ . It is of interest to examine the extent to which the residual difference between the DF approximation and measurement shown in Fig. 2 can be accounted for without considering correlation effects.

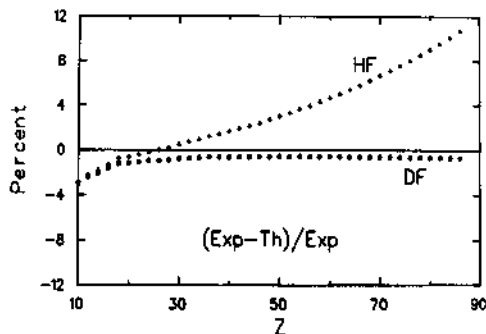


Fig. 2. Relative difference between frozen orbital calculations of K-shell binding energies and the measurements of Ref. 10. HF calculations are from Ref. 11 and DF calculations are from Ref. 12.

Before discussing this problem it should be mentioned that the DF calculations used in Fig. 2 include the effects of finite nuclear size on the atomic orbitals. These finite size effects are incorporated in the single-electron Hamiltonian  $h$  by replacing the Coulomb potential by a potential due to the nuclear charge density  $\rho(\vec{r})$ :

$$- \frac{e^2 Z}{r} + e \int \frac{\rho(\vec{r}')}{|\vec{r} - \vec{r}'|} d^3 r' \quad (1.4)$$

The nuclear charge density is taken to be a Fermi-distribution with parameters determined from electron-nucleus scattering measurements.<sup>13</sup> Finite nuclear size corrections to K-binding energies grow roughly as  $Z^4$  and reduce the theoretical K-binding energy in mercury ( $Z=80$ ) by about 4 Ry.

Even within the DF framework the comparison of orbital eigenvalues with inner electron binding energies is incorrect since such a comparison ignores the relaxation of atomic orbitals when an inner electron is removed from the atom. To account for relaxation one must carry out separate DF calculations for the atom and ion and subtract the resulting total atomic and ionic energies. One then obtains

$$E(\text{atom}) - E(\text{ion}) = \epsilon_i - \Delta E_i \quad (1.5)$$

where  $\epsilon_i$  is the DF eigenvalue of the atomic electron being removed and  $\Delta E_i$  is a relaxation correction to the binding energy of that electron. For the K-shell of mercury the relaxation correction reduces the theoretical binding energy by about 7 Ry.

Table I. Binding Energies of Inner-Shell Electrons (eV) of Noble Gas Atoms.

Shell	Z	Frozen <sup>a</sup>	Relaxed <sup>b</sup>	Experiment <sup>c</sup>
Argon	18			
K		3241.6	3209.2	3206.0 <sup>e</sup>
L <sub>I</sub>		337.7	327.2	
L <sub>II</sub>		262.1	250.5	247.3(3) <sup>d</sup>
L <sub>III</sub>		259.8	248.3	245.2(3)
Krypton	36			
K		14413.6	14359.3	14325.6(8)
L <sub>I</sub>		1961.4	1933.6	1921.2(6)
L <sub>II</sub>		1765.4	1735.0	1722.2(5)
L <sub>III</sub>		1711.1	1681.3	1674.9(5)
Xenon	54			
K		34756.3	34690.0	34561.4(11)
L <sub>I</sub>		5509.4	5472.4	5453.8(4)
L <sub>II</sub>		5161.5	5120.4	5103.7(4)
L <sub>III</sub>		4835.6	4796.0	4782.2(4)

a) Ref. 12, b) Ref. 14, c) Ref. 15, d) Ref. 10

The effect of including relaxation on inner electrons is illustrated in Table I where we list frozen-orbital,<sup>12</sup> relaxed<sup>14</sup> and experimental binding energies<sup>10,15</sup> for the inner K- and L- shells of the noble gases argon, krypton, and xenon. For the K-shell of argon the 1% error in the frozen orbital

approximation is reduced to about 0.1% while in krypton the error is reduced from 0.6% to 0.2% and in xenon from 0.6% to 0.4%. The situation for L-shells is quite similar, inclusion of relaxation effects in inner-shell binding calculations improves the agreement between the DF approximation and experiment substantially.

From Table I we see that the residual difference between theory and experiment is a rapidly increasing function of nuclear charge. This residue is due in part to the omission of terms arising from transverse photon exchange in the Hamiltonian  $H_0$ . Such terms lead to a frequency dependent modification<sup>1,16</sup> of the Breit interaction, viz:

$$H_{\text{trans}} = -e^2 \left( \frac{\cos \omega R}{R} \vec{a}_1 \cdot \vec{a}_2 + \vec{a}_1 \cdot \vec{\nabla} \vec{a}_2 \cdot \vec{\nabla} \frac{\cos \omega R - 1}{\omega^2 R} \right), \quad (1.6)$$

where  $R = |\vec{r}_1 - \vec{r}_2|$  and  $\omega = \omega_1 - \omega_2$ . Neglecting terms of order  $(\omega R)^2 \sim \alpha^2 Z^2$  the transverse interaction reduces to the Breit interaction<sup>1</sup>.

$$H_{\text{Br}} = -\frac{e^2}{2R} (\vec{a}_1 \cdot \vec{a}_2 + \vec{a}_1 \cdot \hat{R} \vec{a}_2 \cdot \hat{R}). \quad (1.7)$$

The influence of the Breit interaction on the binding energies of K-, L-, and M-shell electrons in mercury is illustrated in Table II. In the second column we list the relaxed DF energies as determined by Huang et al.,<sup>17</sup> and in the third column we list the Breit correction to these energies as obtained from a relaxed perturbation theory calculation. Comparison of the resulting DF + Breit energies with the experimental values shows that the Breit interaction accounts for a major part of the discrepancy between the relaxed DF eigenvalues and experiment.

Electron self-energy and vacuum polarization corrections account for most of the remaining difference between DF calculations and experiment. For high Z atoms the electron self-energy has been studied numerically by Desiderio and Johnson<sup>18</sup> for 1s electrons with Z in the range of 70-90 using the method outlined by Brown, Langer and Schaefer,<sup>19</sup> and by Mohr<sup>20,21</sup> for 1s, 2s, and 2p electrons with Z < 137. The effects of

Table II. Breit Interaction and QED Corrections to  
Inner Shell Binding Energies (au) for Mercury.

Shell	DF <sup>a</sup>	Breit	DF+Breit	QED	Exp <sup>b</sup>
K	3070.7	-11.15	3059.6	3053.9	3054.2(3)
L <sub>I</sub>	548.1	-1.23	546.9	546.0	545.5(3)
L <sub>II</sub>	524.5	-2.09	522.4	522.4	522.3(2)
L <sub>III</sub>	453.0	-1.32	451.7	451.6	451.6(2)
M <sub>I</sub>	131.9	-0.22	131.7	131.7	131.1(4)
M <sub>II</sub>	121.4	-0.39	121.0	121.0	120.7(5)
M <sub>III</sub>	105.3	-0.23	105.1	105.1	104.8(2)
M <sub>IV</sub>	88.1	-0.17	88.0	88.0	87.8(1)
M <sub>V</sub>	84.7	-0.11	84.6	84.6	84.5(1)

a) Ref. 17, b) Ref. 10

finite nuclear size on the 1s Lamb shift have been considered by Cheng and Johnson.<sup>22</sup> Vacuum polarization in heavy atoms has been studied by Wichmann and Kroll<sup>23,24</sup> and the finite nuclear size corrections to vacuum polarization have been worked out by Gyulassy<sup>25</sup>.

In column 5 of Table II the influence of the electron self-energy and vacuum polarization corrections on the binding energies of the inner shells of mercury are shown.<sup>17</sup> The resulting theoretical values are seen to agree with the experimental measurements to within one or two times the experimental errors. This comparison for mercury is typical of other heavy atoms and leads to a high degree of confidence in DF calculations for those applications in which correlation effects are expected to be insignificant.

By correlation we understand those effects arising

from the difference between the electron-electron Coulomb interaction and the approximate DF central potential. In the following paragraphs we describe the RRPA which is a natural extension of the DF theory accounting for many of the important effects of correlation, and we give applications to photoexcitation and photoionization problems where both relativistic and correlation effects are significant.

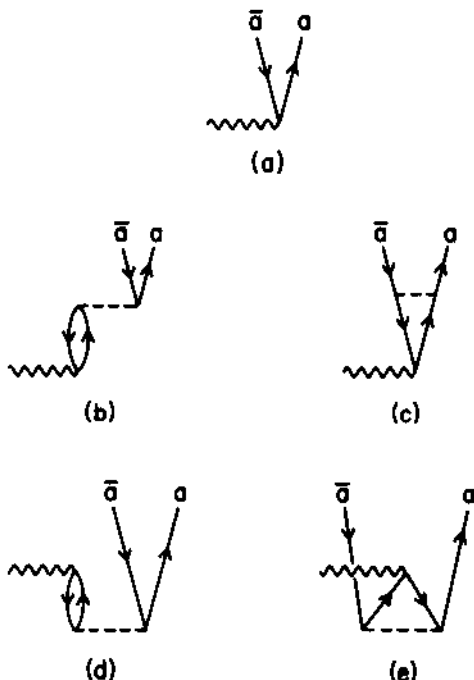


Fig. 3. Lowest order Feynman diagrams contributing to the RRPA amplitude.

— Electron in a Dirac-Fock potential;

--- Coulomb part of the photon propagator;

~~~~ External photon; a and  $\bar{a}$ , electron and hole labels, respectively.

## RELATIVISTIC RANDOM-PHASE APPROXIMATION

The governing equations of the RRPA may be developed from quantum electrodynamics using perturbation theory, or alternatively from time dependent Hartree-Fock (TDHF) theory. In the perturbation approach, the ground state is taken to be the Fermi-level of a closed-shell system with  $N$  electrons, and a diagrammatic method may be used to describe the excitation of the ground state caused by an external photon. The lowest order terms included in photoexcitation processes are illustrated in the Feynman diagrams of Fig. 3. The RRPA transition amplitude is obtained from these diagrams by iteration at the photon vertex.<sup>26</sup>

In Fig. 3, we consider only the Coulomb part of the electron-electron interaction and omit the transverse part which leads to the Breit interaction. We also omit radiative corrections which lead to the Lamb shift. Errors due to the omission of the Breit interaction and the Lamb shift are insignificant for many practical applications, and when corrections for these effects are required, they may be accounted for as perturbations.<sup>27</sup> Errors due to the omitted Coulomb terms in higher order diagrams, on the other hand, are more difficult to assess; nevertheless, experience with a large number of applications of the non-relativistic random-phase approximation with exchange (RPAE) shows that such calculations in general agree very well with experimental measurements.<sup>28</sup> In the past few years, there have been extensive applications of the RRPA to photoexcitation<sup>27,29-36</sup> and photoionization.<sup>37-47</sup> A brief account of the RRPA theory will be given in the next few paragraphs, followed by examples of these calculations.

As mentioned previously, the RRPA equations can be obtained by linearizing the TDHF equations<sup>48</sup> describing the response of an atom to a time dependent external field  $v(t)$ . The Hamiltonian of the system is given by:

$$H = H_0 + \sum_{i=1}^N v_i(t) , \quad (2.1)$$

where  $H$  is the approximate relativistic Hamiltonian given in<sup>49</sup> Eq. (1.1). Starting from the time dependent variational principle<sup>49</sup>

$$\langle \delta \Psi | H - i \frac{\partial}{\partial t} | \Psi \rangle = 0 \quad , \quad (2.2)$$

we seek a stationary solution to the above equation with the trial wavefunction:

$$\Psi(\vec{r}_1, \vec{r}_2, \dots, \vec{r}_N, t) = \frac{1}{\sqrt{N!}} \begin{vmatrix} \phi_1(\vec{r}_1, t) \dots \phi_1(\vec{r}_N, t) \\ \vdots & \vdots \\ \phi_N(\vec{r}_1, t) \dots \phi_N(\vec{r}_N, t) \end{vmatrix} \quad (2.3)$$

In the absence of the time dependent external field, the single electron Dirac wave functions are given by  $\phi(\vec{r}, t) = u(\vec{r})e^{-i\omega t}$ , and the variational calculation leads to the usual Dirac-Fock (DF) equations for the atomic ground state given in Eqs. (1.2) and (1.3). Application of a time dependent external field,  $v(t) = v_+ e^{-i\omega t} + v_- e^{i\omega t}$  induces a time dependent perturbation to the orbitals:

$$u(\vec{r}) \rightarrow u(\vec{r}) + w_+(\vec{r})e^{-i\omega t} + w_-(\vec{r})e^{i\omega t} + \dots \quad . \quad (2.4)$$

Neglecting higher order terms, the RRPA equations for the first order perturbed orbitals,  $w_{i\pm}$ , can be obtained from the linearized TDHF equations as:

$$[h + V - (\epsilon_{i\pm} + \omega)] w_{i\pm} = -V_{\pm}^{(1)} u_i, \quad i = 1, 2, \dots, N, \quad (2.5)$$

where the first order perturbed potential  $V_{\pm}^{(1)}$  is given by:

$$\begin{aligned} V_{\pm}^{(1)} u_i &= \sum_{j=1}^N \int \frac{d^3 r'}{|\vec{r} - \vec{r}'|} \left[ (u_j^\dagger w_{j\pm})' u_i - (u_j^\dagger u_i)' w_{j\pm} \right. \\ &\quad \left. + (w_{j\pm}^\dagger u_j)' u_i - (w_{j\pm}^\dagger u_i)' u_j \right] . \end{aligned} \quad (2.6)$$

If we leave out the driving term  $-V_{\pm}^{(1)} u_i$ , Eq. (2.5) reduces to the excited state DF equation for  $w_{i\pm}$ , with excitation energy  $\omega$  (there is no non-trivial physical solution to  $w_{i-}$  in the DF approximation for  $\omega \ll 2mc^2$ ). Correlation effects are included in the RRPA through the

perturbed potential  $v^{(1)}$  which induces couplings between excitation channels  $u_i \rightarrow w_{i\pm}$ . The eigenvalues  $\omega$  of Eq. (2.5) provide an approximation to the excitation spectrum of the atom, including a discrete range and a continuum. The positive frequency components of the eigenfunctions,  $w_{i+}$ , describe atomic excited states including final state correlations illustrated in Fig. 3(b,c), while  $w_{i-}$  describes ground state correlations illustrated in Fig. 3(d,e). More detailed discussions of the RRPA equations and their physical implications can be found in Refs. 40 and 50.

In radiative processes, the electron-photon interaction in the Coulomb gauge is given by  $v_+ = ea \cdot \vec{A}$  and  $v_- = v_+$ . The transition amplitude from the ground state to an excited state is then given by:

$$T = \sum_{i=1}^N e \int d^3r [w_{i+}^\dagger \vec{a} \cdot \vec{A} u_i^+ + u_i^\dagger \vec{a} \cdot \vec{A} w_{i-}] . \quad (2.7)$$

An important property of the RRPA transition amplitude is that it is gauge invariant. The oscillator strengths calculated in the length gauge are the same as those calculated in the velocity gauge in contrast to other approximate many-body methods (such as DF theory applied to excited states) which give gauge dependent transition amplitudes. In practical applications, we usually truncate the RRPA equations to simplify numerical calculations, with the result that the transition amplitudes are no longer gauge invariant. The degree of gauge dependence can then be used as a measure of the truncation error.

The RRPA has been applied to treat discrete excitations in highly stripped ions where both relativity and correlation are important. Allowed and forbidden transitions for ions in the  $He^{27,29-31}$ ,  $Be^{12}$ ,  $Mg^{12}$ ,  $Zn^{34,35}$  and  $Ne^{36}$  sequences have been studied. We present selected examples here to illustrate the utility of the RRPA technique. A more detailed summary of these results is given in Ref. 51.

In the Be sequence, the electric dipole interaction induces four interaction channels:  $1s \rightarrow np_{1/2}$ ,  $np_{3/2}$  and  $2s \rightarrow np_{1/2}$ ,  $np_{3/2}$  (actually, there are eight coupled channels in RRPA calculations if we count positive and negative frequency channels separately). For the transition of the  $(2s^2)^1S$  ground state to the  $(2s2p)^1P^0$  excited state, we first omit contributions from  $1s$  channels and obtain truncated RRPA

values. As we can see from Table III, the agreement between length and velocity form oscillator strengths is poor for these "frozen-core" calculations. The full RRPA calculation including all excitation channels retains gauge invariance of the transition matrix elements, as reflected in the perfect agreement between length and velocity form results.

Table III. Oscillator Strengths of the Resonance Transition  $(2s^2)^1S - (2s2p)^1P^0$  for Be-like Ions.

|                   |          | Truncated RRPA <sup>a</sup> | Full RRPA <sup>a</sup> | MCDF <sup>b</sup> |
|-------------------|----------|-----------------------------|------------------------|-------------------|
| Ar <sup>14+</sup> | length   | 0.199                       | 0.198                  | 0.208             |
|                   | velocity | 0.228                       | 0.198                  | 0.173             |
| Mo <sup>38+</sup> | length   | 0.140                       | 0.140                  | 0.140             |
|                   | velocity | 0.151                       | 0.140                  | 0.134             |

a) Lin and Johnson, Ref. 32

b) Cheng and Johnson, Ref. 52

We include also in Table III the multiconfiguration Dirac-Fock (MCDF) results of Cheng and Johnson<sup>52</sup> for comparison purposes. As one can see, the length form results in all three calculations are in agreement with each other, while the velocity form results are quite sensitive to approximations involved in the calculations. This suggests that the length gauge may be preferred in transition calculations where gauge invariance is violated.

In Table IV, we present some results of a truncated RRPA calculations for Mg-like ions in which only excitations of the  $3s^2$  valence electrons are included and excitations of the core electrons are omitted. In spite of this approximation, the excitation energies of the resonance transition,  $(3s^2)^1S - (3s3p)^1P^0$ , are in good agreement with experiment. Furthermore, length and velocity form oscillator strengths agree to within one

Table IV. Excitation Energies  $\omega$  (in atomic units) and Length Form Oscillator Strengths  $f_L$  of the Resonance Transition  $(3s^2)^1S-(3s3p)^1po$ , for Mg-like Ions.

|          |                   | $Ar^{6+}$           | $Fe^{14+}$         | $Mo^{30+}$        |
|----------|-------------------|---------------------|--------------------|-------------------|
| $\omega$ | RRPA <sup>a</sup> | 0.7798              | 1.605              | 3.93              |
|          | MCDF <sup>b</sup> | 0.7928              | 1.628              | 3.97              |
|          | Experiment        | 0.7779 <sup>c</sup> | 1.604 <sup>d</sup> | 3.89 <sup>e</sup> |
| $f_L$    | RRPA <sup>a</sup> | 1.27                | 0.83               | 0.55              |
|          | MCDF <sup>b</sup> | 1.25                | 0.82               | 0.54              |

a) Shorer, Lin and Johnson, Ref. 33

b) Cheng and Johnson, Ref. 53

c) Moore, Ref. 54

d) Cowan and Widing, Ref. 55

e) Hinnov, Ref. 56

or two percent, and are in good agreement with corresponding MCDF length form results of Cheng and Johnson.<sup>53</sup> The success of the frozen-core approximation in this case can be attributed to a tight Ne-like core. By contrast, a similar two-channel frozen-core calculation for the resonance transition,  $(4s^2)^1S-(4s4p)^1po$ , in Zn-like ions<sup>54</sup> no longer includes dominant correlation effects, as the 3d10 core is easily polarized, resulting in 10-20% changes in the oscillator strengths when 3d excitation channels are included in the calculation.<sup>55</sup>

The RRPA has been applied to studies of low energy atomic photoionization of rare gas atoms. Subshell cross sections as well as angular distribution and spin polarization of photoelectrons are calculated, and results are in good agreement with experiment. A few examples of these studies are presented here, with emphasis on the interplay between correlation and relativity in photoionization processes. Only length form RRPA results are given, as they agree with velocity form results to within a few percent in all these calculations.

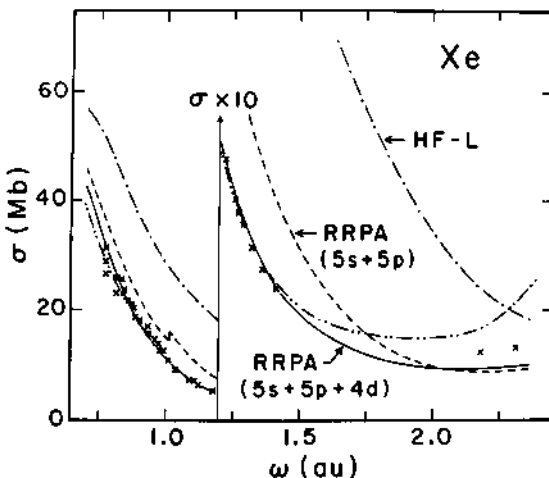


Fig. 4. Photoionization cross sections for xenon as functions of photon energy  $\omega$ . Experiment: —·— West and Morton, Ref. 57;  $\times$  Samson, Ref. 58. Theory: — and —— RRPA, three- and two-shell correlation results, respectively, Ref. 41; —— Kennedy and Manson, Ref. 59.

### i) Total Cross Sections

In Fig. 4, we show total photoionization cross sections for xenon atoms. One general observation that can be made is that correlation effects as measured by the difference between HF<sup>59</sup> and RRPA<sup>41</sup> results are sizeable. Moreover, the inclusion of excitation channels of the 4d shell in the RRPA calculation substantially improves the agreement between theory and experiment, reflecting the importance of core

polarization effects in xenon. It should be mentioned here that no relativistic effects show up in total cross sections and that RRPA results are generally in close agreement with nonrelativistic RPAE calculations<sup>23</sup> for rare gas atoms.

### ii) Partial Cross Section Branching Ratios

Non-relativistically, there is no distinction between subshells of the same fine structure, so the partial cross section branching ratio for two such subshells will be the "statistical ratio" given by their relative occupations. Experimentally, it has been known for some time that the branching ratios of outer np cross sections for rare gases depart from the statistical ratio of 2.60. In Fig. 5, the RRPA branching ratios  $\sigma(2^2P_{3/2}) : \sigma(2^2P_{1/2})$  in xenon are compared with measurements<sup>60,61</sup> and with DF<sup>62</sup> and Dirac-Slater (DS) results.<sup>61</sup>

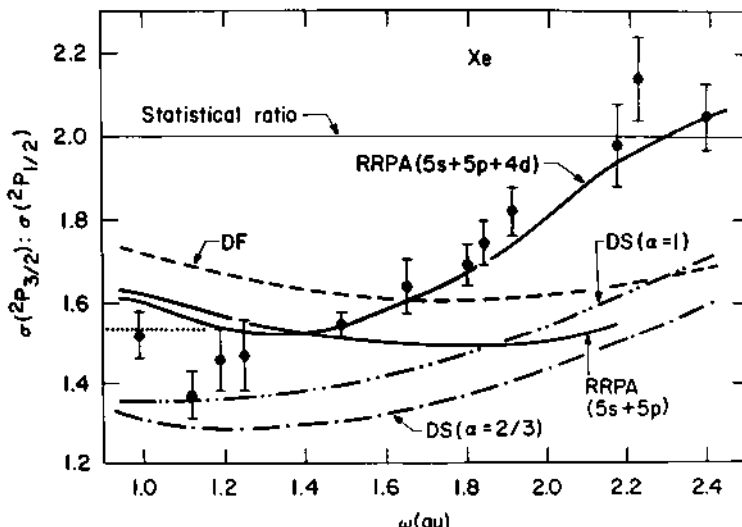


Fig. 5. The  $2^2P_{3/2} : 2^2P_{1/2}$  branching ratios for xenon as functions of photon energy  $\omega$ . Experiment: ..... Samson et al., Ref. 60;  $\pm$  Wuilleumier et al., Ref. 61. Theory — RRPA, Ref. 41; - - - Ong and Manson, Ref. 62; — · — and — · — · — Wuilleumier et al., Ref. 61.

The three-shell ( $5s+5p+4d$ ) RRPA calculation is seen to represent experimental values better than the uncorrelated calculation. Similar RRPA calculations have been reported for the  $\sigma(4^2D_{5/2})$ :  $\sigma(4^2D_{3/2})$  branching

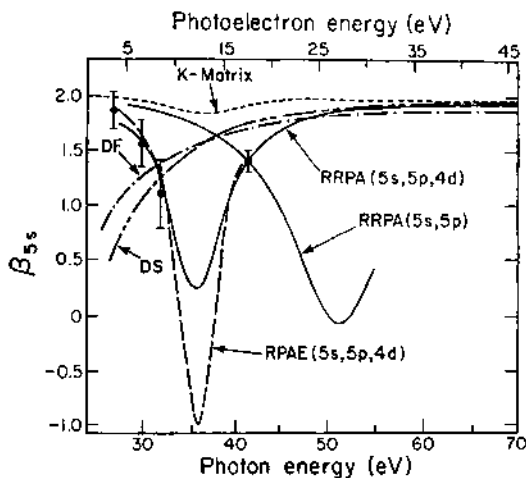


Fig. 6. The asymmetry parameters  $\beta$  for the  $5s$  shell of xenon as functions of photon energy  $\omega$ . Experiment:  $\blacksquare$  Dehmer and Dill, Ref. 63;  $\blacksquare$  White et al., Ref. 64. Theory: — RRPA, Refs. 38, 41; - - - Cherepkov, Ref. 65; - - - Huang and Starace, Ref. 66; - - - Ong and Manson, Ref. 67; - - - Walker and Waber, Ref. 68.

ratio in xenon.<sup>39</sup> Because of the sensitivity of branching ratios to both correlation and relativity, such measurements provide interesting tests of relativistic many-body theories.

## iii) Angular Distributions

In the dipole approximation, the photoionization differential cross section is given by:

$$\frac{d\sigma}{d\Omega} = \frac{\sigma}{4\pi} [1 - \frac{1}{2}\beta P_2(\cos\theta)] . \quad (2.8)$$

Here,  $\theta$  is the angle between the photon momentum  $\vec{k}$  and the electron momentum  $\vec{p}$ ,  $\sigma$  is the photoionization cross section and  $\beta$  is the angular distribution asymmetry parameter.

For the  $5s \rightarrow ep$  photoionization in xenon, nonrelativistic calculation shows that  $\beta = 2$ , independent of photon energy, whereas relativistically,  $\beta$  can depart from 2 because of the interference between  $5s \rightarrow ep_{1/2}$  and  $5s \rightarrow ep_{3/2}$  channels. Experimentally, deviations from the value of 2 for  $\beta_{5s}$  have been observed near the Cooper minimum of the  $5s$  partial cross section.

As shown in Fig. 6, successful explanations of these data again come from relativistic many-body calculations which account for dominant correlation effects - in this case, the RRPA three-shell ( $5s$ ,  $5p$ ,  $4d$ ) correlation calculations.

## iv) Spin Polarization

Even with unpolarized incident radiation, the photoelectron is in general polarized in the direction perpendicular to the reaction plane defined by the incident radiation and the outgoing electron. In the dipole approximation, the degree of polarization  $P_y (y \parallel \vec{k} \times \vec{p})$  is given by:<sup>69-71</sup>

$$P_y = \frac{\eta \sin\theta \cos\theta}{1 - \frac{1}{2}\beta P_2(\cos\theta)} \quad (2.9)$$

In Fig. 7, the measured spin polarization parameters  $\eta$  of the  $5p$  shell are given, along with various theoretical results. Once again, we find good agreement between experiment<sup>72</sup> and the RRPA three-shell calculation.<sup>42</sup> Similar RRPA studies of the  $\eta$ -parameter for  $ns \rightarrow ep$  photoionization in rare gases have been reported.<sup>43</sup> Sizeable polarization is found near the Cooper minima in spite of the non-relativistic

prediction that there should be no spin polarization for the ns photoelectrons.

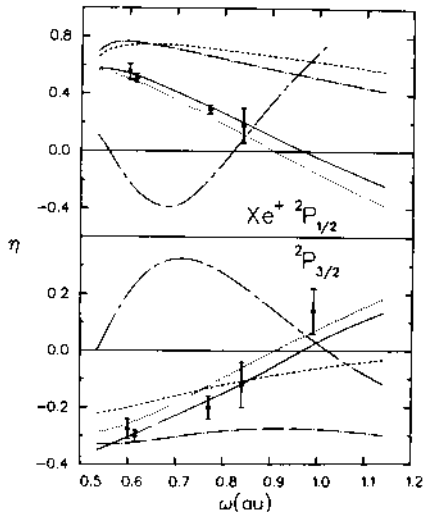


Fig. 7. Spin polarization parameter  $\eta$  of xenon 5p shell photoionization. Experiment: Heinzmann, Schönhense and Kessler, Ref. 72. Theory: — RRPA, Ref. 42; ..... Cherepkov, Ref. 73 (note that there is a sign error in this reference): - - - , - - - , - - - multichannel quantum defect results of Ref. 72 obtained with different sets of parameters from Refs. 74, 75 and 76 respectively.

#### v) Autoionization

To analyze autoionization resonances, it is not convenient to solve the RRPA equations directly, since the computer time required to scan through a family of resonances would be prohibitive. As an alternative, we

use the method of multichannel quantum defect theory (MQDT) pioneered by Seaton<sup>77</sup> and Fano<sup>78</sup> to impose boundary conditions on the RRPA equations. Sets of eigen-channel quantum defect parameters are then obtained at several energies in the autoionizing region of the spectrum. In spite of rapid variations of physical observables such as cross sections, angular distributions, ... etc. in the resonance region, these quantum defect parameters are smooth functions of energy which can be interpolated or extrapolated. At any energy point, we can reconstruct transition amplitudes and hence  $\sigma$ ,  $\beta$ ,  $\eta$ , ... etc. from these parameters. A detailed description of this procedure is given in Ref. 46. Ab initio studies of the inner shell resonances  $1s \rightarrow np$  in Be-like ions<sup>46</sup> and the Beutler-Fano resonances in rare gases<sup>48,47</sup> have been reported. We shall give an example here to show the validity of this method.

The low lying spectra of the rare gases consists of five interacting Rydberg series, three of which arise from excitations of outer  $P_{3/2}$  electrons to  $ns_{1/2}$ ,  $nd_{3/2}$  and  $nd_{5/2}$  states, and two of which arise from excitations of outer  $P_{1/2}$  electrons to  $ns_{1/2}$  and  $nd_{3/2}$  states (termed  $ns'$  and  $nd'$ , respectively). The first three series converge to the  $^2P_{3/2}^0$  threshold, while the remaining two converge to the  $^2P_{1/2}^0$  threshold. Between the  $^2P_{3/2}^0$  and  $^2P_{1/2}^0$  thresholds, we thus have two series of autoionizing resonances - the Beutler-Fano resonances<sup>79,80</sup> - arising from the  $ns'$  and  $nd'$  states. In Fig. 8, we compare our calculated resonance profiles in xenon with recent experimental measurements by Eland.<sup>81</sup> As one can see, the general features of the autoionization profiles consist of sharp  $ns'$  resonances superimposed on broad  $nd'$  resonances. The observed spectrum is well represented by the theory, except for the rapid decrease in the size of the  $ns'$  peaks which is due to finite instrumental resolution.

In Fig. 9, we compare the RRPA prediction of the angular distribution  $\beta$ -parameters for xenon near the  $(6d', 8s')$  resonances with the measurements of Samson and Gardner,<sup>82</sup> and with two MQDT calculations by Dill<sup>74</sup> and by Geiger<sup>76</sup> based on empirical quantum-defect parameters. The overall agreement is good, except for detailed features near the  $8s'$  resonances.

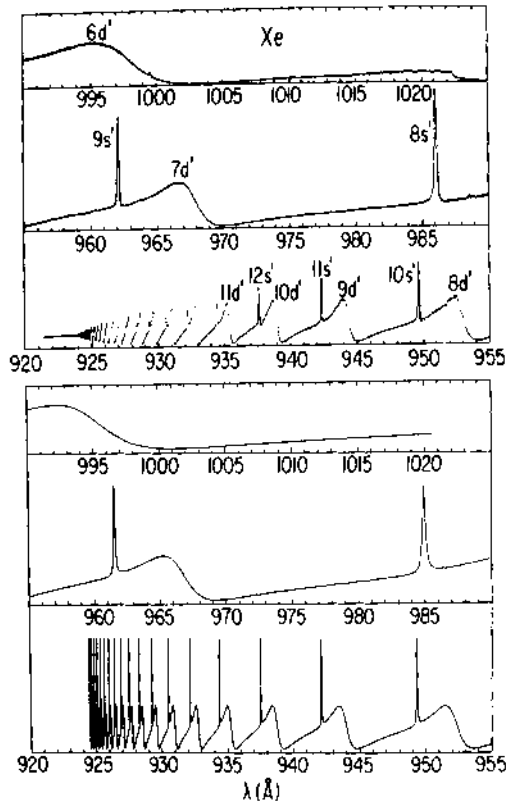


Fig. 8. Photoionization spectra of xenon between the  $2P_{3/2}^0$  and  $2P_{1/2}^0$  thresholds. The upper graph shows experimental data obtained by Eland (Ref. 81) with a photon resolution width of 0.07 Å, and the lower graph shows RRPRA results of Ref. 47.

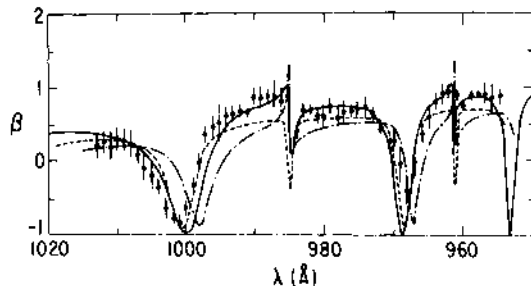


Fig. 9. Angular distribution asymmetry parameters  $\beta$  plotted against photon wavelength  $\lambda$  in the autoionization region of xenon. Experiment:  $\diamond$  Samson and Gardner, Ref. 82. Theory: — RRPA, Ref. 47; —·— Dill, Ref. 74; - - - Geiger, Ref. 76,

## CONCLUSION

In the previous sections, we gave a brief review of atomic structure calculations using the RRPA. There are other possible applications of RRPA in addition to those mentioned here. One important application is the study of elastic scattering of photons, together with associated analysis of atomic susceptibilities and shielding factors, especially for high  $Z$  atoms and ions.<sup>53</sup> Another important application of the RRPA is to the study of parity non-conserving (PNC) neutral weak currents in atoms;<sup>54</sup> relativistic RPA studies of core shielding corrections to PNC interaction have been reported by Harris et al.<sup>55</sup>

The RRPA is found to include dominant correction effects in atomic processes and is very successful in dealing with closed shell systems. It is desirable to develop similar relativistic many-body techniques for open shell systems.

## ACKNOWLEDGEMENTS

The RRPA is developed through the collaboration of C.D. Lin, A. Dalgarno, P. Shorer, C.M. Lee, K.-N. Huang, V. Radojević and M. LeDourneuf. The work of WRJ is supported in part by the National Science Foundation. The work of KTC is supported by the Division of Basic Energy Sciences of the U.S. Dept. of Energy.

## REFERENCES

1. H.A. Bethe and E.E. Salpeter Quantum Mechanics of One- and Two-Electron Atoms (Spring, Berlin, 1957), p. 170.
2. G.E. Brown and D.G. Ravenhall, Proc. Roy. Soc. (London) A208, 525 (1951).
3. J. Sucher, Phys. Rev. A22, 384 (1980).
4. M.H. Mittleman, Phys. Rev. A5, 2395 (1972).
5. G. Feinberg and J. Sucher, Phys. Rev. Lett. 26, 6811 (1971).
6. M.H. Mittleman, Phys. Rev. A (to be published).
7. I.P. Grant, Adv. Phys. 19, 747 (1970).
8. J.P. Desclaux, Comp. Phys. Comm. 9, 31 (1975).
9. T. Koopmans, Physica 1, 104 (1933).
10. J.A. Bearden and A.F. Burr, Rev. Mod. Phys. 39, 125 (1967).
11. C. Froese Fischer, The Hartree-Fock Method for Atoms (Wiley, New York, 1977).
12. J.R. Mann (private communication).
13. R. Hofstadter, Ann. Rev. Nucl. Sci. 7, 231 (1957).
14. N. Beatham, I.P. Grant, B.J. Kinzie, and S.J. Rose, Physica Scripta 21, 423 (1980).
15. R. Deslattes, Phys. Rev. 186, 1 (1969).
16. J.R. Mann and W.R. Johnson, Phys. Rev. A4, 41 (1971).
17. K.-N. Huang, M. Aoyagi, M.H. Chen, B. Crasemann and H. Mark, Atomic Data and Nuclear Data Tables 18, 243 (1976).
18. A.M. Desiderio and W.R. Johnson, Phys. Rev. A3, 1267 (1971).
19. G.E. Brown, J.S. Langer, and G.W. Schaefer, Proc. Roy. Soc. (London) A251, 92 (1959).
20. P.J. Mohr, Ann. Phys. (N.Y.) 88, 26 (1974); 88, 52 (1974).
21. P.J. Mohr, Phys. Rev. Lett 34, 1050 (1975).
22. K.T. Cheng and W.R. Johnson, Phys. Rev. A14, 1943 (1976).
23. E.H. Wichmann and N.M. Kroll, Phys. Rev. 96, 232 (1954).
24. E.H. Wichmann and N.M. Kroll, Phys. Rev. 101,

- 843 (1956).
25. M. Gyulassy, Phys. Rev. Lett. 33, 921 (1974).
26. See for example, A.L. Fetter and J.D. Walecka, Quantum Theory of Many-Particle Systems (McGraw-Hill, New York, 1971), p. 156.
27. W.R. Johnson and C.D. Lin, Phys. Rev. A14, 565 (1976).
28. M. Ya Amusia and N.A. Cherepkov, Case Studies in Atomic Physics 5, 47 (1975).
29. C.D. Lin, W.R. Johnson and A. Dalgarno, Phys. Rev. A15, 154 (1977).
30. W.R. Johnson, C.D. Lin and A. Dalgarno, J. Phys. B9 L303 (1976).
31. C.D. Lin, W.R. Johnson and A. Dalgarno, Astrophys. J. 217, 1011 (1977).
32. C.D. Lin and W.R. Johnson, Phys. Rev. A15, 1046 (1977).
33. P. Shorer, C.D. Lin and W.R. Johnson, Phys. Rev. A16, 1109 (1977).
34. P. Shorer and A. Dalgarno, Phys. Rev. A16, 1502 (1977).
35. P. Shorer, Phys. Rev. A18, 1060 (1978).
36. P. Shorer, Phys. Rev. A20, 642 (1979).
37. W.R. Johnson and C.D. Lin, J. Phys. B10, L331 (1977).
38. W.R. Johnson and K.T. Cheng, Phys. Rev. Lett. 40, 1167 (1978).
39. W.R. Johnson and V. Radojević, J. Phys. B11 L773 (1978).
40. W.R. Johnson and C.D. Lin, Phys. Rev. A20, 964 (1979).
41. W.R. Johnson and K.T. Cheng, Phys. Rev. A20, 978 (1979).
42. K.-N. Huang, W.R. Johnson and K.T. Cheng, Phys. Rev. Lett. 43, 1658 (1979).
43. K.T. Cheng, K.-N. Huang and W.R. Johnson, J. Phys. B13, L45 (1980).
44. K.-N. Huang, W.R. Johnson and K.T. Cheng, Phys. Lett. 77A, 234 (1980).
45. W.R. Johnson and M. LeDourneuf, J. Phys. B13, L13 (1980).
46. C.M. Lee and W.R. Johnson, Phys. Rev. A22, 979 (1980).
47. W.R. Johnson, K.T. Cheng, K.-N. Huang and M. LeDourneuf, Phys. Rev. A22, 989 (1980).
48. A. Dalgarno and G.A. Victor, Proc. R. Soc. A291, 291 (1966).
49. See, G.E. Brown, Unified Theory of Nuclear Models (North-Holland, Amsterdam, 1967) p. 49, 59.
50. P. Shorer, Thesis, Harvard University (1979).

51. W.R. Johnson, C.D. Lin, K.T. Cheng and C.M. Lee, *Physica Scripta* 21, 409 (1980).
52. K.T. Cheng and W.R. Johnson, *Phys. Rev.* A15, 1326 (1977).
53. K.T. Cheng and W.R. Johnson, *Phys. Rev.* A16, 263 (1977).
54. C.E. Moore, Atomic Energy Levels NSRDS-NBS 35 (U.S. Government Printing Office, Washington, D.C., 1971), Vol. I.
55. R.D. Cowan and K.G. Widing, *Astrophys. J.* 180, 285 (1973).
56. E. Hinov, *Phys. Rev.* A14, 1533 (1976).
57. J.B. West and J. Morton, *At. Data Nucl. Data Tables* 22, 103 (1978).
58. J.A.R. Samson, *Adv. At. Mol. Phys.* 2, 177 (1966).
59. D.J. Kennedy and S.T. Manson, *Phys. Rev.* A5, 227 (1972).
60. J.A.R. Samson, J.L. Gardner and A.F. Starace, *Phys. Rev.* A12, 1459 (1975).
61. F. Wuilleumier, M.Y. Adam, P. Bhez, N. Sandner, V. Schmidt and W. Mehlhorn, *Phys. Rev.* A16, 646 (1977).
62. W. Ong and S.T. Manson, *J. Phys.* B11, L163 (1978).
63. J.L. Dehmer and D. Dill, *Phys. Rev. Lett.* 37, 1049 (1976).
64. M.G. White, S.H. Southworth, P. Kobrin, E.D. Poliakoff, R.A. Rosenberg and D.A. Shirley, *Phys. Rev. Lett.* 43, 1661 (1979).
65. N.A. Cherepkov, *Phys. Lett.* 66A, 204 (1978).
66. K.-N. Huang and A.F. Starace, *Phys. Rev.* A21, 697 (1980).
67. W. Ong and S.T. Manson, *J. Phys.* B11, L65 (1978).
68. T.E.H. Walker and J.T. Waber, *J. Phys.* B7, 674 (1974).
69. N.A. Cherepkov, *Sov. Phys.-JETP* 38, 463 (1974).
70. C.M. Lee, *Phys. Rev.* A10, 1598 (1974).
71. K.-N. Huang, *Phys. Rev.* A22, 223 (1980).
72. U. Heinzmann, G. Schönhense and J. Kessler, *Phys. Rev. Lett.* 42, 1603 (1979).
73. N.A. Cherepkov, *J. Phys.* B11, L435 (1978).
74. D. Dill, *Phys. Rev.* A7, 1976 (1973).
75. J. Geiger, *Z. Phys.* A276, 219 (1976).
76. J. Geiger, *Z. Phys.* A282, 129 (1977).
77. M.J. Seaton, *Proc. Phys. Soc.* 88, 801 (1966).
78. U. Fano, *J. Opt. Soc. Am.* 65, 979 (1975).
79. H. Beutler, *Z. Phys.* 93, 177 (1935).
80. U. Fano, *Nuovo Cimento* 12, 154 (1935).
81. See J. Berkowitz, Photoabsorption, Photoionization and Photoelectron Spectroscopy (Academic, New York,

- 1979), p. 181.
82. J.A.R. Samson and J.L. Gardner, Phys. Rev. Lett. 31, 1327 (1973).
83. F.D. Feiock and W.R. Johnson, Phys. Rev. 187, 39 (1969).
84. M.A. Bouchiat and C.C. Bouchiat, Phys. Lett. 48B, 111 (1974); 57B, 284 (1975); J. Physique 35, 899 (1975); 36, 493 (1975).
85. M.J. Harris, C.E. Loving and P.G.H. Sandars, J. Phys. B11, L749 (1978).

## VARIATIONAL METHOD FOR THE TIME-DEPENDENT DIRAC EQUATION

J. Krause and M. Kleber

Physik-Department, Technische Universität München  
8046 Garching, West Germany

### ABSTRACT

The variational method is explained and applied to the time-dependent Dirac equation. As an example we analyse the dynamics of inner-shell electrons during a heavy ion collision. Time-dependent electron trajectories are used to study electron excitation. The classical correspondence is pointed out. Also discussed are flow diagrams in phase space and energy surfaces.

### INTRODUCTION

The use of variational methods for heavy particle impact is not new /1-3/. Unlike perturbation theory, the variational method does not require a small expansion parameter. Instead, it is in the spirit of the method to introduce suitable variational parameters in a trial wave function. The reason why a parametrization of the wave function is not widely used in time-dependent problems may be that it is difficult to find an appropriate set of parameters. We found it very successful to use complex variational parameters /4-8/ because the resulting equations of motion have a classical correspondence (Section 3). This will be of great use in deriving approximate solutions to the time-dependent Dirac equation and in discussing some basic physics (Section 4).

The possibly collective variational parameters must be chosen on physical grounds. But once we have fixed the variational configuration space, it is then straightforward to calculate the time evolution of the parameters (Section 2). Of equal importance is that variational bounds on transition amplitudes exist, and that

variation theory can be related to and combined with perturbation theory (Section 5).

### VARIATIONAL EQUATIONS

The time-dependent Schrödinger equation

$$(H - i\hbar \partial_t) |\psi\rangle = 0 \quad (2.1)$$

can be cast into an eigenvalue problem by separating from the wave function  $\langle r | \psi \rangle$  a purely time-dependent factor  $N(t)$ :

$$|\psi\rangle = N(t) |\phi\rangle \quad (2.2)$$

We put (2.2) in (2.1) with the result that

$$N(t) = N(t_0) \exp\left(\frac{1}{i\hbar} \int_{t_0}^t dt' \frac{\langle \phi | H - i\hbar \partial_{t'} | \phi \rangle}{\langle \phi | \phi \rangle}\right) \quad (2.3)$$

and

$$(H - i\hbar \partial_t) |\phi\rangle = \frac{\langle \phi | H - i\hbar \partial_t | \phi \rangle}{\langle \phi | \phi \rangle} |\phi\rangle \quad (2.4)$$

In contrast to (2.1), the eigenvalue equation (2.4) is automatically invariant under the following change of the Hamiltonian

$$H \rightarrow H + F(t), \quad (2.5)$$

with  $F(t)$  an arbitrary, real time-dependent function. For gauge transformations of type (2.5) the use of (2.3) and (2.4) guarantees the correct transformation properties for all wave functions including approximate ones.

Let us now parametrize the state  $|\phi\rangle$  by a set of  $N$  complex time-dependent parameters  $\underline{\lambda} = (\lambda_1, \lambda_2, \dots, \lambda_N)$

$$|\phi\rangle = (\langle \underline{\lambda} | \underline{\lambda} \rangle)^{-1/2} |\underline{\lambda}\rangle \quad (2.6)$$

With (2.4) we readily find the eigenvalue equation for

$$(H - i\hbar \partial_t) |\underline{\lambda}\rangle = \left[ \frac{\langle \underline{\lambda} | H - i\hbar \partial_t | \underline{\lambda} \rangle}{\langle \underline{\lambda} | \underline{\lambda} \rangle} \right] |\underline{\lambda}\rangle \quad (2.7)$$

which is equivalent to the variational principle

$$\delta I = \delta \int_{t_1}^{t_f} dt \frac{\langle \underline{\lambda} | H - i\hbar \partial_t | \underline{\lambda} \rangle}{\langle \underline{\lambda} | \underline{\lambda} \rangle} = 0 \quad (2.8)$$

Since  $|\underline{\lambda}\rangle$  is assumed to depend on time only through the parameters  $\lambda_i(t)$ , we are allowed to write

$$\partial_t = \sum_{i=1}^N \lambda_i \partial_{\lambda_i} = \dot{\lambda} \cdot \nabla_{\lambda} \quad (2.9)$$

(For a more general time dependence see Refs./5,8/). The integrand in (2.8) is apart from a minus sign the Lagrangian  $L(t)$  of the Schrödinger equation:

$$L(\lambda^*, \lambda, \dot{\lambda}) = - \frac{\langle \lambda | H - i\hbar \partial_t | \lambda \rangle}{\langle \lambda | \lambda \rangle} = -\langle H \rangle + i\hbar \dot{\lambda} \cdot \nabla_{\lambda} \ln \langle \lambda | \lambda \rangle \quad (2.10)$$

In (2.10) we have used an obvious notation for the expectation value of the Hamiltonian. From the variational principle (2.8) we obtain as usual  $N$  Euler-Lagrange equations

$$\partial_{\lambda_i^*} L(\lambda^*, \lambda, \dot{\lambda}) = \frac{d}{dt} \partial_{\dot{\lambda}_i^*} L(\lambda^*, \lambda, \dot{\lambda}), \quad (2.11)$$

which determine the time evolution of the variational parameters  $\lambda_i(t)$ . In our case the right-hand side of (2.11) is zero. We now put (2.10) in (2.11) with the result that

$$\partial_{\lambda_i^*} [\langle H \rangle - i\hbar \lambda_i \cdot \nabla_{\lambda} \ln \langle \lambda | \lambda \rangle] = 0 \quad (2.12)$$

In deriving (2.12) it is understood that the functions  $\lambda_i(t)$  take on prescribed values at  $t_i$  and  $t_f$ , but may be arbitrarily varied in between. In other words, we have omitted possible contributions from the boundaries at  $t_i$  and  $t_f$ . Neglecting them is certainly correct if the number of variational parameters is sufficiently large so that  $|\lambda\rangle$  will remain the exact solution for all times. In practice, however, we shall use only a small number of parameters. But even then there will be no contributions from the boundaries. This can be seen from looking at the error vector

$$|\varepsilon\rangle = (H - i\hbar \partial_t) |\psi\rangle \quad (2.13)$$

Minimization of the corresponding norm

$$\partial_{\lambda_i^*} \langle \varepsilon | \varepsilon \rangle = 0 \quad (2.14)$$

will again yield the equations of motion (2.12) /9/. Note that the error  $|\varepsilon\rangle$  is orthogonal to  $|\psi\rangle$ .

For time-independent problems the equations of motion (2.12) become the Rayleigh-Ritz principle

$$\partial_{\lambda_i^*} \langle H \rangle = 0. \quad (2.15)$$

Then, assuming  $H$  to be real, the wave function will be a real function of the variational parameters  $\lambda_i$ . For this case we find from (2.15) that  $\lambda_i = \lambda_i^*$ . Time-dependent problems arise when  $H$

depends on time, or when the system is not in an eigenstate. As will be pointed out in the next section, both situations are realised in a heavy-ion collision.

#### EXAMPLE AND CLASSICAL CORRESPONDENCE

As an illustrative example we consider monopole excitations of a target electron during the collision between a projectile nucleus and a target atom (Fig. 1) /6/

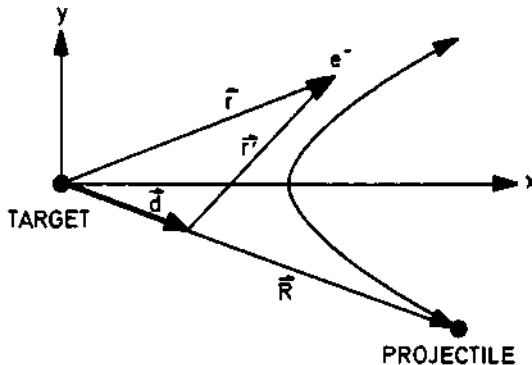


Fig. 1. Coordinates used for the collision between a projectile nucleus (charge  $Z_p$ ) and a target atom (nuclear charge  $Z_t$ ). The electron is denoted by  $e^-$ .

As an approximation, let us ignore all electrons except the K electron under consideration. Then, in the monopole approximation this K electron will feel an effective nuclear charge  $Z$ . In slow collisions  $\lambda$  will vary between  $Z = Z_t$ , the value of the separated configuration ( $R \rightarrow \infty$ ), and  $Z = Z_t + Z_p^p$ , the united atom limit ( $R \rightarrow 0$ ). The corresponding trial wave function becomes

$$\langle \vec{r} | \phi \rangle = \pi^{-1/2} \left( \frac{\lambda + \lambda^*}{2a_0} \right)^{3/2} \exp(-\lambda \frac{r}{a_0}) \quad (3.1)$$

with  $a_0$  the hydrogen Bohr radius. The real part  $\lambda_1$  of the variational parameter  $\lambda$  is proportional to the inverse of the K-shell Bohr radius

$$\lambda_1 = \langle \phi | \frac{a_0}{r} | \phi \rangle, \quad (3.2)$$

whereas the imaginary part  $\lambda_2$  is proportional to the average radial velocity

$$\frac{\langle v \rangle}{r} = \frac{\hbar}{2mi} (\langle \phi | \frac{\partial \phi}{\partial r} - \langle \frac{\partial \phi}{\partial r} | \phi \rangle) = - \frac{e^2 \lambda^2}{\hbar} \quad (3.3)$$

with  $m$  the electron mass. From (3.1) and the one-electron Hamiltonian

$$H = - \frac{\hbar^2}{2m} \vec{\nabla}^2 - \frac{Z_e^2}{r} - \frac{Z_e^2}{|r-R|} \quad (3.4)$$

we calculate the energy of the electron and then, by utilizing (2.12), the equations of motion for  $\lambda_1$  and  $\lambda_2$ :

$$\frac{\hbar}{mc^2} \dot{\lambda}_1 = \frac{2}{3} (\alpha \lambda_1)^2 \lambda_2 \quad (3.5)$$

$$\frac{\hbar}{mc^2} \dot{\lambda}_2 = \frac{2}{3} (\alpha \lambda_1)^2 (Z(t) - \lambda_1)$$

$$\lambda_1 R(t)$$

with  $Z(t) = Z_t + Z_p (1 + 2 \frac{\lambda_1 R(t)}{a_0}) \exp(-2\lambda_1 \frac{R(t)}{a_0})$  and  $\alpha$  the fine structure constant.

The dependence on time enters through  $R(t)$ , the time-dependent internuclear distance.

In strictly adiabatic collisions one has  $\lambda_1 = Z(t)$  and  $\lambda_2 = 0$ . This means that the electron follows a path of minimum energy. In realistic collisions the electron cannot completely follow the changes of  $Z(t)$ . This leads to a non-vanishing radial acceleration  $\lambda_2$  and, therefore, to a finite radial velocity. Hence, if one solves (3.5) for a given internuclear trajectory  $R(t)$  and the initial conditions  $\lambda_1(t \rightarrow -\infty) = Z_t$  and  $\lambda_2(t \rightarrow -\infty) = 0$ , one finds the electron in vibration around the equilibrium radius  $a_0/Z_t$  when the collision is over. This "breathing" signals monopole excitation.

It is useful to point out the close analogy to classical mechanics. To exhibit the classical correspondence we compare the phase in (2.3)

$$\int_{t_0}^t dt' \frac{\langle \phi | H - i\hbar \partial_{t'}, | \phi \rangle}{\langle \phi | \phi \rangle} = \int_{t_0}^t dt' [\langle H \rangle + \text{Im}(\hbar \dot{\lambda} \cdot \vec{\nabla} \ln \langle \lambda | \lambda \rangle)] \quad (3.6)$$

with the classical action

$$S = S_0 - \int_{t_0}^t dt' [H + \sum_{i=1}^N \dot{p}_i q_i] \quad (3.7)$$

From the last two equations it is obvious how one can introduce conjugate variables  $p_i$  and  $q_i$ . For the example given above, a possible choice for the momentum is

$$p = -\text{Im}(\frac{\hbar}{a_0} \lambda) = -\frac{\hbar}{a_0} \lambda_2. \quad (3.8)$$

The corresponding coordinate then becomes

$$q = -a_0 \frac{\partial}{\partial \lambda} \ln \langle \lambda | \lambda \rangle = \frac{3a_0}{2\lambda_1} \quad (3.9)$$

By use of (2.12) we recover Hamilton's equation of motion

$$\dot{p} = -\frac{\partial \langle H \rangle}{\partial q} \quad ; \quad \dot{q} = \frac{\partial \langle H \rangle}{\partial p} . \quad (3.10)$$

#### APPLICATION TO THE TIME-DEPENDENT DIRAC EQUATION

In high Z collision systems the time evolution of the variational parameters is still governed by (2.12); but now H is the time-dependent Dirac Hamiltonian

$$H = \frac{p^2}{2m} + \beta mc^2 - \frac{Z e^2}{r} - \frac{p}{|\vec{r} - \vec{R}|} , \quad (4.1)$$

and  $\alpha$  and  $\beta$  denote the Dirac matrices. The coordinates are the same as in Fig. 1. Note that the equations of motion (2.12) will also hold for spinor wave functions since only expectation values are involved.

Let us again consider monopole excitation of a K-shell target electron. By extending the trial wave function (3.1) to the relativistic case /10/ we have

$$\begin{aligned} \langle \vec{r} | \phi \rangle &= \langle \vec{r} | \lambda \rangle / (\langle \lambda | \lambda \rangle)^{1/2} \\ \langle \vec{r} | \lambda \rangle &= \left( \frac{\lambda r}{a_0} \right)^{s-1} \exp\left(-\frac{\lambda r}{a_0}\right) \begin{pmatrix} \chi^{(s)} \\ i \frac{1-s}{\lambda \alpha} \frac{\vec{p} \cdot \vec{r}}{r} \chi^{(s)} \end{pmatrix} \end{aligned} \quad (4.2)$$

where  $\chi^{(s)}$  is the Pauli spinor,  $\alpha$  the fine structure constant and  $s = (1 - (\lambda \alpha)^2)^{1/2}$ . In analogy to (3.2) and (3.3) we obtain

$$\langle \frac{1}{r} \rangle = \frac{1}{a_0} \frac{\lambda + \lambda^*}{s + s^*} = \frac{mc}{\hbar} \frac{(\lambda + \lambda^*) \alpha}{s + s^*} \quad (4.3)$$

$$\langle v \rangle = \langle \frac{v}{r} \rangle = i c \frac{(\lambda - \lambda^*) \alpha}{s + s^*} . \quad (4.4)$$

The meaning of  $\lambda_1 = \text{Re}(\lambda)$  and  $\lambda_2 = \text{Im}(\lambda)$  is slightly modified compared to the non-relativistic problem ( $s \rightarrow 1$ ) because now the denominator in (4.3) and (4.4) depends on both  $\lambda_1$  and  $\lambda_2$ . This dependence ensures that  $\langle v \rangle$  will never reach  $c$  and that  $\langle 1/r \rangle$  is always finite except for  $\lambda_1 > 137$  and  $\lambda_2 = 0$ .

In order to approximate a dynamical two-centre calculation which is not feasible at present, we allow the electron centre to move a distance  $d$  away from the target (see Fig. 1). This shift  $d(t)$  is taken to be real with  $d(t_\infty) = 0$ . It is not difficult to show that the time dependence of  $d$  follows from

$$\frac{\partial \langle H \rangle}{\partial d} = 0 \quad (4.5)$$

Note that in contrast to the dynamical charge  $\lambda(t)$ , the real parameter  $d(t)$  will adjust instantaneously.

The expectation value of the energy is readily calculated. We find

$$\langle \beta mc^2 \rangle = mc^2 \frac{\lambda\lambda^*\alpha^2 - (1-s^*)(1-s)}{\lambda\lambda^*\alpha^2 + (1-s^*)(1-s)} \quad (4.6a)$$

$$\langle \mathbf{c}_{\alpha\beta}^* \mathbf{c}_{\alpha\beta} \rangle = mc^2 \frac{2\lambda\lambda^*\alpha^2}{s+s^*} \quad (4.6b)$$

$$\langle -\frac{Z_t e^2}{|r-d|} - \frac{Z_p e^2}{|r-R+d|} \rangle = -mc^2 (\lambda+\lambda^*) \alpha \left[ Z_t \alpha F(s+s^*, x) + Z_p \alpha F(s+s^*, \rho-x) \right]. \quad (4.6c)$$

In (4.6) the following quantities have been introduced

$$\rho = (\lambda+\lambda^*) \frac{R}{a} = (\lambda+\lambda^*) \alpha \frac{mc}{\hbar} R$$

$$x = (\lambda+\lambda^*) \frac{d}{a_0} = (\lambda+\lambda^*) \alpha \frac{mc}{\hbar} d$$

The function  $F(k, x)$  is defined by  $F(k, x) = \frac{1}{x} \frac{\gamma_{k+1, x}}{\Gamma(k+1)} + \frac{r(k, x)}{\Gamma(k+1)}$

and the standard notation /11/ for gamma functions has been used.

The function  $F(k, x)$  is of great importance for the average energy and for the time evolution of the variational parameters. It is therefore useful to note that  $F(k, x)$  diverges only for  $k=x=0$ . Consequently, for point nuclei - which we have assumed here - the energy will remain finite, even for collision partners with  $(Z_t + Z_p)\alpha > 1$ , as long as the internuclear distance is different from zero. Realistic collisions, however, will always take place at finite internuclear distances.

As an illustrative example /12/ let us consider the case where a Pb nucleus approaches a Cm nucleus. Fig. 2 shows the energy surface calculated from Eqs.(4.6a-4.6c) for a K electron in Cm in the vicinity of a Pb nucleus ( $R=17$ fm,  $d=0$ ).

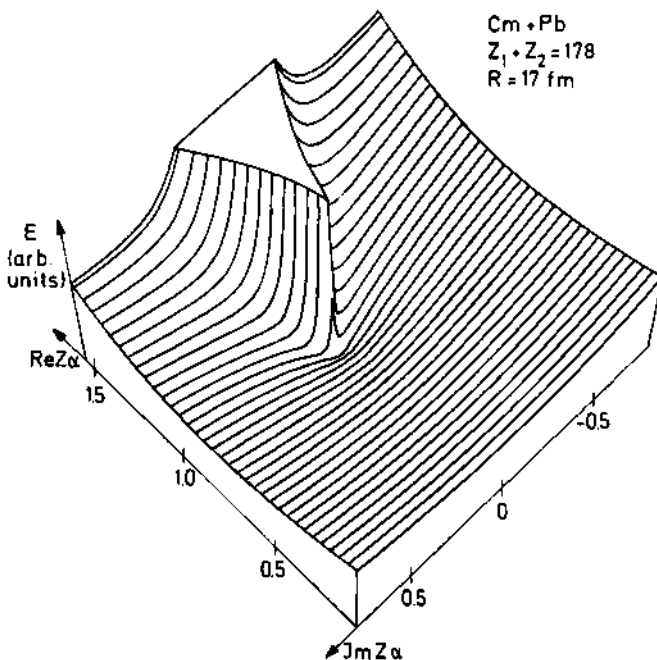


Figure 2. 3-dimensional energy of a K electron in  $Cm$  in the presence of a  $Pb$  nucleus. The plateau is merely a graphical cutoff because  $\langle H \rangle$  becomes infinite for  $(\lambda_1 \alpha) > 1$  and  $\lambda_2 = 0$ .

We next put the expectation value (4.6) of the energy and the expression for the norm overlap  $\langle \lambda | \lambda \rangle$  into (2.12). The resulting equations of motion are similar to the non relativistic equations (3.5). Let us study the behavior of  $\lambda = \lambda_1 + i\lambda_2$  during a 5.9 MeV/u central collision of  $Pb$  on  $Cm$ .

In our variational treatment the K electron in  $Cm$  is characterized by either  $\lambda_1$  and  $\lambda_2$  or, equivalently, by  $\langle 1/r \rangle$  and  $\langle v_r \rangle$ . We show their time evolution in Fig. 3.

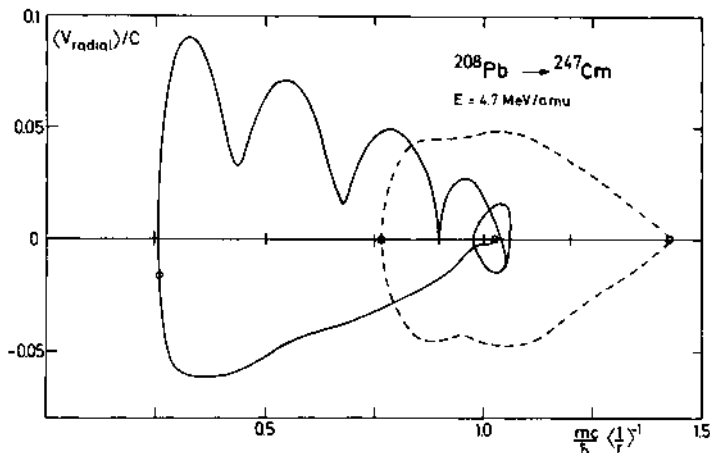


Figure 3. Trajectory for K electron in Cm during a head-on collision between Pb and Cm. Starting point ( $t = -\infty$ ) and point of closest internuclear distance are marked by small circles. Sense of circulation is clockwise. Dashed line is the result of a non-relativistic calculation.

We observe that electron excitation takes place in the second half of the collision. This is, indeed, the finding of a coupled channel analysis /12/. If we compare the relativistic calculation with the corresponding non-relativistic one, then we find relativistic effects responsible for increased non-adiabaticity. The reason why a relativistic electron behaves less adiabatic is because

- i) relativistic electrons cannot speed up beyond the velocity of light and
- ii) relativistic wave functions are more concentrated around the nucleus than non-relativistic wave functions and it is at small internuclear distances where excitation takes place.

The energy transfer to an electron during a collision is found to be

$$\Delta E = \int_{-\infty}^{\infty} dt \langle \phi | \frac{\partial H}{\partial t} | \phi \rangle \quad (4.7)$$

If  $E_0$  is the electron energy prior to the collision, then after the

collision obviously  $E = E_0 + \Delta E$ . For  $E < mc^2$  the electron motion is finite and the trajectories are closed. For  $E \geq mc^2$  the electron motion is unbound. As a result the trajectories are open. In Fig. 4 we plot periodic trajectories of  $\langle v \rangle$  and  $\langle 1/r \rangle^{-1}$  as a function of  $E = \langle B \rangle$  in phase space. Note that in Fig. 3 the closed motion about the equilibrium position begins to develop but the final orbit is not yet reached.

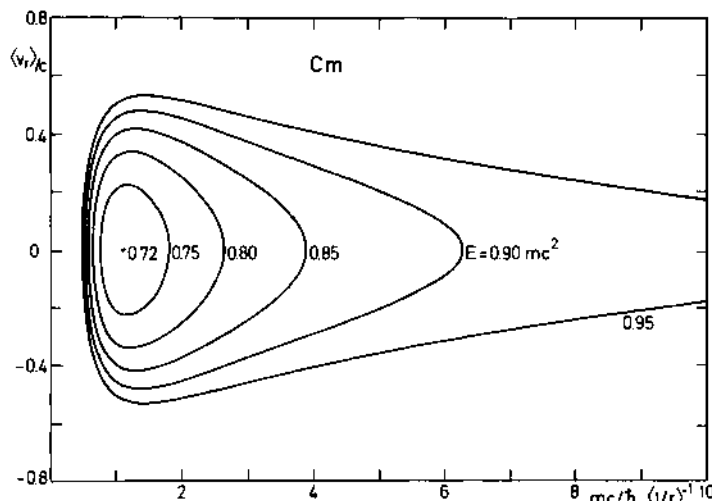


Figure 4. Phase space flow for monopole breathing at different energies  $E$  (in units of  $mc^2$ ). All curves for a hydrogen-like Dirac K electron in Cm.

#### TRANSITION AMPLITUDES AND ESTIMATION OF ACCURACY

In order to calculate transition amplitudes and to estimate the accuracy of a variational wave function of type (2.6) it is convenient to establish the relation between perturbation theory and variational method. For this purpose we follow Demkov's investigation /1/ of the nondiagonal action.

$$I(x_f, x_i) = \int_{t_i}^{t_f} dt \langle x_f | H - i\hbar \partial_t | x_i \rangle \quad (5.1)$$

Here  $|x_i\rangle$  and  $|x_f\rangle$  are normalized trial states which correspond asymptotically to the unperturbed initial or final states of the

target electron(s), for example.

Suppose that  $|\chi_i\rangle$  and  $|\chi_f\rangle$  are close to the true solutions  $|\psi_i\rangle$  and  $|\psi_f\rangle$ ; then we may write

$$|\chi_i(t)\rangle = |\psi_i(t)\rangle + |\eta_i(t)\rangle \quad (5.2)$$

$$|\chi_f(t)\rangle = |\psi_f(t)\rangle + |\eta_f(t)\rangle$$

with  $\langle \eta | \eta \rangle$  a negligibly small quantity. Furthermore, we assume  $|\chi_i(t)\rangle$  to be exact prior to the collision and  $|\chi_f(t)\rangle$  to be exact after the collision:

$$|\eta_i(t_i)\rangle = 0; \quad |\eta_f(t_f)\rangle = 0. \quad (5.3)$$

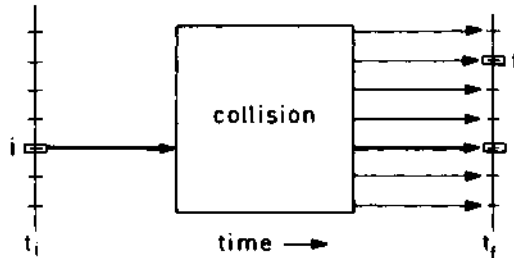


Figure 5. Collision-induced spreading of an initial state  $i$  into various final states  $f$ .

Now the collision takes place between  $t=t_i$  and  $t=t_f$  (see Fig. 5) and, since we are unable to treat the collision correctly we end up with non-vanishing error vectors

$$|\eta_i(t_f)\rangle \neq 0; \quad |\eta_f(t_i)\rangle \neq 0. \quad (5.4)$$

Substituting from (5.2) into (5.1) we get

$$\begin{aligned} I(\chi_f, \chi_i) &= \int_{t_i}^{t_f} dt \langle \psi_f + \eta_f | H - i\hbar \partial_t | \psi_i + \eta_i \rangle \\ &= -i\hbar \langle \chi_f(t_f) | \eta_i(t_f) \rangle + \int_{t_i}^{t_f} dt \langle (H - i\hbar \partial_t) \eta_f | \eta_i \rangle. \end{aligned} \quad (5.5)$$

The last equation is obtained by a partial integration where the boundary condition (5.3) is taken into account. We discard the second term in (5.5) because it is of the order  $\langle \eta | \eta \rangle$ . The first term is related to the exact transition amplitude  $T_{if}$  in a simple way

$$\begin{aligned} T_{if} &= \langle \psi_f(t_f) | \psi_i(t_f) \rangle \\ &= \langle \chi_f(t_f) | \chi_i(t_f) \rangle - \langle \chi_f(t_f) | \eta_i(t_f) \rangle. \end{aligned} \quad (5.6)$$

Combining (5.1), (5.5) and (5.6) we arrive at Demkov's result for the transition amplitude

$$T_{if} = \langle \chi_f(t_f) | \chi_i(t_f) \rangle + \frac{1}{i\hbar} \int_{t_i}^{t_f} dt \langle \chi_f | H - i\hbar \frac{\partial}{\partial t} | \chi_i \rangle \quad (5.7)$$

which is correct up to second order in the error of the wave function. Therefore, the transition amplitude is stationary with respect to a variation of the wave functions. It should be noted that, in order to guarantee gauge invariance of the transition amplitude, one must choose  $|\chi(t)\rangle$  in analogy to equation (2.2)

$$|\chi(t)\rangle = \exp \left[ -\frac{i}{\hbar} \int dt' \frac{\langle \phi | H - i\hbar \frac{\partial}{\partial t'} | \phi \rangle}{\langle \phi | \phi \rangle} \right] |\phi(t)\rangle. \quad (5.8)$$

We observe that (5.7) agrees with perturbation theory

$$T_{if}^{\text{pert}} = \delta_{if} + \frac{1}{i\hbar} \int_{t_i}^{t_f} dt \langle \phi_f | V(t) | \phi_i \rangle \exp \left( \frac{i}{\hbar} (E_f - E_i) t \right) \quad (5.9)$$

if asymptotically unperturbed, time-independent and orthogonal wave functions  $|\phi\rangle$  are used.  $V(t)$  is the perturbation and  $E_f - E_i$  the asymptotic (separated atom) energy difference between the initial and final states.

It can be readily verified that (5.7) becomes the perturbed united-atom approach /13/ if molecular wave functions are used. Variational bounds /14-16/ on the transition amplitude are obtained by inspection of the second order correction to the exact transition amplitude. Writing

$$T_{if} = T_{if}^{\text{var}} + \Delta_{if}, \quad (5.10)$$

introducing  $|\varepsilon\rangle = (H - i\hbar \frac{\partial}{\partial t}) |\chi\rangle$ , and using the Schwarz inequality one finds /16/

$$|\Delta_{if}| \leq \frac{1}{\hbar^2} \int_{t_i}^{t_f} dt \left| \langle \varepsilon_f | \varepsilon_i \rangle \right| \int_{t_i}^{t_f} dt' \left| \langle \varepsilon_f | \varepsilon_i \rangle \right| \quad (5.11)$$

where  $||\epsilon|| = (\langle \epsilon | \epsilon \rangle)^{1/2}$ . Since the variational method minimizes  $||\epsilon||$ , the variational bound

$$|T_{if}^{\text{var}}| - |\Delta_{if}| \leq |T_{if}| \leq |T_{if}^{\text{var}}| + |\Delta_{if}| \quad (5.12)$$

on the amplitude is expected to be useful. Unfortunately, a calculation of  $\Delta_{if}$  requires the computation of the fluctuation term  $\langle (H - i\hbar \partial_t)^2 \rangle$ . For a more practical error estimate we refer to Ref. /17/.

## CONCLUSION

The variational method leads in a very transparent way to generalized force equations (2.12). These equations determine the optimum path within an a priori chosen Hilbert space. Up to now we have used the variational method with success to explain ionization probabilities in collisions with light ions (protons etc.) /8/. Furthermore, dynamical binding has been investigated /17/. In this contribution we have extended the method to very heavy particle systems and have reported on pilot calculations for the time-dependent Dirac equation. A detailed comparison with experimental results on ionization probabilities /18/ and positron production /19-21/ is still to be done. The problem is more involved than for the non-relativistic case. For example, if the bound state approaches the negative continuum, spurious couplings to negative continuum states may show up. But this situation is common to all approximate theories. Nevertheless, we expect the variational method to complement existing theories for very heavy collision systems /12,22-25/.

## ACKNOWLEDGMENT

This work was supported by the Bundesministerium für Forschung und Technologie.

## REFERENCES

1. Yu. N. Demkov; Sov.Phys. JETP 11:1351 (1960).
2. N.C. Sil; Proc.Phys.Soc.75:194 (1960)
3. R. McCarroll, R. D. Piacentini and A. Salin; J.Phys.B3:137 (1970),
4. B. Jancovici and H. D. Schiff; Nucl.Phys.58:678 (1964).
5. M. Kleber and J. Zwiegel; Z. Physik A280:137 (1977).
6. M. Kleber; J.Phys. B11:1069 (1978).
7. M. Kleber and J. Zwiegel; Phys.Rev.A19:579 (1979).
8. M. Kleber and K. Unterseer; Z. Physik A292:311 (1979).
9. P. G. Reinhard, N. Rowley and D. M. Brink; Z. Physik 266:149 (1974).

10. J. J. Sakurai; 'Advanced Quantum Mechanics', Addison-Wesley, Reading 1978, p. 128
11. M. Abramowitz and I. A. Stegun: 'Handbook of Mathematical Functions' Dover Publications, New York 1968, p. 255
12. G. Soff, J. Reinhardt, B. Müller and W. Greiner; Z. Physik A294 137 (1980).
13. J.S. Briggs; J.Phys. B8:L485 (1975).
14. L. Spruch in 'Boulder Lectures in Theoretical Physics', Gordon and Breach, New York 1969, Vol. XI-C, p. 77
15. R. Shakeshaft and L. Spruch; Phys.Rev.A10:92 (1974).
16. D. Storm; Phys.Rev. A10:1008 (1974).
17. K. Unterseer and M. Kleber; to appear in Nucl. Instrum. Meth.
18. P. Armbruster and P. Kienle; Z.Physik A291:399 (1979).
19. H. Backe et al. Phys.Rev.Lett.40:1443 (1978).
20. C. Kozhuharov et al.; Phys.Rev.Lett. 42:376 (1979).
21. D. Liesen et al.; Phys.Rev.Lett. 44:983 (1980)
22. J. Eichler and U. Wille; Phys.Rev. A11:1973 (1975).
23. E. K. U. Gross and R. M. Dreizler; Phys.Rev. A20:1798 (1979).
24. B. Müller et al.; Z.Physik A285 27 (1978).
25. J. Reinhardt et al.; Phys.Lett. 78B:183 (1978).

## RADIATIVE CORRECTIONS IN STRONG FIELDS

Peter J. Mohr

Yale University  
Gibbs Laboratory, Physics Department  
New Haven, CT 06520

### ABSTRACT

Radiative corrections in a strong static external field can be calculated to all orders in the external field by working in the Furry bound-interaction picture. The self-energy correction in a Coulomb field has been calculated for all  $n=1$  or 2 states for a wide range of values of the nuclear charge  $Z$ . In the Wichmann-Kroll approach, the bound-electron propagation function is expanded in angular momentum eigenfunctions. Some aspects of this method as applied to the self-energy calculation, including mass renormalization and numerical methods, are discussed here. The Coulomb field self-energy correction gives the main contribution to the Lamb shift in high- $Z$  hydrogenlike atoms. In high- $Z$  few-electron atoms, energy levels can be calculated by applying perturbation theory where, in lowest order, the electrons are treated as non-interacting Dirac particles. Electron-electron interactions and radiative corrections are then calculated as perturbations. In this framework, the Coulomb-field radiative corrections give the leading radiative corrections for the few-electron system. Comparison to experiment is made for one- and two-electron atoms.

### INTRODUCTION

The purpose of this paper is to review the subject of radiative corrections in strong fields, with attention focused on these effects in one- and two-electron atoms at high  $Z$ .<sup>1</sup> The basic question to be answered is whether the standard formulation of quantum electrodynamics (QED) in strong fields is in agreement with experiment. Rather than address what Professor Greiner has called a "yes or no" question of whether positrons are spontane-

ously produced in heavy-ion collisions, I will examine the quantitative effects of radiative corrections. These effects are of nominal relative order  $\alpha$  compared to atomic binding energies, for values of  $Z$  in the range  $1 \ll Z \ll Z_{cr}$ , where  $Z_{cr} \approx 172$ . A related question is how, in practice as well as in principle, does one calculate QED effects for strongly bound electrons. For high- $Z$  one-electron atoms, the issue seems to be well understood, except possibly near the limit  $Z \rightarrow Z_{cr}$ . For high- $Z$  few-electron atoms, there is a systematic framework based on relativistic perturbation theory that gives accurate predictions. For many-electron atoms, there still remains the problem of consistently incorporating the calculation of radiative corrections into a practical scheme that deals with the many-electron atomic problem. Hopefully, some insight may be gained for this problem from studies of few-electron systems.

Besides the need for quantitative checks of the theory, there are features unique to high- $Z$  atoms that make their study of particular interest. (1) The most striking feature is the fact that the Dirac binding energy, of order  $(Z\alpha)^2 m_e c^2$ , is of the order of the electron rest mass  $m_e c^2$  for large enough  $Z$ . This fact has led to the well-known prediction of spontaneous positron production in heavy-atom collisions. (2) The ratio (radiative corrections) / (binding energy)  $\approx \alpha (Z\alpha)^4 m_e c^2 / (Z\alpha)^2 m_e c^2 = \alpha (Z\alpha)^2$ , shows that the radiative corrections play an increasingly important role in atomic structure as  $Z$  increases. (3) The self-energy correction is strongly  $Z$  dependent, i.e., the asymptotic expansion for small  $Z\alpha$  converges slowly numerically, so that a non-perturbative (in  $Z\alpha$ ) calculation is necessary for good accuracy at high  $Z$ . (4) Weak-field ideas, such as form factors for the electron, are not useful in the high- $Z$  regime. For example, the radiative correction to the  $2p_{1/2} - 2p_{3/2}$  splitting is not simply related to the anomalous magnetic moment at high  $Z$ , as it is at low  $Z$ . In fact, the radiative correction changes sign near  $Z=90$ .

The remainder of this paper is arranged as follows. In Section II, the basic formalism of the Furry picture for dealing with strong fields is reviewed. The Wichmann-Kroll approach to the calculation of the electron propagation function is discussed in Section III. In Section IV, methods of calculation of the self energy at high  $Z$  are discussed, and comparison of theory and experiment is made for the Lamb shift in high- $Z$  one-electron atoms. The perturbation-theory approach to two-electron atoms is described, and comparison to experiment is made in Section V. Concluding remarks are made in Section VI. Natural units are employed everywhere except in formulas giving numerical results.

#### FURRY PICTURE

The basic formalism for the calculation of radiative corrections in strong fields is quantum electrodynamics in the Furry picture.<sup>2</sup> The theory is briefly outlined in this section.

In the Furry picture, the electron-positron field operator

$$\psi(x) = \sum_{n+} b_n \phi_n(x) + \sum_{n-} d_n^* \phi_n(x) \quad (1)$$

is written as a sum over electron destruction operators  $b_n$  and positron creation operators  $d_n^*$  multiplying positive energy ( $n+$ ) and negative energy ( $n-$ ) discrete and continuum eigenfunctions of the Dirac equation,  $\phi_n(x) = \phi_n(\vec{x}) \exp(-iE_n t)$ ,

$$[-i\vec{\alpha} \cdot \vec{v} + V(\vec{x}) + \beta - E_n] \phi_n(\vec{x}) = 0 \quad (2)$$

The electron and positron creation and destruction operators satisfy the usual Fermi anticommutation rules. The important feature of the Furry picture is the fact that the external potential appears in Eq. (2), so that the zero-order (in  $\alpha$ ) states are the bound states of the electron. In this way, the parameter corresponding to the potential  $Z\alpha$  is included to all orders in each order of perturbation theory. The zero-order states are formed by creation operators acting on the vacuum. The one-electron states are given by

$$|n\rangle = b_n^* |0\rangle \quad (3)$$

and the two-electron states are given by

$$|njn'j'JM\rangle = \sum_{mm'} \langle jmj'm' | jj'JM \rangle b_{njm}^* b_{n'm'}^* |0\rangle \quad (4)$$

where the sum over vector addition coefficients produces states of well-defined total angular momentum  $J$ .

The electron-positron field interacts with the radiation field via the interaction Hamiltonian density

$$H_I(x) = -\frac{1}{2}e[\bar{\psi}(x)\gamma^\mu, \psi(x)]A_\mu(x) - \frac{1}{2}\delta m[\bar{\psi}(x), \psi(x)] \quad (5)$$

The bound-state level shift, to any order in  $\alpha$ , is given by the theorem of Gell-Mann and Low<sup>3</sup> in the symmetric form given by Sucher<sup>4</sup>

$$\Delta E_n = \lim_{\substack{\epsilon \rightarrow 0 \\ \lambda \rightarrow 1}} \frac{i\epsilon}{2} \frac{\frac{\partial}{\partial \lambda} \langle n | S_{\epsilon, \lambda} | n \rangle_C}{\langle n | S_{\epsilon, \lambda} | n \rangle_C} \quad (6)$$

where

$$S_{\epsilon, \lambda} = \sum_{n=0}^{\infty} S_{\epsilon, \lambda}^{(n)} \quad (7)$$

and where

$$S_{\varepsilon, \lambda}^{(n)} = \frac{(-i\lambda)^n}{n!} \int d^4x_n \dots \int d^4x_1 e^{-\varepsilon|t_n| - \dots - \varepsilon|t_1|} \times T[H_I(x_n) \dots H_I(x_1)] \quad (8)$$

In (6), the subscript C denotes the fact that only connected graphs are included. Formulas (1)-(8) determine the level shift, provided charge and mass renormalization are carried out.

The formulas for the level shifts are represented by Feynman diagrams, as in free-electron quantum electrodynamics, except that here the electron lines represent propagation of an electron in the external potential. The components of the diagrams are:

- (1) vertex, Fig. 1(a):  $\int d^4x \gamma^\mu$
- (2) legs, Fig. 1(b):  $\phi_n(x)$ ,  $\bar{\phi}_n(x)$
- (3) photon propagator, Fig. 1(c):

$$g_{\mu\nu} D_F(x_2 - x_1) = \frac{2ig_{\mu\nu}}{(2\pi)^4} \int d^4k \frac{e^{-ik \cdot (x_2 - x_1)}}{k^2 + i\epsilon}$$

- (4) electron propagator, Fig. 1(d):

$$S_F(x_2, x_1) = \langle 0 | T[\psi(x_2) \bar{\psi}(x_1)] | 0 \rangle$$

$$= \begin{cases} \sum_{n+} \phi_n(x_2) \bar{\phi}_n(x_1) & t_2 > t_1 \\ -\sum_{n-} \phi_n(x_2) \bar{\phi}_n(x_1) & t_2 < t_1 \end{cases}$$

The main hurdle in calculating radiative corrections for bound systems is finding a practical method of evaluating the electron propagation function. An important solution to this problem is discussed in the next section.

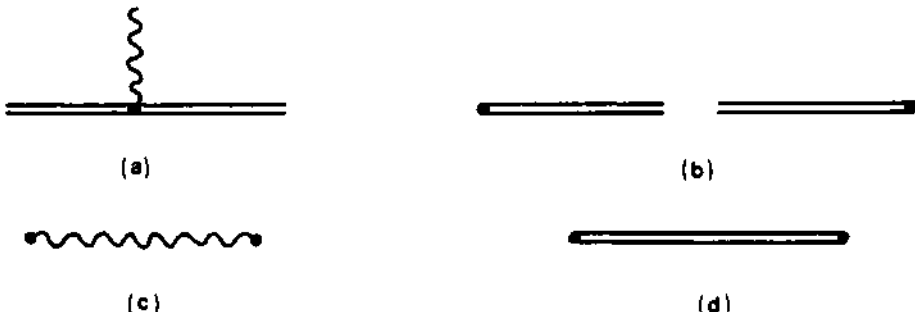


Fig. 1. Components of Furry-picture Feynman diagrams.

## WICHMANN-KROLL METHOD

The generalization of QED from free to Coulomb bound-state problems corresponds to the replacement

$$\frac{1}{\gamma \cdot p - 1} \rightarrow \frac{1}{\gamma \cdot p - \gamma^0 V - 1}$$

for the electron propagator. Feynman integrals containing the bound propagator have been evaluated either (1) by variations on expansion in powers of the potential  $V$ , or (2) by expanding the propagator in angular momentum eigenfunctions. Elsewhere in these proceedings, Professor Erickson describes a calculation based on expansion in powers of the field strength, i.e., in powers of commutators of  $p$  and  $V$ . The angular momentum expansion method is examined below.<sup>5-9</sup>

The bound-electron propagation function can be written in the form

$$S_F(x_2, x_1) = \frac{1}{2\pi i} \int_C_F dz \sum_n \frac{\phi_n(\vec{x}_2) \bar{\phi}_n(\vec{x}_1)}{E_n - z} e^{-iz(t_2 - t_1)} \quad (9)$$

where the sum over  $n$  in the integrand is the Dirac-Coulomb Green's function

$$\sum_n \frac{\phi_n(\vec{x}_2) \phi_n^\dagger(\vec{x}_1)}{E_n - z} = G(\vec{x}_2, \vec{x}_1, z) \quad (10)$$

which satisfies the inhomogeneous Dirac Equation

$$[-i\vec{\alpha} \cdot \vec{\nabla}_2 + V(\vec{x}_2) + \beta - z]G(\vec{x}_2, \vec{x}_1, z) = i\delta^3(\vec{x}_2 - \vec{x}_1) \quad (11)$$

To evaluate the propagation function in a strong field calculation, it is useful to write the Green's function as a sum over eigenfunctions of the Dirac operator  $K = \beta(\vec{\sigma} \cdot \vec{L} + 1)$

$$G(\vec{x}_2, \vec{x}_1, z) = \sum_K G_K(\vec{x}_2, \vec{x}_1, z) \quad (12)$$

where  $KG = -\kappa G$ . The magnitude of the eigenvalue  $\kappa$  is simply related to the angular momentum eigenvalue:  $j = |\kappa| - \frac{1}{2}$ . The advantage of such an expansion is that each term  $G_K$  can be written in  $2 \times 2$  block matrix form, where each block is a product of a radial function and a  $2 \times 2$  spin-angle function. The spin-angle functions are well known, and the radial parts can be written as elements of a  $2 \times 2$  matrix that is the solution of the radial inhomogeneous differential equation

$$\begin{bmatrix} V(r_2) + 1 - z & -\frac{1}{r_2} \frac{d}{dr_2} r_2 + \frac{\kappa}{r_2} \\ \frac{1}{r_2} \frac{d}{dr_2} r_2 + \frac{\kappa}{r_2} & V(r_2) - 1 - z \end{bmatrix} \begin{bmatrix} G_{\kappa}^{11} & G_{\kappa}^{12} \\ G_{\kappa}^{21} & G_{\kappa}^{22} \end{bmatrix} = \frac{1}{r_2 r_1} \delta(r_2 - r_1) \quad (13)$$

The problem of numerically evaluating the electron propagation function is thus reduced to one of evaluating the radial Green's functions via Eq. (13). Two approaches have been employed to do this in calculations of radiative corrections. One method is to numerically solve the coupled differential equations in (13). The other approach takes advantage of the fact that for the Coulomb potential, the solutions to (13) are known linear combinations of Whittaker (confluent hypergeometric) functions. The functions have power series expansions and asymptotic expansions that are suitable for direct numerical evaluation. The angular momentum expansion is thus a key to the evaluation of bound state Feynman diagrams.

### SELF ENERGY

In this section, a calculation of the lowest order (in  $\alpha$ ) self energy, based on the angular momentum expansion, is described.<sup>8</sup> The self-energy Feynman diagram appears in Fig. 2, and the corresponding expression for the energy shift is given by

$$\Delta E_n = -i4\pi\alpha \int d(t_2 - t_1) \int d^3\vec{x}_2 \int d^3\vec{x}_1 D_F(x_2 - x_1) \bar{\phi}_n(x_2) \gamma_\mu S_F(x_2, x_1) \gamma^\mu \phi_n(x_1) - \delta m \int d^3\vec{x} \bar{\phi}_n(\vec{x}) \phi_n(\vec{x}) \quad (14)$$

This formula follows from the formalism outlined in Sect. II. The quantity  $\delta m$  in the second term of (14), the mass renormalization term, is fixed by the condition

$$\lim_{Z\alpha \rightarrow 0} \Delta E_n = 0 \quad (15)$$



Fig. 2. Feynman diagram for the lowest order self energy.

The value of  $\delta m$ , so defined, is formally infinite, i.e., with the conventional regularization prescription

$$\frac{1}{k^2 + i\epsilon} \rightarrow \frac{1}{k^2 + i\epsilon} - \frac{1}{k^2 - \Lambda^2 + i\epsilon} \quad (16)$$

in the definition (see Sect. II) of  $D_F$ , the two terms in (14) are separately of order  $\ln \Lambda$ . The energy shift is then the limit

$$\Delta E_n = \lim_{\Lambda \rightarrow \infty} \Delta E_n(\Lambda) \quad (17)$$

which is finite and independent of  $\Lambda$ . To deal with the divergent term in the numerical evaluation of (14), an auxiliary term is subtracted from the first term in (14) to cancel the divergence, and added to the second term. This subtraction term is constructed by replacing the operator  $G(z) = [\vec{a} \cdot \vec{p} + V + \beta - z]^{-1}$ , corresponding to the Green's function in Eq. (11), by the operator

$$G_A(z) = \frac{1}{\vec{a} \cdot \vec{p} + \beta - z} - V \frac{1}{p^2 + 1 - z^2} - V \frac{2z(\beta + z)}{[p^2 + 1 - z^2]^2} \quad (18)$$

in the first term of Eq. (14). The auxiliary term is similar in form to the first term in (14); it can also be expanded in angular momentum eigenfunctions and subtracted before any integration or summation is carried out, leaving a finite, numerically tractable expression for the difference. On the other hand, the auxiliary term is sufficiently simple that the divergence can be isolated analytically, and cancelled against the second term on the right-hand side in (14).

The calculated values for the level shift due to the self energy can be expressed in the form:

$$\Delta E_n = \frac{\alpha}{\pi} \frac{(Z\alpha)^4}{n^3} F_n(Z\alpha) m_e c^2 \quad (19)$$

in which  $F_n(Z\alpha)$  is a relatively slowly varying function of  $Z$ . A great deal of work has been done on calculations of terms in the small  $Z\alpha$  asymptotic expansion of  $F_n(Z\alpha)$ .<sup>10,11</sup> For  $Z \gg 1$ , the asymptotic expansion converges slowly numerically, and a complete numerical evaluation is necessary. The results of complete evaluations of  $F$  for the  $1S_{1/2}$  state for both a Coulomb field and the field of a finite-size nucleus are shown in Fig. 3. The correction in a Coulomb field appears to approach infinity as  $Z$  approaches 137, while the finite-nucleus values are infinite for all  $Z$  up to 160. There, the curve is increasing rapidly and the value at  $Z_{cr} \approx 172$  is uncertain. On the other hand, the energy shift from the Uehling term of the vacuum polarization (see Gyulassy

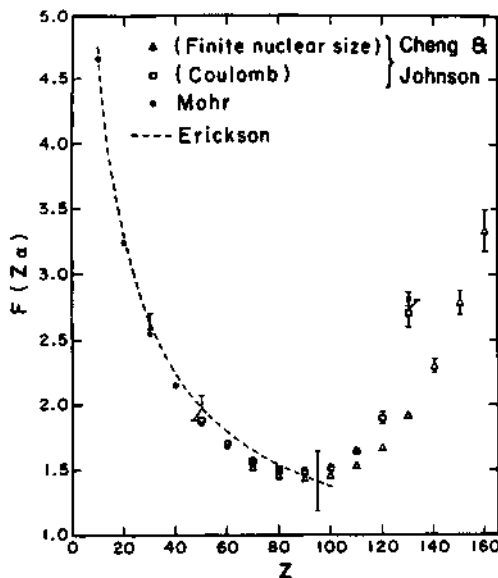


Fig. 3. Calculations of the  $1S_{1/2}$ -state self energy by Cheng and Johnson,<sup>9</sup> Mohr,<sup>8</sup> and Erickson.<sup>12</sup>

in these proceedings) is negative with rapidly growing magnitude as  $Z \rightarrow Z_{cr}$ , such that the sum of the self energy and vacuum polarization corrections is relatively slowly varying at high  $Z$ . Whether the sum remains bounded as  $Z \rightarrow Z_{cr}$  is still unknown and requires further investigation.

The most direct present-day experimental test of radiative corrections in strong fields is measurement of the Lamb shift (splitting of the  $2S_{1/2}$  and  $2P_{1/2}$  energy levels) in high- $Z$  hydrogenlike atoms. The dominant theoretical component of the Lamb shift is the self energy, as shown in Table I which lists the contributions in hydrogenlike argon ( $Z = 18$ ).<sup>13</sup> The functions

Table I. Contributions to the Lamb Shift  
in Hydrogenlike Argon

|                     |                |
|---------------------|----------------|
| Self energy         | 40,544(15) GHz |
| Vacuum polarization | -2,598(3)      |
| Nuclear size        | 283(12)        |
| Everything else     | 22(17)         |
| Total               | 38,250(25) GHz |

$F(Z\alpha)$  for the  $2S_{1/2}$  and  $2P_{1/2}$  states, based on the numerical methods described in Sect. III, are plotted in Fig. 4.<sup>14</sup> High- $Z$  experimental tests of the Lamb shift in hydrogenlike atoms are shown in Fig. 5. These measurements, and particularly the measurements at  $Z = 17$  and 18, are clean tests of strong binding effects in the radiative corrections. There is good agreement between theory and experiment. It is of interest to note that the experiments at  $Z = 17$  and 18 are based on completely different methods. The experiment at  $Z = 18$ , by Gould and Marrus, is based on measurement of the  $2S_{1/2}$  lifetime in an electric field, which in turn, depends

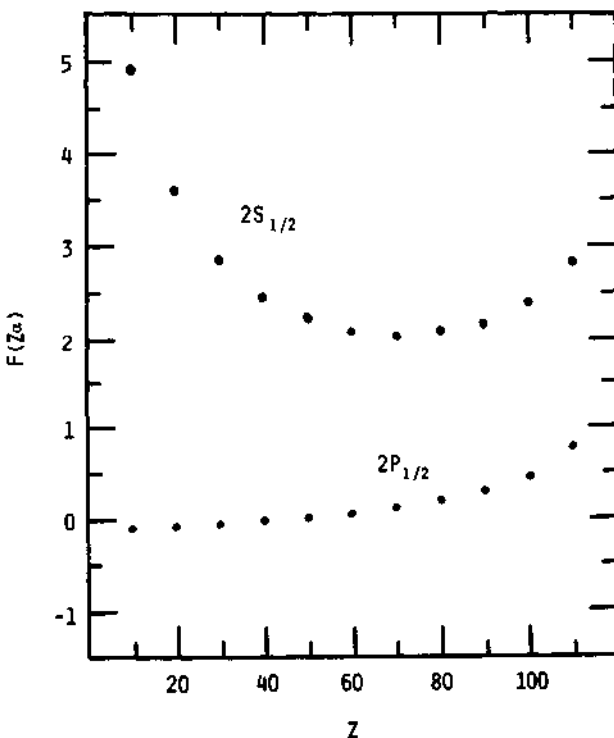


Fig. 4. Graph of the functions  $F_{2s}$  and  $F_{2p}$ .

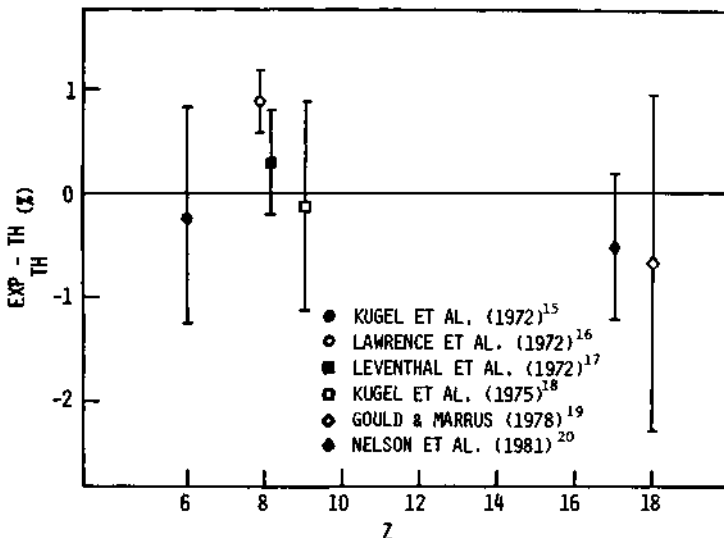


Fig. 5. Comparison of experiment and theory for the Lamb shift in high-Z hydrogenlike atoms.

on the magnitude of the Lamb shift. The recent measurement at  $Z = 17$ , by Nelson et al., is a laser resonance measurement.

#### TWO-ELECTRON ATOMS

It is important to extend the precision tests of QED in simple atoms to stronger fields in order to test the theory under new conditions. This appears to be experimentally difficult for measurements of the Lamb shift in hydrogenlike atoms. An alternative way of carrying out such tests is to compare theory and experiment for energy level splittings in high-Z two-electron atoms. Figure 6 shows energy levels of a high-Z two-electron atom. Such atoms can be produced by passing a fast heavy-ion beam through a thin foil. Some of the ions emerge with two electrons and some of those are in the excited  $2^3P_0$  or  $2^3P_2$  metastable states. The wavelength of photons emitted in transitions to the  $2^3S_1$  state can be directly measured to determine the splittings. The radiative corrections constitute a sizable fraction of the energy splitting for these transitions. Figure 7 shows the ratio of the radiative correction to the total  $2^3S_1$ - $2^3P_0$  energy splitting. This fraction grows rapidly with increasing  $Z$ , from a value of about 0.002% at  $Z = 2$  to a value of about 2% at  $Z = 26$ .

It is possible to formulate the theory for high-Z two-electron

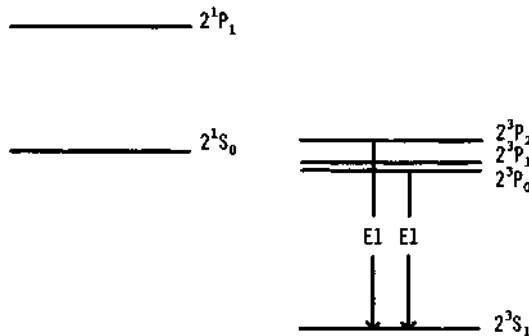


Fig. 6. Energy levels of a high- $Z$  two-electron atom.

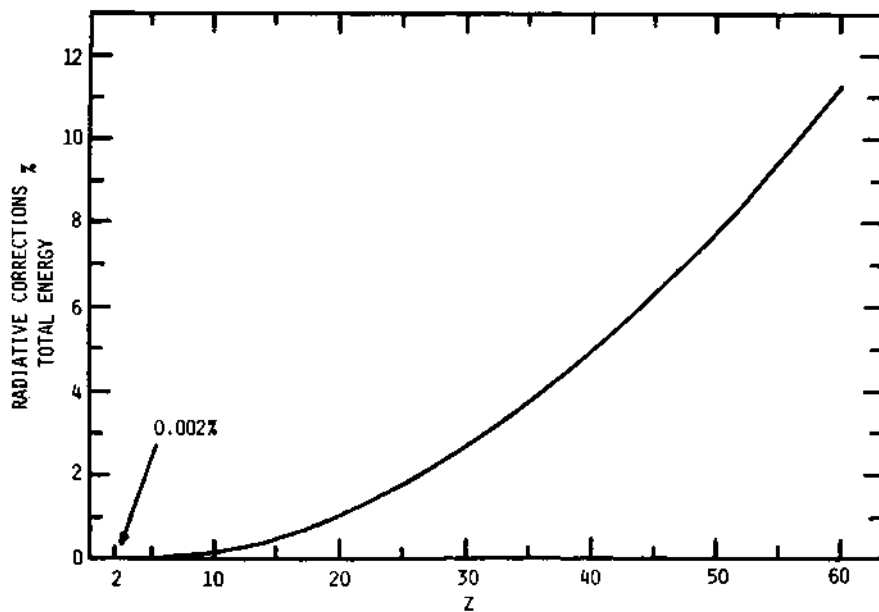


Fig. 7. Ratio of the radiative correction to the total  $2^3S_1-2^3P_0$  energy splitting in two-electron atoms.

atoms in a way which appears as sound as the one-electron formulation. The method is to apply perturbation theory in the Furry picture. As shown subsequently, this procedure generates a series in  $1/Z$  that can give accurate results at high  $Z$ . The physical idea behind the perturbation theory approach is that the electrons in a strong Coulomb field are well approximated as noninteracting Dirac electrons in lowest order; interactions with the high- $Z$  nucleus dominate over the electron interactions. Perturbations due to interaction of the electrons with the electromagnetic field generate the electron-electron interactions and the radiative corrections. This approach to two-electron atoms is complementary

to the two-electron methods that accurately predict the fine structure in neutral helium.<sup>21</sup> In that case, the electron-electron interaction is calculated nonrelativistically to all orders by variational solution of the Schrödinger equation. Radiative and relativistic corrections are then calculated as perturbations by a systematic reduction of the Bethe-Salpeter equation. In the perturbation approach, the relativistic corrections are included exactly in the Furry wave functions and propagator, and the electron interactions are perturbations. This complementarity is illustrated in Table II.

Historically, relativistic perturbation theory has been applied in various forms and contexts. An early application by Christy and Keller was an evaluation of the one-photon electron-electron interaction with Dirac hydrogenic wave functions to estimate the fine structure in the L shell of heavy atoms.<sup>22</sup> Bethe and Salpeter discussed relativistic perturbation theory for two-electron atoms, although experiments with  $Z$  greater than 10 were not foreseen at the time.<sup>23</sup> Relativistic 1/Z expansion methods that include the Breit interaction have been applied by Layzer and Bahcall<sup>24</sup> and by Dalgarno and Stewart.<sup>25</sup> The fully relativistic perturbation approach has been examined by Labsovsky,<sup>26</sup> Klimchitskaya and Labsovsky,<sup>27</sup> and by Ivanov, Ivanova and Safronova.<sup>28</sup>

In order to compare the Furry-picture perturbation theory predictions to experiment, I examine below the order of magnitude of the dominant Feynman diagrams, and collect explicit formulas for the  $2^3S_1-2^3P_0$  energy-level splitting, based on currently available calculations, as an example. The zero-order (in  $\alpha$ ) energy level for the two-electron atom is the sum of the single-electron Dirac hydrogenic energies for the individual electrons. For the  $2^3S_1$  and  $2^3P_0$  states, which are formed from the  $1s_{1/2}2s_{1/2}$  and  $1s_{1/2}2p_{1/2}$  hydrogenic states respectively, the energy difference is zero:

$$\Delta E^{(0)}(2^3S_1-2^3P_0) = 0 \quad (20)$$

Table II. Comparison of Low-Z and High-Z Calculations

|                          | Ordinary Helium | High-Z Two-Electron Atom |
|--------------------------|-----------------|--------------------------|
| Electron Interactions    | Exact           | Perturbation             |
| Relativistic Corrections | Perturbation    | Exact                    |

Feynman diagrams for the corrections of order  $\alpha$  are shown in Fig. 8. The corresponding correction to the energy for the state  $b_i^* b_j^* |0\rangle$  is (omitting the mass renormalization terms)

$$\begin{aligned} \Delta E^{(2)} = & -i4\pi\alpha \int d(t_2-t_1) \int d^3 \vec{x}_2 \int d^3 \vec{x}_1 D_f(x_2-x_1) \\ & \times \left\{ \bar{\phi}_j(x_2) \gamma_\mu \phi_j(x_2) \bar{\phi}_i(x_1) \gamma^\mu \phi_i(x_1) \right. \\ & \quad - \bar{\phi}_j(x_2) \gamma_\mu \phi_i(x_2) \bar{\phi}_i(x_1) \gamma^\mu \phi_j(x_1) \\ & + \bar{\phi}_j(x_2) \gamma_\mu S_F(x_2, x_1) \gamma^\mu \phi_j(x_1) + \bar{\phi}_i(x_2) \gamma_\mu S_F(x_2, x_1) \gamma^\mu \phi_i(x_1) \\ & \left. - [\bar{\phi}_j(x_2) \gamma_\mu \phi_j(x_2) + \bar{\phi}_i(x_2) \gamma_\mu \phi_i(x_2)] \text{Tr}[\gamma^\mu S_F(x_1, x_1)] \right\} \quad (21) \end{aligned}$$

The first two terms on the right side of (21), associated with the first Feynman diagram in Fig. 8, give the leading electron-electron interaction. It is equivalent to the sum of the Coulomb interaction and the transverse photon interaction in the Coulomb gauge. This contribution, which can readily be calculated to high accuracy, is conveniently represented by the first few terms in its power series in  $Z\alpha$ <sup>29,30</sup>

$$\begin{aligned} \Delta E_{pe}^{(2)} (2^3 S_1 - 2^3 P_0) \\ = \alpha(Z\alpha) m_e c^2 \left[ \frac{248}{6561} + 0.1428(Z\alpha)^2 + 0.1(Z\alpha)^4 + \dots \right] \quad (22) \end{aligned}$$

The third-sixth terms in (21), associated with the second and the third Feynman diagrams in Fig. 8, are the one-electron self energy and vacuum polarization corrections. Comparison of Eq. (21) and Eq. (14) shows that the leading two-electron self-energy correction is the sum of the self-energy terms for the zero-order hydrogenic states of the two electrons. This is true for all diagrams with no exchanged photons, so the contribution of such diagrams to the

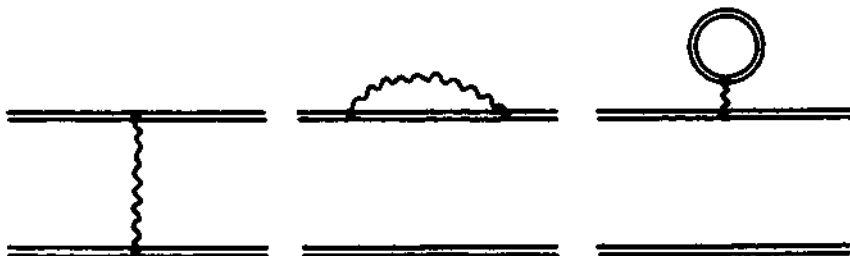


Fig. 8. Second-order Feynman diagrams for the energy-level shift in a two-electron atom.

$2^3S_1-2^3P_0$  splitting is just the negative of the corresponding corrections to the  $2P_{1/2}-2S_{1/2}$  Lamb shift. (The minus sign arises from the fact that the  $2S_{1/2}$  energy level is above the  $2P_{1/2}$  level in hydrogen, while the  $2^3P_0$  level is above the  $2^3S_1$  level in two-electron atoms.)

Fourth-order corrections are represented by the diagrams in Figs. 9-11. These diagrams are grouped into figures according to the number of photon lines that cross from one electron line to the other. This grouping is related to the order of magnitude of the graphs, i.e., graphs with a smaller number of exchanged photons are higher order in  $Z\alpha$ . The dominant fourth-order correction, represented by the two-exchanged-photon graphs in Fig. 9, is known to zero and first order in  $(Z\alpha)^2$ :

$$\Delta E_{pe}^{(4)} (2^3S_1-2^3P_0) = \alpha^2 m_e c^2 [-0.0256 - 0.27(Z\alpha)^2 + \dots] \quad (23)$$

The leading term in (23) is known from nonrelativistic variational perturbation calculations,<sup>31-33</sup> and the first correction has been extracted from variational calculations of the Breit relativistic corrections.<sup>34-36</sup> Diagrams with one exchanged photon shown in Fig. 10, which may be regarded as two-electron corrections to the one-electron radiative corrections, correspond to level shifts of order



Fig. 9. Fourth-order Feynman diagrams with two exchanged photons.

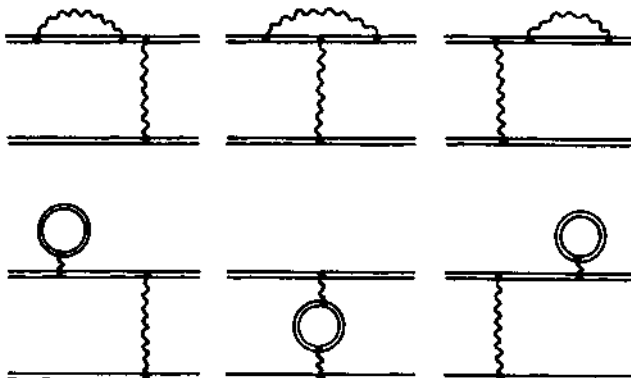


Fig. 10. Fourth-order Feynman diagrams with one exchanged photon.

$$\Delta E_{\text{op}}^{(4)} (2^3S_1 - 2^3P_0) \sim \frac{\alpha}{\pi} (Z\alpha)^4 \frac{1}{Z} m_e c^2 \quad (24)$$

These corrections are included to lowest order in  $Z\alpha$  in calculations for neutral helium,<sup>37-39</sup> but they have not been calculated at high  $Z$ . The third class of fourth-order diagrams, with no exchanged photons, appears in Fig. 11. These diagrams represent the fourth-order hydrogenic radiative corrections which have been calculated to the lowest order in  $Z\alpha$  for hydrogen:<sup>40,10</sup>

$$\Delta E_{\text{np}}^{(4)} (2^3S_1 - 2^3P_0) = \left(\frac{\alpha}{\pi}\right)^2 \frac{(Z\alpha)^4}{6} [-0.3221 + \dots] \quad (25)$$

The lowest-order result is not likely to be valid at high  $Z$ , but it does suggest that this correction is much smaller than other neglected corrections.

Sixth-order corrections are represented by Feynman diagrams with three virtual photons. The dominant correction, in analogy with lower orders, is associated with diagrams with three exchanged photons. As in lower orders, the leading term in  $Z\alpha$  is known from nonrelativistic variational perturbation calculations:<sup>31-33</sup>

$$\Delta E_{\text{pe}}^{(6)} (2^3S_1 - 2^3P_0) = \alpha^3 (Z\alpha)^{-1} m_e c^2 [-0.0117 + \dots] \quad (26)$$

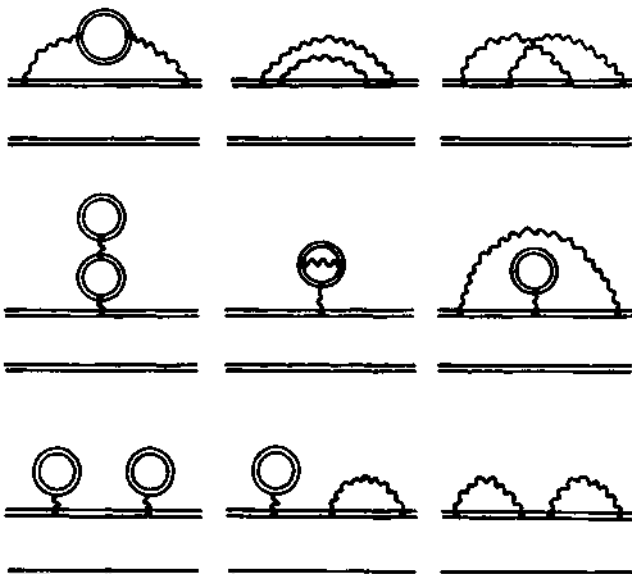


Fig. 11. Fourth-order one-electron Feynman diagrams.

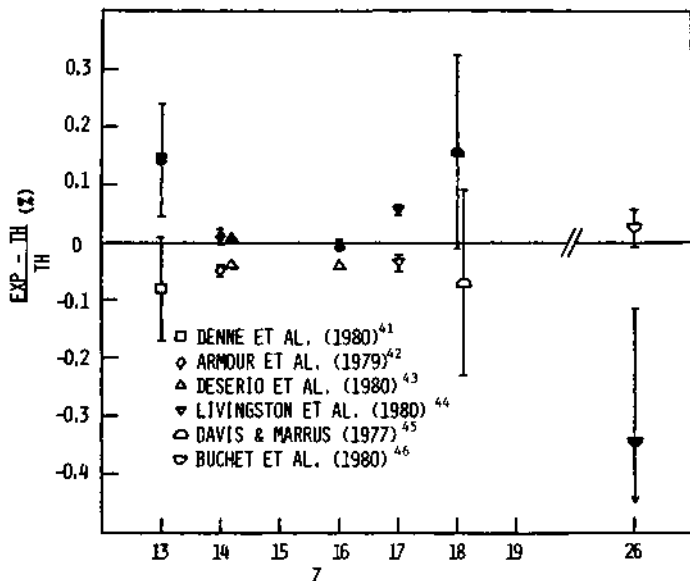


Fig. 12. Comparison of experiment and theory for the  $2\ S_1 - 2^3P_0$  and  $2^3S_1 - 2^3P_2$  energy level separations in high- $Z$  two-electron atoms. The filled (open) shapes correspond to the  $2^3S_1 - 2^3P_0$  ( $2^3S_1 - 2^3P_2$ ) transitions.

The total level splitting, to the accuracy considered here, is summarized as

$$\Delta E(2^3S_1 - 2^3P_0) = -S + \Delta E_{pe}^{(2)} + \Delta E_{pe}^{(4)} + \Delta E_{pe}^{(6)} + \dots \quad (27)$$

The one-electron terms, corresponding to Feynman diagrams with no exchanged photons, are collected in the one-electron Lamb shift  $S$ .<sup>13</sup> The lowest order terms in  $Z\alpha$  in the perturbation expansion, in Eqs. (22), (23), and (26), form a series of increasing powers of  $Z^{-1}$ . Hence, the perturbation scheme is rapidly convergent at high  $Z$ , as would be expected on physical grounds.

Experiment and theory for the  $2^3S_1 - 2^3P_0$  and  $2^3S_1 - 2^3P_2$  energy separations are compared in Fig. 12, which shows the fractional difference as a function of  $Z$  for  $Z > 10$ . Only experimental uncertainties are included in the error bars. The difference between experiment and theory is comparable to uncalculated theoretical contributions. Comparison of Fig. 7 and Fig. 12 shows that the theory and experiments are sufficiently accurate to test the radiative corrections.

## CONCLUSION

The theory of radiative corrections in strong fields in quantitatively successful where it has been tested. In one-electron atoms, the experimental uncertainties presently limit the precision of the tests to an accuracy of about 1%. In two-electron atoms, uncalculated contributions in the theoretical energy splittings limit the accuracy of the tests; however, the basic theory of high-Z few-electron atoms appears to be well understood. With further measurements and calculations, more precise tests of the theory should be possible.

Research supported by the National Science Foundation, Grant No. PHY80-26549.

## REFERENCES

1. For a review of strong field QED, see S.J. Brodsky and P.J. Mohr, in Structure and Collisions of Ions and Atoms, ed. by I.A. Sellin (Springer, Berlin, 1978), Topics in Current Physics, Vol. 5, p.3.
2. S.S. Schweber, An Introduction to Relativistic Quantum Field Theory, Harper and Row, New York, 1961.
3. M. Gell-Mann and F. Low, Phys. Rev. 84, 350 (1951).
4. J. Sucher, Phys. Rev. 107, 1448 (1957); In this paper, it is pointed out that the Gell-Mann-Low formula is a suitable starting point for calculation of high-Z two-electron energy levels.
5. E.H. Wichmann and N.M. Kroll, Phys. Rev. 101, 843 (1956).
6. G.E. Brown, J.S. Langer, and G.W. Schaefer, Proc. Roy. Soc. (London) A 251, 92 (1959).
7. A.M. Desiderio and W.R. Johnson, Phys. Rev. A 3, 1267 (1971).
8. P.J. Mohr, Ann. Phys. (N.Y.) 88, 26, 52 (1974).
9. K.T. Cheng and W.R. Johnson, Phys. Rev. A 14, 1943 (1976).
10. For a review, see B.E. Lautrup, A. Peterman, and E. de Rafael, Phys. Reports 3, 193 (1972).
11. G.W. Erickson, J. Phys. Chem. Ref. Data 6, 831 (1977).
12. G.W. Erickson, Phys. Rev. Lett. 27, 780 (1971).
13. P.J. Mohr, in Beam-Foil Spectroscopy, eds. I.A. Sellin and D.J. Pegg, (Plenum Press, New York, 1976), p. 89.
14. P.J. Mohr, Phys. Rev. Lett. 34, 1050 (1975).
15. H.W. Kugel, M. Leventhal, D.E. Murnick, Phys. Rev. A 6, 1306 (1972).
16. G.P. Lawrence, C.Y. Fan, S. Bashkin, Phys. Rev. Lett. 28, 1612 (1972).
17. M. Leventhal, D.E. Murnick, H.W. Kugel, Phys. Rev. Lett. 28, 1609 (1972).
18. H.W. Kugel, M. Leventhal, D.E. Murnick, C.K.N. Patel, O.R. Wood II, Phys. Rev. Lett. 35, 647 (1975).
19. H. Gould and R. Marrus, Phys. Rev. Lett. 41, 1457 (1978).

20. E.T. Nelson, O.R. Wood II, C.K.N. Patel, M. Leventhal, D.E. Murnick, H.W. Kugel, and Y. Niv, Abstract submitted to the Second Int. Conf. on Precision Meas. and Fund. Const., Gaithersburg, MD, June 1981, p. 92.
21. J. Daley, M. Douglas, L. Hambro, and N.M. Kroll, Phys. Rev. Lett. 29, 12 (1972).
22. R.F. Christy and J.M. Keller, Phys. Rev. 61, 147 (1942).
23. H.A. Bethe and E.E. Salpeter, Quantum Mechanics of One- and Two-Electron Atoms (Springer, Berlin, 1957).
24. D. Layzer and J. Bahcall, Ann. Phys. (N.Y.) 17, 177 (1962).
25. A. Dalgarno and A.L. Stewart, Proc. Phys. Soc. 75, 441 (1960).
26. L.N. Labzovskii, Zh. Eksp. Teor. Fiz. 59, 168 (1970), [Sov. Phys. JETP 32, 94 (1971)].
27. G.L. Klimchitskaya and L.M. Labzovskii, Zh. Eksp. Teor. Fiz. 60, 2019 (1971), [Sov. Phys. JETP 33, 1088 (1971)].
28. L.N. Ivanov, E.P. Ivanova, and U.I. Safronova, J. Quant. Spectrosc. Radiat. Transfer 15, 553 (1975).
29. H.T. Doyle, Advances in Atomic and Molecular Physics, (Academic, New York, 1969), Vol. 5, p. 337.
30. P.J. Mohr, unpublished (1975).
31. R.E. Knight and C.W. Scherr, Rev. Mod. Phys. 35, 431 (1963).
32. F.C. Sanders and C.W. Scherr, Phys. Rev. 181, 84 (1969).
33. K. Aashamar, G. Lyslo, and J. Midtdal, J. Chem. Phys. 52, 3324 (1970).
34. Y. Accad, C.L. Pekeris, and B. Schiff, Phys. Rev. A 4, 516 (1971).
35. P.J. Mohr, in Beam-Foil Spectroscopy, eds. I.A. Sellin and D.J. Pegg, (Plenum Press, New York, 1976), p. 97.
36. A.M. Ermolaev and M. Jones, J. Phys. B 7, 199 (1974).
37. P.K. Kabir and E.E. Salpeter, Phys. Rev. 108, 1256 (1957).
38. J. Sucher, Phys. Rev. 109, 1010 (1958).
39. H. Araki, Progr. Theor. Phys. (Japan) 17, 619 (1957).
40. T. Appelquist and S.J. Brodsky, Phys. Rev. Lett. 24, 562 (1970).
41. B. Denne, S. Huldt, J. Pihl, and R. Hallin, Physica Scripta 22, 45 (1980).
42. I.A. Armour, E.G. Myers, J.D. Silver, and E. Träbert, Phys. Lett. 75A, 45 (1979).
43. R. DeSerio, H.G. Berry, and R.L. Brooks, in Proceedings of the Workshop on Foundations of the Relativistic Theory of Atomic Structure, Argonne National Laboratory, Dec., 1980, Argonne Report ANL-80-126, p. 240.
44. A.E. Livingston, S.J. Hinterlong, J.A. Poirier, R. DeSerio, and H.G. Berry, J. Phys. B 13, L139 (1980).
45. W.A. Davis and R. Marrus, Phys. Rev. A 15, 1963 (1977).
46. J.P. Buchet, M.C. Buchet-Poulizac, P. Ceyzeriat, A. Denis, J. Désesquelles, M. Druetta, and K. Tran Cong, in Proceedings of the Workshop on Foundations of the Relativistic Theory of Atomic Structure, Argonne National Laboratory, Dec., 1980, Argonne Report ANL-80-126, p. 236.

# THE DESCRIPTION OF EXCITATION PROCESSES IN ION-ATOM COLLISIONS

J.S. Briggs

Fakultät für Physik  
Universität Freiburg  
D-7800 Freiburg i. Br., Germany

## INTRODUCTION

From being a subject of fundamental interest in its own right in the early days of quantum mechanics, atomic physics has moved more and more into a role of providing a diagnostic tool to be employed as a 'measuring device' in more complicated physical situations. Good examples of this are to be found in the fields of plasma physics, of astrophysics and in some instances in the interactions of fundamental particles and of course in QED. Atomic physics is unique among the disciplines of modern physics in that the nature of the forces operating, the electromagnetic forces, are well-understood. This knowledge carries with it a responsibility that atomic physics should be capable of an accuracy which is not often demanded in other disciplines. Only when high accuracy in the description of atomic processes is achieved can such processes be applied to monitor the manifestations of more fundamental interactions. The classic example of this type of use of atomic physics is the discovery of the Lamb shift.

The understanding of the collisions between atoms and ions is of course a considerably harder problem than the study of isolated atoms. Nevertheless sufficient progress has been made in this field in the past fifteen years for us to say today that the dominant characteristic processes occurring during the coalescence of two atoms are well-understood. This understanding allows the monitoring of atomic events i.e. the production of vacancies (holes) and their subsequent decay by photon or electron emission to be used to interpret other processes (e.g. nuclear excitation, positron emission) in the close collision of two heavy-ions. That is to say, the nuclear processes affect the electronic environment in a very charac-

teristic way which can be used to provide information on the nuclear processes themselves.

In this paper the theory of electronic excitation and ionisation processes occurring in ion-atom collisions will be developed. Particular emphasis is given to those processes where the nuclear fields are strong compared with the residual electron-electron interactions. This implies effectively the study of inner-shell processes. This is not only appropriate to the theme of this conference but allows considerable simplification of the general theory of ion-atom collisions to be made.

### THEORY OF ION-ATOM COLLISIONS

The general ion-atom collision is a complicated few-body problem which it is still not possible to treat accurately. However as we are mainly interested in inner-shell electrons we will simplify the problem from the outset. The inner-shell electrons are well-separated in space from most other electrons and their motion is dominated by the strong nuclear field. The wavefunction and general behaviour of such electrons becomes increasingly hydrogenic as  $Z$  increases. Even where the wavefunctions depart from hydrogenic behaviour the electrons tend to move independently of one another and a Hartree-Fock basis of one-electron states is generally adequate to describe both ground and excited states. Therefore a three-body problem described by the co-ordinates shown in fig. 1 will be discussed. An electron moves in the field of two nuclei. All the interactions are two-body and Coulombic. For a non-relativistic electron, spin can be ignored (the corrections for relativistic effects are considered later). Choosing the set of co-ordinates  $\underline{r}_2$ ,  $\underline{R}_2$ , the Schrödinger equation reads,

$$H \Psi (\underline{r}_2, \underline{R}_2) = E \Psi (\underline{r}_2, \underline{R}_2) \quad (2.1)$$

where,

$$\begin{aligned} H &= \{ -\frac{\hbar^2}{2\mu_2} \nabla_{\underline{R}_2}^2 - \frac{\hbar^2}{2\mu_2} \nabla_{\underline{r}_2}^2 + V_1(r_1) + V_2(r_2) + V_{12}(R) \} \\ &\equiv \{ T + K + V_1 + V_2 + V_{12} \}, \end{aligned}$$

The usual way to attempt to solve this equation is to use a trial wavefunction of the form

$$\Psi_t = \sum_n \phi_n(\underline{r}_1) F_n(\underline{R}_1) + \sum_m \phi_m(\underline{r}_2) G_m(\underline{R}_2) \quad (2.3)$$

in a variational principle to obtain a set of coupled integro differential equations for the functions  $F_n(\underline{R}_1)$ ,  $G_m(\underline{R}_2)$ . The functions  $\phi_n, \phi_m$  are arbitrary but must be able to represent correctly the bound electronic states in incident and final channels. The asymptotic form

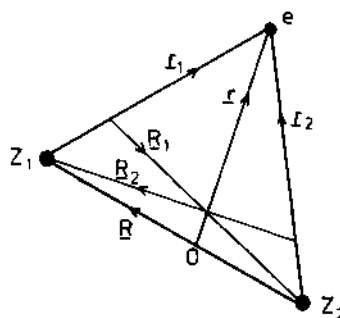


Fig. 1. Co-ordinate system for the two nuclei, one electron problem (not to scale). For simplicity, the centre-of-mass  $O$  of the two nuclei is considered to co-incide with the centre of charge.

of  $F(\underline{R}_1)$ ,  $G(\underline{R}_2)$  for capture or excitation is

$$\begin{aligned} F_n(\underline{R}_1) &\underset{\underline{R}_1 \rightarrow \infty}{\sim} \frac{1}{\underline{R}_1} e^{ik_n \underline{R}_1} f_n(\Omega_1) \\ G_m(\underline{R}_2) &\underset{\underline{R}_2 \rightarrow \infty}{\sim} \frac{1}{\underline{R}_2} e^{ik_m \underline{R}_2} g_m(\Omega_2) \end{aligned} \quad (2.4)$$

where  $f_n$ ,  $g_m$  are the scattering amplitudes for capture or excitation respectively. The coupled equations (2.3) are not easy to solve in their full generality. Either of two approximations is generally made. For fast collisions the basis of atomic eigenstates on nucleus  $Z_1$  and  $Z_2$  is taken. This is appropriate to a situation in which the collision time is much less than electronic orbital times. Then capture is much less probable than simple excitation of the target and the role of target and projectile nucleus is quite different. By contrast, at low velocity where the collision time is much less than orbital times (for an inner-shell this implies roughly that the incident velocity  $v$  in units of the Bohr velocity  $v_0$ , is smaller than both nuclear charges  $Z_1$ ,  $Z_2$ ) it is physically meaningful to employ a basis in which the two nuclei appear on an equal footing. Such a molecular basis is introduced in the following way. To order (electron mass/nuclear mass) the co-ordinates  $\underline{r}$ ,  $\underline{R}$  may be used

with Hamiltonian

$$H = -\frac{\hbar^2}{2M} \nabla_{\underline{R}}^2 - \frac{\hbar^2}{2m} \nabla_{\underline{r}}^2 + V_1(\underline{r}) + V_2(\underline{r}) + V_{12}(\underline{R}) \quad (2.5)$$

The full equivalence of the two nuclear fields is emphasised by using a basis set which diagonalises the molecular Hamiltonian for fixed  $\underline{R}$

$$\text{i.e. } (-\frac{\hbar^2}{2m} \nabla_{\underline{r}}^2 + V_1 + V_2) \chi_n(\underline{r}, \underline{R}) = E_n(\underline{R}) \chi_n(\underline{r}, \underline{R}) \quad (2.6)$$

and where the states are further characterized by the projection of the electronic angular momentum along  $\hat{\underline{R}}$ , the internuclear direction. A trial function composed of a finite superposition of molecular orbital (MO) functions  $\chi_n$  i.e.

$$\text{i.e. } \Psi_t(\underline{r}, \underline{R}) = \sum_n \chi_n(\underline{r}, \underline{R}) F_n(\underline{R}) \quad (2.7)$$

leads to a set of coupled equations

$$\begin{aligned} \{\nabla_{\underline{R}}^2 + k_n^2\} F_n(\underline{R}) &= -2 \sum_{m \neq n} \langle \chi_n | \nabla_{\underline{R}} | \chi_m \rangle \cdot \nabla_{\underline{R}} F_m(\underline{R}) \\ &\quad - \sum_{m \neq n} \langle \chi_n | \nabla_{\underline{R}}^2 + k_n^2 | \chi_m \rangle F_m(\underline{R}) \end{aligned} \quad (2.8)$$

where  $k_n^2 = \frac{2M}{\hbar^2} (E - E_n(\underline{R}) - V_{12}(\underline{R}))$ . After (numerical) solution of the coupled equations the asymptotic behaviour

$$F_n(\underline{R}) \underset{\underline{R} \rightarrow \infty}{\sim} \frac{1}{\underline{R}} \exp(i k_n \underline{R}) f_n(\Omega) \quad (2.9)$$

is examined to extract the scattering amplitude  $f_n$  to final state  $n$ . Two comments must be made concerning the MO basis. Firstly, if the off-diagonal terms in (2.8) are neglected, then only elastic scattering is possible according to

$$(\nabla_{\underline{R}}^2 + k_n^2) F_n(\underline{R}) = 0 \quad (2.10)$$

for each electronic state  $n$ . The functions  $F_n$  are the continuum analogues of the Born-Oppenheimer wavefunctions used to describe the stationary vibrational states of bound molecules. The terms on the r.h.s. of (2.8) couple the electronic and nuclear motion and cause transitions between the adiabatic MO. Such a description of slow inelastic collisions pervades the whole of atomic collision theory<sup>(1)</sup>. The transitions between suitably-defined adiabatic states caused by internuclear motion is used equally well to describe fine-structure changing collisions at impact energies of a few eV as to describe inner-shell transitions in heavy-atom collisions at hundreds of MeV. It is also the basis of the description of so-called vibronic transitions in stable molecules.

The second point concerning the MO basis is that the corresponding choice of co-ordinates  $\underline{r}$ ,  $\underline{R}$  does not allow us to satisfy correctly the boundary conditions on the scattering problem.<sup>(2)</sup> Hence, although the MO may separate correctly to atomic orbitals (AO), it is not permissible to neglect terms of order  $(m/M)$  from the outset. To see this let us suppose that the electron is initially bound to  $Z_1$ . Then the initial form of  $F(\underline{R})$  is not  $\exp(-i \underline{k}_n \cdot \underline{R})$  describing the relative motion of the nuclei, but rather  $\exp(-i \underline{k}_n \cdot \underline{R}_1)$  describing the motion of  $Z_2$  relative to the centre-of-mass of  $(Z_1 + e)$ .

$$\text{i.e. } \Psi(\underline{r}, \underline{R}) \sim \exp(-i \underline{k}_n \cdot \underline{R}_1) \phi_n(\underline{r}_1) \quad (2.10)$$

$$\text{Since, however } \underline{R}_1 = \underline{R} + m \underline{r}_1 / (m+M_1)$$

$$\sim \underline{R} + \frac{m}{M_1} \underline{r}_1 \quad (2.11)$$

The asymptotic wavefunction is seen to contain a factor  $\exp(-i(m/M_1) \underline{k}_n \cdot \underline{r}_1)$ . Since  $\underline{r}_1 = \underline{r} - M_2 \underline{R} / (M_1 + M_2)$  the electronic factor is  $\exp(-i m \underline{v}_1 \cdot \underline{r})$  where

$$\underline{v}_1 = \underline{k}_n / M_1 = (\underline{k}_n / M) \cdot \frac{M_2}{M_1 + M_2} = \underline{v} \cdot \frac{M_2}{M_1 + M_2} \quad (2.12)$$

is the velocity of nucleus  $Z_1$  relative to 0. Hence the MO basis function  $\chi_n(\underline{r})$  must be replaced by  $\chi_n(\underline{r}) \exp(-i m \underline{v}_1 \cdot \underline{r})$  asymptotically to enable it to satisfy the boundary conditions correctly. This is a complication of the adiabatic problem.

The coupled equations (2.8) are usually solved by expansion in partial waves

$$F_n(\underline{R}) = \frac{1}{R} \sum_{\ell} (2\ell+1) F_{n,\ell}(R) P_{\ell}(\cos\theta) \quad (2.13)$$

Then a set of coupled equations for the radial functions  $F_{n,\ell}(R)$  can be obtained. For heavy-particle motion the number of  $\ell$ -values can become prohibitively large. Then  $\ell \hbar$  is approximately equal to the classical angular momentum  $M b v$  of a collision at impact parameter  $b$ . For a transition with inelastic energy  $(E_n - E_0)$  the relevant impact parameter for transition is

$$b \sim \frac{v \hbar}{(E_n - E_0)}$$

which gives  $\ell$ -values of the order of  $Mv^2 / (E_n - E_0)$ . Hence if the inelastic energy of the collision is small i.e. well above threshold, then many  $\ell$ -values contribute and a classical description of the nuclear motion may be possible. The formal derivation of this "semi-classical" treatment of atomic collisions can be made in various ways.<sup>(3)</sup>

In the classical trajectory method the internuclear trajectory is a prescribed function of the collision parameters  $b$  and  $v$  and of

the time  $t$ . The collision problem is now time-dependent, the inter-nuclear potential can be eliminated from the Hamiltonian by a phase transformation and the Schrödinger equ. to be solved is<sup>+)</sup>

$$\{H_e(t) - i \frac{\partial}{\partial t} |_{\underline{r}}\} \Psi(\underline{r}, t) = 0 \quad (2.14)$$

subject to the appropriate boundary conditions. It is emphasised explicitly in (2.14) that time differentiation is performed with electron co-ordinates fixed in a chosen reference frame. The Hamiltonian is

$$H_e = K + V_1(t) + V_2(t) \quad (2.15)$$

in which  $\underline{R}$  appears parametrically.

The requirement that the wave function satisfy the correct boundary conditions appears here as the requirement that the theory be Galilei invariant i.e. that the solution of the Schrödinger equation be independent of the choice of inertial reference frame. For example, consider an arbitrary reference frame with origin  $\hat{O}$  translating with uniform velocity  $\underline{v}$  with respect to  $O$ . The Galilei invariance of (2.14) requires that

$$\Psi(\underline{r}, t) = U \tilde{\Psi}(\hat{\underline{r}}, t)$$

$$\text{and } U(H_e - i \frac{\partial}{\partial t} |_{\hat{\underline{r}}}) U^* = H_e - i \frac{\partial}{\partial t} |_{\underline{r}} \quad (2.16)$$

Utilizing the identity

$$\frac{\partial}{\partial t} |_{\hat{\underline{r}}} g(\underline{r}, t) = \frac{\partial}{\partial t} |_{\underline{r}} g(\underline{r}, t) + \underline{v} \cdot \nabla_{\underline{r}} g(\underline{r}, t) \quad (2.17)$$

for an arbitrary function  $g(\underline{r}, t)$  it is seen that (2.16) is satisfied by

$$U = \exp \{ i \underline{v} \cdot \underline{r} - \frac{1}{2} i \underline{v}^2 t \}, \quad (2.18)$$

the Galilei transform operator. Hence, when a solution of (2.14) is sought with a trial function

$$\Psi = \sum_n a_n(t) \chi_n(t) \quad (2.19)$$

the basis functions must be chosen so that

$$\chi_n(\underline{r}, t) \underset{t \rightarrow \pm \infty}{\sim} \phi_n(\underline{r}_i) \exp(i \underline{v}_i \cdot \underline{r} - \frac{1}{2} i \underline{v}_i^2 t) \quad (2.20)$$

<sup>+)</sup> Since only the electron mass appears we use now atomic units with  $e = m = \hbar = 1$ .

where  $\underline{v}$  is the appropriate nuclear velocity relative to the chosen frame. This requirement has the consequence that the MO basis functions must be multiplied by some kind of 'translational factor' to give the correct asymptotic behaviour. Then the basis is no longer orthonormal and the trial wavefunction (2.19) leads to the coupled equations

$$i \underline{S} \frac{d}{dt} \underline{a} = \underline{M} \underline{a} \quad (2.21)$$

where  $\underline{a}$  is the column matrix of expansion co-efficients,  $\underline{S}$  is the overlap matrix with elements  $S_{k\ell} = \langle \chi_k | \chi_\ell \rangle$  and  $\underline{M}$  is the matrix  $\langle \chi_k | (H_e - i \frac{\partial}{\partial t}) | \chi_\ell \rangle$ .

The Hermiticity of the electronic Hamiltonian implies that the exact solution is of constant norm. Probability conservation is ensured also in the approximate case so long as (2.21) are solved exactly. Consider

$$i \frac{d}{dt} N^2 \equiv i \frac{d}{dt} \langle \psi | \psi \rangle = i \frac{d}{dt} (\underline{a}^T \underline{S} \underline{a})$$

Differentiating one finds

$$i \frac{d}{dt} N^2 = \underline{a}^T (i \frac{d}{dt} \underline{S} + \underline{M} - \underline{M}^T) \underline{a} \quad (2.22)$$

However the Hermiticity of  $H_e$  implies that

$$i \frac{d}{dt} \underline{S} = \underline{M}^T - \underline{M} \quad (2.23)$$

So that the trial solution is of constant norm. (4)

After solution of the set of coupled first-order equations in time (usually numerically) subject to appropriate initial conditions ( $t=-\infty$ ), the probability of occupation of a given orbital after the collision is obtained as

$$P_n(\underline{b}, \underline{v}) = |a_n(+\infty)|^2 \quad (2.24)$$

and the cross-section for excitation as

$$\sigma_n(\underline{v}) = \int db P_n(\underline{b}, \underline{v}) \quad (2.25)$$

The major problem in the use of this method is the necessity to truncate the expansion. Therefore some physical intuition, based largely upon a prior knowledge of the adiabatic MO potentials, is needed to judiciously choose the basis functions to be included. Simple approximate analytic solutions (e.g. the Landau-Zener problem (5)) are also useful to infer the physical processes occurring under given collision conditions. Examples of the solution of the

equations (2.21) for various simple systems are considered in the next section.

### EXAMPLES OF INNER-SHELL PROCESSES

Our aim is to solve (2.21) by a choice of basis functions designed to span those parts of Hilbert space occupied by the electron during a particular collision. In this respect the excitation of K-shell electrons is an outstanding example of the success of this approach. (6) The first task is to compute the adiabatic energy levels, examples of which are shown in fig. 2. The dominant coupling of adiabatic channels is provided by the  $\frac{\partial}{\partial t}$  operator. Since

the adiabatic wavefunctions are quantised along the molecular axis  $\underline{R}(t)$  with an electron co-ordinate  $\underline{r}$ , they are related to wavefunctions described in the laboratory-fixed frame by

$$x_k(\underline{r}, R) = \exp(-i\theta(t)J_y) x_k(\underline{r}', R), \quad (3.1)$$

where  $J_y$  is the component of the electron's angular momentum perpendicular to the  $xz$  collision plane. The angle  $\theta$  is the instantaneous orientation of the molecular axis to the fixed laboratory axes, whose  $z$ -direction is conventionally that of the incident beam. From the form of (3.1) one sees that

$$\frac{\partial}{\partial t} |_{\underline{r}'} x_k(\underline{r}, R) = \{v_R \frac{\partial}{\partial R} |_{\underline{r}} - i \dot{\theta} J_y\} x_k(\underline{r}, R) \quad (3.2)$$

where  $v_R$  and  $\dot{\theta}$  are the radial and rotational velocities respectively.

Hence the coupling consists of two types, radial and rotational. The radial coupling "squeezes" the electron along the molecular axis and thereby attempts to change the radial nodal structure. Apart from the unusual case of pure one-electron systems, this always involves non-adiabatic inelastic energy transfer. By contrast the rotational coupling, which changes the  $\sigma, \pi \dots$  quantum numbers of the MO involves basically a change in the orientation of nodal planes and can be accomplished with small or zero change in the adiabatic energy of the electronic i.e. transitions occur between levels degenerate for certain values of  $R$ . Several examples of the operation of these non-adiabatic couplings are given below.

#### (i) Electron transfer in $H^+ + H(1s)$ collisions

The simplest atomic collision, although unfortunately of limited general importance, is the symmetric proton-hydrogen collision whose levels are shown in fig. 2. In a symmetric nuclear system, the levels are characterized by  $g$  or  $u$  according as their wavefunctions are even or odd under interchange of the nuclei. If, for very slow collisions, the effect of translational factors is neglected, then the coupling operator is simply  $\partial/\partial t$ , which is even under inter-change of the nuclei. Therefore the problem separates into two separate problems,

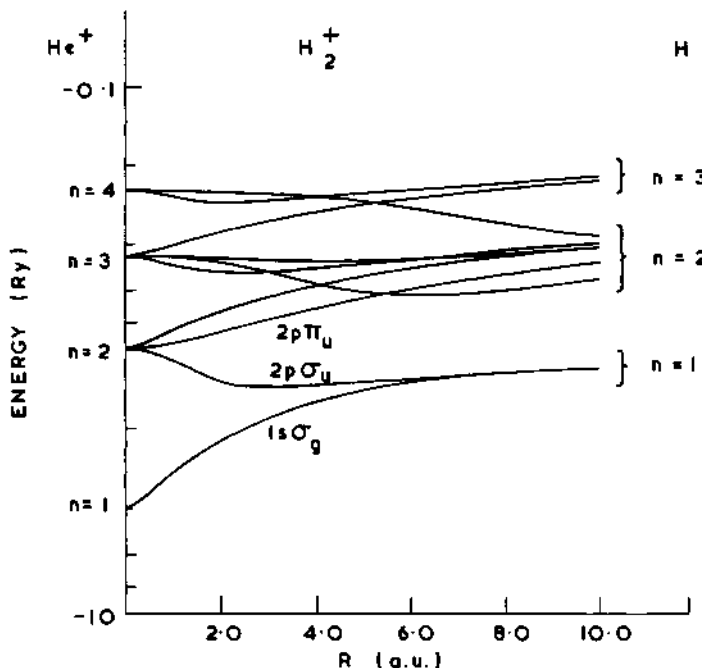


Fig. 2. The correlation diagram for the simplest one-electron molecule  $\text{H}_2^+$ .

one for the  $g$  and one for the  $u$  components. On energetic grounds, at the lowest velocities, since only the two lowest levels are populated adiabatically only these two levels, the  $1s\sigma_g$  and the  $2p\sigma_u$  levels are included in the expansion. In this circumstance the coupled equations for  $a_g(t)$  and  $a_u(t)$  separate and can be solved directly. (7) The probability for electron capture is given asymptotically by

$$|a(t)|^2 = \left| \frac{1}{\sqrt{2}} \{a_g(t) - a_u(t)\} \right|^2 \quad t \rightarrow +\infty$$

and can be written

$$P(b) = \sin^2 \left\{ \int_{-\infty}^{\infty} (E_g - E_u) dt \right\} \quad (3.3)$$

where  $E_g$ ,  $E_u$  are the respective MO energies. Hence one predicts and observes (8) as a function of the collision parameters  $v$  and impact parameter  $b$  (or scattering angle  $\theta$ ) an oscillatory dependence of the capture cross-section.

### (ii) Rotational coupling

The foregoing example results in no change in the internal energy and is untypical. The simplest transition relying upon the

non-adiabatic couplings is the promotion of  $1s$  electrons into the  $2p$  orbital either in homonuclear or heteronuclear systems. The coupling is between the  $2p\sigma$  and  $2p\pi$  MO (or simply the  $1\sigma$  and  $1\pi$  for asymmetric systems). At low velocity the expansion may first be truncated to just these two levels. The pair of coupled equations then reduces to

$$\begin{aligned}\dot{a}_\pi &= \theta f(R) a_\sigma(t) \exp(i\epsilon(t)) \\ \dot{a}_\sigma &= -\theta f(R) a_\pi(t) \exp(-i\epsilon(t))\end{aligned}\quad (3.4)$$

where  $\epsilon(t) = \int_{-\infty}^t (E_\pi - E_\sigma) dt'$  and  $f(R)$  is the matrix element of

the rotational operator  $iLY$  (spin is of course conserved). It is sometimes convenient to emphasise the angular dependence by writing

$$\begin{aligned}\frac{da_\pi}{d\theta} &= f(R) a_\sigma(\theta) \exp(i\epsilon(\theta)) \\ \frac{da_\sigma}{d\theta} &= -f(R) a_\pi(\theta) \exp(-i\epsilon(\theta))\end{aligned}\quad (3.5)$$

These coupled equations must be solved numerically for an electron initially in the  $2p\sigma$  MO. For a repulsive Coulomb trajectory the probability as a function of impact parameter shows a peak rising rapidly with velocity and situated at impact parameters of the order of the K-shell radius of the separated atoms. At higher velocities a second peak appears (fig. 4) whose origin lies solely in the rotation of the molecular axis through a stationary electron i.e. an absolutely non-adiabatic transition at small distances where the  $\sigma$  and  $\pi$  levels are near-degenerate. In this situation the equations (3.5) are solved with  $f = 1$ ,  $\epsilon = 0$  (united atom values) to give simply

$$P(b) = \sin^2 \theta_f \quad (3.6)$$

where  $\theta_f$  is the final scattering angle<sup>(6)</sup>. The solution of the coupled equations (3.4) shows generally very good agreement with experiment<sup>(9)</sup> (fig. 3).

### iii) K-vacancy sharing

Particularly for homonuclear systems and generally at higher velocity, the 2-state expansion is inadequate and several coupled states must be included. Certain coupling processes are dominant in different regions of  $R$  values and often may be effectively separated one from the other. A very important question in the collision of very heavy ions is - how can vacancies be created in the deepest lying  $1\sigma$  MO? One obvious answer is by direct coupling to higher empty levels, mostly in the continuum. This process may

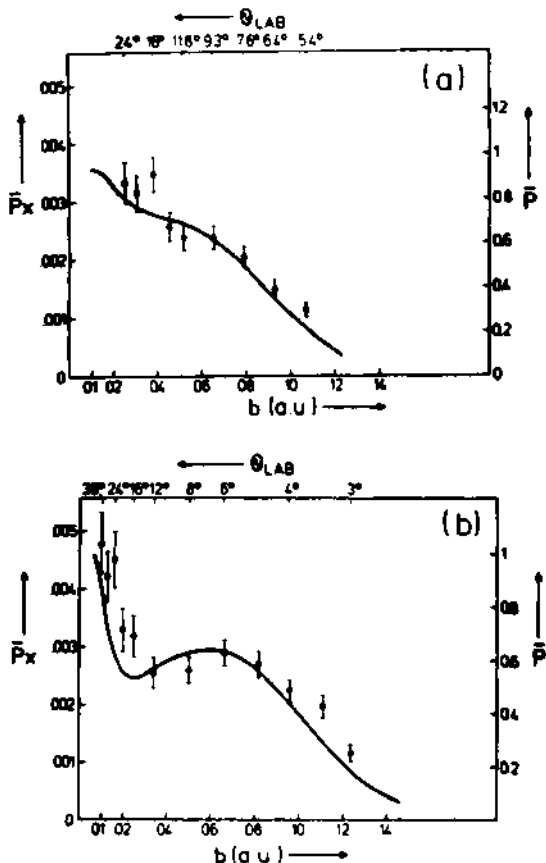


Fig. 3. Experimental x-ray production (left-hand scale) and theoretical vacancy production (full curve, right-hand scale) in  $\text{Ne}^+ - \text{Ne}$  collisions as a function of impact parameter  $b$ .  
 (a) Ion energy 235 keV b) ion energy 363 keV (from ref. 9).

compete unfavourably with a process in which vacancies are gradually fed down into deep levels by non-adiabatic transitions at places of near-approach of adiabatic levels. For example (see fig. 4) a  $1\sigma$  vacancy can be produced by first creation of a  $2p\pi$  vacancy at large distances and then the coupling sequence  $2p\pi - 2p\sigma - 1s\sigma$ . The final radial coupling can only occur on the outgoing half of the trajectory. Given the existence of a  $2p\sigma$  hole at  $t=0$ , the position of closest internuclear approach, an approximate analytical solution can be given of the two-state  $2p\sigma - 1s\sigma$  coupled equations<sup>(10)</sup> resulting in a probability  $\omega$  that after the collision the hole appears in the  $1s\sigma$  orbital

$$\omega = \{1 + \exp (2x)\}^{-1} \quad (3.7)$$

$$\text{where } x \equiv 2\pi (\epsilon_A^{1/2} - \epsilon_B^{1/2})/v$$

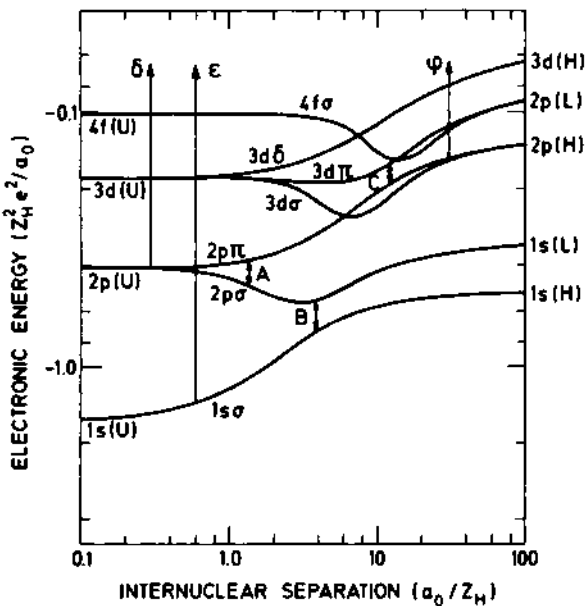


Fig. 4. Possible electronic transitions (indicated by arrows) which are important in the production of K-shell vacancies in an asymmetric ion-atom collision.

This formula has had considerable success in the interpretation of a large amount of data on the creation of K-vacancies in near symmetric heavy-ion collisions (11). It has been tested by comparison with numerical solutions of the coupled equations and the regions of its applicability are well-established.

#### iv) Perturbation theory

It is always sensible to search for perturbation expansions to solve the coupled equations (2.21) in an approximate way. Such perturbation solutions often possess simple scaling properties and serve as standard calculations against which to compare more exact solutions. Two such limits are identified. The first limit is when  $Z_1 \ll Z_2$  so that the influence of the projectile is always small. Then it can be shown that a choice of basis set as undistorted atomic wavefunctions translating with the target nucleus leads to a first-order amplitude

$$a_n = -i \int_{-\infty}^{\infty} \langle \phi_n(r_2) | V_1(t) | \phi_0(r_2) \rangle \exp\{-i(\epsilon_0 - \epsilon_n)t\} dt \quad (3.8)$$

for transition from level 0 to level n of the target. Application of this simple formula has had considerable success in the calculation of excitation of heavy ions by light-ion impact. (12) The

formula (3.8) can be shown to be a consistent first-order expansion of the scattering problem in powers of  $Z_1/Z_2$ . One should note however that it is not possible to give a similar first-order expansion of the amplitude for capture into states of the projectile, indeed the correct description of capture processes at high velocity remains unsolved.

The second limit amenable to perturbation theory is for extremely slow collisions where one considers transitions involving large inelastic energy defects e.g. from a K-shell into the continuum of a heavy ion. Such transitions are of low probability and the probability of excitation of an electron from e.g. the  $1s\sigma$  MO  $\chi_0$  to the continuum described by a wavefunction  $\chi_c$  can be written

$$a_c = -i \int_{-\infty}^{\infty} \langle \chi_c | \frac{\partial}{\partial t} r | \chi_0 \rangle \exp\{-i \int_{-\infty}^t (E_0(t') - E_c(t')) dt'\} dt \quad (3.9)$$

For slow collisions the basis MO refer to the molecular centre as origin and translational factors may be approximated to unity. This formulation has been applied to the calculation of ionisation in slow ion-atom collisions but unfortunately it is of limited validity. Whenever, for example, the initial or final state can be closely coupled, either by radial or rotational coupling, to other MO at same stage of the collision the formula (3.9) will be inapplicable. Since close coupling occurs frequently due to near-degeneracies of MO the simple form (3.9) is rarely a good approximation.

#### (v) Relativistic effects

When the inner-shell excitation of ions with nuclear charge greater than  $Z \sim 50$  is considered then relativistic wavefunction effects come into play, even though the nuclear motion may still be considered classically. The first and most obvious effect is that it is no longer the component of the electron's orbital momentum  $\ell$  along the internuclear axis that is relevant, rather it is the component of the total momentum  $j$ . Then the character of the rotational coupling is changed completely and it is no longer possible to give rotational coupling the simple geometric interpretation as in section (ii). Rather, the addition of the spin-orbit interaction to the Hamiltonian alters the correlation rules. The particular case of the changes in the  $2p\sigma$ - $2p\pi$  rotational coupling occasioned by the introduction of spin-orbit coupling have been examined in detail<sup>(13)</sup>. The relativistic situation is more complicated. Instead of coupling between the degenerate  $2p(m=0)$  and  $2p(m=1)$  levels in the united-atom limit, one has a coupling between the  $2p(j=3/2, m=1/2, 3/2)$  degenerate levels and the non-degenerate  $2p(j=1/2, m=1/2)$  level which correlates to the separated atom K-shell. This type of complication is typical of the relativistic situation.

A more dramatic effect of the relativistic behaviour of inner-

shell electrons is seen in the direct ejection of electrons into the continuum. The relativistic motion results in K-shell electrons with considerably enhanced high momentum components with respect to those of non-relativistic electrons (14,15). Since it is the high-momentum components which are instrumental in the removal of electrons into the continuum, the cross-section for ionisation can be many orders of magnitude greater than that expected on the basis of scaling of non-relativistic cross-sections (15). This much was known and experimentally confirmed in the collision of light ions on heavy atoms (14). Recent work on the collision involving actinides (16) has indicated K-shell vacancy production probabilities approaching unity. This indicates that in such collisions the K-shell appears to be unstable against even slow changes in the Coulomb nuclear potential to which it is bound. Since in these collisions it is highly likely that not all the outer-shell electrons will be ejected simultaneously, the overall effect would be a near 100% population inversion with respect to the K-shell of uranium. This may have practical implications for the production of stimulated X-ray emission. Typical  $P(b)$  values are shown in Fig. 5.

#### DIFFERENTIAL CROSS-SECTION

The assumption of classical internuclear motion is an extreme condition which completely eliminates the coupling between nuclear scattering and scattering off the atomic electrons. The simplest form, a straight line trajectory ignores the internuclear potential altogether. This is rarely a good approximation for slow ion-atom collisions but it is well-established that, for inner-shell excitation, the description of nuclear motion by a screened Coulomb trajectory provides total cross sections in good agreement with experiment. However, the question of differential cross-sections requires closer examination. The link between a quantum-mechanical and a fully classical description of nuclear motion is provided by the eikonal approximation. If the amplitude for a particular inelastic atomic process at impact parameter  $b$  on a classical trajectory decided by an internuclear potential  $V(R)$  is  $a(b)$ , the corresponding differential cross-section (17) for heavy ion scattering through an angle  $\theta$  is<sup>+</sup>

$$\frac{d\sigma}{d\theta} = 2\pi M v^2 \left| \int_0^\infty b J_0(\eta b) e^{i\chi(b)} a(b) db \right|^2 \quad (4.1)$$

where  $\chi(b) = \int_{-\infty}^\infty V(R) dt$  and  $\eta = 2\mu v \sin(\theta/2)$

The formula (4.1) has interesting limiting cases. When  $V=0$  i.e. a straight line trajectory, it can be shown that  $d\sigma/d\theta$  is identical to order  $(m/M)$  with the differential cross section calculated from

<sup>+</sup>) Here we assume for simplicity that the excitation involves no change in magnetic quantum number.

the full quantum-mechanical equations (2.8) under the assumption that the heavy-particle motion is describable by plane waves. This approximation allows one to extract differential cross-sections from calculations of  $a(b)$  using a straight-line trajectory. However the scattering of the incident nucleus is then off the electron alone and this approximation is of doubtful validity for close collisions leading to inner-shell excitations. However it can be shown that (17) in the limit  $Mv \rightarrow \infty$  (both in atomic units) the eikonal integral in (4.1) can be evaluated in stationary phase to give

$$\frac{d\sigma}{d\theta} = \left( \frac{d\sigma}{d\theta} \right)_{\text{class}} P(b(\theta)) \quad (4.2)$$

where  $\left( \frac{d\sigma}{d\theta} \right)_{\text{class}}$  is the classical differential cross-section and  $P(b) = |a(b)|^2$  for impact parameter  $b$  corresponding to classical scattering angle  $\theta$ . Since in slow collisions  $v \ll Z$  still allows  $v$  at least of the order of unity, the approximation (4.2) is well-justified except for the very small angle scattering i.e.  $\theta \sim 1/M$ . The procedure represented by (4.2) is the one usually adopted to compare  $P(b)$  calculations with experimentally measured differential cross-sections.

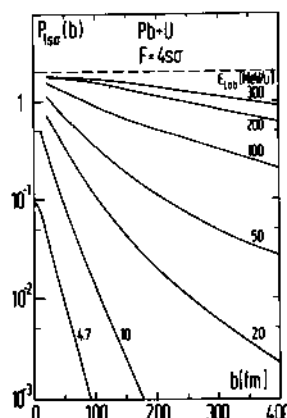


Fig. 5 Number of created  $1s_0$  vacancies per  $\text{Pb} + \text{U}$  collision at impact parameter  $b$  for various bombarding energies  $E_{\text{lab}}$ . The dashed line indicates the maximum possible value of the probability (from ref. 16b)

Recently interest has grown in the understanding of the interplay between nuclear and atomic inner-shell processes (18). Such effects can become prominent particularly near a nuclear resonance, where the united nucleus may exist for a time comparable or greater than K-orbital times, or in the region of a nuclear threshold. Although a semi-classical picture of the nuclear trajectory can still be used to discuss time coherence between excitation of atomic states on the inward and outward halves of the trajectory, a full understanding of the scattering only emerges from a quantum-mechanical treatment of the nuclear and atomic degrees of freedom. Then the full coupled equations (2.8) must be solved, with the additional complication that the nuclear wavefunctions  $F_n(R)$  must include the full effects of the real internuclear potential and not just its long-range part  $V_{12}(R)$ . The study of such effects in light-ion impact on nuclei is in its infancy but similar influence of the details of the nuclear interaction on the formation of inner-shell vacancies is to be expected for the scattering of very heavy ions, although the effects will be of a more complicated nature. Nevertheless, a clear understanding of the concomitant atomic processes may help in the unravelling of the nuclear processes resulting from the energetic collisions of heavy ions.

#### REFERENCES

1. N. F. Mott and H. S. W. Massey, *The Theory of Atomic Collisions* 3rd edn, (Oxford: O. U. P.) 1965.
2. D. R. Bates and R. Mc Carroll, *Proc. Roy. Soc. A245:175* (1958).
3. J. W. Frame, *Proc. Camb. Phil. Soc. 27:511* (1931),  
R. Mc Carroll and A. Salin, *Compt. Rend. Acad. Sci., 263:329* (1966), K. Taulbjerg, *J. Phys. B10:L341* (1977).
4. T. A. Green, *Proc. Phys. Soc., 86:1017* (1965).
5. L. D. Landau, *Z. Phys. Sow. Un., 2:46* (1932),  
C. Zener, *Proc. Roy. Soc., A137:696* (1932).
6. J. S. Briggs, *Rep. Prog. Phys., 39:217* (1976).
7. See ref. 1, p. 433.
8. H. F. Helbig and E. E. Everhart, *Phys. Rev. 140:A715* (1965),  
and ref. 1, p. 657.
9. S. Sackmann, H. O. Lutz and J. S. Briggs, *Phys. Rev. Lett., 32:805* (1974).
10. W. E. Meyerhof, *Phys. Rev. Lett., 31:1341* (1973).
11. W. E. Meyerhof, *Phys. Rev., A10:1005* (1974),  
R. Anholt and W. E. Meyerhof, *Phys. Rev. A16:190* (1977).
12. D. H. Madison and E. Merzbacher, *Atomic Inner-shell Processes* ed. B. Crasemann (New York: Academic) Vol. 1 p. 1 (1975).
13. R. Anholt, W. E. Meyerhof and A. Salin, *Phys. Rev., A16:951* (1977), D. H. Jakubassa and K. Taulbjerg, *J. Phys. B13:757* (1980).
14. P. A. Amundsen, L. Kocbach and J. M. Hansteen, *J. Phys. B9: L203* (1976).
15. B. Müller and W. Greiner, *Z. Naturforsch. 31a:1* (1976).

16. a) F. Bosch, D. Liesen, P. Armbruster, D. Moor and P. H. Mokler, *Zeits. f. Phys.*, A296:11 (1980).  
b) G. Soff, J. Reinhardt, B. Müller, T. de Reus, U. Müller and W. Greiner, G. S. I. Darmstadt Report 1980, p. 150.
17. P. T. Greenland, A. E. R. E. Harwell Report T. P. 850 (to be published in *J. Phys. B*).
18. G. Ciochetti and A. Molinari *Nuovo Cimento* 40:69 (1965),  
J. S. Blair, D. Dyer, K. A. Snover and T. A. Trainor, *Phys. Rev. Lett.* 41:1712 (1978),  
J. M. Feagin and L. Kocbach, *J. Phys. B*. (to be published),  
G. Soff, J. Reinhardt, B. Müller and W. Greiner, *Phys. Rev. Lett.*, 43:1981 (1979).

## PARTICLE CONDENSATES IN STRONGLY COUPLED QUANTUM FIELD THEORY

Johann Rafelski

Institut für Theoretische Physik  
der Johann Wolfgang Goethe-Universität  
Frankfurt am Main, Germany

### INTRODUCTION

The intense study of the behaviour of electrons bound in strong external potentials [1] has stimulated interest in the study of a number of related problems in quantum field theory with the ultimate aim being now the understanding of the vacuum structure of quantum chromodynamics. My lectures describe several attempts to understand the vacuum state of strongly interacting fields.

When the charge  $Z$  of a hypothetical superheavy nucleus is much larger than  $Z_{cr}$ , the real vacuum polarization charge screens a part of nuclear charge. In particular we anticipate that the vacuum charge can screen a substantial part of the source charge. It has been proposed [2] to treat that complex situation for finite size nuclei by the Thomas-Fermi method suitably modified and extended to account for the description of large real vacuum charge density. It will be shown that the real vacuum charge will screen all of the nuclear charge up to a surface dipole layer. Hence, a limiting constant value for the potential is found that depends only on the charge density of the source. To an outside observer the charge of the nucleus appears greatly reduced.

A very similar physical picture emerges from the treatment of bosons bound to strong potentials. Clearly, the concepts here must be very different as it is the Pauli exclusion principle that stabilized the charged vacuum states in the case of Fermi over-critical fields. In order to stabilize the new vacuum state, here, higher order effects must be retained in the Hamiltonian: it has been shown [1,3] that the stabilizing effect is inherent in the Coulomb repulsion of the Bose condensates. Examples of charged

condensates will be discussed.

Similar mechanisms are encountered when in an "Gedanken" experiment the fine-structure constant is increased arbitrarily. At a certain point the bound positronium state could lead to an inherent instability of QED. But even before that point we find a very instructive situation: muons, the heavy partners of electrons, can no more be produced as charged quanta. As  $\alpha \rightarrow \alpha_{cr} \sim 1$  the spontaneous production of a  $e^+ e^-$  pair would become possible leading to a neutralized muon state with the muon charge being carried away by the electron field [4]. Even at greater values of  $\alpha \sim 1.5$  (?) one could argue that the electron field also develops an inherent instability.

The methods developed for the study of supercritical fields can successfully be applied to the study of gauge theories and in particular to the study of the structure of the QCD vacuum. We have to deal here simultaneously with a strongly coupled theory with the Bose field having both attractive and repulsive self-interaction. Ignoring first a possible vacuum structure, i.e. working in the perturbative vacuum we consider the gauge field condensates around a Fermi source and describe the new ground state that must be constructed in order to have a satisfactory theory: a substantial screening of the color charge is found [5].

However, from this study we learn that the essential aspect of the interaction is the supercritical attractive force between the spin 1 gluons and the color magnetic field when both are anti-parallel. This property can be further exploited to construct a new, nonperturbative global vacuum state [6]. This construction is based on an approximate evaluation of the zero point energy of the interacting gauge fields leading to the known concept of 'effective Lagrangian' [7]. The supercritical binding of spin-1 gluons in colour-magnetic fields lowers the energy density of the interacting ground state below that of the perturbative state globally. Hence the usual vacuum state is quite different from the perturbative (naive) vacuum in which (perturbative) quarks are found. The ultimate description of the true QCD vacuum state in terms of the perturbative fields, similar in spirit to the BCS method, but certainly entirely different in its nature has not yet been accomplished.

We begin with the description of the neutralization of a large, supercritical charge density. As we were told by B. Müller at this conference, when the effective coupling constant is sufficiently large, the groundstate of QED undergoes a sudden change, best described by considering the change of the lowest energy state (vacuum) as a function of the external charge. The vacuum state acquires a finite charge when the external source exceeds the critical value  $V_{cr}$ . This is shown schematically in Fig. (1). As the occurrence of the ground state charge is a discontinuous phenomenon, we usually speak of a phase transition from neutral to charged vacuum. This

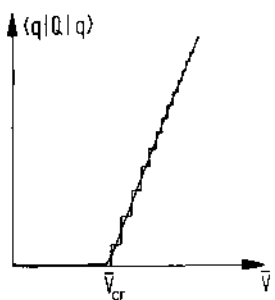


Fig. 1.1 : The charge of the ground state as function of the external potential strength  $\bar{V}$ . For  $\bar{V} > \bar{V}_{cr}$  the ground state is charged.

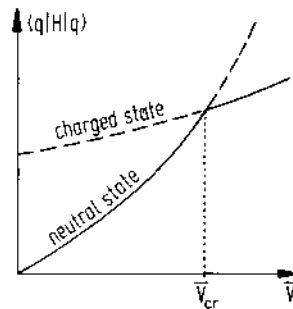


Fig. 1.2. : The lower energy neutral and charged state cross at the critical potential strength.

discontinuity is a consequence of the crossing shown in Fig. (2) between the energies of the neutral and charged states at  $\bar{V} = \bar{V}_{cr}$ .

In the next section we will study the vacuum state for arbitrarily large (nuclear) charge densities and then turn to the resolution of Klein's paradox in the theory of supercritical fields. Our aim is to understand the response of the vacuum to an ever-increasing external potential.

#### SUPERCHARGED ELECTRON VACUUM

Soon, as we increase the nuclear charge above  $Z\alpha = 173$  the charge of the vacuum will rise well above two and the self-interaction of the vacuum charge will become an important aspect. In particular, the vacuum charge may screen a substantial part of the (nuclear) external charge and prevent some states from being supercritical.

It has been proposed [2] to treat this complex situation by use of the relativistic Thomas-Fermi approximation. The charge density of the vacuum is equal to the charge density carried by all the states that have joined the lower continuum. In the Thomas-Fermi model, the sum over all these states is represented by an integral over all states with momentum inside the Fermi sphere of radius  $k_F$ . The density of electrons is related to the Fermi momentum  $k_F(x)$  by

$$\rho_e = \frac{e}{3\pi^2} k_F^3 \quad (2.1)$$

The effect of the spin degeneracy is included in Eq. (1). The relativistic relation between the Fermi energy  $E_F$  and Fermi momentum is

$$k_F^2 = [(E_F - eV)^2 - m^2] \theta(E_F - eV - m) \quad (2.2)$$

The step function ensures that  $k_F^2$  is a positive quantity.

From Eqs. (1) and (2) we now obtain for the charge density of the ground state  $|\Omega\rangle$  characterized by a choice of  $E_F$ :

$$\langle \Omega | \rho_e | \Omega \rangle = \frac{e}{3\pi^2} [(E_F - eV)^2 - m^2]^{3/2} \theta(E_F - eV - m) \quad (2.3)$$

Introducing the total charge density  $\rho_r$ , which is composed of the external "nuclear" part  $\rho_N$  and the electronic part

$$\rho_r = \rho_N + \langle \Omega | \rho_e | \Omega \rangle \quad (2.4)$$

and using Coulomb's law

$$\Delta eV(\vec{r}) = -e\rho_r(\vec{r}) \quad (2.5)$$

we find a self-consistent non-linear differential equation for the average potential  $V$  that depends on the choice of the Fermi surface  $E_F$ , characterizing the groundstate

$$\Delta eV(\vec{r}) = -e\rho_N(\vec{r}) - \frac{e^2}{3\pi^2} [(E_F - eV)^2 - m^2]^{3/2} \theta(E_F - eV - m) \quad (2.6)$$

We consider here Eq. (6) with the Fermi energy fixed at  $E_F = -m$ . This means that only the states accessible to spontaneous decay are filled. Inserting  $E_F = -m$  into Eq. (6) yields

$$\Delta eV(\vec{r}) = -e\rho_N(\vec{r}) - \frac{e^2}{3\pi^2} (2meV + e^2V^2)^{3/2} \theta(-eV - 2m) \quad (2.7)$$

We now proceed to discuss the solution of Eq. (7). Since the charge density of the vacuum must be confined to the vicinity of the external charge, we require a solution such that

$$eV(r) \xrightarrow{r \rightarrow \infty} -\frac{\gamma\alpha}{r} \quad (2.8a)$$

( $\alpha$  is the fine structure constant). For every choice of  $Z, \gamma$  is determined by the boundary condition on the electrostatic potential at the origin

$$\frac{\partial V}{\partial r} \Big|_{r=0} = 0 \quad (2.8b)$$

Eqs. (8a) and (8b) are therefore eigenvalue equations for  $\gamma$ , the

unscreened part of the nuclear charge, and  $Z - \gamma$  gives the charge of the vacuum:

$$\int d^3x \langle \Omega | \rho_e | \Omega \rangle = e(Z - \gamma) \quad (2.9)$$

Neglecting at first the inhomogeneity of the solution, we find that  $V(0) = V_0$  is determined from the condition

$$\rho_r = \rho_N + \langle \Omega | \rho_e | \Omega \rangle = 0 \quad (2.10)$$

in the limit of large  $Z$ , i.e. when the distribution of nuclear charge is large compared with  $1/m$ , then

$$eV_0 = \{m - [m^2 + (3\pi^2 \rho_N)^{2/3}]^{1/2}\}^{1/3} \rightarrow -(3\pi^2 \rho_N)^{1/3} \quad (2.11)$$

Integration of Eq. (7) is straightforward: An equal number of protons and neutrons and normal nuclear density have been assumed for the nuclear charge distribution. The results for  $\gamma$  are plotted in Fig. 1.

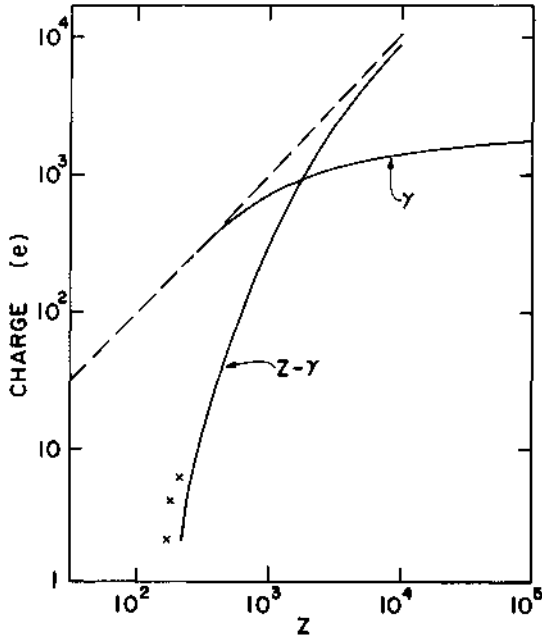


Fig. 2.1. The unscreened charge  $\gamma$  and the total charge of the vacuum  $(Z - \gamma)$  as a function of  $Z$ . The crosses denote points from single-particle calculations. The dashed line denotes the nuclear charge  $Z$ . (Ref. 2)

From the figure we see that  $\gamma$  increases monotonically with  $Z$ , and that  $\gamma/Z$  decreases as  $Z$  increases.

The single-particle results are denoted by crosses in Fig. 1

and agree reasonably well with an extrapolation of the Thomas-Fermi results into the realm of small values of  $Z - \gamma \gtrsim 1$ . In Fig. (2) we consider the approach to infinite nuclear matter. The potential approaches the limit described by Eq. (11) as  $Z$  increases from  $10^4$  to  $10^5$ . The radial total charge density, calculated from the right-hand side of Eq. (7), is shown in Fig. (3). The results are scaled with  $\gamma$  so that each curve is normalized to unity. We see that the charge density resembles more and more that of a surface dipole with clearly defined regions of positive and negative charge.

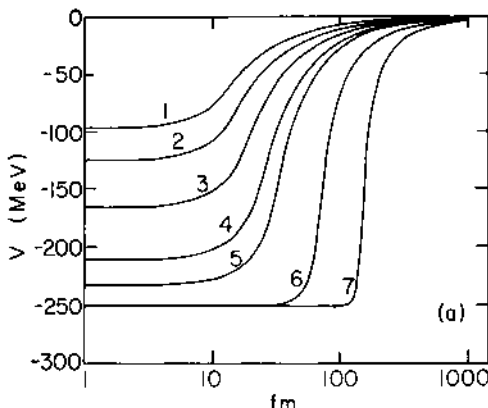


Fig. 2.2. The solutions for the self-consistent potential  $V$  of the relativistic Thomas-Fermi equation for selected values of the nuclear charge as a function of  $r$ . Curve 1,  $Z = 600$ ; curve 2, 1000; curve 3, 2000; curve 4, 5000; curve 5, 10,000; curve 6,  $10^5$ ; curve 7,  $10^6$ . (Ref. 2)

In accordance with our expectations, the charge generated by successive levels joining the lower continuum is sufficient to screen most of the bare nuclear charge as it increases without bound. This property is evident from the fact that for  $Z > 10^5$  the self-consistent potential does not change within the nuclear matter distribution.

Our results show that there is a limit to the coupling strength between electrons and charged matter. The boundary conditions chosen here - that of uniform density background charge - have led to the finite self-consistent potential step,  $V_0$ . We note finally that we could have equally well asked, what happens when a different limit of our equations is considered: for a fixed, large external charge the radius of the background charge distribution is taken to zero. Naturally, the self-consistent potential that emerges must be just subcritical, that is, no further state can become supercritical.

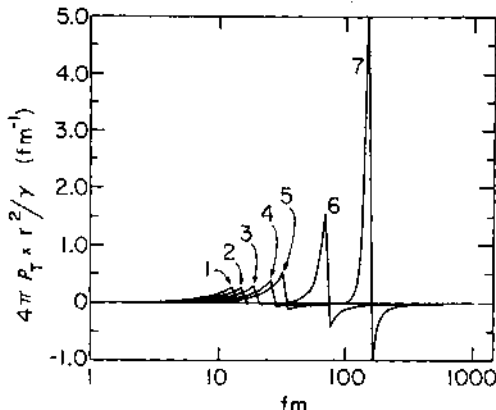


Fig. 2.3. The total charge densities, scaled with  $\gamma$ . Same selected values of nuclear charge as in Fig. (2.2).

This means, however, that the unscreened charge must become

$$Z \sim \gamma \xrightarrow{R \rightarrow 0} \alpha^{-1} \quad (2.12)$$

and the screening is entirely due to the s-states. This latter statement can be qualitatively shown by considering the spectrum of the Dirac equation for pointlike nuclei,  $V = -\frac{Z\alpha}{r}$ , when  $Z\alpha$  approaches one from below: at  $Z\alpha = 1$  all s-states disappear simultaneously. Considering a finite nuclear radius that tends to zero we find that all s-states have dived into the negative energy continuum when  $Z\alpha > 1$ . This supports the above argument.

The intriguing interplay of the different limits has been recently studied in detail numerically by Grtner et al. [8] and the above arguments have been confirmed. In particular, it was found that also the real vacuum polarization charge distribution shrinks to a point at the same pace at which the central nuclear charge radius goes to zero. In this limit all one would detect would be an apparent point charge with  $Z_{\text{eff}}\alpha = 1 + \epsilon$  for pointlike charges of arbitrary strength! Thus we know that there is a limit to the self-consistent strength of interactions. Any supercritical bare charge assembled by (nuclear) interactions will be screened to subcritical values. In the limit of electric point charges we also find that

$$(Z\alpha)_{\text{self-consistent}} \xrightarrow{R \rightarrow 0} 1 \quad (2.13)$$

## KLEIN'S PARADOX

After this preparation we now can turn to the discussion of Klein's paradox (1,9-11). Let us consider an electron of momentum  $p$  and energy  $\epsilon = \sqrt{p^2 + m^2}$ , with spin up that is incident from the left on an electrostatic square-well barrier  $V_0 > 0$ . The discontinuous form of the potential requires that region I outside the potential well and region II inside the potential well be treated separately. In region I the plane wave solution of the free Dirac equation is

$$\Psi_I(z) = ae^{ipz} \begin{bmatrix} 1 \\ 0 \\ p/(\epsilon+m) \\ 0 \end{bmatrix} + be^{-ipz} \begin{bmatrix} 1 \\ 0 \\ -p/(\epsilon+m) \\ 0 \end{bmatrix} \quad (3.1)$$

where the second part of the wave function describes the reflected wave. The form of the wave function in region II (c.f. Fig. 1) depends upon the magnitude of the potential strength. We first consider values of  $V_0$  that are not too large. Then

$$\Psi_{II}(z) = ce^{-\beta z} \begin{bmatrix} 1 \\ 0 \\ ip'/(\epsilon-V_0+m) \\ 0 \end{bmatrix} \quad (3.2)$$

where  $p' = \sqrt{m^2 - (\epsilon - V_0)^2}$ . It is not necessary to add the terms of Eqs. (1) and (2) that describe particles with spin down, since there is no probability of a spin flip. Requiring that the wave function be continuous at  $z = 0$  leads to relations between the coefficients  $a$ ,  $b$ , and  $c$ . The incident current is equal to  $2p|a|^2/(\epsilon + m)$ . The ratio of the reflected current to the incident current is  $|b|^2/|a|^2$ , which is equal to one. The transmitted current is equal to zero. Thus all the incident current is reflected for "small"  $V_0$ ; the situation is analogous to non-relativistic quantum mechanics.

Let us now consider what happens as  $V_0$  is increased beyond  $\epsilon + m$ . The wave function must be written as:

$$\Psi_{II}(z) = de^{ip''z} \begin{bmatrix} 1 \\ 0 \\ p''/(\epsilon+m-V_0) \\ 0 \end{bmatrix}, \quad \epsilon+m < V_0 \quad (3.3)$$

where  $p'' = \sqrt{(V_0 - \epsilon)^2 - m^2}$ . The transmitted current is now equal to  $2p''|d|^2/(\epsilon + m - V_0)$ , which is negative, and the magnitude of the reflected current is larger than that of the incident current. The transmission coefficient, which is the ratio of the transmitted current to the incident current, is given by

$$T = -4\Gamma/(1-\Gamma)^2, \Gamma = \sqrt{\frac{(\epsilon+m)(V_0 - \epsilon+m)}{(\epsilon-m)(V_0 - \epsilon-m)}} \quad (3.4)$$

We note that the transmitted current may be much larger than the incident current. This paradox was first noted by O. Klein [9]. The domain of frequency  $\epsilon$  for which this behaviour is characteristic is shown in Fig. (1). We note the existence of a band of states for which the above behaviour is valid.

Only in the context of a single-particle interpretation does this appear paradoxical. When one appreciates that electrons and positrons are inextricably connected in the Dirac theory, it is natural to identify the negative current in region II with the appearance of positrons. The increase of the reflected current over the incident current is necessary to conserve charge. The reflected current plus the transmitted current is always equal to the incident current.

The result obtained above would imply that the scattering of electrons on a strong potential barrier induces pair production. As we have learned, we also have to consider the spontaneous pair production. In the last section we saw that a saturation in the production may occur.

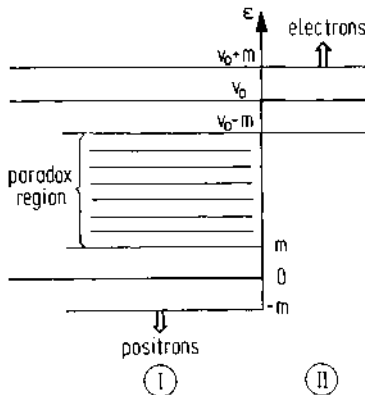


Fig. 3.1. For  $+m < \epsilon < V_0 - m$  ( $V_0 > 0$ ) the transmission coefficient of electrons impinging in region I on potential  $V_0$  is larger than unity.

In order to make a closer connection between the study of supercritical (nuclear) potentials and Klein's paradox, we redefine

the reference point of the energy: we consider the potential step to be strongly attractive in region I ( $0 \rightarrow -V_0$ ) and zero in region II ( $V_0 \rightarrow 0$ ), see Fig. 2. Then we expect that within the range (which may be infinite) of the attractive potential all supercritical states are spontaneously filled with 'electrons', while the positrons are emitted to infinity. Now Klein's gedankenexperiment consists of scattering positrons off the (filled) attractive potential well. Since no final states are available for electrons within the well, we find that the transmission coefficient vanishes - no other particles can be transmitted into the region of the potential. Strictly speaking, this result must be supplemented by a proper quantum field theoretic formulation; however, we will not go into this now.

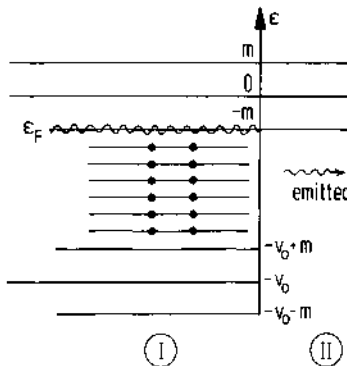


Fig. 3.2. Negative potential step as created by large 'nucleus'. All states with  $-V_0 + m < \epsilon < -m$  in region I are filled by spontaneous positron emission into region II.

However, it is worth noting, that the strength of the potential step must be determined in a selfconsistent manner, similar to one introduced in preceeding section - the background charge and the charge of the filled states must be combined to produce the potential barrier under consideration<sup>1</sup>. We will not persue this interesting point further here and turn now to the study of supercritical Bose fields.

#### BOSONS IN SUPERCRITICAL FIELDS

In this section we continue our study of supercritical fields with the case of relativistic quantum field theory of a charged spin-zero boson field in the presence of the Coulomb field of a prescribed (nuclear) charge distribution. We begin with the

one-boson problem. It is known<sup>1,3,12-16</sup> that for a sufficiently large charge number  $Z = Z_{cr}$ , the deepest bound state reaches the top of the negative energy continuum just as in the case of electrons. Thus there is a solution of the Klein-Gordon equation

$$(-\nabla^2 + m_b^2)\phi = (\epsilon - eV)^2 \phi \quad (4.1)$$

such that  $E$  crosses the point  $-m_b$  at the potential strength  $V$ , and becomes  $-m_b^e$  at  $V_{cr}$  (index  $e$  distinguishes the electron mass from that of the boson  $m_b$ ).

For the norm of any given solution, we compute

$$N = 2 \int d^3x \phi^* (\epsilon - eV) \phi \quad (4.2)$$

Since  $V$  is everywhere negative, the norm Eq. 2 is certainly positive for  $\epsilon > 0$ . On the other hand, for the negative energy continuum solutions (for this discussion, the system enclosed in a box) the norm must be negative, by analytic continuation from the limit  $V = 0$ . We see that, in general, the set of solutions for given  $V$  divides into two subsets,  $\phi_p$  and  $\phi_n$ , characterized by different normalization conditions:

$$\epsilon_p = \langle V \rangle_p > 0 \quad (4.3a)$$

$$\epsilon_n = \langle V \rangle_n < 0 \quad (4.3b)$$

where

$$\langle V \rangle = \frac{\int \phi^* eV \phi}{\int \phi^* \phi} \quad (4.3c)$$

Thus again both particles and antiparticles are described by the same equation, with the sign of the norm being associated with the charges of bose-antibose pair. On occasion we will refer to this pair as  $\pi^-$ - $\pi^+$  pair, but our study at this point is entirely academic.

For a Coulomb potential<sup>14-16</sup> such as that of a finite-size nucleus, the deepest bound orbit behaves in a manner qualitatively similar to the spin 1/2 case. This bound orbit remains normalizable - with positive norm - down to and including the point  $\epsilon = -m_b$ . In Fig. 1 the numerical solution of the Klein-Gordon equation for the lowest energy  $l=0$  state is shown. The Coulomb potential of a charged sphere of radius  $10 \text{ m}^{-1}$  has been chosen, and the lowest eigenvalue is given as a function of the potential depth  $V_0 = -V(0)$ . We find that the discrete state joins the negative energy continuum at  $Z_{cr} = 1986$ , with "nuclear" radius fixed at  $R = 10 \text{ m}_b^{-1}$ . The value of  $Z_{cr}$  increases to 3007 if we assume

$A = 2Z$  and normal nuclear density, where  $A$  is the number of nucleons. The insert in Fig. 1 is an enlargement of the figure in the neighbourhood of the critical point. The dashed line (an antiresonance in the continuum) was obtained from actual numerical integration of the Klein-Gordon equation. The dotted line is the approximate behaviour of the solution after it is modified to include many-body quantum field effects as discussed qualitatively below. The proper formulation of these effects is presented.

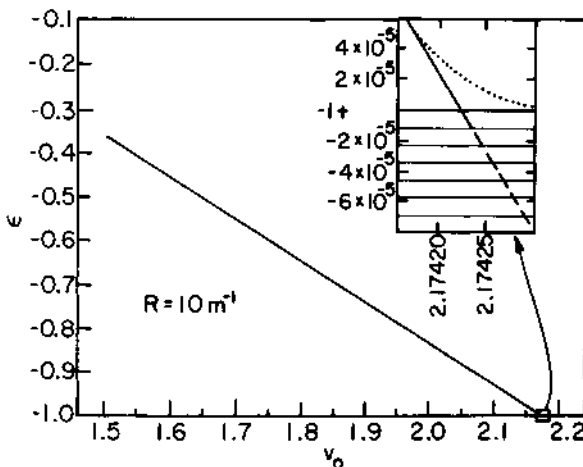


Fig. 4.1. Energy  $\epsilon$  of the lowest bound state of the Klein-Gordon equation as a function of nuclear charge for finite size nuclei. The abscissa is actually the strength of the potential at the origin. The inset magnifies the neighbourhood of the critical point at which  $\epsilon$  reaches the top of the negative energy continuum.

As long as the potential strength is well below  $Z_{cr}$ , the single-particle theory represents perfectly sensible one-particle quantum mechanics provided that we associate the indefinite metric with charge rather than with probability.

For a long-range potential, only negatively charged particles are bound by a field generated by a positive charge, in distinction to a short-range interaction where a "surprise" is found. Here <sup>13, 14</sup> for sufficiently strong interaction a positive pion can also be bound. This is a purely relativistic effect which can be understood if we recall that the charge density is not positive definite, but that for a positive charge it can in fact be negative near the force centre, allowing an average attractive interaction.

For  $Z > Z_{cr}$  the single-particle theory becomes unstable. Unlike the case of electrons, there is no Pauli principle that would

limit the number of spontaneously created pions. Some higher-order effect must be included in the Hamiltonian to stabilize the vacuum in the overcritical case. The physical picture is based on the following considerations: as  $V$  approaches  $V_{cr}$ , the energy necessary to make a meson pair vanishes, allowing an infinite number of pairs to be produced due to the lack of the Pauli principle. To stabilize this situation, a positive definite part in the Hamiltonian is needed that stops the production of the condensate when a certain Boson density is reached. It has also been shown <sup>1, 14, 15</sup> that it is possible to consider the charge of the Bosons as the stabilizing mechanism. Therefore, the (electromagnetic) interaction that leads to the instability in the first place has been shown to have an inherent selfstabilizing mechanism allowing the construction of a proper groundstate. This property is indeed essential in our forthcoming discussion of quantum chromodynamics. The self-charge repulsion is always present in any charge distribution of the Bose condensates and suffices to stabilize the condensate.

The total Coulomb potential  $V_t$  is composed of two contributions (ignoring for the moment the electron field)

$$V_t = V_N + V_{COND} \quad (4.4)$$

originating in the nuclear and condensed Bose charges. With this (self-consistent) potential the Klein-Gordon equation (1) is solved

$$(\mu - eV_t)^2 \phi = (-\nabla^2 + m_b^2) \phi \quad (4.5)$$

where  $\mu$  is a given energy (chemical potential) of the condensate field derived from the physical conditions. In the absence of any further interactions  $\mu = -m_b$ , at which point spontaneous Boson production would begin. Clearly there would be a solution of the above equation only when the potential  $V_t$  has a suitable form derived from the Coulomb equation

$$-\Delta eV_t = e\rho_N + e^2 2\phi (\mu - eV_t) \phi \quad (4.6)$$

where  $\rho_N$  is the nuclear charge. The condensate field  $\phi$  has a norm describing the charge of the condensate and which is controlled by  $\mu$ . Now, however,  $\mu$  is a physical parameter that is fixed by other considerations; hence a field that solves the self-consistent Eqs. 5,6 has a certain norm associated with the screening charge in the condensate. Indeed enclosing Eq. 6 in a large sphere and integrating over the volume we find with ( $\gamma$  is the unscreened charge):

$$V_t \xrightarrow[r \rightarrow \infty]{} - \frac{\alpha \gamma}{r} \quad (4.7)$$

the charge  $q_B$  of the condensate:

$$Z - \gamma = -2 \int d^3x \psi(\mu - eV_t) \phi = -q_B, \quad (4.8)$$

as stated above.

It remains to determine what value is assumed by the chemical potential  $\mu$  of the Bose field. The physical value of  $\mu$  corresponds to the point at which spontaneous particle creation can occur and is the energy of the last boson added, thus we find in the absence of other interactions

$$\mu_b = -m_b \quad (4.9a)$$

corresponding to the reaction  $|\text{vacuum}\rangle \rightarrow |\Omega\rangle + B^-$ <sup>\*</sup>. The introduction of a strong self-consistent potential and the associated supercritical electron field leads us to the requirement that  $\mu_b$  in Eq. 6 must be:

$$\mu_b = -m_e \quad (4.9b)$$

As a first exercise let us consider the external charge distribution  $\rho_N$  in Eq. 6 to contain already the electron charge density. Then the coupled system Eqs. 5, 6 with  $\mu$  given by Eq. 9 can be solved numerically for a given finite size  $\rho_N$ . Two remarkable results are found:

---

\* However, pions can be created easily by inverse  $\beta$ -decays, e.g.

$$\mu^- \rightarrow \pi^-_{(\text{bound})} + \nu_\mu$$

$$e^- \rightarrow \pi^-_{(\text{bound})} + \nu_e$$

if the Fermispheres of  $e, \mu$  are filled, according to spontaneous decay described in previous section. Therefore sufficient supply of  $\mu^-$  and  $e^-$  are locally found in any charge distribution. The spontaneous decay

$$|\text{vacuum}\rangle \rightarrow \pi^-_{(\text{bound})} + e^+ + \nu$$

can only proceed on the surface as otherwise it is hindered by the Coulomb barrier. However,  $\pi^-$  will only diffuse very slowly from the surface to inside of any nuclear charge distribution. Thus we find that due to the dominant channel,  $\mu_\pi$  is fixed at the same value as  $E_F$  that had to be chosen for electrons:  $\mu_\pi = -m_e$ . This can be understood easily in a different language: There is only one Lagrange parameter  $\mu_b = E_f^e = E_f^\mu = \mu_q$  that fixes the total charge of a physical system and is the Lagrange multiplier for the total charge operator, used in the variational principle (that commutes with the Hamiltonian).

- i) the charge of the bose condensate becomes quite similar to that of the external charge - with only small portion of external charge remaining unscreened.
- ii) within the distribution  $\rho_N$  the total potential  $V_t$  is just

$$eV_t = -m_B - m_e + O\left(\frac{1}{R}\right) \quad (4.10)$$

This latter property can be derived from Eq. 5, assuming that  $\epsilon$  changes little with  $r$ .

To illustrate (ii), we show the numerical solution for the total potential  $V_t$ , the Coulomb potential of the nucleus  $V_n$ , and the condensate potential  $V_{\text{cond}}$  for  $Z = 1800$  in Fig. 2. We see that although the pion potential reaches about  $-m_{\pi} \cdot \frac{r}{2}$  in that case, the total potential remains at the limiting value described by Eq. 10.

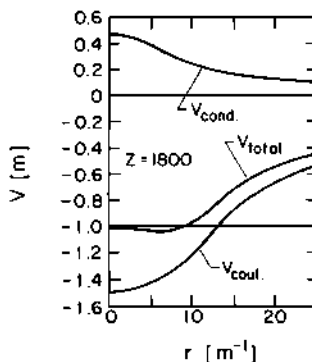


Fig. 4.2. Comparison of the total potential  $V_t$ , the condensate potential  $V_{\text{cond}}$ , and the Coulomb potential  $V_n$  of the nucleus for  $Z = 1800$ . (Ref. 15)

Again we may qualitatively discuss what happens when the radius of the charge distribution  $\rho_N$  becomes much smaller than the Compton wavelength of the Bose field,  $m_B^{-1}$ .

The unscreened potential must just be supercritical for the 1s-state. Thus again a pointlike source of any strength will appear to an outside observer as having the strength  $Z\alpha \sim 1$ . This remark will be deepened later - we will apply the above methods to the problem of gluon condensation in nonabelian theories. Before introducing the quantum field theoretic formulation of the above qualitative discussion we will discuss straightforward an

important physical application in next section: the neutralization of charged nuclear matter (e.g. in 'neutron' stars) by spontaneous particle production.

### NEUTRALIZATION OF CHARGED NUCLEAR MATTER

The behaviour of the solutions obtained numerically for the condensate suggests that the potential generated by the external "nuclear" charge distribution cannot much exceed the value  $(-m_B - m_e)$  in view of the ensuing neutralization by the condensed charged meson distribution. In this section we will consider the interplay between the neutralization effects expected when fermion and meson fields are considered simultaneously. We take the fermion field of both electrons and muons. The meson field discussed here is that of pions. We neglect the non-electromagnetic interactions in order to simplify the presentation of the principal mechanism.

The problem of supercritical electrons for very large  $Z$  has been treated in section 2 by an extension of the Thomas-Fermi approximation. We have seen that a constant limiting value  $V_{\lim}$  of the potential  $V$  is reached as the charge of the nucleus increases, provided that the nuclear charge density is kept at a constant value. This means that aside from surface effects, exact neutralization of the charges must occur in finite, large distributions. Since  $m_e \ll |V_{\lim}|$  for supercritical nuclear matter, the limit indicated in Eq. 2.11 follows. With  $\rho_N^0$  the equilibrium nuclear density,  $0.17 \text{ N/fm}^3$ , we find<sup>2</sup>

$$V_0 = -340 \text{ [MeV]} \cdot \left( f \cdot \frac{\rho_N^0}{\rho_N} \right)^{1/3} \quad (5.1)$$

Here  $f$  is the fraction of protons in nuclear matter ( $f = Z/A$ ). For  $f = 1/2$  and  $\rho_N^0 \sim \rho_N$ , we find  $V_0 = -250 \text{ MeV}$ . In view of this value of  $V_0$ , we must also consider the pion condensation effect.

We note that the channel for the muonic vacuum charge is also open. The charge density associated with the muonic spontaneous decay is:

$$e\rho_\mu = -\frac{e^2}{3\pi^2} [(E_F^\mu - eV)^2 - m_\mu^2]^{3/2} \quad (5.2)$$

Since the muonic states with  $-m_e > E_\mu > -m_\mu$  are fed by the weak decay from the electron channel, we have as discussed before

$$E_F^\mu = E_F^e = -m_e \quad (5.3)$$

This introduces a small correction of Eq. 5.1. The simultaneous consideration of lepton and pion fields leads to the more restrictive

limit for the electrostatic potential:

$$|V_{\text{lim}}| = \min (m_{\pi} + m_e, |V_0|) . \quad (5.4)$$

This limit implies that the nuclear charge is completely neutralized, with some remaining surface charge  $\gamma = Z - (q_e + q_\mu + q_\pi)$  such that for  $Z \rightarrow \infty$ :

$$\gamma/Z \rightarrow 0, \quad \gamma/(q_e + q_\mu + q_\pi) \rightarrow 0 \quad (5.5)$$

The spontaneous neutralization process thus cancels the  $Z^2$ -proportional Coulomb energy - the price is the kinetic energy of the vacuum (i.e. of fermions and pions that neutralize the nuclear matter) which must be considered.

The energy per nucleon residing in the charged fields (again except for the nuclear energy) is found to be<sup>1,15</sup>

$$E/A = m_\pi q_\pi/A + \frac{3}{4} |V_{\text{lim}}| (C(V_0) q_\mu/A + q_e/A) , \quad (5.6)$$

$$C(-m_\pi) = 1.21.$$

Neglecting the surface charge (as we have neglected the surface energy) we have  $q_\pi = Z - q_\mu - q_e$ .

The most important consequence of the considerations presented above is that the essentially complete neutralization of the charged nuclear matter, the Coulomb energy which normally grows like  $Z^2/A^{17/3}$  cannot exceed the kinetic energy of the neutralizing fields proportional to  $Z$ .

It is interesting to note the parallelism in our description of nuclear matter and that of neutron stars (with some small proton fraction present). Our description is the correct one based on an observer outside the star gauged to zero potential. Then inside of the star is a region of a negative Coulomb potential  $V \sim -m_\pi$ . Our theory allows us to have a continuous description from small nuclei to neutron stars. It is worth noting the common language, also shown in the Fig. 1. For an observer inside the star, there is an electron Fermi gas beginning at  $(V) + m_e$  and reaching to  $-m_e$ .

#### QUANTITATION OF SUPERCRITICAL BOSE FIELD

In this section we put the qualitative discussion of the pion condensation phenomena introduced in section 4 on a firm theoretical foundation<sup>1,14,15</sup>. For purposes of technical development, we shall work with a first order formalism<sup>17</sup> where we write the Klein-Gordon equation in the form

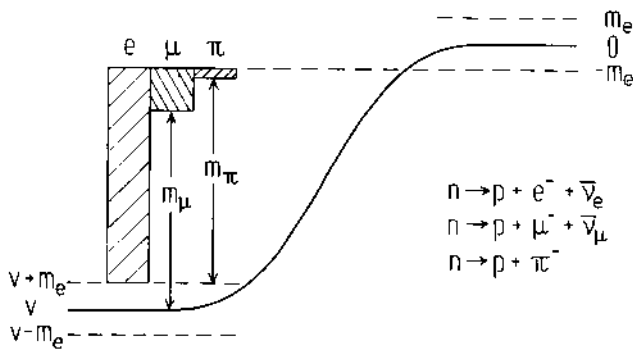


Fig. 5.1. Comparison of two different descriptions of macroscopic charge distributions.

$$\epsilon \tau_1 \phi = H\phi \quad (6.1)$$

where  $\phi$  is the two component hybrid

$$\phi = \begin{pmatrix} \epsilon \sqrt{m} \\ \epsilon - v \\ \sqrt{m} \psi \end{pmatrix} \quad (6.2)$$

and

$$\mathcal{H} = \frac{1}{2}(1+\tau_3) \frac{p^2 + m^2}{m} + \frac{1}{2}(1-\tau_3)m + \tau_1 v \quad (6.3)$$

Here  $\tau_i$  ( $i = 1, 2, 3$ ) are the conventional Pauli spin matrices. Since  $H$  is Hermitian, we recognize that the fundamental scalar product is the integral of the density

$$d_{ab}(\vec{r}) = \phi_a^*(\vec{r}) \tau_1 \phi_b(\vec{r}) \quad (6.4)$$

providing then an orthogonality theorem for two solutions of Eq. 1 belonging to different energies. For the norm of any given solution, we compute

$$\int \phi^+ \tau_1 \phi = 2 \int \phi^* (\epsilon - V) \phi \quad (6.5)$$

we see that the solution set for given  $V$  divides as before into two subsets  $\phi_p$  and  $\phi_n$ , characterized by different normalization conditions:

$$\int \phi_p^+ \tau_1 \phi_p = 1, \quad \int \phi_n^+ \tau_1 \phi_n = -1 \quad (6.6)$$

When the two sets of solutions defined by Eq. 6 are separated, we have a completeness relation

$$\sum_p \phi_p(\vec{r}) [\phi_p^+(\vec{r}') \tau_1] - \sum_n \phi_n(\vec{r}) [\phi_n^+(\vec{r}') \tau_1] = I \delta^3(\vec{r} - \vec{r}') \quad (6.7)$$

where  $I$  is the unit  $2 \times 2$  matrix. The completeness relation guarantees a satisfactory quantum theory when used in conjunction with the expansion (the subscripts  $p$  and  $n$  referring in general to the sign of the single particle energy)

$$\hat{\phi}(\vec{r}) = \sum_p \hat{a}_p \phi_p(\vec{r}) + \sum_n \hat{b}_n^+ \phi_n(\vec{r}) \quad (6.8)$$

where the  $\hat{a}_p$  are destruction operators for negative mesons and the  $\hat{b}_n^+$  creation operators for positive mesons satisfying

$$[\hat{a}_p, \hat{a}_p^+] = \delta_{pp}, \quad [\hat{b}_n, \hat{b}_n^+] = \delta_{nn}, \quad (6.9)$$

while other commutators vanish.

The quantum Hamiltonian associated with Equation 3 is

$$\hat{H}' = \int \hat{\phi}^+ \mathcal{H} \hat{\phi} \quad (6.10)$$

which we consider together with the charge operator

$$\hat{Q} = -|e| \int \hat{\phi}^+ \tau_1 \hat{\phi}, \quad [\hat{H}', \hat{Q}] = 0. \quad (6.11)$$

The vacuum state is defined by

$$\hat{a}_p |\text{vac}\rangle = \hat{b}_n |\text{vac}\rangle = 0 \quad (6.12)$$

We then find from Eqs. 8 - 11

$$\hat{H}' = \sum_p \hat{a}_p^+ \hat{a}_p + \sum_n (-\epsilon_n) \hat{b}_n^+ \hat{b}_n + E_0 \quad (6.13)$$

$$\hat{Q} = -|e| [\sum_p \hat{a}_p^+ \hat{a}_p - \sum_n \hat{b}_n^+ \hat{b}_n] \quad (6.14)$$

with the zero point energy.

$$E_0 = \frac{1}{2} (\sum_p \epsilon_p + \sum_n (-\epsilon_n)) \quad (6.15)$$

For  $Z < Z_c$  this standard quantization is acceptable. We note that for  $Z > Z_c$  the completeness relation 7 can not be satisfied<sup>1</sup> and that no satisfactory quantization exists.

However by adding the Coulomb interaction of the charged meson field, in accordance with the discussion in section 4, we obtain a palatable theory: We study the Hamiltonian supplemented by the Coulomb energy of the meson field:

$$\hat{H} = \hat{\phi}^\dagger \hat{\phi} + \frac{1}{2} e^2 \int \hat{\rho}(\vec{r}) \hat{\rho}(\vec{r}') \frac{1}{|\vec{r}-\vec{r}'|} , \quad (6.16)$$

$$\hat{\rho} = \hat{\phi}^\dagger \tau_1 \hat{\phi} ,$$

defined up to ordering problems, i.e., up to additional constants and single-particle operators which will not enter our discussion directly in the approximations which will be considered. The operator  $\hat{Q}$  of Eq. 14 continues to be a constant of the motion.

We now develop a mean field approximation valid for  $Z - Z_c \gg 1$ . We assume that the ground state has charge  $q$  and that it can be described in good approximation by the trial state vector

$$|q\rangle \approx (q!)^{-1/2} (\hat{\alpha}^\dagger)^q |vac\rangle \quad (6.17)$$

where

$$\hat{\alpha}^\dagger = \int d^3r \hat{\phi}^\dagger(\vec{r}) \tau_1 \phi_0(\vec{r}) \quad (6.18)$$

is the creation operator for a particle bound in the orbit  $\phi_0(\vec{r})$  which is to be determined self-consistently. The function  $\phi_0$  has a positive norm

$$\int \phi_0^\dagger \tau_1 \phi_0 = 1 \quad (6.19)$$

and we suppose that

$$\hat{\alpha} |vac\rangle = 0 \quad (6.20)$$

We next calculate the expectation value of  $\hat{H}$ , Equation 16 with respect to the state 17 taken as a trial function. The result contains a semi-classical part which is extracted by simply replacing  $\hat{\phi}^\dagger \phi$  in Eq. 16 and calculating the resulting expectation value. There are also quantum fluctuations to which we shall return in the last part of this section. We thus find

$$W(q) = \langle q | \hat{H} | q \rangle \approx q \int \phi_0^* \hat{\mathcal{H}} \phi_0 + \frac{1}{2} q^2 e^2 \int \frac{\rho_0(\vec{r}) \rho_0(\vec{r}')}{|\vec{r} - \vec{r}'|} \quad (6.21)$$

$$\rho_0(\vec{r}) = \phi_0^*(\vec{r}) \tau_1 \phi_0(\vec{r})$$

We shall determine  $\phi_0$  and  $q$  from the constrained variational principle

$$\delta J(q) = \delta [W(q) - \mu q \int \rho_0(\vec{r})] = 0 \quad (6.22)$$

where  $\mu$  is the Lagrange multiplier for the condition 19. Varying with respect to  $\phi_0^*$  at fixed  $q$ , we obtain the condensate equation

$$\mu \tau_1 \phi(\vec{r}) = \hat{\mathcal{H}} \phi(\vec{r}) + \tau_1 v_{\text{COND}}(\vec{r}) \phi(\vec{r}) \equiv H_{\text{eff}} \phi(\vec{r}) \quad (6.23)$$

where we have introduced the (macroscopic) condensate wave function

$$\phi = \sqrt{q} \phi_0 \quad (6.24)$$

and the condensate potential

$$v_{\text{COND}}(\vec{r}) = e^2 \int d^3 r' \frac{\rho(\vec{r}')}{|\vec{r} - \vec{r}'|} \quad (6.25)$$

$$\rho = \phi^* \tau_1 \phi \quad ,$$

Here the physical significance of the parameter  $\mu$  as chemical potential is established by computing  $\langle q+1 | \hat{H} | q+1 \rangle$  in the same approximation as led to Eq. 21. This yields

$$\langle q+1 | \hat{H} | q+1 \rangle = W(q) + \mu \quad (6.26)$$

We thus see that  $\mu$  is the energy of the last meson added.

In general, due to the approximations made,  $q$  will not be an integer - but this is of no practical or fundamental importance since the validity of our model requires  $q \gg 1$  anyway. With Eqs. 23, 25, 26 we have established the required quantum field theory description implied in section 4. An independent derivation of Eq. 22 can be based on the definition

$$\langle q | \hat{\phi}(\vec{r}) | q+1 \rangle = \sqrt{q} \phi_0(\vec{r}) \equiv \phi(\vec{r}) \quad (6.27)$$

and the Heisenberg equation for  $\hat{\phi}$ , but we shall not develop this remark in detail. Still another description valid for large  $q$  replaces the charge eigenstate 17 by a coherent state

$$|\alpha_0\rangle = \exp[\alpha_0 \hat{\alpha}^\dagger] |vac\rangle \quad (6.28)$$

where  $\alpha_0 = q^{1/2}$ . At this point we note that  $q$  may be considered a continuous function of  $Z$  with  $\mu$  fixed at  $-m_e$ .

We conclude this section by indicating how one shows that the (charged) ground state is stable with respect to fluctuations of zero charge. This emphasizes the role played by the subsidiary condition in Eq. 22. The approximate, coherent ground state, Eq. 28, is in fact an approximate eigenstate of the operator

$$\hat{H}' = \hat{H} - \mu \hat{Q} \quad (6.29a)$$

$$\hat{Q} = \int \hat{\phi}^\dagger \tau_1 \hat{\phi} \quad (6.29b)$$

The coherent state is furthermore characterized by the condition

$$\langle \alpha_0 | \hat{\phi}(\vec{r}) | \alpha_0 \rangle = \phi(\vec{r}) \quad (6.30)$$

which is equivalent to Eq. 27. One then writes

$$\hat{\phi}(\vec{r}) = \phi(\vec{r}) + \hat{\chi}(\vec{r}) \quad (6.31)$$

where  $\hat{\chi}(\vec{r})$  describes the small oscillations around the new ground state. Standard procedures may then be followed to show that  $|\alpha_0\rangle$  is locally stable under these fluctuations. We shall not pursue this further here.

#### GLUON CONDENSATION IN QCD

Quantum chromodynamics (QCD), the quantized gauge theory of the gauge group  $SU(3)$ , is the prime candidate for a fundamental theory of the strong interactions<sup>18</sup>. Of the several features which make this theory particularly attractive, we quote the following:

- (1) QCD is known to be renormalizable;
- (2) the coupling constant  $\alpha_s = g^2/4\pi$  becomes small at short distances (asymptotic freedom);
- (3) the structure of baryons (3 quarks) and of mesons (quark-anti-quark) is readily understood as being caused by the color singlet structure of particles.
- (4) the mutual interaction of the quanta of the gauge field, gluons, is very likely responsible for the phenomenon of quark confinement.

However, the low-momentum, large-distance properties of the  $SU(3)$  gauge theory are at present far from being understood. The main

reason for this, and also the basis for the widespread belief that QCD explains quark confinement, is that the coupling strength  $\alpha_s$  increases for large separations and the nature of the interaction changes from being perturbative into the strong-coupling regime.

The gauge field Lagrangian is not quadratic in the gauge-potentials  $A_\mu^a$  ( $a=1, \dots, 8$ ) but contains higher order terms:

$$L = -\frac{1}{4} F_{\mu\nu}^a F^{a\mu\nu} + g j_a^\mu A_\mu^a \quad (7.1)$$

$$\text{with } F_{\mu\nu}^a = \partial_\mu A_\nu^a - \partial_\nu A_\mu^a + g f_{abc} A_\mu^b A_\nu^c \quad (7.2)$$

where the  $f_{abc}$  are the antisymmetric structure constants of SU(3) and  $j_a^\mu$  is the source current generated by quarks. Writing Eq. 2 in momentum space:

$$F_{\mu\nu}^a(k) = k_\mu A_\nu^a(k) - k_\nu A_\mu^a(k) + g f_{abc} \int \frac{d^4 q}{(2\pi)^4} A_\mu^b(q) A_\nu^c(k-q) \quad (7.3)$$

it is evident that the non-linear term becomes important for low enough momenta  $k_\mu$ , independent how weak the potential is. Let us assume for the moment that we have a Coulomb-type solution for the potential  $A_0 \sim Qg/4\pi r$ . Since the  $f_{abc}$  are of order one, we can estimate crudely that the non-linear term in Eq. 2 becomes comparable to the gradient term when

$$\frac{Qg}{4\pi r^2} = \frac{\partial A_0}{\partial r} \sim g (A_0)^2 = g \frac{(Qg)^2}{16\pi^2 r^2}$$

or

$$Q\alpha_s = Qg^2/4\pi \sim 1 \quad (7.4)$$

The way the self-coupling of the gluon field affects the equation of motion, given a quark source will be given in the remainder of this section. Our treatment is considerably simplified, if we pass from the gauge group SU(3) to the group SU(2) which has only three generators and therefore only three gauge potentials  $A_\mu^a$  ( $a=1, 2, 3$ ). We note that SU(2) is a subgroup of SU(3). Therefore, even this simplification is directly relevant to the understanding of QCD.

We study the response of the gauge quantum field to the presence of a colored charge of strength  $Q$  located near to  $r=0$ .<sup>5, 19-23</sup> We assume (without loss of generality) that it points in the colour "direction"  $a=3$ :

$$j_a^\mu = Q \delta_{\mu 0} \delta_{a3} \delta(\vec{r}) = \rho(\vec{r}) \delta_{\mu 0} \delta_{a3} \quad (7.5)$$

Since the structure constants  $f_{abc} = \epsilon_{abc}$  (for SU(2)) do not allow for a coupling of any direction in color space to itself, but only

for couplings between different colors, we employ the following approximation scheme: the charge, Eq. 5 is a source of a static Coulomb-potential in its rest frame - we assume that the vector potential in the  $a=3$  direction vanishes i.e.

$$A_{\mu}^3 = (\phi(\vec{r}), \vec{0}) . \quad (7.6)$$

In the treatment of the colour components  $a=1,2$  it is useful to apply the "temporal" gauge  $A_{\mu}^a = 0$  ( $a=1,2$ ) which is a gauge condition and not an approximation. We are then dealing with three coupled fields  $\phi, \vec{A}^1, \vec{A}^2$ :

$$A_{\mu}^a = \begin{pmatrix} 0 & \vec{A}^1 \\ 0 & \vec{A}^2 \\ \phi & 0 \end{pmatrix} \quad (7.7)$$

The components of the field strength Tensor  $F_{\mu\nu}^a$  are:

$$\begin{aligned} \vec{E}^1 &= -\dot{\vec{A}}^1 + g\phi\vec{A}^2 & \vec{B}^1 &= \text{curl } \vec{A}^1 \\ \vec{E}^2 &= -\dot{\vec{A}}^2 - g\phi\vec{A}^1 & \vec{B}^2 &= \text{curl } \vec{A}^2 \\ \vec{E}^3 &= -\nabla\phi & \vec{B}^3 &= -g\vec{A}^1 \times \vec{A}^2 \end{aligned} \quad (7.8)$$

It is advantageous to combine the neutral vector fields  $\vec{A}^1$  and  $\vec{A}^2$  into one complex field:

$$\vec{W} = \frac{1}{2}(\vec{A}^1 + i\vec{A}^2) \quad (7.9)$$

In terms of this field the Lagrangian can be written after some elementary manipulations as:

$$\begin{aligned} L &= \frac{1}{2}(\nabla\phi)^2 + \left(\frac{\partial}{\partial t} + ig\phi\right)\vec{W}^* \cdot \left(\frac{\partial}{\partial t} - ig\phi\right)\vec{W} - \\ &\quad - (\text{curl } \vec{W}^*) \cdot (\text{curl } \vec{W}) + \frac{g}{2}(\vec{W}^* \times \vec{W})^2 + g\phi\phi \end{aligned} \quad (7.10)$$

The nonlinear classical field equations are obtained by variation with respect to  $\phi$  and  $\vec{W}^*$ , yielding:

$$\nabla^2\phi = g[\rho - \vec{W}^* \cdot (i\frac{\partial}{\partial t} - g\phi)\vec{W} + (i\frac{\partial}{\partial t} + g\phi)\vec{W}^* \cdot \vec{W}] \quad (7.11a)$$

$$[(i\frac{\partial}{\partial t} - g\phi)^2 + \nabla^2 - \text{grad div} - g^2(\vec{W}^* \times \vec{W})x]\vec{W} = 0 \quad (7.11b)$$

These equations have an extremely interesting structure. Eq. 11a, the one for the Coulomb potential  $\phi$ , is essentially the Poisson equation, but with a crucial modification: the source term

contains not only the external color charge density but also the color density generated by the complex vector field  $\vec{W}$ :

$$\rho_w = \vec{W}^* \cdot [ (i \frac{\partial}{\partial t} - g\phi) \vec{W} ] - [ (i \frac{\partial}{\partial t} + g\phi) \vec{W}^* ] \cdot \vec{W} \quad (7.12)$$

The  $\vec{W}$ -field can therefore screen the external charge  $\rho$ , when it becomes too strong. That indeed the expected effect is in general a screening and not antiscreening can be easily seen, if one neglects the time-dependence of  $\vec{W}$ . Then Eq. 11a can be written in the form

$$[-\nabla^2 + 2g^2 (\vec{W}^* \cdot \vec{W})] \phi = -\rho \quad (7.13)$$

where the complex field acts as an effective mass term for the Coulomb-like field  $\phi$  and reduces the range of  $\phi$ . Eq. 11b for the  $\vec{W}$ -field does not contain a source term, except for the third-order term  $g^2 (\vec{W}^* \vec{W}) \vec{W}$ . It is up to this term the usual wave equation for a charged vector boson in an external Coulomb field  $\phi$ . Hence the problem we find here in gauge theory is formally the same as the one treated in sections 4 and 6!

As discussed there, the Coulomb problem develops unstable modes when the external charge is too large. Our intention now is to construct, given Eqs. 11a, b a variational groundstate that will eliminate the 'Coulomb' instability. In quantum field theory the instability of classical modes means that we cannot expect these modes of the Yang-Mills field  $\vec{W}$  to be absent in the vacuum state. Indeed, the true groundstate will be characterized by the presence of a finite number of the  $\vec{W}$ -particles, a state we have called 'condensate' in the last section. Naturally, we will not be able to give the "exact" new stable groundstate since this would imply the complete solution of a nontrivial interacting quantum field theory, but we can construct an approximate variational groundstate which can be improved by successive refinements.

The path to the solution of the condensate problem has been already described at length. Hence we shall only repeat the essential points. For quantization of the  $\vec{W}$ -field we require a complete set of solutions of the linearized Eq. 11:

$$[(i \frac{\partial}{\partial t} - g\phi)^2 + \nabla^2 - \text{grad div}] \vec{W}_n^{(\pm)} = 0. \quad (7.14)$$

Here the third-order term has been omitted - it will be included later as perturbation. The quantum field operator  $\vec{W}$  is then decomposed into contributions from modes with positive and negative norm:

$$\hat{\vec{W}} = \sum_n \hat{\alpha}_n \vec{W}_n^{(+)}(x) + \sum_n \hat{\beta}_n^+ \vec{W}_n^{(-)}(x), \quad (7.15)$$

where

$$\int d^3x \vec{W}_n(\varepsilon) \cdot \left( i \frac{\partial}{\partial t} - 2g\phi \right) \vec{W}_m(\varepsilon') = \varepsilon \delta_{nm} \delta_{\varepsilon\varepsilon'} . \quad (7.16)$$

The normal vacuum state  $|\text{vac}\rangle$  is defined to be annihilated by all particle destruction operators  $\alpha_i$ ,  $\beta_i$ . When the potential  $\phi$  is time-independent and a function of the radial variable  $r = |\vec{x}|$  only, we can introduce stationary modes

$$\vec{W}_n(\vec{x}, t) = \vec{W}_n(\vec{x}) \exp(-i\omega t) . \quad (7.17)$$

First consider the perturbative state in which the charge density, Eq. 13, generated by the charged field  $W$  is zero. Then the potential outside the source is  $g\phi(r) = -Q\alpha_s/r$ . It is possible to show<sup>2,3</sup> that the positive parity modes  $h_{lm}(r)$  are least stable and we consider them now. As  $\text{div } \vec{W}$  vanishes for these modes, Eq. 14 reduces to

$$\left[ \frac{1}{r} \frac{\partial^2}{\partial r^2} r + (\omega - g\phi)^2 - \frac{l(l+1)}{r^2} \right] h(r) = 0 \quad (l \geq 1) . \quad (7.18)$$

This is just the radial Klein-Gordon equation for a particle in a Coulomb potential. It is well-known that in the case of a pure  $1/r$ -potential the condition for the occurrence of unstable modes in this equation is  $|Q\alpha_s| > 1 + \frac{1}{2}$ .

Beyond these critical values of  $Q\alpha_s$  the standard perturbative groundstate becomes unstable as has been discussed in the literature. Our aim is to construct the new "condensate" groundstate for which

- (a) there exists a complete set of well-behaved (stable)  $W$ -modes of Eq. 14, and
- (b) which has lower energy than the perturbative vacuum state  $|\text{vac}\rangle$ .

If condition (a) can be satisfied, we have found with (b) a new and better groundstate.

The actual mechanism for the stabilization is the build-up of a gluon condensate which screens the potential  $\phi$  to below the critical strength. To show that this is so we follow the formalism for the description of charged bose condensates developed in section 6. Since the "magnetic" quantum number does not enter in Eq. 18, the modes  $l=1$ ,  $m=0, \pm 1$  share the same radial wavefunction  $h(r)$ . It is therefore plausible, and in fact necessary to obtain a spherically symmetric condensate charge distribution  $\rho_W$ , that the gluon condensate will have equal strength in all these three  $m$ -channels. With the creation operators for the condensate  $m$ -quanta:

$$\hat{\alpha}_{c,m}^+ = 2\int d^3x \hat{\vec{W}}(\vec{x}) (\omega - g\phi) h(r) \hat{T}_{1lm}(\theta, \phi) , \quad (7.19)$$

$$\hat{T}_{1lm}(\theta, \phi) = \sum_{m\mu} (\ell+1) 1/\mu \mu' m Y_{\ell\mu} \xi_{\mu} ,$$

we approximate the condensate state vector by the spherically symmetric expression

$$|q\rangle = (q!)^{-3/2} (\hat{\alpha}_{c,-1}^+ \hat{\alpha}_{c,0}^+ \hat{\alpha}_{c,1}^+)^q |vac\rangle \quad (7.20)$$

where  $q$  is an integer denoting the number of quanta in each of the magnetic sub-states of the condensate mode. We cannot exclude the possibility that an unequal occupation of the  $m$ -modes could result in an even lower energy state. This would not change the principal conclusions while leading to much more involved equations. However, as all  $m$ -modes are entirely equivalent this would then imply the dynamical breaking of rotational invariance.

The following coupled equations for the radial trial wavefunction  $h(r)$ , the potential  $\phi(r)$  and the condensate strength  $q$  are found following the procedure put forward in sections 4,6:

$$\nabla^2 \phi = g(\rho + \frac{3q}{\pi} g\phi h^2) , \quad (7.21a)$$

$$[\frac{1}{r} \frac{d^2}{dr^2} r + (g\phi)^2 - \frac{2}{r^2}] h(r) = 0 . \quad (7.21b)$$

Before we proceed to solve this set of coupled nonlinear equations we must check for the consistency of our approximations. It turns out that the source terms of wave equation for  $\vec{A}^3$  vanish in the condensate state. Hence  $\langle \vec{A}^3 \rangle = 0$  is a solution of the field equation, also in the presence of a condensate. Furthermore we find for the neglected quartic  $W$ -term

$$\langle q | \hat{\vec{W}} \times \hat{\vec{W}} |^2 |q\rangle = \langle 0 | \hat{\vec{W}} \times \hat{\vec{W}} |^2 |0\rangle + \frac{g}{32\pi^2} q^2 h(r)^4 \quad (7.22)$$

we will see that the  $h^4$  term is indeed negligible.

In order to solve the condensate Eq. 21 we impose the boundary conditions for a shell source<sup>21</sup>:

$$(\text{at } r=R) \quad \frac{d\phi}{dr} \Big|_R = \frac{Qg}{4\pi R^2} , \quad h(R) = 0 , \quad (7.23a)$$

$$(\text{at } r=\infty) \quad \phi(\infty) = 0 , \quad h(\infty) = 0 . \quad (7.23b)$$

For practical purposes it is necessary to choose a finite integration limit  $r_{\max}$ . In this case one must require that

$$\frac{d}{dr} (r\phi) \Big|_{r_{\max}} = 0, \quad h(r_{\max}) = 0 \quad (7.23c)$$

in order to obtain a  $1/r$ -potential for  $r > r_{\max}$ . The quantity of physical interest is  $(gr\phi)$ , which would be equal to  $-Q_0$  in the absence of screening. Its value at  $r = r_{\max}$  gives the remaining asymptotically unscreened gauge charge  $\gamma = (Q-3q)$ .

In the numerical example presented here<sup>5</sup> the parameters were:  $\alpha_s = 0.5$  and  $Q = 8$ , corresponding to a source where eight "quarks" with parallel "isospin" are homogeneously distributed on a shell with radius  $R = 1$ . As the solution depends on the position of the outer boundary  $r_{\max}$ , we have plotted in Fig. 1a the function  $(gr\phi)$  for a number of different choices of  $r_{\max}$ . For  $r_{\max}/R = 89$  we find  $q = 2$  and the asymptotic strength is  $\gamma\alpha_s = 1$ . The surprise is that the potential is screened below the critical coupling strength,  $Q_{\text{cr}}\alpha_s = 1.5$ . In Fig. 2, we show the variation, with the position of the outer boundary, of the condensate strength  $q$  (Fig. 2a) and of the energy gain  $\Delta\xi$  (Fig. 2b) for our self-consistent solution. It is obvious from the figures that a finite limit is approached when  $r_{\max}/R \rightarrow \infty$ . By explicit calculation we find that the quartic term  $E^{(4)}$  makes only a minor contribution to the condensate energy, in support of our strategy to include this term as a perturbation. Thus we have shown that the in-

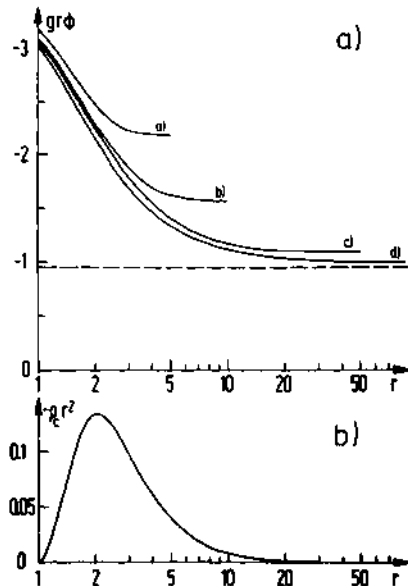


Fig. 7.1. (a) The screened potential  $(gr\phi)$  for various positions of the outer boundary  $r_{\max}$ . The values of  $r_{\max}/R$  are a) 5, b) 10, c) 50, d) 89. (b) The radial distribution of the condensate charge for case d).

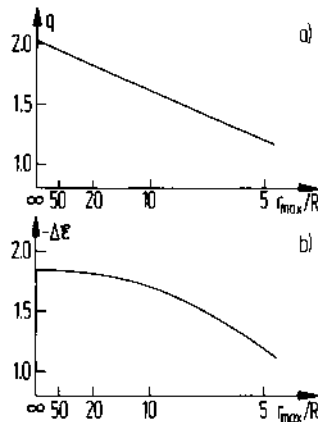


Fig. 7.2. Variation of the condensate charge (part a) and condensate energy (part b) with the outer boundary  $r_{\max}$ . A finite limit is approached for  $r_{\max} \rightarrow \infty$ .

stability of the Coulomb solution of the SU(2) gauge field around a strong external gauge source can be removed by properly choosing a condensate groundstate. The screening of the source is almost complete - in the example treated<sup>5</sup> 75% of the source charge is balanced by the condensate. It is conceivable that the overscreening due to the massless quanta might actually lead to complete source screening in the limit of arbitrarily large source strength, contrary to the expectations and examples from massive theories discussed in previous sections.

#### SOME CONSIDERATIONS ABOUT LARGE $\alpha$ IN THE FERMISECTOR

It is quite natural to ask whether the theory developed at this conference for supercritical fields with external sources is applicable when we actually consider Quantum Electrodynamics for large coupling constant between particles. In part, our interest in this problem is motivated by the quark confinement puzzle, as was our work in the preceding section. We have introduced in the last section a valid candidate for the theory of strong interactions - Quantum Chromodynamics - and we have seen that the gauge sector by itself leads us to a picture similar to the supercritical Bose condensation. Unlike in QED we have to face several complications simultaneously: the non-perturbative treatment of relatively strongly coupled non-Abelian gauge theory. Therefore we regress here to study the relevant aspects of an Abelian gauge theory in the limit of strong coupling<sup>4</sup>. Clearly such a theory must be QED, but with an "unphysically" large value of the coupling constant  $\alpha$ . In next section we will address the problem of nonabelian gauge theory in mean 'magnetic' field approximation.

Let us consider the quantum field theory of two charged Fermi fields, hence forth called " $\mu$ " and "e", e being much lighter than  $\mu$ :

$$m_\mu/m_e \gg 1 \quad (8.1)$$

Our objective is to show that when the coupling  $e^2$  becomes large

$$\alpha = \frac{e^2}{4\pi} \gtrsim 1 \quad (8.2)$$

it is impossible to create a free heavy Fermion. This will be the case when "muonium", the bound state of  $(\mu e)$ , and a free e are energetically a more favourable state than the free  $\mu$  particle. All that follows now is a (trivial) elaboration of this observation. From this point of view confinement seems to be more the rule than an exception in strongly coupled theories; where confinement is understood as the absence of Lagrangian field particles from asymptotic states.

It is the condition (1) which allows us to find a simple approximate solution to the difficult mathematical problem posed by Eq. 2; therefore we cannot yet derive similar results for the light Fermion confinement. In the limit indicated by Eq. 1, up to corrections of the order of  $(m_e/m_\mu)^2$ , the transition amplitude

$$\Psi_e = \langle \mu e | \hat{\Psi}_e | \mu \rangle \quad (8.3)$$

of the light Fermion field  $\hat{\Psi}_e$  from the state consisting of one heavy Fermion to the (possibly bound) state of  $\mu$  and e satisfies the Dirac equation ( $\hat{m}_e$  is the reduced mass of the light Fermion):

$$[\gamma \cdot (p - eA) - \hat{m}_e] \Psi_e = 0 \quad (8.4)$$

Here "A" is the electromagnetic potential generated by the heavy Fermion:

$$\partial_\nu F^{\nu\alpha} = \langle \mu | \hat{e} j^\alpha | \mu \rangle \quad (8.5a)$$

$$F^{\nu\alpha} = \partial^\nu A^\alpha - \partial^\alpha A^\nu \quad (8.5b)$$

$$\hat{j}^\alpha = -\frac{e}{2} [\hat{\Psi}_\mu, \gamma^\alpha \hat{\Psi}_\mu] - \frac{e}{2} [\hat{\Psi}_e, \gamma^\alpha \hat{\Psi}_e] \quad (8.5c)$$

Let us approximate a solution of Eq. 5 by the Coulomb potential

$$eA_\alpha = \delta_{\alpha 0} V \quad (8.6a)$$

$$V = \begin{cases} -\frac{e^2}{4\pi r} & : r > a \\ -\frac{e^2}{4\pi a} & : r < a \end{cases}, \quad r = |\vec{x}| \quad (8.6b)$$

with a suitable cut-off radius

$$a \ll m_e^{-1} \quad (8.7)$$

We will justify this ansatz further below.

Now we turn to the description of solutions of Eq. 4, of which the details are given above in section 2. In particular, we consider the stationary ansatz

$$\Psi_e(\vec{x}, t) = e^{-i\epsilon t} \Psi_e'(\vec{x}) \quad (8.8)$$

which leads us to the Dirac eigenvalue problem for  $\Psi_e'$  discussed previously. The lowest discrete eigenvalue  $\epsilon$  is shown schematically in Fig. 1. As indicated there, for  $\alpha$  not much larger than 1 and called the critical strength  $\alpha_{cr}$ , the eigenvalue disappears from the discrete spectrum and becomes a resonance in the continuum with  $\epsilon < -m_e$ . Beyond this point, a naked  $\mu^-$  will have higher energy than the state of a bound muonium ( $\mu^+ e^-$ ) and a free  $e^-$ . As was shown in the lectures of B. Müller the associated decay time is governed by the width of the resonance in the continuum and is in general a very small fraction of  $m_e^{-1}$  when we are not too close to the critical coupling constant. Thus if  $\alpha > \alpha_{cr}$

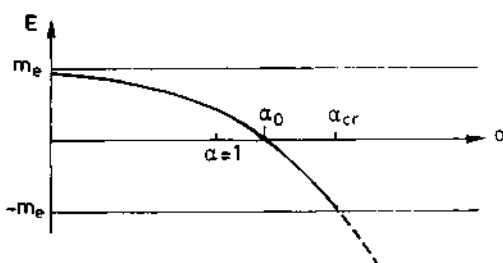


Fig. 8.1. Lowest bound state of the Dirac equation for a cut-off Coulomb potential as a function of  $\alpha$ . At  $\alpha_0$  the binding equals  $m_e$  and at  $\alpha_{cr}$  it is  $2m_e$ ; beyond the naked muon becomes unstable and is degenerate with muonium and a free positron.

a naked heavy Fermion would quickly be neutralized by spontaneous production of a light lepton pair.

Since the heavy leptons would be produced in pairs, the self-screening described above must be now generalised to the case of an initial state consisting of a heavy Fermion pair. Let us first assume that the relative velocity  $v_r$  of the  $\mu^+ \mu^-$  pair in its centre of mass system is small as compared to the velocity of light. Then the previous considerations are fully applicable to this case, with some changes in the potential  $V$ . It must now be the potential of two charges fixed at a distance  $2R$ . Thus, instead of Eq. 6.b we now have

$$V = \frac{\alpha}{|x-R|} f^- - \frac{\alpha}{|x+R|} f^+ \quad (8.9)$$

where  $f^\pm$  are the suitable cut-off factors which ensure that when  $|x \pm R| < a$  the singularity of Eq. (9) is cut off in a similar fashion as in Eq. 6.b. A cut of the two-centre potential (9) along the vector  $R$  and going through the centre of mass is shown schematically in Fig. 2. As indicated there we can have simultaneously  $e^+$  and  $e^-$  bound mainly to  $\mu^-$  and, respectively,  $\mu^+$ . For a given  $\alpha > \alpha_0$

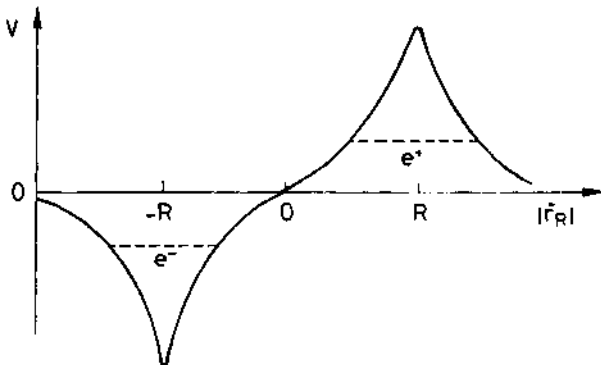


Fig. 8.2. Two-centre potential cut along the axis going through the centre of mass and connecting a heavy particle-antiparticle pair separated by the distance  $2R$ .

( $\alpha_0$  is as defined in Fig. 1, the point at which the eigenvalue  $\epsilon$  descends below 0) we can draw the eigenvalue spectrum of the Dirac equation as a function of  $R$  as shown in Fig. 3. For some  $R$ , called  $R_{cr}$ , the eigenvalue of  $e^+$  and  $e^-$  solutions join. Since the difference between the curves so denoted is the energy required to make a  $e^+, e^-$  pair bound to  $\mu^-, \mu^+$ ; beyond  $R_{cr}$  the naked  $\mu^+, \mu^-$  state is unstable and makes a spontaneous transition to the state with a muonium-antimuonium pair. Thus as the distance between a

pair of heavy Fermions increases, there is a point beyond which a light Fermion pair can be created in order to screen the charges of the heavy Fermion field. It is possible to view the pair creation process as if originating in the strong constant electric fields: an expression non-analytic at  $\alpha = 0$  has been first given by Schwinger<sup>24</sup>. Thus in the adiabatic approximation, when the heavy Fermions move sufficiently slowly, only muonium is seen asymptotically. Even when the relative momentum of the  $\mu^+, \mu^-$  pair is large, the neutralization will proceed more likely without creation of free light Fermions. However, it can then occur before or after  $R_{cr}$ , the  $e$  pair energy being shared with the kinetic energy of the  $\mu$  pair. Still, there is always a (very) small chance that the  $\mu$ 's will separate before being neutralised. Then the process described in the first part of this section leads to the required neutralisation. The fate of the free light Fermions is unclear at the present time, we will return to this point further below.

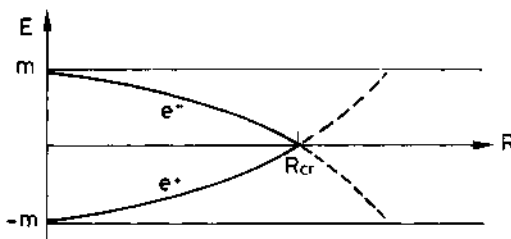


Fig. 8.3. Lowest bound states for particles and antiparticles of the Dirac equation in the potential of a heavy particle-antiparticle pair. At  $R_{cr}$  the spontaneous neutralisation of the heavy particles begins.

It remains to justify the validity of Eqs. 4,6,9. In the limit given in Eq. 1, it has been shown<sup>25</sup> that the Dirac equation 4 is the proper limit of the Bethe Salpeter equation when the kernel includes the ladder and crossed ladder diagram. However, when  $\alpha \gtrsim 1$  we must also consider further contributions. This can be done more easily taking as the starting point the basis provided by the solutions of the Dirac equation. In particular, we have to consider the vertex corrections of the light Fermion as well as its self-energy. Scaling the results of QED we conjecture that these contributions cannot alter the qualitative character of our discussion. Clearly, all quantitative work demands extensive computation of all these contributions. This is the reason why at present we can only estimate:  $\alpha_{cr} \sim 1$ ,  $R_{cr} \sim m_e$ . Since we take

the heavy Fermion as the source of a static Coulomb field, we had to simulate the relevant effect of recoil, e-field vacuum polarization as well as vertex corrections introducing the cut-off radius "a" in Eq. 6. Both recoil and vertex corrections tend to smear out the point-like character of the source. We note that in QED (unlike QCD) the singularity of a point-like source increases when vacuum polarisation is considered, however for already smeared-out source it only leads to further smearing.

Let us return now to the discussion of the fate of the light Fermions. In the spirit of our discussion they would be confined if the bound particle-antiparticle state would lie below the empty vacuum state. This seems to be the case for  $\alpha > 3/2$  in massless electrodynamics and for  $\alpha > 9/8$  in QCD with massless quarks<sup>26,27</sup>. However, to solve the confinement problem here one has to construct a new global vacuum state which would provide a lower bound for the Hamiltonian. In this language our muonium state is the local ground state in the presence of a heavy Fermion.

To obtain the description of the global vacuum state we must guess the essential physical interaction that characterizes the system near to the critical strength. Quite in analogy to the spin pairing in the BCS theory we think that the important effect is the colour charge pairing of the gauge particles.

#### ZERO-POINT ENERGY, SUPERCRITICAL FIELDS AND THE QUARK CONFINEMENT

To obtain the ground state of strongly interacting quantum field theory we must find a configuration, usually in terms of perturbative fields, for which the zero point energy aquires a minimum as function of an order parameter - see Fig. 9.1. In theories with spontaneous symmetry breaking this quantity is identified as the ground-state expectation value of a Higgs field and the exercise is rather trivial. In cases of dynamic symmetry breaking the identification of the proper collective coordinate that leads to a straight forward description of the new ground state is perhaps the most important aspect of the entire problem-solving process.

In order to understand better this situation, let us imagine that the vacuum state of QED and/or QCD would have properties similar to those of a ferromagnet. In particular there may be a local magnetization. In such a case the local magnetic field  $B(x)$  seems to be a useful collective coordinate and we will below consider the zero point energy of the ferromagnetic vacuum as a function of  $B$ .

The framework for such a calculation has been developed since 1935 in the context of 'Effective Lagranian' of Kockel-Euler-Heisenberg<sup>7,24,28,29</sup>: Our intention is to compute the zero point energy of a quantum field in the presence of a background, classical

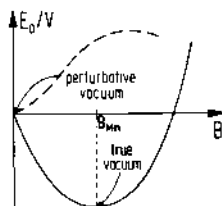


Fig. 9.1. The behaviour of the zero-point energy density  $E_0/V$  as a function of an order parameter  $B$ . Full line: there is a nonperturbative minimum at  $B_{\text{min}} \neq 0$ . Dashed line: there is a (perturbative) minimum at  $B=0$  and perhaps a maximum at some  $B$ .

$B$ -field. The word background means that the field may be a combination of an external and spontaneous fields or, as is the case with ferromagnets, just be the spontaneous magnetization.

Though we would be more interested in a solution of this problem for arbitrary magnetic field  $B(x)$ , the problem can so far be only solved for constant background fields both in case of QED and QCD: In such a relatively simple field configuration the exact diagonalization of single particle Hamiltonian for spin-1/2 (QED) or spin-1 (QCD) particles is possible; from the known spectrum  $[E_n(B)]$  we can compute the zero point energy.

For spin-1/2 particles we have:  $E =$ energy of particle states,  $E_n =$ energy of antiparticle states ( $E_n < 0$ )

$$E_0^e = - \frac{1}{2} \left( \sum_p E_p - \sum_n E_n \right), \quad (9.1)$$

$$E_0^{e(0)} = - \frac{1}{2} \cdot 4 \cdot V \cdot \frac{\infty}{m} \sqrt{p^2 + m^2} \frac{4\pi p^2 dp}{(2\pi)^3} = -\infty. \quad (9.2)$$

Here the second line Eq. 2 is the result for non-interacting particles;  $V$  is the volume; there are four degrees of freedom of a relativistic spinor field and we have the usual phase-space integral over all particle states with energy  $E_p = \sqrt{p^2 + m^2}$ . Let me reemphasize that our interest is just in the deviation of the zero point energy Eq. 1 from the free field result Eq. 2.

For spin-1, massless particles we have similarly

$$E_0^g = \frac{1}{2} \cdot 2 \cdot \sum_p E_p \quad , \quad (9.3)$$

$$E_0^{g(0)} = \frac{1}{2} \cdot 2 \cdot (N^2 - 1) \cdot \sqrt{\int_0^\infty p \frac{4\pi p^2 dp}{(2\pi)^3}} = +\infty \quad . \quad (9.4)$$

In the Eq. 4 we have again shown the free field result: there are two transverse degrees of freedom of a SU(N) gauge theory with  $N^2 - 1$  different gluons. Only in a gauge theory ( $N > 1$ ) is the discussion of zero point energy of interest, as only charged glue can self interact and there can be a modification of the free field result, Eq. 4.

In passing we notice that though infinite, the free field zero point energies are of opposite sign for Fermions and Bosons - hence we should always keep in mind that in principle a theory could be found with finite or perhaps vanishing total zero point energy - it is important to appreciate that the large number of relationships required between masses, coupling constants etc. for such a case require a suitable 'supersymmetric' point of departure.

Returning now to our main line of investigations, let us recall the results of Euler and Kockel [28]: they discovered that there is a lowest order contribution

$$E_0^e = v \cdot \left( -\frac{2\alpha^2}{45} \frac{1}{m^4} B^4 + \dots \right) + E_0^{e(0)} \quad (9.5)$$

to the zero point energy.  $m$  is electrons mass. In terms of Feynman diagrams, this expression corresponds to the lowest light-light scattering diagram, Fig. 2a. The  $q$ -dependence of the electromagnetic field strengths must be neglected. The  $(1/m^4)$  factor is

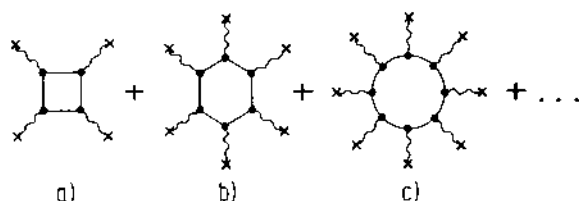


Fig. 9.2. Contributions to the effective Lagrangian as power series in the background field, indicated by a cross.

reminiscent of four electron propagators connecting the photon lines. Passing from energy to action and including the free field Lagrangian they found the effective action:

$$\mathcal{L}_{\text{eff}}^e = \frac{1}{2}(E^2 - B^2) + \frac{2\alpha^2}{45} \frac{1}{m^4} \left[ (E^2 - B^2)^2 + 7(E \cdot B)^2 + \dots \right] \quad (9.6)$$

Actually, also a  $E^2$ -term was found. But it had to be reabsorbed in the renormalization of the coupling constant.

The exact result is in QED for a constant B-field:

$$-\int d^4x \mathcal{L}_{\text{eff}}^e = E_0^e + \frac{1}{2}B^2 = V \left[ \frac{1}{2}B^2 + \frac{1}{8\pi^2} \int_0^\infty \frac{ds}{s^3} e^{-m^2 s} \cdot \left\{ (seB) \operatorname{ctg}(seB) - 1 - \frac{(seB)^2}{3} \right\} \right] \quad (9.7)$$

The two subtractions in the parentheses are in turn the free field zero point energy and the contribution to the charge renormalization. The integration parameter  $s$  is sometimes called 'proper time'. A power series expansion in  $B$  is possible and corresponds to the expansion given in Fig. 2. For large  $B$  the limit of Eq. 7 is

$$E_0^e \xrightarrow[eB/m^2 \gg 1]{} V \left( -\frac{\alpha}{6\pi} B^2 \ln \frac{eB}{m^2} + \dots \right) \quad (9.8)$$

The validity of the limit  $eB/m \gg 1$ , Eq. 8, is limited, as it can be shown that higher orders in  $e^2$  are required to find the proper behaviour of the zero point energy at large magnetic fields. The zero point energy, as given by Eq. 7 (including the Maxwell term) is shown qualitatively by dashed line in Fig. 1. For large  $B$  the logarithmic term dominates and there seems to be a maximum of  $E_0^e$ .

It is important to appreciate the effect these terms can have on physics: e.g. modified Maxwell equations that follow from Eqs. 6,7 are nonlinear and there is the possibility of light-light scattering. At present there is an effort to measure the influence of the  $E \cdot B$  term, Eq. 6, on the polarization of laser light in strong external magnetic fields<sup>30</sup>.

Before turning to the spin-1 QCD case let us consider a crucial technical detail of QED calculations that will be so different in QCD. In order to obtain the spectrum of the spin-1/2 particles we solve in a constant B-field the Dirac equation

$$[i\alpha_x \frac{\partial}{\partial x} + i\alpha_y \frac{\partial}{\partial y} + i\alpha_z (i \frac{\partial}{\partial z} - eB_x y)] \Psi - \beta m \Psi = E_n \Psi \quad (9.9)$$

with the magnetic field pointing here in the x-direction. As is well known, the electron spirals around the field lines and propagates in the direction of the field: hence the eigenvalues are

$$E_n^e(k_x, s_x) = \pm \sqrt{k_x^2 + m^2 + 2eB_x(n + \frac{1}{2} - s_x)} \quad (9.10)$$

where  $k_x$  is the longitudinal momentum,  $n=0, 1 \dots$  is the quantum number of the 'oscillator' orbit around the  $x$ -axis and  $s_x = \pm \frac{1}{2}$  is the spin projection on the magnetic field vector. We notice<sup>2</sup> that the smallest (absolute value) of  $E_n(k_x, s_x)$  is obtained for  $n=0$ ,  $k_x=0$  and  $s_x=1/2$ . However we always have  $|E_n| \geq m$ .

Turning now our attention to QCD we discover that the above formula is preserved. Replacing  $e$  by  $Q$ , where  $Q$  is a suitable colour factor and with the spin projection  $s_x$  being now  $\pm 1$  we find<sup>31</sup>:

$$E_n^g(k_x, s_x) = \sqrt{k_x^2 + 2QgB_x(n + \frac{1}{2} - s_x)} \quad (9.11)$$

Hence for  $s_x = -1$ ,  $n = 0$  only for  $k_x^2 > QgB$  will the eigenvalues be real. In the preceding sections and in particular also in the

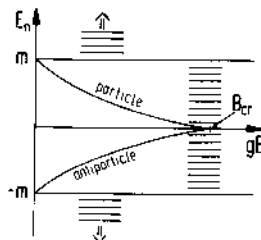


Fig. 9.3. For a massive spin-1 particle there exists a magnetic field  $B_{cr}$  at which the lowest energy states meet each other.

lectures by B. Müller this situation has been discussed at length. In particular, for a massive spin-1 field the spectrum, as shown in Fig. 3, is similar to the supercritical behaviour found for bose fields. At a certain value  $B_{cr}$  the gap between particle and anti-particle solutions vanishes and there is a nonvanishing probability for pair production. In analogy to our previous discussions we anticipate the formation of a bose condensate that will screen the applied magnetic field near to the critical value.

In real QCD the gauge invariance of the theory requires that the perturbative quanta are massless. Hence as documented by Eq. 11 there is an inherent supercriticality of the theory associated with small  $k_x$  modes<sup>32</sup>. In my opinion the only sensible physical way to circumvent the supercriticality in the massless case (which differs from  $m \neq 0$ , but  $m \neq 0$ ) is the domainization of the volume filled with the magnetic field lines<sup>33</sup>. The assumption  $B = \text{const.}$  is inconsistent, instead we should have  $B = \text{const.}$  in a certain domain  $V_d$ ; in another domain  $B^a$  points in a different space (and possible colour) direction. We can estimate the elementary size of a domain by requiring that the small  $k_x$  supercritical modes be cut out in the spectrum (11). Hence we find for the typical radius of the domain:

$$R_d \sim \frac{1}{\sqrt{QgB}} . \quad (9.12)$$

This breaking of the homogeneity of space eliminates all low momentum components from the glue spectrum - their absence lowers the value of the positive, infinite zero point energy of the spin-1 field. Hence we can anticipate that at a finite value of the magnetic field the zero point energy will be reduced (due to the absence of these modes) as compared to  $B=0$  case. The actual expression found by Savvidy et al.<sup>34</sup> for constant  $B$  is (through order  $g^2$ )

$$E_0^g = V \frac{B^2}{2} \left[ 1 + \frac{11}{12} \frac{g^2 N}{8\pi^2} \left( \ln \frac{(gB)^2}{\mu^4} - 1 \right) \right] \quad (9.13)$$

where the renormalised coupling constant has been chosen such that<sup>34</sup>

$$\frac{\partial (E_0^g / V)}{\partial B^2} \left|_{gB=\mu^2} \right. = \frac{1}{2} \quad (9.14)$$

This procedure introduces a dimensional quantity  $\mu$  into the calculations in a fashion similar to the introduction of a scale in the running coupling constant of QCD.

We notice that the minimum of Eq. 13 is at

$$(gB)_{\text{Min}}^2 = \mu^4 \exp \left\{ - \frac{96\pi^2}{11Ng^2} \right\} \quad (9.15a)$$

where

$$E_0^g / \text{Min} = V B_{\text{ag}}^{(M)} = - \frac{11N\mu^4}{192\pi^2} \exp \left\{ - \frac{96\pi^2}{11Ng^2} \right\} \quad (9.15b)$$

The energy density at the minimum has been denoted by  $B_{\text{ag}}^{(M)}$  as it is a first approximation to the value of the bag constant found

phenomenologically in the study of hadronic spectra<sup>35</sup>:

$$B_{ag} \approx (170 \text{ MeV})^4 \sim (145 \text{ MeV})^4 \quad (9.16)$$

It describes the positive energy density inside hadrons, in regions of space occupied by perturbative quarks.

Our description of the vacuum state, though yet incomplete, shows this particular behaviour: the true vacuum at finite spontaneous magnetization has a lower energy density than the 'perturbative' state at  $B=0$ . However our value  $B^{(M)}$  can not be directly related with the phenomenological value Eq. 16. We have computed the groundstate for constant  $B$  in all space, Eq. 13 and not in a domainised world. This point has been studied in more detail<sup>33</sup> <sup>36</sup> and an improvement of the vacuum structure was found to lower the energy of the ground state by approximately 20%. In this process Poincare invariance can be restored to the vacuum state.

More relevant is the observation<sup>37</sup> that the choice of a colour carrying collective coordinate such as  $\vec{B}^a$  implies that in a local space domain glue quanta couple together to a colour octet, such that a net colour field remains. However, when two colour gluons are coupled to a colour singlett we have a stronger glue-gluue attractive interaction. Hence we conclude that we should have used a colourless collective coordinate, perhaps

$$\lambda \sim \langle \text{Tr}(\vec{B}^2 - \vec{E}^2) \rangle . \quad (9.17)$$

As we see there are several conceptual and technical improvements necessary, however the main message of this section is very likely invariant against further improvements: the true ground-state in QCD is a complicated structure that arises as a consequence of the supercritical glue-gluue interaction of massless particles. With this understanding of the vacuum state, the quark confinement puzzle can be resolved by observing that the true vacuum structure is incompatible with the presence of colour field lines. We recall that the electric colour field lines must begin and end on colour sources (quarks). As we attempt to separate quarks from each other, the volume occupied by the field lines grows. The presence of these field lines leads to an increase in the energy density of the perturbative ground state. To create a colour source with an 'infinite' range to the field lines requires an infinite energy. [There is a backdoor out of this argument - if the perturbation drops like  $E^2$  or higher power, the quark ionization energy would remain finite].

Let us finally record an interesting test of the above ideas: the possible observation of a change in the vacuum state as a function of temperature. In Fig. 4 we show that at  $T \sim 1.5 B^{1/4} \sim 250 \text{ MeV}$  the structure of the magnetic vacuum will be dissolved<sup>6</sup>. The

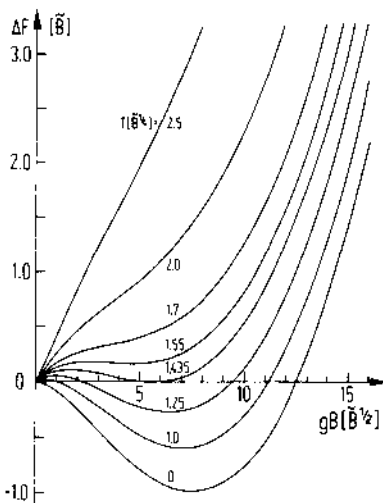


Fig. 9.4. The change in the zero point energy at finite temperature is shown: all quantities in units of  $\tilde{B}$ , the minimum value of the effective action at  $T=0$ , Ref. 6.

experimental problem is the creation of a hot and large heat bath. In a laboratory the most suitable tool seems to be a relativistic collision of two heavy nuclei. Over the volume occupied by participating hadrons suitable temperature could be reached for projectile energies of 10-100 GeV/Nucleon<sup>38</sup>. The participating quarks could be liberated within the heated volume.

#### SUMMARY

We have seen that the physics of strong fields, originally developed for the description of novel phenomena occurring in super-heavy atomic systems, has equally important applications towards the neutralization of nuclear matter, pion condensation and the physics of quarks and gluons. We have completely passed by a wealth of applications with respect to strong gravitational fields (black holes, etc.). A review of possible phase transitions of the vacuum state under the influence of strong gravity can be found in Ref. <sup>39</sup>.

In order to recall the common characteristics of all these phenomena, let us summarize the basic results: when the field of force acting on some species of particles (electrons, pions, gluons, etc.) exceeds a certain critical strength, the vacuum state is suddenly forced to change its symmetry properties. For instance, in the original case of a supercritical atomic nucleus the vacuum state becomes charged, and positrons are emitted at the same time. In general, the vacuum state is rearranged in such a way as to diminish the effect of the applied "external" force, i.e. the vacuum acts as a screening agent. In the academic case of a pointlike Coulomb source the screening effect would be such that an outside observer could not even detect the fact that the "bare" source was originally of supercritical strength. We wish to emphasize this point again, since also for weak fields the vacuum is a polarizable medium, but whether the virtual vacuum polarization results in a weakening or an enhancement of the external field depends on the nature of the interaction.

The two cases of greatest importance are probably

- (1) supercritical heavy ion collisions and
- (2) gluon condensation in quantum chromodynamics.

Heavy ion collisions draw their importance from the fact that they form the unique testing ground for quantum electrodynamics of strong fields as we have seen during this conference. On the other hand, the phenomenon of gluon condensation and nonperturbative vacua (discussed in sections 7,8,9) may prove to be the clue for understanding the elusiveness of quarks. While the experimental evidence for the presence of quark-like constituents in the proton and other hadrons is overwhelming, the fact that these constituents seem to be permanently confined to the interior of elementary particles is not yet fully understood. Recent investigations, however, have yielded preliminary evidence that the true vacuum of quantum chromodynamics is characterized by a condensate of gluons interacting among themselves. It is likely that the methods developed to describe the charged electronic vacuum and pion condensates will prove to be successful also in the description of the vacuum state for the strong interactions. If this development is as fruitful as it now promises to be, it will be a gratifying experience to see that atomic physics, after having been a source of new developments for almost hundred years, has again made an important contribution to our understanding of the fundamental laws of nature.

#### REFERENCES

1. J. Rafelski, L. P. Fulcher, and A. Klein, Phys. Reports, 38C:227 (1978).

2. B. Müller and J. Rafelski, Phys. Rev. Lett., 34:349 (1975).
3. A. Klein and J. Rafelski, Z. f. Physik, A284:71 (1978).
4. J. Rafelski, Phys. Lett., 79B:419 (1978).
5. B. Müller and J. Rafelski, "Self-consistent gluon screening of a strong  $SV(2)$ -source", Phys. Rev., In print.
6. B. Müller and J. Rafelski, Phys. Lett., 101B:111 (1981) and references therein.
7. See e.g. V. S. Weisskopf "Über die Elektrodynamik des Vakuums auf Grund der Quantentheorie des Elektrons", reprinted in J. Schwinger, "Quantum Electrodynamics", Dover Pubs., New York. Original published in Kongelige Danske Videnskabernes Selskab, Mathematisk-fysiske Meddelelser XIV:6 (1936).
8. P. Gärtner, B. Müller, J. Reinhardt, and W. Greiner, Phys. Lett., 95B:181 (1980).  
B. Müller, this conference.
9. O. Klein, Z. f. Physik, 53:157 (1929).
10. F. Beck, H. Steinwedel, and G. Süssmann, Z. f. Physik, 171:189 (1963).
11. H. G. Dosch, J. D. H. Jensen, and V. F. Müller, Physica Norvegica, 5:151 (1971).
12. H. Snyder and J. Weinberg, Phys. Rev., 57:307 (1940).
13. A. B. Migdal, Sov. Phys. JETP 34:1189 (1972); Zh. Eksp. Theor. Fiz. 61:2209 (1971).
14. A. Klein and J. Rafelski, Phys. Rev., D11:300 (1975).
15. A. Klein and J. Rafelski, Phys. Rev. D12:1194 (1975).
16. M. Bavin and J. P. Lavine, Phys. Rev., D12:1192 (1975).
17. H. Feshbach and F. Villars, Rev. of Mod. Phys., 30:24 (1958).
18. For an introduction see the review articles:  
E. S. Abers and B. W. Lee, Phys. Lett., 9C:1 (1973);  
W. Marciano and H. Pagels, Phys. Lett., 36C:137 (1978).  
See also the lecture of M. Baker at this conference.
19. J. E. Mandula, Phys. Rev., D14:3497 (1976); Phys. Lett., 67B:175 (1977).
20. A. B. Migdal, Pis'ma Zh. Eksp. Teor. Fiz. 28:37 (1978), (JETP Letters 28:35 (1978)).
21. M. Magg, Phys. Lett., 74B:246 (1978).
22. P. Houston and D. Pottinger, Z. Physik, C3:83 (1979).
23. M. Magg, Nucl. Phys. B158:154 (1979).
24. J. Schwinger, Phys. Rev., 82:664 (1951).
25. W. Dittrich, Phys. Rev., D1:3345 (1970).
26. A. J. G. Hey, D. Horn, and J. E. Mandula, Phys. Lett., 80B:90 (1978).
27. J. Finger, D. Horn, and J. E. Mandula, Phys. Rev., D20:3253 (1979).
28. H. Euler and B. Kockel, Naturwiss. 23:246 (1935);  
H. Euler, Ann. d. Phys. V. 26:398 (1935).
29. W. Heisenberg and H. Euler, Z. f. Physik, 38:714 (1936).

30. E. Iacopini and E. Zavattini, *Phys. Letters*, 85B:151 (1979).
31. N. K. Nielsen and P. Olesen, *Nucl. Phys.*, B144:376 (1978);  
*Phys. Lett.*, 79B:304 (1978).
32. This has been noted in a different context already G. Velo  
and D. Zwanziger, *Phys. Rev.*, 186:1337 (1969); 188:2218  
(1969).  
V. Schanbacher "Gluon Propagator and Effective Lagran-  
gian in Quantum Chromodynamics", Tübingen preprint 1981.
33. H. B. Nielsen and P. Olesen, *Nucl. Phys.*, B160:380 (1979).
34. G. K. Savvidy, *Phys. Lett.*, 71B:133 (1977); T. A. Batalin,  
S. G. Matinyan, and G. K. Savvidy, *Sov. J. Nucl. Phys.*,  
26:214 (1977) [*Yad. Fiz.* 26:407 (1977)].
35. For a review see e.g.  
K. Johnson, *Acta Phys. Polon.*, B6:865 (1975).
36. J. Ambjørn and P. Olesen, *Nucl. Phys.*, B170:60 (1980).
37. K. Johnson, private communication.
38. R. Hagedorn and J. Rafelski, *Phys. Lett.*, 97B:136 (1980)  
and manuscript in preparation for *Phys. Reports*.
39. B. Müller and W. Greiner, *Acta Physica Austriaca, Suppl*  
XVIII:153 (1977).

NON-PERTURBATIVE APPROACH TO THE LONG DISTANCE BEHAVIOR OF  
YANG-MILLS THEORY AND THE PROBLEM OF QUARK CONFINEMENT IN QCD

M. Baker

Department of Physics FM-15  
University of Washington  
Seattle, Washington 98195

INTRODUCTION

Quantum chromodynamics (QCD), the theory of interacting quarks and gluons, is a natural generalization of quantum electrodynamics (QED), the theory of interacting electrons and photons. In QCD the gauge symmetry of QED is generalized to a non Abelian  $SU(3)$  local symmetry in which the vector fields transform like the octet (adjoint) representation of  $SU(3)$  and hence carry the charge (color) associated with symmetry. This means that the gluons contribute to the vacuum polarization of the color charge which determines the forces and energies in QCD. All known hadrons are color singlets, i.e., their wave functions are invariant under  $SU(3)$  color rotations. This phenomenon, called color confinement, could be explained if the solution of the equations of QCD yield long range forces which impede the separation of color charge or equivalently give infinite energy to an isolated state of non-zero color.

In these lectures we first review the motivation and formulation of QCD. We then compare the forces of QED produced by the vacuum polarization of electric charge to those of QCD. In QED the long distance force is given by Coulomb's law while the short distance force is still unknown. In QCD the effective coupling at short distance becomes small (asymptotic freedom) and can be calculated using perturbation theory. The long distance forces, relevant for confinement, must however be calculated using non-perturbative methods.

We present such a non-perturbative approach based upon the

Schwinger-Dyson equations and Ward-Slavnov-Taylor identities of Yang-Mills theory. The Schwinger-Dyson equations describe the propagation of gluons in a dielectric medium, the vacuum. The dielectric constant  $\epsilon(\vec{x}-\vec{y})$  in electrodynamics determines the relation between the electric field  $\vec{E}(\vec{x})$  and the external charge density  $\rho(\vec{x})$  via Gauss' Law,

$$\vec{\nabla} \cdot \int dy \epsilon(\vec{x}-\vec{y}) \vec{E}(\vec{y}) = \rho(\vec{x}). \quad (a)$$

Similarly in QCD the dielectric constant  $\epsilon^{ab}$  determining the polarization of color charge in the vacuum is defined as

$$\vec{\nabla} \cdot \epsilon^{ab}(\vec{x}, \vec{y}) = \frac{\delta \rho^a(\vec{x})}{\delta \vec{E}^b(\vec{y})}, \quad (b)$$

where  $\rho^a(\vec{x})$  is the color charge density and  $\vec{E}^b(\vec{y})$  is the color electric field. The Schwinger-Dyson equations are a set of coupled integral equations for  $\epsilon^{ab}$  and its derivatives with respect to  $\vec{E}^c(\vec{x})$ . We have developed a systematic non-perturbative procedure for studying their long distance behavior. At each stage of our approach the requirements of gauge invariance are exactly satisfied as is necessary to preserve the correct long distance properties of the theory.

In the first stage of our procedure we find that  $\epsilon^{ab}(\vec{x}, \vec{y})$  vanishes when  $|\vec{x}-\vec{y}|$  becomes large; i.e., over large distances the QCD vacuum behaves like a medium of zero dielectric constant. Using Eq. (b), we then find that the color electric field  $\vec{E}^a(\vec{x})$  due to a color charge source  $\rho^a(\vec{y})$  behaves as a constant at large distances from the source and produces a linear long range potential between two sources. Thus any system with non-zero color charge will have infinite energy. In this first stage of our procedure we have used gauge invariance to approximate the dependence of the dielectric constant on the field  $\vec{E}^a(\vec{x})$ . The Ward-Slavnov-Taylor identities indicate that this approximation should not affect the long distance behavior of QCD. We can then conclude that the color electric field does not fall off at large distances from the source and hence QCD confines color.

#### THE QUARK MODEL AND QCD

We begin with a brief review of the evidence for the non-relativistic quark model, in order to motivate QCD as a model for strong interactions. In this model<sup>1</sup> a meson is a composite particle of a pair of spin 1/2 constituents, a quark  $q$  and an anti-quark  $\bar{q}$ , while a baryon is a composite of three quarks: There is evidence for a number of different kinds of quarks characterized by quantum numbers referring to the weak and electromagnetic interactions.

There are quarks with charge  $Q = +2/3$  denoted by  $u$ ,  $c$ , and quarks with charge  $-1/3$  denoted by  $d$ ,  $s$ , and  $b$ . The  $s$ ,  $c$  and  $b$  are more massive than  $u$  and  $d$  and the heavier mesons and baryons are composites of these quarks. Some examples are:

$$p_{938}^{+}(\text{uud}), \quad \pi_{140}^{+}(\bar{d}u), \quad \Lambda_{1115}^0(\text{uds})$$

$$\Delta_{1238}^{++}(\text{uuu}), \quad \psi_{3095}^{+}(\bar{c}c), \quad \tau_{9452}^{+}(\bar{b}\bar{b}).$$

The properties of essentially all low energy meson and baryon resonances can be understood by associating these hadrons with ground states or low-lying excited states of  $(q\bar{q})$  or  $(qqq)$ .

However a problem immediately arises: This is most easily seen by considering the particle  $\Delta_{1238}^{++}$  which is the lowest mass  $J = 3/2$ ,  $Q = 2$  baryon. In the quark model this state is just a product of  $u$  quarks with their spins aligned, i.e.,

$$\Delta_{1238}^{++}(1,2,3) = u_{\uparrow}^{+}(1)u_{\uparrow}^{+}(2)u_{\uparrow}^{+}(3).$$

Now if the spatial wave function had relative orbital angular momentum zero (which is the usual situation for the lowest energy state for a given spin) i.e., if it was a relative  $s$  state, the  $\Delta_{1238}^{++}$  wave function would be symmetric under interchange of the space and spin coordinates of any pair and would have spin  $3/2$ . This would contradict the connection between spin and statistics which is based on the most general principles of quantum field theory.

One can avoid this problem by assuming there are three quarks of each type denoted red, yellow, and blue.<sup>2</sup> Thus  $u^i u^j$  ( $i = R, Y, B$ ),  $d^i d^j$ , etc. With this multiplicity of quarks we can construct completely antisymmetric wave functions for all baryons. For example:

$$\begin{aligned} \Delta_{1238}^{++}(1,2,3) &= u_{\uparrow}^R(1)u_{\uparrow}^B(2)u_{\uparrow}^Y(3) - u_{\uparrow}^R(2)u_{\uparrow}^B(1)u_{\uparrow}^Y(3) \\ &+ u_{\uparrow}^R(2)u_{\uparrow}^B(3)u_{\uparrow}^Y(1) - u_{\uparrow}^R(1)u_{\uparrow}^B(3)u_{\uparrow}^Y(2) \\ &+ u_{\uparrow}^R(3)u_{\uparrow}^B(1)u_{\uparrow}^Y(2) - u_{\uparrow}^R(3)u_{\uparrow}^B(2)u_{\uparrow}^Y(1) \\ &= \sum_{i,j,k} \epsilon_{ijk} u_{\uparrow}^i(1)u_{\uparrow}^j(2)u_{\uparrow}^k(3), \end{aligned}$$

where  $\epsilon_{123} = 1 = -\epsilon_{213} \dots$  etc., and where  $u_{\uparrow}^i(1)$  is the amplitude

that quark 1 be a spin up u quark of color i. Thus the  $\Delta$  wave function is an antisymmetric linear combination of simple product wave functions, each of which has  $J = 3/2$  and  $Q = 2$ , and the usual relation between spin and statistics is preserved. We conclude that the combination of the quark model and the spin-statistics relation suggests the existence of a new quantum number (color) yielding a triplet of degenerate quarks of each type.

We will now see that this seemingly ad hoc hypothesis made to explain a basic problem with the quark model contains the seeds of the current dynamical theory of strong interactions QCD. The degeneracy of states having different color quantum numbers suggests that the underlying dynamical theory possesses a symmetry, just as the degeneracy of states  $q_\uparrow$  having  $S_z = 1/2$  and  $q_\downarrow$  having  $S_z = -1/2$  reflects the invariance of the Hamiltonian under the transformation corresponding to ordinary spatial rotations:

$$q_i (i = \uparrow, \downarrow) \rightarrow q'_i = \sum_{j=\uparrow, \downarrow} \Lambda_{ij}^s (\theta) q_j, \quad (2)$$

$$\text{where } \Lambda^s \Lambda^{s\dagger} = 1, \quad \det \Lambda^s = 1.$$

Analogously the color degeneracy suggests that the dynamics is invariant under rotations in color space in which

$$q_i (i = R, Y, B) \rightarrow q'^i = \sum_{j=R, Y, B} \Lambda_{ij}^c q^j, \quad (3)$$

where  $\Lambda^c \Lambda^{c\dagger} = 1$ ,  $\det \Lambda^c = 1$ . That is, it is natural to assume that the theory has an  $SU(3)$  color symmetry and that each triplet of quarks  $q^R q^Y q^B$  transforms as the fundamental representation of the group.

The implications of such an invariance are most readily seen by considering an infinitesimal  $SU(3)$  rotation  $\Lambda_{ij}^c (\delta\omega)$  characterized by eight angles  $\delta\omega_a$   $a = 1, 2, 3, \dots, 8$ , (since there are eight independent  $3 \times 3$  unitary, unimodular matrices).

$$\Lambda_{ij}^c (\delta\omega) = \delta_{ij} + i \sum_{a=1}^8 (T_a)_{ij} \delta\omega_a, \quad (4)$$

where  $T_a$  are 8 Hermitian matrices satisfying

$$[T_a, T_b] = i \sum_c f_{abc} T_c. \quad (5)$$

The constants  $f_{abc}$  are completely antisymmetric in their indices

and are the SU(3) analogues of the  $\epsilon_{abc}$  determining the commutation relation of the Pauli matrices  $\sigma_a$ ,  $a = 1, 2, 3$  via the equation

$$[\sigma_a, \sigma_b] = 2i \sum_{c=1,2,3} \epsilon_{abc} \sigma_c. \quad (6)$$

The matrices  $\sigma_a$  determine the  $\Lambda_{ij}^s$  for rotations by infinitesimal angles  $\delta\omega_a$ ,  $a = x, y, z$ , as

$$\Lambda_{ij}^s(\delta\omega_a) = \delta_{ij} + i/2 \sum_{a=1}^3 (\sigma_a)_{ij} \delta\omega_a. \quad (7)$$

The invariance of the theory under spatial rotations, (7), then implies the existence of 3 angular momentum operators  $J_x, J_y, J_z$  which are the generators of spatial rotations. These operators commute with the Hamiltonian and satisfy the commutation relations of the matrices  $\sigma_a$ , i.e.,

$$[J_a, J_b] = i \sum_c \epsilon_{abc} J_c, \quad [J_a, H] = 0. \quad (8)$$

Similarly invariance under color rotations implies the existence of eight color charge operators  $Q_a$  which generate rotations in color space and satisfy the commutation relations

$$[Q_a, Q_b] = i \sum_c f_{abc} Q_c, \quad [Q_a, H] = 0.$$

How do states transform under rotations? Consider the  $\Delta^{++}$  wave function, Eq. (1). Under the transformation (3)

$$\Delta^{++} \rightarrow \Delta^{++'} = \sum_{i,j,k} \epsilon_{ijk} u_{\uparrow}^i u_{\uparrow}^j u_{\uparrow}^k = \Delta^{++}(1,2,3). \quad (9)$$

Thus the  $\Delta^{++}(1,2,3)$  is invariant under rotations in color space and hence has 0 color charge. The wave function (1) is an SU(3) color singlet just as the wave function

$$\psi_{s=0}(1,2) = q_{\uparrow}(1)q_{\downarrow}(2) - q_{\uparrow}(2)q_{\downarrow}(1)$$

is invariant under the spatial rotation, Eq. (2), and is a spin singlet carrying zero angular momentum.

Next consider the wave function for the  $\pi^+$  meson

$$\pi^+(1,2) = d^R u^R + d^B u^B + d^Y u^Y.$$

This state is clearly also an  $SU(3)$  color singlet. We can invert the argument and assume that all baryons and mesons are  $SU(3)$  color singlets. It then follows that mesons are  $qq$  pairs and baryons are  $qqq$  states. Color singlets cannot be formed from other combinations of quarks and antiquarks such as four quarks. Both  $3 \times 3 = 1 + 8$  and  $3 \times 3 \times 3 = 1 + 8 + 8 + 10$  contains the  $SU(3)$  singlet representation. Furthermore since a free quark transforms like an  $SU(3)$  color triplet, no free quarks can exist.

Thus the assumption of an  $SU(3)$  color symmetry with all particles color singlets resolves the spin-statistics problem and shows why only  $q\bar{q}$  or  $qqq$  states exist. We must then explain why the dynamics selects out only color singlets, i.e., confines color.

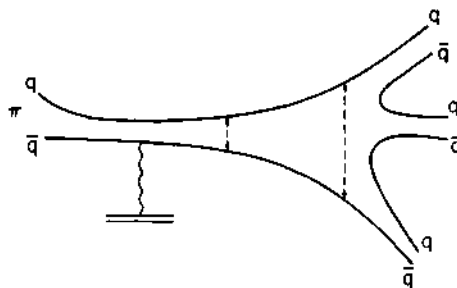


Fig. 1. Elementary picture of quark confinement.

(Since the color charge operators  $Q_a$  generate color rotations, all noninvariant states must carry color charge, just as states which transform nontrivially under spatial rotations have nonvanishing values of angular momentum.) Color confinement, and in particular quark confinement, could possibly be understood as the consequence of a strong long range attraction between colored particles such as quarks, making it energetically favorable to produce  $q\bar{q}$  pairs from the vacuum which could then annihilate to ordinary hadrons (color singlets). See Figure 1. To see if this picture is realized we must construct a dynamical theory of interacting quarks.

We want to construct a theory of the strong interactions

which contains (a) spin 1/2 particles, (b) SU(3) color symmetry, (c) long-range forces. As a guide to constructing such a theory let us recall the construction of quantum electrodynamics (QED) which very accurately describes physics on an atomic and molecular scale. QED describes the interaction of spin 1/2 particles electrons ( $e$ ) and positrons ( $\bar{e}$ ) with massless vector particles, photons ( $\gamma$ ). To each particle we associate a local field

$$e \rightarrow \psi_\alpha(x), \quad \bar{e} \rightarrow \bar{\psi}_\alpha(x), \quad \gamma \rightarrow A_\mu(x).$$

The system of noninteracting electrons and positrons is then described by the Lagrangian

$$\mathcal{L}_0(\psi, \bar{\psi}) = \bar{\psi} \gamma^\mu i \left( \frac{\partial}{\partial x^\mu} \right) \psi(x) - m \bar{\psi}(x) \psi(x). \quad (10)$$

In Eq. (10)  $m$  is the mass of the electron.  $\gamma_\mu$  are Dirac  $\gamma$  matrices whose spin indices have been suppressed.  $\mathcal{L}_0$  is invariant under the phase transformation

$$\begin{aligned} \psi(x) &\rightarrow \psi'(x) = e^{ie_0^\omega} \psi(x), \\ \bar{\psi}(x) &\rightarrow \bar{\psi}'(x) = e^{-ie_0^\omega} \bar{\psi}(x), \end{aligned} \quad (11)$$

corresponding to the symmetry  $U(1)$ . The constant phases  $e^\omega$  are  $1 \times 1$  unitary matrices. The invariance  $\mathcal{L}_0(\psi) = \mathcal{L}_0(\psi')$  then implies the existence of a conserved charge  $Q$ ,  $[Q, H] = 0$ , which is the generator of infinitesimal  $U(1)$  transformations.

The coupling of electrons to photons is determined by requiring that the Lagrangian  $\mathcal{L} = \mathcal{L}_0 + \mathcal{L}_{\text{INT}}$  be invariant under the local  $U(1)$  transformation

$$\begin{aligned} \psi(x) &\rightarrow \psi'(x) = e^{ie_0^\omega(x)} \psi(x) \\ \bar{\psi}(x) &\rightarrow \bar{\psi}'(x) = e^{-ie_0^\omega(x)} \bar{\psi}(x). \end{aligned} \quad (12)$$

$\mathcal{L}$  is determined by making the replacement

$$i \frac{\partial}{\partial x^\mu} \rightarrow i \frac{\partial}{\partial x^\mu} - e_0 A_\mu \quad (13)$$

in  $\mathcal{L}_0$ , which gives

$$\mathcal{L} = \bar{\psi} \gamma^\mu (i \frac{\partial}{\partial x^\mu} - e_0 A_\mu(x)) \psi - m \bar{\psi} \psi . \quad (14)$$

$\mathcal{L}$  is invariant under (12) provided  $A_\mu(x)$  transforms as

$$A_\mu(x) \rightarrow A'_\mu(x) = A_\mu(x) - \frac{\partial}{\partial x^\mu} \omega(x) \quad (15)$$

Finally we must add to  $\mathcal{L}$  a term  $\mathcal{L}^Y$  describing noninteracting photons.

$$\mathcal{L}^Y = -\frac{1}{4} F^{\mu\nu} F_{\mu\nu} , \quad (16)$$

where

$$F_{\mu\nu} = \frac{\partial}{\partial x^\mu} A_\nu - \frac{\partial}{\partial x^\nu} A_\mu .$$

$\mathcal{L}^Y$  is automatically invariant under the transformation (15) since the fields  $F_{\mu\nu}$  are themselves invariant. Thus QED is determined by the requirements of local  $U(1)$  symmetry Eqs. (12) and (15); (also denoted as an Abelian gauge symmetry). To couple electrons to massless vector particles we must use potentials  $A_\mu$  coupled according to Eq. (14).

We can construct QCD following exactly the same prescription. First we associate with color quark  $q^i$  a local field  $\psi_i(x)$ . The system of non-interacting quarks is then described by a Lagrangian  $\mathcal{L}_0$  given by

$$\mathcal{L}_0 = \sum_{i,j=R,Y,B} \psi_i \gamma^\mu i \frac{\partial}{\partial x^\mu} \delta_{ij} \bar{\psi}_j - m_q \bar{\psi}_i \psi_i \quad (17)$$

where  $m_q$  is the bare quark mass.  $\mathcal{L}_0$  is under  $SU(3)$  color rotations

$$\psi_i \rightarrow \psi'_i = \sum_j \Lambda_{ij}^c \psi_j . \quad (18)$$

For infinitesimal rotations  $\Lambda_{ij}^c$  takes on the form of Eq. (4), and the invariance of  $\mathcal{L}_0$  under the transformation Eq. (18) implies the existence of eight color charges  $Q_a$ ,  $a = 1, 2, \dots, 8$  which are the generators of this transformation and which commute with the Hamiltonian

$$[Q_a, H] = 0 \quad a = 1, 2, 3, \dots, 8 .$$

Now we introduce interactions as we did in QED by requiring that  $\mathcal{L} = \mathcal{L}_0 + \mathcal{L}_{\text{INT}}$  is invariant under the local SU(3) color transformation,  $\delta\omega_a + \delta\omega_a(x)$  in Eq. (4), i.e.,

$$\psi_i \rightarrow \psi_i' = [\delta_{ij} - ig_0 \sum_{a=1}^8 (T_a)_{ij} \delta\omega_a(x)] \psi_j. \quad (19)$$

$\mathcal{L}$  is determined by requiring the existence of an octet of massless vector fields  $A_\mu^a(x)$ ,  $a = 1, 2, 3, \dots, 8$  and constructing  $\mathcal{L}$  by making the replacement

$$i \delta_{ij} \frac{\partial}{\partial x^\mu} \rightarrow i \delta_{ij} \frac{\partial}{\partial x^\mu} - g_0 \sum_{a=1}^8 (T_a)_{ij} A_\mu^a(x) \quad (20)$$

in  $\mathcal{L}_0$ . This substitution yields

$$\mathcal{L} = \bar{\psi}_i \gamma^\mu [i \delta_{ij} \frac{\partial}{\partial x^\mu} - g_0 \sum_{a=1}^8 (T_a)_{ij} A_\mu^a(x)] \psi_j(x). \quad (21)$$

$\mathcal{L}$  is then invariant under the transformation Eq. (19) provided the fields  $A_\mu^a(x)$  are transformed simultaneously according to the rule

$$\begin{aligned} A_\mu^a(x) \rightarrow A_\mu^{a'}(x) &= A_\mu^a(x) + \frac{\partial}{\partial x^\mu} \delta\omega_a(x) + \\ &+ g_0 \sum_{b,c=1}^8 f_{abc} A_\mu^b(x) \delta\omega_c(x), \end{aligned} \quad (22)$$

where  $f_{abc}$  are the structure constants of the SU(3) color group determining the commutation relations of the matrices  $T_a$  according to Eq. (5). The gradient term in Eq. (22) is the ordinary gauge transformation analogous to the transformation (Eq. (15)) of the electromagnetic field  $A_\mu(x)$ . The last term in Eq. (22) is a local SU(3) color rotation which is necessary to compensate the local rotation of  $\psi_i$  in Eq. (19) and preserve the invariance of  $\mathcal{L}$ . Thus the "gluon" fields  $A_\mu^a(x)$  transform even when  $\delta\omega_c$  is independent of  $x$ . This means that the gluons themselves carry color charge  $Q_a$  unlike the photon field  $A_\mu(x)$  which remains unchanged under a constant gauge transformation and hence does not carry electric charge.

Finally we must add to  $\mathcal{L}$  a term  $\mathcal{L}^A$  depending only upon the fields  $A_\mu^a(x)$  which is the contribution of the kinetic energy of the gluons. The requirement that  $\mathcal{L}^A$  be invariant under the transformation Eq. (22) essentially determines the form of  $\mathcal{L}^A$ .

$$\mathcal{L}^A = -\frac{1}{4} \sum_{a=1}^8 F_{\mu\nu}^a(x) F^{\mu\nu,a}(x), \quad (23)$$

where

$$F_{\mu\nu}^a(x) = \frac{\partial}{\partial x^\mu} A_\nu^a(x) - \frac{\partial}{\partial x^\nu} A_\mu^a(x) + g_0 f_{abc} A_\mu^b(x) A_\nu^c(x). \quad (24)$$

The last term in Eq. (24) is necessary to make  $\mathcal{L}^A$ , (Eq. (23)) invariant under the local SU(3) color rotation Eq. (22). It induces cubic and quadratic contributions to  $\mathcal{L}^A$  which result in gluon-gluon interactions. This interaction is a consequence of the fact that the gluon carries color charge and hence contributes to the color current to which the gauge field must couple universally in order to preserve gauge invariance. This gluon-gluon interaction is the essential feature distinguishing QCD from QED.

To summarize: The existence of an SU(3) color symmetry makes it possible to construct a local SU(3) symmetry. This leads to the existence of massless vector fields  $A_\mu^a(x)$  which couple to quarks according to Eq. (21) and necessarily couple to themselves in  $\mathcal{L}^A$  (Eqs. (23) and (24)). The QCD Lagrangian is  $\mathcal{L} + \mathcal{L}^A$  where  $\mathcal{L}$  is given by Eq. (21) and  $\mathcal{L}^A$  by Eqs. (23) and (24). The theory containing only interacting gluons described by the Lagrangian  $\mathcal{L}^A$  is Yang-Mills theory.<sup>3</sup>

To understand more clearly the physics of QCD we introduce a color electric field  $\vec{E}^a$  and a color magnetic  $\vec{B}^a$  defined by the equations

$$\vec{E}_i^a = F_{0i}^a, \quad \vec{B}_i^a = -\frac{1}{2} \sum_{jk} \epsilon_{ijk} F_{jk}^a. \quad (25)$$

Then the Yang-Mills Lagrangian  $\mathcal{L}^A$  takes on the form

$$\mathcal{L}^A = \frac{1}{2} \sum_{a=1}^8 (\vec{E}^a \cdot \vec{E}^a - \vec{B}^a \cdot \vec{B}^a), \quad (26)$$

and Eq. (24) becomes\*

$$\vec{E}^a = -\frac{\partial \vec{A}^a}{\partial t} - \vec{\nabla} A_0^a + g_0 f_{acb} \vec{A}_0^c A_0^b, \quad (27a)$$

\*Henceforth in these lectures summation over repeated color indices will be understood.

$$\vec{B}^a = \vec{\nabla} \times \vec{A}^a - \frac{g_0 f}{2} \epsilon_{abc} \vec{A}^c \times \vec{A}^b. \quad (27b)$$

Defining a quantity  $\vec{D}_{ab}$

$$\vec{D}_{ab} = \delta_{ab} \vec{\nabla} - f_{acb} \vec{A}^c. \quad (28)$$

we can write Eqs. (27) in the form

$$\vec{E}^a = - \frac{\partial \vec{A}^a}{\partial t} - \vec{D}_{ab} A_0^b \quad (29a)$$

$$\vec{B}^a = \vec{D}_{ab} \times \vec{A}^b. \quad (29b)$$

Equations (29) can be obtained from the corresponding equations of electromagnetism by the replacement  $\vec{\nabla} \rightarrow \vec{D}_{ab}$ .

Because of the invariance (22) we can impose an additional condition on  $A_\mu^a(x)$ , which corresponds to a choice of gauge. We will work in the temporal gauge

$$A_0^a = 0. \quad (30)$$

In this gauge Eq. (27b) becomes

$$\vec{E}^a = - \frac{\partial \vec{A}^a}{\partial t}. \quad (31)$$

Furthermore in this gauge the equations of motion are obtained from the Lagrangian  $\mathcal{L} + \mathcal{L}^A$  in the usual way.<sup>4</sup> Varying  $A_\mu^a$  in the action  $S = \int dx (\mathcal{L} + \mathcal{L}^A)$  then yields the equation of motion

$$D_{ab}^\mu F_{\mu\nu}^b = J_\nu^a, \quad (32)$$

where

$$D_{ab}^\mu = \frac{\partial}{\partial x_\mu} \delta_{ab} + g_0 f_{acb} A^\mu c$$

and  $J_\nu^a = g_0 \bar{\psi}_i \gamma_\mu T_{ij}^a \psi_j$  is the color current due to the quarks. Again Eqs. (32) can be obtained directly by making the replacement

$$\frac{\partial}{\partial x_\mu} \rightarrow D_{ab}^\mu, \quad F_{\mu\nu} \rightarrow F_{\mu\nu}^b$$

in the equations of electromagnetism. It is easy to show that

Eq. (32) implies

$$D_{ab}^{\mu} J_{\mu}^a = 0 \quad (33)$$

i.e., the color current  $J_{\mu}^a$  appearing in Eq. (32) must be "covariantly" conserved, Eq. (33), in order for the field equations, (32), to be consistent.

If we write  $J^{\mu, a} = (\rho^a, \vec{J}^a)$  where  $\rho^a$  is the color charge density and  $\vec{J}^a$  is the vector color current density the field equations (32) assume the form

$$\vec{\nabla} \cdot \vec{E}^a = \rho^a + g_0 f_{abc} \vec{A}^b \cdot \vec{E}^c \quad (v=0) \quad (34a)$$

$$\vec{\nabla} \cdot \vec{B}^a - \frac{\partial \vec{E}^a}{\partial t} = \vec{J}^a + g_0 f_{abc} (A_0^b \vec{E}^c + \vec{A}^b \times \vec{E}^c) \quad (v=k). \quad (34b)$$

Equations (34) differ from Maxwell's Equations by having additional terms on the right hand side representing the gluon contributions to the charge and current densities respectively. The total charge and current density obtained by adding the gluon charge and current densities to quark densities  $\rho^a$  and  $J^a$  is then conserved. The quark contribution,  $(\rho^a, \vec{J}^a)$ , to the current is not by itself conserved as is made clear by writing Eq. (33) in terms of  $\rho^a, \vec{J}^a$

$$\frac{\partial \rho^a}{\partial t} + \vec{\nabla} \cdot \vec{J}^a = - g_0 f_{abc} (A_0^b \rho^c - \vec{A}^b \cdot \vec{J}^c). \quad (33')$$

YANG-MILLS THEORY IN THE PRESENCE OF AN EXTERNAL CURRENT SOURCE  $J_{\mu}^a$

As we shall see, the charge distribution of the quarks does not play an essential role in producing the confining force. (This might be expected since it is the presence of a gluon cloud carrying color charge which distinguishes QED from QCD.) In this work we will therefore replace the quark current density  $J_{\mu}^a(x)$  by a classical prescribed color current distribution. Equations (32), (33), and (34) remain unchanged in form:  $\rho^a(x)$  and  $\vec{J}^a(x)$  are now prescribed external sources of colored charge and current. These equations then describe Yang-Mills theory in the presence of an external source.

To determine whether color is confined we calculate the energy  $U(R)$  induced in the vacuum by introducing an external color charge density  $\rho^a(\vec{x})$  corresponding to two static point color charges separated by a distance  $R$ ; i.e.,

$$\rho^a(\vec{x}) = Q_1^a \delta(\vec{x} - \vec{x}_1) + Q_2^a \delta(\vec{x} - \vec{x}_2), \quad (35)$$

where  $R = |\vec{x}_1 - \vec{x}_2|$ , and  $Q_1^a$  and  $Q_2^a$  are the color charges of the two sources. (In the temporal gauge a static charge distribution  $J^\mu, a = (\rho^a(\vec{x}), 0)$  satisfies the conservation law Eq. (33).) If  $U(R)$  increases as  $R$  for large  $R$ , then it will be impossible to separate these color charges; i.e., the color will be confined.

In order to calculate  $U(R)$  we first calculate  $\langle \vec{E}^a(x) \rangle$ , the color electric field induced in the vacuum by the charge distribution  $\rho^a(\vec{x})$ . Taking the vacuum expectation value of Eq. (34a) we obtain

$$\vec{\nabla} \cdot \langle \vec{E}^a(x) \rangle = \rho^a + g_0 f_{abc} \langle \vec{A}^b(x) \cdot \vec{E}^c(x) \rangle. \quad (36)$$

The quantity

$$g_0 f_{abc} \langle \vec{A}^b(x) \cdot \vec{E}^c(x) \rangle \equiv \rho^{(in)a}(x) \quad (37)$$

is then induced color charge density produced by the gluon cloud surrounding the source  $\rho^a(\vec{x})$ . Neglecting quantum fluctuations we have

$$\langle \vec{A}^b(x) \cdot \vec{E}^c(y) \rangle = \langle \vec{A}^b(x) \rangle \cdot \langle \vec{E}^c(y) \rangle,$$

and Eq. (36) reduces to the classical Yang-Mills equation for  $\langle \vec{A}^a(x) \rangle$ . However the quantum fluctuations are essential for determining the vacuum polarization charge density  $\rho^{(in)a}(x)$ . These fluctuations are determined by the gluon propagator  $\Delta_{ij}^{bc}(x, y)$  defined by the equation

$$\langle A_i^b(x) A_j^c(y) \rangle \equiv \langle A_i^b(x) \rangle \langle A_j^c(y) \rangle + \Delta_{ij}^{bc}(x, y). \quad (38)$$

Knowing the dependence of  $\Delta_{ij}^{bc}$  upon  $\langle \vec{A}^a \rangle$  gives the dependence of  $\rho^{(in)a}(x)$  on  $\langle \vec{A}^a \rangle$ . We can then expand  $\rho^{(in)a}(x)$  in a power series in  $\langle \vec{A}^a(x) \rangle$ . The linear terms in the expansion determine the color electric susceptibility of the Yang-Mills vacuum, and the high order terms determine the field dependence of this susceptibility. Using this expansion we will show that Eq. (36) takes on the form

$$\rho^a = \vec{\nabla} \cdot \int dy \epsilon^{ab}(x, y) \langle \vec{E}^b(y) \rangle + O(\langle \vec{A}^a \rangle^2). \quad (39)$$

Thus in the linear approximation, Eq. (36) reduces to Gauss' Law in a medium with dielectric constant  $\epsilon^{ab}(x, y)$ .

Using expression (37) for  $\rho^{(in)a}(x)$ , we will then obtain a set of coupled integral equations for  $\epsilon^{ab}$  and its derivatives with respect to  $\langle \vec{E}^a \rangle$ . (The Schwinger-Dyson equations). We have developed a systematic non-perturbative procedure for studying their long distance behavior.<sup>5-7</sup> We will show that in the first stage of this procedure  $\epsilon^{ab}(x,y)$  vanishes when  $|\vec{x} - \vec{y}|$  becomes large; i.e., over large distances the QCD vacuum behaves like a medium of zero dielectric constant. From Gauss' Law, Eq. (39), we will see that  $\langle \vec{E}^a(x) \rangle$  will remain constant at large distances from the source and will yield a field energy  $U(R)$  which increases linearly with  $R$ .

Before carrying through this program we will review in the next two sections what is known about the forces in QED and QCD and compare the two.

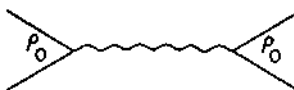


Fig. 2. One photon exchange graph.

#### FORCES IN QED

In QED the force between the two electrons is due to the exchange of photons. In lowest order it is determined by the single photon exchange amplitude  $a(q)$  for electron-electron scattering represented by the Feynman diagram of Fig. 2. It is convenient to give the bare electron a charge distribution  $\rho_0(x)$  such that

$$\int d\vec{x} \rho_0(\vec{x}) = e_0, \quad (40)$$

where  $e_0$  is the bare charge of the electron. We then have, omitting  $\gamma$  matrices,

$$a(q) = \frac{-\rho_0^2(\vec{q})}{q^2} \quad (41)$$

where

$$\rho_0(\vec{q}) = \int d\vec{x} \rho_0(\vec{x}) e^{-i\vec{q} \cdot \vec{x}}$$

and  $q^2 = (q^0)^2 - \vec{q}^2$  is the four momentum transfer in the scattering. In the limit of large electron mass the energy transfer  $q^0 = 0$ , and  $\rho_0(\vec{q}) \Big|_{q^0=0}$  is the Fourier transform of the static potential  $U_0(R)$ , where  $R$  is distance between the two electrons. That is,

$$U_0(\vec{q}) = \frac{\rho_0^2(\vec{q})}{\vec{q}^2},$$

and hence

$$U_0(R) = \int \frac{d\vec{x}_1 d\vec{x}_2}{4\pi} \frac{\rho_0(\vec{x}_1) \rho_0(\vec{x}_2 + \vec{R})}{|\vec{x}_1 - \vec{x}_2|}. \quad (42)$$

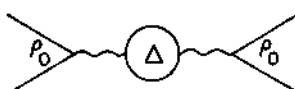


Fig. 3. One photon exchange graph including vacuum polarization.

In higher order the photon emitted by one electron can create a virtual electron-positron pair. This subsequently annihilates into a photon which is then absorbed by the second electron. This process leads to the Feynman graph of Fig. 3 in which the bare photon propagator  $-1/q^2$  has been replaced by a full photon propagator  $\Delta(q)$ . The static potential  $U_0(\vec{q})$  is then replaced by

$$U(\vec{q}) = \rho_0^2(\vec{q}) \Delta(\vec{q}), \quad (43)$$

where

$$\Delta(\vec{q}) \equiv \Delta(q) \Big|_{q=0}.$$

We can then regard the vacuum as a polarizable medium with dielectric constant

$$\epsilon(\vec{q}) \equiv (\vec{q}^2 \Delta(\vec{q}))^{-1}, \quad (44)$$

since

$$U(\vec{q}) = \frac{\rho_0^2(\vec{q})}{\epsilon(\vec{q})\vec{q}^2} \equiv \frac{\rho^2(\vec{q})}{\vec{q}^2}, \quad (45)$$

where

$$\rho^2(\vec{q}) \equiv \frac{\rho_0^2(\vec{q})}{\epsilon(\vec{q})} \quad (46)$$

is the charge distribution surrounding the physical electron.

Before discussing the behavior of the potential  $U(\vec{q})$  we will show how to obtain an equation for the dielectric constant  $\epsilon$ . To do this we consider the electric field  $\langle \vec{E}(\vec{x}) \rangle$  induced in the vacuum by a single electron of charge density  $\rho_0(\vec{x})$ . By Gauss' Law we have

$$\vec{\nabla} \cdot \int d\vec{x}' \epsilon(\vec{x}, \vec{x}') \langle \vec{E}(\vec{x}') \rangle = \rho_0(\vec{x}) \quad (47)$$

where

$$\epsilon(\vec{x}, \vec{x}') = \epsilon(\vec{x} - \vec{x}') = \int \frac{d\vec{q}}{(2\pi)^3} e^{i\vec{q} \cdot (\vec{x} - \vec{x}')} \epsilon(\vec{q}).$$

Equivalently,  $\langle \vec{E}(\vec{x}) \rangle$  is determined by the total charge density

$$\rho(\vec{x}) \equiv \int \frac{d\vec{q}}{(2\pi)^3} e^{i\vec{q} \cdot \vec{x}} \rho(\vec{q}),$$

as

$$\vec{\nabla} \cdot \langle \vec{E}(\vec{x}) \rangle = \rho(\vec{x}). \quad (48)$$

The induced charge  $\rho^{(in)}(\vec{x})$  surrounding the electron is

$$\rho^{(in)}(\vec{x}) \equiv \rho(\vec{x}) - \rho_0(\vec{x}). \quad (49)$$

Differentiating Eq. (47) with respect to  $\langle \vec{E}(\vec{x}) \rangle$  we obtain

$$\vec{\nabla} \cdot \epsilon(\vec{x}, \vec{x}') = \frac{\delta \rho_0(\vec{x})}{\delta \langle \vec{E}(\vec{x}') \rangle}. \quad (50)$$

Using Eqs. (48), (49), and (50) we obtain,

$$\vec{\nabla} \cdot \epsilon(\vec{x}, \vec{x}') = \vec{\nabla} \delta(\vec{x} - \vec{x}') - \frac{\delta \rho^{(in)}(\vec{x})}{\delta \langle \vec{E}(\vec{x}') \rangle}. \quad (51)$$

Defining the susceptibility  $\chi(\vec{x}, \vec{x}')$  as

$$\epsilon(\vec{x}, \vec{x}') = \delta(\vec{x} - \vec{x}') + \chi(\vec{x}, \vec{x}') \quad (52)$$

we then have

$$\vec{\nabla} \cdot \chi(\vec{x}, \vec{x}') = - \frac{\delta \rho^{(in)}(\vec{x})}{\delta \langle \vec{E}(\vec{x}') \rangle}. \quad (53)$$

The induced charge density, however, is determined in terms of the propagator  $\Delta(\vec{x}, \vec{x}')$ . (See Eqs. (37) and (38) for the case of Yang-Mills' theory.) The propagator is determined by the dielectric constant, Eq. (44). Thus  $\rho^{(in)}(\vec{x})$  is a functional of  $\epsilon$ , i.e.,  $\rho^{(in)} = \rho^{(in)}(\epsilon)$ . Equation (53) then expresses  $\chi$  as a function of  $\epsilon$  and  $\delta \epsilon / \delta \langle \vec{E} \rangle$ ,

$$\vec{\nabla} \cdot \chi(\epsilon, \frac{\delta \epsilon}{\delta \langle \vec{E} \rangle}) = \frac{\delta \rho^{(in)}(\epsilon)}{\delta \langle \vec{E} \rangle}. \quad (54)$$

The Fourier transform of Eq. (52) gives  $\epsilon(\vec{q})$  in terms of  $\chi(\vec{q})$ ,

$$\epsilon(\vec{q}) = 1 + \chi(\vec{q}), \quad (55)$$

where  $\chi(\vec{q})$  is determined in terms of  $\epsilon(\vec{q})$  and  $\delta \epsilon / \delta \langle \vec{E} \rangle$  by the Fourier transform of Eq. (54). This is the Schwinger-Dyson equation. Since the susceptibility  $\chi(\vec{q})$  depends on both  $\epsilon$  and  $\delta \epsilon / \delta \langle \vec{E} \rangle$ , the Schwinger-Dyson equation (54) and (55), is a functional differential equation for  $\epsilon$ . Successive differentiation of Eqs. (54) and (55) with respect to  $\langle \vec{E} \rangle$  yields the infinite set

of coupled integral equations for  $\epsilon$  and its derivatives with respect to  $\langle \vec{E} \rangle$  referred to earlier.

We now return to our discussion of the static force between two electrons, determined by  $U(\vec{q})$ , Eq. (45). At large distances we need  $\lim_{\vec{q} \rightarrow 0} U(\vec{q})$  which is

$$\lim_{\vec{q} \rightarrow 0} U(\vec{q}) = \frac{\rho_0^2(\vec{q})}{\vec{q}^2} = \frac{e^2}{\vec{q}^2}, \quad (56)$$

where

$$e = \lim_{\vec{q} \rightarrow 0} \rho(\vec{q}) = \int d\vec{x} \rho(\vec{x}) \quad (57)$$

is the total charge contained in a large sphere surrounding the electron. The Fourier transform of Eq. (56) then gives  $U(R)$  as  $R \rightarrow \infty$ , i.e.,

$$\lim_{R \rightarrow \infty} U(R) = \frac{e^2}{4\pi R} \quad (58)$$

where  $e^2/4\pi \approx 1/137$  is the physically measured charge.

The force at some finite distance  $R$  is determined by the charge  $e(R)$  contained in a sphere of radius  $R$  surrounding the electron. The charge  $e(R)$  is of order  $\rho(\vec{q}) \Big|_{|\vec{q}|=1/R}$  and hence from Eq. (46)

$$e^2(R) = \frac{\rho_0^2(\vec{q})}{\epsilon(\vec{q})} \Big|_{|\vec{q}|=1/R}. \quad (59)$$

We assume that the bare charge of the electron is confined to a sphere of radius  $a$  and consider distances  $R > a$ . Then

$$\rho_0^2(\vec{q}) \Big|_{|\vec{q}|=1/R} \approx e_0^2$$

and

$$e^2(R) = \frac{e_0^2}{\epsilon(\vec{q})} \Big|_{|\vec{q}|=1/R}. \quad (60)$$

Figure 4 represents a picture of the charge distribution surrounding the electron. The total charge contained in the sphere of radius  $R$  is  $e(R)$ , and the charge contained in the sphere of radius  $a$  is the bare charge  $e_0$ .

In lowest order  $\chi(q)$  is determined by the graph of Fig. 5, representing virtual creation in the vacuum of a single electron-positron pair. Using Eqs. (60), (55) and the perturbation expression for  $\chi(q)$  we obtain

$$e^2(R) = \frac{e_0^2}{\frac{2}{1 + \frac{e_0^2}{12\pi^2} \log R^2/a^2}}. \quad (61)$$

Thus  $e^2(R) < e_0^2$ , i.e., the vacuum polarization shields the bare charge. In fact, Eq. (61) predicts infinite shielding ( $e^2(R)=0$ )<sup>8</sup> in the limit of a point electron,  $a \rightarrow 0$ , for any value of  $e_0^2$ . However the approximation (61) is justified only when

$$\frac{e_0^2}{12\pi^2} \log R^2/a^2 \leq 1,$$

and hence the conclusion  $e^2(R) = 0$ , as  $a \rightarrow 0$  is not necessarily valid.

An alternate way of viewing the problem is to eliminate  $e_0^2$  from Eq. (61) and express the charge  $e^2(R)$  in terms of the physical charge contained in a sphere of radius  $R_1^2$  as represented by Fig. 6. Equation (61) then gives

$$e^2(R) = \frac{e^2(R_1)}{1 - \frac{e^2(R_1)^2}{12\pi^2} \log R_1^2/R^2}. \quad (62)$$

Thus if we fix the physical charge,  $e^2(R_1)$ , contained in a sphere of radius  $R_1$ , then  $e^2(R) > e^2(R_1)$  for  $R < R_1$  since the shielding is less effective at short distances. In fact, according to Eq. (62)  $e^2(R)$  becomes infinite at  $R^2 = R_G^2$  where

$$R_G^2 = R_1^2 e^{-12\pi^2/e^2(R_1)}.$$

This singularity<sup>8</sup> (Landau Ghost) at  $R^2 = R_G^2$  can be avoided by

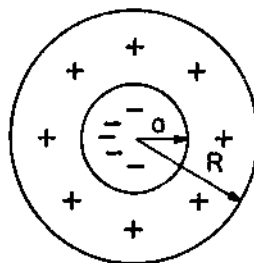


Fig. 4. Charge distribution surrounding an electron

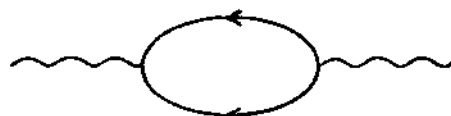


Fig. 5. Lowest order graph for the susceptibility  $\chi$  (vacuum polarization).

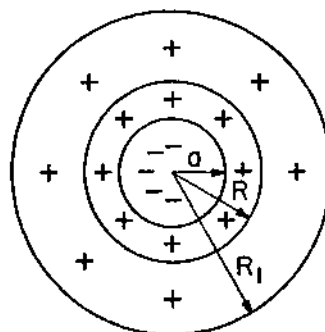


Fig. 6. Electric charge  $e^2(R)$  at small distance  $R$  for  $e^2(R_1)$  fixed.

taking  $e^2(R_1) = 0$ . Thus Eq. (62) also leads to zero physical charge.

Of course Eq. (62) is not valid at a distance  $R^2 \approx R_G^2$  and we do not know the short distance behavior of the full QED. However one can show in a simplified model of QED that the term  $(e_0^2 \log R^2/a^2)/12\pi^2$  in the denominator of Eq. (61) is replaced by  $f(e_0^2) \log R^2/a^2$ , when all higher orders are included.<sup>9</sup> The function  $f(e_0^2)$  has been calculated to order  $(e_0^2)^3$  and is given by<sup>10</sup>

$$f(e_0^2) = \frac{e_0^2}{8\pi^2} \left[ \frac{2}{3} + \frac{e_0^2}{8\pi^2} - \frac{1}{4} \left( \frac{e_0^2}{8\pi^2} \right)^2 + \dots \right]. \quad (63)$$

In this model there is then no zero charge if  $e_0^2$  is a nonvanishing root of the equation  $f(e_0^2) = 0$ . Furthermore one can show that if such a root exists, then the exact QED with non zero charge has a well behaved short distance behavior without the Landau Ghost.<sup>11</sup> However since  $f(e_0^2)$  has not been calculated beyond Eq. (63), the self-consistency of the short distance behavior of QED has not been established.

#### FORCES IN QCD

We now carry through an analogous discussion in QCD for the forces between quarks, the carriers of color charge. Gluon exchange between quarks leads to a potential

$$U_C(\vec{q}) \equiv \rho_{0C}^2(\vec{q}) \Delta_C(\vec{q}), \quad (64)$$

where  $\rho_{0C}(\vec{q})$  is the Fourier Transform of the color charge distribution surrounding a bare quark, and  $\Delta_C(q)$  is the gluon propagator\*

---

\* The gluon propagator  $\Delta_{ij}^{ab}(x,y)$  defined by Eq. (38) is a second rank tensor in color space and hence is proportional to the only available second rank tensor  $\delta^{ab}$ . It is also a tensor in the space indices  $k$  and  $j$ , whose explicit form will be given later. For the purposes of this section it is sufficient to replace

$$\Delta_{ij}^{ab} \rightarrow \Delta_C \delta^{ab}$$

where  $\Delta_C$  is the scalar function which multiplies the known tensor structure of  $\Delta_{ij}^{ab}$  and which contains all the dynamics.

( $\rho_{0C}(0) = g_0$ , the bare color charge of the quark.) Since the gluon carries color charge,  $\Delta_C(q)$  is not invariant under a color charge rotation (Eq. (22)), and hence unlike the photon propagator depends upon the choice of gauge. However we will show that the gluon propagator in the temporal gauge,  $A_0 = 0$ , determines the color dielectric constant  $\epsilon_C(\vec{q})^*$  via the equation, (analogous to Eq. (44)),

$$\epsilon_C(\vec{q}) = [\vec{q}^2 \Delta_C(\vec{q})]^{-1}. \quad (65)$$

We can then interpret  $\rho_C(\vec{q})$  defined by

$$\rho_C^2(\vec{q}) = \rho_{0C}^2(\vec{q}) / \epsilon_C(\vec{q}) \quad (66)$$

as the Fourier Transform of the color charge distribution surrounding a quark in the physical vacuum. Furthermore in analogy with Eqs. (54) and (55),  $\epsilon_C(\vec{q})$  can be obtained from the Schwinger-Dyson equation

$$\epsilon_C(\vec{q}) = 1 + \chi_C(\vec{q}) \quad (67)$$

where  $\chi_C(q)^{ab} = \chi^{ab}(q)$  is the Fourier Transform of the color charge susceptibility  $\chi^{ab}(\vec{x}, \vec{x}') \equiv \chi_C(\vec{x}, \vec{x}') \delta^{ab}$ , determined from the induced color charge density  $\rho^{(in)}a(\vec{x})$  by the equation

$$\vec{\nabla} \chi^{ab}(\vec{x}, \vec{x}') = - \frac{\delta \rho^{(in)}a(\vec{x})}{\delta \vec{E}^b(\vec{x}')}. \quad (68)$$

Thus  $\chi_C(\vec{x}, \vec{x}')$  gives the change in  $\rho^{(in)}a(\vec{x})$  due to a fluctuation of the color electric field  $\langle \vec{E}^b(\vec{x}') \rangle$ . Equation (37) gives the expression for  $\rho^{(in)}a(\vec{x})$  in Yang-Mills theory.

To lowest order in  $g_0^2$ ,  $\chi_C$  is determined by the graphs of Fig. 7, representing the virtual creation and annihilation in the vacuum of a quark-antiquark pair and of a gluon pair. The quark-antiquark pair gives a positive contribution to  $\chi_C$ . However the gluon contribution to  $\chi_C$  is negative and dominates. The resulting dielectric constant  $\epsilon_C$  is less than 1, i.e., we have antishielding.

As in QED we can interpret  $g(R) \equiv \rho_C(\vec{q}) \Big|_{|\vec{q}|=1/R}$  as the color charge contained in a sphere of radius  $R$  surrounding a quark.

\* The color dielectric constant  $\epsilon^{ab}$  (see Eq. (39)) is also proportional to  $\delta^{ab}$ . We then have  $\epsilon^{ab} = \delta^{ab} \epsilon_C$  where  $\epsilon_C$  is related to  $\Delta_C$  by Eq. (65).

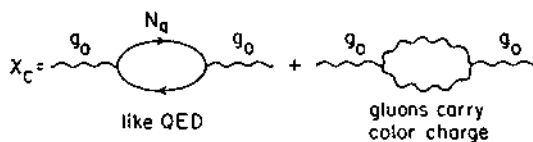


Fig. 7. Lowest order graph for the color susceptibility  $x_C$  of QCD vacuum.

Then

$$g^2(R) = \frac{g_{0C}^2(\vec{q})}{\varepsilon_C(\vec{q}) \Big|_{|\vec{q}|=1/R}} = \frac{g_0^2}{\varepsilon_C(\vec{q}) \Big|_{|\vec{q}|=1/R}}, \quad (69)$$

where we assume that the bare charge of the quark is confined to a sphere of radius  $a$  and take  $R > a$ . Figure 8 represents a picture of the color charge distribution surrounding the quark. The perturbation expression for  $x_C$  determined from the graph of Fig. 7 gives

$$g^2(R) = \frac{g_0^2}{1 - \frac{g_0^2}{12\pi^2} \left( 11 - \frac{2N_q}{3} \right) \log \frac{R^2}{a^2}}, \quad (70)$$

where  $N_q$  is the number of quark-antiquark pairs contributing to

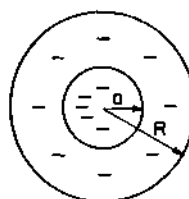


Fig. 8. Color charge distribution surrounding a quark.

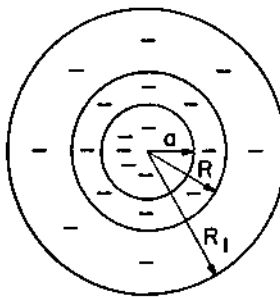


Fig. 9. Color charge  $g^2(R)$  at small distance  $R$  for  $g^2(R_1)$  fixed.

Fig. 6. Setting  $N_q = 5$  corresponding to the "known" quarks  $u, d, s, c, b$  gives  $\chi_C < 0$ . Thus  $g^2(R) > g_0^2$ , and the antiscreening produced by the gluon contribution to  $\rho(\text{in})a(\vec{x})$  has eliminated the problem of zero charge possibly occurring in QED.

As in QED it is convenient to eliminate  $g_0^2$  from Eq. (70) and express the color charge  $g(R)$  contained in a sphere of radius  $R$  in terms of the color charge  $g(R_1)$  contained in a sphere of radius  $R_1$  as represented in Fig. 9. We obtain

$$g^2(R) = \frac{g^2(R_1)}{1 + \frac{g^2(R_1)}{16\pi^2} (11 - \frac{2}{3} N_q) \log \frac{R_1}{R}}. \quad (71)$$

Thus if we fix the color charge  $g(R_1)$  contained in a sphere of radius  $R_1$ , then  $g^2(R) < g^2(R_1)$  for  $R < R_1$ , i.e., the antiscreening is less effective at smaller distances. There is no Landau Ghost at short distances and as  $R \rightarrow 0$

$$g^2(R) \rightarrow \frac{1}{b \log R_1^2/R^2}, \quad (72)$$

$$\text{where } b = \frac{1}{16\pi^2} (11 - \frac{2}{3} N_q).$$

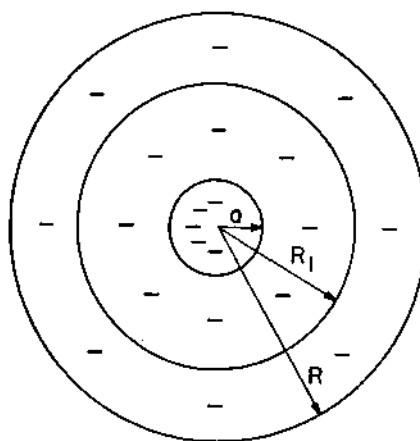


Fig. 10. Color charge  $g^2(R)$  at large distance  $R$  with  $g^2(R_1)$  fixed.

Thus in QCD the coupling constant becomes small at short distances (asymptotic freedom) and perturbation theory is applicable. Then by comparing Eq. (72) to appropriate high momentum phenomena we can determine

$$1/R_1^2 \equiv \Lambda^2 \approx (200 \text{ MeV})^2.$$

We now consider the long distance behavior of QCD, which will be complicated, just as QED is complicated at short distances. Choosing  $R > R_1$  corresponding to the diagram of Fig. 10 we have

$$g^2(R) = \frac{g^2(R_1)}{1 - g^2(R_1) b \log R^2/R_1^2} > g^2(R_1). \quad (73)$$

According to Eq. (73)  $g^2(R)$  continues to grow as we increase  $R$  and becomes infinite at  $R^2 = R_{CG}^2$  where

$$R_{CG}^2 = R_1^2 e^{1/(b g^2(R_1))}. \quad (74)$$

Of course the "Landau Approximation", Eq. (73) based on perturbation theory for  $\chi_C(\vec{q})$  is not valid at small  $\vec{q}^2$ . Thus we must find a non-perturbative procedure for calculating the small  $\vec{q}^2$  behavior of QCD. One possibility is that after the non-perturbative effects are included, the low momentum instability represented by the pole, "Landau Ghost", in Eq. (73) at  $\vec{q}^2 \equiv 1/R^2 = 1/R_{CG}^2$ , would be reflected by a pole at  $\vec{q}^2 = 0$  in the exact solution. From Eq. (69) or (66) this would mean that

$$\epsilon_C(\vec{q}) \xrightarrow[\vec{q}^2 \rightarrow 0]{} \vec{q}^2 \quad (75)$$

which corresponds to a dielectric constant  $\epsilon_C(\vec{x} - \vec{y})$  which vanishes as  $|\vec{x} - \vec{y}| \rightarrow \infty$ . As we have seen this behavior would lead to a confining potential between quarks.

The increase Eq. (73) of the QCD charge at long distances was due to the antishielding nature of the gluon contribution to the vacuum polarization. It is these gluon contributions which fundamentally distinguish QCD from QED. Determining the long distance behavior of Yang-Mills theory would then be an important step in understanding the long distance behavior of QCD. In our work we omit the quark contribution to the current density and consider the problem of a pure Yang-Mills theory in the presence of an external current source  $J_\mu^a(x)$ . As discussed earlier this current will polarize the vacuum and we will show that its long-range response to this current is characterized by a color dielectric constant,  $\epsilon_C(\vec{q})$ , which for small  $\vec{q}^2$  (large distances) is proportional to  $\vec{q}^2$  as anticipated in Eq. (75).

#### GENERALIZED "MAXWELL EQUATIONS" FOR A DIELECTRIC MEDIUM

In this section we will show, using "covariant current conservation", Eq. (33), that  $\langle \vec{E}^a(x) \rangle$  and  $\langle \vec{B}^a(x) \rangle$  are related to the external current  $J^\mu, a = (\rho, \vec{J})$  by a set of equations resembling Maxwell's equations in a nonlinear dielectric medium. The linear terms in the equations will be the ordinary Maxwell's equations in a dielectric medium, one of which is simply Gauss' Law, Eq. (39). The general nonlinear equations are just the formal manifestation of the fact that vacuum of quantum field theory is a nonlinear polarizable medium as we have discussed earlier. This discussion will make use only of gauge invariance, (Eq. (33)), and Lorentz invariance, and will contain as yet undetermined parameters like the dielectric constant  $\epsilon^{ab} = \delta^{ab} \epsilon_C$  appearing in Eq. (39). In the next section we will determine the long distance behavior of  $\epsilon_C(\vec{x} - \vec{y})$  using the Schwinger-Dyson equations.

We recall we are working in the temporal gauge  $A_0^a = 0$ . It is sometimes convenient to write this equation as

$$n^\mu A_\mu^a = 0,$$

where  $n^\mu = (1, 0, 0, 0)$ . The vacuum expectation value of Eq. (32)

$$\langle D_{ab}^\mu F_{\mu\nu}^b \rangle = J_\nu^a \quad (76)$$

determines the expectation value  $\langle A_\mu^a(x) \rangle$  induced in the vacuum in terms of the external current  $J_\mu^a(x)$ . The  $\nu = 0$  component of Eq. (76) is Eq. (36). Equation (76) differs from the classical Yang-Mills equations by the presence of the quantum fluctuations determined by the gluon propagator  $\Delta_{ij}^{bc}(x, y)$ , Eq. (38). If the propagator  $\Delta_{ij}^{bc}(x, y)$  is known as a functional of  $\langle A_\mu^a(x) \rangle$ , the left hand side of Eq. (76) expresses  $J_\nu^a$  as a functional of  $\langle A_\mu^a(x) \rangle$ . This functional  $J_\nu^a(\langle A_\mu^a \rangle)$  must satisfy the equation

$$\langle D_{ab}^\mu \rangle J_\mu^a(x) = 0, \quad (77)$$

obtained by taking the vacuum expectation value of Eq. (33). Using the definition, Eq. (32), of  $D_{ab}^\mu$ , we can write Eq. (77) as

$$\frac{\partial}{\partial x_\mu} J_\mu^a(x) + g_0 f_{ars} \langle A^r, \mu \rangle J_\mu^s(x) = 0. \quad (78)$$

Equation (78) is the constraint on the functional  $J_\mu^a$  required by gauge invariance. Any solution of Eq. (76) must yield a  $J_\mu^a$  satisfying Eq. (78). Equation (76) contains all dynamics and yields the explicit form of the Schwinger-Dyson Equation which we obtain in the next section. In this section we will make use only of Eq. (78) in order to determine the general structure of  $J_\mu^a(x)$  allowed by gauge invariance. It is this analysis which will give us the generalized Maxwell equations.

We begin by expanding  $J_\mu^a(x)$  as a power series in  $\langle A_\nu^a \rangle$ , using Eq. (78) to put restrictions upon the expansion coefficients. Since  $J_\mu^a = 0$  when  $\langle A_\nu^a \rangle = 0$  (see Eq. (76)), we can write

$$J_\mu^a(x) = \int dy \frac{\delta J_\mu^a(x)}{\delta \langle A_\nu^b(y) \rangle} \bigg|_{\langle A \rangle = 0} \langle A_\nu^b(y) \rangle$$

$$+ \int dy_1 dy_2 \frac{\delta^2 J_\mu^a(x)}{\delta \langle A_\nu^b(y_1) \rangle \delta \langle A_\lambda^c(y_2) \rangle} \bigg|_{\langle A \rangle = 0} \langle A_\nu^b(y_1) \rangle \langle A_\lambda^c(y_2) \rangle + \dots$$

The coefficients of the first two terms in the expansion define tensors

$$\Pi_{\mu\nu}^{ab}(x, y) \equiv \left. \frac{\delta J_{\mu}^a(x)}{\delta \langle A_{\nu}^b(y) \rangle} \right|_{\langle A \rangle = 0}, \quad (80)$$

$$\Gamma_{\mu\nu\lambda}^{abc}(x, y, z) \left|_{\langle A \rangle = 0} \right. \equiv \left. \frac{\delta^2 J_{\mu}^a(x)}{\delta \langle A_{\nu}^b(y) \rangle \delta \langle A_{\lambda}^c(z) \rangle} \right|_{\langle A \rangle = 0}. \quad (81)$$

We call  $\Pi_{\mu\nu}^{ab}(x, y)$  (Eq. (80)) the color dielectric tensor since by Eq. (39) it is clearly related to the color dielectric constant  $\epsilon^{ab} = \epsilon \delta^{ab}$ .<sup>\*</sup> We will obtain the precise form of the relation below. Equation (80) without the restriction  $\langle A \rangle = 0$  defines the field dependent color dielectric tensor. The quantity  $\Gamma_{\mu\nu\lambda}$  is the triple gluon vertex function, which by Eqs. (80) and (81) is a measure of the field dependence of  $\epsilon$ , i.e.,

$$\Gamma \sim \frac{\delta \epsilon}{\delta \langle A \rangle}.$$

Similarly the coefficients of the higher powers of  $\langle A \rangle$  in the expansion (79) are related to higher derivatives of  $\epsilon$  with respect to  $\langle A \rangle$ . Equation (78) imposes restrictions upon these coefficients (The Slavnov-Taylor identities).<sup>13</sup> Differentiating Eq. (78) with respect to  $\langle A^{\nu},^b(y) \rangle$  yields (using Eq. (80))

$$\begin{aligned} \frac{\partial}{\partial x_{\mu}} \Pi_{\mu\nu}^{ab}(x, y) + g_0 f_{ars} \langle A^r,^{\mu}(x) \rangle \Pi_{\mu\nu}^{sb}(x, y) \\ = - g_0 f_{abs} J_{\nu}^s(x) \delta(x - y). \end{aligned} \quad (82)$$

In Eq. (82) we have used the notation  $\Pi_{\mu\nu}^{ab}(x, y)$  for the right hand side of Eq. (80) even when  $\langle A \rangle \neq 0$ . Differentiation of Eq. (82) with respect to  $\langle A^c,^{\lambda}(z) \rangle$  yields (using Eqs. (80) and (81) without setting  $\langle A \rangle = 0$ )

$$\begin{aligned} \frac{\partial}{\partial x_{\mu}} \Gamma_{\mu\nu\lambda}^{abc}(x, y, z) + g_0 f_{ars} \langle A^r,^{\mu}(x) \rangle \Gamma_{\mu\nu\lambda}^{sbc}(x, y, z) \\ = - g_0 f_{abs} \Pi_{\nu\lambda}^{sc}(x, z) \delta(x - y) - g_0 f_{acs} \Pi_{\lambda\nu}^{sb}(x, y) \delta(x - z). \end{aligned} \quad (83)$$

\*Since in the remainder of these lectures we consider only color charge we will omit the subscript  $C$  on the dielectric constant  $\epsilon_C$  and the susceptibility  $\chi_C$ , making the replacements  $\chi_C \rightarrow \chi$ ,  $\epsilon_C \rightarrow \epsilon$ .

In Eq. (83) we have used the notation  $\Gamma_{\lambda\mu\nu}^{abc}(x,y,z)$  for the right hand side of Eq. (81) also when  $\langle A \rangle \neq 0$ . Further differentiation of Eq. (83) yields identities expressing the four divergences of higher order vertex functions (higher order field derivatives of the color dielectric tensor) in terms of derivatives of one lower order. These are Slavnov-Taylor identities,<sup>13,14</sup> which as we have seen, are immediate consequences of Eq. (78).

In these lectures we make use of two special cases of these identities.

(I) Set  $\langle A \rangle = 0$  in Eq. (82). Then since  $J_\mu^a$  is then zero, Eq. (82) becomes

$$\frac{\partial}{\partial x_\mu} \Pi_{\mu\nu}^{ab}(x,y) = 0. \quad (84)$$

Equation (84) states that the zero field color dielectric tensor is transverse (in the four-dimensional sense) i.e., its longitudinal part vanishes.

(II) Set  $\langle A \rangle = 0$  in Eq. (83). We obtain

$$\begin{aligned} \frac{\partial}{\partial x_\mu} \Gamma_{\mu\nu\lambda}^{abc}(x,y,z) = & - g_0 f_{abs} \Pi_{\nu\lambda}^{sc}(x,z) \delta(x-y) \\ & - g_0 f_{acs} \Pi_{\lambda\nu}^{sb}(x,y) \delta(x-z). \end{aligned} \quad (85)$$

Equation (85) states that the longitudinal part of the vertex function (the field derivative of the dielectric tensor) is determined in terms of the color dielectric tensor  $\Pi_{\mu\nu}^{ab}(x,y)$  itself.

We now show using Eq. (84) that the linear term in Eq. (79) yields Maxwell's Equations in a linear dielectric medium. Taking the Fourier Transform of the linear term in Eq. (79) we obtain

$$J_\mu^a(q) = \Pi_{\mu\nu}^{ab}(q) A^\nu, b(q), \quad (86)$$

where

$$J_\mu^a(x) = \int \frac{dq}{(2\pi)^4} e^{-iq \cdot x} J_\mu^a(q),$$

and

$$A_\nu^b(y) = \int \frac{dq}{(2\pi)^4} e^{-iq \cdot y} A_\nu^b(q).$$

and

$$\Pi_{\mu\nu}^{ab}(x, y) = \int \frac{dq}{(2\pi)^4} e^{-iq \cdot (x-y)} \Pi_{\mu\nu}^{ab}(q).$$

In Eq. (86) we have used translational invariance,

$$\Pi_{\mu\nu}^{ab}(x, y) \Big|_{\langle A \rangle = 0} = \Pi_{\mu\nu}^{ab}(x - y).$$

Furthermore since  $\delta^{ab}$  is the only available second rank color tensor,

$$\Pi_{\mu\nu}^{ab}(q) = \delta^{ab} \Pi_{\mu\nu}(q). \quad (87)$$

The transversality condition Eq. (84) yields

$$q^\mu \Pi_{\mu\nu}(q) = 0. \quad (88)$$

The most general Lorentz covariant solution of Eq. (88) is

$$\Pi_{\mu\nu}(q) = -Z^{-1}(q)(q^2 g_{\mu\nu} - q_\mu q_\nu), \quad (89)$$

where

$$g_{00} = 1, \quad g_{ij} = -\delta_{ij},$$

and  $Z^{-1}(q)$  is a function of the scalar  $q^2$ . In general  $\Pi_{\mu\nu}$  could depend upon the vector  $n^\mu$  defining the temporal gauge. However, we will assume that the  $n^\mu$  dependence of  $\Pi_{\mu\nu}(x, y)$  is not important at small  $q^2$ ; in which case Eq. (89) is the most general solution of (88). We will later check the consistency of this ansatz.

Equations (86), (87) and (89) then yield

$$J_\mu^a(q) = -Z^{-1}(q)(q^2 g_{\mu\nu} - q_\mu q_\nu) \langle A^\nu, a(q) \rangle. \quad (90)$$

Taking the  $\mu = 0$  component of Eq. (90), and using the gauge condition Eq. (30) we obtain

$$\rho^a(q) = -Z^{-1}(q) q_0 q_k \langle A_k^a(q) \rangle. \quad (91)$$

Remember we use a time like metric  $a_\mu^a b^\mu = a^0 b^0 - \vec{a} \cdot \vec{b}$ .

Now the Fourier Transform of the vacuum expectation value of Eq. (31) gives

$$\langle \vec{E}^a(q) \rangle = i q_0 \langle \vec{A}^a(q) \rangle. \quad (92)$$

Hence Eq. (91) becomes

$$\rho^a(q) = i \vec{q} \cdot \vec{z}^{-1}(q) \langle \vec{E}^a(q) \rangle. \quad (93)$$

We then define a vector  $\vec{D}^a(q)$ ,

$$\vec{D}^a(q) \equiv \vec{z}^{-1}(q) \langle \vec{E}^a(q) \rangle. \quad (94)$$

Equation (93) then becomes (in coordinate space)

$$\vec{\nabla} \cdot \vec{D}^a(x) = \rho^a(x). \quad (95)$$

Hence the 0 component of Eq. (90) is Gauss' Law in a dielectric medium with a dielectric constant whose Fourier Transform  $\epsilon(q)$  is

$$\epsilon(q) = \vec{z}^{-1}(q). \quad (96)$$

Next we take the  $k$  component of Eq. (90). Writing  $q^2 = (q^0)^2 - \vec{q}^2$ , we obtain

$$\begin{aligned} -J_k^a(q) &= \vec{z}^{-1}(q) (q^0)^2 \langle A_k^a(q) \rangle \\ &\quad - \vec{z}^{-1}(q) (\vec{q}^2 \delta_{kl} - q_k q_l) \langle A_l^a(q) \rangle. \end{aligned} \quad (96)$$

Using Eqs. (92) and (94), we can write Eq. (97) as

$$\vec{J}^a(q) = i q^0 \vec{D}^a(q) - \vec{q} \times (\vec{z}^{-1}(q) \vec{q} \times \langle \vec{A}^a(q) \rangle). \quad (98)$$

Now it is convenient to define

$$\vec{B}_{\text{classical}}^a(x) \equiv \vec{\nabla} \times \langle \vec{A}^a \rangle - \frac{g_0}{2} f_{abc} \langle \vec{A}^c(x) \rangle \times \langle \vec{A}^b(x) \rangle. \quad (99)$$

Comparing Eqs. (27b) and (99) we see

$$\vec{B}_{\text{classical}}^a(x) \quad \text{differs from} \quad \langle \vec{B}^a(x) \rangle$$

because of the omission of the quantum fluctuations in the

quadratic term in (27b). This is the reason for the nomenclature  $\vec{B}_{\text{classical}}^a(x)$ . Since Eq. (97) is accurate to first order in  $\langle \vec{A}^a \rangle$ , we can use the linear term in Eq. (99) to write Eq. (98) in the form

$$\vec{J}^a(q) = i q^0 \vec{D}^a(q) + i \vec{q} \times z^{-1}(q) \vec{B}_{\text{classical}}^a(q). \quad (100)$$

It can be shown that the quadratic terms in Eq. (79) include a contribution of the form of Eq. (100) with  $\vec{B}_{\text{classical}}^a$  given by the quadratic term in Eq. (99). (Of course, there is no need to define  $\vec{B}_{\text{classical}}^a(q)$  except for heuristic purposes, since the variable  $\langle \vec{A}^a \rangle$  is usually more convenient.)

We now define a quantity

$$\vec{H}^a(q) \equiv z^{-1}(q) \vec{B}_{\text{classical}}^a(q) = z^{-1}(q) i \vec{q} \times \langle \vec{A}^a(q) \rangle, \quad (101)$$

to first order in  $\langle \vec{A}^a \rangle$ . Then in coordinate space Eq. (98) or (100) becomes

$$\vec{\nabla} \times \vec{H}^a(x) - \frac{\partial \vec{D}^a(x)}{\partial t} = \vec{J}^a. \quad (102)$$

Equation (102) is just Maxwell's Equation in a medium of magnetic permeability

$$\mu(q) = z(q). \quad (103)$$

Thus using Eqs. (86) and (89) we have seen that the linear term in the expansion (79) reduces to Maxwell's equations in a dielectric medium of color dielectric constant  $\epsilon(q)$  and color magnetic permeability  $\mu(q)$  given by

$$\epsilon(q) = \frac{1}{\mu(q)} = z^{-1}(q), \quad (104)$$

where  $z^{-1}(q)$  is the scalar function determining  $\Pi_{\mu\nu}(q)$  via Eq. (89).

Similarly we can use Eq. (85) to determine the structure of the quadratic terms in Eq. (79). They will lead to the classical Yang-Mills equations in a dielectric medium with additional quadratic terms due to quantum fluctuations.

Finally we calculate the static limit by setting  $q^0 = 0$  in Eq. (93). Then

$$\rho^a(\vec{q}) = - i \vec{q} \cdot z^{-1}(\vec{q}) \langle \vec{E}^a(\vec{q}) \rangle, \quad (105)$$

where

$$\begin{aligned}\rho^a(\vec{q}) &= \rho^a(q) \Big|_{\substack{0 \\ q=0}} = \int d\vec{x} e^{-i\vec{q} \cdot \vec{x}} \int dt \rho^a(\vec{x}, t) \\ &= \int d\vec{x} e^{-i\vec{q} \cdot \vec{x}} \rho^a(\vec{x}),\end{aligned}$$

where  $\rho^a(\vec{x})$  is the time average of the external charge distribution. In coordinate space Eq. (105) becomes

$$\vec{\nabla} \cdot \int d\vec{y} \epsilon(\vec{x} - \vec{y}) \langle \vec{E}^a(\vec{y}) \rangle = \rho^a(\vec{x}), \quad (106)$$

where  $\langle \vec{E}^a(\vec{y}) \rangle$  is the time average of the expectation value of the color electric field and

$$\epsilon(\vec{x} - \vec{y}) = \int \frac{dq}{(2\pi)^3} e^{i\vec{q} \cdot (\vec{x} - \vec{y})} z^{-1}(\vec{q}). \quad (107)$$

The static color dielectric constant is then the Fourier Transform of

$$z^{-1}(\vec{q}) \equiv z^{-1}(q) \Big|_{\substack{0 \\ q=0}}.$$

Thus if  $z^{-1}(q)$  is finite at  $q^0 = 0$ , then the static limit exists and we obtain Gauss' Law, Eq. (106), with a static color dielectric constant given by Eq. (107). In the presence of singular long range forces the finiteness of  $z^{-1}(\vec{q})$  is nontrivial. We will show in the next section using the temporal gauge Schwinger-Dyson equations and the Slavnov-Taylor identity (85) that this limit does exist. This result is of course essential for the calculation of the energy of separation of two static charge distributions which we carry out in the final section.

Finally we remark the static color dielectric constant is related to  $\Pi_{\mu\nu}$  in the temporal gauge via Eqs. (107) and (89). In other gauges in general the Slavnov-Taylor identities do not have the simple form of Eqs. (84) and (85) and the quantity  $\Pi_{\mu\nu}$  has no direct physical interpretation. On the other hand we will see that the long distance behavior of the static dielectric constant Eq. (107) will determine the large distance energy of separation of two static color sources and is hence a physically observable quantity. Thus the value of the gauge dependent quantity defined by Eq. (80) yields a physical measurable quantity when evaluated in the temporal gauge.

THE SCHWINGER-DYSON EQUATION FOR THE COLOR DIELECTRIC CONSTANT  $\epsilon(q)$ 

The Schwinger-Dyson Equation for the color dielectric constant of Yang-Mills theory is obtained by combining Eqs. (67), (68) and (37). We will first do this without keeping track of kinematic factors in order to understand qualitatively the structure of the equation.

From Eqs. (37) and (38) we see that  $\rho^{(in)a}(x)$  is proportional to the gluon propagator  $\delta_{ij}^{bc}.$ \* Equation (37) then yields

$$\nabla \chi^{\rightarrow ad} = - \frac{\delta \rho^{(in)a}}{\delta \langle \vec{E}^d \rangle} = g_0 f_{abc} \frac{\delta \Lambda^{bc}}{\delta \langle \vec{E}^d \rangle}. \quad (108)$$

Using Eq. (65), omitting color indices and kinematic factors we obtain

$$\chi^{\rightarrow a} = g_0 f \frac{\delta(\frac{1}{\epsilon})}{\delta \langle \vec{E}^a \rangle} \sim g_0 f \frac{1}{\epsilon} \frac{\delta \epsilon}{\delta \langle \vec{E}^a \rangle} \frac{1}{\epsilon}. \quad (109)$$

Equations (109) and (37) then yield

$$\epsilon = 1 + g_0 f \frac{1}{\epsilon} \frac{\delta \epsilon}{\delta \langle \vec{E}^a \rangle} \frac{1}{\epsilon}. \quad (110)$$

Equation (110) (with the inclusion of proper kinematic factors and color indices) is the Schwinger functional differential equation for the field dependent color dielectric constant  $\epsilon(\langle \vec{E}^a \rangle).$  Evaluated at  $\langle \vec{E}^a \rangle = 0$ , it expresses the zero field dielectric constant  $\epsilon$  in terms of  $\delta \epsilon / \delta \langle \vec{E}^a \rangle.$  Differentiating Eq. (110) with respect to  $\langle \vec{E}^a \rangle$  yields an expression for  $\delta \epsilon / \delta \langle \vec{E}^a \rangle$  in terms of  $\delta^2 \epsilon / \delta \langle \vec{E}^a \rangle \delta \langle \vec{E}^b \rangle$ , etc.

We seek a nonperturbative procedure to truncate these equations which satisfies the requirements of gauge invariance so as to preserve the correct long distance properties of the theory. Gauge invariance requires that the color dielectric tensor  $\Pi_{\mu\nu}$  is transverse (Eq. 84), and relates the longitudinal part of the triple gluon vertex  $\Gamma_{\mu\nu\lambda}$  to  $\Pi_{\mu\nu}.$  Since  $\Pi_{\mu\nu}$  determines  $\epsilon$ , and  $\Gamma_{\mu\nu\lambda}$  is related to  $\delta \epsilon / \delta \langle \vec{E}^a \rangle$ , Eq. (85) is essentially a relation between  $\delta \epsilon / \delta \langle \vec{E}^a \rangle$  and  $\epsilon$ , which does not of course uniquely determine  $\delta \epsilon / \delta \langle \vec{E}^a \rangle.$  However in the first stage of our approximation procedure we choose a particular solution of Eq. (85) which expresses

\* The first term in Eq. (38) is trivial and furthermore does not contribute to Eq. (68) for  $\chi^{ab}$ , since we will eventually set  $\langle \vec{A}^a \rangle = 0.$

$\delta\varepsilon/\delta\langle\hat{A}^a\rangle$  in terms of  $\varepsilon$ . Equation (110) then becomes a closed nonlinear integral equation for  $\varepsilon$ . We then find a selfconsistent solution of this equation in which  $\varepsilon(q) \rightarrow q^2$  as  $q^2 \rightarrow 0$ .

Let us now carry out the procedure indicated above. We define the vacuum polarization tensor  $\hat{\Pi}_{\mu\nu}$  as

$$\hat{\Pi}_{\mu\nu} = -[(q^2 g_{\mu\nu} - q_\mu q_\nu) - \hat{\Pi}_{\mu\nu}]. \quad (111)$$

Equation (111) is just the tensor generalization of Eq. (67). If  $\varepsilon = 1$ , then Eqs. (111) and (89) give  $\hat{\Pi}_{\mu\nu} = 0$ , and hence  $\hat{\Pi}_{\mu\nu}$  is the tensor analog of the color susceptibility  $\chi$ . Using the definition (80) of  $\Pi_{\mu\nu}$  and the field equation (76) to determine  $J_\mu^a(\langle\hat{A}^a\rangle)$ , we find the following expression for  $\hat{\Pi}_{\mu\nu}$  which is the analog of Eq. (109) for  $\chi$ :

$$\begin{aligned} \hat{\Pi}_{\mu\nu}^{ab}(q) = & \quad (112) \\ \frac{g_0^2}{2} \int \frac{dp}{(2\pi)^4} \Gamma_{\mu\lambda\sigma}^{(0)adc}(-q, -p, -r) \Delta_{\lambda\lambda'}^{dd'}(p) \Delta_{\sigma\sigma'}^{cc'}(r) \Gamma_{\nu\lambda'}^{bd'c'}(q, p, r) \end{aligned}$$

where  $r = - (p + q)$  and

$$\Gamma_{\mu\lambda\sigma}^{(0)adc}(q, p, r) \equiv f_{adc}[(q-p)_\sigma g_{\lambda\mu} + (p-r)_\mu g_{\lambda\sigma} + (r-q)_\lambda g_{\mu\sigma}]. \quad (113)$$

The momentum factors in Eq. (113) arise from the derivatives in Eq. (76) relating  $J_\mu^a$  to  $\langle\hat{A}^a\rangle$ .

The gluon propagator  $\Delta_{\mu\nu}^{ab}(p)$  and the triple gluon vertex  $\Gamma_{\nu\lambda}^{bd'c'}(q, p, r)$  are the Fourier transforms of the corresponding coordinate space quantities defined by Eqs. (38) and (81) respectively.  $p$ ,  $q$ , and  $r$  are the momenta entering the vertex  $\Gamma$ . The gauge condition  $n^\mu A_\mu = 0$  implies

$$n^\mu \Delta_{\mu\nu}^{ab} = 0 \quad (114)$$

which means  $\Delta_{\mu\nu}^{ab} = 0$  unless both  $\mu = i$  and  $\nu = j$ . Its spatial components  $\Delta_{ij}^{ab}$  are determined by Eq. (38).

Equation (112) is represented graphically in Fig. (11)\* and is derived in Appendix A of Ref. [6]. We briefly indicate the argument. The only relation not already presented in the lectures

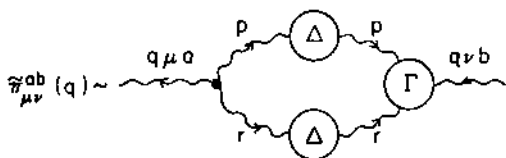


Fig. 11. Graph representing the vacuum polarization tensor  $\Pi_{\mu\nu}^{ab}(q)$  in Yang-Mills theory.

which is needed to complete the derivation is the following:

$$\Delta_{\mu\nu}^{ab}(x, y) = \frac{\delta \langle A_\mu^a(x) \rangle}{\delta J_\nu^b(y)} . \quad (115)$$

That is, the propagator is the change in the potential at  $x$  due to a change in the current at  $y$ . Alternatively  $\Delta_{ij}^{ab}(x, y)$  can be defined by Eq. (115). Then Eq. (38), relating  $\Delta_{ij}^{ab}(x, y)$  to the correlations of the vacuum fluctuations of  $A_i^a(x)$ , can be derived. Comparing Eqs. (115) and Eq. (80) we see that  $\Pi_{\mu\nu}^{ab}(x, y)$  is essentially the inverse of  $\Delta_{\mu\nu}^{ab}(x, y)$ . The precise relation is<sup>6,13</sup>

$$\Pi_{\mu\lambda}^{ab}(q) \Delta_{\lambda\nu}^{bc}(q) = \delta^{ac} [g_{\mu\nu} - \frac{n_\mu q_\nu}{(n \cdot q)}] . \quad (116)$$

\*There is another contribution to  $\Pi_{\mu\nu}$  which involves the quadruple gluon vertex  $\Gamma_4$ . However it does not contribute to  $\Pi_{0\nu}^{ab} \equiv n_\nu \Pi_{\mu\nu}^{ab}$  which involves only the fluctuations in the charge density operator ( $\Pi_{0\nu}^{ab} = \delta J_0^a / \delta \langle A_\nu^b \rangle$ ). Since  $\Pi_{\mu\nu}$  has the structure, Eq. (89), we will only need the equation for  $\Pi_{0\nu}^{ab}$  in order to determine  $Z^{-1}$ . Having determined  $Z^{-1}$  from the equation for  $\Pi_{0\nu}^{ab}$ , we can calculate  $\Pi_{\mu\nu}^{ab}$  from Eq. (112) and then  $\Pi_{i\nu}^{ab}$  from Eq. (111). We find, for  $q_0 = 0, q \rightarrow 0$ , consistency with the value of  $\Pi_{i\nu}^{ab}$  obtained from Eq. (89), i.e., with the ansatz that the color dielectric tensor  $\Pi_{\mu\nu}^{ab}$  does not depend upon the gauge vector  $n_\mu$ . We can thus apply our results to calculate the long range static forces. This will be carried out in the last section.

The additional term on the right hand side of Eq. (116) makes it consistent with Eqs. (88) and (114). Equations (116) and (89) then yield the following expression for the propagator:

$$\Delta_{\mu\nu}^{ab}(q) = \delta_{ab} Z(q) \Delta_{\mu\nu}^0(q) \quad (117)$$

where

$$\Delta_{\mu\nu}^0(q) = \frac{-1}{q^2} [g_{\mu\nu} - \frac{(n_\mu q_\nu + q_\mu n_\nu)}{(n \cdot q)} + \frac{n^2 q_\mu q_\nu}{(n \cdot q)^2}]. \quad (118)$$

Recalling that  $Z = \varepsilon^{-1}$ , Eqs. (117) and (118) yield  $\Delta_{\mu\nu}^{ab} \sim 1/\varepsilon q^2$  aside from kinematic factors. Furthermore, since  $\Gamma$  is related to  $\delta\varepsilon/\delta\langle\hat{A}^a\rangle$ , Eq. (112) for  $\hat{\Pi}$  then has the same structure as Eq. (109) for the color susceptibility.

Combining Eqs. (89) and (111), we write the Schwinger-Dyson equation in the form

$$(Z^{-1}(q) - 1)(q^2 g_{\mu\nu} - q_\mu q_\nu) \delta^{ab} = \hat{\Pi}_{\mu\nu}^{ab}(q) \quad (119)$$

where  $\hat{\Pi}_{\mu\nu}^{ab}(q)$  is expressed in terms of  $Z(p)$ ,  $Z(r)$  and  $\Gamma$  via Eq. (112) (Fig. 11). (Equation (119) is of the form of Eq. (119) with the replacement  $Z^{-1}(q) = \varepsilon(q)$  (Eq. (96)). The vertex  $\Gamma$  is related to  $\Pi_{\mu\nu}$  via the Fourier Transform of the Slavnov-Taylor identity Eq. (85) which is

$$i q_\mu \Gamma_{\mu\lambda\nu}^{abc}(q, p, r) = f_{abc} [\Pi_{\lambda\nu}(r) - \Pi_{\lambda\nu}(p)]. \quad (120)$$

The relation between the Slavnov-Taylor identities and the Schwinger-Dyson equation is the following:

Any triple gluon vertex  $\Gamma_{\mu\lambda\nu}^{abc}(q, p, r)$  satisfying Eq. (120) yields a vacuum polarization tensor  $\hat{\Pi}_{\mu\nu}^{ab}$  via Eq. (112), (Fig. 11) which is transverse, i.e.,

$$q^\mu \hat{\Pi}_{\mu\nu}^{ab}(q) = 0,$$

or equivalently from Eq. (111)  $\Pi_{\mu\nu}^{ab}(q)$  satisfies its Slavnov-Taylor identity Eq. (88).

This statement, which is straightforward to prove<sup>6</sup>, tells us that in order to be consistent with gauge invariance we must use vertices  $T$  in the Schwinger-Dyson expression for  $\hat{\Pi}_{\mu\nu}^{ab}$  which are exact solutions of the Slavnov-Taylor identity Eq. (120). An

analogous result holds for the Schwinger-Dyson equation for  $\Gamma$ , obtained by differentiating Eq. (112) with respect to  $\langle \hat{A}^a \rangle$ . This equation involves the quadruple gluon vertex  $\Gamma_4$ . The longitudinal part of  $\Gamma_4$  is expressed in terms of  $\Gamma$  by the Slavnov-Taylor identity obtained by differentiating Eq. (83) with respect to  $\langle \hat{A}^a \rangle$ . We can show that any vertex  $\Gamma_4$  satisfying this Slavnov-Taylor identity, when used in the Schwinger-Dyson equation for  $\Gamma$ , yields a triple gluon vertex  $\Gamma$  which satisfies Eq. (120). More generally, the Schwinger-Dyson equation for  $\Gamma_n$ , the  $n$  gluon vertex, involves  $\Gamma_{n+1}$ . The Slavnov-Taylor identity relates the longitudinal part of  $\Gamma_{n+1}$  back to  $\Gamma_n$ . Then, if any vertex  $\Gamma_{n+1}$  satisfying this Slavnov-Taylor identity is used in the Schwinger-Dyson equation for  $\Gamma_n$ , this expression for  $\Gamma_n$  automatically satisfies its Slavnov-Taylor identity.

These results provide a natural non-perturbative systematic approximation procedure to truncate the Schwinger-Dyson equations such that at each stage the requirements of gauge invariance are exactly satisfied. In the first stage we study the Schwinger-Dyson equation for  $\Pi_{\mu\nu}$  using a vertex  $\Gamma$  which is an exact solution of Eq. (120). Inserting the expression for  $\Pi_{\mu\nu}(q)$  given by Eq. (89) into the right hand side of Eq. (120), we can show that the most general solution of this equation for  $\Gamma$  which satisfies Bose Symmetry and is free of kinematic singularities has the following form<sup>15</sup>:

$$\Gamma_{\lambda\mu\nu}^{abc}(p, q, r) = \Gamma_{\lambda\mu\nu}^{(L)abc}(p, q, r) + \Gamma_{\lambda\mu\nu}^{(T)abc}(p, q, r) \quad (121)$$

where

$$\Gamma_{\lambda\mu\nu}^{(L)abc}(p, q, r) = f_{abc} \{ g_{\lambda\mu} [z^{-1}(p)p_\nu - z^{-1}(q)q_\nu] \quad (122)$$

$$- \frac{[z^{-1}(p) - z^{-1}(q)]}{p^2 - q^2} [p \cdot q g_{\lambda\mu} - q_\lambda p_\mu] (p - q)_\nu \}$$

$$+ \text{cyclic permutations of } (p, \lambda, a)(q, \mu, b)(r, \nu, c)$$

and

$$\begin{aligned} \Gamma_{\lambda\mu\nu}^{(T)abc}(p, q, r) = & f^{abc} \{ F(p^2, q^2, r^2) [p \cdot q g_{\lambda\mu} - p_\mu q_\lambda] [p_\nu r \cdot q - q_\nu r \cdot p] \\ & + G(p^2, q^2, r^2) [g_{\lambda\mu} (p_\nu q \cdot r - q_\nu p \cdot r) + \frac{(r_\lambda p_\mu q_\nu - q_\lambda p_\nu r_\mu)}{3}] \} \end{aligned}$$

$$+ \text{cyclic permutations.} \quad (123)$$

$F$  and  $G$  are undetermined functions which are free of kinematic singularities and which have the following symmetry properties:

$$F(p^2, q^2, r^2) = F(q^2, p^2, r^2).$$

$$G(p^2, q^2, r^2) = G(q^2, p^2, r^2) = G(q^2, r^2, p^2) = G(r^2, q^2, p^2) \text{ etc.}$$

The longitudinal vertex  $\Gamma^{(L)}$  satisfies

$$q^\mu \Gamma_{\lambda\mu\nu}^{(L)abc}(p, q, r) = f_{abc} [\Pi_{\lambda\nu}(r) - \Pi_{\lambda\nu}(p)].$$

The transverse vertex  $\Gamma^{(T)}$  satisfies

$$q^\mu \Gamma_{\lambda\mu\nu}^{(T)abc}(p, q, r) = 0,$$

and vanishes linearly when any one of three momenta  $p$ ,  $q$ , or  $r$  approaches zero, since each term in Eq. (123) contains an explicit factor  $p \times q \times r$ . The low momentum structure of  $\Gamma$  is then determined explicitly in terms of  $Z^{-1}$  according to Eq. (122).

#### THE SCHWINGER-DYSON EQUATIONS IN THE PRESENCE OF LONG RANGE FORCES AND THE EXISTENCE OF A STATIC DIELECTRIC CONSTANT

In this section we note that the Schwinger-Dyson expression Eq. (112) for the vacuum polarization with  $\Gamma$  given by Eqs. (121), (122) and (123) is infrared finite even if  $Z(p) \rightarrow A/p^2$  as  $p^2 \rightarrow 0$ . This low  $p^2$  behavior of  $Z(p)$  corresponds to a confining color dielectric constant  $\epsilon(q^2) \rightarrow q^2/A$  as  $q^2 \rightarrow 0$ . It introduces a potential  $\int dp/(p^2)^2$  singularity in Eq. (112) for  $\tilde{\Pi}$ , since under such circumstances  $\Delta_{\lambda\lambda}^{dd}(p) \sim 1/(p^2)^2$  as  $p \rightarrow 0$  (see Eq. (118)). However, this potential infrared divergence is not present in Eq. (112) since the angular average of the temporal gauge gluon propagator can be shown to vanish, that is

$$\int d\Omega_p \Delta_{\lambda\lambda}^{dd}(p) = 0. \quad (124)$$

Equation (124) is a consequence of a particular spinor or structure of  $\Delta_{\mu\nu}^0(q)$ , Eq. (118).\* However in order to have a finite static dielectric constant  $\epsilon(q) \equiv Z^{-1}(q)$  the vacuum polarization tensor  $\tilde{\Pi}_{\mu\nu}(q)$  must also be infrared finite when  $q^0 = 0$ . Setting  $q^0 = 0$  introduces new potential infrared divergences in Eq. (112) since the

---

\*The  $1/n \cdot p$  singularities in  $\Delta_{\mu\nu}^0(p)$  were evaluated with a principal value prescription which corresponds to a further specification of the gauge.

propagator  $\Delta_{\text{GG}}^{\text{cc}}(r)$ , as well as  $\Delta_{\lambda\lambda}^{\text{dd}}(p)$ , then becomes singular at  $p^0 = 0$ , that is, with  $q^0 = 0$ ,  $-n \cdot r = n \cdot (p + q) = n \cdot p = p^0$ . The  $1/n \cdot r$  singularity in  $\Delta_{\text{GG}}^{\text{cc}}(r)$  then becomes a  $1/p^0$  singularity which multiplies the  $1/p^0$  singularity of  $\Delta_{\lambda\lambda}^{\text{dd}}(p)$  in Eq. (112). Equation (124) is then not applicable and there must be additional cancellations of these  $1/p^0$  singularities in Eq. (112) in order that

$$\tilde{\Pi}_{\mu\nu}(\vec{q}) \equiv \tilde{\Pi}_{\mu\nu}(q) \Big|_{q^0=0}$$

be finite. To see whether they occur we insert the explicit form Eqs. (121), (122) and (123) of the triple gluon vertex  $\Gamma_{\nu\lambda}^{\text{bd},\text{c}}(q,p,r)$  into Eq. (112) and set  $q^0 = 0$ .

We first note that the  $p \times q \times r$  kinematic factors appearing in each term in Eq. (123) for  $\Gamma^T$  compensate the additional  $1/p^0$  factors in Eq. (112) generated by setting  $n \cdot q = 0$  in  $\Delta_{\text{GG}}^{\text{cc}}(r)$ . Since the undetermined functions  $F$  and  $G$  have no kinematic singularities, the contribution of the transverse vertex  $\Gamma^T$  to the static dielectric constant  $\epsilon(\vec{q})$  is then finite even if  $\epsilon^{-1}(p) = Z(p) + 1/p^2$ , and  $\epsilon^{-1}(r) \rightarrow 1/r^2$  in Eq. (112). On the other hand, the longitudinal vertex  $\Gamma^L$  (Eq. (122)) does not contain kinematic factor which might make it vanish when one of the momentum vanishes. The individual terms of Eq. (122) then yield infrared divergent contributions to Eq. (112) for  $\tilde{\Pi}_{\mu\nu}(\vec{q})$  and hence to  $\epsilon(\vec{q})$ . However, because of the detailed structure, Eq. (122), of  $\Gamma^L$ , imposed by gauge invariance, these divergences in Eq. (112) when  $\epsilon^{-1}(p) \sim 1/p^2$  cancel and  $\epsilon(\vec{q})$  is finite.

To summarize: The Schwinger-Dyson Eq. (112), when combined with the general solution Eq. (121), Eqs. (122) and (123) of the Slavnov-Taylor identity (120), yields an infrared finite expression for  $\epsilon(\vec{q})$  even if  $\epsilon^{-1}(p) \rightarrow 1/p^2$  as  $p^2 \rightarrow 0$ . That is, Eq. (112) yields a finite static color dielectric constant even in the presence of singular long range forces and a confining solution of the Schwinger-Dyson equations could exist.

#### INTEGRAL EQUATION FOR $\epsilon(q)$ AND ITS LOW MOMENTUM STRUCTURE

In the last section we pointed out that because of the extra  $p \times q \times r$  factor in Eq. (123) potential infrared divergent contributions to  $\tilde{\Pi}_{\mu\nu}^{\text{ab}}(\vec{q})$  came only from  $\Gamma^L$  and were insensitive to  $\Gamma^T$ . Assuming that  $\Gamma^T$  does not dominate the low  $q^2$  behavior of  $\tilde{\Pi}_{\mu\nu}^{\text{ab}}(q)$ , we omit  $\Gamma^T$  and set  $\Gamma = \Gamma^L$  in Eq. (112) for  $\tilde{\Pi}_{\mu\nu}^{\text{ab}}(q)$ .\* The vacuum polarization tensor  $\tilde{\Pi}_{\mu\nu}$  then depends only on  $Z^{-1} = \epsilon$  and Eq. (119) becomes a nonlinear integral equation for  $\epsilon(q)$  of the

following form:

$$\epsilon(q) \approx 1 + g_0^2 \int dp \frac{K(p, q)}{\epsilon(p)} + g_0^2 \epsilon(q) \int dp \frac{L(p, q)}{\epsilon(p) \epsilon(p + q)}. \quad (125)$$

The explicit forms of the kernels  $K$  and  $L$  can be written<sup>5,6</sup> using the expression (122) for  $\Gamma^{(L)}$  with  $Z^{-1} = \epsilon$ . The kernel  $K$  comes from the terms in  $\Gamma^{(L)}$ , Eq. (122), proportional to  $\epsilon(p)$  or  $\epsilon(r)$ , while the kernel  $L$  comes from the terms in Eq. (122) proportional to  $\epsilon(q)$ . In these lectures we will only make use of the fact that both  $K$  and  $L$  contain the factor  $(1/p^2)(1/(p + q)^2)$  arising from the product  $\Delta_{\lambda\lambda}^{dd}(p)\Delta_{\lambda\lambda}^{cc}(r)$  in Eq. (112). (See Eq. (118)). We have seen in the last section that the approximation  $\Gamma = \Gamma^{(L)}$  leading to Eq. (125) is consistent with current conservation (Eq. (88)) as well as with the existence of a static limit in the presence of singular long range forces. Equation (125) then preserves the low momentum properties of the theory and should be appropriate for determining the behavior of  $\epsilon(q)$  at small  $q^2$ .

We now try to determine what low momentum behavior of  $\epsilon(q)$  is compatible with Eq. (125). We will make various ansätze about the low momentum behavior of  $\epsilon^{-1}(p)$  to insert into the right hand side of Eq. (125). For each input  $\epsilon_{in}^{-1}(p)$  we will estimate the low  $q^2$  behavior of  $\epsilon_{out}(q)$ , the output obtained from the integration on the right hand side, and will then compare for consistency.\* The arguments will usually depend only on the dimensions and convergence properties of the resulting integrals.

Assume

a)  $\epsilon_{in}^{-1}(p) \xrightarrow[p^2 \rightarrow 0]{} \text{const.}$

Then the logarithmic singularity at  $q^2 = 0$  generated by the factor  $(1/p^2)(1/(p + q)^2)$  in  $K$  and  $L$  yields an output

\* At the next stage of our approximation procedure we would retain the full vertex  $\Gamma$  in Eq. (112) for  $\tilde{\Gamma}_{\mu\nu}(q)$  and approximate the quadruple vertex  $\Gamma_4$  appearing in the Schwinger-Dyson Equation for  $\Gamma$  by its longitudinal part. We would then be left with a nonlinear integral equation for  $\Gamma$  whose solution automatically satisfies the Slavnov-Taylor identity (120).

\*\* These arguments are similar to those used by Mandelstam<sup>16</sup> to study the low momentum behavior of an integral equation similar to Eq. (125) with  $L = 0$ .

$$\epsilon_{\text{out}}(q^2) \xrightarrow[q^2 \rightarrow 0]{} 1 + \text{const} \log q^2.$$

Similarly

$$b) \quad \epsilon_{\text{in}}^{-1}(p) \xrightarrow[p^2 \rightarrow 0]{} \log p^2,$$

gives

$$\epsilon_{\text{out}}(q) \xrightarrow[q^2 \rightarrow 0]{} 1 + \text{const}(\log q^2)^2.$$

$$c) \quad \epsilon_{\text{in}}^{-1}(p) \xrightarrow[p^2 \rightarrow 0]{} \frac{1}{\log p^2}$$

gives

$$\epsilon_{\text{out}}(q) \xrightarrow[q^2 \rightarrow 0]{} 1 + (\text{const}) \log(\log q^2).$$

All the above ansätze are clearly inconsistent; perhaps the infrared logarithms sum to a power. We try

$$d) \quad \epsilon_{\text{in}}^{-1}(p) \xrightarrow[p^2 \rightarrow 0]{} \left(\frac{M^2}{p^2}\right)^\alpha, \quad 0 < \alpha < 1.$$

The integrals in Eq. (125) are then all infrared finite and their low momentum behavior is determined by their dimension, i.e.,

$$\epsilon_{\text{out}}(q) \xrightarrow[q^2 \rightarrow 0]{} 1 + \text{const}(M^2/q^2)^\alpha.$$

Suppose

$$e) \quad \epsilon_{\text{in}}^{-1}(p) \xrightarrow[p^2 \rightarrow 0]{} M^2/p^2.$$

Then the integrals in Eq. (125) are still infrared finite because of Eq. (124). Hence

$$\epsilon_{\text{out}}(q) \xrightarrow[q^2 \rightarrow 0]{} 1 + C(M^2/q^2).$$

This output would lead to a gluon mass term which would violate gauge invariance. Hence  $C$  must vanish because of the gauge invariance of our approximation procedure Eq. (88). Note in example (d) a nonvanishing coefficient of the  $(M^2/q^2)^\alpha$  output is to be expected since it does not violate gauge invariance. This output then dominates the 1 and is inconsistent with the input just as in the first three examples.

Thus only the ansatz  $\epsilon$  could possibly be self-consistent. To obtain consistency the output  $\epsilon(q)$  must behave as  $q^2$  for small  $q^2$ , that is the 1 term in the equation for  $\epsilon(q)$  must be canceled by the contributions to  $\chi(q)$  generated by the corrections to the leading  $M^2/q^2$  behavior of  $\epsilon_{\text{in}}^{-1}(p)$ . We now consider various possibilities for these corrections.

Suppose

$$(f) \quad \epsilon_{\text{in}}^{-1}(p) \xrightarrow[p^2 \rightarrow 0]{} M^2/p^2 + \text{const.}$$

Then

$$\epsilon_{\text{out}}(q) \xrightarrow[q^2 \rightarrow 0]{} 1 + (\text{const}) \log q^2.$$

The  $\log q^2$  output is generated by the constant part of the input just as in case (a). Thus there can be no constant term in  $\epsilon_{\text{in}}^{-1}(p)$ .

Suppose

$$g) \quad \epsilon_{\text{in}}^{-1}(p) \xrightarrow[p^2 \rightarrow 0]{} A \left(\frac{M^2}{p^2}\right) + B \left(\frac{p^2}{M^2}\right)^\nu, \quad (126)$$

which for small  $q^2$  is equivalent to

$$\epsilon_{\text{in}}(q) = \frac{q^2}{AM^2} - \frac{B}{A^2} \left(\frac{q^2}{M^2}\right)^{\nu+1}. \quad (127)$$

The output generated from Eq. (126) by the right hand side of

Eq. (125) is of the form

$$\epsilon_{\text{out}}(q) = 1 + D_0(v) \left(\frac{q^2}{M^2}\right)^v + D_1 + D_2 \frac{q^2}{M^2}. \quad (128)$$

The term  $D_0(v)(q^2/M^2)^v$  in the output arises from the infrared region of integration in Eq. (125) and  $D_0(v)$  can be calculated analytically. For consistency the output Eq. (128) must match the input Eq. (127). Since there is no  $(q^2)^v$  term in Eq. (127) we must have

$$D_0(v) = 0, \quad (129)$$

from which we find  $v \approx .18$ . The term  $D_1 + D_2 q^2/M^2$  in Eq. (128) receives contributions from the entire range of the  $p$  integration and a numerical study<sup>7</sup> shows that a self-consistent choice of  $A$  and  $B$  in Eq. (126) can be found such that  $1 + D_1 = 0$ , and  $D_2 = 1/A$ .

Thus a simple analysis of the infrared consistency of Eq. (125) leads naturally to Eq. (126) with  $v \approx .18$ . All other simple ansätze that we have tried are inconsistent. The simple perturbation theory ansatz (a) for example led to the Landau Ghost. In our solution Eq. (126), the Landau Ghost has moved to  $q^2 = 0$  and consistency is restored. Thus the combination of the Schwinger-Dyson equations and Slavnov-Taylor identities upon which Eq. (125) is based led to a confining dielectric constant  $\epsilon(\vec{q}) \rightarrow \vec{q}^2/AM^2$  as  $\vec{q}^2 \rightarrow 0$ , where  $M^2$  is an arbitrary mass scale.

In order to solve Eq. (125) numerically for all  $q^2$ , it first has to be renormalized to account for the usual ultraviolet divergences.<sup>6</sup> We subtract Eq. (125) at an arbitrary point and rescale, writing

$$\epsilon_R(q) \equiv Z_3 \epsilon(q)$$

where  $Z_3$  is chosen such that

$$\epsilon_R(M) = 1.$$

The rescaled Eq. (125) for  $\epsilon_R(q)$  is then free from ultraviolet infinities when expressed in terms of an appropriate renormalized coupling constant  $g^2(M)$ .<sup>6</sup> We define the arbitrary scale  $M$  such that

$$g^2(M) = \frac{4\pi}{3}. \quad (130)$$

We use the renormalization group<sup>11</sup> to solve Eq. (125) for

large  $q^2$ , and find<sup>5,6</sup>

$$\epsilon_R^{-1}(q) \xrightarrow[q^2/M^2 \rightarrow \infty]{} \frac{\text{const}}{(\log q^2/M^2)^{11/16}} \quad (131)$$

Equation (131) of course differs from the known large  $q^2$  result of asymptotic freedom,<sup>12</sup> (Eq. (72) with  $N_q = 0$ )

$$\epsilon_R^{-1}(q) \rightarrow \frac{1}{b_{YM} \log q^2/\Lambda^2}, \quad (132)$$

where

$$b_{YM} \approx \frac{11}{16\pi^2}, \quad \Lambda^2 \approx (200 \text{ MeV})^2,$$

because our approximation procedure was adapted to the infrared region. However, it is reassuring that the difference is not drastic. The mass  $M^2$  defined by Eq. (130) can be related to  $\Lambda^2$ .<sup>7</sup> We find

$$M^2 \approx 65 \Lambda^2 \approx (10) \text{ GeV}^2. \quad (133)$$

A trial form for  $\epsilon_R^{-1}(q)$  which extrapolates between the known infrared and ultraviolet behavior is

$$\epsilon_R^{-1}(q) = \frac{AM^2}{-q^2} + \left( \frac{q^2}{q^2 + \mu_1^2} \right)^\nu F(q),$$

where

$$F(q) = \frac{1}{\left( 1 + \frac{16}{11} b_{YM} g^2(M) \log \frac{q^2 + \mu_2^2}{M^2 + \mu_2^2} \right)^{(11/16)}}. \quad (134)$$

The condition  $\epsilon_R^{-1}(M) = 1$  gives the relation,

$$1 - A = \left( \frac{M^2}{M^2 + \mu_1^2} \right)^\nu.$$

The trial form, Eq. (134) was inserted into the right hand side of Eq. (125) and the parameters,  $A$ ,  $\mu_2^2$  and  $\nu$  were determined to

optimize the consistency over the largest possible range of values of  $q^2$ . The best values were  $A \approx .21$ ,  $\mu_2^2 \approx .2M^2$ ,  $v = .18$ . The value of  $v$  agrees with that determined analytically from Eq. (129).\* Figure 12 shows  $\epsilon_R(q)$  vs  $-q^2/M^2$  over the range of the fit. The solid line is the input  $\epsilon_R(q)$ , Eq. (134) and the circles are the output  $\epsilon_R(q)$  calculated from the right-hand side of the integral equation (125).

We have thus found a self-consistent numerical solution to Eq. (125) which for small  $q^2$  has the behavior Eq. (126). The dielectric constant  $\epsilon(q)$  then has the long distance behavior:

$$\epsilon(q) \xrightarrow[q^2/M^2 \rightarrow 0]{} \frac{1}{A}(-q^2/M^2). \quad (135)$$

As pointed out after Eq. (129), the constant  $A$  in Eq. (135) receives contributions from the entire range of integration in Eq. (125).

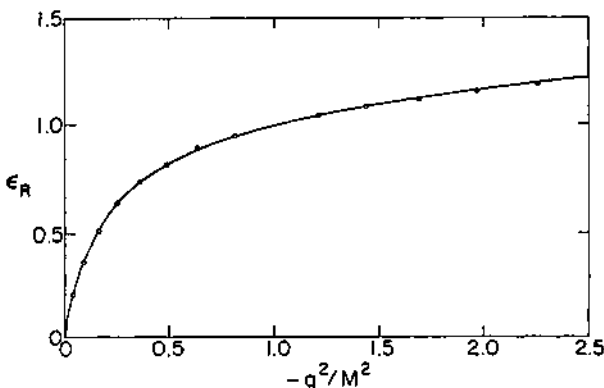


Fig. 12. The solution to the integral equation, Eq. (125), for  $\epsilon_R(q)$ . The solid curve is the input  $\epsilon_R(q)$  obtained from Eq. (134). The circles are the output  $\epsilon_R(q)$  calculated from the right-hand side of the integral equation.

\* The analytic calculation was carried out at  $q_0 = 0$ . This reflects again the consistency of the static limit.

Its value,  $A \approx .21$ , determined from our numerical solution of Eq. (125), might then change when we proceed to the second stage of our approximation procedure. However the form,  $\epsilon(q) \propto q^2$ , of the low momentum solution should be preserved at each stage of our approximation procedure and be a feature of the full theory. We now consider the implications of this result on the problem of confinement.

### THE ENERGY OF TWO STATIC POINT COLOR CHARGES

We have seen that the linear terms in the expansion of  $J_\mu^a$  in terms of  $\langle A_\mu^a(x) \rangle$  yielded Maxwell's equations (95), (102) in a dielectric medium with  $\epsilon(q) = 1/\nu(q)$ . The behavior of  $\epsilon(q)$  at small  $q^2$  was determined from a self-consistent solution of the Schwinger-Dyson equations describing the fluctuations of charges and currents in the vacuum of Yang-Mills theory. We now want to calculate the energy of two static point color charges, Eq. (35), embedded in this medium, when they are a long distance apart. We then replace  $\epsilon(q)$  by its low  $q^2$  limit, Eq. (135), for all  $q^2$ , i.e., we take

$$\epsilon(\vec{q}) = b \vec{q}^2 \quad (136)$$

where  $b = 1/AM^2$  is a length determined in terms of the measured QCD scale  $\Lambda^2$ . Using Eq. (133) and the value  $A \approx .21$  gives  $b \approx 1/2(\text{GeV})^2$ .

We must then solve the static problem

$$\begin{aligned} \vec{\nabla} \times \vec{E}^a(\vec{x}) &= 0 \\ \vec{\nabla} \cdot \vec{D}^a(\vec{x}) &= \rho^a(\vec{x}) \end{aligned} \quad (137)$$

where  $\rho$  is given by Eq. (135), and from Eq. (136)

$$\vec{D}^a(\vec{x}) = -b \vec{\nabla}^2 \vec{E}^a(\vec{x}). \quad (138)$$

In the usual way one can derive from Eq. (137) the expression for the field energy  $U$  produced by the color charge distribution  $\rho^a(\vec{x})$  as

$$U = \frac{1}{2} \int d\vec{x} \vec{E}^a(\vec{x}) \cdot \vec{D}^a(\vec{x}). \quad (139)$$

The solution of Eq. (137) can be expressed as a superposition

$$\begin{aligned}\vec{D}^a(\vec{x}) &= Q_1^a \vec{D}_1(\vec{x}) + Q_2^a \vec{D}_2(\vec{x}) \\ \vec{E}^a(\vec{x}) &= Q_1^a \vec{E}_1(\vec{x}) + Q_2^a \vec{E}_2(\vec{x}) ,\end{aligned}\tag{140}$$

where

$$\vec{v} \cdot \vec{D}_i(\vec{x}) \approx \rho_i(\vec{x}), \quad i = 1, 2$$

and

$$\vec{E}_1(\vec{x}) = -\frac{1}{b\vec{v}^2} \vec{D}_1(\vec{x}) . \tag{141}$$

We choose  $\vec{x}_1 = \vec{R}$  and  $\vec{x}_2 = -\vec{R}$  in Eq. (35). Then  $\rho_1(\vec{x}) = \delta(\vec{x} - \vec{R})$ ,  $\rho_2(\vec{x}) = \delta(\vec{x} + \vec{R})$ . The solution of Eq. (140) is clearly

$$\begin{aligned}\vec{D}_i(\vec{x}) &= -\vec{v} \frac{1}{4\pi r_i} , \\ \vec{E}_i(\vec{x}) &= \frac{1}{b\vec{v}^2} \vec{v} \frac{1}{4\pi r_i} = \frac{1}{b} \vec{v} \frac{r_i}{8\pi} ,\end{aligned}\tag{142}$$

with  $r_1 = |\vec{x} - \vec{R}|$ ,  $r_2 = |\vec{x} + \vec{R}|$ .

To obtain Eq. (142) we used the result

$$\vec{v}^2 r_i = \frac{2}{r_i} .$$

We fix the strengths of  $Q_i^a$  of the color charges,

$$(Q_i^a)^2 \equiv \sum_{a=1}^8 Q_i^a a^2$$

and take  $Q_1^2 = Q_2^2 \equiv Q^2$ . We choose  $Q_1^a$  to be along the direction 8, i.e.,  $Q_1^a = \delta^a_8 Q$ . Then it is easy to see that the energy  $U$ , Eq. (139), is minimized by taking  $Q_2^a = -\delta^a_8 Q$ , in which case Eqs. (139), (140), and (142) give

$$\begin{aligned}U &= \frac{1}{2} \int d\vec{x} (\vec{D}_1(\vec{x}) - \vec{D}_2(\vec{x})) \cdot (\vec{E}_1(\vec{x}) - \vec{E}_2(\vec{x})) \\ &= -\frac{Q^2}{64\pi^2 b} \int d\vec{x} \vec{v} \left( \frac{1}{r_1} - \frac{1}{r_2} \right) \cdot \vec{v} (r_1 - r_2) .\end{aligned}\tag{143}$$

The integral (143) converges both at small  $\vec{x}$  and large  $\vec{x}$ . By power counting it is clearly convergent at small  $\vec{x}$ . At large  $\vec{x}$ , ( $|\vec{x}| \gg R$ ), the dominant term in  $r_1 - r_2$  cancels and the integrand in Eq. (143), which then behaves as  $1/|\vec{x}|^4$ , is convergent.

We integrate Eq. (143) by parts. The surface terms at both large and small  $\vec{x}$  vanish and we obtain

$$\begin{aligned} U &= \frac{Q^2}{64\pi^2 b} \int d\vec{x} \vec{v}^2 \left( \frac{1}{r_1} - \frac{1}{r_2} \right) (r_1 - r_2) \\ &= -\frac{Q^2}{16\pi b} \int d\vec{x} [\delta(\vec{x} - \vec{R}) - \delta(\vec{x} + \vec{R})] (|\vec{x} - \vec{R}| - |\vec{x} + \vec{R}|) \\ &= \frac{Q^2}{16\pi b} \int d\vec{x} (\delta(\vec{x} - \vec{R}) |\vec{x} + \vec{R}| + \delta(\vec{x} + \vec{R}) |\vec{x} - \vec{R}|) = \frac{Q^2}{8\pi b} (2R). \end{aligned} \quad (144)$$

Thus the potential energy of a system of 2 point sources of opposite color charge increases linearly with the distance  $2R$  between the sources, and hence it is impossible to separate them with a finite amount of energy. The strength of this linearly rising potential,  $Q^2/8\pi b$ , is determined by the low  $q^2$  behavior of  $\epsilon(q)$ , Eq. (136), obtained from the Schwinger-Dyson equation for the dielectric constant. There is no ultraviolet self energy of the individual sources since we have used Eq. (136) for all  $q^2$ . Using the correct  $\epsilon(q)$  would produce additional terms in  $U$  but would not change its  $R$  dependence at large  $R$ .

The long range color electric field of course produces an infinite self energy  $U_1$  for a single source of strength  $Q$ . We have

$$U_1 = \frac{Q^2}{2} \int d\vec{x} \vec{D}_1(\vec{x}) \cdot \vec{E}_1(\vec{x}). \quad (145)$$

Using Eq. (142) and integrating Eq. (145) over  $|\vec{x}| < L$ , we obtain

$$\begin{aligned} U_1 &= -\frac{Q^2}{64\pi^2 b} \int d\vec{x} \vec{v} \cdot \left( \frac{1}{r_1} \right) \cdot \vec{v} r_1 \\ &= -\frac{Q^2}{64\pi^2 b} \int d\vec{x} [r_1 (-\nabla^2 \frac{1}{r_1}) + \vec{v} \cdot (r_1 \vec{v} \frac{1}{r_1})] = (\frac{Q^2}{16\pi b}) L \xrightarrow{L \rightarrow \infty} \infty. \end{aligned} \quad (146)$$

This infinity cancels when the field of two oppositely charged

sources are added and a finite energy proportional to their distance, Eq. (144), remains. Equations (144) and (146) are two basic aspects of confinement.

However the field configuration,  $\vec{E}(\vec{x}) \equiv \vec{E}_1(\vec{x}) - \vec{E}_2(\vec{x})$  produces a tube of flux between the two sources which is not limited in the transverse direction. At large distances the color electric field  $\vec{E}(\vec{x})$  behaves like  $1/r^2$ , which could give rise to long range forces between color singlets (hadrons). A suppression of this long range field could result from the nonlinear corrections to Maxwell's equations due to the field dependence of the dielectric constant, represented by the vertex  $\Gamma$ , (Eq. (81)), determining the quadratic term in Eq. (79).

An explicit expression for the low momentum behavior of the quadratic terms in Eq. 79 results from the replacement of  $\Gamma$  by  $\Gamma^L$ , Eq. (122) with  $Z^{-1} = \epsilon = -bq^2$ . Similarly, at low momentum the cubic terms in Eq. (79) can be obtained by using the solution of the Slavnov-Taylor identity relating  $\Gamma_4$  to  $\Gamma$ .<sup>17</sup> Continuing in this manner we can find the complete low momentum expansion for  $J_\nu^b(\langle A_\mu^a \rangle)$ . The final result can be obtained more directly by the following observation:

We have seen that the linear term in Eq. (79) gives Maxwell's equations, Eqs. (95) and (102). These equations with  $\epsilon = b(\partial/\partial x^\sigma)(\partial/\partial x_\sigma)$  can be derived from the following Lagrangian:

$$\mathcal{L}^{(2)}(\langle A_\mu^a \rangle) \equiv -\frac{1}{4} F^{\mu\nu,a} (b \frac{\partial}{\partial x^\sigma} \frac{\partial}{\partial x_\sigma}) F_{\mu\nu}^a. \quad (147)$$

$\mathcal{L}^{(2)}(\langle A_\mu^a \rangle)$  is obtained by introducing the factor  $b(\partial/\partial x^\sigma)(\partial/\partial x_\sigma)$  in the Lagrangian, Eq. (16), of electromagnetism. In Eq. (147)  $F_{\mu\nu}^a$  is given by the Maxwell expression, Eq. (16), with  $A_\mu$  replaced by  $\langle A_\mu^a \rangle$ .

The complete low momentum expansion of Eq. (79) can then be derived from a Lagrangian  $\mathcal{L}(\langle A_\mu^a \rangle)$  which is obtained from  $\mathcal{L}^{(2)}(\langle A_\mu^a \rangle)$ , Eq. (147), as follows:

- Define  $F^{\mu\nu,a}$  in Eq. (147) by the Yang-Mills expression, Eq. (24), with  $A_\mu^a \rightarrow \langle A_\mu^a \rangle$ .
- Make the following replacement in Eq. (147):

$$\frac{\partial}{\partial x_\sigma} \rightarrow D_\sigma^{ab} \quad \text{where } D_\sigma^{ab} \text{ is given by Eq. (32).}$$

The rules (i) and (ii) yield a Lagrangian  $\mathcal{L}(\langle A_\mu^a \rangle)$  which is clearly invariant under the gauge transformation Eq. (22). It thus gives rise to a current

$$J_\nu^b(x) = J_\nu^b(\langle A_\mu^a \rangle) \equiv \frac{\delta \mathcal{L}(\langle A_\mu^a \rangle)}{\delta \langle A_\nu^b(x) \rangle} \quad (148)$$

which is covariantly conserved; Eqs. (33) and (89). Hence the expression (148) must agree with the expansion (79) when  $\epsilon = -bq^2$ . In particular since  $\mathcal{L}(\langle A_\mu^a \rangle)$  is of order  $(\langle A_\mu^a \rangle)^6$  and hence  $J_\nu^b(\langle A_\mu^a \rangle)$  is of order  $(\langle A_\mu^a \rangle)^5$ , all terms in the low momentum expansion of Eq. (79) beyond  $(\langle A_\mu^a \rangle)^5$  must vanish when  $\epsilon = -bq^2$ .

Equation (148) then yields a set of nonlinear differential equations for  $\langle A_\mu^a(x) \rangle$  which describes the low momentum behavior of exact Yang-Mills theory. These equations have the form of classical Yang-Mills equations in a dielectric medium where  $\epsilon = b\overrightarrow{q}^2$ , with additional currents determined from the conservation equation, (79). (The quantum fluctuations are accounted for by our self-consistent low momentum solution for  $\epsilon(q)$ .) We are now studying these nonlinear differential equations to see how the nonlinear effects modify the field configurations Eq. (140), obtained in the linear approximation.

## SUMMARY

We have shown that the zero field static color dielectric constant  $\epsilon(\vec{q})$  vanishes like  $\vec{q}^2$  as  $\vec{q}^2$  approaches zero. This is a consequence of self-consistency in the presence of antiscreening imposed by the Schwinger-Dyson equation and Slavnov-Taylor identities for  $\epsilon$ . This color dielectric constant when inserted into Maxwell's equations, yields an infinite long distance self-energy for a single colored source, and gives rise to an energy for two colored sources of opposite charge, which increases linearly with their distance of separation.

I would like to thank my collaborators, J.S. Ball and F. Zachariasen, for their invaluable help in making these lectures possible. I would also like to thank D. Gross and L. McLerran for useful conversations, and W. Greiner and the organizers of this school for their hospitality and encouragement.

## REFERENCES

1. M. Gell-Mann, Phys. Lett. 8 (1964) 214, G. Zweig, CERN Report Nos. TH401, 412, (1964). Unpublished.
2. O.W. Greenberg, Phys. Rev. Lett. 13 (1964) 598.

3. C.N. Yang and R.L. Mills, Phys. Rev. 96 (1954) 191.
4. L.S. Faddeev and V.N. Popov, Phys. Lett. 25B (1967) 29.
5. R. Anishetty, M. Baker, J.S. Ball, S.K. Kim, and F. Zachariasen, Phys. Lett. 86B (1979) 52; M. Baker, J.S. Ball, P. Lucht, and F. Zachariasen, Phys. Lett. 89B (1980) 211; J.S. Ball and F. Zachariasen, Phys. Lett. 95B (1980) 273; M. Baker, Acta Physica Polonica, D12 (1981) 3.
6. M. Baker, J.S. Ball, and F. Zachariasen, CALT-68-807, November, 1980.
7. M. Baker, J.S. Ball, and F. Zachariasen, CALT-68-808, November, 1980.
8. L. Landau on "The Quantum Theory of Fields" in Niels Bohr and the Development of Physics (ed. W. Pauli) Pergamon Press (London, 1955) p. 52.
9. K. Johnson, R. Wiley, and M. Baker, Phys. Rev. 163 (1967) 1699.
10. J. Rosner, Phys. Rev. Lett. 17 (1966) 1190.
11. M. Gell-Mann and F.E. Low, Phys. Rev. 95 (1954) 1300; M. Baker and K. Johnson, Phys. Rev. 183 (1969) 1292; S.L. Adler, Phys. Rev. D5 (1972) 3021.
12. D. Gross and F. Wilczek, Phys. Rev. Lett. 30 (1973) 1343; H.D. Politzer, Phys. Rev. Lett. 30 (1973) 1346.
13. A.A. Slavnov, Teor. Fiz. 10 (1972) [Theor. Math. Phys. 10 (1972) 99]; J.C. Taylor, Nucl. Phys. 10 (1971) 99.
14. W. Kummer, Acta Physica Austriaca, 41 (1975) 315.
15. S.K. Kim and M. Baker, Nucl. Phys. B164 (1980) 152.
16. S. Mandelstam, UCB-PTH-7918 (1979).
17. S.K. Kim, University of Washington Thesis 1979 (unpublished). See also M. Baker in High-Energy Physics in the Einstein Centennial Year (1979) (ed. B. Kursunoglu et al.) Plenum, N.Y. p. 247.

This work was supported in part by the U.S. Department of Energy.

## PION CONDENSATION

J. Maxwell Irvine

Department of Theoretical Physics  
The University  
Manchester M13 9PL  
U.K.

### INTRODUCTION

I have been asked to talk about pion condensation and the relevance of this to an Institute on "Quantum Electrodynamics of Strong Fields" may not be immediately apparent. I presume that the idea was to stress the universality of the concept of symmetry breaking induced by supercritical fields whatever their nature.

I shall not attempt to provide a complete survey of the literature of pion condensation suffice to say that the idea was pioneered by Migdal (1973) and the early keynote papers were, for me, by Sawyer and Scalapino (1973), Baym and Flowers (1974), Campbell, Dashen and Manassah (1975). More recently the subject has been given an overview in the reviews by Migdal (1978) and Weise and Brown (1976). I shall concentrate on describing the physics of pion condensation and the consequences for astrophysics and nuclear physics. The specific calculational techniques involved are described in our publications Irvine (1975), Irvine and Rodgers (1977), Goodwin, Meinhart and Irvine (1980) and Irvine (1981).

To promote a common view of strong field phenomena let me begin by reproducing in figure 1 a diagram which has become synonymous with super strong QED. Note that instead of labeling the horizontal axis with an increasing charge strength  $Z$  I have deliberately used an arbitrary coupling constant  $g$  to an undefined corresponding field  $F$ . The critical field is of course

$$F_{\text{crit}} = \frac{2mc^2}{g} \quad (1)$$

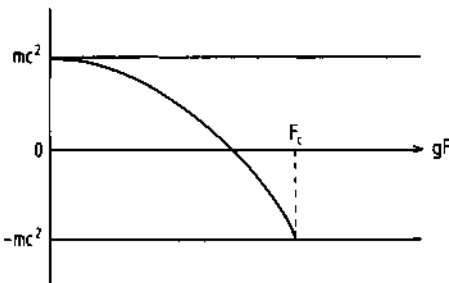


Fig. 1. The Dirac spectrum of a single-particle coupled to a scalar field  $F$  with a coupling constant  $g$ .

Note that the critical field depends on the ratio of the mass to the coupling constant. In principle spontaneous production of particles could begin at smaller fields when the self-energy of the particle becomes zero. If the particles carry any conserved quantum number then a super symmetry will prevent their production, this is the case for all fermions. Because of the mass in equation (1) the first critical field depends on the mass of the lightest particle which couples to it and hence the discussions of spontaneous  $e^+e^-$  pairs in supercritical QED.

An alternative view of figure 1 would be to consider a fixed charge  $Ze$  and ask at what distance from it does the field become critical. It is

$$R_{\text{QED}} = \frac{1}{2} \frac{Ze}{c^2} \left( \frac{e}{m_e} \right) \quad (2)$$

and of course depends on the charge to mass ratio. Had we instead considered a point mass  $M$  then the critical field is reached at the Schwarzschild radius

$$R_G = 2 \frac{M}{c^2} \quad (3)$$

and we see that in the case of the gravitational field the critical field is independent of the probing mass. The translation of the factor  $\frac{1}{2}$  in eqtn. (2) to the factor 2 in eqtn. (8) is due to general relativistic corrections to Newtonian gravitational theory.

The two 'classical' fields of electromagnetism and gravitation differ from nuclear fields in that they are propagated by massless bosons and hence are of long range. It is then possible to consider critical field strengths far removed from the source of the field and thus to discuss 'vacuum' polarization. Nuclear forces on the other hand are short ranged and critical field strengths occur only within the source material. Thus it is not the 'vacuum' which is strictly relevant. We are more interested in the excitations of the 'normal' ground state of a many-body system than the polarization of the vacuum.

In the Dirac picture of figure 1 the inverse mass in eqtn. (2) is simply the density of states at the Fermi surface. The larger the mass the smaller the density of states and the more stable the vacuum. In the many-body system the charge to mass ratio of eqtn. (2) translates into the product of the coupling constant and the density of states at the Fermi surface. A particularly low density of states at the Fermi surface implies exceptional stability of the 'normal' ground state as in the case of inert gas atoms, magic number nuclei and solid state insulators.

In the case of critical coulombic or gravitational fields we envisaged achieving the necessary field strengths by cranking up remote sources of charge Z or mass M. In the nuclear case the analogue is to increase the density either by compressing the nuclear material in enormous gravitational fields in neutron stars or by generating high density shock waves in heavy ion collisions. In the coulombic case the critical field strength could be obtained either by cranking up the external source strength or increasing the density of states (decreasing the probe mass). In the nuclear case these processes are strongly coupled since the density of states is a function of the number density of nucleons.

In nuclear physics we have long been aware of phase transitions associated with increasing the density of states. In figure 2 we present for the even isotopes of samarium the energy levels of the first  $J^\pi = 2^+$  and  $4^+$  states.  $^{144}\text{Sm}$  contains a closed shell of 82 neutrons and its high stability is illustrated by the high excitation energy of the first  $2^+$  state. The isotopes  $^{146}\text{Sm}$ ,  $^{148}\text{Sm}$  and  $^{150}\text{Sm}$  have in common that the energy of the  $4^+$  state is approximately twice the excitation energy of the  $2^+$  state which is characteristic of quadrupole vibrations of the spherical ground state. The steady fall in the energy of the  $2^+$  state (the one quadrupole phonon state) indicates the 'softening' of the normal ground state as the density of states increases. If that sequence was to continue

eventually the  $2^+$  state would become degenerate with the  $0^+$  normal ground state. The physical ground state would then be a linear combination of a  $J = 0$  and a  $J = 2$  state and thus not having good angular momentum would no longer be spherical. In an ensemble average of microscopic states we have to average over orientations of the intrinsic deformation to recapture states of good angular momentum. The low lying spectra is now that of the collective rotation of an intrinsically deformed nucleus with

$$E_J = \frac{\hbar^2}{2I} J(J + 1) \quad (4)$$

where  $I$  is the effective moment of inertia, as indicated in isotopes  $^{154}\text{Sm}$ ,  $^{156}\text{Sm}$  and  $^{158}\text{Sm}$ . The point of this example is that it clearly illustrates that the loss of symmetry during a phase transition is associated with the quantum numbers of the Goldstone bosons. In the case of the gravitational field, since the critical field is independent of the mass of the boson, all bosons simultaneously become soft and this is the origin of the assertion that "black-holes have no hair".

#### PION CONDENSATION

Turning now to the pionic spectrum in nucleon matter, our first

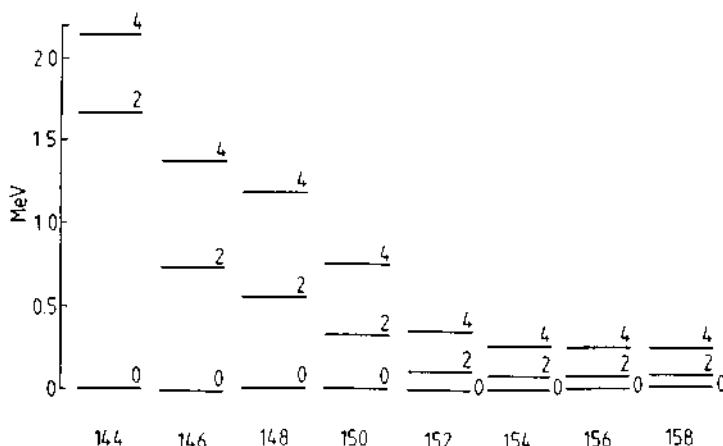


Fig. 2. The energy levels of the first excited  $J^\pi = 2^+$  and  $J^\pi = 4^+$  states in the samarium -144 to 158 isotopes.

problem is that unlike electromagnetism or gravitation, there is no accepted underlying field theory. Quantum chromodynamics (QCD) is a possible gauge theory of the strong interactions but its non abelian nature means that it is extremely unlikely that QCD will ever provide a workable description of pionic physics. The reason for this is immediately obvious in figure 3 where we schematically indicate the quark-quark interaction. In region 1  $V_{qq} \sim 1/r$  consistent with asymptotic freedom, in region 2 common assumptions are that  $V_{qq} \sim r$  or  $r^2$  the force is still weak and perturbation theory is applicable. The force diverges in region 3 where we approach the "bag" radius. The degree of divergence depends on the level of quark "confinement". The bag radius is  $\sim 0.8\text{fm}$  for nucleons. In region 3 perturbation theory does not work. The Compton wavelength of the pion is  $\lambda_\tau \approx 1.4\text{fm}$  and hence encompasses region 3. On the other hand, the next lightest hadron is the kaon with a Compton wavelength  $\lambda_K \approx 0.4\text{fm}$  which is safely within the perturbation regime. The result is that elementary QCD calculations do extremely well in reproducing hadron spectroscopy with the notable exception of the mass of the pion which is always over estimated by a factor two.

The absence of an underlying gauge field theory means that at best any relativistic field theory treatment must be of a phenomenological nature. Luckily we have a long history of pion phenomenology.

The dominant  $\pi$ -N interaction is an attractive p-wave

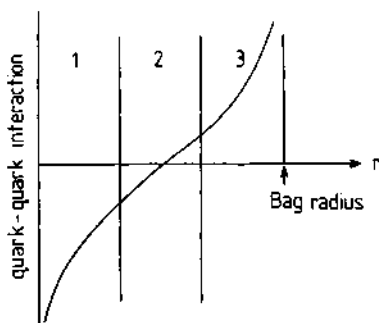


Fig. 3. The  $q$ - $q$  interaction.

force which, ignoring isospin, has the non-relativistic form

$$V_{\pi N} = -g_{\pi N} \sigma_N \cdot \underline{k}_\pi \quad (5)$$

where  $\sigma_N$  is the nucleon spin and  $\underline{k}_\pi$  is the pion momentum. Hence the non-relativistic pion dispersion relation is

$$\epsilon_\pi(\underline{k}) = m_\pi c^2 + \frac{1}{2} k_\pi^2 - \sum_N g_{\pi N} \sigma_N \cdot \underline{k}_\pi \quad (6)$$

If the nucleon spins are randomly orientated then the last term in eqtn. (6) is zero. If the nuclear spins are ordered then the self-energy of the pion will be considerably reduced. Since the pions are bosons, they will tend to condense into the lowest energy momentum state given by

$$\frac{\partial \epsilon}{\partial \underline{k}_\pi} = 0 \quad (7)$$

which because of the linear momentum term in eqtn. (6) is not  $\underline{k}_\pi = 0$ .

Since the pions condense to macroscopically populate a single momentum eigenstate we may replace relativistic pionic field operators  $\pi(\underline{r}, t)$  by their quantum field expectation values

$$\pi(\underline{r}, t) \rightarrow \langle \pi(\underline{r}, t) \rangle = A_\pi(t) e^{i \underline{k}_\pi \cdot \underline{r}} \quad (8)$$

The value of the pionic amplitude  $A_\pi(t)$  may be obtained by minimisation of the field theory Hamiltonian  $H(\pi, P_\pi)$  where the conjugate field operators  $P_\pi$  are defined by the corresponding Lagrangian density  $\mathcal{L}$

$$P_\pi = \frac{\delta \mathcal{L}}{\delta \pi} \quad (9)$$

Now we must introduce isospin. The pion exists in three possible electric charge states conveniently expressed in a three component isospin vector notation  $\underline{\pi}$ . Since electric charge is conserved, we must introduce an associated chemical potential  $\mu_\pi$  so that the variational calculation becomes

$$\delta \langle H - \mu_\pi \rho_\pi \rangle = 0 \quad (10)$$

where  $\rho_\pi$  is the pionic charge density

$$\rho_\pi = i(\underline{\pi}^\dagger \cdot P_\pi - P_\pi^\dagger \cdot \underline{\pi}) \quad (11)$$

Hamilton's equations

$$\begin{aligned}\langle \delta^H / \delta \underline{P}_\pi^\dagger \rangle &= \langle \dot{\underline{\pi}} \rangle \\ \langle \delta^H / \delta \underline{\pi}^\dagger \rangle &= -\langle \dot{\underline{P}}_\pi \rangle\end{aligned}\quad (12)$$

then yield

$$\begin{aligned}\langle \dot{\underline{\pi}}(r, t) \rangle &= -i\mu_\pi \langle \underline{\pi}(r, t) \rangle \\ \langle \dot{\underline{P}}_\pi(r, t) \rangle &= -i\mu_\pi \langle \underline{P}_\pi(r, t) \rangle\end{aligned}\quad (13)$$

Since there is no conservation of pion number as opposed to electric charge we have

$$\mu_\pi^0 = 0, \quad \mu_\pi^- = \mu_\pi^+ = -\mu_\pi \quad (14)$$

and thus

$$\begin{aligned}\langle \underline{\pi}^\pm(r, t) \rangle &= A e^{\pm i(k_\pi \cdot r - \mu_\pi t)} \\ \langle \underline{\pi}^0(r, t) \rangle &= A_0 e^{i k_\pi \cdot r}\end{aligned}\quad (15)$$

We note a distinct difference between the three possible pionic condensates: (i) A neutral pion condensate is a standing wave with chemical potential zero, (ii) a charged pion condensate is a travelling wave. While the masses of free  $\pi^+$ 's and  $\pi^-$ 's are equal in general their self-energies in the condensed phase are quite different. Because of the existence of a preferred vector  $k_\pi$ , the condensate does not have good parity. This should not surprise us since pions carry a negative parity quantum number. The other symmetry lost on condensation is that of charge since pions also carry an isospin quantum number. In model calculations on pure neutron matter or pure nuclear matter the isotopic spin degree of freedom is usually not invoked and this distinction between the three possible condensate modes is artificially obscured. In calculations on beta stable matter charge symmetry is broken because the lightest fermion contained in the matter, the electron, carries negative charge. This means that  $\pi^-$  condensation is much more likely to be physically realised than either  $\pi^0$  or  $\pi^+$  condensation.

Normal beta stable matter is in thermal equilibrium with respect to

$$n \leftrightarrow p + e^- \quad (16)$$

Neutrinos are not explicitly indicated in eqtn. (16), it being assumed that any neutrinos will diffuse out of any finite distribution of matter in a time short compared with the relaxation time for the matter. While this is probably not true during super novae

collapse, it is certainly true for stable neutron stars or dense shock waves induced in heavy ion collisions. The equilibrium abundances of neutrons, protons and electrons is then governed by the requirement that

$$\mu_n - \mu_p = \mu_e , \quad (17)$$

the chemical potentials  $\mu$  being simply related to the Fermi energies by the inclusion of the corresponding rest mass. For charge neutral matter the electron and proton number densities are equal. Thus, at densities of the order of the nuclear saturation density  $\rho_0 \approx 0.17 \text{ Nfm}^{-3}$  or  $2.8 \times 10^{14} \text{ gm cm}^{-3}$ , the electron chemical potential is

$$\mu_e \approx 316 n_n^{2/3} \text{ MeV} \quad (18)$$

where  $n_n$  is the neutron number density in  $\text{fm}^{-3}$ . At  $n_n \approx 0.2 \text{ Nfm}^{-3}$   $\mu_e \approx 110 \text{ MeV}$ , i.e. the minimum energy required to maintain an electron in the system is greater than the rest mass of a muon,  $m_\mu c^2 = 105 \text{ MeV}$ . Hence the equilibrating reaction (16) is supplemented by



As the density increases there is a developing fermi sea of muons, the equilibrium condition (17) is extended to

$$\mu_n - \mu_p = \mu_e = \mu_\mu \quad (20)$$

According to eqtn. (18)  $\mu_e$  reaches the pion rest mass at a density  $\approx 1.6 \rho_0$ . At this point we would expect eqtns. (19) and (20) to become supplemented by



and

$$\mu_n - \mu_p = \mu_e = \mu_\mu = \mu_\pi \quad (22)$$

Thereafter the fact that the pion is a boson while the electron and muon are fermions makes an enormous difference, because as the density increases the fermi energies of the leptons rises sharply and they become energetically more and more expensive to maintain while the boson pions condense and hence become better and better value. At twice the nuclear saturation density electrons and muons are present in only negligible abundances and the role of cancelling the proton

charge density has evolved almost exclusively onto the pions. Indeed this process may well occur at even lower densities since the other difference between the pion and the leptons is that being a baryon the pion's effective mass may be substantially reduced through its interaction with the surrounding nucleons whereas the renormalization of the leptonic masses by weak and electromagnetic interactions is totally negligible.

#### NUCLEAR INTERACTIONS

By replacing the pion field operators by their expectation values [eqtn. (8)] we do not make any great error in our treatment of the condensate. However, we do eliminate all virtual pion effects, including the generation of any N-N interaction arising from the pion exchange. The effect of N-N interactions must therefore be "put in by hand". There are two principle effects of N-N interactions:

Nuclear matter is bound by  $\sim 16$  MeV per nucleon at nuclear saturation densities. Pure neutron matter at the same density is unbound by  $\sim 16$  MeV per nucleon. Thus the symmetrisation of nucleon matter by a  $\pi^-$  condensate will yield  $\sim 32$  MeV per nucleon and note that

$$\mu_e = m_\mu c^2 \approx (m_\pi c^2 - 32) \text{ MeV} \quad (23)$$

This energy saving comes in almost equal parts from the kinetic energy saving produced by the reduced nucleon fermi energy associated with the increased spin-isospin degeneracy of nuclear matter compared with neutron matter and the potential energy decrease due to the opening up of the attractive  $T = 0$  interaction channels, predominately the  $1^3S_1$  channel. Note that this lowering of energy only occurs for a  $\pi^-$  condensate and again emphasises the likely realization of this phase at lower densities than  $\pi^0$  or  $\pi^+$  condensation.

The N-N interaction at short distances  $\lesssim 0.5$  fm becomes strongly repulsive. This generates strong two-body correlations in nucleon matter keeping the nucleons apart. This pionic phenomena known as the Ericson-Ericson (1966) effect is the analogue of the well known Lorentz-Lorenz (1880) effect in photon propagation. The result is to increase the critical density at which pion condensation is predicted to occur.

The  $\pi$ -N system supports a p-wave resonance at  $1234$  MeV. This occurs in the angular momentum  $J = 3/2$ , isospin  $T = 3/2$  channel and is variously known as the 3-3 resonance,  $\Delta(1234)$  or  $N^*(1234)$ . We shall adopt the latter notation.

In a mix of nucleons and pions at high density  $N^*$ 's will continually be formed and decay. In thermal equilibrium the Saha equation will predict the relative abundances of  $N^*$ 's and free pions and

nucleons. In normal nuclear matter at a density  $\sim \rho_0$  the relative abundance of  $N^*$ 's is predicted to be  $\sim 0.1\%$ . This increases significantly in the condensed phase. The increased spin and isospin of the  $N^*$  compared with the  $N$  increases the effective tensor force (nuclear analogue of the electromagnetic dipole-dipole interaction) which is the dominant ordering force in the system. This increase in the effective tensor force decreases the critical density for pion condensation.

In their effect on the critical density for pion condensation the inhibiting effect of the short range repulsive  $N$ - $N$  correlations and the encouraging role of the  $N^*$ 's largely cancel each other out. The net effect is that once nuclear interactions are allowed for the critical density for the onset of pion condensation is  $\sim \rho_0$  in bulk nucleon matter.

#### THE EQUATION OF STATE

Qualitatively the equation of state for electrically neutral matter can be deduced from figure 4 and the result is indicated in figure 5. At very low densities matter is composed of electrons and protons in the form of hydrogen. As the density increases the fermi energy of the lowest mass component, the electrons, rises fastest; when it exceeds the proton-neutron mass difference the neutron abundance begins to grow. At densities only slightly below the critical density  $\sim \rho_0$  we have matter composed predominately of neutrons with traces of electrons and protons. At higher densities when the condensation is complete we have equal abundances of neutrons, protons and negative pions. In figure 5 we see that the resulting equation of state has the traditional form associated with a phase transition and in thermal equilibrium the usual equal areas Maxwell construction is required to describe the phase separation. A density discontinuity clearly exists between the two phases. In the fully condensed phase we have the long range ordering of spin and isospin illustrated in figure 6.

#### NEUTRON STARS

Matter at a density  $1 - 2 \times \rho_0$  in thermal equilibrium is unstable against phase separation with matter pion condensing out of a neutron rich fluid just as water droplets condense out of supercooled steam. The density discontinuity between the phases is  $\sim 3\rho_0$ .

Given an equation of state describing the pressure  $P$  as a function of density  $\rho$  one can solve the Tolman-Oppenheimer-Volkov equation

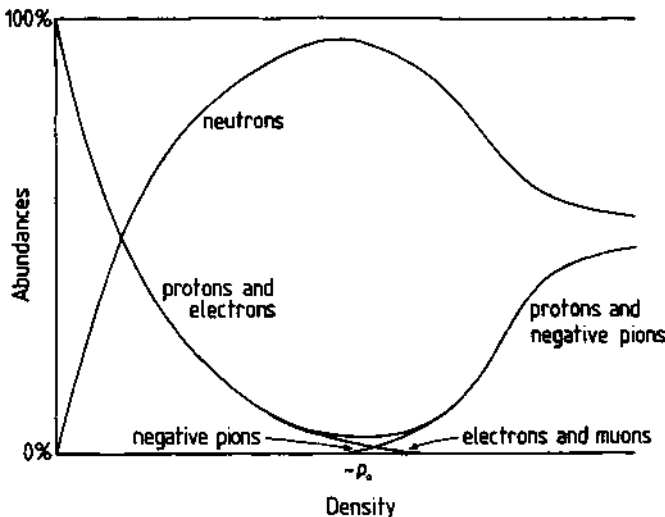


Fig. 4. The relative abundances of various species of particles in electrically neutral matter as a function of density.

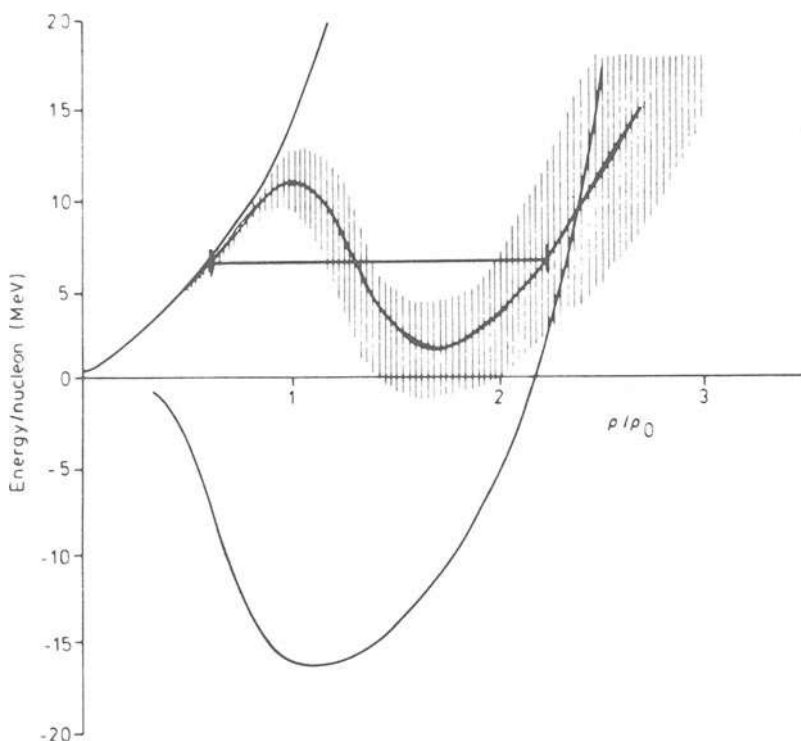


Fig. 5. The equation of state is close to that for neutron matter below  $\rho_0$  and close to pure nuclear matter once condensation is complete.

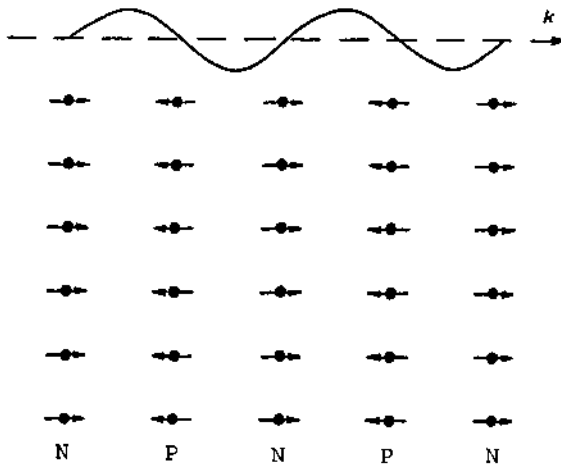


Fig. 6. Long range spin-isospin ordering.

$$\frac{dP(\rho)}{dr} = -\frac{G}{r} [M(r) + 4\pi P(\rho) r^3/c^2] [\rho + P(\rho)/c^2] [r - 2GM(r)/c^2]^{-1}$$

$$M(r) = 4\pi \int_0^r \rho(r') r'^2 dr' , \quad (24)$$

describing hydrodynamic equilibrium in a spherical non-rotating star, for the density profile of the star. Being a first order equation a single boundary condition determines the solution uniquely. Thus the central density determines a unique mass for the star. Typical results for equations of state ignoring pion condensation are presented in figure 7. This curve represents equilibrium stellar configurations, not all of which are stable. The stability condition is that the mass of the star should be an increasing function of the central density. Hence we have the prediction of a minimum and maximum mass for stable neutron stars. Looking at the central density associated with the lightest stable neutron star configuration we see that it lies in the region spanned by the Maxwell construction of figure 5. Hence when pion condensation is allowed for such configurations are no longer stable but will develop a pion condensed core with a density discontinuity and the surrounding neutron star matter of  $\sim 3\rho_0$ . This changes the density profile of the star slightly and also makes a small increase in the minimum mass of a

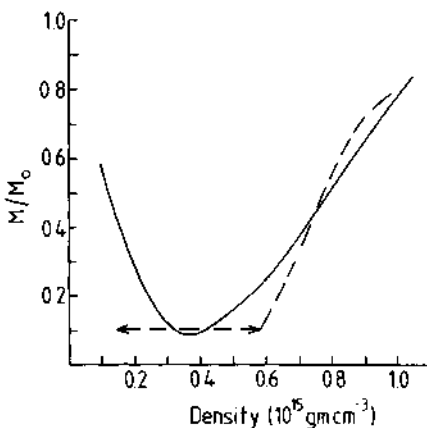


Fig. 7. Masses of stars as a function of central density given by equation (24).

stable configuration. More significantly such cores are potential sources of enormous magnetic fields. From figure 6 we see that the magnetization of the core is  $\sim \mu_N n_N$  where  $\mu_N$  is the nuclear magneton and  $n_N$  is the nucleon density. At  $\sim 3\rho_0$ ,  $n_N \approx 0.5 \text{ fm}^{-3}$  and hence the surface polar field in a star of radius  $R$  with a pion condensed core of radius  $R_C$  is

$$B \approx 10^{10} \frac{R_C^3}{R} \text{ Tesla} \quad (25)$$

Pulsars are believed to have characteristic surface magnetic fields in the range  $10^8 - 10^{10}$  T.

#### HEAVY ION COLLISIONS

There are three possible situations to be examined:

- (i) Normal nuclear ground states contain a pion condensate.
- (ii) Normal nuclear ground states do not contain a pion condensate but are so close to it in phase space that quantum fluc-

tuations (frequently called precursor phenomena) are observable.

- (iii) High density matter created in heavy ion collisions may contain condensates.

Since pion condensation is a collective phenomena it is most probably manifested in extremely heavy nuclei. Such nuclei contain a substantial neutron excess and asymmetry energy is available to favour  $\pi^-$  condensation. Consider the nucleus  $^{238}_{92}\text{U}$  viewed as composed of 92 protons and 146 neutrons. The two conserved quantum numbers are the electric charge and total baryon number. A fully condensed state with the same quantum numbers can be constructed from 119 protons, 119 neutrons and 27 negative pions. It is clear however that this condensation does not occur in the normal ground states of nuclei since if it did the large magnetic fields, so attractive in neutron stars, would cause havoc with the systematics of hyperfine splittings and electron scattering experiments would detect the substantial reduction in nuclear size associated with the condensed phase.

Looking for evidence of precursor phenomena has been popular for some time. Close to the phase transition we would expect excitations of the pionic degrees of freedom to be enhanced. Thus we should expect enhancement of ( $\pi$ ,  $2\pi$ ) or ( $e$ ,  $e\pi$ ) reactions. We might expect to see large numbers of parity doublets in the low lying spectra of nuclei. The results of these searches have so far been negative. Unfortunately they have to date been concentrated on light  $N = Z$  nuclei where we have tried to indicate they will probably not be seen, so that a final conclusion must await further studies of much heavier nuclei.

Finally we turn to energetic heavy ion collisions capable of generating high density nucleonic matter. We are faced with three problems (i) Does the high density phase survive long enough to thermalise; (ii) If it does, is the equilibrium temperature above or below the critical temperature for pion condensation; (iii) If pion condensation does occur what is the most likely signature to be seen in the laboratory?

While I believe that the answer to (i) is negative, it is clear that to have any chance of success we require to study the heaviest possible target-projectile system, i.e.  $^{238}\text{U}$  on  $^{238}\text{U}$ . This has the advantage of maximum neutron excess again favouring the formation of  $\pi^-$  condensation. In the entrance channel we have 184 protons and 292 neutrons. To date the reaction has been studied with charged particle detectors which have seen large quantities of  $\alpha$ 's,  $^{12}\text{C}$ 's,  $^{16}\text{O}$ 's, etc., i.e. light  $N = Z$  nuclei. The key question is then what happened to the large neutron excess? If the neutrons simply evaporated off in the heat of the collision, then their number and

characteristic spectrum are well defined. Suppose some significant fraction of them were compressed and the compressed phase equilibrated with respect to



If all the protons in the initial compound configuration could be accounted for by the light  $N = Z$  fragments, we could be left with an  $A \approx 100$ ,  $Z \approx 0$  fragment composed of  $\sim 50$  neutrons, 50 protons and 50 negative pions. Such an exotic object far from the line of beta stability if observed would be a sure signature for a whole new world of exciting physics. The direct observation of such an object must be viewed as extremely unlikely but its decay would also provide a characteristic signature with



and the neutrons tunneling through the potential barrier of figure 5. We might hope to see a spectrum of delayed neutrons of fixed energy rather than the thermal evaporation spectrum predicted if no condensation were to occur.

#### REFERENCES

- Baym, G. and Flowers, E., 1974, Nucl. Phys. A222: 29.  
 Campbell, D., Dashen, R. and Manassah, J., 1975, Phys. Rev. D12: 1010.  
 Ericson, M. and Ericson, T., 1966, Ann. Phys. (N.Y.), 36: 323.  
 Goodwin, N.H., Meinhart, M. and Irvine, J.M., 1980, Jour. Phys., G6: 455.  
 Irvine, J.M., 1975, Rep. Prog. Phys., 38: 1385.  
 Irvine, J.M., 1981, Prog. Part. and Nucl. Phys., 5: 1.  
 Irvine, J.M. and Rodgers, I.R., 1977, Jour. Phys., G3: 1699.  
 Lorenz, L., 1880, Ann. Phys. (Lpz.), 11: 70.  
 Migdal, A.B., 1973, Nucl. Phys., A210: 421.  
 Migdal, A.B., 1978, Rev. Mod. Phys., 50: 107.  
 Sawyer, R. and Scalapino, D., 1973, Phys. Rev. D7: 953.  
 Weise, W. and Brown, G.E., 1976, Phys. Reports, 27C: 1.

## CLASSICAL SOLUTIONS OF YANG-MILLS-THEORY

H. Mitter

Institut für Theoretische Physik der Universität  
A-8010 Graz, Austria

In this lecture I shall present a review on classical, static solutions of the Yang-Mills field equations in presence of charge- and current sources. I shall consider only the SU(2) theory and concentrate essentially on solutions describing spherically symmetric situations. Thus the solutions to be discussed can be considered as the simplest non-Abelian generalization of the well known Coulomb-Biot-Savart solution in classical electrodynamics. The idea behind studying classical solutions is that investigations in quantum theory should perhaps not be performed without any reference to the classical theory (though the relation between classical and quantum mechanics may differ in Abelian and non-Abelian theories). In addition, some peculiar features on non-Abelian theories can be studied already on the classical level.

The material to be covered here is contained essentially in two papers<sup>1,2</sup>. I shall try to give an outline of these results, which avoids too sophisticated machinery and is intended for non-experts; only some familiarity of the reader with classical electrodynamics is assumed; detailed calculations are, however, omitted in many places. The notation is as follows: The field is described by potentials  $\Phi_a, A_a$  and field strengths  $\vec{E}_a, \vec{B}_a$ . The sources are described by  $\rho_a, j_a$ . The SU(2) index  $a$  takes values 1,2,3 and we shall adopt the summation convention for repeated indices. We shall call  $\vec{E}_a$  the "electric",  $\vec{B}_a$  the "magnetic" field,  $\rho_a$  the "charge" density, etc.; one should, however, keep in mind, that this is meant only per analogiam: the physical meaning of these quantities in a non-Abelian theory is richer than in electrodynamics. The full Yang-Mills equations read:

$$\vec{E}_a = -\vec{\nabla}\Phi_a - \frac{1}{c} \frac{\partial}{\partial t} \vec{A}_a + g\epsilon_{abc} \vec{A}_b \Phi_c$$

$$\vec{B}_a = \vec{\nabla} \times \vec{A}_a - \frac{g}{2} \epsilon_{abc} \vec{A}_b \times \vec{A}_c$$

$$\vec{\nabla} \cdot \vec{E}_a - g\epsilon_{abc} \vec{A}_b \cdot \vec{E}_c = \rho_a$$

$$\vec{\nabla} \cdot \vec{B}_a - g\epsilon_{abc} \vec{A}_b \cdot \vec{B}_c = 0$$

$$\vec{\nabla} \cdot \vec{B}_a - g\epsilon_{abc} (\vec{A}_b \times \vec{B}_c + \Phi_b \vec{E}_c) =$$

$$= \vec{j}_a + \frac{1}{c} \frac{\partial}{\partial t} \vec{E}_a$$

$$\vec{\nabla} \times \vec{E}_a - g\epsilon_{abc} (\vec{A}_b \times \vec{E}_c - \Phi_b \vec{B}_c) =$$

$$= - \frac{1}{c} \frac{\partial}{\partial t} \vec{B}_a$$

$$\vec{\nabla} \cdot \vec{j}_a + g\epsilon_{abc} (\Phi_b \rho_c - \vec{A}_b \cdot \vec{j}_c) = - \frac{\partial}{\partial t} \rho_a$$

Here  $g$  is a coupling constant and  $\epsilon_{abc}$  denotes the familiar Levi-Civita symbol (with  $\epsilon_{123}=+1$ ). The first two equations are the relations between potentials and field strengths. The following four equations are the analog of Maxwell's equations. The last equation is a consequence of these and is the analog of the continuity equation. The whole set is invariant under local SU2-transformations (non-Abelian gauge transformations):

$$\Phi_a \rightarrow \Phi'_a = K_{ab} \Phi_b + \Omega_a, \quad \vec{A}_a \rightarrow \vec{A}'_a = K_{ab} \vec{A}_b + \vec{\Omega}_b$$

$$(\vec{E}_a, \vec{B}_a, \rho_a, \vec{j}_a) \rightarrow (\vec{E}'_a, \vec{B}'_a, \rho'_a, \vec{j}'_a) = K_{ab} (\vec{E}_b, \vec{B}_b, \rho_b, \vec{j}_b)$$

where

$$K_{ab} = \delta_{ab} \cos\theta + n_a n_b (1 - \cos\theta) + \epsilon_{abc} n_c \sin\theta$$

with an arbitrary angle  $\theta = \theta(\vec{x}, t)$  and an arbitrary unit vector

$$n_a = n_a(\vec{x}, t) \quad n_a n_a = 1$$

and

$$g\Omega_a = \frac{1}{2c} \epsilon_{abc} \left( \frac{\partial}{\partial t} K_{bd} \right) K_{cd}, \quad g\vec{\Omega}_a = - \frac{1}{2} \epsilon_{abc} (\vec{\nabla} K_{bd}) K_{cd}.$$

It has to be noted that (in contrast to electrodynamics) also the field strengths and sources are changed by gauge transformations.

This change is, however, by no means an arbitrary one: despite of the arbitrariness in the quantities  $\theta$ ,  $n_a$  one may not change every information contained in the fields at will; also gauge-dependent quantities contain information on the physics they describe, like the potentials in electrodynamics. There are important combinations of the field strengths, which are manifestly gauge invariant. One example, which we shall use, is the total field energy

$$E = \frac{1}{8\pi} \int (\vec{E}_a \cdot \vec{E}_a + \vec{B}_a \cdot \vec{B}_a) d^3x.$$

In order to obtain an unique solution of the field equations it is necessary to fix the gauge completely. The solution obtained will then refer to this particular gauge. The gauge fixing should be done in such a way, that the field equations become as simple as possible. Other solutions can be obtained from the result by gauge transformations and may be envisaged as "the same solution in another gauge frame". They may look, however, completely different: for instance field (and sources) which are static ( $\partial/\partial t = 0$ ) in one gauge, may depend on time in another one. The term "static" is nevertheless appropriate for the corresponding situation: any time dependence can be gauged away. Corresponding remarks apply to a situation, which shows some symmetry in a particular gauge.

#### ABELIAN STATIC SOLUTION

In electro-resp. magnetostatics the potentials can be written in terms of integrals of the sources. The same expressions turn out to be also static solutions of the nonabelian theory.

The solution reads

$$(\Phi_3(\vec{r}), \vec{A}_3(\vec{r})) = \frac{1}{4\pi} \int \frac{d^3r'}{|\vec{r}-\vec{r}'|} (\epsilon \rho_3(\vec{r}'), \vec{j}_3(\vec{r}'))$$

$$\Phi_1 = \Phi_2 = \vec{A}_1 = \vec{A}_2 = \rho_1 = \rho_2 = \vec{j}_1 = \vec{j}_2 = 0$$

and refers to gauges, in which the 3-direction is distinguished (this is called the Abelian gauge frame). We shall use this solution for reference purposes later on for spherically symmetric situations. In order to describe such a situation we write for the sources

$$cgr^3 \rho_3(\vec{r}) = q(x), \quad gr^3 j_{3,k} = -\epsilon_{3ki} e_i m(x) .$$

Here we have taken out an arbitrary length scale  $r_0$  and have used the abbreviations  $\vec{r} = \vec{r}/r$ ,  $x = r/r_0$ . The function  $q(x)$  describes the "charge" distribution, whereas  $m(x)$  characterizes the current distribution and simulates a source of static "magnetism". We shall

call the corresponding solution the (abelian) Coulomb solution and shall compare its field energy

$$\varepsilon_c = \frac{g^2 r_0}{4\pi} \quad E_c = \int_0^\infty dx \int_0^\infty dy [x q(x) q(y) + \frac{2}{9} y m(x) m(y)]$$

with the corresponding one for nonabelian solutions for the same sources.

### NONABELIAN SOLUTIONS FOR SPHERICAL SYMMETRY

In accordance with the remarks made in the introduction we shall call a situation spherically symmetric, if any deviation from the symmetry can be gauged away. This notion of symmetry is less restrictive than the usual one: it does, for instance, not imply, that the charge density  $\rho_a$  must be scalar under rotations; if we take  $\rho_a = r_a k(r)$  this will transform as a vector under rotations, the change can, however, be removed by the corresponding SU2 rotation about the same axis with opposite angle. In the same way one may use a tensor form  $A_a$ . The most general ansatz for sources describing spherically symmetric situations can be written in terms of four scalar functions

$$g r_0^3 c \rho_a = e_a q(x)$$

$$g r_0^3 j_{a,k} = e_a e_k v(x) + (e_a e_k - \delta_{ak}) v(x) = \varepsilon_{aki} e_i m(x) ,$$

and refers to a class of gauges, which we shall call the radial frame. We may still do gauge transformations within this frame (e.g. SU2-rotations about  $e_a$ , which mix  $v$  and  $m$ ). The radial flow term  $\sim v$  cannot be removed, however. We shall assume here  $v = \dot{v} = 0$  (for the general situation see Ref. 2). For the potential a similar ansatz can be made. Here it is, however, possible to remove the  $e_a e_k$ -term (without leaving the radial frame) via the inhomogeneous part  $\vec{\Omega}$  of the transformation. A further gauge fixing within the radial frame allows for a choice with only two radial functions  $g \Phi_a = f(x)/r$

$$g A_{a,k} = -\varepsilon_{aki} e_i (1-a(x))/r .$$

After some calculational steps we obtain for the field strengths

$$g E_{a,k} = e_a e_k (f - x f')/r^2 + (e_a e_k - \delta_{ak}) a f / r^2$$

$$g B_{a,k} = e_a e_k (1 - a^2)/r^2 + (e_a e_k - \delta_{ak}) x a' / r^2 ,$$

where the prime denotes the derivative with respect to  $x$ . Thus both

fields display a radial component ( $e_a e_k$ ) and a tangential one. The field equations reduce to two coupled nonlinear differential equations

$$-x^2 f'' + 2fa^2 = x^3 q \quad ; \quad x^2 a'' + a(f^2 + 1 - a^2) = x^3 m .$$

The field energy becomes

$$\epsilon = \frac{g^2 r_0}{4\pi} E = \frac{1}{2} \int_0^\infty dx [(f - xf')^2 + 2f^2 a^2 + (a^2 - 1)^2 + 2x^2 (a')^2] / x^2 .$$

We shall be interested in solutions, for which  $\epsilon$  is finite. Then  $f$  must vanish for  $x=0$ , whereas  $a$  has to assume the value  $\pm 1$ . We take the + sign (which fixes the gauge completely). For the source functions we assume  $q(0)=m(0)=0$ . The behaviour of  $f$  and  $a$  near  $x=0$  is then determined from the differential equations. We have

$$f = f_2 x^2 + f_4 x^4 + \dots , \quad a = 1 + a_2 x^2 + a_4 x^4 + \dots$$

with certain coefficients  $f_2, f_4, a_2, a_4$  etc. If  $f_2$  (resp.  $a_2$ ) differs from zero, the two components of  $E_a$  (resp.  $B_a$ ) are finite at the origin and have opposite sign.

The behaviour of large  $x$  is less simple. Since we are interested in sources of finite extent we shall assume that  $q$  and  $m$  fall off rapidly for large  $x$  (faster than  $x^{-4}$ ). For the behaviour of the fields it is crucial, whether an electric source  $q$  is present or not. We shall first discuss the former situation  $q \neq 0, f \neq 0$ . Then we may have two types (I,II) of solutions:

$$(I) \quad f = f_{-1}^I / x + \dots \quad a = 1 + a_{-1}^I / x + \dots$$

$$(II) \quad f = f_{-1}^{II} / x + \dots \quad a = -1 + a_{-1}^{II} / x + \dots$$

The vector potential tends asymptotically to a pure gauge potential  $\sim 1/r$  for type II, whereas it falls off quadratically for type I. The only difference is that the leading terms in the two components of  $E_a$  (and  $B_a$ ) have equal sign for type I and opposite sign for type II. It has not been possible so far to find any other criterion, by means of which the types can be distinguished.

In absence of an electric source,  $q=0$ , one may show that  $f$  must vanish, so that  $\Phi_a = E_a = 0$ . There can be still solutions of type I and II. Besides these there is, however, also a third type III possible, for which  $a$  falls off quadratically or faster. In this case the magnetic field is

$$gB_{a,k}^{\text{III}} = e_a e_k / r^2 + \dots$$

which is the field of a magnetic monopole of fixed strength. It is a particular feature of nonabelian gauge theories, that they may contain magnetic monopoles. Note, however, that (in the situation considered here: spherical symmetry) this field is possible only in absence of electric sources and fields.

If one wants to have analytical results, one may start with an ansatz for  $f$  and  $a$  with the correct behaviour at small and large  $x$  and compute the corresponding sources from the differential equations. It is very easy to find explicit examples of monopole solutions in this way<sup>2</sup>. In absence of magnetic sources ( $m=0$ ) the problem is less easy, but some results have been found recently<sup>3</sup>. In general the sources turn out very reasonable.

There is one important question, however, which is not easily answered in this way: whether or not the various types of solutions may coexist for the same sources. In order to decide upon that one must solve the differential equations numerically. This has been done for a very simple model, in which the sources have shell structure

$$q(x) = Q\delta(x-1), \quad m(x) = M\delta(x-1)$$

where  $Q(>0)$  and  $M$  are constant parameters. Ref. 1 contains rather accurate results for  $m=0$ . In Ref. 2 these results were extended to a limited number of values  $m\neq 0$ ; the purely magnetic situation  $q=0$  has been covered rather completely by curve discussion almost without need of numerical work. I shall give here a brief qualitative review of the results, discussing the solutions (found numerically) and their field energy  $\epsilon$ , which I shall compare with the corresponding energy  $\epsilon_c$  of the abelian Coulomb solution with the same sources.

For  $Q=0$  there is no coexistence: type I exists for  $M<0$ , the monopole (type III) for  $M=M_0 \approx 1.458$ , type II for  $M \geq M_1 \approx 2.33$ . Between these values, i.e. for  $0 < M < M_0$  and  $M_0 < M < M_1$  there are no solutions (this result is exact, only the values of  $M_0$ ,  $M_1$  are calculated numerically). The energy  $\epsilon$  grows with increasing  $|M|$  and is always larger than the Coulomb energy.

For  $Q \neq 0$  the numerical procedure adopted in Ref. 2 becomes inaccurate for too large values of  $|M|$ , so that I can make reliable statements only for  $|M| < 3$ . Type I is found for all values of  $Q$  sifted so far, if  $M \leq 0$ . For  $Q \neq 0$  we have found type I also for positive values of  $M$ . Type II exists only, if the sources are strong enough, i.e. above a certain curve in the  $(Q, M)$  plane. Three points on this curve  $(5, 0.35)$ ,  $(5.8, 0)$ ,  $(10, -2.65)$  have been determined so

far. Probably it extends to  $(0, M_1)$ . Above this curve two different solutions type II (a,b) are found, which differ also in energy. Thus we have not only coexistence of type I and II, but even a bifurcation of the latter type for sufficiently large  $Q$  and  $M$ . In contrast to the purely magnetic situation we find for fixed  $Q \neq 0$ ,  $M$  for the energy  $\epsilon_1 < \epsilon_{IIa} < \epsilon_{IIb} < \epsilon_c$  (there may be changes in this sequence for large values of  $|M|$ ).

The meaning of the field energy should perhaps not be overestimated in this context. One reason for this is that its meaning is not clear at all in the context of quantum theory, for which these classical investigations could provide at most a first step. Even in a purely classical context we should also not forget that any search for static (soliton) solutions should be supplemented by a stability analysis in a nonlinear theory. Only solutions which are stable in the sense that they remain close to static ones during a development in time, can be trusted. A local minimum in energy is a sufficient, but by no means a necessary criterion for stability. A stability analysis has been done so far only for  $M=0$ <sup>4</sup>. The result is that the Abelian solution becomes unstable above  $Q=1.5$ . The type I solution is shown to be stable for sufficiently small  $Q$ . What happens for larger values, is not known. The energetically lower branch of the type II solution can be shown to be stable exactly for all values of  $Q$ , for which it exists ( $Q > 5.8$ ) (though type I has lower energy!), the other branch is always unstable.

It is not clear at present whether and how this rich structure of solutions will carry over to quantum theory. In addition one might expect an even richer structure for other symmetries (e.g. axial symmetry, which should allow also for vortex type fields). Thus many questions of interest remain still open in this nonlinear field theory.

#### REFERENCES

1. R. Jackiw, L. Jacobs, C. Rebbi, Phys. Rev. D20:474 (1979).
2. L. Mathelitsch, H. Mitter, F. Widder, Phys. Rev. D, in print.
3. C. H. Oh, R. Teh, W.K. Koo, Cambridge preprint DAMTP 81/2 (1981).
4. R. Jackiw, P. Rossi, Phys. Rev. D21:426 (1980).

## PARTICLES IN STRONG PERIODIC FIELDS

H. Mitter

Institut für Theoretische Physik der Universität  
A-8010 Graz, Austria

Quantum electrodynamics of electrons in external electromagnetic fields has been of interest since a very long time, since the Coulomb field of nuclei can be described in good approximation by a given potential. Later on other fields, as for instance homogeneous magnetic or electric ones, have been studied, which can be realized and allow for a solution of the relativistic wave equation as well. It is one of the main goals of this meeting to discuss specific effects, which might happen in strong Coulomb fields. I shall try to detract the attention of the participants to some other types of fields, which might compete in a certain sense with respect to their strength with nuclear Coulomb fields. In order to obtain some rough notion of what is a "strong" field, we shall start from the wave equation for an electron in an external field:

$$[\gamma_\mu (i\partial^\mu - eA^\mu) - \kappa] \psi(x) = 0$$

Here  $\epsilon = e/mc$  with the elementary charge  $e$  and  $\kappa = mc/\hbar$  with the electronic mass  $m$ . The vector potential  $A^\mu(x)$  describes the external field. Dividing by  $\kappa$  and scaling the coordinates to the Compton wavelength  $1/\kappa$  everything becomes dimensionless, but  $A^\mu$  may contain one or more dimensionless numbers, which determine its strength relative to the mass term and/or derivative term. If possible, such a number  $v$  is factored off  $eA/\kappa$  in such a way that the remainder has order of magnitude unity in the relevant domain. We shall call the field "weak", if this number is small:  $v \ll 1$ . A perturbative solution of the equation (with the potential as a perturbation) is then an expansion in powers of a small quantity (the expansion may not always converge, however). In contrast, a field is called "strong", if we have  $v \approx 1$  or larger. For the Coulomb field of a point charge  $Ze$  we obtain for this number  $v = Z\alpha$ . For a constant, homogeneous magnetic resp. electric field we obtain the ratio of

the actual field strength to a critical or natural field strength:

$$v = \epsilon B / \kappa^2 \quad \text{resp.} \quad v = \epsilon E \kappa^2$$

where the natural field strength is

$$\kappa^2 / \epsilon = m^2 c^3 / e \hbar = 4.41 \cdot 10^{13} \text{ Gauß resp. } 1.32 \cdot 10^{18} \text{ V/m}$$

What may happen for  $Z \alpha \gtrsim 1$  is a topic at this meeting. What may happen for strong constant fields is of academic interest. There are, however, some other fields, for which the corresponding parameter may become appreciable. Consider any periodic function of the coordinate and take e.g. a cosine function as a candidate for one of the components of  $A^\mu$ . Then we have for this component

$$A = a \cos \xi(x)$$

where  $a$  measures the maximal amplitude of the vector potential. Our number is then

$$v = \epsilon a / \kappa$$

For a plane wave field produced by a laser we have in terms of the wave length  $\lambda_L$  (m) and the irradiation density  $S$  (W/m<sup>2</sup>)

$$v^2 \approx 7.5 \cdot 10^{-11} \lambda_L^2 S$$

Devices for laser fusion realize values of 1 and larger for this parameter. I shall therefore consider as an example a circulary polarized plane wave field (CPPW). Another example of a periodic field with unexpected consequences is a standing light wave made up from two such plane waves propagating in opposite directions. One may think of a plane wave reflected by a mirror or look into the interior of the resonance cavity of a laser. The polarization of the two beams may be opposite or equal (circular) and the corresponding standing wave will be called SWOP resp. SWEP (I shall consider only circular polarization; for linear polarization the calculations are quite formidable). The parameter  $v$  is essentially the same as for the running wave, but we shall see, that there is another parameter present in this case, which may control nonperturbative effects even for smaller values of  $v$ . Another example is a magnetic field constant in time and periodic in space  $\vec{B} = B (\cos \omega z, \sin \omega z, 0)$ . Such a field is produced in the axis of a solenoid made up from one layer of a bifilar wire wound loosely on a cylinder, whereby the two files are connected with each other on one end and with a current source at the other end. This so-called magnetic wiggler field (MW) is an essential piece of the free electron laser in operation at Stanford. The parameter  $v$  is in this case

$$v = \frac{\epsilon B}{\omega k} = \frac{eB}{mc^2 \omega}$$

The wiggler is realized by a superconducting solenoid. The wave length  $\lambda_w = 2\pi/\omega$  of the winding is 3.2 cm and the field strength is  $B=2.4$  kG. With these data (which are certainly not at the limits of technology) we have  $v=0.71$ . It seems therefore worthwhile to review briefly some of the physics of electrons in these fields, which I shall attempt to do in this lecture. As a general pattern we have to observe, that the parameter  $v$  is a classical quantity for all four fields to be studied (in contrast to Coulomb- or homogeneous fields, where  $h$  does not cancel out). Thus we have always to face the possibility, that some effects will turn out to be classical ones at the end, in spite of the fact, that we shall use relativistic quantum mechanics.

A general procedure to obtain information on the solutions of the wave equation of an electron in these fields can be obtained by observing, that the vector potential can be written as

$$A^\mu = a(0, a_1(x_0, z), a_2(x_0, z), 0)$$

in all four situations. We shall consider the Klein-Gordon-equation

$$(\pi_\mu \pi^\mu - \kappa^2) \psi = 0 \quad \pi^\mu = i \partial^\mu + e A^\mu$$

for simplicity and shall discuss the influence of spin effects (Dirac equation) qualitatively later on. Since the vector potential is independent of  $x, y$  we may split off an exponential

$$\psi = \exp [i(xp_x + yp_y)] \phi(x_0, z)$$

where the components  $(p_x, p_y) \equiv (p_i, i=1,2)$  are conserved. Then we have in two-vector notation

$$\left( \frac{\partial^2}{\partial z^2} - \frac{\partial^2}{\partial x_0^2} - 2i\epsilon a_i a_i - \epsilon^2 a_i^2 a_i a_i - \kappa^2 \right) \phi = 0$$

(Here  $x_0 = ct$ ,  $p_i$  and  $\omega$  have the dimension of wave numbers:  $hp_i$  are momenta,  $2\pi/\omega$  is a wave length).

For the plane wave field it is convenient to use the light-like coordinates

$$\left( \frac{u}{v} \right) = (x_0 \mp z)/2^{1/2} \quad \frac{\partial^2}{\partial z^2} - \frac{\partial^2}{\partial x_0^2} = -2 \frac{\partial}{\partial u} \frac{\partial}{\partial v}$$

instead of  $x, z$ . The various types encountered can be discussed using the following table

| Field     | CPPW                       | MW                | SWOP                                | SWEP                               |
|-----------|----------------------------|-------------------|-------------------------------------|------------------------------------|
| $a_1$     | $\cos \sqrt{2\omega_0 u}$  | $\cos \omega_0 z$ | $2\cos \omega_0 z \cos \omega_0 x$  | $2\cos \omega_0 x \cos \omega_0 z$ |
| $a_2$     | $-\sin \sqrt{2\omega_0 u}$ | $\sin \omega_0 z$ | $-2\cos \omega_0 z \sin \omega_0 x$ | $2\cos \omega_0 x \sin \omega_0 z$ |
| $a_i a_i$ | 1                          | 1                 | $4\cos^2 \omega_0 z$                | $4\cos^2 \omega_0 x$               |

Thus we see, that the "effective mass" of the particle defined by

$$\kappa_{\text{eff}}^2 = \kappa^2 + \epsilon^2 a_i^2 a_i a_i = \kappa^2 (1 + \epsilon^2 a_i a_i)$$

is in general intensity-dependent, but constant for the first two fields of our table. In both of these cases we have an additional conserved quantity, since the potential depends only on one coordinate. For the CPPW this is  $p_y = (p_0 - p_z)/2$  for the wiggler this is the energy  $p_0$  of the particle. For the standing wave fields the effective mass depends on space (resp. time) and things are more complicated. In order to simplify further we consider only the motion along the field direction ( $p_x = p_y = 0$ ). This is not really necessary for the CPPW where both the Dirac and Klein-Gordon equation can be solved without this assumption. For the MW this is, however, necessary, since the field considered here is only realistic along the axis of the wiggler and the electrons move only along this direction in the free electron laser. For the standing wave fields our restriction means, that we shall not discuss the (transverse) Dirac-Kapitza effect (i.e. the Bragg-type scattering of the electrons off the periodic lattice formed by the standing wave field): this effect could be discussed by semi-classical methods<sup>1</sup>. We shall rather consider the corresponding longitudinal motion, which shows typical quantum mechanical features.

The solution of the Klein-Gordon-equation is very easy for the first two fields because of the additional conserved quantities: we obtain a plane wave in either case. The result reads (up to a normalization factor)

$$\phi = \exp [i(x_0 \pi_0 - z \pi_z)] = \exp [i(u \pi_u + v \pi_v)]$$

where the "effective" energy-momentum fulfills

$$\pi_0^2 - \pi_z^2 = 2\pi_u \pi_v = \kappa^2 + \epsilon^2 a^2$$

It is convenient to consider the corresponding quantities for a free electron

$$(p_0, p_z) \quad p_0^2 - p_z^2 = 2p_u p_v = \kappa^2$$

i.e. the energy-momentum of the electron without (or outside of) the field: these values are, for instance, those with which the electron enters the field (which is of finite extension in practice.) We may think of these quantities as labels of the electronic state in the field. In terms of these we have

$$\text{CPPW: } \pi_v = p_v, \pi_u = p_u + \frac{\epsilon^2 a^2}{2p_v}$$

$$\pi_o = p_o + \frac{\epsilon^2 a^2}{2(p_o - p_z)}, \pi_z = p_z + \frac{\epsilon^2 a^2}{2(p_o - p_z)}$$

$$\text{MW: } \pi_o = p_o, \pi_z = (p_z^2 - \epsilon^2 a^2)^{1/2}$$

The propagation is therefore not limited for the CPPW field, whereas particles may propagate through the wiggler only, if  $p > \epsilon a = \epsilon B/\omega$ : it is a well-known general fact, that wave propagation along a periodic medium can be restricted by the properties of the latter. If we introduce a wave vektor  $k^\mu$  of the field, we can write for the effective momentum

$$\pi^\mu = p^\mu + K k^\mu$$

where

|         | CPPW                     | MW                                                           |
|---------|--------------------------|--------------------------------------------------------------|
| $k^\mu$ | $\omega(1,0,0,1)$        | $\omega(0,0,0,1)$                                            |
| $K$     | $\epsilon^2 a^2 / 2(pk)$ | $k^{-2} \{-(pk)^{\pm} [(pk)^2 - \epsilon^2 a^2 k^2]\}^{1/2}$ |

This formal notation is sometimes useful for the discussion of QED processes in the field.

The inclusion of the spin via Dirac's equation introduces a spin factor (dependent on  $\gamma$ -matrices) in both cases. For the CPPW the exponential is the same for both spin directions. For the MW we obtain a superposition of plane waves with four different effective momenta

$$\pi_z = \frac{\pm \omega}{2} + \sqrt{(p_z \frac{\pm \omega}{2})^2 - \epsilon^2 a^2}$$

and appropriate spin factors. Details can be found for the CPPW e.g. in Ref. 2 (where also motion with  $p_z \neq 0$  and more general wave forms are considered) and for the MW in Ref. 3.

The only propagation phenomenon, which would test the wave functions, is therefore the trapping for  $p_z < \epsilon a$  for the MW. This is, however, not particularly interesting, since it is a classical phenomenon: the limiting momentum is (in our units)  $\hbar \epsilon a = eB/\omega c$  and does not contain  $\hbar$ .

For the standing wave fields we have an additional conserved component for  $p_x = p_y = 0$ , which is  $p_o$  for opposite polarization,  $p_z$  for equal polarization. Splitting off the corresponding exponential we obtain Mathieu's equation

$$\left( \frac{d^2}{d\zeta^2} + \Lambda - 2\ell^2 \cos 2\zeta \right) \phi(\zeta) = 0$$

with the same parameter

$$\ell = \epsilon a/\omega = v\kappa/\omega$$

in both cases. The other quantities can again be read off a table:

|      | $\phi$                        | $\zeta$      | $\Lambda$                                  |
|------|-------------------------------|--------------|--------------------------------------------|
| SWOP | $\exp(-ix_o p_o) \phi(\zeta)$ | $\omega z$   | $-2\ell^2 + (p_o^2 - \kappa^2) / \omega^2$ |
| SWEP | $\exp(izp_z) \phi(\zeta)$     | $\omega x_o$ | $+2\ell^2 + (p_z^2 + \kappa^2) / \omega^2$ |

The solutions of Mathieu's equation display a stability pattern: there are stable (oscillatory) resp. unstable (exponentially behaving) solutions according to whether the characteristic exponent  $\tau(\Lambda, \ell^2)$  is real resp. complex. In order to have a probability interpretation one must select the stable solutions. For given  $\ell^2$  these exist only for certain domains of  $\Lambda$ , which have to be determined from the stability chart of Mathieu's equation. This amounts to a band structure for the energy  $p_o$  (SWOP) resp. the momentum  $p_z$  (SWEP). Thus the standing wave field acts as a one-dimensional lattice. The quantitative pattern is determined by the fact, that  $\ell^2$  can easily become large, even for moderate intensities. I shall discuss only the SWOP case in some detail. In the asymptotic region  $\ell^2 \gg \Lambda$  the energy bands become very narrow (i.e. quasi-discrete) and one may use the approximate formula ( $n=0,1,2,\dots$ )

$$E_n \approx mc^2 [1 + (2n+1)\Delta], \quad \Delta = \ell\omega^2/\kappa^2 = v\omega/\kappa$$

where the level splitting  $\Delta$  is very small in practice. On the other end (small  $\ell^2$ ) the energy becomes continuous. The band structure should be observable in the neighbourhood of

$$\Lambda = 2\ell^2 \quad E = E_{th} = mc^2 (1+4v^2)^{1/2}$$

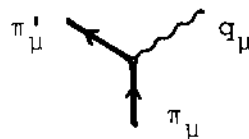
which marks the classical threshold for the transmission of particles<sup>4</sup>. Unfortunately this means, that the band structure shows up at small energies. In order to have  $E_{th} = mc^2 \approx 1 \text{ keV}$  one needs  $v^2 \approx 10^{-3}$ , which is already a rather strong laser. There are much stronger ones available in fusion devices, but one can hardly realize a clean standing wave in the focus, where the intensity

is high. For the momentum bands in the SWEP case the situation is entirely hopeless, since the positive sign in  $\Lambda$  implies  $\Lambda \gg \ell^2$  even for appreciable  $\ell^2$  and the momentum becomes continuous in this limit.

The inclusion of spin effects via the Dirac equation<sup>6</sup> makes things more complicated. For a SWOP we obtain different energy bands for the two spin components. Since the energy splitting due to the spin is very small in practice, this does not affect the qualitative pattern very much. In the SWEP case this is different: here the momentum bands are completely absent in the Dirac theory. Thus we have a qualitative difference between Bose- and Fermi-statistics already on the level of a one-particle theory for this external field.

The only possibility for an experimental test is to look for the transmission of particles through a sufficiently long SWOP arrangement. The corresponding transmission- and reflection coefficients have been calculated in Ref. 5 for the Klein-Gordon theory and in Ref. 6 for the Dirac theory. It turns out, that one may have some domains below the classical threshold where the transmission coefficient differs from zero. Above this threshold the transmission zones become broad and approach each other rapidly. The reflection coefficient above threshold (which would show the quantum pattern like the transmission coefficient below threshold) is, however, rather small. The actual difficulties involved in possible experiments are more on the side of the electron beam than the laser. One needs a beam with a small and rather sharp value of the kinetic energy, which is difficult to produce. It were nevertheless quite nice to observe these quantum effects of an electron in a macroscopic field experimentally.

The next possibility, which we shall consider, is the emission of a photon by an electron travelling in the field. In terms of Feynman graphs this is the process



where the heavy line denotes the wave function of the particle in presence of the field. It is in fact possible to develop a graph formalism for such processes (see e.g. Ref. 2 for the CPPW), but I shall discuss here only the results of the calculation for the CPPW and the MW (for standing waves no reliable results are known). The emitted frequencies can be found in a very simple way using energy-momentum balance for effective momenta ( $\pi^\mu$ ) for the electron and taking account of the fact, that these momenta are

only conserved up to multiples of the "field momentum"  $k^{\mu}$ , since the external field can take up momentum. For our process this means

$$\pi'_{\mu} + q_{\pi} = \pi_{\mu} - nk_{\mu}$$

From this and the mass shell condition

$$\pi_{\mu} \pi^{\mu} = \pi'_{\mu} \pi^{\mu} = \kappa^2 \epsilon^2 a^2$$

one obtains a formula expressing the emitted frequency  $q_0$  in terms of  $n$  and the initial resp. final energy-momenta  $(p, p')$  of the electron. In order to obtain the transition probabilities, one has to compute matrix elements, traces etc., which is of course harder, but can be done in both cases even with the Dirac solutions. For the plane wave field the results are known since a long time under the name of stimulated Compton scattering: one photon from the Laser wave is considered as the "incoming" photon of a Compton process, which is stimulated by the other laser photons emitted or absorbed by the electron in interaction with the field. As a result of the appearance of the integer  $n$  in our momentum formula we can have harmonic generation. The formula for the frequency of the  $n$ th harmonic becomes

$$q_0(n) = \frac{n\omega}{1 + (2n\frac{\omega}{K} + v^2) \sin^2 \theta/2}$$

The formula refers to the rest system of the incoming electron,  $\theta$  is the angle between the directions of the field and the emitted photon and we have assumed  $p_i \neq 0$ . The well-known Compton formula corresponds to  $n=1$ , there is, however an additional indensity-dependent frequency shift due to  $v^2$ . This shift comes from the effective mass of the particle. It has so far not been observed experimentally, though it survives even in the non-relativistic (Thomson) limit. The cross section is an incoherent sum of partial cross sections for the various harmonics, which are proportional to  $v^{2n}$  in the nonrelativistic limit. Details can be found in literature, see e.g. Ref. 7. There have been many discussions on whether the mass shift can be found in other processes. Detailed calculations for almost all other quantum electro-dynamical effects have been done. None of these predictions has been tested by any experiment so far. The reason is, that  $v^2$  may be sufficiently large in laser fusion devices, but these are used for other purposes.

The situation is different for the MW. Here the same procedure with the effective momenta gives for  $n=+1$  and  $q_z = +q_0$  (forward emission).

$$q_0 = \frac{\omega(2\sqrt{p_z^2 - \epsilon^2 a^2} - \omega)}{2[p_0 - \sqrt{p_z^2 - \epsilon^2 a^2} + \omega]}$$

For highly relativistic electrons the corresponding formula for the wavelength  $\lambda = 2\pi/q_0$  becomes

$$\lambda = \frac{\omega}{v^2} [1 + v^2 + 2\gamma\omega/\kappa]^{1/2}, \quad \gamma = (1 - v^2/c^2)^{-1/2}, \quad \gamma_w = 2\pi/\omega$$

For  $n=-1$  we would obtain analogous formulas for absorption ( $q_0 < 0$ ). In the corresponding formula for the wavelength the last term has then the opposite sign, which shows, that this (very small) term corresponds to the recoil of the electron. The wave length is controlled practically by the energy of the electron beam via  $\gamma'$ . For the Stanford<sup>8</sup> equipment the data are  $\lambda_w \approx 3.2$  cm,  $\gamma \approx 84$ ,  $v^2 \approx 0.5$ . This gives an infrared radiation, which is observed at the predicted frequency. Thus the mass shift (which accounts for  $v^2$ ) is measured here. The recoil term is by far too small to be observed, but it is responsible for the possibility to obtain a laser by stimulation. The frequency distribution for emission is peaked at a somewhat lower frequency than the distribution for absorption due to the recoil term. If the operating frequency is chosen somewhat below the mean frequency of both distributions, emission will be predominant and one has a positive gain.

If the Dirac equation is used, one finds a zeroth harmonic ( $n=0$ ) and a first harmonic ( $n=2$ ) in addition to the fundamental frequency ( $n=1$ ). These extra harmonics correspond to spin flip processes and have very small probabilities relative to the fundamental transition. Also the energy splitting due to the spin for the fundamental frequency is very small in comparison with the recoil term, so that the spin is of no practical influence in this context. The absence of higher harmonics is due to the circular "polarization" of the wiggler field. For a linearly polarized field one would find higher harmonics.

The gain factor has been calculated for small stimulating signal in Ref. 4. The result is proportional to  $v^2 e^2 / mc^2 \lambda_w \gamma^3$  and is to a very good approximation independent of  $\hbar$ . It confirms corresponding earlier calculations, which were done either with the Weizsäcker-Williams approximation or with purely classical methods. The extension to stimulation signals of arbitrary strength has been done along the same lines in Ref. 9 and with somewhat different methods before in Ref. 10. In order to perform the calculation<sup>9</sup> it was necessary to find the Green's function of the particle for

longitudinal propagation, for which an integral representation in terms of Mathieu functions is available. The result allows for a calculation of the saturation behaviour of the laser. It is interesting to observe that a cancellation of higher order contributions to the gain occurs, which is due to the infrared cancellation mechanism in QED. The detailed energy distribution of the electrons after the interaction is of quantum mechanical origin, in contrast to the gain, which is classical also for strong signals. Apart from these results, which are important for understanding the laser, no other QED processes have been investigated (to my knowledge) so far for the MW field.

## REFERENCES

1. F. Ehlotzky, C. Leubner, Opt. Commun. 10: 175 (1974) and J.Phys. A8: 1806 (1975).
2. H. Mitter, Acta Phys. Austr. Suppl. XIV: 397 (1975)  
For more literature see the article in Multiphoton Processes,  
J.H. Eberly and P. Lambropoulos (ed.), J. Wiley N.Y. 1978.
3. W. Becker, H. Mitter, Z. Physik B35: 399 (1979).
4. H. Latal, Phys. Lett. A64: 175 (1977).
5. W. Becker, R. Meckbach, H. Mitter, J. Phys. A12:799 (1979).
6. W. Becker, H. Mitter, J. Phys. A12: 2407 (1979).
7. L.S. Brown, T.W.B. Kibble, Phys.Rev. 133: A705 (1964).
8. D.A.G. Deacon et.al., Phys. Rev. Lett. 38:892 (1977).
9. W. Becker, Z. Physik B38: 287 (1980).
10. M.V. Fedorow, J.K. McIver, JETP 79: 1996 (1979) and Phys. Lett. A72: 83 (1979).

## PRECISION LASER SPECTROSCOPY OF HYDROGEN

Theo W. Hänsch

Department of Physics  
Stanford University  
Stanford, California 94305

### ABSTRACT

Advances in laser technology and coherent light techniques have opened interesting opportunities for precision spectroscopy of atomic hydrogen and other simple quantum electrodynamic systems. The present state of such experiment will be reviewed, and possible future precision measurements will be discussed.

### INTRODUCTION

Quantum electrodynamics is one of the most accurate and successful theories of physics. In order to test the possible limits of QED, the experimentalist has to resort to extremes. Other lectures in this course report on experiments at extremely high fields, as they occur in the collision of fast highly stripped heavy ions. And we have learned about experiments which can test QED at extremely high energies. This paper will deal with a third alternative: measurements with extreme precision.

At first glance, the third choice may appear as the most difficult one. A closer look, however, may convince us that this is not necessarily true. One field of physics where high precision has traditionally been a virtue is optical spectroscopy. Recent advances in laser technology and coherent light techniques have led to dramatic further advances in possible resolution and precision. We shall see how laser spectroscopy of simple quantum mechanical systems can indeed provide a powerful tool to determine more precise values of fundamental constants and to probe the limits of quantum electrodynamic theory.

At present, only the hydrogen atom and its isotopes, the heavier hydrogen-like ions, and certain hydrogen-like exotic atoms permit sufficiently accurate model calculations for such an approach. Future theoretical progress should make it possible to add three body systems such as the neutral helium atom or the hydrogen molecular ion to the list of promising candidates. Of these candidates, only hydrogen and deuterium have so far been studied extensively by precision laser spectroscopy,<sup>1</sup> and the work on these two simplest of the stable atoms will be at the center of our discussions.

#### HIGH RESOLUTION LASER SPECTROSCOPY OF THE BALMER- $\alpha$ LINE OF HYDROGEN AND DEUTERIUM

Spectroscopy of atomic hydrogen has played a crucial role in the development of atomic physics and quantum mechanics.<sup>1</sup> The simple and regular Balmer spectrum, reaching from the red into the near ultraviolet, has been studied extensively for about 100 years. More than once, seemingly minute discrepancies between experiment and theory have led to major revolutions in our understanding of quantum physics, from Bohr and Sommerfeld to Schrödinger, Dirac, and modern QED.

The Balmer lines can be observed most readily in the light emitted by a glow discharge. However, no classical spectroscopic observation has ever succeeded in fully resolving the intricate fine structure of these lines. The spectra remained always blurred by Doppler broadening due to the rapid thermal motion of the light hydrogen atoms.

#### Doppler-Free Saturation Spectroscopy

Dramatic progress in spectral resolution became possible only with the advent of highly monochromatic tunable dye lasers<sup>2</sup> together with techniques of Doppler-free laser spectroscopy. One of the oldest and most widely used of these techniques is a method of saturated absorption spectroscopy illustrated in Fig. 1: Two monochromatic laser beams are sent in opposite directions through the absorbing gas sample. When the laser is tuned to the center of a Doppler broadened line, both beams can interact with the same atoms, those with zero axial velocity. The signal is observed as a bleaching of the absorption of the probe beam, caused by the saturating beam.

The prominent red Balmer- $\alpha$  line was the first hydrogen line to be studied by Doppler free saturated absorption spectroscopy.<sup>3</sup> Even though only a relatively simple pulsed dye laser was available in our initial experiments at Stanford, we were thrilled by the

spectra (Fig. 2) that could be recorded in a simple Wood type gas discharge. We were able to resolve single fine structure components of the Balmer- $\alpha$  line, and we could observe the  $n=2$  Lamb shift directly in the optical spectrum.

It was immediately clear that the new spectra would permit a more precise absolute wavelength measurement than any of the classical experiments, which had to resort to troublesome deconvolutions of blends of unresolved line components. And a comparison with theoretical computations<sup>4,5</sup> could provide a more accurate value of the Rydberg constant, which describes the binding energy between electron and nucleus and provides one of the cornerstones in the determination of other fundamental constants.<sup>6</sup> In 1974, Munir Nayfeh at Stanford<sup>7</sup> completed an absolute wavelength measurement of the strong  $2P_{3/2} - 3D_{5/2}$  component of hydrogen and deuterium which yielded an eightfold improved value of the Rydberg constant, compared to the value recommended in the 1973 adjustment of the fundamental constants.<sup>6</sup>

Since then, frequency stabilized cw dye lasers have become readily available, whose resolution is not limited by pulse length. Moreover, new techniques of saturation spectroscopy have been developed, which can reach shot-noise limited sensitivity despite laser intensity fluctuations.<sup>8,9</sup> One of these is the method of polarization spectroscopy, introduced in 1975 by C. E. Wieman and the author.<sup>8</sup> A polarization spectrometer (Fig. 3) is rather similar to a saturation spectrometer (Fig. 1). However, the probe beam monitors not the bleaching, but rather the dichroism and birefringence of the sample induced by optical pumping with a circularly or linearly polarized saturating beam. The technique takes advantage of the fact that small changes in light polarization can be detected with higher sensitivity than changes in intensity. Because of its higher sensitivity, the method permits measurements at lower atom densities and lower laser intensities, so that pressure broadening, power broadening, and related problems can be much reduced.

In 1978, J. E. M. Goldsmith et al. at Stanford<sup>10</sup> completed a new measurement of the Rydberg constant, observing the hydrogen Balmer- $\alpha$  line in a mild helium-hydrogen discharge by polarization spectroscopy with a cw dye laser. Examples of the new spectra are shown in Fig. 4. The resolution of the weak but narrow  $2S_{1/2} - 2P_{1/2}$  fine structure component was at least 5 times better than in the earlier pulsed experiments. The absolute wavelength of this component was measured relative to the  $i$ th hyperfine component of the  $^{127}I_2$  B-X R(127) 11-5 transition at 632.8 nm, using a near-coincident  $I_2$  line (the  $i$ th hyperfine component of the  $^{127}I_2$  B-X R(73) 5-5 transition) as an intermediate reference.<sup>11</sup>

Systematic line shifts due to the discharge plasma were

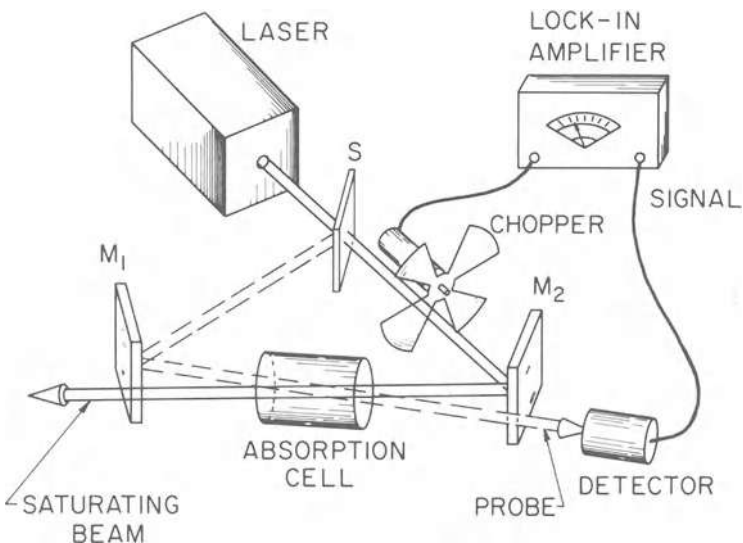


Fig. 1. Apparatus for Doppler-free saturated absorption spectroscopy of a gas sample.<sup>2</sup>

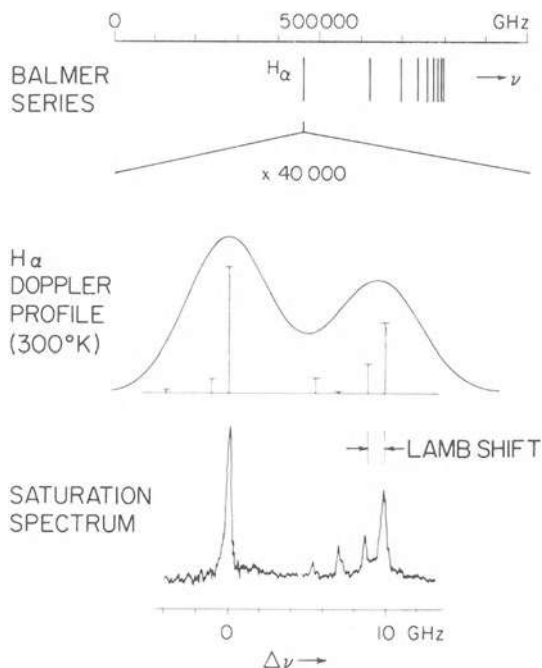


Fig. 2. Top: Balmer spectrum of atomic hydrogen. Center: Doppler-profile of the red Balmer- $\alpha$  line at room temperature and theoretical fine structure components. Bottom: Doppler-free spectrum of Balmer- $\alpha$ , recorded by saturated absorption spectroscopy with a pulsed dye laser.<sup>3,7</sup>

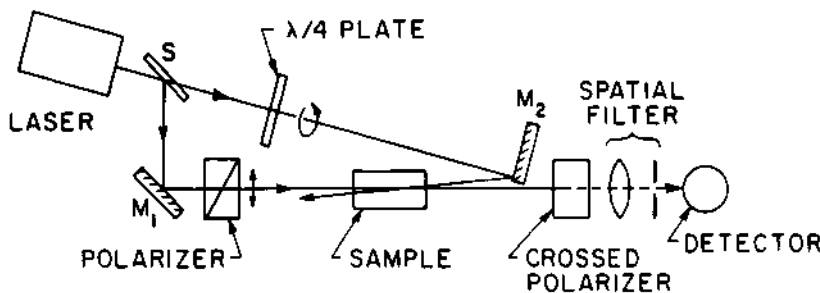


Fig. 3. Setup for Doppler-free polarization spectroscopy.<sup>8</sup>

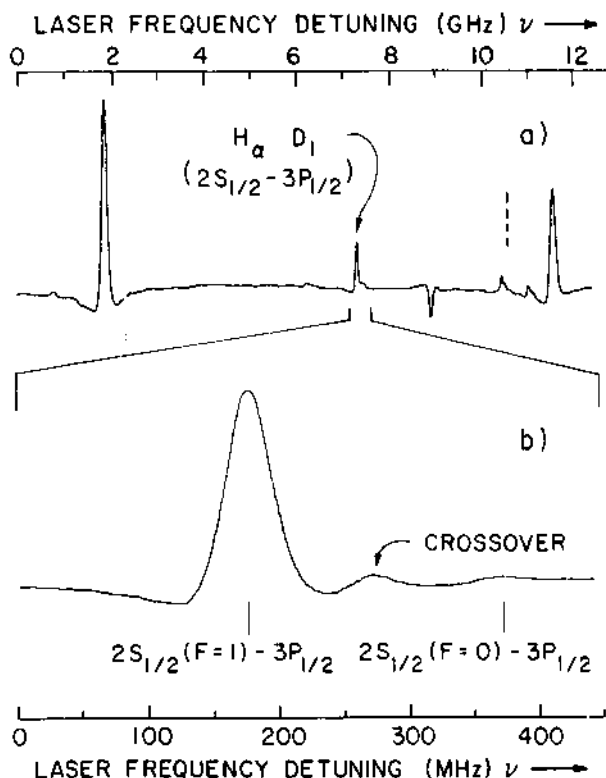


Fig. 4. Doppler-free polarization spectrum of the Balmer- $\alpha$  line, recorded with a cw dye laser in a mild He-H<sub>2</sub> discharge.<sup>10</sup>

studied very carefully in a series of measurements which yielded several results interesting in their own right.<sup>12,13</sup> For instance, anomalous pressure shifts have been observed which could be explained in terms of collisional decoupling of the 3P hyperfine structure.<sup>12</sup> The final evaluation of all measurements gave a threefold improvement in the accuracy of the Rydberg value. The results, as shown in Fig. 5, are in good agreement with the 1974 measurement. The values given in Table 1 have been slightly adjusted to be consistent with the rounded value of the iodine reference wavelength, 632.991 339 nm, as recommended by the Committee for the Definition of the Meter.<sup>14</sup>

Table 1 and Fig. 5 also give the results of an independent measurement of the Rydberg constant, reported in 1980 by B. W. Petley et al.<sup>15</sup> The Balmer- $\alpha$  line of hydrogen was observed in a Wood type gas discharge by saturated absorption spectroscopy with a cw dye laser. The result is in good agreement with the earlier Stanford values.

#### Laser Spectroscopy of an Atomic Beam

The accuracy of the best measurements in hydrogen discharges<sup>10</sup> does not appear to be limited by pressure shifts or Stark effect in the discharge plasma. Nonetheless, it has long been obvious that a collisionless beam of metastable hydrogen atoms would be a more ideal sample for precision laser spectroscopy.<sup>7</sup>

S. R. Amin et al. of Yale University are the first who have succeeded with such an atomic beam experiment, and they have reported very recently on a new Rydberg measurement.<sup>16</sup> The Balmer- $\alpha$  line of hydrogen and deuterium is observed by exciting the metastable 2S ( $F=1$ ) atoms with cw dye laser beams which cross the atomic beam at a right angle. Most of the excited 3P atoms quickly decay into the 1S ground state, and the resulting quenching of the 2S state can be observed with a detector for metastable atoms, just as in the classical Lamb Rutherford experiment.<sup>17</sup> Such linear atomic beam spectroscopy requires fewer systematic corrections than nonlinear saturation spectroscopy, and a wavelength measurement by direct comparison with an iodine stabilized He-Ne laser has yielded a new Rydberg value accurate to one part in  $10^9$ , as shown in Table 1 and Fig. 5.

Although the accuracy of linear laser spectroscopy of a metastable hydrogen beam appears amenable to further improvements, the resolution of the narrowest Balmer- $\alpha$  components will always be limited by the short lifetime of the upper 3P state to no better than 29 MHz.

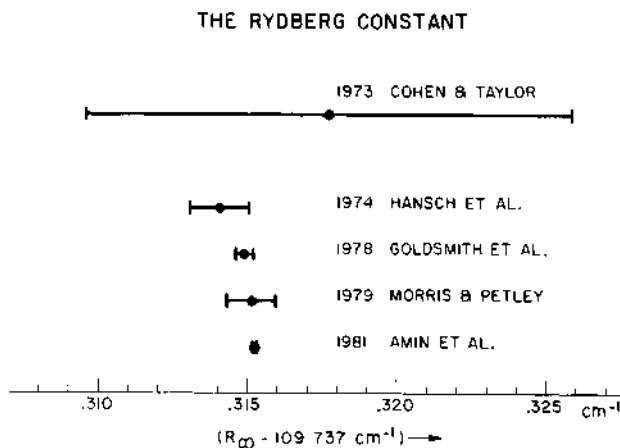


Fig. 5. Recent measurements of the Rydberg constant.

Table 1. Measurements of the Rydberg Constant

|    |                                                | $R_{\infty}$ [ cm <sup>-1</sup> ] |
|----|------------------------------------------------|-----------------------------------|
| 73 | COHEN, TAYLOR (6)                              | 109 737.317 70 ± 0.008 30         |
| 74 | HANSCH<br>NAYFEH, LEE,<br>CURRY,<br>SHAHIN (7) | 109 737.314 10 ± 0.001 00         |
| 78 | GOLDSMITH,<br>WEBER,<br>HANSCH (10)            | 109 737.314 90 ± 0.000 32         |
| 79 | PETLEY,<br>MORRIS,<br>SHAWYER (15)             | 109 737.315 13 ± 0.000 85         |
| 81 | AMIN,<br>CALDWELL,<br>LICHEN (16)              | 109 737.315 21 ± 0.000 11         |

Radiofrequency-Optical Double-Quantum Spectroscopy

D. E. Roberts and E. N. Fortson<sup>18</sup> were the first to point out that narrower lines can be obtained if an additional radiofrequency field is applied so that radiofrequency optical double quantum transitions are induced from the  $2S_{1/2}$  level to the longer living  $3S_{1/2}$  and  $3D_{1/2}$  level. E. W. Weber and J. E. M. Goldsmith<sup>19</sup> have observed lines as narrow as 20 MHz by applying this technique to hydrogen atoms in a gas discharge, and they have been able to measure the small  $3P_{3/2} - 3D_{3/2}$  Lamb shift directly by comparing single- and double-quantum signals. C. E. Wieman and collaborators<sup>20</sup> have recently begun to apply the same technique to a beam of metastable hydrogen atoms, and they expect to reach a resolution better than 1 MHz, corresponding to the natural width of the  $3S$  level.

Doppler-Free Two-Photon Spectroscopy

The same narrow lines could also be observed by excitation with two laser photons of equal frequency. If the two photons come from opposite directions (Fig. 6), first order Doppler broadening is automatically eliminated without any need to select slow atoms, because from a moving atom the two photons have equal but opposite Doppler shifts, so that their sum-frequency is constant.<sup>21</sup> Although Doppler-free two-photon excitation has become a widely used technique of high resolution laser spectroscopy,<sup>22</sup> its application to the Balmer- $\alpha$  transition has so far been stifled by the lack of a suitable highly monochromatic tunable lasers in the near infrared. But visible dye lasers should make it possible to study transitions from  $2S$  to high Rydberg levels by this technique.

TWO-PHOTON SPECTROSCOPY OF HYDROGEN  $1S-2S$ 

There is another, even more intriguing transition in hydrogen which can be studied by Doppler-free two-photon spectroscopy: the transition from the  $1S$  ground state to the metastable  $2S$  state. The  $1/7$  sec lifetime of the upper level implies an ultimate natural linewidth as narrow as 1 Hz or a spectral resolution better than 1 part in  $10^{15}$ .

There is no intermediate near resonant level which would enhance the two-photon transition rate. However, even small numbers of excited  $2S$  hydrogen atoms can be detected with high sensitivity, by monitoring the vacuum ultraviolet Lyman- $\alpha$  radiation emitted after conversion to the  $2P$  state by collisions or external fields, or by photoionizing the  $2S$  atoms and observing charged particles.

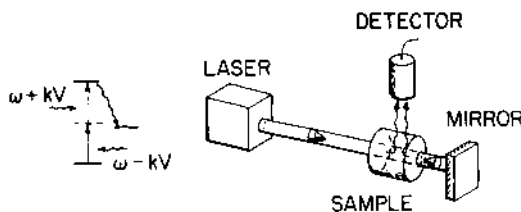


Fig. 6. Scheme of Doppler-free two-photon spectroscopy.<sup>21</sup>

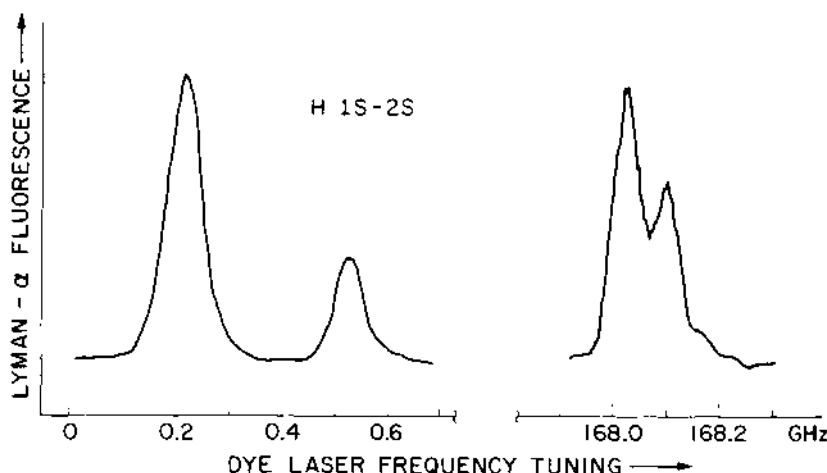


Fig. 7. Doppler-free two-photon spectrum of the 1S-2S transition in hydrogen and deuterium with resolved hyperfine splitting.<sup>25</sup>

Unfortunately, however, two-photon excitation of 1S-2S requires monochromatic ultraviolet radiation near 243 nm, where there are still no good tunable laser sources available. Intense coherent radiation at this wavelength can be generated by frequency doubling of a pulsed dye laser in a nonlinear optical crystal, and 1S-2S two-photon spectra have been observed at Stanford with such sources.<sup>23-25</sup> But the resolution remained limited by the large bandwidth of the pulsed lasers.

### Spectroscopy with Pulsed Lasers

The best 1S-2S spectra so far have been recorded by C. E. Wieman,<sup>25</sup> who reached a resolution of 120 MHz (fwhm at 243 nm) with the help of a blue single mode cw dye laser oscillator with nitrogen-pumped pulsed dye laser amplifier chain and lithium niobate frequency doubler. The hydrogen atoms were generated in a Wood type discharge tube and carried by gas flow and diffusion into the observation chamber, where they were excited by two counterpropagating beams from the laser system. The emitted vacuum ultraviolet Lyman- $\alpha$  photons were observed through a magnesium fluoride side window by a photomultiplier. Although the spectral resolution remained short of the envisioned ultimate limit by a factor of 100 million, it was sufficient to resolve the hyperfine doublets (Fig. 7). And even these crude spectra permitted a measurement of the 611 GHz H-D isotope shift to within 6.3 MHz and provided a first qualitative confirmation of the predicted small 11.9 MHz relativistic correction due to nuclear recoil.<sup>25</sup>

In the same series of experiments,<sup>23-25</sup> the 1S-2S energy interval was compared with the n=2-4 interval, by simultaneously observing the Balmer- $\beta$  line with the visible dye laser output. If the simple Bohr theory were correct, the n=1-2 interval would be exactly four times the n=2-4 interval, and both transitions would be observed at exactly the same laser frequency. In reality, this degeneracy is lifted by relativistic and quantum electrodynamic corrections, and we expect line splittings and displacements as illustrated in Fig. 8. By measuring the separation of the 1S-2S resonance from one of the Balmer components, one can determine an experimental value of the Lamb shift of the 1S ground state, which cannot be measured by radiofrequency techniques, because there is no 1P state which could serve as a reference.

In the most recent Stanford experiments<sup>25</sup> the predicted  $8149.43 + 0.08$  MHz Lamb shift of the hydrogen 1S state has been confirmed within 0.4%, by comparing the 1S-2S spectrum with a polarization spectrum of the Balmer- $\beta$  line, observed with the cw dye laser output in a Wood type gas discharge. The uncertainty in this

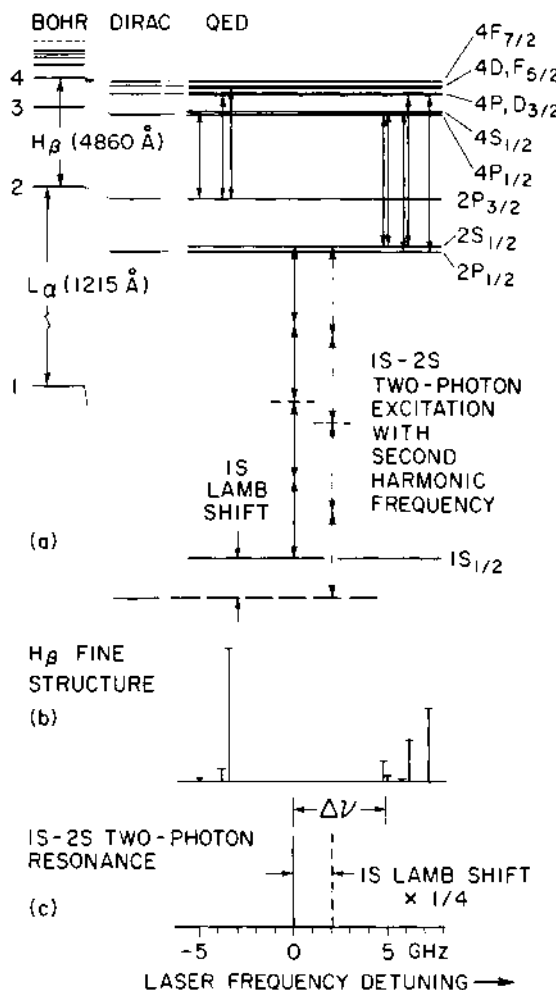


Fig. 8. Top: Simplified diagram of hydrogen energy levels and transitions. The Dirac fine structure and QED corrections are shown on an enlarged scale, hyperfine structure has been ignored. Bottom: Fine structure spectrum of the Balmer- $\beta$  line and relative position of the 1S-2S two-photon resonance, as recorded with the second harmonic frequency. The dashed line gives the hypothetical position of the 1S-2S resonance if there were no 1S shift.

experiment was dominated by laser frequency shifts due to rapid refractive index changes in the pulsed dye amplifiers. Such chirping introduces unknown phase parameters into the calculation of the line-shape of the two photon signals. Pressure shifts of the Balmer- $\beta$  spectrum were the next largest source of error. Both problems can be overcome with mere technical improvements, and the intrinsic narrow natural linewidths of the observed transitions make it appear likely that measurements of the 1S Lamb shift will eventually reach a higher accuracy than radiofrequency measurements of the 2S Lamb shift.<sup>26</sup> The latter provide one of the current most stringent low-energy tests of quantum electrodynamics, but they are plagued by a 100 MHz natural linewidth due to the short lifetime of the 2P state. And persisting discrepancies between experiment and the predictions of different computational approaches<sup>27,28</sup> make further accurate Lamb shift measurements highly desirable.

#### Envisioned CW Two-Photon Spectroscopy of 1S-2S

In order to avoid the limitations of a pulsed laser source, A. I. Ferguson, J. E. M. Goldsmith, B. Couillaud, A. Siegel, J. E. Lawler and other collaborators at Stanford have invested considerable efforts into an experiment designed to observe the hydrogen 1S-2S two-photon transition with low power continuous wave ultraviolet radiation. While known nonlinear optical crystals do not permit efficient 90 degrees phase matched second harmonic generation down to 243 nm, cw ultraviolet radiation at this wavelength can be produced as the sum frequency of a blue krypton ion laser and a yellow rhodamine 6G dye laser in a crystal of ammonium dihydrogen phosphate (ADP), cooled close to liquid nitrogen temperature.<sup>29</sup> With frequency stabilized single frequency lasers of 0.6 and 2.5 watts power, respectively, focused to a waist diameter of 100  $\mu\text{m}$  inside a 5 cm long ADP crystal, about 700  $\mu\text{W}$  of tunable cw ultraviolet power have been produced. A frequency locked external passive enhancement cavity increases this power to several mW at the sample. Such a power should be sufficient for a resonant signal of several hundred Lyman- $\alpha$  photons per second under the chosen experimental conditions.

Unfortunately, however, the ADP crystal is damaged within less than a minute under these conditions. We speculate that the ultraviolet light produces color centers, perhaps associated with heavy ion impurities, and that these centers then absorb enough of the intense primary beams to damage the crystal. We are presently investigating whether mixing of more widely separated primary wavelengths in ADP near room temperature can provide a cure for this problem, and we are actively pursuing alternative approaches. Once the damage problem is solved, it should be possible reduce the bandwidth of such a cw ultraviolet source to a few kHz with the help of fast servo controls.

However, other causes of line broadening, in particular pressure broadening, transit broadening, and transverse Doppler broadening have to be overcome before such a resolution can be approached in the 1S-2S two-photon spectrum.<sup>29</sup> A beam of ground state hydrogen atoms, cooled close to liquid helium temperature, and interacting with nearly collinear counterpropagating laser beams could minimize such problems, and it appears technically quite feasible to observe the 1S-2S two-photon transition with a line width of a few tens of kHz, or a resolution approaching one part in  $10^{11}$ . The line center could then be determined to within 1 part in  $10^{13}$  or better, once accurate frequency standards become available in the visible and ultraviolet region.

Such a precise measurement of the 1S-2S frequency could, of course, be used to determine a still better value of the Rydberg constant. However, the current uncertainty of the electron/proton mass ratio<sup>31</sup> (about 0.14 ppm) limits the accuracy of such a Rydberg value to about 1 part in  $10^{10}$ . Considerable improvements of direct measurements of the electron/proton mass ratio have been predicted.<sup>31</sup> Alternatively, a better mass ratio could be determined from a precision measurement of the 611 GHz H-D isotope shift of the 1S-2S frequency. However, uncertainties of the fine structure constant and of the mean square radii of the nuclear charge distributions would still impose error limits of about 4 parts in  $10^{11}$  for the Rydberg.

If the electron/proton mass ratio and the fine structure constant can be measured independently with improved accuracy, then a precise measurement of the 1S-2S H-D isotope shift could provide an accurate probe for nuclear structure and recoil shifts.

To determine a precise Rydberg value that is not limited by nuclear structure corrections, one could combine the 1S-2S measurement with a precise measurement of a two-photon transition from 2S to one of the higher nS levels. Taking advantage of the fact that the lowest order nuclear structure corrections scale with the inverse cube of the principal quantum number n, one can easily construct differences of transition frequencies which are no longer sensitive to the exact nuclear sizes.

Obviously, neither a measurement of the 1S-2S frequency nor of the isotope shift by itself can provide a very stringent test of quantum electrodynamics, because we are free to adjust the values of fundamental constants until the calculations agree with the observations. However, if we form the ratio of the 1S-2S frequency to the frequency of a different hydrogenic transition, such as a Balmer transition, or a transition to or between Rydberg states, we arrive at a dimensionless quantity, which, to lowest order, no longer depends on the Rydberg constant, and which can be calculated with very high precision. An accurate measurement of such a

frequency ratio would permit a very interesting test of theory. In this way, one might detect, for instance, some small deviations from Coulomb's law, which may exist within atomic dimensions, but which may have escaped detection in the past.

## TWO-PHOTON SPECTROSCOPY OF POSITRONIUM 1S-2S

The observation of the hydrogen 1S-2S interval by Doppler-free two-photon spectroscopy suggests that a similar experiment should be possible for positronium. In principle, this simplest, purely leptonic atom could provide an even more ideal testing ground for quantum electrodynamic theory, because calculations do not involve large nuclear structure correction.

On the other hand, this relativistic two-body system can no longer be closely approximated by the Dirac equation, describing an electron of reduced mass in a fixed Coulomb potential. Instead, one has to resort to the more general Breit equation, which cannot be solved in closed form. And although numerical computations of the optical energy intervals in positronium are certainly possible, they have not yet been carried out with a precision comparable to that for hydrogen.

However, the main obstacles are experimental ones. The rapid annihilation even of orthopositronium makes it difficult to produce a sufficient number of slow positronium atoms, despite recent considerable improvements in conversion techniques.<sup>32,33</sup> And although the envisioned experiment requires only visible laser radiation with a wavelength near 486 nm, the intensities would have to be on the order of 10 to 100 MW/cm<sup>2</sup> to ensure the excitation of a positronium atom during its short annihilation lifetime. Unfortunately, there exist still no tunable lasers which can produce such intensities with good duty cycle. A typical Nd:YAG pumped pulsed dye laser system has a duty cycle of only 10<sup>-7</sup>. And although it appears possible to detect the excitation of a positronium atom with near 100% efficiency, by observing the subsequent photoionization in the intense radiation field, it appears difficult to reach final count rates of more than a few per minute, even if one starts with a radioactive positron source of 100 Curies. Somewhat higher count rates should be achievable with clever storage and bunching techniques, or with an accelerator-based pulsed positron source.

Another serious difficulty is the expected line broadening due to the relativistic transverse Doppler effect, which is not cancelled in the excitation with counterpropagating beams. Most converters produce positronium atoms with kinetic energies of a sizeable fraction of 1 eV, and the corresponding transverse Doppler shifts would be on the order of 1 GHz. Recently introduced surface

converters<sup>32</sup> can produce positronium of thermal or even subthermal energies, and could alleviate this problem. However, the rapid photoionization of the 2S state in the intense laser field would still produce substantial line broadening, and it will be very difficult to approach the 1 MHz natural linewidth of the positronium 1S-2S transition, as limited by the annihilation of the ground state.

In summary, it does not appear likely that positronium will soon compete with hydrogen as a testing ground for quantum electrodynamics by precision laser spectroscopy. On the other hand, even a relatively poor resolution of the positronium 1S-2S transition would permit a welcome test of the theory of relativistic two-body systems.

This work was supported by the National Science Foundation under Grant PHY80-10689, and by the U.S. Office of Naval Research under Contract ONR N00014-78-C-0403.

#### REFERENCES

1. T. W. Hänsch, G. W. Series, and A. L. Schawlow, *Scientific American* 240, 94 (1979).
2. T. W. Hänsch, *Applied Optics* 11, 895 (1972).
3. T. W. Hänsch, I. S. Shahin, and A. L. Schawlow, *Nature* 235, 63 (1972).
4. J. D. Garcia and J. E. Mack, *J. Opt. Soc. Am.* 55, 654 (1965).
5. G. Erickson, *J. Chem. Phys. Ref. Data* 6, 831 (1977).
6. E. R. Cohen and B. N. Taylor, *J. Phys. and Chem. Ref. Data* 2, 663 (1973).
7. T. W. Hänsch, M. H. Nayfeh, S. A. Lee, S. M. Curry, and I. S. Shahin, *Phys. Rev. Letters* 32, 1336 (1974).
8. C. E. Wieman and T. W. Hänsch, *Phys. Rev. Letters* 36, 1170 (1976).
9. R. K. Raj, P. Bloch, J. J. Snyder, G. Camy, and M. Ducloy, *Phys. Rev. Letters* 44, 1251 (1980).
10. J. E. M. Goldsmith, E. W. Weber, and T. W. Hänsch, *Phys. Rev. Letters* 41, 940 (1978).
11. J. E. M. Goldsmith, E. W. Weber, F. V. Kowalski, and A. L. Schawlow, *Applied Optics* 18, 1983 (1979).
12. E. W. Weber and J. E. M. Goldsmith, *Physics Letters* 70A, 95 (1979).
13. E. W. Weber, *Phys. Rev. A* 20, 2278 (1979).
14. Comité Consultatif pour la Définition du Mètre, 5e Session - 1973, Bureau International des Poids et Mesures, p. M23.
15. B. W. Petley, K. Morris, and R. E. Shawyer, *J. Phys. B: Atom. Molec. Phys.* 13, 3099 (1980).
16. S. R. Amin, C. D. Caldwell, and W. Lichten, *Phys. Rev. Letters* (to be published).

17. W. E. Lamb and R. C. Rutherford, Phys. Rev. 79, 549 (1950).
18. D. E. Roberts and E. N. Fortson, Phys. Rev. Letters 31, 1539 (1973).
19. E. W. Weber and J. E. M. Goldsmith, Phys. Rev. Letters 41 940 (1978).
21. L. S. Vasilenko, V. P. Chebotaev, and A. V. Shishaev, JETP Letters 12, 113 (1971).
22. N. Bloembergen and M. D. Levenson, in *High Resolution Laser Spectroscopy*, K. Shimoda, ed. (Topics in Applied Physics, Vol 13), Springer-Verlag, Berlin, Heidelberg, New York (1976), pp. 315.
23. T. W. Hänsch, S. A. Lee, R. Wallenstein, and C. E. Wieman, Phys. Rev. Letters 34, 307 (1975).
24. S. A. Lee, R. Wallenstein, and T. W. Hänsch, Phys. Rev. Letters 35, 1262 (1975).
25. C. E. Wieman and T. W. Hänsch, Phys. Rev. A22, 192 (1980).
26. S. R. Lundeen and F. M. Pipkin, Phys. Rev. Letters 46, 232 (1981).
27. G. W. Erickson, Phys. Rev. Letters 27, 780 (1971).
28. P. J. Mohr, Phys. Rev. Letters 34, 1050 (1975).
29. A. I. Ferguson, J. E. M. Goldsmith, T. W. Hänsch, and E. W. Weber, in *Laser Spectroscopy IV*, H. Walther and K. W. Rothe, eds. (Springer Series in Optical Sciences, Vol. 21) Springer-Verlag, Berlin, Heidelberg, New York (1979), pp. 31.
30. S. B. Crampton, T. J. Greytag, D. Kleppner, W. D. Phillips, D. A. Smith, and A. Weinrib, Phys. Rev. Letters 42, 1039 (1979).
31. R. S. Van Dyck, Jr., and P. B. Schwinberg, Phys. Rev. Letters 47, 395 (1981).
32. A. P. Mills and L. Pfeiffer, Phys. Rev. Letters 43, 1061 (1979).
33. A. P. Mills, J. Appl. Phys. 22, 1 (1980).

## NON-LINEAR VACUUM POLARIZATION IN STRONG FIELDS

M. Gyulassy

Nuclear Science Division  
Lawrence Berkeley Laboratory  
University of California  
Berkeley, CA 94720

### INTRODUCTION

A particularly interesting consequence of the Dirac equation and hole theory is the phenomenon of spontaneous  $e^+e^-$  pair creation in strong static electric fields<sup>1-3</sup>. Normally, pair creation in a static field costs energy,  $\Delta E = 2m_e - B$ , where  $B$  is the binding energy of the electron. Consequently, spontaneous pair creation is normally a virtual process lasting only a short time,  $\Delta\tau \sim 1/\Delta E \sim (2m_e - B)^{-1}$ . This virtual process is called vacuum polarization in Quantum Electrodynamics (QED). However, if the external fields become so strong that  $B \rightarrow 2m_e$ , then  $\Delta\tau \rightarrow \infty$ , and the virtual pair can "materialize". In terms of QED this would be called real or on-shell vacuum polarization.

The necessary condition ( $B > 2m_e$ ) for real vacuum polarization has been estimated<sup>1-3</sup> to occur for very high nuclear charges  $Z > Z_c \approx 175$ . This range of  $Z$  is fortunately accessible via heavy ion collisions. In such high fields  $Z\alpha > 1$  and relativistic non-linear effects are important.

While in the Dirac equation it is formally possible to increase  $Z$  indefinitely (for finite size nuclei), it is not clear a priori whether a full QED calculation allows arbitrary large fields and bindings. In particular, it could be that radiative corrections such as self-energy and vacuum polarization effects could increase so rapidly with  $Z$  that the diving condition,  $B = 2m_e$ , is significantly delayed or even prevented.

Even classically it could be that non-linear effects, unobserved in low field ( $Z < 100$ ) experiments, could become important in the strong field limit  $Z \rightarrow Z_c$ . As an example of non-linear electrodynamics Rafelski, et al.<sup>4</sup> applied the Born-Infeld<sup>5</sup> Lagrangian to calculate  $B(Z)$ . In that theory there is an upper bound of  $E_{BI} = 1.2 \times 10^{18}$  V/cm on the electric field strength. While the non-linearities do not prevent  $B$  from reaching  $2m_e$ , the critical charge was shifted to  $Z_c > 200$ , beyond the range accessible via heavy ion collisions. Later, Soff et al.<sup>6</sup> showed that high precision experiments on muonic atoms require a lower bound on the maximum field strength  $E^* > 100 E_{BI}$ . In that case, classical non-linear effects could change  $Z_c$  by at most a few units. Therefore, this type of classical non-linear electrodynamics cannot prevent diving.

On the other hand, the QED calculations of Wichmann and Kroll<sup>7</sup> showed that non-linear vacuum polarization screening has a singular derivative with respect to  $Z$  at  $Z = 137$ . This singularity was due to the assumed point nuclear charge distribution. Nevertheless, it indicated that vacuum polarization screening could be expected to grow rapidly with  $Z$  beyond 137 when finite nuclear size effects are taken into account. In this review, I focus on this aspect of non-linear vacuum polarization in strong fields. The basic question addressed is whether virtual pair creation (vacuum polarization) can screen the nuclear charge sufficiently to prevent real vacuum polarization (spontaneous  $e^+e^-$  production). As I show below, the answer is no.

The remainder of this review is organized as follows: The Wichmann-Kroll formalism for calculating the vacuum polarization density to first order in  $\alpha$  but to all orders in  $Z\alpha$  is derived. The most essential quantity is shown to be the electrons Green's function in these calculations. The method of constructing that Green's function in the field of finite radius nuclei is then presented.

Comparing the calculations with data on muonic atoms shows good agreement with data and gives us confidence in extending the calculations beyond  $Z = 137$ . The  $1S_{1/2}$  shift is then calculated as  $Z \rightarrow Z_c$ . The main result is that the screening due to non-linear vacuum polarization remains small all the way up to  $Z_c$ . In terms of an effective screening charge,  $Q_{eff}$ , the vacuum screens the nuclear charge by only  $Q_{eff} \approx e/20$  at  $Z_c \approx 175$ . Therefore, vacuum polarization cannot prevent diving and is nonsingular in the strong field limit. Finally, it is shown that the charge density of the overcritical vacuum ( $Z > Z_c$ ) is highly localized and represents the smooth continuation of the He-like charge density for  $Z < Z_c$ .

## WICHMANN-KROLL FORMALISM

The first step is to write the vacuum polarization charge density as

$$\rho_{VP}(x) = -\frac{|e|}{2} \langle 0 | [\psi^\dagger(x), \psi(x)] | 0 \rangle , \quad (1)$$

where  $\psi$  is the electron field operator and  $|0\rangle$  is the vacuum state. It is necessary to write the commutator of  $\psi^\dagger$  and  $\psi$  to insure correct charge conjugation properties. In general,  $\psi(x)$  and the photon field  $A_\mu(x)$  satisfy coupled Dirac and Maxwell field equations. However, in order to calculate the vacuum polarization density to lowest order  $\alpha$  but to all orders in  $Z\alpha$ , it is possible to decouple these equations. To lowest order in  $\alpha$ ,  $\psi(x)$  satisfies the Dirac equation

$$(i\vec{\sigma} - Z\alpha V(r)\gamma_0 - m_e) \psi(x) = 0 , \quad (2)$$

with the external c-number field  $A_{ex}^\mu = \delta\mu_0 Ze V(r)$  satisfying the classical Maxwell equations  $\nabla^2 V = -\rho_{ex}$ . To solve eq. (2),  $\psi(x)$  can be expanded in terms of the complete set of positive and negative energy eigenfunctions,  $\psi_E(x)$ , of the Dirac equation

$$\psi(x) = \sum_{E>E_F} \psi_E(x) b_E + \sum_{E<E_F} \psi_E(x) d_E^+ , \quad (3)$$

with  $b_E$  and  $d_E$  being the anticommuting destruction operators of electrons and positrons. The sum over spin projections is implicit in eq. (3). Also  $E_F$  is the Fermi energy,  $-m_e < E_F < m_e - B(1S_{1/2})$ . Equation (3) defines the Furry bound interaction picture. We can now evaluate eq. (1) giving

$$\rho_{VP}(x) = \frac{|e|}{2} \left\{ \sum_{E>E_F} |\psi_E(x)|^2 - \sum_{E<E_F} |\psi_E(x)|^2 \right\} . \quad (4)$$

As  $Z \rightarrow 0$ ,  $\rho_{VP} \rightarrow 0$  due to the symmetry between positive and negative energy plane wave solutions.

The main trick in the Wichmann-Kroll approach is to calculate  $|\psi(x)|^2$  from the residues of the electron Green's function. Observe that

$$G(x, y; \omega) = \sum_E \frac{\psi_E(x) \psi_E^\dagger(y)}{E - \omega} \quad (5)$$

is a solution to the equation

$$(H_x - \omega)G(x, y; \omega) = \delta^3(x - y) \quad (6)$$

with  $H_x = -i\alpha \cdot \nabla + \beta m_e + V(r)$ , because  $\{\psi_E(x)\}$  form a complete set of solutions of the Dirac equation,  $(H - E)\psi_E = 0$ . For an isolated pole of  $G$ , it is obvious from eq. (5) that

$$|\psi_E(x)|^2 = - \operatorname{Res}_{\omega=E} \operatorname{Tr} G(x, x; \omega) \\ = \int_{C_E} \frac{d\omega}{2\pi i} \operatorname{Tr} G(x, x; \omega) \quad , \quad (7)$$

where  $C_E$  is a clockwise contour around  $E$ . Therefore, we can express the vacuum polarization density from eq. (4) as

$$\rho_{VP}(x) = \frac{|e|}{2} \left\{ \int_{C_+} + \int_{C_-} \right\} \frac{d\omega}{2\pi i} \operatorname{Tr} G(x, x; \omega) \quad , \quad (8)$$

where the contour  $C_+$  goes clockwise around all the positive energy singularities of  $G$  and where  $C_-$  goes counter-clockwise around all the negative energy singularities. Noting that  $G$  has no singularities away from the real  $\omega$  axis, these contours can be rotated for convenience so that  $1/2(C_+ + C_-) = C_F$ , where the Feynman contour  $C_F$  is illustrated in Fig. 1.

We obtain finally the contour integral representation of  $\rho_{VP}$  as

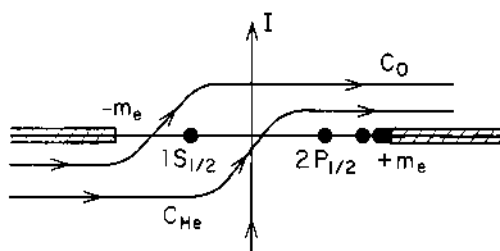


Fig. 1. Singularities of Green's function in complex energy plane. Contour  $C_0 = C_F$  in eq. (9) and  $C_{He}$  is for eq. (31).

$$\rho_{\text{vp}}(x) = |e| \int_{C_F} \frac{d\omega}{2\pi i} \text{Tr} G(x, x; \omega) \\ = i|e| \text{Tr}(S_F(x, x') \gamma_0) \Big|_{x' \rightarrow x} , \quad (9)$$

where  $iS_F(x, x') = \langle 0 | T(\psi(x)\bar{\psi}(x')) | 0 \rangle$  is the familiar Feynman propagator<sup>9</sup>. What has been accomplished by rotating the contours into  $C_F$  is a relation between  $\rho_{\text{vp}}$  and the equal time-equal space point value of the Feynman propagator. This is useful because we know how to draw Feynman diagrams for  $S_F(x, x')$  and consequently we obtain a diagrammatic expansion of  $\rho_{\text{vp}}(x)$ :

$$\rho_{\text{vp}}(x) = \text{---} x + \text{---} x + \text{---} x + \dots \quad (10)$$

where  $\text{---}$  is the diagram corresponding to the amplitude to propagate an electron from  $x'$  to  $x$  in the absence of interactions. Thus,  $\rho_{\text{vp}}(x)$  can be pictured as a "besoffenes" electron that staggers from point  $x$  back to  $x$  occasionally drinking (---) "einen Schluck edlen Rheinweins".

Because the trace of an odd number of  $\gamma_\mu$  matrices vanishes, only terms with an odd number of external interactions (or Schluck) survive [note the extra  $\gamma_0$  at the point  $x$  from eq. (9)]. This is Furry's theorem, which guarantees that only odd powers of  $Z\alpha$  occur in the expansion of  $\rho_{\text{vp}}$ .

$$\rho_{\text{vp}}(x) = Z\alpha \rho_1 + (Z\alpha)^3 \rho_3 + \dots \quad (11)$$

Having a diagrammatic expansion of  $\rho_{\text{vp}}$  we can see that not all diagrams are free from ambiguity. In particular, the first order diagram diverges quadratically since the internal loop integration,  $\int d^4 p \text{Tr}[\gamma_0 S_F(p) \gamma_0 S_F(p + q)]$ , behaves in the ultraviolet limit as  $\int d^4 p / p^2 \rightarrow \infty^2$ . Actually, if we look in more detail (see Bjorken and Drell<sup>9</sup>, for example) imposing gauge invariance reduces the degree of divergence such that  $\rho_1 \rightarrow \ln \infty$ . This remaining divergence can be removed because it merely renormalizes the bare nuclear charge,  $Z\alpha \rho_{\text{ex}}^{\text{bare}}$ . To see this it is convenient to regulate the expression for  $\rho_1$  according to the Pauli-Villars method<sup>9</sup>

$$\rho_1^{\text{reg}} = \lim_{M \rightarrow \infty} [\rho_1(m_e) - \rho_1(M)] , \quad (12)$$

In eq. (12)  $\rho_1(M)$  corresponds to the first order diagram with the electron mass replaced by  $M$ . The regulated first order density in momentum space is then found to be<sup>9</sup>

$$Z_{\alpha p}^{\text{reg}}(q) = Z_{\alpha p}^{\text{bare}}(q)$$

$$x \left\{ -\frac{\alpha}{3\pi} \log \frac{M^2}{m_e^2} + \frac{2\alpha}{\pi} \int_0^1 dx \, x(1-x) \log \left[ 1 + \frac{q^2 x(1-x)}{m_e^2} \right] \right\}. \quad (13)$$

The total charge density to order  $\alpha(Z\alpha)$  is then

$$Z_{\alpha p}^{\text{ex}}(q) = Z_{\alpha p}^{\text{bare}}(q) + Z_{\alpha p}^{\text{reg}}(q) . \quad (14)$$

We now see that the  $\log M^2$  term in eq. (13) simply rescales the bare nuclear charge density. The sign of this effect is in accord with our intuition that vacuum polarization should screen the nuclear charge. The second term vanishes in the  $q \rightarrow 0$  limit, which implies that it contains no net charge. This second term is the finite physical part of the first order (Uehling) VP density. It is interesting to note the famous "asymptotic slavery" property of QED in eq. (14). As  $q^2 \rightarrow \infty$ ,

$$\rho_{\text{ex}}(q) \rightarrow \rho_{\text{ex}}^{\text{bare}}(q) \left\{ 1 - \frac{\alpha}{3\pi} \log \frac{M^2}{m_e^2} + \frac{\alpha}{3\pi} \log \frac{q^2}{m_e^2} \right\} . \quad (15)$$

Therefore, with increasing momentum transfers, corresponding to smaller  $r$ , the strength of the nuclear charge increases.

Expressed in coordinate space, Blomqvist<sup>10</sup> found the small  $r$  behavior of the screened nuclear potential to be

$$Z\alpha V(r) = -\frac{Z\alpha}{r} \left\{ 1 + \frac{2}{3} \left[ \log \frac{1}{m_e r} - 1.41 + 0(m_e r) \right] \right\} . \quad (16)$$

Equation (16) shows explicitly that the strength of the potential increases in the small  $r \ll \lambda_e$  limit. (For large  $r$ , the Uehling potential falls off exponentially.)

Having reviewed the first order  $\alpha(Z\alpha)$  part of the VP density, I turn next to the non-linear parts of order  $\alpha(Z\alpha)^{n-3}$ . From the diagrams in eq. (10), the ultraviolet behavior of the  $n$ th order density goes as  $\sim \int d^4 p / p^{n+1}$ . For order  $\alpha(Z\alpha)^{n-5}$  this is manifestly finite. For order  $\alpha(Z\alpha)^3$  it shows an apparent logarithmic divergence. However, gauge invariance eliminates this divergence and all higher order diagrams  $\alpha(Z\alpha)^{n-3}$  are finite and well behaved for bounded external potentials. Thus, only the first order diagram requires special care. Since we now know the analytic form of first order density, the higher order density can be calculated from eq. (9) simply by subtracting the first order Green's function.

In order to carry out this subtraction, it is convenient for spherically symmetric systems to expand the Green's function in eigenfunctions of the Dirac angular momentum  $K = \gamma_0(\mathbf{r} \cdot \mathbf{L} + 1)$ . The eigenvalues are  $k = \pm(j + 1/2)$  in terms of the total angular momentum  $j$ . Details of this expansion can be found in Ref. 11. For the trace needed in eq. (9), the expansion is particularly simple

$$\text{Tr } G(\mathbf{r}, \mathbf{r}; \omega) =$$

$$\sum_{j=1/2, 3/2, \dots} \frac{2j+1}{4\pi} \text{Tr} [G_{k=j+1/2}(\mathbf{r}, \mathbf{r}; \omega) + G_{k=-j-1/2}(\mathbf{r}, \mathbf{r}; \omega)], \quad (17)$$

where  $G_k(\mathbf{r}, \mathbf{r}'; \omega)$  is the radial Green's function, that satisfies<sup>11</sup>

$$\begin{bmatrix} m_e + V(r) - \omega & -\frac{1}{r} \frac{d}{dr} r + \frac{k}{r} \\ \frac{1}{r} \frac{d}{dr} r + \frac{k}{r} & m_e + V(r) - \omega \end{bmatrix} G_k(\mathbf{r}, \mathbf{r}'; \omega) = \frac{\delta(\mathbf{r} - \mathbf{r}')}{r r'}, \quad (18)$$

With eq. (17) we can now define the vacuum polarization density due to a particular angular momentum  $j$  as

$$\rho_j(\mathbf{r}) = |e| \frac{(2j+1)}{4\pi} \int_{C_F} \frac{d\omega}{2\pi i} \text{Tr} [G_{j+1/2}(\mathbf{r}, \mathbf{r}; \omega) + G_{-j-1/2}(\mathbf{r}, \mathbf{r}; \omega)]. \quad (19)$$

It is straightforward to show<sup>8c</sup> that  $\rho_j(\mathbf{r})$  is an odd function of  $Z\alpha$  as required by Furry's theorem.

Converting eq. (18) into an integral equation, the first order contribution for a given  $k$  is

$$\text{Tr } Z\alpha G_k^1(\mathbf{r}, \mathbf{r}; \omega) = Z\alpha \int_0^\infty dr' r'^2 V(r') \text{Tr} [G_k^0(\mathbf{r}, \mathbf{r}'; \omega) G_k^0(\mathbf{r}', \mathbf{r}; \omega)], \quad (20)$$

where  $G_k^0$  is the free space radial propagator involving spherical Bessel functions<sup>8,11</sup>.

Finally, the expression for the non-linear  $\alpha(Z\alpha)^{n-3}$  vacuum polarization density for a given  $j$  can be written as

$$\begin{aligned} \rho_j^{3+}(\mathbf{r}) = & |e| \frac{2j+1}{4\pi} \int_{C_F} \frac{d\omega}{2\pi i} \\ & \times \text{Tr} [G_{j+1/2}(\mathbf{r}, \mathbf{r}; \omega) + G_{-j-1/2}(\mathbf{r}, \mathbf{r}; \omega) - 2Z\alpha G_{j+1/2}^1(\mathbf{r}, \mathbf{r}, \omega)]. \end{aligned} \quad (21)$$

This expression is now finite and well behaved. In practical calculations, it is most convenient to rotate the  $C_F$  contour to the imaginary  $\omega$  axis.

The real power of the Wichmann-Kroll method lies in the ease with which the radial Green's functions can be constructed. The following theorem<sup>7</sup> is all we need: Let  $\psi_R(r)$  and  $\psi_I(r)$  be the regular and irregular solutions of the radial Dirac equation,  $(H - \omega)\psi = 0$ , where  $(H - \omega)$  is the matrix in eq. (18). The regular solution is that one which is integrable near  $r \rightarrow 0$ , while the irregular solution is the one which is integrable at  $r \rightarrow \infty$ . The Green's function is then

$$G_k(r, r'; \omega) = \frac{1}{W(\omega)} \left\{ \theta(r' - r) \psi_R(r) \psi_I^+(r') + \theta(r - r') \psi_I(r) \psi_R^+(r') \right\}, \quad (22)$$

where the  $W(\omega)$  is the Wronskian given by

$$W(\omega) = r^2 \left\{ \psi_{R2}(r) \psi_{I1}(r) - \psi_{R1}(r) \psi_{I2}(r) \right\}. \quad (23)$$

It is easy to verify that eq. (22) does satisfy eq. (18). For the trace needed in eq. (21),

$$\text{Tr } G_k(r, r; \omega) = \psi_I^+(r) \psi_R(r) / W(\omega). \quad (24)$$

An important example of the above construction is for the case of a pure Coulomb potential  $Z\alpha V(r) = -Z\alpha/r$ . The solutions<sup>8,11</sup> are  $\psi_R(r) = M(r)$  and  $\psi_I(r) = W(r)$ , where  $M$  involves linear combinations of regular Whittaker functions  $M_{v\pm 1/2, S}(2cr)$  and  $W$  involves linear combinations of the irregular Whittaker functions  $W_{v\pm 1/2, S}(2cr)$ .

The parameters on which  $M$  and  $W$  depend are  $S = \sqrt{k^2 - (Z\alpha)^2}$ ,  $c = \sqrt{m_e - \omega}$ , and  $v = Z\alpha\omega/c$ . Whittaker functions are related to confluent hypergeometric functions for which rapid, high precision numerical techniques are readily available<sup>11</sup>. The most important parameter in the case of strong fields ( $Z\alpha \gg 1$ ) is  $S = \sqrt{1 - (Z\alpha)^2}$  for  $k = +1$ ,  $j = 1/2$ , states. At  $Z\alpha = 1$ ,  $S$  and consequently  $M$  have a branch point as a function of  $Z\alpha$  for  $j = 1/2$ . Although it seems that  $W$  would also have a branch point at  $Z\alpha = 1$ ,  $W_{\alpha, S}$  is an even function of  $S$  and therefore nonsingular at  $Z\alpha = 1$ . It is the nonanalytic behavior of the  $M$  function that causes a singularity of  $\text{Tr } G_{k=+1}$  for this point nuclear charge case at  $Z\alpha = 1$ . Higher angular momentum states ( $j \geq 3/2$ ) are, on the other hand, well behaved near  $Z\alpha = 1$ . Therefore, to extend  $Z\alpha$  beyond 1, it is necessary to include finite size corrections for the  $j = 1/2$  contribution to the VP density. As we shall see, it is also sufficient to modify only the  $j = 1/2$  case.

In order to include finite nuclear size, a definite nuclear model must be adopted. The simplest finite size nuclear density is a shell distribution, for which  $V(r) = -1/R$  for  $r < R$  and  $V(r) = -1/r$  for  $r > R$ ,  $R$  being the nuclear radius. With this model it is possible to solve the problem analytically<sup>8</sup>. For  $r < R$ , the solutions are  $j(r)$  and  $h(r)$ , simply related to spherical Bessel functions. For  $r > R$ , the Coulomb  $M$  and  $W$  solutions apply. Continuity at  $r=R$  determines the particular linear combination of  $M$  and  $W$  that joins the interior  $j(r)$  solution giving the regular solution. Continuity at  $r=R$  also determines that linear combination of the  $j$  and  $h$  solutions that join the exterior  $W$  function that gives the irregular solution. With these solutions for finite nuclear systems, eq. (24) yields<sup>8</sup>

$$TrG_k(r, r; \omega) = \begin{cases} TrG_k^0(r, r; \omega + \frac{Z\alpha}{R}) + Tr\Delta G_k^<, & r < R \\ TrG_k^{Coul}(r, r; \omega) + Tr\Delta G_k^>, & r > R \end{cases}, \quad (25)$$

where  $G_k^0$  is the free radial Green's function,  $G_k^{Coul}$  is the point nucleus Coulomb Green's function, and  $\Delta G_k^{<(>)}$  are finite size correction functions. Explicit formulas are given in Ref. (8c). It is straightforward to show that  $TrG_k \rightarrow TrG_k^0$  if  $R \rightarrow \infty$ , while  $TrG_k \rightarrow TrG_k^{Coul}$  if  $R \rightarrow 0$ . Furthermore, for  $Z < 137$ , a useful analytic expression for  $\Delta G_k^>$  can be derived by setting the electron mass to zero<sup>12</sup>. With this approximation, the contour integration in eq. (19) for the  $Tr\Delta G_k^>$  part can be performed analytically. In this way, the finite size correction to the vacuum polarization potential is found to be<sup>12</sup>

$$\delta V(r) = \frac{\alpha(Z\alpha)}{15\pi r} \left( \frac{R}{r} \right)^{\sqrt{1-(Z\alpha)^2}} f[(Z\alpha)^2] \quad (26)$$

valid for  $r \gg R$  and  $Z\alpha \ll 1$ . Eq. (26) is particularly useful in computing finite size VP corrections for muonic atoms.

#### MUONIC ATOMS

High  $Z$  muonic atoms provide a good test of vacuum polarization since typical 4f, 5g muonic radii  $\sim 50$  fm, which satisfy  $R \ll a \ll \lambda_e$ . Hence, these orbits are insensitive to nuclear details but probe the structure of the vacuum polarization cloud. Furthermore, since  $m_\mu \gg m_e$  self-energy corrections are small. The example of muonic Pb is listed in table 1. The contributions to the energy levels were taken from the compilation in Ref. 13. The latest experimental results are in agreement with theory. Comparing the contribution  $\Delta E^{3+} = 45$  eV, due to

Table 1. Contributions<sup>13</sup> to Energy Levels in Muonic Pb (eV)

| Diagram                                                   | Order                           | $4f_{7/2}$ | $5g_{9/2}$ |
|-----------------------------------------------------------|---------------------------------|------------|------------|
| 1.                                                        | $\alpha^0 (Z\alpha)^{n \geq 1}$ | -1188318   | -758970    |
| 2.                                                        | $\alpha^1 (Z\alpha)^1$          | -3664      | -1565      |
| 3.                                                        | $\alpha^1 (Z\alpha)^{n \geq 3}$ | +104       | +59        |
| 4.                                                        | $\alpha^1 (Z\alpha)^{n \geq 1}$ | +10        | +3         |
| 5.                                                        | $\alpha^2 (Z\alpha)^1$          | -25        | -11        |
| 6.                                                        | $\alpha^2 (Z\alpha)^2$          | -9         | -3         |
| 7.                                                        | $\alpha^2 (Z\alpha)^2$          | -1         | 0          |
| 8. Nuclear + Atomic Effect                                |                                 | -97        | -173       |
| $\Delta E(5g_{9/2} - 4f_{7/2}) = 431,332 \pm 5$ eV theory |                                 |            |            |
| $431,331 \pm 8$ eV Dubler, et al. <sup>14</sup>           |                                 |            |            |
| $431,360 \pm 11$ eV Tauscher, et al. <sup>15</sup>        |                                 |            |            |

non-linear vacuum polarization (line 3) with the experimental uncertainties ( $\pm 10$  eV), we can say that the current experiments test and confirm non-linear vacuum polarization effects at the level of  $\sim 20\%$ . Encouraged by this success, we now push the theory beyond  $Z=137$  up to  $Z_c$ .

NON-LINEAR SCREENING AS  $Z \rightarrow Z_c$ 

For a point charge, Wichmann and Kroll showed that the non-linear vacuum polarization density has the form

$$\rho_{VP}^{3+}(r) = Q_{wk}^{3+}\delta(r)/4\pi r^2 + \tilde{\rho}_{wk}(r) , \quad (27)$$

where  $Q_{wk}^{3+}$  is a point screening charge at the origin and  $\tilde{\rho}_{wk}$  is a finite compensating VP charge density extending to  $r \sim \lambda_e$ . The net charge of  $\rho_{VP}^{3+}$  is, of course, zero. As a function of  $Z\alpha$ , they found that

$$Q_{wk}^{3+} = -|e| \left\{ (Z\alpha)^3 (0.021) + (Z\alpha)^5 (0.007) F[(Z\alpha)^2] \right\} , \quad (28)$$

where  $F$  is close to 1 except near  $Z\alpha = 1$ . In the limit  $Z\alpha \rightarrow 1$ ,  $Q_{wk}^{3+} \rightarrow e/20$ , approximately. However, due to the nonanalytic behavior of the  $j=1/2$  Green's function at  $Z\alpha = 1$ , they found that  $dQ_{wk}^{3+}/dZ \rightarrow -\infty$  at  $Z\alpha = 1$ . The contribution of higher partial waves ( $j \geq 3/2$ ) to  $Q_{wk}^{3+}$  was found<sup>8,12b</sup> to be less than 10% over the entire range  $Z \leq 137$ . Almost all the screening charge, therefore, is due to  $j=1/2$  pairs.

This last observation greatly simplifies the calculations of  $\rho^{3+}$  for  $Z > 137$ . To high accuracy, we need only include finite size effects in the  $j=1/2$  term, while continuing to use the point charge form of  $\rho_j^{3+}$  for  $j \geq 3/2$  (valid up to  $Z\alpha = 2$ ). In table 2, the energy shift<sup>8b</sup> of the  $1S_{1/2}$  state due to non-linear vacuum polarization is given for  $Z \rightarrow Z_c$ . The nuclear charge density was taken to be a shell of radius  $R = 10$  fm. While the energy shift increases very rapidly for  $Z > 137$ ,  $\Delta E^{3+}(Z) \sim Z^{10}$ , we see that it nevertheless remains small ( $\lesssim 1$  keV) and nonsingular as  $Z \rightarrow Z_c$ . Also, it can be seen that the third order,  $\alpha(Z\alpha)^3$ , contribution accounts for about one-half the repulsion.

It is important to compare these numbers to the first order Uehling shift, which is attractive and hence of opposite sign to  $\Delta E^{3+}$ . From eq. (16) a simple estimate of  $\Delta E^1$  can be made<sup>13</sup> by replacing  $1/r$  by  $\langle 1/r \rangle_{1S}$  as listed in table 2. For  $Z \rightarrow Z_c$ , we get in this way  $\Delta E^1 \sim -10$  keV. Detailed calculations<sup>16</sup> give in fact  $\Delta E^1(Z_c) = -11.8$  keV. Therefore,  $\Delta E^{3+}(Z_c) \approx -\Delta E^1(Z_c)/10$ , and the net effect of vacuum polarization to all orders in  $Z\alpha$  is attractive at the critical charge! Diving,  $B > 2m_e$ , is therefore enhanced by vacuum polarization.

An interesting way to characterize the effect of non-linear vacuum polarization is to define an effective point screening charge  $Q_{eff}^{3+}$  such that

$$\Delta E^{3+} \equiv Q_{eff}^{3+} \langle \alpha/r \rangle_{1S} . \quad (29)$$

Table 2. Energy Shift (eV) Due to Non-linear Vacuum Polarization for  $R = 10$  fm Nuclear Shell Density

| $Z$ | $E(1S_{1/2})V/m_e$ | $\langle \alpha_e/r \rangle_{1S}$ | $\Delta E^{3+}$ | $\Delta E^3$ | $Q_{eff}^{3+}$       | $Q_{eff}^3$          |
|-----|--------------------|-----------------------------------|-----------------|--------------|----------------------|----------------------|
| 82  | 0.79               | 0.8                               | 2               | 2            | $6 \times 10^{-4}$   | $6 \times 10^{-4}$   |
| 130 | 0.362              | 2.1                               | 63              | 47           | $8 \times 10^{-3}$   | $6 \times 10^{-3}$   |
| 153 | -0.137             | 4.2                               | 307             | 197          | $2.0 \times 10^{-2}$ | $1.3 \times 10^{-2}$ |
| 165 | -0.550             | 5.9                               | 641             | 368          | $2.9 \times 10^{-2}$ | $1.7 \times 10^{-2}$ |
| 175 | -0.990             | 7.6                               | 1140            | 566          | $4.1 \times 10^{-2}$ | $2.0 \times 10^{-2}$ |
| 175 | -0.999             | 7.6                               | 1150            | 570          | $4.1 \times 10^{-2}$ | $2.0 \times 10^{-2}$ |

Since  $\langle \alpha/r \rangle_{1S} = -dE_{1S}/dZ = dB_{1S}/dZ$ , we can determine  $Q_{eff}$  from

$$Q_{eff}^{3+} = -\Delta E^{3+}/(dE_{1S}/dZ) . \quad (30)$$

Similarly, we can define an effective third order screening charge using  $\Delta E^3$ . The resulting screening charges are illustrated as a function of  $Z$  in Fig. 2.

The rapid increase of screening as  $Z \rightarrow Z_c$  is obvious. However, the magnitude of  $Q_{eff}^{3+} \approx 0.04e$  remains much smaller than the nuclear charge even at  $Z_c$ . Furthermore,  $dQ_{eff}^{3+}/dZ$  remains finite at  $Z_c$ . Also shown for comparison is the Wichmann-Kroll charge, eq. (28), obtained for a point nuclear density. The small contribution of higher angular momenta ( $j \geq 3/2$ ) at  $Z = 137$  is indicated by  $Q_{|k| \geq 2}$ . Qualitatively, it is suggestive to say that finite nuclear size simply shifts the  $Q_{wk}(Z)$  curve to higher  $Z$ :  $Q_{eff}(Z) \approx Q_{wk}(Z - Z_c + 137)$ . Note also that for  $Z < 137$ ,  $Q_{eff}(Z) \ll Q_{wk}(Z)$  because for lower  $Z$ , the  $1S_{1/2}$  radius lies outside the vacuum polarization cloud, and the compensating density  $\rho_{wk}$  in eq. (27) shields the VP point charge,  $Q_{wk}$ .

In conclusion, non-linear vacuum polarization is nonsingular and small compared to the linear (Uehling) effect in  $Z \rightarrow Z_c$ .

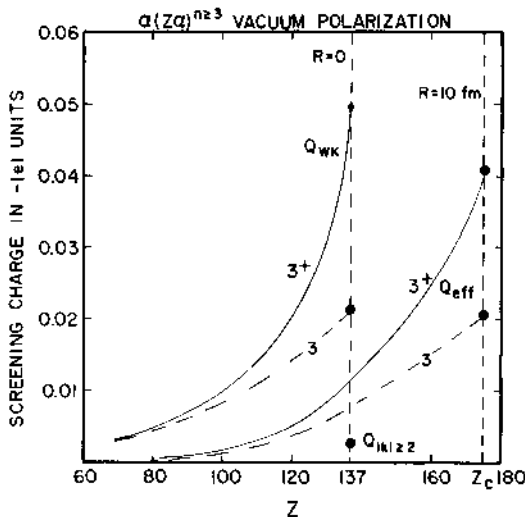


Fig. 2. Effective non-linear screening charge for orders  $\alpha(Z\alpha)^{n=3}$  labeled  $3^+$  and order  $\alpha(Z\alpha)^3$  labeled 3.

Therefore, virtual pair creation does not prevent real pair creation for  $Z > Z_c$ .

#### CHARGED VACUUM FOR $Z > Z_c$

For  $Z > Z_c$ , the  $1S_{1/2}$  pole in Fig. 1 moves off the physical sheet through the branch point at  $\omega = -m_e$ . The original contour integration over  $C_F$  is then no longer well defined beyond  $Z_c$ . Therefore,  $\rho_{\text{vp}}$  is nonanalytic at  $Z = Z_c$ , although the limit  $Z \rightarrow Z_c$  from below  $\rho_{\text{vp}}$  remains small and nonsingular. The nonanalytic behavior signals a breakdown in the assumption that the chargeless vacuum state is the one of lowest energy. Beyond  $Z_c$ ,  $B > 2m_e$  and the state with two electrons bound around the nucleus and two free positrons has lower energy and will therefore define the new vacuum<sup>1-3</sup>.

We expect therefore, that the vacuum charge density  $\rho_{VP}$  should be a smooth continuation of the helium-like density  $2e|\psi_{1S_{1/2}}(x)|^2$ . However, the  $1S_{1/2}$  state no longer exists as part of the Dirac spectrum for  $Z > Z_c$ . This poses no difficulty, however, if we realize that the physical helium-like density includes the vacuum polarization cloud:

$$\begin{aligned} \rho_{He}(x) &= 2e|\psi_{1S_{1/2}}(x)|^2 + \rho_{VP}(x) \\ &= |e| \int_{C_{He}} \frac{d\omega}{2\pi i} \text{Tr } G(x, x; \omega) , \end{aligned} \quad (31)$$

where  $C_{He}$  is the contour  $C_F$  shifted to the right of the  $1S_{1/2}$  pole in Fig. 1. For  $Z \leq Z_c$  the first line is well defined. However, the contour integral is perfectly well defined both below and above  $Z_c$ . It is manifestly analytic in  $Z$  in the neighborhood of  $Z_c$ . Therefore, the contour integral representation allows<sup>8</sup> us to compute the continuation of the helium-like density and hence the overcritical vacuum density for  $Z > Z_c$ . (The Green's function must, of course, be regulated as in eq. (12) for all  $Z$ .) The highly localized character of the overcritical charged vacuum density is shown in Fig. 3. In this example, the  $1S_{1/2}$  state dives at  $Z_c \approx 1.274$ . However, we can see that the vacuum density defined by eq. (31) for  $Z > Z_c$  is a smooth analytic continuation of the He-like density from  $Z < Z_c$  all the way up to the diving point of the  $2P_{1/2}$  state. Finally, the smooth increase in the localization of the vacuum density beyond  $Z_c$  can be seen from the average inverse radius in Fig. 3b.

## SUMMARY

In this review, I have shown how the Wichmann-Kroll formalism can be applied to finite radius nuclei with very large  $Z$ . The non-linear vacuum polarization was shown to remain too small to prevent spontaneous pair production for  $Z \sim 175$ . Finally, the density of the overcritical charged vacuum was shown to be highly localized and continuous up to the  $2P_{1/2}$  diving point.

This work was supported by the Director, Office of Energy Research, Division of Nuclear Physics of the Office of High Energy and Nuclear Physics of the U.S. Department of Energy under Contract W-7405-ENG-48.

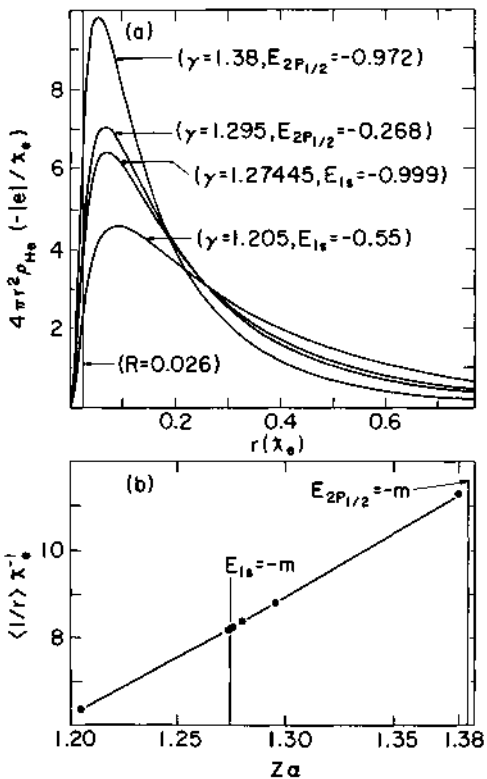


Fig. 3. a) Charge density of He-like state which corresponds to the vacuum density for  $Z\alpha > 1.275$ .  
 b) Average inverse radius of He-like state.

## REFERENCES

1. W. Pieper, W. Greiner, Z. Phys. 218:327 (1969).
2. B. Muller, J. Rafelski, W. Greiner, Z. Phys. 257:62 (1972); Z. Phys. 257, 83 (1972); Nucl. Phys. B68:585 (1974).
3. Ya.B. Zel'Dovich, V.S. Popov, Sov. Phys. Usp. 14:673 (1972).
4. J. Rafelski, L.P. Fulcher, W. Greiner, Phys. Rev. Lett. 27:958 (1971).
5. M. Born, L. Infeld, Proc. Roy. Soc. (London) A144:425 (1934).
6. G. Soff, J. Rafelski, W. Greiner, Phys. Rev. A7:903 (1973).
7. E.H. Wichmann, N.M. Kroll, Phys. Rev. 96:232 (1954); 101, 843 (1956).

8. M. Gyulassy, (a) Phys. Rev. Lett. 32:1393 (1974), (b) Phys. Rev. Lett. 33:921 (1974), (c) Nucl. Phys. A244:497 (1975).
9. J.D. Bjorken, S.D. Drell, "Relativistic Quantum Fields," vols. I,II (McGraw-Hill, New York, 1965).
10. J. Blomquist, Nucl. Phys. B48:95 (1972).
- 11a. P.J. Mohr, Phys. Rev. Lett. 34:1050 (1975); Ann. Phys. (N.Y.) 88:26, 52 (1974);  
b. K.T. Cheng, W.R. Johnson, Phys. Rev. A14:1943 (1976).
- 12a. J. Arafune, Phys. Rev. Lett. 32:560 (1974);  
b. L.S. Brown, R.N. Cahn, L.D. McLerran, Phys. Rev. Lett. 32:562 (1974); Phys. Rev. D12, 609 (1975).
13. S.J. Brodsky, P.J. Mohr, in "Structure and Collisions of Ions and Atoms," I.A. Sellin, ed., New York, Springer (1978).
14. T. Dubler, K. Kaesser, B. Robert-Tissot, L.A. Schaller, L. Schellenberg, H. Schnenwly, Nucl. Phys. A294:397 (1978).
15. L. Tauscher, G. Backenstoss, K. Fransson, H. Koch, A. Nilsson, J. de Raedt, Z. Phys. A285:139 (1978).
16. G. Soff, B. Müller, J. Rafelski, Z. Naturforsch A29:1267 (1974).

## DOES PION CONDENSATION PREVENT PION CONDENSATION?

Amand Faessler

Institut für Theoretische Physik  
Universität Tübingen  
D-7400 Tübingen, W. Germany

### ABSTRACT

Pions which are moving through nuclear matter are attracted by nucleons. The binding of these pions increases with increasing density. Midgal, Sawyer and Scalapino realized that there might be the possibility that pions are more bound than their rest mass and then one can produce pions without needing additional energy. This phenomenon has been called pion condensation. Several groups studied this phenomenon extensively by calculating the propagator of a pion through nuclear matter. They obtained the pion self energy by including particle-hole excitations of the nucleons and also  $\Delta$  particle-nucleon hole excitations. In all cases they assumed for the particle-hole force in the pion channel a momentum independent constant expression which is characterized by the quantity  $g' \approx 0.5$ . In this calculation one obtains pion condensation near twice nuclear matter density. In our investigation we used realistic nucleon-nucleon interactions for the particle-hole force for scattering a particle-hole pair into another one. The correlations between the nucleons are included by calculating the Brueckner reaction matrix. For the transition potential into  $\Delta$  excitations we include  $\pi$ - and  $\rho$ -meson exchange and sum the nucleon-nucleon correlations again with Brueckner theory. This calculations yield roughly the same result as the one of Brown and Weise with the constant momentum independent particle-hole force.

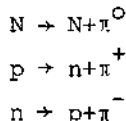
But in addition to the particle-hole excitation one needs also to include exchange forces within a particle-hole bubble. These exchange forces have also to be extended to include again an RPA series within particle-hole bubbles. This force is called the induced particle-hole interaction. It consists among others out of

the same diagrams which lead to pion condensation but since it is an exchange force it has the opposite sign. Near the phase transition where one expects pion condensation without the induced particle-hole exchange force these terms are diverging and shield against pion condensation. In this sense pion condensation is preventing pion condensation. But if one goes a step further and considers also bubbles in bubbles in bubbles then the next hierarchy is also diverging and shielding the shielding of pion condensation. Therefore this approach to calculate the critical density for pion condensation can not be successful if one does not include the sequence of diagrams with bubbles in bubbles, in bubbles ... summed up to infinity. The Mean Field theory is a possibility to go around this problem. With forces which include  $\pi$  and  $\rho$  exchange pion condensation is studied in a simplified Mean Field approach in  $^{160}$ O including also the possibility of exciting the nucleons into  $\Delta$ 's. Temperature below the single particle gap is assisting pion condensation in double closed shell nuclei, while higher temperatures move the critical density for pion condensation to higher values.

## INTRODUCTION

Pions which move with a larger momentum  $k$  in nuclear matter are attracted. The attraction increases with increasing density of the nuclear matter. If this attraction is stronger than the kinetic energy and the rest mass of the pion it is possible to create "dressed" pions without additional energy. This phenomenon is known as "Pion Condensation". It has first been discussed by Migdal<sup>1)</sup> and by Sawyer and Scalapino<sup>2)</sup>. Later on this effect has been studied by Brown and Weise<sup>3)</sup> and by Bäckman and Weise<sup>4)</sup>. Investigations of pion condensation in view of heavy ion collisions have been done by Gyulassy, Greiner and coworkers<sup>5)</sup>. The studies which I want to present here have been done together with Dickhoff, Meyer-ter-Vehn and Müther<sup>6)</sup>. The investigation of the effect of  $\Delta$ -isobars and  $\rho$ -meson exchange in the transition potentials on pion condensation has been worked out together with Tripathi and Shimizu<sup>7)</sup>.

Pion condensation in symmetric nuclear matter is due to the following microscopic processes:



The only force for nucleon pion interaction which can be strong enough to produce eventually pion condensation is the  $p$ -state interaction between pions and nucleons,

$$H_{\pi NN} = i \frac{f_\pi}{m_\pi} \psi_N^+ (\vec{\sigma}_N \cdot \vec{k}_\pi) (\vec{\tau}_N \cdot \vec{\phi}_\pi) \psi_N. \quad (1)$$

Fig. 1 shows a stationary  $\pi^0$ -wave in nuclear matter and the processes which are produced by interaction (1). One sees that one expects in nuclear matter a laminated structure with the layers perpendicular to the direction of the pion momentum. In these layers one finds alternatingly protons with spin up, neutrons with spin down and in the next layer protons with spin down and neutrons with spin up. The pion which runs through nuclear matter is polarizing the surrounding nucleons. The mechanism can be discussed with the help of Fig. 2. Fig. 2 corresponds to the energy spectrum of phonons as a function of their momentum  $k$  in solids. The pion corresponds to the photon which probes the material from the outside. Thus one often calls the pion spectrum  $E_\pi = \sqrt{m^2 + k^2}$  the unperturbed optical branch. The nucleon particle-hole interaction  $NN^{-1}$  corresponds then to the acoustical branch. The figure also contains  $\Delta$ -isobar nucleon-hole excitations ( $\Delta N^{-1}$ ). If the interaction between the free pion and the particle-hole interaction is switched on the spectrum of Fig. 2 is distorted. If one of the branches is distorted in such a way that it reaches zero excitation energy at a finite momentum we speak of pion condensation. This means that in nuclear matter such an excitation mode corresponding to the quantum numbers of the pions can be excited without additional energy. Such a state is not a pure pion but is a strong mixture of pions and particle-hole excitations. A possibility for the nature of such a polarization mode of nuclear matter is shown in Fig. 3. The double lines correspond to  $\Delta$ -isobars. The particle-hole interactions needed for the so-called direct diagram,

$$G_{ph}^{\text{direct}} = \text{Diagram} \approx g_{ph} \sigma_1 \cdot \sigma_2 \tau_1 \cdot \tau_2, \quad (2)$$

has to exchange the quantum numbers of the  $\pi$ , which are  $S=1$  and  $T=1$ . This is easily obtained from the pion-nucleon interaction if one puts the momentum of the pion in  $z$ -direction,

$$\begin{aligned} \tau_N^0(k) &= \text{Diagram} = \frac{f_\pi}{m_\pi} \Gamma(k) \sigma_Z k_\pi \tau_Z \left[ \psi_N^+ \psi_N \right]_{ST} \\ &= \frac{f_\pi}{m_\pi} \Gamma(k) 2k_\pi \delta_{T,1} \delta_{S,1} \delta_{M_S,0} \end{aligned} \quad (3)$$

$\Gamma(k)$  is the monopole form factor for the pion-nucleon vertex,

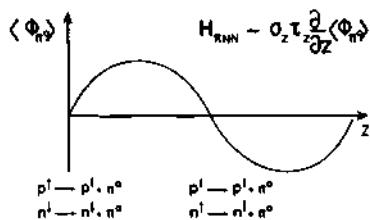


Fig. 1. Expectation value of a stationary  $\pi^0$  wave in nuclear matter. The pion nucleon interaction is strongest at places where the expectation value oscillates through zero due to the derivative. If the derivative is positive it favours for example the concentration of protons with spin up and neutrons with spin down and if the derivative is negative it favours the concentration of protons with spin down and neutrons with spin up. Pion condensed nuclear matter has, therefore, a laminated structure with an oscillating spin-, isospin-density. Our calculation shows that pion condensation happens preferentially at a pion momentum close to the Fermi momentum  $k_F$  for empirical nuclear matter density. Thus the wave length of the above oscillations is  $\lambda \approx (2\pi)/k_F \approx 4.7$  fm.

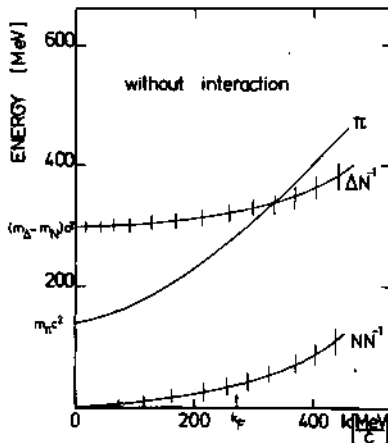


Fig. 2. Sketch of the excitation energy in nuclear matter by non-interacting nucleon-particle nucleon-hole ( $NN^{-1}$ ) and  $\Delta$ -isobar particle nucleon-hole ( $\Delta N^{-1}$ ) excitation for different momenta  $k$  of the particle-hole state compared with the energy of a pion with the momentum  $k$  travelling through nuclear matter. The interaction of the  $\pi$  with the particle-hole excitations and the interaction between the different  $ph$  excitations modifies this diagram. At higher nuclear matter densities this interaction can be so strong that the pion branch (often called optical branch in analogy to photon and phonon excitations in solids) is lowered at a finite momentum  $k$  down to zero energy. Then one speaks of pion condensation.

$$\Gamma(k) = \left| \frac{\Lambda^2 - m_\pi^2}{\Lambda^2 + k^2} \right| \quad . \quad (4)$$

Since one needs the proper self energy as discussed in chapter 2, one has to subtract the direct particle-hole matrix element of the one pion exchange force with the pion quantum numbers. Bäckman and

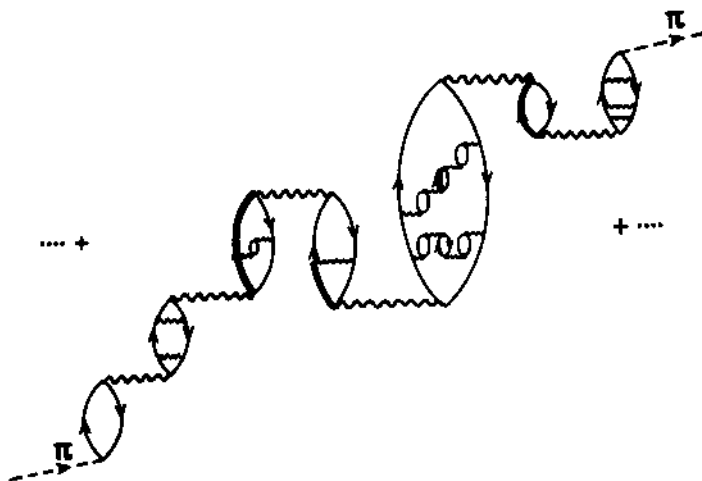


Fig. 3. A diagram which shows the polarization of nuclear matter by a pion travelling through the nuclear medium. Double lines indicate  $\Delta$ -isobars. The first bubble is a pure nucleon-particle nucleon-hole ( $NN^{-1}$ ) excitation. The two interactions in the second bubble are the so-called exchange particle-hole interactions represented by the Brueckner reaction matrix. The interaction between the bubbles (direct particle-hole interaction) has the one-pion exchange potential subtracted. The interactions in bubble 3 and 5 are induced ph-interactions which diverge at the critical density in nuclear matter at which pion condensation can set in. Each bubble represents a Lindhard function. Its value increases with the density. Bubble 6 with a  $\Delta$ -particle nucleon-hole state is proportional to the density  $\rho$ .

and Weise checked that after averaging the reaction matrix transformed into the particle-hole channel over the initial and final relative momenta and over the starting energy yields roughly an expression which is independent on the total particle-hole momentum  $k$ .

$$\begin{aligned}
 G_{ph} - v_p \text{ (OPE)} &= \\
 G(p, p'; k, \omega, w, \rho) &= \frac{f_\pi^2}{m_\pi} |\Gamma(k)|^2 \frac{k^2}{\omega^2 - k^2 - m_\pi^2} \\
 &= \frac{f_\pi^2}{m_\pi^2} g_N^2
 \end{aligned} \tag{5}$$

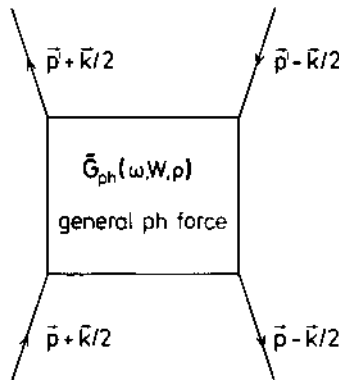


Fig. 4 Nomenclature for the general particle-hole force  $\tilde{G}_{ph}$ . It depends on the relative momenta of the initial and final particle-hole states  $\vec{p}$ ,  $\vec{p}'$ , respectively and on the total particle-hole momentum  $\vec{k}$ , on the total particle-hole energy  $\omega$ , on the starting energy  $W$  (single-particle energies of the incoming particle lines) and on the nuclear matter density  $\rho$ .

Definition of the initial and final relative momenta  $\vec{p}$ ,  $\vec{p}'$  and of the total particle-hole momentum  $\vec{k}$  is shown in Fig. 4. The particle-hole force depends further on the total energy  $\omega$  of the particle-hole states on the starting energy  $W$  (sum of the single-particle energies of the ingoing lines) and on the density in nuclear matter  $\rho$ . The quantity  $g'_N$  is shown in Fig. 5. this figure contains also direct contribution of the pion exchange potential in the pion channel. The purpose of this lecture is to go beyond the constant approximation for the particle-hole force for  $NN^{-1}$  and  $\Delta N^{-1}$ . In addition we want not only to describe the particle-hole force by the Brueckner reaction matrix but also to include higher order terms (induced particle-hole interaction). At the end we will also study pion condensation in finite nuclei. In detail the different

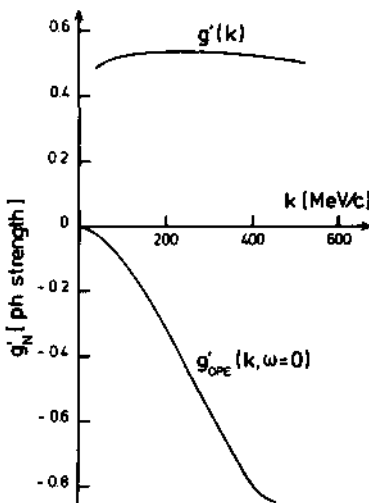


Fig. 5. Particle-hole strength  $g'_N$  defined in eq. (5) derived from the Reid soft core potential. The lower part shows the one pion exchange contribution for the "direct" particle-hole interaction with the pion quantum numbers ( $T=1, S=1$ ) as a function of the total particle-hole momentum  $k$ .

section will concentrate on the following topics:

In chapter 2 we will shortly outline the formal theory for the pion self energy.

In chapter 3 the pion self energy will be calculated taking into account the mixing between pions and the pure nucleon particle-hole ( $NN^{-1}$ ) states. It will be also tested how well one can reproduce this result with a constant particle-hole force.

In chapter 4 we shall switch on the full interaction between pions, nucleon particle-hole states ( $NN^{-1}$ ) and isobar particle and nucleon-hole states ( $\Delta N^{-1}$ ). Again we shall test how well these results may be reproduced using constant particle-hole forces.

In chapter 5 we will also include higher order terms and not only the pure Brueckner reaction matrix as the particle-hole interaction.

Especially we shall study the influence of the induced particle-hole

interaction on pion condensation.

Chapter 6 concentrates on the influence of the  $\Delta$ -isobars and the  $\rho$ -meson exchange for pion condensation in finite nuclei. The main conclusions of this lecture are summarized in chapter 8.

### PION SELF ENERGY

The propagation of a pion through a nucleus or nuclear matter is described by the following propagator (Green's function):

$$D(\vec{k}, \omega; \rho) = \left[ \omega^2 - k^2 - m_\pi^2 - \Pi(\vec{k}, \omega; \rho) \right]^{-1} \quad (6)$$

which differs from the pion propagator by the proper selfenergy  $\Pi(\vec{k}, \omega; \rho)$ . It depends on the pion momentum  $\vec{k}$ , on its energy  $\omega$  and on the density in nuclear matter  $\rho$ . The proper self energy is irreducible with respect to a one pion line. It is connected in the local density approximation to the pion-nucleus optical potential by the following relation:

$$\Pi(\vec{k}, \omega; \rho(\vec{r})) = 2\omega U_{\text{opt}}(\vec{k}, \omega; \vec{r}) \quad . \quad (7)$$

From the fits of the optical potential  $U_{\text{opt}}$  to the spectra in  $\pi$ -mesic atoms one knows also that the contribution of the s-wave pion-nucleon interaction is very small in symmetric nuclear matter, since

$$\Pi_S \approx \left\{ 0.03 \frac{\rho_n + \rho_p}{\rho_0} + 0.57 \frac{\rho_n - \rho_p}{\rho_0} \right\} \frac{m_\pi^2}{m_n^2} \quad (8)$$

Pion condensation can therefore only be due to the p-wave nucleon-pion interaction. If we want to obtain real pions we have to look to the pole of the propagator (6). Pion condensation means now, as discussed in connection with Fig. 2 that the energy  $E=\omega$  of the pion goes to zero,

$$E^2 = \omega^2 = 0 = k^2 + m_\pi^2 + \Pi(\vec{k}, \omega=0; \rho) \quad (9)$$

To find a condition for pion condensation means, therefore, to calculate the proper pion self energy in nuclear matter for energy  $\omega=0$  and different pion momenta  $\vec{k}$  and nuclear matter densities  $\rho$ . If this quantity added to the square of the free pion energy  $m_\pi^2 + k^2$  yields zero we have found pion condensation.

### MIXING OF PIONS WITH $NN^{-1}$

The proper pion self energy in nuclear matter due to the polarization of the nuclear medium by particle-hole excitations is shown in Fig. 6.

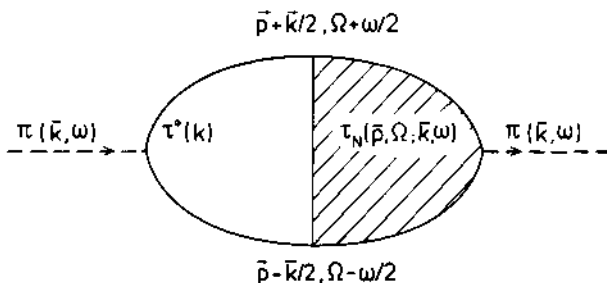


Fig. 6. Graph for the proper pion self energy. Proper pion self energy does not contain the free single-particle propagator which is indicated here only for the better understanding of the graph on the left and right hand side. The selfenergy contains on the right and the left only the vertices.  $\vec{k}, \omega$  are the momentum and the energy of the pion  $\vec{p}$  and  $\Omega$  are the momentum and the energy "rotating" in the loop.  $\vec{p}$  can also be understood as the relative momentum of the intermediate particle-hole-state. The free vertex function  $\tau^0(k)$  is defined in eq. (3). The dressed vertex function  $\tau_N(\vec{p}, \Omega; \vec{k}, \omega)$  has to be calculated according to the integral equation pictured in Fig. 7. The analytical expression of the graph given in this figure is shown in eq. (11).

The propagator of the ingoing and outgoing free pion does not belong any more to the proper self energy but it is defined including the vertex function

$$\tau^0(k) = \text{---} \sqrt{\text{---}} = \frac{f}{m_\pi} 2k_\pi (k) \delta_{T,1} \delta_{S,1} \delta_{M_S,0} \quad (10)$$

by the expression:

$$\Pi(\vec{k}, \omega=0; p) = \int \frac{d\Omega}{2\pi i} \int \frac{d^3 p}{(2\pi)^3} \quad (11)$$

$$\tau^0(k) \frac{n^p/h(\vec{p} + \frac{\vec{k}}{2})}{\Omega - \epsilon_{\vec{p} + \frac{\vec{k}}{2}} + i\eta} \frac{n^h/p(\vec{p} - \frac{\vec{k}}{2})}{\Omega - \epsilon_{\vec{p} - \frac{\vec{k}}{2}} + i\eta} \tau_N(\vec{p}, \Omega; \vec{k})$$

The integration over the energy  $\Omega$  in the loop can be performed with the help of the residues of the single-nucleon propagator in the upper half of the complex  $\Omega$ -plane, since the poles of the reaction matrix are in the lower part. The integration over the momenta is restricted by the functions  $n^p/h(\vec{p} + \vec{k}/2)$ . They are unity for the particle states ( $p$ ) above the Fermi surface and for the hole states ( $h$ ) below the Fermi surface. One obtains therefore two contributions in which in Fig. 6 the particle-hole character of the nucleon lines is exchanged. This corresponds to a forward or backwardgoing diagram.

The dressed pion-nucleon vertex  $\tau_N(\vec{p}, \Omega; \vec{k}, \omega=0)$  is determined by an integral equation which is pictured in Fig. 7.

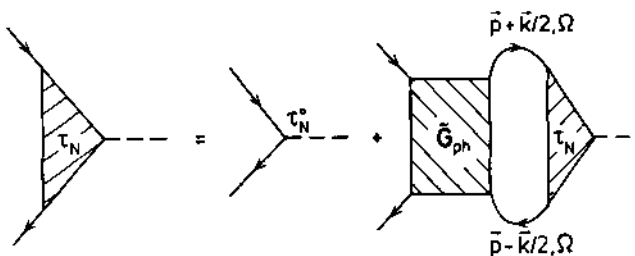


Fig. 7. Graphical equation for the integral equation which determines the dressed vertex function  $\tau_N(\vec{p}, \Omega; \vec{k}, \omega)$ . The vertex  $\tau_N^0$  is defined in eq. (3). The general particle-hole force  $G_{ph}$  is defined in Fig. 4.

The particle-hole interaction  $\tilde{G}_{ph}$  has to be irreducible with respect to a one-pion line and with respect to particle-hole excitations. This means that  $\tilde{G}_{ph}$  can not be separated in two parts by cutting either a pion line or a particle and a hole line. This irreducible particle-hole interaction has usually been approximated by a constant particle-hole force. Naturally we also do not know the exact full particle-hole interaction  $\tilde{G}_{ph}$ . We shall use different approximations. In this and the next chapter we will approximate the irreducible particle-hole interaction by the Brueckner matrix minus the direct part of the one-pion exchange potential as indicated in Fig. 8.

$$\tilde{G}_{ph} \approx G(\vec{p}, \vec{p}; k, \omega=0; W, \rho) - V_m^{\text{one-pion}}(\text{OPE})$$

Fig. 8. Irreducible direct part of the particle-hole interaction approximated by Brueckner reaction matrix for the particle-hole channel with the pion quantum number  $S=1$ ,  $M_S=0$ ,  $T=1$ . For the calculation of the proper self energy the direct part of the one-pion exchange potential has to be subtracted.

$$\tilde{G}_{ph} \approx G(\vec{p}, \vec{p}'; k, \omega=0; W, \rho) + \left( \frac{f_\pi \Gamma(k)}{m_\pi} \right)^2 \frac{4k^2}{m_\pi + k^2} \quad (12)$$

The proper self energy calculated in this way is shown graphically in Fig. 9. The one-pion exchange particle-hole force has naturally only to be subtracted in the direct part of the particle-hole interaction and not in the exchanged part. The result of this

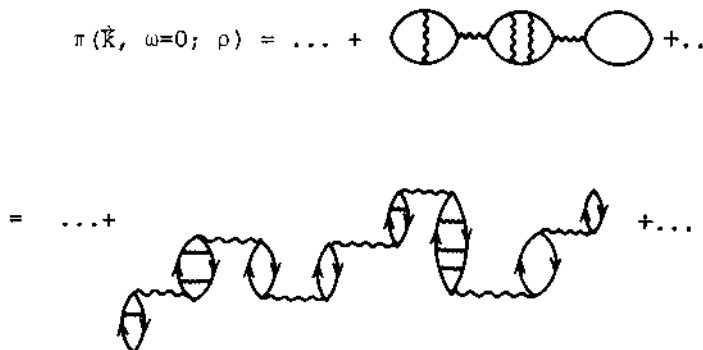


Fig. 9. Perturbation expansion of the proper self energy shown in Fig. 6. The horizontal particle-hole interaction is approximated by the Brueckner reaction matrix with the one-pion exchange subtracted as shown in Fig. 8. The particle-hole interaction indicated by the vertical wavy line is the full Brueckner reaction matrix without any subtraction. In the upper part a diagram is given without specifying the time structure. The lower part shows a diagram with time structure and indicates that the perturbation expansion may contain forward- and backward-going graphs.

calculation in form of the square of the energy as a function of the pion momentum is shown in Fig. 10. The result is only correct for the energy  $E = \omega = 0$ . It shows that at the empirical nuclear matter density different realistic forces (Reid soft core potential<sup>8</sup>) and the Bonn potential HM2 +  $\Delta$ <sup>9</sup>) yield no pion condensation. It shows also that the result is insensitive to the choice of the single particle energies. The selfconsistent Brueckner choice and the Landau recipe yield practically the same result. An increase to twice the empirical nuclear matter density does also not yield pion condensation. After we have calculated the proper self energy with the unapproximated Brueckner reaction matrix as the particle-hole force we can ask: How good would the same result for the proper self energy be reproduced with a constant particle-hole force for a given nuclear matter density  $\rho$ . If we assume that the direct particle-hole interaction minus the corresponding one-pion exchange diagram is

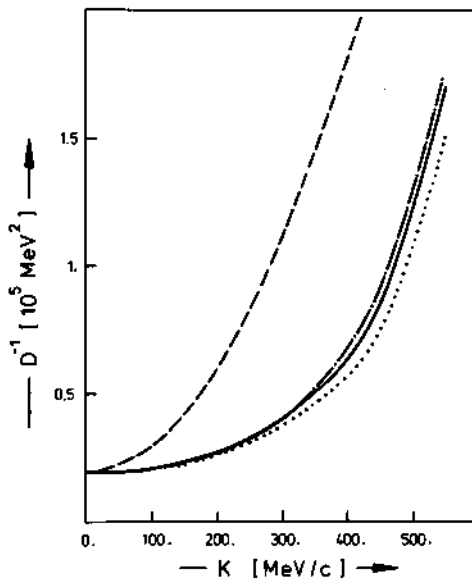


Fig. 10. The negative value of the inverse static pion propagator  $D$  defined in eq. (6) for  $\omega=0$  as a function of the momentum of the pion field. It shows the square of the energy as a function of the pion momentum with the restriction to the pion energy  $\omega=0$  in the proper pion-self energy  $\Pi(k, \omega=0; \rho)$ . Thus the expression would be only correct for  $E = \omega=0$  where pion condensation occurs. The dashed curve displays the free propagator of the pion. The dashed-dotted and the solid curves are obtained calculating the pion-self energy  $\Pi$  for a Fermi momentum  $k_F=1.4 \text{ fm}^{-1}=276.2 \text{ MeV}/c$  using the NN potentials HM2+ $\Delta$  and Reid soft core, respectively. While for these two calculations the single-particle spectrum is characterized by the Landau effective mass  $m^*(\epsilon=k^2/2m^*+C)$  a selfconsistent "Brueckner" spectrum and the Reid potential were used to obtain the dotted curve.

constant and if we neglect the exchange term of the particle-hole interaction the proper self energy can be written,

$$\Pi(\vec{k}; \rho) = \Pi_0(\vec{k}; \rho) \left[ 1 - g' \Pi_0 / k^2 \right]^{-1} , \quad (13)$$

using the particle-hole force according to eq. (5). The zero order approach  $\Pi_0$  for the proper selfenergy is defined with the help of the Lindhard function.

$$\Pi_0(\vec{k}; \rho) = - \frac{f^2}{\frac{m^2}{\pi}} k^2 \Gamma^2(k) 4P \int \frac{d^3 p}{(2\pi)^3} \frac{n(\vec{p}) - n(\vec{p} + \vec{k})}{\epsilon_{p+k} - \epsilon_k} , \quad (14)$$

where P indicates the principal value integral. The step function  $n(p)$  is unity within the Fermi sphere and zero outside. From the calculated proper selfenergy  $\Pi$  and its zero order approach  $\Pi_0$  we can extract for each pion momentum  $k$  the constant  $g'$  and see if it is independent on the pion momentum  $k$  as assumed in previous calculations. The result for different realistic forces and different nuclear matter densities is given in Fig. 11 ( $\gamma=g'$ ). One sees that using a constant particle-hole force is quite a good approximation. One also sees that the tensor force has to be included to obtain this result. The pure central part varies very drastically with the pion momentum.

Table 1. Coupling constants, masses and cutoff masses (both in MeV) that were used in the calculations in nuclear matter presented in the chapters 3, 4 and 5. The cutoff masses  $\Lambda$  are used in monopole form factors as shown in eq. (4).

|                         |       |                         |       |
|-------------------------|-------|-------------------------|-------|
| $f_\pi$                 | 0.978 | $f_\rho$                | 5.416 |
| $f_\pi^*$               | 1.956 | $f_\rho^*$              | 9.192 |
| $\Lambda_{NN}^\pi$      | 1200  | $\Lambda_{NN}^\rho$     | 1800  |
| $\Lambda_{N\Delta}^\pi$ | 1200  | $\Lambda_{\Delta}^\rho$ | 1800  |
| $m_\pi$                 | 139   | $m_\rho$                | 770   |
| $m_N$                   | 938.9 | $m_\Delta$              | 1236  |

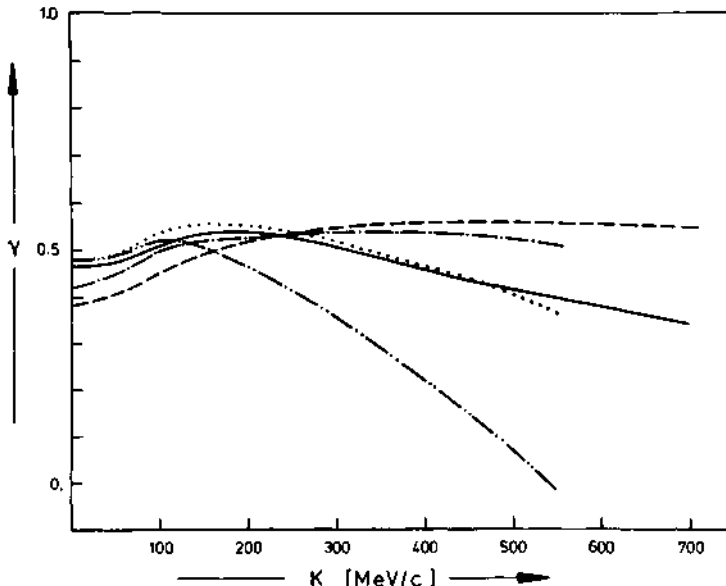


Fig. 11. Effective interaction strengths in the pion channel  $T=1$ ,  $S=1$ ,  $M_S=0$  as defined in eq. (5). The strengths are deduced from the calculation of pion self energies for two different Fermi momenta and two different NN potentials. They are presented by a solid curve ( $k_F=1.77 \text{ fm}^{-1}$ , Reid), a dashed-dotted curve ( $1.4 \text{ fm}^{-1}$ , Reid), a dashed curve ( $1.77 \text{ fm}^{-1}$ , HM2+), and dotted curve ( $1.4 \text{ fm}^{-1}$ , HM2+ $\Delta$ ). The dashed-dot-dot curve is obtained if only the central part of the Reid potential ( $k_F=1.4 \text{ fm}^{-1}$ ) is considered. The particle-hole strengths  $\gamma$  in this Figure are identical with the particle-hole strength  $g_N$  (or sometimes  $g'_N$ ) in the text.

INCLUSION OF  $\Delta$ - ISOBAR STATES

Fig. 2 shows that the  $\Delta$ -isobar nucleon-hole states are quite far away (300 MeV and more) from zero energy where pion condensation happens. But the importance of those states is revealed by the size of the matrix elements. The particle-hole matrix elements between nucleon-particle and nucleon-hole states is of the order of 1 MeV while the transition potential from a  $\Delta N^{-1}$  to a  $NN^{-1}$  state is about

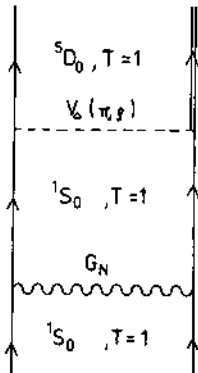


Fig. 12. The only contribution to the  $NN-\Delta$  transition potential where  $NN$  correlations could be important. It almost vanishes, however due to momentum mismatch.

5 MeV. The matrix elements for the transition from one  $\Delta N^{-1}$  to another one is of the order of 25 MeV. The particle-hole forces involving  $\Delta$ -isobars are much less known than the nucleon-nucleon particle-hole forces. We use here a one boson exchange approximation. At a  $\Delta$ -nucleon vertex only an isovector meson can interact. Thus we describe the transition potential by  $\pi$  and  $\rho$  exchange. The correlations are taken into account only between nucleons as indicated in Fig. 12.

$$\begin{aligned}
 G_{\Delta} &= \text{Diagram with a wavy line and two external lines} = v_{\Delta} + v_{\Delta} \frac{Q}{4} G_N \\
 &= v_{\Delta} (1 + \frac{Q}{4} G_N) = v_{\Delta} f_{\text{corr}} (q_{12}) \quad , \quad (15)
 \end{aligned}$$

where  $f_{\text{corr}} (q_{12})$  is the nucleon-nucleon correlation function calculated by Brueckner theory.

The proper selfenergy is now defined as a sum of a nucleon and a  $\Delta$ -isobar contribution. The two different  $\Delta$ -isobar contributions represent forward and backward going diagrams since the  $\Delta$  has always to be a particle going forward in time. The coupled system of integral equations for the dressed vertices  $\tau_N^o(p, \Omega; \vec{k})$ ,  $\tau_{\Delta}^o(p, \Omega; \vec{k})$  and  $\tau_{\Delta}^*(p, \Omega; \vec{k})$  are pictured in Fig. 13.

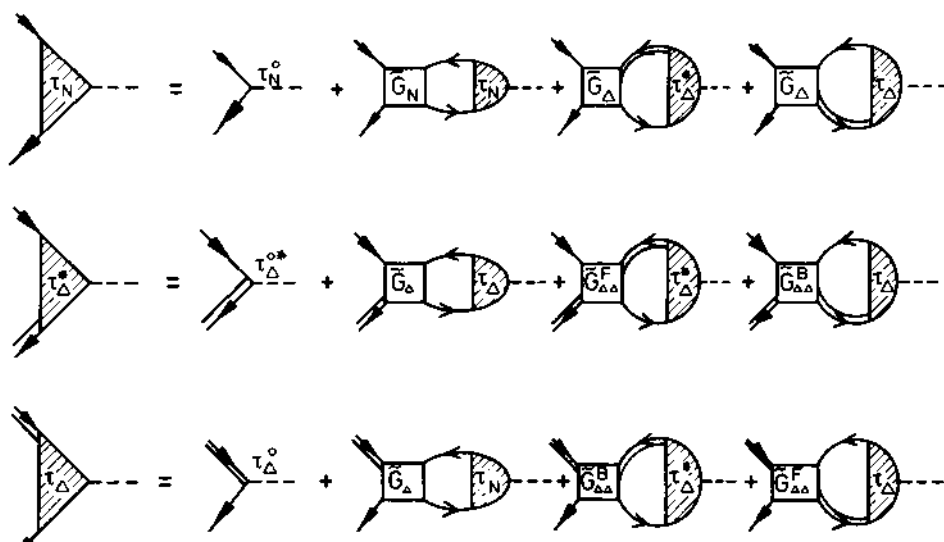


Fig. 13. Coupled set of integral equations for the dressed  $\pi NN$  and  $\pi N\Delta$  vertices  $\tau_N^o$ ,  $\tau_{\Delta}^o$  and  $\tau_{\Delta}^*$ .

$$\Pi(k, \omega=0; \rho) = \Pi_N + \Pi_\Delta$$

$$= \tau_N^0 + \tau_N + \tau_\Delta + \tau_\Delta^* \quad (16)$$

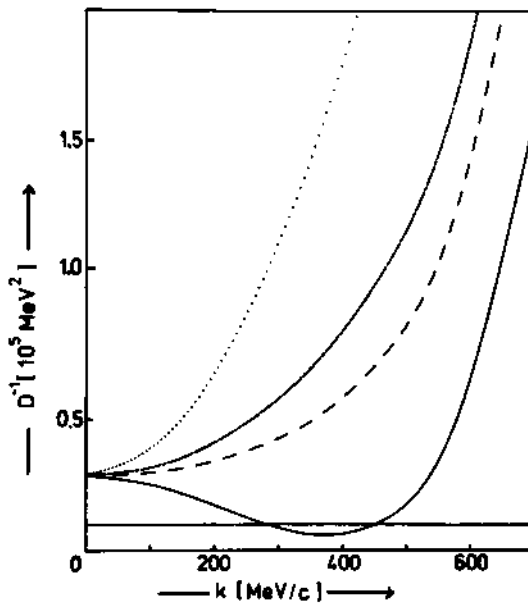


Fig. 14. The inverse of the negative static pion propagator  $D$  (see eq. (6) with  $\omega=0$ ,  $E^2 = m_\pi^2 + k^2 + \Pi(k, \omega=0; \rho)$ ) as a function of the pion field at a Fermi momentum  $k_F = 1.77 \text{ fm}^{-1} = 349.2 \text{ MeV/c}$ . The Reid soft core potential has been used for the NN interaction. The full curve represents for the total self energy with inclusion of isobars whereas the dashed-dotted curve gives the result if only contributions displayed in Fig. 6 are considered. The solid line is obtained calculating the dressed vertices with inclusion of isobars. For a reference this Figure also contains the results for the free pion (dotted curve) propagator and for the case where all isobar contributions are neglected (dashed curve).

The results are shown in Fig. 14 for twice the empirical nuclear matter density. One finds pion condensation at a pion momentum which corresponds roughly to the empirical Fermi momentum  $k_F = 1.4 \text{ fm}^{-1}$ . It is interesting to see that the nucleon proper selfenergy  $\Pi_N$  from eq. (16) without any inclusion of  $\Delta$ -isobars as calculated according to eq. (11) lies closer to pion condensation than the proper self energy  $\Pi_N$  from the coupled system of Fig. 13, which includes some  $\Delta$ -isobar contributions. The decisive term which leads to pion condensation in this approximation is  $\Pi_\Delta$ .

Former calculations<sup>3,4)</sup> use also for the transition potentials with constant particle-hole forces

$$\begin{aligned}
 G_{Nph} - v_{OPE} &= \text{Diagram} = \frac{f^2}{m_\pi^2} g'_N \\
 G_{\Delta ph} - v_{\Delta OPE} &= \text{Diagram} = \frac{f_\pi f^{*\pi}}{m_\pi^2} g'_\Delta \quad (17) \\
 G_{\Delta\Delta ph} - v_{\Delta\Delta OPE} &= \text{Diagram} = \frac{f_\pi^{*2}}{m_\pi^2} g'_{\Delta\Delta}
 \end{aligned}$$

The three-particle-hole constants  $g'_N$ ,  $g'_\Delta$  and  $g'_{\Delta\Delta}$  can be determined as a function of the pion momentum  $k$  in the following way:  $g'_N$  has already been determined from eq. (13) where no  $\Delta$ -isobars are included. The two missing constants  $g'_\Delta$  and  $g'_{\Delta\Delta}$  are now determined by  $\Pi_N$  and  $\Pi_\Delta$  from eq. (16) which are the solutions of the coupled integral equations of Fig. 13. The result of this analysis is contained in Fig. 15 and 16, for the empirical nuclear matter density and twice the empirical nuclear matter density ( $g' \equiv \gamma$ ). Two figures contain also the particle-hole strength under the assumption that all three coupling constants  $g'_N = g'_\Delta = g'_{\Delta\Delta}$  are identical. Again one sees that one finds slight variations of this coupling strength with the pion momentum. But in general the assumption of a constant value is a good approximation.

#### HIGHER TERMS IN THE PARTICLE-HOLE INTERACTION

Till now we used for the particle-hole interaction between nucleons the Brueckner reaction matrix and if a  $\Delta$ -isobar was involved the one-boson-exchange potential with  $\pi$  and  $\rho$  mesons and correlations between the nucleons. But this is only part of the nucleon-nucleon interaction. Fig. 17 shows some of the terms which also should

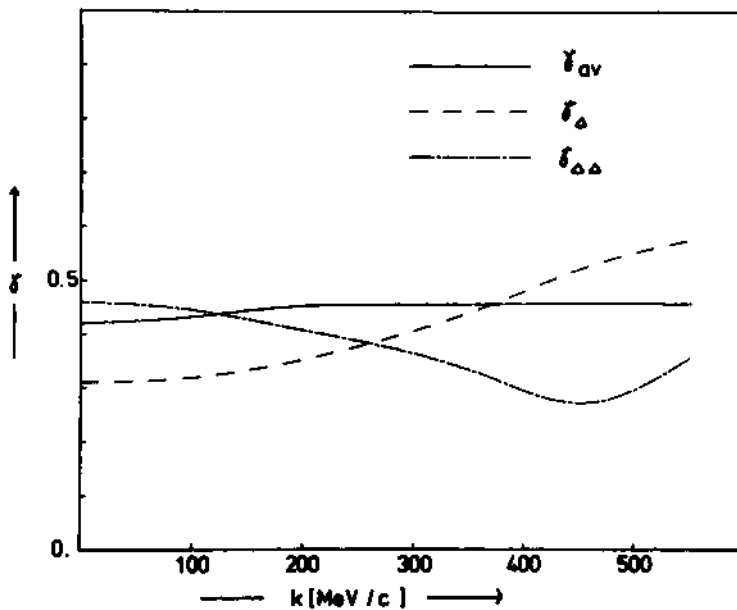


Fig. 15. Effective interaction strength  $g'_\Delta$  (identical with  $Y_\Delta$  in the Figure; dashed curve) and  $g'_{\Delta\Delta}$  (in the figure identical with  $Y_{\Delta\Delta}$ ; dashed-dotted curve) as obtained from analysing the self energy as described in the text. The solid curve represents  $g'_{av}$  ( $= Y_{av}$ ) which is obtained with the assumption  $g'_{av} = g'_N = g'_\Delta = g'_{\Delta\Delta}$  (see eq.(17)). The calculations are performed for  $k_F=1.4^{-1}$  ( $\rho=\rho_0$ ) using the Reid soft core potential.

be included in the particle-hole interaction. The calculations presented till now include only the first two terms. In the present chapter we do not want to include diagrams of the type indicated in the second line of Fig. 17. These are the so-called induced particle-hole interactions due to the polarization of neighbouring nuclear matter. To see how this induced force affects the particle-hole interaction we again look at the particle-hole force constant  $g'_N$  defined in eq. (5). For the comparison we simplified the particle-hole force into the Landau limit. This means that all ingoing and outgoing momenta have an absolute value which is

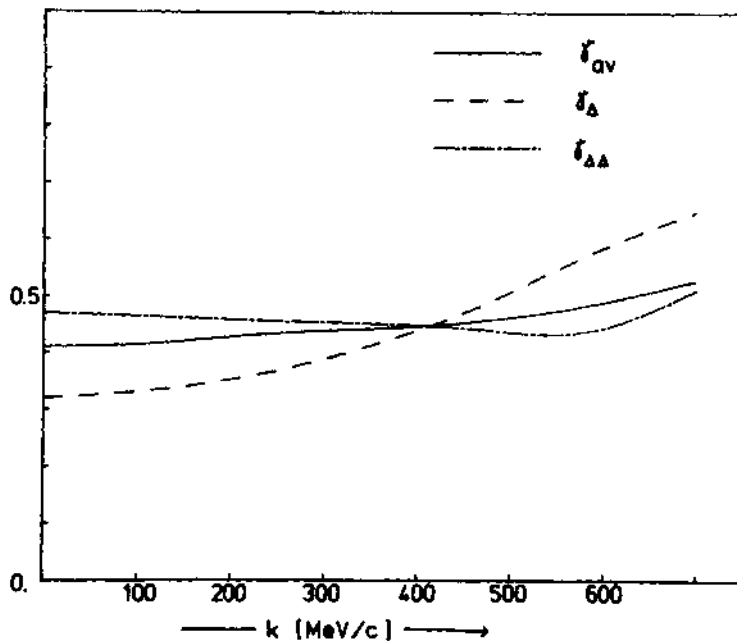


Fig. 16. Effective interaction strengths at  $k_F = 1.77 \text{ fm}^{-1}$  ( $p = 2p_0$ ), further details see Fig. 15.

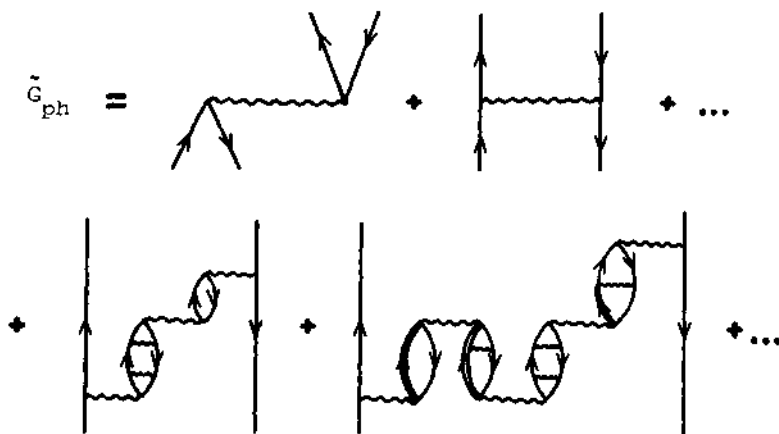


Fig. 17. Full particle-hole interaction. The first line is the so-called direct and exchange contribution from the Brueckner reaction matrix. The second line are examples for induced contributions to the particle-hole force. They are due to the polarization of the surrounding nuclear medium. Double lines indicate  $\Delta$ -isobars. The wiggly interaction lines always represent the Brueckner reaction matrix of a realistic potential.

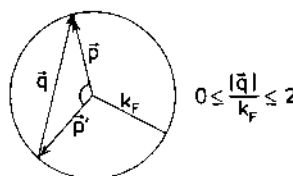


Fig. 18. In the Landau limit all ingoing and outgoing particle and hole momenta have the absolute value of the Fermi momentum  $k_F$ . The total particle-hole momentum  $k$  goes to zero. Thus the ph-force depends only on the angle between the relative momenta in the initial  $\vec{p}$  and the final state  $\vec{p}'$ . This angle can be represented by the absolute value of the vector  $q = |\vec{p} - \vec{p}'|$ . The Figure shows that  $q$  can take values between zero and  $2k_F$ . The ratio  $q/k_F$  can therefore vary between zero and 2.

identical with the Fermi momentum  $k_F$ . In addition the Landau limit requires that the total momentum of the particle-hole states goes to zero. In this limit the force depends only on the angle between the relative momentum  $p$  in the initial and the relative momentum  $p'$  in the final state (see Fig. 4). This situation is indicated in a Fermi sphere in Fig. 18. This figure also shows that the angle between  $\vec{p}$  and  $\vec{p}'$  can also be represented by the absolute value of the difference vector  $\vec{q}$ .  $q$  varies between zero and  $2k_F$ . Thus  $q/k_F$  varies between zero and 2. The result for  $g'_N$  is shown in Fig. 19 as a function of the ratio  $q/k_F$  for different approximations of the particle-hole force. The solid line shows the result including all diagrams indicated in Fig. 17 at normal nuclear density  $\rho_0$ . The dashed line includes only the induced interaction due to nucleon particle-hole states. The dashed-dotted line is the strength of the nucleon particle-hole interaction calculated only with the Brueckner reaction matrix as the particle-hole force. Important for the pion condensation is only the strength  $g'_N$  averaged over all momenta  $q$ . This yields for  $\rho = \rho_0$  ( $\rho = 1.5\rho_0$ )  $g'_N = 0.48$  ( $g'_N = 0.49$ ) for the Brueckner reaction matrix,  $g'_N = 0.58$  ( $g'_N = 0.59$ ) including the induced interaction with nucleon particle-hole states only and  $g'_N = 0.66$  ( $g'_N = 0.75$ ) including also  $\Delta$ -isobars. This increase of the particle-hole strength reduces drastically the probability for pion condensation as indicated in Fig. 20.

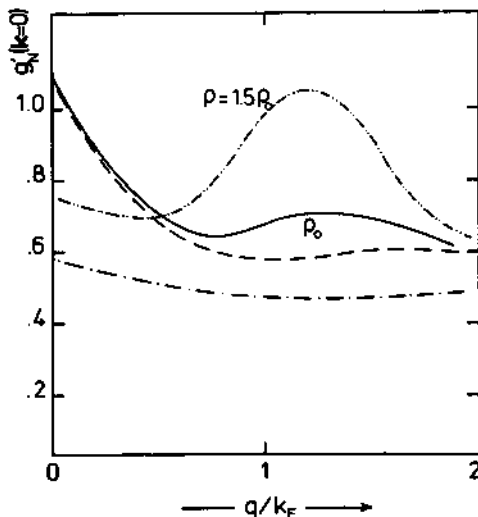


Fig. 19. The nucleon-nucleon particle-hole strength  $g_N^<0>$  for the Landau limit is shown at normal nuclear matter density  $\rho_0$  and  $1.5\rho_0$  as a function of the difference between the relative initial and final momenta  $q$  defined in Fig. 18. For pion condensation only the values averaged over all  $q$ 's are important. The dashed-dotted curve corresponds to the particle-hole interaction included also in Fig. 11. The value of the particle-hole strength averaged over  $q$  is  $g_N^<0>=0.48$ . The dashed curve includes the induced interaction shown in the first diagram in the lower part of Fig. 17. This means the intermediate bubbles in the induced interaction contain only  $NN^{-1}$  states. The particle-hole strength averaged over  $q$  has the value  $g_N^<0>=0.60$ . The solid line calculated for  $\rho=\rho_0$  includes also  $\Delta$ -isobars in the induced interaction as indicated in the last graph shown in Fig. 17. The particle-hole strength averaged over  $q$  is  $g_N^<0>=0.66$ . Experimentally it seems that the particle-hole strength  $g_N^<0>$  lies in nuclei at  $0.7 \pm 0.1^{10}$  and 0.66 (for  $^{48}\text{Ca}$ )<sup>12</sup>). The dashed-double dotted curve is calculated for  $\rho=1.5\rho_0$  and yields averaged  $g_N^<0>=0.75$ .

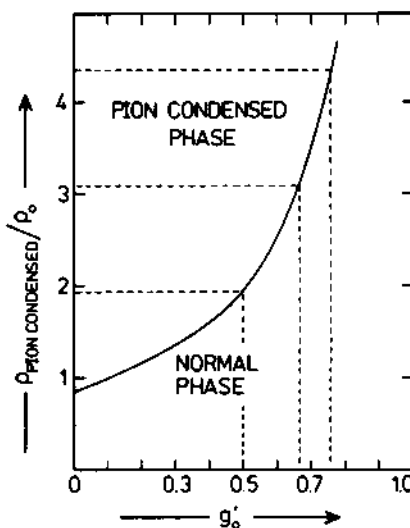


Fig. 20. Critical nuclear matter density  $\rho_{\text{cond}}$  in units of the empirical nuclear matter density  $\rho_0$  as a function of the averaged particle-hole strength  $g'_{\text{av}}$ .

Fig. 20 shows the nuclear matter density  $\rho_C$  at which pion condensation occurs in units of the empirical nuclear matter density  $\rho_0$  as a function of the averaged particle-hole strength  $g'_{\text{av}}$  defined in eqs. (5), (17) and determined from the proper selfenergy by assuming that  $g'_N = g'_{\Delta\Delta} = g'_{\text{av}}$ .

Thus we can draw the conclusion that the induced particle-hole interaction with diagrams as shown in the lower part of Fig. 17 shield inside the RPA-bubbles nuclear matter from pion condensation up to a very high nuclear matter density. This is obvious from the fact that the induced ph-force contains the same diagrams as the pion selfenergy. If these diagrams get so important that they drive to pion condensation, the induced force gets important in shielding the bubbles against pion condensation. At twice nuclear matter density  $\rho = 2\rho_0$  the strength  $g'_{\text{N}}$  diverges to infinity in this approximation. Pion condensation acts therefore as a shield against pion condensation.

But that does not mean that we are not getting pion condensation. The bubbles inside bubbles which shield against pion condensation are shielded again by a sequence of bubbles in these bubbles. Thus one has to sum up the series of bubbles in bubbles, in bubbles, ... up to infinity, since each finite sum would diverge. In solid state physics such sums are performed with the help of the renormalisation group method. But in solid state physics one uses also simpler methods to describe phase transitions. The Mean Field approach has the advantage that one is not doing the calculation relative to the normal state which leads into difficulties in a phase transition where one has tremendous changes relative to the normal state which can not be handled in for example the RPA approach.

In the following chapter we even simplify the Mean Field approach and study pion condensation in  $^{16}\text{O}$  and its temperature dependence.

#### PION CONDENSATION IN FINITE NUCLEI

Since nuclear matter is anyway a fictitious invention of the theoreticians one easily agrees to vary the density  $\rho$  in nuclear matter to test which minimal density is needed to achieve pion condensation. The density in finite nuclei is given and all theoretical calculations<sup>3,4,6,7)</sup> and also an experimental analysis<sup>10)</sup> show that we can not expect pion condensation in empirical finite nuclei. The only possibility to achieve the high nuclear matter densities needed might be in heavy ion collisions with appreciably high energies. At the moment we are still far away from a realistic calculation of a collision between two heavy ions to test if pion condensation occurs. In addition to the nuclear many body problem complicated by the  $\Delta$ -isobars and the pions one has to tackle the reaction problem, the high temperature of nuclear matter in the collision and the time element. It is not obvious that in a volume of nuclear matter in which pion condensation happens in a stationary state that it will also lead to pion condensation if this state is only reached for a short time. The eigentime of a pion  $\hbar/mc^2 \approx 5 \times 10^{-22}$  sec seems to be the minimum time needed for the phase transition leading to pion condensation. This is comparable to the reaction time in a heavy ion collision. We are studying at the moment in Tübingen the influence of the time element and of high temperature on pion condensation in finite nuclei. I can present here only some preliminary results for an adiabatic compression of  $^{16}\text{O}$  at zero temperature. Specifically we want to study the influence of the  $\Delta$ -isobars and the  $\rho$ -meson exchange on pion condensation in  $^{16}\text{O}$  if the density in this nucleus is increased by reducing its radius.

Fig. 1 shows that pion condensation in finite nuclear matter leads to a laminated structure of protons with spin up and neutrons

with spin down alternating with protons with spin down and neutrons with spin up. Fig. 13 shows that the pion momentum at which pion condensation occurs lies around the Fermi momentum  $k_F$ . The wave length of the stationary pion wave in the condensed state is thus around 5 fm. Since the radius of  $^{16}\text{O}$  is smaller than this value we expect that the pion condensed phase of  $^{16}\text{O}$  consists of a wave function which has only for example protons with spin up and neutrons with spin down as indicated in Fig. 21.

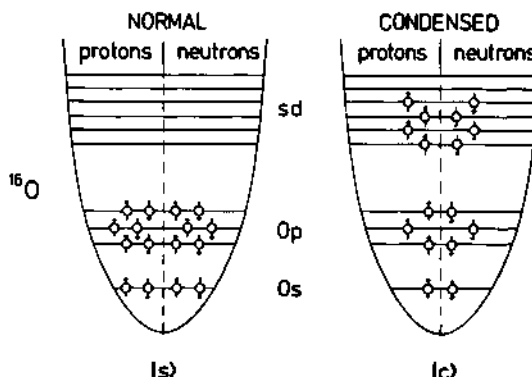


Fig. 21. Structure of the normal and the pion condensed solution of  $^{16}\text{O}$ . In the normal solution each spatial state is fourfold occupied. In the condensed solution as indicated in the text we have only a proton with spin up and a neutron with spin down. The condensed solution is represented by a Slater determinant of oscillator wave functions allowing for axially symmetric deformations with only a proton with spin up and a neutron with spin down in each spatial state. In the condensed solution we furthermore allow  $\Delta$  admixtures. The minimization of the total energy including the residual interaction  $\pi$  and  $\rho$  meson exchange yields a  $\Delta$  probability of 2.5% for the single-particle states.

This figure shows that a spatial single-particle state is occupied fourfold in a normal shell model Slater determinant:  $p\uparrow$ ,  $p\downarrow$ ,  $n\uparrow$ ,  $n\downarrow$ . A condensed Slater determinant has in every spatial wave function only two nucleons:  $p\uparrow$ ,  $n\downarrow$ . Therefore we approximate the normal shell model wave function of  $^{16}\text{O}$  by the usual Slater determinant  $|S\rangle$  of

oscillator wave functions in the  $0s$ ,  $0p$ , shells. The Slater determinant which represents the condensed phase  $|C\rangle$  is occupied as indicated in Fig. 21 and can be axially-symmetrically deformed. The averaged density in both wave functions is the same by requesting volume conservation.

$$\begin{aligned} b_z b_{\perp}^2 &= b_s^3 \\ b_o^2 &= \left(\frac{\hbar}{m_c}\right)^2 \frac{m_c^2}{\hbar\omega_o} \\ \hbar\omega_o &= 41/A^{1/3} \text{ [MeV]} \\ \rho/\rho_o &= (b_o/b_s)^3 \end{aligned} \quad (18)$$

$b_o$  is here the oscillator length for the ground state of  $^{16}\text{O}$  which reproduces the experimental root mean square radius.  $b_s$  is the oscillator length for the compressed normal Slater determinant. The oscillator lengths of the condensed solution are  $b_z$  and  $b_{\perp}$ .

We assume that the selfconsistent potential of  $^{16}\text{O}$  is well represented by an oscillator and that the residual interaction can be described by one-pion and one  $\rho$ -meson exchange.

$$H = \sum_{i=1} \left( \frac{p_i^2}{2m} + \frac{1}{2} m \sum_{v=x,y,z} \omega_v^2 x_{vi}^2 \right) + V_{\text{res}}$$

$$V_{\text{res}} = V_{\pi}(k) + V_{\rho}(k) \quad (19)$$

$$V_{\pi}(k) = -\frac{f_{\pi}^2}{m_{\pi}^2} \frac{1}{(2\pi)^3} \frac{(\vec{\sigma}_1 \cdot \vec{k})(\vec{\sigma}_2 \cdot \vec{k})}{m_{\pi}^2 + k^2}$$

$$V_{\rho}(k) = -\frac{f_{\rho}^2}{m_{\rho}^2} \frac{1}{(2\pi)^3} \frac{(\vec{\sigma}_1 \times \vec{k})(\vec{\sigma}_2 \times \vec{k})}{m_{\rho}^2 + k^2}$$

The  $\pi N$  and  $\rho NN$  coupling constants are taken to be  $f_{\pi}^2/(4\pi) = 0.08$  and  $f_{\rho}^2/(4\pi) = 5.0$ . We have included monopole type form factors with the cutoff masses  $\Lambda_{\pi} = 1000$  MeV and  $\Lambda_{\rho} = 2000$  MeV. We further generalized the single-particle states to include the admixtures of  $\Delta$ -isobars,

$$|\alpha\rangle = (|N\alpha\rangle + A|\Delta\alpha\rangle)/(1+A^2)^{1/2} \quad (20)$$

$A$  is the mixing amplitude for the  $\Delta$ -isobar. To simplify the calculation we assume that this value is the same for each single-particle

state. The inclusion of  $\Delta$ -isobars means that we have also to calculate the transition matrix elements:  $N\Delta-N\Delta$ ,  $NN-\Delta\Delta$ ,  $N\Delta-\Delta\Delta$ ,  $NN-N\Delta$  and  $\Delta\Delta-\Delta\Delta$ . The expectation value of the Hamiltonian (19) supplemented by the transition potentials is compared for the normal  $|S\rangle$  and the condensed  $|C\rangle$  solution.

$$E_C - E_S = \langle C | H | C \rangle - \langle S | H | S \rangle \quad (21)$$

The condensed solution  $|C\rangle$  is found by minimizing  $\langle C | H | C \rangle$  with respect to the mixing amplitude  $A$  of the  $\Delta$ -isobars and the ratio  $b_1/b_2$ . The results are given in Fig. 22. Keeping in the spirit of the mean field approximation we restrict ourselves here to the direct terms only and consider  $\pi^0$  condensation. That means we are not assuming that the single-particle wave functions are mixed states out of protons and neutrons.

The result of Fig. 22 without  $\Delta$ -isobars and with only  $\pi$ -meson exchange has been calculated by Do Dang<sup>11)</sup> for the case of  $^{12}\text{C}$ . This approximation yields for this (not realistic) model pion condensation at 8 times the normal nuclear matter density. Inclusion of  $\rho$  exchange reduces this value  $\rho/\rho_0 = 6$ .  $\Delta$ -isobar admixture reduces further the critical value of nuclear matter density at which pion condensation sets in. In our model we obtain with  $\pi$  and  $\rho$  meson exchange a value of about 3 times normal nuclear matter density. Compared to our previous calculations in nuclear matter this model for a finite nucleus is not very realistic: (i) we include nucleon-nucleon correlations through the introduction of a form factor.

(ii) The interaction contains only  $\pi$  and  $\rho$  exchange and is not realistic and does therefore not fit the nucleon-nucleon phase shifts. (iii) The induced particle-hole interactions which played such an important role in nuclear matter are not included. But in spite of all these limitations the calculation demonstrates that any study of pion condensation in finite nuclei which does not take into account the admixture of  $\Delta$ -isobars in addition to  $\pi$  also  $\rho$ -meson exchange can not be taken seriously. But this model indicates that calculations which do not take into account  $\Delta$ -isobars and  $\rho$ -meson exchange are not realistic.

This model is easily extended to include also temperature. This extension is important since the compression of a nucleus in a heavy ion collision is always connected with heating up the nucleus during the collision.

#### PION CONDENSATION AT FINITE TEMPERATURE

We want to consider now in the above nuclear model for  $^{16}\text{O}$  pion condensation at a fixed temperature and a fixed density<sup>5,13,14)</sup>. Under these conditions we have to minimize the free energy.

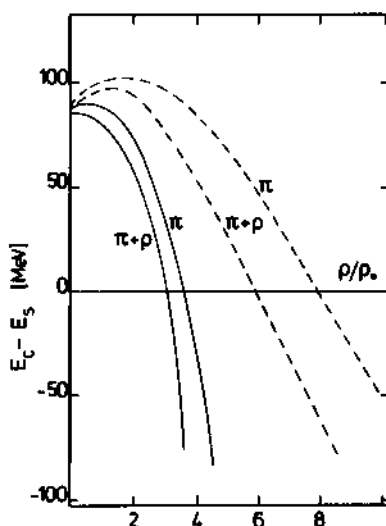


Fig. 22. Energy difference between the condensed solution and the usual shell model Slater determinant as a function of the density in  $^{16}\text{O}$  in units of the empirical nuclear matter density  $\rho_0$ . The density is varied by compressing the volume of the nucleus. The shell model and the condensed solution occupy the same volume ( $b_z b^2 = b_s^3$ ). The density in units of the nuclear matter density is defined by  $\rho/\rho_0 = (b_0/b_s)^3$ . The oscillator  $b_0$  reproduces the correct root mean square radius for the ground state in  $^{16}\text{O}$ . It is defined by the oscillator energy  $\hbar\omega_0 = 41/\text{A}^{1/3}$  [MeV]. The dashed curves show the difference between the condensed and the normal solution including only  $\pi$  and including  $\pi$  and  $\rho$  meson exchange for the residual interaction. This model calculation would yield pion condensation at 8 and at 6 times the nuclear matter density if no  $\Delta$ -isobars are included. The solid lines include also admixtures of  $\Delta$ -isobars in the single-particle states. The minimization of the total energy yields an admixture of 2.5%. The two curves are the results for  $\pi$  and  $\pi + \rho$  meson exchange for the residual interaction. This model would yield if all effects are included pion condensation in  $^{16}\text{O}$  if it is compressed to about 3 times the nuclear matter density.

$$F = E - T \cdot S \quad (22)$$

The temperature is defined by the usual Fermi distribution of the nucleons over the single particle levels.

$$\rho_i = [1 + \exp \{(\epsilon_i - \mu_f)/T\}]^{-1} \quad (23)$$

The Fermi surface  $\mu_f$  has to be determined by having the correct nucleon number for the protons and neutrons. The entropy is given by:

$$S = - \sum_i [\rho_i \ln \rho_i + (1 - \rho_i) \ln (1 - \rho_i)] \quad (24)$$

Again we describe the normal state by a spherical oscillator potential with  $p_\uparrow$ ,  $p_\downarrow$ ,  $n_\uparrow$  and  $n_\downarrow$  in a spatial level. For the condensed state we allow for axial symmetric deformation and put only a  $p_\uparrow$  and a  $n_\uparrow$  in each spatial level. Pion condensation is then obtained if  $F_C - F_N < 0$ .

Fig. 23 shows the phase diagram of the temperature against the density in units of  $\rho_0$ . The general trend is (as already found by Greiner and coworkers<sup>5</sup>) that the critical density shifts to higher values with increasing temperature. (An opposite result which was recently obtained by Glendenning and Lumbroso<sup>14</sup>) is not correct since it minimizes the energy  $E$  instead of the free energy  $F$ .) At low temperature one sees in fig. 23 that surprisingly pion condensation is facilitated with increasing temperature. This is connected with the closed shell character of normal  $^{16}\text{O}$  and the open shell character of condensed  $^{16}\text{O}$ . At temperatures below the shell energy ( $T < \hbar\omega$ ) an increase of  $T$  does not enhance the entropy  $S$  for normal  $^{16}\text{O}$ . In condensed  $^{16}\text{O}$  which has no closed shell an increase of  $T$  enhances the entropy  $S$  and thus lowers the free energy  $F_C = E_C - S_C \cdot T$ . If it is possible to compress in a heavy ion (HI) collision a magic nucleus without destroying the closed shell character up to the critical density a moderate increase in temperature would assist pion condensation. But probably one can not compress a nucleus in a HI collision up to the critical density  $\rho_c$  without destroying the shell closure.

## CONCLUSIONS

First we studied the influence of realistic nucleon-nucleon interactions on pion condensation in nuclear matter. If a pion travels through nuclear matter, its interaction with the nucleons lowers the energy. If the lowering is equal or larger than the kinetic energy and the rest energy of the pion we speak of pion condensation. This means that such polarized pion states in nuclear matter can be created without additional energy. The polarization

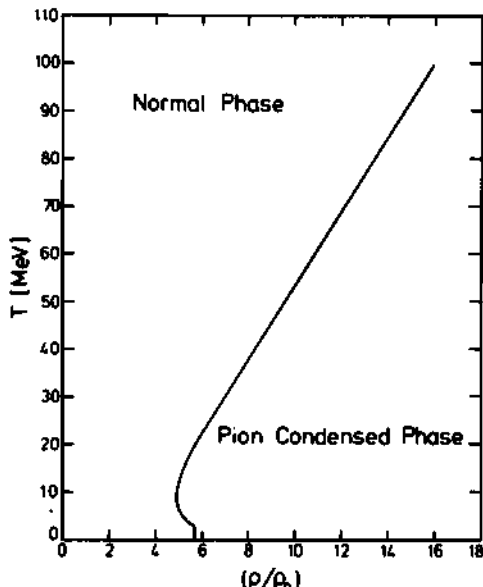


Fig. 23. Critical temperature for the transition from the normal to the pion condensed phase as a function of the density  $\rho/\rho_0 = b_0^3/(b_\perp^2 b_z)$  in  $^{16}\text{O}$ . For the pion condensed nucleus we allow for axially symmetric deformation with a different oscillator length  $b_z$  in  $z$  direction and  $b_\perp$  in  $x, y$  directions.  $b_0$  is the oscillator length for the ground state of  $^{16}\text{O}$ . Small temperatures below  $\hbar\omega$  assist pion condensation.

of the surrounding nuclear matter is due mainly to nucleon-particle and nucleon-hole excitations and also due to  $\Delta$ -isobar and nucleon-hole states. In addition the surrounding nuclear matter modifies also the particle-hole interaction by the so-called induced nucleon-nucleon force.

We asked the following questions:

- (a) Can the interaction of the pion with the nucleon particle-hole states  $NN^{-1}$  lower the energy of the pion down to zero and produce by that pion condensation? We found that with realistic interaction this is not possible at a reasonable nuclear matter density.
- (b) We included then not only the interaction of the pion with nucleon ph ( $NN^{-1}$ ) states but also with  $\Delta$ -isobar nucleon hole ( $\Delta N^{-1}$ ) configurations. Using the Reid soft core and one of the Bonn ( $HM2+\Delta$ ) potentials we found a particle-hole strength parameter of about  $g'_0 = 0.5$  and pion condensation at twice the normal nuclear matter density.
- (c) What happens to pion condensation if one takes into account that the particle-hole interaction is not only represented by the Brueckner reaction matrix but is modified by the polarization of the neighbouring nucleons in nuclear matter? It turned out that this induced interaction increases inside the RPA-bubbles and increases  $g'_0$  to 0.66 at normal nuclear density and shields nuclear matter from pion condensation up to higher nuclear matter densities (around  $3 \rho_0$ ). But at densities  $\rho=2\rho_0$  the particle-hole strength  $g'_0(\rho)$  in the pion channel is diverging. The induced interaction contains among others the same propagator as in the pion channel. Since it is there an exchange interaction it shields inside the bubbles against pion condensation. Thus pion condensation is shielding against pion condensation if one includes terms up to bubbles in bubbles. But there it does no stop: Bubbles inside the bubbles in bubbles shield against the shielding and so on. Thus one has to sum at least the sequence of bubbles in bubbles in bubbles ... up to infinity to get a reasonable answer for the critical density. Since this is too difficult at the moment we propose to use the mean field approach which is successful in solid physics in describing phase transitions.
- (d) In the 6. chapter we discussed pion condensation in the finite nucleus  $^{16}O$  with the mean field method. Here we did not use realistic forces but we restricted the residual nucleon-nucleon interaction to  $\pi$  and  $\rho$  meson-exchange. We found that the inclusion of  $\Delta$ -isobars and the  $\rho$ -meson exchange is essential. These effects reduce pion condensation in a compressed  $^{16}O$  from  $8 \rho/\rho_0$  to  $3 \rho/\rho_0$ . It means that any calculation of pion condensation in finite nuclei which does not take into account  $\Delta$ -isobars and effects of  $\rho$ -meson exchange is not realistic.

- (e) In chapter 7 we studied in  $^{16}\text{O}$  the temperature dependence of pion condensation. We found that in doubly closed shell nuclei an increase of the temperature  $T$  below the shell energy  $\hbar\omega$  is assisting pion condensation. But the general trend is that the critical density increases with the temperature.

The problem of pion condensation in nuclei is even after the investigations presented here far away from its final solution. One still has to solve the main questions:

- (1) Is the critical density for pion condensation finite? What is the critical density? Can this density be obtained in heavy ion collisions? To answer at least part of these questions one has to perform mean field calculations in finite nuclei which improve on the simple model wave functions and on the forces employed in chapter 6. We are working at the moment on such investigations.
- (2) One should include realistic information about the temperature connected with HI reactions which compress the nucleus to the critical density  $\rho_c$ . Compression in a cold HI collision would be preferential. This suggests for pion condensation a collision of a closed shell nucleus with an other closed shell nucleus. Investigations of corresponding HI collisions allowing for temperature are needed.
- (3) Pion condensation is a phase transition which needs time. The times in which one finds the high densities in HI collisions are according to hydrodynamic calculations<sup>15)</sup> of the order of  $3 \times 10^{-23}$  sec. The pion condensation needs at least the eigentime of the pion  $\hbar/(m_\pi c^2) \approx 0.5 \times 10^{-23}$  sec but probably more. To study this question we do time dependent Hartree-Fock calculations.
- (4) An open problem are the experimental fingerprints of pion condensation. Gyulassy<sup>16)</sup> estimated that kinetic energy might be transferred from the relative motion of the HI's to the condensed pion to bring them on energy shell. Nagamiya et al<sup>17)</sup> showed experimentally that in the  $\text{Ne} + \text{NaF} \rightarrow \pi^- (\theta_{CM} = 90^\circ) + \text{X}$  reaction this is not the case in the degree estimated by Gyulassy<sup>16)</sup>.

If one asks me finally if it will be possible to find once pion condensation in HI collisions, I would answer that I am not prepared to bet money on it if it is my own.

The above investigations have been done in collaboration with W.H. Dickhoff, A. Goodman, J. Meyer-ter-Vehn, H. Müther, K. Shimizu and R.K. Tripathi.

## REFERENCES

1. A.B. Migdal, ZhETF 61 2210 (1971); Nucl. Phys. A210: 421 (1973)
2. R.F. Sawyer, Phys. Rev. Lett. 29: 386 (1972)  
D.J. Scalapino, Phys. Rev. Lett. 29: 386 (1972)  
R.F. Sawyer, D.J. Scalapino, Phys. Rev. D7: 953 (1973)
3. G.E. Brown, W. Weise, Phys. Rep. 27C: 2 (1976)
4. S.O. Bäckman, W. Weise, in "Mesons and Nuclei", ed. M. Rho,  
D.H. Wilkinson (North-Holland, Amsterdam 1979) p. 1095
5. V. Ruck, M. Gyulassy, W. Greiner, Z. Physik A277: 391 (1976)  
M. Gyulassy, W. Greiner, Ann. Phys. 109: 485 (1977)
6. W.H. Dickhoff, A. Faessler, J. Meyer-ter-Vehn, H. Müther,  
to be published.
7. R.K. Tripathi, A. Faessler, K. Shimizu, Z. Physik A297: 275 (1980)
8. R.V. Reid, Ann. Phys. (N.Y.) 50: 411 (1968)
9. K. Holinde, R. Machleidt, Nucl. Phys. A280: 429 (1977)
10. J. Meyer-ter-Vehn, Z. Phys. A287: 241 (1978)
11. G. Do Dang, Phys. Rev. Lett. 43: 1708 (1979)
12. A. Richter, private communications
13. P. Hecking, Nucl. Phys. A348: 493 (1980)
14. N.K. Glendenning, A. Lumbroso, preprint LBL-12108 (1981)
15. R. Nix and W. Greiner, private communications
16. M. Gyulassy, Nucl. Phys. A354: 395 (1981)
17. S. Nagamayi et al. LBL-7766 (1981)

## SHORT-RANGE NUCLEON-NUCLEON INTERACTION AND QCD POTENTIAL MODELS

C.S. Warke

Tata Institute of Fundamental Research  
Bombay, India, and Institut für Theoretische  
Physik, Frankfurt (M), West Germany

### INTRODUCTION

In this conference we are already introduced to the quantum-chromo-dynamics (QCD) field theory. Therefore, instead of repeating the theoretical ideas, the experimental results leading to the specific theoretical points are summarized before I come to the main theme of the talk. The strongly interacting particles are grouped into mesons and baryons depending on their integral or half-integral spin. Gellman and Zweig proposed the SU(3) (eight fold way) to classify hadrons into groups of particles having similar masses, spins, parities and reaction properties. Now we believe that hadrons are bound states of a few fundamental particles of spin  $s=1/2$ , the constituent quarks, interacting through gluons.

$(\frac{u}{d})$ ,  $(\frac{c}{s})$ ,  $(\frac{t}{b})$  with charge and baryon number  $(\frac{2/3}{-1/3}, \frac{1/3}{1/3})$ .

The striking success of these concepts has been in classifying and accounting of hadrons and in the understanding of their spin-parity assignments, magnetic moments and transition matrix elements. Further details of spectroscopy requires the knowledge of quark-quark (qq) interaction. The essential properties of this interaction can be inferred from the following experimental observations. Free quarks not yet seen: qq interaction strongly binding (confining). Hadron binding is small compared to quark masses and that flavour is conserved in strong interactions: qq interaction flavour independent, can be mediated by flavour independent field.

$m(\pi) < m(\rho)$ ,  $m(\kappa) < m(\kappa^*)$ ,  $m(D) < m(D^*)$ : As in positronium  $e^+e^-$   $m(^1S_0) < m(^3S_1)$ , where the Coulomb interaction arises from vector photon exchange, similarly  $qq$  interaction is mediated by a vector gluon field.  $\Delta^{++}(3,3)$ ,  $\Omega^-(s^3)$  with  $s=3/2$ : lowest configuration space symmetric, spin and flavour wave functions are also symmetric; quark statistics therefore requires three colored quarks.  $\alpha_{\text{expt}}(\pi \rightarrow 2\gamma) = 9 \alpha_{\text{theo}}$ : 3-colored quarks being  $\alpha_{\text{expt}} = \alpha_{\text{theo}} \cdot m(N) < m(\Delta)$ : If spin-spin splitting is due to uncolored gluons,  $m(N) > m(\Delta)$ ; for colored gluons  $m(N) < m(\Delta)$ . Therefore  $qq$  interaction is color magnetic.

In order to observe the quark structure of the proton, a resolution of distances of the order 0.1 proton radius  $\approx 0.1$  fm ( $= \lambda$ ) would require beam energy  $E = pc = 2\pi\hbar c/\lambda = 2$  GeV. For clean experimental situation, the projectile should be a point particle, its dynamics and interaction with proton should be accurately known. The conclusion of such experiments are summarized below.

- (a)  $e^-P$  scattering  $5 < E < 100$  GeV, scaling:  $\lim F_{e^-, m}(q^2, \gamma) = F_{e^-, m}(x)$  as  $q^2, \gamma \rightarrow \infty$ ;  $x = q^2/2M$ . It leads to non-interacting point like constituents of  $P$ , scattering arises from  $e^-q$  interaction.  $\langle 2xF_{e^-, m} \rangle = 0.94 \pm 0.03$ , spin  $1/2$  quarks with  $g = 2$  gives this value to be 1.0.
- (b)  $\nu + N \rightarrow \mu^+x$ ;  $\bar{\nu} + N \rightarrow \mu^- + x$ ;  $2 < E < 100$  GeV: Measured  $R = \sigma(\bar{\nu}N)/\sigma(\nu N) = 0.38 \pm 0.2$  independent of  $E$ , SU(3) quark model gives  $R = 1/3$ . The experimental value of average charge square of proton  $\bar{A}_V(z^2) = 0.29 \pm 0.03$  and number of quarks in proton  $N(q) - N(\bar{q}) = \sum_i 3.2 \pm 0.6$  while SU(3) model predicts their value  $1/3$  and 3 respectively.
- (c)  $e^+ + e^- \rightarrow \text{hadrons}$ : The theoretical SU(3) colored quark prediction for  $R = \sigma(e^+e^- \rightarrow h)/\sigma(e^+e^- \rightarrow \mu^+\mu^- + h) = 3 \sum_i e^2 q_i$  for  $E < m_c$  which agrees with its measured value.

The observed properties are compatible with a gauge field theory of quarks and gluons; color SU(3) is an exact symmetry of strong interactions and hadrons are color singlet objects.

A strong interaction theory that explains hadrons provides a natural foundation for the theory of nuclear physics. The forces between elementary strongly interacting particles, quarks and gluons, which determine the structure of baryons and mesons should also determine the interactions between them. This is analogous to the calculation of molecular potential curves which are determined from the Coulomb interaction between charges, which determine the structure of atoms. The Coulomb interaction itself being deduced from the electromagnetic interaction between charges and photons, the elementary constituents. The difficulty is that unlike QED, QCD is a non-abelian field theory and that the coupling is strong. Therefore, one uses models based on some of the essential properties of QCD.

## QCD POTENTIAL MODELS

The non-relativistic potential models have some validity for heavier mesons having heavier quark constituents. Unfortunately, in nuclear physics, lighter mesons are most important - in which case such an approximation is most likely incorrect. Moreover, nuclear physics necessarily involves many-body complications for which there exists no relativistic theoretical framework of composite system. Even though the use of Schrödinger equation with Breit interaction (or its modification) could be a fairly bad approximation, it could still be of use in finding qualitative correlation and mutual consistency between nuclear physics and high energy physics strong interaction data. Pioneering work on hadron spectroscopy within this model is that of Dalitz et al.<sup>1</sup>. Later, Robson<sup>2</sup> developed it extensively in order to carry it through in nuclear physics. Shanker and Warke<sup>3</sup> used it to derive the NN potential using the Feshbach-Rubino method. The basic question is: Is there a simple explanation of the simple features of the NN interaction? - Such as short-range repulsion for all 1, parity, spin and isospin states of NN system; sign and strength of NN  $\vec{L} \cdot \vec{S}$  interaction which is the basis of nuclear shell model; difference between AN (and  $\Sigma N$ ) force at short distances and the NN repulsion. In our calculations we used Breit interaction and the correct dynamical degrees of freedom to construct the appropriate configuration space-symmetric wave functions which included two-body correlations. Using the generalized Pauli principle, the baryon masses and the corresponding wave functions  $\mathbf{f}_i(1,2,3)$  were obtained. The four parameters in the Hamiltonian  $m_u$ ,  $m_s$ ,  $\alpha_s$  and  $\alpha$  were fixed from the lowest octet baryon masses. The decuplet masses, magnetic moments and charge radii provided the consistency check. The masses agreed within 50 MeV, magnetic moments required a small quark anomalous moment and the proton charge radius came out to be too small 0.3 fm. Using these color "atomic" wave functions (color singlet) six quark antisymmetric color "molecular" wave functions were constructed:

$$\psi(1,2,3--6) = \frac{1}{\sqrt{20}} \sum_{\alpha=1}^{20} (-1)^\alpha P_\alpha \{ \mathbf{f}_a^S(123) \mathbf{f}_b^T(456)$$

$$F_{ST}(\vec{r}_1 + \vec{r}_2 + \vec{r}_2 - \vec{r}_4 - \vec{r}_5 - \vec{r}_6/3) \}$$

The six quark Schrödinger equation is then reduced to the following wave equation for

$$\psi_{ST} = [ F_{ST}(\vec{R}) + (-1)^{S+T+1} F_{ST}(-\vec{R}) ] / \sqrt{2} ,$$

$$\frac{\vec{p}_2}{3m} \psi_{ST} + \langle \mathbf{f}_a \mathbf{f}_b | \sum_{i \in a} \sum_{j \in b} V(ij) (1-9 P_{36}) | \mathbf{f}_a \mathbf{f}_b \psi_{ST} \rangle / N = \epsilon \psi_{ST} .$$

The interaction term involves integration over internal variables of the clusters  $a$  and  $b$ . Because of the action of  $P_{36}$  on  $\psi_{ST}$  the above NN interaction is nonlocal. However, consistent with well known NN interactions, the nonlocality is kept only to lowest order expansion in the momentum operator. The denominator  $N(R)$  is the normalization integral over the internal variables. After performing the spin, flavour and color algebra, one finds for the central and color magnetic  $qq$  interaction,

$$V_e(R) = -4 \langle \mathbf{s}_a \mathbf{s}_b | [V_e(14) + V_e(36) - 2V_e(16)] P_{36}^{\infty} | \mathbf{s}_a \mathbf{s}_b \rangle f(ST)$$

$$V_{\sigma\sigma}(R) = \frac{32\pi^2\alpha_s}{3m^2c^2} \langle \mathbf{s}_a \mathbf{s}_b | \delta(14)f_{ST}(14) + \delta(36)f_{ST}(36) - 2\delta(16)f_{ST}(16) | \mathbf{s}_a \mathbf{s}_b \rangle$$

where  $f_{ST}(ij) = (1/486, 0); (19/108, 55/108); (-7/108, -7/108)$  corresponding to ST values  $(10,01)$  for  $ij = (14), (36)$  and  $(16)$  respectively. As all the radial integrals are positive, there is a large cancellation at short distances in the case of  $V_e$  while due to the appropriate change in phase of  $f_{ST}(ij)$ , there is a coherent addition in  $V_{\sigma\sigma}$  at short distances where  $p^* \approx 1$ . Thus the color magnetic  $qq$  interaction is responsible for the short range NN repulsion arising from the quark exchange mechanism. It was also found that the 1.5 and tensor  $qq$  interaction gave rise to the corresponding NN interaction of correct sign but these were too weak. There was no attraction in the intermediate range of  $r=1.2\text{fm}$  and no long range pion tail. Shanker, Greiner and Warke<sup>4</sup> used this wave function with a Gaussian relative cluster wave function, whose oscillator parameter was fixed from the deuteron radius, to calculate the spectroscopic factor of  $\Delta\Delta$  component in the deuteron wave function. The calculated theoretical value of 0.32% is in reasonable agreement with its measured value 0.4 - 0.9%. Earlier attempts<sup>4</sup> required an additional repulsion at short distances. The conclusion is that the nucleon q-structure in antisymmetric 6q deuteron wave function correctly incorporates the short-range repulsive correlation. There is no additional source of such correlation arising from the gluon exchange mechanism.

Harvey<sup>5</sup> finds that the effect of the color octet cluster mixing in the deuteron wave function reduces the short range repulsion to zero. Within such a theoretical model, it is questionable whether one should mix the colored baryon states in calculating the NN interaction. This is so because color octet states would be strongly coupled to the gluon field, not included in the theory, and this will make these states decay quickly to the color singlet baryon clusters. Even though such states may exist in

bound states they should not be mixed into scattering states of color singlet baryons. It is not a question of closed or open channels energetically but of the physical requirement that a color singlet six quark state of two color octet baryons can not be unconfined. Matsuyama<sup>6</sup> et al. and Gavela<sup>7</sup> et al. find that the confining  $qq$  interaction leads to the van der Waals force  $\propto -\text{const}/R^3$  inconsistent with the known nuclear interaction. Part of the difficulty is related to the fact that the confining interaction does not confine colored states of multi-quark systems, and may even confine such color singlet clusters. There have been attempts to introduce relativistic effects<sup>8</sup> by taking the kinetic energy operator to be  $\sqrt{p^2+m^2}$  and replacing the Breit interaction with that which has both the asymptotic freedom and the confinement property<sup>9</sup>. Liberman<sup>10</sup> used two center shell model with Gaussian wave functions, fitted to reproduce proton radius. With no other consistency checks of any kind, his NN interaction agrees reasonably well with the known soft core interaction except the pion tail.

#### THE MIT BAG MODEL

In this model quarks and gluons are confined to a bag. The real vacuum pressure from outside the bag balances the quark and gluon pressure from inside to keep the bag's surface in equilibrium. Inside the bag perturbative free vacuum allows one to use perturbative methods to calculate baryon masses and their static properties. The extensive application of this model to the baryon and meson static properties are carried out by de Grand et al., Jaffe, Isgur et al. and Johnson et al.<sup>11</sup>. DeTar<sup>12</sup> used this model to derive the NN interaction model. Using the baryon structure wave functions and eigenvalues, he took the trial six quark variational wave function,  $\psi(1,2..6) = [L\bar{L}L\bar{R}R\bar{R}]$ , where the cluster single quark molecular orbitals  $q_{L,R} = q_s + r_{\mu}q_p$ , and  $q_s$  and  $q_p$  are the quark orbitals derived from baryon structure. The variation is performed with the constraint that the NN separation defined by  $R_{12}^2 = \langle \psi | \sum (3z_i^2 - r_i^2) | \psi \rangle$  is constant. The NN interaction is then defined to be  $\langle H_F^i \rangle + BV - 2M_N$ . Firstly it is to be noticed that the 6 quarks are always confined to the spherical bag, only the  $q$ -orbitals inside are deformed. The above interaction definition has the following disadvantage: It includes in the NN interaction spurious center of mass kinetic energy. Secondly, Wong<sup>13</sup> pointed out that the relative motion kinetic energy has to be subtracted from DeTar's definition of  $V_{NN}$ . The result is that the NN interaction is very strongly attractive in the intermediate range and has an unphysical long range repulsion arising from the 6-quark confinement in the bag. Besides one does not know in which equation this interaction is to be used. Contrary to known nuclear interaction properties, Wong<sup>13</sup> finds strong nuclear many-body interactions within MIT bag model.

## THE LITTLE BAG MODEL

It is well known that MIT bag model violates the chiral invariance, i.e. the axial vector current is not conserved across the bag. Brown and Rho<sup>14</sup> argue that the MIT bag size of  $R \approx 1$  fm is too large to be consistent with nuclear properties. Therefore they introduce a bag of size  $R \approx 0.3$  fm and a pion as a structureless particle in order to restore chiral invariance. For such a bag of high mass density, chiral symmetry is spontaneously broken outside the bag to have a Goldstone boson-a pion. Inside the bag  $\mathbf{f}_\pi = 0$  and  $\mathbf{f}_\pi$  outside the bag is connected to the bag's surface by matching the pion axial vector current to the quark axial current at the bag's surface. This model has the advantage that it now reproduces the one pion exchange tail of the NN interaction besides the short distance repulsion. With the use of Goldberger-Treiman relation, it gives axial vector coupling constant  $g_A = 1$  and predicts  $\Delta^{++} \rightarrow p + \pi^+$  width to be 94 MeV whose measured value is 110 to 120 MeV. However, the disadvantages are the pion and Goldberger-Treiman relation do not come from the QCD model but are additional inputs. Secondly, in order to restore the baryon mass, one has to carry out perturbative theory whose lowest order contribution is 50% of the unperturbed value. One is faced again with the difficulty of perturbative theory for large coupling constant.

## SHORT RANGE CORRELATIONS IN THE DEUTERON WAVE FUNCTION

Brodsky and Chertok<sup>15</sup> extract this information from the large momentum transfer elastic electron scattering off deuteron. For large  $q^2$  binding effects are negligible. The elastic form factor has the same short distance scaling behaviour as the amplitude of electron scattering from on shell N and P each with equal share of total momentum. Nucleus being a system of several scales of compositeness, they define a reduced form factor  $f_A(q^2) = F_A(q^2)/\prod_i f_i(q_i^2)$  where  $q_i = m_i \vec{q}/m_A$ . The baryon form factors  $f_i$  remove the minimal fall of  $F_A$ . For large  $q^2$  the dimensional scaling law then leads to  $(q^2)^{A-1} f_A(q^2) \rightarrow \text{constant}$ . From pp and NP scattering data fixed  $\theta_{cm}$  and the e-d scattering they extract the deuteron wave function value at zero separation to be  $\sqrt{4\pi} \psi_a(0) \approx 0.1(m_\pi)^{3/2}$ , which is close to that derived from soft core potentials. This clearly demonstrates that at least up to distances  $r \geq 0.08$  fm there is no hard core in the NN interaction. They further show that for large  $q^2$ , the effective interaction scales with the square of the nucleon form factor. Once again this demonstrates that the entire fall of the NN potential at short distances is due to the dynamical structure of the nucleons in the deuteron with no additional fall from the exchange force. The same conclusion was reached by Shanker, Greiner and Warke from their study of the isobar component of the deuteron wave function which also sensitively depends on the short range NN correlation.

## THE OZI RULE AND THE NN INTERACTION

The one boson exchange potential (OBEP) is by far the best NN known interaction. While doing the best fit to the observed phase shifts, the optimum value of the  $\delta$ ,  $\delta^*$  and  $s^*$  coupling to nucleon is found to be  $1/30$  times the coupling of other mesons to nucleon. The question is, can we understand this from the point of view of QCD models and why does the second order OBEP form work so well. In the OBEP the essential NN attraction arises from the hypothetical scalar  $\epsilon$  and  $\sigma$  meson exchange. Does QCD model provide a possibility of simulating  $\epsilon$  and  $\sigma$  boson exchanges? Lovas<sup>16</sup> found that these points are consistent with the OZI rule. The emission of a strange  $s\bar{s}$  pair by a nucleon, carrying three ( $u,d$ ) quarks, is possible only by creating a disconnected  $s\bar{s}$  quark line. This requires at least two gluon creation and annihilation. According to the OZI rule this graph is forbidden. As the constituents of  $\delta$ ,  $\delta^*$  and  $s^*$  are  $s\bar{s}$  quarks, their coupling to nucleons is expected to be smaller from the OZI rule as observed in OBEP. The other non-strange mesons can be emitted by simply bending one quark line (after cutting) of the non-strange constituent quarks through one gluon exchange. As there are three quarks in a nucleon, at most three mesons can be simultaneously exchanged by bending three quark lines. The exchange of one lighter meson includes the contribution coming from graphs in which only one quark line is bent. The exchange of  $\epsilon$  and  $\sigma$  includes the contribution of two simultaneous exchanges or graphs corresponding to the bending of two simultaneous quark lines. The simultaneous bending of three quark line graphs is the only one not included in the OBEP. This is why the OBEP works so well.

## REFERENCES

1. R. Horgan and R.H. Dalitz, Nucl. Phys. B66:135 (1973).  
R.H. Dalitz, "Topics in Quantum Field Theory and Gauge Theories", ed. J.A. de Azcarraga, Springer Verlag, Heidelberg (1977).
2. D. Robson, Nucl. Phys. A308:381 (1978).  
D.P. Stanley and D. Robson, Phys. Rev. D22:165 (1980).
3. R. Shanker and C.S. Warke, Z. Phys. 6:17 (1980); Hadronic J., 3:1108 (1980); Phys. Rev. C21:2643 (1980); Phys. Lett. 89B:17 (1979).
4. C. S. Warke, R. Shanker, and W. Greiner, J. Phys. G7:L1 (1981); Y.F. Smirnov and Y.M. Tchuvilsky, J. Phys. G4:L1 (1978).
5. M. Hsirvey, Nucl. Phys. A353:301 (1981).
6. S. Matsuyama and H. Miyazawa, Progr. Theor. Phys. 61:942 (1979).
7. M. B.Gavela et al., Phys. Lett. 82B:228 (1981).  
D. Robson, Erice Spring School "Quarks and Nucleus" Ettore Majorana, ed. H. Wilkinson, 1981.

8. R. K. Bhaduri et al., Phys. Rev. Lett. 44:1369 (1980).  
D. Robson, Phys. Rev. D13:2004 (1976).
9. J. L. Richardson, Phys. Lett. 82B:272 (1979).
10. D. A. Liberman, Phys. Rev. D16:1542 (1977)
11. T. DeGrand et al., Phys. Rev. D12:2060 (1975).  
R. W. Jaffe, Phys. Rev. D15:267, 281 (1977).  
N. Isgur and G. Karl, Phys. Rev. D18:4187 (1978).  
K. Johnson and C.B. Thorn, Phys. Rev. D13:1934 (1976).
12. C. DeTar, Phys. Rev. D17:323 (1978); D19:1451 (1979).
13. C. W. Wong, Erice Spring School 'Ettore Majorana' on "Quarks and Nucleus, ed. H. Wilkinson, 1981; Phys. Rev. D - to be published, UCLA preprint, 1981.  
C.W. Wong and K.F. Liu, Phys. Rev. D21:2039 (1980).
14. G. E. Brown and M. Rho, Phys. Lett. 82B:177 (1979); Phys. Lett. 97B:423 (1981).
15. S. J. Brodsky and B.T. Chertok, Phys. Rev. D14:3003 (1976).
16. I. Lovas, "Few-Body Nuclear Physics", IAEA, Vienna, 1978.

## QUARK INTERCHANGE IN BAG-MODEL QCD

H.J. Weber\*

Department of Physics  
University of Virginia  
Charlottesville, VA 22901

Over the past 45 years Yukawa's pion exchange has evolved into a sophisticated one-boson-exchange (OBE) plus two-pion-exchange representation for elastic nucleon-nucleon (NN) scattering.<sup>1</sup> Similar meson exchange models hold more generally for baryon-baryon, meson-baryon and meson-meson scattering at low energy and low momentum transfer. The couplings involved are governed by the broken SU(6) symmetry (constituent quark model). The success of this local model in light nuclei is surprising and calls for an explanation because of the empirically known size of about 1 fm of the baryons and mesons so that, for example, four nucleons barely fit into  ${}^4\text{He}$  without overlapping.

According to quantum chromodynamics, a color SU(3) gauge model which is now widely accepted as a candidate for a strong interaction theory, hadrons consist of fundamental point-like quarks and antiquarks whose interaction is mediated by eight gluons which are massless, colored gauge bosons.<sup>2</sup> Thus, in contrast to the conventional local model of nuclear forces in terms of point-like baryons, the latter are composite, extended particles consisting of three valence quarks predominantly while mesons are quark-antiquark composites. Thus, meson (or  $Q\bar{Q}$ ) exchange at low  $q$  is equivalent to some form of valence quark interchange which is required to be local for color singlet hadrons if the OBE + TBE + ... representation is valid. In this form Yukawa's meson exchange can serve as a guide in the search for the underlying, fundamental quark-gluon mechanism.

It is generally expected that QCD will explain the OBE + TBE + ... representation, particularly the unknown short range regime but also its local character in color singlet channels at long

range, and the presently fitted form factors involving large regulator masses ( $1.5-2 \text{ GeV}/c^2$ ), the static  $SU(6)$  symmetry broken according to ideal mixing, and the chiral properties characteristic of the pseudoscalar mesons, like the pion, as Nambu-Goldstone bosons.

Since QCD is asymptotically free, the effective quark-gluon coupling  $\alpha_c = g^2/4\pi$  is small at high  $q$  so that perturbation theory is applicable. At low  $q$ , when  $\alpha_c$  is large, color is expected to be confined; but it is not well understood how this comes about. In the confinement regime of QCD, therefore, phenomenological models have been developed which incorporate quark confinement in terms of a local potential, e.g. a linearly rising one<sup>3</sup> or an infinite square well in the MIT bag model.<sup>4</sup> Moreover, when  $\alpha_c$  becomes sufficiently large, gluons appear to condense in the QCD vacuum<sup>5</sup> and for  $\alpha_c > 9/8$  it has been suggested<sup>6</sup> that color flux strings form between quark-antiquark pairs which leads to pair instability and  $Q\bar{Q}$  condensation. Such condensates imply nonlocal effective quark interactions which cannot be generated perturbatively nor be represented by a local confinement potential.<sup>7</sup> These processes are ignored in recent attempts<sup>8</sup> to obtain the NN interaction from perturbative diagrams involving gluon exchange between six valence quarks using usually bag wave functions for the latter. This may well cause the difficulty to make contact with meson theoretic models such as the OBE, TBE, vector-meson dominance and chiral algebra, even at small internucleon distances.

Because of color confinement uncorrelated quark interchange can only contribute to the NN force at short range, when both nucleons overlap significantly and/or both quarks have the same color. And this also applies to van der Waals mechanisms involving two uncorrelated gluons. Correlations among exchanged gluons essentially lead to glueball formation whose mass is estimated<sup>9</sup> to be  $\gtrsim 1.5 \text{ GeV}/c^2$ , so that this is also an unlikely candidate for the OBE.

Therefore, it seems reasonable to start with a quark interchange mechanism which is mediated by gluon exchange. This quark exchange scattering process (see Fig.1) is color singlet with the same color matrix element 4/9 for baryon-baryon, meson-baryon and

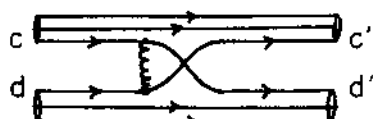


Fig. 1. Quark exchange scattering mediated by gluon exchange, as it occurs in baryon-baryon OBE.

meson-meson reactions. However, in the strong coupling regime at low  $q$ , the perturbative amplitude is modified when the aforesaid nonperturbative condensation effects in the QCD vacuum are included.

When hadrons get sufficiently close, within a coherence length of the order  $m_\pi^{-1}$ , say, color flux may penetrate into the vacuum and induce its quark-antiquark condensate to establish a coherent link between valence quarks in different hadrons. Then, in analogy with processes in condensed matter, e.g. (anti)ferromagnetic materials, it is conceivable that two valence quarks exchange their spin, flavor and color along such an ordered  $Q\bar{Q}$  chain between two different points  $x$  and  $y$  of the interacting hadrons and not just locally. By antisymmetry this amounts to a space exchange  $P(x \leftrightarrow y)$  in the resulting nonperturbative quark interchange amplitude<sup>10</sup>

$$T_Q = -\frac{8}{9}(ig)^2 \int d^3x d^3y \bar{\psi}_c^1(y) (\gamma_\mu l^f)_{c'd} \psi_d(y) P(x \leftrightarrow y) G \bar{\psi}_d^1(x) (\gamma^\mu l^f)_{d'c} \psi_c(x) \quad (1)$$

where  $l^f$  denotes the unit matrix in flavor space.\* When its spin-flavor part is Fierz rearranged,

$$\begin{aligned} 2\delta_{c'd'd'c} \delta_{d'd'c} (\gamma_\mu)_{c'd} (\gamma^\mu)_{d'c} &\equiv \sum_\alpha O_{c'c}^\alpha O_{d'd}^\alpha \equiv [1_{c'c} 1_{d'd} (\gamma_5)_{c'c} (\gamma_5)_{d'd} \\ &\quad - \frac{1}{2} (\gamma_v)_{c'c} (\gamma^v)_{d'd} - \frac{1}{2} (\gamma_5 \gamma_v)_{c'c} (\gamma_5 \gamma^v)_{d'd}] \\ &\quad [1_{c'c} 1_{d'd} + (\gamma)_{c'c} \cdot (\gamma)_{d'd}] \quad , \end{aligned} \quad (2)$$

\*Thus  $P(x \leftrightarrow y)$  in (1) may have a similar dynamical origin as the coordinate permutations in the scattering part of the wave function in the Bethe Ansatz for such ordered systems. For a recent application of the Bethe Ansatz in finding the exact solution of the closely related Gross-Neveu model see ref. 11.

The similar but perturbative amplitude  $T_F$  does not involve  $P(x \leftrightarrow y)$  when it is expressed in coordinate space. After Fierz-ing, therefore,  $T_F$  involves bilocal quark matrix elements  $\bar{\psi}(x)O\psi(y)$  so that the  $x$  and  $y$  integrations are not separable, contrary to reported results.<sup>12</sup> Weise and Werner<sup>12</sup> avoid this problem by assuming a contact form for the effective gluon propagator  $G$  which is unrealistic in the strong coupling regime. Technically more important, though, is that these authors overlook the cancellation of the  $\gamma_5 \tau$  and  $\gamma_5 \gamma_v \tau$  terms<sup>13</sup> resulting in negligible pion-nucleon coupling.

this  $T_Q$  generates precisely those vertex invariants  $O^\alpha$  which occur in the OBE representations. Moreover, in conjunction with valence quark wave functions

$$\psi(\vec{r}) = \begin{pmatrix} R_0(r) \\ -iR_1(r)\vec{\sigma} \cdot \vec{r} \end{pmatrix} \chi, \quad R_0 \sim (-1)^\ell j_\ell(x_0 r/R), \quad r \leq R \quad (3)$$

of the static MIT bag model,<sup>4</sup> the Fierzing in (1), (2) is crucial for generating the proper relationships of the static SU(6) symmetry among the coupling constants. It is broken here according to ideal mixing due to quark interchange. That is to say, e.g. when two strange quarks are interchanged, the exchanged mesons corresponding to the vertices  $O^\alpha = 1, Y_5, Y_V, Y_5 Y_V$  in elastic  $\Lambda\Lambda$  scattering, i.e.  $S^*(980)$ ,  $\eta^*(958)$ ,  $\phi(1020)$ ,  $E(1420)$  respectively, have pure  $s\bar{s}$  valence quark content. When the valence quarks are interchanged the flux transmits the momentum  $q$ . The implied momentum correlation among the interchanged valence quarks amounts to an anticorrelation of quark-antiquark momenta in the equivalent exchanged  $Q\bar{Q}$ -gluon system. Thus the color flux penetration is taken to be controlled by different selfenergies  $m_0^2$  in the propagator  $G$  corresponding to each term  $O^\alpha$  in (2). Putting these prescriptions together yields the effective valence quark interaction

$$T_Q = \frac{4}{9} g^2 \sum_\alpha \int d^3y \bar{\psi}_c(y) O^\alpha_{c'c} \psi_c(y) e^{-i\vec{q} \cdot \vec{y}} (q^2 - m_0^2)^{-1} \cdot \int d^3x \bar{\psi}_d(x) O^\alpha_{d'd} \psi_d(x) e^{i\vec{q} \cdot \vec{x}}. \quad (4)$$

Clearly,  $T_Q$  has the local structure characteristic of the OBE. And Eq. (4) involves no other adjustable parameter besides those already determined by the bag-model spectroscopy provided the  $m_0$  are taken to be the appropriate  $(Q\bar{Q})JT$  meson masses in each channel. This procedure is consistent with the role of the one-gluon exchange in the mass splittings of the low-lying hadron spectrum. Incidentally, a linear confinement potential produces similar coupling constants and form factors at low  $q$ .

When the spin-isospin matrix elements of the effective quark interaction  $T_Q$  are evaluated using three-quark wave functions for the relevant baryons, various OBE amplitudes are obtained.<sup>10,14,15</sup> The coupling constants obey the SU(6) symmetry. For example, the  $\pi NN$  coupling is given by

$$g_0 = -\frac{4m_N}{q} F_1(R_0 R_1), \quad \alpha_c = g^2/4\pi = \begin{cases} 2.2, & m_Q = 0 \\ 3.0, & m_Q = 0.108 \text{ GeV}/c^2 \end{cases}$$

$$\frac{1}{4\pi} g_{\pi NN}^2 = \frac{4}{9} \alpha_c \left(\frac{5}{3}\right)^2 g_0^2 (\vec{q}^2 = 0) = \begin{cases} 12.2 & , m_Q = 0 \\ 13.4 & , m_Q = 0.108 \text{ GeV}/c^2 \end{cases}$$

$$F_\lambda(f) \equiv 4\pi \int_0^R dr r^2 j_\lambda(qr) f(r) \quad , \quad (5)$$

involving the effective quark mass  $m_Q$ . The latter is the only bag-model parameter that is not well determined by the spectroscopy. The full OBE for the NN interaction is

$$\begin{aligned} T_{NN} = & \frac{4}{9} g^2 \{ F_0^2 (R_0^2 + R_1^2) [9(q^2 - m_\pi^2)^{-1} + \frac{1}{2} \cdot \frac{1}{2} (q^2 - m_\delta^2)^{-1}] \\ & - g_0^2 \gamma_5' \gamma_5 [(q^2 - m_\eta^2)^{-1} + \frac{25}{9} \cdot \frac{1}{2} (q^2 - m_\pi^2)^{-1}] \quad (6) \\ = & \frac{1}{2} [F_{10} \gamma_\mu' + F_{20} i \sigma_{\mu\nu} q^\nu / 2m_N] (q^2 - m_\omega^2)^{-1} [F_{10} \gamma^\mu - F_{20} i \sigma^{\mu\nu} q_\nu / 2m_N] \\ = & \frac{1}{2} [F_{11} \gamma_\mu' + F_{21} i \sigma_{\mu\nu} q^\nu / 2m_N] (q^2 - m_\rho^2)^{-1} \cdot \frac{1}{2} [F_{11} \gamma^\mu - F_{21} i \sigma^{\mu\nu} q_\nu / 2m_N] \\ = & \frac{1}{2} [g_{A,0} \gamma_5' \gamma_\mu' + g_{P,0} \gamma_5' q_\mu] [(q^2 - m_D^2)^{-1} + \frac{25}{9} \cdot \frac{1}{2} (q^2 - m_{A_1}^2)^{-1}] \\ & \cdot [g_{A,0} \gamma_5 \gamma^\mu - g_{P,0} \gamma_5 q^\mu] \end{aligned}$$

which is to be sandwiched between plane-wave Dirac spinors for the nucleons. The resulting coupling constants resemble those of the Bonn potential.<sup>1</sup> Similarly complete OBE representations can be obtained for other baryons.<sup>15</sup>

The vector-meson form factors  $F_{ij}$  take a form corresponding to the electromagnetic current of the nucleon and, therefore, reproduce vector-meson dominance. Here, the Sachs form factors are

$$G_{E,T}(q^2) = 3^{1-T} F_0 (R_0^2 + R_1^2) , \quad G_{M,T} = \left(\frac{5}{3}\right)^T g_0 , \quad (T=0,1) \quad (7)$$

and the axial-vector form factor is

$$g_{A,T}(q^2) = \left(\frac{5}{3}\right)^T [F_0 (R_0^2 - \frac{1}{3} R_1^2) + \frac{2}{3} F_2 (R_1^2)] \quad . \quad (8)$$

The axial-vector form factor  $g_{A_1,1}$  agrees with the empirical dipole shape, as does  $G_{E,1}$  with that of the proton charge form factor up to  $q^2 \sim 0.5$  GeV/c. Beyond 1/2 GeV/c, the bag model matrix elements become unphysical due to spurious oscillations which are caused by the underlying infinite square well.

The fast fall-off of the form factors in  $T_{NN}$  and other OBE amplitudes with increasing  $q^2$  is one of the predictions of this bag-model scheme. Its main effect is to deplete the conventional, elastic and inelastic, meson and baryon channels at short range suggesting a soft core. Another new feature is axial-vector meson  $A_1(1100)$ ,  $D(1285)$ ,  $Q(1280)$ ,  $E(1420)$  exchanges with specific couplings wherever allowed in the OBE.

In second and third order the quark interchange,  $T_Q$ , generates the TPE. The  $2\pi$ -exchange part of the once iterated  $T_Q$  with intermediate  $\Delta N$  and  $\Delta\Delta$  states (see Fig. 2) corresponds to the isobar configurations which turn out to be small and provide only 20% of the needed scalar-isoscalar (effective  $\sigma_0$ -meson exchange) attraction

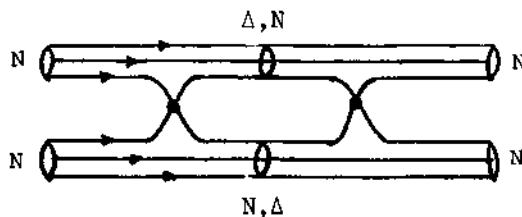


Fig. 2. TBE, isobar configurations; 2nd order quark interchange

at medium range. In third order,  $T_Q$  generates TPE triangle mechanisms involving  $\pi N$  scattering on one nucleon and an intermediate  $N$  or  $\Delta$  at the other nucleon (see Fig. 3). Again the results can be parametrized as effective  $\sigma_0$  exchange of the correct strength to reproduce phase shifts and low energy parameters<sup>14</sup>. These results test the predicted dipole shape of the form factors.

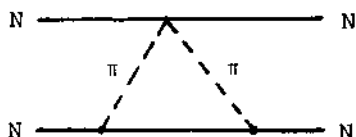


Fig. 3. TPE triangle mechanism; 3rd order quark interchange.

Moreover, in the direct  $\Lambda N$  amplitude<sup>15</sup> the  $\omega$ -exchange turns out to contain only the convection current which, together with a small  $\epsilon$ -exchange and the resulting Thomas term, is consistent with the recent measurements of small spin-orbit coupling in  $\Lambda$ -hyper-nuclei<sup>16</sup>. The calculated coupling constants are close to empirical values or those from SU(6); e.g.

$$\frac{1}{4\pi} g_{\pi\Lambda\Sigma}^2 = \frac{4}{9} \alpha_c \cdot \frac{4}{3} \cdot \left( \frac{4m_{\Sigma\Lambda}}{q} F_1 \right)^2 / q^2 = \begin{cases} 8.8, & m_Q = 0 \\ 9.7, & m_Q = 0.108 \text{ GeV}/c^2 \end{cases}$$

$$\frac{1}{4\pi} g_{K\Lambda\Lambda}^2 = \frac{4}{9} \alpha_c \cdot 3 \cdot \left( \frac{4m_{\Lambda\Lambda}}{q} F_1 \right)^2 / q^2 = \begin{cases} 15.5, & m_Q = 0 \\ 17.1, & m_Q = 0.108 \text{ GeV}/c^2 \end{cases} .$$

The effective quark interchange has also been applied to meson-baryon and meson-meson collisions. To be specific, consider (in Fig. 4) elastic  $\pi N$  (S-wave) scattering at low energy. Here two amplitudes enter which both involve the exchange of a  $Q\bar{Q}$ -gluon system with anti-correlated  $Q$  and  $\bar{Q}$  momenta, and differ from each other by a G-parity phase. As a result, cancellation among various meson exchanges occur. For  $\pi N$  S-wave scattering at low  $q$ , only  $\epsilon$  and  $\rho$  exchange remain in agreement with the standard results from current algebra and PCAC.



Fig. 4. Quark interchange mechanism for meson-baryon scattering

However, besides its role as an equal partner of other mesons of the SU(6) symmetry, the pion is as a Nambu-Goldstone boson an ingredient of chiral algebra. It is intriguing that  $T_Q$  is able to reproduce the Goldberger-Treiman relation (GTR) and axial-vector coupling for the  $\pi NN$  vertex involving a real pion<sup>13</sup>. The GTR results from cancellation between the  $\gamma_5 T$  and  $\gamma_5 \gamma_5 T$  terms in  $T_Q$  upon emission or absorption of a real pion in  $A$ ,  $B$ , where both  $A$  and  $B$  are described by a three-quark (S-state) wave function (see Fig. 5);

$$\begin{aligned}
 & \langle 0 | (i\gamma_5 \gamma_5) | \pi(q) \rangle \cdot \langle N(p+q) | (i\gamma_5 \gamma_5) | N(p) \rangle \\
 & + \frac{1}{2} \langle 0 | (i\gamma_5 \gamma_5) | \pi(q) \rangle \cdot \langle N(p+q) | (i\gamma_5 \gamma_5) | N(p) \rangle \quad (10) \\
 & \propto f_\pi g_{\pi NN} + \frac{1}{2} (-2m_N) g_A = 0
 \end{aligned}$$

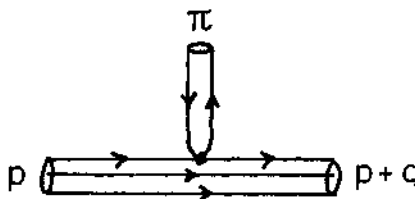


Fig. 5. Real pion absorption/emission on a baryon of momentum  $p$  with a three-valence quark wave function component in the initial and final state. The dot denotes the quark interchange mechanism.

The transition  $A + \pi \rightarrow B$  can only occur for a real pion, when the quark wave function of  $B$  contains an additional  $(QQ) {}^3P_0$  component in the sense of a BCS-like chiral expansion (see Fig. 6). This results in effective axial-vector  $\pi NN$  coupling, and relates  $T_Q$  to the  ${}^3P_0$  quark pair creation model for baryon decays<sup>17</sup>.

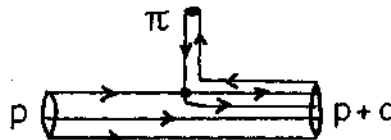


Fig. 6. Real pion absorption on a baryon of momentum  $p$  leading to a final baryon state with an additional  $(QQ) {}^3P_0$  pair component.

In conclusion we note that the effective, nonlocal quark interchange  $T_Q$  of Eqs. (1,2,4) generates the hadronic, color singlet couplings at low  $q$ . This includes the space-like OBE, TBE, ... governed by the static  $SU(6)$  symmetry, that is broken here by ideal mixing, vector-meson dominance, and low-energy theorems due to the chiral properties of the pion such as the Goldberger-Treiman relation and axial-vector pion-nucleon coupling. We expect the

unusual nonlocal nature of  $T_Q$ , which is inconsistent with perturbative QCD, to be intimately related to quark-antiquark and gluon condensates in the strong coupling regime of QCD. The unifying aspect of  $T_Q$  becomes understandable by the similarity of the exchanged quark-antiquark-gluon to Nambu's nonlinear spinor model<sup>18</sup> and BCS-superconductivity.

## REFERENCES

1. R. Vinh Mau, in Mesons in Nuclei, Vol. 1, p. 151, North-Holland (Amsterdam, 1979);  
K. Erkelenz, Phys. Reports C13: 191 (1974);  
K. Holinde, *ibid.* C68: 121 (1981).
2. Quantum Chromodynamics, W. Frazer and F. Henyey, eds., AIP Conf. Proc. 18 (1979).
3. C.L. Critchfield, Phys. Rev. D12: 923 (1975).
4. T. DeGrand, R. Jaffe, K. Johnson, J. Kiskis, Phys. Rev. D12: 2060 (1975).
5. J. Ambjørn and P. Olesen, Nucl. Phys. B170: 60 (1980), *ibid.* p. 265.
6. R. Fukuda, Phys. Lett. 73B: 33 (1978);  
J. Finger, D. Horn, J. Mandula, Phys. Rev. D20: 3253 (1979);  
M.A. Shifman, A.I. Vainstein, V.I. Zakharov, Nucl. Phys. B147: 385, 448, 519 (1979).
7. H. Leutwyler, Phys. Lett. 98B: 447 (1981).
8. C. DeTar, Phys. Rev. D17: 302 (1978);  
M. Harvey, Nucl. Phys. A352: 326 (1981), *ibid.* p. 301.
9. P.M. Fishbane, "Glueballs, A Little Review", Univ. Va. preprint.
10. H.J. Weber, Z. Phys. A297: 261 (1980).
11. N. Andrei and J.H. Lowenstein, Phys. Rev. Lett. 43: 1698 (1979).
12. M. Kislinger, Phys. Lett. 79B: 474 (1978);  
H.J. Pirner, *ibid.* 85B: 190 (1979);  
W. Weise and E. Werner, revised version of Univ. Regensburg preprint, Phys. Lett. 101B: (1981) 223.
13. H.J. Weber, Z. Phys. A301: (1981) 141.
14. B.L.G. Bakker, J.N. Maslow, H.J. Weber, Uva preprint, to be published in Phys. Lett. 104B: (1981).
15. H.J. Weber, J.N. Maslow, Z. Phys. A297: 271 (1980).
16. B. Povh, Comments Nucl. Part. 9: 15 (1979).
17. A. LeYaouanc, L. Oliver, O. Pène, J.-C. Raynal, Phys. Rev. D11: 1272 (1975), and references therein.
18. Y. Nambu, G. Jona-Lasinio, Phys. Rev. 122: 345 (1961).

\* Supported in part by the U.S. National Science Foundation.

# NONPERTURBATIVE TREATMENT OF MAGNETIC INTERACTIONS AT SHORT DISTANCES AND A SIMPLE MAGNETIC MODEL OF MATTER

A. O. Barut

Department of Physics  
The University of Colorado  
Boulder, Colorado 80309. USA

## INTRODUCTION

In these lectures I discuss some properties of large magnetic dipole fields, the phenomenon of magnetic resonances in dipole fields, and a dynamical model of hadrons and heavy leptons based on magnetic resonances.

Because the general idea has been already reviewed<sup>1</sup> I shall concentrate on more recent results and new viewpoints. In particular, some of the nonperturbative results which may be relevant to heavy ion physics are mentioned, although the main effect, the resonance phenomenon, comes in probably still at shorter distances than those occurring at present in heavy ion physics.

## PART I -

### THEORY OF MAGNETIC INTERACTIONS

#### Some Properties of Magnetic Dipole Fields

We assume, in agreement with the latest experiments<sup>2</sup> that the electron is a point particle with a charge  $e$  and magnetic moment

$$\vec{\mu} \equiv g\mu_o \vec{S}, \quad \mu_o = \frac{e}{2m}, \quad g = 2\left(1 + \frac{\alpha}{2\pi}\right) \quad . \quad (1)$$

I shall use the units  $c = \hbar = 1$ . Then  $e^2 = \alpha$ . To the following characteristic lengths and energies we shall often refer in this report:

|        | Coulomb<br>Levels           | Scattering<br>Problems | Normal<br>Magnetic<br>Resonances    | Anomalous<br>Magnetic<br>Resonances |
|--------|-----------------------------|------------------------|-------------------------------------|-------------------------------------|
| Length | $r_0 = \frac{1}{\alpha}$    | $r = \frac{1}{m}$      | $r_{\text{mag}} = \frac{\alpha}{m}$ | $\frac{\alpha^2}{m}$                |
| Energy | $R_y = \frac{m\alpha^2}{2}$ | $m$                    | $E_{\text{mag}} = \frac{m}{\alpha}$ | $\frac{m}{\alpha^2}$                |

For  $m = m_{\text{electron}}$ ,  $\frac{\alpha}{m} = 2.8$  Fermis,  $\frac{m}{\alpha} = 70$  MeV,  $\frac{m}{\alpha^2} = 9.5$  GeV.

The product of a charge  $e$  and a magnetic moment  $\mu$  is a length in our units, and will appear predominantly in the following:

$$e \mu_0 = \frac{1}{2} \frac{\alpha}{m} . \quad (2)$$

The magnetic fields near the electron or the proton are extremely strong. At a distance  $r = \alpha/m$  from the electron

$$B(r = \frac{\alpha}{m}) \approx \frac{\mu_0}{r^3} = \frac{1}{2} \frac{(m^2)}{e} \frac{1}{\alpha^2} , \quad (3)$$

which is about  $10^{17}$  gauss, four orders of magnitude larger than the magnetic fields on neutron stars. The magnetic energy of an electron in the field of another becomes equal to its rest energy i.e.  $\vec{\mu} \cdot \vec{B} = m$  at  $B = 2 \frac{(m^2)}{e}$ , or at a distance

$$r = \frac{1}{m} \left( \frac{\alpha}{4} \right)^{1/3} , \quad (4)$$

around 40 fermis, hence the magnetic interactions cannot be treated as a perturbation at these distances and below. The same is true for the electron magnetic energy at about a few fermis from the proton.

The importance of large magnetic effects is not always realized. For example in the electromagnetic mass problem one equates the electrostatic energy to the rest energy of the electron,

$$\frac{1}{8\pi} \int_{r_m}^{\infty} E^2 dV = m ,$$

whereas the magnetic energy in the same volume is 10 times larger<sup>3</sup>

$$\frac{1}{8\pi} \int_{r_m}^{\infty} B^2 dV = \frac{1}{12} \frac{m}{\alpha} \approx 11.4 m .$$

For this reason the length  $r_m = \alpha/m$  is not quite the classical electron radius. I prefer to call it the "magnetic length", for reasons which will be clear below.

A particle with charge  $e$  and dipole moment  $\vec{\mu}$  produces a vector potential at a distance  $r$  given by

$$A_{\mu} = \left[ \frac{e}{r}, \frac{\vec{\mu} \times \vec{r}}{r^3} \right] . \quad (5)$$

This potential can be derived from field theory (see Section - "Quantum Theory of Magnetic Dipole Resonances").

The corresponding fields are

$$F_{\mu\nu} : \left\{ \vec{E} = \frac{e}{r^2} \hat{r}, \quad \vec{B} = \frac{3\hat{r} \vec{\mu} \cdot \hat{r} - \vec{\mu}}{r^3} + \frac{8\pi}{3} \mu \delta^3(\vec{r}) \right\} . \quad (6)$$

Note also that

$$B^2 = \frac{\mu^2}{r^6} (3 \cos^2 \theta + 1) . \quad (7)$$

### Electron in the Field of a Charged Magnetic Dipole

We shall study now the motion, orbits and quantized states in a dipole field, similar to what we do in a Coulomb field.

The Dirac Hamiltonian for the electron in a charged dipole field is

$$H = \vec{\alpha} \cdot (\vec{p} - e_1 \vec{A}) + \beta m + \frac{e_1 e_2}{r} , \quad (8)$$

where  $\vec{A}$  is given in eq. (5). In the course of solving for the stationary states of this Hamiltonian one arrives, as usual, to the second-order form of the Hamiltonian

$$H = [ \vec{p}^2 - e_1 (\vec{p} \cdot \vec{A} + \vec{A} \cdot \vec{p}) + e_1^2 A^2 + m^2 + e_1 \vec{\sigma}_1 \cdot \vec{B} + i e_1 \vec{\alpha}_1 \cdot \vec{E} ]^{1/2} + \frac{e_1 e_2}{r} \quad (9)$$

and, further to the eigenvalue equation

$$\begin{aligned} & \left[ (E - \frac{e_1 e_2}{r})^2 - m^2 \right] \psi \\ & = \left[ - \frac{d^2}{dr^2} + \frac{1(1+1)}{r^2} - \underbrace{\frac{4e\mu}{r^3} \vec{\sigma}_2 \cdot \vec{L} + \frac{2e^2 \mu^2}{r^4} + e\mu S_{12} + i e_1 e_2 \vec{\alpha}_1 \cdot \vec{E}}_{(10)} \right] \psi \end{aligned}$$

We have to explain the origin and meaning of some of the terms in eq. (10).

The cross term  $-e_1(\vec{p} \cdot \vec{A} + \vec{A} \cdot \vec{p})$  gives with (5)

$$-2e\mu \frac{\vec{p} \cdot \vec{\sigma}_2 \times \vec{r}}{r^3} = -4e\mu \frac{\vec{S}_2 \cdot \vec{L}}{r^3},$$

where  $\vec{S}$  is the spin of the dipole. This is the spin-orbit potential. The  $e_1^2 A^2$ -term in (9) becomes on squaring  $2e_1^2 \mu^2 / r^4$ . This term is usually neglected in atomic physics, but is in fact very important and should not be neglected, as we shall see, as a matter of principle. The term  $e_1 \vec{\sigma}_1 \cdot \vec{B}$ , using (6), becomes  $e_1 \mu S_{12}$ , where

$$S_{12} = \frac{3\vec{\sigma}_1 \cdot \hat{r} \vec{\sigma}_2 \cdot \hat{r} - \vec{\sigma}_1 \cdot \vec{\sigma}_2}{r^3} + \frac{8\pi}{3} \vec{\sigma}_1 \cdot \vec{\sigma}_2 \delta(\vec{r}) . \quad (11)$$

This is the spin-spin interaction term, or the tensor force. Finally the last term  $ie_1 \vec{d} \cdot \vec{E}$  in (9) is another kind of spin-orbit term and must be further diagonalized.

In atomic physics one treats, since Fermi's first calculation of hyperfine effects<sup>4</sup>, the last four terms in eq. (10), as a perturbation to the exact solutions of the Coulomb problem. Now the term  $2e^2 \mu^2 / r^4$  is too singular, the integrals do not converge. One drops this term with the justification that its coefficient, proportional to  $e^2$ , is too small. The remaining Hamiltonian with  $1/r^3$ -term is then not essentially self-adjoint. Nevertheless, one takes its expectation value. Two incorrect steps cancel each other and one obtains for atomic states at large distances reasonable values.

It is clear that we must treat the equation (10) as it stands without dropping the  $1/r^4$ -term, and without using perturbation theory. The most singular part,  $1/r^4$ -term, is always repulsive, it dominates at  $r \rightarrow 0$ , hence we know the exact behavior of the solution at origin. With this information, we can rigorously modify and justify the perturbation theory for the Coulomb problem. In addition, moreover, we get new unexpected resonance states. These cannot be seen in perturbation theory, but only in an exact treatment of  $1/r^3$ - and  $1/r^4$ -terms which dominate for small  $r$ .

There is in fact a classical problem where the magnetic dipole field must be treated nonperturbatively and the formation of resonances occurs:

Störmer Problem: This is the problem of the motion of charged particles in the magnetic dipole field of the earth. Neglecting the

spin of the charged particles, the classical relativistic Hamiltonian can be written in polar coordinates as

$$H_{\text{class}} = m \left[ 1 + \frac{1}{m^2} \left( \frac{p_r^2}{r} + \frac{1}{r^2} p_\theta^2 + \frac{1}{r^2 \sin^2 \theta} (p_\phi - e\mu \frac{\sin^2 \theta}{r})^2 \right) \right]^{1/2} . \quad (12)$$

Assuming the direction of the dipole to be fixed, the angular momentum in the  $z$ -direction is a constant of the motion,  $p_z = l_z$ . In the meridian plane we have an effective potential

$$V^2 = (l_z - e\mu \frac{\sin^2 \theta}{r})^2 ,$$

which is repulsive at  $r \rightarrow 0$ , has a minimum at  $r_m = \frac{e\mu \sin^2 \theta}{l_z}$  and a maximum at  $2r_m$ .

In this potential well the charged particles can be trapped. They go up and down around a magnetic field line, crossing the equator plane irregularly. (This problem is an example of non-integrable classical systems).

The order of magnitude of the size of trapped orbits from earth is

$$r_m \sim \frac{g_E}{l_z} \cdot \frac{\alpha}{m} , \quad (13)$$

where  $g_E$  is the g-value of the earth in Bohr magnetons, and  $m$  the electron mass. The energy of the resonance is

$$E_{\text{max}} \sim \frac{l_z}{g_E} \cdot \frac{m}{\alpha} . \quad (14)$$

This is a remarkable example of a "resonance" in classical mechanics. Note, for future reference, that the energy  $E_m$  of the resonance is larger than the rest mass of the particle (i.e. positive binding energy), contrary to a Coulomb type bound state. This is due to the potential barrier, and the extra mass comes from the kinetic and potential energies of the trapped particle.

This problem is more than an example. We shall obtain the same type formulas (13), (14) in the dipole fields of electrons or protons, when  $g_E$  and  $l_z$  become numbers of the order of unity.

#### Spectroscopy in a Magnetic Dipole Field

It is remarkable that the spectroscopy of narrow resonances in a dipole field can be treated analogous to the spectroscopy of bound states in a Coulomb field. There exist quantum rules for them (Bohr-Sommerfeld or WKB-approximations), as well as a formulation as an

eigenvalue-problem. In order to show these we consider some simple cases.

(i) Charge-Dipole System. If the spin-orbit term in eq.(10) dominates over the spin-spin term (e.g. for a spin 0 particle in a dipole field) we have the simple Hamiltonian

$$H = \left[ \frac{p^2 + m^2}{r^3} - \frac{4e\mu}{r^3} \vec{S} \cdot \vec{L} + \frac{2e^2 \mu^2}{r^4} \right]^{1/2} - \frac{\alpha}{r} . \quad (15)$$

Semi-classical Spectrum: For circular orbits in a dipole field the equation of motion is given by

$$\frac{mv^2}{\sqrt{1-v^2}} - \frac{1}{r} \approx \frac{\alpha}{r^2} - \frac{e\mu vr}{r^3} . \quad (16)$$

The Bohr-Sommerfeld quantization is

$$\frac{mv^2 r}{\sqrt{1-v^2}} = N . \quad (17)$$

Solving eqs. (16) and (17) we find two types of states for which  $v$ ,  $r$  and total energy  $E$  are shown in the next Table I.

Table I

|     | Solutions of Type I                                         | Solutions of Type II        |
|-----|-------------------------------------------------------------|-----------------------------|
| $v$ | $\sim \alpha/N$                                             | $\sim (1 - \alpha^2/8N^2)$  |
| $r$ | $\sim \frac{N^2}{m\alpha} (1 - \frac{\alpha^2}{N^2})^{1/2}$ | $\sim \alpha/2mN$           |
| $E$ | $\sim m (1 - \frac{\alpha^2}{N^2})^{1/2}$                   | $\sim \frac{m}{\alpha} N^2$ |

These two solutions are widely separated in size, velocity and energy so that in I Coulomb potential dominates and magnetic term is a small perturbation, and in II the magnetic force dominates and Coulomb term is a small perturbation. The values in the Table correspond to pure Coulomb terms and pure dipole terms, resp.

Note on High Z-Limit: The relativistic Coulomb problem fails, as we see from Table I, as  $\alpha/N \rightarrow 1$  (e.g.  $Z \rightarrow 137$  for  $N=1$ ). But with a dipole term, there is no difficulty at  $Z \rightarrow 137$ . I suggest therefore

to use the magnetic dipole field of the proton as a physical regularization mechanism, instead of a phenomenological finite size of the proton, when treating the  $Z \rightarrow 137$  limit of the relativistic Coulomb problem. A theory for noncircular orbits in the dipole case does not yet exist, as the elliptic orbit theory of Sommerfeld for the Coulomb field.

WKB-Spectrum: Returning to the Hamiltonian (15), we look for the spectrum of states when  $\vec{S} \cdot \vec{L}$  has the eigenvalue  $\lambda$ . If we set in (15)  $p = N/r$  and find the extrema of the Hamiltonian, i.e.

$$\frac{dH}{dr} = 0 \quad , \quad (18)$$

we find again two sets of solutions:

(a) Solutions dominated by the Coulomb term with  $r$  and  $E$  as given in Table I.

Positronium: The WKB-quantization is rather accurate for the relativistic positronium. The 2-body Hamiltonian

$$H = [(\vec{p}_1 - e_1 \vec{A}_1)^2 + m_1^2]^{1/2} + [(\vec{p}_2 - e_2 \vec{A}_2)^2 + m_2^2]^{1/2} + \frac{\alpha}{r} \quad (19)$$

reduces, in the center of mass frame ( $\vec{p}_2 = -\vec{p}_1$ ,  $m_1 = m_2$ ), to

$$H = 2[p^2 + m^2 - \frac{4e\mu}{r^3} \vec{S} \cdot \vec{L} + \frac{2e^2 \mu^2}{r^4}]^{1/2} - \frac{\alpha}{r} \quad . \quad (20)$$

The conditions  $p = N/r$  and  $dH/dr = 0$  give for the Type I Solutions the spectrum

$$E_N = 2m \left[ 1 - \frac{\alpha^2}{4N^2} \right]^{1/2} \quad (21)$$

which agrees with the spectrum of the Bethe-Salpeter equation in Ladder approximation. The spin-orbit and spin-spin terms can be treated as perturbation to Type I solutions. The results are

$$|\Delta E| = \frac{1}{4} m \alpha^4 \frac{\lambda}{N^6} \quad \text{with} \quad \lambda = \langle \vec{S} \cdot \vec{L} \rangle \quad , \quad (22)$$

for spin-orbit, and

$$|\Delta E| = \frac{1}{16} m \alpha^4 \frac{\langle \sigma_1 \cdot \sigma_2 \rangle}{N^6} \quad (23)$$

for the  $\frac{\sigma_1 \cdot \sigma_2}{r^3}$  part of the spin-spin interaction.

$$\langle \sigma_1 \cdot \sigma_2 \rangle = \begin{cases} -3 & (S=0) \\ +1 & (S=1) \end{cases} \quad (24)$$

(b) Solutions of (18) dominated by the spin-orbit term again give the values in Table I for Type II solutions. Here the Coulomb perturbation gives

$$|\Delta E|_{\text{Coulomb}} = \frac{\alpha}{r} = 2mN \quad . \quad (25)$$

Thus electromagnetic mass-differences to magnetic resonances are of the order of a few electron-mass. [This is indeed the case experimentally for the mass-differences within iso-spin multiplets of mesons and baryons (see identifications in Part II)].

(ii) Dipole-Dipole System. For type II solutions we can neglect the Coulomb term and the mass term in the Dirac Hamiltonian. Consider therefore

$$H = \vec{\alpha} \cdot (\vec{p} - e\vec{A}) \quad . \quad (26)$$

The eigenvalues of  $H$  are given by

$$E^2 = (\vec{p} - e\vec{A})^2 + e\vec{\sigma} \cdot \vec{B} \quad , \quad (27)$$

where  $\vec{A}$  is as in eq.(5).

The semi-classical spectrum of (26) for circular orbits is obtained by putting again  $p = N/r$ , replacing  $(\vec{p} - e\vec{A})^2$  by  $(p - \frac{e\mu}{r^2})^2$ , and then determining the extremum of the energy:

$$E = \left[ \left( p - \frac{e\mu}{r^2} \right)^2 - e\mu \frac{\langle \sigma_1 \cdot \sigma_2 \rangle}{r^3} \right]^{1/2}, \quad C = \langle \sigma_1 \cdot \sigma_2 \rangle \quad .$$

The result is

$$\frac{dE}{dr} = 0 \quad \text{at} \quad r_m = \frac{3}{4} e\mu \left( \frac{2N+C}{N^2} \right) \rho; \quad \rho = 1 \pm \left( 1 - \frac{32}{9} \frac{N^2}{(2N+C)^2} \right)^{1/2}$$

and at energy

$$E(r=r_m) = \frac{4}{3} \frac{1}{e\mu} \cdot \frac{N^3}{(2N+C)\rho} \left[ 1 - \frac{4}{3\rho} + \frac{16}{9\rho^2} \left( \frac{N}{2N+C} \right)^2 \right]^{1/2}$$

For  $N = 2$  ( $l=1$ ) and  $C=1$  (triplet)  $S=1$ ,  $2N+C=5$ ,  $\rho \sim 5/3$ , and we get approximately

$$E \approx \frac{2m}{\alpha} = m_\pi \quad , \quad (28)$$

the absolute value of the pion mass. (We shall see later that the lowest magnetic resonance has the quantum numbers  $l = 1, S = 1$ ).

### Quantum Theory of Magnetic Dipole Resonances

We go back now to our Eq.(10) and try to solve the eigenvalue problem. The last term ( $\vec{\alpha}_1 \cdot \vec{E}$ ) needs still to be diagonalized. Neglecting this term for the time being (it modifies the  $1(l+1)/r^2$ -term), and also neglecting the Coulomb term in the region of magnetic resonances, we obtain the following eigenvalue problem:

$$\left[ \frac{d^2}{dr^2} + (E^2 - m^2) - V_{\text{rad}}(r) \right] \psi = 0 , \quad (29)$$

where the effective radial potential is of the form

$$V_{\text{rad}} = \frac{v_2}{r^2} + \frac{v_3}{r^3} + \frac{v_4}{r^4} . \quad (30)$$

This potential is shown schematically in Fig. 1 for negative  $v_3$  (we have added the Coulomb tail in the figure to make a comparative discussion).

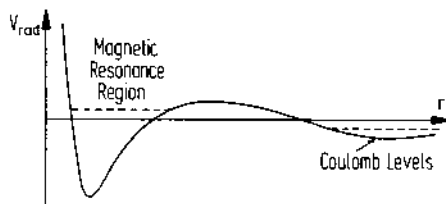


Fig. 1

For large  $Z$ , the two potential wells in Fig. 1 approach each other, the Coulomb well becomes broader and deeper so that eventually it cannot support the 1s-bound level, and then, with increasing  $Z$ , the 2s-, 2p-levels, etc.; i.e. these wave functions are no longer normalizable. The change in the resonance region with increasing  $Z$  depends on the magnetic moment of the nucleus. The potential barrier disappears when  $k(k+1) - Z^2\alpha^2 = 0$ , i.e. at  $Z = 194$  for  $k = 1$ .

A Class of Exactly Soluble Potentials. For special values of  $v_3$  and  $v_4$  the eigenvalue problem (29)-(30) is exactly soluble for resonances and/or bound states<sup>5</sup>, namely, when

$$v_3/\sqrt{v_4} = -2M-2, \quad M = 0, 1, 2, \dots . \quad (31)$$

Here  $M$  appears as a quantum number characterizing the resonances which are treated on the same footing as bound states. They correspond to complex eigenvalues of (29), and their wave function have the characteristic asymptotic behavior

$$\psi \xrightarrow[r \rightarrow \infty]{i\lambda r} e^{-i\lambda r}; \quad \lambda = \text{complex} . \quad (32)$$

Some models of magnetic resonances lead exactly to the case (31). In other cases when  $v_3$  slightly deviates from (31) we can use a perturbation theory around these exact solutions.

An interesting problem would be to extend the class of exactly soluble problems when the Coulomb potential  $v_1/r$  is added to (30). Then the asymptotic behavior (32) has to be modified to an asymptotic Coulomb tail.

Numerical Solutions of Complex Eigenvalue Problems. A method has been developed to locate the very narrow resonances in potential wells as shown in Fig. 1.<sup>6</sup>. The phase shift jumps by about  $\pi$  at  $E = E_{\text{res}}$  within a very narrow energy interval  $\Delta E$  which corresponds to the width of resonance.

Dirac Particle with an Anomalous Magnetic Moment. We shall now include into the Dirac equation, eq. (8), an effective Pauli interaction term representing the anomalous magnetic moment of the electron:

$$[\gamma^\mu (i\partial_\mu - eA_\mu) - m]\psi = -a \frac{e}{4m} \gamma^\mu F_{\mu\nu} \gamma^\nu \psi . \quad (33)$$

Here  $a$  is the anomalous magnetic moment, in units of  $e/2m$ . In perturbation theory,  $a = \frac{\alpha}{2\pi} + O(\alpha^3)$ , and  $\alpha$  is a constant. Eq. (33) is used in the calculation of Lamb shift and other radiative effects<sup>7</sup>. This equation is also important for the magnetic interactions of the neutrino with an anomalous magnetic moment, for which the right hand side of (33) is the only interaction term.

For a Coulomb field  $A_\mu = (\frac{e}{r}, \vec{0})$ , eq. (33) has been completely analysed<sup>8</sup>. One obtains in this case a deep potential well at much shorter distances,  $r \sim \frac{\alpha}{m}$ .

In general, a Dirac particle interacting with a scalar potential  $V_s$ , an electric  $V_e$  and a magnetic potential  $V_m$ , satisfies the radial equations

$$\begin{aligned}\frac{df}{dr} &= \frac{k-1}{r}f + (m + V_s - E)g + V_e g + V_m f \\ \frac{dg}{dr} &= -\frac{k+1}{r}g + (m + V_s + E)f - V_e f + V_m g\end{aligned}. \quad (34)$$

These can be written as a second order Sturm-Liouville equation for one or the other component (f or g) as

$$\psi_{(1)}'' + [(E^2 - m^2) - V_{\text{eff}}^{(1)}] \psi_{(1)} = 0, \quad (35)$$

where the effective potential is

$$\begin{aligned}V_{\text{eff}}^{(1)} &= \frac{k(k+1)}{r^2} + 2EV_e - V_e^2 + V_s^2 + 2mV_s + V_m^2 + 2\frac{k}{r}V_m \\ &- V_m^2 + \frac{1}{2} \frac{V_e'' - V_s'' + 2(V_s' - V_e')(\frac{k}{r} + V_m)}{(m + E + V_s - V_e)} + \frac{3}{4} \frac{(V_s' - V_m')^2}{(m + E + V_s - V_e)^2}, \\ V_{\text{eff}}^{(2)}(k, E, V_e, V_m) &= V_{\text{eff}}^{(1)}(-k, -E, -V_e, -V_m) .\end{aligned} \quad (36)$$

Bound States or the Resonances of the Neutrino. A 4-component neutrino with an anomalous magnetic moment is a special case of the previous equations (33) or (35). Even in the Coulomb field alone there are resonance solutions<sup>9</sup> determined by the equation

$$\begin{aligned}[\frac{d^2}{dy^2} + \lambda^2 - V_{\text{eff}}] u(y) &= 0 \\ V_{\text{eff}}^{(1)} &= \frac{k(k+1)}{y^2} + \epsilon \frac{2(k+1)}{y^3} + \frac{1}{y^4}, \quad \epsilon = \text{sign}(e\mu), \\ [\text{or } V_{\text{eff}}^{(2)} &= \frac{k(k-1)}{y^2} + \epsilon \frac{2(k-1)}{y^3} + \frac{1}{y^4}].\end{aligned} \quad (37)$$

Here  $\lambda^2 = (e\mu)^2 E^2$ ,  $r = (e\mu)y$ . There is an exact zero energy solution of eq. (37):

$$f = C r^{k-1} e^{+r_0/r}, \quad g = C' r^{-(k+1)} e^{-r_0/r}. \quad (38)$$

The normalizable solutions, for  $\epsilon = -1$ , for example, exist when  $k = +1$ , of the form

$$\begin{pmatrix} ig_{k=+1} \\ 0 \end{pmatrix}, \text{ i.e. with large components only.}$$

Only one of the two parity states can bind.

### Field Theory of Magnetic Interactions

One can introduce a fundamental Lagrangian, and an effective Lagrangian. The latter one arises when one derives from perturbation theory with the fundamental Lagrangian effective electric and magnetic potentials which are then used in bound-state problems, for example.

The basic electromagnetic Lagrangian is

$$\begin{aligned} L = & \sum_i \bar{\psi}_i (\gamma^\mu i \partial_\mu - m_i) \psi_i + \frac{1}{4} F_{\mu\nu} F^{\mu\nu} \\ & + \sum_i (e_i \bar{\psi}_i \gamma_\mu \psi_i) A^\mu + \sum_i (a_i \bar{\psi}_i \sigma_{\mu\nu} \psi_i) F^{\mu\nu}. \end{aligned} \quad (39)$$

The sum goes over the basic particles (which we shall take in Part II to be proton, the electron and the neutrino). The last two interaction terms in (39) are the most general couplings of spin- $1/2$  particles. For electron it is sufficient to take at present only the minimal electric coupling, although a very small intrinsic anomalous magnetic moment,  $a_e$ , cannot be excluded.

For neutrino with an anomalous magnetic moment there is only the second term. For the proton both terms are present effectively, until we have a more detailed theory of the proton.

In the derivation of effective potentials between electron, proton and the neutrino we can use (39) also as an effective Lagrangian.

The Pauli-coupling in (39) as a fundamental Lagrangian is not renormalizable in the perturbation theory. It may be however renormalizable in a more subtle way in the so called "bound state" representation. This happens also for the non-renormalizable four-Fermi coupling<sup>10</sup>. Roughly speaking, it means that sums of families of graphs give rise to renormalizable integrals.

The effective potentials are derived most simply from the interaction action obtained from (39) which contains the usual QED-terms like

$$e_i e_j \int dx dy \bar{\psi}_i(x) \gamma_\mu \psi_i(x) D(x-y) \bar{\psi}_j(y) \gamma^\mu \psi_j(y), \quad (40)$$

as well as the new terms like

$$e_i a_j \int dx dy \bar{\psi}_i(x) \gamma_\mu \psi_i(x) \frac{\partial D(x-y)}{\partial x_\nu} \bar{\psi}_j(y) \sigma_{\nu\mu} \psi_j(y) \quad (41)$$

$$a_i a_j \int dx dy \bar{\psi}_i(x) \sigma^{\mu\nu} \psi_i(x) \frac{\partial^2 D(x-y)}{\partial x^\nu \partial x^\lambda} \bar{\psi}_j(y) \sigma_{\lambda\mu} \psi_j(y) \quad . \quad (42)$$

The first term, eq. (40), gives for localized current distributions the well known Breit-potential and its generalizations. The other terms give the relativistic form of the more singular charge-dipole and dipole-dipole potentials that we used in simple models in previous Sections.

## PART II -

### MAGNETIC RESONANCES AND A THEORY OF HADRONS AND HEAVY LEPTONS

#### Historical Remarks

We have argued that only stable particles should be considered to be the true building blocks of matter<sup>1</sup>. All unstable states of matter eventually decay into proton, electron and neutrino. The stability criterion puts a limit on how far we can go with hypothetical chains of substructures. Other virtue of this point of view is that it removes the problem of confinement of unobserved hypothetical constituents ("quarks"), and of course brings back an extraordinary simplicity, economy and conservatism to particle physics ("occam's razor").

The story of particle physics and magnetic resonances begins with Pauli's hypothesis of neutrino, and of neutron being a bound state of proton, electron and neutrino,  $n = (pe\nu)$ , into which it decays<sup>11</sup>. The number of stable particles has not changed in the last fifty years. Even if proton decays, with a life-time of some  $10^{32}$  years or greater, eventually into electron and neutrino, this lifetime is so long that proton still is safely a building block of all baryons and nuclei. It is a problem at a different level, to study the structure of proton,  $e$  and  $\nu$ . First we must see, given  $(p, e, \nu)$ , to what structures they can give rise to. The bound state  $(pe\nu)$  of the neutrino with proton and electron must be due to the magnetic moment of the neutrino which was also postulated by Pauli.

If  $\nu$  has a small magnetic moment a number of electromagnetic processes can happen, e.g. pair production  $e^+ + e^- \rightarrow \bar{\nu} + \nu$ , and also the scattering

$$\nu + e \rightarrow \bar{\nu} + e \quad , \quad (43)$$

which is nowadays called, a "neutral-current" process. The process (43) was first calculated by Carlson and Oppenheimer<sup>12</sup> and then by Bethe<sup>13</sup>. A comparison with the present experiments on the process (43) gives a value for the neutrino magnetic moment of the order of

$$a_{\nu} \sim (10^{-9} - 10^{-10}) \mu_0 . \quad (44)$$

We shall see that even such a minute value of the neutrino magnetic moment can also give rise to bound states at very small distances. But such a deep potential well was not known in the thirties, and the Pauli-model of the neutron was gradually replaced by an iso-doublet of primary nucleons, and the neutron decay was described by Fermi phenomenologically by a new coupling constant  $G_F$  and by creation of  $p, e^-, \bar{\nu}$  and annihilation of neutron<sup>14</sup>.

However, during the years around Yukawa's theory<sup>15</sup> a great deal of work has been done by Tamm and Ivanenko, Wentzel, Heisenberg, Wick, von Weizsäcker, Gamow and Teller<sup>16</sup> on various properties of strong interactions and nuclear magnetic moments by  $e\nu$ ,  $e^+e^-$  and  $\nu\bar{\nu}$  exchange forces between the nucleons. Although these developments have been overshadowed by Yukawa's concept of meson exchanges, it will appear from our model below that they are more general than the Yukawa theory, and the latter is, in present day language, a "mean field approximation" to these earlier theories.

In 1971 I have reconsidered Pauli's model of the neutron,  $n = (p\bar{\nu})$ , in connection with the dyonium theory of the proton, and showed that if magnetic interactions are used,  $(e\nu)$ -system could bind to the proton at nuclear sizes<sup>17</sup>.

The idea that leptons could be building blocks of hadrons has been considered by other authors<sup>18</sup>. They have not used the magnetic interactions, but other possible new forces. The magnetic resonances in  $(e^+e^-)$ -system were suggested in 1975 in connection with the then new  $\psi$ -resonances<sup>19</sup>.

### Neutrino Magnetic Moment

The magnetic moment of the neutrino  $a_{\nu}$  is the only unknown parameter in the present theory. We shall try to put limits to its value from different processes. One value is already given in eq.(44). The properties of the neutrino magnetic moment have been recently reviewed<sup>20</sup>. I give here only the result for the differential cross-section of the electron-neutrino scattering, eq. (43).

For  $m_{\nu} \ll E_{\nu}$ , the result is

$$\frac{1}{S} \frac{d\sigma}{dy} = \frac{d\sigma}{dt|t|} = a_{\nu}^2 \pi r_o^2 \frac{1+t/s}{t} = a_{\nu}^2 \pi r_o^2 \frac{(1-y)}{sy} . \quad (45)$$

Here  $a_\nu$  is the neutrino magnetic moment,  $r_0 = \alpha/m$ ;  $s = 2m_e(E_\nu + m_e)$ ,  $E_\nu$  = energy of incoming  $\nu$  in the Lab-frame of the electron,  $t = -2m_e(E_e - m)$ ;  $E_{e'}$  = energy of the scattered electron, and  $y = E_{e'}/E_\nu$ . Compared to the standard model, eq. (45) predicts a large forward picking of the cross section. The energy and angular distribution for  $e + \nu \rightarrow e + \nu$ , when they become available would put more stringent limits on  $a_\nu$  and on the relative magnitude of magnetic neutral currents as compared with possible other neutral currents (e.g.  $Z^0$ -exchange).

#### Problems with Leptonic Constituents

There are a number of immediate apparent difficulties if one wants to build hadrons from leptons. The idea seems at first to clash sharply with our experience or intuition. That is why new types of fields and interactions have been postulated to account for nuclear forces and the  $\beta$ -decay. These problems have all been mentioned since early days in one form or another:

(a) The problem of the force: Can we reconcile the apparent relatively "weak" interactions of electrons and neutrinos with the "strong" interactions of hadrons.

(b) The problem of mass: How can we obtain the large meson and heavy lepton masses from the light electron and neutrino and the large baryon masses from  $p$ ,  $e$  and  $\nu$ ?

(c) The problem of magnetic moment: How can one compensate the large magnetic moment of the electron to obtain hadrons which have a small magnetic moment?

(d) The problem of localization: The force must be strong and short-ranged to localize  $e$  and  $\nu$  in a volume of at most the nuclear size.

(e) The problem of internal quantum numbers and multiplets: How to obtain the multitude of states of heavy leptons, mesons and hadrons from just three stable particles proton, electron and neutrino?

The dynamical theory of magnetic resonances of Part I has already answered most of these questions:

(a) The magnetic forces had been treated as a small perturbation in atomic physics. In nuclear physics, they have been tacitly lumped into strong interactions. Although spin-orbit type forces are very important in nuclear physics, they have been thought to be not of electromagnetic origin. The fact that the magnetic forces become very strong at a fairly localized short distance with

a repulsive core, and far separated from the Coulomb force has not been realized before. It just acts as a completely separate force from the Coulomb field.

(b) One important characteristic of magnetic resonances is that the mass of the resonance is larger than the sum of the masses of the constituents

$$E_{\text{res}} > m_1 + m_2 , \quad (46)$$

as one can see from Fig. 1. We have a positive binding energy. In fact  $E_{\text{res}}$  can be quite large for higher  $l$  when the barrier is high. The mass is created so to speak from the magnetic field; it resides in the kinetic and potential energy of the constituents. This is an important point to emphasize. All composite models so far tried to construct stable bound states with a large negative binding energy, hence very heavy constituents. Magnetic resonances work against such an intuition. The instability that the mass creation brings with it, is actually physically correct and desirable, and we shall relate it to the lifetime of unstable particles.

(c) The magnetic moments must be calculated relativistically from the wave function of the resonance; they are not simply the sums of the magnetic moment of the constituents as in the additive quark model; orbital contributions play an important role. We note also that the relativistic magnetic moment operator of a Dirac particle is given by<sup>21</sup>

$$\hat{\mu} = \frac{e}{2} (\vec{L} + 2\vec{S}) H^{-1} , \quad (47)$$

so that a fast moving constituent electron inside the hadron would have a highly reduced magnetic moment. We shall apply this to the calculation of the magnetic moment of the  $\mu$ -meson.

(d) This question is already answered by the shape of the potential well in Fig. 1.

The remaining problem (e) I will now discuss in the next Section.

#### Internal Quantum Numbers, Multiplets and Group Structure

We begin with three simple but useful statements:

(a) Absolutely stable constituents provide absolutely conserved quantum numbers. Thus the proton number  $P$ , the electron number  $E$ , and the neutrino number  $N$  are conserved in all particle processes (for times shorter than the lifetimes of  $p, e, \nu$ ).

(b) The electromagnetic interactions (the only one so far in this already unified theory) can produce or annihilate pairs of  $p$ ,  $e$ ,  $\nu$  which do not change the internal quantum numbers of hadrons.

(c) A metastable state, formed from  $p$ ,  $e$ ,  $\nu$  and their anti-particles, of lifetime  $\tau$  provides a constituent for new states with lifetimes less than  $\tau$ , and with a conserved quantum number for all processes shorter than  $\tau$ . An example is the muon, which is built from  $\mu^- = (e^- \bar{\nu}_e \nu_\mu)$ ,  $\tau = 10^{-6}$  sec. Thus, the muon number is conserved in strong interactions which last about  $T \sim 10^{-22}$  sec. We shall see that the muon number is identified in the present theory with "strangeness" quantum number.

Leptons. We begin with the stable doublet  $(e, \nu_e)$ . The  $\mu$ -meson is a resonance in the channel  $(e^- \bar{\nu}_e \nu_\mu)$ . (Strictly speaking the two neutrinos in the  $\mu$ -decay have not been experimentally identified as  $\nu_e$  and  $\nu_\mu$ ). A dynamical model of the  $\mu$  as a  $(e \bar{\nu}_e \nu_\mu)$ -resonance will be calculated in Section "Interpretation of Isospin, Strangeness and other Internal Quantum Numbers".

The muon neutrino  $\nu_\mu$  is postulated to be a resonance (or bound state) in the  $(\nu_e \bar{\nu}_e \nu_\mu)$ -channel. At present it is not known experimentally if  $\nu_\mu$  decays. The upper bound of the mass of  $\nu_\mu$  is of the order of an electron mass.

We proceed similarly with  $\nu_\tau = (\nu_\mu \bar{\nu}_\mu \nu_\tau)$ , or  $(\nu_e \bar{\nu}_e \nu_\tau)$ , ... and with  $\tau = (\nu \bar{\nu})$ , and arrive at the following sequence of leptons

|        |            |
|--------|------------|
| :      | :          |
| $\tau$ | $\nu_\tau$ |
| $\mu$  | $\nu_\mu$  |
| $e$    | $\nu_e$    |

doublet      quartet      sextet

It is possible to visualize the heavy lepton sequence as excitation of the stable  $(e \bar{\nu}_e)$ -system. The transitions between the lepton sequences take place with the emission and absorption of  $(\nu \bar{\nu})$ -pairs (instead of the  $\gamma$  as in atomic physics). Semi-classical arguments show that perhaps magnetic self-energy of the electron is quantized in units of  $\frac{3}{2} \frac{m_e}{\alpha}$ , and a semi-classical mass formula for the lepton may be derived<sup>22</sup>.

The idea of a magnetic excitation of the electron with  $(\nu \bar{\nu})$ -quanta and the idea of a magnetic resonance  $(e \bar{\nu} \nu)$  are probably the same thing in two slightly different forms. The  $\mu$ -meson mass is given with great accuracy by the formula

$$m_\mu = m_e + \frac{3}{2} \frac{m_e}{\alpha} \quad . \quad (48)$$

Mesons. We build the mesons as lepton-antilepton magnetic resonances:

$$M = (1 \otimes \bar{1}) . \quad (50)$$

However, there may be some mixing effects. Considering the quartet of leptons,  $(e, \nu_e, \mu, \nu_\mu)$ , as a representation of  $U(4)$ , there are two ways of decomposing it with respect to the  $SU(3)$ -subgroup 23: We denote the leptons

$$1 : (SU(3) \text{ triplet } e^- \nu_e \mu^-, \text{ singlet } \nu_\mu)$$

$$1' : (SU(3) \text{ triplet } e^- \nu_e \nu_\mu, \text{ singlet } \mu) .$$

Accordingly we can also write eq. (50) as

$$M = (1 \otimes \bar{1}) + (1' \otimes \bar{1}') . \quad (51)$$

Physically eq. (51) means that the states  $e^- \mu^+$  and  $\nu_\mu \bar{\nu}_e$ , for example, are mixed. At this  $U(4)$  level, the multiplets are the same as in the quark-model:

$$[4] \times [4] = [15] + [1]$$

The [15] dimensional representation of  $U(4)$ -decomposes with respect to  $U(3)$  as:

$$[15] + [1] + [8] + [3] + [\bar{3}] .$$

Baryons. All baryons eventually decay into a proton and lepton-antileptons. Hence we build the baryons as

$$B = p \otimes 1 \otimes \bar{1} \otimes (1\bar{1}) \dots \quad (52)$$

The neutron becomes  $n = (p \ e^- \bar{\nu}_e)$ , i.e. Pauli's original neutron. The multiplets are given in Ref. 1.

Correspondence with the Integrally and Fractionally Charged Quarks. In the form (52), baryons in general need more than three constituents 1. In order to establish contact to the  $U(4)$ -structure of baryons (as we did for mesons), it is possible to take 4 baryons as forming a basic quartet and then build others by direct products of these. So if we take  $23 \ b \equiv (p, n, \lambda_s, \lambda_c)$  as a basic quartet:

|    |             |             |
|----|-------------|-------------|
| b: | $\lambda_s$ | $\lambda_c$ |
|    | p           | n           |

where  $n = (p e^- \bar{v}_e)$ ,  $\lambda_s = (p \mu^- \bar{v}_e)$  and  $\lambda_c = (p e^- \bar{v}_\mu)$  (the last two can also be the superpositions  $\lambda_s = [p(\mu^- \bar{v}_e + \bar{v}_e^- \mu)]$ ) then we can rewrite eq. (52) in the form

$$B = b \times l \times \bar{l}' \quad (53)$$

with  $l$  and  $\bar{l}'$  given in eq. (51). Then at the  $U(4)$  level we have the following multiplets and their  $SU(3)$ -reduction:

$$U(4): [4] \times [4] \times [4] = [20] + 2 [20] + [4]$$

$$\downarrow \quad \downarrow$$

$$[8] + [6] + [3] + [\bar{3}]$$

$$\downarrow$$

$$[10] + [6] + [\bar{3}] + [1]$$

The resulting correspondance with the quark model is shown in

Table II

|   | $b$           | $l$     | $\bar{l}'$  | Average Charge |
|---|---------------|---------|-------------|----------------|
| u | $p^+$         | $v_e$   | $e^+$       | $2/3$          |
| d | $n$           | $e^-$   | $\bar{v}_e$ | $-1/3$         |
| s | $\lambda_s$   | $\mu^-$ | $\bar{v}$   | $-1/3$         |
| c | $\lambda_c^+$ | $v_\mu$ | $\mu^+$     | $2/3$          |

"green" "blue" "red"

Our constituents  $b$ ,  $l$ ,  $\bar{l}'$  are in one-to-one correspondance with the Han-Nambu integrally charged quarks<sup>24</sup>, except that ours are real physical particles. We also show the correspondance to fractionally charged quarks (u d s c). Note that the average charge in each row of the physical particles equals the quark charges. Furthermore, a correspondance to the so called "colour" degree of freedom may be established: By eq.(53) we take, in forming the baryons, one particle from each column, i.e. from each "colour". But "colour" in our case does not increase the number of basic constituents.

#### Interpretation of Isospin, Strangeness and Other Internal Quantum Numbers

The notion of iso-spin originated in the 2-nucleon system<sup>25</sup>. The states  $|p,p\rangle$  and  $|n,n\rangle$  are symmetric with respect to exchange,

but for  $|np\rangle$  we must form the combinations

$$\frac{1}{\sqrt{2}} (|p,n\rangle \pm |n,p\rangle) . \quad (54)$$

We interpret eq. (54) as the symmetry or antisymmetry with respect to the exchange of  $(e^-v)$  between two protons, exactly in the same way as the symmetric and antisymmetric states of  $H^+$ -ion with respect to the exchange of  $(e^-)$  between the two protons (the  $\sigma_g$  and  $\sigma_u$ -states). The third component of isospin can be identified with the number of stable constituents as

$$I_3 = \frac{1}{2} ( (P - \bar{P}) + (E^+ - E^-) + (N - \bar{N}) ) , \quad (55)$$

where  $P$ ,  $E$ ,  $N$  are the numbers of protons, electrons and neutrinos. We shall denote eq. (54) schematically by

$$p \xrightarrow{(e\bar{v})} p \quad (56)$$

We also denote the transformation between proton and neutron by

$$p \xrightarrow{(e\bar{v})} n \quad (57)$$

which can be identified with the isospin lowering operator  $I^-$  on the single particle case.

The isospin selection rules can only be verified experimentally on at least 2-body reactions. For example, for the two pion system, if we write

$$\pi^+ \xrightarrow{(e\bar{v})} \pi^0 \xrightarrow{(e\bar{v})} \pi^- , \quad (58)$$

then, we obtain the following symmetrizations with respect to exchange of  $(e\bar{v})$

$$\begin{aligned} \pi^+ \xleftrightarrow{(e\bar{v})} \pi^+ & \text{ corresponds to } \frac{1}{\sqrt{2}} (|\pi^+ \pi^0\rangle \pm |\pi^0 \pi^+\rangle) \\ \pi^0 \xleftrightarrow{(e\bar{v})} \pi^0 & \text{ corresponds to } \frac{1}{\sqrt{2}} (|\pi^- \pi^0\rangle \pm |\pi^0 \pi^-\rangle) \end{aligned}$$

and

$$\begin{aligned} \pi^+ \xleftrightarrow{(e\bar{v})} \pi^0 & \text{ gives the } 2|\pi^0 \pi^0\rangle + |\pi^+ \pi^-\rangle + |\pi^- \pi^0\rangle \\ \pi^0 \xleftrightarrow{(e\bar{v})} \pi^+ & \text{ symmetry } \} \text{ types} \quad \text{etc.} \end{aligned} \quad (59)$$

Similarly using (57) and (58) we have the symmetric states under exchange of  $(e\bar{v})$  in the  $\pi N$ -system:

$$\begin{aligned}
 \pi^+ \leftrightarrow p &\implies \frac{1}{\sqrt{2}} (|\pi^0 p\rangle \pm |\pi^+ n\rangle) \\
 \pi^0 \leftrightarrow p &\implies \frac{1}{\sqrt{2}} (|\pi^- p\rangle \pm |\pi^0 n\rangle)
 \end{aligned} \tag{60}$$

All selection rules in particle reactions due to the law of conservation of isotopic spin can be obtained from the symmetrization of states with respect to  $(e\bar{v})$ -exchanges. It was observed long ago, that isospin selection rules can be derived by the use of finite subgroups of the  $SU(2)$ , one does not need the full  $SU(2)$ -Lie algebra<sup>26</sup>. We have now derived in our model a physical realization of these finite subgroups.

We have already remarked the interpretation of strangeness as

$$S = N_{\mu^+} - N_{\mu^-} \tag{61}$$

and its conservation in strong interactions during which  $\mu$  is stable. This can be generalized to the conservation of the numbers  $v_\mu$ ,  $v_\tau$ ,  $v_\tau$ , ... .

The lowering and raising operators in  $SU(3)$ - or  $SU(4)$ -representation space can be interpreted as the excitation of  $e^-$  into  $\mu^-$ ,  $v_e \leftrightarrow v_\mu$ ,  $\mu \leftrightarrow \tau^-$ , etc.

These together with the absolutely conserved additive quantities  $B$ ,  $L$ ,  $Q$ , ... comprise all the observed internal quantum numbers.

We may therefore conclude that the only fundamental continuous symmetry group in particle physics is the space-time group (extended perhaps to the conformal group to account for the electron-neutrino doublet), hence the only fundamental quantum numbers are mass, spin, parity, and the identity of absolutely stable constituents (i.e.  $B$ ,  $L$ ,  $Q$ ). All other approximate symmetries are due to the structure of the resonances formed from  $p$ ,  $e$ ,  $v$ . Note that usually the  $SU(2)$ -invariance of strong interaction, for example, is postulated (say by a phenomenological Lagrangian), but is not explained.

#### Strong and Weak Interactions from Magnetic Forces

Having discussed the formation of resonances and their multiplets we ask "how do the weak and strong interactions arise from magnetism". The answer is given in Fig. 1. We interpret the deep potential well at short distances as the region of strong interactions and the barrier penetration of a resonance as the weak decays of hadrons. Thus  $\beta$ -decay, for example, has exactly the same basic quantum explanation as the  $\alpha$ -decay. The weak interactions of the neutrino we have already discussed in terms of its magnetic

moment. The interaction of two hadrons are due to (i) van der Waals forces, as usual (but this is small), (ii) exchange and or rearrangement of constituents, (iii) pair production or annihilation of  $p, e, \nu$  and subsequent exchange and rearrangement of constituents. Thus strong interactions are just like the chemical interactions (except the pair production). There are no fundamental coupling constants in both weak and strong interactions; they are derivable.

Why are the  $pp$ ,  $\pi p$ ,  $ep$ ,  $ee$ , ... scatterings apparently so different? This is due largely to the phenomenon of scattering against a potential barrier. It is well known that in the scattering problem with a potential of the type of Fig. 1, the phase shifts essentially follow at high energies the Born approximation phase shifts, except at definite energies where a resonance in a partial wave  $l$  exists in the potential well. At this energy the  $l^{\text{th}}$  partial wave phase shift jumps by about  $\pi$  which gives a sharp resonance peak in the cross-section superimposed on a general background coming from all other partial waves. This is the resonance penetration process first introduced by Gurney. We note that the many resonances observed in the  $e^+e^-$ -scattering, for example, appear as such sharp bumps on a background. Now pion, having spin 0 and no magnetic moment can come very close to the proton (no spin-spin force) when constituents of pions and nucleons would interact and exchange, whereas for electrons there are strong spin-spin barriers. It would be important to perform experiments with polarized electrons and targets to select spin states in which the spin-spin forces are attractive. If these show very strong spin effects as in the case of polarized  $pp$ -experiments (see Section - "Further Results and Conclusions"), this would be a very clear support for the magnetic effects.

#### Decays of Charged Pions and Muons

I shall now discuss a more specific dynamical model of charged pions and muons in order to illustrate the formation of these resonances and their subsequent weak decays<sup>27</sup>. In particular, we shall calculate the weak Fermi coupling constant from the magnetic moment of the neutrino which we have estimated from the neutral current process (43).

The muon is  $\mu = (e\bar{\nu}_e v_\mu)$ , and pion  $\pi^- = (e\bar{\nu}_e)(v_\mu\bar{\nu}_\mu)$ . The additional  $(v_\mu\bar{\nu}_\mu)$  is added in  $\pi^-$  to incorporate the two decay modes

$$\pi^- = (e\bar{\nu}_e)(v_\mu\bar{\nu}_\mu) \quad \begin{array}{l} \xrightarrow{(e\bar{\nu}_e v_\mu)\bar{\nu}_\mu = \mu\bar{\nu}_\mu} \\ \xrightarrow{e\bar{\nu}_e \text{ with annihilation of } (v_\mu\bar{\nu}_\mu)} \end{array}$$

and also for parity reasons:  $(e\bar{\nu}_e)$ -magnetic resonance is in the  $l = 1, S = 1$  ( $J = 0$ ) state; we give  $(-1)$  relative parities to

$(e^- \bar{\nu}_e)$  and  $(\nu_\mu \bar{\nu}_\mu)$ .

The three- or four-body problems with neutrinos are difficult to handle at the moment. So approximately we couple the neutrinos in  $\pi^-$  and  $\mu$  into a spin  $1/2$  and spin 1 dipole moment, respectively. The models are then

$\pi$ : Electron in the field of a fixed spin  $1/2$  dipole moment,  $J = 0^-$  state.

$\mu$ : Electron in the field of a fixed spin 1 dipole moment,  $J = 1/2^+$  state.

Surely these models are crude, but we want to have an idea of the binding and decay rate, and these are the simplest models that one can calculate.

For the  $\pi$ , we obtain the equation

$$\frac{d^2u}{dy^2} - \left[ \frac{1}{y^4} - \frac{4}{y^3} + \frac{2}{y^2} \right] u + \eta^2 u = 0,$$

where  $y$  is a dimensionless variable,  $y = \frac{mr}{|a|a}$ ,  $|a| =$  anomalous magnetic moment of the fixed dipole, and  $\eta^2 = |a|^2 \alpha^2 (E^2 - m^2) / m^2$ . The effective potential is like that in Fig. 1. We see the possibility of a resonance but the resonance in this approximation has zero-energy, i.e.  $M = m_\pi$ . A form factor for the fixed dipole of the form  $a(r) = a(1 - e^{-(y/Y)^2})$ , with a reasonable choice  $Y = .044$ , yields  $E_{res} = m_\pi$ . Such a form factor modifies the potential in Fig. 1 only at distances around and less than  $Y = .044$ . For  $y \geq 1$ , the potential is unchanged.

Now we can evaluate the lifetime  $\tau$  of the resonance so formed using the WKB-formula

$$\frac{1}{\tau} = \text{frequency} \times e^{-2A}, \quad A = \int_b^t \left[ \frac{1}{y^4} - \frac{4}{y^3} + \frac{2}{y^2} - \eta^2 \right]^{1/2} dy.$$

The decay is independent of the form factor. We compare the decay rate so calculated with the usual formula for  $\pi \rightarrow \mu \nu$ , and obtain a relation between the Fermi coupling constant  $G$  and the anomalous magnetic moment  $a$ . The result is  $a \approx -3 \times 10^{-10}$ . The magnetic moment of the neutrino is negative (like electron) and of the same order of magnitude as obtained from the scattering experiments:  $e + \nu \rightarrow e + \nu$ , eq. (44).

For the muon,  $\mu = (e \bar{\nu}_e \nu_\mu)$ , we couple  $(\bar{\nu}_e \nu_\mu)$  to a spin 1 state and solve the equation of the electron in the dipole field of spin 1,

$$A = \frac{\vec{S}_1 \times \vec{r}}{r^3}, \quad S_1 = 3 \times 3, \text{ Spin 1 matrices,}$$

namely

$$[\vec{a} \cdot (\vec{p} - e\vec{A}) - E + \beta m] \psi = 0. \quad (63)$$

We couple spin 1 with spin  $1/2$  of the electron to a total  $S_1^+$  and then  $S$  with the orbital angular momentum  $L$  to a total  $J = \frac{1}{2}$ . The resultant 4 coupled radial equations can be analyzed. We get degenerate  $\frac{1}{2}^+$ -states, and a potential well with a barrier for the  $\frac{1}{2}^+$  state.

The lifetime  $\tau$  is calculated as in the  $\pi$ -decay. We find for the anomalous magnetic moment of the  $(\nu_\mu \bar{\nu}_e)$ -system  $|a| = .6 \times 10^{-10}$ . If we write  $a = a_{\bar{\nu}_e} + a_{\nu_\mu}$ , and use the value of  $a_{\nu_\mu}$  from pion decay, we have  $a_{\bar{\nu}_e} \approx +3 \times 10^{-10}$ . The signs of both  $a_{\bar{\nu}_e}$ ,  $a_{\nu_\mu}$  are negative ( $a_{\bar{\nu}_e}$  then positive).

This model gives a point-like structure to muon: The size is determined by

$$e a \mu_0 = \frac{\alpha}{2m_e} |a| \approx 10^{-13} \times 10^{-10} \sim 10^{-23} \text{ cm,}$$

and is independent of the masses of the constituents; depends on the magnetic moment. For  $\tau$ , for example, we would find approximately the same magnitude, if in  $\tau = (\mu \bar{\nu})$  the neutrinos have the same magnetic moment. From experiments  $e^+ + e^- \rightarrow \mu^- + \mu^+$ , or  $\tau^- + \tau^+$ , one can already deduce that sizes of  $\mu, \tau, \dots$  are all less than  $10^{-16}$  cm.<sup>2</sup>

The magnetic moment of the composite muon can be estimated from eq. (47). For an electron at rest  $H$  in eq. (47) is equal to  $m_e$ , but for the electron inside the muon which is moving very fast,  $H$  is of the order of the mass of the magnetic resonance,  $H \sim m_\mu$ . This explains why the magnetic moment of a particle of mass  $M$  is very close to the value of  $e/2M$ .

### Further Results and Conclusions

I believe that the framework I have described gives a very good intuitive picture of all phenomena in particle physics and in high energy physics. It is conservative, economical, and is based on the common sense that hadrons are essentially built from stable particles into which they disintegrate. This extends the basic tradition and attitude of physicists from atomic and molecular physics to nuclear and particle physics, and establishes a continuity which perhaps was missing with the introduction of many hypothetical unobserved (or unobservable) particles and fields. It is always legitimate to ask what kind of forces between the decay products would describe

the strong and weak interactions. It is gratifying that, unexpectedly, the seemingly small and so far neglected spin-effects may just do the job, in which case we would have an already unified theory in electromagnetism itself.

The fact that spin-effects are indeed very important in strong interactions has been dramatically demonstrated in recent years in the polarized pp and pn-scattering experiments<sup>28</sup>. Not only does one find large differences between parallel and antiparallel spin orientations, but also possible new narrow diproton resonances.

I feel that only after a very careful study of magnetic resonances at short distances we can say if there is another new type of force in nature other than electromagnetism. We have made only a beginning in this study.

The most important immediate problem is to have more and more accurate methods of solving dynamical models of interacting particles with magnetic potentials, and to derive more accurate magnetic potentials from field theory. I am of course aware that some of the potential models we used might appear to be too crude. But on the other hand, since perturbation expansions, hence terms like vacuum polarization etc., do not apply, it is possible that effective potentials between point-like objects do already sum the perturbation terms. Other methods might also be useful. For example, the so called "Bag Model" of hadrons applies equally well to our model, in fact more so than the quark model: Here one takes massless constituents (in our case electron and neutrino) in a volume of radius R (e.g. our potential well of Fig. 1), and solves the Dirac equation in such a volume. With these states one constructs an effective Hamiltonian with 2-body interactions which is of the form  $\sum \alpha_i \cdot \alpha_j$ , i.e. has the form of spin-spin interactions. In this way, one obtains an interpretation of the mass formula of the type given by Zeldovich and Sakharov<sup>29</sup>.

The Bag model, parton model, various exchange models, ... are different approximate forms, substitutes, of a full relativistic many-body dynamical problem. They can be applied (with minor modifications) to any kind of constituents. For further results we refer to reviews in<sup>1</sup>.

In conclusion, the simple theory presented here gives a good overall intuitive picture to all particle physics as in atomic and molecular physics. It is testable. A number of experimental predictions may give crucial information soon, such as angular distribution in  $e+v \rightarrow e+v$ ; no contribution of weak interactions in  $e^+ + e^- \rightarrow e^+ + e^-$ ; polarized  $e^+, e^-$ -experiments; prediction of new massive (ep)-resonances, etc., effects of neutrino magnetic moment (astrophysical tests), and so on. There are no new hypothetical

particles or fields, no new interactions, but electrodynamics; hence no problems like confinement. It is also very restrictive because there are no parameters, except the properties of the three stable particles:  $p, e, \nu$ . We must be able, however, to make more quantitative predictions by dynamical calculations to really understand the properties of magnetic forces at short distances.

## REFERENCES

1. (a) For previous reviews see A.O. Barut, *Surveys in High Energy Physics*, Vol.1, No. 2:113-140 (1980).  
 (b) in "Group Theory-1980", AIP Conference Proceedings, Vol.71 (edit. by T. Seligman), p.73-108 (1981).
2. see A. Böhm, these Proceedings.
3. F. Rasetti and E. Fermi, *Nuovo Cim.* 3:26 (1926).
4. E. Fermi, *Z.F.physik* 60:320 (1930)
5. A. O. Barut, M. Berrondo and G. Garcia-Calderón, *J. Math. Phys.* 21:1851 (1980).
6. A. O. Barut and A. Skorupski (to be published).
7. See for example, C. Itzykson and J.-B. Zuber, *Quantum Field Theory*, McGraw Hill, N.Y. 1980; p. 347ff.
8. A. O. Barut and J. Kraus, *J. Math. Phys.* 17:506 (1976).
9. A. O. Barut, *J. Math. Phys.* 21:568 (1980).
10. C. M. Bender, F. Cooper, G.S. Guralnik, *Ann. of Phys.* 109:165 (1977);  
*Phys. Rev. Lett.* 40:1620 (1978); *Phys. Rev. D4*:2755 (1976).
11. W. Pauli, *Collected Scientific Papers*, Vol. 2, (Interscience) p.1313.
12. J. F. Carlson and J.R. Oppenheimer, *Phys Rev.* 41:763 (1932).
13. H. Bethe, *Proc. Cambr. Phil. Soc.* 35:108 (1935).
14. E. Fermi, *Z.f.Physik* 88:161 (1934).
15. H. Yukawa, *Proc. phys. math. soc. (Japan)* 17:48(1935).
16. D. Ivanenko and I. Tamm, *Nature* 133:981 (1934).  
 G. Wick, *Atti Acad. Lincei* 21:170 (1935).  
 C. von Weizsäcker, *Z. f. Physik* 102:572 (1936).  
 G. Wentzel, *Helv. Phys. Acta* 10:107(1936).  
 G. Gamow and E. Teller, *Phys. Rev.* 51:289 (1937).
17. A. O. Barut, in *Structure of Matter*, Proceedings of the Rutherford Centenary Conference, Univ. of Christchurch Press (1971).
18. Z. Maki, M. Nakagura, Y. Ohnuki, S. Sakata, *Progr. Theor.Phys.* 23:1174 (1960).  
 J. Pati, A. Salam and J. Strathdee, *Phys. Lett.* 59B:265 (1975).  
 E. Novak, J. Sucher and C.H. Woo, *Phys. Rev. D16*:2874 (1975).
19. A. O. Barut and J. Kraus, *Phys. Lett.* 59B:175 (1975).
20. A. O. Barut, *Proceedings of the Neutrino Workshop*, Univ. of Wisconsin Press, Madison, Wisc. (1981).
21. A. O. Barut and A.J. Bracken, *The Magnetic Moment Operator of the Relativistic Electron* (to be published).

22. A. O. Barut, Phys. Lett. 73B:310 (1978).  
Phys. Rev. Letters 42:1251 (1979).
23. A. O. Barut and S.A. Basri (to be published).
24. M. Y. Han and Y. Nambu, Phys. Rev. B139:1006 (1965).
25. W. Heisenberg, Z.f.Physik 77:1 (1932); 156 (1932); 80:582 (1932); 96:473 (1935).
26. K. M. Case, R. Karplus and C.N. Yang, Phys. Rev. 101:874(1956).
27. A. O. Barut and G. Strobel (to be published).
28. A. D. Krisch, Scientific American 240:68, May 1979, and  
Orbis Scientific (1979).
29. Ya. B. Zeldovich and A.D. Sakharov, Sov. J. Nucl. Phys. 4:288 (1967).

## STRONG MAGNETIC FIELDS

N.D. Hari Dass

The Niels Bohr Institute  
University of Copenhagen  
DK-2100 Copenhagen Ø, Denmark

I wish to describe in this talk a summary of a variety of problems pertaining to strong external electromagnetic fields that have been tackled by the proper time techniques due to Schwinger. These techniques were first discovered by Schwinger as gauge invariant regularisation schemes to tackle a host of problems in quantum electrodynamics. We shall follow Schwinger and discuss the derivation of the Euler-Heisenberg effective action for the self coupling of the electromagnetic field induced by vacuum polarisation.

The starting point is the Dirac equation for an electron in an external e.m. field described by  $A_\mu(x)$ :

$$(\gamma_\mu \pi_\mu + m)\psi = 0 \quad \text{where} \quad \pi_\mu = p_\mu - eA_\mu \quad (1)$$

The current density four vector is given by

$$j_\mu(x) = \frac{ie}{\hbar} [\bar{\psi}(x), \gamma_\mu \psi(x)] \quad (2)$$

The vacuum expectation value of  $j_\mu(x)$  is given by

$$\langle j_\mu(x) \rangle = ie \operatorname{tr} \gamma_\mu G(x', x)_{x \rightarrow x} \quad (3)$$

Writing  $G(x', x)$  symbolically as  $G(x', x) = \langle x' | G | x \rangle$  the operator form of the equation satisfied by  $G$  is

$$(\gamma \cdot \pi + m)G = 1 \quad (4)$$

The modification of the action due to the additional current induced by the vacuum  $\langle j_\mu \rangle$  is given by

$$\delta W = \int dx \delta A_\mu(x) \langle j_\mu \rangle = ie \operatorname{Tr}(\gamma \delta A) G \quad (5)$$

The formal solution of (4) being  $G = (\gamma \cdot \pi + m)^{-1}$  we find

$$\begin{aligned} G &= (\gamma \cdot \pi + m)^{-1} = (-\gamma \cdot \pi + m) \left| m^2 - (\gamma \cdot \pi)^2 \right|^{-1} \\ &= (-\gamma \cdot \pi + m) \int_0^\infty ds \exp -is \left| m^2 - (\gamma \cdot \pi)^2 \right| \quad (6) \end{aligned}$$

Now  $\delta W$  is recast as

$$\begin{aligned} \delta W &= -\operatorname{Tr} \delta(\gamma \cdot \pi) G \\ &= \operatorname{Tr} \delta(\gamma \cdot \pi) \gamma \cdot \pi \int_0^\infty ds e^{-is} \left| m^2 - (\gamma \cdot \pi)^2 \right| \quad (7) \end{aligned}$$

$$= \delta \left| \frac{i}{2} \int_0^\infty ds s^{-1} \operatorname{Tr} \exp -is \left| m^2 - (\gamma \cdot \pi)^2 \right| \right| \quad (8)$$

Hence

$$W = \frac{i}{2} \int_0^\infty ds s^{-1} \operatorname{Tr} \exp -is \left| m^2 - (\gamma \cdot \pi)^2 \right| \quad .$$

We will now demonstrate that for constant e.m. fields this action is explicitly calculable. Introduce

$$H = -(\gamma \cdot \pi)^2 = \pi^2 - \frac{e}{2} \sigma_{\mu\nu} F^{\mu\nu} \quad .$$

Then

$$W = \frac{i}{2} \int_0^\infty ds s^{-1} \operatorname{Tr} e^{-isH} \quad (9)$$

Writing  $A(s) = e^{isH} A e^{-isH}$  one finds

$$\frac{dA(s)}{ds} = +is[H, A(s)] \quad .$$

$$\text{Thus we find } \frac{dx_\mu}{ds} = 2\pi_\mu; \frac{d}{ds} \pi_\mu = 2eF_{\mu\nu}\pi_\nu \quad (10)$$

Equations (10) are easily solved to yield

$$\pi(s) = e^{2eFs} \pi(0); x(s) - x(0) = (e^{2eFs} - 1)\pi(0) \quad (11)$$

Now

$$\text{Tr } e^{-isH} = \text{tr} \langle x | e^{-isH} | x \rangle = \text{tr} \langle x' | e^{-isH} | x \rangle_{x' \rightarrow x} \\ = \langle x'(s) | x(0) \rangle_{x' \rightarrow x} .$$

Now

$$i \frac{\partial}{\partial s} \langle x'(s) | x(0) \rangle = \langle x'(s) | H | x(0) \rangle$$

and

$$H + \frac{e}{2} \sigma_{\mu\nu} F^{\mu\nu} = \pi^2(s) \\ = |x(s) - x(0)| + \frac{1}{4} e^2 F^2 \sinh^2 eFs |x(s) - x(0)|$$

Using  $|x(s), x(0)| = i(eF)^{-1} (e^{2eFs} - 1)$  one gets

$$i \frac{\partial}{\partial s} \langle x'(s) | x(0) \rangle = \left[ -\frac{1}{2} e F + (x' - x) \cdot K \cdot (x' - x) \right] \langle x'(s) | x(0) \rangle$$

has the solution

$$\langle x'(s) | x(0) \rangle = C(x', x'') \frac{e^{-L(s)}}{s^2} \exp \left[ \frac{ie}{2} \sigma Fs + \frac{i}{4} (x' - x) eF \coth eFs \cdot (x' - x) \right] \\ C = -i/(4\pi)^2 ; \quad L(s) = \frac{1}{2} \text{tr} \ln \frac{\sinh eFs}{eFs}$$

This way one gets

$$\langle x \rangle = \frac{i}{2} \int_0^\infty ds s^{-3} \exp -im^2 s + e^{-L(s)} \text{tr} \exp \frac{i}{2} e\sigma Fs . \quad (12)$$

After the usual renormalisation one finds

$$= 1(E^2 - H^2) + \frac{2\alpha^2}{45} \cdot \frac{1}{4} |(E^2 - H^2)^2 + 7(\bar{E} \cdot \bar{H})^2| + \dots \quad (13)$$

Equation (12) is the famous Euler-Heisenberg result. It is clear that a new scale for the e.m. fields has appeared in  $E, H \sim m^2/\alpha \sim 10^{16}$  Gauss. It is therefore instructive to ask for the behaviour of (12) for strong fields without the weak field approximation (12) reads

$$= - \frac{1}{8\pi^2} \int_0^\infty ds s^{-3} \exp -m^2 s \left| (es)^2 G \frac{\text{Re} \cosh esx}{\text{Im} \cosh esx} - 1 - \frac{2}{3} (es)^2 \right| \quad (14)$$

$$\text{where } = \frac{1}{4} F_{\mu\nu}^2 ; \quad G = \frac{1}{4} F_{\mu\nu} F_{\mu\nu}^* = \vec{E} \cdot \vec{H} ; \quad \vec{X} = \vec{E} + i\vec{H} = \frac{1}{2}(H^2 - E^2) .$$

As it stands the integrand of (14) has singularities on the real axis unless  $G=0$   $>0$  which implies a pure magnetic field. The physical interpretation of this result is that a pure magnetic field is stable against pair creation. We shall come back to this later on. If on the other hand one has a pure electric field for which  $G=0$ ,  $<0$ , the singularities are at  $s=s_n = n\pi/e$ . Taking the path of integration to lie above the real axis one finds

$$2\text{Im} = \frac{\alpha^2}{\pi^2} \varepsilon^2 \sum_{n=1}^{\infty} n^{-2} \exp \frac{-n\pi m}{e} \quad (15)$$

This is the probability per unit time per unit volume for the constant field to produce a pair.

When  $H$  is very strong, we can drop the  $m^2$  dependence in (14) and one finds, for the energy density of the field,

$$= \frac{1}{2} H^2 + \frac{11}{48\pi^2} g^2 H^2 \left( \ln \frac{gH}{2} - \frac{1}{2} \right) \quad (16)$$

This expression has a minimum not at  $H=0$  but at

$$gH_{\min} = \Lambda^2 \exp - \frac{24\pi^2}{11g} .$$

This result has figured prominently in discussions regarding the vacuum structure in QCD.

In the early 70's Schwinger generalised the proper time techniques to study the radiative corrections to the electron propagator: The Dirac equation is now modified to

$$(\gamma^\mu \pi + m + M) G = 1 \quad (17)$$

$$\text{where } M = ie^2(2\pi)^{-4} \int dk \gamma^\nu k^{-2} |m - \gamma(\pi-k)| m^2 - e\sigma F + (\pi-k)^2|^{-1} \gamma_\nu .$$

The proper time parametrisation is introduced as

$$k^{-2} |m^2 - e\sigma F + (\pi-k)^2|^{-1} = - \int_0^\infty ds s \int_0^1 du e^{is\chi} \quad (18)$$

where  $\chi = (k-u\pi)^2 + u(1-u)\pi^2 + u(m^2 - e\sigma F)$ . Introducing variable  $\xi_\nu$  "conjugate" to the integration variables  $k_\mu$  according to

$$|k_\mu, \xi_\nu| = -ig_{\mu\nu}$$

one can write  $M$  as

$$M = -ie^2 \langle \xi' | \int ds s du e^{-is\chi} |m - \gamma^\nu(\pi-k)| |\xi' \rangle \quad (19)$$

The trick now is to develop the "equations of motion" for  $k_\mu$ ,  $\pi_\mu$ ,  $\gamma_\mu$  etc. and the final form of  $M$  is

$$\begin{aligned} M = & \frac{\alpha}{2\pi} \int \frac{ds}{s} du e^{-ism^2 u^2} \Delta^{-\frac{1}{2}} \exp - \frac{ius}{x} \{ \beta - (1-u)x \} \pi_H^2 \\ & \cdot e^{i\xi ux} \cdot |1 + ue^{-2i\xi ux} + \frac{1-u}{m} \{ \frac{1-u}{\Delta} + \frac{u}{\Delta} \frac{\sin x}{x} e^{-2i\xi x} \} \gamma^\nu \pi_H| - (1+u)\xi \end{aligned} \quad (20)$$

where  $\xi = \pm 1$  is the spin along the magnetic field direction,  $\pi_H$  is the projection of  $\pi$  onto the 1-2 plane defined by the magnetic field;  $x = esHu$ ,  $\beta = \tan^{-1} \{ (1-u)\sin x \{ (1-u)\cos x + u\sin x/x \}^{-1} \}$  and  $\Delta = (1-u)^2 + 2u(1-u) \sin x \cos x/x + u^2 \sin^2 x/x^2$ .

Thus  $M$  has been reduced to an expression involving only diagonal operators and can be evaluated easily. As an application of

(20), let us consider the ground state of the system. Here it is easy to check that  $M$  is real characteristic of the stability of the ground state.

For weak fields the result is

$$\operatorname{Re} M = - \frac{\alpha}{2\pi} \frac{eH}{2m} \left| 1 - \frac{8}{3} \frac{eH}{m^2} \left\{ \log \frac{m^2}{2eH} - \frac{13}{24} \right\} + \dots \right| .$$

For strong fields the energy of the ground states is

$$E = \frac{m\alpha}{2\pi} \left( \log \frac{2eH}{m^2} \right)^2 + m \quad (21)$$

We see from (21) that the anomalous magnetic moment  $\alpha/2\pi$  is modified by a field dependent term that tends to reduce it and that even for very strong fields the energy of the ground state is shifted by only  $\sim \alpha m_e$  thus making it impossible for pair creation.

Applying (20) to an excited state it is easy to see that  $M$  is imaginary and this imaginary part can then be related to the power emitted by synchrotron radiation. The final result one obtains is

$$P = \frac{2}{3} \alpha \left( \frac{eH}{m} \right) \left( \frac{E}{m} \right)^2 \left| 1 - \frac{55}{16} \sqrt{3} \frac{eH}{m^2} \frac{E}{m} \left( 1 - \frac{8}{55} \sqrt{3} \zeta' \right) \right| \quad (22)$$

This sums up the first quantum correction to the synchrotron power emitted. In pulsars  $eH/m^2 \sim 1/50$  and  $E/m \sim 10^6$  we see that quantum corrections are significant.

As a final illustration of the proper time techniques we consider vector potentials to be  $A_\mu^{\text{ext}} + a_\mu$ . Considering for example processes involving only external photons,  $H$  as defined in (9) becomes

$$H = H_0 + H_1 \text{ with } H_0 = \pi^2_{\text{ext}} - \frac{e}{2} \sigma_{\mu\nu} F_{\mu\nu}^{\text{ext}}; H_1 = -2e\pi^* a + e^2 a^2 - \frac{e}{2} \sigma_{\mu\nu} f_{\mu\nu}$$

The exponential  $e^{-ish}$  has the expansion

$$e^{-ish} = e^{-ish_0} - is \int_{-1}^{+1} \frac{dv}{2} e^{-is \frac{1+v}{2} H_0} H_1 e^{-is \frac{1-v}{2} H_0} + \dots \quad (23)$$

Thus one can evaluate processes like photon splitting, refractive index of the vacuum, photon pair creation, pair creation due to  $\gamma\gamma$  collisions etc. As a typical example let us consider the probability of photon pair creation in a magnetic field. For weak fields  $eH/m^2 \ll 1$ ,  $\omega/m > 1$  such that  $eH/m^2 \omega/m > 1$  we find for the absorption coefficient

$$\kappa \sim \alpha \sin\theta \frac{\omega H}{2} \frac{\sqrt{3}}{\sqrt{2}} \frac{e^{-\frac{1}{3} \frac{mH_c}{\omega}}}{e} \quad (24)$$

In pulsars with  $H_c \sim 50H$  and  $\omega \sim 2\text{MeV}$ , this length is about  $\sim 10^4$  cms and we see that the photon disintegrates into a pair easily in the magnetosphere. The electric field induced by the rotation accelerates these pairs which in turn emit curvature radiation in the MeV range and soon one has an avalanche of charged particles.

The same techniques can be used to calculate photon decay into neutrinos in a magnetic field.

As a more complicated example of the radiative processes in a strong magnetic field consider compton scattering. With the identification  $A_\mu = A_{\mu}^{\text{ext}} + a_\mu$ , the  $\chi$  introduced in (18) becomes

$$\chi = \chi_0 + \chi' = \{k-u(\pi_{\text{ext}} - ea)\}^2 + u(1-u)(\pi_{\text{ext}} - ea)^2 + u(m^2 - e^2 F_{\text{ext}} - e\omega) \quad (25)$$

$e^{is\chi}$  has now an expansion similar to (23). The electron field in the combined vector potential has likewise the expansion

$$\psi^{A+a} = \psi^A + (\gamma \cdot \pi + m)^{-1} \psi^A + \dots \quad (26)$$

Combining (25) and (26) we can expand the mass operator  $\psi^{A+a} \gamma^0 M \psi^{A+a}$  to quadratic powers in  $a$  to yield the radiative correction to forward compton scattering in external magnetic fields. The imaginary part of this amplitude then yields the cross section for compton scattering in external fields. For  $eH/m^2 < 1$ , for example, the correction to the Klein-Nishina formula is (electron rest frame)

$$\Delta\sigma = \frac{\pi\alpha^2}{m\omega} \frac{eH}{m^2} (2n+1)A(\omega) \quad (27)$$

I would like to end this talk with a brief mention of some work I am currently engaged in concerning the problem of electron gas in a strong magnetic field. At  $T = 0^{\circ}\text{K}$ , the energy levels are filled from  $m$  to  $E_F$ . If there are positrons also present, the levels are empty from  $-E_F$  to  $-m$ . The correction to the vacuum effective action can then be expressed as

$$\Delta = \frac{eH}{4\pi^{5/2}} \int_m^{E_F} dE \int_0^\infty \frac{ds}{s^{5/2}} (\coth esH - \frac{1}{esH}) e^{-(E^2 - m^2)s} \quad (28)$$

This can be used to calculate the susceptibility of the system, its refractive index etc. Applying the perturbation scheme outlined before one can also calculate various radiative processes in such a magnetised electron gas. Generalisations to finite temperatures are under investigation.

## REFERENCES

1. J. Schwinger, Phys. Rev. 82, p. 664 (1951)
2. W.Y. Tsai, Phys. Rev. D10, 4, p. 1342 (1974) and references therein.
3. N.D. Hari Dass, Annals of the New York Academy of Sciences 257 (1975) and references therein.
4. L.L. De Raad, K.A. Milton, N.D. Hari Dass, Phys. Rev. D14, p. 3326 (1976).

## PARTICLE PRODUCTION BY THE GRAVITATIONAL FIELD

P. Candelas

Center for Theoretical Physics  
The University of Texas at Austin  
Austin, Texas 78712

### INTRODUCTION

My aim, in these lectures, will be to review some aspects of the theory of particle production by gravitational fields. Roughly speaking this theory deals with two rather different topics: particle production by black holes and particle production in cosmological contexts. Of these the former process is more completely understood, the latter, which may well lead to significant effects in the theory of the early universe, is less well understood since it is currently bedevilled by the question of what should be chosen as the quantum state of the field. For this reason as well as the exigencies of the available time I shall leave the subject of cosmological particle production entirely aside and concentrate instead on gaining an elementary understanding of the phenomenon of black hole radiance. Quite apart from its considerable intrinsic interest this will serve also to highlight the principal difference between electrodynamic and gravitational particle production namely the role played by boundary conditions and the global structure of the space-time manifold.

Below is displayed an intuitive picture of the mechanism by which the gravitational field creates particles. Some geodesics which are initially close and parallel are caused to diverge by the curvature of space-time. Virtual particles which are present in the vacuum state would, it might be thought, like to follow geodesics and if the tidal gravitation is strong enough to separate the two members of a virtual pair by a distance greater than a compton wavelength within a compton time then we might expect significant production of real particles.

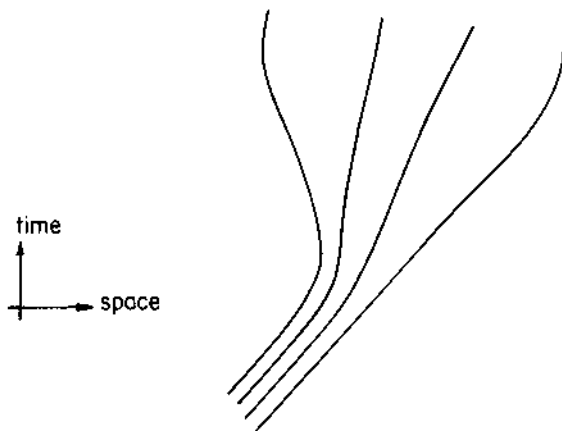


Fig. 1. Some geodesics which are initially close and parallel are caused to diverge by the action of a tidal gravitational field.

In order to draw attention to the difference between the electromagnetic and gravitational case let us consider the Feynman propagator for a massless scalar field say

$$G(x, x') = i\langle 0 | T\hat{\phi}(x)\hat{\phi}(x') | 0 \rangle$$

most of the quantities of interest may be computed from  $G$  which may be found by solving the Green function equation

$$\left[ g^{-1/2} \frac{\partial}{\partial x^\alpha} \left( g^{1/2} g^{\alpha\beta} \frac{\partial}{\partial x^\beta} \right) - m^2 \right] G(x, x') = -g^{-1/2} \delta(x, x') . \quad (1)$$

In the electrodynamic case an analogous equation obtains for the Feynman propagator for a charged scalar field in flat space-time

$$\left[ \eta^{\alpha\beta} \left( \frac{\partial}{\partial x^\alpha} - ieA_\alpha \right) \left( \frac{\partial}{\partial x^\beta} - ieA_\beta \right) - m^2 \right] G(x, x') = -\delta(x, x') . \quad (2)$$

The form of these two equations is rather similar with the metric tensor  $g_{\alpha\beta}$  playing a role analogous to that of the electromagnetic potential  $A_\alpha$ . Note however that there is an important difference that is implicit between these two equations because, while a particular vector potential  $A_\alpha$  in (2) may make the equation difficult to solve it does not affect the boundary or positive frequency conditions which the propagator must satisfy. By contrast the geometry in (1) hits twice: once in that the explicit appearance of the metric makes the equation difficult to solve and again in that the metric determines the global geometry of the space-time manifold on which (1) is to be solved and hence enters into the boundary or positive frequency conditions to which  $G$  is subject.

The question of positive frequency conditions is equivalent to the question of what defines a particle, a question that turns out to be somewhat subtle. In conventional quantum field theory the statement is often made that a particle is an irreducible representation of the Poincaré group. A moments reflection reveals that this statement is singularly unhelpful in the sort of situation that we shall consider. In a curved space-time the symmetries of the Poincaré group are no longer available to us, moreover they become less and less relevant the greater the curvature of space-time and the greater the curvature of space-time the greater we expect the particle production to be.

In the following we shall not address the question *what is a particle?* directly but rather we shall cleave to more operationally defined quantities. We shall, in fact, infer the rate of particle production by calculating two other quantities: the vacuum expectation value of the stress energy tensor ( $\hat{T}_{\mu\nu}$ ) and the response of an idealized "particle detector" of the type proposed by Unruh [1]. Neither of these quantities is a direct measure of particle production since in the case of the vacuum expectation value of the stress-energy tensor there is a contribution due to vacuum polarization as well as from "real particles" while in the case of the response of an idealized "particle detector" we shall see that under some circumstances the detector responds not so much to particles as to the spectrum of vacuum fluctuations.

In the following we shall adhere to the maxim that before seeking to understand effects due to gravitation it is wise first to understand those due to acceleration. The remainder of this lecture will be devoted to a review of a calculation due originally to Unruh [1] and later DeWitt [2] of the effect of accelerating a model "particle detector" through empty Minkowski space-time. The second lecture will examine a vacuum state that is itself accelerated and in the third lecture we shall see how gravity and black holes fit into the picture.

## ACCELERATED DETECTORS

Unruh's idealized detector consists of a Schrödinger particle confined to a box and which is weakly coupled to the field that is being detected. Inside the box the Schrödinger particle has certain discrete energy levels. In normal circumstances we might think that if the box is initially prepared in its ground state and at a later time, due to its coupling to the field, is observed to be in a higher state then the box might reasonably be said to have detected a particle.

For simplicity we shall couple the Schrödinger particle to a scalar field via an interaction Lagrangian of the form

$$\mathcal{L}_I = \mu(\tau)\phi(x(\tau)) \quad (3)$$

where  $x(\tau)$  denotes the position of the box, assumed small, at time  $\tau$  and  $\mu(\tau)$  denotes some sort of monopole charge (our box is, in fact, a relativist's atom and the interaction Lagrangian (3) is an analogue of the familiar p.E coupling between the electromagnetic field and the atomic dipole moment).

We shall now examine the response of a uniformly accelerated detector. Uniform acceleration being defined as a motion such that the acceleration as measured in the instantaneous rest frame of the body is a constant. This is also the motion produced by a constant force.

A useful parametrization [3] of the space-time path of the detector is obtained by writing

$$\begin{aligned} x &= \alpha^{-1} \cosh t \\ t &= \alpha^{-1} \sinh t \end{aligned} \quad . \quad (4)$$

Then  $\alpha$  is the constant proper acceleration of the detector and  $\alpha^{-1}t$  is its proper time.

We shall suppose that the scalar field is in the familiar vacuum state which we shall denote by  $|M\rangle$  (we shall avoid the usual symbol  $|0\rangle$  in order to avoid confusion between the various vacua that we shall encounter in due course) and that the detector is initially (at  $\tau = -\infty$ ) in a stationary state  $|\Psi_n\rangle$ . Since the regime inside a uniformly accelerated box does not change with time it is clear that such stationary states exist in just the same way that they exist if the box is held fixed in a uniform and constant gravitational field.

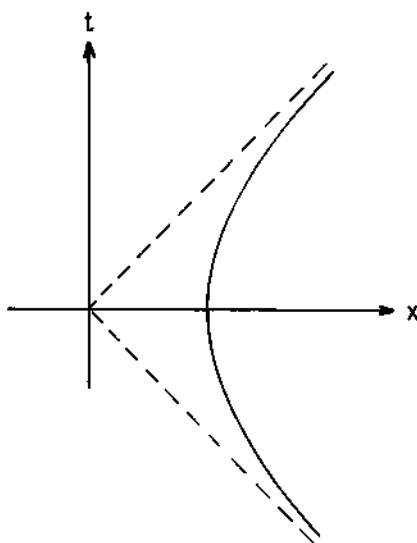


Fig. 2. The space-time path of the uniformly accelerated detector.

The amplitude that the box will (when  $\tau = +\infty$ ) be found to be in a state  $|\Psi_m\rangle$  while the field is found to be in a state  $|\sigma\rangle$  is

$$\langle \Psi_m, \sigma | T \exp \left( i \int_{-\infty}^{\infty} \mathcal{L}_I \alpha^{-1} d\tau \right) | \Psi_n, M \rangle$$

which for weak coupling and  $\Psi_n$  orthogonal to  $\Psi_m$  is just

$$i \int_{-\infty}^{\infty} \alpha^{-1} d\tau \langle \Psi_m, \sigma | \mu(\tau) \phi(x(\tau)) | \Psi_n, M \rangle . \quad (5)$$

We are interested in the probability that the box makes a transition from  $\Psi_n$  to  $\Psi_m$ . This may be found by taking the squared modulus of the above amplitude and summing over a complete set of the field states  $|\sigma\rangle$ , after some elementary manipulations we obtain

$$\alpha^{-2} |\langle \Psi_n | \mu(0) | \Psi_m \rangle|^2 \int_{-\infty}^{\infty} d\tau \int_{-\infty}^{\infty} d\tau' e^{-i(E_m - E_n)(\tau - \tau')/\alpha} \langle M | \phi(\tau) \phi(\tau') | M \rangle \quad (6)$$

where we use the abbreviation  $\phi(\tau)$  to denote  $\phi(x)$  evaluated at  $x(\tau)$ . The matrix element  $\langle M | \phi(\tau) \phi(\tau') | M \rangle$  is an expectation value evaluated with respect to the Minkowski vacuum since that is the state that the field is in, and is a function of the time difference  $(\tau - \tau')$  only as a consequence of the fact that the parameter  $\tau$  corresponds to the boost parameter of the Poincaré transformations that connect the instantaneous rest frames of the box. Thus the integrand in (6) is a function of  $(\tau - \tau')$  only. This corresponds to the fact that we have computed a transition probability for a process which, due to its stationary character, takes place at a uniform rate. We therefore change variables of integration in (6) from  $\tau$  and  $\tau'$  to  $(\tau - \tau')$  and  $\tau'$  and by dividing out by

$$\alpha^{-1} \int_{-\infty}^{\infty} d\tau'$$

we arrive at an expression for the rate at which these transitions take place

$$R_{nm} \approx \alpha^{-1} |\langle \Psi_n | \mu(0) | \Psi_m \rangle|^2 \int_{-\infty}^{\infty} d\tau e^{-i(E_m - E_n)\tau} \langle M | \phi(\tau) \phi(0) | M \rangle \quad .$$

Thus we see that the rate is in all its essential features determined by the quantity

$$\Pi(v) = \alpha^{-1} \int_{-\infty}^{\infty} d\tau e^{-iv\tau} \langle M | \phi(\tau) \phi(0) | M \rangle \quad (7)$$

which is the Fourier transform of the autocorrelation function of the field and by the Wiener-Khinchin theorem is just the power spectrum of the field fluctuations.\*

Standard analysis reveals that for a massless scalar field

$$\langle M | \phi(x) \phi(x') | M \rangle = \frac{1}{4\pi^2} \frac{1}{[-(t - t' - i\varepsilon)^2 + (x - x')^2]} \quad (8)$$

where we have introduced an infinitesimal  $\varepsilon$  in order to specify correctly the singularities of the autocorrelation function.

\*It is interesting to recall that a classical analogue of the fact that the rate at which a detector absorbs energy is essentially determined by the power spectrum of the field fluctuations was discovered by Planck in 1899 [4] in connection with his investigation of the rate an oscillator absorbs energy when it interacts with a bath of black body radiation.

The analysis so far would, of course, apply equally well for the case of an inertially moving detector. If we specialize (7) and (8) to this case we find that

$$\Pi_{\text{inertial}}(\omega) = -\frac{1}{4\pi^2} \int_{-\infty}^{\infty} \frac{dt e^{-i\omega t}}{(t - i\varepsilon)^2} \quad (9)$$

with  $t$  denoting the proper time along the worldline of the box. Evaluation of the integral by residues immediately reveals that

$$\Pi_{\text{inertial}}(\omega) = -\frac{\omega}{2\pi} \theta(-\omega)$$

where  $\theta$  denotes the step function. The fact that  $\Pi_{\text{inertial}}$  is zero for  $\omega$  positive means that if we prepare the box in its ground state then we will never find it in a higher state whereas if we prepare the box in an excited state then we would expect to find at a later time that the box had decayed into its ground state.

Now let us return to our accelerated detector. By employing the parametrization (4) we see that

$$\langle M | \phi(\tau) \phi(0) | M \rangle = \frac{\alpha^2}{16\pi^2 \sinh^2 \left( \frac{\tau}{2} - i\varepsilon \right)} \quad (10)$$

The functional form of the right hand side is different from that in equation (9) but this is no more than the statement that the distance between  $x(\tau)$  and  $x(0)$  is different if measured along the accelerated worldline of the box from the distance measured along the geodesic that joins them (see Fig. 3). Substituting (10) into (7) we find

$$\Pi_{\text{accelerated}}(v) = -\frac{1}{4\pi^2} \int_{-\infty}^{\infty} dt \frac{e^{-ivt}}{4 \sinh^2 \left( \frac{\tau}{2} - i\varepsilon \right)}.$$

This integral may be evaluated conveniently by integrating the function

$$f(\tau) = -\frac{\alpha}{16\pi^2} \frac{e^{-iv\tau}}{\sinh^2 \left( \frac{\tau}{2} - i\varepsilon \right)}$$

around the contour  $C$  as shown in Fig. 4. The integral over the lower part of the contour yields  $\Pi(v)$  while that over the upper part yields  $e^{-2\pi v} \Pi(v)$ . The sum of these contributions is related to the residue of  $f(\tau)$  at  $\tau = 0$ . Thus we find

$$\Pi_{\text{accelerated}}(v) = \frac{1}{2\pi} \frac{v\alpha}{(e^{2\pi v} - 1)}$$

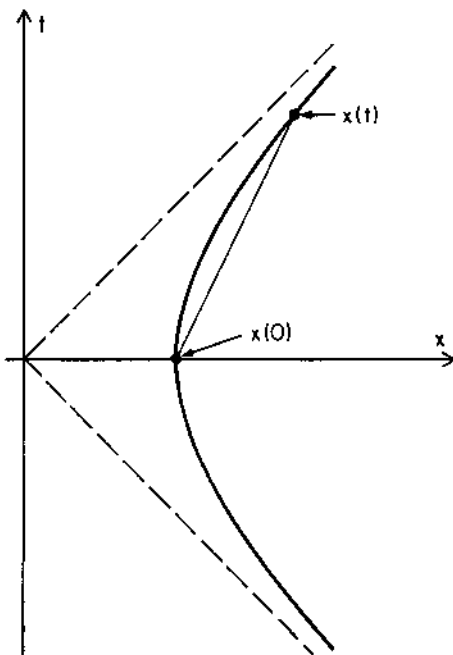


Fig. 3. The autocorrelation function is determined by the geodetic interval between  $x(\tau)$  and  $x(0)$ .

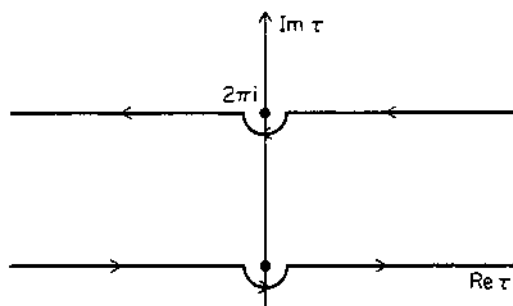


Fig. 4. The contour of integration used to evaluate  $\Pi_{\text{accelerated}}(v)$ .

so that, restoring the dimensions, the uniformly accelerated detector will be excited to a temperature

$$T = \frac{\hbar\alpha}{2\pi k c}$$

as first pointed out by Unruh [1] (see also Davies [5] for a related result).

We have found that the box behaves *as if* immersed in black-body radiation at a temperature  $\alpha/2\pi$  however it cannot be the case that the observed "particles" are real since:

(i) The renormalized value of the vacuum expectation value of the stress energy tensor vanishes in the Minkowski vacuum and since this is a tensorial quantity it must vanish in all frames including an accelerated one. To underscore this point we observe also that

(ii) Two observers with the same acceleration but very different velocities see the same blackbody spectrum characterized by the same temperature. If the observed "particles" were real we would expect the two observers to observe spectra that differed by the appropriate Doppler shift factor.

Our conclusion is that an Unruh box measures the power spectrum of the vacuum fluctuations rather than real particles and can be said reliably to be detecting real particles only if the detector is moving inertially.

As a final point it is of interest to draw attention to the field states  $|\sigma\rangle$  that contribute when the box makes a transition from its ground state to a higher state. From (5) we see that the only field states that make a non-zero contribution are those for which

$$\langle \sigma | \phi(x) | M \rangle$$

does not vanish. Thus the relevant states  $|\sigma\rangle$  are one particle states and we see that the box makes a transition from its ground state to an excited state and at the same time a quantum of the  $\phi$ -field is emitted. The energy for both these events being derived ultimately from the agency that is accelerating the box.

#### AN ALTERNATIVE VACUUM STATE FOR FLAT SPACE-TIME

We shall discuss in this lecture an accelerated state in flat space-time which by contrast to our previous discussion concerning the readings of accelerated detectors in the Poincaré invariant (inertial) vacuum refers to a vacuum which is itself accelerated.

Historically Fulling [6] noticed that although the formalism of Lagrangian field theory has the appearance of being covariant, the choice of a time coordinate defines what is meant by positive and negative frequency thereby defining what is meant by the vacuum state. It was pointed out by Fulling that the field theory that is 'natural' in Rindler coordinates is not unitarily equivalent to the usual one; a fact that is intimately linked with the existence of a horizon.

In order to examine this state of affairs let us introduce Rindler coordinates  $(\xi, \tau)$  in the  $x - t$  plane by a transformation regular in the region  $x > |t|$

$$x = \xi \cosh \tau$$

$$t = \xi \sinh \tau$$

the Minkowski space line element becomes

$$ds^2 = -\xi^2 d\tau^2 + d\xi^2 + dy^2 + dz^2 .$$

We recall from the previous lecture that the curves  $\xi = \text{constant}$ ,  $x = \text{constant}$  are curves of constant proper acceleration  $\xi^{-1}$ ,  $\xi\tau$  being the proper time along such a curve.

The curves  $\xi = \text{constant}$  are all asymptotic to the planes  $x = \pm t$ . It is clear from Fig. 5 that these planes are horizons for uniformly accelerated observers since an observer following one of the curves  $\xi = \text{constant}$  cannot communicate with any space-time point in regions II and IV and cannot receive any communication from regions II or IV. These interesting causal properties associated with uniformly accelerated observers in Minkowski space-time have long been known and have received a certain amount of attention over the years, much of it related to the question of whether a uniformly accelerated charge radiates.

Following Fulling let us consider the problem of quantizing, say, a massless scalar field  $\phi$  using Rindler coordinates instead of the more usual Minkowski set. The wave equation

$$\square\phi = 0$$

can be separated in Rindler coordinates and possesses normal mode solutions that are of positive frequency with respect to Rindler time

$$u(x|\nu, k) = \frac{\sqrt{sh\nu\pi}}{2\pi^2} e^{-i\nu\tau} K_{i\nu}(k\xi) e^{ik \cdot y} \quad (11)$$

where  $y$  denotes the two-vector  $(y, z)$ . The normalization in (11)

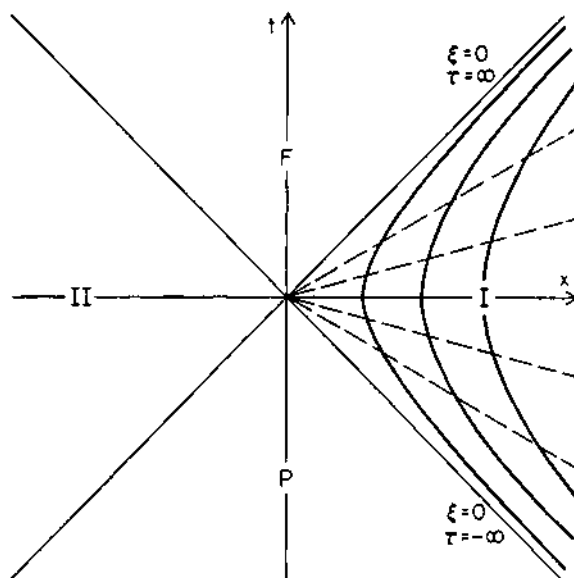


Fig. 5. Rindler coordinates cover the region  $x > |t|$ . The curves of constant  $\xi$  are hyperbolae while those of constant  $\tau$  are straight lines through the origin.

has been chosen such that  $u(x|\underline{v},\underline{k})$  is of unit norm with respect to a Klein Gordon inner product taken over any of the surfaces  $T =$  constant (and hence over any spacelike surface originating at the origin in Fig. 5).

We may now expand  $\phi$  in the form

$$\phi(x) = \int_0^\infty dv \int d^2 \underline{k} \frac{\sqrt{sh v \pi}}{2\pi^2} K_{\underline{v}\underline{k}}(\underline{k}\xi) \times \\ \times \left\{ e^{-i v T + i \underline{k} \cdot \underline{y}} a(\underline{v}, \underline{k}) + e^{i v T - i \underline{k} \cdot \underline{y}} a^\dagger(\underline{v}, \underline{k}) \right\}$$

where ' $\dagger$ ' denotes hermitian conjugation.

The canonical commutation relations then require that

$$[a(\underline{v}, \underline{k}), a^\dagger(\underline{v}', \underline{k}')] = \delta(\underline{v} - \underline{v}') (\underline{k} - \underline{k}')$$

with all commutators independent of this one vanishing. Let us now define a "vacuum state"  $|F\rangle$  by the requirement that it be annihilated by the annihilation operators i.e.

$$a(\underline{v}, \underline{k}) |F\rangle = 0 \text{ for all } \underline{v}, \underline{k} .$$

Fulling's observation was that the theory that is thereby constructed is not unitarily equivalent to the usual free field theory on Minkowski space. Of even greater surprise was the subsequently discovered fact that the usual Poincaré invariant vacuum state appropriate to Minkowski space  $|M\rangle$  contains a thermal distribution of quanta with respect to the Fulling Fock space.

Indeed  $|M\rangle$  has properties identical with a thermal Fulling mixture of local temperature  $(2\pi\xi)^{-1}$ . If the field is in the Minkowski vacuum state, then the quantum expectation value of any observable on the Fulling Fock space is the same as its statistical ensemble average in thermal equilibrium at a temperature  $(2\pi\xi)^{-1}$  [7]. Two bodies can be in thermal equilibrium at different points in a gravitational field if and only if the ratio of their temperatures is equal to the gravitational redshift that light would suffer in travelling from one to the other. Thus the dependence of the temperature on position should cause no surprise, being just that which is required to maintain equilibrium.

What, more precisely, is meant by this is as follows. We have said that for any observable  $\hat{O}[\hat{\phi}(x)]$  confined to the Rindler wedge, that is when  $\hat{O}$  depends only on the field  $\hat{\phi}(x)$  at points for which  $x > |t|$ ,

$$\langle M | \hat{O}[\hat{\phi}(x)] | M \rangle = \text{Tr} \hat{\rho}_{2\pi\xi} \hat{O}$$

where  $\hat{\rho}_{2\pi\xi}$  is the density operator

$$\left\{ \sum_{|m,n\rangle} e^{-2\pi E_m \xi} \right\}^{-1} \sum_{|m,n\rangle} e^{-2\pi E_m \xi} |m,n\rangle \langle m,n|$$

of a thermal Fulling state of temperature  $(2\pi\xi)^{-1}$ .  $|m,n\rangle$  is the  $n^{\text{th}}$  Fulling state of energy  $E_m$ .

We shall now seek to gain a physical understanding for the Fulling vacuum  $|F\rangle$ . Rindler coordinates are suggestive of acceleration so let us, with a certain prescience, examine the effect of accelerating the vacuum by taking an infinite plane conductor and accelerating it normal to itself with acceleration  $a$ . If we choose coordinates appropriately then the path swept out by the mirror can be taken to be the line  $\xi = a^{-1}$  in Fig. 5. This situation is moreover relevant to gravity since instead of regarding it as an accelerated mirror which drives the vacuum before it we might alternatively care to think of it as the vacuum in the gravitational field of an infinite flat earth. The vacuum would, in some sense, like to fall through the floor but it is prevented from doing so by the fact that the floor is perfectly reflecting. The vacuum adjusts to this situation by acquiring a non-vanishing vacuum expectation value for  $\hat{T}_{\mu\nu}$ . Thus the ether takes on the appearance of an equilibrium atmosphere loaded under the action of a gravitational field. The relevant field theory calculations can be performed exactly [8] and we shall briefly review the results of these calculations. We have used the language of electromagnetism but it is equally possible to consider analogous problems for fields of different spin.

Far above the mirror (i.e. as  $\xi a \rightarrow \infty$ ) we find

$$\langle \hat{T}_{\mu}^{\nu} \rangle \underset{\xi \rightarrow \infty}{\sim} \frac{h(s)}{2\pi^2 \xi^4} \int_0^{\infty} \frac{dv v(v^2 + s^2)}{e^{2\pi v} - (-1)^s} \text{diag} \left[ -1, \frac{1}{3}, \frac{1}{3}, \frac{1}{3} \right] \quad (12)$$

where  $h(s)$  is the number of helicity states of a massless field of spin  $s$ . Thus far above the mirror we find that  $\langle \hat{T}_{\mu}^{\nu} \rangle$  is reduced below zero by an amount corresponding to black body radiation at a "temperature"  $(2\pi\xi)^{-1}$ , the dependence of the "temperature" on position being just that which would be required to maintain thermal equilibrium in a gas of massless scalar particles in the gravitational field of an "infinite flat earth." This asymptotic expression for  $\langle \hat{T}_{\mu}^{\nu} \rangle$  is independent of the acceleration of the barrier in the sense that it depends only on the acceleration of the local Killing trajectory. It may also be shown that the relation (12) is independent of the precise nature of the boundary conditions applied to the field at the mirror.

The form of the stress tensor seems rather remarkable at first, though with the benefit of hindsight we can see that some of the

features of  $\langle \hat{T}_\mu^\nu \rangle_{\text{Ren}}$  might have been anticipated had we had the confidence to assert that the precise nature of the boundary condition becomes unimportant far from the barrier. In virtue of the symmetries of the problem the expectation value of the stress energy tensor would be expected to assume the form

$$\langle \hat{T}_\mu^\nu \rangle_{\text{Ren}} = \text{diag}(\alpha, \beta, \gamma, \gamma)$$

with  $\alpha, \beta, \gamma$  functions of  $\xi$  only. In order that  $\langle \hat{T}_\mu^\nu \rangle_{\text{Ren}}$  be trace-free and conserved these functions are required to satisfy

$$\alpha + \beta + 2\gamma = 0$$

and

$$\alpha = \frac{d}{d\xi} (\beta \xi) \quad .$$

If the components of the stress tensor are to be 'local', i.e. asymptotically independent of  $a$ , then on dimensional grounds they must vary as  $\xi^{-4}$ . (13) then determines the ratios  $\alpha:\beta:\gamma$  so that up to a constant or proportionality  $\langle \hat{T}_\mu^\nu \rangle_{\text{Ren}}$  becomes

$$\xi^{-4} \text{ diag} \left[ -1, \frac{1}{3}, \frac{1}{3}, \frac{1}{3} \right] \quad . \quad (14)$$

Now the Minkowski vacuum is that state which minimizes the energy subject to the constraint of invariance under the full Poincaré group. The ground state for the present problem is that state which (aside from boundary effects) minimizes the energy subject to the constraint of invariance under the homogeneous Lorentz transformations of the  $x - t$  plane and the Euclidean transformations of the  $y - z$  plane. Since this latter symmetry group is a subgroup of the Poincaré group the energy is to be minimized subject to a less onerous constraint, resulting in the attainment of a lower minimum. We might therefore expect the energy density far from the barrier to be depressed *below* that of the Minkowski vacuum and the constant that multiplies (14) to be negative.

We see from (12) that the energy density has a thermal distribution. The factor  $(v^2 + s^2)$  that occurs in the integrand is a density of states factor. The reason that one would normally expect this factor to be  $v^2$  is that usually the density of states factor is computed under the assumption that the wavelengths involved are very much smaller than the size of the container. Now when note is taken of the fact that the proper time measured along a world-line is  $\xi\tau$  rather than  $\tau$  then it is readily seen from (12) that the relevant "wavelengths" are of order  $\xi$  and hence are of the same order as the distance to the mirror. The surprise then, if any, is that the deviation of the spectrum from the more usual Planckian form is so simple. The reason for this is that the density of states fac-

tor is a property which the Rindler manifold shares with a related manifold which has the metric

$$ds^2 = -dt^2 + \frac{d\xi^2 + dy^2 + dz^2}{\xi^2} . \quad (15)$$

It is a somewhat remarkable fact that the spatial metric in (15) is the metric on the three-hyperboloid. It is the simplicity of the geometry of this related space that is responsible for the concise form that the density of states factor assumes.

We have not discussed the form of  $\langle \hat{T}_{\mu}^{\nu} \rangle_{\text{Ren}}$  when  $\xi$  is comparable to  $a^{-1}$ . In this regime the effects and the precise nature of the boundary conditions become important. The point that we wish to stress is the fact that for the region  $\xi a \gg 1$  the vacuum state above an accelerated mirror is a very good approximation to the Fulling vacuum. The agreement between these states becomes better the greater the acceleration of the mirror and becomes exact in the limit that the acceleration of the mirror becomes infinite. In this limit the motion of the mirror is as in Fig. 5 with the mirror travelling along the path  $\xi = 0$ , initially the mirror moves along the negative  $x$  direction at the speed of light until it reaches the origin and then instantaneously reverses its motion. In this limit the expression (12) for  $\langle \hat{T}_{\mu}^{\nu} \rangle$  is exact and is valid for all  $\xi$ . The components of  $\langle \hat{T}_{\mu}^{\nu} \rangle$  are seen to be unbounded as  $\xi \rightarrow 0$  but this is hardly surprising since the vacuum is being made to accelerate infinitely hard there.

We wish to stress that the Fulling vacuum and the corresponding field theory are not to be regarded as some sort of wrong quantization but rather a quantum field theory adapted to a particular physical situation. It is thus hardly surprising that this field theory should not be unitarily equivalent to the more usual Poincaré invariant one.

It is of interest to inquire how an Unruh box would respond if accelerated appropriately through the Fulling vacuum. This is equivalent to the question of how the box would respond if held stationary in the gravitational field of an infinite flat earth. It is easy to see that if the box is prepared in its ground state then it will never be found in an excited state. This follows from the fact that the state  $|F\rangle$  has been constructed such that the autocorrelation function

$$\langle F | \phi(\tau) \phi(0) | F \rangle$$

contains no positive frequency component. Thus an accelerated detector will not register if the vacuum is correspondingly accelerated but, as we saw in the previous lecture, will register if the vacuum is inertial.

Both the Poincaré invariant vacuum and the Fulling vacuum have close analogues in black hole space-times and, just as is the case in flat space-time, these different vacua are most easily discussed in terms of different coordinate systems. In order that we may shortly draw attention to these similarities we are led to ask if there is any 'natural' way to extend the Rindler coordinate system in such a way as to cover the entire space-time. If we wish to do this in such a way that  $\partial/\partial t$  remains a generator of boosts then we are led to the following sets of transformations, which are illustrated in Figure 6

$$\left. \begin{array}{l} x = \xi \cosh t \\ t = \xi \sinh t \end{array} \right\} \text{region I}$$

$$\left. \begin{array}{l} x = \xi \sinh t \\ t = \xi \cosh t \end{array} \right\} \text{region F}$$

$$\left. \begin{array}{l} x = -\xi \cosh t \\ t = -\xi \sinh t \end{array} \right\} \text{region II}$$

$$\left. \begin{array}{l} x = -\xi \sinh t \\ t = -\xi \cosh t \end{array} \right\} \text{region P}$$

The line element induced by these transformations is

$$ds^2 = \mp \xi^2 dt^2 \pm d\xi^2 + dy^2 + dz^2$$

with the upper signs holding in I and II and the lower signs holding in F and P. We note that  $t$  is a time coordinate in I and a space coordinate in F and P. In region II  $t$  is again a time coordinate but runs backwards. We shall meet this phenomenon also in the curved space-times with horizons that we shall consider. We remark also that even the above set does not quite cover the space-time since the transformations are not regular on the planes  $x = \pm t$ .

#### FIELD THEORY ON BLACK HOLE SPACE-TIMES

We wish now to discuss quantum field theory in a black hole space-time; for simplicity we shall take the black hole to be non-rotating. We begin by briefly reviewing the geometry of the extended Schwarzschild manifold. The close analogies between the structure of Schwarzschild space-time and the properties of accelerated observers in Minkowski space-time will become apparent as we proceed.

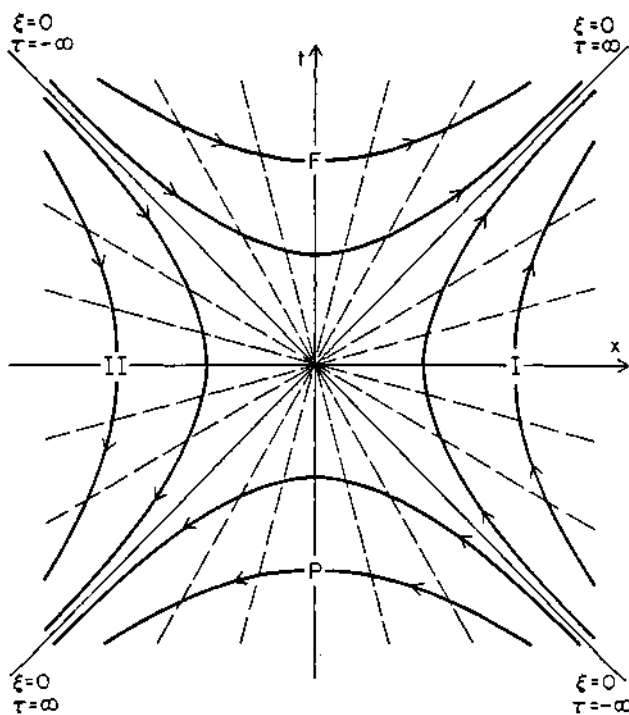


Fig. 6. The extended Rindler coordinates. The arrows denote the direction in which  $\tau$  increases.

The Schwarzschild metric describes the gravitational influence of a spherically symmetric body of mass  $M$ . The metric was first presented in the form

$$ds^2 = - \left(1 - \frac{2M}{r}\right) dt^2 + \frac{dr^2}{\left(1 - \frac{2M}{r}\right)} + r^2(d\theta^2 + \sin^2\theta d\phi^2) \quad .$$

It was not until 1960 [9] that the nature of the coordinate singularity at  $r = 2M$  was properly elucidated. Schwarzschild coordinates are singular at  $r = 2M$  but the curvature of the manifold is not. It is possible to introduce non-singular coordinates which may be used to analytically continue the manifold from the domain of its original definition  $r > 2M$  to encompass the points for which  $r < 2M$ . It is usual to do this in terms of Kruskal coordinates in which the metric takes the form

$$ds^2 = \frac{32M^3}{r} e^{-r/2M} (-dv^2 + du^2) + r^2(d\theta^2 + \sin^2\theta d\phi^2) \quad (16)$$

in which  $r$  is to be understood as a function of  $u$  and  $v$  given implicitly by

$$\left(\frac{r}{2M} - 1\right) e^{r/2M} = u^2 - v^2 \quad .$$

The metric (16) is singular only at the curvature singularities where  $r = 0$ , and with the coordinate ranges

$$-\infty < v < \infty, \quad -\infty < u < \infty, \quad u^2 - v^2 > -1$$

represents the maximal analytic extension of the Schwarzschild manifold. In addition to the Kruskal coordinates we shall have occasion to refer to the null coordinates  $U$  and  $V$  defined by

$$U = v - u \quad (17)$$

$$V = v + u$$

Figure 7 is a Kruskal diagram which exhibits the structure of the  $(u, v)$  plane. The transformation between the Kruskal coordinates and Schwarzschild coordinates take the explicit forms

$$\left. \begin{aligned} u &= \left(\frac{r}{2M} - 1\right)^{1/2} e^{r/4M} \cosh(t/4M) \\ v &= \left(\frac{r}{2M} - 1\right)^{1/2} e^{r/4M} \sinh(t/4M) \end{aligned} \right\} \text{region I}$$

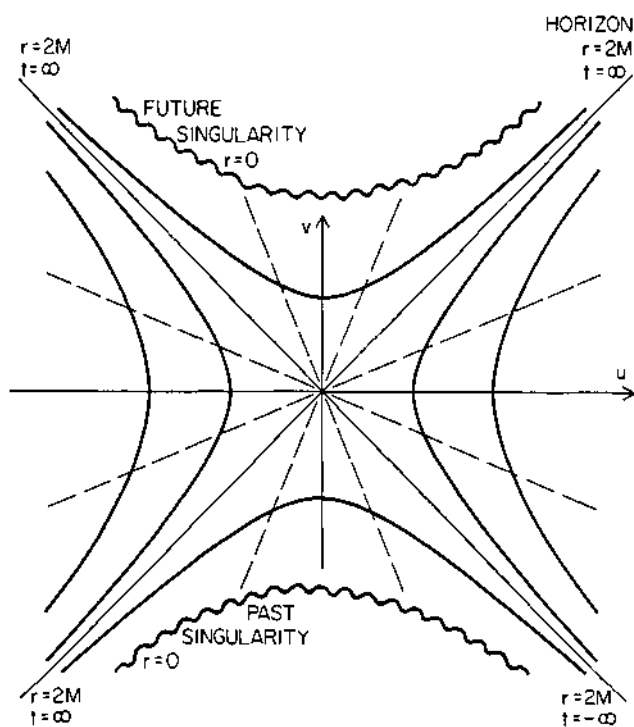


Fig. 7. The analytically extended Schwarzschild manifold. The hyperbolae represent curves of constant  $r$  while the straight lines represent those of constant  $t$ .

$$\left. \begin{array}{l} u = \left(1 - \frac{r}{2M}\right)^{1/2} e^{r/4M} \sinh(t/4M) \\ v = \left(1 - \frac{r}{2M}\right)^{1/2} e^{r/4M} \cosh(t/4M) \end{array} \right\} \text{region F}$$

$$\left. \begin{array}{l} u = -\left(\frac{r}{2M} - 1\right)^{1/2} e^{r/4M} \cosh(t/4M) \\ v = -\left(\frac{r}{2M} - 1\right)^{1/2} e^{r/4M} \sinh(t/4M) \end{array} \right\} \text{region II}$$

$$\left. \begin{array}{l} u = -\left(1 - \frac{r}{2M}\right)^{1/2} e^{r/4M} \sinh(t/4M) \\ v = -\left(1 - \frac{r}{2M}\right)^{1/2} e^{r/4M} \cosh(t/4M) \end{array} \right\} \text{region P}$$
(18)

The complete analogy between the relationship that Kruskal coordinates bear to Schwarzschild coordinates and the relationship that Minkowski coordinates bear to Rindler coordinates is clear from the above. The fact that the maximally extended Schwarzschild manifold contains two singularities and two asymptotically flat regions is perhaps surprising on first acquaintance. It should, however, be kept in mind that if a black hole is formed by the collapse of an extended object then it is only a portion of this manifold that is relevant as the solution exterior to the extended body and this must be joined to an interior solution. In Fig. 8 we present a diagram of the space-time appropriate to a star that collapses to form a black hole.

Because it is easier to handle the equations on the Kruskal manifold rather than working on the non-analytic manifold which is the one that in fact corresponds to the way that a black hole would actually form, many authors have considered the problem of how to "formulate correctly" a quantum field theory on the Kruskal manifold. It is to this problem that we now turn. Our conclusion will be that the problem consists not so much of how to formulate correctly such a field theory but rather of recognizing that different theories correspond to different physical situations.

Let us consider a scalar field theory. In the exterior region of Schwarzschild space-time a complete set of normalized basis functions that satisfy the equation

$$\square u = 0$$

is [10]:

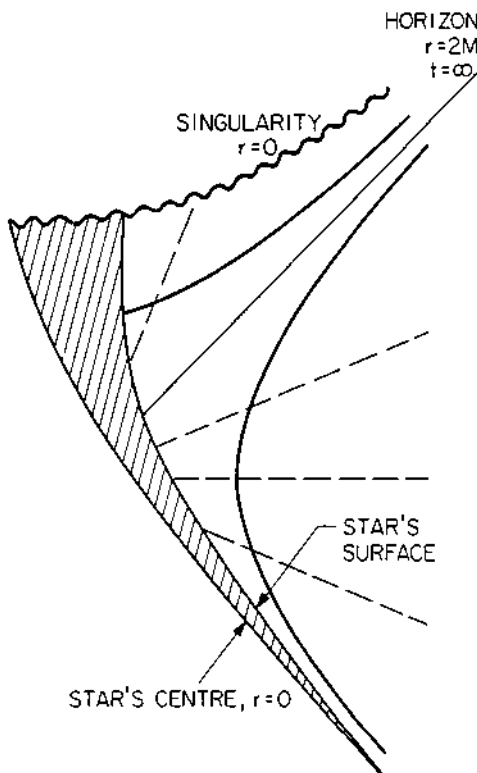


Fig. 8. The manifold appropriate to an extended body that collapses to form a black hole. The Schwarzschild metric describes the geometry exterior to the body. When this is smoothly joined to the geometry interior to the body the unphysical regions II and P are eliminated.

$$\begin{aligned}\vec{u}_{\omega\ell m}(x) &= (4\pi\omega)^{-1/2} e^{-i\omega t} \vec{R}_\ell(\omega|r) Y_{\ell m}(\theta, \phi) \\ \hat{u}_{\omega\ell m}(x) &= (4\pi\omega)^{-1/2} e^{-i\omega t} \hat{R}_\ell(\omega|r) Y_{\ell m}(\theta, \phi) \quad .\end{aligned}$$

The  $Y_{\ell m}$  are the spherical harmonics and the radial functions have the asymptotic forms

$$\begin{aligned}\vec{R}_\ell(\omega|r) &\sim \begin{cases} \frac{1}{r} e^{i\omega r_*} + \frac{1}{r} \vec{A}_\ell(\omega) e^{-i\omega r_*}, & r \rightarrow 2M \\ \frac{1}{r} B_\ell(\omega) e^{i\omega r_*} & , \quad r \rightarrow \infty \end{cases} \\ \hat{R}_\ell(\omega|r) &\sim \begin{cases} \frac{1}{r} B_\ell(\omega) e^{-i\omega r_*} & , \quad r \rightarrow 2M \\ \frac{1}{r} e^{-i\omega r_*} + \frac{1}{r} \hat{A}_\ell(\omega) e^{i\omega r_*}, & r \rightarrow \infty \end{cases} \quad .\end{aligned}$$

in which

$$r_* = r + 2M \log\left(\frac{r}{2M} - 1\right)$$

denotes the Regge-Wheeler coordinate. The physical interpretation of these modes is illustrated in Fig. 9. The  $\vec{u}$  modes emerge from the past horizon and the  $\hat{u}$  modes come in from infinity.

The scalar field is quantized by writing

$$\begin{aligned}\hat{\phi}(x) &= \sum_{\ell m} \int_0^\infty d\omega \{ \vec{a}_{\ell m}(\omega) \vec{u}_{\ell m}(x|\omega) + \hat{a}_{\ell m}(\omega) \hat{u}_{\ell m}(x|\omega) \\ &\quad + \vec{a}_{\ell m}^\dagger(\omega) \vec{u}_{\ell m}^*(x|\omega) + \hat{a}_{\ell m}^\dagger(\omega) \hat{u}_{\ell m}^*(x|\omega) \} \quad .\end{aligned}$$

and demanding that the creation and annihilation operators should satisfy the usual commutation relations.

We are concerned with the question of how to choose a vacuum state. It is fairly clear how we should treat the incoming modes since they originate at infinity where the space is flat and the time coordinate  $t$  with respect to which they are of positive frequency is a good time coordinate. We can therefore safely assert that the vacuum state should be annihilated by the corresponding annihilation operators

$$\hat{a}_{\ell m}(\omega) |vac\rangle = 0$$

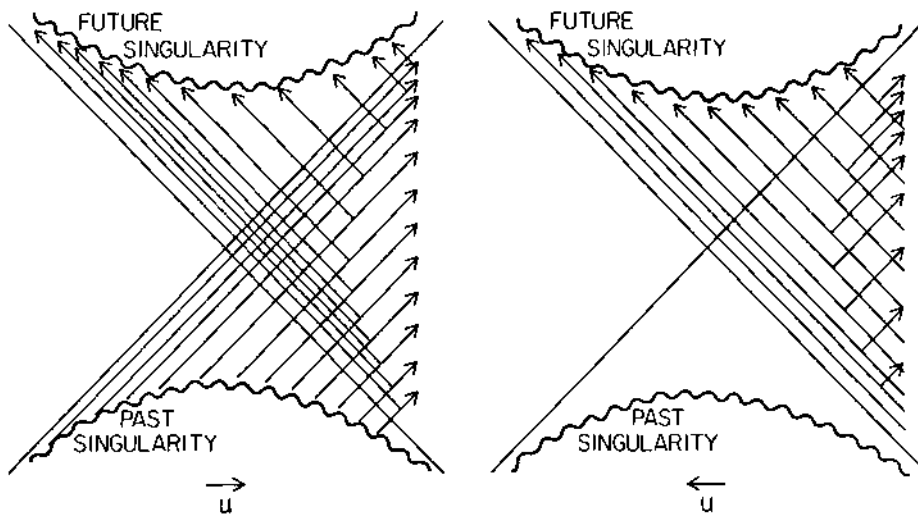


Fig. 9. A schematic representation of the behavior of the outgoing and incoming modes. The outgoing modes of  $\vec{u}$  represent waves that are outgoing across the past horizon. The space-time curvature deflects part of the wave across the future horizon. The incoming modes  $\vec{u}$  represent waves that are incoming from infinity. The geometry deflects part of the wave while the remainder is transmitted across the future horizon.

for all  $(\omega, \ell, m)$ . The problem really hinges on how we deal with the outgoing modes  $u$  which emanate from the past horizon which is where the  $(t, r)$  coordinates are singular.

We shall first examine the state that results if we demand that the outgoing annihilation operators should also annihilate the "vacuum." This yields the Boulware vacuum  $|B\rangle$  which therefore satisfies

$$\vec{a}_{\ell m}(\omega)|B\rangle = 0, \quad \vec{a}_{\ell m}^*(\omega)|B\rangle = 0. \quad .$$

This state is the analogue of the accelerated state  $|F\rangle$  that we have discussed in relation to flat space-time and we therefore expect it to manifest the same behavior near the horizon. Indeed it does, explicit calculation reveals that for a massless conformally invariant field of spin  $s$  ( $=0, \frac{1}{2}, 1$ ) the leading behavior of  $\langle B | \hat{T}_\mu^\nu | B \rangle_{\text{Ren}}$  near the horizon is given, in Schwarzschild coordinates, by

$$\langle B | \hat{T}_\mu^\nu | B \rangle \underset{r \rightarrow 2M}{\sim} -\frac{h(s)}{2\pi^2 \left(1 - \frac{2M}{r}\right)^2} \int_0^\infty \frac{d\omega (\omega^2 + s^2 \kappa^2)}{e^{2\pi\omega/\kappa} - (-1)^s} \times \\ \times \text{diag} \left[ -1, \frac{1}{3}, \frac{1}{3}, \frac{1}{3} \right] \quad (19)$$

where  $\kappa = (4M)^{-1}$  is the so-called surface gravity of the black hole. We see that in this state the vacuum expectation value of the stress tensor is depressed below zero by an amount corresponding to black body radiation at the black hole temperature  $T = 2\pi/\kappa$ . The expectation value is unbounded as  $r \rightarrow 2M$  due to the gravitational redshift factor. (Strictly speaking we have shown only that the components of  $\langle B | \hat{T}_{\mu\nu} | B \rangle_{\text{Ren}}$  are unbounded in Schwarzschild coordinates. In order to infer that  $\langle B | \hat{T}_\mu^\nu | B \rangle_{\text{Ren}}$  is physically unbounded as  $r \rightarrow 2M$  we should examine its components in a coordinate system, such as the Kruskal coordinates (18), that is regular at  $r = 2M$ . It is straightforward to check that our conclusion still holds when this is done.) If we are seeking a vacuum state for the space-time of a star that collapses to form a black hole then we see that the Boulware vacuum is unacceptable.

The solution that suggests itself is to add a thermal distribution of outgoing quanta, corresponding to a temperature  $2\pi/\kappa$ , to  $|B\rangle$ . This yields the Unruh vacuum  $|U\rangle$ . This state may also be defined by choosing as positive frequency mode functions  $\vec{v}_{\ell m}(x|\omega)$  which are linear combinations of  $\vec{u}_{\ell m}(x|\omega)$  and  $\vec{u}_{\ell m}^*(x|\omega)$  chosen such that the resulting mode function is of positive frequency with respect to the Kruskal null coordinate  $U$  of equation (17) which is regular on the past horizon.

By adding a thermal distribution of outgoing quanta we cancel the leading behavior of the diagonal components of the vacuum expectation value of the stress tensor as manifested by equation (19). However since we have added an outgoing *flux* the *t* and *r* components of the expectation value of the stress tensor for a scalar field, say, manifest the following behavior as  $r \rightarrow 2M$

$$\langle U | \hat{T}_a^b | U \rangle_{Ren} \underset{r \rightarrow 2M}{\sim} \frac{L}{4\pi} \begin{pmatrix} \frac{1}{\left(1 - \frac{2M}{r}\right)} & -\frac{1}{r^2} \\ \frac{1}{r^2 \left(1 - \frac{2M}{r}\right)^2} & -\frac{1}{\left(1 - \frac{2M}{r}\right)} \end{pmatrix}$$

where

$$L = \int_0^\infty \frac{d\omega}{2\pi} \frac{\omega \sum (2\ell+1) |B_\ell(\omega)|^2}{(e^{2\pi\omega/\kappa} - 1)}$$

is the luminosity of the black hole. At first sight this would seem to spoil the hoped for regularity of the expectation value of the stress tensor on the horizon. However if we examine the components of  $\langle U | \hat{T}_{\mu\nu} | U \rangle_{Ren}$  in a regular coordinate system then we find that they are well behaved on the future horizon but are unbounded on the past horizon. This constitutes an acceptable resolution since only the future horizon is relevant to the space-time of the collapsing star (see Fig. 8). The price paid for the finiteness of the expectation value of the stress tensor on the future horizon is that an outgoing flux of radiation escapes to infinity.

Note the nature of the cancellation that occurs near the future horizon. Expression (19), which we might regard as the "vacuum polarization part" of  $\langle U | \hat{T}_{\mu\nu} | U \rangle_{Ren}$ , and the contribution from the "real particle part" of  $\langle U | \hat{T}_{\mu\nu} | U \rangle_{Ren}$ , which corresponds to an outgoing flux of quanta, are each separately unbounded near the horizon but their sum which is the physically observable quantity remains bounded.

The spectrum of vacuum fluctuations  $\Pi(\omega | r)$  which determines the response of an Unruh box can be calculated both near to the horizon and at infinity. The results are displayed in the Table. From the Table we see that an Unruh box held at constant radius just outside the horizon of a black hole would register furiously, but this is just what is to be expected from the fact that the box has to have a very large acceleration in order to remain at a constant radius and in no way contradicts the finiteness of  $\langle U | \hat{T}_{\mu\nu} | U \rangle_{Ren}$  there. At infinity where the readings of the box are to be trusted they indicate a flux of radiation. This conclusion is confirmed by a computation of the expectation value of the

Table 1. The asymptotic values of the function

$$\Pi(\omega|r) = \int_{-\infty}^{\infty} dt e^{-i\omega t} \langle 0|\hat{\phi}(t)\hat{\phi}(0)|0\rangle$$

which determines the response of an Unruh box.  $\theta$  denotes the step function.

|                        | Boulware Vacuum                                                    | Unruh Vacuum                                                                                                                           |
|------------------------|--------------------------------------------------------------------|----------------------------------------------------------------------------------------------------------------------------------------|
| $r \rightarrow 2M$     | $\frac{-\omega\theta(-\omega)}{2\pi\left(1 - \frac{2M}{r}\right)}$ | $\frac{\omega}{2\pi\left(1 - \frac{2M}{r}\right)(e^{2\pi\omega/\kappa} - 1)}$                                                          |
| $r \rightarrow \infty$ | $-\frac{\omega}{2\pi}\theta(-\omega)$                              | $\frac{1}{r^2} \frac{\sum (2\ell+1)  B_{\ell}(\omega) ^2}{8\pi\omega(e^{2\pi\omega/\kappa} - 1)} - \frac{\omega}{2\pi}\theta(-\omega)$ |

stress tensor, it may be shown that

$$\langle U|\hat{T}_{\mu}^{\nu}|U\rangle_{\text{Ren}} \underset{r \rightarrow \infty}{\sim} \frac{L}{4\pi r^2} \begin{pmatrix} -1 & -1 & 0 & 0 \\ 1 & 1 & 0 & 0 \\ 0 & 0 & 0 & 0 \\ 0 & 0 & 0 & 0 \end{pmatrix}.$$

It is apparent what situation the Boulware vacuum is appropriate to: It is relevant to the region exterior to a massive body that is only just outside its Schwarzschild radius. One could, for ease of visualization, consider a spherical body with a perfectly conducting surface just outside the body's Schwarzschild radius. The vacuum, in some sense, would like to fall through the surface but is prevented from doing so by the boundary condition. It therefore comes to equilibrium loaded under the action of the gravitational field, and its response to this loading is to set up in itself certain energy densities and stresses. If the body is now slowly shrunk down towards its Schwarzschild radius then the stresses that are required to support the vacuum become larger and ultimately infinite in the limit that the radius of the body actually equals its Schwarzschild radius. Thus the aether is no more able to support itself under such circumstances than is a more conventional atmosphere.

This provides us with an intuitive picture of black hole radiance: When the body passes through its Schwarzschild radius the vacuum must collapse. The negative energy of the accelerated vacuum (19) falls into the hole. An observer at infinity perceives an inward flux of negative energy which is equivalent to an outward flux of positive energy. This is precisely the Hawking radiation.

## REFERENCES

1. W. G. Unruh, Phys. Rev. D14:870 (1976).
2. B. S. DeWitt, contribution to "General Relativity, An Einstein Centenary Survey," S. W. Hawking and W. Israel, eds., Cambridge University Press, Cambridge (1979).
3. W. Rindler, "Essential Relativity: Special, General and Cosmological," Van Nostrand (1969).
4. M. Planck, Annln Phys. 1:69 (1900).
5. P. C. W. Davies, J. Phys. A8:609 (1975).
6. S. A. Fulling, Phys. Rev. D7:2850 (1973).
7. See, for example, D. W. Sciama, P. Candelas, and D. Deutsch, Adv. in Phys. 30:327 (1981), especially appendix C and references cited therein.
8. P. Candelas and D. Deutsch, Proc. Roy. Soc. Lond. A354:79 (1978), ibid. A362:251.
9. M. D. Kruskal, Phys. Rev. 119:1743 (1960).

## CONFINING THE AETHER

P. Candelas

Center for Theoretical Physics  
The University of Texas at Austin  
Austin, Texas 78712 U.S.A.

### INTRODUCTION

Insight and heuristic guidance in a number of areas including the bag model for hadrons and the surface properties of metals ought to be afforded by a theory in which a quantum field is restricted by a surface on which it is constrained to satisfy certain boundary conditions.

Perhaps the most celebrated calculation of this type was that performed by Casimir in 1948 [1] which showed that two uncharged plane conductors placed parallel to each other *in vacuo* experience an attractive force per unit area, proportional to the inverse fourth power of their separation

$$F = \frac{\hbar c \pi^2}{240 a^4} \quad (1)$$

and that this force may be ascribed entirely to the change, brought about by the presence of boundaries, in the energy of the electromagnetic vacuum. It was not until 1969 that the local form of this result was obtained. Brown and Maclay [2] showed that  $\langle \hat{T}_{\mu\nu} \rangle_{\text{Ren}}$  the renormalized vacuum expectation value of the stress energy tensor takes the constant value

$$\langle \hat{T}_{\mu\nu} \rangle_{\text{Ren}} = \frac{\hbar c \pi^2}{720 a^4} \text{ diag}(-1, -3, 1, 1) \quad (2)$$

relative to Minkowski coordinates  $(t, x, y, z)$ , with the plates at rest with their normals along the  $x$ -axis.

The results (1) and (2) are deceptively simple and seemingly could have been anticipated on the basis of dimensional analysis. Consider, however, a scalar field  $\hat{\phi}(x)$  in the presence of a single, infinite, plane "conductor" on which  $\hat{\phi}$  is constrained to vanish. The vacuum expectation value of the stress tensor for this field may be represented as the result of acting on the Feynman propagator  $G(x, x')$  for  $\phi$  with a certain differential operator  $\hat{T}_{\mu\nu}$  and taking the coincidence limit  $x' \rightarrow x$

$$\langle \hat{T}_{\mu\nu}(x) \rangle = \lim_{x' \rightarrow x} T_{\mu\nu} G(x, x') . \quad (3)$$

This expression contains, of course, the usual infinite zero point energy of free field theory. We are really interested in the change in  $\langle \hat{T}_{\mu\nu}(x) \rangle$  ascribable to the presence of the "conductor." We therefore renormalize  $\langle \hat{T}_{\mu\nu} \rangle$  by subtracting the value it would have in the absence of the conductor, obtaining thereby the finite expression

$$\langle \hat{T}_{\mu\nu}(x) \rangle_{\text{Ren}} = \lim_{x' \rightarrow x} T_{\mu\nu}(G(x, x') - G_0(x, x')) \quad (4)$$

where

$$G_0(x, x') = \frac{i}{4\pi^2(x - x')^2} \quad (5)$$

is the familiar Feynman propagator appropriate to the entire space-time.

For a plane conductor  $G$  is expressible as a simple image sum

$$G(x, x') = G_0(x, x') - G_0(x, \bar{x}') \quad (6)$$

with  $\bar{x}'$  the image of  $x'$  in the "conductor." Thus (4) becomes

$$\langle \hat{T}_{\mu\nu}(x) \rangle_{\text{Ren}} = \lim_{x' \rightarrow x} T_{\mu\nu} G_0(x, \bar{x}') . \quad (7)$$

Now from (5) we see that as  $x$  approaches the conductor  $G_0(x, \bar{x})$  varies as  $\delta^{-2}$  where  $\delta$  is the distance from the point  $x$  to the conductor, since  $T_{\mu\nu}$  is a differential operator of second order this suggests that  $\langle \hat{T}_{\mu\nu}(x) \rangle_{\text{Ren}}$  should vary as  $\delta^{-4}$ . Similar considerations apply also to the electromagnetic field. We are therefore led to consider the question of why it is that, as we know from (2),  $\langle \hat{T}_{\mu\nu}(x) \rangle_{\text{Ren}}$  does in fact remain bounded near the conductors. The answer lies in the exceptional degree of symmetry enjoyed by the electromagnetic field in the presence of an infinite plane boundary [2]. It turns out that the Lorentz invariance of  $\langle \hat{T}_{\mu\nu} \rangle_{\text{Ren}}$  with respect to arbitrary boosts parallel to the mirrors combined with the fact that  $\langle \hat{T}_{\mu\nu} \rangle_{\text{Ren}}$  is traceless and conserved forces  $\langle \hat{T}_{\mu\nu}(x) \rangle_{\text{Ren}}$  to be independent of position and therefore bounded.

This is an important point because it shows that (1) and (2) are unlikely to be representative of a generic situation and detailed calculation shows this indeed to be the case.

Thus it is that if the Lorentz invariance of an infinite plane conductor is disturbed by introducing a smooth deformation of the conductor then in the vicinity of a point  $p$  of the conductor, where the principal curvatures are  $\kappa_1$  and  $\kappa_2$ , the energy density of the electromagnetic field may be shown [3] to satisfy the asymptotic relation

$$\langle \hat{T}_{00}(x) \rangle_{\text{Ren}} \underset{x \rightarrow p}{\sim} \frac{\hbar c(\kappa_1 + \kappa_2)}{60\pi^2 \delta^3} \quad (8)$$

where  $\delta$  is the distance from  $x$  to  $p$ .

A result of a similar character is obtained if the energy density is calculated in the vicinity of a plane interface between two polarizable media characterized by dielectric constants  $\epsilon_1, \epsilon_2$  and magnetic permeabilities  $\mu_1, \mu_2$  owing to the fact that these properties confer on the system a preferred rest frame. If  $x$  is a point in region 2, say, the energy density is given asymptotically by

$$\begin{aligned} \langle \hat{T}_{00}(x) \rangle_{\text{Ren}} \sim & \frac{1}{16\pi^2 \delta^3} \int_0^\infty dv \left\{ \frac{\epsilon_1(iv) - \epsilon_2(iv)}{\epsilon_1(iv) + \epsilon_2(iv)} \frac{1}{\epsilon_2(iv)} \frac{d}{dv} (v\epsilon_2(iv)) + \right. \\ & \left. + \frac{\mu_1(iv) - \mu_2(iv)}{\mu_1(iv) + \mu_2(iv)} \frac{1}{\mu_2(iv)} \frac{d}{dv} (v\mu_2(iv)) \right\} \end{aligned} \quad (9)$$

with  $\delta$  the distance from the point  $x$  to the boundary.

Taken naively (8) and (9) would seem to imply that an infinite amount of energy is associated with the surface. In reality, of course, there are no perfect conductors and in the case of metals, say, it is more appropriate to regard the metal as a dielectric at high frequencies than as a conductor. Moreover a continuum picture of a dielectric is valid only for wavelengths long compared to the interatomic spacing. The burden of these remarks is that (8) and (9) indicate in fact that the energy associated with a dielectric boundary, say, depends quadratically on a cutoff determined by the microstructure of the media. This cutoff dependence is well known in the theory of metal surfaces [4] and with a suitable choice for the cutoff is known to account reasonably for the surface tensions of liquid helium [5] and of many metals [6,7].

A simple but essential point is that in the presence of boundaries vacuum energies will generically depend on a cutoff and therefore will take values very different from those that might be inferred on the basis of naïve dimensional analysis. Unfortunately this fact has been widely overlooked and this has led to persistent fallacies, particularly concerning the vacuum energies of conducting shells. A topic which has received a certain amount of attention over the years in connection with Casimir's semi-classical model for the electron. Moreover the theory has been, in addition, beset by misconceptions relating to the correct identification of the energy density in polarizable media and the analyticity properties enjoyed by the dielectric constant and magnetic permeability.

The primary aim of this lecture is to indicate that when these errors are corrected geometrical expansions exist for the vacuum energy associated with a boundary. These expansions take the form

$$\mathcal{E} = \mathcal{E}^S \int dS + \mathcal{E}^C \int dS(\kappa_1 + \kappa_2) + \mathcal{E}_I^C \int dS(\kappa_1 - \kappa_2)^2 + \\ + \mathcal{E}_{II}^C \int dS \kappa_1 \kappa_2 + \dots \quad (10)$$

and express the surface energy in terms of integrals of geometrical features of the boundary and certain *shape tensions* (the first of these,  $\mathcal{E}^S$ , is the surface tension) which are independent of the particular geometry of the boundary and depend only on the type of field under consideration and the boundary conditions to which it is subject.

We shall discuss here only the case of dielectric boundary conditions. The interested reader may care to refer to Ref. 8 for a more detailed treatment that treats also the case of perfect conductor boundary conditions.

#### THE SURFACE ENERGY OF DIELECTRICS

In order to discuss surface tension it is sufficient to consider a plane interface between two semi-infinite dielectric media. We shall take the interface to be the plane  $x = 0$  and we shall suppose the region  $x < 0$  to be filled with a uniform medium characterized by the properties  $(\mu_1, \epsilon_1)$  while the region  $x > 0$  is filled with a uniform medium with properties  $(\mu_2, \epsilon_2)$ .

It is straightforward to calculate the electromagnetic Feynman propagators corresponding to this situation and to obtain the renormalized value of the energy density from them in a manner similar to that which has been outlined above in relation to the scalar field  $\phi$ . We obtain the following result for the region  $x > 0$

$$\mathcal{E}(x) = \mathcal{E}^V + \mathcal{E}^S(x) \quad (11)$$

with

$$\mathcal{E}^V = -\frac{i}{2} \int \frac{d\omega}{2\pi} \int \frac{d^2 k}{(2\pi)^2} \frac{\omega}{p_2} \frac{d}{d\omega} (\omega^2 \mu_2 \epsilon_2) \quad (12)$$

and

$$\begin{aligned} \mathcal{E}^S(x) = & -\frac{i}{4} \int \frac{d\omega}{2\pi} \int \frac{d^2 k}{(2\pi)^2} \frac{1}{p_2 \epsilon_2} \frac{d}{d\omega} (\omega \epsilon_2) \left[ (k^2 + p_2^2) \left( \frac{\epsilon_1 p_2 - \epsilon_2 p_1}{\epsilon_1 p_2 + \epsilon_2 p_1} \right) \right. \\ & \left. + \mu_2 \epsilon_2 \omega^2 \left( \frac{\mu_1 p_2 - \mu_2 p_1}{\mu_1 p_2 + \mu_2 p_1} \right) \right] e^{-2p_2 x} + (\epsilon \leftrightarrow \mu) \end{aligned} \quad (13)$$

where  $p_r^2 = k^2 - \mu_r \epsilon_r \omega^2$  for  $r = 1, 2$ .

As it is independent of  $x$  we identify  $\mathcal{E}^V$  as a volume energy density. This term can itself be decomposed into three parts

(i) the zero point energy of the electromagnetic field (ii) the electromagnetic self energy of the charges and (iii) an interaction energy. This is simply illustrated for the particular case of a gas of electrons described by a charge  $e$  mass  $m$  and number density  $N$ . Such a gas has dielectric properties

$$\mu = 1, \quad \epsilon = 1 - \frac{Ne^2}{m\omega^2}. \quad (14)$$

If we deform the contour of the  $\omega$ -integration\* so as to envelop one of the branch cuts associated with  $p$  (see Figure) and introduce a three vector  $K$  it is easy to show that

$$\mathcal{E}^V = \int \frac{d^3 K}{(2\pi)^3} \omega(K) \quad (15)$$

with

$$\omega(K) = \sqrt{K^2 + \frac{Ne^2}{m}}. \quad (16)$$

We recognize (15) as representing an energy  $\frac{1}{2}\omega$  per mode which is indeed the ground state energy appropriate to a uniform medium. If, following Power [9] we expand this energy in terms of the electronic charge then we recognize the zeroth order term

$$\int \frac{d^3 K}{(2\pi)^3} K$$

\*We discard the contribution of the arc at infinity that is required by this deformation.

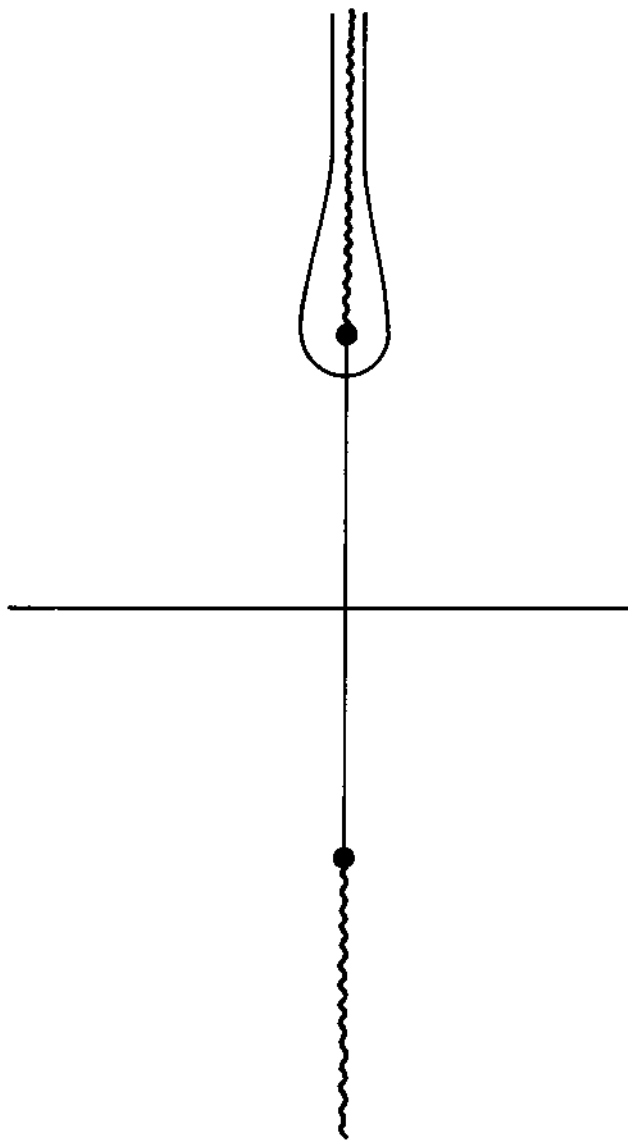


Figure. The contour for the frequency integration deformed so as to envelop one of the branch cuts of the function  $(Ne^2 + \kappa^2 - \omega^2)^{1/2}$  as required in the derivation of the representation (15) for  $\mathcal{E}_V$ .

as the quartically divergent zero point energy of the electromagnetic field. The first order term is the quadratically divergent quantity

$$\frac{Ne^2}{2m} \int \frac{d^3 K}{(2\pi)^3} \frac{1}{K}$$

corresponding to the electromagnetic self-mass of the electrons. This is easily verified by, say, calculating the vacuum expectation value of the  $e^2 \underline{A}^2$  term in the Schrödinger equation of a single electron.

We shall not here pursue the volume energy any further save to draw the reader's attention to the elegant result of Power [9] that if, instead of a gas of electrons, a gas of hydrogen atoms is considered then it is possible to derive the Lamb shift from  $\mathcal{E}^V$ .

We turn now to the surface energy term  $\mathcal{E}^S(x)$ . This quantity is finite for each positive  $x$  due to the presence of the exponential factor in (13). However since the integrand is  $O(ke^{-kx})$  for large  $k$  we see that  $\mathcal{E}^S(x)$  is unbounded as  $x$  approaches zero. The asymptotic behavior of  $\mathcal{E}^S(x)$  for small  $x$  may be computed by integrating term by term the large  $k$  asymptotic series for the integrand in (13). This yields

$$\begin{aligned} \mathcal{E}^S(x) = & - \frac{i}{32\pi^2 x^3} \int d\omega \left\{ \left( \frac{\epsilon_1 - \epsilon_2}{\epsilon_1 + \epsilon_2} \right) \frac{1}{\epsilon_2} \frac{d}{d\omega} (\omega \epsilon_2) \right. \\ & + \left. \left( \frac{\mu_1 - \mu_2}{\mu_1 + \mu_2} \right) \frac{1}{\mu_2} \frac{d}{d\omega} (\omega \mu_2) \right\} - \frac{i}{16\pi^2 x} \int d\omega \frac{\omega^2 (\mu_1 \epsilon_1 - \mu_2 \epsilon_2)}{(\mu_1 + \mu_2)(\epsilon_1 + \epsilon_2)} \\ & \times \left\{ \left[ \mu_2 + \epsilon_1 \left( \frac{\mu_1 + \mu_2}{\epsilon_1 + \epsilon_2} \right) \right] \frac{d}{d\omega} (\omega \epsilon_2) \right. \\ & \left. + \left[ \epsilon_2 + \mu_1 \left( \frac{\epsilon_1 + \epsilon_2}{\mu_1 + \mu_2} \right) \right] \frac{d}{d\omega} (\omega \mu_2) \right\} + O(x^0) . \end{aligned} \quad (17)$$

Thus the energy density near the surface varies as  $x^{-3}$  no matter how fast the dielectric properties approach unity at high frequency. This leads us to expect that the integrated surface energy will be quadratically divergent. Indeed it is, as is readily seen by integrating (17) with respect to  $x$  and adding the corresponding expression obtained by interchanging the suffices 1 and 2. However a more elegant expression may be achieved by returning to (13) and integrating under the integral sign. With a certain prescience we may write  $\mathcal{E}_2^S$ , that part of the surface energy that resides in region 2, in the form

$$\mathcal{E}^S = \frac{i}{4} \int \frac{d\omega}{2\pi} \int \frac{d^2 k}{(2\pi)^2} \left( \frac{d}{d\omega} (\omega \epsilon_2) \frac{\partial}{\partial \epsilon_2} + \frac{d}{d\omega} (\omega \mu_2) \frac{\partial}{\partial \mu_2} \right) \times \times \log \left[ \frac{(\epsilon_1 p_2 + \epsilon_2 p_1)^2 (\mu_1 p_2 + \mu_2 p_1)^2}{16 \mu_1 \mu_2 \epsilon_1 \epsilon_2 p_1^2 p_2^2} \right] \quad (18)$$

and by interchanging suffices and adding we find the total surface energy per unit area to be

$$\mathcal{E}^S = \frac{i}{4} \int \frac{d\omega}{2\pi} \int \frac{d^2 k}{(2\pi)^2} \omega \frac{\partial}{\partial \omega} \log \left[ \frac{(\epsilon_1 p_2 + \epsilon_2 p_1)^2 (\mu_1 p_2 + \mu_2 p_1)^2}{16 \mu_1 \mu_2 \epsilon_1 \epsilon_2 p_1^2 p_2^2} \right]. \quad (19)$$

#### COMPARISON WITH EXPERIMENTAL VALUES

As has been anticipated  $\mathcal{E}^S$  is quadratically divergent owing to the fact that the integrand becomes independent of  $k$  as  $k$  tends to infinity. It would seem reasonable to employ a cutoff  $\Lambda$  for the  $k$ -integration corresponding roughly to the interatomic spacing since our picture of a uniform medium certainly ceases to be valid for such wavelengths.

If we specialize (19) to the case of a dielectric-vacuum interface i.e.  $\mu_1 = \mu_2 = \epsilon_1 = 1$ ,  $\epsilon_2 = \epsilon$  and retain only the leading order in  $\Lambda$  we find

$$\mathcal{E}^S \approx \frac{i\Lambda^2}{32\pi^2} \int d\omega \omega \frac{\partial}{\partial \omega} \log \left[ \frac{(\epsilon + 1)^2}{4\epsilon} \right]. \quad (20)$$

The frequency integration may be performed by enumerating the zeros and poles of the function enclosed by the square brackets. If we denote the zero of  $\epsilon + 1$  by  $\alpha_E$ , the zero of  $\epsilon$  by  $\beta_E$  and the pole of  $\epsilon$  by  $\omega_E$  we may write

$$\mathcal{E}^S \approx \frac{\Lambda^2}{16\pi} (2\alpha_E - \beta_E - \omega_E). \quad (21)$$

Thus we recover the Schmit-Lucas formula [6] which is in semi-quantitative agreement with experimentally observed values for a number of materials [6,7].

In the case of metals, for example, Schmit and Lucas take as a model dielectric constant

$$\epsilon = 1 - \frac{\omega_p^2}{\omega^2} \quad (22)$$

for which  $\alpha_E = \omega_p/\sqrt{2}$ ,  $\beta_E = \omega_p$  and  $\omega_E = 0$ . The cutoff is chosen

to be\*

$$\Lambda = \frac{\omega_p}{v_F \sqrt{2}} \quad (23)$$

where  $v_F$  denotes the Fermi velocity of the valence electrons. This choice being motivated by a desire to achieve a reasonable separation between collective and single particle excitations of the electron gas. The resulting surface tension

$$\sigma_{\text{metal}}^S \approx \frac{(\sqrt{2} - 1)}{16\pi} \omega_p \Lambda^2 \quad (24)$$

agrees with experimentally observed values not only for the alkali series but also for the transition metals<sup>†</sup> to an accuracy of better than 30%. We note that these authors claim also reasonable agreement with experiment for the rare gas solids.

A point that deserves emphasis is that the facts that (i) the observed values for surface tensions are in semi-quantitative agreement with (20) and (ii) that the predicted value (20) follows the observed variation in surface tensions over four orders of magnitude (from 0.37 erg cm<sup>-2</sup> for He to the range 2000 - 3000 erg cm<sup>-2</sup> for some of the transition metals) argues strongly for the reality of the quadratic cutoff dependence.

It is interesting that the quadratic cutoff dependence elevates the vacuum polarization energy to the status of a *macroscopic* quantity, in the face of which it is hard to deny the existence of the ether.

#### THE CURVATURE TENSION

By considering the effect of deforming the surface it is possible to calculate the curvature tension  $\sigma^C$ . The result is

$$\begin{aligned} \sigma^C = & - \frac{1}{16} \int \frac{d\omega}{2\pi} \int \frac{d^2k}{(2\pi)^2} \frac{\omega}{k} \frac{\partial}{\partial \omega} \left[ \log \left( \frac{\mu_1 \epsilon_1 (p_2 + k)^2}{\mu_2 \epsilon_2 (p_1 + k)^2} \right) - 2k \left( \frac{1}{p_2} - \frac{1}{p_1} \right) \right. \\ & \left. + \frac{4k^3}{3} \left( \frac{1}{p_2^3} - \frac{1}{p_1^3} \right) - \frac{2k}{p_1^2 p_2^2} \left( \frac{\epsilon_1 p_1^2 - \epsilon_2 p_2^2}{\epsilon_1 p_2 + \epsilon_2 p_1} + \frac{\mu_1 p_1^2 - \mu_2 p_2^2}{\mu_1 p_2 + \mu_2 p_1} \right) \right] \quad (25) \end{aligned}$$

\*Curiously, this is the only point at which the Fermionic nature of the electrons makes itself felt.

<sup>†</sup>Schmit and Lucas determine an effective value for the number of valence electrons by making reference to the most stable oxidation state of the metal.

In order to gauge the importance of the curvature tension relative to the surface tension we shall again consider a dielectric-vacuum interface obtained by setting  $\mu_1 = \mu_2 = \epsilon_1 = 1$  and  $\epsilon_2 = \epsilon$ . If we also retain only the leading term in  $\Lambda$  we find that (25) reduces to

$$\begin{aligned}\epsilon^C &\approx \frac{1\Lambda}{64\pi^2} \int d\omega \omega \frac{\partial}{\partial\omega} \left[ \log \epsilon - 2 \left( \frac{\epsilon - 1}{\epsilon + 1} \right) \right] \\ &= \frac{\Lambda}{32\pi} \left[ \beta_E - \omega_E - \frac{4}{\epsilon'(\alpha_E)} \right] \quad .\end{aligned}\quad (26)$$

For the case of metals  $\beta_E = \omega_p$ ,  $\omega_E = 0$  and  $\epsilon'(\alpha_E) = 4\sqrt{2}/\omega_p$  yielding

$$\epsilon_{\text{metals}}^C \approx \frac{\Lambda\omega_p}{64\pi} (2 - \sqrt{2}) \quad . \quad (27)$$

For the case of an insulator described by a dielectric constant

$$\epsilon = 1 - \frac{\omega_p^2}{\omega^2 - \omega_E^2} \quad (28)$$

we have

$$\alpha_E = \left( \omega_E^2 + \frac{\omega_p^2}{2} \right)^{\frac{1}{2}}, \quad \beta_E = \left( \omega_E^2 + \omega_p^2 \right)^{\frac{1}{2}} \quad \text{and} \quad \epsilon'(\alpha_E) = \frac{8\alpha_E}{\omega_p^2} \quad . \quad (29)$$

If, for definiteness, we specialize in the direction of liquid helium for which  $\omega_p \ll \omega_E$  we find

$$\begin{aligned}\epsilon_{\text{He}}^C &\approx \frac{\Lambda}{2048\pi} \frac{\omega_p^6}{\omega_E^5} \\ &\approx 1.1 \times 10^{-10} \text{ erg cm}^{-1}\end{aligned}\quad (30)$$

where we have used the values

$$\omega_E \approx 3.5 \times 10^{16} \text{ sec}^{-1}, \quad \frac{\omega_p^2}{\omega_E^2} \approx 0.05 \quad (31)$$

and have chosen the cutoff such that the surface tension computed from (20) yields the observed value ( $\approx 0.37 \text{ erg cm}^{-2}$ ).

For a sphere of dielectric material of radius  $R$  the ratio of the total curvature energy to the total surface energy is

$$\frac{2g_C}{R\varepsilon^S} = \begin{cases} \frac{1}{\sqrt{2} R\Lambda} & , \text{ for metals} \\ \frac{1}{4R\Lambda} \left( \frac{\omega_P}{\omega_E} \right)^2 \approx \frac{1}{80R\Lambda} & , \text{ for liquid helium} . \end{cases} \quad (32)$$

Thus it seems that it may be possible to observe the effect of the curvature tension in small droplets of radius a few atomic separations.

## REFERENCES

1. H. B. G. Casimir, Proc. K. Ned. Akad. Wet. 51:793 (1948).
2. L. S. Brown and G. J. Maclay, Phys. Rev. 184:1272 (1969).
3. D. Deutsch and P. Candelas, Phys. Rev. D20:3063 (1979).
4. G. Barton, Rep. Prog. Phys. 42:963 (1979).
5. J. Schwinger, L. L. DeRaad, Jr., and K. A. Milton, Ann. Phys. (N.Y.) 115:1 (1978).
6. J. Schmit and A. A. Lucas, Solid St. Comm. 11:475 (1972).
7. J. Schmit and A. A. Lucas, Solid St. Comm. 11:419 (1972).
8. P. Candelas, "Vacuum Polarization in the Presence of Dielectric and Conducting Surfaces." Preprint, Center for Theoretical Physics, The University of Texas at Austin, Austin, Texas 78712. U.S.A.
9. E. A. Power, Amer. J. Phys. 34:516 (1966).

## EARLY GERMS OF QUANTUM FIELD THEORY

### IN THE HISTORY OF QUANTUM PHYSICS

Friedrich Hund

Institut für Theoretische Physik der Universität  
D-3400 Göttingen

#### INTRODUCTION

The main concepts of quantum electrodynamics: duality of fields and particles, field quanta, antiparticles, creation and annihilation of particles, reactions based on a coupling, these concepts are common for all quantum field theory. Roots and germs of them we find already in the early history of quantum physics.

Up to creation and physical understanding of quantum mechanics (1927) we can distinguish three steps. The first, ranging from black body radiation to specific heat (1900-1913) was essentially low temperature physics;  $h$  became the natural unity for counting cases in statistics. The second step was search for atomic mechanics (1913-1925): it was guided by a special law of atomic spectra, the combination principle  $\nu = F(n, l, \dots) - F(n', l', \dots)$ ; it ranged from the "correspondence" between the frequencies of a classical model and the really emitted or absorbed frequencies up to the substitution of classical observables by matrices or by  $q$ -numbers with commutation relations. The third step (1923-1927), De Broglie's transfer of duality from light to matter, Schrödinger's equation, the concept of probability amplitudes, led to a general mathematical formalism and its physical understanding. While at the end of the second step quantum mechanics was an alteration of classical particle mechanics to such an extent that the combination principle for spectra worked, from 1927 quantum mechanics could be regarded as an alteration of classical particle mechanics for making matter waves possible, and the same quantum mechanics as an alteration of a classical field theory of matter for making particles possible.

During the first of these historical steps duality of light was detected and a sort of quantization of the light field took place; during the second step this duality remained in the background; during the third step duality of light and matter were seen as the center of quantum physics.

#### DUALITY OF LIGHT

It was detected by Einstein. He saw 1905 that Wien's radiation formula requires an entropy  $S(E)$  depending on energy  $E$  like a gas of particles each with an energy  $\epsilon = h\nu$ . While a system of light waves corresponds to equation (1), Wien's formula says equation (2), Planck's formula says (3):

$$-\frac{d^2S}{dE^2} \sim \frac{1}{E^2} \quad (1)$$

$$-\frac{d^2S}{dE^2} \sim \frac{1}{\epsilon E} \quad (2)$$

$$-\frac{d^2S}{dE^2} \sim \frac{1}{E^2 + \epsilon E} \quad (3)$$

Some years later (1908/09) Einstein recognized, that Planck's formula according to (3) means energy fluctuation in a radiating cavity coming from waves and from particles side by side (the fluctuations are expressed by the reciprocal of  $-d^2S/dE^2$ ). This fluctuation paper of Einstein clearly shows the concept of duality of light.

Ehrenfest, during his attempts to understand Planck's quantum hypothesis, preferred to consider the modes, the eigen vibrations of the radiation field instead of Planck's material oscillators, modes each with energies  $E = h\nu \cdot n$  (1906). This was early quantum field theory. Same was Debye's short derivation of the radiation formula, counting the number of modes in the interval  $d\nu$  and multiplying it with their mean energy:

$$n(T, \nu) d\nu = \frac{8\pi}{c} \nu^2 d\nu \cdot \frac{h\nu}{e^{h\nu/kT} - 1}.$$

After the detection of commutation relations for canonical variables (1925) these relations could be used for the modes of the radiating field. By reason of the special symmetry between coordinate  $q$  and momentum  $p$  for harmonic oscillators it was convenient to use the complex variables  $b_r = q_r + ip_r$ ,  $b_r^* = q_r - ip_r$  (suitable factors are omitted) and the commutation relations  $b_r b_s^* - b_s b_r^* = \delta_{rs}$ . The  $b$  and  $b^*$  matrices have a simple form and were later named annihilation and creation operators. Dirac used them 1927 for emission and absorption of light by matter. This was quantization of a field by commutation relations.

## DUALITY OF MATTER

In the first years after 1905 the light quantum was not taken much seriously. Some eminent physicists spoke of an unnecessary transcription of the quantum hypothesis. However it was taken seriously when (1922) the Compton-effect was detected and explained by collision of a photon against an electron on classical lines. The only non classical point in the explanation was measuring not momentum but frequency of light. Soon after (1923) De Broglie founded duality of matter. Instead of a circulating electron in an atom there was a standing wave, an integer number  $n$  of wave lengths  $\lambda = h/p$ . With

$$2\pi r = n\lambda = \frac{nh}{p}$$

$$rp = n \frac{h}{2\pi} ;$$

this explained Bohr's quantum condition, the moment of momentum was a multiple of  $h/2\pi$ , "la première explication physiquement plausible".

Schrödinger's equation of 1926, based on De Broglie's ideas was mathematically equivalent to quantum mechanics of 1925, but it was more convenient to handle. In those days partial differential equations with boundary conditions were better known to physicists than non commuting algebra. Schrödinger himself believed his "wave mechanics" to be a sort of physical explanation of quantum phenomena; others took it only for a convenient method to fulfill commutation relations ( $h\partial/\partial x$  for  $p_x$ ).

Among the flood of applications starting in 1926 two had principal significance. Treating unperiodic motions like collisions now was possible, so Born found the probability interpretation of Schrödinger's wave function. Treating an atom with two electrons by Heisenberg showed atomic states with an orbital function symmetric with respect to the two electrons, and states with an antimetric orbital function. Adding the spin function both are completed to an antimetric function according to Pauli's principle.

A more general formulation of quantum mechanics than matrix mechanics and wave mechanics soon was found, containing both as special forms. From this general formulation, which he regarded as a finished theory which could define its concepts, Heisenberg (1927) deduced the uncertainty relation  $\Delta x \Delta p \geq h$ . Coordinate  $x$  of a particle and  $x$ -component  $p$  cannot have fixed values simultaneously, determination of future is reduced. Bohr, disinclined to trust a mere mathematical formalism, expressed the physical meaning of quantum mechanics by the concept of complementarity. Matter waves are as real as particles and photons as real as light waves. Waves (or fields) and particles are two complementary aspects of reality restricting each other. When e.g. an object is looked at by means of a light microscope, then the accuracy of its coordinate  $x$  is limited by the wave

length of the light,  $\Delta x \approx \lambda / \sin \zeta$ ; on the other side the particle aspect of light leads to an uncertainty  $\Delta p = p \cdot \sin \zeta$  of the x-component of the momentum of the object, then  $\Delta x \Delta p \approx \lambda p = h$ . Uncertainty is a result of using the two complementary aspects. Since Bohr's symmetrical use of particle and wave (1927) quantum mechanics can be understood as an alteration (by commutation relations or by differential operators) of classical particle mechanics, just as far as necessary for the possibility of waves. The same quantum mechanics should also be an alteration of a so to speak classical field theory of matter, just as far as necessary for getting particles.

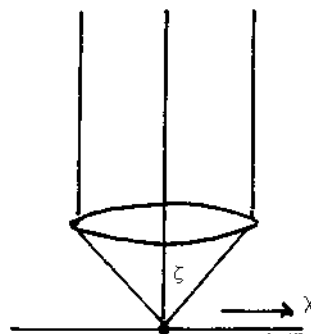


Fig. 1. Uncertainty relation

Bohr's program may be illustrated by the following confrontation (minor details omitted).

Matter consists of particles with an energy and a momentum

$$\vec{E}, \vec{p}$$

and a velocity

$$v = \frac{dE}{dp}$$

for  $v \ll c$  proportional to  $p$

$$\frac{dE}{dp} = \frac{p}{m} \quad .$$

A homogeneous matter beam has wave properties expressed by frequency and wave number

$$\omega, \vec{k}$$

giving a group velocity

$$v = \frac{d\omega}{dk}$$

for  $v \ll c$  proportional to  $k$

$$\frac{d\omega}{dk} = \frac{k}{\sigma} \quad .$$

Integration and inclusion of an electric field gives

$$\frac{\vec{p}^2}{2m} + eU - E = 0 .$$

$$\frac{\vec{k}^2}{2\sigma} + \zeta U - \omega = 0 .$$

Such waves (with slowly varying  $U$ ) come from a field equation for a complex function  $\psi(x, t)$

$$- \frac{1}{2\sigma} \Delta \psi + \zeta U \psi - i \dot{\psi} = 0 .$$

$U$  contains the interaction with other particles of the system. the matter itself ( $\Delta U - \zeta \psi^* \psi$ ).

This all is classical description of the two aspects. The non classical alterations may be given for the special case of one particle. To make waves possible, we introduce differential operators  $\hbar \partial / i \partial x \dots i \hbar \partial / \partial t$  and get:

As one particle has no interaction with itself,  $U$  is external potential,  $\psi^* \psi$  is probability for the particle

$$\int \psi^* \psi d\tau = 1 ,$$

and between wave properties and particle properties holds the relation

$$(\sigma, \zeta, \omega, \vec{k}) \hbar = (m, e, \vec{E}, \vec{p})$$

so we get:

$$- \frac{\hbar^2}{2m} \Delta \psi + e U \psi - i \hbar \dot{\psi} = 0$$

the Schrödinger equation for one particle.

Erection of Schrödinger equation for more particles from the field aspect was 1927 still to do. Jordan and O.Klein did it. They started with the field equations for  $\psi, \psi^*, U$ , developed  $\psi$  and  $\psi^*$  into a suitable orthogonal system of functions, and quantized by introducing operators instead of the coefficients with commutation relations  $a_s a_s^* - a_s^* a_s = \delta_{rs}$ . This procedure gave the symmetric solutions of the Schrödinger equation in configuration space. To get the anti-symmetric solutions, required by Fermi-statistics, Jordan and Wigner quantized with  $a_s a_s^* + a_s^* a_r = \delta_{rs}$  etc. In both cases quantization of a three-dimensional matter field was equivalent to Schrödinger equation of  $n$  particles in a  $3n$ -dimensional configuration space. At the beginning of 1928 the concept of quantization of light field and of quantization of a non relativistic matter field was clear.

## RELATIVISTIC FIELD

Transformation of the classical equation for one particle

$$\frac{E^2}{c^2} - \vec{p}^2 - m^2 c^2 = 0$$

$$\frac{(E-eU)^2}{c^2} - \left(\vec{p} - \frac{e\vec{A}}{c}\right)^2 - m^2 c^2 = 0$$

into a field equation of differential operators, the Klein-Fock-Gordon-Schrödinger-equation, was for the present not much trusted. To get first order in time derivative Dirac split 1928 the equation, using his matrices  $\alpha$  and  $\beta$ , and got his relativistic equation for one electron. It allowed positive and negative values of the kinetic energy  $E-eU$  and transitions between them, "Klein's paradoxon". With the assumption of normally occupied negative energy states, incidentally occurring free places, "holes", in the negative region behave like particles with positive energy and opposite sign of electric charge. So, the theory makes creation of pairs  $e^-$  and  $e^+$  possible. The concept of antiparticles was coined (about 1930).

In the meantime a general scheme of a quantum field theory with canonical commutation relations was established by Heisenberg and Pauli (1929). Additional insight into the important concept of antiparticle gave then the quantization of a scalar matter field by Pauli and Weißkopf in 1934. Production of matter and antimatter with opposite sign of the electric charge could not be understood in an elementary manner. Consider a matter wave

$$\left(\frac{\omega}{c} - \eta U\right)^2 - \vec{k}^2 - \kappa^2 = 0$$

then  $\omega/c - \eta U > \kappa$  (with  $\eta > 0$ ) means positive charge and  $\omega/c - \eta U < -\kappa$  negative charge. The theory contains both signs for charge, while the energy is always positive (Diracs theory gave originally one sign for charge and both signs for energy). Let now a matter wave with (let us say) negative charge run from left against a very deep precipice of the electric potential from 0 to  $\eta U < -2\kappa$ . Then if  $\omega/c < -\kappa$  and  $-\kappa > \omega/c > \eta U + \kappa$  the incoming wave will give rise to a reflected wave with negative charge and a passing through wave with positive charge. As conservation of charge holds in this theory, the reflected wave must have a higher intensity than the incoming wave. Already in this still unquantized theory we find production of matter and antimatter. In the quantized theory pair production of particles and antiparticles takes place, also without incoming matter. Possible production of particles and antiparticles is a fundamental feature of a relativistic quantized field theory of charged matter. From about 1934 the difficulties coming from divergent calculations were discussed.

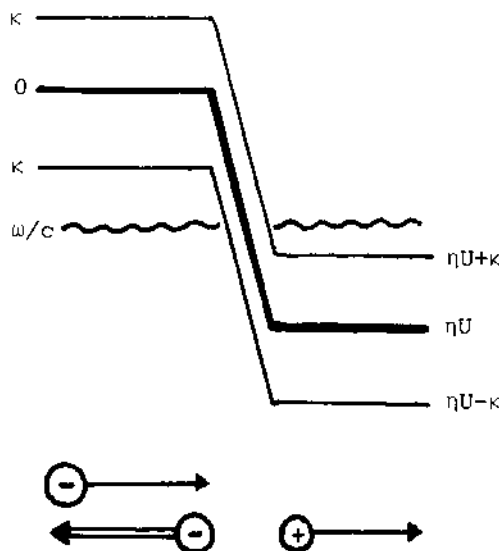


Fig. 2. Matter production

About this time a new stimulus came to quantum field theory from new fields. The  $\beta$ -decay  $n \rightarrow p + e^- + \nu$  and (in a nucleus)  $p \rightarrow n + e^+ + \nu$  led Fermi 1934 to coupling four particles, the first example of a weak coupling. In 1935 Yukawa conceived a strong coupling. A static field

$$\Delta\phi - \kappa^2\phi = 0$$

can have the spherically symmetric form  $\phi \sim e^{-Kr}/r$  with a finite range  $1/K$ . Since nuclear forces have a range somewhat larger than  $10^{-15} \text{ m}$ , Yukawa explained them by such a field, the corresponding field quanta had a mass of about 200 electron masses ( $mc = \hbar\kappa$ ); they were the later found  $\pi$ -Mesons. The concept of "force" was much extended: to gravitation and electromagnetic force came new "strong" and "weak" force.

## SUMMARY

- Let us now repeat the main steps in early quantum field theory:
- (1) QED began with the photon (1905), with treating radiation as a system of quantized modes,  $E = h\nu n$  (1906) and with duality of light (1909).
  - (2) Understanding quantum mechanics as the expression of duality of matter meant quantization of a non relativistic matter field with commutation relations for Bosons and Fermions (1927).
  - (3) Quantization of relativistic matter fields coined the concepts of antimatter, antiparticles and pair production (1930-34). Experiments gave different examples of fields and their coupling.

I will end with the mid-thirties. Afterwards came "out off" rules, renormalization, strange particles, rules for leptonic and hadronic coupling, isospin, quarks with colour and flavour. We do not know, whether the essential features are still detected. But this conference perhaps will confirm the belief that matter gets simpler if we proceed to smaller dimensions and higher energies.

## SUMMARY TALK: THEORETICAL

L.C. Biedenharn

Physics Department  
Duke University  
Durham, N.C., 27706

### INTRODUCTION

It was with considerable trepidation, and no little hesitancy, that I accepted Professor Greiner's invitation to give this summary talk. The subject of the conference--quantum mechanics of strong fields--runs the gamut of physics: from high precision QED, quarks and pion condensation to radiating black holes. Only a very brave, very foolish, or very unwary person would accept this responsibility --and I leave it to you to decide which fits best.

But there are special hazards that deserve mention. Walter Greiner arranged the schedule to leave open most of the day before the summary talk. I thought this very thoughtful of him to give me time to prepare. But alas, he dived into this vacuum and filled the available time with more talks.

The second special hazard has been the unusually large number of really beautiful talks--experimental as well as theoretical-- for which any summary is both hopeless as well as hapless. It has been said that a summary talk is a good way to please a few friends at the expense of making a larger number of enemies. Hence I shall not tell you who gave these superb talks--you already know this!-- but shall only say that if I don't summarize your talk, then you and I already agree on one such speaker.

Let me now give an overview of how I shall attempt this summary. I will divide the conference by major themes, and consider the talks made under each theme. Since, as stated, summaries are scarcely possible, I shall proceed by reminding you of the

concluding remarks of the speakers themselves.\* Then I shall take the opportunity to make some pedagogical remarks on the topic, under the pretext that this is, after all, a school and there may be some students who enjoy non-profound comments. After having discussed the major themes, I will conclude with the outlook.

QUANTUM ELECTRODYNAMICAL CALCULATIONS FOR STRONG FIELDS  
(Talks by: Erickson, Gyulassy, Mohr)

Talks on this basic theme initiated the conference. The talks by Erickson concluded with a very enlightening survey of precision calculations and precision measurements of the Lambshift in hydrogen, illustrating graphically how discrepancies came and went as the field progressed to the fabulous current accuracy of 1 part in  $10^{10}$ . The question was raised during these talks as to usefulness of measuring, say, the Lambshift in heavy atoms to which Erickson gave the surprising answer: "to check the calculations which are of differing reliability"! To illustrate this point, let me remind you of the VU-graph concluding Erickson's talks which summarized the status of the current precision calculations for large  $Z$ . This is a most interesting VU-graph for it shows the basic honesty of physics: note that the discrepancies *exceed* the estimated errors, so that the VU-graph, in a sense, self-destructs. We saw later in Hänisch's talk that the  $C1^{17}$  Lambshift verifies that Mohr's calculations do fit experiment marginally better than Erickson's (but the final decision is still unclear.)

Let me now comment on this. A famous intuitive explanation of the Lambshift was given by Welton. During the conference the question arose as to whether one could give an intuitive explanation of the large value of the lower cut-off on the Bethe logarithm term. To answer this, Ted Welton has supplied me with the following guest comment.

Explanation of the Large Value of Bethe's Lower Cut-off (T.A. Welton)

An elementary semi-classical argument indicates that a free electron subjected to the zero-point fluctuations of the electromagnetic field would suffer a mean-square fluctuation in position given by

$$\langle |(\delta \vec{x})^2| \rangle = \frac{2\alpha}{\pi m^2} \int_{\epsilon}^{\kappa} \frac{d\omega}{\omega} = \frac{2\alpha}{\pi m^2} \log(\kappa/\epsilon) , \quad (1)$$

\*In the talk as actually given, this enabled me to use their VU-graphs.

where  $\kappa$  is an upper cut-off frequency, approximately equal to  $mc^2/\hbar$ , above which the response of the electron is strongly limited by recoil and relativistic considerations. The lower cut-off  $\epsilon$  is more subtle in its character, it being clear that the finding of the electron in an atom will somehow restrict its response for  $\hbar \omega \approx Z^2 \alpha^2 mc^2$  (= the approximate binding energy for the lowest state of a hydrogen atom if  $j = 1/2$ .) The argument proceeds to calculate the energy shift of a bound state of the atom by finding the perturbation in the potential energy:

$$\begin{aligned} \langle \nabla(\vec{x} + \delta\vec{x}) \rangle &= V(\vec{x}) + \langle \delta\vec{x} \cdot \nabla V(\vec{x}) \rangle + \frac{1}{2} \langle (\delta\vec{x} \cdot \nabla)^2 V(\vec{x}) \rangle + \dots \\ &= V(\vec{x}) + \frac{1}{6} \langle (\delta\vec{x})^2 \rangle \nabla^2 V(\vec{x}) + \dots, \end{aligned} \quad (2)$$

or:

$$\begin{aligned} \delta E_n &= \frac{\alpha}{3\pi m^2} \left( \log \frac{mc^2}{\hbar\epsilon} \right) \langle n | \nabla^2 \left( -\frac{Ze^2}{r} \right) | n \rangle \\ &= \frac{\alpha}{3\pi m^2} \left( \log \frac{1}{\lambda Z^2 \alpha^2} \right) \langle n | 4\pi Z e^2 \delta(\vec{x}) | n \rangle \end{aligned} \quad (3)$$

$$\begin{aligned} &= \frac{\alpha}{3\pi m^2} \left( \log \frac{1}{\lambda Z^2 \alpha^2} \right) \cdot 4\pi Z \alpha |\Psi_n(0)|^2 \\ &= \frac{\alpha}{3\pi m^2} \left( \log \frac{1}{Z^2 \alpha^2} - \log \lambda \right) \cdot 4\pi Z \alpha [n^3 \pi (a_H/Z)^3]^{-1} \\ &= \frac{4}{3\pi} \cdot \frac{\alpha (Z\alpha)^4}{n^3} \cdot \left( \log \frac{1}{Z^2 \alpha^2} - \log \lambda \right) \cdot mc^2. \end{aligned} \quad (4)$$

(Here we have introduced the dimensionless parameter  $\lambda$  as  $\epsilon = \lambda \cdot Z^2 \alpha^2 mc^2 / \hbar$ .)

It comes as something of a surprise that  $\lambda$  must be a fairly large number ( $\approx 17$ ) to yield agreement with Bethe's calculation. This can be rendered less surprising by a somewhat more detailed attention to the cut-off mechanism. The S-state of a hydrogenic atom become very "stiff" near the nucleus, that is, an increasingly high frequency for a harmonic driving force must be used to get a response approximating to the free electron response at the same frequency. Thus,  $\epsilon$  should really be taken to be a function of  $r$ , and then an appropriate spatial average of  $\epsilon$  should be used. The basic idea is one proposed by Aage Bohr to explain the fact that the hyperfine structure of deuterium is not calculated quite correctly by using the deuteron magnetic moment. Rather, the electron wave function, with its (non-relativistic) cusp at the position of the proton, follows the proton motion in the deuteron, and the neutron is always at a point of somewhat lower electron density. Bohr suggested (the argument is not fully quantitative!) that the electron wave function would follow the proton out to distance  $r$ , if the proton oscillation frequency  $\epsilon$  is given by:

$$\hbar \epsilon(r) = \frac{\hbar^2}{mr^2}$$

$$\text{or } \epsilon(r) = \frac{\hbar}{mr^2} , \quad (5)$$

which gives us the required expression for the lower cut-off frequency at each  $r$ -value.

We then rewrite the energy shift as

$$\delta E_n = 4\pi \int_0^\infty r^2 dr \left( -\frac{2e^2}{r} \right) \cdot \delta \rho_n \quad (6)$$

where:

$$\rho_n = |\psi_n(r)|^2 ,$$

and

$$\delta \rho_n = \frac{\alpha}{3\pi m^2} \log \frac{(mc^2/\hbar)}{(\hbar/mr^2)} \vec{\nabla}^2 \rho_n .$$

This is not quite correct because  $\int_0^\infty r^2 dr \delta \rho_n \neq 0$ , but this is easily remedied by a slight change:

$$\delta \rho_n = \frac{\alpha}{3\pi m^2} \vec{\nabla} \cdot \log \left( \frac{mc^2}{\hbar} \right)^2 \vec{\nabla} \rho_n . \quad (7)$$

Finally, for the ground state of the atom:

$$\delta E_1 = -4\pi Z\alpha \cdot \frac{2\alpha}{3\pi m^2} \int_0^\infty r^2 dr \left( \frac{1}{r} \right) \frac{1}{r^2} \frac{d}{dr} r^2 \log \frac{mc^2}{\hbar} \frac{d}{d\hbar} \frac{e^{-(2Zr/a_H)}}{\pi a_H^3 Z^3} .$$

The logarithm must be taken to vanish when  $\frac{mc^2}{\hbar} < 1$ , so an integration by parts yields:

$$\begin{aligned} \delta E_1 &= -\frac{8\alpha(Z\alpha)^4 mc^2}{3\pi} \int_{\hbar/mc}^\infty dr \left( \log \frac{mc^2}{\hbar} \right) \frac{d}{dr} \left( e^{-2Z\alpha \frac{mc^2}{\hbar}} \right) \\ &= \frac{8\alpha(Z\alpha)^4 mc^2}{3\pi} \int_{2Z\alpha}^\infty \frac{ds}{s} e^{-s} , \end{aligned} \quad (8)$$

If we equate (4), with  $n = 1$ , and (8), we obtain:

$$\log \frac{1}{Z\alpha} - \log \sqrt{\lambda} = \int_{2Z\alpha}^\infty \frac{ds}{s} e^{-s} = \log \frac{1/\gamma}{2Z\alpha} + O(Z\alpha) ,$$

where  $\gamma$  is the Euler-Mascheroni constant.

Therefore:  $\lambda \approx 4\lambda^2$ , or numerically  $\lambda \approx 12.7$ .

Strictly, Bethe's  $\epsilon$  was calculated for the 2S state. The above argument leads to  $\lambda \approx 14.2$ , which compares reasonably well with the value  $\lambda \approx 17$  from Bethe's calculation.  $\square$

The talk by Miklos Gyulassy answered the question: "Can Non-linear Electromagnetic Effects Prevent or Delay Diving?" Gyulassy used the following concluding VU-graph:

Summary: (Gyulassy)

1. Wichmann-Kroll formalism has been applied to finite R nuclei.
2. High Z muonic atoms confirm vacuum polarization  $\alpha(Z\alpha)^{n>3}$  to  $\approx 20\%$ .
3. For  $Z > 137$ ,  $\alpha(Z\alpha)^{n>3}_{j=\frac{1}{2}}$  vacuum polarization screening increases rapidly, but remains non-singular and small  $Q_{\text{eff}} \approx \frac{e}{20}$  at  $Z_c \approx 175$ .
4. Beyond  $Z_c$ , chargeless vacuum density  $\langle 0 | J_0 | 0 \rangle$  is not defined, but charged vacuum state (He-like) exists and remains localized past  $Z_c$ .

Thus the answer to Gyulassy's question is: no.

Before turning to another conference topic, let me note that Hari-Dass, in a contribution, used Schwinger's elegant methods to give, among other things, a very succinct derivation of the Euler-Heisenberg Lagrangian.

#### DECAY OF THE VACUUM, SUPERHEAVY QUASI-MOLECULES, POSITRON CREATION, STABILIZATION OF THE VACUUM FOR STRONG FIELDS

(Talks by Müller, Rafelski, Reinhardt, Soff)

This was a major (if not *the* major) theme of the conference, and one can only admire the enormous ingenuity and effort that has gone into understanding the physical processes of colliding, say, uranium on uranium. This forms a composite system of 576 nucleons and 184 electrons (and innumerable more particles on the quark, rishon level). The physical processes are mind-boggling to untangle: bremsstrahlung,  $\delta$ -electrons, Coulomb excitation, internal conversion; direct-, spontaneous-, and induced emission of positrons, to say nothing of nuclear interactions, and, as I will discuss later, possibly "Fairbank-quark" production.

Let me remind you of a few details from the work of Müller, Soff, Reinhardt. They established the very useful scaling law (VU-graph from Müller):

Scaling Law

$$P_k = D(Z_1 + Z_2) \exp \left( -\frac{\alpha R_{\min} E_k(R_{\min})}{\hbar v} \right)$$

(G. Soff + B. Müller, Bosch et al., Bang + Hansteen: also correct in 2nd order perturbation theory)

$D, \alpha, R_{\min}, v$  known  $\rightarrow$  "measure"  $E_k(R_{\min})$ .

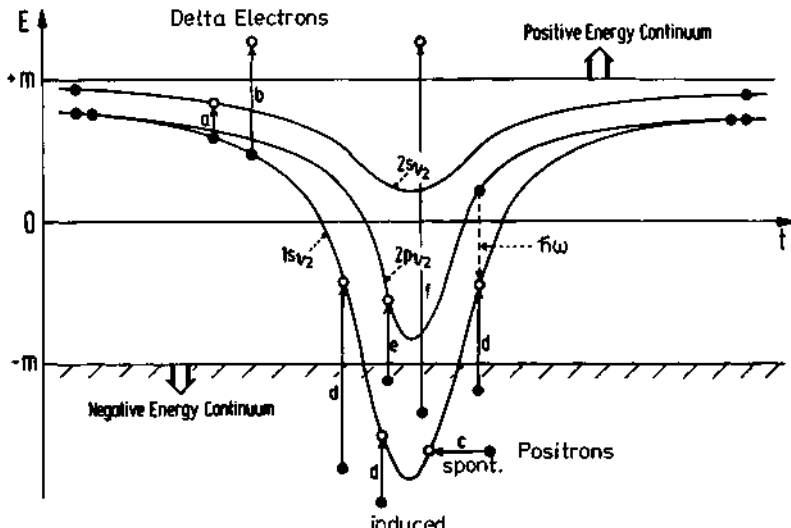


Figure 1.

Using this law they could fit the experimental data (e.g. Pb + Cm fit from Müller's talk).

They carried out extensive calculations on the properties of the "diving levels", and applied this work to determine the theoretically expected direct-, induced-, and spontaneous-positrons as indicated in their familiar slide:

Comments and Discussion

The relativistic Kepler problem--more precisely, the Dirac electron in a Coulomb field--plays a very large role in studies on the decay of the vacuum. Since this Dirac problem is one of the few things I have studied intensively, I thought perhaps I would explain some of the curious physical features of this system. I take the point of view that *every detail of the Dirac-Coulomb solution is of genuine physical interest.*

Intuitive physical explanations always mean semi-classical explanations and I begin by reminding you of Sommerfeld's treatment of this problem in 1916. Non-relativistic Kepler motion gives conic sections, the bound orbits being ellipses with the attracting center (the nucleus) as a focus.

What does relativity do to this motion?

Consider the electron at peri-helion. Here it moves *fastest*, and therefore appears to be *more* massive. Thus the product  $m_{\text{eff}} v r$  would tend to increase. But this is not possible, since angular momentum is conserved relativistically and thus the velocity must decrease to compensate. In other words, the ellipse rotates as Sommerfeld showed. Which way does it rotate? (This is a nice question for doctoral exams.) Clearly, it rotates in such a direction as to (apparently) *decrease* the angular momentum.

Thus we get the famous rosette pattern of relativistic Kepler motion.

*The relativistically induced orbital rotation has just that frequency so that in a rotating frame we get again closed orbits.*

Very nice, you may say, but old hat. What does this have to do with the Dirac problem where we have spin and other complications? To answer this, let me remind you of an operator that naturally occurs in the Dirac-Coulomb problem which I re-discovered\* (to my chagrin about 25 years after G. Temple). I call it *Temple's operator*:  $\Gamma \equiv K + i\alpha Z \rho_1 \vec{\sigma} \cdot \vec{f}$ , where  $K$  is Dirac's operator,  $K \equiv -\rho_3 (\vec{\sigma} \cdot \vec{L} + 1)$ .

(Dirac's operator  $K$  is a marvelous operator. It has no zero in its spectrum so that the inverse  $K^{-1}$  is well defined, and hence it may be normed to unity:  $K$ , with  $K^2 = 1$ . Then  $K, \rho_1 \vec{\sigma} \cdot \vec{r}, \rho_1 \vec{\sigma} \cdot \vec{r} K$  form a set of three anti-commuting units.)

The eigenvalues of  $\Gamma$  are just the mysterious quantum numbers:

$$\gamma = |\kappa^2 - (\alpha z)^2|^{\frac{1}{2}}.$$

\* Phys. Rev. 126(1962)845-851.

Clearly we should diagonalize this operator  $\Gamma$ , and not  $K$  as is usually done, a step Temple did not carry out. We can easily do so by a unitary transformation around the  $p_2$  direction. Astonishing things happen!

What we find is that in this new reference frame the Dirac-Coulomb problem becomes *completely non-relativistic in appearance*: one obtains "non-relativistic Coulomb wave functions" where the quotes mean that relativistic parameters are to be used:

$$\gamma_{\text{rel}} = \frac{Z_1 Z_2 e^2}{\hbar v_{\text{rel}}} = \frac{Z_1 Z_2 e^2 E_{\text{rel}}}{\hbar p_{\text{rel}} c}; \quad "l"_{\text{rel}} = \gamma, \gamma^{-1};$$

$$\hbar k_{\text{rel}} = p_{\text{rel}}.$$

Anyone who has actually worked with the Dirac solutions will understand what I mean when I say they are highly counter-intuitive. It takes considerable technical skill simply to find the non-relativistic limit. It is the clear implication from the above result that one is simply looking at things in the wrong frame of reference.

But what about the Sommerfeld construction? Things are not quite so clear-cut since a continuous rotation is not an inertial transformation. Hence we cannot claim the transformation diagonalizing  $\Gamma$  is Sommerfeld's transformation. But it is close. In the classical limit, the transformation diagonalizing  $\Gamma$  corresponds to an instantaneous Lorentz transformation to a frame that would be Sommerfeld's moving frame at that instant. Thus we may use this idea qualitatively.

What do we learn? One sees from the fact that the orbital angular momentum is decreased (in rotating frame) that the change in the centrifugal potential has effectively an *attractive* effect. This causes the *relativistic shrinking* emphasized by Kienle as so essential to observing vacuum decay. Moreover, one sees that the rotation *lowers* the velocity at peri-helion but *increases* it ap-helion. Thus, in the limit we find  $v$  will exceed  $c$  unless the orbit shrinks. The effect is greatest for S-states, which are the famous pendelbahnen (highly eccentric elliptical orbits) that stick out the furthest from the nucleus.

One last point. The relativistic splitting of the energy levels occurs from the interaction of the spin with this "relativistic rotation": there are two equivalent directions of rotation relative to the spin direction, hence a *doubling* of states. But the orbits with largest angular momentum are circular. This explains the fact that these states of highest  $j$  are *not* doubly degenerate, since a circle is invariant to rotation. (There are textbooks that have this

degeneracy wrong.)

It is an unsolved problem why Sommerfeld got the exact Dirac energy levels in 1916, and famous people (Schrödinger, Mandelstam, among others) have asserted that the problem doesn't exist, i.e., it is all an accident. In my opinion it was not an accident at all, and the answer may lie in making more quantitative the above observations.

#### Further Remarks

Now I would like to turn to the decay of the vacuum. Let me apologize in advance for these remarks, for I fear the Frankfurt school may be annoyed with me, but my duty as summarizer requires some comment.

There is no doubt about the physics of the vacuum decay, but in my opinion the diving has been made unduly provocative and complicated by using the concept of a Bound State Embedded in the (negative energy) Continuum (B.S.E.C.).

I claim the B.S.E.C. does not exist in the sense it has been used.

Consider the free one-particle Dirac equation: the spectrum is uncontroversial, there is a positive continuum with  $E \geq mc^2$  and a negative energy continuum with  $E \leq -mc^2$ .

But the quantized Dirac theory is absolutely essential. One way to look at this theory, although admittedly a bit perverse, is that it *linearizes* the (non-linear, one-particle) charge conjugation operator which relates bijectively the two sets of one-particle solutions of the free equation. Thus for the quantized free-particle spectrum one has two distinct positive energy continua ( $E > mc^2$ ), split by a super-selection rule (for charge), whose one-particle states are related linearly by the charge-conjugation operator.

Now turn on a weak Coulomb field. Bound levels pop out of the negative-charge zero-energy ("parabolic orbits") continuum. Charge conjugation has been *broken*; these solutions are effectively real and have no partners. *One is not free to regard these as "positrons" even if their energies do become negative.* (The bijective conjugation pairing still exists in the two continua.) Physically this is obvious since these bound solutions are big near the nucleus, i.e., attraction exists (as appropriate to negative charge).

The picture we have obtained continues\* smoothly through  $E=0$  and even through  $E=-mc^2$ . The  $1s_{\frac{1}{2}}$  levels "dive" smoothly

\*for finite sized nuclei.

But notice: *these diving levels never appear in either continuum.* (Continuum means motion at infinity and these states vanish there.) There is--in this sense!--*no B.S.E.C.* The diving levels and the "negative energy continuum" are split by the charge quantum number.

But clearly there is a new effect at  $E_{1s_{1/2}} = -mc^2$ , for now this electron level can combine with the continuum at  $E = mc^2$  for positrons (this is the zero-energy continuum) and the vacuum state is degenerate (in zeroth order) to this continuum of states of  $(e^- e^+)$  zero energy pairs. The vacuum is unstable, just as Walter Greiner asserted years ago. Only the details have changed.

But note now a curious point. *If we neglect vacuum polarization and self-energy terms, then these pair states are certainly bound.* (Proof: the omitted shielding and interaction energies are *all attractive.*) Johann Rafelski was kind enough to discuss this with me, and he told me that Migdal proposed these states some time ago, but that it was (and still is) felt that they do not exist. In my view, the problem should be re-examined critically.

To conclude: the *one particle B.S.E.C.* does not exist; there *is*, however, a form of the B.S.E.C. which does exist: this is the vacuum state and arbitrarily many pair states when  $Z$  becomes critical. Physically this is exactly what one would expect: the virtual pairs become real (but still localized I believe) then for very large charges the positrons drift to infinity and we get vacuum decay. There is no sharp transition, in my view.

#### METHODS FOR TREATING MANY BODY RELATIVISTIC SYSTEMS

- a. Density Functional Methods (Dreizler, Gross)
- b. Electron Correlation in High-Z Atoms (Johnson)
- c. Ion-Atom Collisions (Briggs, Kleber)
- d. Sticking Collisions (Meyerhof)

The necessity to treat correctly the difficult many-body problems posed by the GSI experiments has generated much interest in new approaches, such as the papers noted above.

Let me comment briefly on the interesting new developments in extending the Thomas-Fermi method discussed here by Dreizler and Gross. My comment is technical. In the application of their methods to the Dirac equation they used the Foldy-Wouthuysen series

development for the Dirac-Coulomb field, partly from the practical necessity of reducing  $4^N \times 4^N$  structures to  $2^N \times 2^N$ . The Foldy-Wouthuysen expansion is in powers of  $c^{-1}$ , and it is very probable that this expansion is not convergent (Dreizler noted that it is not unique.)

Using the freedom of the additional anti-commuting structure mentioned earlier, my colleagues and I found that the free Dirac equation, with mass, permitted an exact two-component splitting distinct from the Foldy-Wouthuysen form. This result extends to interactions, in particular, it extends to the Coulomb field so that there exist *exact two-component* Dirac-Coulomb relativistic wave functions. This technical simplification might be helpful for the extended Thomas-Fermi calculations reported at this conference.

The paper of Johnson was impressive for the large amount of theoretical and experimental results presented, and I would like to use some of his VU-graphs to summarize this:

1) Dirac-Fock Calculations

$$h = \frac{p^2}{2m} - \frac{e^2 Z}{r}$$

replaced by

$$h = \vec{a} \cdot \vec{p} + \beta m - \frac{e^2 Z}{r}$$

$$H_0 = \sum_i h_i + \sum_{i>j} \frac{e^2}{r_{ij}}$$

Hartree-Fock Approximation  
(Dirac-Fock)

$$(h+v) u_k = \epsilon_k u_k; \quad k=1, 2, \dots, N$$

$$v_u = \sum_{k=1}^n e^2 \int \frac{d^3 r'}{R} [ (u_k^\dagger u_k)^\dagger u - (u_k^\dagger u)^\dagger u_k ]$$

$-\epsilon_k$  = "Frozen-Orbital" approximation  
to binding energy for  $k^{\text{th}}$  electron

4) Difficultiesi) Correlation Effects

| Argon Energies (eV)   |      |                   | Diff | Corr <sup>d</sup> |
|-----------------------|------|-------------------|------|-------------------|
| L <sub>I</sub>        | 33.0 | 29.2 <sup>a</sup> | -3.8 | -4.3              |
| L <sub>II</sub>       | 14.5 | 15.9 <sup>b</sup> | 1.4  | 1.0               |
| L <sub>III</sub>      | 14.3 | 15.8 <sup>b</sup> | 1.5  | 1.0               |
| Krypton Energies (eV) |      |                   | Diff | Corr <sup>d</sup> |
| M <sub>I</sub>        | 31.0 | 27.5 <sup>c</sup> | -3.5 | -3.3              |
| M <sub>II</sub>       | 13.7 | 14.7 <sup>b</sup> | 1.0  | 0.9               |
| M <sub>III</sub>      | 13.0 | 14.0 <sup>b</sup> | 1.0  | 0.9               |
| Xenon Energies (eV)   |      |                   | Diff | Corr <sup>d</sup> |
| N <sub>I</sub>        | 26.5 | 23.4 <sup>c</sup> | -3.1 | -3.5              |
| N <sub>II</sub>       | 12.5 | 13.4 <sup>b</sup> | 0.9  | 0.9               |
| N <sub>III</sub>      | 11.2 | 12.1 <sup>b</sup> | 0.9  | 0.9               |

a) Sevier, Low Energy Spectrometry (1972).b) Moore, Atomic Energy Levels (1971).

c) Beorden and Burr, R.M.P. (1967).

d) Aoyagi et al., ICAP V Abst. (1976).

ii)  $K_{\alpha_1}$  hypersatellite

| State                             | Tm (Z=69)           | Hg (Z=80)                                  |
|-----------------------------------|---------------------|--------------------------------------------|
| [1s <sub>1/2</sub> ]              | 309,412.9           | 450,597.7                                  |
| [2p <sub>1/2</sub> ]              | 360,150.9           | 521,408.7                                  |
| [1s <sub>1/2</sub> ] <sup>2</sup> | 248,781.1           | 365,919.8                                  |
| [1s, 2p] <sub>J=1</sub>           | <u>300,438.4</u>    | <u>437,906.3</u>                           |
| $k_{\alpha_1}^h - k_{\alpha_1}$   | 917.0 <sup>a</sup>  | 1,175.5 <sup>a</sup> (1178.7) <sup>b</sup> |
| Exp.                              | 902(9) <sup>c</sup> | 1,145(12) <sup>d</sup>                     |

a) van Eijk and Wijnhorst, Phys. Rev. A15:1794 (1977).

b) Schreckenbach et al., Phys. Lett. 63A:33C (1977).

c) Desclaux, Physica Scripta 21:438 (1980).

d) Beatham et al., Physica Scripta 21:428 (1980).

The paper by Meyerhof, on sticking collisions, does not quite fit under this general heading but certainly under heading (c). This work is interesting because it shows that *the proper formulation of the interference structure due to sticking still requires both theoretical and experimental work*. Meyerhof is presently repeating the crucial experiment, but the theory should also be straightened out. The interference effect is physically understandable as a variation on the two-slit problem (as pointed out by Barut). Other examples were given in the talk by Hänisch: two-photon spectroscopy with two pulses show a similar interference effect, and there is a (spatial) version of the same general effect given by 'Ramsey fringes'.

#### PION CONDENSATION (Faessler, Irvine, Rafelski)

The subject of pion condensation is rather vexed. It is clearly important, and could be truly fundamental, but it has been plagued by controversy, even error. The very evident progress represented by the papers presented in this conference is not without paradoxical aspects--as witness Faessler's title "Does Pion Condensation prevent Pion Condensations?" One clear result, emphasized by Faessler, is that this phenomenon definitely causes the Brown-Weise calculation to self-destruct!

In searching for an adequate response to the erudite (and amusing) formulation of Greek philosophical thought by Fritz Bosch, I tried--and eliminated--several possibilities which I pass over here.

The only satisfactory theme (thanks to W. Greiner) for our conference appeared to stem from Aristoteles: *Horror Vacuii* ("Der Abschen der Natur vor dem leeren Raum"). But as I thought about it this possibility turned out to be just as controversial to the Eleatic school as pion condensation is for this conference.

##### Pro-vacuum:

Leukippus  
Anaxogoras  
Empedocles  
Demokritos

##### Anti-vacuum:

Parmenides  
Aristoteles

The controversy developed in two versions: micro-vacuum (the space between atoms) and macro-vacuum (space with atoms absent). This is rather closely paralleled by the split between proponents of fermion (quark) condensation ('microvacuum') and boson (pion) condensation ('macrovacuum').

But do not scoff at the vacuum problem! As you know it reaps

peared as the ether (Aristotle's fifth substance) only to be eliminated by Michelson-Morley. But not for long--it now reappears as the 3°K. background radiation, reestablishing(?) the old absolutes.

## TWO SHORT REMARKS

(1) The talks by Candelas aroused intense interest since it is very counter-intuitive that an accelerated system should have heated up internally! My colleague, Hank van Dam, (working with W. Troost\*) found a very differently appearing formulation of this same phenomenon: the accelerated observer finds himself, formally, in a multiply-connected space-time with the fundamental group  $\mathbb{Z}$ . (In this latter formulation it is not so obvious that the system is not reversible.) I should also mention that Greiner, Müller, and Rafelski found what appears to be the same phenomenon in their interpretation of external fields as temperature. I don't pretend to understand these matters, but (using that pretext again) students may find the references helpful.

(2) The Fairbank quark experiment has forced theorists to contend with the fact that a very tiny fraction of the quarks may be free. Doesn't this destroy the QCD confinement? No, says Slansky, et al, in a recent preprint\*\*. The idea is to break  $SU_3^c$  to  $SO_3^8$  (the nuclear physics way) and to insist that *only*  $SO_3^8$  singlets exist. (g stands for "glow").

Surprisingly, the baryon 56 remains unaffected. But now the di-quarks can escape to infinity and these carry fractional charge.

The  $e^+e^-$  interest for this conference is that (unlike the high energy  $e^+e^-$  experiments at PETRA), heavy-ion experiments, such as the U-U experiments at GSI, could show "copious production of di-quarks" according to these authors.

## CURRENT STATES AND FUTURE

Where do we stand? I think the only fair verdict is the Scottish one: Not proven. But I strongly feel that the experiments are well on the way to proving:

(1) That the vacuum does indeed decay as claimed, and

(2) That the superheavy quasi-atoms exist and live for at least  $10^{-19} - 10^{-20}$  seconds. If the  $\rho$ -meson with a lifetime of order

\* W. Troost and H. van Dam, Nucl. Phys. B152(1979) 442-460.

\*\* Slansky, Goldman and Shaw, "Observable Fractional Electric Charge in Broken QCD", LASL preprint LA-UR-81-1378.

$10^{-23}$  sec. can be said to "exist", then surely these superheavies could have a valid claim!

Establishing these results is the task of the near future. Beyond that lies the possibility of super-heavy atomic as well as nuclear spectroscopy. The fascinating possibility is open that this quasi-atom may even decay into a more stable super-heavy nucleus, a possibility noted in this conference by Müller and Greiner.

#### CONCLUDING REMARK

I come now to the pleasant part of my task. Organizing a conference, or a school, is unbelievably hard work. The local committee has done a fine job of organizing this school and selecting such a beautiful part of Germany for the locale. The trips to the Loreley and the splendid *Ritterliches Mahl* at the Marksburg, especially, bear witness to superb organizing. In the name of the conferees, I wish to thank Professor Walter Greiner for initiating, organizing, and conducting this school, NATO and the Bundesministerium for support, the local committee represented by Professor Dreizler, and the secretarial staff Mrs. Lasarzig and Pfister, for a splendid conference!

## SUMMARY: EXPERIMENTAL ASPECTS

J. S. Greenberg

A. W. Wright Nuclear Structure Laboratory  
Yale University  
New Haven, Connecticut 06511

### INTRODUCTION

A natural hesitancy accompanies all summary speakers approaching their task. But I feel particularly timid this morning because you may recall that the organizing committee, earlier this week, saw fit to generously award me a bottle of wine in anticipation of my effort this morning. I appreciate their confidence in me, but I want to assure them that I have taken the precaution of leaving the bottle unopened, although tempted otherwise, in case they may want to retrieve it with the termination of this talk.

As always, doing justice to summarizing a conference such as this one with two weeks of lectures discussing diverse phenomena with forays into completely new domains is a formidable challenge, if not an impossible task. Such as it is, my expertise certainly does not extend to all the territory covered during these past two weeks and, as you have probably experienced in the past, uninformed comments by the summary speaker can be painful both to the audience and to the speaker. In pondering how to deal with this familiar problem yesterday, my thoughts turned to the preachings of our adopted conference philosopher, Fritz Bosch. His informative and entertaining lecture and his comments from the floor were much appreciated by us all. I refer particularly to the "golden rules" he developed for achieving experimental success as he presented the experimental assault on the problem of ionization in the very-heavy collision systems. Among the complex structure of rules that emerged from his treatise, the call above all to be clever and then simple had an

especially ringing appeal. I reasoned that what applies to experiments may also be useful for summary talks. Failing to think of a clever approach, however, I have settled for the option of keeping my comments simple.

With this guiding principle in mind, possibly the best service I can perform for you today is to direct my remarks at those experiments which most directly deal with the central questions addressed at this Conference. Although they have been dealt with in many forms during the past two weeks, let me restate these questions, albeit in simplified form.

1. Can spectroscopic information on the relativistic structure of superheavy atomic species be extracted from studying superheavy collision systems?

2. Does supercritical binding exist in atoms?

3. In particular, can collision systems such as U+U and U+Cm be utilized to observe the spontaneous decay of the supercritically bound hole-state?

4. An intriguing question which has emerged from the most recent data concerns the possibility of exploiting atomic processes, such as positron creation, as probes of exotic nuclear properties such as the formation of superheavy nuclear species which has been one of the holy grails long sought by nuclear physicists.

Since I will attempt to tie together the experiments discussed at this conference which bear on these questions most directly, the emphasis, therefore, will be on the positron search experiments. But it is also important to appreciate and comment on the very important roles played by the other investigations which have been instrumental in developing the physics associated with very-heavy ion-atom collisions and with the formation of transient superheavy atomic systems. In discussing the past, I will also try to look ahead. I apologize to those people who have discussed the many interesting aspects of QED which I cannot touch base with, but which are in exciting states of development, such as precision laser spectroscopy, high energy probes of QED, and the interface of atomic and nuclear physics.

## PRINCIPAL DEVELOPMENTS

The history of experiments on this subject is short. We observe

that a serious experimental challenge was first issued only about a decade ago in 1968, particularly by the Frankfurt school. The theorist at that time even suggested the vehicle for achieving overcritical fields. It is very fortunate that their suggestion for using heavy-ion collisions to form superheavy quasiatoms coincided with the development of heavy-ion accelerators for nuclear physics investigations. The scenario, shown in Fig. 1, of how the formation of the quasimolecule can simulate the conditions for observing supercritical phenomena is very familiar to you at this stage of the conference, so that for the time being I only want to draw your attention again to the two important ingredients associated with the detection of the diving process to which we return later. One of these concerns the crucial role played by vacancy formation, which is a prerequisite for observing the decay of the vacuum by positron emission. The other is the duration of time spent in the collision when energy levels are supercritically bound, which is the significant factor determining the relative amplitudes for spontaneous and dynamic positron production. The success of the search for the "sparking of the vacuum" depends very much on how nature has arranged for both.

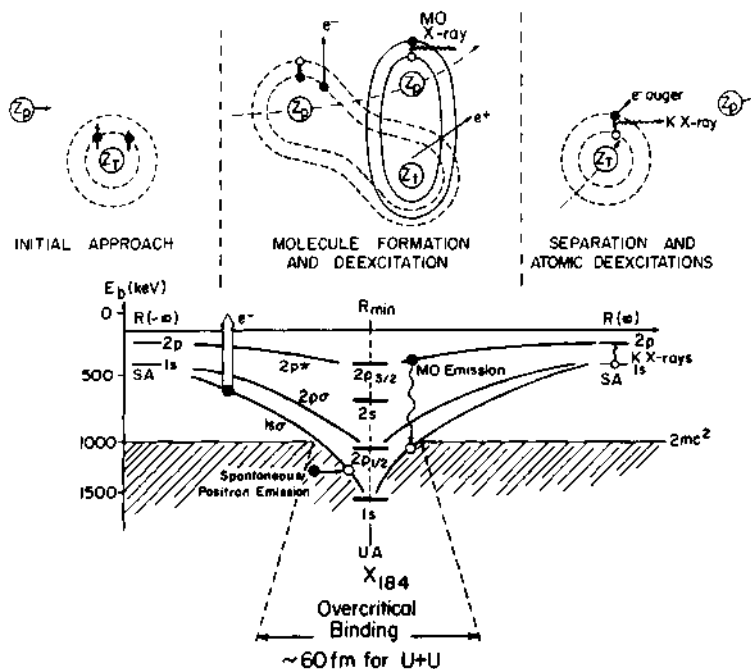


Figure 1. Schematic presentation of the evolution of quasimolecular orbitals in U+U collisions with united atom Z=184. Over-critical binding occurs at  $\sim \pm 30$  fm about  $R_{\min}$ , corresponding to a time of  $\sim 2 \times 10^{-21}$  sec for a Rutherford trajectory.

Progress beyond Gedanken experiments actually only came after April 1976 when the first uranium beams were accelerated at GSI to energies sufficient to reach the Coulomb barrier for the heaviest nuclear species. With this new experimental capability, a new field of investigation emerged dealing with atomic processes in strong fields with couplings  $Z\alpha > 1$ . The fact that two uranium atoms could be brought together to transiently form a quasiatom with  $Z=184$  was the catalyst to mount an assault on a whole range of fundamental questions which, for a long time, had been considered only academic. Although in the five years that have elapsed since that achievement at GSI we have not been able to categorically answer the two questions posed by Walter Greiner a few days ago regarding the detection of spontaneous positron emission and the formation of a superheavy nuclear composite system, an impressive amount of progress has nevertheless been documented at this conference. In fact, my impression is that presently we are in a very exciting period with a pervasive sense of expectation, and that the answers to Greiner's questions may very well be available in the near future.

In particular, a number of speakers have shown that the following important information has already been accumulated.

1. It has been established that the formation of superheavy quasi-molecules in collision systems such as  $\text{Pb}+\text{U}$ ,  $\text{U}+\text{U}$ ,  $\text{Pb}+\text{Cm}$ , and  $\text{U}+\text{Cm}$  is a meaningful concept.
2. The K-vacancy formation process has been shown to exhibit properties that are favorable to observing the spontaneous emission of positrons, both as regards to its amplitude and to its dependence on the internuclear separation.
3. In superheavy collision systems  $e^+$  production is observed considerably in excess of the intensity expected from nuclear internal pair conversion decay of nuclear states excited in the collision.
4. The magnitude of the  $e^+$  production cross section, its strong dependence on the minimum internuclear separation,  $R_{\min}$ , and the rapid increase of the  $e^+$  production probability with total projectile-target charge cannot be accounted for without invoking the quasiatom as the source.
5. A good theoretical understanding of the dynamic  $e^+$  production processes in heavy-ion collisions has been achieved.
6. Most recently, structure has been observed in positron spectra

which indicates the presence of a source of positrons in addition to the well-established dynamic processes. It seems to be connected with specific kinematic conditions. Its association with either nuclear processes or with spontaneous positron decay of an overcritically bound state is under investigation.

Using the work presented at this meeting, let me try to comment briefly on the main points of these major steps in developing answers to the four questions I posed earlier, and attempt to put them in perspective.

### INNER-SHELL IONIZATION

Access to information on the strong-binding phenomena in quasi-atoms all starts with the ionization process involving the inner-shells. While the excitation process leads to delta electron emission, the de-excitation of the vacancy can occur via the emission of characteristic X-rays, Auger electrons, molecular orbital X-rays and positrons. The detection of these emissions, as we have heard, constitute the experimental probes for the problem. It is also worthwhile to point out, as a general observation, that for superheavy collision systems, a dominant common feature governing the electron, X-ray and positron emission processes is the very strong increase of transition matrix elements at small internuclear separations. The important implication that follows this fact is that the structure of the quasiatom at small internuclear separation can be studied.

In this connection, Bosch, in an excellent summary of recent work concerning inner-shell ionization, brought out several critical points. He illustrated with Fig. 2 how the Doppler Shift technique, introduced by Greenberg and coworkers to measure the impact parameter dependence of K X-ray emission, established that the ionization of the  $1s\sigma$  state in superheavy quasimolecules is predominantly concentrated at small internuclear separations. This observation together with a concurrent determination that the cross section for  $1s\sigma$  ionization was of the order of several barns for these heavy systems are, of course, central to the spontaneous positron search experiments. It is clear that to observe spontaneous positron production requires that  $1s\sigma$  vacancies be present at small internuclear separations. It was noted by Armbruster that the large experimental ionization cross sections conflict with the pessimistic estimates from non-relativistic calculations. In fact, if this discrepancy had not been so large, the positron search experiments would have been relegated to failure.

Both Dr. Bosch and Professor Armbruster impressed us further with the quantity and variety of data that has been accumulated on the

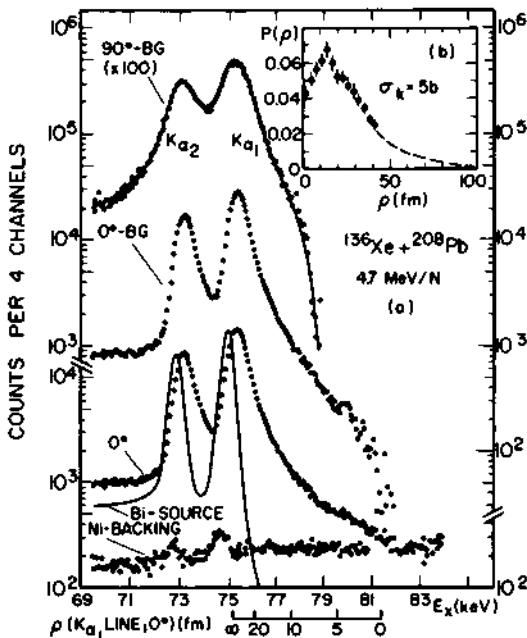


Figure 2. Doppler broadening of K X-rays emitted at  $0^\circ$  to the beam direction used to measure the impact parameter dependence of the  $1s\sigma$  ionization probability by Greenberg, *et al.* (a)  $K\alpha_1$ - $K\alpha_2$ -line profiles of Pb from  $^{136}\text{Xe} + ^{208}\text{Pb}$  collisions observed at  $0^\circ$  before and after background (BG) subtraction, and at  $90^\circ$  after BG subtraction. Also shown (bottom of figure) is the normalized background from the Ni beam stop, and the  $K\alpha_1$  and  $K\alpha_2$  lines of Pb from  $^{208}\text{Bi}$  decay. The solid line through the  $90^\circ$  spectrum represents the  $90^\circ$  line shape calculated with a  $P(\rho)$  [inset (b)] extracted from the  $0^\circ$  line shape.

inner-shell ionization of superheavy collision systems. For example, the confinement of the  $1s\sigma$  ionization probability for these heavy systems at small impact parameters is now well documented (see Fig. 3) using a more conventional scattered-ion, X-ray coincidence technique. This feature was first predicted by Greiner, Müller, Soff, Betz, and their co-workers as originating with the extreme relativistic properties associated with the strong fields generated by the superheavy quasiatoms. More specifically, the underlying properties responsible for this behavior are the rapid increase of the binding energies of the deepest bound quasimolecular states with decreasing internuclear separation, and the accompanying typical relativistic collapse of the wave functions about the nuclear centers. I draw your attention to the particular point that it is the molecular description of the ionizing process that leads to these special properties which in turn lead to the important consequences predicted by

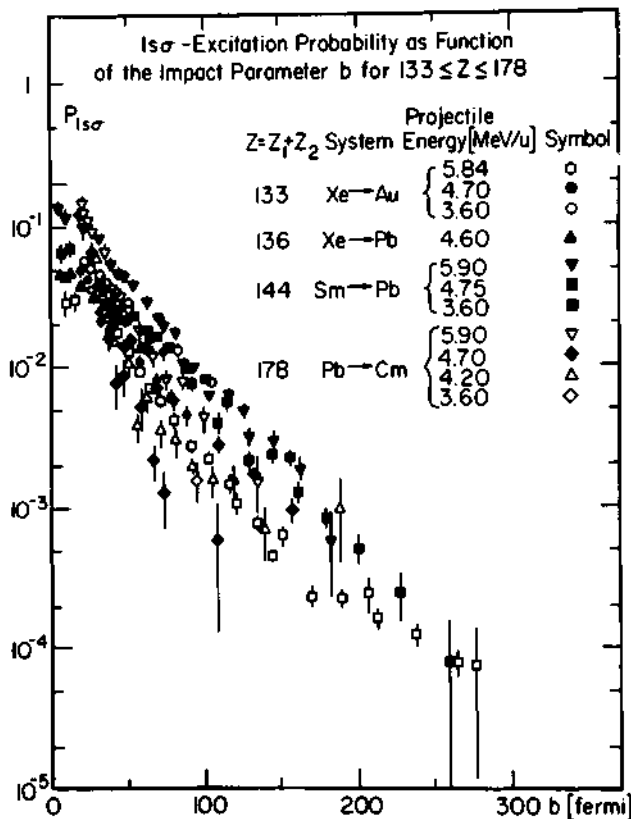
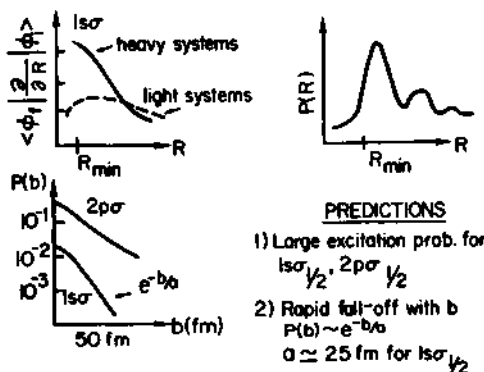


Figure 3. The  $1s\sigma$ -excitation probability,  $P_{1s\sigma}$ , for a number of superheavy collision systems as a function of the impact parameter  $b$ , from data by Armbruster, Bosch, Liessen, Mokler, et al. The maxima for the excitation cross sections are confined well within 50 fm.

the Frankfurt theory and sketched in Fig. 4. These are (1) The radial coupling matrix elements are large and dominate at small  $R$  contrary to the behavior found in light collision systems. (2) The ionization probability is concentrated at the distance of minimum approach,  $R_{\min}$ , since it is here the states are changing so rapidly that the electrons cannot keep up. These features produce the observed  $P(b)$ . The large minimum momentum transfer required, which is characteristic of the strongly bound states of the quasimolecule (and not of the individual atoms), sets the scale for this spacial confinement. The very large enhancement of the electron wave function at small distances about the two nuclear centers leads to the large cross sections observed.

The interplay of the momentum transfer and the spacial confine-

ment for the ionization probability has also been demonstrated to be of some quantitative interest to us. Müller developed the explicit relationship in the form of a scaling law, shown in Fig. 4, which is derived from an analytical model based on first order perturbation theory. It is also inherent in the Bang-Hansteen scaling rule for Coulomb ionization,  $\Delta E = \hbar C v / b$ . Bosch, Armbruster and their coworkers have developed this idea further and have demonstrated in their lectures how successful it is in unifying the large body of data shown in Fig. 5. However, this success is somewhat tempered by questions regarding the range in  $R_0^*$  over which the scaling is valid, the effect of smearing out the ionization over a range of internuclear distances, and the theoretical justification for using first order perturbation theory in a situation where multistep processes are known to be important. The consequences of all the approximations made have yet to be determined.



$$P_{1s\sigma}(b) = D(Z) \exp \left[ -\gamma R_{\min} E_{1s\sigma}(R_{\min}) / \hbar v \right] = D(Z) \exp \left[ \gamma \tau E_{1s\sigma}(R_{\min}) / \hbar \right]$$

$$\Delta E = C \frac{\hbar v}{b}$$

Figure 4. Sketch of the behavior of the radial matrix elements and excitation probabilities,  $P(b)$ , as a function of the internuclear separation and impact parameter for the ionization of the inner-shells of superheavy collision systems (after calculations by Betz, Soff, Müller, Greiner, *et al.*). The first order perturbation theory scaling law by Müller, *et al.*, is shown.

A case in point has centered around the discussion to exploit the scaling law to extract the binding energy of the quasimolecular state being ionized at the distance of closest approach. In this connection,

\*  $R_0$  and  $R_{\min}$  have been used interchangeably by various authors.

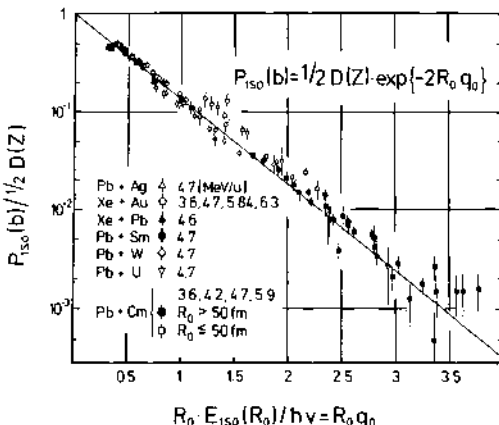


Figure 5. Unification of the  $1s\sigma$  excitation data for superheavy collision systems by the scaling law derived by Müller, *et al.*, and Bosch, *et al.* Here  $R_0$  is the minimum internuclear separation and  $q_0$  is the minimum momentum transfer.

Armbruster discussed several collision systems for which this procedure was taken literally to deduce the  $1s\sigma$  quasimolecular energy level structure. The results obtained for the  $1s\sigma$  state in the  $\text{Pb}+\text{Cm}$  system, shown in Figs. 6, 7, imply rather startling deviations from the solutions of the two-center Dirac equation. It is clear that this challenge cannot be taken too seriously without further consideration of the theoretical details and some of the experimental ambiguities. On the other hand, although the scaling law may be a limited spectroscopic tool, it is very useful for anticipating the behavior of Coulomb ionization with kinematic variables including some aspects of positron creation in heavy-ion collisions.

There is one more important aspect to emphasize regarding the role played by the inner-shell vacancy production studies in the developments I listed earlier. They have provided us with some of the more convincing evidence for quasimolecule formation in superheavy collision systems by showing that quasimolecular levels are participating in the excitation mechanism. We have seen that the cross sections and the spacial confinement of the ionization probability depend very sensitively on the binding energies and would be quite different if the projectile or target atomic energy levels were involved. Moreover, the shapes of the cross-sections for target and projectile excitation shown by Arm-

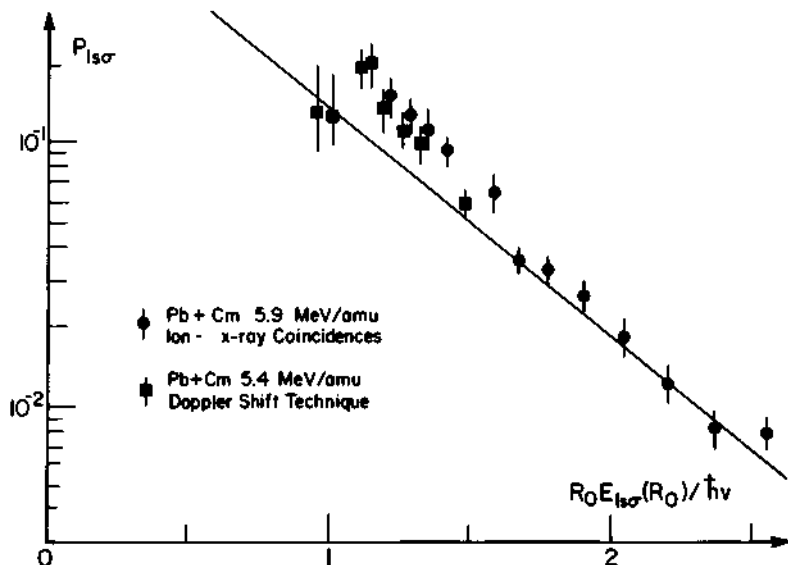


Figure 6.  $P_{1\text{iso}}$  vs.  $R_0 E_{1\text{iso}}(R_0) \hbar v$  obtained by ion-K X-ray coincidence and Doppler shift techniques (see lecture by Bosch).

$$P_{1\text{iso}}(b) = D(Z) \exp(-\gamma E_{1\text{iso}}(R_0) R_0 / \hbar v)$$

measured at two energies,  $R_0$  Constant

$$E_{1\text{iso}}(R_0) = \frac{\hbar v_1 v_2 \ln(P_{1\text{iso}}(b_1)/P_{1\text{iso}}(b_2))}{\gamma R_0 (v_1 - v_2)}$$

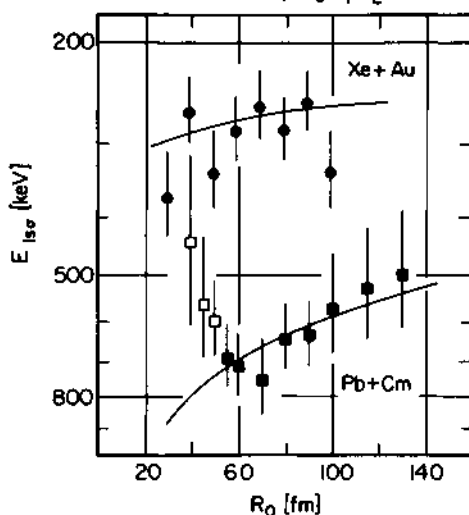


Figure 7.  $E_{1\text{iso}}$  derived from the scaling law shown using the ion-K X-ray coincidence technique measurements for the  $Xe + Au$  and  $Pb + Cm$  collision systems (see lecture by Armbruster).

bruster is very indicative of a primary excitation of a molecular orbital followed by a Meyerhof-Demkov sharing mechanism near a matching of molecular orbitals. Figure 8 illustrates how impressive the data has become in tracing this mechanism from the K-shell to some of the higher orbitals. This is a very characteristic molecular effect. The fact that the cross-sections for  $1s\sigma$  and  $2p\sigma$  ionization only seem to depend on  $(Z_1 + Z_2)$ , shown in Fig. 9 from data by P. Mokler and colleagues, further reinforces the view that it is the states of the quasi-atom  $(Z_1 + Z_2)$  which determine the ionization probability.

### DELTA-ELECTRON EMISSION

Complementing the study of characteristic X-rays,  $\delta$ -electron

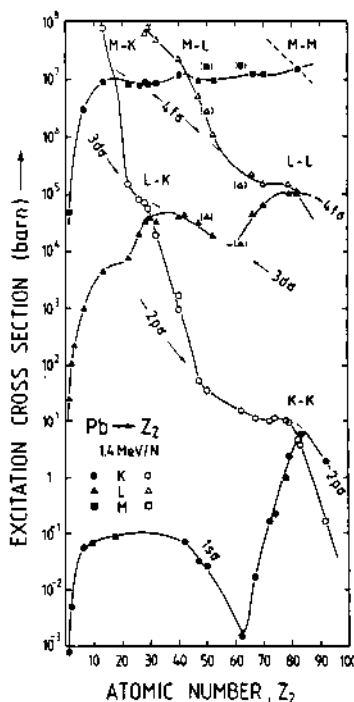


Figure 8. Survey of projectile and target atom excitation for 1.4 MeV/amu  $\text{Pb}+Z_2$  collisions (Schönfeldt, Mokler, Armbruster, et al.). The cross-sections for the different shells are plotted as a function of  $Z_2$ .)

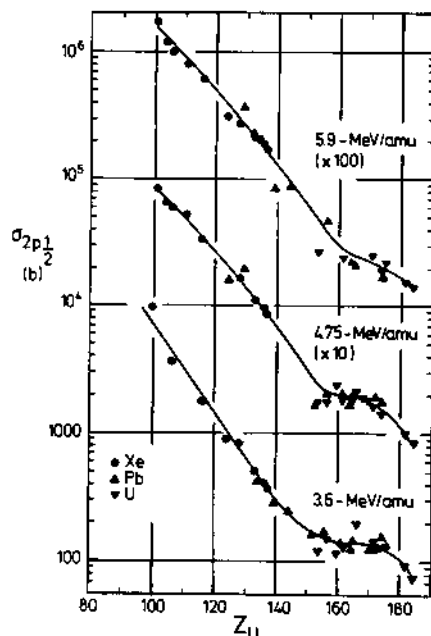
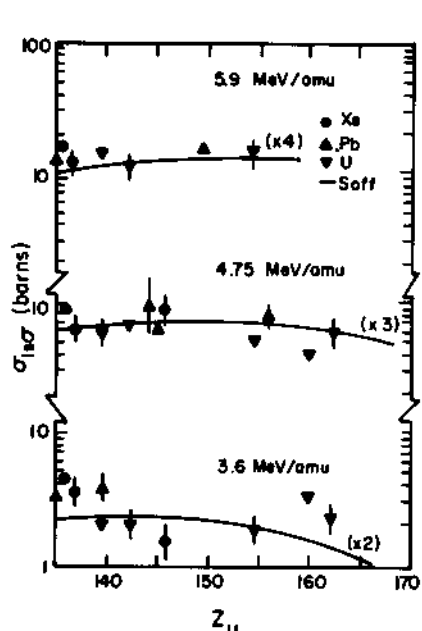


Figure 9.  $1s\sigma$  and  $2p_{1/2}\sigma$  excitation cross-sections as a function of  $Z_u = Z_1 + Z_2$  for  $X_e$ ,  $Pb$  and  $U$  projectiles on  $Z_2$  targets at 3.6, 4.7 and 5.9 MeV/amu bombarding energies. Data are from Anholt et al., and Behncke et al.

emission has recently also become a source of information on the quasi-atomic wave function. It is obvious that in detecting the delta electrons we are obtaining one more differential piece of information not available in the total vacancy production studies via X-ray deexcitation; i.e., we define the energy transferred to the ejected electron. In particular, the high energy component of this spectrum reflects the high momentum components of the quasiatomic wave functions, which, in turn, provide the information regarding close encounters. In fact, the  $\delta$ -electron spectrum is a probe of the inner-shell electronic form factor corresponding to the distance of closest approach, since the ionization predominantly is concentrated in this region. Since we are dealing with a scattering system and not a stable atom, measuring this form factor, while fixing the distance of closest approach, may provide one of the more powerful tools to study quasiatoms.

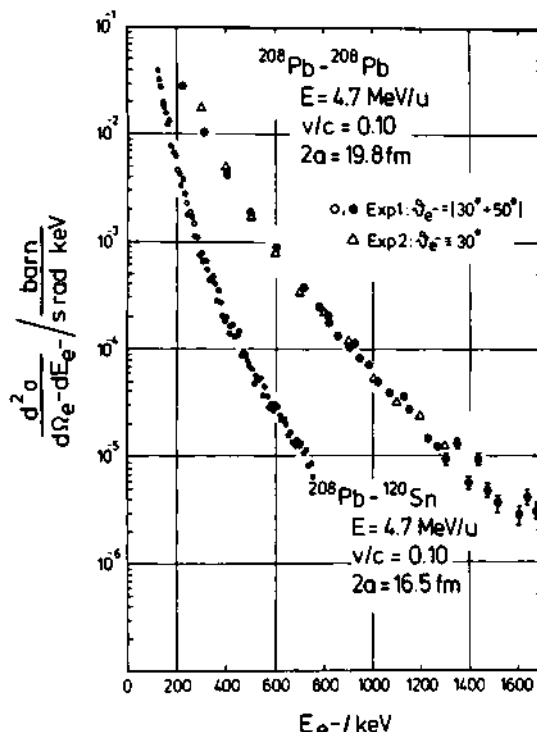
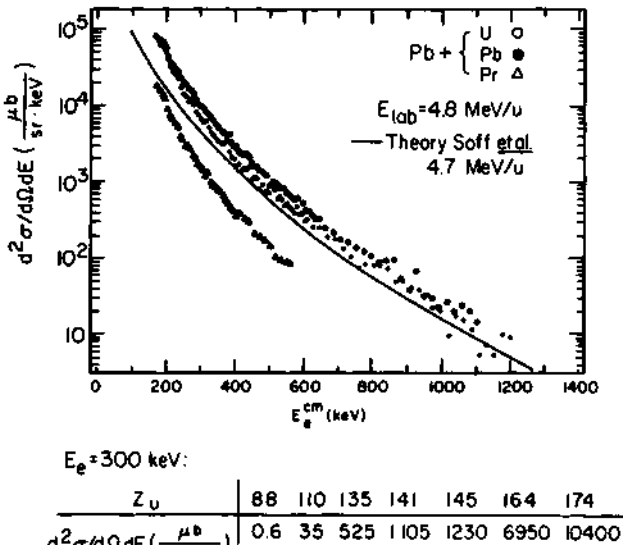


Figure 10. Delta-electron spectra from Pb-Sn ( $Z_u = 132$ ) and Pb-Pb ( $Z_u = 164$ ) collisions. Excited states not specified. Data from Kozhuharov, et al.

Kozhuharov showed us some interesting results. With data like that shown in Fig. 10 he illustrated the detection of the high energy electron component which, of course, reflects the deep binding in the quasimolecule and demonstrates that we are not dealing with the atomic states of the individual atom. With Fig. 11 he showed how the cross section at a particular electron energy grows with the united atom  $Z_u$ , exposing in a dramatic fashion the relativistic contraction of the wave function. The exploitation of X-ray, electron coincidences in data as shown in Fig. 12, indicates that we can now isolate individual inner-shell transitions, and further emphasizes the utilization of  $\delta$ -electron detection as a powerful tool for the future.

#### MOLECULAR ORBITAL X-RAYS

Let us turn briefly to the other potential source of information on quasimolecular structure, MO X-ray emission. Several lectures were given on this subject by Dr. Heinig and Dr. Vincent. It would be expected that among all the probes available MO transitions would provide



$$d^2\sigma(Z_u=174)/d^2\sigma(Z_u=88) = 1.7 \cdot 10^4$$

Figure 11. Dependence of delta-electron cross-section on combined charge of the collision system  $Z_u$ . Data by Kozhuharov *et al.*, and calculation by Soff *et al.* (see lectures by Ch. Kozhuharov and G. Soff).

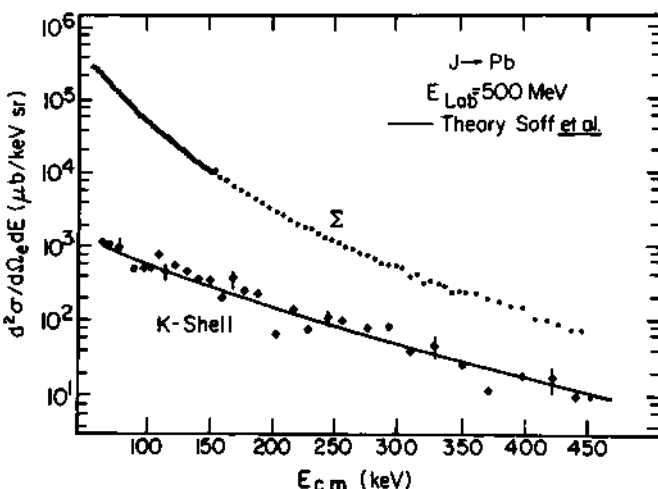


Figure 12. Delta-electron spectra from I-Pb collisions ( $\frac{v}{c} = 0.09$ ) associated with Pb K X-rays. The solid line represents a calculation by Soff *et al.* Also shown is the singles delta-ray spectrum ( $\Sigma$ ). Data are from Kozhuharov *et al.* (see lectures by Ch. Kozhuharov and G. Soff).

one of the more direct sources of information on molecular orbitals, and in our optimistic moods, we hoped that it would be possible to trace the MO energy level structure, if not into the negative energy continuum, into the region prior to diving. This has not come to pass for a variety of reasons discussed by our lecturers, although a valiant effort has been made by many workers.

Figures 13 and 14 illustrate some typical spectra that have been obtained for both low and high Z systems. They are characteristically what one expects, an undistinguished continuum with, unfortunately, prominent collision broadened high energy tails. A general scaling with Z is evident, but the identification of such spectra with MO transitions has only been qualitative. Some of these qualitative signatures are as follows:

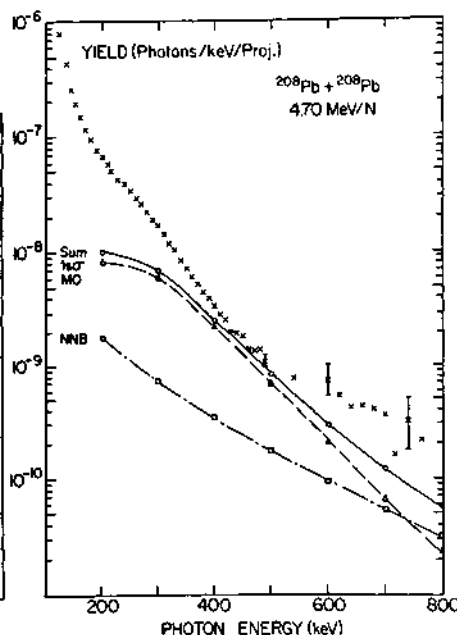
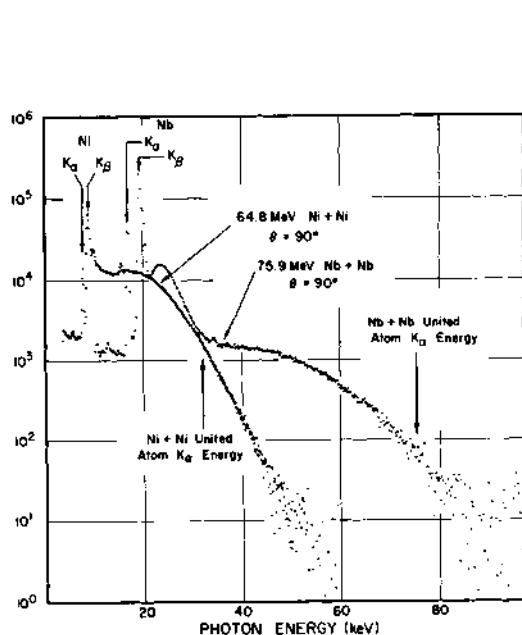


Figure 13. MO X-ray spectra from Ni - Ni and Nb - Nb collisions. Measurements are by Vincent and Greenberg.

Figure 14. MO X-ray spectra from Pb + Pb collisions by Meyerhof et al. (see lecture by P. Vincent).

1. A general agreement has been found between the experimental spectral shapes and intensities and theoretical calculations.
2. The observation of a predicted photon frequency dependent emission anisotropy has been verified.
3. The emitter velocity corresponds to the center of mass.
4. Backgrounds such as nucleus-nucleus bremsstrahlung, electron bremsstrahlung, radiative electron capture, etc., have been excluded as possible explanations for the total intensities observed.

However, extracting quantitative information from these spectra in the traditional spectroscopic sense has proven to be a much more formidable task. The limitations have been set by the availability of mostly total spectra of complex character to which many transitions contribute and are not resolved. Collision broadening further complicates matters. In an attempt to develop further quantitative information, more difficult differential-type measurements have been pioneered recently. Fig. 15 shows results from an attempt to map the impact parameter dependence of the MO spectrum from  $\text{Pb}+\text{Pb}$  collisions. A successful effort has recently been made to establish a conventional one-to-one spectroscopic correlation between energy levels and specific

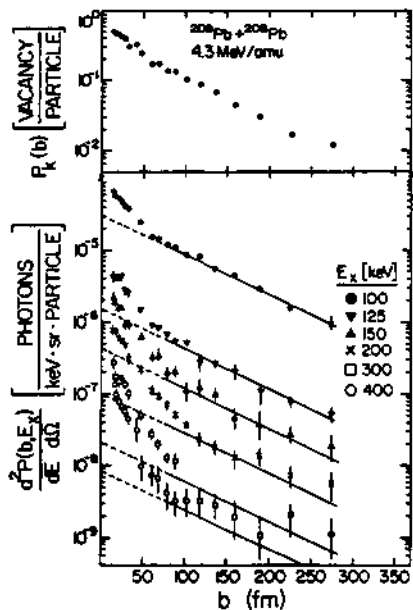


Figure 15.  
Impact parameter dependence of X-ray production in 4.3 MeV/amu  $^{208}\text{Pb}+^{208}\text{Pb}$  collisions showing two component structures of  $P(b)$  curves (data by Schmidt-Böcking, et al.).

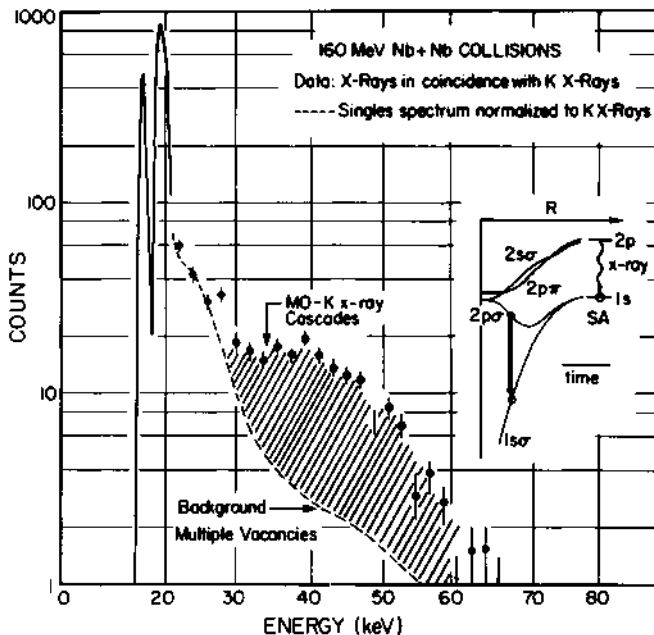


Figure 16. MO X-rays observed in coincidence with K X-rays to isolate transitions to the  $1s\sigma$  state. The shaded area corresponds to intensity of cascade transitions (data by Liarokapis, O'Brien and Greenberg).

transitions by isolating transitions to the  $1s\sigma$  state by a coincidence technique illustrated in Fig. 16. Even with these more penetrating probes, however, it is difficult to see how the study of MO radiation can develop into a real spectroscopic tool in the conventional sense. Most probably it will stand with the other tests of quasimolecular wave functions and transition matrix elements.

#### THE ROLE OF DYNAMIC PROCESSES

My overview of your lectures thus far has been mainly slanted towards emphasizing the first two important points of progress in this field which I listed earlier. They are that we seem to be forming superheavy quasimolecules in collisions near the Coulomb barrier with very deeply bound  $1s\sigma$  states, and that the essential  $1s\sigma$  vacancy production probability is large and concentrated at small internuclear separations where the vacancies are needed to observe the spontaneous positron emission process. With these essential ingredients available, the obvious question then naturally follows as regards to why a positive identification of the spontaneous positron emission process has yet to be made.

Part of the answer to this question is supplied by the experiments I just discussed which have established one other very relevant point. It is evident that we are not dealing with a static system and dynamic effects permeate, and sometimes dominate, all of quasimolecular physics. They are responsible for the vacancies, the  $\delta$ -electrons, and they complicate the MO spectra. Fig. 17 illustrates this point by sketching the difference in the roles played by collision broadening in heavy systems colliding near the Coulomb barrier, and in light systems at energies used in conventional atomic collision physics.

The dynamic effects are a major source of positrons in heavy-ion collisions and constitute the major obstacle in the search for spontaneous positron emission. Our speakers have pointed out the positron production amplitudes, shown schematically in Fig. 18, which are associated with the time-varying fields, and discussed the complications introduced by coherence. The same matrix elements responsible for ionization of bound electrons can induce the excitation of negative energy electrons into unfilled bound states and into the positive energy continuum. In fact, the behavior of the dynamic positron production probability much resembles the ionization process. In addition, we have seen that the situation is further complicated by pair creation from nuclear excitations, so that the task has been to extract spontaneous positron emission embedded in this complex positron spectrum. The progress in achieving this goal, so far, reflects the complexity of this task.

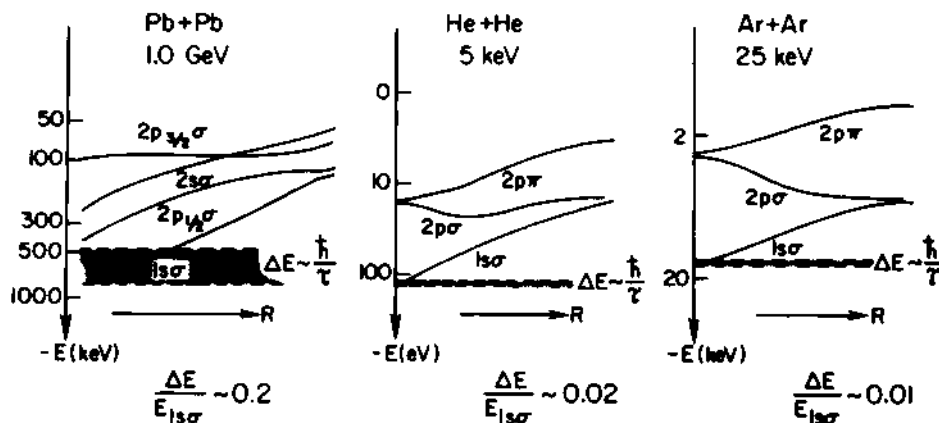


Figure 17. Collision broadening in heavy and light systems under difference bombarding conditions.

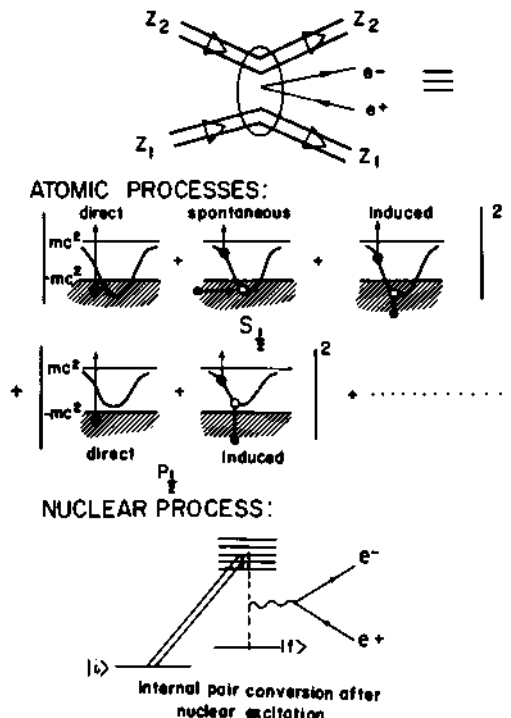


Figure 18. Atomic and nuclear positron production mechanisms in time-varying fields of the collision partners.

#### THE SEARCH FOR SPONTANEOUS POSITRON EMISSION

Of course, any separation of the positron production processes depends on identifying a characteristic behavior of each of these processes (or coherent combinations) with the experimental variables available. The latter include the total charge of the colliding system,  $Z_{ua}$ , the distance of minimum approach between nuclear centers,  $R_{min}$ , the relative velocity of the collision,  $v$ , the positron energy spectrum and emission angle, and the nuclear parameters. For the case of sub-Coulomb scattering, they determine, in an interrelated way, the strength of the central perturbing field and the potential binding of quasimolecular states, the spacial extent of the states, the Fourier frequencies inherent in the collision, the energy transfer to the leptons, and the nuclear excitations. In general, a contribution from the spontaneous emission process has to be sought at small  $R_{min}$ , well within the critical radius, as a deviation from dynamic processes acting alone. In the static limit,  $R_{min}$  and  $Z_{ua}$  are the only parameters associated with spontaneous emission.

Reinhardt has told us that for the sub-Coulomb scattering situation the positron emission features, as a function of the variables mentioned, merge from subcritical to critical systems without any distinguishing signatures to identify the transition. This is evident in the calculated positron spectra, shown in Fig. 19, a very discouraging prediction. If nuclear reactions contribute, however, the situation can change appreciably. In this case, the important new quantities to measure in addition are the mass transfer, the energy loss, and the emission angles for the reaction products and their identification. The theorists have emphasized that the significant new ingredient is the time delay associated with the reactions. As shown by Reinhardt in Fig. 20, interference wiggles are expected to appear in the positron spectrum, and as the threshold for critical systems is passed, the spontaneous amplitude builds up with delay time which can lead to a sharp peaked structure

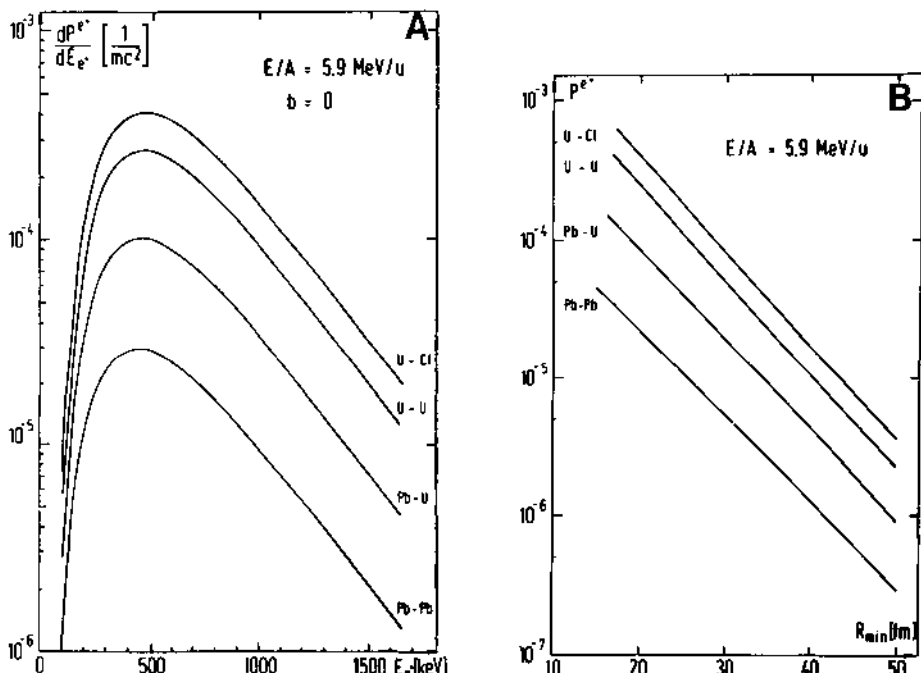


Figure 19. a) Calculated energy spectra of positrons created in 5.9 MeV/amu head-on collisions of  $Pb+Pb$ ,  $U+Pb$ ,  $U+U$ , and  $U+Cl$ .  
 b) Emission probability of positrons in 5.9 MeV/amu collisions as a function of  $R_{min}$  (see lecture by J. Reinhardt).

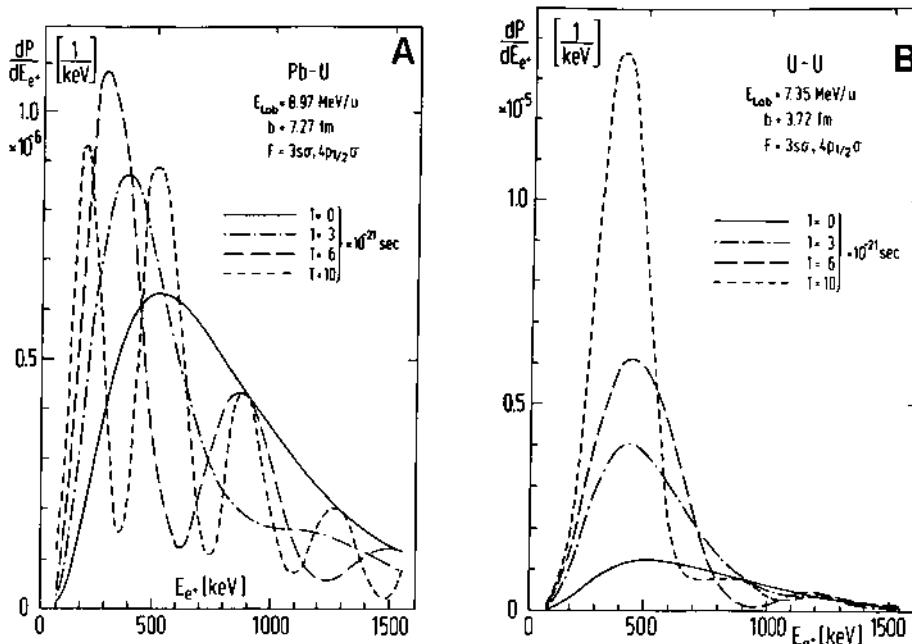


Figure 20. Spectra of positrons created in a subcritical (a), and in a supercritical (b) collision system, taking into account in a schematic model time delay,  $T$ , due to nuclear reactions. Calculations have been carried out by U. Müller, *et al.* Whereas, for the subcritical system, modulations in the positron spectra are present, a distinct peak at the "resonance" energy  $E_{1s0}(R_{\min})$  builds up for systems with  $Z_u > 175$  (see lecture by J. Reinhardt).

easily identifiable. In view of these open-ended scenarios and the possibility that reality may not entirely conform to any of these theoretical descriptions, the option for the experimentalist seems to be, as Kienle alluded to, measure everything. This also, as always, seems to be the theorist's clarion call. As we have seen during the discussions of the past weeks, the experimentalists have tried to comply valiantly.

We have heard from three groups reporting their work. All have carried out their experiments at GSI, Darmstadt, so that there is some interdependence of the measurements or the approach. However, the experiments are sufficiently diverse in their detection systems to pro-

vide complementary emphasis on the information gathered, as well as important comparisons of results for what are inherently very difficult measurements. Small cross-sections, and the requirement for differential information, have dictated the small data accumulation rates, long irradiation times, and the slow assimilation of information.

The positron detection systems all feature some version of the following capabilities:

1. A transport system for  $e^+$  and  $e^-$  to remove them from the target area.
2. An  $e^+$  energy measurement.
3. Discrimination against  $e^-$ .
4. Identification of  $e^+$ .
5. Scattered-ion detection: angle, energy, various degrees of kinematics.
6. Gamma-ray detection for monitoring nuclear reactions.

I refer you for details to the original presentations, but I do want to emphasize one important aspect of the experiments.

The ability to closely define the scattered-ion kinematics seems to constitute an essential part of the measurements. As was demonstrated in the work reported by Bokemeyer, the coincidence detection of both scattered particles to specify a class of events corresponding to a narrow angular region of scattering and a narrow region of energy loss close to the elastic scattering seems to be responsible for revealing the interesting peak structures in the positron spectrum that are observed in these experiments. From these observations, it becomes clear that poor kinematic selection which can accompany the detection of only one particle in the final state with poor energy resolution or averaging over a large angular region may reduce the selectivity against backgrounds which obscure these features under some experimental conditions. Such considerations may account for some of the apparent differences in the observation of structure in the positron spectra reported by the three groups to date, and for some of the inconsistency in reproducing data in some of the experiments.

### (1) Early Experiments

Let me begin an overview of the results from the positron detection experiments with some of the results on which everybody agrees. One reason for the unanimity is that all the experimenters were then involved together in these particular measurements. Being the first experiments of this type, the goals were modest. At that time there were only the theorist's predictions that positrons related to atomic processes would be seen in sufficient numbers not to be overwhelmed by positron production from nuclear origin, such as internal pair conversion of gamma-ray transitions. One of the first tasks was to determine the level of signal to background.

In this regard, the first measurements on the  $^{208}\text{Pb} + ^{208}\text{Pb}$  collision system, using the small solenoid described by Backe, played an important role. With the nuclear background particularly simple to evaluate in this case because of the exceptional stability of  $^{208}\text{Pb}$  to nuclear excitation, results such as shown in Fig. 21 are the first convincing demonstration of positron production from QED processes in heavy ion collisions not associated with nuclear structure. The

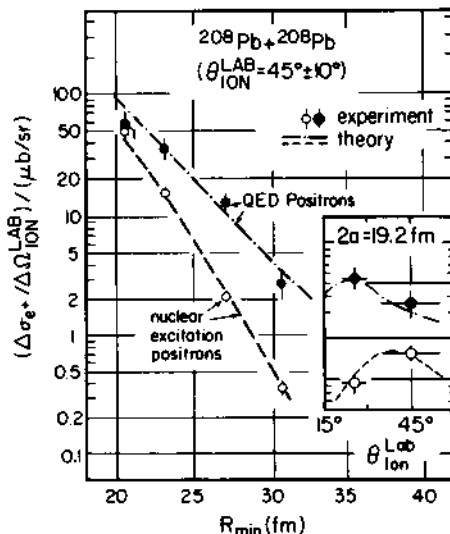


Figure 21. Differential positron cross sections as a function of  $R_{\min}$  for  $^{208}\text{Pb} + ^{208}\text{Pb}$  collisions. The inset shows an angular distribution for  $2a = 19.2$  fm. The nuclear excitation positrons form only a fraction of the whole differential cross-section (see lecture by H. Backe).

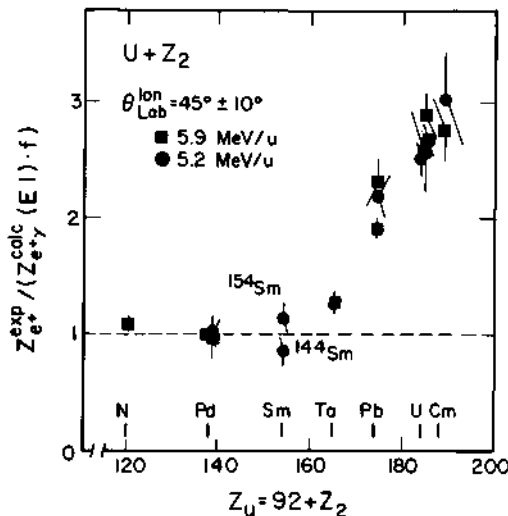


Figure 22. The ratio of measured positron yields to those calculated from the  $\gamma$ -ray yields assuming E1 multipolarity. The factor  $f$  is close to unity. The measurements were carried out with the spectrometer described by H. Backe. For  $Z_u > 174$ , there is a rapid increase of positron production with increasing  $Z_u$  over that expected from the  $\gamma$ -ray intensities.

good agreement with theory associates the excess positron production with the strong, time-varying Coulomb field of the quasiamionic complex.

The measurements on the collision systems Pb+U and U+U carry these investigations into another heavier subcritical system, but with different background considerations, and into a supercritical system, respectively. The interesting qualitative observation, illustrated in Fig. 22, is the spectacular increase in positron production over that expected from nuclear internal pair conversion alone as  $Z_{ua}$  increases. The data in Fig. 23 and 24 show that the positron emission probability behaves very similarly with  $R_{min}$  and with the relative ion velocity for all three systems. There are no surprises. These first experiments principally developed information on the dynamic positron creation mechanisms associated with the time-varying fields generated by the combined nuclear charge, and the results can be summarized as follows:

- (i) Atomic QED processes account for the major fraction of the total positron creation cross-section in superheavy collision systems.

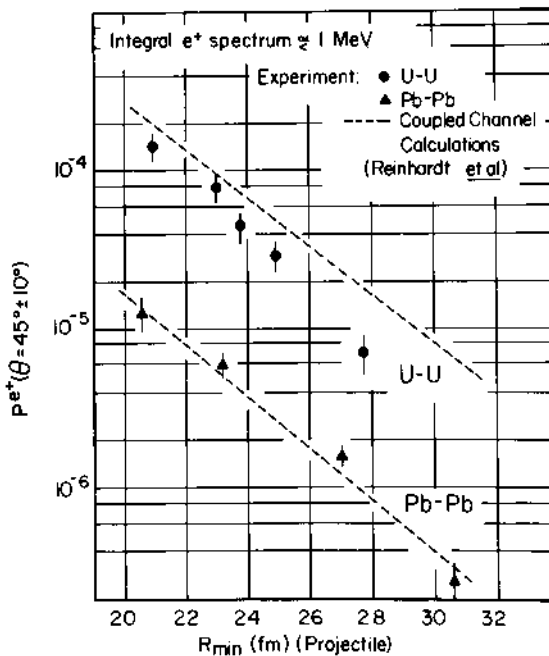


Figure 23. Positron production probabilities for a fixed scattering angle of  $45 \pm 10^\circ$ , but with relative ion velocity,  $v$ , varied to determine  $R_{\min}$  (see lecture by H. Backe).

(ii) The positron creation probability associated with quasi-atomic processes exhibits a rapid exponential fall-off with  $R_{\min}$  at constant collision velocity. This behavior parallels that found for the ionization probability of inner-shell electrons and reflects similar mechanisms. In this case, the minimum energy transfer is given by the energy gap  $2mc^2$  for pair creation which sets the scale for the spacial confinement of this process as it did for the ionization process through  $e^- \alpha R_{\min} \Delta E / \hbar v$ .

(iii) The most striking feature of the data is the almost exponential increase of the positron excitation probability with increasing  $Z_p + Z_T$  shown in Fig. 25, reflecting the relativistic enhancement of the wave functions about the nuclear centers.

All these earlier experiments, of course, represent very significant steps in developing confidence in our understanding of the dynamic aspects of pair creation in heavy-ion collisions. But they also indicated that a signature for a contribution from spontaneous positron emission is

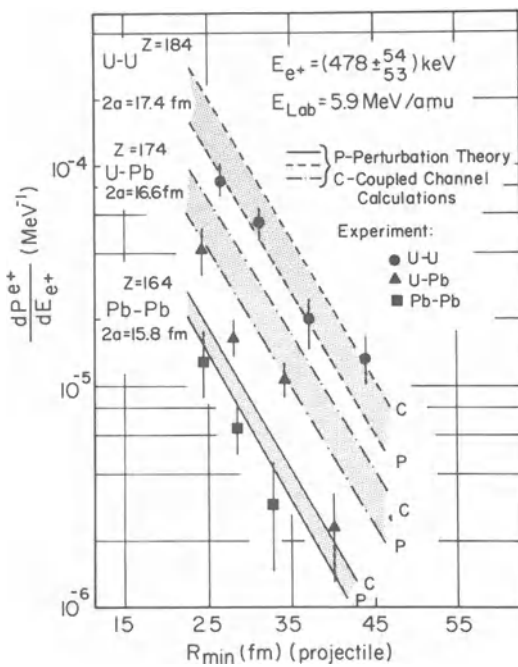


Figure 24. Positron production probabilities at 5.9 MeV/amu as a function of  $R_{\min}$  (see lecture by P. Kienle).

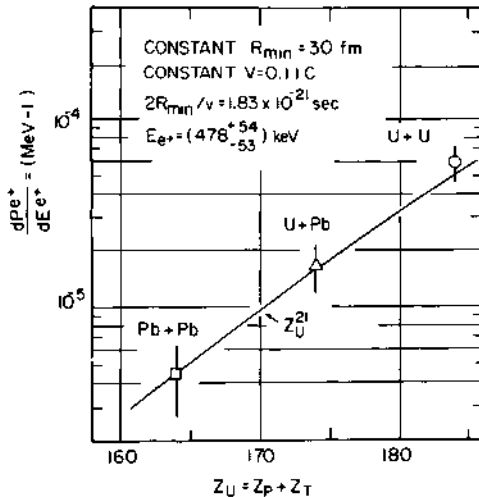


Figure 25. The dependence of the positron emission probability on the total charge of the collision system. This extraordinary behavior reflects the relativistic properties of the super-heavy quasatomic system.

not readily forthcoming in any gross feature, such as in a dramatic change in the  $R_{\min}$  dependence of the total positron excitation probability as  $R_{\text{crit}}$  is passed. It is clear that the effect has to be sought in finer details. For instance, long-lived nuclear composites, which would enhance the spontaneous amplitude, could be expected to be reflected in a strong correlation between the positron energy distribution and the reaction kinematics, but still contribute little to the total positron creation probability. Therefore, the fact that one did not observe any dramatic effects in the  $R_{\min}$  dependence of the total positron creation probability as the critical internuclear separation is passed in U+U collisions is not too surprising. None would be expected if the ions followed Rutherford trajectories, and any nuclear reactions leading to time delay may comprise only a very small part of the total cross-section. It is clear that such arguments lead into a search for effects that are focussed in bombarding energy at specific kinematic scattering conditions and into selected positron energies.

## (2) Recent Experiments

These are the directions embarked on by the most recent experiments, so let me conclude by discussing the progress in these latest attempts to plunge into the vacuum in the order in which they were presented. It must be kept in mind that in all cases the data is very preliminary, and most likely should be more indicative of the kind of information being accumulated, rather than of a final result.

Kienle, Kozhuharov, Bosch and collaborators, recently have been investigating the positron spectra emitted in U+U and U+Th collisions near the Coulomb barrier in association with the angle of scattering of the colliding ions. Their data, as it was discussed at this conference, involves the detection of one scattered particle in the final state between scattering angles of  $20^\circ$  to  $50^\circ$ . The limited ability to select out elastic scattering events, or to specify reaction kinematics in general, reflects this somewhat unrestrictive condition of detecting only one particle with somewhat moderate energy resolution.

Some of their first results, shown in Fig. 26, exhibit an interesting enhancement of the positron spectrum from 5.9 MeV/amu U+U collisions near low positron energies and  $45^\circ$  scattering over that expected from pair production induced by the dynamic processes we discussed earlier. With further, more elaborate, measurements (see Fig. 27) this enhancement turns into a line-like structure at a positron energy of 370 keV which is superimposed on a broad distribution which

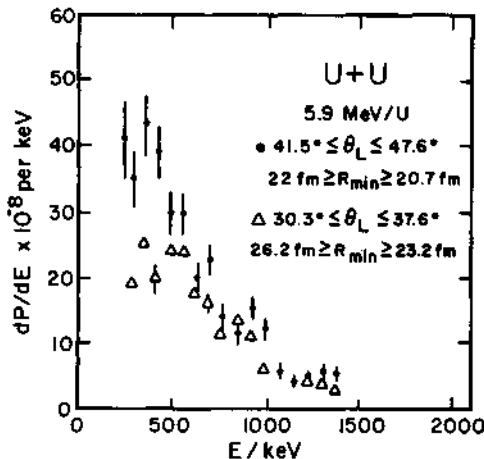


Figure 26. The positron production probability as a function of positron kinetic energy,  $E$ , for  $U+U$  collisions in coincidence with ions scattered into two angular ranges. Data from Kienle *et al.*

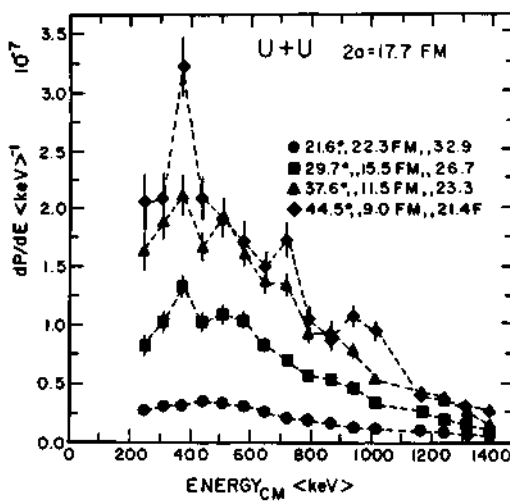


Figure 27. The positron production probability as a function of positron kinetic energy for  $U+U$  collision in coincidence with ions scattered into designated angular regions (see lecture by P. Kienle).

may or may not have structure itself. In another measurement, a similar line structure seems to be found in the U+Th collision system (5.9 MeV/amu) at a somewhat lower energy of  $\sim$ 270 keV. With the possible implication that finding such structures can have, it was disappointing, as Kienle put it, that attempts to reproduce these interesting results by the same apparatus were, apparently, not very successful.

Fig. 28 shows the results of some of these more recent measurements. The peaked structure appears to be a much less prominent effect, and the mean energy of the peak location is shifted to a lower energy of  $\sim$ 310 keV. At a bombarding energy of 6.0 MeV/amu, the peak structure is not evident within the statistical accuracy of the data. If not statistical in origin, the non-reproducibility of the data is a troubling aspect which is presently not well understood.

But, irrespective of some of these difficulties, some gross features of these new data reported are also very indicative that some interesting new phenomena are occurring. As shown in Fig. 29, Kienle, et al. find that for selected positron energies between 300 to 600 keV, and predominantly for particle emission near  $45^\circ$ , there is a rapid increase in the positron production cross-section with increasing bombarding energy which exceeds the expected increase from dynamic processes and is not mirrored in an equal increase in the  $\gamma$ -ray production by reactions. One implication is that the enhanced positron production may be associated with the formation of nuclear structures as the Coulomb barrier is being crossed. Of course, there is a question of whether this source of positrons is atomic in origin or whether it reflects a process like internal pair conversion of monopole transitions which are excited as we cross the threshold for nuclear reactions, but are not detectable through  $\gamma$ -ray emission.

The work presented by Backe, Kankeleit and coworkers, in general, seems to give a similar impression; there are some features in the positron spectrum that cannot be associated with the dynamic positron production processes where the scattered ions follow purely Coulomb trajectories.

One of these interesting results presented by Backe is reproduced in Fig. 30. All the data is for 5.9 MeV/amu U ions, for which a coincidence was required between the positrons and one of the scattered ions detected in a plastic scintillator at  $45 \pm 10^\circ$  in the laboratory with rather poor energy resolution. The spectrum for the low  $Z_{ua} = 138$  system, U+Pd, for which only nuclear positrons are expected with a measurable

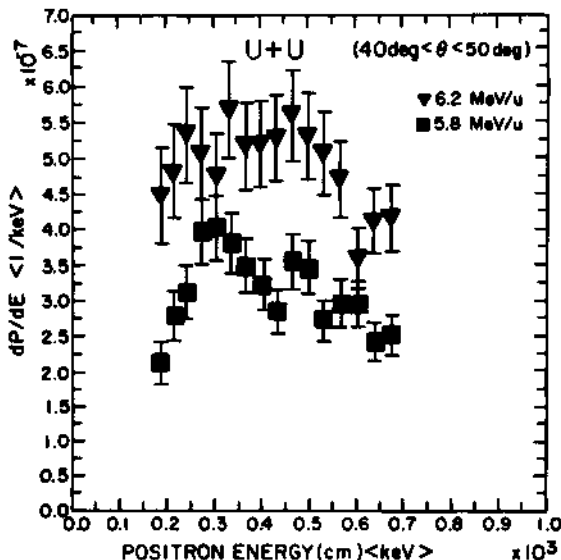


Figure 28. The positron production probability as a function of positron kinetic energy for U+U collision in coincidence with ions scattered into designated angular regions (see lecture by P. Kienle).

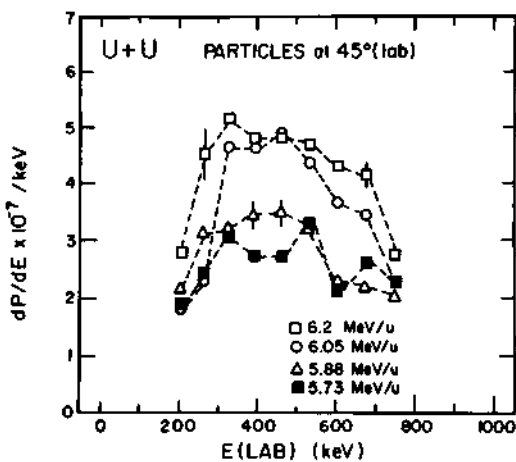


Figure 29. Positron production probability for U+U collisions at 5.73, 5.88, 6.05, and 6.2 MeV/amu. Ions are scattered near 45° (see lecture by P. Kienle).

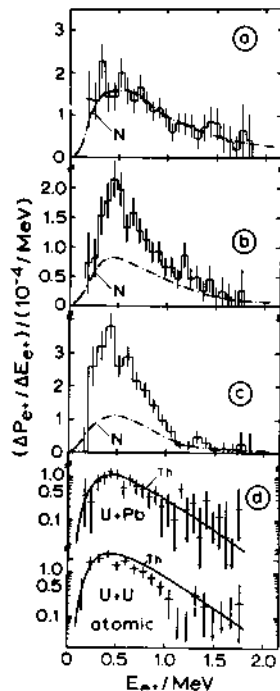


Figure 30. Positron spectra for (a) the nuclear U+Pd, (b) the undercritical U+Pb, (c) the overcritical U+U systems at a U beam energy of 5.9 MeV/amu and  $\Theta_{\text{lab}} = 45 \pm 10^\circ$ . The curves "N" are derived from  $\gamma$ -ray spectra assuming E1 multipolarity. In (d) the semi-logarithmic presentations of the spectra after "N" has been subtracted are compared with calculations by Reinhardt, Soff, Müller, Greiner et al.

intensity, can be accounted for by converting the target  $\gamma$ -rays into a positron spectrum assuming E1 electron-positron internal pair conversion. The nuclear contributions to the positron emission spectra from the U+Pb and U+U systems have been evaluated similarly. We see that the theory for dynamically induced positron emission reproduces the measured spectrum from the subcritical U+Pb system, but is not successful in the U+U system where over-critical binding of the  $1s\sigma$  electrons can be achieved. In itself, this is not an overwhelming effect, but, when considered together with the other data from independent measurements, it forms part of a pattern of evidence.

However, it is again disconcerting to find that the inconsistency observed for some of the measurements reported by Kienle is repeated here. A subsequent experiment was not able to reproduce the deviations from theory found in the initial data on the U+U system. This begins to suggest that controlling the bombarding conditions carefully may be a crucial ingredient in studying these effects. As I noted already, the underlying reason for this sensitivity is presently not understood, unfortunately.

There was another interesting aspect reported by Backe, which should be noted. For U+U collisions significantly above the Coulomb

barrier, 7.5 and 8.4 MeV/amu, the positron spectrum above 700 keV exhibits the interesting feature that it decreases more rapidly than the reference spectrum taken at 5.9 MeV/amu. (For the former, coincidences are required with reaction products, while for the latter, coincidences are taken with Rutherford scattering into  $45 \pm 10^\circ$  in the laboratory.) Calculations based on pure Rutherford trajectories predict a behavior opposite to these observations. This effect, therefore, may indicate the presence of the time delay phenomenon during nuclear contact which was discussed by Reinhardt for deep inelastic collisions.

But even more detailed and convincing evidence for deviations from the theory based on Rutherford scattering alone has emerged from the detailed experiments reported by Bokemeyer, using the EPOS device. As I mentioned earlier, a well-defined kinematic identification of the collision by kinematic coincidences seems to be necessary to isolate the effects, such as structure in the positron spectrum. The coincident detection of two particles in the final state provide a selection of reaction channels, an unambiguous definition of  $R_{\min}$  for asymmetric systems such as U+Pb, and even in symmetric systems it provides a measure of the intrinsic energy loss in a collision.

Both the gross features and the finer details of the data reported by Bokemeyer exhibit interesting effects. We have seen that within the sensitivity of the earlier experiments nothing unexpected occurs in the  $R_{\min}$  dependence of the total positron excitation probability as  $R_{\text{crit}}$  is passed. However, in this regard, a new and interesting aspect emerges with these new experiments by comparing the  $R_{\min}$  dependence for the low energy and high energy parts of the spectrum from U+Cm collisions at 5.8 MeV/amu. As shown in Fig. 31, it was observed that the slope of

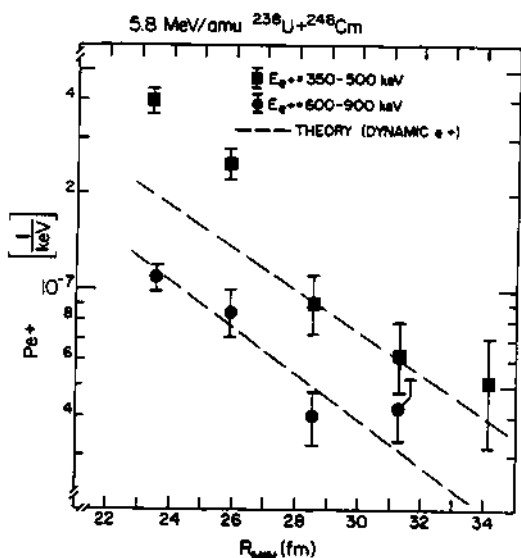


Figure 31.  
The dependence of the positron production probability for selected kinetic energy regions of the positron spectrum on the distance of minimum separation in  $^{238}\text{U} + ^{248}\text{Cm}$  collisions. Nuclear background due to internal pair production has been subtracted. The dashed lines show the slopes theory predicts (Reinhardt et al.) for the two kinetic energy regions of the positron spectra (see lecture by H. Bokemeyer).

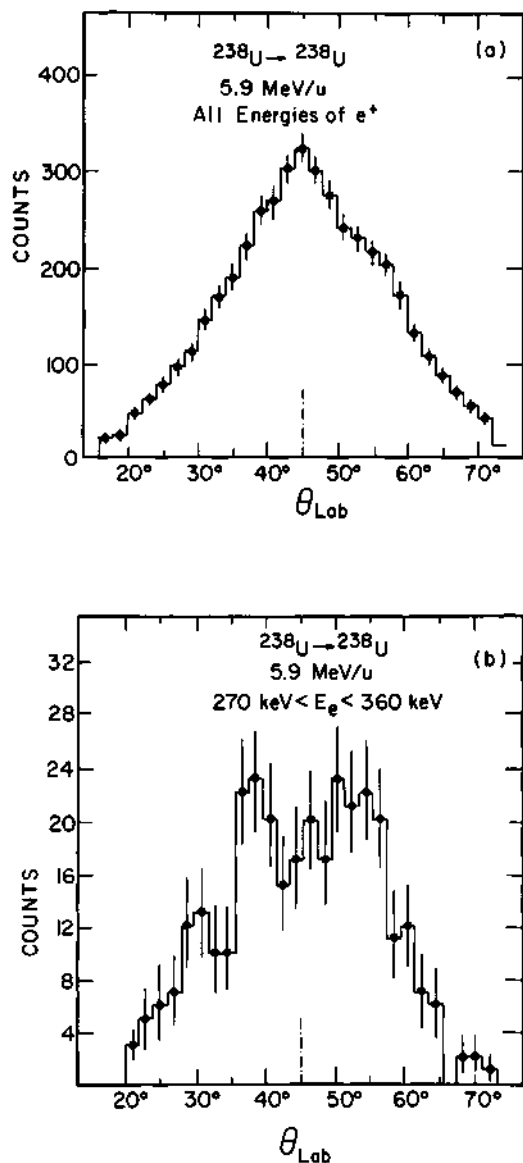


Figure 32:  
Measured angular distribution of positrons from 5.9 MeV/amu U+U collisions:  
a) The total positron spectrum is detected. (b) Positron energies are selected between 270 and 360 keV. The angular distribution shown in (b) also involves a selection of events within a window of approximately 15 MeV energy loss from elastic scattering, while in (a) all events have been chosen which approximate elastic scattering within  $\pm 30$  MeV. Elastic scattering is determined by two body kinematic coincidences. (Data from spectrometer EPOS.)

$dP_e^+/dE_e^+$  vs.  $R_{\min}$  is greatest for the low energy component of the positron spectrum. The significance of this observation is that it contrasts with expectations for dynamically induced positrons. In fact, theory predicts that it should be the higher energy positron band which should reveal the larger slope in the ratio  $\sim C^{-\text{const}} (\Delta E)$ , where  $\Delta E$  is the energy transferred to the positrons. As related by our speakers, these data provided an incentive to search further into details.

In fact, with more detail, such as a more selective choice of positron energies, the effect becomes more prominent. Bokemeyer showed with Fig. 32 that singling out positron energies between 270 to 360 keV in the  $U^+ U$  spectrum taken at 5.9 MeV/amu, and selecting two body final state events favoring an energy loss within a few tens of MeV of elastic scattering, leads to an angular distribution for the scattered ions which differs considerably from the distribution obtained when the entire positron energy spectrum is accepted. The implication, of course, is one of structure in the positron spectrum. Indeed, structure becomes evident even in the total positron spectrum (unrestricted by a selection of scattering angles) when events are selected to cluster about elastic scattering, defined by the two body kinematic coincidences to beat down the background. Fig. 33 shows examples of such total spectra from  $U^+ U$  collisions at 5.8, 5.9, and 6.0 MeV/amu, and from  $U^+ Cm$  collisions at 5.8 MeV/amu. There are obvious statistically significant deviations from an overall bell-shape positron energy distribution with the maximum near  $\sim 500$  keV expected from the dynamically induced positron emission processes.

Bokemeyer also demonstrated that imposing restricted kinematic conditions develops this structure even further, and rather impressively, as expected from the angular distribution shown in Fig. 32(b). With Fig. 34, it was illustrated that the peaked structures present for one set of scattering angles and energy loss do not seem to be evident when the scattering angles are changed, but otherwise all other conditions are unaltered. Moreover, theoretical spectra for dynamically induced positrons can account for the data from one set of angles, but clearly only provide the smooth background to which the peak structures add for the data from the other set of scattering angles.

Thus, these last experiments, like the others we have discussed, suggest very convincingly that there are excess positrons above the dynamically induced background, but they go even further in pointing out that the additional positrons are associated with selected kinematic conditions possibly reflecting a focussed nuclear reaction.

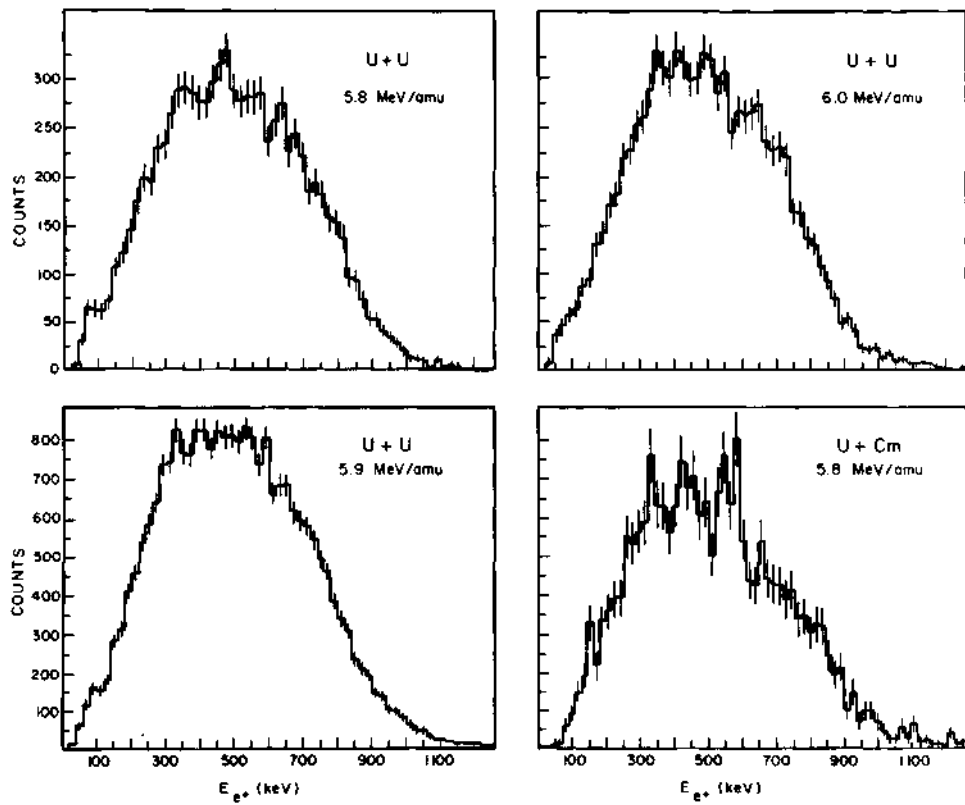


Figure 33. Total positron spectra after near elastic scattering events are selected. The spectra are not corrected for spectrometer transport efficiency which primarily affects the smallest and largest energies (see lecture by H. Bokemeyer).

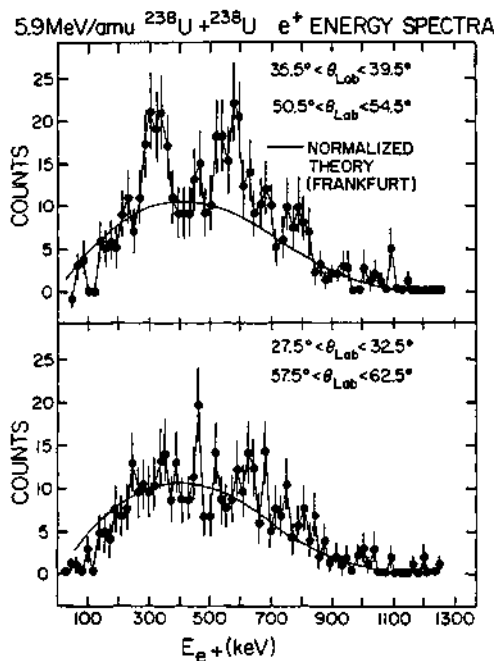


Figure 34. Positron spectra from 5.9 MeV/amu U+U collisions obtained by the spectrometer EPOS after a selection is made both in the scattering angles and energy loss. Structure in the spectra seems to be associated with selected kinematic conditions. The solid lines represent spectra for dynamically induced processes calculated by Reinhardt and coworkers at the University of Frankfurt, adjusted in relative magnitude at the two angular regions in conformity with the theoretically determined impact parameter dependence.

## OUTLOOK

The search for spontaneous positron emission (the sparking of the vacuum) has taken us into a new domain of atomic physics, a domain where the binding energy of electrons in atoms can exceed the rest-mass energy and where relativistic effects dominate the landscape. The vehicle that is capable of reaching this region is the superheavy quasimolecule formed in very heavy-ion collisions. In our quest, we have found that signatures for the formation of these superheavy quasi-atomic systems are clearly observed. The dynamic effects provide us with the sources of information on the quasimolecule; because of the very relativistic behavior of the wave functions all effects are focussed at the turning points of the heavy ion trajectory so that they especially probe the properties of the quasiatom ( $Z_1 + Z_2$ ) in the united atom limit. In particular, the dynamically induced positron production processes considered theoretically have been confirmed, with theory in good agreement with experiment. An overall, good understanding has been achieved of the background positron production mechanisms which are associated with the time-varying fields of the nuclear motion.

The detection of peaked structures in the positron spectra emitted from collisions where overcritical binding can be achieved not only opens up the exciting possibility that we may be observing spontaneous positron emission but, if indeed this is spontaneous positron emission, it simultaneously implies that we must be forming metastable super-heavy nuclear composites at bombarding energies close to the Coulomb barrier which prolong the nuclear contact time sufficiently to observe the relatively narrow peaked structures. Widths of 100 keV or narrower correspond to lifetimes for the dinuclear system larger than  $\sim 40$  times the collision time for Rutherford trajectories where the  $1s\sigma$  state can be overcritically bound. Thus, the picture of the collision, as worked out by J. Reinhardt, U. Müller, B. Müller, W. Greiner and G. Soff, is that of two uranium atoms colliding with low angular momentum partial waves (small impact parameter) and forming a metastable nuclear system of  $Z = 184$  for a time corresponding to  $\geq 4 \times 10^{-20}$  secs. If a  $1s\sigma$  vacancy is available during this time, its spontaneous decay leads to a peaked positron energy distribution which is centered at an energy corresponding to the overcritical binding fraction of the resonance state with a width which reflects the lifetime of the metastable nuclear system, as well as any variation in the binding of the resonance due to a fluctuating nuclear shape during the sticking time.

However, as Reinhardt mentioned, this is not the only possible source of peak-like structures in the positron spectrum, even if we confine ourselves to atomic effects only. Peak-like structures can also be produced, without requiring overcritical binding, by interference between incoming and outgoing dynamically induced positron emission amplitudes separated by a time delay. But in this case also, the formation of a long-lived nuclear composite is necessary. Indeed, it is difficult to invent a mechanism, associated with atomic positron emission, which would produce structures in the positron spectrum but not involve the formation of an intermediate superheavy nucleus that lives a long time compared to sub-Coulomb scattering collisions times.

We also have to keep in mind that these structures can be connected with pure nuclear effects. There are two prominent candidates; one is the internal pair conversion of a nuclear transition which leads to a positron energy distribution which may be peaked in character, and the other is the internal pair conversion process followed by the capture of the electron into empty atomic orbits, which leads to positron line spectra. The possibility that the former is responsible for the peak structures is diminished by the relatively narrow peak shapes observed, while intensity considerations seem to exclude the latter by many orders of magnitude. Obviously direct measurements of both these effects have to be pursued further.

Thus, we presently have the situation where evidence for structure in the positron spectrum for overcritical systems persists and is found in several independent measurements. The appearance of structure can imply the presence of a mechanism for positron production, in superheavy collision systems, which does not originate with dynamic effects and Coulomb trajectories. If eventually completely proven to be non-nuclear in origin, except for the introduction of a time delay in the collision, the observation of this structure leads to the speculation that we are seeing metastable superheavy nuclear systems formed as the nuclei barely touch in just overcoming the Coulomb repulsion. This partly unforeseen new phenomenon opens the way to the two engaging possibilities. If the positron peaks are found to reflect spontaneous positron emission, then for the first time we will have observed the spontaneous change in the ground state in a fundamental field theory. On the other hand, finding that the structure in the positron spectrum results from a time delay effect on induced positron emission would reveal the equally significant consequence that the energy levels do not penetrate the negative energy continuum in a situation where the Dirac theory pre-

dicts that they should. In either case, the peaked positron structure would be a characteristic feature of an atomic clock indicating the existence of the superheavy nucleus and measuring its lifetime.

The directions for future experiments are self-evident:

(i) It has to be determined whether the positrons of interest originate with separated atoms, implying nuclear sources of positrons, or with quasimolecules. For this purpose the Doppler broadening and shift that otherwise plagues the resolution of the spectrometers can be utilized to advantage. In this connection, it would be very useful to track down nuclear EO transitions via internal electron conversion decays.

(ii) Questions associated with the nuclear physics aspects of the problem have to be addressed in more detail. Are we forming metastable superheavy nuclear species? Here the techniques of nuclear physics have to be mobilized with careful excitation functions and many-body break-up studies. It would be preferable to carry out these studies independent of the positron probe, if the level of sensitivity allows. Most likely, this will not be the case, and the heavy-ion detection in the positron spectrometers will have to be developed into more elaborate configurations. It is also of particular importance to compare our measurements near the Coulomb barrier with measurements using projectile energies that ensure the absence of nuclear reactions. Unfortunately, the latter consume excessive accelerator time, which explains the absence of such data to date.

(iii) The electrodynamic aspects have to be explored with studies of the  $Z$  dependence. Here the possibilities for supercritical systems is limited, but the obvious tracking of positron peak energies with  $(Z_1+Z_2)$  and nuclear shapes is a major aspect to be studied.

#### POSTSCRIPT

Your many excellent, interesting lectures have been a testimony to the impressive progress that has been made towards understanding the questions I posed at the beginning of this summary. Much has been accomplished in just one decade in this emerging field associated with the physics of strong fields. You have made it clear that we may be at an exciting threshold of new observations, and that, indeed, the answers to Greiner's questions I referred to earlier may very well be in the affirma-

tive. I am sure that it won't be too long before we will be meeting again to consider the resolution of these issues. I hope that such a meeting will take place under the same most pleasant circumstances provided by our hosts these past two weeks. To our host I would like to take this opportunity to add my appreciation for organizing such an enjoyable conference.

In concluding, I would like to add one more observation. One of the pleasant aspects of the decade of work which I just attempted to summarize has been the close coordination between experiment and theory which has marked the progress in the search for spontaneous positron emission. As a participant in the experiments, this coordination has been very gratifying for me personally. In this and in many other aspects of the field's development, our host, Walter Greiner, occupies a singular role. I am sure that I speak for all the experimentalists here in extending special recognition of the guidance his work, and that of his colleagues, has provided in stimulating the experimental progress in this field of physics.

## CONTRIBUTORS

Professor P. Armbruster  
Gesellschaft für Schwerionen-  
forschung mbH  
P.O. Box 110 541  
D-6100 Darmstadt - FRG

Dr. H. Backe  
Institut für Physik  
Universität Mainz  
Jakob-Welder-Weg 14  
D-6500 Mainz - FRG

Professor M. Baker  
Department of Physics FM-15  
University of Washington  
Seattle, Washington 98195 - USA

Professor A.O. Barut  
Department of Physics  
The University of Colorado  
Boulder, Colorado 80309 - USA

Professor L.C. Biedenharn  
Physics Department  
Duke University  
Durham, N.C. 27706 - USA

Professor A. Böhm  
III. Phys. Institut  
RWTH Aachen  
D-5100 Aachen - FRG

Dr. K. Bokemeyer  
Gesellschaft für Schwerionen-  
forschung mbH  
P.O. Box 110 541  
D-6100 Darmstadt 11 - FRG

Dr. F. Bosch  
Gesellschaft für Schwerionen-  
forschung mbH  
P.O. Box 110 541  
D-6100 Darmstadt 11 - FRG

Professor J.S. Briggs  
Fakultät für Physik  
Universität Freiburg  
Hermann-Herder-Str. 3  
D-7800 Freiburg i.Br. - FRG

Professor P. Candelas  
Center for Theoretical Physics  
The University of Texas  
Austin, Texas 78712 - USA

Dr. N.D. Hari Dass  
The Niels Bohr Institute  
University of Copenhagen  
DK-2100 Copenhagen Ø - Denmark

Professor R. Dreizler  
Institut für Theoretische Physik  
Universität Frankfurt  
P.O. Box 11 19 32  
D-6000 Frankfurt/Main - FRG

Professor G.W. Erickson  
Physics Department  
University of California at Davis  
Davis, California 95616 - USA

Professor A. Faessler  
Institut für Theoretische Physik  
Universität Tübingen  
D-7400 Tübingen - FRG

Professor J. Greenberg  
 Physics Department  
 Yale University  
 217 Prospect Street  
 New Haven, Connecticut 06511 -USA

Professor W. Greiner  
 Institut für Theoretische Physik  
 Universität Frankfurt  
 P.O. Box 11 19 32  
 D-6000 Frankfurt/Main - FRG

Dr. E.K.U. Gross  
 Institut für Theoretische Physik  
 Universität Frankfurt  
 P.O. Box 11 19 32  
 D-6000 Frankfurt/Main - FRG

Dr. M. Gyulassy  
 Nuclear Science Division  
 Lawrence Berkeley Laboratory  
 University of California  
 Berkeley, California 94720 -USA

Professor T.W. Hänsch  
 Department of Physics  
 Stanford University  
 Stanford, California 94305 - USA

Dr. K.-H. Heinig  
 Akademie der Wissenschaften  
 der DDR  
 Zentralinstitut für Kernforschung  
 Rossendorf b. Dresden  
 P.O. Box 19  
 DDR-8051 Dresden - GDR

Professor F. Hund  
 Institut für Theoretische Physik  
 der Universität  
 D-3400 Göttingen - FRG

Professor J. Maxwell Irvine  
 Department of Theoretical Physics  
 The University  
 Manchester M13 9PL - UK

Professor W.R. Johnson  
 Department of Physics  
 University of Notre Dame  
 Notre Dame, Indiana 46556 - USA

Professor K.-H. Kaun  
 Akademie der Wissenschaften  
 der DDR  
 Zentralinstitut f. Kernforschung  
 Rossendorf b. Dresden  
 P.O. Box 19  
 DDR-8051 Dresden - GDR

Professor P. Kienle  
 Physik Department E12  
 Technische Universität München  
 James-Franck-Strasse  
 D-8046 Garching - FRG

Professor M. Kleber  
 Physik Department  
 Technische Universität München  
 James-Franck-Strasse  
 D-8046 Garching - FRG

Dr. C. Kozhuharov  
 Gesellschaft für Schwerionen-  
 forschung mbH  
 P.O. Box 110 541  
 D-6100 Darmstadt 11 - FRG

Dr. J. Krause  
 Physik Department  
 Technische Universität München  
 James-Franck-Strasse  
 D-8046 Garching - FRG

Professor W.E. Meyerhof  
 Department of Physics  
 Stanford University  
 Stanford, California 94305 - USA

Professor H. Mitter  
 Institut für Theoretische Physik  
 der Universität Graz  
 A-8010 Graz - Austria

**Dr. P.J. Mohr**  
Gibbs Laboratory, Physics Dept.  
Yale University  
New Haven, Connecticut 06520 -USA

**Professor Berndt Müller**  
Institut für Theoretische Physik  
Universität Frankfurt  
P.O. Box 11 19 32  
D-6000 Frankfurt/Main - FRG

**Professor E. Picasso**  
C E R N (Theory Group)  
CH-1211 Genève - Suisse

**Professor J. Rafelski**  
Institut für Theoretische Physik  
Universität Frankfurt  
P.O. Box 11 19 32  
D-6000 Frankfurt/Main - FRG

**Dr. J. Reinhardt**  
Institut für Theoretische Physik  
Universität Frankfurt  
P.O. Box 11 19 32  
D-6000 Frankfurt/Main - FRG

**Dr. G. Soff**  
Gesellschaft für Schwerionen-  
forschung mbH  
P.O. Box 110 541  
D-6100 Darmstadt - FRG

**Professor P. Vincent**  
Department of Physics and  
Astronomy  
Rutgers University  
New Brunswick, New Jersey 08903  
U.S.A.

**Professor C.S. Warke**  
Tata Institute of Fundamental  
Research  
Homi Bhabha Road  
Bombay 400 005 - India

**Professor H.J. Weber**  
Department of Physics  
University of Virginia  
Charlottesville, VA 22901 - USA

## INDEX

- Adiabatic model, 80, 383  
Aether, 817f  
Asymptotic freedom, 560, 583, 607, 627, 639, 741, 746  
Atomic clock, 233, 891  
Atomic structure calculations, 463, 483  
Axial vector  
  coupling, 742, 751  
  current, 742  
  form factor, 749f
- Bag  
  constant, 577  
  model, 741f, 746, 748  
  radius, 639, 742
- Black hole, 791, 808, 813  
  particle production, 789  
  radiance, 789, 837  
  space time, 804
- Born approximation, 104  
Born-Oppenheimer wave functions, 383, 524  
Bose condensate, 551, 553, 567, 576  
  equation, 559  
  potential, 559  
  wave function, 559
- Boulware vacuum, 812, 814
- Breit  
  interaction, 468, 739  
  potential, 767
- Bremsstrahlung, 338, 373, 416, 841, 845
- Brückner  
  reactions matrix, 701, 712, 722
- Brückner (continued)  
  theory, 701, 718
- Chiral algebra, 746  
Chiral symmetry, 742  
Coincidence method, 164, 365, 371  
Collision, 42, 128, 137, 163, 179, 233, 305, 308, 323, 327, 366f
- Color  
  charge, 561ff, 583f, 594f, 604, 606  
  screening, 540, 563  
  current, 593f  
  dielectric constant, 584, 610ff, 621f, 626, 631ff  
  flux, 747  
  flux strings, 746  
  magnetic field, 540  
  magnetic permeability, 614  
  magnetic qq interaction, 740  
  singlet, 560  
  symmetry group SU(3), 586ff, 591ff, 737
- Correlation, 143, 336, 368, 386
- Coulomb  
  barrier, 158, 294, 320, 360, 870, 899  
  excitation, 207, 374  
  field, 503  
  radiative corrections, 503  
  repulsion, 539  
  fission, 207
- Coupled channel calculation, 185, 203, 305

- δ-electron, 89, 203, 233, 238, 256, 274, 317, 360, 368, 384, 864, 870
- detection, 865
- emission, 320, 857, 863
- spectrum, 93, 864
- Δ-isobar, 717ff, 726, 728
- nucleon vertex, 717
- Density functional method, 383
- Dirac-equation, 13, 45, 80, 180, 197, 235, 360
- Dirac-Fock theory, 399, 463
- Doppler
  - broadening corrections, 330
  - free Laser spectroscopy, 670
  - free two photon spectroscopy, 676
  - shift, 115, 375, 797
  - technique, 170, 857
- Dynamical model, 335
- Effective coupling constant, 540, 583
- Electric monopole transition, 195
- Electron, 79, 475
  - electromagnetic structure, 29, 425, 441
  - in strong electromagnetic fields, 41, 195, 273
  - radiative capture, 338, 373
  - screening, 195, 248
  - wave function, 179, 317, 368
- Fission, 128, 151, 214
- Form factor, 30, 417, 426
- Fulling
  - Fock space, 800
  - vacuum, 800, 803f
- Furry
  - bound-interaction picture, 503
  - picture, 504f, 513f
  - Feynman diagram, 506
  - theorem, 689, 691
- Gauge field
  - condensate, 540, 563, 566f
  - ground state, 564, 566
- Gauge field (continued)
  - group SU(3), 560
- Gauge transformation
  - for non-abelian theory, 652ff
- Glueball formation, 746
- Goldberger-Treiman relation, 742, 751f
- Goldstone boson, 638, 742, 746, 751
- g-2 experiments, 413, 441, 459
- Hartree-Fock approximation, 46, 386, 471
- Heavy-ion
  - deep inelastic reaction, 94
- Higgs field, 572
- High-Z
  - muonic atoms, 841
  - nucleus, 513f
  - two electron atoms, 512
- Hyperfine splitting, 25, 28
- Impact parameter, 152, 275, 297, 336, 355, 366, 384
- Inner shell
  - excitations, 159, 533, 535
  - ionization, 143, 857f
  - process, 528, 536
  - transition, 865
- Ion
  - atom collision, 522
- Ionization, 47, 77, 144f, 179, 185, 373, 475, 480
- Klein-Nishina formula, 788
- Klein's paradoxon, 8, 42, 199, 546f
- K-shell, 533
  - Bohr radius, 492
  - electron, 492, 495f, 528, 534
  - radius, 530
  - target monopole excitation, 492, 494
  - vacancies, 170, 203, 238, 530, 532, 534
- Kruskal
  - coordinates, 806, 808, 812
  - manifold, 808

- Lambshift, 5, 25, 34, 503, 516, 521, 671, 678, 680  
in hydrogen-like atoms, 510ff, 838  
in heavy atoms, 838
- Landau-ghost, 601, 606ff, 626
- Laser  
spectroscopy, 669  
of an atomic beam, 674  
of hydrogen-like atoms, 670
- Level  
effects of a diving ~, 126  
crossing, 143
- Line  
shape method, 159
- Magnetic dipole fields, 755, 758ff
- Magnetic interaction at short distances, 755, 779
- Magnetic moment, 26, 443, 445
- Magnetic monopole, 656
- Magnetic resonances, 755ff, 762ff, 767, 769ff, 776f
- Many-body problem, 383
- Minkowski vacuum, 794, 797, 800, 802
- Molecular orbital, 525, 527f, 530, 533  
energies, 529  
functions, 524  
potential, 527  
radiation, 869f  
spectrum, 869f  
transitions, 865ff  
x-ray emission, 865
- Multistep process, 185, 191, 205, 263, 325
- Muonic atoms, 692
- Negative energy continuum, 544, 549
- Neutron  
matter, 643  
stars, 642, 644, 646, 648
- Non-linear vacuum polarization, 694, 696, 698  
screening, 686  
in strong fields, 685, 686
- Nuclear charge distribution, 196
- Nuclear excitation, 221
- Nuclear structure effect, 123
- One-boson-exchange (OBE), 745f, 748ff
- Overcritical binding, 889, 890
- Overcritical charged vacuum, 698
- Overcritical fields, 539, 855
- Overcritical systems, 890
- Overcritical vacuum, 686  
density, 698
- OZI-rule, 743
- Pair  
conversion (internal), 890  
creation, 9, 43, 274f, 293, 414
- Particle  
hole, 701  
bubble, 701  
excitations, 701ff, 710ff  
force, 701, 708ff, 712ff, 717, 720ff, 729  
interactions, 703, 712, 722, 725, 733  
pair, 701  
states, 707, 723
- production  
by black holes, 789  
by gravitational fields, 789ff  
in cosmological context, 789ff
- PCAC, 751
- Perturbation theory, 89, 100
- Phantom spectroscopy, 133, 186
- Pion  
condensation, 17, 554ff, 580, 635, 641ff, 646ff, 701ff, 707ff, 713, 720, 725ff, 729ff, 837, 849  
in heavy ion collisions, 647f  
and mean field approach, 702
- exchange potential, 707, 712
- self-energy, 701, 708f, 725

- Poincaré  
 group, 791, 802  
 invariant vacuum, 797, 800, 804
- Point charge problem, 69
- Positron  
 creation, 854, 876f, 881  
 detection experiments, 875  
 emission, 43, 79, 87, 368, 856,  
 869ff, 872, 877, 889ff  
 nuclear background, 120, 295  
 production (direct), 842  
 production (dynamically  
 induced), 842, 855, 881, 886,  
 889f  
 production (spontaneous), 87,  
 221, 274, 503f, 841, 855,  
 857  
 production amplitudes, 870  
 search experiments, 854, 857  
 spectra, 107, 122, 126, 202,  
 275, 294, 306, 311, 313,  
 879ff
- Projection operator technique,  
 197
- QCD (quantum chromodynamics),  
 560, 567, 577f, 583f,  
 590ff, 639, 737f, 745f,  
 753  
 long distance behavior, 584,  
 596, 607  
 non-perturbative approach,  
 583ff, 608  
 vacuum, 584, 596, 746f
- Quark, 540, 578, 583ff, 590ff,  
 837, 850  
 confinement, 560f, 567ff, 572,  
 578, 583, 588, 629, 639,  
 741, 745f, 850  
 confining potential, 608, 746  
 current, 594  
 -quark interaction, 737, 738  
 -quark interchange, 748ff
- Quasiatom, 856f, 864, 889
- Quasimolecule, 273, 321, 855,  
 859, 861, 865  
 superheavy, 12
- Radial coupling, 80
- Radiative corrections, 416  
 in a Coulomb field, 503  
 in strong fields, 503, 510ff,  
 519
- Radioactivity, 374
- Random phase approximation, 463,  
 483
- Regge-Wheeler coordinates, 810
- Resonance, 78f, 196
- Rindler  
 coordinates, 798ff, 808  
 system, 804
- Rutherford trajectory, 128f, 179,  
 204, 296, 320
- Rydberg constant, 671, 674f, 681
- Scaling law, 179, 183, 188, 266,  
 271, 375
- Scattering, 5, 78, 107, 338, 414
- Schwarzschild  
 coordinates, 806, 808, 812  
 manifold, 806  
 metric, 805f  
 radius, 814  
 space time, 808
- Schwinger-Dyson equation, 584,  
 596, 599, 604, 608f,  
 615ff, 622f, 626, 629,  
 631, 633
- Self-coupling of gluon fields,  
 561
- Self-energy, 509f, 571  
 correction, 504, 515, 685  
 correction in a Coulomb field,  
 503  
 Feynman diagram, 508
- Self-interaction of the vacuum  
 charge, 541
- Shell model, 13
- $\sigma$ -State  
 1 s, 163, 169, 199, 210, 234,  
 238, 261f, 362, 367  
 2 p, 190, 335, 361
- Slater determinant, 727ff
- Spectrometer, 112, 129, 209,  
 217, 275, 294, 317
- Spin, 258, 449, 475
- Spontaneous  $e^+e^-$  production, 685
- Spontaneous pair production, 536,

Spontaneous pair production (continued)  
 547, 570f, 576, 685, 698  
 Spontaneous particle production, 552, 636  
 Spontaneous symmetry breaking, 572  
 Sticking, 14, 89, 233  
 Strong periodic fields, 659ff  
 Supercritical binding, 854  
 Supercritical electron fields, 552  
 Supercritical fields, 540f, 567, 635  
 Supercritical nuclear matter, 554  
 Supercritical phenomena, 584  
 Supercritical potentials, 547  
 Supercritical systems, 891  
 Supercritical vacuum, 743  
 Superheavy atomic systems, 152, 157, 228, 378, 854, 891  
 Superheavy quasiatom, 850, 855, 858  
 Superheavy quasimolecules, 856f, 869, 889

Thomas-Fermi  
 approximation, 541, 554  
 method, 846f  
 model, 218, 248, 389, 392, 541, 544  
 Thomas precession, 449  
 Time delay effect, 78, 89, 102, 202, 210, 256

Unruh  
 box, 813f  
 vacuum, 812, 814

Vacuum  
 charge, 63, 196, 539, 541, 697  
 density, 542, 687f, 691, 698  
 decay, 841, 843f, 846, 850, 855  
 energy, 820  
 fluctuations, 31  
 polarization, 5, 43, 49, 416

Vacuum (continued)  
 polarization (continued)  
 445, 509f, 515, 572, 583, 601, 608, 621, 637, 685f, 690ff, 783, 841, 846  
 charge, 539, 545, 687  
 of color changes, 584, 595, 598  
 energy, 825  
 tensor, 617, 619, 621  
 pressure, 741  
 state, 6, 8, 539, 541, 563, 572, 578, 580, 791f, 798, 800, 846  
 structure, 22, 50, 540, 578  
 of QCD, 539f, 580, 584, 741, 747, 786  
 Variational method for time-dependent Dirac-equation, 489ff  
 Ward-Slavnow-Taylor identity, 584, 611, 615, 619f, 626  
 Weak interaction, 428, 431  
 Wichmann-Kroll  
 approach, 503ff, 692, 696  
 formalism, 687, 698, 841

X-Rays, 78, 151  
 characteristic, 133, 274, 324, 360  
 compound nucleus, 77, 82  
 continuum, 359  
 molecular-orbital, 80, 274, 362, 375  
 non-characteristic, 354  
 quasimolecular, 14, 335, 359  
 separated atom, 80  
 target, 78, 89

Yang-Mills  
 field, 563  
 Lagrangian, 592  
 theory, 584, 592, 594, 599, 604, 608, 633  
 and classical SU(2) solutions, 651  
 and nonabelian solutions for spherical symmetry, 654

**Zero-point energy**  
of the electromagnetic field,  
821, 828